المجلة العراقية الوطنية لعلوم الارض

INJES

P- ISSN 1682 – 3222
E- ISSN 2664 – 2816



https://earth.uomosul.edu.iq Scopus E-mail injes@uomosul.edu.iq

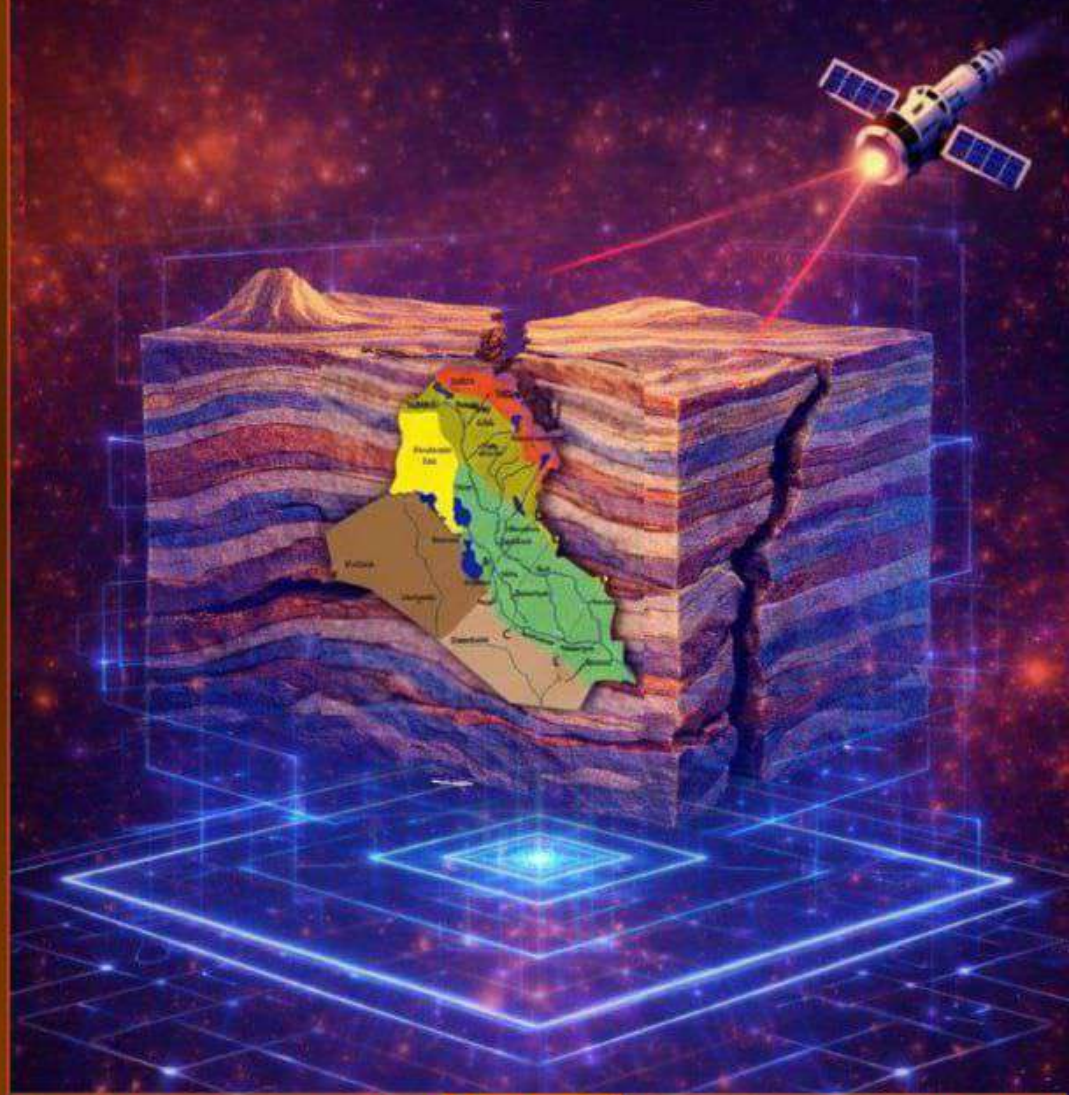
[1] العدد كانون الثاني 2026 [26] المجلد

Iraqi National Journal of Earth Science No. [1] Jan. 2026 Vol. [26]

Iraqi National Journal of Earth Science

INJES

P- ISSN 1682 – 3222
E- ISSN 2664 – 2816



https://earth.uomosul.edu.iq Scopus E-mail injes@uomosul.edu.iq

Vol. [26] Jan. 2026 No. 1

المجلة العراقية الوطنية لعلوم الأرض

المجلد السادس وعشرون كانون الثاني 2026 العدد الأول

رئيس التحرير

الأستاذ الدكتور ريان غازي ذنون

مدير التحرير

الاستاذ المساعد الدكتور عزالدين صالح الجوادي

أعضاء هيئة التحرير

الأستاذ الدكتور ماجد مجدي عبد المجيد

الأستاذ الدكتور حاجي رحاب (الجزائر)

الأستاذ الدكتور عزالدين نجم الدين بابان

الأستاذ الدكتور ألين بريت (بلجيكا)

الأستاذ الدكتورة سوسن حميد فيصل الهزاع

الأستاذ الدكتور رافع إبراهيم عبدالله الحميدي

الأستاذ المساعد الدكتور محمد فوزي عمر

الأستاذ المساعد الدكتور عمر عبدالله إسماعيل

الاستاذ المشارك الدكتور هيثم إسماعيل حامد

الأستاذ المساعد الدكتور مهدي رهناما (ايران)

الأستاذ المساعد الدكتور بشار عزيز محمود

الأستاذ الدكتور معز بن فاضل (تونس)

الأستاذ الدكتور شريف فاروق محمد (مصر)

الأستاذ الدكتور باسم سيد نبوي (مصر)

الأستاذ الدكتور مصدوق محمد إبراهيم التاج (الأردن)

الأستاذ الدكتور ستار جبار رشيد الخفاجي

الأستاذ المساعد الدكتور عاهد يونس عبدالله الملاح

الأستاذ المساعد الدكتور نمام محمد صالح

الأستاذ المساعد الدكتور فلاح عبد محمد المعماري

الأستاذ المساعد الدكتور صدام عيسى مصطفى الخاتوني

الأستاذ المساعد الدكتور راشد بورميزراني (ايران)

إدارة المنظومة الالكترونية للمجلة

الأستاذ المساعد الدكتور صدام عيسى مصطفى الخاتوني

الشؤون الفنية والتنسيق والنشر

المدرس المساعد مُيسر سمير محمود السراج

الشؤون الإدارية: سجى سالم عبدالهادي

إصدار: كلية العلوم/ جامعة الموصل

p-ISSN: 1682-3222

e-ISSN: 2664-2816

البريد الالكتروني: injes@uomosul.edu.iq

الموقع الالكتروني: http://www.iasj.net

https://earth.uomosul.edu.iq

الموبايل: 009647701610916

رقم الإيداع في دار الكتب و الوثائق ببغداد (**1310** لسنة **2009**)

المحتويات

تقييم نوعية مياه نهر دجلة في مدينة الموصل: تأثير المخلفات السائلة المطروحة به

محمد احمد عبد الله الطائي، عبد القادر عبش سباك الحديدي، وحيدة علي احمد البدراني.....1

الخصائص المورفومترية لحوض وادي الكومل- شمال العراق

نوزاد يوسف عبدالرحمن سلي، فواز حميد حمو النيش 18

التحليل الهيدرومورفومتري لحوض وادي سماقولي، شمالي شرقي العراق

كاروان سردار حسين الداوودي، عبدالسلام مهدي صالح الجبوري 42

التمثيل الخرائطي للخصائص الفيزيائية والكيميائية لترب ناحية بعشيقة، محافظة نينوى

محمد عباس حسن، لمياء حسين علي 59

Iraqi National Journal of Earth Science

www.earth.uomosul.edu.iq

تقييم نوعية مياه نهر دجلة في مدينة الموصل: تأثير المخلفات السائلة المطروحة به

محمد احمد عبد الله الطائي [1]* ، عبد القادر عبش سباك الحديدي [2] ، وحيدة علي احمد البدراني [3]

[1] *كلية الزراعة، جامعة تلعفر، تلعفر، العراق.*

[2،3] *قسم علوم التربة والموارد المائية، كلية الزراعة والغابات، جامعة الموصل، الموصل، العراق.*

معلومات الارشفة

تاريخ الاستلام: 11- يوليو -2024

تاريخ المراجعة: 02- ديسمبر -2024

تاريخ القبول: 18- فبراير -2025

تاريخ النشر الالكتروني: 01- يناير -2026

الكلمات المفتاحية:

نهر دجلة،

التلوث،

مصبات الصرف،

المراسلة:

الاسم: محمد احمد عبد الله الطائي

Email: mohammed.a.abdullah@uotelafer.edu.iq

الملخص

يعد نهر دجلة مصدرا مهما للمياه للاستخدام المنزلي والأنشطة الاقتصادية في العراق ومدينة الموصل وقد زاد هذا الاستخدام بالوقت الحالي مع قلة معدلات تصريفه وزيادة كمية المخلفات السائلة المطروحة به عن طريق مياه الصرف الصحي غير المعالجة. اختيرت ثمانية مواقع لمياه نهر دجلة المحاذية لمصبات مياه الصرف الصحي ضمن مدينة الموصل بالإضافة الى موقع للمقارنة في منطقة شريخان خلال فصل الربيع لسنة 2022 .اشارت النتائج الى ان قيم متوسط درجة حرارة المياه والاملاح الذائبة الكلية TDS والدالة الحامضية والعكورة والعسرة تراوحت ما بين (18.0-19.1°) سيليزية و(352-422) ملغم.لتر$^{-1}$ و(7.65 -7.93) و(12-24) NTU و(355-485) ملغم.لتر$^{-1}$ على التوالي وفاقت قيم العكورة للمياه في مواقع الدراسة المواصفات القياسية لمنظمة الصحة العالمية (WHO) لغرض الشرب وكانت المياه عسرة في جميع المواقع. تراكيز الاوكسجين المذاب في نهر دجلة يتراوح ما بين (3.1-2.4) ملغم. لتر$^{-1}$ وتجاوزت التركيز العالمي المسموح لمياه الشرب وحياة معظم أنواع الأسماك. تراوحت تراكيز ايونات النترات والفوسفات والكلوريدات والكبريتات بين (3.1-5.9) و(0.9-4.0) و(38-61) و (3.1-5.9) ملغم. لتر$^{-1}$ على التوالي في حين تراوحت تراكيز العناصر الثقيلة (النحاس والزنك والرصاص والكوبلت والنيكل) (nil – 0.211) و (1.13 – 1.76) و (0.099 -0.615) و (0.013-0.042) و(0.102 -0.361) ملغم. لتر$^{-1}$ على التوالي. تراكيز الرصاص في مواقع مياه نهر دجلة فاقت المحددات العالمية للشرب الري وسقي الدواجن والماشية ولحياة الأسماك في حين ان تراكيز النيكل في جميع المواقع فاقت المحددات العالمية لمياه الشرب. اصناف مياه نهر دجلة كانت (رديئة – رديئة جدا) للشرب وسقي الدواجن بالاعتماد على تصنيف دليل جودة المياه water quality index (WQI) و(جيدة – رديئة) للري وسقي المواشي وللحياة المائية. مياه نهر دجلة في موقع المقارنة في شريخان كانت ذات جودة أفضل للاستخدامات المختلفة من المواقع الأخرى والسبب يعود الى تأثير المخلفات السائلة المطروحة بالنهر.

DOI: 10.33899/injes.v26i1.60178, ©Authors, 2026, College of Science, University of Mosul.
This is an open-access article under the CC BY 4.0 license (http://creativecommons.org/licenses/by/4.0/).

Water Quality Assessment of the Tigris River in Mosul city: Effects of Wastewater Discharge

Mohammed A. Altaee [1]*, Abd Al-kader A. Alhadede [2], Waheeda Ali Ahmad Al-badrani [3]

[1] *College of Agriculture, University of Telafer, Telafer, Iraq.*
[2,3] *Department of Soil Science and Water Resources College of Agriculture and Forestry, University of Mosul, Mosul, Iraq.*

Article information

Received: 11- Jul -2024

Revised: 02- Dec -2024

Accepted: 18- Feb -2025

Available online: 01- Jan – 2026

Keywords:
Tigris River,
Pollution,
Sewage Valleys,

Correspondence:
Name: Mohammed A. Altaee

Email: mohammed.a.abdullah@uotelafer.edu.iq

ABSTRACT

The Tigris River is an important source of water for domestic use and economic activities in Iraq and the city of Mosul. This use has increased at present with the low rates of its discharge and the increase in untreated wastewater discharged into it. Eight (8) sites were selected for the waters of the Tigris River after the sewage valleys in the city of Mosul, in addition to a comparison site in the Sharekhan area. Samples were collected during the spring season. The results indicated that the average water temperature, total dissolved salts (TDS), pH, turbidity, and total hardness ranged between (18.0–19.1 C◦), (352–442 mg/L), (7.65–7.93), (12–24 NTU), and (355–485 mg/ L), respectively. The turbidity values of the water in the study sites exceeded the standard specifications of the World Health Organization (WHO) for drinking purposes, and the water was hard in all sites. Concentrations of dissolved oxygen in the Tigris River ranged between 2.4 and 3.1 mg/L and exceeded the global concentration limit for drinking water and the lives of most fish species. The concentrations of nitrate, phosphate, chloride, and sulfate ions ranged between (3.1–5.9), (0.9–4.0), (38–61), and (3.1–5.9) mg/L, respectively, while the concentrations of heavy metals copper, zinc, lead, cobalt, and nickel ranged between (nil–0.211), (1.13–1.76), (0.099–0.615), (0.013–0.042), and (0.102–0.361), respectively. Lead concentrations in river water sites exceeded global limits for drinking, irrigation, and watering of poultry, livestock, and fish life, while nickel concentrations at all sites exceeded global limits for drinking water. The results of the Tigris River water class were (poor–very poor) for drinking and watering poultry, based on the Water Quality Index (WQI) classification, and (good–poor) for irrigation, livestock watering, and aquatic life. The Tigris River water at the comparison site in Sherekhan was of better quality for different uses than the other sites due to the effect of the liquid waste discharged into the river.

DOI: 10.33899/injes.v26i1.60178, ©Authors, 2026, College of Science, University of Mosul.
This is an open-access article under the CC BY 4.0 license (http://creativecommons.org/licenses/by/4.0/).

المقدمة

يعد نهر دجلة مصدرا مهما للمياه للاستخدام المنزلي والأنشطة الاقتصادية في العراق ومدينة الموصل خصوصا وقد زاد هذا الاستخدام بالوقت الحالي مع قلة معدلات تصريفه وزيادة كمية المخلفات السائلة المطروحة به عن طريق مياه الصرف الصحي غير المعالجة (Oleiwi and Al-Dabba, 2022). تعرف مياه الصرف بانها نفايات سائلة ناتجة من الأنشطة البشرية كمخلفات المنازل والمستشفيات والمصانع والمخلفات الحيوانية والزراعية، يتم تصريفها باستخدام قنوات او انابيب تمتد عبر المدن وتنتهي الى الأنهار والمياه السطحية غالباً دون أي معالجة حقيقية (Henze and Comeau, 2008). تحتوي مياه الصرف على كائنات حية دقيقة مرضية كالبكتيريا والفيروسات والديدان ومواد عضوية قابلة للتحلل تسبب الرائحة الكريهة فيها ومواد عضوية أخرى مثل المنظفات والمبيدات والدهون والزيوت والشحوم والتلوين والمذيبات والفينولات فضلا عن العناصر الغذائية مثل النيتروجين والفوسفور والأمونيوم التي تشجع نمو بعض النباتات المائية التي

تستنفذ الاوكسجين المذاب في الماء ، كذلك تحتوي مياه الصرف على العناصر الثقيلة السامة مثل الزئبق والرصاص والكادميوم والكروم والنيكل بالإضافة الى مواد واحماض غير عضوية أخرى مثل كبريتيد الهيدروجين والمواد ذات القاعدية (Manasa and Mehta, 2020 and Karri et al., 2021).

عملية طرح مياه الصرف غير المعالجة الى الأنهار تؤثر في نوعية المياه للشرب عن طريق زيادة تراكيز الملوثات او المواد السامة فيها كالعناصر الثقيلة التي تمتاز بالتراكم الحيوي داخل جسم الكائنات الحية والانسان والتي تؤثر سلباً على صحته وتسبب امراض سرطانية (Machate, 2023).

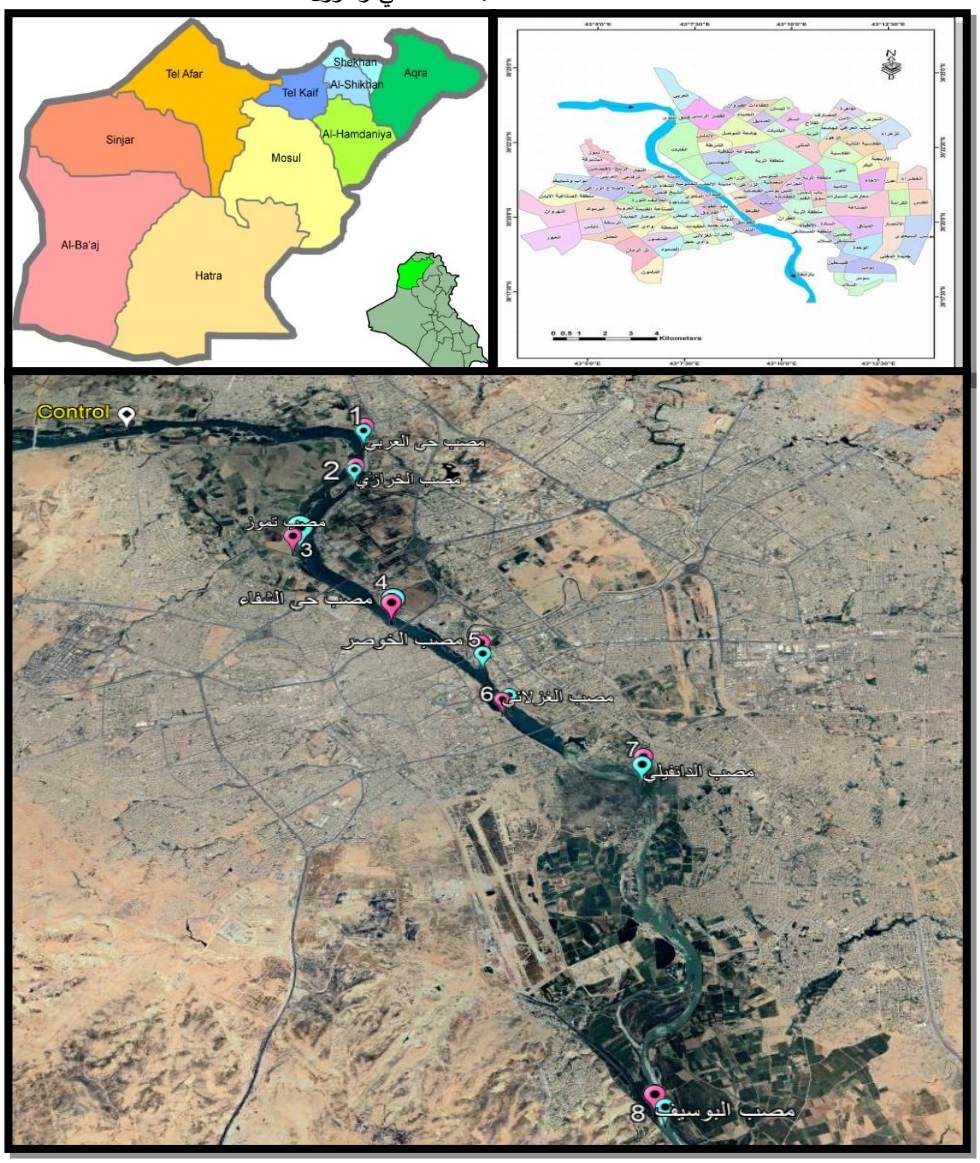
تؤثر المياه ذات النوعية الرديئة او الملوثة سلبا على الصفات الفيزيائية والكيميائية للتربة مما يؤدي الى تدهورها وقلة انتاجيتها وتسمم النباتات وإلحاق الضرر بالمستهلك سواء كان حيوانا ام انسانا عن طريق تناول المحاصيل الملوثة فضلا عن الاضرار الاقتصادية نتيجة تراكم الملوثات في التربة (Mukherjee et al., 2023). يشكل استخدام المياه رديئة النوعية في سقي حيوانات المزرعة مثل الدواجن والماشية خطرا على صحتها ويؤثر على وظائف العديد من الأعضاء كالقلب والكلى والكبد ويسبب اضراراً اقتصادية عن طريق تقليل إنتاج اللحوم والبيض والحليب ، فضلا عن ذلك فإنها تسبب مشاكل صحية للإنسان خلال تناوله للمنتجات الحيوانية الحاوية على المواد السامة او العناصر الثقيلة من خلال ما يعرف بالسلسلة الغذائية (Al-Assaf et al., 2020) و (Hossini et al., 2022).

أصبح من الضروري تقييم نوعية المياه العذبة بسبب القلق المحلي والعالمي كونها ستكون مورداً نادراً في المستقبل وعرضة دائمة للتلوث، لذا تهدف هذه الدراسة الى تقييم نوعية مياه نهر دجلة لأغراض (الشرب وري المزروعات وسقي الماشية والدواجن وللحياة المائية وحياة الأسماك) باستخدام دليل جودة المياه ودراسة تأثير مياه الصرف الصحي المطروحة فيه على بعض صفاته الفيزيائية والكيميائية من خلال مقارنتها مع المواصفات القياسية العالمية للاستعمالات المتعددة.

المواد وطرائق العمل

منطقة الدراسة

استُعين ببعض الخرائط الهيدرولوجية وأُجري مسح لحوض نهر دجلة في مدينة الموصل وتم جمع عينات مياه من (17) موقعاً (8) مواقع لمياه الصرف الصحي من المصبات المطروحة في مياه نهر دجلة و (8) مواقع أخرى لمياه نهر دجلة عند التقائها مع مياه تلك المصبات. الموقع الأول قرب فندق نينوى الدولي، والموقع الثاني مقابل الجزيرة السياحية، والموقع الثالث في منطقة الغابات مقابل حي النجار، في حين كان الموقع الرابع بين قلعة قره سراي والجسر الخامس، والموقع الخامس قرب الجسر القديم، وبالنسبة للموقع السادس فكان مقابل منطقة الدندان، والموقع السابع بالقرب من حي المزارع، وبالنسبة للموقع الثامن فكان في منطقة البوسيف، فضلا عن ذلك أُخذ موقع من نهر دجلة للمقارنة (Control) في منطقة شريخان وامتدت منطقة الدراسة على مسافة (20) كم تقريبا وحددت احداثيات المواقع بجهاز GPS وكما مبين في الشكل (1).



الشكل 1. خارطة وصورة جوية تظهر مواقع مياه المصبات ونهر دجلة

جمع العينات

جمعت عينات مياه نهر دجلة ومياه المصبات من المواقع الموضحة في الجدول (1) والشكل (1) خلال فصل الربيع للفترة بين اذار الى ايار لسنة 2022 باستخدام علب بلاستيكية غُسلت بماء الموقع ثم ملئت.

الجدول 1: مواقع واحداثيات عينات المياه

الموقع	المصب القريب	خط الطول	خط العرض
المقارنة(Control)	–	43.076853	36.396793
الأول	حي العربي	43.1117687	36.3915251
الثاني	الخرازي	43.1117687	36.3915251
الثالث	تموز	43.1108927	36.3726315
الرابع	حي الشفاء	43.123136	36.3571307
الخامس	الخوصر	43.1354935	36.3471517
السادس	الغزلاني	43.1438274	36.3390694
السابع	الدانفيلي	36.32169	36.32169
الثامن	البوسيف	43.1575091	36.2867438

القياسات الحقلية والمختبرية للمياه

رشحت عينات المياه باستخدام ورق ترشيح واضيفت لها قطرات من التلوين لتقدير الايونات السالبة والموجبة واضيف حامض النتريك للعينات التي قيست فيها العناصر الثقيلة وحفظت في الثلاجة بدرجة حرارة (4)° سيليزية، وقيست صفات المياه الحقلية والمختبرية لثلاثة اشهر وفقا للطرائق الواردة من قبل (APHA, 2017) وحسب المتوسط لها، وقيست درجة حرارة الماء والدالة الحامضية pH والتوصيلية الكهربائية EC والمواد الصلبة الذائبة الكلية TDS والاوكسجين المذاب Do لمواقع الدراسة حقليا اثناء جمع العينات باستعمال اجهزة الكترونية محمولة ، واجريت التحاليل المختبرية للمياه في مختبرات قسم علوم التربة والموارد المائية والمختبر المركزي لكلية الزراعة والغابات في جامعة الموصل ، اذ قيست ايونات الكالسيوم Ca^{+2} والمغنسيوم Mg^{+2} بالتسحيح مع EDTA (0.01)ع، وقيست ايونات البوتاسيوم K^{+} والصوديوم Na^{+} قيست بجهاز (Flame-photometer) كما في (Al-Hamandi et al., 2019). قيست الكلوريدات Cl^{-} بالتسحيح مع نترات الفضة $AgNO_3$ (0.005) م وقيست الكبريتات $SO_4^{=}$ بطريقة الترسيب بكلوريد الباريوم ($BaCl_2$) باستخدام جهاز المطياف الضوئي Spectrophotometer بطول موجي (492) نانومتر. اما النترات، فقيست باستخدام جهاز Spectrophotometer بطول موجي (206) نانوميتر وبالنسبة لأيونات الفوسفات، فقيست باستخدام موليبدات الامونيوم $(NH_4)_2MoO_4$ وكلوريد القصديروز $SnCl_4$ ثم قياس شدة الامتصاصية بجهاز Spectrophotometer وبطول موجي (690) نانومتر، وقيست العسرة الكلية باستخدام المحلول المنظم لكلوريد الامونيوم NH_4Cl والتسحيح مع EDTA (0.02)ع واستخدم جهاز قياس شدة الضوء Turbidty Lovidond لتقدير العكورة ، وقدرت العناصر الثقيلة (النحاس والزنك والكوبلت والرصاص والنيكل) باستخدام جهاز مطياف الامتصاص الذري (Atomic Absorption) .

تقييم نوعية المياه تبعا لدليل جودة المياه Water quality index (WQI)

قيمت نوعية المياه لأغراض (الشرب وري المزروعات وسقي الدواجن والماشية وللحياة المائية) باستعمال دليل جودة المياه حسب ما أشار اليه (Mhaske et al., 2022) ويتم اختيار بعض الصفات المهمة او المؤثرة والتي كانت قريبة من المحددات العالمية لكل استخدام وفقا للمعادلات الاتية:

$$Rwi = \frac{wi}{\sum wi} \quad \text{..... (1)}, \qquad qi = \frac{ci}{si} * 100 \quad \text{..... (2)}$$

$$SLi = RWi * Qi \quad \text{..... (3)}, \qquad WQI = \sum SLi \quad \text{..... (4)}$$

حيث ان (RWi) الوزن النسبي والتي حسبت في الجدول (3) و(wi) وزن الصفة والتي عوض عنها بالعدد (1−5) اعتمادا على شدة تأثير الصفة على جودة المياه و(ci) القيمة المقاسة للصفة خلال الدراسة و(si) القيمة القياسية للصفة تبعا للمحددات العالمية والموضحة في الجدول (2) و(SLi) قيمة الدليل الفرعي وتستخرج قيمتها من خلال المعادلة (3).

الجدول 2: قيم (Si) في تصنيف نوعية المياه للأغراض المختلفة

الصفة	الوحدة	الشرب	الري	سقي حيوانات المزرعة		حياة الاسماك
				الدواجن	الماشية	
pH	-	7.5	7.5	7.0	-	7.5
EC	($\mu S.cm^{-1}$)	400	-	-	-	-
Turbidity	NTU	5	−	5	-	-
TDS	mg/L	600	2000	2000	3000	500
Cl^{-}		250	100	250	-	860
SO_4^{-2}		250	920	250	1000	-
Zn		4	2	1.5	50	0.12
Cu		2	0.2	0.6	5.0	0.01
Co		-	0.05	−	1.0	-
Ni		0.02	0.2	−	1.0	0.47
Pb		0.01	5	0.2	0.1	0.065
NO^{-3}		50	45	45	100	2.7

PO_4^{-3}	-	-	-	-	-
Ca^{+2}	75	400	60	1000	-
Mg^{+2}	100	61	125	-	-
Na^{+}	250	100	32	-	-
K^{+}	-	78	–	-	-
Hardness	500	–	180	200	-
التصنيف العالمي	(WHO, 2022)	(FAO, 1985)	(CCME, 2005)	(EPA, 1994)	(EPA, 2024)

الجدول 3: قيم (wi) و(RWi) للصفات المستخدمة في تصنيف نوعية المياه للأغراض المختلفة

الصفة	نوع الاستعمال									
	الشرب		الري		الدواجن		الماشية		الحياة المائية	
	Wi	RWi	Wi	RWi	Wi	RWi	Wi	RWi	Wi	RWi
pH	4	0.085	4	0.093	4	0.105	-	-	1	0.091
EC	-	-	-	-	-	-	-	-	1	0.091
TDS	5	0.106	5	0.116	5	0.132	5	0.200	1	0.091
Cl^{-}	5	0.106	4	0.093	4	0.105	-	-	1	0.091
SO_4^{-2}	5	0.106	4	0.093	4	0.105	4	0.160	-	-
Zn	2	0.043	2	0.047	2	0.053	2	0.080	-	-
Cu	2	0.043	2	0.047	1	0.026	2	0.080	-	-
Co	-	-	1	0.023	–	–	2	0.080	-	-
Ni	-	-	2	0.047	–	–	2	0.080	3	0.243
Pb	-	-	2	0.047	1	0.026	1	0.040	-	-
NO^{-3}	5	0.106	4	0.093	3	0.132	3	0.120	4	0.364
Ca^{+2}	3	0.064	3	0.070	3	0.079	4	0.160	-	-
Mg^{+2}	3	0.064	3	0.070	3	0.079	-	-	-	-
Na^{+}	4	0.085	5	0.116	2	0.053	-	-	-	-
K^{+}	-	-	2	0.047	–	–	-	-	-	-
Hardness	4	0.085	–	–	4	0.105	-	-	-	-
Turbidity	5	0.106	–	–	–	–	-	-	-	-
∑	43	1.0	38	1.0	36	1.0	25	1.0	11	1.0

النتائج والمناقشة

تأثير المخلفات السائلة على الصفات النوعية لمياه نهر دجلة

يبين الجدول (4) متوسط درجات الحرارة والاملاح الصلبة الكلية والعكورة والدالة الحامضية والنترات لمياه نهر دجلة ، اذ كانت أدنى قيمة لمتوسط درجة الحرارة في الموقع الاول بمقدار (18.0°) سيليزية واعلى قيمة كانت في الموقع السابع بمقدار (19.1°) سيليزية في حين ان درجة حرارة موقع المقارنة في شريخان كانت (17.9°) سيليزية، وقد يعود سبب الاختلاف بين المواقع الى اختلاف سرعة ومعدل الجريان وطوبوغرافية المنطقة والظروف المناخية والغطاء النباتي على جانبي النهر بين المواقع كذلك الابتعاد عن سد الموصل، فقد اشار (Adamo et al., 2020) الى ان تصريف المياه من السدود إلى الأنهار يؤدي الى حدوث تغيرات كبيرة في درجات الحرارة والاحمال العضوية والرواسب وهذا ما يفسر انخفاض درجة حرارة مياه نهر دجلة في مدينة الموصل كلما اقتربنا باتجاه سد الموصل نتيجة تصريف المياه العميقة الباردة منه وهذه النتائج تتفق مع (Al-Hamdani, 2010) الذي اشار الى ارتفاع درجة حرارة مياه نهر دجلة كلما ابتعدنا عن سد الموصل باتجاه جنوب المدينة.

تراوحت قيم متوسط المواد الصلبة الذائبة الكلية TDS لمياه نهر دجلة ما بين (352-442) ملغم.لتر$^{-1}$، أدنى قيمة كانت في الموقع الثالث والاعلى في الموقع الثامن في حين ان قيمة TDS في موقع المقارنة كانت (244) ملغم.لتر$^{-1}$، وهذه الزيادة عن موقع المقارنة تعود الى الاملاح العضوية والمعدنية المحمولة مع مياه الصرف الصحي الناتجة من المخلفات المنزلية والصناعية الحاوية على الاملاح فضلا عن المخلفات الزراعية وانتقال الاملاح من التربة نتيجة التعرية المائية عبر المصبات الى مياه نهر دجلة، وعند مقارنة قيم المواد الصلبة الذائبة الكلية لمياه نهر دجلة مع المحددات العالمية الواردة في الجدول (2) فإنها تعد صالحة للشرب والري وسقي الحيوانات الماشية والدواجن ومناسبة لحياة الاسماك.

الجدول 4: متوسط درجات الحرارة والاملاح الكلية الذائبة والعكورة والدالة الحامضية والنترات لمياه نهر دجلة

NO_3 mg/L	pH -	Turbidity NTU	TDS mg/L	Tem. C°	الموقع
0.61	7.51	4.0	244	17.9	المقارنة
3.1	7.75	12	422	18.0	الأول
5.0	7.65	13	393	18.4	الثاني
4.6	7.85	16	352	18.9	الثالث
3.5	7.77	18	397	18.1	الرابع
5.9	7.93	22	401	2.18	الخامس
4.5	7.72	19	391	18.5	السادس
4.0	7.89	21	422	19.0	السابع
5.3	7.83	24	442	19.1	الثامن

بينما تراوحت قيم العكورة لمياه نهر دجلة ما بين(12-24) NTU أدنى قيمة كانت في الموقع الاول واعلى قيمة كانت في الموقع الثامن وبزيادة كبيرة عن قيمة موقع المقارنة والذي بلغ (4.0)NTU وهذه الزيادة ناتجة عن حجم وطبيعة المواد العالقة والذائبة في مياه النهر سواء كانت املاح او مواد عضوية غير متحللة او حوامض عضوية ومعدنية ذائبة بالماء او مواداً عالقة كحبيبات الطين وبقايا النباتات ومخلفات صناعية كالأصباغ وزيوت المحركات ومخلفات الوقود التي يتم طرحها فيه من خلال المياه العادمة الصناعية، فضلا عن المخلفات المنزلية وما تحمله من مواد عالقة وذائبة بالماء كمساحيق الغسيل ومخلفات المطابخ التي تنتقل الى النهر عن طريق مياه المصبات وبحسب (Nisa, and Kishor, 2021) فان عكورة مياه الأنهار تنتج عن طريق طرح مخلفات الصرف الصحي الحاوية على كميات متفاوتة من المواد الرغوية مثل مخلفات النفط والوقود ومستحضرات الغسيل والاستحمام ومخلفات المراحيض والاملاح الذائبة العضوية والمعدنية والاسمدة والمخلفات الأخرى.وبالنتيجة، تعد مياه نهر دجلة باستثناء موقع المقارنة شديدة العكورة وغير صالحة للشرب حسب مواصفات منظمة الصحة العالمية (WHO, 2022) الواردة في الجدول (2).

وكذلك تراوحت قيم الدالة الحامضية لمياه نهر دجلة ما بين (7.65 –7.93) وأدنى قيمية كانت في الموقع الثالث واعلى قيمة كانت في الموقع الخامس اما في موقع المقارنة، فبلغت (7.51)، ان ارتفاع قيمة الدالة الحامضية لماء النهر قد يكون سببه اختلاط بعض الملوثات الكيميائية مع مياه النهر وما تحمله من عناصر قاعدية. اشار (APHA, 2017) الى ان الدالة الحامضية لمياه نهر دجلة تميل للقاعدية بسبب اذابة ايون الكاربونات والبيكاربونات والتي تصل اليه نتيجة تحلل مكونات التربة الحاوية هذه الايونات ومن خلال المواد القاعدية المحمولة مع مياه الصرف الصحي، وتتفق النتائج مع (Oleiw and Al-Dabbas, 2024) اللذان أشارا الى ان قيمة pH لمياه نهر دجلة في مدينة الموصل تتراوح بين (8.0–7.0) ، وأشار (Marin and Rusănescu, 2023) الى ان اختلاف الدالة الحامضية بين مواقع مياه نهر دجلة يعود الى ان المخلفات السائلة للمدن تحتوي على أنواع وكميات مختلفة من المواد المعدنية والعضوية ذات دالة حامضية متباينة اذ ان المواد العضوية المتحللة بواسطة الاحياء المجهرية تعمل على تكوين غاز CO_2 وحامض الكربونيك الذي يقلل درجة تفاعل المياه والمخلفات المنزلية والصناعية الأخرى الواصلة للنهر كمساحيق الغسيل والاملاح والمواد القاعدية الذائبة تعمل على زيادة القاعدية. تعد مياه نهر دجلة في جميع المواقع ضمن الحدود المسموح بها عالميا ومحليا للاستخدام لأغراض الشرب وري المزروعات وسقي الماشية والدواجن وحياة الاسماك تبعا للمواصفات العالمية لقيم pH (الجدول 2).

تراوح تركيز النترات ما بين (3.1-5.9) ملغم. لتر$^{-1}$ وكانت أدنى قيمة لها في الموقع الأول واعلى قيمة في الموقع الخامس لنهر دجلة، وبلغ تركيز النترات في موقع المقارنة (0.61) ملغم. لتر$^{-1}$، وهذا ما يدل على التأثير الواضح لمياه الصرف المطروحة في النهر على تركيز النترات، وأشار (Zhai et al., 2021) الى ان زيادة تراكيز النترات في الأنهار يعود الى المخلفات الزراعية والحيوانية المطروحة به وذلك لان النترات تدخل في تركيب الأسمدة الكيميائية والعضوية ويستخدم على نطاق واسع في الترب لذلك يصل الى المياه عن طريق التعرية، وان أكثر من (50)% من تلوث المياه

السطحية والجوفية بالنترات يعود إلى استخدام المبيدات والأسمدة في الاراضي الزراعية التي تتسرب إلى المسطحات المائية. تبعا للمواصفات العالمية الواردة في الجدول (2)، فان مياه نهر دجلة في جميع المواقع تعد صالحة للشرب والري وسقي الماشية والدواجن وعلى الرغم من ذلكم الا ان دول الاتحاد الأوربي (EU, 2014) وضعت تركيزا ضئيلا للنترات في مياه الشرب (0.5) ملغم. لتر$^{-1}$. وبالنسبة لوكالة حماية البيئة الامريكية (EPA, 2012)، فان المستوى المسموح للنترات في المياه السطحية يجب ان لا يتجاوز (1) ملغم. لتر$^{-1}$، فالتراكيز الأعلى من (10) ملغم. لتر$^{-1}$ تعد سامة للأحياء المائية.

يبين الجدول (5) متوسط قيم تركيز الفوسفات والعسرة الكلية والاوكسجين المذاب والكلوريد والكبريتات في مياه نهر دجلة، فقد وجد ان تركيز الفوسفات لنهر دجلة يتراوح ما بين (0.9-4.0) ملغم.لتر$^{-1}$ وكانت ادنى قيمة في الموقع الثاني واعلى قيمة في الموقع الثامن وبلغ تركيز الفوسفات (0.39) ملغم.لتر$^{-1}$ في موقع المقارنة وهذا الاختلاف بين المواقع يعود الى اخلاف نوع وكمية مخلفات الصرف الصحي بين مواقع النهر التي تعد المصدر الرئيس للفسفور واشار (Ruzhitskaya and Gogina, 2017) الى ان مخلفات الصرف الصحي تكون غنية بعنصر الفسفور و(40)% منه يأتي عن طريق المخلفات المنزلية نتيجة الاستخدام الواسع للمنظفات ومساحيق الغسيل التي يشكل فيها (60)% بالإضافة الى المركبات العضوية القابلة للذوبان والمخلفات الزراعية الغنية بالفسفور بفعل استخدام الأسمدة المعدنية والعضوية فضلا عن المخلفات الحيوانية.

فيما تراوحت قيم العسرة الكلية لنهر دجلة ما بين (355-485) ملغم. لتر$^{-1}$، وكانت أدنى قيمة في الموقع الاول واعلى قيمة في الموقع الرابع، وكانت القيم اعلى من موقع المقارنة والذي بلغت فيه (223) ملغم. لتر$^{-1}$. تعد مياه نهر دجلة صالحة للشرب بينما تجاوزت الحد المسموح به لسقي الدواجن تبعا للمواصفات العالمية وتبعا تصنيف (Todd, 1980) كما في الجدول (6). وان مياه نهر دجلة تعد عسرة الى عسرة جدا في جميع المواقع، وقد اشار (Schiavon and Moore, 2021) الى ان استخدام المياه التي تزيد فيها العسرة الكلية عن (300) ملغم. لتر$^{-1}$ في الري يؤدي إلى ترسبات وانسداد انابيب الري مما يؤدي الى تلف انظمة الري وأشارت بعض الدراسات إلى أن ارتفاع عسرة الماء تجعله غير مناسب للاستخدامات المنزلية والصناعية وتسبب مضار صحية كأمراض القلب والأوعية الدموية والكلى لدى الانسان (Al-Naqib et al., 2018).

الجدول 5: معدل قيم تركيز الفوسفات والعسرة الكلية والاوكسجين المذاب والكلوريد والكبريتات في مياه نهر دجلة

الموقع	PO_4	Hardness	Do	Cl	SO_4
	mg/L				
المقارنة	0.39	223	7.3	28	132
الأول	1.2	355	2.7	38	168
الثاني	0.9	372	2.9	42	155
الثالث	2.9	367	3.0	45	174
الرابع	1.9	485	3.1	41	180
الخامس	3.1	417	2.4	52	149
السادس	2.6	415	2.8	51	139
السابع	3.0	448	2.6	58	168
الثامن	4.0	457	2.4	61	173

الجدول 6: تصنيف المياه تبعا للعسرة الكلية

	العسرة الكلية (ملغم. لتر$^{-1}$)	نوع المياه
1	اقل من 75	يسر
2	180	عسرة نسبيا
3	360–180	عسرة
4	أكثر من 360	عسرة جدا

(Todd, 1980)

تراوح متوسط تركيز الاوكسجين المذاب في نهر دجلة ما بين (3.1-2.4) ملغم.لتر$^{-1}$، وكانت ادنى قيمة في الموقعين الخامس والثامن واعلى قيمة في الموقع الرابع وقد يعود سبب الاختلاف الى تباين كمية النفايات السائلة المطروحة الى مياه نهر دجلة او عوامل أخرى كما اشار (Lwang et al., 2003) مثلا الى ان زيادة سرعة جريان المياه يؤدي الى زيادة تعرضه الى تيار الهواء الجوي مما يؤدي الى زيادة التدفق الكتلي للهواء فيه وبالتالي زيادة الاوكسجين المذاب على عكس المياه الراكدة والنتائج جاءت اقل من قيم الاوكسجين المذاب التي حصل عليها (Al-Sarraj, 2020)، فقيمة Do في موقع المقارنة كانت اكبر من المواقع الاخرى وبلغت (7.3) ملغم.لتر$^{-1}$ مما يدل على ارتفاع تركيز الاوكسجين المذاب فيه نتيجة عدم او قلة تعرضه للمخلفات السائلة الحاوية على مواد عضوية كون منطقة شريخان تعد اول منطقة حضرية يمر فيها نهر دجلة في مدينة الموصل ولا يتم طرح المخلفات السائلة في النهر الا بعد حوالي 3 كم عن موقع شريخان من خلال مصب حي العربي الذي يعد اول مصب كبير يطرح مياهه في نهر دجلة داخل مدينة الموصل، ولم تضع منظمة الغذاء والزراعة العالمية (FAO) قيمة قياسية لتركيز الاوكسجين المذاب في مياه الري ، واشارت بعض الدراسات الى ان تركيز الاوكسجين المذاب في مياه الري تعد مقبولة عند التركيز الاكبر من (5) ملغم.لتر$^{-1}$، ويكون نمو وانتاج معظم المحاصيل افضل وخاصة محاصيل البيوت الزجاجية عندما يكون التركيز اكبر من (8) ملغم.لتر$^{-1}$ ، وعندما يكون تركيزه اقل من (4) ملغم.لتر$^{-1}$ فان الري بهذه المياه يسبب مشاكل في نمو النبات والمياه التي يكون فيها التركيز اقل من (0.5) ملغم.لتر$^{-1}$ حيث انها غير صالحة للري، لذا فان مواقع نهر دجلة المدروسة ذات تراكيز قليلة من الاوكسجين المذاب. تجاوزت تراكيز الاوكسجين المذاب المحددات العالمية لمياه الشرب الواردة في الجدول (2)، اشار (Coenen, 2019) الى ان الاوكسجين المذاب في الماء يؤثر على تنوع الاسماك والتركيز يجب ان يكون اعلى من (5) ملغم. لتر$^{-1}$ لكي تعيش معظم انوع الاسماك وعندما يقل تركيزه عن (2) ملغم. لتر$^{-1}$ تنعدم الحياة المائية ويحدث نفوق للأسماك واستنادا الى ذلك فان مياه نهر دجلة تعد غير ملائمة لمعظم أنواع الأسماك.

في حين تراوح متوسط تركيز الكلوريد لمواقع نهر دجلة ما بين (38–61) ملغم. لتر$^{-1}$ وكانت أدنى قيمة في الموقع الأول في حين اعلى قيمة سجلت في الموقع الثامن وان التباين في تركيز الكلوريد بين المواقع يعود الى كمياته المطروحة في مياه النهر نتيجة اختلاف تركيزه في مياه المصبات والمشار اليها في الجدول (7) وان مصدره فيها ناتج من المخلفات المنزلية لكونه يدخل في تركيب مستحضرات التنظيف ومساحيق الغسيل ومياه الاسالة المعالج بالكلوريد. واشار (Geilfus, 2019) الى ان الكلوريد يصل الى الانهار بعدة مصادر من خلال التعرية المائية للتربة كون المادة الام والاسمدة المضافة اليها تحتوي على تراكيز من ايون الكلوريد وقد تنتقل ايضا الى المياه عن طريق غبار المصانع وحرق الفحم والنفايات المحمولة بالهواء الجوي والنتائج اعلى من التركيز الذي حصل عليه (Al-Hamdani, 2022) والبالغ (31.19–26.1) ملغم. لتر$^{-1}$ للمياه نهر دجلة قرب مشروع مياه وادي حجر والغزلاني (الموقع السادس). تعد مياه نهر دجلة في موقع المقارنة والمواقع الاخرى صالحة للشرب ولحياة الاسماك وسقي الدواجن وري المزروعات بالنسبة لتركيز ايون الكلوريد وفقا للمحددات العالمية الواردة في الجدول (2).

الجدول 7: الصفات الكيميائية والفيزيائية لمياه مصبات الصرف الصحي

الصفة	موقع المصب							
	حي العربي	الخرازي	تموز	حي الشفاء	الخوصر	الغزلاني	الدانفيلي	البوسيف
Temperature (C°)	18.2	18.1	18.5	18.4	18.9	19.0	19.3	19.5
TDS	499	507	582	544	589	509	653	794
EC (µS.cm^{-1})	0.78	0.79	0.91	0.85	0.92	0.83	1.02	1.24
pH	7.85	7.85	7.85	7.81	7.93	7.89	7.93	8.01
Do (mg/L)	2.7	2.2	2.3	2.5	1.9	2.1	1.5	1.3
Po_4 (mg/L)	2.4	2.3	4.5	4.0	5.3	4.7	5.4	6.2
Cl^-	61	55	59	61	60	69	65	80
SO_4^{-2} (mg/L)	177	185	194	193	174	170	226	257
Zn (mg/L)	1.55	1.68	1.61	2.12	2.17	2.16	1.84	1.77
Cu (mg/L)	Nil	Nil	0.095	Nil	0.124	0.05	0.390	0.095
Co (mg/L)	0.028	0.026	0.037	0.041	0.064	0.038	0.066	0.049

0.530	0.543	0.517	0.510	0.230	0.610	0.450	0.330	Ni (mg/L)
0.714	0.931	0.510	0.431	0.274	0.667	0.329	0.179	Pb (mg/L)
7.5	6.5	6.9	8.9	5.8	5.2	6.5	4.9	NO^{-3} (mg/L)
91	95	73	61	70	74	72	66	Ca^{+2} (mg/L)
72	66	44	53	55	58	54	50 j	Mg^{+2} (mg/L)
48	68	40	61	50	55	42	43	Na^{+} (mg/L)
19	13	19	13	24	17	15	16	K^{+} (mg/L)
806	700	628	811	601	598	558	534	Hardness (mg/L)
50	55	42	59	38	31	24	23	Turbidity (NTU)

تراوحت معدل قيم تركيز الكبريتات لمواقع نهر دجلة ما بين (139–180) ملغم. لتر$^{-1}$ وكانت أدنى قيمة في الموقع الثاني واعلى قيمة سجلت في الموقع الرابع، وبلغ تركيز الكبريتات في موقع المقارنة (132) ملغم. لتر$^{-1}$، وهذا يتفق مع (Al-Shanona et al., 2020) الذين اشاروا الى ان تركيز الكبريتات لمياه نهر دجلة تراوحت ما بين (130–188) ملغم. لتر$^{-1}$. ان ارتفاع تراكيز الكبريتات في بعض مواقع مياه نهر دجلة يعود الى المخلفات السائلة التي يتلقاها النهر من مياه المصبات الغنية بالكبريتات والناتجة بحسب (Talaiekhozani et al., 2016) من تحليل البكتريا والفطريات للمواد العضوية في المياه العادمة والتي ينتج منها ايونات الكبريتات المسببة للرائحة الكريهة فيها، تعد مياه نهر دجلة في جميع المواقع بما فيها موقع المقارنة صالحة للشرب والري وسقي الماشية والدواجن حسب المواصفات العالمية في الجدول (2).

اما بالنسبة لتراكيز العناصر الثقيلة في مياه نهر دجلة فقد اظهرت النتائج في الجدول (8) الى ان تراكيز النحاس تراوحت ما بين (Nil – 0.211) ملغم.لتر$^{-1}$ ولم تسجل في (الموقع الأول والثاني والرابع وموقع المقارنة) وكان اعلى تركيز في الموقع السابع؛ والنتائج تتفق مع (Kannah and Shihab, 2022) اللذان لم يسجلا أي تراكيز للنحاس في مياه نهر دجلة في مدينة الموصل في منطقة القبة ، يعزى ارتفاع تراكيز النحاس في الموقع السابع الى تأثير مياه مصب الدانفيلي المطروحة فيه ذات التركيز العالي من النحاس والمشار اليها بالجدول (7) والسبب في ذلك هو ان مصب الدانفيلي يمر عبر الحي الصناعي في الساحل الايسر لمدينة الموصل (صناعة الكرامة) وتُطرح فيه المخلفات الصناعية السائلة والصلبة الحاوية على تراكيز عالية من النحاس كونه يستخدم بشكل كبير في عمليات اللحام و يدخل في صناعة اجزاء السيارات مثل أنظمة التبريد (الراديترات) والاسلاك وانابيب الفرامل ويدخل في تركيب ملفات الداينمو والسلف ومحركات النوافذ وغيرها وهذا يتفق مع (Ibrahim and Al-Youzbakey, 2023) اللذان أشارا الى ان مصب الدانفيلي ملوث بالنحاس، فضلا عن ذلك فقد أشار (Zubair et al., 2008) الى ان مصدر النحاس بالمياه بالإضافة الى المياه العادمة الصناعية قد يكون من مياه الصرف الزراعية الحاوية على الأسمدة والمبيدات والمخلفات الحيوانية والمواد العضوية والمخلفات المنزلية السائلة التي تسهم في رفع تركيز النحاس في مصب الدانفيلي الذي يعد من المصبات الكبيرة الذي يجمع المخلفات السائلة الصناعية والحضرية والزراعية في مدينة الموصل. تعد مياه نهر دجلة في جميع المواقع غير ملوثة بالنحاس وصالحة للشرب والري وسقي الماشية والدواجن تبعا للمحددات والعالمية في الجدول (2).

اشارت النتائج الى ان متوسط تراكيز الزنك لمواقع مياه نهر دجلة تراوحت ما بين (1.13 – 1.76) ملغم. لتر$^{-1}$ وكان اقل تركيز في الموقع الأول في حين اعلى تركيز كان في الموقع الرابع الواقع بعد مصب الخوصر ذي التركيز الأعلى من الزنك عن المصبات الأخرى والمشار اليها بالجدول (7). قد يعود السبب الى ان مصب الخوصر يعد من المصبات الكبيرة الذي يمر بالعديد من القرى والاحياء السكنية لمدينة الموصل ويحتوي على المخلفات الزراعية والحيوانية والمنزلية ذات المحتوى العالي من الزنك. تعد مياه نهر دجلة صالحة للشرب والري ولسقي الماشية والدواجن وقد فاقت الحدود المسموحة لحياة الأسماك تبعا لتركيز الزنك فيها وفقا للمحددات العالمية في الجدول (2)، في حين بلغ تركيز الزنك في موقع المقارنة في شريخان (0.73) ملغم. لتر$^{-1}$ وكان ضمن الحدود المسموحة للاستعمالات أعلاه.

الجدول 8. تركيز النحاس والزنك والرصاص والكوبلت والنيكل في نهر دجلة

الموقع	Cu	Zn	Pb	Co	Ni
	mg/L				
المقارنة	Nil	0.73	Nil	0.003	0.015
الأول	Nil	1.13	0.099	0.013	0.193
الثاني	Nil	1.26	0.114	0.021	0.185
الثالث	0.091	1.36	0.345	0.028	0.472
الرابع	Nil	1.76	0.150	0.022	0.102
الخامس	0.060	1.70	0.214	0.042	0.293
السادس	0.078	1.57	0.313	0.026	0.254
السابع	0.211	1.35	0.615	0.036	0.361
الثامن	0.093	1.45	0.201	0.031	0.310

اشارت النتائج الى ان تركيز الرصاص لمواقع مياه نهر دجلة تراوحت ما بين (0.099 –0.615) ملغم.لتر$^{-1}$ وكان اقل تركيز في الموقع الأول واعلى تركيز في الموقع السابع وقد يعود سبب تلك الزيادة الى تأثر الموقع السابع بالمخلفات السائلة لصناعة الكرامة خلال مصب الدانفيلي الملوث بالرصاص، اذ ان مخلفات الوقود والديزل واسلاك اللحام وورش صيانة الراديترات والبطاريات تعد احد مصادر التلوث بالرصاص ولهذا السبب نلاحظ ارتفاع تراكيز الرصاص في مصب تموز المشار اليه في الجدول (7) الذي يجمع المخلفات السائلة لصناعة الجانب الأيمن (وادي عقاب). تعد مياه نهر دجلة في جميع المواقع غير صالحة للشرب والري وسقي الدواجن والماشية ولحياة الاسماك تبعا للمحددات العالمية، فالرصاص يعد من العناصر السامة بالمطلق للكائنات الحية ولا يمكن ان يتحلل ويتراكم (Bioaccumulation) داخل انسجتها فيسبب مشاكل صحية خطيرة واشارت بعض الابحاث ان التعرض للرصاص يسبب مليون حالة وفاة سنويًا و(30)% من حالات الاعاقة الفكرية للأطفال (Shadbegian et al., 2019) وفيما يخص موقع المقارنة، فلم تسجل تراكيز محسوسة للرصاص.

بالنسبة لتركيز الكوبلت في المياه فقد اشارت النتائج الى ان متوسط تراكيز الكوبلت لمواقع مياه نهر دجلة تراوحت ما بين (0.013–0.042) ملغم.لتر$^{-1}$ وكان اقل تركيز له في الموقع الأول في حين اعلى تركيز كان في الموقع الخامس وكان تركيزه ضئيلا جدا في موقع المقارنة البالغ (0.003) ملغم.لتر$^{-1}$.ان ارتفاع تراكيز الكوبلت عن موقع المقارنة يعود الى الكميات التي يتلقاها النهر عن طريق النفايات السائلة الحاوية على الكوبلت اذ اشار (Bhardwaj et al., 2017) الى ان النيكل يصل الى المياه من خلال دخان عوادم السيارات والمواد العضوية والمخلفات الحيوانية والنباتية والطبية فضلا عن مخلفات الورش الصناعية كونه يدخل في تركيب الأجهزة الالكترونية واشباه الموصلات وأدوات القطع الثقيلة وصناعة السبائك والبطاريات والزجاج والخزف والاصباغ. وبحسب (Al-Rawi, 2005)، فان نهر دجلة يعد المصدر الوحيد للمياه السطحية في مدينة الموصل وتستخدم مياهه لأغراض مختلفة منها المنزلية والصناعية فضلا عن الزراعية ويتم تصريف مخلفات جميع تلك الاستخدامات اليه لذا يمكن ان ترتفع تراكيز الكوبلت فيه وتتباين بين المواقع بالاعتماد على كمية المخلفات المطروحة فيه ونوع الأنشطة الناتجة عنها، فزيادة الكلوبلت في الموقع الخامس ناتج من تأثير مصب الخوصر الملوث به. لم تضع المنظمات العالمية حداً حرجاً لتركيز الكوبلت في مياه الشرب كونه يعد عنصرًا ضروريا لمكونات فيتامين B_{12} ويستخدم كمكمل غذائي لعلاج فقر الدم وكذلك يعتبر عنصراً غير مسرطن بحسب وكالة حماية البيئة الامريكية (Harikrishnan et al., 2025)، وعلى الرغم من ذلك، فقد اشارت بعض الدراسات الى حصول حالات تسمم بالكوبلت وتسبب امراض الجهاز التنفسي والكبد والكليتين نتيجة التعرض الى كميات كبيرة منه (EPA, 2016). تعد مياه نهر دجلة في جميع المواقع صالحة للري وسقي الماشية عند مقارنتها بالمحددات العالمية في جدول (2).

تراوحت تراكيز النيكل في مياه نهر دجلة ما بين (0.102–0.472) ملغم.لتر$^{-1}$ وكان اقل تركيز في الموقع الرابع واعلى تركيز كان في الموقع الثالث المتأثر بمخلفات صناعة الكرامة والتي تضم ورش صباغة السيارات ومعامل تصنيع

المواد الكيميائية والاصباغ ومخلفات الديزل وزيوت المكائن ومواد اللحام الحاوية على النيكل والمحمولة للنهر خلال مصب الدانفيلي، وهذا ما أيده (Al-dabbagh, 2022) من ان مصب الدانفيلي يبلغ طوله تقريبا 6 كم ويبدأ من منطقة شقق الخضراء شرقي الموصل ويمر بالمنطقة الصناعية في الكرامة ويصب في نهر دجلة وهو احد أكثر المصبات تلوثا نتيجة انتشار المخلفات الصناعية والمنزلية فيه. واستنادا الى المحددات العالمية تعد مياه نهر دجلة في جميع المواقع باستثناء موقع المقارنة البالغ (0.015) ملغم. لتر$^{-1}$ غير صالحة للشرب نتيجة التصريف العشوائي للنفايات السائلة اليه دون معالجة وقد تسبب مشاكل صحية للإنسان، مثل السرطان والطفرات وامراض الجلد والجهاز الهضمي والعقم (Buxton et al., 2019). وقد تجاوزت اغلب المواقع قد تجاوزت الحدود المسموح بها للري وقد تسبب تلوث للتربة وتقليل انبات البذور وضعف نمو الجذور والتمثيل الضوئي للنبات فضلا عن تسمم النبات وعرقلة العمليات الفسيولوجية داخل الخلية النباتية وتكون الجذور الحرة (Hassan et al., 2019). تصلح مواقع المياه المدروسة لسقي الماشية والدواجن وللحياة المائية تبعا الى تركيز النيكل المسموح عالميا الجدول (2).

تقييم نوعية المياه للاستخدامات المختلفة تبعا لدليل جودة المياه (WQI)

يستخدم دليل (WQI) لتفسير صفات المياه خاصة عندما تكون أقل من المعايير القياسية العالمية عن طريق جمع العديد من هذه الصفات بقيمة رقمية واحدة يسهل مقارنتها مع قيم مرجعية لتقييم جودة المياه للاستعمالات المختلفة وبالتالي تقديمها الى الجمهور بطريقة سلسة فضلا عن ذلك يسهل على صانعي القرار عمليات اعداد الخطط البيئية لمعالجة تلوث المياه (Syeed et al., 2023) ، واشارت النتائج الموضحة بالجدول (9) الى ان قيم دليل جودة مياه نهر دجلة (WQI) لموقع المقارنة في شريخان كانت (39 و 24.2 و 47.1 و 4.9 و 16.2) للشرب والري وسقي الدواجن والماشية وللحياة المائية. اما بالنسبة للمواقع الأخرى، فتراوحت ما بين (64– 98) للشرب وكانت أدنى قيمة في الموقع الأول في حين اعلى قيمة سجلت في الموقع الثامن وهذا يدل على تأثير المخلفات السائلة المطروحة في نهر دجلة والتي تزداد بشكل ملحوظ كلما اتجهنا الى جنوب مدينة الموصل باتجاه الموقع الثامن في منطقة البوسيف نتيجة زيادة المخلفات المحمولة مع مياه النهر واشار (Al-Sudani et al., 2022) الى ان تصريف المياه العادمة الى نهر دجلة دون معالجة تعد أحد أسباب تردي نوعية مياهه للشرب، وتؤدي الى مشاكل صحية وبيئية خطيرة. تراوحت قيم (WQI) للري وللحياة المائية تراوحت بين (35.5– 54.3) و(37.2–57.6) على التوالي وكانت ادنى قيمة في الموقع الاول واعلى قيمة في الموقع الثامن ، تراوحت قيم دليل (WQI) لسقي الدواجن والماشية ما بين (63.9 –86.5) و (12.5 –36.4) على التوالي وكانت ادنى قيمة في الموقع الأول واعلى قيمة في الموقع السابع ، وان زيادة قيم دليل جودة مياه نهر دجلة في الموقع الأول عن المواقع الأخرى يعود لسببين هما حجم الملوثات الضئيلة المختلطة مع النهر كونه يقع بعد اول مصب للصرف الصحي ولا توجد مصبات أخرى قبله تزيد من الاحمال والمخلفات فيه كما في المواقع الأخرى باتجاه جنوب المدينة والسبب الاخر هو قلة حجم التصريف لمصب حي العربي فضلا عن التراكيز والقيم المنخفضة لأغلب الصفات المدروسة بالمقارنة مع المصبات الأخرى والموضحة بالجدول (7)، وقد يعزى ذلك الى ان مصب حي العربي لا يطرح مخلفات زراعية وصناعية وكذلك العدد القليل من الاحياء السكنية التي يمر بها فضلا عن الكثافة السكانية المنخفضة في تلك الاحياء. كانت أصناف مياه نهر دجلة في موقع المقارنة كانت ممتازة للري وسقي الماشية وجيدة للشرب وسقي الدواجن وبالنسبة للمواقع الأخرى لمياه نهر دجلة فكانت نوعية المياه (رديئة – رديئة جدا) للشرب وسقي الدواجن بالاعتماد على تصنيف دليل جودة المياه (WQI) في الجدول (10) وهذا يدل على تباين تأثير المصبات على نوعية مياه النهر اذ يؤثر كل من كمية ونوع الفضلات المحمولة مع مياه المصبات وحجم ومعدل تصريفه على جودة ونوعية مياه نهر دجلة ، وبحسب (Al-Assaf et al., 2020)، فان استخدام المياه ذات الجودة المنخفضة في سقي الدواجن تؤثر على إنتاج البيض واللحوم وتسبب مشاكل صحية لها.

الجدول 9: قيم دليل جودة مياه نهر دجلة للاستخدامات المختلفة (WQI)

الموقع	الشرب	الري	الدواجن	الماشية	الحياة المائية
المقارنة	39	24.2	47.1	4.9	16.2
الأول	64	35.5	63.9	12.5	37.2
الثاني	68	39.1	68.0	13.9	42.2
الثالث	76	47.1	75.3	24.4	50.0
الرابع	84	49.1	82.4	18.2	58.0
الخامس	90	42.5	76.3	17.5	39.0
السادس	82	46.9	75.6	23.3	53.3
السابع	91	54.3	86.5	36.4	54.1
الثامن	98	51.6	80.4	20.2	57.6

كانت أصناف مياه النهر كانت (جيدة – رديئة) للري ولسقي المواشي ونلاحظ ان جودة مياه نهر دجلة لسقي المواشي كانت أفضل من سقي الدواجن والسبب يعود بحسب (Gupta et al., 2021) الى ان الملوثات والعناصر الثقيلة في أنسجة الطيور والدواجن تتراكم بعشرة اضعاف عن تراكمها في حيوانات الماشية لكون الدواجن والطيور أكثر حساسية لزيادة تركيز العناصر الثقيلة من الماشية (العجول والاغنام). والسبب في ذلك يعود الى التركيبة الفسجلية والايضية المختلفة بين الصنفين فضلا عن القدرة على مقاومة اجهاد تراكم المواد السامة التي تجعل التراكم البيولوجي للعناصر الثقيلة في الدواجن أكثر من الماشية، وصنفت مياه نهر دجلة ما بين (جيدة– رديئة) النوعية للحياة المائية وهذا يتفق مع (Enad, and Jaeel, 2019) اللذان أشار الى ان مياه نهر دجلة غير مناسبة للحياة المائية وحياة الأسماك نتيجة تصريف الملوثات المختلفة له من مياه الصرف الصحي بدون معالجة.

الجدول 10. تصنيف قيم دليل جودة المياه (WQI) للاستخدامات المختلفة (Gupta and Misra, 2018)

الصنف	Unsuitable Water	Very Poor Water	Poor Water	Good Water	Excellent Water
قيم WQI	100 <	75-100	51– 75	26-50	0 – 25

الاستنتاجات

1.كانت اصناف مياه نهر دجلة (رديئة – رديئة جدا) للشرب وسقي الدواجن بالاعتماد على تصنيف دليل جودة المياه (WQI) و(جيدة – رديئة) للري وسقي المواشي وللحياة المائية بينما أصناف مياه نهر دجلة في موقع المقارنة كانت ممتازة للري وسقي الماشية وجيدة للشرب وسقي الدواجن وهذا يدل على التأثير الواضح لمياه الصرف الصحي المطروحة في نهر دجلة خلال المصبات المتوزعة على جانبي النهر التي عملت على تردي جودة مياه النهر نتيجة اختلاط الملوثات المختلفة فيه.

2.كانت تراكيز النحاس والرصاص والنيكل في الموقع السابع اعلى من المواقع الاخرى والسبب يعود الى ان مياه نهر دجلة تتأثر بمياه مصب الدانفيلي ذات التراكيز العالمية من النحاس والرصاص والنيكل كونه يعد احد المصبات الصناعية الكبيرة في مدينة الموصل الذي يبلغ طوله تقريبا 6 كم ويبدأ من منطقة شقق الخضراء شرقي الموصل ويمر بالمنطقة الصناعية في منطقة الكرامة التي تضم ورش صيانة السيارات والصباغة وصيانة البطاريات وورش اللحام ومعامل تصنيع المواد الكيميائية والاصباغ ومخلفات الديزل وزيوت المكائن على تراكيز عالية من النحاس والرصاص والنيكل ويصب في نهر دجلة وهو احد أكثر المصبات تلوثا ، وتراكيز الزنك والكوبلت كانت مرتفعة في الموقع الرابع والسبب يعود الى تأثير مياه مصب الخوصر ذي التركيز العالي من الزنك الناتج من المخلفات الزراعية والحيوانية والمنزلية ذات المحتوى العالي من الزنك لكون مصب الخوصر يعد من المصبات الكبيرة الذي يمر بالعديد من القرى والاحياء السكنية لمدينة الموصل الحاوية على تراكيز عالية من الزنك

3. تميل الدالة الحامضية في اغلب المواقع الى القاعدية، والسبب يعود الى ايون الكاربونات والبيكاربونات الذائبة في المياه والتي قد تصل الى النهر عن طريق مكونات التربة الذائبة او من خلال المواد القاعدية المحمولة مع مياه الصرف، ومياه نهر دجلة كانت عسرة الى عسرة جدا في جميع المواقع، وقيم العكورة للمياه في مواقع الدراسة فاقت المواصفات القياسية لمنظمة الصحة العالمية (WHO) لغرض الشرب وتراكيز الاوكسجين المذاب Do أيضا كانت غير صالحة للشرب وحياة معظم أنواع الأسماك، وبالنسبة لتراكيز الرصاص في مواقع مياه النهر فقد فاقت المحددات العالمية للشرب والري وسقي الدواجن والماشية ولحياة الأسماك في حين ان تراكيز النيكل في جميع المواقع كانت غير صالحة للشرب، وتراكيز الزنك في مياه نهر دجلة كانت غير ملائمة لحياة الأسماك، وقيم العسرة الكلية كانت ضمن الحدود المسموح بها للشرب وتجاوزت الحد المسموح لسقي الدواجن تبعا للمحددات العالمية، وتراكيز والنترات والكبريتات والكلوريدات والكوبلت والمواد الصلبة الذائبة الكلية كانت صالحة للشرب والري وسقي حيوانات المزرعة وللحياة المائية.

4.كانت مياه نهر دجلة في موقع المقارنة في شريخان ذات نوعية أفضل من المواقع الاخرى للاستعمالات المتنوعة، أي ان جميع الصفات المدروسة كانت بتراكيز اقل من مواقع نهر دجلة الأخرى المتأثرة بمياه الصرف الصحي.

شكر وتقدير

يتقدم الباحث بالشكر والتقدير الى القائمين على مختبرات قسم علوم التربة والموارد المائية والمختبر المركزي التابع لكلية الزراعة والغابات /جامعة الموصل لتسهيل مهمة اجراء التحاليل الخاصة بالبحث.

المصادر

Adamo, N., Al-Ansari, N. and Sissakian, V., 2020. How dams can affect freshwater issues in the Euphrates-Tigris basins. Journal of Earth Sciences and Geotechnical Engineering, 10(1), pp. 43-76.

Al-Assaf, A.Y., Talat, R.A. and Al-Saffawi, A.Y.T., 2020. Suitability of water for irrigation and livestock watering purpose using IWQI Model: The case study, groundwater quality of some quarters of Mosul city, Iraq. Plant Archives, 20(1), pp. 1797-1802. https://www.researchgate.net/publication/339940063

Al-Dabbagh A.H., 2022. Geochemical assessment of heavy metals in sediments of main Wadis of Mosul City/Iraq. MSc. Thesis, University of Mosul, Mosul. 121P. (In Arabic). https://doi.org/10.4408/IJEGE.2023-01.O-04

Al-Hamandi, H.M., Al-Obaidi, M.A. and Aljumaily, M.M., 2019. Study on quantity and intensity of potassium in the alluvial soils in Baghdad, Plant Archives, 19(2), pp. 123-130.

Al-Hamdani, I.O. and Malko, S., 2010. Environmental Survey for Some Selection Water Resources, Sanitary Waste and Phytoremediation in Mosul City and its Suburbs. PhD Thesis. University of Mosul, College of Science.

Al-Naqib S., Al-Youzbakey K. and Sulaiman A., 2018. - Hydrochemistry and groundwater level fluctuations (2009-2011) in selected wells at the eastern part of Mosul city, northern Iraq. The 9th Periodical Scientific Conference for Dams and Water Resources Research Center, pp. 19-34. (In Arabic)

Al-Rawi, S.M., 2005. Contribution of Man–Made Activities to the Pollution of the Tigris within Mosul Area/IRAQ. International journal of environmental research and public health, 2(2), pp. 245-250. https://doi.org/10.3390/ijerph2005020007

Al-Sarraj, E.S.Y., 2020. Effect of Seasonal Variations on Some Physio-Chemical Properties of Tigris River Water in Mosul City. DOI: 10.33899/edusj.2020.126256.1027

Al-Shanona, R.A., Al-Maathide, A.T. and Al-Asaaf, A.Y., 2020. The environmental status of Tigris River water in Mosul city, northern of Iraq. Plant archives (09725210), 20(1).

Al-Sudani, I.M., Al-Razzaq, H.T.A., Khraibet, A.C. and Mohammed, H.J., 2022. Impacts of untreated sewage effluent on Tigris River water quality using (NSF-WQI) index. Journal of Genetic and Environmental Resources Conservation, 10(1), pp. 7-13.

APHA. (American Public Health Association), 2017. Standard methods for the examination of Water and wastewater. American Public Health Association, 23rd Ed., Washington, DC, USA.

Bhardwaj, R., Gupta, A. and Garg, J.K., 2017. Evaluation of heavy metal contamination using environmetrics and indexing approach for River Yamuna, Delhi stretch, India. Water science, 31(1), pp. 52-66. https://doi.org/10.1016/j.wsj.2017.02.002

Buxton, S., Garman, E., Heim, K.E., Lyons-Darden, T., Schlekat, C.E., Taylor, M.D. and Oller, A.R., 2019. Concise review of nickel human health toxicology and ecotoxicology. Inorganics, 7(7), pp. 89. S https://doi.org/10.3390/inorganics7070089

CCM., 2005. Canadian Council of Ministers of the Environment, Canadian Water.

Coenen, W., 2022. Analysis of the water quality dynamics of Lake Vomb: Interactions between water quality profile and cyanobacterial bloom in a eutrophic lake in Sweden. TVVR 5000.

Enad, H.Y. and Jaeel, A.J., 2019. Water quality index of Tigris River in Wasit Governorate for aquatic life. In IOP Conference Series: Materials Science and Engineering (Vol. 584, No. 1, p. 012029). IOP Publishing. DOI 10.1088/1757-899X/584/1/012029

EPA Environmental Protection Agency, 1994. Poultry Water Quality Handbook.

EPA., 2012. What are nitrates and why are they important.

EPA., 2016. Cobalt Compounds.

EPA., 2024. National Recommended Water Quality Criteria - Aquatic Life Criteria Table

EU., 2014. European Union (Drinking Water) Regulations 2014.

FAO., 1985.Ayers, R.S. and D.W. Westcot. Water for agriculture. Irrigation and Drainage Paper (29 Rev. I). FAO, Rome, Italy

Geilfus, C.M., 2019. Chloride in soil: From nutrient to soil pollutant. Environmental and Experimental Botany, 157, pp. 299-309. https://doi.org/10.1016/j.envexpbot.2018.10.035

Gupta, A.R., Bandyopadhyay, S., Sultana, F. and Swarup, D., 2021. Heavy metal poisoning and its impact on livestock health and production system. Indian J. Anim. Health, 60(2). DOI: https://doi.org/10.36062/ijah.2021.spl.00421

Gupta, R. and Misra, A.K., 2018. Groundwater quality analysis of quaternary aquifers in Jhajjar District, Haryana, India: Focus on groundwater fluoride and health implications. Alexandria Engineering Journal, 57(1), pp. 375-381 https://doi.org/10.1016/j.aej.2016.08.031

Harikrishnan, S., Kaushik, D., Kumar, M., Kaur, J., Oz, E., Proestos, C. and Oz, F., 2025. Vitamin B12: prevention of human beings from lethal diseases and its food application. Journal of the Science of Food and Agriculture, 105(1), pp. 10-18. https://doi.org/10.1002/jsfa.13661

Hassan, M.U., Chattha, M.U., Khan, I., Chattha, M.B., Aamer, M., Nawaz, M., and Khan, T.A., 2019. Nickel toxicity in plants: reasons, toxic effects, tolerance mechanisms, and remediation possibilities—a review. Environmental Science and Pollution Research, 26, pp. 12673-12688. https://doi.org/10.1007/s11356-019-04892-x

Henze, M. and Comeau, Y., 2008. Wastewater characterization. Biological wastewater treatment: Principles modelling and design, 27.

Hossini, H., Shafie, B., Niri, A.D., Nazari, M., Esfahlan, A.J., Ahmadpour, M. and Hoseinzadeh, E., 2022. A comprehensive review on human health effects of chromium: Insights on induced toxicity. Environmental Science and Pollution Research, 29(47), pp. 70686-70705. https://doi.org/10.1007/s11356-022-22705-6

Ibrahim, I.F. and Al-Youzbakey, K.T., 2023. A geochemical study of the main valleys' waters on the left part of Mosul (Iraq). Italian journal of engineering geology and environment, (1), pp. 45-60. https://doi.org/10.4408/IJEGE.2023-01.O-04

Kannah, A.M. and Shihab, H.F., 2022. Heavy Metals Levels in the Water of the Tigris River in the City of Mosul, Iraq.

Karri, R.R., Ravindran, G. and Dehghani, M.H., 2021. Wastewater—sources, toxicity, and their consequences to human health. In Soft Computing Techniques in Solid Waste and Wastewater Management, pp. 3-33. Elsevier. https://doi.org/10.1016/B978-0-12-824463-0.00001-X

Lwanga, M.S., Kansiime, F., Denny, P., and Scullion, J., 2003. Heavy Metals in Lake George, Uganda with Relation to Metal Concentrations in Tissues of Common Fish Species. Hydrobiol. J., 499(1-3): pp. 83-93. https://doi.org/10.1023/A:1026347703129

Machate, D.J., 2023. Anthropogenic hyperactivity for natural resources increases heavy metals concentrations in the environment: Toxicity of healthy food and cancer risks estimated. Journal of Trace Elements and Minerals, 4, 100057. https://doi.org/10.1016/j.jtemin.2023.100057

Mahto, A. and Mishra, S., 2021. Guar gum grafted itaconic acid: a solution for different wastewater treatment. Journal of Polymers and the Environment, pp. 1-14. https://doi.org/10.1007/s10924-021-02125-2

Manasa, R.L. and Mehta, A., 2020. Wastewater: sources of pollutants and its remediation. Environmental Biotechnology Vol. 2, pp. 197-219. https://doi.org/10.1007/978-3-030-38196-7_9

Marin, E. and Rusănescu, C.O., 2023. Agricultural use of urban sewage sludge from the wastewater station in the municipality of Alexandria in Romania. Water, 15(3), 458. https://doi.org/10.3390/w15030458

Mhaske1and3, G.D., Bhalla, R. and Nalawade, P.M., 2022. Study of groundwater hydrochemistry and drinking appropriateness using Water Quality Index (WQI) modelling in the Jam River basin, India. http://doi.org/10.53550/EEC.2022.v28i08s.071

Mukherjee, S., Chatterjee, N., Sircar, A., Maikap, S., Singh, A., Acharyya, S. and Paul, S., 2023. A comparative analysis of heavy metal effects on medicinal plants. Applied Biochemistry and Biotechnology, 195(4), pp. 2483-2518 https://doi.org/10.1007/s12010-022-03938-0

Nisa, A.M. and Kishor, B., 2021. Removal of turbidity and TDS from wastewater by using natural coagulants-a review. In IOP Conference Series: Earth and Environmental Science, Vol. 889, No. 1, p. 012074. IOP Publishing. DOI 10.1088/1755-1315/889/1/012074

Oleiwi, A.S. and Al-Dabbas, M., 2022. Assessment of contamination along the Tigris River from Tharthar-Tigris canal to Azizziyah, middle of Iraq. Water, 14(8), 1194. https://doi.org/10.3390/w14081194

Oleiwi, A.S. and Al-Dabbas, M., 2024. The Parameters Discharge, Salinity and Dissolved loads of Tigris River from Mosul to Baghdad, Iraq. Iraqi Journal of Science, pp. 3176-3194. https://doi.org/10.24996/ijs.2024.65.6.19

Ruzhitskaya, O. and Gogina, E., 2017. Methods for removing of phosphates from wastewater. In MATEC Web of Conferences, Vol. 106, p. 07006. EDP Sciences. https://doi.org/10.1051/matecconf/201710607006

Schiavon, M. and Moore, K.K., 2021. How to Properly Read Your Irrigation Water Analysis for Turf and Landscape: ENH1352/EP616, 12/2021. EDIS, 2021(6). https://doi.org/10.32473/edis-EP616-2021

Shadbegian, R., Guignet, D., Klemick, H. and Bui, L., 2019. Early childhood lead exposure and the persistence of educational consequences into adolescence. Environmental research, 178, 108643. https://doi.org/10.1016/j.envres.2019.108643

Syeed, M.M., Hossain, M.S., Karim, M.R., Uddin, M.F., Hasan, M. and Khan, R.H. 2023. Surface water quality profiling using the water quality index, pollution index and statistical methods: A critical review. Environmental and Sustainability Indicators, 100247. https://doi.org/10.1016/j.indic.2023.100247

Talaiekhozani, A., Bagheri, M., Goli, A. and Khoozani, M.R.T., 2016. An overview of principles of odor production, emission, and control methods in wastewater collection and treatment systems. Journal of Environmental Management, 170, pp. 186-206. https://doi.org/10.1016/j.jenvman.2016.01.021

Todd, D.K., 1980. Groundwater Hydrology, Second Edition. John Wiley and Sons, Inc., New York

WHO. (World Health Organization), 2022. Guidelines for drinking-water quality: incorporating the first and second addenda. World Health Organization.

Zhai, S., Jacob, D.J., Wang, X., Liu, Z., Wen, T., Shah, V., and Liao, H., 2021. Control of particulate nitrate air pollution in China. Nature Geoscience, 14(6), pp. 389-395. https://doi.org/10.1038/s41561-021-00726-z

Zubair, A., Farooq, M.A. and Abbasi, H.N., 2008. Toxic Trace Element Pollution in Storm Water of Karachi: A Graphical Approach. The Pacific Journal of Science and Technology, 9(1), pp. 238-253.

Iraqi National Journal of Earth Science

www.earth.uomosul.edu.iq

الخصائص المورفومترية لحوض وادي الكومل- شمال العراق

نوزاد يوسف عبدالرحمن سلي [1]* ، فواز حميد حمو النيش [2]

[2،1] قسم الجغرافيا، كلية التربية للعلوم الإنسانية، جامعة الموصل، الموصل، العراق.

معلومات الارشفة

تاريخ الاستلام: 30- اغسطس-2024

تاريخ المراجعة: 08- اكتوبر-2024

تاريخ القبـول: 21- نوفمبر -2024

تاريخ النشر الالكتروني: 01- يناير -2026

الكلمات المفتاحية:

المورفومتري،

أنماط الصرف،

تكوين بيلاسبي،

رواسب المنحدرات،

الاستطالة،

المراسلة:

الاسم: نوزاد يوسف عبدالرحمن سلي

Email: nowzad.22ehp147@student.uomosul.edu.iq

الملخص

يهدف البحث إلى استخدام تقنيات نظم المعلومات الجغرافية في الكشف عن الخصائص المورفومترية لحوض وادي الكومل في العراق المتمثلة بالخصائص المساحية والشكلية والتضاريسية والخصائص التصريفية للشبكة المائية، فضلاً عن الأنماط التصريفية للحوض، لبناء قاعدة معلومات رقمية مورفومترية للحوض. اعتمد البحث على تحليل المرئيات الفضائية Land Sat8 (OLI) وأنموذج الارتفاع الرقمي (DEM) والدراسة الميدانية، واستخدام برنامج Arc GIS Desktop 10.8 في أعداد الخرائط لشبكات التصريف المائي وتحديد المراتب للمجاري المائية وحساب المعاملات المورفومترية. تمَ الاعتماد على بيانات محطات الرصد الجوية للتعرف على نوعية مناخ المنطقة، كما تمَ الاعتماد على المنهج التحليلي والمنهج الكمي لتحليل وقياس المتغيرات المورفومترية، وانتاج خريطة الشبكة النهرية وتصنيف مراتبها حسب طريقة ستريلر. من ثم تمَ تحليل الخصائص الطبيعية المؤثرة في الحوض منها التكوينات الجيولوجية والخصائص الطبوغرافية والمناخ والتربة والنبات الطبيعي. يقع حوض وادي الكومل في الجزء الشمالي والشمالي الشرقي من العراق ضمن المنطقة المتموجة والجبلية العالية بين محافظتي نينوى ودهوك. بلغت مساحة الحوض الكلي (926.29) كم^2 وبطول يقارب من (70) كم، وبلغَ عدد المراتب النهرية ستة تباينت في أعداد جداول وأطوالها بحسب مراتبها، فبلغَ مجموع أعداد مجاري جداول الحوض (3242) مجرى، يرجع هذا التباين إلى عمليات تكوينها ونشأتها فضلاً عن التباين في الخصائص البيئية المكونة لها، كذلك ظهر تباين في الخصائص التضاريسية للحوض بين أجزائهِ المختلفة لاختلاف طبوغرافية المنطقة.

DOI: 10.33899/injes.v26i1.60184, ©Authors, 2026, College of Science, University of Mosul.
This is an open-access article under the CC BY 4.0 license (http://creativecommons.org/licenses/by/4.0/).

Morphometric Characteristics Wadi Al-Kumel Basin Northern Iraq

Nowzad Y. Seli [1*], **Fawaz H. Al-Nish** [2]

[1,2]*Department of Geography, College of Education for Humanities, University of Mosul, Mosul, Iraq.*

Article information

Received: 30- Aug -2024

Revised: 08- Oct -2024

Accepted: 21- Nov -2024

Available online: 01- Jan – 2026

Keywords:
Morphometrics,
Drainage Patterns,
Pila Spi Formation,
Slope Deposits,
Elongation,

Correspondence:
Name: Nowzad Y. Seli

Email: nowzad.22ehp147@student.uomosul.edu.iq

ABSTRACT

This research aims to utilize GIS techniques to identify the morphometric characteristics of the Wadi Al-Kumel basin in Iraq, encompassing its spatial, morphological, topographical, and drainage characteristics, as well as the drainage patterns of the basin, to establish a digital morphometric information base for the basin. The research is based on the analysis of Landsat 8 (OLI) satellite images, digital elevation models (DEM), and field studies, utilizing ArcGIS Desktop 10.8 to prepare maps for drainage networks, determine waterway ranks, and calculate morphometric parameters. The data of the meteorological stations are relied upon to identify the type of climate of the region. The analytical and quantitative approaches are also relied upon to analyze and measure the morphometric variables, producing a map of the river network and classifying its ranks according to the Strehler method, and then analyzing the natural characteristics affecting the basin, including geological formations, topographic characteristics, climate, soil, and natural vegetation. The Wadi Al-Kumel basin is located in the northern and northeastern parts of Iraq within the undulating and high mountainous region between Nineveh and Dohuk Governorates. The total basin area reaches (926.29) km^2 and a length of approximately (70) km. The number of river levels reaches six, varying in streams number and lengths according to their levels. The total number of basin streams reaches 3242 streams. This variation is due to the processes of their formation and origin, in addition to the variation in the environmental characteristics that compose them. There is also a variation in the topographic characteristics of the different parts of the basin due to the difference in the topography of the region.

DOI: 10.33899/injes.v26i1.60184, ©Authors, 2026, College of Science, University of Mosul.
This is an open-access article under the CC BY 4.0 license (http://creativecommons.org/licenses/by/4.0/).

المقدمة

تمثل دراسة الاحواض المائية جانبا كبيرا من اهتمام الجومورفولوجيين، لما لهذه الاحواض من دلالات جيومورفية وبيئية عديدة. ترتبط الأحواض المائية عامةً ارتباطاً مباشراً بالعوامل الطبيعية خاصة (البنية والجيولوجيا وانحدار السطح والمناخ والتربة والغطاء النباتي)، كما يعتمد التحليل المورفومتري بدرجة كبيرة على تحليل الارتفاع ودرجات الانحدار واتجاهاتهِ، معظم البيانات المورفومترية من خلال الخرائط الطبوغرافية لمنطقة الدراسة وأنموذج الارتفاع الرقمي لها.

تعد دراسة الأحواض المائية أتجاه حديث في الجيوموفولوجيا الكمية التي تعتمد على التحليل الإحصائي والمعادلات الرياضية لدراسة الأشكال الأرضية، ويعد دراسة الأحواض المائية أساساً في الدراسات الهيدرولوجية والجيومورفولوجية.

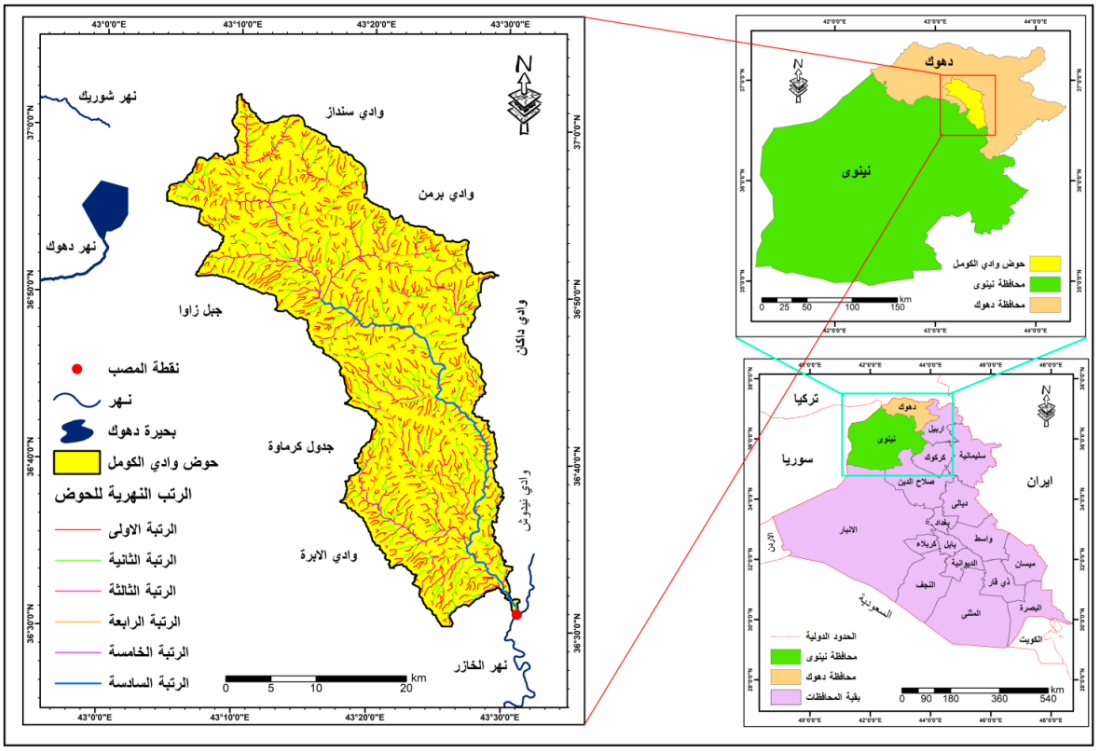
هذه الدراسة قاعدة ضرورية لاهتمامات علمية أخرى كتلك المتعلقة بالمصادر المائية والتربة والهندسة الجيولوجية، إذ تتفاعل هذه العوامل لتساهم في تطوير السمات الجيومورفولوجية التي تميز هذا الحوض. تمثل منطقة الدراسة وحدة طبيعية جيومورفولوجية وهيدرولوجية متكاملة تساعد في الكشف عن العديد من المظاهر والأشكال الأرضية فيها.

تهدف الدراسة إلى تحليل الخصائص الطبيعية لحوض منطقة الدراسة (الجيولوجيا، الانحدار، المناخ، التربة، النبات الطبيعي)، والتعرف على مكونات وتفاصيل هذهِ الخصائص ومدى تأثيرها على مظاهر سطح الأرض في المنطقة وتأثير هذه الخصائص على الخصائص الهيدرومورفومترية والعمليات الجيومورفية في حوض منطقة الدراسة.

تهدف تحليل المعاملات المورفومترية من خلال المعادلات الرياضية الى التعرف على خصائص الحوض وخصائص الشبكة التصريفية فيها والمراحل التي وصلَ إليها الحوض وتأثير عامل الانحدار والتضرس ودرجة الوعورة على الكثافة التصريفية وأنماط شبكات الصرف في حوض وادي الكومل.

موقع وحدود منطقة الدراسة

يشغل حوض وادي الكومل مساحة تقدر بـ (926.29 كم^2) ويمتد عبر أراضي محافظتي نينوى ودهوك ويصب في نهر الخازر أحد روافد نهر الزاب الكبير شمالي العراق. يمتد الحوض فلكياً بين دائرتي عرض ("43 '29 º36) و ("41 '02 º37) شمالاً، وبين خطي طول ("46 '03 º43) و("55 '31 º43) شرقاً. يحد المنطقة طبيعياً من جهة الشرق عدد من الوديان منها (سبندار، برمن، داكان، نيدوش)، ومن الشمال الغربي نهر شوريك، ومن الغرب جبل زاوا وجدول كرماوة، ومن الجنوب الغربي وادي الابرة، ومن الجنوب نهر الخازر، حيث يصب النهر فيهِ في الجزء الجنوبي الشرقي من الحوض عند التقائهِ بنهر الخازر بطول يصل الى ما يقارب (70) كم.



الشكل 1. موقع حوض وادي الكومل في العراق.

الخصائص الطبيعية لمنطقة الدراسة

الجيولوجيا

تعمل البنية الأرضية الجيولوجية على إظهار المكاشف الصخرية نتيجةً لعوامل بنيوية وترسيبية من العمليات التي حدثت وتحدث في المنطقة وهي أحد أبرز العوامل التي لها علاقة بتشكيل المظهر الأرضي وإحدى الخصائص التي ترتكز عليها الدراسات الجيوموفولوجية المرافقة للتطورات البيئية عبر الزمن من خلال الحركات الأرضية الناتجة بفعل العمليات الباطنية من طي الطبقات والتصدع والشقوق والفواصل الصخرية. وتوفر فهماً أعمق للعمليات الجيولوجية والتأثيرات البيئية

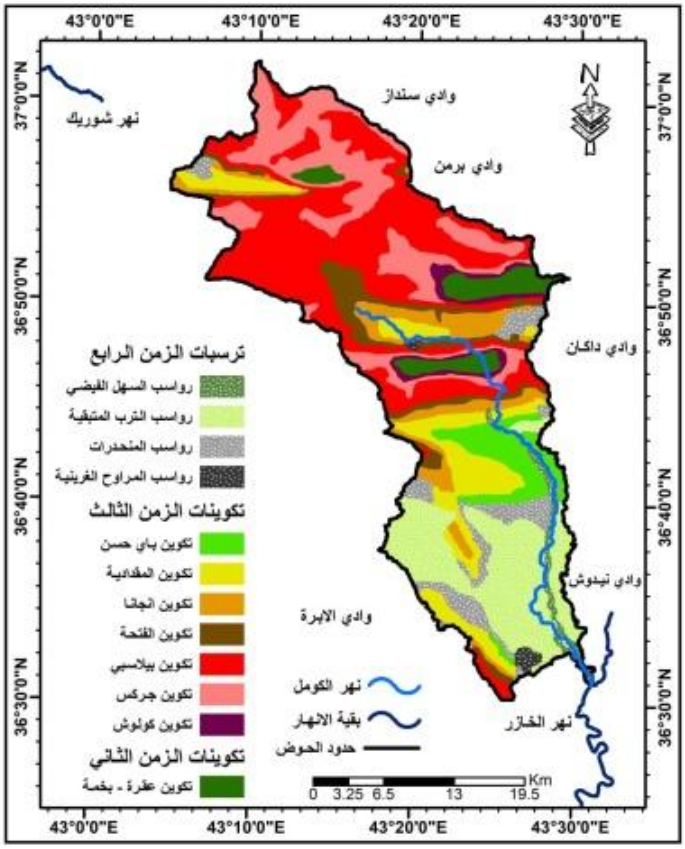
والموارد الطبيعية في هذهِ المنطقة، وتساعد في تحسين التخطيط لغرض التنمية المستدامة وتقليل المخاطر الجيومورفية المحتملة. والتي كما تقوم عليها مختلف العمليات الجيوموفولوجية سواءً كانت في هذهِ المنطقة أو في مناطق أخرى.

التكوينات الجيولوجية (الطباقية) في منطقة الدراسة

أبرز التكوينات الجيولوجية التي ظهرت في منطقة الدراسة التي تنحصر ما بين تكويني (عقرة – بخمة) التابع إلى تكوينات الزمن الجيولوجي الثاني وتكوينات الزمن الجيولوجي الرابع والمتمثل بـ (رواسب السهل الفيضي) حسب الخريطة الجيولوجية للمنطقة (الشكل 2) ومعطيات الجدول (1) وتم تصنيفها من الاقدم الى الاحدث بالشكل التالي:

تكوينات الزمن الجيولوجي الثاني

تكوين عقرة – بخمة: يشكل التكوينان كتلة سميكة واحدة من الحجر الجيري، بعمر الكريتاسي الاعلى الذي ينتمي إلى نهاية العصر الجيولوجي الثاني، ويتكون هذان التكوينان من صخور جيرية شعابية وصخور جيرية شعابية أمامية، وتشير بعض الدراسات إلى القول بأن وحدة بخمة أكثر تدلمتاً من وحدة عقرة (Sayab et al., 1982).



الشكل 2. التكوينات الجيولوجية المنكشفة في منطقة الدراسة (المصدر: جمهورية العراق وزارة الصناعة والمعادن، الهيئة العامة للمسح الجيولوجي والتعدين، ولوحة الموصل الجيولوجية 13 - 38 – Nj، بمقياس رسم 1:250000، لسنة 1995، ومخرجات برنامج Arc GIS Desktop V.10.8).

تكوينات الزمن الجيولوجي الثالث

1- تكوين كولوش: يعد هذا التكوين من ترسبات الباليوسين، وهو عبارة عن كميات هائلة من صخور المدملكات والحصى والرمال التي تعود جميعها إلى عصر الباليوسين والايوسين المبكر والتابعان إلى الزمن الثالث (Al-Omari and Alisadik, 1977).

2– تكوين جركس: هو من ترسبات الايوسين وجزء من الباليوسين، ويسمى بطبقات دهوك الحمراء والتي يميل لونها ما بين الأحمر والأرجواني والتي تظهر في هذه المنطقة تنوعاً ما بين صخور سجيلية حمراء وصخور أرجوانية وصخور طينية وصلصال رملي حبيبي مع وجود حصى ورمال ومدملكات وعدسات من الجبس وبقايا اللغنايت وعدسات من الصخور الملحية أو بدونها (Sayab, 1982).

3– تكوين بيلاسبي: يعود هذا التكوين الى عصر الايوسين من الزمن الجيولوجي الثالث وهو أكثر انتشاراً في منطقة الدراسة، وهو يتشكل من جزأين علوي وسفلي، الجزء العلوي منهُ يتكون من طبقة الحجر الجيري الابيض والرمادي والمارل الطباشيري مع الصوان، بينما نلاحظ معدن الكوارتز نحو الاعلى، أما الجزء السفلي من هذا التكوين يتمثل بطبقة من الحجر الجيري مع متحجرات من الطحالب أو الصدف والحجر الجيري والدولومايت والطباشيري مع الصوان (Jassim and Goff, 2006).

الجدول 1: مساحات ونسب التكوينات الجيولوجية في منطقة الدراسة.

ت	الزمن	العصر	التكوينات الجيولوجية	مكونات الصخور	اللون	المساحة / كم^2	النسبة %
1	الرباعي	الحديث بلايستوسين – هولوسين	رواسب السهل الفيضي	خليط من الرسوبيات المتكونة من الحصى والرمل والطين والغرين		17.280	1.865
2			رواسب الترب المتبقية			137.307	14.823
3			رواسب المنحدرات			53.441	5.770
4			رواسب المراوح الغرينية			5.484	0.592
5	الثالث ميوزين سينوزيك	البلايوسين	تكوين باي حسن	الطفل والمدملكات والحجر الطيني والغريني والحجر الرملي		43.722	4.720
6			تكوين مقدادية	الحجر الرملي والحجر الغريني والطيني		86.806	9.371
7		المايوسين	تكوين أنجانا	الحجر الطيني الاحمر والحجر الغريني والحجر الرملي		61.862	6.679
8			تكوين فتحة	الانهيدريت والجبس والملح، متداخلة مع الحجر الجيري والمارل		53.700	5.799
9		الايوسين	تكوين بيلاسبي	صخور جيرية وحجر جيري طباشيري		263.476	28.444
10			تكوين جركس	صخور سجيليه حمراء وصخور ارجوانية وصخور طينية وصلصال مع رمال ومدملكات		143.975	15.543
11		الباليوسين	تكوين كولوش	احجار وصخور المدملكات والحصى والرمال		19.660	2.122
12	الثاني ميزوزيك	الكريتاسي الأعلى	تكوين عقرة – بخمة	صخور جيرية شعابية وصخور جيرية شعابية أمامية أو صخور ضحضاحيه		39.577	4.272
						926.29	%100

4– تكوين فتحة: يتبع هذا التكوين ترسبات عصر المايوسين التابع إلى الزمن الجيولوجي الثالث. ومن المعروف أن هذا العصر حدثت فيهِ معظم الحركات الألبية، يتألف هذا التكوين من الانهايدريت والجبس والملح والمتداخلة مع الحجر الجيري والمارل، كما ويُعد هذا التكوين ضمن منطقة انتقالية تتكون من الانهايدريت والحجر الطيني والحجر الجيري الرقيق (Jassim and Goff, 2006).

5- تكوين انجانة : يعود هذا التكوين أيضاً لعصر المايوسين، وهو من أكثر ترسبات عصر المايوسين المتأخر انتشاراً في شمال العراق، يحتوي على الحجر الرملي والحجر الطيني والغريني (Mohsen, 2018) .

6- تكوين مقدادية : يعد من تكوينات عصر البلايوسين، ويتألف من طبقات متداخلة من الحجر الطيني الاحمر والحجر الغريني والحجر الرملي، ويوجد في الغالب عند أقدام الجبال، حيثُ يكون لون طبقاتهِ رمادياً فاتحاً ذا حبيبات ناعمة (Al-Janabi, 2016).

7- تكوين باي حسن : يُعتبر هذا التكوين من ترسبات عصر البلايوسين أيضاً، ويتألف من ترسبات المولاس والمدملكات والحجر الطيني والغريني والحجر الرملي الذي يشكل القسم الاكبر ولاسيما الجزء الاسفل، بينما تشكل المدملكات الجزء الاعلى منه (Mohsen, 2018).

ترسبات الزمن الجيولوجي الرابع

1- رواسب المراوح الغرينية: هي من ترسبات عصر البلايستوسين، ويتمثل هذا التكوين بوجود الحصى ورمال مخلوطة مع ترسبات حصوية أو على شكل عدسات، ويشترك الغرين والطين الغريني مع الرمال لتكوين المراوح الغرينية بمساحات واسعة في أغلب المناطق المشابهة لهذه الرواسب (Al-Obaidi, 2015).

2- رواسب المنحدرات: هي رواسب حديثة تعود لعصر الهولوسين، وتُعد من الترسبات المتباينة في خصائصها الشكلية والحجمية التي تتراوح ما بين الحصى المتباين والرمل والغرين فضلاً عن قطع الحجارة التي تسقط من أعالي المرتفعات، ناهيكَ عن الطين وخليط من الرسوبيات (Allawi, 2021).

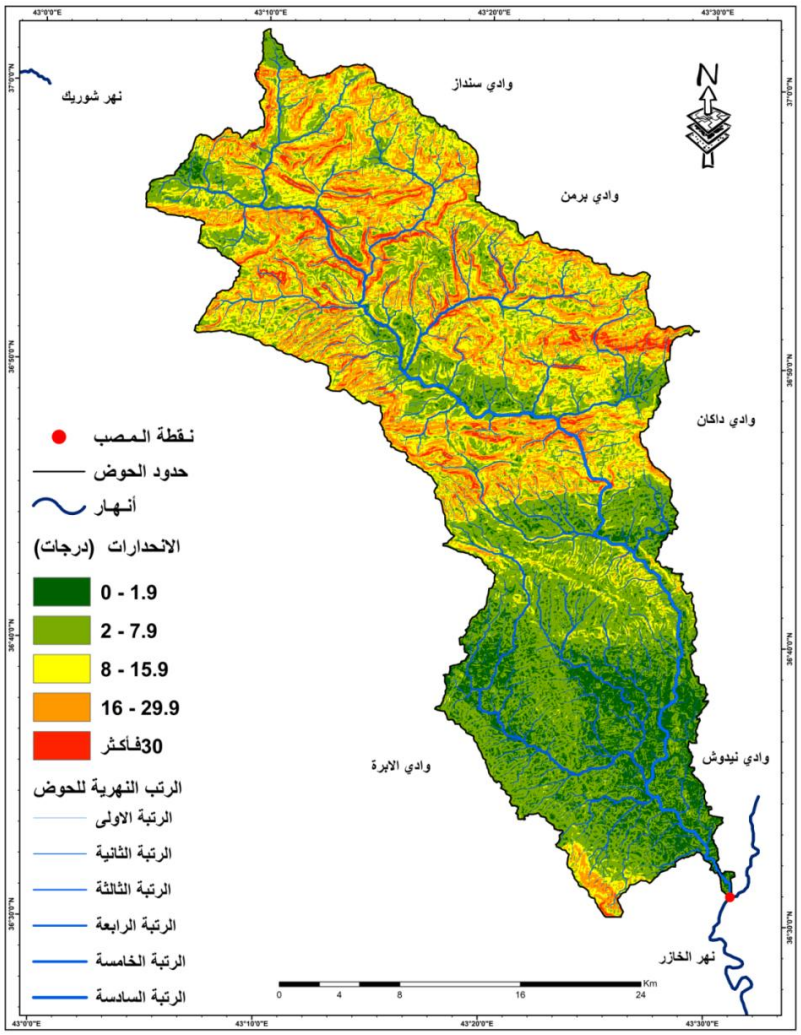
3- رواسب الترب المتبقية: هي كذلك رواسب حديثة من ترسبات عصر الهولوسين مشتقة من الصخور التي تستند عليها وتبقى فوق تلك الصخور، فهي تحتوي على المعادن الأولية نفسها الموجودة في صخور الأساس لأنها ناتجة من عملية التجوية الموضعية للصخور ذاتها، حيثُ عُدت القشرة جبسية في بعض المناطق بسبب احتوائها على نسبة عالية من الجبس الثانوي، وتشمل هذه الرواسب مواد رملية وغرينية وطينية مع فتات صخري من حجر الكلس بلون بني مصفر الى رمادي (Al-Halbousi, 2005) اعتمادا بالأصل على صخور الأم التي تستند عليها.

4- رواسب السهل الفيضي: يتراوح عمرها ما بين (البلايستوسين والهولوسين)، تعد من الرسوبيات الحديثة التكوين التي تتميز بانبساطها، وتتكون من الطين والغرين والرمل، وفي بعض الاحيان توجد فيها قطع صخرية بحجم الجلاميد ويكون ترسيبها معتمدا على كمية المياه الموسمية الجارية (Al-Maamourimohamed, 2016).

خصائص الانحدار

1- المنحدرات: المنحدر هو ميل سطح الأرض عن خط الأفق أو الميلان الذي يربط بين نقطتين مختلفتي المنسوب، ويعبر عن الانحدار بالدرجة أو النسبة المئوية (Salama, 2004)، إذ تمثل أحد عناصر مظاهر السطح التي يتم تحليلها باستخدام أساليب قياسية وتحليلية لعلاقتها الوطيدة بالنشاط البشري بأشكالهِ المختلفة (Al-Dulaimi, 2018). تم الاعتماد على بيانات أنموذج الارتفاع الرقمي (DEM) لحوض وادي الكومل، واستخدام تصنيف زنك (Zink) لتصنيف درجات الانحدار في المنطقة والتي تضم خمس فئات تصنيفية لدرجات الانحدار كما موضح بالخريطة (3) والجدول (2)، وهي تستخدم في تحديد أنواع التضاريس والاشكال الارضية على مستوى الارض، كما أن خريطة المنحدرات تساعد في توضيح وإبراز المتغيرات الجيومورفية. تسود في منطقة الدراسة أنظمة معقدة من المنحدرات المحدبة والمقعرة وبامتدادات متباينة منها الطويلة والمتوسطة والقصيرة، إذ تختلف أطوالها باختلاف القوى المؤثرة في نشأتها فضلاً عن العوامل والعمليات الجيومورفية ضمن المنطقة والحافات المعقدة التركيب بسبب التكوينات الصخرية والمتمثلة بتعاقب الصخور الصلبة واللينة فضلاً عن تأثرها الشديد بالحركات التكتونية.

2– تصنيف زنك Zink: أعدهُ العالم زنك Zink عام (1988–1989)، وهو تصنيف جيومورفولوجي هرمي متسلسل يتكون من خمسة مستويات تصنيفية للمنحدرات الارضية. من مميزات هذا التصنيف أنهُ يعطي صورة أكثر وضوحاً عن المنحدرات الارضية (Al-Dulaimi, 2018). إذ تم تطبيقهُ على حوض وادي الكومل لبيان زوايا الانحدار ضمن منطقة الدراسة حسب هذا التصنيف، وتبين الخريطة (3) والجدول (2) الخصائص والصفات الإنحدارية الآتية:



الشكل 3. أصناف الانحدار بالدرجات ومستويات التضرس حسب تصنيف زنك (Zink, 1988-1989) لمنطقة الدراسة.

الجدول 2: أصناف الانحدار ومستويات التضرس ومساحة ونسب الانحدارات حسب تصنيف (Zink) لمنطقة الدراسة.

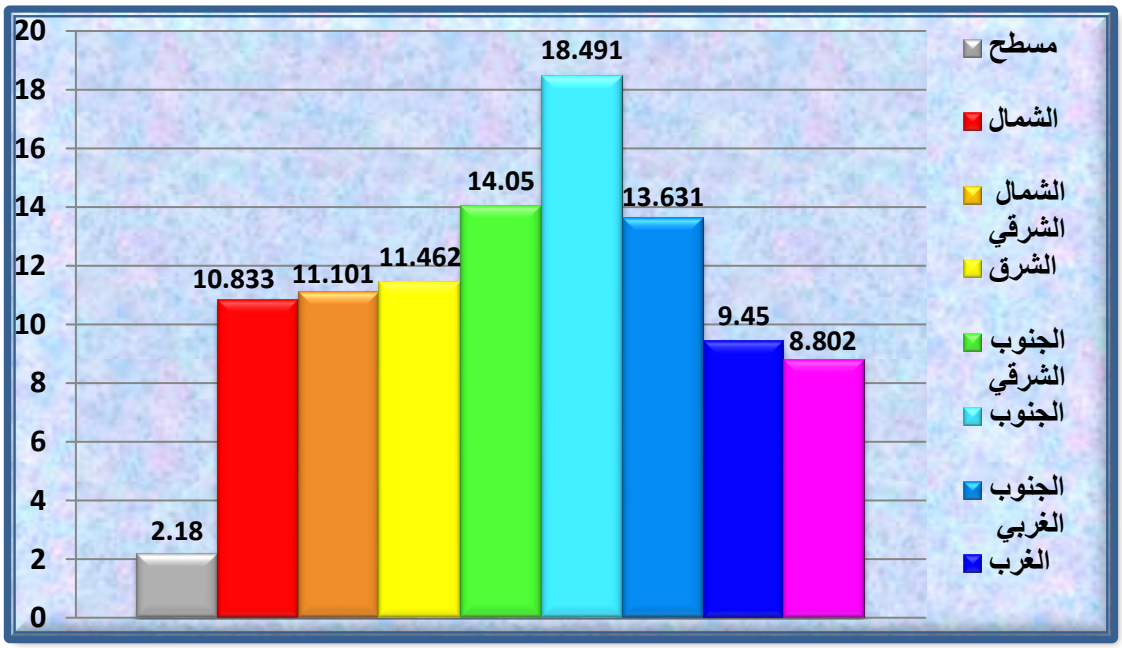
ت	شكل التضرس	درجة الانحدار	تصنيف السطح	المساحة كم²	النسبة %	مجموع النسب لمعرفة المرحلة التي تمر بها المنطقة
1	مسطح – مستوي	$1.9^0 – 0^0$	سهول الوديان	126.540	13.661	53.205
2	تموج خفيف	$7.9^0 – 2^0$	سهول نهرية – أقدام جبال	366.292	39.544	
3	متموج	$15.9^0 – 8^0$	تلال منخفضة	235.926	25.470	25.470
4	مقطعة – مجزأة	$29.9^0 – 16^0$	تلال مرتفعة	166.002	17.921	21.325
5	مقطعة بدرجة عالية	30^0 فأكثر	جبال	31.530	3.404	
	المجموع			926.29	% 100	100

3– اتجاه الانحدار: يعرف اتجاه الانحدار بأنه الجهة التي ينحدر منها أو يميل نحوها السطح، فمن العوامل التي تؤثر في تباين نشاط العمليات المورفومناخية والمورفوديناميكية على السطح هي جهة الانحدار أو ميل السطح نحوها، ومقدار ما تستلمهُ هذهِ الجهة من عناصر مناخية وأي عنصر مناخي يغلب تأثيرهُ على جهة الانحدار هذهِ دون الأخرى (Al-Obaidi, 2022). ان دراسة الانحدارات من حيث اتجاه المنحدر لها اهمية كبيرة في الدراسات الجيومورفية والهيدروجيومورفية، إذ تساعد على التنبؤ باتجاه حركة المياه وحركة مواد السطح، كما يمكن من خلالها ابراز القيمة

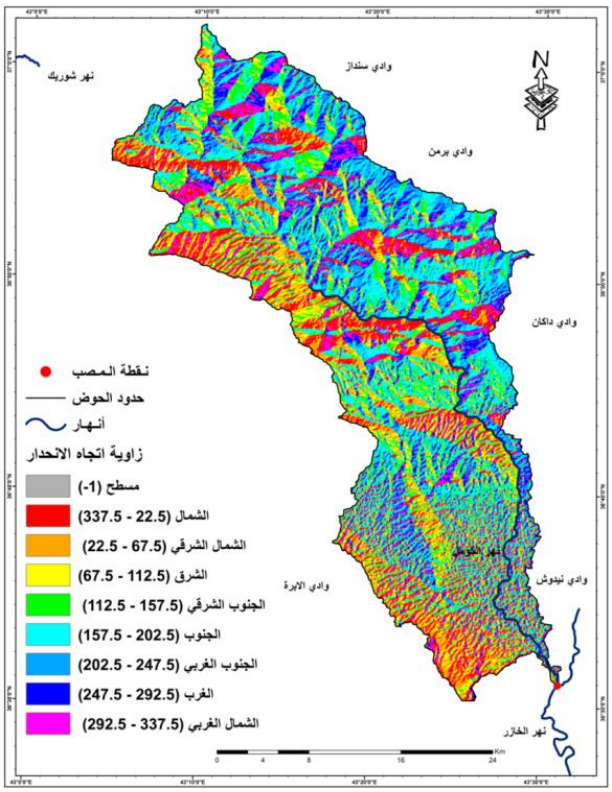
المكانية للمنحدر ومعرفة العديد من المحددات منها انماط التصريف حيث لها تأثير على درجة انجراف التربة، وتحديد المناطق المعرضة لعمليات النحت والترسيب. فعند ملاحظة خريطة الاتجاه (4) لانحدارات منطقة الدراسة، المصمم في برنامج Arc GIS (10.8) من خلال عملية الاشتقاق من أنموذج الارتفاع الرقمي (DEM)، يتضح أن هناك تعدد في اتجاهات الانحدار للحوض التي بلغت (9) اتجاهات تتفق مع اتجاهات التضرس للحوض وبعض المناطق القليلة المسطحة، وحسب الجدول (3) ظهر أقل فئة أتجاه للمسطح بدرجة انحدار (0 – 1)º بمساحة (20.186) كم^2 وبنسبة (2.180)%، وأعلى فئة أتجاه للجنوبي بدرجة انحدار (157.5–202.5)º بمساحة (171.279) كم^2 ونسبتها (18.491)% (الجدول 3).

الجدول 3: مساحات ونسب زوايا اتجاه الانحدار في منطقة الدراسة.

ت	درجة الزاوية	اتجاه الانحدار	المساحة (كم^2)	النسبة المئوية (%)	اللون
1	0 -1	مسطح	20.186	2.180	
2	337.5 -22.5	الشمال	100.345	10.833	
3	22.5 – 67.5	الشمال الشرقي	102.826	11.101	
4	67.5 – 112.5	الشرق	106.178	11.462	
5	112.5 – 157.5	الجنوب الشرقي	130.145	14.050	
6	157.5 – 202.5	الجنوب	171.279	18.491	
7	202.5 – 247.5	الجنوب الغربي	126.263	13.631	
8	247.5 – 292.5	الغرب	87.526	9.450	
9	292,5 – 337.5	الشمال الغربي	81.541	8.802	
	المجموع		926.29	100	



الشكل 4. النسب المئوية لزوايا اتجاه الانحدار.



الشكل 5. زوايا اتجاه الانحدار لحوض وادي الكومل.

المناخ:

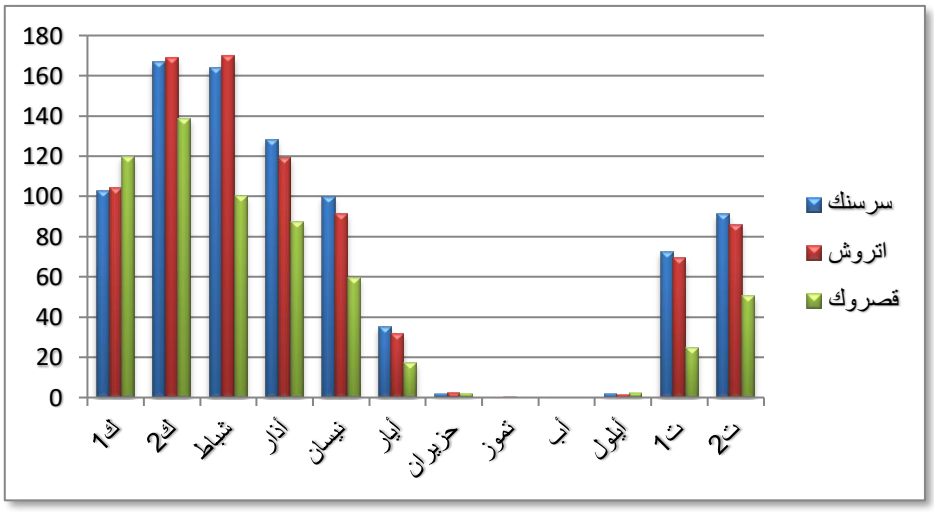
يعد المناخ من أهم المكونات البيئة الطبيعية والمسبب في التغيرات التي تحصل ضمن البيئة، لذا تبرز أهمية دراستهِ لكونهِ الأساس المهم الذي تتألف منه الصورة الكاملة للبيئة الطبيعية السائدة في منطقة الدراسة.

ولمعرفة طبيعة المناخ في أي منطقة يتطلب دراسة تتسم بشيء من التفصيل حتى يمكن إعطاء صورة واقعية عن ظروفها المناخية الخاصة وذلك بالاعتماد على ما يتم تسجيله من قبل هيئة الأرصاد الجوية (Alganaby, 2013). فالأمطار تُعد المصدر الرئيس لكل المياه التي تجري فوق سطح الأرض وما يترشح منها الى باطن الأرض؛ والماء الجاري وما يقوم بهِ من عمليات النحت والنقل والترسيب هو أهم عوامل التعرية وأكثرها أثراً في تشكيل مظاهر سطح الأرض. وعليهِ يمكن توضيح أثر المناخ على جيومورفولوجية حوض وادي الكومل من خلال معرفة المناخ في الزمن الحالي:

1- الامطار: هناك عدة عوامل تتحكم في التباين الزماني والمكاني لكميات الامطار الساقطة ضمن منطقة الدراسة، فالارتفاع عن مستوى سطح البحر يزيد من كميات الامطار وبالعكس، وكذلك لاتجاه السلاسل الجبلية والمرتفعات من الجهة التي تواجه أو تعاكس أتجاه الرياح الدور الكبير في تباين كميات الامطار الساقطة في الأجزاء المختلفة من منطقة الدراسة، كما تعد المنخفضات الجوية المصدر الاساس للرطوبة والامطار في العراق وخاصةً في فصلي الشتاء والربيع. وعليهِ فأن المدة التي تسقط فيها أعلى كميات المطر فوق العراق هي المدة نفسها التي تكثر فيها المنخفضات الجوية (Majed, 2008). وإن الموقع الفلكي للمنطقة جعلها ضمن نطاق مرور المنخفضات الجوية المتوسطية والتي يبدأ وصولها بأعداد محدودة من منتصف تشرين الأول ثم تزداد تدريجياً بتقدم فصل الشتاء. تعد الامطار من العوامل المناخية المؤثرة بصورة مباشرة وغير مباشرة في التصريف المائي للأنهار، ويبدو المناخ فيها مناخاً جبلياً رغم أمطارهِ التي ربما تصل إلى 25 سم أو أكثر والتي تسببها الرياح الغربية وأعاصيرها (Maaruf et al, 2016). وكانت قيم الأمطار المسجلة في محطة أتروش التي تم الاعتماد عليها في المعادلات الرياضية بكونها واقعة في منتصف منطقة الدراسة تقريباً، وكميات الامطار فيها بلغت أدنى قيمة في محطة أتروش في شهر آب (0.1) ملم، وبلغت أعلى قيمة لها في شهر شباط (169.6) ملم، وكان مجموع الساقط المطر السنوي فيها (805.3) ملم (الجدول 4).

الجدول 4: المعدلات الشهرية للأمطار(ملم) للمدة (2012-2022) في محطات منطقة الدراسة.

الأشهر / المحطات	ك1	ك2	شباط	أذار	نيسان	أيار	حزيران	تموز	آب	أيلول	ت1	ت2	المعدل الشهري	المجموع
سرسنك	102.5	166.8	164.1	128	99.6	35.2	1.8	0	0	1.9	72.3	91.2	71.2	854.4
اتروش	104.3	168.9	169.6	119.4	91.4	31.8	2.4	0.1	0	1.7	69.4	85.9	57.5	805.3
قصروك	119.8	138.7	100.3	87.6	59.7	17.2	1.9	0	0	2.1	24.8	50.5	48	575.6

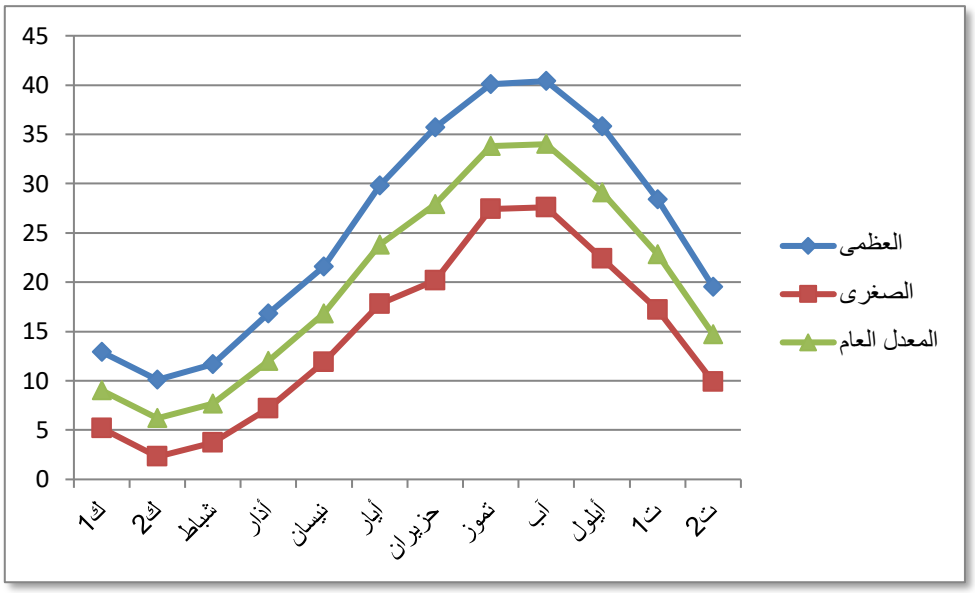


الشكل 6. المخطط البياني للمعدلات الشهرية للأمطار (ملم) لمحطات منطقة الدراسة.

2- درجة الحرارة: إن لدرجات الحرارة تأثيراً كبيراً في أشكال الأرض، فضلاً عن العوامل الأخرى، ويظهر هذا التأثير من خلال دورها في عمليات التجوية وبشكل خاص الفيزيائية منها، ولهذا فالتباين الكبير في درجات الحرارة ومن فصل الى آخر والمدى الحراري واختلاف درجات الحرارة بين الليل والنهار تعمل على تمدد المعادن الموجودة في الصخور وتقلصها. ومع تكرار عملية التمدد والتقلص هذهِ يحدث ظاهرة التقشر الصخري وتفتيت الصخور، إذ أن التباين في الارتفاع عن مستوى سطح البحر بين أجزاء المنطقة وتأثرها بالرياح والكتل الهوائية المتباينة في الخصائص تخلق تبايناً في الخصائص الحرارية لأجزاء منطقة الدراسة. ومن خلال الجدول (5) نستنتج ما يلي: بلغ المعدل السنوي لدرجات الحرارة للمحطة المختارة ضمن منطقة الدراسة وهي أتروش الواقعة في وسط منطقة الدراسة (19.8) م°، وقد بلغ معدل درجة الحرارة لشهر كانون الثاني وهو أبرد الشهور (6.2) م°، وسبب هذا الانخفاض في درجات الحرارة هو تعرض المنطقة الى الكتل الهوائية الباردة القادمة من المرتفع السيبيري والأوربي وخاصةً في فصل الشتاء بالإضافة الى عامل الارتفاع لمنطقة الدراسة.

الجدول 5: المعدل العام للمعدلات الشهرية والسنوية لدرجات الحرارة (سيليزية°) لمحطات منطقة الدراسة (2012 – 2022).

الأشهر / الحرارة سليزية°	ك1	ك2	شباط	أذار	نيسان	أيار	حزيران	تموز	آب	أيلول	ت1	ت2	المعدل السنوي
العظمى	12.9	10.1	11.7	16.8	21.6	29.8	35.7	40.1	40.4	35.8	28.4	19.5	25.2
الصغرى	5.2	2.3	3.7	7.2	11.9	17.8	20.2	27.4	27.6	22.4	17.2	9.9	14.4
المعدل العام	9.05	6.2	7.7	12	16.8	23.8	27.9	33.8	34	29.1	22.8	14.7	19.8
المعدل الفصلي	7.7		17.5			31.9			22.2			19.8	



شكل 7. معدلات الحرارة لمنطقة الدراسة.

– دي مارتون: أستخدم دي مارتون قرينة الجفاف حسب المعادلة التالية (AlSamurai, 2008) بالاعتماد على بيانات محطة أتروش كحالة وسطية بين محطات منطقة الدراسة:

$$\text{قرينة الجفاف} = \frac{\text{كمية المطر السنوي}}{\text{متوسط درجة الحرارة السنوي} + 10}$$

$$\text{قرينة الجفاف} = \frac{805.3}{10 + 19.8} = 27.02$$

وعلى أساس نتائج المعادلة، فأن مناخ الأقاليم يكون كالتالي:

مناخ جاف = أقل من 5

مناخ شبه جاف = 5 – 10

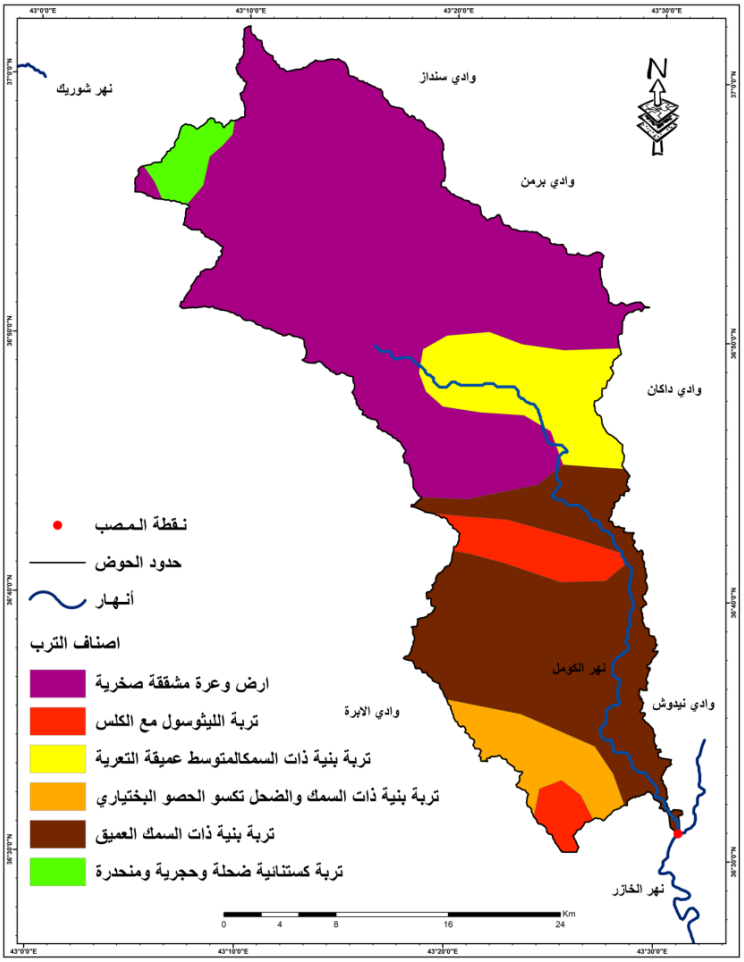
مناخ شبه رطب = 10 – 20

مناخ رطب = 20 – 30

إذن بالاعتماد على بيانات محطة أتروش كانت نتيجة المعادلة (27.02)، وهذا يشير بأن المنطقة تقع ضمن المناخ الرطب.

التربة:

يقصد بها الطبقة المفتتة من القشرة الارضية التي تكونت نتيجة لتفتت الصخور الاصلية عبر أزمنة جيولوجية قديمة بفعل العوامل المختلفة من (ماء وهواء وتجوية وتعرية) وأكسبها الخصائص الفيزيائية والكيميائية، وهي الطبقة الهشة التي لا يتجاوز عمقها بضع سنتمترات الى بضعة أمتار والتي يعيش بها الإنسان والنبات والحيوان الذي يتأثر بها ويؤثر عليها (Al-Muzaffar, 2016). تتكون التربة من العناصر الناتجة عن التجوية للصخور الأم تحت تأثير عوامل مناخية وبيولوجية (Anaab, 2006). وانطلاقاً من هذا، يمكن تصنيف الترب حسب المكان الذي نشأت فيهِ، وفي حوض وادي الكومل نجد ستة أنواع من الترب حسب الشكل (8) والجدول (6) التي تم استخراجها بالاعتماد على تصنيف و خريطة بيورنك (Burring, 1960) والمعدة من قبلهِ، وعن طريق برنامج Arc GIS Desktop 10.8 من خلال أنموذج الارتفاع الرقمي (DEM) وهي كالتالي:



الشكل 8. أصناف الترب في منطقة الدراسة حسب تصنيف بيورنك (Buringh, 1960).

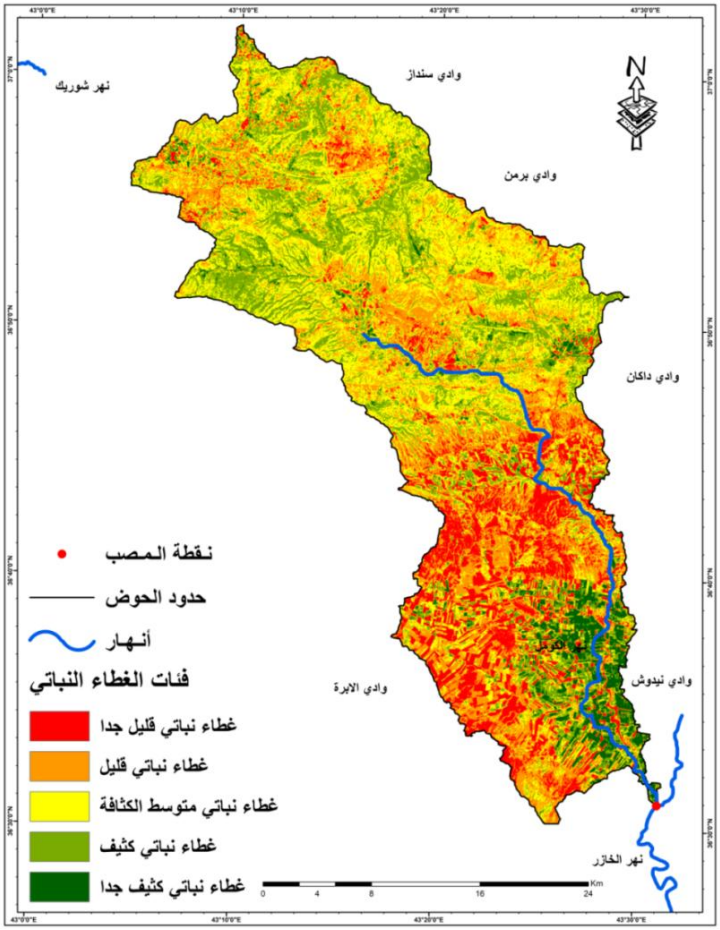
الجدول رقم 6: أصناف الترب في منطقة الدراسة حسب تصنيف بيورنك (Buringh, 1960).

ت	الصنف	المساحة (كم²)	النسبة المئوية (%)
1	أراضي وعرة مشققة صخرية	495.602	53.504
2	ترب الليثوسول مع الكلس	47.591	5.137
3	ترب بنية ذات السمك المتوسط عميقة التعرية	45.61	4.924
4	ترب بنية ذات السمك الضحل تكسو الحصو البختياري	82.050	8.857
5	ترب بنية ذات السمك العميق	236.087	25.488
6	ترب كستنائية ضحلة وحجرية ومنحدرة	19.350	2.090
	المجموع	926.29	100

الغطاء النباتي:

تم تصنيف الغطاء النباتي ضمن منطقة الدراسة حسب الشكل (9) والجدول (7) كما يلي:

1- أنواع الغطاء النباتي: يتكون الغطاء النباتي بشكل عام نتيجةً لتفاعل عدة عوامل طبيعية فيما بينها، منها المناخ والتضاريس والتربة والموارد المائية، ويكون نتيجة مباشرة لها. ويعد المناخ من أهم العوامل، إذ يساعد في تحديد أنواع النباتات الطبيعية من خلال معرفة الظروف المناخية السائدة في المنطقة. كما يؤثر النبات الطبيعي تأثيراً واضحاً في التصريف المائي للأحواض من خلال عرقلة الجريان المائي السطحي على سطح الأرض مما يؤدي الى زيادة نسبة التسرب في التربة. وعلى ضوء ما تقدم ظهرت أعلى نسبة غطاء نباتي (34.167)% وهو متوسطة الكثافة، وأقل نسبة غطاء نباتي (4.843) % وهو كثيف جداً حسب بيانات الجدول (7) المستخرجة من أنموذج الارتفاع الرقمي (DEM) عن طريق برنامج Arc GIS Desktop V 10.8.



الشكل 9. التوزيع الجغرافي للغطاء النباتي باستخدام مؤشر (NDVI) في منطقة الدراسة.

الجدول 7: مساحات ونسب الغطاء النباتي في منطقة الدراسة.

ت	كثافة الغطاء النباتي	المساحة (كم2)	النسبة المئوية (%)
1	غطاء نباتي قليل جداً	135.383	14.616
2	غطاء نباتي قليل	234.784	25.346
3	غطاء نباتي متوسطة الكثافة	316.486	34.167
4	غطاء نباتي كثيف	194.786	21.028
5	غطاء نباتي كثيف جداً	44.851	4.843
	المجموع	926.29	100

2– الخصائص المورفومترية لشبكات التصريف Morphometric Characteristics For Drainage Network: تشكل خصائص الأحواض المائية نظاماً مفتوحاً مثالياً يعكس درجة عالية من العلاقات المتبادلة ذات حساسية عالية قائمة بين الخصائص الحوضية من جهة وبينها وبين الخصائص البيئية من جهة أخرى (Salama, 2007). ويمكن توضيح ذلك من خلال الخصائص الحوضية التالية:

الخصائص المساحية والشكلية لحوض الكومل

1 الخصائص المساحية Areas Morphometric: إنّ لمساحة الأحواض النهرية أهمية كبيرة لأنها تؤثر بصورة مباشرة على حجم الجريان المائي، ومن المعلوم أنّ الأحواض المائية تتباين في مساحاتها طبقاً للظروف المناخية السائدة في المنطقة ونوعية الصخور التي تتكون منها الطبقات والحركات الأرضية التي حدثت في المنطقة وكذلك التضاريس الأرضية للمنطقة، بالإضافة إلى عامل الزمن، إضافةً إلى عوامل أخرى تساهم في تشكّل الحوض. كما أنّ الأحواض المائية تميل إلى زيادة مساحتهِ إذ تنشط فيها عملية الحت المائي في ظل الظروف المناخية الرطبة، وإذا كانت الصخور لينة يسهل تعريتها، كذلك إذا تعرضت إلى حركات تكتونية تؤدي إلى انخفاض أراضي مجاورة أو رفع أخرى مما تؤدي بالنتيجة إلى تغيير مجاري بعض الأودية والأنهار إلى أحواض أخرى (Albabawaty, 1995). كما نجد أن الأحواض

الكبيرة تقل فيها نسبة التضرس مما يقلل من معدلات الحت أو التعرية المائية (Adra, 2007). يوضح الجدول (8) ادناه هذه الخصائص.

الجدول (8) الخصائص المساحية لحوض وادي الكومل.

المساحة/ كم2	الطول المثالي/ كم	عرض الحوض/ كم	محيط الحوض / كم
926.29	65.22	14.2	213.96

أ- مساحة الحوض Basin Area: تُعد مساحة الحوض من المتغيرات المورفومترية المهمة التي لها تأثير واضح على حجم التصريف المائي داخل الحوض. وتوجد علاقة طردية بين كل من مساحة الحوض وحجم التصريف المائي في الحوض (Aldaraji, 2010). وتختلف المساحات الحوضية التي تغذي الأنهار بالمياه من إقليم إلى آخر (Al-Maliki, 2016) ، كما يمكن الاستفادة منها في القياسات المورفومترية الأخرى مثل (كثافة التصريف، الكثافة العددية والمعامل الهبسومتري وغيرها من الخصائص). وتبلغ المساحة الكلية لحوض الدراسة (926.29) كم^2. تختلف الأحواض في مردودها المائي ومقدار مساهمتها في الكثافة التصريفية. وبالنظر لمساحة الحوض الحالي، فأن حجم التصريف المائي وكميات الرواسب تكون كبيرة في الحوض لكون مساحته كبيرة ويحتوي على كميات كبيرة من الرسوبيات بسبب كبر حجم الحوض.

ب- طول الحوض Basin Length: هو الخط المستقيم الذي يبدأ من مصب الحوض إلى أبعد نقطة في محيطهِ. ولطول الحوض دور مهم في عملية الجريان السطحي، فهو يتحكم بمدة تفريغ الحوض لمياههِ وحمولتهِ الترسيبية، كما تتناسب معدلات التسرب لطبقات التربة والتبخر مع طول الحوض تناسياً طردياً وذلك لتباطؤ سرعة المياه الجارية بالاتجاه نحو مصب الحوض بسبب قلة عامل انحدار السطح واتساع القنوات والمجاري المائية (Al-Shammari). وللأحواض المائية نوعان من الأطوال وهما الطول الحقيقي والطول المثالي. ومن خلال الدراسة والاطلاع، فأنّ زيادة طول المجرى يقلل من خطر الفيضان في القنوات والمجاري المائية لضياعهِ أثناء الجريان عن طريق فقدان كميات من المياه عن طريق الترشح لطبقات الأرض وتبخر كميات أخرى بفعل الحرارة.

ج- عرض الحوض Basin Width: هو المسافة المستقيمة العرضية بين أبعد نقطتين في محيط الحوض. وفي هذا الجانب لا يمكن الاعتماد على قياس أحادي البعد لعرض الحوض نظراً لاختلاف أشكال أحواض المياه بسبب تباين الشكل وكثرة المنحنيات والتعرجات في محيط الحوض (Al-Jubouri, 2024). يعّد عرض الحوض من المتغيرات المورفومترية المهمة التي تساعد في تحديد شكل الحوض من خلال النسبة بين مساحة الحوض (كم^2) إلى طول الحوض (كم). من أجل الدقة في الاستنتاج وبيان أشكال الأحواض المائية ومحيطها، فقد تمَ الاعتماد على المعادلة التالية (Aldaraji, 2010) :

$$\text{متوسط العرض} = \frac{\text{مساحة الحوض كم}^2}{\text{طول الحوض كم}}$$

وأتضحَ من خلال تطبيق المعادلة وكما موضح في الجدول (8) بأنّ متوسط عرض الحوض بلغَ (14.2) كم. أن زيادة عرض الحوض يؤدي إلى زيادة ما يتلقاهُ من كميات التساقط ومن ثمَ زيادة الجريان السطحي، كما ان له تأثيراً في زيادة معدل التبخر.

د- محيط الحوض Basin Perimeter: يُعد محيط الحوض عاملاً مهماً في القياسات المورفومترية التي تُعبر عن أشكال الأحواض التصريفية وتضاريسها. ويتم قياسه بتتبع خطوط تقسيم المياه التي تفصل الحوض عن الأحواض المجاورة، أي انه هو الإطار الخارجي الذي يُحيط بالحوض ويفصل بينهُ وبين الأحواض الأخرى (Al-Shammari, 2021). وبزيادة طول المحيط يزداد انتشار الحوض وتوسعه، ثمَ يزداد تطوره الجيومورفي. من خلال الجدول (8) بلغَ محيط الحوض في منطقة الدراسة (213.96) كم.

2- الخصائص الشكلية Shapes Morphometric: تعكس أشكال الأحواض النهرية في أغلب الأحيان خصائص تكوينها الجيولوجي في مرحلة مبكرة، وعوامل أخرى في مرحلة متأخرة، ويؤثر الشكل الذي يتخذهُ الحوض على الخصائص التصريفية للمياه وعلى العمل الحتي لهُ، وتعّد الخصائص الشكلية أحد العوامل المؤثرة في هيدرولوجية الروافد النهرية وخصائصها المورفومترية فهي تؤثر على وقت التركيز الذي يحددهُ قوة وسرعة ذروة التصريف النهري في الحوض فتزداد هذهِ الفيضانات قوةً مع التناقص في زمن التركيز نتيجةً للانخفاض المحتمل في كمية المياه المتبخرة والمتسربة من التدفقات المائية في مجاري الروافد النهرية (Al-Azzawi, 2021).

نسبة المطابقة Fitness Ratio: يُقصد بهِ نسبة طول القناة الرئيسة على محيط الحوض المائي وهي مقياس لمدى نسبة تطابق الطبوغرافية، ويوضح مدى نسبة التطابق التضاريسي للحوض، تتراوح قيمها ما بين (0 – 1) وتشير القيم المنخفضة أو القريبة من الصفر إلى تضاريس وعرة ومنحدرات شديدة، في حين تشير القيم المرتفعة أو القريبة من الواحد الصحيح إلى تضاريس منبسطة نسبياً وقليلة الانحدار في الحوض (Salman, 2022) ، ويمكن التعبير عن نسبة المطابقة بـ (RF) من خلال المعادلة الآتية (Hasan, 2023):

$$RF = Lc / P$$

حيث أن: Lc= طول القناة الرئيسي (كم)؛ P = محيط الحوض

بعد تطبيق المعادلة أعلاه تم الحصول على النتيجة وبلغَت نسبة المطابقة في الحوض (0.30) وهذا دليل بأنّ النهر ينحدر من مناطق ذات تضاريس وعرة وأراضي شديدة الانحدار.

ب- نسبة الاستدارة Circularity: إن هذهِ القرينة أقترحها ميلتون (Melton, 1958) ومعرفة نسبة الاستدارة تبين مدى اقتراب أو ابتعاد شكل الحوض من الشكل الدائري، إذ كلما أقترب قيم نسبة الاستدارة من العدد الواحد الصحيح يعني اقتراب الحوض من الشكل الدائري، وفي هذهِ الحالة يُوصف الحوض بأنهُ بلغَ قمة التطور والحت الجانبي والتراجعي من خلال مناطق تقسيم المياه وتطور الجريانات القنوية المجاورة، وكلما أقترب من الصفر يعني ابتعاد الحوض عن الشكل الدائري (Al-Taai, 2017).

ويمكن حساب نسبة الاستدارة (Rc) من خلال العلاقة التالية (Kartick and Sutapa, 2019) :

$$Rc = 4\pi \ A/P^2$$

حيث أن: A= مساحة الحوض؛ π = 3.14؛ P= محيط الحوض

من خلال المعادلة كانت نتيجة نسبة الاستدارة في الحوض (0.25)، بما أنّ النتيجة قريبة من الصفر،فهذا يعني ابتعاد شكل الحوض عن الشكل الدائري ودليل على أنّ خط تقسيم المياه متعرج وربما يحصل أسر نهري في الحوض، وأن الحوض في بداية دورته الحتية.

ج- نسبة الاستطالة Elongation Ratio: تصف نسبة الاستطالة امتداد مساحة الحوض المائي بمقارنتها بشكل مستطيل، وتنخفض هذهِ النسبة عادةً في الأحواض الطويلة، بينما تزداد في الاحواض التي يختلف عرضها مع امتدادها، أي يزيد عرضها باتجاه مساواتهِ مع طول الحوض. كما تعبّر استطالة الحوض عن شكل الحوض وهو يُعد انعكاساً لأثر الخصائص الجيولوجية والبنيوية إلى جانب أهميتهِا في معرفة سرعة الوصول إلى قمة الفيضان في حالة حدوث السيل، كما تفيد في تحديد المراحل الحتية التي وصل إليها الحوض النهري. وتتراوح نسبة الاستطالة مابين (0 – 1)، فإذا كانت النتيجة أقرب من الواحد الصحيح، يكون الشكل قريباً من الاستطالة، وإذا كانت قريبة من الصفر، كان لهُ شكل مختلف (Alganay, 2013).

ويمكن الحصول على معامل الاستطالة (Re) من خلال المعادلة التالية (Kartick and Sutapa, 2019) :

$$Re = \frac{\sqrt[2]{A/\pi}}{LB}$$

حيث أن: A= مساحة الحوض؛ π = 3.14؛ LB= طول الحوض

من خلال نتيجة المعادلة، كان معامل الاستطالة مساوياً لـ (0.53)، وكما مبين في الجدول (9)، فهو قريب من الصفر، مما يدل على اقتراب الحوض من الاستطالة، ومثل هذهِ الأشكال تميل إلى تقليل أطوالها وزيادة أعدادها خاصةً في المراتب الدنيا، ويزداد طول المجرى الرئيس للحوض، مما يعمل على تناقص الصبيب المائي بسبب طول المسافة التي يقطعها المجرى والزمن المستغرق ويؤدي إلى زيادة الترب فيه وزيادة التبخر من مياههِ.

د- نسبة تماسك المحيط: يُعد مقياس نسبة تماسك المحيط مقياساً آخر لتأكيد اقتراب الحوض من الشكل الدائري أو الابتعاد منهُ. فكلما كان الناتج قريباً من العدد (1) الصحيح، أبتعدَ شكل الحوض عن الشكل الدائري ويتم استخراجهِ من المعادلة التالية (Ismael, 2017) :

$$\text{نسبة تماسك المحيط} = \sqrt{\frac{1}{\text{نسبة تماسك المساحة (الاستدارة)}}}$$

اظهرَت نتيجة المعادلة اعلاه اقتراب النتيجة من العدد الواحد الصحيح كما في الجدول (9)، وهذا يعني أنّ الحوض ابتعدَ عن الشكل الدائري، وهو دليل على زيادة نسبة تعرجات محيطهِ وقلة درجة تناسقهِ.

هـ- معامل شكل الحوض Form Factor Ratio: يعطي هذا المعامل فكرة عن مدى تناسق و انتظام الشكل العام لأحواض التصريف المائي من خلال العلاقة بين مساحة الحوض وطول الحوض ، فتشير القيم المنخفضة البعيدة عن العدد واحد الصحيح إلى عدم تناسق و انتظام شكل الحوض وتغير عرضهِ من منطقة إلى أخرى ، واقترابه من الشكل الثلاثي ، بينما القيم المرتفعة القريبة من العدد واحد الصحيح تشير إلى اقتراب الشكل من شكل المربع ، فإذا كانت النتائج تتراوح ما بين (0.1 – 0.4) فأن شكل الحوض قريب من شكل المثلث شديد التعرج ، أما إذا كانت النتائج ما بين (0.4 – 0.6) فأن شكل الحوض أقرب إلى الشكل المربع شديد التعرج ، وإذا كانت النتيجة أكبر من (0.6) فأن شكل الحوض مربع شديد الانتظام، ويتم استخراج معامل شكل الحوض من خلال المعادلة التالية (Al-Saadi, 2023) وضعها Horton عام (1932) :

$$\frac{\text{كم}^2\text{الحوض}}{\text{كم}}$$

بعد تطبيق المعادلة ظهرت النتيجة (0.21)، لذا فأن شكل الحوض غير منتظم وقريب من شكل المثلث شديد التعرج.

الجدول 9: الخصائص الشكلية لحوض وادي الكومل.

نسبة المطابقة	معامل الشكل	نسبة الاستدارة	نسبة الاستطالة	نسبة تماسك المحيط	معامل الانبعاج
0.30	0.21	0.25	0.52	1	1.15

و- معامل الانبعاج Lemniscates: يدل معامل الانبعاج على العلاقة بين مربع طول حوض التصريف إلى أربعة أمثال مساحتهِ كما في المعادلة أدناه، وهو يدل على مدى التشابه بين شكل الحوض التصريفي والشكل الكمثري، نظراً إلى أنّ معظم أحواض التصريف المتناسقة الشكل تميل إلى الشكل الكمثري وليس الدائري تماماً، حيثُ تدل القيمة المرتفعة للمعامل إلى الزيادة في الاستطالة لحوض التصريف، وسيادة عمليات النحت الرأسي أكثر من النحت الجانبي، بينما تدل القيم المنخفضة إلى زيادة انبعاج شكل الحوض، مما يدل على زيادة أطوال المجاري وأعدادها في الرتب الدنيا مع زيادة عمليات النحت الرأسي والجانبي (Hamid, 2016) . يمكن إيجاد معامل الانبعاج (*K*) من خلال تطبيق المعادلة التالية:

$$K = \frac{LB^2}{4 \times A}$$

حيث أن: LB^2= مربع طول الحوض؛ A= مساحة الحوض

ظهرت نتيجة المعادلة (1.15)، وبما أنّ القيمة أكبر من واحد، فإن الحوض يتميز بانبعاج شديد وزيادة استطالة حوض التصريف وبالتالي قلة أعداد مجاريها المائية وقلة أطوالها وخاصةً في المراتب الدنيا، وسيادة عمليات النحت الرأسي أكثر من النحت الجانبي.

الخصائص التضاريسية للحوض Basin Relief Characterizes

تُعّد هذهِ من الخصائص المهمة في الدراسات المورفومترية، ولنتائج هذهِ الخصائص دلائل مهمة فهي تساعد في معرفة القدرات الحتية للمجرى المائي وتقدير حجم الرواسب المنقولة، فضلاً عن معرفة طبيعة ونوع الأشكال الأرضية المرتبطة بها، وكذلك معرفة المرحلة الجيومورفية التي يمر بها الحوض المائي (Al-Azzawi, 2021).

1- معدل التضرس Relief Ratio : (يعرف ايضاً بنسبة التضرس أو معامل التضرس) وهو أحد المقاييس المهمة لمعرفة الطبيعة الطبوغرافية لأي منطقة. تُعد قيمته مؤشراً جيداً لتقدير حجم الرواسب المنقولة، إذ تزداد نسبتها مع زيادة التضرس، وتساهم في تكوين الأشكال الجيومورفية المختلفة، وتعمل على زيادة سرعة وصول الناتج المائي نحو الانحدارات القليلة أو الأراضي المنبسطة باتجاه المصب، كما لها دور في زيادة فعالية التعرية النهرية وما يرتبط بها من نقل كميات كبيرة من الرواسب، وتنخفض نسبة التضرس في الأحواض ذات المساحة الكبيرة، وتدل القيم المرتفعة لنسبة التضرس إلى زيادة الكثافة التصريفية وعمق المجاري المائية (Salman, 2021). ويمكن التعبير عن معامل أو نسبة التضرس من خلال إيجاد الفرق بين أخفض نقطة وأعلى نقطة في الحوض مقسوماً على طول الحوض، ويمكن الحصول على معامل التضرس من خلال تطبيق المعادلة التالية (Al-Dulaimi, 2017):

$$\text{معامل التضرس} = \frac{\text{تضرس الحوض } (\text{أعلى نقطة} - \text{أدنى نقطة})}{\text{طول الحوض } (\text{م})}$$

من خلال نتيجة المعادلة التي بلغَ (19.69) فهي منخفضة مما يدل على انخفاض بحجم الرواسب المنقولة وبطء وصول الناتج المائي نحو الانحدارات القليلة والأراضي المنبسطة.

2- التضاريس النسبية: وهي تعبير عن العلاقة بين قيمة التضرس ومحيط الحوض، حيثُ تشير القيم المنخفضة إلى ضعف مقاومة الصخور ونشاط عمليات التعرية، في حين تدل القيم المرتفعة على صلابة الصخور ومقاومتها لنشاط عمليات التعرية، وتعطي هذه النسبة صورة واضحة عن مساحة الحوض، فتدل القيم المرتفعة على صغر المساحة الحوضية، في حين تدل القيم المنخفضة على كُبر المساحة الحوضية، وناتج المعادلة هو إيجاد علاقة ارتباط سالبة بين التضاريس النسبية ودرجة مقاومة الصخور لعمليات التعرية عندَ تشابه الأحوال المناخية، كما أنهُا تُعبر عن درجة التضرس الطبوغرافي في الحوض، ويتم إيجاد التضرس النسبي من خلال المعادلة التالية (Al-Dulaimi, 2017):

$$\text{التضاريس النسبية} = \frac{\text{تضاريس الحوض /م}}{\text{محيط الحوض/ كم}}$$

بلغَ القيمة (6) (الجدول 10) وهي قليلة وتدل على ضعف مقاومة الصخور ونشاط عملية التعرية، كما تدل على كبر المساحة الحوضية.

الجدول 10: الخصائص التضاريسية لحوض وادي الكومل.

أعلى ارتفاع / م	أدنى ارتفاع / م	التضرس / م	طول الحوض /كم	محيط الحوض /كم	معامل التضرس	التضاريس النسبية م/كم	قيمة الوعورة	التكامل الهبسومتري
1589	305	1284	65.22	213.29	19.69	6	2.16	0.72

3- قيمة الوعورة Ruggedness Number: تشير قيمة الوعورة إلى مدى تضرس الحوض ومدى انحدار الحوض المائي فيهِ ويعني ارتفاع هذهِ القيمة شدة التضرس وسيادة التعرية المائية ونقل الرواسب من المنابع العليا للأحواض إلى أسفل المنحدرات، أي أنّ قيمة الوعورة تزداد بزيادة الكثافة التصريفية في الحوض من جهة وزيادة التضرس ومن ثم زيادة عملية الحت المائي ونقل الرواسب. ويتم الحصول على قيمة الوعورة من خلال المعادلة الآتية (Ismael, 2017):

$$\text{قيمة الوعورة} = \frac{\text{تضاريس الحوض x الكثافة التصريفية كم / كم}^2}{1000}$$

من خلال المعادلة ظهر النتيجة (2.16) وهي قيمة مرتفعة تدل على شدة التضرس للحوض وخاصةً في الأجزاء الشمالية منه أي في مناطق المنابع وسيادة التعرية المائية فيهِ وتدل كذلك على نقل الرواسب من المنابع العليا الشديدة الانحدار نحو أسفل المنحدرات وزيادة الكثافة التصريفية في هذهِ المناطق الوعرة.

4- التكامل الهبسومتري Hypsometric Integral : يُعد التكامل الهبسومتري من أدق المعاملات المورفومترية تمثيلاً للفترة الزمنية التي قطتعها الدورة النحتية للأحواض التصريفية، فضلاً عن قياسهِ لدرجة التضرس الحوضي وإعطاء فكرة واضحة عن الارتباط بين الأشكال التضاريسية الحالية والأشكال التضاريسية القديمة. من خلال نتائج هذا المعامل يمكن معرفة المرحلة المورفولوجية التي وصلَ إليها الحوض كلياً أو أيةِ تباينات أخرى في أجزاء الحوض نفسهِ، فالمناطق الشديدة الانحدار تدل على أنها مازالت في مرحلة الشباب وبداية النضوج، بينما تشير الأجزاء القليلة الانحدار على أنها وصلت إلى مرحلة متقدمة من الدورة النحتية (Al-Saadi, 2023)، إذ تُشير القيم المرتفعة للمعامل إلى زيادة مساحة أحواض التصريف وانخفاض المدى التضاريسي لهُ مما يدل على التقدم العمري لهذهِ الأحواض. ويتم حساب المعامل وفق المعادلة التالية :

$$\text{التكامل الهبسومتري} = \frac{\text{مساحة الحوض / كم}^2}{\text{تضاريس الحوض / م}}$$

أظهرت نتيجة المعادلة قيمة (0.72) وهي تشير إلى كبر مساحة الحوض وتقدم عمره ووصولهِ إلى مرحلة نضج متقدمة ومرحلة متقدمة من الدورة النحتية.

خصائص الشبكة النهرية : يمكن دراسة الشبكة المائية للحوض من خلال الخصائص التالية:

1- المراتب النهرية Stream Order: صنفت المراتب النهرية وفقاً لطريقة (ستريلر)، الذي يبين أنّ الأودية والمجاري الصغيرة لاتلتقي بأي مجرى أخر ببدايتها وهي تعد مرتبة أولى، وبالتقاء مجريين من المرتبة الأولى يتشكل مجرى المرتبة الثانية، وباتحاد مجريين من المرتبة الثانية تتشكل المرتبة الثالثة ... وهكذا تتشكل بقية المراتب من التقاء مجاري أدنى منها لتشكل مجرى أعلى مرتبةً، حتى بلوغ الحوض أعلى مرتبة نهرية (Al-Jaaf, 2005)، يبين الجدول (11) أعداد ومراتب المجاري النهرية للحوض.

الجدول 11: المراتب النهرية وأعداد المجاري ونسبة التشعب لحوض وادي الكومل.

الحوض	أعداد المجاري المائية بحسب رتبها في الحوض						أجمالي عدد المجاري
	الأولى	الثانية	الثالثة	الرابعة	الخامسة	السادسة	
الكومل	1242	570	292	13	3	1	2121

2- نسبة التشعب Bifurcation Ratio: هي درجة تفرع الشبكة النهرية أو مقدار التباين الحاصل بين فروع المراتب المختلفة للحوض، وتقاس حسب طريقة (Harton) المعدلة، وهي عبارة عن النسبة بين عدد المجاري في مرتبة ما على عدد المجاري في المرتبة التي تليها، وتعد هذهِ النسبة أحد العوامل التي تتحكم في معدل التصريف الذي بدورهِ يؤثر في تشكيل المراوح الفيضية، حيثُ زيادة معدل التصريف تتبعها زيادة في طاقة المياه وقدرتها على القيام بعمليات التعرية لأسطح أحواض التصريف (Slman, 2022).

$$\text{نسبة التشعب} = \frac{\text{مجموع أطوال المجاري في مرتبة ما}}{\text{عدد المجاري في المرتبة التي تليها}}$$

بلغَ نسبة التشعب (6.79) (الجدول 12) وهي أكثر من (5) حسب الحدود التي وضعها ستريلر، مما يدل على أنّ الحوض يقع ضمن المنطقة الجبلية الشديدة التضرس والانحدار والتقطع خاصةً في مناطق منابع الحوض في أجزائهِ الشمالية، وشكلهِ القريب من الاستطالة الذي زاد من نسبة التشعب مما ساعد على تمرير وحركة المياه بمدة زمنية طويلة.

الجدول 12: نسبة التشعب لحوض وادي الكومل.

الحوض	الرتب						نسبة التشعب
	1	½	3/2	4/3	5/4	6/5	
وادي الكومل		2.18	1.95	22.46	4.34	3	6.79

3– أطوال المجاري Stream length : إنّ لدراسة أطوال المجاري المائية أهمية كبيرة في الدراسات المورفومترية إذ أنّ هناك علاقة بين حوض المجرى المائي وأطوال المجاري المختلفة، وإنّ مجاري المرتبة الأولى تكون أقصر طولاً، وكلما تقدمت رتبة المجرى المائي زادَ طول ذلك المجرى، ويبين الجدول (13) أطوال المجاري (كم) حسب المراتب النهرية لحوض منطقة الدراسة.

الجدول 13: أطوال المجاري/ كم حسب المراتب النهرية لحوض الكومل.

الحوض	أطوال المجاري المائية بحسب رتبها في الحوض						أجمالي أطوال المجاري
	الأولى	الثانية	الثالثة	الرابعة	الخامسة	السادسة	
الكومل	823.60	397.67	166.03	73.72	41.96	52.91	1555.89

4– كثافة التصريف Drainage Density:

أ– كثافة الصرف الطولية Longitudinal Drainage Density : تمثل كثافة الصرف الطولية مجموعة أطوال المراتب النهرية في الحوض إلى مساحتهِ الكلية، ويمكن استخراجها من خلال المعادلة التالية (Al-Majidi, 2023) :

$$\text{كثافة الصرف الطولية} = \frac{\text{مجموع أطوال المجاري / كم}}{\text{مساحة الحوض / كم}^2}$$

بلغَ الكثافة التصريفية للحوض (1.68) كم/كم^2 وهي كثافة منخفضة بحسب الحدود التي وضعها ستريلر، ويعود هذا إلى الظروف المناخية التي تؤثر على تشكل المجاري المائية وكذلك النفاذية العالية التي تتميز بها المنطقة بسبب نوعية التكوينات الجيولوجية والصخرية التي تتميز بنفاذية عالية نوعاً ما منها الصخور الرملية والصخور الكلسية التي تتشكل منها منطقة الدراسة.

ب– كثافة الصرف العددية Numerical Drainage Density : وتسمى أيضاً التكرار النهري، ويقصد بها النسبة بين عدد الجداول المائية لجميع الرتب المسجلة للحوض إلى مساحتهِ، إنّ زيادة عدد المجاري بواسطة التعرية يؤدي إلى زيادة في أطوال مجاريها ويمكن التعبير عنها من خلال المعادلة التالية (Al-Majidi, 2023):

$$\text{كثافة الصرف العددية} = \frac{\text{مجموع أعداد المجاري}}{\text{مساحة الحوض / كم}^2}$$

بحسب نتيجة المعادلة بلغَ الكثافة العددية للصرف (2.29) مجرى/كم (الجدول 14). لذا، فأن هذهِ الزيادة في العدد تعكس زيادة عامل التعرية الذي يؤدي إلى زيادة عدد المجاري وأطوالها، كما يؤدي إلى الزيادة في كمية التصريف المائي للحوض.

الجدول 14: كثافات التصريف الطولية والعددية لحوض وادي الكومل.

مجموع أطوال المجاري/ كم	مجموع أعداد المجاري	المساحة / كم^2	الكثافة الطولية كم/ كم^2	كثافة كثافة الصرف	الكثافة العددية للصرف (مجرى/ كم)
1555.89	2121	926.29	1.68	منخفض	**2.29**

5- النسيج الحوضي Basin Texture: إنّ دراسة مؤشر النسيج الحوضي يتأثر بمجموعة من العوامل، لاسيما العوامل المناخية وطبيعة التراكيب الخطية وخصائص التربة والغطاء النباتي (Al-Zarfi, 2021)، ويوضح نسيج شبكة التصريف وكثافة الوحدة المساحية فضلاً عن شدة التطور النحتي للمجاري المائية، ويستخرج من خلال المعادلة الآتية (Al-Zuhairi, 2020):

$$\text{النسيج الحوضي} = \frac{\text{أعداد أودية الحوض}}{\text{محيط الحوض / كم}}$$

بعد تطبيق المعادلة أعلاه ظهر لدينا النتيجة (9.94)، وحسب تصنيف (Smith)، فأن الحوض يقع ضمن الفئة الخامسة ذات النسيج الناعم جداً.

6- معامل الانعطاف Reflecting Factor: هو نسبة الطول الحقيقي للمجرى المائي إلى الطول المثالي، إذ يُقصد بالطول الحقيقي هو المسافة التي يقطعها المجرى من منبعهِ إلى مصبهِ على اليابسة، أما الطول المثالي فهو يمثل أقصر مسافة يسلكها المجرى ما بينَ المنبع والمصب، ويُحسب من المعادلة التالية (Al-Zuhairi, 2020):

$$\text{معامل الانعطاف} = \frac{\text{طول المجرى الحقيقي / كم}}{\text{طول المجرى المثالي / كم}}$$

من خلال النتيجة التي تم الحصول عليها من تطبيق المعادلة بلغَ معامل الانعطاف (1.34) وبهذا فإن شكل النهر ملتوي.

الجدول 15: النسيج الحوضي ومعامل الانعطاف لحوض وادي الكومل.

طول النهر الحقيقي	طول النهر المثالي	النسيج الحوضي	نوع النسيج	معامل الانعطاف	شكل النهر
87.43	65.22	9.94	ناعم جداً	1.34	**ملتوي**

أنماط التصريف النهري لحوض منطقة الدراسة

تُعد أنماط التصريف للأنهار خلاصة التأثيرات المناخية والتضاريسية والبشرية والعوامل الطبيعية الأخرى على أحواض التصريف ومن أهم هذهِ العوامل التي تتحكم بأشكال التصريف للأنهار (Jarei and Diya al-din, 2018) هي:

1- طبيعة الانحدار
2- اختلاف التراكيب الصخرية ونظام بنية الطبقات
3- مدى التجانس الصخري
4- الظروف المناخية التي يتعرض لها الإقليم ولاسيما التساقط
5- التطور الجيومورفي لحوض التصريف
6- تأثير حركات الرفع، والتصدع في تعديل شكل التصريف النهري

وأهم أنماط التصريف النهري هي:

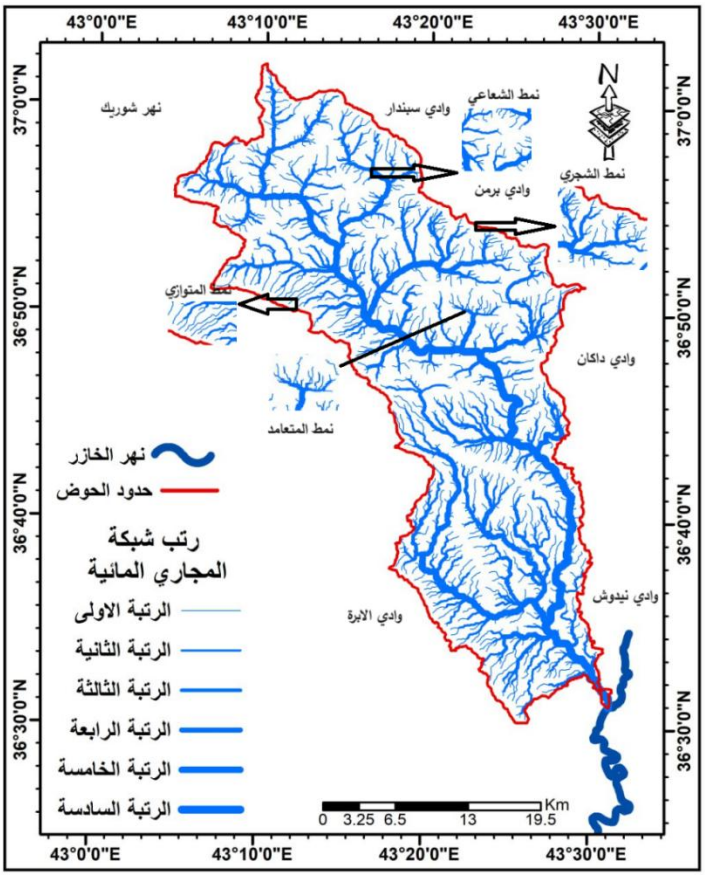
1- نمط التصريف المتوازي Parallel Drainage Pattern: مجاري طويلة تجري بشكل متواز وتفصل بينها مسافات متقاربة ومتساوية.

2- نمط التصريف الشجري Dendritic Drainage Pattern: يعد من أكثر الأنماط انتشاراً ويتميز بتشعب الروافد النهرية بشكل غير منتظم يشبه تفرعات الشجرة، وعادةً ما تكون الزوايا التي تكونها الوديان غير قائمة، وهذا النوع من التصريف

ينشأ فوق الصخور الرسوبية بشكل خاص والأراضي التي تكون قليلة التضرس إلى سهلية وتكون البنية فيها ضعيفة ومتجانسة صخريا. وظهرَ هذا النمط في العديد من مناطق حوض منطقة الدراسة (Al-Dulaimi, 2017).

3- نمط التصريف الشعاعي Radial Drainage Pattern: تتجه المجاري التي تنحدر من أعلى القمم الجبلية في اتجاهات عديدة متخذةً شكلاً شعاعياً.

4- نمط التصريف المتعامد: يتكون هذا النوع في المناطق التي تحتوي على فواصل وشقوق وصدوع التي تتبعها المجاري وتلتقي مع بعضها بزوايا شبه قائمة.



الشكل 10. الشبكة النهرية وأنماط التصريف لحوض وادي الكومل.

الاستنتاجات

1- أثرت العوامل الطبيعية من بنية جيولوجية وطبوغرافية السطح والانحدار وعناصر المناخ في الخصائص المورفومترية والكثافة التصريفية للحوض.

2- ينبع حوض نهر الكومل من المناطق الجبلية في شمال وشمال شرق العراق وهي من الانهار المؤقتة الجريان، وبلغَ مساحة حوضهِ (926.29 كم^2)، وبارتفاع بلغَ بين (305 – 1589) م فوق مستوى سطح البحر.

3- وجود تباين في الخصائص الشكلية للحوض منها (الاستدارة، الاستطالة، معامل شكل الحوض، معامل الانبعاج، الاندماج، قيمة الوعورة والتكامل الهبسومتري).

4- تتباين الخصائص التضاريسية لحوض نهر الكومل من حيث (التضرس، نسبة التضرس، قيم الوعورة، التكامل الهبسومتري)، إذ يمر النهر بمرحلة الشباب وبداية النضج حسب نتائج التكامل الهبسومتري.

5- أظهرت شبكة التصريف عدة أنماط تصريفية تبعاً للبنية الجيولوجية وتأثير درجة الانحدار وهي (الشجري، المتوازي، الشعاعي والمتعامد).

6- ينتهي حوض وادي الكومل بالمرتبة السادسة وفقاً لتصنيف ستريلر، ويعد من الأحواض الكبيرة في المنطقة حيثُ بلغ مساحتهُ (926,29) كم^2 وهو متباين في خصائصه المساحية والشكلية والتضاريسية وخصائص الشبكة التصريفية وفقاً للخصائص الطبيعية المختلفة للحوض.

7- إن استخدام برنامج Arc GIS واداة التحليل المورفومتري Morphometric Toolbox اعطت كفاءة ودقة وسرعة كبيرة في اجراء التحليل الموفومتري للأحواض الكبيرة في المساحة، حيث من الصعوبة إجراء مثل هذهِ التحليلات بالطرق التقليدية.

8- ظهرَ اثنا عشرَ تكويناً جيولوجياً في حوض منطقة الدراسة تعود إلى عدة عصور وأزمنة جيولوجية، وتتميز هذهِ التكوينات بمكونات وخصائص مختلفة لها تأثير كبير في أشكال السطح والخصائص المورفومترية للحوض في منطقة الدراسة.

التوصيات

من خلال النتائج التي توصل إليها البحث نوصي بما يلي:

1- ضرورة إجراء دراسة هيدرولوجية تفصيلية وإنشاء محطات هيدرولوجية تهدف إلى تقدير حجم التصريف المائي والاستفادة منها في المشاريع التنموية، لكون أغلب الوديان والمجاري المائية في المنطقة موسمية الجريان.

2- العمل على بناء السدود والخزانات المائية والسدود الترابية الصغيرة تهدف إلى حصاد المياه الأمطار في موسم التساقط والاستفادة منها في تنمية النشاط الزراعي والثروة الحيوانية وتغذية المياه الجوفية.

3- دراسة كمية ونوعية الرواسب المنقولة خلال مواسم الفيضانات التي تحدث في الوادي، وإجراء مسح أرضي للرواسب المنقولة للاستفادة منها في الصناعات المختلفة.

References

Al-Maamouri, M.K.M., 2016. Geomorphological analysis of material movement of the northeastern slopes of the Makhoul hill range overlooking the village of Mashak using digital modeling, PhD Thesis (unpublished), College of Education, Tikrit University, 155 P. (In Arabic)

Adra, N.A.M., 2007. Geomorphology of the upper river drainage basin of the Hebron Valley, MSc Thesis (unpublished), An-Najah National University, Nablus, Palestine, 118 P. (In Arabic)

Al-Azzawi, H.M.F., 2021. A geomorphological model for estimating the volume of surface runoff in the Wadi Izyana Basin in Erbil Governorate, MSc Thesis (unpublished), College of Education for Girls, University of Baghdad, 162 P. (In Arabic)

Albabawaty, A.A.H., 1995. Wadi Al-Ajeej Basin in Iraq and uses its terrestrial forms, PhD Thesis (unpublished), College of Arts, University of Baghdad, 164 P. (In Arabic)

Aldaraji, S.A.M., 2010. Fundamentals of Geomorphology, Kunuz Al-Ma'rifa, Amman, Jordan, 1st Edition, 134 P. (In Arabic)

Al-Dulaimi, A.M.K., 2018. A geomorphological analysis of the land slopes in Shaqlawa district and its impact on human activity using remote sensing techniques and geographic information systems (unpublished PhD Thesis), Anbar University, College of Education for the Humanities, 111 P. (In Arabic)

Al-Dulaimi, K.H., 2017. Rivers, an applied geohydromorphometric study, Safaa Publishing and Distribution House, Amman, Jordan, 1st edition, 92 P. (In Arabic)

Al-Dulaimi, K.H., 2018. Landforms, a field study, Anbar University, Iraq, Safaa Publishing and Distribution House-Amman, 1st Edition, 190 P. (In Arabic)

Alganay, J.M., 2013. Geomorphology of the Wadi Suf El-Jin Basin, MSc Thesis (unpublished), Faculty of Arts, University of Sirte, 155 P. (In Arabic)

Al-Halbousi, F.J.K., 2005. Geomorphology of the Wadi Al-Asadi Basin, MSc Thesis (unpublished), Ibn Rushd College of Education, University of Baghdad, 122 P. (In Arabic)

Al-jaf, J.R.A.F., 2005. Geomorphology of Barakra Mountain and its river basins and its applications, unpublished MSc Thesis, College of Arts, University of Baghdad, 132 P.

Al-Janabi, B.A.A.H., 2016. Geomorphological evaluation of the slopes of the Garh Range, PhD Thesis (unpublished), College of Education - Ibn Rushd, Baghdad, 221 P. (In Arabic)

Al-Jubouri, S.I.I.A, 2024. Geomorphological assessment of the Wadi Amlak Basin in Dohuk Governorate, MSc Thesis (unpublished), College of Education for Human Sciences, Tikrit University, 175 P. (In Arabic)

Allawi, S.J.H., 2021. Geomorphology of Wadi Badush Basin (Baghal), MSc Thesis (unpublished), College of Education, University of Mosul, 130 P. (In Arabic)

Al-Majidi, M.H.J., 2023. Hydrological indicators of the main morphometric parameters of the Diyala River Basin, MSc Thesis (unpublished), College of Education for Human Sciences, University of Basra, 174 P. (In Arabic)

Al-Maliki, A.S, 2016. Basics of Geomorphology, Al-Wadah Publishing House, Jordan, Dijlah Library for Printing and Publishing, Baghdad, 1st Edition, 186 P. (In Arabic)

Al-Muzaffar, S.M., 2016. Soil Geography, College of Arts, University of Kufa, 180 P. (In Arabic)

Al-Obaidi, A.H.M., 2015. Geomorphology of the Wadi Naft Basin-eastern Diyala Governorate/Iraq, PhD Thesis (unpublished), College of Education, University of Diyala, 227 P. (In Arabic)

Al-Obaidi, D.K., 2022. Geomorphological assessment of Altun Kubri district in Kirkuk Governorate, MSc Thesis (unpublished), College of Education for Human Sciences, Tikrit University, 139 P. (In Arabic)

Al-Omari, F.S. and Ali, S., 1977. Geology of Northern Iraq, National Library, Baghdad, 117 P. (In Arabic)

Al-Rubaie, S.A.B., 2021. A hydrogeomorphological assessment of the Wadi Abu Dalaiya basin in Al-Jazeera region for the purposes of water harvesting, MSc Thesis (unpublished), College of Education for Human Sciences, Anbar University, 109 P. (In Arabic)

Al-Saadi, H.M.A., 2023. Landforms of Wadi Roser Basin in Dohuk Governorate using Geographic Information Systems, MSc Thesis (unpublished), University of Maysan, College of Education, 100 P. (In Arabic)

Al-Samurai, Q.A.M., 2008. Climate and Climate Regions, Dar Al-Yazurdi for Publishing and Distribution, Amman, Jordan, 148 P.

Al-Shammari, M.A.A., 2023, Characteristics of surface runoff in the Wadi Ghariba Basin and the possibility of investing in water harvesting, MSc Thesis (unpublished), College of Education, Al-Mustansiriya University, 150 P. (In Arabic)

Al-Shammari, M.H. and Abdel, A.R.M., 2021. Hydrogeomorphological risk assessment of the Bashadr region in Sulaymaniyah Governorate, PhD Thesis (unpublished), Ibn Rushd College of Education, for the Human Sciences, University of Baghdad, 148 P. (In Arabic)

Al-Ta'i, A.T.H., 2017. Geomorphology of the Duerig Flood Fan using GIS (GIS) and remote sensing (RS), MSc Thesis (unpublished), College of Arts, University of Basra, 97 P. (In Arabic)

Al-Zarfi, N.Q.M., 2021. Hydrological assessment of the possibility of harvesting rainwater in the Muthanna Desert (Wadi Al-Ghadhari - an applied study), MSc Thesis (unpublished), College of Education for Human Sciences, Muthanna University, 76 P. (In Arabic)

Al-Zuhairi, N.S.H., 2020. Hydrogeomorphological assessment of the northeastern Kalar basins and its impact on sustainable development, College of Education for Human Sciences, PhD Thesis (unpublished), University of Diyala, 103 P. (In Arabic)

Anaab, R., 2006. Estimating the risk of erosion in the Timgad Basin and its impact on the Kedia Dam-a multi-criteria approach, MSc Thesis (unpublished), People's Democratic Republic of Algeria, Batna, Colonel Hadj Lakhdar University, Faculty of Science, Department of Earth Sciences, 137 P. (In Arabic)

Hamid, H.T.M., 2016. Geomorphological characteristics of the Glatt region, northeast of Maysan Governorate, MSc Thesis (unpublished), College of Education, University of Wasit, 74 P. (In Arabic)

Hasan, I.J.D., 2023. Hydrology of valley basins and water harvesting west of Lake Sawa, MSc Thesis (unpublished), College of Education for Girls, University of Baghdad, 154 P. (In Arabic)

Ismael, G.J., 2017. Geomorphological characteristics of the Wadi Kani Masi basin in Dohuk, MSc Thesis (unpublished), University of Baghdad, College of Education / Ibn Rushd, 73 P. (In Arabic)

Jarei, T.M. and Diya, A.H., 2018. Morphometry of the Saffron River Basin in the Northeast of Maysan Governorate, A Study in Applied Geomorphology, Journal of the College of Education, Issue 10, Wasit, 343 P. (In Arabic) DOI:10.31185/eduj.Vol1.Iss10.449

Jassim, S.Z.J. and Goff, J.C., 2006. Published by Dolin, printed in the Czech Republic, first edition, 166 P.

Kartick, C.M., Sutapa, S., and Pritam, Z., 2019. Morphometric Analysis of Ajay River Basin Using Geospatial Technique, Geographical Review of India, 361 P.

Maaruf, F.J., 2016. The Natural, Demographic, and Economic Geography of Iraq: A Study in Regional Geography, Dar Degla, Amman, Jordan, pp. 79-80. (In Arabic)

Majed, H.M.S., 2008. The effect of geomorphological processes on land use in the district of Kosanjak (unpublished PhD Thesis), College of Education for Girls, University of Baghdad, 147 P. (In Arabic)

Mohsen, S. H, 2018, Geomorphology of Wadi Nidush Basin, PhD Thesis (unpublished), College of Education for Girls, University of Baghdad, 197 P. (In Arabic)

Salama, H.R., 2004. Fundamentals of Geomorphology, Al Masirah Publishing House, Amman - Jordan, 1st edition, 140 P. (In Arabic)

Salama, H.R., 2007. Fundamentals of Geomorphology, Dar Al Masirah for Publishing and Distribution, Amman, Jordan, 2nd Edition, 73 P. (In Arabic)

Salman, J.F.M., 2022. Morphological changes of the Rania Al-Faydiya fan (northern Iraq), a geomorphological study, PhD Thesis (unpublished), College of Education for Girls, University of Baghdad, 258 P. (In Arabic)

Sayab, A., Faruk, S.A., Jassm, A.J., and Nadir, A., 1982. Geology of Iraq, University of Mosul, 112 P.

Iraqi National Journal of Earth Science

www.earth.uomosul.edu.iq

التحليل الهيدرومورفومتري لحوض وادي سماقولي، شمالي شرقي العراق

كاروان سردار حسين الداوودي[1*] ، عبدالسلام مهدي صالح الجبوري[2]

[2،1] قسم علوم الأرض التطبيقية، كلية العلوم، جامعة تكريت، تكريت، العراق.

معلومات الارشفة

تاريخ الاستلام: 24- سبتمبر -2024

تاريخ المراجعة: 25- اكتوبر -2024

تاريخ القبـول: 28- نوفمبر -2024

تاريخ النشر الالكتروني: 01- يناير -2026

الكلمات المفتاحية:

سماقولي،

الهيدرومورفومتري،

التحليل الجيولوجي،

الشبكة المائية،

الخصائص التضاريسية،

المراسلة:

الاسم: كاروان سردار حسين الداوودي

Email: kkarwan328@gmail.com

الملخص

إن جانبا من جوانب أهمية هذا البحث هو في كونه يوفر معلومات شاملة وبيانات متكاملة عن الجيولوجية والهيدرومورفومترية ويركز بشكل خاص على مواضيع عدة منها كيفية الاستفادة من الامطار الموسمية واستغلالها بأفضل شكل لصالح في خزان سد سماقولي. وقد اكتشف أن للحوض خصائص الهيدرومورفومترية ومنها خصائصه الشبكة المائية، والخصائص التصريفية، والخصائص المساحية، والخصائص الشكلية، والخصائص التضاريسية، ونمط التصريف، كما وقد اكتشف أن الحوض المائي من الرتبة السادسة اعتمادا على طريقة (Strahler). شكل ونمط مستطيل. وكذلك تم استخدام نموذج الارتفاعات الرقمية (DEM) بدقة وضوح (x1414) متراً والذي هو مساحة البكسل الواحدة في التحليل الهيدرومورفومتري لخزان سد سماقولي، كأساس من أساسيات في التحليل الجيولوجي والهيدرومورفومتري للخزان شمالي شرقي العراق.

DOI: 10.33899/injes.v26i1.60207, ©Authors, 2026, College of Science, University of Mosul.
This is an open-access article under the CC BY 4.0 license (http://creativecommons.org/licenses/by/4.0/).

Hydromorphometric Analysis of Smaquli Basin, North-Eastern Iraq

Karwan Sardar Hussien[1*] , Abdulsalam Mehdi Altarif [2]

[1,2] *Department of Applied Geology, College of Science, University of Tikrit, Tikrit, Iraq.*

Article information

Received: 24- Sep-2024

Revised: 25- Oct-2024

Accepted: 28- Nov-2024

Available online: 01- Jan– 2026

Keywords:
Smaquli,
Hydromorphometric,
Geological analysis,
Characteristics,
Water network,

Correspondence:
Name: Karwan Sardar Hussien
Email: kkarwan328@gmail.com

ABSTRACT

One aspect of the importance of this research is that it provides comprehensive information and integrated data on geology and hydromorphometry, and focuses in particular on several topics, including how to benefit from seasonal rains and exploit them in the best way to supply the Smaquli Dam reservoir. It is discovered that the basin has hydromorphometric characteristics, including the characteristics of the water network, drainage characteristics, areal characteristics, formal characteristics, topographic characteristics, and drainage pattern. It was also discovered that the water basin is of the sixth order based on the (Strahler) method, the drainage shape, and a rectangular pattern. Based on the Strahler method, it is also a digital elevation model (DEM) with a resolution of (x1414) meters, which is the area of one pixel, is used in the hydromorphometric analysis of the Smaquli Dam reservoir as a basis for geological and hydromorphometric analysis of the reservoir in northeastern Iraq.

DOI: 10.33899/injes.v26i1.60207, ©Authors, 2026, College of Science, University of Mosul.
This is an open-access article under the CC BY 4.0 license (http://creativecommons.org/licenses/by/4.0/).

المقدمة

تعد الدراسات الهيدرومورفومترية تعد احدى الاتجاهات الحديثة في دراسة الاحواض النهرية، ونعني بذلك التحليل الكمي (العددي) لخصائص شكل الارض وايجاد العلاقات الرياضية التي تربط بين الطوبوغرافية وشبكات التصريف المائي (Morisawa, 1985)، دراسة الاحواض المائية و ايجاد خصائصها اهمية في الدراسات الهيدرولوجية والجيومورفولوجية، لما لها من دلالات هيدرولوجية معينة مثل خصائص الصرف المائي وهيدرولوجية القنوات والمجاري المائية واوديتها، اذ تعبر عن العلاقات بين عوامل وعمليات الحت والترسيب والظواهر الارضية المرتبطة بها والناشئة عنها (Al-Sahhaf, and Musa, 1998)، الظواهر الارضية للأحواض المائية والعمليات المكونة لها تكون معقدة ومتنوعة غالبا، الا انه يمكن معالجتها وتحليلها عن طريق مجموعة من القوانين التي كانت تعتمد سابقا على الدراسات الوصفية في تحليل صفاتها والتي وضع اساسياتها العالم (Horton, 1945) والتي قام بتطويرها بعد ذلك العالم(Strahler, 1957)، والذي اعتمد فيها الاسلوب الرياضي والكمي في دراسة الاحواض المائية وشبكات تصريفها والعلاقات بين اعداد الروافد واطوالها ومساحات احواضها وانحدارها.

اذ تم في هذه الدراسة ايجاد الخصائص الهيدرومورفومترية لحزان سد سماقولي بالاعتماد على نموذج الارتفاعات الرقمية للمنطقة (Digital Elevation Model) (DEM) وكانت دقة (مساحة البكسل الواحدة) بمقدار (14×14) متر باستخدام برنامج (Arc Map) في نظام (Arc GIS 10.4)، وتوظيف وربط نواتج وتأثيرات هذه الخصائص المتمثلة بالخصائص المساحية، والتضاريسية، والشكلية، والتصريفية.

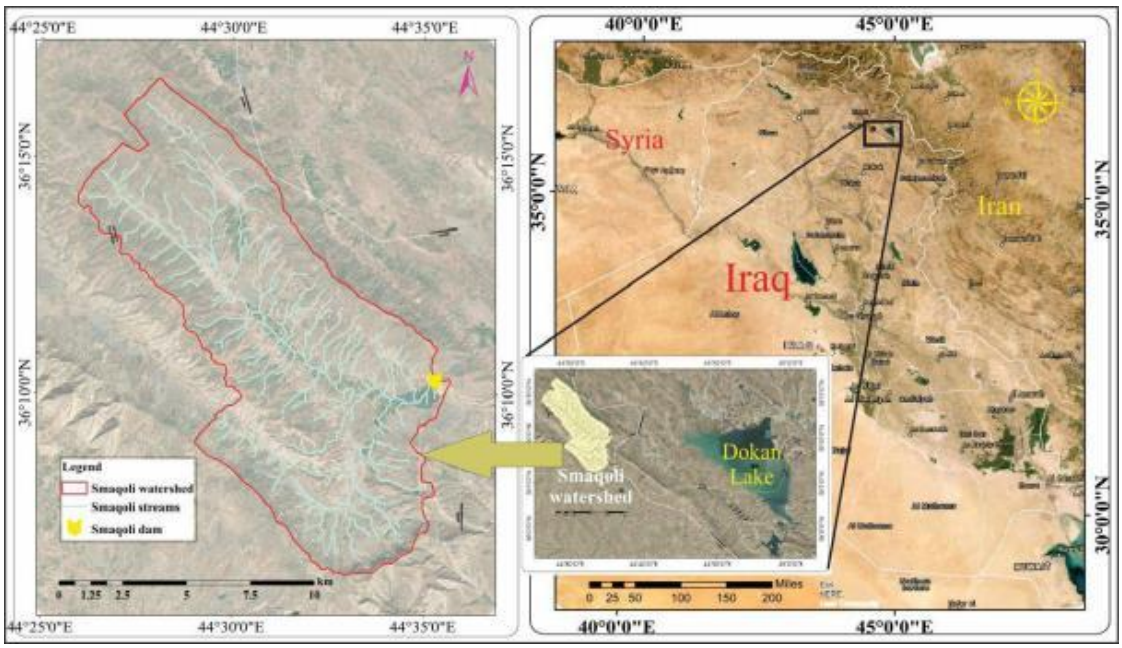
موقع منطقة الدراسة

وتقع المنطقة في قرية سماقولي Smackoli في محافظة السليمانية شمالي شرقي العراق وتنحصر بين خطي طول (10.52″ ′ 10 ° 36 الى11.37″ ′ 10 ° 36 شمالا) ودائرتي عرض (17.67″ ′ 35 ° 44 الى 19.15″ ′ 35

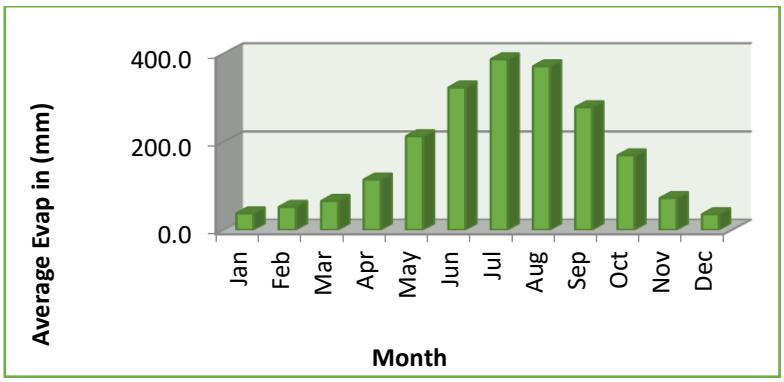
°44 شرقا) (الشكل 1). ويتأثر مقدار التبخر في موقع الدراسة بالإشعاع الشمسي ودرجة الحرارة ومساحة المنطقة المتعرضة للتبخر والطاقة المخزونة تحت السطح فضلا عن سرعة الرياح التي تؤدي الى زيادة نسبة التبخر (Al-Hussein, 2014).

لوحظ من الشكل (2) ان اعلى قيمة لمعدل التبخر الشهري للفترة من (2014–2023) كانت في شهر تموز (Jul.) حيث بلغت(386.9 mm) ، بينما تكون اقل قيمة لمعدل التبخر الشهري في شهر كانون الثاني (Dec.) إذ بلغت (35.8 mm)، وكما موضح في الجدول (1).

ان المعدل السنوي للتبخر للفترة (2014–2023) بلغت قيمته (2118.6 mm).



الشكل 1. خارطة موقعية لمنطقة الدراسة ضمن نطاق الحوض.



الشكل 2. يبين المعدل الشهري للتبخر للفترة (2014-2023).

الجدول 1: يبين المعدل الشهري لقيم التبخر للفترة (2014-2023).

Months	Jan.	Feb.	Mar.	Apr.	May.	Jun.	Jul.	Aug.	Sep.	Oct.	Nov.	Dec.
Av.	37.6	52.3	65.9	114.2	212.4	322.9	386.9	371.1	278.1	169.1	72.3	35.8

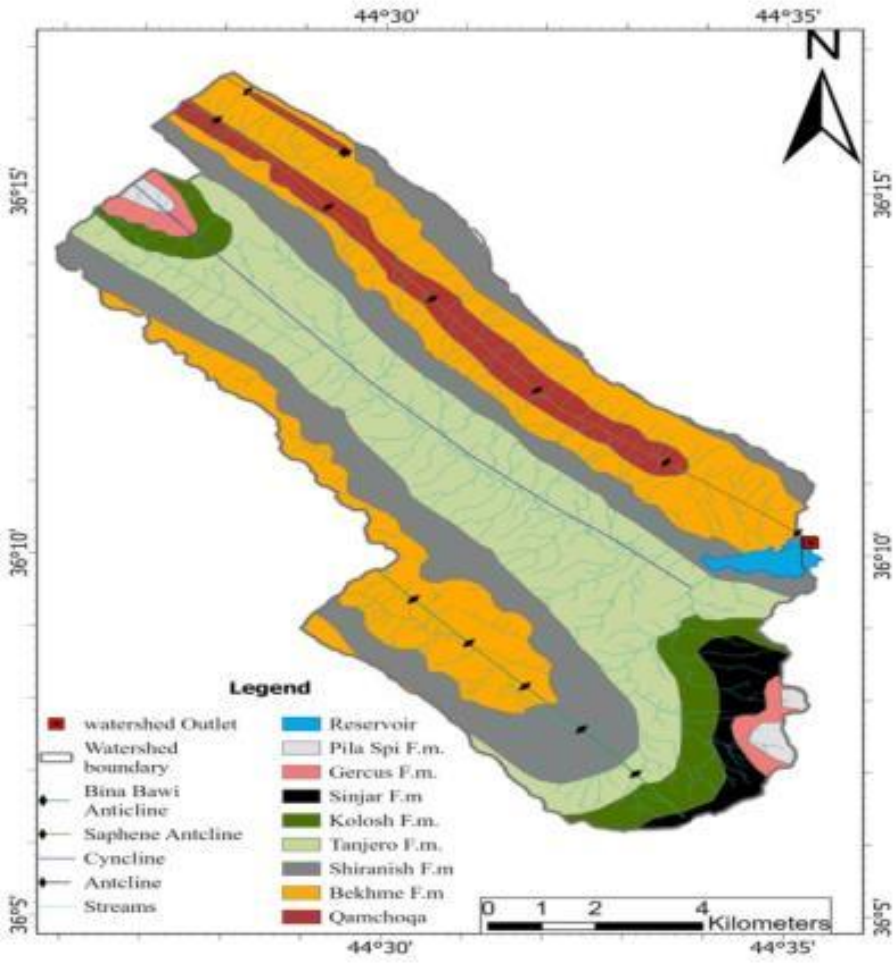
جيولوجية منطقة الدراسة:

تنكشف في المنطقة الدراسة عدة تكوينات جيولوجية هذه التكوينات من الأقدم الى الاحدث، من اهم ما تتناوله هذه الدراسة هي (الطباقية) لان المنكشفات تربط بالموضوع قيد الدراسة كمصدر للرسوبيات لذلك كل عنصر طباقي وكل منكشف لكل تكوين يختلف بتولد الرسوبيات الطباقية. ولأن لكل تكوين لأن الاستجابة فيها تختلف في مسألة تهيئة

الرسوبيات المنقولة من منكشف الى اخر، وبالتالي اصبحت التكوينات المنكشفة بالحوض هي الأساس في كمية ونوعية الترسبات المنقولة بالخزان ومن اهم هذا التكوينات (تكوين قمجوقة، تكوين بخمة، تكوين شرانش، تكوين تانجيرو، تكوين كولوش، تكوين سنجار، تكوين جركس، تكوين بيلاسبي).

تعّد طية سفين (Safeen) واحدة من مجموعة من الطيات المحدبة ذات المحاور المتوازية تقريباً والممتدة باتجاه (شمال غرب– جنوب شرق) والمنفصلة عن بعضها بتراكيب مقعرة ضيقة نسبياً كما في الشكل (3)، وهي تقع في نطاق الطيات العالية High Folded Zone ضمن الرصيف غير المستقر Unstable Shelf من العراق .(Buday, 1980) يبلغ ارتفاع الطية سفين حوالي (1500 متراً) وتمتاز طية سفين بوجود الحواجز الصخرية Ridges والوديان. طية سفين المحدبة هي طية ثنائية الغطس Double plunging، ومحورها يمتد باتجاه (N 45° W) وهي أيضاً غير متناظرة Asymmetricalحيث جناحها الجنوبي الغربي هو الأشد ميلاً (90–25 º) وأحياناً مقلوب Overturned في حين أن جناحها الشمالي الشرقي أقل ميلاً (º 60 – 20) .(Sissakian and Youkhana, 1979)

تعّد طية باني باوة (Bina Bawi) هذه واحدة من مجموعة من الطيات المحدبة ذات المحاور المتوازية تقريباً والممتدة باتجاه (شمال غرب– جنوب شرق) والمنفصلة عن بعضها بتراكيب مقعرة ضيقة نسبياً، وهي تقع في نطاق الطيات العالية High Folded Zone ضمن الرصيف غير المستقر Unstable Shelf من العراق (Buday, 1980). وتمتاز طية باني باوة بوجود الحواجز الصخرية Ridges والوديان. طية باني باوة المحدبة هي طية ثنائية الغطس Double plunging، وهي أيضاً غير متناظرة (Sissakian and Youkhana, 1979) Asymmetrical.



الشكل 3. خارطة جيولوجية موضح علية حدود الخزان وتكوينات جيولوجية.

طرائق العمل

يتضمن هذا الجانب إعداد المعلومات المتوفرة لمنطقة الدراسة من دراسات السابقة وتقارير وخرائط (جيولوجية وتكتونية وطبوغرافية وهيدرولوجية) بالإضافة الى المعلومات الهيدروجيولوجية والجيولوجية كما هو موضح أدناه:

1. خريطة جيولوجية للعراق صادرة عن الشركة العامة للمسح الجيولوجي والتعدين بمقياس رسم (1:100000) وضعه (Sissakian et al., 2020).
2. التقارير والمعلومات الصادرة عن وزارة الموارد المائية في اقليم كردستان.
3. نموذج الارتفاع الرقمي (DEM) بدقة (14*14) م لمنطقة الدراسة.

تمت عملية اشتقاق الحوض المائي لمنطقة الدراسة (Catchment area) باستخدام مجموعة برمجيات واستخراج الخصائص المورفومترية له، واشتقاق الشبكة المائية للحوض المائي حيث تم تحديد رتبة الحوض وعدد وطول وديان كل رتبة ونسبة تشعبها، وايجاد مساحة الحوض ومحيطه وعرضه وطوله، وايضا طول الوادي المثالي والحقيقي وارتفاع اعلى و اوطأ نقطة ضمن الحوض المائي بالاعتماد على نموذج الارتفاعات الرقمية (DEM) ، ثم اعتمدت هذه المعلومات في حساب الخصائص الهيدرومورفومترية للحوض المائي، وتم جدولة هذه النتائج، وتتلخص خطوات منهجية التحليل المورفومتري(Badowi and Abbood, 2024) بالنقاط التالية:

1. يتم العمل على برنامج (Global Mapper 13) وقد راقبنا المرئية الرادارية من خلال البرنامج، وتبعًا للاستدعاء تم تصحيح مسقط المرئية وفق المسقط التربيعي (UTM)، وقد تم بعد ذلك تصدير المرئية الى امتداد (Elevation Grid Format) ويتم اختيار نوع وصيغة الملف (DEM) من النافذة المنبثقة.
2. ما ذكرناه آنفًا هو الملف الذي يطالب به برنامج (ArcGIS 10.4) لاستخراج الحوض المائي وحساب المميزات والخصائص المورفومترية.
3. يتطلب منا بعد ذلك إضافة المرئية المصدرة في الخطوة السابقة لبرنامج (ArcGIS 10.4) وذلك بواسطة الامر (Add) وبالتالي تظهر المرئية باللون الأسود.
4. نذهب إلى (Table of Contents) ثم نقوم بالضغط على اسم المرئية ونختار (Data) ثم اختيار (Export Data) فتظهر نافذة جديدة هي (Export Raster) ثم من الخيار (Format) ونقوم لاختيار صيغة (GRID) بعد ذلك نقوم بكتابة الاسم المناسب والمعين للمرئية المخرجة الجديدة.
5. نختار صندوق (Spatial Analyst Tools) في برنامج (Arc Toolbox)  بالتالي يفتح لنا الامر (Hydrology) الاداة (Fill) وآنذاك تظهر لنا نافذة تضاف فيها المرئية الجديدة من الخطوة التي ذكرناها ونعطي لها اسم جديد، وبهذه الخطوة تصبح هناك طبقة جديدة ثالثة.
6. نختار صندوق (Spatial Analyst Tools) في برنامج (Arc Toolbox)  ، ثم يفتح الأمر (Hydrology) ونختار أداة (Flow Direction) وبعد ذلك تظهر لنا نافذة نضيف فيها الطبقة الاخيرة المنتجة حسب الخطوات السابقة وثم نضغط على خيار ok، فتظهر لنا طبقة جديدة تحتوي على نقاط ملونة غير مفهومة إلا أن الطبقة الأهم لأن من خلالها يتم اخراج جميع الوديان ضمن المرئية.
7. نختار صندوق (Spatial Analyst Tools) ونفتح الامر (Hydrology) بعد ذلك نختار الاداة (Flow Accumulation) فتظهر لنا نافذة نرى فيها الطبقة الأخيرة التي انتجت وفق الخطوات السابقة، وحينها ستظهر المرئية الجديدة بشكل خطوط بيضاء في ارضية سوداء، ويستخرج من خلالها شكل الوديان وشكل المجرى ونمط اتصال الوديان.

8. نطلب من برنامج (ArcGIS 10.4) ان يخرج الخطوط البيضاء المتواجدة في الصورة السابقة ونستطيع ان نجعل البرنامج أكثر تحسسًا وذلك بأن يخرج لنا أكثر مما هو معروض في الصورة من خلال صندوق (3D Analyst Tools) نفتح (Raster Reclass) ونختار اداة (Reclassify) فيظهر البرنامج لنا طبقة جديدة.
9. نختار صندوق (Spatial Analyst Tools) ونفتح الامر (Hydrology) بعد ذلك نختار اداة (Stream Order) فيظهر البرنامج لنا نافذة نضع فيها الطبقة الأخيرة المنتجة وفق الخطوات السابقة، وبذلك يتم انتاج طبقة الرتب المائية.
10. نحول الطبقة المنتجة وفق الخطوات السابقة إلى (Features) ومن النوع الخطي (Polyline) بواسطة صندوق (3D Analyst Tools) نفتح الأمر (Convert) ثم الأداة (Raster to Features) ونحدد نضع نوع الإخراج (Polyline) وبالتالي نحصل على الشبكة الهيدرولوجية في المنطقة التي اجرينا دراستنا عليها بشكل (Vector).
11. نضيف الموقع النفطي للمنطقة التي نريد ايجاد الحوض المائي لها، وبذلك عن طريق ذهابنا الى (Editor) و (Snapping) ونفعل طبقة الـ(Shapefile) النفطي من الأمر (Edit Sketch)، ثم يتوجب علينا الذهاب الى المنطقة التي استخرجناها في الخطوات السابقة، وبعد ذلك نختار (Symbology) ثم (Categories) ثم نحدد الحقل (Grid Code) ثم (Add all value).
12. يتوجب علينا ان نجد الحوض المائي عن طريق الصندوق (Spatial Analyst Tools) ونفتح (Hydrology) ثم نختار الأداة (Watershed) فيظهر البرنامج لنا نافذة نضع فيها الموقع النفطي المنتج وفق الخطوات السابقة ويتم وضع الطبقة المنتجة في الخطوة التاسعة فنحصل على الحوض المائي للمنطقة التي اجرينا عليها الدراسة بصيغة (Raster).
13. نحول صيغة الحوض المائي من (Raster) الى (Polygon) فنختار من صندوق (Conversion Tools) الامر (From Raster) وبعدها نختار الاداة (Raster to Polygon) وبالتالي تظهر لنا نافذة نضيف لها الطبقة المستخرجة وفق الخطوات السابقة.
14. نستخرج الحوض المائي الى منطقة الدراسة مع حدوده من هذه الطبقة وشريطة الاستقلال بوحدة ونفتح من صندوق (Analyst Tools) الامر (Extract) ثم نختار الاداة (Clip) فيظهر البرنامج لنا نافذة جديدة نضع فيها الطبقة المنتجة وفق الخطوات السابقة، وبذلك نكون قد أكملنا عملية الاشتقاق للحوض المائي ولشبكته (Catchment area) للمنطقة التي اجرينا عليها الدراسة.
15. حينها تصبح عندنا قاعدة بيانات للشبكة المائية والتي تحتوي على متغيرات عديدة، ونلاحظ ان رتب الشبكة المائية (Attributes Table) قد تكرر ولتجميعها او توحيدها نجري لها عملية احلال (GRID_CODE) فالصندوق (Dissolve) نفتحه بـ (Data Management Tools) ونختار (Generalization) ثم اختيار الاداة (Dissolve) فيظهر النظام لنا نافذة نضع فيها الخطوات المطبقة والتي ذكرناها آنفًا، ونؤشر على حقل (GRID_CODE) فيظهر النظام لنا رتب الشبكة المائية في قالب موحد ومجمع.
16. يتم استخراج الخصائص المورفومترية بواسطة قوانين معينة ونعتمد على الشبكة المائية وقاعدة بياناتها.

النتائج والمناقشة

استخدمت تقنيات الاستشعار عن بعد ونظم المعلومات الجغرافية في اشتقاق شبكة التصريف من نموذج الارتفاعات الرقمية، واجراء التحليل الهيدرومورفومتري لحوض سماقولي، ووجد أن نمط التصريف المتشابك هو السائدة. ووصلت رتب الوديان التي تم اشتقاقها الى الرتبة السادسة. تشير قيم الكثافة التصريفية الى النسيج الناعم وهناك العديد من الخصائص العددية والتصريفية والمورفولوجية والمكانية والطوبوغرافية التي تقلل من تصريف المياه في الأودية وتقلل من سرعة الجريان السطحي، كما تسبب انخفاض من نشاط التعرية مثل انخفاض الصرف، وقلة استقامة الأودية، وقلة عددها، وانخفاض

الكثافة النسبية، وزيادة طول الحوض على حساب العرض، وتكون سرعة الجريان عالية في المنابع المياه ومن ثم تنخفض مع قلة الانحدار اثناء تحركها نحو المصب في خزان سد سماقولي.

بينت الخصائص الهيدروموفومترية ان سد سماقولي يمكنه توفير كمية كبيرة من المياه للاستخدامات المختلفة، وفي المناطق العليا يكون التدفق سريعاً ويمكن ان يحمل كمية كبيرة من الرواسب الى الخزان بوجود تكوينات ذات صخارية فتاتية تغطي مساحات كبيرة من الحوض المتمثلة بتكويني تانجيرو وسيرانش، ويتمتع الحوض بقدرته العالية على الاحتفاظ بالمياه، مما يستلزم الحذر من السكان قرب السد لتجنب الكوارث من الموجات الفيضانية، بالإضافة الى ذلك فإن منطقة نشطة تكتونياً.

خصائص الشبكة المائية

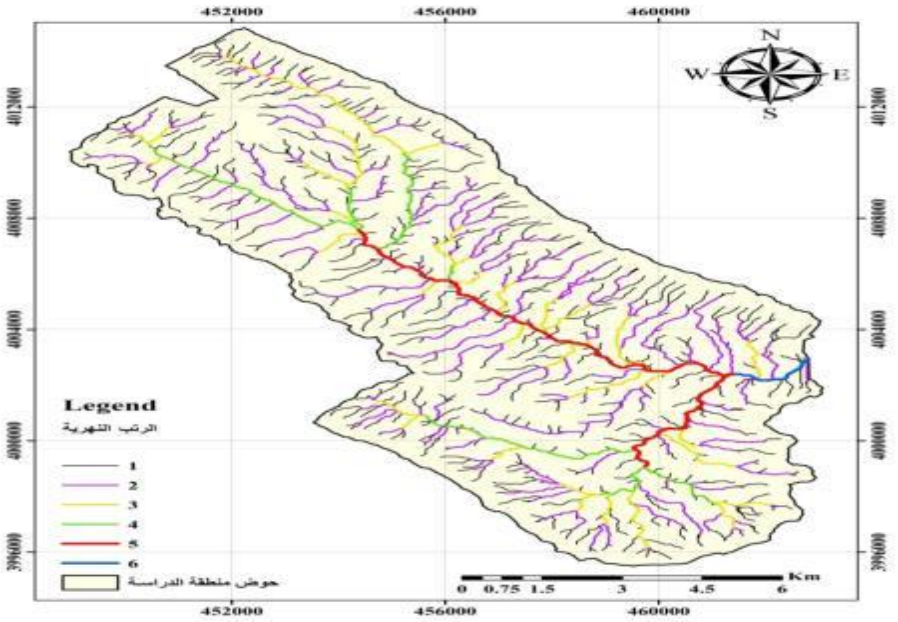
شبكة التصريف المائية في اي منطقة هي انعكاس للمكونات البيئية لها والمتمثلة بالعوامل الجيولوجية والتضاريسية والمناخية (Al-Ani, 2010).تم اشتقاق الحوض المائي واستحصال البيانات الهيدرومورفومترية له، وايجاد مساحته، حدوده، ارتفاع أعلى وأدنى نقطة فيه من نموذج الارتفاعات الرقمية للمنطقة (Digital Elevation Model) (DEM) وكانت وضوحيتها بمقدار (14×14) متراً باستخدام برنامج (Arc Map) في نظام (Arc GIS 10.4)، اذ اشتقت الشبكة المائية للحوض واتضح ان الحوض المائي من الرتبة السادسة للرتب المائية بالاعتماد على طريقة (Strahler) وتتكون الرتبة الثانية عند إلتقاء رافدين من الرتبة الثالثة، بالتالي تتشكل الرتبة الخامسة عندما يلتقي رافدين من الرتبة الرابعة، بينما الرتبة السادسة فتتكون عند إلتقاء رافدين من الرتبة الخامسة، وبهذا الشكل تستمر العلمية الى ان يصل المجرى الرئيسي لأعلى رتبة (Strahler, 1957) كما في الشكل (4). تم استخراج اعداد الوديان واطوالها لكل رتبة مائية من قواعد البيانات المستحصلة من نموذج الارتفاعات الرقمية للمنطقة (Digital Elevation Model) (DEM) بوضوحية (14×14) متر (مساحة البكسل الواحدة) باستخدام برنامج (Arc Map) في نظام (Arc GIS 10.4) للحوض المائي وادراجها مع قيم الرتب المائية في الجدول (2). تعد نسبة التشعب من العوامل المهمة التي تتحكم في معدل التصريف السطحي، ويقصد بها النسبة بين عدد المجاري المائية في رتبة مائية ما إلى عدد المجاري في الرتبة التي تعلوها (Al-Babawati, 1995). كما في المعادلة التالية: –

نسبة التشعب = (عدد مجاري رتبة ما / عدد مجاري الرتبة التي تعلوها)

كما تم استخراج الطول الحقيقي والمثالي والعرض للحوض، واُعتمدت هذه المعلومات العددية والمساحية والطولية لحساب الخواص الهيدرومورفومترية للحوض.

الجدول 2: الرتب النهرية وخصائص شبكة الاودية النهرية المحسوبة لخزان سد سماقولي.

الرتبة	عدد الوديان	طول الوديان كم	نسبة التشعب
1st	649	203.5	4.80
2nd	135	127.9	3.97
3rd	34	45.5	4.85
4rd	7	21.0	3.5
5rd	2	15.4	2
6rd	1	1.8	–
المجموع	828	415.4	



الشكل 4. الشبكة المائية لحوض سد سماقولي ورتبها بالاعتماد على المرئية الرادارية باستخدام برنامج (Arc GIS 10.4).

خصائص الشبكة التصريفية

1- الكثافة التصريفية السطحية: هي عبارة عن معيار لقابلية الوديان على نقل الساقط المطري باتجاه المصب، فكلما ازدادت الكثافة كلما زاد تصريفها السطحي، ويلاحظ انها تزداد عادة في المناطق التي تمتاز بتساقط الأمطار فيها بغزارة والتي تمتاز تربتها او صخاريتها السطحية بالنفاذية الواطئة (Al-Jubouri, 2009). يتم استخراج قيمتها بقسمة مجموع اطوال وديان الشبكة المائية لجميع الرتب على مساحة الكلية الحوض المائي حسب (Horton, 1945) على وفق المعادلة الاتية:

الكثافة التصريفية = (مجموع اطوال وديان الحوض (كم)/ مساحة الحوض (كم^2)).

بلغت قيمة الكثافة التصريفية للحوض المائي (3.29 كم/ كم^2) كما موضح في الجدول (3)، وهي كثافة تصريف منخفضة حسب تصنيف (Strahler,1957)، وبالتالي فان هذه القيمة ينعكس تأثيرها على الخزان المائي، اذ ان عملية نقل الساقط المطري تكون بطيئة لحين تجمع المياه امام جسم السد، وتقل فرصة تطوير المجاري المائية في اعلى الحوض وزيادة مساحتها.

2- معامل الانعطاف: يمثل نسبة الطول الحقيقي للوادي المائي الرئيسي الى الطول المثالي له (أقصر مسافة بين المنبع والمصب)، ويعد ذا اهمية في معرفة قدرة المجرى المائي على الإزاحة والتحرك جانبيا وتقييم انعطافات المجرى المائي، اذ ان معامل الانعطاف يعكس المشاكل التي تسببها الانعطافات النهرية (Schumm, 1956)، ويمكن حسابه على وفق المعادلة التالية: -

معامل الانعطاف = (طول الوادي الحقيقي (كم)/ طول الوادي المثالي المستقيم (كم))

إن ارتفاع نسبة معامل الانعطاف يفسر زيادة الالتواءات وتعقد الوضع الهيدروجيومورفولوجي على جانبي المنعطف وبالتالي زيادة التبخر والترشيح في مجرى الوادي، وتحدث التعرية على احدى الجهتين والترسيب على الجهة الأخرى، اذ بلغت قيمة معامل انعطاف الحوض المائي (1.20) وحسب تصنيف (Schumm, 1956) ، فان هذه القيمة تمثل استقامة عالية وتوحي الى قلة الانحناءات وزيادة سرعة الجريان ووصول المياه بفترة زمنية قليلة الى منطقة المصب عند جسم السد، وبالتالي فهي تنطبق مع الكثافة التصريفية وتؤدي هذه الحالة الى تقليل فرصة تطوير المجاري المائية في اعلى الحوض وزيادة مساحتها، كما موضح في الجدول (3).

3- التكرار النهري: هو عبارة عن العلاقة النسبية بين مجموع عدد الوديان في كل الرتب إلى مساحة الحوض (Al-Moumani, 1997)، لذا فان زيادة عدد الوديان او الروافد يزيد من الكثافة التصريفية العددية (التكرار النهري) وكمية الجريان المائي، وبالتالي زيادة نشاط عمليات التعرية، ويمكن ايجاده حسب (Horton, 1945) وفق المعادلة التالية:

التكرار النهري = (مجموع عدد الوديان في كل الرتب/مساحة الحوض(كم^2))

وقد بلغت قيمة كثافة التصريف العددية لحوض سماقولي (6.57 وادي/كم^2)، وهي كثافة متوسطة حسب تصنيف (Strahler, 1957). وهو دليل على قلة عدد الوديان والروافد اي انخفاض كمية الجريان المائي وبالتالي انخفاض نشاط التعرية للخزان.

4- شدة التصريف: هي عبارة عن النسبة العددية بين الكثافة الطولية (الكثافة التصريفية) الى الكثافة العددية (التكرار النهري)، وهي خاصية ذات أهمية كبيرة لأنها تعكس سرعة انتقال الموجات التصريفية من أجزاء الحوض المائي المختلفة نحو القناة المائية الرئيسية لإيصالها الى قمة التصريف (Al-Ananza, 2005)، ويمكن حسابها وفق المعادلة التالية:

شدة التصريف = (كثافة التصريف الطولية/كثافة التصريف العددية)

بلغت نسبة شدة التصريف للحوض المائي (0.5) وهي قيمة قليلة تدل على ان الحوض المائي لايزال في مرحلة الشباب وذو طاقة تصريفية عالية، وبالتالي تنعكس على تخزين المياه ضمن الخزان المائي حيث تدل على انخفاض سرعة انتقال الموجات التصريفية من أجزاء الحوض المائي المختلفة نحو القناة المائية الرئيسية.

5- الكثافة النسبية: وهي تمثل نسبة الكثافة العددية (التكرار النهري) الى مربع الكثافة الطولية (الكثافة التصريفية) كما في المعادلة التالية: -

الكثافة النسبية = (الكثافة العددية (وادي/كم^2) / مربع الكثافة الطولية (كم/كم^2))

وقد بلغت قيمتها (0.61 وادي/كم)، وهي قيمة منخفضة تدل على قلة توزيع الوديان وبالتالي التقليل من سرعة انتقال الموجات المائية من اجزاء الحوض المختلفة نحو القناة المائية الرئيسة، مما يؤدي الى انخفاض عمليات ونشاط التعرية ضمن الخزانات المقترحة.

الجدول 3: الخصائص التصريفية لخزان سد سماقولي.

التكرار النهري وادي/كم2	كثافة التصريف الطولي كم/كم2	الكثافة النسبية للوديان وادي/كم	شدة التصريف	معامل الانعطاف
6.57	3.29	0.61	0.5	1.20

الخصائص المساحية

وهي تختص بالأبعاد الهندسية للحوض المائي، الطول والعرض والمساحة والمحيط والنسب بين هذه الأبعاد، وتأثيرها بحجم الجريان المائي، وعلاقتها بتطور اطوال واعداد الاودية المائية (Huggett, 2007)، وهي تتأثر بمجموعة من العوامل المناخية والجيومورفولوجية ونوع الصخور والحركات التكتونية اذ تزداد بشكل طردي مع زيادة النحت المائي وضعف مقاومة الصخور والترب مما قد يؤدي الى انخفاض مستوى القاعدة او حدوث أسر نهري (Garde, 2006). تم حساب الخصائص المساحية للحوض المائي بعد اشتقاقها من نموذج الارتفاعات الرقمية باستخدام برنامج (ArcGIS 10.4) بعد استخراج الشبكة المائية وتحديد الحوض المائي، ويتم استخراج بعض الخصائص باستخدام قوانين تطبق من خلال البرنامج.

1. مساحة الحوض: تعد خاصية مهمة في الدراسات الهيدرولوجية والجيومرفولوجية، وذلك لإيجاد الخصائص الهيدرومورفومترية الاخرى كالكثافة التصريفية، الكثافة العددية، المعامل الهبسومتري وغيرها، وايضا الحصول على علاقات كمية يتم من خلالها تقييم هيدرولوجية الحوض، وكذلك لها أهمية كبيرة في التحكم بحجم الجريان المائي (Strahler, 1958). تعد مساحة الحوض منطقة تغذية مائية (Catchment Area) متكاملة لما لها من دور في

تحديد كمية المياه الواردة في الشبكة المائية الموجودة فيها (Al-Tamimi, 2016). وقد بلغت مساحة الحوض قيد الدراسة (125.977 كم^2) كما موضح في الجدول (3)، ويتضح من خلال هذه المساحة ومحيط الحوض ان الحوض المائي يمكنه ان يؤدي الغرض المنشود لجمع حجم جريان مائي.

2. طول الحوض: هو أحد المتغيرات المورفومترية المهمة المرتبطة بمميزات اخرى من خصائص حوض التصريف المائي، ويعرف بانه المسافة المقاسة لمحور الحوض والممتدة بين نقطة المصب المائي وابعد نقطة فوق منطقة تقسيم المياه بأعلى محيط الحوض المائي (Schumm, 1956). وتكون العلاقة طردية فبما بين طول الحوض ومساحته اي عند زيادة طول الحوض تكبر مساحته (Horton, 1945). وبلغ طول حوض منطقة الدراسة (18.871 كم) كما موضح في الجدول (3). الفرق بين طول الحوض وعرضه واضح ومميز بحيث يؤدي هذا التباعد الى نقصان سرعة الدفقات المائية القادمة اثناء فترة الزخات المطرية الغزيرة، مما يجب ان يؤخذ بنظر الاعتبار عن اختيار موقع السد عند المنخفض الطوبوغرافي المرشح وتصميمه.
3. اطوال الوادي: للوادي نوعان من الاطوال هما الطول الحقيقي والطول المثالي، ويعرف الطول الحقيقي بانه تلك المسافة التي يقطعها النهر او المجرى المائي من منبعه الى مصبه على اليابسة، اما الطول المثالي فأنه يمثل أقصر مسافة يمكن ان يسلكها المجرى المائي بين المنبع والمصب (Morisawa, 1985). غالباً ما يكون الطول الحقيقي أكبر من المثالي، وقد بلغ الطول الحقيقي للوادي (19.884 كم) بينما بلغ الطول المثالي له (16.525 كم) كما موضح في الجدول (3–3)، ولهذه الاطوال اهمية في ايجاد قيمة معامل الانعطاف الذي يعد من اهم خصائص الشبكة المائية التصريفية.
4. محيط الحوض: يعرف بانه خط تقسيم المياه ما بين الحوض قيد الدراسة وما يجاوره من احواض اخرى (Al-Eryani, 2000)، تؤثر به عوامل عديدة منها، تطور المجاري والوديان المائية وبالأخص مجاري الرتبة الاولى التي تتوسع وتتعمق مجاريها اثناء موسم سقوط الامطار بتأثير عملية النحت الرأسي والجانبي، وكذلك امتداد الفواصل والصدوع والشقوق والتراكيب الخطية مما انعكس على زيادة الرتب الاولى (Al-Aqeel, 2001). بلغت قيمة محيط الحوض (61.046 كم) كما موضح في الجدول (3)، وقد عكس محيط الحوض اضافة الى مساحته بان الحوض المائي ربما سيؤدي الغرض المنشود لخزن المياه.
5. عرض الحوض: هو معدل اطوال مجموعة الخطوط التي تتعامد على الخط المستقيم الذي يمثل طول الحوض المائي، ويبلغ عرض حوض منطقة الدراسة (8.579 كم) كما موضح في الجدول (4)، والدلالة الجيومورفولوجية للاختلاف ما بين منطقة المنبع والمصب ناتجة بسبب اختلاف الخصائص المناخية والانحدارية (Zureikat, and Al-Hasban, 2015). لعرض الحوض أثر مماثل كما للطول في تحديد شكل الحوض، ويؤثر عرض الحوض على كمية الساقط المطري وجريانه والتبخر والترشيح، اذ تزداد كمية الساقط المطري التي يتلقاها الحوض بزيادة عرضه وبالتالي يزداد الجريان السطحي والعكس صحيح (Mahsoub, 1997).

الجدول 4: الخصائص المساحية لخزان سد سماقولي.

مساحة الحوض المائي – كم^2	الطول المثالي للوادي – كم	الطول الحقيقي للوادي–كم	محيط الحوض كم	عرض الحوض كم	طول الحوض المائي–كم
125.977	16.525	19.884	61.046	8.579	18.871

الخصائص الشكلية

1– نسبة الاستدارة (نسبة تماسك المساحة): يعنى بها بيان مدى اقتراب او ابتعاد الحوض المائي من الشكل الدائري (Melton, 1958)، وتسمى ايضا نسبة تماسك المساحة، اذ للحوض المائي اشكال تشبه الاشكال الهندسية كالمستطيل والمربع والمستدير والمثلث، وتتراوح نسبة الاستدارة ما بين (0–1) فيبقة الارتفاع التي تكون قريبة من الرقم الواحد، (أي اقتراب الأحواض من الشكل الدائري) لأن الرقم واحد هو ممثل الاستدارة الكاملة، وتدل هذه الى تقدم الدورة

التعروية للحوض وزيادة فعالية مجراه المائي عن طريق تعميق المجرى على حساب التوسعة، بينما القيمة المنخفضة التي تبتعد من الرقم واحد فتدل على ابتعاد الحوض عن الشكل الدائري وان دورة التعرية مازالت تقوم بدورها (Reddy, et al., 2004) يتم قياس نسبة الاستدارة من قسمة مساحة الحوض المائي (كم^2) على مساحة دائرة محيطها الذي يساوي محيط الحوض نفسه (كم^2) كما في المعادلة التالية:

نسبة الاستدارة = مساحة الحوض (كم^2) / مساحة دائرة محيطه الذي يساوي محيط الحوض نفسه (كم^2)

بلغت نسبة الاستدارة خزان سد سماقولي (0.38) كما موضح في الجدول (4)، مما يدل على ابتعاد الحوض عن الشكل الدائري واقترابه من الشكل المستطيل، وهذا يدل على زيادة طول الحوض على حساب عرضه والتي تكونت نتيجة تأثير العامل البنيوي.

2- نسبة الاستطالة: هي نسبة تدل إلى مدى اقتراب وتشابه شكل الحوض المائي الى الشكل المستطيل أو ابتعاده، وقد حدد (Schumm, 1956) بان نسبتها تنحصر ما بين (0-1)، اذ كلما اقتربت قيمتها من الصفر (0)، فان ذلك يدل على شدة استطالة الحوض، بينما يدل ارتفاع القيمة واقترابها من الواحد الصحيح (1) دل ذلك على اقتراب الحوض من الشكل الدائري، وتستخرج نسبة الاستطالة من المعادلة التالية: -

نسبة الاستطالة = طول قطر دائرة بمساحة الحوض نفسه (كم)/ اقصى طول للحوض (كم)

اذ ان طول قطر دائرة بمساحة الحوض نفسه بلغت (12.66 كم)، وبالتالي فان نسبة الاستطالة لخزان سد سماقولي بلغت (0.67) كما موضح في الجدول (4)، مما يدل على اقتراب الحوض من الشكل المستطيل، وهو يتطابق مع ما تم التوصل اليه من قيمة نسبة الاستدارة، اذ تكون طبيعة الصرف لهذا الحوض اقل من الاحواض الدائرية او القريبة من ذلك بسبب طول المجاري على حساب عرضها والذي يؤدي الى فقدان كميات كبيرة من المياه خلال الجريان الطويل.

3- نسبة تماسك المحيط: وهي خاصية ومؤشر آخر لتأكيد اقتراب او ابتعاد شكل الحوض من الشكل الدائري، اذ كلما ارتفعت النسبة عن الواحد الصحيح (1) فان شكل الحوض يكون أكثر استطالة ويبتعد عن الشكل الدائري، علما ان ناتج نسبة تماسك المحيط دائماً يكون أكثر من الواحد الصحيح (Sharif, 2000)، وتستخرج نسبة تماسك المحيط من المعادلة التالية:

نسبة تماسك المحيط =1/ نسبة تماسك المساحة (الاستدارة)

بلغت نسبة تماسك المحيط لخزان سد سماقولي (1.63) كما موضح في الجدول (4)، والذي قد ابتعد عن المعدل مما يدل على استطالة الحوض المائي واقترابه من الشكل المستطيل وابتعاده عن الشكل الدائري، وهو دليل على تعرج خط تقسيم المياه او محيط الحوض، وبالتالي فان الحوض مازال يعيش في مرحلة تطوير من الناحية الجيومورفولوجية وان طبيعة الصرف لهذا الحوض قليلة بسبب طول المجاري على حساب عرضها الامر الذي يؤدي الى فقدان كميات كبيرة من المياه خلال الجريان الطويل، وبهذا ينطبق مع ما تم التوصل اليه من خلال نسبة الاستدارة ونسبة الاستطالة.

4- معامل شكل الحوض: يوضح مدى تناسق الشكل العام للحوض أي مدى انتظام عرض الحوض المائي على طول امتداده من منطقة المنبع وحتى المصب، بواسطة العلاقة بين مساحة الحوض المائي وطول الحوض، اذ ان القيمة المنخفضة المبتعدة عن الواحد الصحيح (1) توضح الى اقتراب شكل الحوض المائي من الشكل المثلث، بينما القيمة المرتفعة المقتربة من الواحد الصحيح (1) فإنها تشير الى الابتعاد عن الشكل الثلاثي (Al-Sahhaf, and Musa 1998). يتأثر شكل ونمط حوض التصريف المائي وشبكة التصريف الممتدة بداخله بالخصائص الأخرى لحوض التصريف مثل نوعية الصخر ودرجة الانحدار بالإضافة إلى أن الشكل يؤثر على العمليات الجيومورفولوجية خاصة فيما

يتعلق بكفاءة الحوض المحتملة وشبكة التصريف المائي به (Al-Mashat, 1995)، وقد استخدم (Horton ,1945)، معامل الشكل لتحديد أشكال الأحواض النهرية على وفق المعادلة التالية:

معامل شكل الحوض = مساحة الحوض (كم^2)/ مربع طول الحوض (كم^2)

بلغ معامل شكل الخزان سد سماقولي (0.35) كما موضح في الجدول (5)، وهي قيمة منخفضة عن الواحد الصحيح (1) وتدل على ان شكل الحوض يقترب من الشكل المثلث، وتدل ايضا على صغر مساحة الحوض المائي نسبة الى طوله، ويشير ذلك الى تشابه اجزاء الحوض في طبيعة المناخ، ونوعية الصخور، مع وجود الاختلافات الصغيرة في بنية الصخور كوجود بعض الفواصل والشقوق والصدوع (Abdulla, 2024). يؤثر انخفاض قيمة معامل الشكل واقترابه من الشكل المثلث على نظام التصريف المائي، فعندما تشكل منطقة المنابع رأس المثلث ومنطقة المصب قاعدته فإن التصريف المائي يزيد بعد سقوط الامطار مباشرة مؤدياً الى ارتفاع منسوب الماء بشكل سريع وذلك لقرب الجداول والمسيلات من المصب الرئيسي، بينما في الاحواض التي تكون فيها منطقة المصب ممثلة لرأس المثلث وقاعدته عند المنابع فأن المياه تصل اليها بشكل متعاقب نتيجة بعد الجداول والمسيلات عن المصب (Gregory and Walling, 1973). والحالة الثانية هي التي تنطبق على حوض الدراسة.

الجدول 5: الخصائص الشكلية خزان سد سماقولي

الاستدارة	تماسك المحيط	الاستطالة	معامل الشكل
0.38	1.63	0.67	0.35

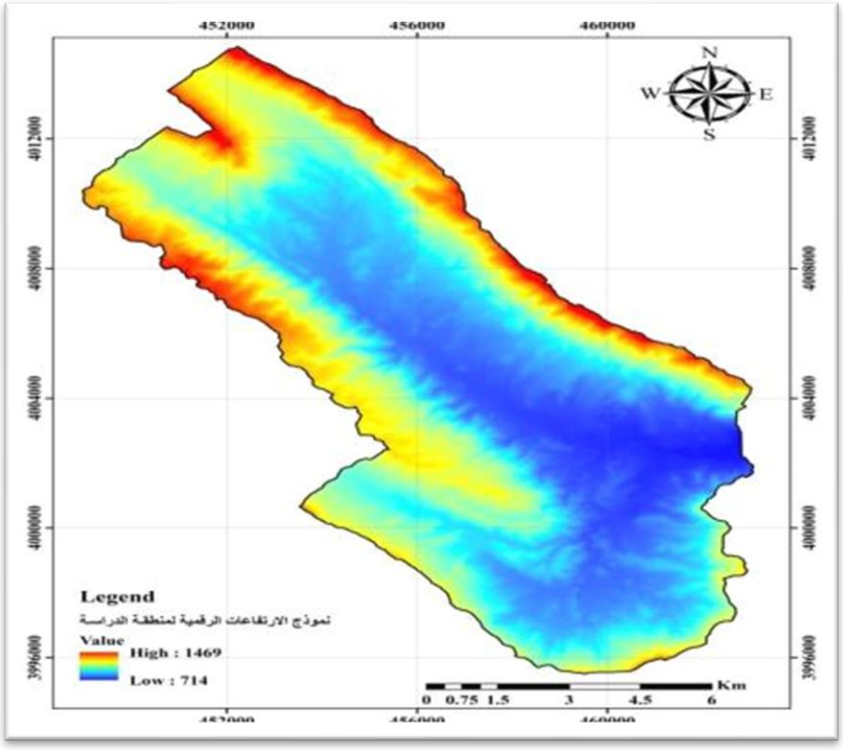
الخصائص التضاريسية

تعتبر من الخصائص المهمة بالنسبة للباحث في الدراسات الجيومورفولوجية والهيدرولوجية، لأهميتها في تحديد مراحل عمليات التعرية المائية والهوائية وعمليات التجوية ودورها في تشكيل سطح الارض، وتعد ايضا انعكاساً للطبيعة الصخرية وخصائصها البنيوية، ومعرفة مدى تطور الحوض المائي ودورته الحتية وعمليات التجوية السائدة، لذا تنوعت مقاييس الخصائص التضاريسية من قبل الباحثون وهي كالتالي:

1- معدل التضرس: تعد من الخصائص التضاريسية المهمة لأهميتها في معرفة الطبيعة الطوبوغرافية ومدى تضرس الحوض المائي من حيث التباينات في الارتفاع ما بين المنبع والمصب وانعكاس ذلك على قابلية المجرى المائي في انجاز العمليات الجيومورفولوجية المتمثلة في التعرية عند اعلى الحوض والترسيب في منطقة المصب، ويقاس معدل التضرس حسب (Strahler, 1957) بالطريقة التالية:

معدل التضرس = الفرق بين اعلى وأدنى نقطة بالحوض (م)/ طول الحوض (كم)

بلغت اعلى نقطة في الحوض (m1469) فوق مستوى سطح البحر، بينما أدنى نقطة في الحوض بلغت (714 m) فوق مستوى سطح البحر كما في الشكل (5). ترتفع قيمة التضرس في الاحواض صغيرة المساحة، وهو دليل على قلة نشاط عمليات الحت بفعل المياه وان الحوض مازال لديه الكثير من النشاط الجيومورفولوجي لتحقيق التوازن في مجاريه وهو ما ينطبق على حوض منطقة الدراسة فقد بلغ معدل التضرس له (40.01) م/كم كما موضح في الجدول (5). بينما تنخفض نسبة معدل التضرس في الاحواض كبيرة المساحة، وهو يؤثر في زيادة سرعة وصول الموجات المائية وينعكس ذلك على زيادة الرواسب المنقولة بشكل أكبر (Schumm, 1956).



الشكل 5. يوضح بين اعلى و ادنى نقطة في حوض سد سماقولي.

2- نسبة التضرس (التضاريس النسبية): تعتبر مقياساً اخر مهم لقياس شدة التضرس للحوض المائي، وتمثل العلاقة بين قيمة تضاريس الحوض (الفرق بين اعلى وادنى نقطة بالحوض (م)) ومحيط الحوض نفسه (Strahler, 1957). وتبين مدى العلاقة بين مساحة الحوض من جهة ودرجة مقاومة الصخور لعمليات التعرية من جهة اخرى، حيث توجد علاقة ارتباط سالبة بين التضاريس النسبية ودرجة مقاومة الصخور لعمليات التعرية في حالة تشابه الاحوال المناخية، وتقاس حسب القانون التالي: –

نسبة التضرس = الفرق بين اعلى وأدنى نقطة بالحوض (م)/ محيط الحوض (كم)

بلغت نسبة التضرس خزان سد سماقولي (12.37م/كم) كما موضح في الجدول (5)، وهي نسبة منخفضة ناتجة عن قلة معدلات الانحدار وتعرض الحوض الى تعرية منخفضة.

3– قيمة الوعورة: خاصية مهمة تستخدم لمعرفة مدى تضرس الحوض، ودرجة تقطع سطح حوض الوادي الناتج عن نحت المجاري المائية، ومدى انحدار المجرى المائي بالاعتماد على كثافة التصريف الطولية للحوض (Al-Mashat, 1995)، وتقاس على وفق الطريقة التالية: –

قيمة الوعورة = (الفرق بين اعلى وادنى نقطة بالحوض (م)×كثافة التصريف الطولية (كم/كم^2))/1000

ترتفع قيمة الوعورة عند زيادة تضرس الحوض إلى جانب زيادة أطوال المجاري على حساب المساحة، وتتباين قيمة الوعورة خلال مراحل الدورة الحتية، اذ تنخفض قيمة الوعورة في بداية الدورة، ثم تبدأ بالزيادة تدريجيا حتى تصل اقصاها عند بداية مرحلة النضج، ثم تنخفض مرة اخرى لتصل مرحلة الشيخوخة ونهاية الدورة الحتية (Ashour, 1986). بلغت قيمة الوعورة لحوض وادي ابو خشب (2.48كم/كم^2) كما موضح في الجدول (5)، وهي قيمة منخفضة تدل على ان الحوض وقع ضمن مرحلة النضوج المبكر.

4- النسيج الحوضي: يعد من الخصائص المهمة في التحليل الهيدرومورفومتري والذي يعني بأنه المباعدة النسبية لخطوط تصريف الشبكة المائية (Reshma, et al., 2012). ومعرفة مدى تضرس وتقطع سطح الارض وكثافة الصرف فيها، فكلما تزاحمت خطوط شبكة التصريف ازداد عدد الاودية واقتربت من بعضها البعض، مما يدل على شدة التقطع ومدى حجم معدلات الحت فيها، وتتأثر بعوامل طبيعية مثل المناخ، والساقط المطري، ونوعية الصخور والتربة، وسعة الترشيح، وطبيعة الغطاء النباتي (Schumm, 1977). ويتم حساب قيمة النسيج الحوضي حسب (Ritter, et al., 1995) وفق المعادلة التالية:

النسيج الحوضي = اعداد اودية الحوض/ محيط الحوض (كم)

اذ يصنف النسيج الحوضي حسب (Schumm, 1977) الى اربعة اصناف هي كالتالي: –

1. خشن جدا: إذا كان معدل النسيج اقل من (2) اودية.
2. خشن: إذا كان معدل النسيج بين (2–4) اودية.
3. متوسط: إذا كان معدل النسيج بين (4–10) اودية.
4. ناعم: إذا كان معدل النسيج أكثر من (10) اودية.

بلغ النسيج الحوضي لمجرى وادي سد سماقولي (13.5) كما موضح في الجدول (6)، وهو بذلك يعد نسيجا ناعم.

الجدول 6: الخصائص التضاريسية خزان سد سماقولي.

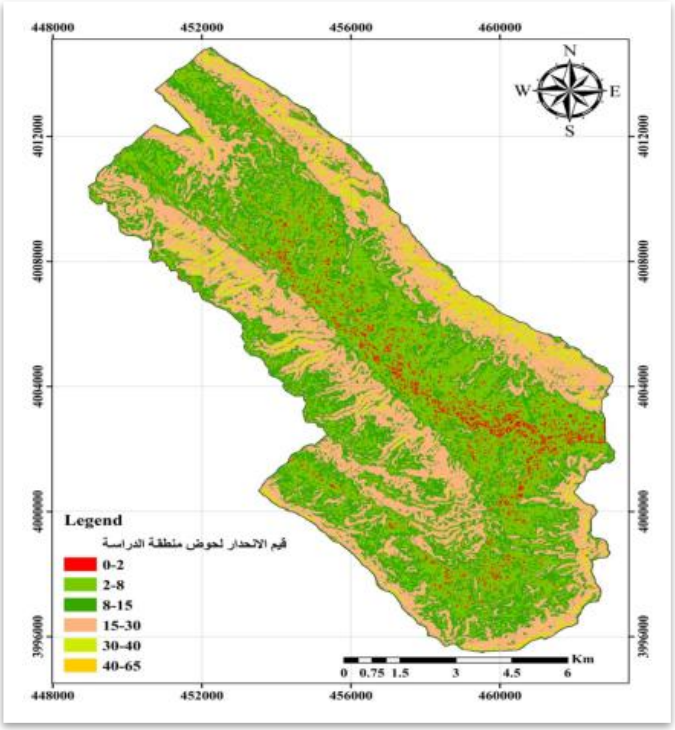
النسيج الحوضي	قيمة الوعورة (كم/كم2)	معدل التضرس	نسبة التضرس (م/كم)
13.5	2.48	40.01	12.37

شدة الانحدار

تمثل المنحدرات نتاجا طبيعيا استمر تشكيله لمدة زمنية قديمة جدا، و قد افرزتها تداخل مجموعة من العناصر البيئية المختلفة حيث يمكن تحديدها بخمسة عوامل اساسية هي (التضاريس والمناخ والوضع والجيولوجي، التربة والعمليات الجيومورفولوجية والغطاء النباتي)، تمثل الانحدارات من الدراسات الجيومورفولوجية المهمة التي تبرز اهم العمليات الجيومورفولوجية المتمثلة بالتجوية و التعرية .توضح خريطة شدة الانحدار ملامح نوع و شدة العملية الجيومورفولوجية التي تسود وتأثيرها كبير وواسع في اراضي المنطقة، إذ تعكس أصنافها مديات انواع الأساس الذي تركز عليه مسببات مخاطر الوضع البيئي، إذ تمثل احد الأركان الأساسية في معايير أوزان المخاطر البيئية، فمن خلالها يمكن تقييم تطور حركة المنحدرات التي استرعت اهتمام العديد من الجيومورفولوجين، لما تسببه من تغيرات مهمة على سطح الارض. وهي تنعكس على الغلاف الصخري والحياتي وما يتعلق بالجوانب التطبيقية في حياة الإنسان استخلصت خارطة شدة الانحدار بالاعتماد على نموذج الارتفاع الرقمي (DEM) ومن خلال برنامج (Arc GIS) أجري اعادة تصنيف لفئاتها المخرجة وتم تصنيفها الى خمسة اصناف لتمثل صفة المنحدر من اذ شدة انحداره، وكما موضح في الشكل (6)، واعتمدت الدراسة على التصنيف الجيومورفولوجي (Zink) والذي يكون تصنيفاً هرمياً متسلسلاً يقع في خمسة مستويات تصنيفية مع زيادة في التعميم عند المستويات العالية. ويستخدم هذا التصنيف في تحديد انواع التضاريس والأشكال الأرضية على مستويات الانحدار الأراضي. ومن خلالها تمثلت الأصناف بما يلي:

1. **الصنف الأول:** شدة الانحدار تتراوح فيه ما بين (0–2) درجة، إذ تظهر في مناطق الاستواء التضاريسي لاسيما في الأجزاء السهلية والمستوية من منطقة الدراسة التي أصبحت تستقبل الرواسب من سلاسل المرتفعات المنتشرة في المنطقة لتشكل سهول مستوية طفيفة الانحدار، وتعد الميزات الأساسية التي جعلتها من الأراضي التي تصلح للاستخدامات الزراعية والاروائية والسكنية.

2. **الصنف الثاني:** يتمثل بالأراضي قليلة الانحدار التي تراوحت قيم الانحدارها ما بين (2–8) درجة، واتسمت اراضيها بتموج خفيف إلى متوسط وتوزعت فيها المراوح الفيضية المنحدرة من سلاسل المرتفعات.
3. **الصنف الثالث:** تتراوح شدة انحداره ما بين (8–15) درجة، فتظهر فيها مناطق متوسطة الانحدار تقع في مناطق أسفل المنحدرات وفي مناطق القدمات وتمثل اراضي وعرة تتخللها بعض التلال الواطئة وتقطعها وديان الشبكة المائية التي تبدأ عملياتها الترسيبية الاولى فيها وتكون أرض ذات رواسب خشنة.
4. **الصنف الرابع:** تراوحت شدة الانحدار فيه تراوحت ما بين (15–30) درجة، عبرت عن مناطق اتسمت بمنحدرات شديدة تسود ضمن جزء سلاسل الحافات المنتشرة على أجنحة و سفوح الطيات المنطقة، و تحديدا في منطقة المنابع (مخارج الوديان)، إذ تظهر فيها الحافات تمثل خطوط تقسيم المياه بين الروافد الأساسية لمجاري الشبكة المائية و تبدو مجاريها بهية أخدوديه عميقة جدا، و تشكلت الانحدارات بسبب طول الانحدارات من جهة و وجود تعاقب مستمر من الحافات الصخرية من جهة اخرى للعديد من المنكشفات الجيولوجية و التي تفصل فيما بينها أودية طولية شبه مستقيمة تزداد اتساعا و عمقا كلما ابتعدنا عن محاور الطيات تشكلت فيها شبكة كثيفة من المراتب الثانوية القصيرة المنحدرة نحو الوديان الرئيسية.
5. **الصنف الخامس:** تتراوح شدة الانحدار فيه ما بين (30–40) درجة، اتصفت بالمناطق بانحدار شديد.
6. **الصنف السادس:** يمثل المواقع التي يتراوح الانحدارها ما بين (40–65) درجة واتصفت بانحدارات شديدة جدا مثل مناطق ذروات قمم الطيات المنتشرة في منطقة الدراسة بهيئة سلاسل جبلية طويلة.



الشكل 6. يمثل خارطة شدة الانحدار للخزان والمناطق المجاورة منه.

الاستنتاجات

1. واتضح ان الحوض المائي من الرتبة المائية السادسة بالاعتماد على طريقة (Strahler)، وان مساحة الحوض تبلغ (125.9 كم^2)، ويبلغ طول حوض منطقة الدراسة (18.8 كم)، وقد بلغ الطول الحقيقي للوادي (19.884 كم)، بينما بلغ الطول المثالي له (16.525 كم)، وبلغت قيمة محيط الحوض (61.046 كم)، بينما يبلغ عرض حوض منطقة الدراسة (8.579 كم).

2. تشير الخصائص الشكلية الى اقتراب الحوض المائي من الشكل المستطيل أي زيادة طول الحوض نسبة الى عرضه ودلت نسبة الاستدارة، ونسبة الاستطالة بلغت، ونسبة تماسك المحيط، ومعامل شكل الحوض، على ان دورة التعرية مازالت تقوم بدورها وان الحوض مازال يعيش في مرحلة تطوير من الناحية الجيومورفولوجية.
3. تشير الخصائص التضاريسية الى ان الحوض ذو تضرس مرتفع وان التعرية فيه قليلة ومازال لديه الكثير من النشاط الجيومورفولوجي لتحقيق التوازن في مجاريه.
4. من خلال شبكة التصريف المائية لحوض منطقة الدراسة فقد تم اكتشاف نوع مميز من انماط التصريف وهو النمط المستطيل (المتعامد).

References

Abdulla, H.H., 2024. Morphometric parameters study for the lower part of lesser zap using GIS technique, Diyala Journal for Pure Sciences, Vol. 7, 2010, 138 P. https://iasj.rdd.edu.iq/journals/uploads/2024/12/09/83c6c8b81b1673ddd3713602c0c7a5fa.pdf

Al-Ananza, A.A.A., 2005. The Extent of Exploitation of Natural and Human Resources of Wadi Ibn Hammad in Karak Governorate, Jordan, King Abdulaziz University Journal, Volume 13, Issue 3, pp. 185-213. (In Arabic).

Al-Ani, R.A.M., 2010. Geomorphology of Sindhi Plain, unpublished PhD Thesis, University of Mosul. (In Arabic).

Al-Aqeel, H.M.S., 2001. Geomorphology of the Wadi Laha Basin, one of the tributaries of the Wadi Hanifa Basin in the Kingdom of Saudi Arabia, unpublished PhD Thesis, University of Riyadh. (In Arabic).

Al-Babawati, A.A.H., 1995. Wadi Al-Ajej Basin in Iraq and the Uses of Landforms, Unpublished PhD Thesis, University of Baghdad. (In Arabic).

Al-Eryani, A.S.A., 2000. Wadi Banah Basin in the Republic of Yemen, unpublished MSc Thesis, University of Baghdad. (In Arabic).

Al-Hussein, A.A.M., 2014. A hydromorphometric sedimentary study of the regulatory reservoir of Mosul Dam, northern Iraq, unpublished PhD Thesis, University of Mosul. (In Arabic). https://iasj.rdd.edu.iq/journals/uploads/2024/12/05/81ada88afed276b6a6411a40f20fa7c5.pdf

Al-Jubouri, M.Y.H., 2009. Morphology of Wadi Al-Shor Basin - A Comparison of the Use of Multiple Data Sources and Technologies, Unpublished PhD Thesis, University of Mosul. (In Arabic).

Al-Mashat, H.A.R., 1995. Wadi Liyah Basin in the Kingdom of Saudi Arabia: A Geomorphological Study, Unpublished PhD Thesis, University of Jeddah. (In Arabic).

Al-Moumani, L.R., 1997. Hydrology of the Main Mujib Basin in Jordan, A Study in Applied Geography, Ministry of Culture Press, Jordan. (In Arabic).

Al-Sahhaf, M.M. and Musa, K., 1998. Hydromorphometry of the Diyala Basin: A Study in Applied Geomorphology, Journal of Al-Mustansiriya Arts, Issue 16, p. 788. (In Arabic).

Al-Tamimi, B.F.M., 2016. Hydrological Modeling of Jamjamal Water Basin Using Geographic Information Systems (GIS) and Remote Sensing (RS), Unpublished PhD Thesis, Tikrit University (In Arabic). https://aladabj.uobaghdad.edu.iq/index.php/aladabjournal/article/view/1807

Ashour, M.M., 1986. Methods of Morphological Analysis of Water Drainage Networks, Annals of the College of Humanities and Social Sciences, Qatar University, Issue 9, 1986, 496 P. (In Arabic).

Badowi, S. and Abbood, A., 2024. Dam Breakdown and Response of Protection Dam, Case Scenarios of Mosul-Badush Dams, Northern Iraq, https://tjes.com/ojs/index.php/tjes/article/view/1032

Buday, T. and S.Z. Jassim, 1987. The regional Geology of Iraq, Vol. 2 Tectonism, Magmatism and Metamorphism, Baghdad, Iraq.

Grade, R.J., 2006. River Morphology, New Delhi, New Age International.

Gregory, K.J. and Walling, D.E., 1973. Drainage basin form and Process: A geomorphological approach, Edward Arnold.

Horton, R.E., 1945. Erosional development of streams and their drainage density: hydrophysical approach to quantitative geomorphology, Geol. Soc. Amer. Bull.

Huggett, R.J., 2007. Fundamentals of Geomorphology, 2nd Edition, London and New York, Routledge Taylor and Francis Group.

Mahsoub, M.S., 1997. Geomorphology of Landforms, Cairo University, Dar Al-Fikr Al-Arabi for Printing and Publishing. (In Arabic).

Melton, M.A., 1958. Correlation structure of morphometric properties of drainage system and their controlling agents, Journal of Geology, Vol. 66, pp. 442-460.

Morisawa, M., Geomorphology Texts, River's form and process, 1985, pp. 91-94.

Reddy, G.P.O., Maji, A.K. and Gajbhiye, K.S., 2004. Drainage Morphometry and its influence on Land form characteristics in a Basaltic Terrain, central India, International Journal of Applied Earth Observation and Geo Information, 16 P.

Reshma P., Kumar, U. and Singh, V.K., 2012. Geomorphometric Characterization of Upper South Koel Basin, Jharkhand, Journal of Water Resource and Protection, India, Vol. 4, pp. 1042-1050.

Ritter D.F., Kochel R.C. and Miller J.R., 1995. In Process Geomorphology, Dubuque, William C. Brown.

Schumm S.A., 1977. The Fluvial System, United States of America, Jon Wiley and Sons.

Schumm, S.A., 1956. Evolution of drainage systems and slopes in Badlands at Perth Anboy, New Jersey, Bulletin of the Geological Society of America.

Sharif, A.J., 2000. Hydromorphology of the Khabur River Basin, Journal of the Iraqi Geographical Society, Issue 34, 2nd Edition, pp. 182. (In Arabic).

Sissakian, V.K., Mohammed J.A. and Rahel K.I., 2020. Industrial Assessment of the Carbonate Rocks of the Pila Spi formation at Haibat Sultan Mountain, Iraqi Kurdistan Region. Department of Natural Resources Engineering and Management, University of Kurdistan Hewler Erbil, Kurdistan Region-F.R. Iraq, Vol. 8, No.1, pp.24-30. https://aro.koyauniversity.org/index.php/aro/article/view/ARO.10546

Strahler, A.N., 1957. Quantitative analysis of watershed geomorphology, Transactions of American Geophysical Union, Vol. 8, pp. 913-920.

Zureikat, D.A. and Al-Hasban, Y.A., 2015. Morphometric Characteristics of the Zarqa River Basin in Jordan Using Geographic Information Systems and Digital Relief Model, Journal of Humanities and Social Sciences Studies, Vol. 42, Supplement 1, pp. 1482. (In Arabic).

Iraqi National Journal of Earth Science

www.earth.uomosul.edu.iq

التمثيل الخرائطي للخصائص الفيزيائية والكيميائية لترب ناحية بعشيقة، محافظة نينوى

محمد عباس حسن [1*]، لمياء حسين علي [2]

[2،1] قسم الجغرافيا، كلية التربية للعلوم الانسانية، جامعة الموصل، الموصل، العراق.

معلومات الارشفة

تاريخ الاستلام: 09- اغسطس-2024

تاريخ المراجعة: 01- اكتوبر-2024

تاريخ القبول: 03- نوفمبر-2024

تاريخ النشر الالكتروني: 01-يناير-2026

الكلمات المفتاحية:

التمثيل،

الخرائطي،

الفيزيائية،

الكيميائية،

بعشيقة،

المراسلة:

الاسم: محمد عباس حسن.

Email: mohammedabbas3223@gmail.com

الملخص

تعد هذه الدراسة تمثيلاً للخصائص الفيزيائية والكيميائية لترب ناحية بعشيقة، شمال شرقي محافظة نينوى. وجغرافياً تقع منطقة الدراسة بين دائرتي عرض ("47 '20°36-"54 '35°36) شمالاً، وبين خطي طول ("55 '10°43-"42 '32°43) شرقاً، بمساحة تقدر بحوالي (511.40) كم^2. تم إختيار (23) عينة دراسية موزعة على عموم منطقة الدراسة بغية إجراء الفحوصات الحقلية والمخبرية التي تتضمن الخصائص الفيزيائية والكيميائية للتربة من (اللون، النسجة، الرطوبة، الكثافة، المسامية، درجة تفاعل pH، والملوحة EC). كما تم التحليل النتائج للعمل المختبري ورسم الخرائط للمتغيرات في المواقع المدروسة والاعتماد على بيانات تم الحصول عليها لغرض التمثيل الخرائطي وقد وجد أن الترب تتباين من حيث اللون الذي يمثل لون المعادن الموجودة في المنطقة، فيتغير اللون بتغير المعادن ,وتبين ايضاً ان أهم نسجة للترب في منطقة البحث هي النسجة المزيجية، وان كمية ونوعية الرطوبة والمسامية والكثافة تختلف من منطقة لأخرى وفق متغيرات عدة كالمناخية (الامطار والحرارة والرياح) والخصائص التكوينية لكل منطقة وعوامل تكوين التربة. وهذا المتغيرات تؤثر ايضاً على درجة تفاعلpH والملوحة EC.

DOI: 10.33899/injes.v26i1.60215, ©Authors, 2026, College of Science, University of Mosul.
This is an open-access article under the CC BY 4.0 license (http://creativecommons.org/licenses/by/4.0/).

Mapping of the Physical and Chemical Properties of the Soils of Bashiqa District, Nineveh Governorate

Mohammed Abbas Hassan [1*], Lamia Hussein Ali [2]

[1,2] *Department of Geography, College of Education for Humanities, University of Mosul, Mosul, Iraq.*

Article information

Received: 09- Aug -2024

Revised: 01- Oct -2024

Accepted: 03- Nov -2024

Available online: 01- Jan – 2026

Keywords:
Representation,
Maps,
Physical,
Chemical,
Bashiqa,

Correspondence:
Name: Mohammed Abbas Hassan

Email: mohammedabbas3223@gmail.com

ABSTRACT

This study is a representation of the physical and chemical properties of the soils in the Bashiqa district, northeast of Nineveh Governorate. Geographically, the study area is located between latitudes (36°20'47-35°36'54) north and longitudes (43°10'55-43°32'42) east, with an estimated area of about 511.40 km^2. (23) samples distributed throughout the study area are collected to conduct field and laboratory tests, including the physical and chemical properties of the soil (color, texture, moisture, density, porosity, pH reaction degree, and salinity EC). The results of the laboratory work have been analyzed, and maps of the variables in the studied sites have been drawn, relying on the obtained data required for map representation. It is found that the soils vary in terms of color, which represents the color changes of the minerals present in the region. It is also shown that the worthiest soil texture in the region is mixed one, and that the quantity and quality of moisture, porosity, and density differ from one region to another according to several variables such as climate (rain, temperature, and wind), the compositional characteristics of each region, and soil formation factors. These variables also affect the degree of interaction between pH and salinity EC.

DOI: 10.33899/injes.v26i1.60215, ©Authors, 2026, College of Science, University of Mosul.
This is an open-access article under the CC BY 4.0 license (http://creativecommons.org/licenses/by/4.0/).

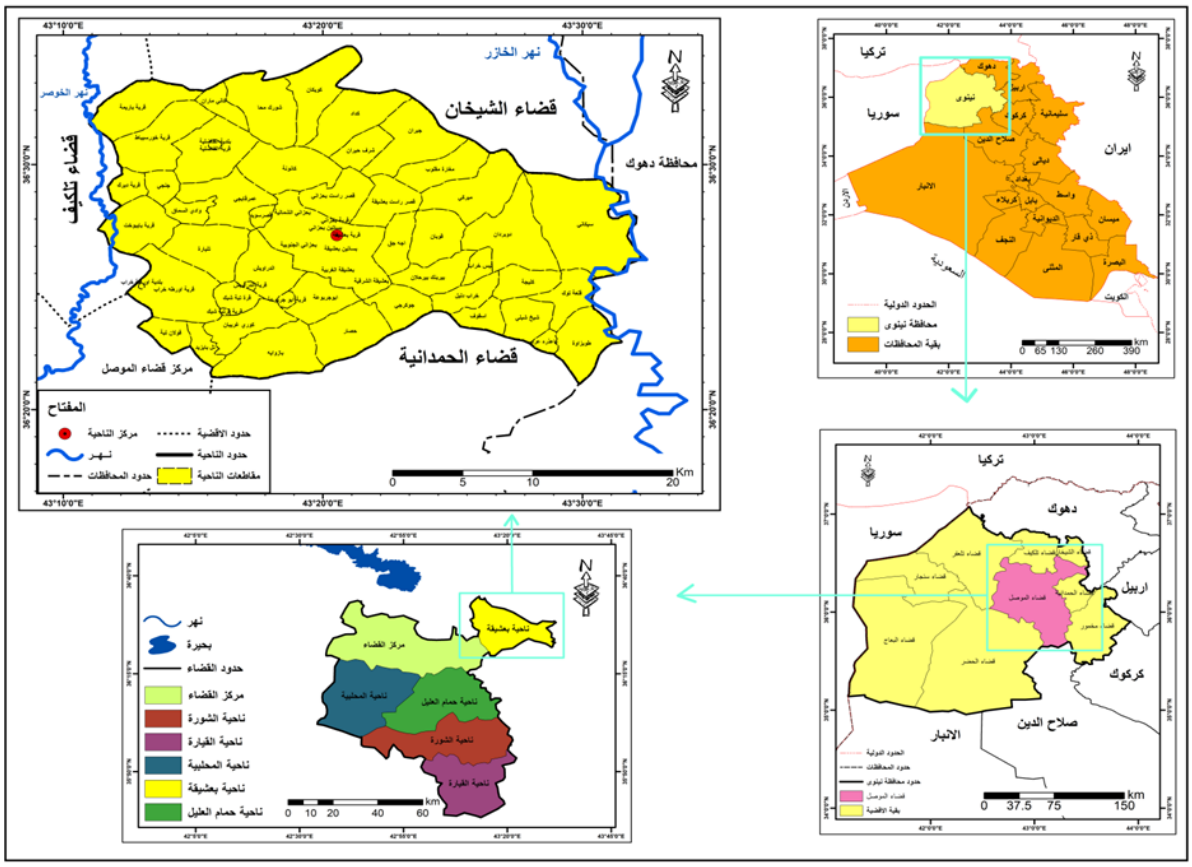
المقدمة

تعد التربة من العوامل المهمة للإنسان الى جانب الماء والهواء، فهي مورد متجدد غير قابل للنفاذ اذا ماتم استخدامها بشكل صحيح. وإنها موضع اهتمام للعديد من المجالات العلمية، اذ تتم دراستها في العديد من الاقسام العلمية مثل الهندسة والموارد المائية والزراعة والجغرافية وعلوم الارض؛ وهذا يؤكد اهميتها مما يجعلها مرتبطة بهذه المجالات. وتتأثر جميع استخدامات التربة بشكل كبير بالخصائص الفيزيائية والكيميائية؛ وإن دراستها تهدف الى فهم التربة والوصول الى اساسياتها من خلال النظر الى النظام الجيوفيزيائي للقشرة السطحية، فالجغرافية تهتم بدراسة خصائص التربة من حيث توزيعها الجغرافي في منطقة معينة او العالم، والزراعة تدرس الخصائص العامة الفيزيائية والكيمياوية بهدف توضيح علاقتها بالإنتاج الزراعي؛ فكل علم يهتم بدراسة التربة وفقاً لمجال تخصصه.

من الممكن ان تختلف خصائص التربة من مكان لأخر في منطقة الدراسة بسبب اختلاف عوامل تكوين التربة في ناحية بعشيقة. ومما تجدر الاشارة اليه ان الزراعة موجودة في جميع جهات ناحية بعشقية فهي منطقة تشتهر بالزراعة بمختلف أنواعها (Al-Salem, 1989)، وأن التطبيقات الفيزيائية والكيميائية للتربة تهدف الى استعمال الآلات الخاصة في إدارة التربة من خلال عمليات الري والبزل، وصيانة التربة والمياه وحراثة التربة وبناء التربة عن طريق تحسين التهوية، وتنظيم حرارة التربة (Hassan, 1990) فضلاً عن استعمال التربة كمواد بناء وشق الطرق وبناء السدود واستخدامها كحواجز طبيعية بين دولة واخرى.

موقع منطقة الدراسة

تقع منطقة الدراسة في شمالي العراق والشمال الشرقي من مدينة الموصل، وهي تابعة إدارياً لقضاء الموصل؛ وبين دائرتي عرض ("47 '20°36–"54 '35°36) شمالاً وبين خطي طول ("55 '10°43 – "42 '32°43) شرقاً؛ أما الحدود الادارية للناحية فيحدها من الشمال قضاء الشيخان، ومن الجنوب قضاء الحمدانية؛ ومن الشرق محافظة دهوك؛ ومن الغرب قضاء تلكيف؛ و من الجنوب الغربي مركز قضاء الموصل (حدود بلدية الموصل) كما موضح في الخريطة ادناه (شكل 1).



الشكل 1. خريطة العراق الادارية بمقياس (1000000:1) بالاعتماد على: جمهورية العراق، وزارة الزراعة، ومديرية ناحية بعشيقة، شعبة الحاسبة، سجلات غير منشورة، سنة 2012 تبين موقع الدراسة(Republic of Iraq, 2012)

التكاوين الجيولوجية لناحية بعشيقة

تتكون ناحية بعشيقة من عدة تكوينات جيولوجية يمكن ان نوضحها كما يأتي:

تكوين بيلاسبي (الايوسين الأوسط): يتألف هذا التكوين بصورة رئيسة من الحجر الدولوماتي والحجر الجيري المتدلمت، الذي يكون ذا لون أبيض أو رمادي فاتح. يظهر هذا التكوين بالدرجة الأولى في منطقة بعشيقة ويبلغ سمكه حوالي 191م ويكون حد التماس العمودي للتكوين غير متوافق مع تكوين فتحة، كما أن سطح التماس السفلي غير متكشف على السطح. ويغطي هذا التكوين معظم أجزاء طية مقلوب المرتبطة بطية منددان .(Khalid, 2016) وتبلغ مساحة التكوين (90.51) كم2 وبنسبة تشمل حوالي.% (17.70)

تكوين فتحة (المايوسين الأوسط): يظهر هذا التكوين في الاطراف المستوية المحيطة بطيات المنطقة المحدبة كطية بعشيقة والفاضلية وعين الصفرة ومقلوب، ويظهر بشكل حزام حول المنطقة .(Al-Bassam, 2012) وتقدر مساحته بـ (35.80) كم2 وبنسبة (7) %. يصل أعلى سمك للتكوين في منطقة الدراسة إلى (200) م، ويتكون من الحجر الجيري

والطيني والطفل التي تشكل المواد الأساسية للبناء والإسمنت وغيرها، فضلاً عن احتوائه على كسور وفواصل تساعد على حركة المياه الجوفية.(Al-Rawi, 1986)

تكوين إنجانة (الميوسين الأعلى): ويمثل رواسب فتاتية. فالحركات التي حدثت آنذاك جعلت منطقة المصدر أكثر انحداراً نحو الحوض الترسيبي مما جعل صخارية التكوين تتكون بصورة رئيسة من تعاقبات أطيان حمراء أو خضراء وغرين ورمل، إذ تزداد نسبة المواد الفتاتية الخشنة الحجم باتجاه أعلى التكوين، أما في أجزائه السفلى فهناك نعومة للحبيبات مع ازدياد المكونات الجيرية والطفل، وسمك هذا التكوين متباين من موقع إلى آخر ويصل أقصى سمك له في هذه الدراسة الى (150) متراً .(Alridha et al., 2013) من الصعب التعرف على سمك التكوين في منطقة الدراسة لتغطيته بالترسبات الحديثة. أن الحوض الرئيس لتكوين إنجانة يقع في الجزء الجنوبي الشرقي لمدينة الموصل ويتراوح سمكه عموماً في مواقع اخرى مابين (30–220) متراً من خلال سجل حفر الآبار المائية في المنطقة .(Ramzi et al., 2020) وتبلغ مساحته (93.46) كم2 وبنسبة تصل الى.% (18.28)

تكوين مقدادية (الباليوسين) توجد مكاشف هذا التكوين الصخري في الجزء الشمالي من طية مقلوب والجنوب الشرقي من منطقة الدراسة وعلى امتداد نهر الخازر من طية مقلوب الى نهاية حدود بعشيقة عند طية عين صفرة، ويتكون من صخور رملية حاوية على الحصى وصخور طينية وصخر صواني مع المتكتلات، وتبلغ مساحة هذا التكوين (26.33) كم2 وبنسبة.% (5.15)

ترسبات العصر الرباعي :(Quaternary) تشغل ترسباته تقريباً نصف الخصائص الجيولوجية في منطقة الدراسة، إذ تبلغ المساحة التي يشغلها (259.81) كم2 ما نسبته (53.68) % من مساحة المنطقة، وتتميز هذه التكوينات بانها نواتج تعرية الانهار على التكوينات في منطقة الدراسة حيث ترسبت فوق التكوينات الاقدم عمراً منها، ويعود عمر هذا الترسبات الى عصر البلايستوسين والهولوسين.(Jassim and Goff, 2006)

انواع الرواسب في منطقة الدراسة بالاعتماد على الخريطة في الشكل (2):

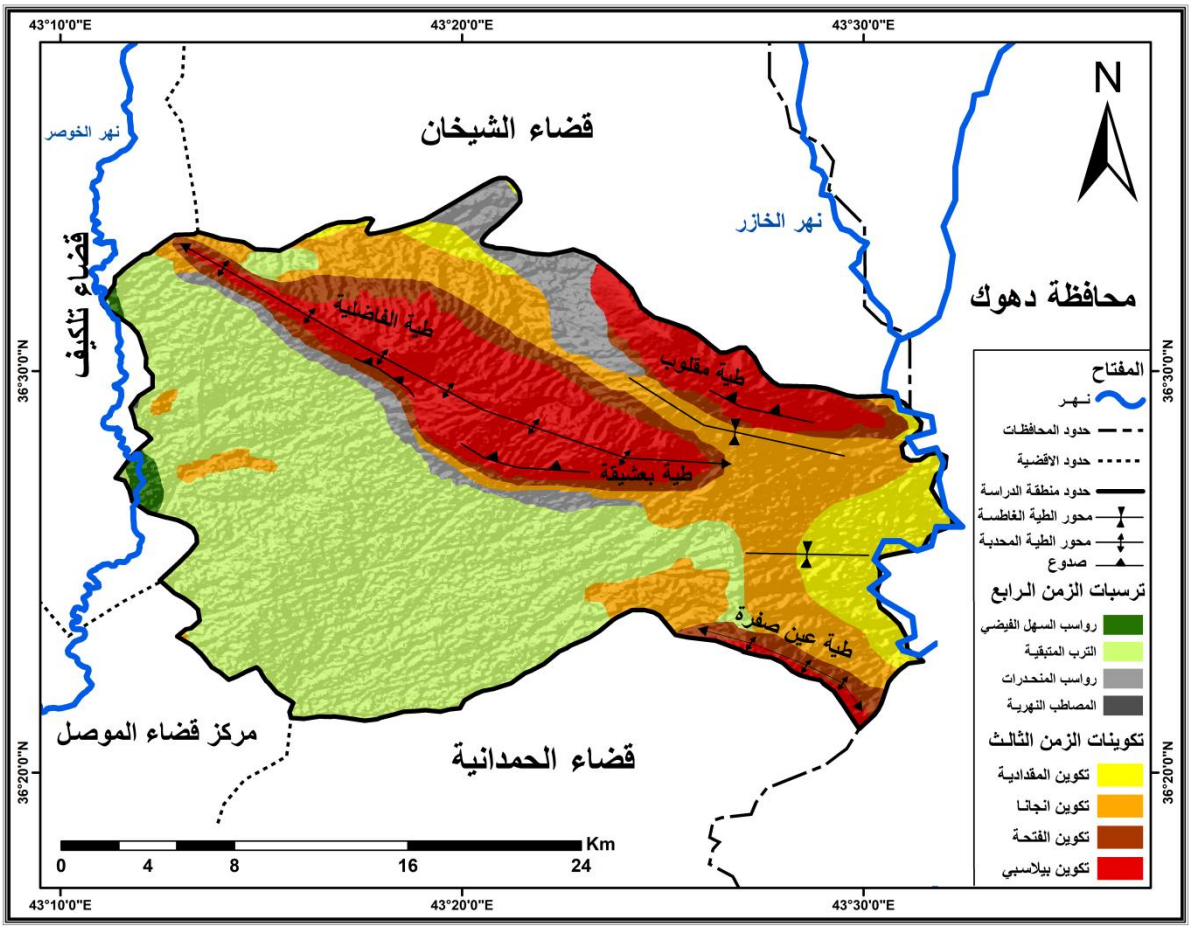
أ–رواسب المنحدرات: تتكون هذه الرواسب من مواد طينية وغرينية وحصى بأحجام مختلفة فضلاً عن الرمل وفتات من الحجر الكلسي وقطع صخرية مختلفة في الحجم والتركيب الصخري، وتظهر ترسبات المنحدرات ضمن منطقة الدراسة في العديد من الأجزاء بشكل الامتداد مع طية بعشيقة والفاضلية ومقلوب حيث تتجمع هذه الترب أسفل الطيات في منطقة الدراسة، وأن المساحة التي تغطيها (28.21) كم^2 وبنسبة (5.51) % من مجموع التكوينات في ناحية بعشيقة.

ب– الترب المتبقية: هي عبارة عن ترب اشتقت من الصخور التي ترتكز عليها، لذا فهي غنية بالمعادن التي تتكون منها هذه الصخور، وتنتشر في منطقة الدراسة في الاراضي المستوية وذات التموج الخفيف وتمتد من بداية الشمال الشرقي وحتى نهاية الجنوب الشرقي وبالامتداد داخل المنطقة وتوقفت عند الوصول الى الطيات الثلاثة (الفاضلية، بعشيقة، عين صفرة) وبهذا الامتداد تغطي مساحة قدرها (228.03) كم^2 ونسبته (44.59) %.

ج–رواسب السهل الفيضي: تتألف من ترسبات متباينة من الحصى والرمل والغرين والطين، ترسبت بشكل دورات ترسيبية متتالية، وتنتشر بشكل واضح على ضفاف نهر الخوصر في القسم الغربي من منطقة الدراسة. وعلى الرغم من وجود نهر الخازر على جهة الشرقي الا أنها لا تظهر انواع ترب السهل الفيضي، وتغطي السهول الفيضية ما يقارب (3.44) كم^2 وبنسبته (0.67) %.

د–المصاطب النهرية: مكونات هذه الرواسب من الرمل والغرين والطين وقليل من الحصى على شكل عدسات صغيرة وفتات الحجر الجيري، وهي بمجملها تمثل رواسب الأودية النهرية والتي لا تزال مستمرة بالترسيب إلى الوقت الحاضر، وتوجد في جانبي بعشيقة على امتداد نهر الخازر ونهر الخوصر وبارتفاع منسوبها في فصل الشتاء وانخفاضها في

فصل الصيف لتتشكل المصاطب النهرية (0.12) كم^2 ونسبته (0.02) %. كما موضح في الشكل (2) جيولوجية منطقة الدراسة.



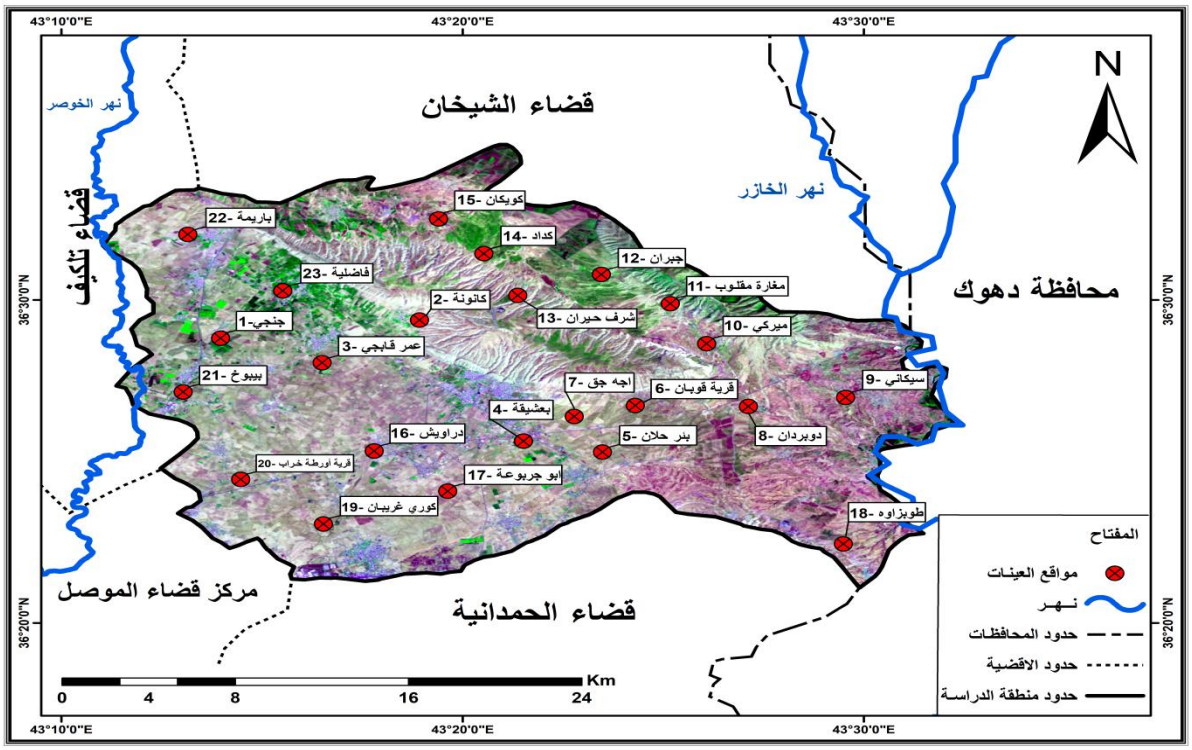
الشكل 2. خريطة ناحية بعشيقة الجيولوجيا، بالاعتماد على خريطة العراق الجيولوجيا، وزارة الصناعة والتعدين، المنشأة العامة للمسح الجيولوجي والتعدين، بغداد، 1995، بمقياس 1:250000(GEOSURV, 1995)

طرائق ونتائج العمل

ان القيام بعمل ميداني يتطلب الإلمام بأمور عدة ومنها موقع المنطقة المدروسة ونوع الدراسة وانتخاب الادوات للقيام بالعمل المطلوب والمعرفة التامة بمنطقة الدراسة ليسهل القيام بالعمل الميداني (اللوحة 1). لذا أُخذت العينات وفقاً للنمط العشوائي بحيث تغطي منطقة الدراسة بالكامل ليسهل معرفة خصائصها الفيزيائية والكيميائية وانتخاب مواقعها؛ وللقيام بذلك تم جمع العينات من (23) موقعاً في منطقة الدراسة للقيام بالتحاليل المختبرية عن طريق تحديد إحداثيات كل موقع بشكل تقريبي مسبقاً. واعتماداً على نظام تحديد الموقع العالمي (GPS) وباستخدام جهاز (Garmin) بعد اخذ العينة، وعليه أُخذت الترب من عمق (30) سم وتعبئتها في اكياس لإجراء الفحوصات المطلوبة كما موضح في الجدول (1) والشكل (3).

الجدول1: مواقع اخذ عينات التربة ضمن ناحية بعشيقة.

تسلسل العينة	خطوط الطول	دوائر العراض
1-جنجي	43° 13' 58.117" E	36° 28' 49.013" N
2-كانونة	43° 18' 55.569" E	36° 29' 22.814" N
3-عمر قابجي	43° 16' 30.223" E	36° 28' 3.381" N
4-بعشيقة	43° 21' 31.055" E	36° 25' 38.036" N
5- بئر حلان	43° 23' 29.360" E	36° 25' 17.755" N
6-قرية قوبان	43° 24' 18.372" E	36° 26' 43.948" N
7-اجه جق	43° 22' 47.108" E	36° 26' 23.667" N
8-دوبردان	43° 27' 7.378" E	36° 26' 42.258" N
9-سيكاني	43° 29' 32.724" E	36° 26' 59.159" N
10-ميركي	43° 26' 4.846" E	36° 28' 38.873" N
11-مغارة مقلوب	43° 25' 10.764" E	36° 29' 53.236" N
12-جبران	43° 23' 27.670" E	36° 30' 47.318" N
13-شرف حيران	43° 21' 22.605" E	36° 30' 8.446" N
14-كداد	43° 20' 31.903" E	36° 31' 26.189" N
15-كويكان	43° 19' 24.300" E	36° 32' 30.412" N
16-دراويش	43° 17' 47.966" E	36° 25' 19.445" N
17-ابو جربوعة	43° 19' 37.821" E	36° 24' 5.082" N
18-طوبزاوة	43° 29' 29.344" E	36° 22' 27.058" N
19-كوري غريبان	43° 16' 31.913" E	36° 23' 4.240" N
20-قرية أورطة خراب	43° 14' 28.538" E	36° 24' 27.053" N
21-بابيوخ	43° 13' 2.345" E	36° 27' 9.299" N
22-باريمة	43° 13' 9.105" E	36° 32' 1.681" N
23-فاضلية	43° 15' 31.071" E	36° 30' 16.897" N



الشكل 3. مواقع عينات الترب لناحية بعشيقة بالاعتماد على جدول (1) باستخدام برنامج.(ArcGIS10.8)



اللوحة 1: طريقة العمل الميداني.

وفي المختبر تم اجراء الفحوصات للحصول على نتائج خصائص الكيميائية والفيزيائية للتربة وكما مبين في اللوحة (2).



اللوحة 2: المختبر المركزي، قسم التربة والموارد المائية، كلية الزراعة والغابات، جامعة الموصل.

ان لكل تربة خصائص وان هذه الخصائص تتكون من جزيئات معدنية وعضوية واملاح ذات أحجام مختلفة؛ وهذه الجزيئات تتكون من مسامات وان 50 % من مساحة هذه المسامات تشغلها الماء والهواء. وينتج عن ذلك نظام ثلاثي الطور من المواد الصلبة والسوائل والغازات (Foth, 1991).

أن خصائص الترب التي سنتطرق اليها هي الخصائص الفيزيائية (اللون، النسجة، الرطوبة، الكثافة، المسامية)؛ والخصائص الكيميائية (درجة تفاعل pH– الملوحة EC).

الخصائص الفيزيائية

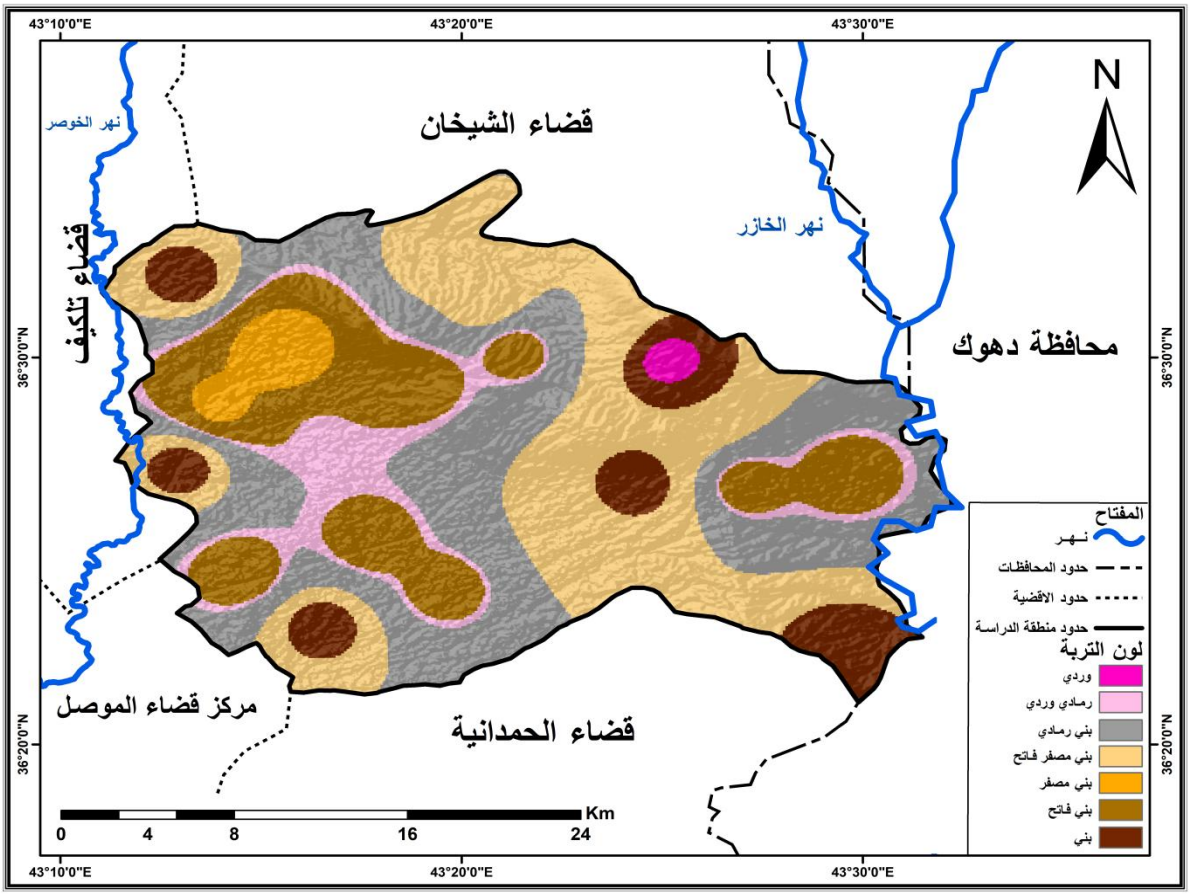
لون التربة (Soil Color)

يعد لون التربة من أكثر خصائص التربة وضوحا وأسهلها في القياس وأول ما يلاحظه الإنسان بالعين المجردة، ويعتمد لون التربة على عدد من العوامل منها المادة الأصل التي تكونت منها التربة وما تحتويه من معادن، ودور كل من نسبة الرطوبة ودرجة الحرارة في حصول عملية الغسل أو الترشيح، وهل أن التربة جيدة التهوية أم أنها من الترب اللاهوائية، فضلاً عن عامل المناخ لاسيما الأمطار ودورها في تشكيل وزيادة نسبة والمادة العضوية العضوي.

يعكس لون التربة التأثير المتداخل الألوان مكونات التربة وخواصها الكيميائية والطبيعية والحيوية، كما يبين اللون حالة الصرف وظروف التهوية ومستوى الماء الأرضي. وتتراوح التربة في ألوانها بين الأصفر والأحمر والبني الغامق والأسود. ويساعد لون التربة علماء التربة في تقدير كمية الهواء والماء والمواد العضوية وبعض العناصر في التربة. فقد يدل اللون الأحمر مثلاً على وجود مركبات الحديد في التربة ويدل اللون الابيض على وجود الاملاح في تربة وهكذا بالنسبة لباقي الألوان (Abu Sammour, 2009). يعد اللون الغامق أحد أكثر الالوان انتشاراً في ناحية بعشيقة حيث تكون ألوان ترب اغلب مناطق الدراسة (بني، بني فاتح، بني مصفر فاتح، بني مصفر، وبني رمادي) ومنطقة او منطقتين ذات الألوان (رمادي وردي، وردي) موزعة في عموم منطقة الدراسة. وتتكون منطقة الدراسة من (23) عينة موزعة على منطقة الدراسة بشكل عشوائي منتظم بحيث تغطي كافة المنطقة. وتم فحص انواع الترب من حيث اللون بالاعتماد على كتاب (Munsell Soil Color Charts) وهو كراس أو فهرست الالوان يوضح انواع الترب بحسب التدرج اللوني لكل تربة، كما موضح في الجدول (2).

الجدول 2: التحليل المختبري للخصائص الفيزيائية والكيميائية لناحية بعشيقة.

تسلسل العينة	رمز اللون الجاف	اسم اللون	مفصولات التربة			صنف النسجة	رطوبة التربة	الكثافة الظاهرية	مسامية الترب	قيم الملوحة (Ece)	درجة تفاعل التربة (pH)
			الرمل/ Sand	الطين/ Clay	الغرين/ Silt						
1	10YR 5/4	بني مصفر	44.05	39.45	16.5	طينية رملية/Sandy clay	1.28	1.49	43.8	0.4	7.1
2	7.5YR 6/4	بني فاتح	26.55	39.45	34	مزيجية طينية/Clay loam	3.17	1.07	59.6	0.8	7.2
3	7.5YR 6/2	رمادي وردي	19.05	51.95	29	طينيةClay	6.46	0.91	65.6	0.6	7.4
4	10YR 5/2	بني رمادي	44.05	21.95	34	طينية/Clay	1.62	0.72	72.8	0.6	7.3
5	10YR 6/4	بني مصفر فاتح	44.05	24.45	31.5	مزيجية/Loam	1.04	0.85	67.9	0.4	7.6
6	10YR 5/3	بني	31.55	29.45	39	مزيجية طينية/Clay loam	2.29	1.55	41.5	0.4	7.6
7	10YR 6/4	بني مصفر فاتح	46.55	21.95	31.5	مزيجية/Loam	1.15	1.05	60.3	0.3	7.6
8	7.5YR 6/4	بني فاتح	31.55	44.45	24	طينية/Clay	3.36	1.06	60	0.6	7.2
9	7.5YR 6/4	بني فاتح	30.14	43	23.46	طينية/Clay	7.22	1.54	41.8	0.5	7.3
10	10YR 6/4	بني مصفر فاتح	40.11	32.27	21.15	مزيجية طينية/Clay loam	1.33	0.73	72.4	0.3	7.8
11	7.5YR 7/4	وردي	41.55	35.95	22.5	مزيجية طينية/Clay loam	1.94	1.87	29.4	0.6	7.6
12	10YR 5/2	بني رمادي	69.05	20.95	10	مزيجية طينية رملية /Sandy clay loam	2.27	0.61	76.9	0.4	7.7
13	7.5YR 6/4	بني فاتح	36.55	38.45	25	مزيجية طينية/ Clay loam	2.37	1.72	35	0.6	7.4
14	10YR 6/4	بني مصفر فاتح	61.55	23.45	15	مزيجية طينية رملية/ Sandy clay loam	2.57	0.8	69.8	0.5	7.2
15	10YR 6/4	بني مصفر فاتح	34.55	34.45	31	مزيجية طينية/Clay loam	5.26	1.01	61.8	0.6	7.3
16	7.5YR 6/4	بني فاتح	54.55	26.95	18.5	مزيجية طينية رملية/ Sandy clay loam	2.29	1.52	42.6	0.8	7.3
17	7.5YR 6/4	بني فاتح	49.55	26.95	23.5	مزيجية طينية رملية/ Sandy clay loam	3.11	0.9	66	0.6	7.6
18	10YR 5/3	بني	37.05	34.45	28.5	مزيجية طينية/Clay loam	3.14	1.58	40.3	0.5	7.6
19	10YR 5/3	بني	44.55	24.45	31	مزيجية/ Loam	1.82	0.6	77.3	0.8	7.4
20	7.5YR 6/4	بني فاتح	34.55	39.45	26	مزيجية طينية/ Clay loam	2.18	1.51	43	0.7	7.3
21	7.5YR 5/2	بني	37.05	29.45	33.5	مزيجية طينية/Clay loam	6.96	0.62	76.6	2.6	7.4
22	7.5YR 5/4	بني	21.55	42.45	36	طينية/Clay	4.63	1.22	53.9	1	7.6
23	10YR 5/4	بني مصفر	19.05	39.95	41	طينية غرينية/Silty clay	4.73	0.7	73.5	0.8	7.5
المعدل			39.07	27.20	33.29		3.13	1.11	57.90	0.66	7.43



الشكل 4. التوزيع الجغرافي لألوان الترب في منطقة الدراسة.

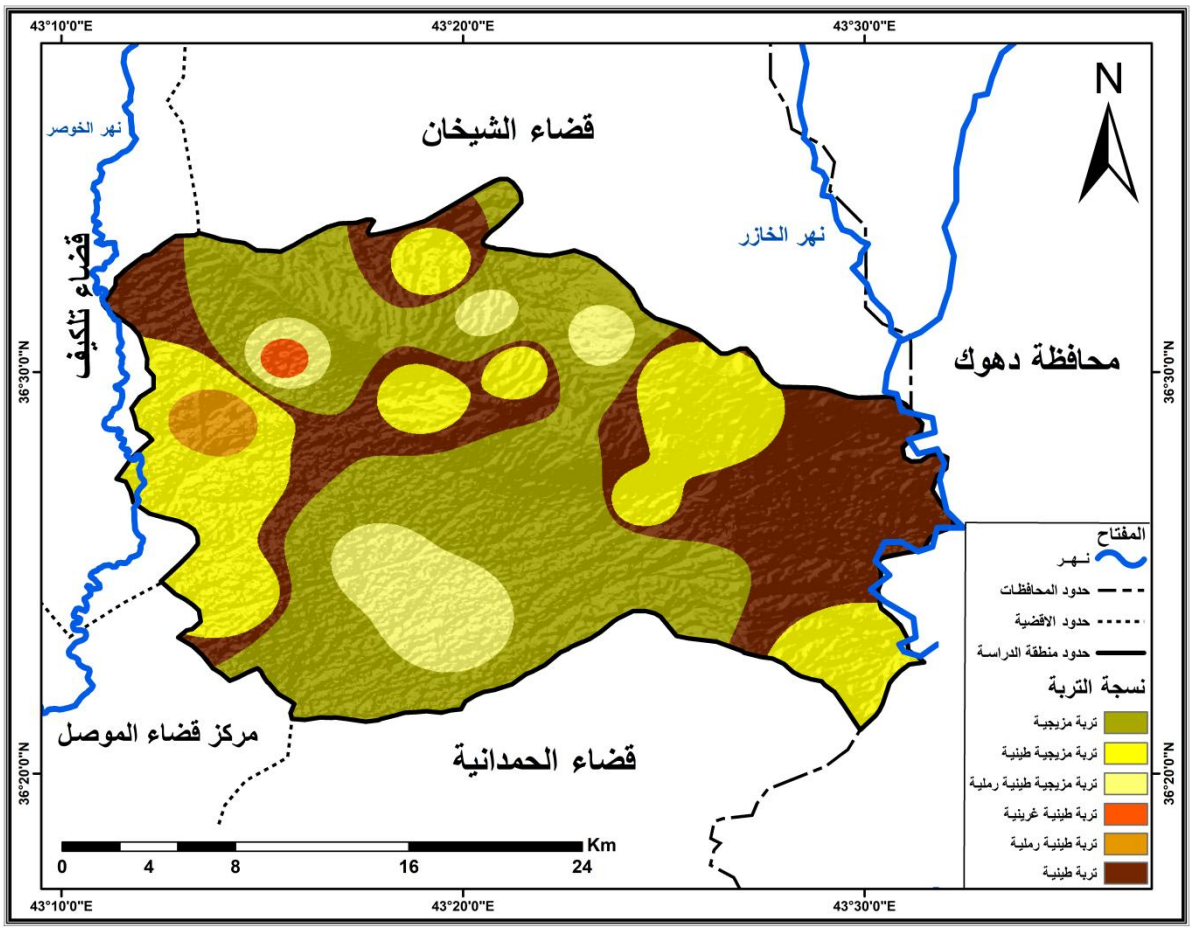
الجدول 3: يوضح مساحة ونسب التوزيع الجغرافي للون في منطقة الدراسة.

ت	لون التربة	المساحةكم^2	النسبة%
1	بني مصفر	16.20	3.16
2	بني فاتح	92.77	18.14
3	رمادي وردي	41.91	8.19
4	بني رمادي	152.91	29.90
5	بني مصفر فاتح	159.14	31.11
6	بني	45.02	8.80
7	وردي	3.43	0.67
8	المجموع	511.40	100%

نسجة التربة (Soil Texture)

هي التوزيع النسبي لمجاميع الاحجام المختلفة لمفصولات التربة (الرمل Sand، الطين Clay، الغرين Silt) اي مدى نعومة وخشونة التربة (Roth, 2012)، ويتدرج التوزيع النسبي لمفصولات التربة من نسيج رملي خشن جداً الى نسيج طيني، وتحدد النسجة المساحة السطحية النوعية للتربة والتي تعتمد عليها الكثير من الخواص الكيميائية والفيزيائية والحيوية. ويتم تحديد النسجة اما عن طريق اللمس أو قياس النسب المختلفة للرمل والغرين والطين في المختبر(Al-Mawsiliand Al Khafaji 2013). نادراً ما تتكون التربة من مجموعة واحدة من الذرات (الرمل Sand، الطين Clay، الغرين Silt) وإنما هي في الغالب تتكون من خليط من ذرات متباينة الأحجام، ولكن دائماً ما يبرز نوع من ذرات الترب على باقي الأنواع ولذلك يسمى النسيج باسم الذرات المهيمنة في التربة. أن اصناف النسجة لترب منطقة الدراسة مكونة من 6 اصناف وهي العينة (1) التي تتكون من نسجة طينية رملية Sandy clay، والعينة (23) التي تتكون من

نسجة طينية غرينية Silty clay، وتتكون العينات (12–14–16–17) من نسجة مزيجية طينية رملية Sandy clay loam، وان العينات (4–5–7–19) تتكون من نسجة مزيجية Loam، وكذلك العينات (3–8–9–22) تتكون من نسجة طينية Clay، كما ان العينات(2–6–10–11–13–15–18–20–21) تتكون من نسجة مزيجية طينية Clay loam؛ اي ان اقل نسجة في المنطقة تظهر في النسجة الطينية الرملية والنسجة الطينية الغرينية بواقع عينة واحدة لكل منهما؛ واعلى نسبة هي للنسجة المزيجية الطينية loam Clay بواقع (9) عينات. ان أعلى نسبة من بين نسب النسجة هي الرمال Sand والتي بلغت (39.07) % من اجمالي الانسجة الموجودة في منطقة الدراسة ويأتي الغرين Silt بعدها من حيث النسبة حيث يشكل (33.29) % من اجمالي النسجة وتكون نسبة الطين Clay هي الاقل في منطقة الدراسة بنسبة (27.20)%.



الشكل 5. التباين المكاني لتوزيع اصناف النسجة في منطقة الدراسة.

الجدول 4: مساحة ونسب اصناف النسجة في منطقة الدراسة.

ت	نسجة التربة	المساحة كم2	النسبة%
1	طينية رملية/Sandy clay	7.97	1.55
2	مزيجية طينية/Clay loam	117.26	22.92
3	طينية/Clay	135.60	26.51
4	مزيجية/Loam	201.99	39.49
5	مزيجية طينية رملية /Sandy clay loam	46.02	8.99
6	طينية غرينيةSilty clay/	2.53	0.49
	المجموع	511.40	%100

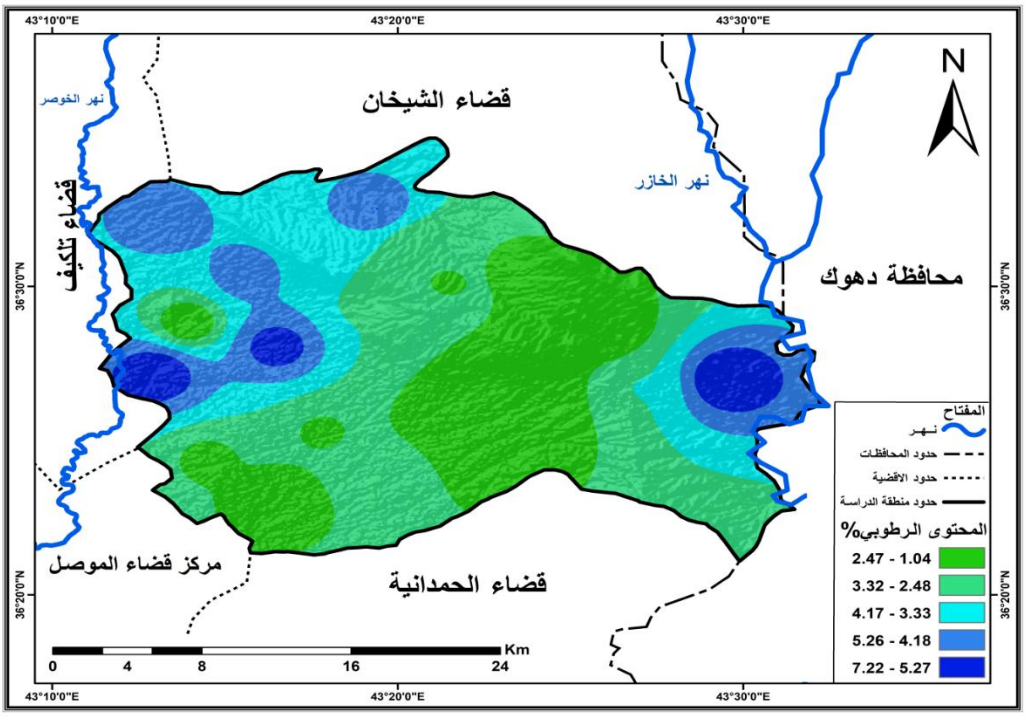
رطوبة التربة(Soil moisture)

يقصد برطوبة التربة نسبة المياه الموجودة في التربة، وتتباين هذه النسبة بحسب فصول السنة وتتباين من تربة لأخرى تبايناً كمياً بحسب التركيب الحبيبي والكيميائي ومسامية التربة. وتعد الرطوبة من اهم صفات التربة الفيزيائية ولها دور كبير في تكوين وتطور التربة اذ توفر الرطوبة الوسط المناسب للتفاعلات الكيميائية المختلفة فيها وفي توفير الوسط المناسب للنشاط الحيوي أذ تعتمد كمية الرطوبة التي تحصل عليها التربة على مجموعة من العوامل (نفاذية التربة، الانحدار، التساقط المطري، معدل التبخر والنتح، والتغيرات الموسمية) (Habib, 2008). ولمعرفة محتوى الرطوبة لعينات ترب مواقع الدراسة تم استعمال ميزان حساس، فرن كهربائي حراري، أوعية فرن مرقمة فارغة، وعينات التربة لكل موقع، فتم وزن الأوعية (البيكر) وهي فارغة (w1 وزن الوعاء) وبعد ذلك نضع عينات التربة في الأوعية بمقدار يقارب (250) غم أو أكثر ومن ثم وزنها مجدداً ثم نضع البيكر في الفرن الحراري لمدة (24) ساعة وعلى حرارة (105)° نستخرج العينة من الفرن ثم نوزنها (w3 وزن الوعاء +التربة بعد التسخين). ولاستخراج معدل الرطوبة يتم تطبيق المعادلات الثلاثة الآتية:

$$\text{الرطوبة على اساس وزن رطب \%} = 100 \times \frac{w3 - w2}{w1 - w2}$$

$$\text{الرطوبة على اساس وزن الجاف \%} = 100 \times \frac{w3 - w2}{w1 - w3}$$

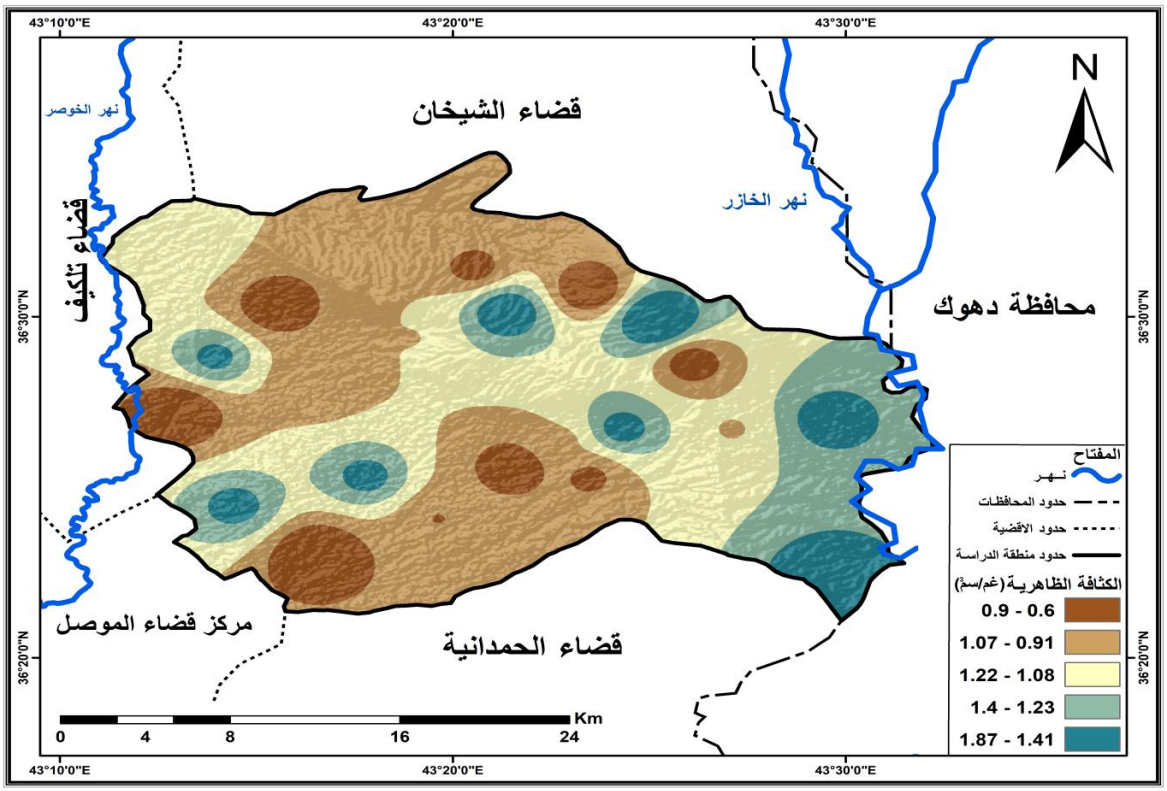
وبعد تطبيق الخطوات اعلاه التي تعني قياس وزن العينة للتربة قبل التسخين وتسجيل نسبتها وقياسها بعد التسخين وقياس نسبتها التي تكون (نسبة ماقبل التسخين ناقص نسبة مابعد التسخين مطروح منها وزن الوعاء وبذلك يظهر صافي نسبة الرطوبة في التربة). تم الحصول على النسبة المئوية للرطوبة في ناحية بعشيقة وبلغت اعلى درجة للرطوبة في العينة (7–سيكاني) بمعدل (7.22) % التي تقع شرقي ناحية بعشيقة، وبلغت اقل درجة للرطوبة في العينة (5–بئر حلان) وبمعدل (1.04) % في الجنوب الشرقي من منطقة الدراسة، وبلغ المعدل العام لرطوبة التربة في ناحية بعشيقة (3.13) % كما مبين في الجدول (2) والشكل (6).



الشكل 6. محتوى رطوبة التربة لمنطقة الدراسة.

الكثافة الظاهرية(Bulk density)

تعرف الكثافة الظاهرية على أنها كتلة وحدة الحجم الظاهري للتربة الجافة والتي تحتفظ ببنائها الطبيعي ويشمل الحجم الجزء الصلب للتربة والمسامات الموجودة بينها، اي انها مقياس يعبر عن كثافة التربة بما في ذلك الفراغات الموجودة بين الجسيمات. تستخدم هذه القيمة لتحديد مدى تراص التربة والقدرة على تخزين الماء والمغذيات، وتمثل عادة بالغرامات في السنتمتر المكعب(Foth, 1991) وتتراوح قيمتها في معظم الترب مابين (0.6–1.87) في منطقة الدراسة. ويشير ارتفاع قيم الكثافة الظاهرية الى ان التربة متماسكة وهي نوع من التربة التي تلتصق ببعضها البعض وذات نفاذية قليلة للماء لتكونها من الطمي والطين الذي يؤثر بدوره في نمو وتنفس جذور النباتات، بينما تنخفض هذه النسبة في التربة المفككة غير المتماسكة. فقيمة الكثافة الظاهرية تعكس خصائص التربة من نسجة وبناء ونوع المعادن، لذلك فالترب الثقيلة تكون كثافتها الظاهرية اقل مما عليه الترب الخفيفة لان المسامية في الترب الثقيلة اصغر من مسامية الترب الخفيفة (Al-Ameri, 2005)، وبالنسبة للكثافة الحقيقية فهي تعبر عن كثافة حبيبات الترب الجافة تماماً دون الاخذ بالاعتبار للفراغات المسامية الموجودة بين حبيبات التربة، وبلغ معدل العام للكثافة الحقيقية في المنطقة المدروسة(2.65) غم/سم^3 استناداً الى الدراسات السابقة على ان الكافة الحقيقية للترب الفقيرة بالمادة العضوية تتراوح مابين (2.60 –2.75) غم/سم^3، وعليه وفق الدراسات السابقة يمكن الاستدلال على قلة المادة العضوية في ترب المنطقة بسبب العلاقة العكسية بينها وبين الكثافة الحقيقية؛ اي إن الكثافة الظاهرية تكون اقل دائماً من الكثافة الحقيقية لنفس التربة، فإن كانت الفراغات البينية تمثل نصف الحجم الكلي للتربة، فإن الكثافة الظاهرية تصبح نصف الكثافة الحقيقية، ولا يمكن بأي حال من الأحوال ان تزيد الكثافة الظاهرية عن الكثافة الحقيقية، كما انه ليس من المعقول أن تتساوى هاتان القيمتان والا فان المسامية تكون صفراً. تتأثر قيمة الكثافة الظاهرية ببناء التربة أي درجة انضغاطها أو تفككها وذلك بعمليات الخدمة المختلفة وكذلك بتمددها وانكماشها والتي تعتمد بدورها على محتوى التربة من الطين ومحتواها الرطوبي وكذلك تتأثر بنسبة المادة العضوية الموجودة بالأرض (Abdel Hady, 1998) (الشكل 7).



الشكل 7. الكثافة الظاهرية لترب منطقة الدراسة.

المسامية(porosity)

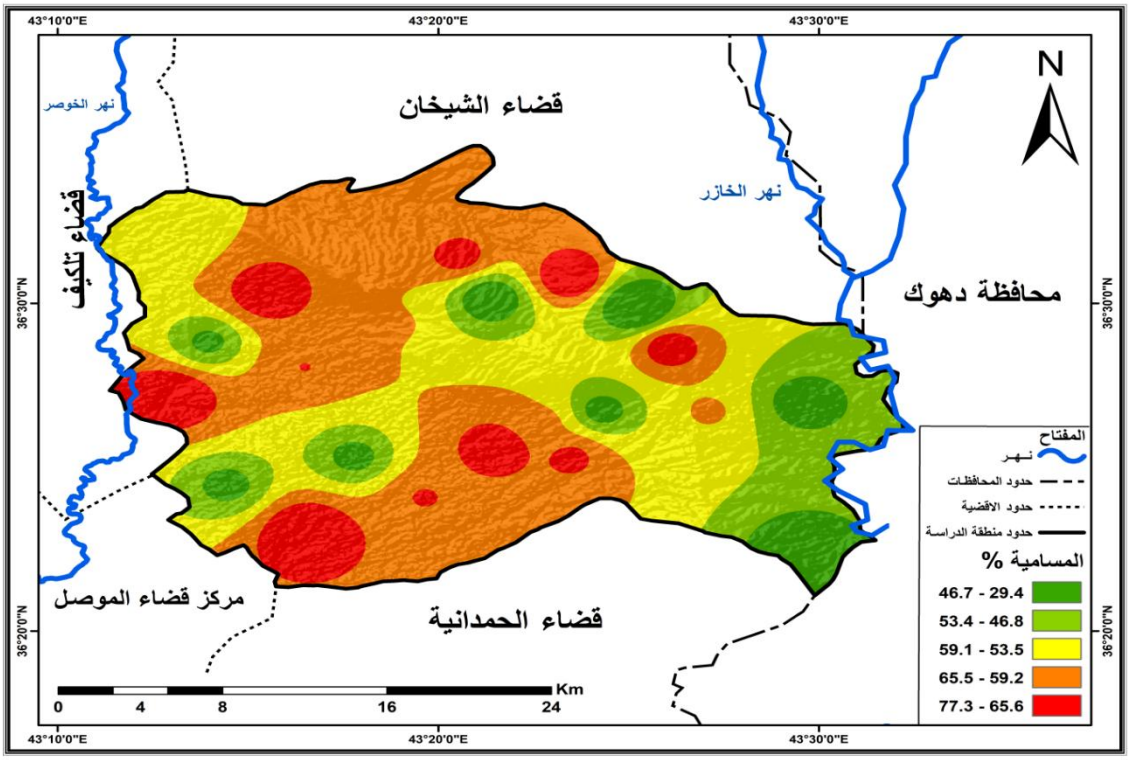
يقصد بالمسامية النسبة المئوية بين حجم الفراغات الموجودة في التربة والحجم الكلي لها التي تشير إلى الفراغات الموجودة بين حبيبات التربة، والتي يمكن أن تحتوي على الماء أو الهواء (Al-Musawi, 2005). وتستعمل المسامية كدليل نسبي لحجم الفراغات الموجودة في التربة. تقع قيم المسامية لمعظم الترب ضمن المديات 0.3–0.6 اي من (30–60) %. فالترب ذات النسجة الخشنة تميل لأن تكون اقل مسامية من الترب ذات النسجة الناعمة، رغم أن معدل حجم المسامات المفردة تكون كبيرة في التربة ذات النسجة الخشنة عند مقارنتها مع التربة ذات النسجة الناعمة. تمتاز الترب الطينية بمساميتها المختلفة وذلك بسبب قدرتها على التمدد والانكماش والتجميع والتفرقة والانضغاط والتشقق Hassan, (1990).

يكون حساب واستخراج المسامية عن طريق معادلة حسابية تعتمد على الكثافة الظاهرية والكثافة الحقيقية في حين تكون وفق المعادلة والمثال الآتي:

$$\%\text{المسامية} = (1 - \frac{\text{الكثافةالظاهرية}}{\text{الكثافةالحقيقية}} \times 100)$$

$$\%\text{المسامية} = (1 - \frac{1.49}{2.65}) \times 100 = (0.562 - 1) \times 100 \text{ المسامية} = (43.8) \%.$$

بقسمة الكثافة الظاهرية على الكثافة الحقيقية نتخلص من الجذر ونطرح الناتج من سالب واحد ونضربه في مئة ليظهر لنا الناتج بالسالب وتهمل اشارة السالب لتكون قيمة المسامية (43.8) % ونطبق المعادلة على باقي العينات لتعطينا نتائج المسامية كما موضح في الشكل (8) الذي يوضح قيم المسامية بعد تطبيق المعادلة. حيث تمثل اعلى قيمة للمسامية في العينة 19 وتقدر بـ (77.3) % واقل قيمة للمسامية في العينة 11 وتقدر بـ (29.4) % وإن معدل المسامية في ناحية بعشيقة يقدر بـ(57.90) %. لو رجعنا الى قيمة الكثافة الظاهرية لرأينا ان اعلى قيمة هي (11– مغارة مقلوب) غم/سم^3 واقل قيمة في (19–كوري غريبان) غم/سم^3 وهذا يعني ان العلاقة بين المسامية والكثافة الظاهرية علاقة عكسية.



الشكل 8. قيم المسامية في منطقة الدراسة.

الخصائص الكيميائية (Chemical properties)

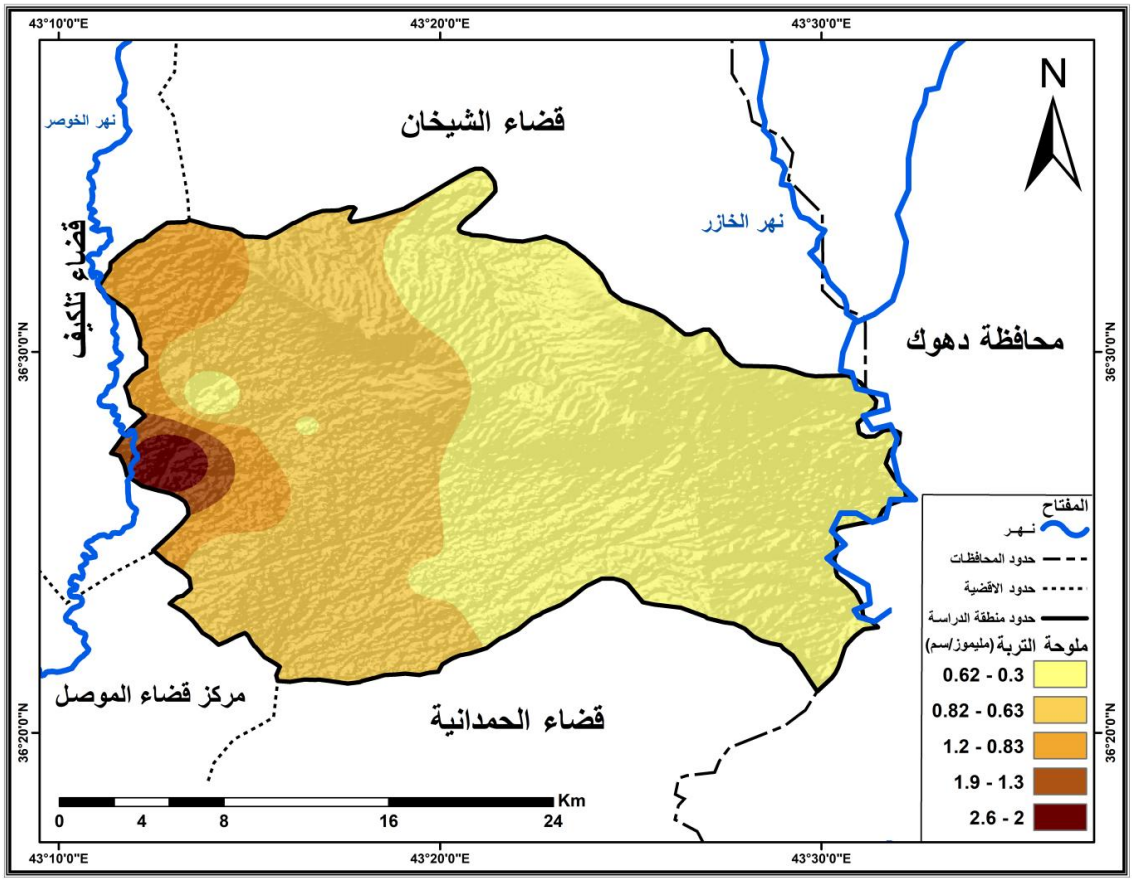
ملوحة التربة (Soil salinity)

الملوحة عبارة عن التركيز الكلي للأملاح المعدنية الذائبة في مستخلص التربة المائي وتوجد الأملاح الذائبة بشكل دائم في التربة، وبعضها يمثل مواد اساسية للتربة وغذائية للنبات إذا وجدت بكميات محدودة وبعضها إن وجدت بتركيز مرتفع فأنها تكون مصدر ضرر للتربة وللنباتات ايضاً (Jallabi and Mahali, 2020)، وان الترب المتأثرة بالأملاح تحدث في جميع القارات وتحت جميع الظروف المناخية تقريباً. ومع ذلك فإن توزيعها يكون أكثر اتساعاً نسبياً في المناطق القاحلة وشبه القاحلة مقارنة بالمناطق الرطبة. كما تتنوع طبيعة وخصائص هذه التربة بحيث تتطلب أساليب محددة لاستصلاحها وإدارتها للحفاظ على إنتاجيتها على المدى الطويل؛ بالنسبة لأي حلول طويلة المدى، من الضروري فهم طريقة منشأ التربة المتأثرة بالملوحة، مع الأخذ في الاعتبار الخصائص الفيزيائية والكيميائية والعمليات التي تؤدي إلى تكوينها والنهج المحتملة لاستصلاحها والإدارة الناجحة. المصدر الرئيس لجميع الأملاح الموجودة في التربة هو المعادن الأولية الموجودة في الطبقة المكشوفة من القشرة الأرضية أثناء عملية التجوية الكيميائية التي تتضمن التحلل المائي، والترطيب، والمحلول، والأكسدة، والكربنة وغيرها من العمليات، يتم إطلاق مكونات الملح تدريجيًا وتصبح قابلة للذوبان. يتم نقل الأملاح المنطلقة بعيداً عن مصدرها الأصلي عبر مجاري المياه السطحية أو الجوفية. وتتركز الأملاح الموجودة في مجرى المياه الجوفية تدريجيا حيث تنتقل المياه ذات الأملاح الذائبة من المناطق الأكثر رطوبة إلى المناطق الأقل رطوبة والقاحلة نسبيا. الأيونات السائدة بالقرب من موقع التجوية في وجود ثاني أكسيد الكربون ستكون كربونات وكربونات الهيدروجين من الكالسيوم والمغنيسيوم والبوتاسيوم والصوديوم؛ إلا أن تراكيزها منخفضة. وعندما ينتقل الماء ذو المواد المذابة من المناطق الأكثر رطوبة إلى المناطق القاحلة، تتركز الأملاح وقد يصبح التركيز مرتفعاً بما يكفي ليؤدي إلى ترسيب أملاح منخفضة الذوبان وبصرف النظر عن هطول الأمطار، تشير ملوحة التربة إلى تركيز الأملاح غير العضوية القابلة للذوبان في التربة. يتم قياسها عادة عن طريق استخراج عينة التربة مع الماء أو في مستخلص عجينة مشبعة. وتكون هذه المستخلصات سريعة، ويتم قياس الملوحة بواسطة التوصيل الكهربائي (EC) باستخدام جسر التوصيلية. ويمكن تقدير إجمالي محتوى الملح في التربة من هذا القياس. تتضمن الطريقة الأكثر دقة تبخر المستخلص المائي ووزن البقايا (إجمالي المواد الصلبة الذائبة،TDS). تعتبر الملوحة من القياسات المختبرية الهامة لأنها تعكس مدى ملاءمة التربة لزراعة المحاصيل. ومع ذلك تؤثر الملوحة على النباتات في جميع مراحل النمو، وبالنسبة لبعض المحاصيل تختلف حساسية النباتات من مرحلة نمو إلى أخرى. وفي حين أن الملوحة تشكل مصدر قلق إلى حد كبير في المناطق المروية (المسقية) وفي المناطق ذات التربة المالحة، فإنها غالبا ما تكون أقل أهمية في الزراعة البعلية*. مع زيادة استخدام الري، سيكون هناك تركيز أكبر على قياس التوصيلية الكهربائية في المستقبل (Estefan et al., 2013). وان الري ايضاً يساعد على نشاط الخاصية الشعرية للتربة التي تعد خاصية فيزيائية ينتقل بها السائل من الأسفل الى الاعلى (دون تأثير قوة خارجية عليه) في الانابيب الشعرية كانتقال الماء من الاسفل الى الاعلى. فبصعود الماء الى الاعلى ينقل معه جميع المواد المذابة التي يمكن ان تذوب بالماء ومنها الاملاح التي ترتفع الى الاعلى مع الماء وبتبخر الماء يتجمع الاملاح فوق التربة وبتكرار عملة الارواء يؤدي الى اذابة الاملاح ونزولها الى الاسفل. ومن خلال الخاصية الشعرية ستصعد الى الاعلى مرة اخرى مما يؤدي الى تكوين السبخات الملحية فوق سطح الارض التي تظهر باللون الابيض على شكل غيوم. وان ترب ناحية بعشيقة يكثر تأثرها بهذا النوع من الاملاح لأنها تعتمد على مياه الابار في ارواء المحاصيل الزراعية المختلفة، وهذا يعني ان الخاصية الشعرية تنشط في الاماكن التي تزرع ويتم سقيها اكثر من المناطق التي تزرع بالمحاصيل الشتوية كالحنطة والشعير التي تعتمد على مياه الامطار فقط في الارواء؛ وذلك لان الزراعة الري وبالاخص السقي بكميات كبيرة يؤدي الى تكوين الاملاح على شكل بقع بيضاء والتي تسمى بـ(السبخات الملحية). إن الشكل (9)

يظهر شذوذاً في كمية الملوحة في منطقة بيبوخ التي تصل إلى (2.6) مليوز/سم ويعود سبب في ذلك الى العامل البشري إذ يستخدم الملح في العديد من الصناعات الغذائية (الزيتون– والطرشي) وغيرها؛ وبعد الانتهاء من استخدامها يجري الملح في التربة مع مياه مما أدى الى إضافة كميات كبيرة من الاملاح إلى ترب هذه المناطق (اللوحة 3).



اللوحة 3: تملح التربة في منطقة الدراسة.

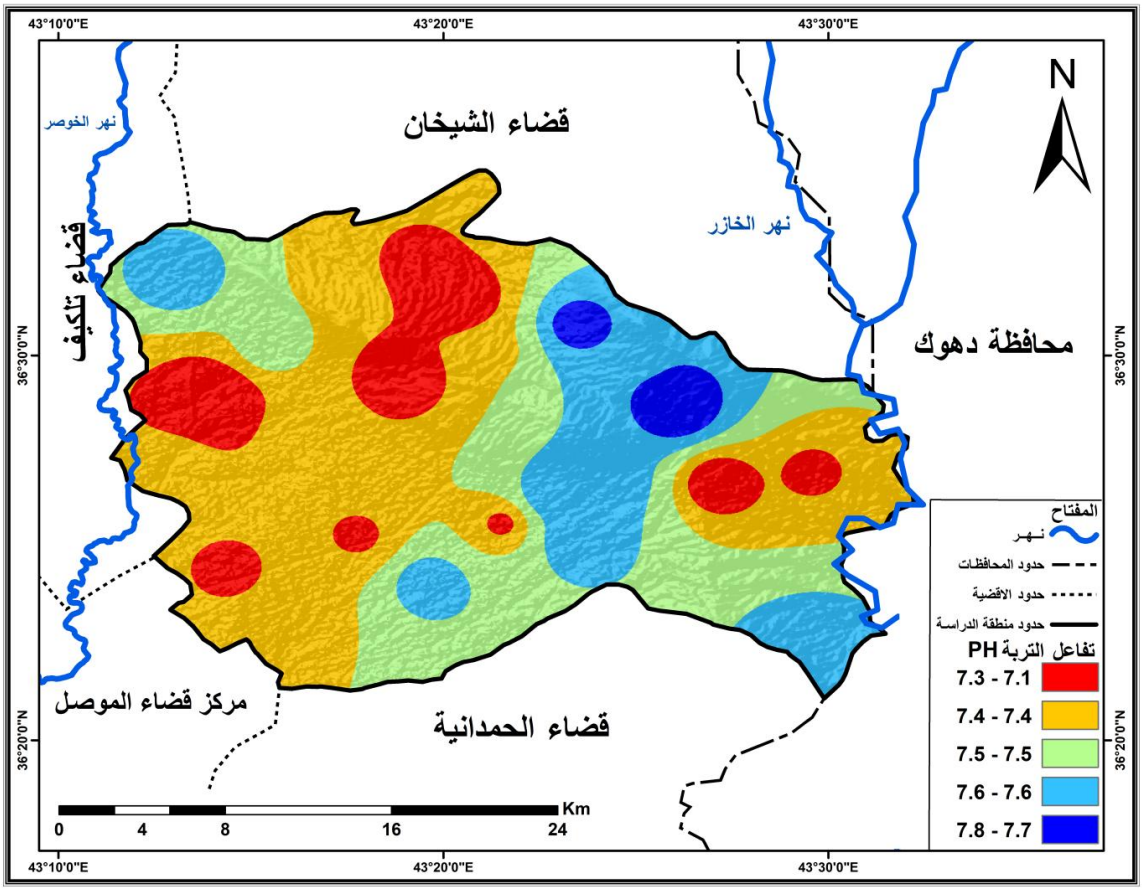


الشكل 9. توزيع قيم الملوحة.(Ece)

درجة تفاعل التربة (pH):

تعرف (pH) بأنها اللوغارتيم السالب لنشاط وفعالية أيون الهيدروجين في التربة وتسمى بقيم الحموضة والقاعدية للتربة وهي صفة كيميائية لنظام التربة والتي يمكن أن يرمز لها كمياً بدرجة تفاعل التربة (pH) وتستخدم لتوضيح درجة حموضتها وقاعديتها، حيث تكون التربة حامضية التفاعل عندما تكون قيمة أقل من (7) وتكون قاعدية التفاعل عندما تكون قيمة أكثر من(7)، أما إذا كانت قيمة تساوي (7) فتعني القيم متعادلة الحموضة والتي تعبر عن درجة تفاعل الماء

النقي جداً(Al-Nuaimi, 1999). ولقد أثبتت التجارب أن درجة تفاعل الهيدروجين في محلول التربة عامل مهم جداً لتحديد خصوبتها ومن ثم قدرتها الانتاجية إذ إن إذابة بعض المعادن تتوقف بالدرجة الأولى على مقدار (pH) فيها. فاذا أرتفع مقدارها في تربة حامضية فأن ذلك يجعلها أقل حموضة كما تؤثر قابلية ذوبان عدد من العناصر المعدنية مثل الحديد والمنغنيز والنحاس والقصدير وغيرها. وأن ارتفاع الحموضة أو القلوية يؤدي الى تأثير سام ومباشر أيضا الى هدم جذور النباتات وهذا التأثير يحدث اذا كان (pH) أقل من (4) أو أكثر من (9) قد يؤدي الى الاخلال بالتوازن بين العناصر التي يمتصها النبات عن طريق التنافس المباشر بين ايون الهيدروجين والايونات الأخرى عند الامتصاص بواسطة النبات خصوصاً مع أيونات الكالسيوم والبوتاسيوم اللازمة للنمو، في حين تعد الترب ذات التراكيز لأيونات الهيدروجين (7) بأنها ترب حيادية وهي ترب مثالية لجميع المحاصيل الزراعية والاحياء الدقيقة التي تعيش في التربة كما وتقوم الأحياء الدقيقة بوظائفها على أكمل وجه عندما يكون مقدارها قريباً من الحيادية والتي تتراوح مابين (6.6 – 7.3) (Al-Barakat, 2016) (الشكل 10).



الشكل 10. قيم درجة تفاعل التربة (pH) في منطقة الدراسة.

الاستنتاجات والتوصيات

- اظهرت نتائج التحاليل ان هنالك تنوعاً في الخصائص الفيزيائية والكيميائية لترب منطقة الدراسة التي تم توصل اليها في المختبر من خلال العينات التي جمعت من المنطقة المدروسة؛ وقد وضحت من خلال التمثيل الخرائطي لها.
- ضرورة تبني مشروع اعداد أطلس طبيعي لمحافظة نينوى يتضمن كافة المظاهر الطبيعية ليكون دليل عمل ووسيلة للباحثين الجغرافيين.
- التشجيع على استخدام التقنيات الحديثة في مجالات التربة والزراعة وجغرافيا وغيرها من العلوم التي تهتم بدراسة التربة وربطها مع بعضها لينتج لنا محتوى متكامل عن التربة.

References

Abdel Hady, Y.M., 1998. Soil Physics, Dar Wael for Printing and Publishing, First Edition, Oman, (In Arabic)

Abu Sammour, M., 2009. Biogeography and Soil, Dar Al-Maysara for Publishing, Distribution and Printing, Oman - Jordan, 293 P. (In Arabic)

Al-Bassam, K.S., 2012. Mineral deposits and occurrences of the low folded zone. Iraqi Bulletin of Geology and Mining, (5), pp.159-188.

Al-Ameri, I.D.S., 2005, Spatial variation of soil characteristics in the districts of Buhriz and Bani Saad and their spatial relations with climate and water resources, College of Education, Ibn Al-Rashid, University of Baghdad, 260 P. (In Arabic)

Al-Barakat, M.M.M., 2016. Spatial variation of soil properties in Warka district and its impact on agricultural production, MSc Thesis, Department of Geography, Faculty of Arts, University of Thi-Qar, 93 P. (In Arabic)

Al-Mawsili, M.A. and Al-Khafaji, M.A.Q., 2013. Fundamentals of General Soil, Dar Dijlah for Printing and Publishing, 1st Edition, 46 P. (In Arabic)

Al-Musawi, N.A.S.A.H., 2005. Spatial Variation of the Soil Properties of Basra Governorate (A Study in Soil Geography), PhD thesis (unpublished), College of Arts, University of Basra, 102 P. (In Arabic)

Al-Nuaimi, S.N.A., 1999. Fertilizers and Soil Fertility, Dar Al-Kutub Directorate for Printing and Publishing, 2nd Edition, College of Agriculture and Forestry, University of Mosul, Mosul, 71 P. (In Arabic)

Al-Rawi, Y., 1980. Petrology and sedimentology of the Gercus red beds Formation (Eocene), Northeastern Iraq. Iraqi Journal of Science, 21(1), pp.132-171.

Alridha, N., Al-Yasi, A. and Wadhah, A.K., 2013. The Role of (Geoelectric and Hydrogeologic) Parameters in the Evaluation of Groundwater reservoir at South of Jabal Sinjar area. Iraqi Journal of Science, 54(3), pp. 628-637.

Al-Salem, E.T.A.M., 1989. From the characteristics of the soil of Maysan Governorate, MSc Thesis, Department of Geography, College of Arts, University of Basra, 40 P. (In Arabic)

Estefan, G., Sommer, R. and Ryan, J., 2013. Methods of soil, plant, and water analysis. A manual for the West Asia and North Africa region, 3(2), pp. 65-119.

Foth, H.D., 1991. Fundamentals of Soil Science, 8th Edition, John Wiley and Sons, New York, USA, 360 P.

GEOSURV, 1995. Geological map of Bashiqa district, based on the Geological map of Iraq, Ministry of Industry and Mining, General Establishment for Geological Survey and Mining, Baghdad, 1995, at a scale of 1:250,000.

Habib, H.S., 2008. Soil Origin and Composition (Theoretical Part), Faculty of Agriculture, Damascus University, Al-Rawda Press, 125 P. (In Arabic)

Hassan, H.M., 1990, Soil Physics, Mosul, Directorate of Dar Al-Kutub for Printing and Publishing, 138 P. (In Arabic)

Jallabi, A. and Mahali, S., 2020. The effect of salinity on the germination strength of wheat in the valley wheat rows, MSc Thesis, Department of Biology, Faculty of Science, University of Martyr Hama Lakhdar-Al-Wadi, 123 P. (In Arabic)

Jassim, S.Z. and Goff, J.C. eds., 2006. Geology of Iraq. DOLIN, sro, distributed by the Geological Society of London, 186 P.

Khalid, K.A., 2016. The Effect of Land Use on the Development of Some Limestone Soils in Northern Iraq, PhD thesis, Department of Soil Science and Water Resources, College of Agriculture and Forestry, University of Mosul, 135 P. (In Arabic)

Ramzi, M.S.M., Hamadi, A.F. and Amer, A.R., 2020. A morphometric study of the plain of Bashiqa, north of Iraq and northeast of Mosul using the WMS7.1 program, Department of Earth Sciences, College of Science, University of Mosul, College of Basic Education Research Journal, Volume 16, Issue 2, p 1021-1032. (In Arabic)

Republic of Iraq, Ministry of Agriculture, Directorate of Bashiqa District, Computer Division, 2012. Unpublished Records, Administrative Map of Iraq at Scale (1:1000000).

Roth, K., 2012. Soil Physics, Institute of Environmental Physics, Heidelberg University, 48 P.

البحوث باللغة الانكليزية

Arabic Section

Iraqi National Journal of Earth Science

www.earth.uomosul.edu.iq

Monitoring Changes of Rivers Using Remote Sensing Technique: Articles Review

Kareem Tarik Jayed [1*], Hussein Kareem Shather [2]

[1] *Department of Surveying Engineering Technologies, College of Engineering Technical, University of Middle Technical Baghdad, Baghdad, Iraq.*

[2] *Engineering Technical College, University of Middle Technical Baghdad, Baghdad, Iraq.*

Article information

Received: 13- Jul -2024

Revised: 14- Sep -2024

Accepted: 23- Nov -2024

Available online: 01- Jan –2026

Keywords:
Deposition,
Erosion,
Morphology,
Remote Sensing,

Correspondence:

Name: Kareem Tarik Jayed

Email:

Kareemxx12xxx@gmail.com

ABSTRACT

The morphological changes of rivers and lakes continue as a result of several factors, including natural and human. These changes include rivers' pathways, deposition of sediment, erosion, and flooding due to water level fluctuation. It is therefore necessary to understand these changes, which are the basis for the sustainable management of water resources. The Remote Sensing (RS) technique is often regarded as very efficient for monitoring natural events, including the morphological characteristics of river basins. This study has addressed the worldwide morphological changes of rivers and lakes. It has monitored them using modern techniques such as remote sensing techniques and its effectiveness in assessing these changes. Remote sensing technology is an advanced tool brought about a significant shift in the field of studying the morphological changes of rivers and lakes. This technology has provided the capability to collect and analyze data on a large scale, offering precise and up-to-date information about morphological changes not only for aquatic systems but also for landforms and physical alterations. This technology relies on multiple applications for assessing morphological changes, including satellite imaging, LiDAR (Light Detection and Ranging) techniques, and radar systems. The results show the effectiveness of remote sensing techniques and geographic information systems in analyzing and monitoring the morphological changes of rivers, lakes, and the aquatic environment in general, as these techniques save effort, time, and accuracy compared to traditional methods and fieldwork. The findings of this research indicate that remote sensing technology and geographic information systems are highly effective in monitoring morphological changes in rivers and lakes. These methods provide precise results in a significantly shorter timeframe compared to conventional approaches. Additionally, they offer precise and dependable outcomes capable of encompassing extensive regions and gathering crucial and varied information such as terrain heights, water movement, sediment dispersion, and early identification of geological problems.

DOI: 10.33899/injes.v26i1.60192, ©Authors, 2026, College of Science, University of Mosul.
This is an open-access article under the CC BY 4.0 license (http://creativecommons.org/licenses/by/4.0/) .

مراجعة ادبية لمراقبة التغيرات المورفولوجية للانهار باستخدام تقنية التحسس النائي

كريم طارق جايد [1*] ، **حسين كريم شذر** [2]

[1] *قسم تقنيات هندسة المساحة، كلية الهندسة التقنية، الجامعة التقنية الوسطى ببغداد، بغداد، العراق.*

[2] *الكلية التقنية الهندسية، الجامعة التقنية الوسطى ببغداد، بغداد، العراق.*

معلومات الارشفة

تاريخ الاستلام: 13- يوليو-2024

تاريخ المراجعة: 14- سبتمبر-2024

تاريخ القبول: 23- نوفمبر-2024

تاريخ النشر الالكتروني: 01- يناير-2026

الكلمات المفتاحية:

الترسيب،

التاكل،

موفولوجيا،

التحسس النائي،

المراسلة:

الاسم: كريم طارق جايد

Email: Kareemxx12xxx@gmail.com

الملخص

تستمر التغيرات المورفولوجية في الأنهار والبحيرات نتيجة لعدة عوامل التي تشمل الطبيعة والبشر. تشمل هذه العوامل تغيير مسارات الأنهار، وترسيب الرواسب، والتعرية، والفيضانات نتيجة لتغير مستويات المياه. لذا فمن الضروري فهم هذه التغيرات التي تشكل أساس إدارة الموارد المائية بطريقة مستدامة. تُعتبر أساليب التحسس النائي (RS) فعالة لمراقبة الأحداث الطبيعية بما في ذلك الخصائص المورفولوجية لحوض الأنهار. قدمت هذه الدراسة تقييماً للتغيرات المورفولوجية في الأنهار والبحيرات باستخدام تقنيات حديثة مثل تقنيات التحسس النائي، وفعالية هذه التقنيات في تقييم هذه التغيرات. أظهرت النتائج فعالية تقنيات التحسس النائي وأنظمة المعلومات الجغرافية في تحليل ومراقبة التغيرات المورفولوجية في الأنهار والبحيرات، حيث توفر هذه التقنيات جهدًا ووقتًا ودقة أكبر مقارنة بالأساليب التقليدية والعمل الميداني. تشير نتائج هذه الورقة البحثية إلى أن تقنيات التحسس النائي وأنظمة المعلومات الجغرافية فعالة للغاية في مراقبة التغيرات المورفولوجية في الأنهار والبحيرات، حيث توفر هذه الأساليب نتائج دقيقة في فترة زمنية أقصر بشكل كبير مقارنة بالطرق التقليدية. بالإضافة إلى ذلك، تقدم نتائج دقيقة وموثوقة، وتتمتع بالقدرة على شمول مناطق واسعة وجمع معلومات حيوية ومتنوعة مثل ارتفاعات التضاريس، وحركة المياه، وتوزيع الرواسب، والكشف المبكر عن المشاكل الجيولوجية.

DOI: 10.33899/injes.v26i1.60192, ©Authors, 2026, College of Science, University of Mosul.
This is an open-access article under the CC BY 4.0 license (http://creativecommons.org/licenses/by/4.0/).

Introduction

Rivers' Morphology (RM) has a decisive role in the planning and upkeep of infrastructure projects like levees, dams, and bridges. Meander patterns are often presented in straight rivers, where the meandering of rivers is sinuous in plan, with efficient equilibrium features (Southard, 1984). The meander patterns are characterized by the non-linear geometry of the river plan, which is influenced by the stability of the riverbanks and the presence of midstream bars, along with potential obstructions.

Various elements, including water discharge, water velocity, water surface slope, width, and depth of the riverbed material, determine river morphology (RM). These factors shape the patterns, forms, and banks of the river. These elements are interconnected and cannot be considered separately (Rinaldi et al., 2016).

Rivers are natural channels that convey a large amount of water flow from catchment areas as runoff. This water streams from the mountains, runs through the plains, and eventually joins the sea or ocean. Rivers play a significant role in the hydrological cycle, and transport a considerable amount of silt or sediment carried down from the catchment region and eroded from the riverbed and banks, in addition to water. In alluvial soils, silt plays a crucial role in river behavior (Kim et al., 2009). Floods in rivers create enormous havoc and misery for human beings when there is no river control in the early days. River behavior is now well understood

because of advances in science and technology with RS and GIS, and many river training methods are applied.

Remote sensing technology is an advanced tool that has brought about a significant shift in the field of studying the morphological changes of rivers and lakes. These technologies have provided the capability to collect and analyze data on a large scale, offering precise and up-to-date information about morphological changes not only for aquatic systems but also for landforms and physical alterations.

This technology relies on multiple applications for assessing morphological changes, including satellite imaging, LiDAR (Light Detection and Ranging) techniques, and radar systems.

Remote sensors commonly record wavelengths throughout a wide range, including visible and infrared rays (near, medium, and far), ultraviolet rays, and other categories. The energy is transformed, recorded as data, and saved for later use (Forestier et al., 2012).

These technologies can facilitate the adaptive development of all fields. At the same time, remote sensing techniques are necessary to regularly supply information about the condition and nature of the research area at various levels. Recent innovations have enhanced remote sensing (RS) technology, enabling it to better address multiple stakeholders' needs in agricultural applications. These applications include monitoring agricultural land use, predicting crop productivity and species distribution, and assessing ecosystem services related to soil and water resources and biodiversity loss. RS offers a range of substantial and effective solutions and services to enhance and deliver long-term, cost-efficient operational services for applications in green lands (Weiss et al., 2020).

It is worth mentioning that traditional methods require extensive field efforts, which result in higher costs and lower accuracy, whereas remote sensing techniques provide the ability to analyze large areas with higher efficiency.

Previous studies

Previous research on river and gulf morphological changes has explored potential negative impacts like flooding, air pollution, water supply loss, agricultural land degradation, and Earth's average surface temperature. Remote sensing and geographic information systems could be crucial tools.

Ghoshal et al. (2010) focused on the velocities and types of channels and floodplain change analysis, emphasizing the importance of examining historical records from the latter half of the 19th century in the Sierra Nevada of northeastern California. The current area held great importance because of the swift accumulation of sediment in channels and the transformation of floodplains caused by hydraulic mining operations. The temporal scope of this investigation, during which accurate topographic data were accessible, was from 1906 to 2006 (Fig. 1).

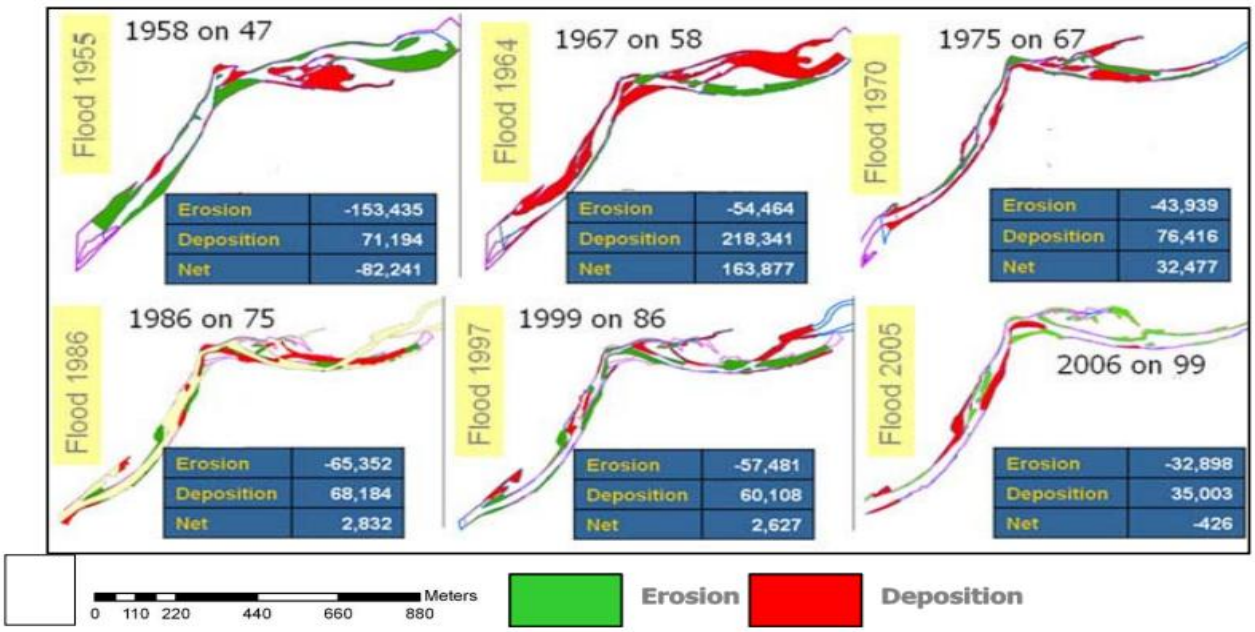


Fig. 1. Deposition and erosion polygons showing areas (m^2) of sediment reworked by each flood (Ghoshal et al., 2010).

The piedmont deposits originating from "the Yuba, Bear, and lower Feather Rivers" were found to contain an estimated 38% of the high-magnitude sediment produced in the northern Sierra Nevada region. Before mining activities, the rivers in the Sacramento Valley exhibited distinct features, including high, steep banks and relatively restricted areas of healthy and nutrient-rich soil.

The Yuba River revealed substantial and prolonged modifications to its channel due to the unexpected influx of sediment from the Hydraulic Mining System (HMS) and human interventions aimed at its management (Ghoshal et al., 2010).

Farooq and Siddique (2015) examined the morphology of the river Jamuna in Bangladesh by means of (GIS) and (RS) methodologies. Vulnerabilities and changes were identified over five years, including 2010, 2003, 1989, 1980, and 1973 (Fig. 2). Settlement identification and analysis were conducted using Landsat Enhanced Thematic Mapper Plus, Multispectral Scanner images, and Thematic Mapper. Topographic maps from 1947 were employed to map river channels. Image classification was performed using eCognition/Definiens object-based methods for river mapping, while ArcGIS provided data on river channel dynamics and bank erosion. The average rates of bank erosion and siltation were significantly elevated. The average bank erosion and siltation rates were quantified and determined to be exceptionally elevated. The annual average erosion measured 1235.25 square kilometers, whereas siltation amounted to 29.82 square kilometers. The highest recorded river displacement was 35,847 m in 2003, while the lowest was 16,415m in 2010.

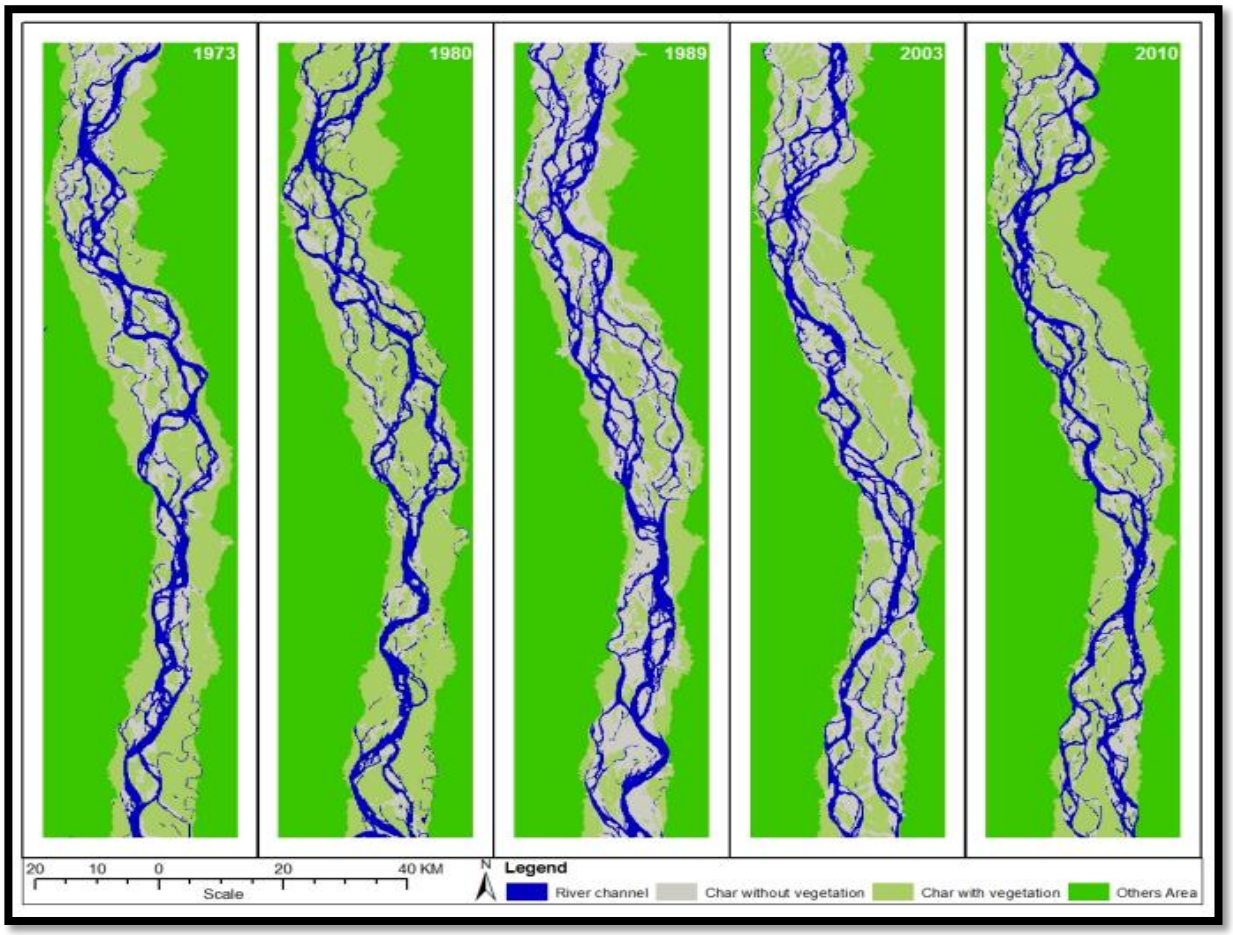


Fig. 2. Map of Jamuna River channel (1973-2010) with associated land cover (Farooq and Siddique, 2015).

Fashae and Faniran (2015) examined the physical characteristics of the river channels of the Ogun River, Nigeria. The collection of data about the morphological parameters of the channel involved the measurement of the river's bank full cross-sectional qualities as well as the determination of its longitudinal characteristics. Sonar equipment mounted on a boat was utilized to measure the maximum depth and width of the river at each of the cross-sections. The bank full width exhibited a strong positive association of 0.8 for the wetted perimeter and 0.9 cross-sectional area. The study additionally demonstrated a strong positive correlation of 0.9 between the gradient and discharge. The study assessed the extent of variation in the physical features of the Ogun River, providing a scientific basis for the management and maintenance of the river (Fig. 3).



Fig. 3. Migratory sand bars along the Lower River Ogun channel (Fashae and Faniran, 2015).

Donovan et al. (2019) examined river systems and suggested optimal methodologies for quantifying boundary alterations, including glacier retreat, erosion, and vegetation expansion. To avoid spatial autocorrelation, it is recommended to assess planform changes over spatial intervals bigger than the coherent units of adjustment. Remotely sensed imaging enhanced the precision of analyzing the movement and breadth changes of the Root River, located in southeastern Minnesota within the region of North America. Nevertheless, there needed to be a framework specifically designed to address this dataset's uncertainty issue. The primary factor contributing to uncertainty in manual riverbank delineations was the inconsistency among users rather than the image quality or environmental circumstances. The digitations traced the vegetation boundary that most closely represented the river's width at the bank full stage. The study also suggested utilizing a spatially variable threshold for error detection to improve data accuracy. The investigation revealed little to no spatial autocorrelation in the rates at which channels migrate over distances of 1-4 channel widths (50-200 m). This finding was consistent with the observed patterns of irregularity in user digitizing (Fig. 4).

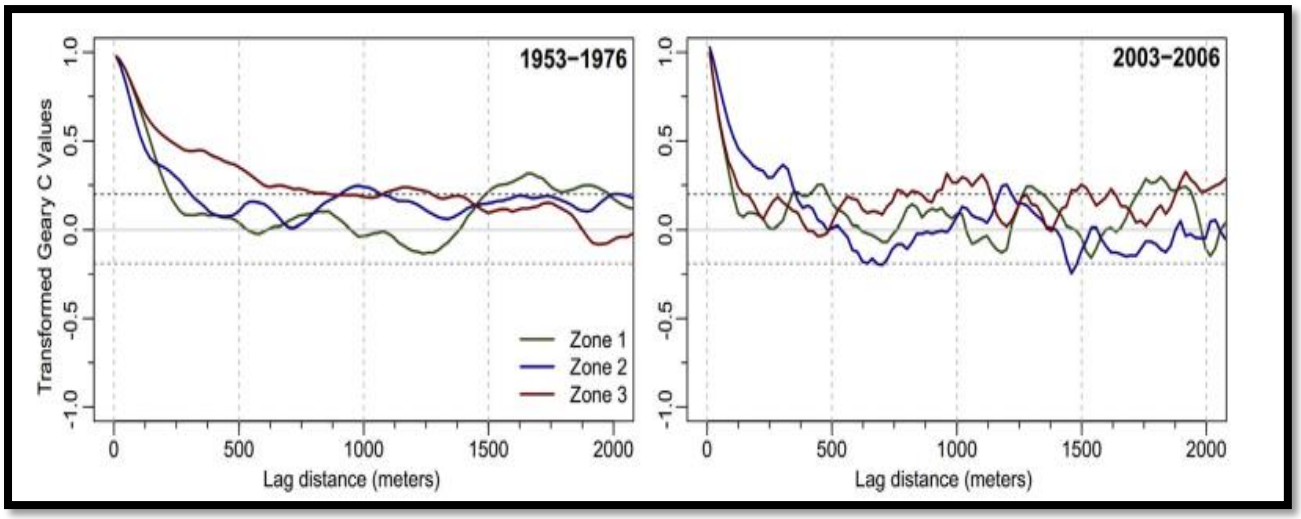


Fig. 4. Correlograms showing spatial autocorrelation to measure channel movement. Lag distance denotes the length over which autocorrelation was measured. Geary's C values, generally ranging from 0 to 2, were changed to the standard correlation range of -1 to 1 (Donovan et al., 2019).

Langat et al. (2019) conducted the flow duration curve using geospatial methodologies to examine the Tana River's current hydromorphological properties in Kenya. The goal was to obtain a clearer knowledge of human impacts during the last twenty years and the consequences for future development projects. For 17 years, the results indicated that all extreme peak, low, and average discharges exhibited significant upward trends. The analysis of hydrological changes after regulations showed a significant rise of 56% and 40% in high and low flows, respectively. However, the construction of the dam equipment led to a notable decline of 13% in the highest level of discharge and a substantial 30% drop in low flows. The primary water flow has had a 33% increase in the previous decade compared to the present decade (Fig. 5).

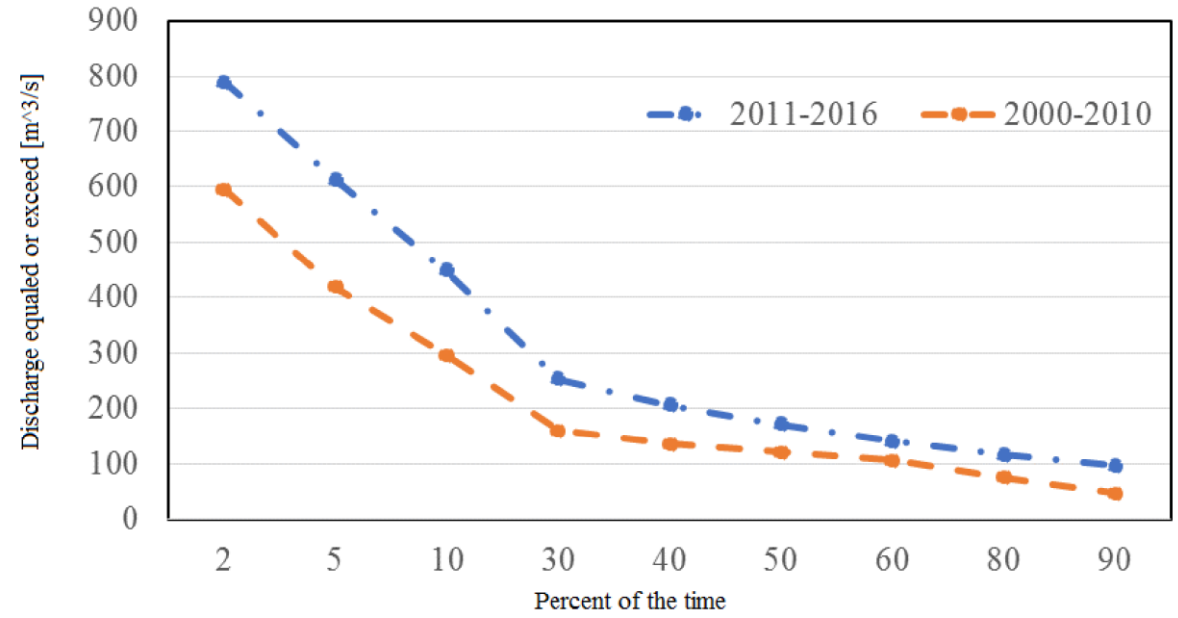


Fig. 5. Flow characteristics of the Garissa gauging station, including the discharge equaled or surpassed and the proportion of time (%) for the periods 2000-2010 and 2011-2016 (Langat et al., 2019).

Aziz et al. (2020) analyzed the structural characteristics of the Diyala River and the parameters of its basin using geographic information systems (GIS) and image processing. The study was able to define watersheds and examine their physical characteristics using GIS hydrology methods and DEM information collected by the Shuttle Radar Topography Mission (SRTM). As part of this study focused on geometry, the morphometric aspects of the sub-basins were also analyzed, such as their area, perimeter, frequency of streams, maximum breadth and length, drainage density, and stream orders. Five distinct sub-basins were identified, each with its stream order and drainage density ranging from 0.47 to 0.99 km/km^2, as shown in Fig. 6.

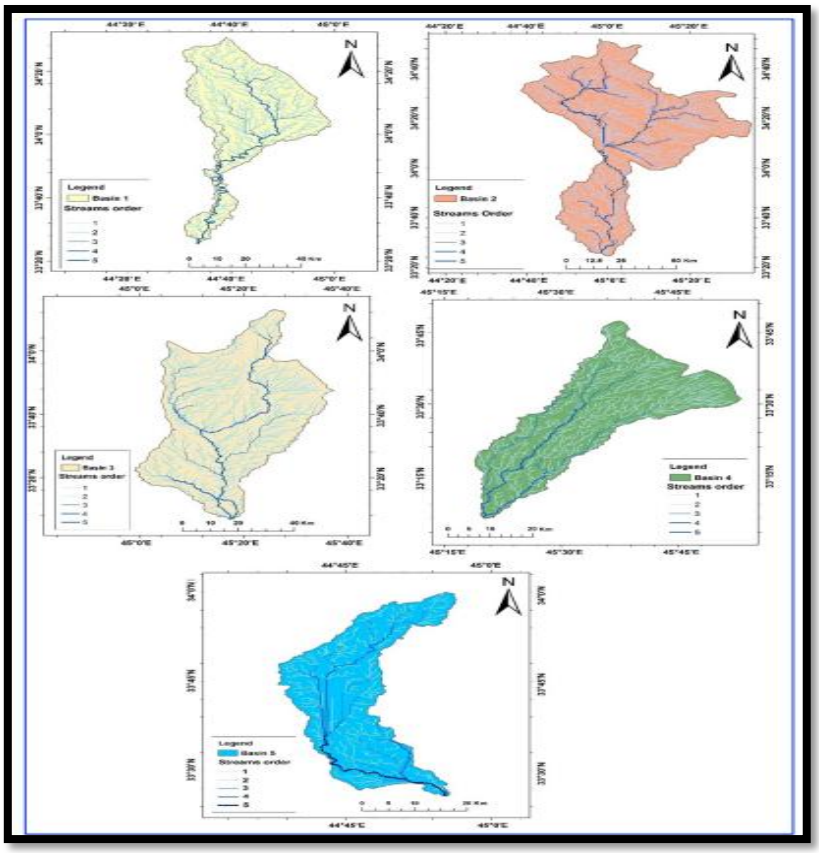


Fig. 6. Stream order of the sub-basins 1, 2, 3, 4, and 5 (Aziz et al., 2020).

Li et al. (2021) studied a comprehensive analysis of the physical structure and form of the Yongding River across its 92 km stretch in Beijing, China, during four separate periods spanning from 1964 to 2018. The changes in the river channel's structure were rebuilt at both the macro and micro levels using data analysis by Geographic Information System (GIS). The results indicated a substantial alteration in the morphology of the river. The channel's diameter had decreased by 31%, and there were discernible changes in the temporal and spatial patterns (Fig. 7). By evaluating the impact of human actions on climate change over various historical periods, it was determined that human involvement is the primary governing force.

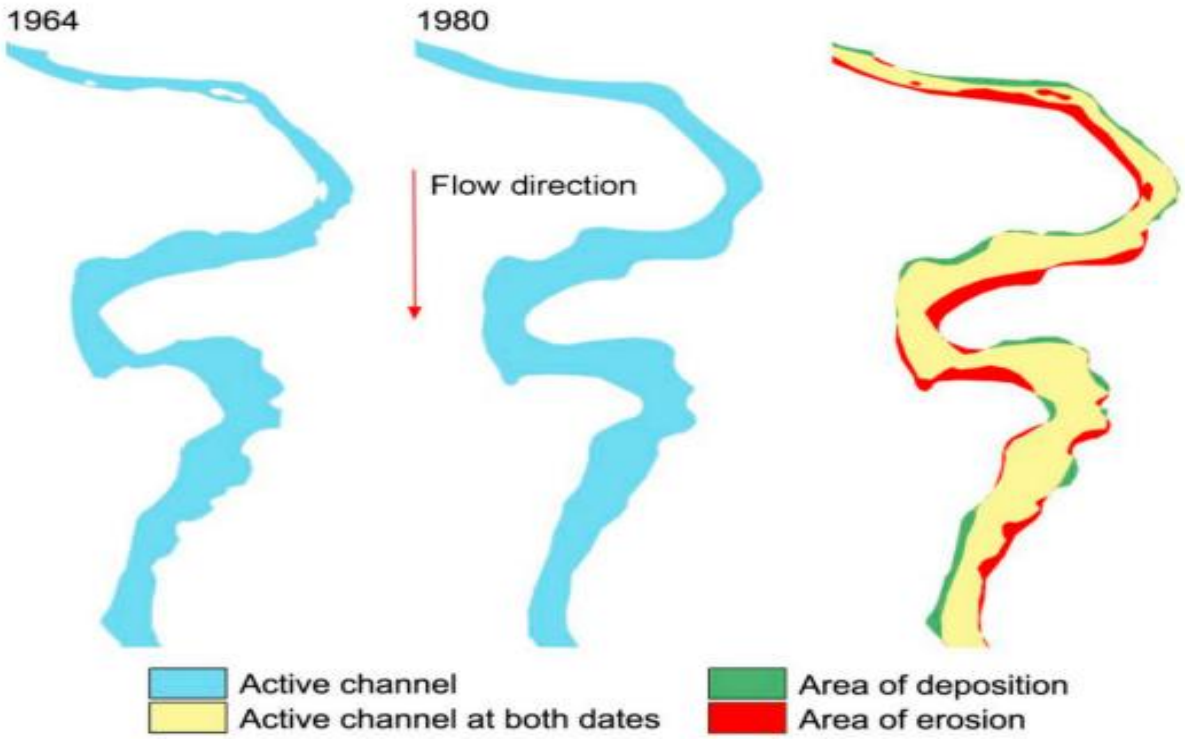


Fig. 7. Erosion/deposition area determined by superimposing two channel positions (Li et al., 2021).

Ibitoye (2021) analyzed the morphological features of the Niger River by utilizing Landsat images captured in 1990, 2002, and 2017. Between 1990 and 2017, the data showed a 27.64% reduction in water bodies and a 9.77% drop in riparian vegetation. Nevertheless, there was a significant 75.61% increase in sediment yield. The river channel exhibited substantial spatial variations, with the central axis migrating 1347.3 meters eastward in the upper segment and westward in the lower section. The study determined that the channel had seen significant structural alterations, primarily due to erosion and accretion processes, which were well documented using remote sensing imagery (Fig. 8).

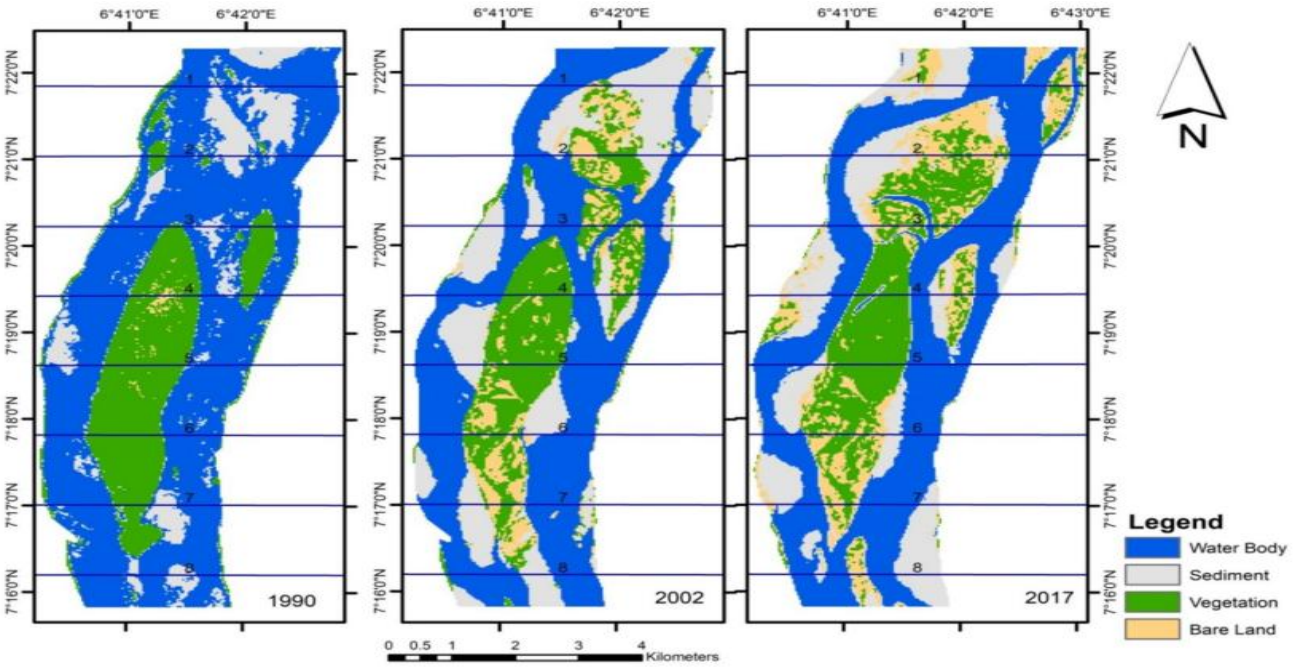


Fig. 8. Land cover classification over the study period (Ibitoye, 2021).

Zhang et al. (2022) investigated the reported variations in water levels and modifications in the principal river channel that links Wuzhou and Zhaoqing, China, over the past few decades. Throughout a continuous 27-year period from 1987 to 2013, the quantities of suspended sediment ejected consistently surpassed the quantities imported. The observed phenomena could be attributed to a significant decrease in the concentration of suspended silt particles. Consequently, a notable occurrence of riverbed erosion took place, transforming the riverbed into a primarily silt-based reservoir. Between 2004 and 2014, a noticeable decrease in the average elevation of the riverbed was noticed, amounting to a magnitude of 2.21 meters.

Hossain et al. (2023) examined the possibility of morphological alterations in land use, erosion-sedimentation patterns, coastal dynamics, and sediment accumulation on Sonadia Island in Southeast Bangladesh. To assess the phenomenon of unusually high sediment accumulation, the researchers employed various methodologies, including the analysis of toposheets, historical maps, multiple satellite pictures, and on-site fieldwork observations. The findings of the inquiry indicated that the coastline of the island experienced frequent and rapid alterations. In 1779, the island had an area coverage of 1.65 km², which subsequently expanded by a factor of 21 to reach 36 km² in 2021. The study conducted between 1972 and 2021 examined the alterations in land use and land cover on Sonadia Island as seen in Figs. 9 and 10.

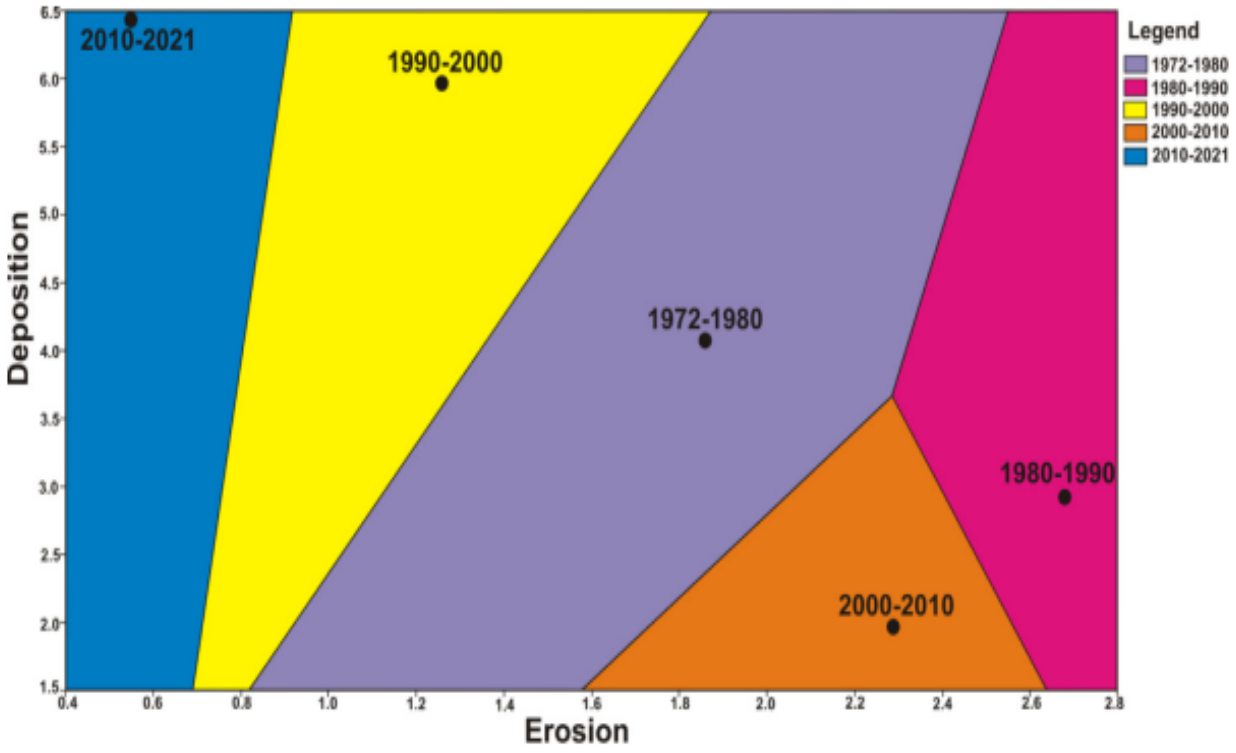


Fig. 9. Analyzed erosion and sedimentation trends of Sonadia Island from 1972 to 2021 by employing a Voronoi diagram (Hossain et al., 2023).

Vu et al. (2024) investigated the significant morphological changes in the Vietnamese Mekong Delta and their impacts on local economic and social conditions. Utilizing satellite data from 1988 to 2020 and population density and (LU/LC) maps from 2002, 2008, and 2015, the study provided a comprehensive analysis of these changes. The islets in the delta showed a trend of accretion, with an increase in area by 13.3 km^2. This accretion led to a narrowing of the river width over the years.

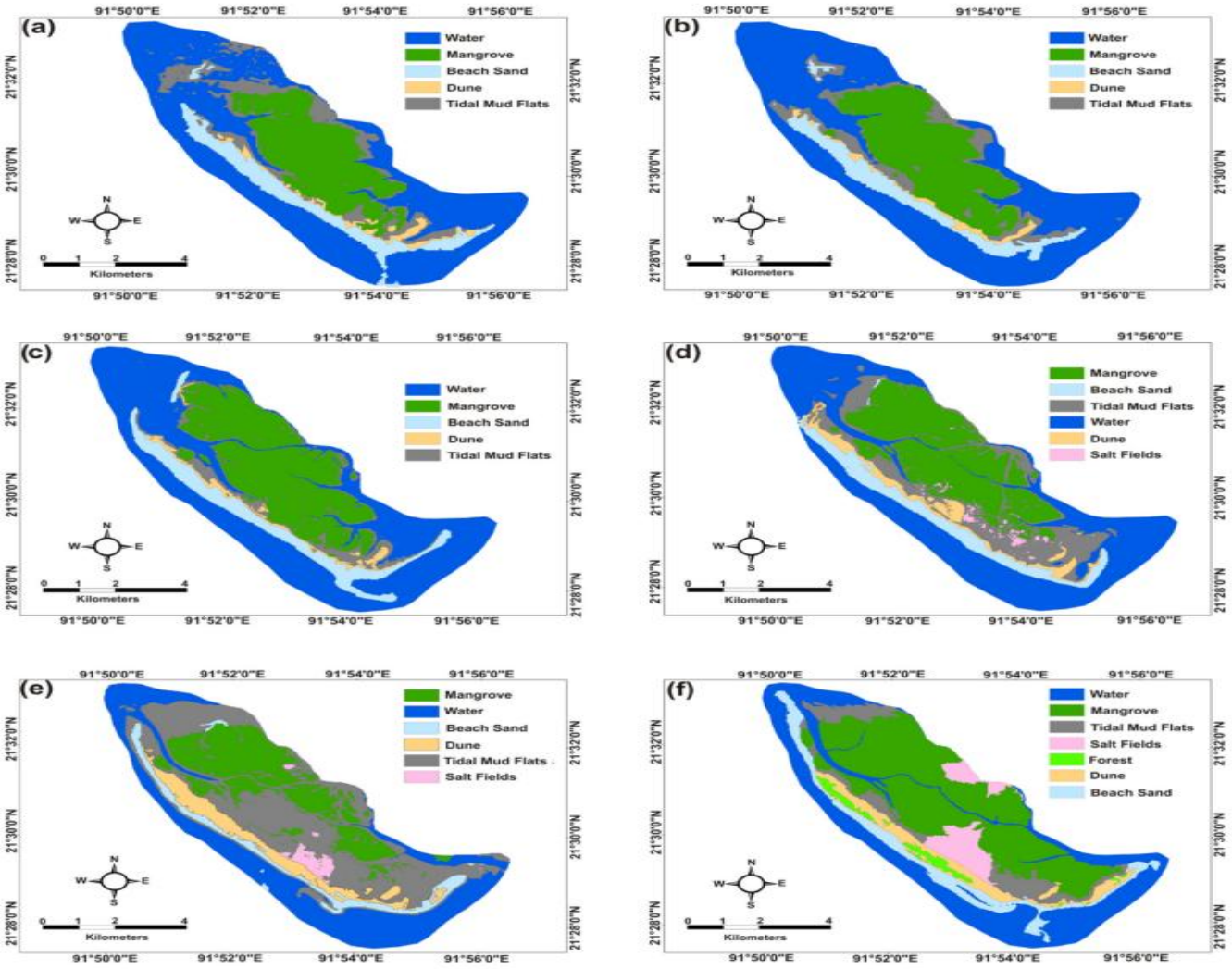


Fig.10. Morphological change maps of Sonadia Island's study area (a) 1972, (b) 1980, (c) 1990, (d) 2000, (e) 2010, and (f) 2021(Hossain et al., 2023).

River Meandering

Meandering rivers are highly dynamic sedimentary processes on Earth. River bends, particularly those with high sediment discharge, can move several meters annually (Constantine et al., 2014). Predicting how meanders develop over time has significant engineering and geological ramifications, such as managing agricultural land, reducing infrastructure loss, designing bridges, and distributing heterogeneities in porous sediments and rocks. The meandering process is characterized by erosion occurring on the outer bank and deposition occurring on the inner bank. An uneven distribution of flow velocity and shear stress in curved segments of the channel produces this (Sylvester et al., 2019).

Riverbank Erosion

Riverbank erosion has a significant detrimental influence on the river's ecosystem and floodplain. Riverbank erosion is an important issue with long-term effects on human life and the river ecosystem. Riparian land loss, capital expenditure damage, sediment generation and deposition downstream are among the most significant repercussions (Das et al., 2014).

The river bank side slope affects the erosion process, where a steep slope is taken as a trigger of erosion, the steep slope will increase the number and speed of runoff, causing erosion to accelerate owing to more carried and dissolved materials (Kumsa and Assen, 2022). There are many effective erosion control solutions to keep soil from washing away on a side slope;

these include riprap, baffles, barriers, terraces, plants, and erosion control wattles. The soil type can be considered to specify the maximum slope to prevent soil erosion (Ali et al., 2012).

Sediment Transport

Sediment serves as the fundamental component for fluvial processes. Sediment transport initiates the process of soil erosion. Hence, the implementation of erosion control measures is crucial for the stabilization of river networks. The sediment load of rivers originates from the hilly region due to slope erosion, rill erosion, gully erosion, and erosion of the channel bed and banks.

Sand-bed rivers convey a comparatively substantial quantity of sediment as suspended load. On the contrary, gravel-bed rivers typically exhibit the opposite trend, with bed-load accounting for 10 to 50 percent of the total burden (Peckham, 2003).

Rive Banks Riprap

Riprap is a commonly used method for protecting riverbanks (Fig. 12). Various techniques exist for designing riprap effectively, but they typically involve using medium-sized chunks dropped into place. However, enhanced protection against erosion may be attained by strategically positioning individual stones in one or more layers instead of haphazardly depositing them (Jafarnejad et al., 2019).



Fig. 12. Riprap with blocks of 4 to 4.5 t individually laid by a machine atop a geotextile functioning as a filter (Jafarnejad et al., 2019).

Impacts of climate and land use/land cover change on river hydromorphology

Fig. 13 shows the interrelationships between the various components. Land cover changes impact the atmosphere's energy balance, influencing rainfall and temperature patterns. Similarly, weather patterns impact LULC, which affects both watershed hydrology and river morphology through an exact feedback mechanism. Climate change and hydrology unidirectionally impact river morphology. To achieve effective and sustainable land and water

resource management, it is crucial to comprehend the hydro-morphological reactions of watersheds to climate and land use/land cover change (LULC), especially in tropical nations that experience alternating wet and dry seasons. While there has been substantial research on the impact of LULC and CC on basin hydrology, less attention has been given to morphological and hydrological feedback in tropical settings (Watershed, 2020).

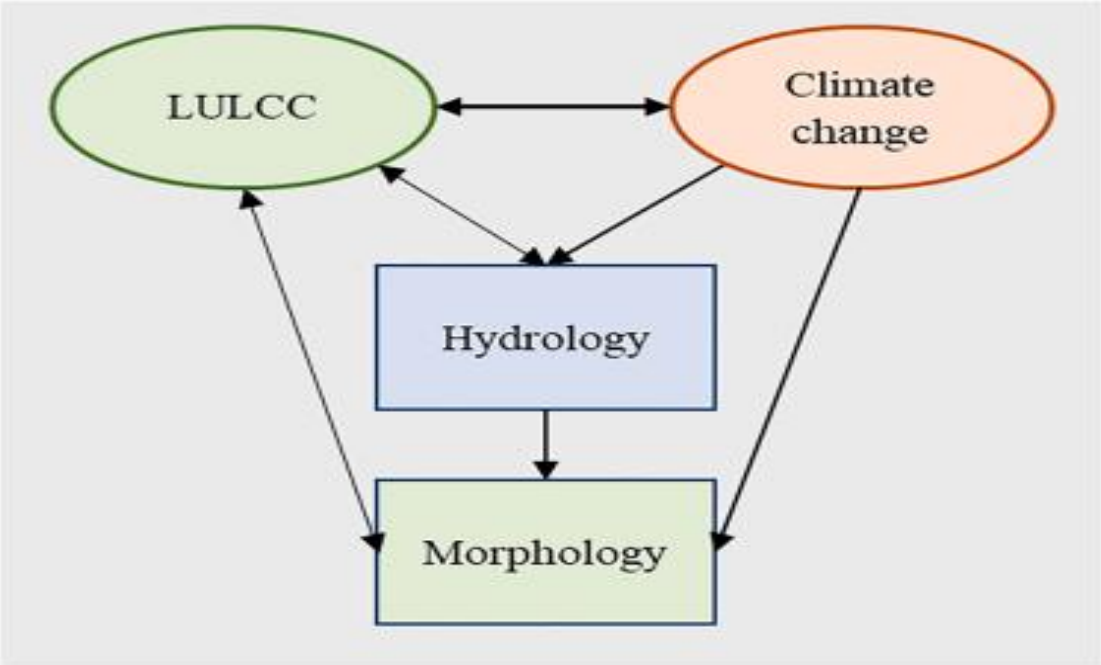


Fig. 13. LULC, CC, hydrology, and morphological interactions. Arrows indicate the direction of causality (Watershed, 2020).

Results and discussion

The results of this study, through the analysis of previous studies, have shown that the use of modern remote sensing technology and geographic information systems has made it possible to accurately determine the morphological changes in water bodies such as rivers and lakes over specific periods. It is also found that Landsat data have been widely used in the study and analysis of water bodies, and the best tool was the remote sensing technique, especially when analyzing long-term time series with high spatial resolution, because the Landsat satellite provides the longest continuous time series of any environmental satellite program, making it an effective and primary tool in studies spanning long periods. Consequently, all newer remote sensing technology has yet to reach the same level of usage as the Landsat satellite.

The results show that this technology represents a revolution in monitoring and analyzing the morphological changes of water bodies, as it has been able to provide accurate, detailed, and rapid data compared to traditional methods. Using satellite images and analyzing them with geographic information systems allows for the assessment and monitoring of changes in river courses and lake boundaries, as well as identifying areas of erosion and deposition over long and consistent time periods.

The utilization of these technologies yields precise, rapid, and dependable outcomes. This technology can cover large areas and capture important data such as land elevations, water flow patterns, and sediment distribution. Additionally, it aids in the prompt identification of morphological issues, facilitating swift intervention. Therefore, this technology greatly enhanced water resource planning and management, thereby improving the efficiency of decision-makers and individuals involved in the management of rivers and lakes.

Conclusion

The following points can be concluded from the current review:

1. The effectiveness of the remote sensing (RS) technique and geographic information system (GIS) in assessing and monitoring morphological changes in aquatic environments such as lakes and rivers.
2. These capabilities contribute to providing accurate and comprehensive data that have aided in the development of sustainable water resource management.
3. It is essential to monitor the morphological changes in rivers and lakes to reduce the occurrence of floods.
4. The use of remote sensing technologies, such as Landsat-8 satellite images and Google Earth Pro, in monitoring the morphological changes of water areas, detecting violations along the banks of rivers and lakes.
5. More data must be obtained from GIS and RS for buildings with a unified database among the concerned departments for updating it continuously, accurately, and systematically due to the social, economic, and urban changes. Developing appropriate solutions to problems before they occur accurately and thoughtfully.

Effective water resource management requires the use of modern remote sensing technologies and advanced data analysis tools. By expanding the use of these technologies, developing integrated analytical tools, and enhancing training programs, the ability to monitor and analyze morphological changes in rivers and lakes will be improved, leading to more sustainable water resource management.

Acknowledgement

I would like to express my gratitude first to my Creator and the Department of Surveying Engineering at the Technical College - Baghdad. Many thanks to my wife and friends for their support.

References

Ali, A.A., Al-Ansari, N.A., and Knutsson, S., 2012. Morphology of Tigris River within Baghdad City. Hydrology and Earth System Sciences, 16(10), pp. 3783–3790. https://doi.org/10.5194/hess-16-3783-2012

Aziz, N.A., Abdulrazzaq, Z.T., and Mansur, M.N., 2020. GIS-based watershed morphometric analysis using DEM data in Diyala River, Iraq. Iraqi Geological Journal, 53(1), pp. 36–49. https://doi.org/10.46717/igj.53.1c.3rx-2020.04.03.

Constantine, J.A., Dunne, T., Ahmed, J., Legleiter, C., and Lazarus, E.D., 2014. Sediment supply as a driver of river meandering and floodplain evolution in the Amazon Basin. Nature Geoscience, 7(12), pp. 899–903. https://doi.org/10.1038/NGEO2282

Das, T.K., Haldar, S.K., Gupta, I.D., and Sen, S., 2014. Riverbank erosion induced human displacement and its consequences. Living Reviews in Landscape Research, 8(1), pp. 1–35. https://doi.org/10.12942/lrlr-2014-3

Donovan, M., Belmont, P., Notebaert, B., Coombs, T., Larson, P., and Souffront, M., 2019. Accounting for uncertainty in remotely-sensed measurements of river planform change. Earth-Science Reviews, 193 (December 2018), pp. 220–236. https://doi.org/10.1016/j.earscirev.2019.04.009

Farooq, M., and Siddique, K.H.M., 2015. Conservation agriculture. Conservation Agriculture, 1(1), 665. https://doi.org/10.1007/978-3-319-11620-4

Fashae, O.A., and Faniran, A., 2015. Downstream Morphologic Characteristics of the Alluvial Section of Lower River Ogun, Nigeria. Journal of Environmental Geography, 8(1–2), pp. 1–10. https://doi.org/10.1515/jengeo-2015-0001

Forestier, G., Puissant, A., Wemmert, C., and Gançarski, P., 2012. Knowledge-based region labeling for remote sensing image interpretation. Computers, Environment and Urban Systems, 36(5), pp. 470–480. https://doi.org/http://dx.doi.org/10.1016/j.compenvurbsys.2012.01.003.

Ghoshal, S., James, L.A., Singer, M.B., and Aalto, R., 2010. Channel and floodplain change analysis over a 100-year period: Lower Yuba River, California. Remote Sensing, 2(7), pp. 1797–1825. https://doi.org/10.3390/rs2071797

Li, H., Xu, X., Wu, M. and Liu, Z., 2021. Spatiotemporal evolution trajectory of channel morphology and controlling factors of Yongding River, Beijing, China. Water, 13(11), p.1489. https://doi.org/https://doi.org/10.3390/w13111489 Academic

Hossain, M.S., Yasir, M., Shahriar, M.S., Jahan, M., Liu, S., and Niang, A.J., 2023. Morphological change assessment of a coastal island in SE Bangladesh reveal high accumulation rates. Regional Studies in Marine Science, 62, 102969. https://doi.org/10.1016/j.rsma.2023.102969

Ibitoye, M.O., 2021. A remote sensing-based evaluation of channel morphological characteristics of part of lower River Niger, Nigeria. SN Applied Sciences, 3(3), pp. 1–12. https://doi.org/10.1007/s42452-021-04215-1

Jafarnejad, M., Franca, M.J., Pfister, M., and Schleiss, A.J., 2019. Design of Riverbank Riprap Using Large, Individually Placed Blocks. Journal of Hydraulic Engineering, 145(12), pp. 1–12. https://doi.org/10.1061/(asce)hy.1943-7900.0001641

Kim, H., Yeh, P.J.F., Oki, T., and Kanae, S., 2009. Role of rivers in the seasonal variations of terrestrial water storage over global basins. Geophysical Research Letters, 36(17), pp. 2–6. https://doi.org/10.1029/2009GL039006

Kumsa, A., and Assen, M., 2022. GIS and Remote Sensing Based Land Degradation Assessment and Mapping: Case Study Adea Woreda. Journal of Electrical Electronics Engineering, 1(1), pp. 21–30. https://doi.org/10.33140/jeee.01.01.01

Langat, P.K., Kumar, L., Koech, R., and Ghosh, M.K., 2019. Hydro-morphological characteristics using flow duration curve, Historical data and remote sensing: Effects of land use and climate. Water (Switzerland), 11(2), pp. 1–18. https://doi.org/10.3390/w11020309

Peckham, S.D., 2003. Fluvial landscape models and catchment-scale sediment transport, Global and Planetary Change, 39(1-2), pp. 31–51. https://doi.org/10.1016/S0921-8181(03)00014-6

Rinaldi, M., Gurnell, A.M., Del Tánago, M.G., Bussettini, M., and Hendriks, D., 2016. Classification of river morphology and hydrology to support management and restoration. Aquatic Sciences, 78, pp. 17–33. https://doi.org/10.1007/s00027-015-0438-z

Southard, J., 1984. The environment of medicine. Ohio State Medical Journal, 80(4), pp. 258–261, 302. https://doi.org/10.5014/ajot.44.7.668c

Sylvester, Z., Durkin, P., Covault, J.A., and Sharman, G.R., 2019. High curvatures drive river meandering. Geology, 47(10), pp. e486–e486. https://doi.org/10.1130/G46838Y.1

Vu, T.H., Binh, D. Van, Tran, H.N., Khan, M.A., Bui, D.Du, and Stamm, J., 2024. Quantifying Spatio-Temporal River Morphological Change and Its Consequences in the Vietnamese Mekong River Delta Using Remote Sensing and Geographical Information System Techniques. Remote Sensing, 16(4). https://doi.org/10.3390/rs16040707

Watershed, G., 2020. Impacts of Climate and Land Use Change on Hydrological. In Ecohydrology and Hydrobiology. https://doi.org/10.1016/j.ecohyd.2020.12.001

Weiss, M., Jacob, F., and Duveiller, G., 2020. Remote sensing for agricultural applications: A meta-review. Remote Sensing of Environment, 236, 111402. https://doi.org/https://doi.org/10.1016/j.rse.2019.111402

Zhang, M., Feng, X., Yan, T., and Wang, X., 2022. Human impacts on riverbed morphology and hydrology in the lower reaches of the West River, China. River Research and Applications, 38(5), pp. 952–964. https://doi.org/10.1002/rra.3960

Iraqi National Journal of Earth Science

www.earth.uomosul.edu.iq

Assessment of Rock Masses Exposed at the Khanas Dam Site in the Southeastern Part of Sheikhan Anticline, Northern Iraq.

Safwan Taha Yasin Al-Habity[1*], Mohammed Rashid Abood [2], Ibrahim saad Ibrahim Aljumaily [3]

[1] *Ministry of Oil, North Oil Company, Iraq.*

[2] *Department of Applied Geology, College of Science, University of Tikrit, Tikrit, Iraq.*

[3] *Department of Mining, College of Petroleum and Mining Engineering, University of Mosul, Mosul, Iraq.*

Article information

Received: 28- Mar -2024

Revised: 25- Jul -2024

Accepted: 07- Oct -2024

Available online: 01- Jan –2026

Keywords:
Rock Mass Rating
Dam Mass Rating
Geological Strength Index
Khanas Dam
Banks of the Dam

Correspondence:
Name: Safwan Taha Yasin Al-Habity

Email: Alhabitysafwan1982@gmail.com

ABSTRACT

This study is based on assessing rock masses exposed on the banks of the Khanas Dam reservoir in the southeastern part of the Sheikhan Anticline in northern Iraq. The rock masses are of the Pila Spi Formation. The study includes field data, laboratory tests, and office work. During the study, seven stations were chosen and distributed on both banks, four stations on the right and three stations on the left, considering that the Pila Spi Formation is the dominant and representative geological formation of the study area, and it represents the foundation of the dam, Shoulders, and banks overlooking the reservoir. The rock masses of the Pila Spi Formation are represented by limestone, chalky limestone, and dolomitic limestone as a result of the diagenetic process. Three classifications are used to assess rock masses: Rock Mass Rating (RMR), Dam Mass Rating (DMRSTA), and Geological Strength Index (GSI). As a result of the classification of rock masses, they range between (50-61) on the right bank, while on the left bank, they range between (53-62). The results of the assessment of the stability of the Dam Mass Rating on the right bank range between (61-66), while on the left bank range between (58-67). The results of the geological strength index values for rock mass on the right bank are between 41-56, while the results on the left bank are between 48-57. The Roclab program was also used, through which the mechanical properties of rock masses, represented by cohesion strength(C) and angle of internal friction(Ø), are determined using the Hoek-Brown failure criterion. Cohesion strength on the right bank range is between (0.362-0.877MPa), while on the left bank, their values range between (0.385-0.869MPa). The angle of internal friction on the right bank ranges between (24.26°-28.15°), while on the left bank, the values range between (25.31°- 28.51°).

DOI: 10.33899/injes.v26i1.56213, ©Authors, 2026, College of Science, University of Mosul.
This is an open-access article under the CC BY 4.0 license (http://creativecommons.org/licenses/by/4.0/) .

تقييم الكتل الصخرية المنكشفة في موقع سد خنس في الجزء الجنوبي الشرقي من طية الشيخان، شمالي العراق.

صفوان طه ياسين الحبيطي[1*]، محمد راشد عبود [2]، ابراهيم سعد ابراهيم الجميلي[3]

[1] وزارة النفط، شركة نفط الشمال، العراق.

[2] قسم علم الارض التطبيقية ، كلية العلوم، جامعة تكريت، تكريت، العراق.

[3] قسم التعدين ، كلية هندسة النفط و التعدين، جامعة الموصل، الموصل ، العراق.

معلومات الارشفة

تاريخ الاستلام: 28- مارس -2024

تاريخ المراجعة: 25- يوليو-2024

تاريخ القبول: 07- اكتوبر -2024

تاريخ النشر الالكتروني: 01- يناير-2026

الكلمات المفتاحية:

تصنيف الكتل الصخرية

تصنيف كتلة السد

مؤشر القوة الجيولوجية

سد خنس

ضفاف السد

المراسلة:

الاسم: صفوان طه ياسين الحبيطي

Email: Alhabitysafwan1982@gmail.com

الملخص

تعتمد هذه الدراسة على تقييم الكتل الصخرية المنكشفة على ضفاف خزان سد خنس في الجزء الجنوبي الشرقي من طية الشيخان، شمالي العراق. وتمثلها صخور تكوين البلاسبي. وتشمل الدراسة البيانات الحقلية والفحوصات المختبرية، والعمل المكتبي. خلال الدراسة تم اختيار سبع محطات متوزعة على الضفتين، اربعة منها على الضفة اليمنى وثلاث محطات على الضفة اليسرى، باعتبار ان تكوين بلاسبي هو التكوين السائد والممثل لمنطقة الدراسة. ويمثل تكوين البلاسبي اساس السد والاكتاف والضفاف المطلة على الخزان. بالنسبة للكتل الصخرية المكونة من تكوين البلاسبي والمتمثلة بالحجر الجيري والحجر الجيري الطباشيري والحجر الجيري المتدلمت نتيجة العمليات التحويرية. فقد استخدمت ثلاث تصانيف لتقييم الكتل الصخرية، وهي كالاتي: تصنيف الكتلة الصخرية وتصنيف كتلة السد ومؤشر القوة الجيولوجية، وكنتيجة لتصنيف الكتلة الصخرية، فأنها تراوحت ما بين (50–61) على الضفة اليمنى، بينما على الضفة اليسرى حيث كانت ما بين (53–62)، وتراوحت نتيجة تقييم استقراريه تصنيف كتلة السد على الضفة اليمنى بين (61– 66)، بينما على الضفة اليسرى فكانت ما بين (58–67). اما نتائج قيمة مؤشر القوة الجيولوجية للكتل الصخرية على الضفة اليمنى فكانت بين (41–56)، بينما على الضفة اليسرى فهي ما بين (48–57). كما تم استخدام برنامج (الروك– لاب)، والذي يتم من خلاله معرفة الخواص الميكانيكية الصخرية المتمثلة بقوة التماسك وزاوية الاحتكاك الداخلي التي تم تحديدها باستخدام معايرة الفشل لـ (هوك – براون). حيث بلغت قوة التماسك (C) على الضفة اليمنى ما بين (0.877– 0.326) ميكا باسكال، بينما على الضفة اليسرى فقد تراوحت ما بين (0.689– 0.385) ميكا باسكال. تراوحت زاوية الاحتكاك الداخلي على الضفة اليمنى ما بين (°28.15– °24.26)، بينما على الضفة اليسرى فان القيم تراوحت ما بين (°28.51–°25.31).

DOI: 10.33899/injes.v26i1.56213, ©Authors, 2026, College of Science, University of Mosul.
This is an open-access article under the CC BY 4.0 license (http://creativecommons.org/licenses/by/4.0/).

Introduction

The study area is located about 56 km Northeast of Mosul City, in Al-Sheikhan District, represented by the Khanas Dam located within Sheikhan Anticline in its southeastern part. The coordinate of the studied area is between latitudes (36°55’301”) (36°45’150”) N and longitudes (43°25’09.11”) (43°25’36.888”) E, as shown in Figure 1 and Plate 1.

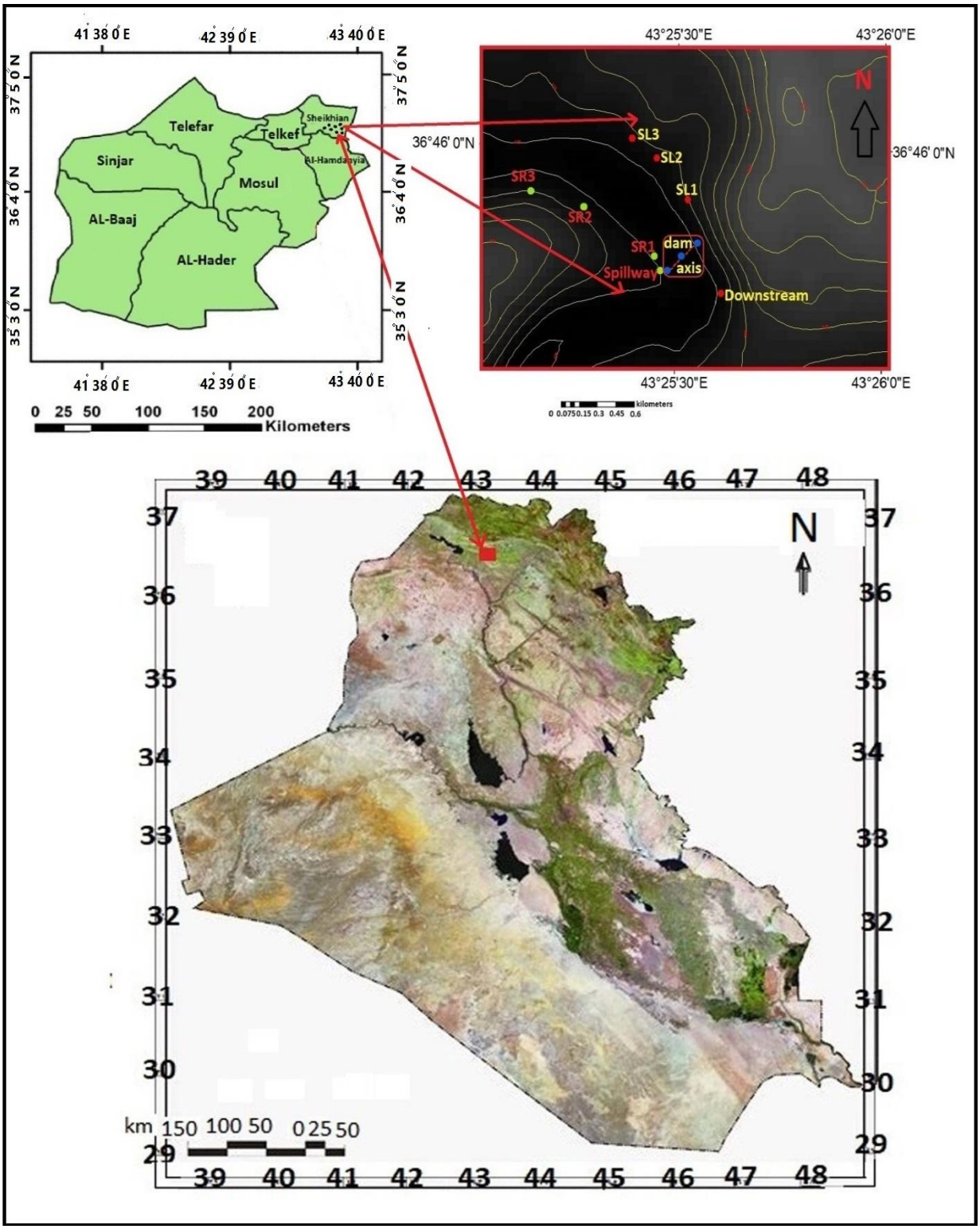


Fig. 1. Location map of the studied Area

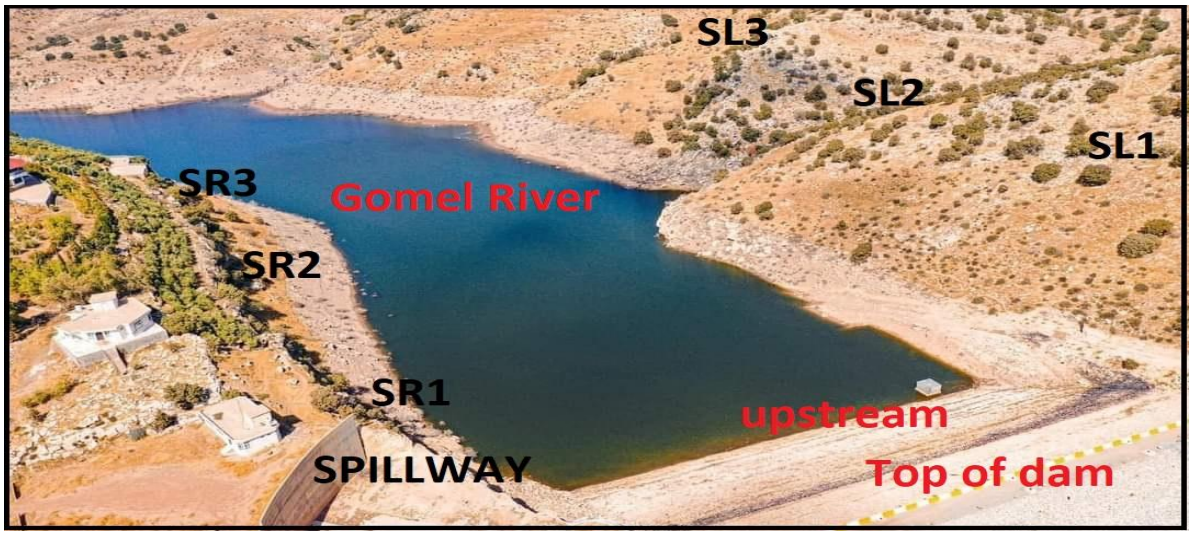


Plate 1: An aerial photo of the Khanas Dam, showing the locations of the stations distributed on both banks, right and left.

Geology of the study area

It is a very important factor and affects the rock masses located on the banks of the Khanas Dam. The dam is located in a complex geological area, with its flank located in the southeastern part, as the stream of the river is perpendicular to the axis of the fold from the time it enters the fold, then it continues vertically and deviates from the axis of the fold near the archaeological site of Khanas, where the axis of the dam is located.

Stratigraphy

It includes the exposed study rock, which is represented by limestone belonging to the Pila Spi Formation (Middle-Late Eocene). Fragile and disintegrated red clay deposits represented by the Gercus Formation (Middle Eocene) underlie the Pila Spi Formation. Recent deposits are at the top (Ahmed, 1980; AlHmedy, 2007).

Tectonically:

The study area is located within the unstable shelf with a foothill zone according to Jassim and Goff (2006) and Fouad (2012) within the Butmah-Ghemcheml subzone Taurus Mountains range (East-West trend). In the section in which the dam is located, the direction of the anticline axis deviates (E-NE) (W-SW). Al-Khatony (2009) also prepared a geological and structural map of the Sheikhan anticline, and it is modified by the projection of the axis of the dam (Fig. 2). The dip value of bedding planes on the right bank ranges between 20-24 degrees with very large differences in the dip direction. The amount of dip of the bedding planes on the left bank of the dam ranges between (22-26) degrees, with large differences in the amount of dip direction shown in Plates 2 and 3.

Khanas Dam is a water dam constructed on the Gomel River. It is used as a water harvester in the wet season of the year, and also for the purpose of controlling floods, as well as for irrigation. It is a small dam and does not generate electric energy. The study includes the assessment of the rock masses located on the banks of the reservoir; it is represented by the Gercus Formation and Pila Spi Formation, and recent deposits. A study of the effect of the erosion of the Gercus Formation on the Dohuk Dam, which is built on the Pila Spi Formation (Al-Talib et al., 2021). Therefore, the rock mass classification system must be assessed. The rock mass rating is a geomechanics classification developed by Bieniawski (1973) for tunnels and slopes, and foundations. The classification of the Rock Mass Rating is diverse, mostly frequent in subsurface works, very rarely in slopes, and essentially non-existent in foundation. (Romana,2003a) Thus, the suggested dam Mass Rating is a new classification used in the dam foundations as an adaptation

to rock mass rating due to the difficulty use of RMR for dam foundation. In addition to previous studies related to dams, the use of rock mass rating and dam mass rating has been reviewed. Shaflei and Dusseault (2015) studied the Rock Mass characterization at the proposed Kangir Dam Site. Hamasur (2009) evaluated the rock mass engineering of the proposed Basara Dam Site. Singh (2020) studied the Dam Mass Rating of the rock mass of the Dhap Dam Site. Al-Jawadi (2013) studied the effect of structural discontinuities on the engineering structure at the Bekhme Dam site. Maleki (2011) studied engineering geological problems of Havsan Dam. Al-Jawadi et al. (2020) studied the possibility of constructing a dam in the Bandawaya Stream Valley in the plunge area of the Alqush and Dehkan anticlines, based on an evaluation of the rock masses. Zadeh et al. (2022) described the engineering properties assessment of the rock mass of the Darband Dam site using DMR. Ghart et al. (2023) evaluated the foundation rocks at the proposed Makhol Dam site. Badowi (2023) evaluated the geometrical and geoengineering characteristics of the Badush Dam site. Mohammed et al. (2023) evaluated the rock masses for the dam foundation in where Kanarwe River Basin, Sulaymainyah is a case study. Al-Jawadi et al. (2023) used the proposed reduction system of the rock mass strength in the evaluation of the Bekhme Dam site.

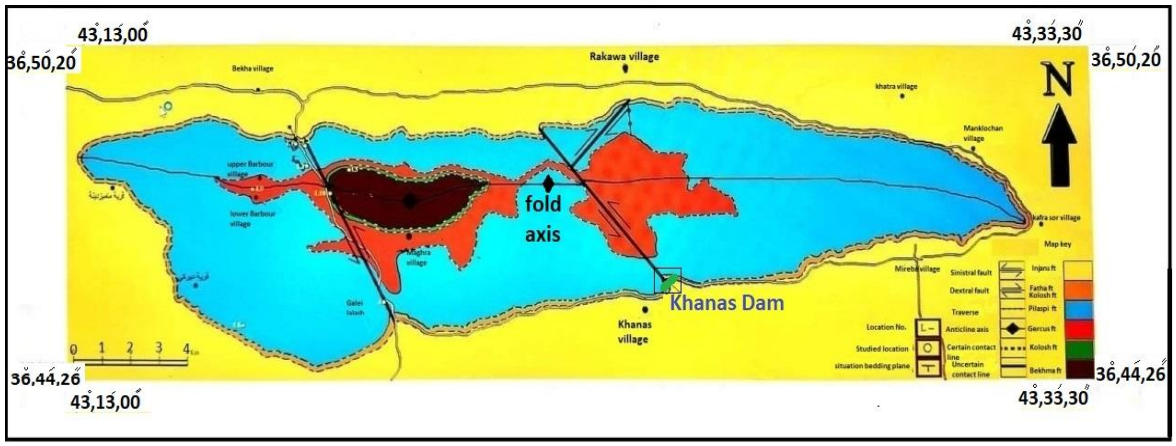


Fig. 2. Structural and geological map of the Sheikhan anticline (Al-Khatony, 2009)

Methodology

During the fieldwork, the largest amount of field information was collected for each station as a preliminary stage for the site investigation of rocks present on the two banks of the reservoir lake of Khanas Dam. This is done by measuring the dip direction/dip amount for the bedding planes and discontinuities, and determination of the volumetric joints through the discontinuities existing at the bed and determination of the Rock Quality Designation (RQD), as well as the determination of the Geological Strength Index (GSI) following Hoek and Marino's(2000) and after Hamasur (2009) through the intersection between structure rating and surface engineering investigation present by determination of the slope dip for rock mass and slope dip for Gercus Formation. Then determining the parameters required for evaluation of rock mass rating by RQD, uniaxial compressive condition rating, and determination of the rock mass thickness for each station, as well as the site strength, discontinuities situation for a prominent and distinctive joint represented by length of discontinuities and spacing of discontinuities, surface discontinuities (rough, very rough, smooth) aperture, and ground water condition, orientation of discontinuities, as well as these parameter involved in emulating the rock masses located on the banks and determining the stability for the each station on the two banks using the Dam Mass Rating in the same way as the stability of foundation. Additionally, finding the properties of rock mass by inputting the special parameters in the analysis of rock strength using the Roclab program. It is represented by uniaxial compressive strength (Ϭc) for intact rock and Geological Strength Index (GSI), and the value of the constant (mi) for intact rock by rock group, and estimated (Marino and Hoek, 2001). Since limestone is micrite, the estimated value is (9). The estimating disturbance factor for limestone is (0.4) (Hoek et al.,2002), and the Modulus Ratio (MR) value is between

(800-1000) with an average of (900), and the intact modulus (Ei) is obtained by multiplying the compressive strength by the modulus ratio. After entering these transactions, the following transactions will be obtained: Hoek – Brown criterion (mb, s, a). Mohor–Coulomb fit (Cohesion, Friction angle), Rock Mass Parameters: Tensile strength, Uniaxial compressive strength, Global strength, Deformation Modulus. shown in Figure 6 of the spillway station.

Engineering classification system

Rock Mass Rating System

It is a geomechanical system and was initially postulated by Bieniawski (1973) and is used in the subway, downhills, and foundations. It went through many developments during the following years (1973, 1974, 1975, 1976, and 1989) as given in Table 1. The Rock Mass Rating System uses six different parameters, which can be determined by field and through field observations, to laboratory tests (Bieniawski,1989), as follows: 1-UCS Unconfined compressive strength, 2-RQD-Rock Quality Designation, 3-Spacing of Discontinuities. 4-Condition of Discontinuities, 5-Ground Water condition, 6-Orientation of Discontinuities. The results for both banks are shown in Tables 4 and 5.

Table 1: Evolution of RMR rating (Modified from Milne et al., 1998)

RMR Parameters	**Period**				
	1973	1974	1975	1976	1989
Uniaxial Compressive Strength	10	10	10	15	15
RQD	16	20	20	20	20
Discontinuity spacing	30	30	30	30	20
Groundwater condition	10	10	10	10	15
Condition of Joints	34	30	30	25	30
Discontinuity strike and dip orientation in the tunnel	− (3−15)	− (0−15)	− (0−12)	− (0−12)	− (0−12)

The parameters affecting the evaluation of the rock masses are summarized as follows: the higher value of uniaxial compressive strength caused a higher quality of the rock mass, and vice versa. Rock quality designation depends on the volumetric joints in the m^3; the higher the value of volumetric joints, the lower the quality of the rock mass, and the lower the value of (jv), leading to a higher quality. The conditions of the discontinuities are represented by the persistence of discontinuities, the width of the aperture, infilling material, roughness of discontinuities, and weathering. All affect the evaluation of the rock mass. The effect of groundwater is negative; it reduces the cohesive strength of the rock and reduces the angle of internal friction. The highest rating of the rock is when it is dry. It decreases if it is damp, wet, dripping, or flowing.

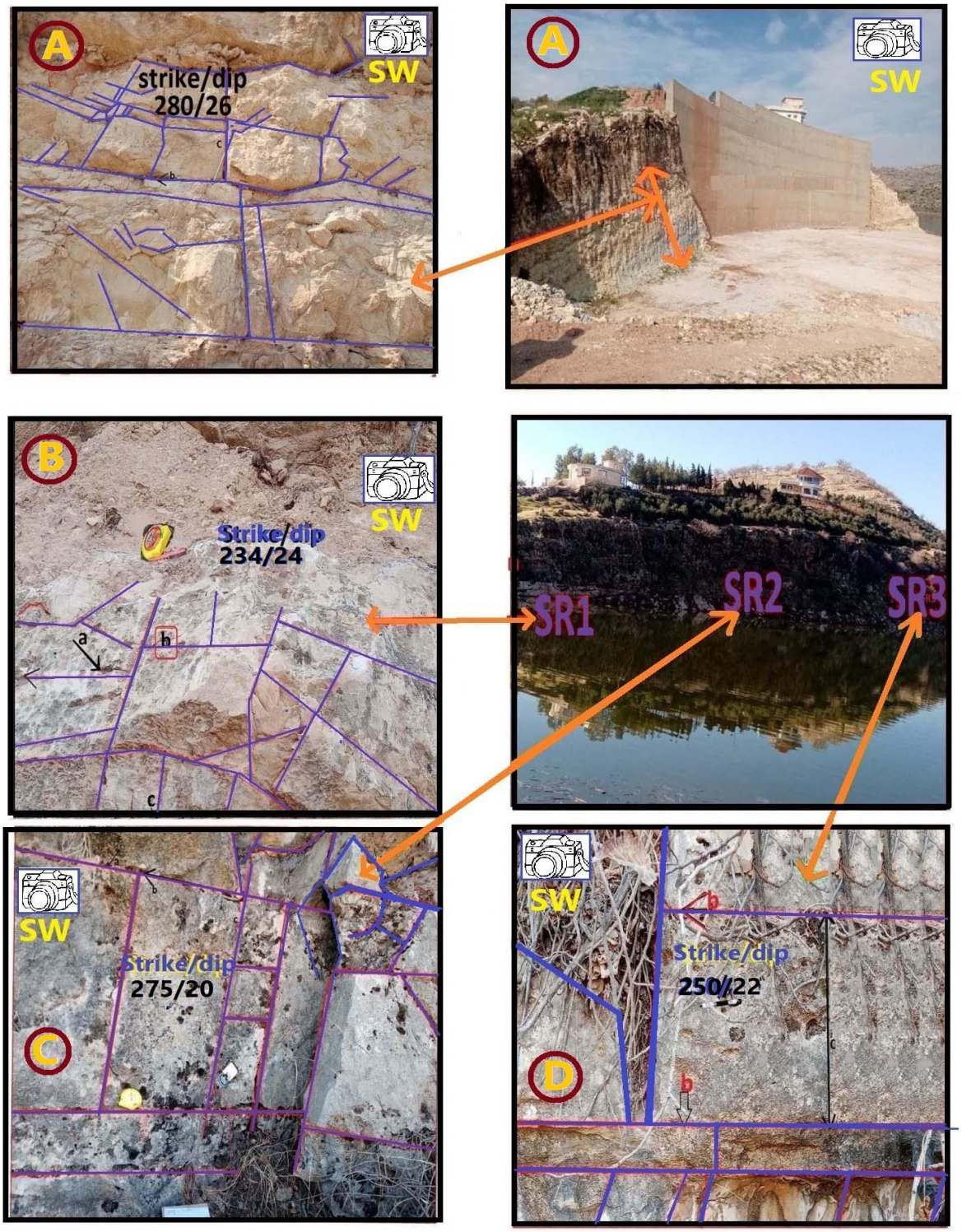


Plate 2: Pictures of A-Spillway station, B- First station (SR1), C- Second Station (SR2), and D- Third station (SR3), with shooting directions at the right bank of Khanas Dam.

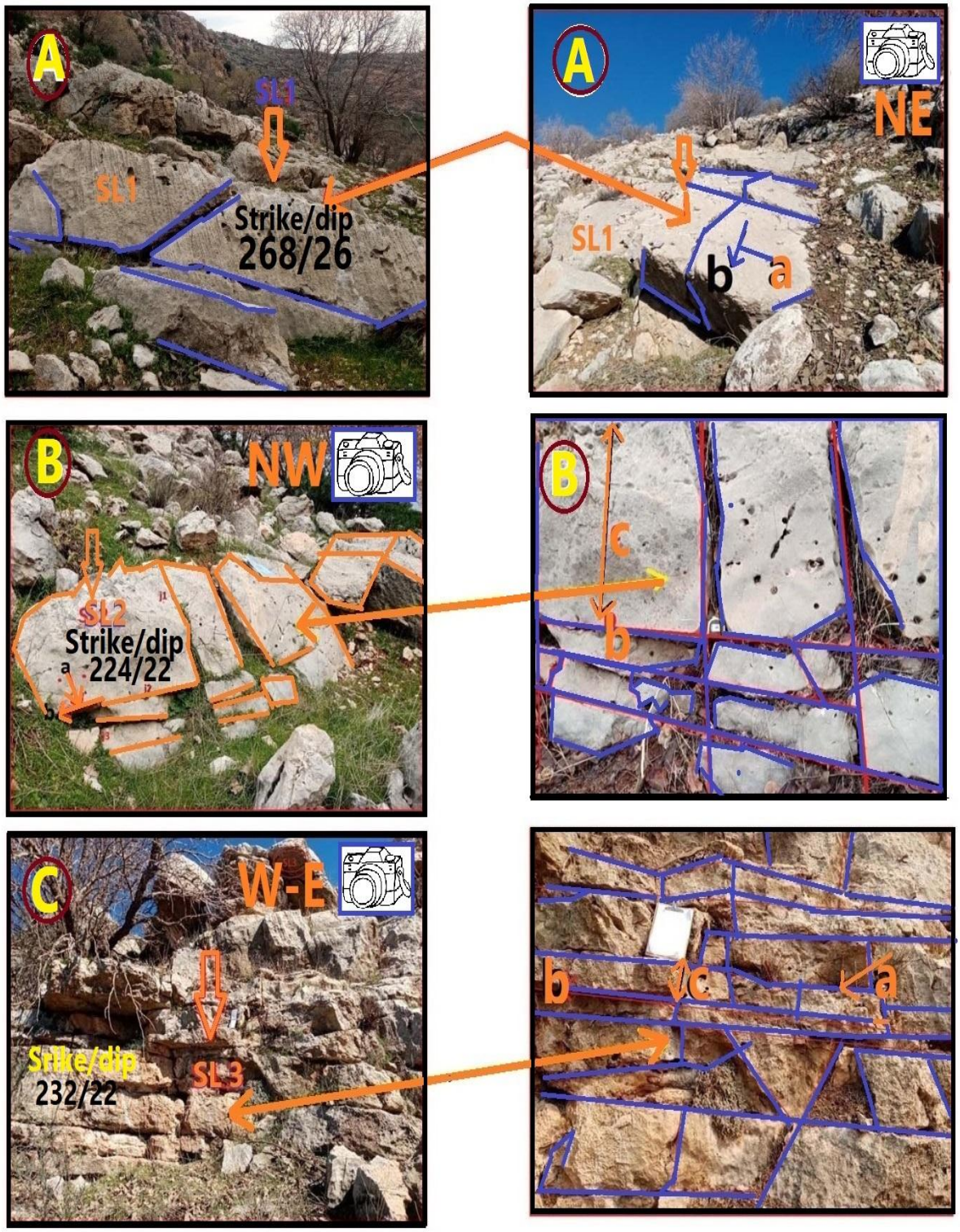


Plate 3: Pictures of A- First Station (SL1), B- Second Station (SL2), and C- Third Station (SL3), with shooting directions at the left bank of Khanas Dam.

Dam Mass Rating System (DMR)

It is known as the new geomechanical classification system created by scientists (Romana, 2003a). It is used in the foundations of dams and is better than the Rock Mass Rating system in the dam foundations for the following reasons:

1-Water pressure calculations are questionable as the water pressure ratio of voids changes along the length of the dam foundation.

2-There is no specific parameter that cares about the direction of joints. The idea of using a dam mass rating system is the same basis that is also used in studying the banks located towards the dam reservoir lake. The dam mass rating system is also used to evaluate the Rock Mass Rating located on the two banks of the Khanas Dam reservoir lake, which will be discussed in the following paragraph.

Stability Rocks for Khanas Dam Area

As stated by Snell and Knight (1991), the problem of the stability of the dam is dealt with systematically, taking into account all forces and pressures exerted dam. Depending on their study and other factors, a different set of adjustment factors must be applied. (Table 2) suggested by Romana (2003a) shows these new temporary adjusting factors that appeared according to the major discontinuity orientation. The numerical rating values originally proposed by Bieniawski were retained. When the dip direction of a joint is distinct and often not parallel to the inflow direction of the dam, the danger of sliding decreases because of the geometrical difficulties of sliding. It is possible to take into account this effect by multiplying the rating of the adjusting factor for dam stability (R_{STA}) by the geometrical correction factor (CF).

Table 2: Rating of the adjusting factor for the dam stability (R_{STA}) according to joints orientation"(Romana,2003a)

Type of Dam	VF	F	FA	U	VU
	Very Favorable	Favorable	Fair	Unfavorable	Very Unfavorable
Fill	Others	10-30DS	0-10A	-	-
Gravity	10-60DS	30-60, 60-90A	10-30US	0-10A	-
Arch	30-60DA	10-30DS	30-60US, 60-90A	10-30US	0-10A
R_{STA}	0	-2	-7	15	-25

DS = dip Downstream, US = dip Upstream, A = any dip

The Dam Mass Rating of the rock block was calculated according to Rommana (2003b), where the relationship is as follows:

$$DMR_{(STA)} = RMR_{BD} + CF \times R_{(STA)}$$

Where, $DMR_{(STA)}$= Dam Mass Rating for the dam stability; (RMR_{BD})= the first four-parameters of Rock Mass Rating + water rating of 15)

$$CF = (1 - Sin\,|\alpha d - \alpha j\,|)^2$$

CF = Geometric correction factor

Where (α d) = inflow direction, (α j) = Dip direction of the significant discontinuity

The rating of the adjusting factor for dam stability (R_{STA}) is the adjusting factor for dam stability as in Table 2. Therefore, the DMR_{STA} is calculated, and the relationship between the value of DMR_{STA} and the degree of safety of the dam against sliding is suggested as a regional rule in Table 3 due to a lack of data that would allow such a correlation to be established (Romana,2003a). The results for both banks are shown in Tables 6 and 7.

Table 3: Correlation between (DMRSTA) and Degree of Safety (Romana,2003a).

DMR_{STA}	<30	30−60	>60
Degree of Safety	Serious Concern	Concern	No primary Concern

Geological Strength Index (GSI) For the Studied Area

The Geological Strength Index (GSI) was submitted by Hoek (1994), Hoek et al. (1995), and Hoek and Brown (1997) to overcome the deficiencies or shortcomings in Bieniawski for (very poor–quality rock blocks). The geological strength index evaluates the reduction in the strength of a rock block for different circumstances as determined through field notes. The rock block is characterized by visual viewing of a structure, in terms of blackness and surface condition of the

discontinuities indicated by joint roughness and alteration (Hoek,1994). The geological strength index is expanded as experience is gained in its application to practical rock engineering dilemmas. During this current study, the geological strength index is evaluated through the following equation, through the Rock Mass Rating.

$$GSI = (RMR_{89}-5).$$

Alternatively, the quantitative modified geological strength index (Sonmez and Ulusay, 2002; Hamasur, 2009) is used. It is based on the relationship between the surface condition rating (SCR) of discontinuities along the X-axis on the chart and the structure rating along the Y-axis. This depends on the volumetric joint, with each being a limit whose value is calculated. The intersection of these values indicates the geological strength index of the rock block, as determined by the discontinuities present, as shown in figure (5). This index is calculated as follows:

Structure Rating (SR)=100 – 17.5322 *ln (j.v)*

Surface Condition Rating. (SCR)= R_r (rough)+R_w (weathering)+R_f (filling).

There is a difference between the values of the Geological Strength Index in Figure 3 and the values in Tables 4 and 5. Where it is relied upon, GSI = RMR_{89}-5.

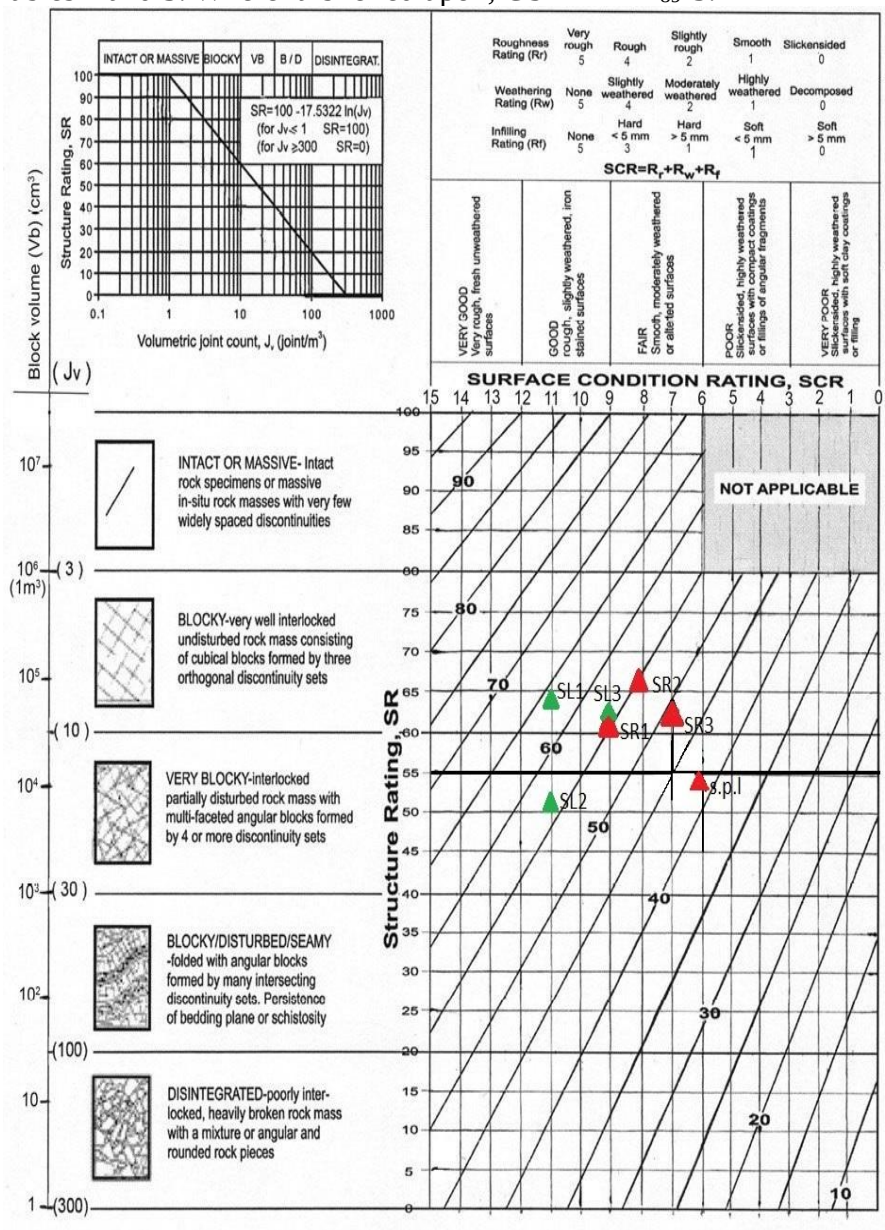


Fig. 3. The Quantitative modified geological strength index (SonmezandUlusay, 2002; Hamasur, 2009)

Table 4: Assessment of the (RMR) system in the spillway, first, second, and third stations at the right bank.

Geological Unit	Pila Spi Formation			
Rock mass unit	Spillway Station S.P.ST	First Right Station SR1	Second Right Station SR2	Third Right Station SR3
Height (above sea level)	478m	468m	492m	490m
The thickness of the unit (m)	0.40m	0.60m	0.69m	0.85m
Rock type	Limestone	Limestone	Limestone	Limestone
Strength of intact rock material USC(MPa)	16.600 MPa	10.61023 MPa	7.87425 MPa	20.642988 MPa
RQD	75.70%	87.3343%	92.680%	88.843%
The Average spacing of all discontinuities = $\frac{1}{Average\ j.v}$ According (Bieniawski,2011)	291.603mm	330.89mm	433.039mm	354.493mm
Condition of Discontinuities	1-Length of Discontinuities = (0.51) m 2- Separation = (3mm 3-Roughness rating = (rough) 4-Infilling soft filling (<5mm) 5-Weathering= (Moderate)	1-Length of Discontinuities = (0.60) m 2-Separation =(1mm) 3-Roughness rating = (rough) 4-Infilling soft filling (<5mm) 5-Weathering = (Slight)	1-Length of Discontinuities =(1.30)m 2-Separation(1mm) 3-Roughness rating =(very rough) 4-Infilling soft filling (<5mm) 5-Weathering =(Moderate)	1-Length of Discontinuities =(1.39) m 2-Separation= 1mm) 3-Roughness rating = (rough) 4-Infilling soft filling (<5m) 5-Weathering=(Moderate)
Groundwater condition	Dripping 4	Flowing 0	Damp 10	Damp 10
Volumetric joint count (joint vm^3)	13.71727	9.066279	6.92778	8.46277
RMR_{89}	50	51	61	57
Modulus Ratio of Intact rock (MR)	900	900	900	900
The material constant of intact rock (mi)	9	9	9	9
GSI	41	46	56	52

Table 5: Assessment of the (RMR) system in the first, second, and third stations at the left bank.

Geological Unit	Pila Spi Formation		
Rock mass unit	First Left Station SL1	Second Left Station SL2	Third Left station SL3
Height (above sea level)	506m	483m	496m
The thickness of the unit (m)	0.50m	0.40m	0.50m
Rock type	Chalky- limestone	Limestone	Limestone
Strength of intact rock material USC(MPa)	8.2018 MPa	11.97158 MPa	22.1267 MPa
RQD	91.3428%	71.173%	86.75%
The Average spacing of all discontinuities = $\frac{1}{Average\ j.v}$ According (Bieniawski,2011)	535.98mm	257.55mm	430.10mm
Condition of Discontinuities	1-Length of Discontinuities = (0.75) m 2-Separation (>5mm) 3-Roughness rating = (rough) 4-Infilling soft filling = (None) 5-Weathering = (Moderate)	1-Length of Discontinuities = (0.69) m 2- Separation (>5mm) 3-Roughness rating = (rough) 4-Infilling soft = (None) 5-Weathering = (Moderate)	1-Length of Discontinuities = (0.75) m 2-Separation (> 5mm) 3-Roughness rating = (rough) 4-Infilling soft filling(>5m) 5-Weathering = (Moderate)
Groundwater condition	Damp 10	Damp 10	Damp 10
Volumetric joint count (joint vm^3)	7.462857	15.530	9.3
RMR_{89}	62	55	53
Modulus Ratio of Intact rock (MR)	900	900	900
The material constant of intact rock (mi)	9	9	9
GSI	57	50	48

Table 6: Assessment of the (DMR_{STA}) system in the spillway, first, second, and third stations at the right bank.

Geological Unit	Pila Spi Formation			
Rock mass unit	Spillway Station S.P.ST	First Right Station SR1	Second Right Station SR2	Third Right Station SR3
Height (above sea level)	478m	468m	492m	490m
Rock type	Limestone	Limestone	Limestone	Limestone
Strength of intact rock material USC(MPa)	16.600 MPa	10.61023 MPa	7.87425 MPa	20.642988 MPa
RQD	75.70%	87.3343%	92.680%	88.843%
The Average spacing of all discontinuities = $\frac{1}{Average\ j.v}$ According (Bieniawski,2011)	291.603mm	330.89mm	433.039mm	354.493mm
Condition of Discontinuities	1-Length of Discontinuities = (0.51) m 2-Separation = (3mm) 3-Roughness rating = (rough) 4-Infilling soft filling (<5mm) 5-Weathering = (Moderate)	1-Length of Discontinuities = (0.60) m 2-Separation= (1mm) 3-Roughness rating = (rough) 4-Infilling soft filling (<5mm) 5-Weathering= (Slight)	1-Length of Discontinuities = (1.30) m 2-Separation= (1mm) 3-Roughness rating = (very rough) 4-Infilling soft filling (<5mm) 5-Weathering= (Moderate)	1-Length of Discontinuities = (1.39) m 2-Separation = (1mm) 3-Roughness rating = (rough) 4-Infilling soft filling (<5mm) 5-Weathering=(Moderate)
(first four parameters) of RMR	46	51	51	47
$RMR_{BD\ (89)}$= Four first five parameters of the Rock Mass Rating +15	61	66	66	62
Dip direction/dip for significant joints αj	190/26	144/24	185/20	160/22
Average of dip direction /dip amount	170/23			
The direction of the Dam axis	40NE			
Dip direction of upstream-downstream αd	130SE			
$R_{STA\ =}$ (Fill Dam)	-2			
CF= $(1\text{-Sin }\lvert\alpha d\text{- }\alpha j\rvert)^2$	0.4131759112			
(CF ×R sta)	-0.8263518224			
$DMR_{STA}=RMR_{BD}+CF\times R_{STA}$	60.1736	65.1736	65.1736	61.1736

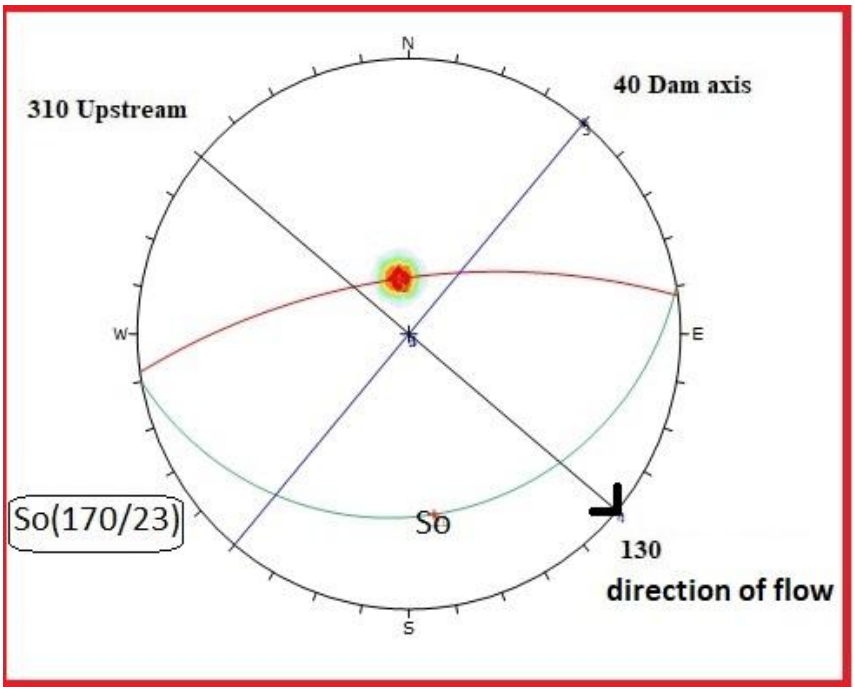


Fig. 4. Spatial projection showing the dip direction of bedding planes, the axis of the dam, and the direction of flow from upstream to downstream of the Gomel River, represented by the spillway, first, second, and third stations of the right bank of Khanas Dam.

Table 7: Assessment of the (DMR_{STA}) system in the first, second and third stations at the left bank.

Geological Unit	Pila Spi Formation		
Rock mass unit	First left Station SL1	Second left Station SL2	Third left Station SL3
Height (above sea level)	506m	483m	496m
Rock type	Chalky - Limestone	Limestone	Limestone
Strength of intact rock material USC(MPa)	8.2018 MPa	11.97158 MPa	22.1267 MPa
RQD	91.3428%	71.173%	86.75%
The Average spacing of all discontinuities = $\frac{1}{Average\ j.v}$ According (Bieniawski,2011)	535.98mm	257.55mm	430.10mm
Condition of Discontinuities	1-Length of Discontinuities = (0.75) m 2-Separation (>5mm) 3- Roughness rating = (rough) 4-Infilling soft filling = (None) 5-Weathering= (Moderate)	1-Length of Discontinuities = (0.69) m 2-Separation = (1mm) 3-Roughness rating = (rough) 4-Infilling soft = None 5-Weathering= (Moderate)	1-Length of Discontinuities =(0.75) m 2-Separation (> 5mm) 3-Roughness rating = (rough) 4-Infilling soft filling (>5mm) 5-Weathering= (moderate)
(first four parameters) of RMR	52	45	43
$RMR_{(89)}$= Four first five parameters of the Rock Mass Rating + 15	67	60	58
Dip direction/dip for significate joints αj	178/26	136/22	142/22
Average of dip direction /dip amount		152/23	
The Direction of the Dam axis		40NE	
Dip direction of upstream-downstream αd		130SE	
R_{STA} = (Fill Dam)		-2	
CF= $(1\text{-Sin }\lvert\alpha d - \alpha j\rvert)^2$		0.1403300998	
(CF × Rsta)		-0.2806601997	
$DMR_{STA}=RMR_{BD}+CF \times R_{STA}$	66.4386	58.4386	57.4386

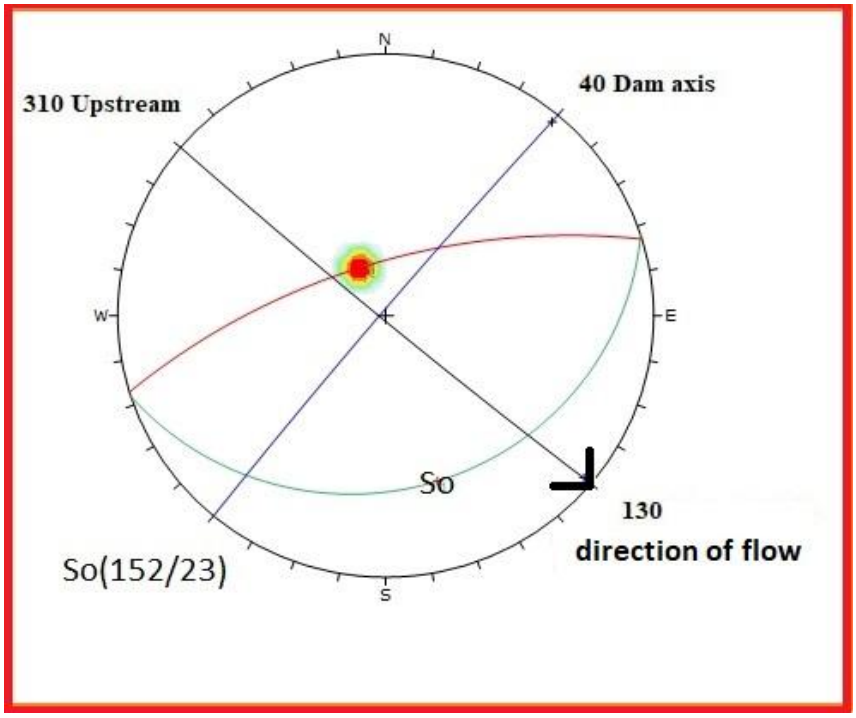


Fig. 5. Spatial projection showing the dip direction of bedding planes, the axis of the dam, and direction of flow from upstream to downstream of Gomel River, represented by the first, second, and third stations of the left bank of Khanas Dam.

Table 8: Analysis of rock strength for stations at the right bank (Pila Spi Formation) using the Roclab program.

Geological Unit	**Pila Spi Formation**			
Rock mass unit	Spillway Station S.P.ST	First Right Station SR1	Second Right Station SR2	Third Right Station SR3
Height (above sea level)	478m	468m	492m	490m
Rock type	Limestone	Limestone	Limestone	Limestone
Strength of intact rock material USC(MPa)	16.600	10.61023	7.87425	20.642988
GSI	45	46	56	52
Values of the constant mi for intact rock	9	9	9	9
Disturbance Factor	0.4	0.4	0.4	0.4
Modulus ratio (MR)	900	900	900	900
Ei= Modulus of elasticity of intact rock Ei= MR *σ_{CI}	14940	9549	7086.82	18578.7
Cohesion	0.615MPa	0.401MPa	0.362MPa	0.877MPa
Friction angle	24.26°	24.61°	28.15°	26.72°
Mb	0.772	0.808MPa	1.262MPa	1.056MPa
S	0.0009	0.0010	0.0035	0.0021
a	0.508	0.508	0.504	0.505
Rock mass parameters				
Tensile strength	-0.019MPa	-0.013MPa	-0.022MPa	-0.042MPa
Uniaxial compressive strength	0.462MPa	0.316MPa	0.459MPa	0.923MPa
Global strength	1.903MPa	1.249MPa	1.207MPa	2.846MPa
Deformation modulus	1841.60MPa	1257.81MPa	1769.93MPa	3623.45MPa

Table 9: Analysis of rock strength for stations at the left bank (Pila Spi Formation) using the Roclab program.

Geological Unit	**Pila Spi Formation**		
Rock mass unit	First left Station SL1	Second left Station SL2	Third left Station SL3
Rock type	Chalky-Limestone	Limestone	Limestone
Strength of intact rock material USC(MPa)	8.2018MPa	11.975186MPa	22.12670MPa
GSI	57	50	48
Values of the constant mi for intact rock	9	9	9
Disturbance Factor	0.4	0.4	0.4
Modulus ratio (MR)	900	900	900
Ei= Modulus of elasticity of intact rock Ei= MR *σ_{Ci}	7381.26	10777.7	19914.03
Cohesion	0.385MPa	0.489MPa	0.869MPa
Friction angle	28.51°	26.02°	25.31°
Mb	1.320	0.966	0.883
S	0.0040	0.0016	0.0013
a	0.504	0.506	0.507
Tensile strength	-0.025MPa	-0.020MPa	-0.032Mpa
Uniaxial compressive strength	0.511MPa	0.468MPa	0.755MPa
Global strength	1.291MPa	1.566MPa	2.746MPa
Deformation modulus	1955.11MPa	1847.75MPa	2994.44MPa

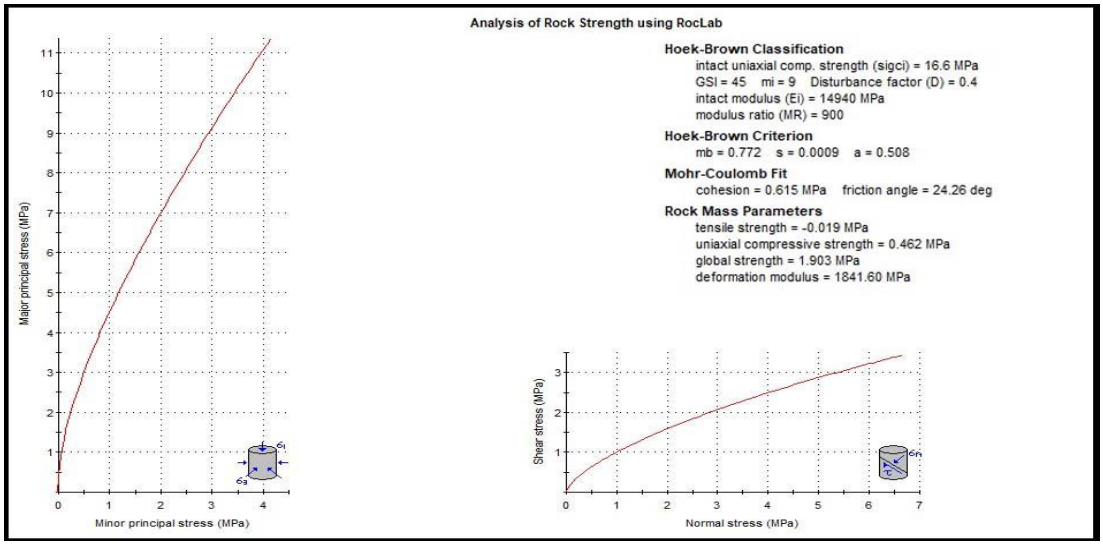


Fig. 6. Analysis of rock strength for spillway station (Pila Spi Formation-limestone), using RocLab program.

Conclusion

The following conclusions are reached to evaluate the rock masses belonging to the Pila Spi Formation rocks, which represent the foundation rock of the dam and the reservoir area.

Assessment of the rock masses according to the Rock Mass Rating System (RMR) is fair for rock masses, except second station on the right bank and except for the first station on the left bank of the dam, which have good rock masses.

The degree of safety using the Dam Mass Rating System (DMR_{STA}) of the rock masses of the right bank of the dam is (a nonprimary concern), while on the left bank of the dam is (concern), except the first station on the left bank of the dam is (nonprimary concern).

According to the Geological Strength Index (GSI), the rock masses are of fair quality on the right bank of the dam, except for the second station is of good quality, while the rocks on the left bank are of fair quality, except for the rocks of the first station are of good quality.

According to the results of the Uniaxial Compressive Strength obtained through the RocLab program, the right bank rocks have (0.462MPa), (0.316MPa), (0.459MPa) and (0.923MPa) for the (spillway, first, second, third) stations respectively, while the values of (USC) on the left bank are (0.511 MPa),(0.468 MPa)and(0.755 MPa) for the (first, second, and third) stations respectively..

According to the results of Tensile Strength obtained using the RocLab program, for the right bank rocks have (-0.019 MPa), (-0.013 MPa), (-0.022 MPa) and (-0.042 MPa) for the (spillway, first, second and third) stations respectively, while the values of Tensile strength on the left bank rocks are (-0.025MPa), (-0.020MPa), and (-0.032MPa) for the (first, second and third) stations respectively.

Reference:

Ahmed, M.A., 1980. Geology of Sheikhan Area. Unpublished M.Sc. Thesis, University of Mosul. 178 P.

Al-Hemdy, R., 2007. Facies Analysis and Depositional Environment of Sequence (Upper Campanian-Middle Eocene) in Sheikhan Anticline. Unpublished PhD Thesis. University of Mosul. 156 P.

Al-Jawadi, A.S, Al-Jumaily, I.S., Al-Dabbagh, T.H., and Davie, C., 2023. Evaluation of the Bekhme Dam Site-NE Iraq Using the Proposed Reduction System of the Rock Mass Strength, Iraqi National Journal of Earth Science, Vol. 23, No. 1, pp. 85-106. DOI: 10.33899/earth.2023.137501.1036

Al-Jawadi, A.S.H., 2013. Rock Mass Classification and the Effect of Structural Discontinuities on Engineering Structures at the Bekhme Dam Site, NE Iraq. PhD Thesis. University of Mosul. 204 P.

Al-Jawadi, A.S., Abdul Baqi, Y.T., and Sulaiman, A.M., 2020, Qualifying the Geotechnical and Hydrological Characteristic of the Bandawaya Stream Valley-Northern Iraq, Scientific Review – Engineering and Environmental Sciences, 29 (3), pp. 319–331, DOI: https://doi.10.22630/PNIKS.2020.29.3.27.

Al-Khatony S., 2009. Structural Analysis and Tectonic Interoperation for Sheikhan Anticline. Unpublished M.Sc. thesis. University of Mosul. 160 P.

Al-Talib, S.A., Al-Jawadi, A.S., and Al-Sanjari, A.A., 2021. Impact of Gercus Formation Erosion and Rock Sliding on Duhok Dam Reservoir – Northern Iraq, Iraqi Journal of Science, Vol. 62, No. 5, pp. 1562-1569, DOI: https://10.24996/ijs.2021.

Badowi, M.S., 2023. Evaluation of Hydrological Geometrical and Geoengineering Characteristics, for Badush Dam, Northern Iraq. Unpublished PhD Thesis. University of Tikrit. 326 P.

Bieiawsk1, Z.T., 1973. Engineering Classification of Jointed Rock Masses. Transaction, South Africa Institution of Civil Engineering, Vol. 15, No. 12, pp. 335-344.

Bieniawski, Z.T., 2011, Misconceptions in the Application of Rock Mass Classifications and Their Corrections. Proc. Seminar on Advanced Geotechnical Characterization for Tunnel Design, ADIF, Vol. 29. Madrid, Spain, pp. 4-9.

Bieniawski, Z.T., 1989. Rock Mass Classification in Rock Engineering: A Complete Manual for Engineering and Geologist in Mining and Petroleum Engineering. John Wiley and Sons.

Fouad, S.F.A., 2012, Western Zagros Fold-Thrust Belt, Part1: The Low Folded Zone. Iraqi Bulletin of Geology and Mining, Vol. 5, pp. 39-62.

Ghart, I.H., Hamasur, G.A., and Abood, M.R., 2023. Assessment of Foundation Rocks of the proposed Makhol Dam in Salah-Aladdin-Iraq, The Iraqi Geological Journal. DOI: 10.46717/igj.56.1F.10ms-2023-6-18

Hamasur, G.A., 2009. Rock Mass Engineering of the Proposed Basara Dam Site. Sulaimani, Kurdistan Region/ NE- Iraq. Published PhD Thesis, College of Science, University of Sulaimani/ Sulaimani- Iraq, 202 P.

Hoek, E. and Brown, E.T., 1997. Practical Estimates of Rock Mass Strength. International Journal of Rock Mechanics and Mining Science and Geomechanics Abstracts, Vol. 34, No. 8, pp. 1165-1186.

Hoek, E., 1994. Strength of Rock and Rock Masses. ISRM, News journal 2 (2), pp. 4-16.

Hoek, E., Kaiser, P.K., and Badwen, W.F., 1995. Support of Underground Excavation in Hard Rocks, Rotterdam. AA Balkema, pp. 84-97.

Hoek, E. and Marino's, P., 2000. Predicting tunnel squeezing. Tunnels and Tunneling International, part 1, 32/11, pp. 45-51- November 2000, part 2, 32/12, pp. 33-36

Jassim, M.A. and Goff, J.C., 2006. Geology of Iraq, Published by Dolin, Prague and Moravian. Museum, Brno, 304 P.

Maleki, M.R., 2011. Study of Engineering Geological Problem of the Havsan Dam with Emphasis on Clay Filled Joint in the Right Abutment, Rock Mechanics and Rock Engineering, Vol. 44, pp. 695-710.

Milne, D., Hadjigeorgiou, J., and Pakalnis, R., 1998. Rock Mass Characterization for Underground Hard Rock Mines. Tunneling and Underground Space Technology, Vol. 13, No. 4, pp. 383-391.

Mohammed, O.F., Hamasur, G.A., and Al-Manimi, D.A., 2023. Evaluation of Carbonate and Heterogeneous Rock Masses for the Dam Foundations: A Case Study at the Kanarwe River Basin, Sulaymainyah, NE Iraq. Iraqi Geological Journal. DOI: 10.46717/igj.56.1F.11ms-2023-6-19

Romana, M., 2003a. DMR (Dam Mass Rating): An Adaptation of RMR Geomechanic Classification for Use in Dam Foundation. Int. Cong. On Rock Mechanics (Technology Roadmap for Rock Mechanics), South Africa Inst. Of Min. and Meta. pp. 977-980.

Romana, M., 2003b. DMR. A New Geomechanic Classification Focus in Dam Foundations Adapted from RMR 4th International Symposium on Roller Compacted Concrete (RCC) Dams, Madrid, pp. 9.

Shaflei, A. and Disseault, M.B., 2015. Rock Mass Characterization the Proposed Kangir Dam Site in Western Iran. Earth and Environment Science, University of Waterloo, Canada, N2L3G.

Singh, S., 2020. Dam Mass Rating, A Geomechanic Classification of the Rock Mass of DHAP Dam Site, Shivpouri- Nagrun National Park, Central Nepal. MSc. Thesis in Engineering Geology. 87 P.

Snell, E. and Knight, K., 1991. Susceptibility of Dams to Failure by Sliding on Sun-Foundation Strata that Dip Upstream. International Congress on Large Dams. 17, pp. 1643-1665.

Sonmez, H. and Ulusay, R., 2022. An Application of Fuzzy Sets to the Geological Strength Index (GSI) System Used in Rock Engineering, Engineering Application of Artificial Intelligence, Vol. 16, Issue 3, pp. 251-269.

Zadeh, M.K., Feredooni, D., and Diamante, K., 2022. An Engineering Geological Assessment for the Darband Dam Site, NE of Iran, Using the Eight Rock Mass Classifications System, Springer Nature Switzerland AG22/ Vol. 7, article No. 151. DOI: 10.1007/s41062-022-00741-y

Iraqi National Journal of Earth Science

www.earth.uomosul.edu.iq

Integrating Geophysical and Geotechnical Methods to Optimize Foundation Design of a Power Station Site in Basrah, Iraq

Iman M. Jaafar [1*], Emad H. Al-Khersan[2], Amer A. Al-Khalidy [3], Amer J. Al-Khafaji [4]

[1]*Department of Geology, College of Science, University of Basrah, Basrah, Iraq.*

[2]*Department of Oil and Gas Engineering, College of Oil and Gas Engineering, Basrah University for Oil and Gas, Basrah, Iraq.*

[3,4] *Department of Applied Geology, College of Science, University of Babylon, Hillah, Iraq.*

Article information

Received: 24- Jul -2024

Revised: 10- Sep -2024

Accepted: 08- Nov -2024

Available online: 01- Jan – 2026

Keywords:
Cross-hole Seismic Refraction,
Geotechnical,
Template load,
Foundation,
Siba District,

Correspondence:
Name: Iman M. Jaafar

Email: Eman.jaafar@uobasra.edu.iq

ABSTRACT

The geotechnical soil investigation in Al-Siba District in southern Iraq for a Gas Power Plant Project reveals soft to very soft silty clay soil with varying elastic moduli values across different depths. The soil is divided into six layers, with modulus values ranging from 342.23 m/sec to 548.02 m/sec and 215.43 m/sec to 307.73 m/sec starting from 1.0 to 24.0 m depths, respectively. The Poisson's ratio and Young's modulus values are found to be between 0.21 and 0.325 in BH.3, with the minimum and maximum values being 74.5 and 171.5 MPa. The study has identified zones of weakness at depths of 5-19 meters based on low N-values (Number of blows). The foundation soil demonstrated the ability to withstand double the design load without settlement. Plate load tests and elasticity theory results aligned closely, indicating allowable bearing capacity values between 13 to 25.5 T/m2. A strong correlation is found between subgrade reaction and permanent deformation moduli. Overall, the site's soil characteristics and gas production potential support the recommendation for implementing the Gas Power Plant in Al-Siba District.

DOI: 10.33899/injes.v26i1.60177, ©Authors, 2026, College of Science, University of Mosul.
This is an open-access article under the CC BY 4.0 license (http://creativecommons.org/licenses/by/4.0/) .

دمج الطرق الجيوفيزيائية والجيوتكنيكية لتحسين تصميم الأساس لموقع محطة كهرباء في البصرة، العراق

ايمان مال الله جعفر[1]* ، عماد حسن الخرسان[2] ، عامر عطية الخالدي[3] ، عامر جاسم الخفاجي[4]

[1] *قسم علم الارض، كلية العلوم، جامعة البصرة، البصرة، العراق.*

[2] *قسم هندسة النفط والغاز، كلية هندسة النفط والغاز، جامعة النفط والغاز، البصرة ، العراق.*

[4،3] *قسم علم الارض التطبيقي، كلية العلوم، جامعة بابل، الحلة، العراق.*

معلومات الارشفة

تاريخ الاستلام: 24– يوليو –2024

تاريخ المراجعة: 10– سبتمبر –2024

تاريخ القبول: 08– نوفمبر –2024

تاريخ النشر الالكتروني: 01– يناير –2026

الكلمات المفتاحية:

الانكسار الزلزالي المتقاطع عبر الابار،

الجيوتكنيك،

تحميل القالب،

الاساس،

منطقة السيبة،

المراسلة:

الاسم: ايمان مال الله جعفر

Email: Eman.jaafar@uobasra.edu.iq

الملخص

اجري فحص هندسي لتقييم تربة موقع لإنشاء محطة لتوليد الكهرباء في منطقة السيبة جنوب العراق. اشتملت الدراسة على تقنية الانكسار الزلزالي عبر الفتحات واختبارات تحميل الألواح لتقييم معاملات المرونة والخصائص الجيوتقنية للتربة. تم تقسيم التربة إلى ست طبقات تتراوح قيم معاملات المرونة فيها من 342.23 م/ثانية إلى 548.02 م/ثانية و 215.43 م/ثانية إلى 307.73 م/ثانية تبدأ من 1.0 إلى 24.0 م على التوالي. وجد ان تربة الموقع تقع ضمن الطين الغريني الضعيف الى ضعيف جدا . تراوحت نسبة بويزون مابين 0.21 و 0.325 ، وكان الحد الأدنى والحد الأقصى لقيم معامل يونغ 74.5 و 171.5 ميكا باسكال على التوالي في الحفرة رقم3. وان معامل التقلص الحجمي الذي يصف تشوه التربة تحت حمولة معينة 183 في الحفرة رقم.1 و 533.8 في حفرة.3. كانت قيمة معامل يونك للمواد الصلبة عالية، بينما كانت القيم المنخفضة للمواد الاقل صلابة. تم تقسيم التربة تحت السطحية إلى ست طبقات . كانت الطبقات باعماق تتراوح من 5 إلى 19 مترا ذات قيم اختراق قياسي Standard Penetration Test, (SPT) منخفضة (1.5–2) تمثل مناطق ضعف في التربة. كان الحد الأقصى للهبوط – 3.7 ملم عند 61 طن/م 2 ، مما يشير إلى أن تربة الأساس يمكن أن تتحمل ضعف حمل التصميم المتوقع دون هبوط. كانت تجارب اختبار تحميل اللوحة ونتائج نظرية المرونة قريبة من بعضها البعض مع قيم قدرة تحمل مسموح بها تتراوح من 13 إلى 25.5 طن/م2. لوحظت علاقة قوة قوية بين رد الفعل الارضي ومعامل التشوه الدائم ، مع معامل ارتباط R2 يساوي 1. في الختام ، يوصى بتنفيذ محطة توليد الكهرباء بالغاز في منطقة السيبة نظرا لخصائص التربة الملائمة لذلك وإمكانية إنتاج الغاز .

DOI: 10.33899/injes.v26i1.60177, ©Authors, 2026, College of Science, University of Mosul.
This is an open-access article under the CC BY 4.0 license (http://creativecommons.org/licenses/by/4.0/).

Introduction

Geophysical methods have been used successfully in recent years for civil engineering purposes related to soil investigation and foundation. The cross-hole seismic refraction method is the most common method of geophysical exploration. It has critical applications in engineering investigations, as it is used in determining the depths and quality of rock layers and detailed investigations of the sites of tunnels, dams, and mega projects because of excellent penetrability and high-accuracy interpretation (Al-Zubaidi et al., 2022). They are non-destructive test methods for locating subsurface weak zones and determining dynamic elastic moduli. (Mohsain and Al-Khalidy, 2022; Saify and Al-Khalidy, 2023). The study area in Basrah Governorate, at Al-Siba District in Basrah Governorate is severely damaged due to many circumstances resulting in subsurface soil settlements. The settlements caused many problems for the subsurface utilities (like

pipes, cables, channels, etc.). Cross-hole seismic refraction is one of the methods that can be considered suitable for such a problem. Yet, there are certain restrictions to using this procedure, notably in Basrah's soil conditions. With the reconstruction of Iraq, particularly in the Basrah area, there is an urgent need for cross-hole seismic techniques for identifying and monitoring subsurface utilities in areas where the water table is shallow, and the soil is composed of clay, silt, and sand with high salt content. Zahraa et al. (2023) and Jaafar et al. (2024) outlined superficial subsurface layering. Using seismic refraction tomography and multi-channel evaluations of shear wave techniques, they determined their geotechnical properties in the Al-Bayt University Campus in Mafraq, NE, Jordan. The main objectives of this investigation are to obtain the elastic moduli, the underlying geotechnical engineering foundation (using cross-hole seismic refraction), and the plate load test of the study site located in Basrah Governorate, Siba District, southern Iraq.

Geology and Tectonic Settings

The geology of the studied area is marked by the existence of Quaternary deposits covering the Pleistocene period - Holocene Mesopotamian plain regions in Iraq. (Al-Siyab, et al. 1982; Al-Heety, et al. 2016). The studied area comprises alluvial and floodplain deposits, representing the Dibdibba Formation (Quaternary deposits). The Dibdibba Formation is widely exposed in southern Iraq and is slightly inclined towards the northeast, forming the Dibdibba Plain. This formation belongs to the Upper Miocene-Pliocene Cycle, whose sediments are generally characterized by a gradual change from marine sediments to estuary and river sediments, as their quantities and grain sizes increase from the oldest to the youngest, in addition to being almost devoid of significant fossils (Al-Dabbas et al., 1989; Al-Ameri et al., 2011). The formation is also distinguished by the inclusion of mud lenses, which reflect a quiet sedimentation environment in closed or semi-closed local basins within the deltaic environment, which may have been affected by tides due to its proximity to the sea during the late Miocene (Buday and Jassim, 1987). The relevance of Quaternary deposits is becoming a basis for many engineering and building deep or shallow foundations.

This type of foundation works in Basrah City and is the source of numerous underground water reservoirs (Hatzfeld and Molnar, 2010). Three boreholes (BH.1, BH.2, and BH.3) were drilled in the study site during the year 2021. The typical stratigraphic column for this site mainly consists of sandy, silty clay in shallow depth and silty sand in moderate depth, as shown in Figure 1 below.

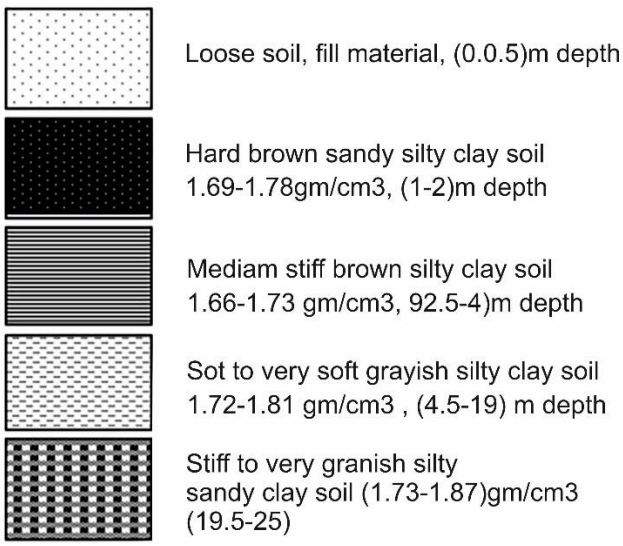


Fig. 1. Typical soil stratigraphic column in the studied area

Depending on the longitudinal and transverse tectonic divisions of Iraq, the location of the research area is in the southeastern part of the unstable shelf belonging to the Basrah block / Zubair sub-zone and forming a part of the Mesopotamian sedimentary plain. The research site is inside

the Basrah block, the southern sub-block of the Al-Batin boundary, and the Takhadid-Qurna transverse fault at the north (Fig. 2). The Zagros complex represents a youthful collisional orogeny, where many shallow and deep mechanisms of continental deformation and mountain construction are underway. (Al-Kadhimi et al., 1996). The study area is considered one of the tectonically calm areas. Still, approximately in the last five years, the region was exposed to many earthquakes whose values ranged between 1-4.5 degrees on the Richter scale, which were represented by aftershocks resulting from the collision between the Arabian and the Iranian plate and the formation of the Zagros Mountains since the Miocene.

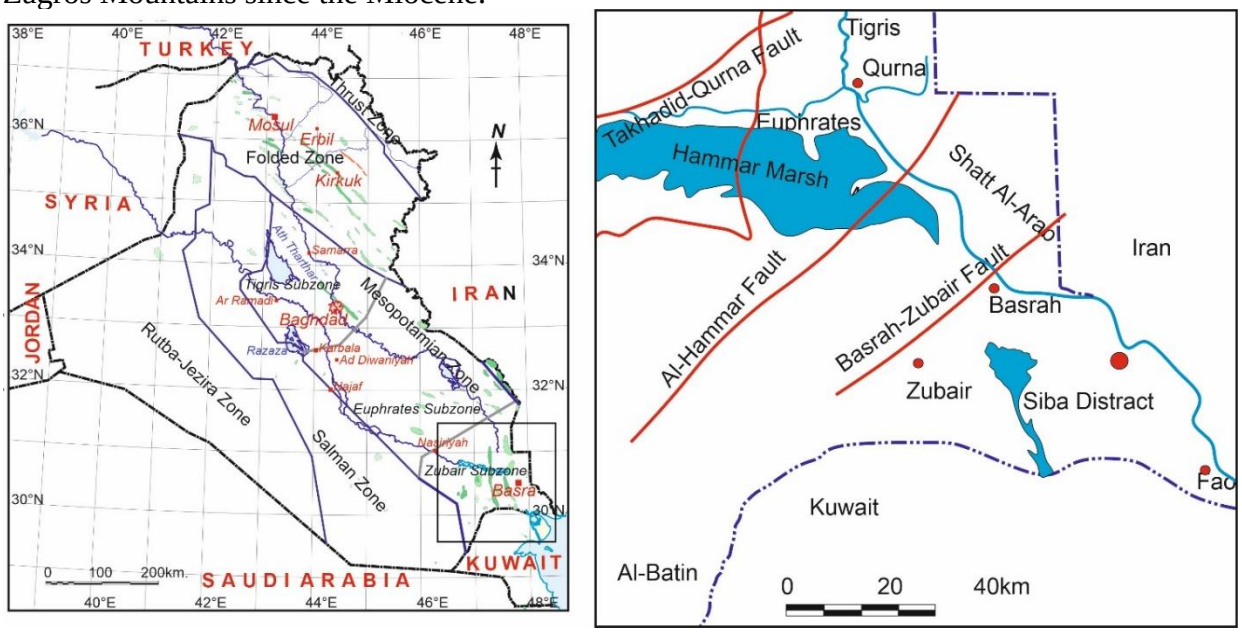


Fig. 2. Tectonic map of Iraq (left), Location of the study area (right) within the Basrah block division, modified from Al-Ameri et al., 2014.

Materials and Methods

The approach used to meet the aims of the current study is outlined in the chart below (Fig. 3). In this study, down cross-hole seismic refraction and plate load engineering tests are done as follows:

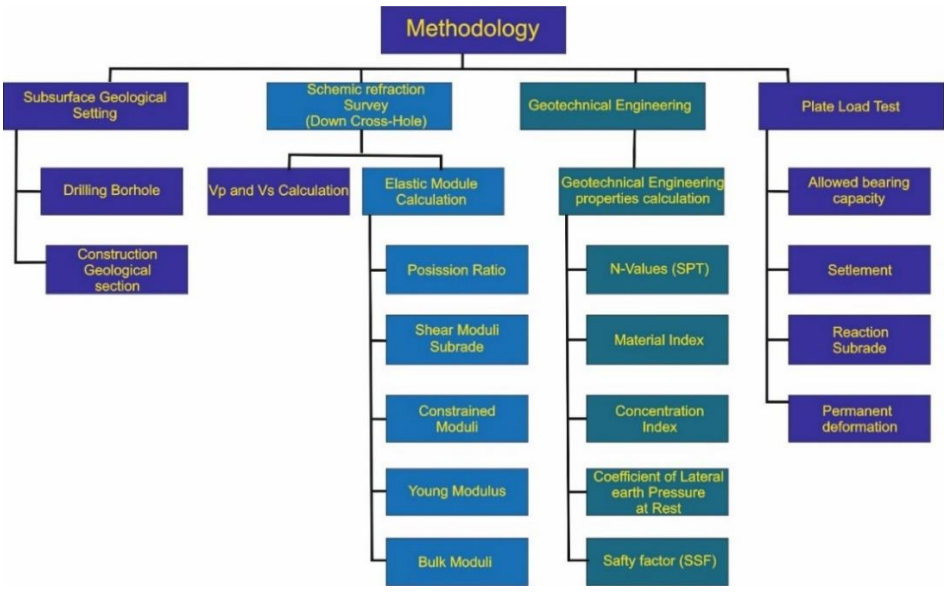


Fig. 3. Flow diagram indicating the adopted approach used in the study site.

Seismic refraction survey in boreholes

Three boreholes were drilled to 24 m depth to allow the performance of this seismic refraction survey (Fig. 4). The coordinates of these boreholes are illustrated in Table 1. Geophone orientation must remain fixed for all depths to ensure the proper wave type, which is recorded and analyzed. One or two tri-axial geophones are used as receivers. The horizontal (tangential) component is used to record horizontally polarized shear (S_h) waves (Uyanik, 2010). The cross-hole seismic refraction survey was designed and carried out to determine the variations of in situ V_p and V_s of soils and rocks with depth at a selected site in Al-Siba Field, Basrah Governorate, southern Iraq, using Olson Instruments WinGeo in addition to their geotechnical properties based on Dobrin and Savit (1988) and Kennedy et al. (2024).

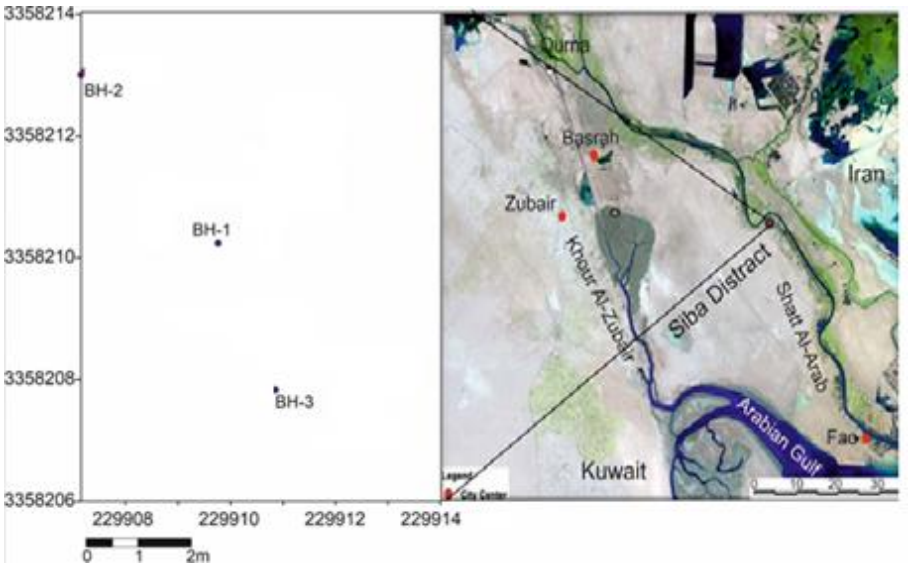


Fig. 4. Landsat satellite image of the study area showing the drilled boreholes BH.1, BH.2 and BH.3.



(a) **(b)**

Fig. 5. Photos of seismic test in the study site.

Table 1: Study site's distances and locations of the drilled boreholes.

BH. No	Coordination using UTM (meter)	
	Easting	Northing
1	229909.7	3358210
2	229907.2	3358213
3	229910.3	3358207

At this study site, the method is used for both P- and S-wave velocities separately. A source capable of producing shear and compressional waves is decreased in BH.1, and a pair of corresponding three-component geophone receivers is brought down to the identical depth in BH.2

and BH.3, which are distributed evenly in a line generally between 10 and 20 feet away from the drill source to conduct a detailed survey of the area. The receivers are set up on the borehole casing's side to detect shear and compressional waves. A three-component geophone is placed at the same elevation in the reception hole to receive the seismic signal as an elastic wave.

Plate Load Test

The plate load test results show that the foundation can be shallow or deep. However, the key criteria that influence these tests include water level, shear strength, permeability, soil density, angle of internal friction, and void ratio. (Ameen, 2006).

A linear equation can be extracted from the plot between subgrade reaction and permanent deformation of moduli or this test. The test was carried out in August 2015 in five locations and conducted at the site under study. It is performed according to the ASTM D-1194- 2003. The hearing test, as shown in Figure 6.

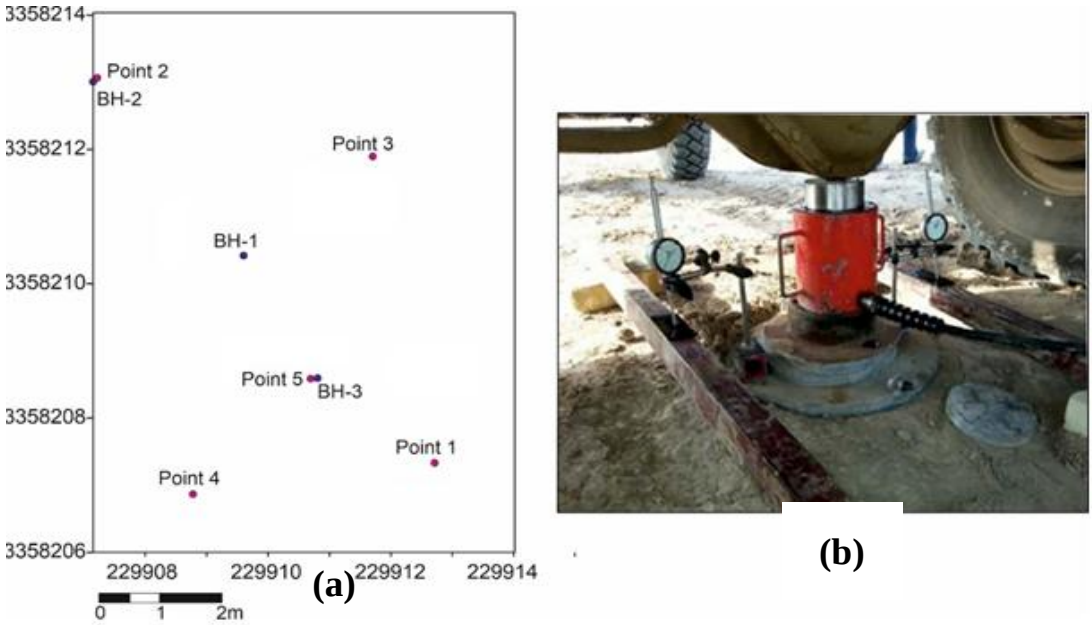


Fig. 6. (a) Base map of the study site showing five plate load test points and boreholes. (b) Photo of field plate load test.

Results and discussion

Vp and Vs outputs

A three-component geophone placed at the same elevation in the reception hole receives the seismic signal as an elastic wave. The WinGeo application selected the initial arrival times (Tp and Ts) for each seismogram (seismic segment) between boreholes. Vp and Vs are calculated using the following equations from the source to receiver boreholes (Dobrin and Savit, 1988).

$$V_p = \frac{X}{T_p} \ldots\ldots\ldots\ldots (1)$$

$$V_s = \frac{X}{T_s} \ldots\ldots\ldots\ldots (2)$$

Equations 1 and 2 are used to calculate the Vp and Vs values, as shown in Table 2. The average Vp ranges from 342.23 m/sec to 548.02 m/sec, while the average Vs ranges from 215.43 m/sec to 307.73 m/sec, beginning at 1.0 and 24.0 m depths, respectively, according to this data. Figure 7 shows significant correlations between average velocities (x-axis) and depths (y-axis) for both P and S-waves. It appears that depth causes a partial drop in Vp and Vs. It provides

information on the differences in the lithology of soil and its constituent parts. Where the density and water content of the soil influence the velocity, the soil lacks adequate stiffness.

Table 2: Calculated values of Vp, Vs., Vp/Vs., and average velocities in the studied boreholes.

Depth (m)	Borehole No.1			Borehole No.2			Borehole No.3			Average velocities (m/sec)	
	Vp (m/sec)	Vs (m/sec)	VP/Vs	Vp (m/sec)	Vs (m/sec)	VP/Vs	Vp (m/sec)	Vs (m/sec)	VP/Vs	Vp	**Vs**
1	475.0	285.0	1.7	467.2	276.7	1.7	518.2	290.8	1.8	486.8	**284.2**
2	483.1	276.7	1.7	475.0	271.4	1.8	483.1	282.2	1.7	480.4	**276.8**
3	518.2	296.9	1.7	500.0	290.8	1.7	508.9	300.0	1.7	509.0	**295.9**
4	548.1	306.5	1.8	537.7	300.0	1.8	558.8	316.7	1.8	548.0	**307.7**
5	537.7	296.9	1.8	527.8	290.8	1.8	518.2	293.8	1.8	527.9	**293.8**
6	508.9	296.9	1.7	500.0	287.9	1.7	475.0	287.9	1.6	494.6	**290.9**
7	475.0	282.2	1.7	483.1	276.7	1.7	467.2	268.9	1.7	475.1	**275.9**
8	445.3	259.1	1.7	452.4	252.2	1.8	445.3	252.2	1.8	447.7	**254.5**
9	401.4	243.6	1.6	425.4	237.5	1.8	401.4	235.5	1.7	409.4	**238.9**
10	365.4	229.8	1.6	395.8	219.2	1.8	380.0	228.0	1.7	380.4	**225.7**
11	347.6	220.9	1.6	375.0	217.6	1.7	375.0	212.7	1.8	365.9	**217.1**
12	390.4	235.5	1.7	395.8	231.7	1.7	380.0	222.7	1.7	388.7	**230.0**
13	356.3	220.9	1.6	360.8	214.3	1.7	360.8	211.1	1.7	359.3	**215.4**
14	331.4	235.5	1.4	351.9	219.2	1.6	343.4	217.6	1.6	342.2	**224.1**
15	375.0	245.7	1.5	375.0	235.5	1.6	370.1	229.8	1.6	373.4	**237.0**
16	419.1	237.5	1.8	395.8	229.8	1.7	390.4	224.4	1.7	401.8	**230.6**
17	445.3	231.7	1.9	438.5	224.4	2.0	419.1	219.2	1.9	434.3	**225.1**
18	413.0	229.8	1.8	419.1	220.9	1.9	407.1	226.2	1.8	413.1	**225.6**
19	401.4	256.8	1.6	401.4	247.8	1.6	419.1	243.6	1.7	407.3	**249.4**
20	413.0	235.5	1.8	419.1	226.2	1.9	419.1	228.0	1.8	417.1	**229.9**
21	438.5	252.2	1.7	431.8	247.8	1.7	445.3	235.5	1.9	438.5	**245.2**
22	452.4	259.1	1.7	445.3	252.2	1.8	459.7	237.5	1.9	452.5	**249.6**
23	459.7	256.8	1.8	452.4	247.8	1.8	475.0	231.7	2.1	462.4	**245.4**
24	**475.0**	**268.9**	**1.8**	**467.2**	**266.4**	**1.8**	**491.4**	**250.0**	**2.0**	**477.9**	**261.8**

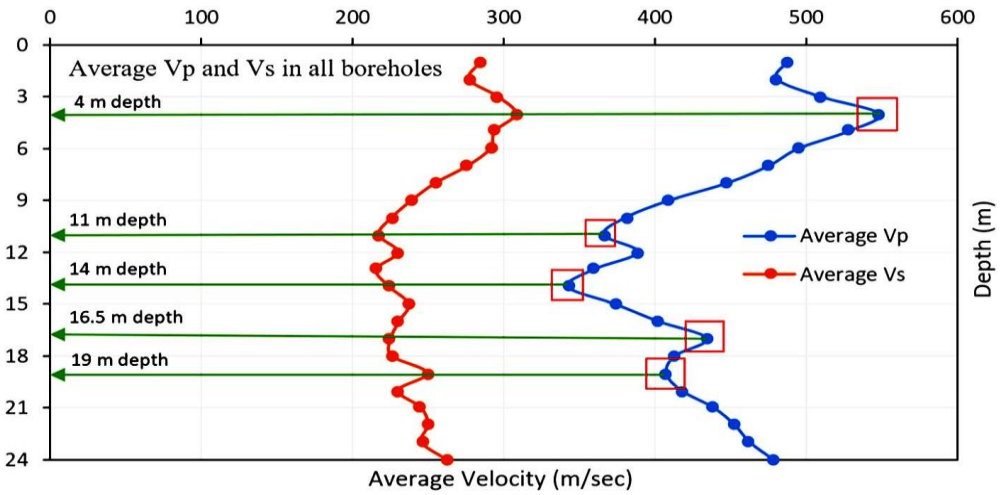


Fig.7. Relationship between depth and average velocities of (Vp, Vs) for each chosen site borehole.

Six layers can be identified within the soil of the research site, as shown in the above figure, and by variations in the values of Vp and Vs with depth. There are 1st layer (2-4) m, 2nd layer (5-11) m, 3rd layer (12-14) m, 4th layer (15-16.5), 5th layer (17-19) m, and 6th layer (20-24). The decrease in Vp and Vs at the top of layers 3 and 4 may indicate the existence of soft, silty clay soil. This fact can be noticed in the elastic modulus versus depth relationships at nearly the same depths, as shown in Figure 8.

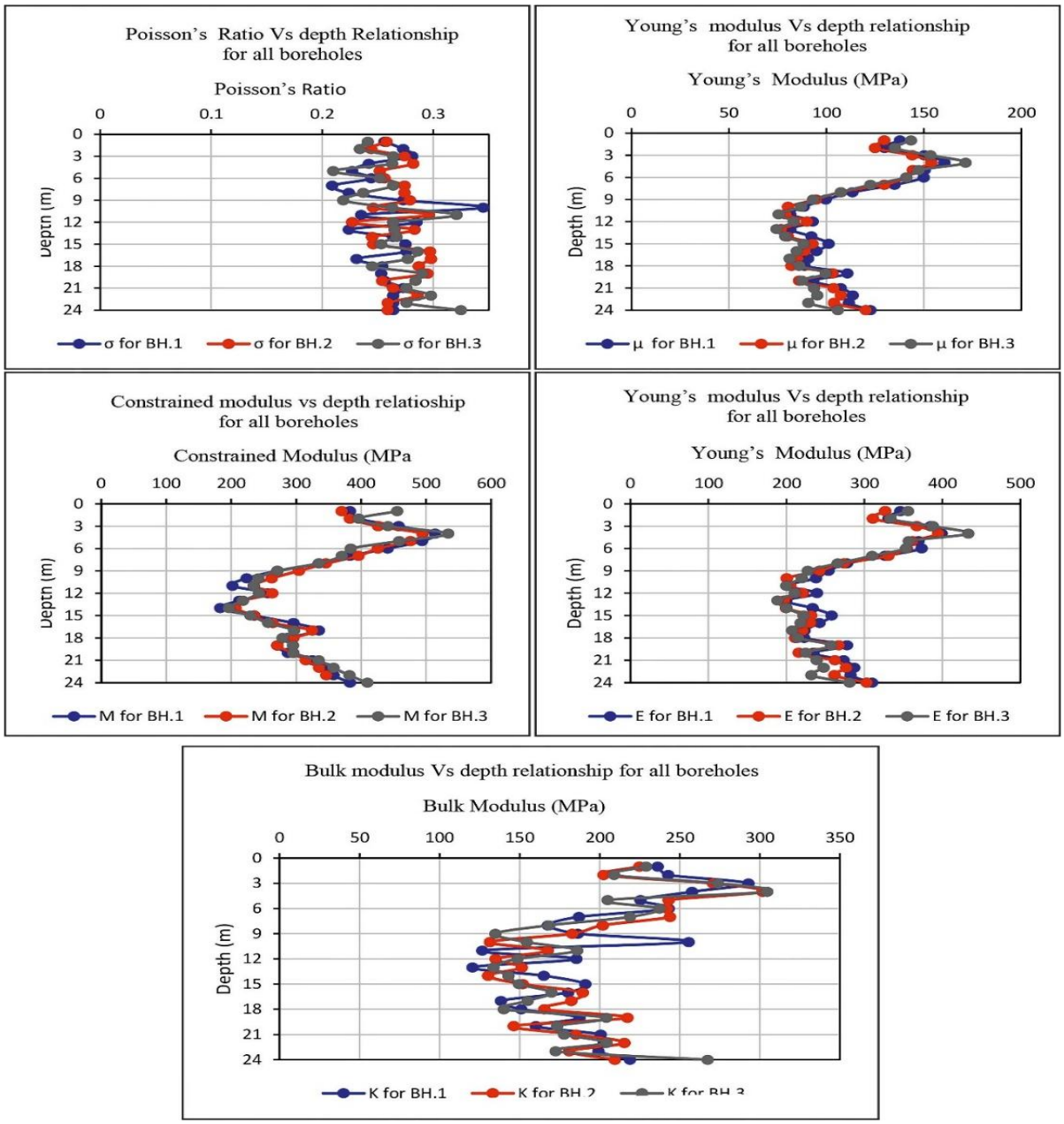


Fig. 8. Relationship between the elastic modulus values and depth for all boreholes in the site, the blue circle tends to decrease these values corresponding to the third layer.

The Poisson's ratio value ranges between 0.21 and 0.325 in BH.3 from depths 1.0 to 24.0 m. This is owed to the lithological changes, the variants in consolidation ratio, moisture content, and the proportion of water saturation in the soil, consistent with engineering parameter results. The variety of (σ) suggests that the soil of these layers is classified from stiff sandy clay soil to silty soil (loose-medium) in the investigated site. Shear modulus reflects the cohesion and stiffness of soil (Hunt, 1986). The moduli's lowest and most excellent values are 74.5 and 171.5 MPa in BH.3. The constrained modulus of elasticity values range between 183 in BH.1 and 533.8 in BH.3. The results range from 196.9 MPa in BH.2 to 433.1 MPa in BH.3. This indicates the presence of soft clay to stiff silty clay. Bulk modulus values range between 120.6 MPa in BH.1 and 304.6 MPa in BH.3, indicating the compacted layers underlying the ground surface.

Geotechnical Properties

Material Index (Im) is a significant geotechnical feature since it shows the degree of material efficiency. However, it affects the joints, degree of consolidation, material composition,

fractures, and liquid in pores (water content). Consequently, seismic wave velocities and material elasticity are also affected. This index has limits ranging from -1 (when μ = 0) for liquid materials to 1. It is obtained using the following equation (Craig, R.F., 2004).

$$I_m = \frac{3\left(V_s/V_p\right)^2 - 1}{1 - \left(V_s/V_p\right)^2} \ldots\ldots\ldots\ldots (3)$$

Soil suitability as a foundation material can be categorized based on Poisson's ratio and material index values. The average material index values in BH.2 and BH.1 vary from (-0.29) to (1.5), respectively, indicating the presence of somewhat to moderately competent individuals based on their classification.

Concentration Index (Ic)

For rock or soil, the concentration index combines material qualities. The foundation and other civil engineering targets view it as a degree of expertise. It can be computed using the values of the (Vs/Vp) ratio, as described below (equation 4):

$$I_c = \frac{3-4\left(V_s/V_p\right)}{1-2\left(V_s/V_p\right)^2} \ldots\ldots\ldots\ldots\ldots (4)$$

The average concentration index in BH.1 at the investigated site varies from -15.80 to 2.68. The soil research site's natural values are soil density, stiffness, and natural cohesiveness at shallow and deep depths.

Coefficient of Lateral Earth Pressure at Rest (Ko)

In BH.1 and BH.2, the tabulated values of Ko vary from (-0.01) to 0.48, respectively. Consequently, the site's soil is classified as over-normally consolidated clay. In general, there is a complete correspondence in the behavior of the curves of geometrical properties with depth to those curves of elastic constants, as we notice sudden changes at the beginning of the third layer at a depth of 11 meters, which may indicate the presence of soft to very soft silty clay soil, as shown in Figure 9.

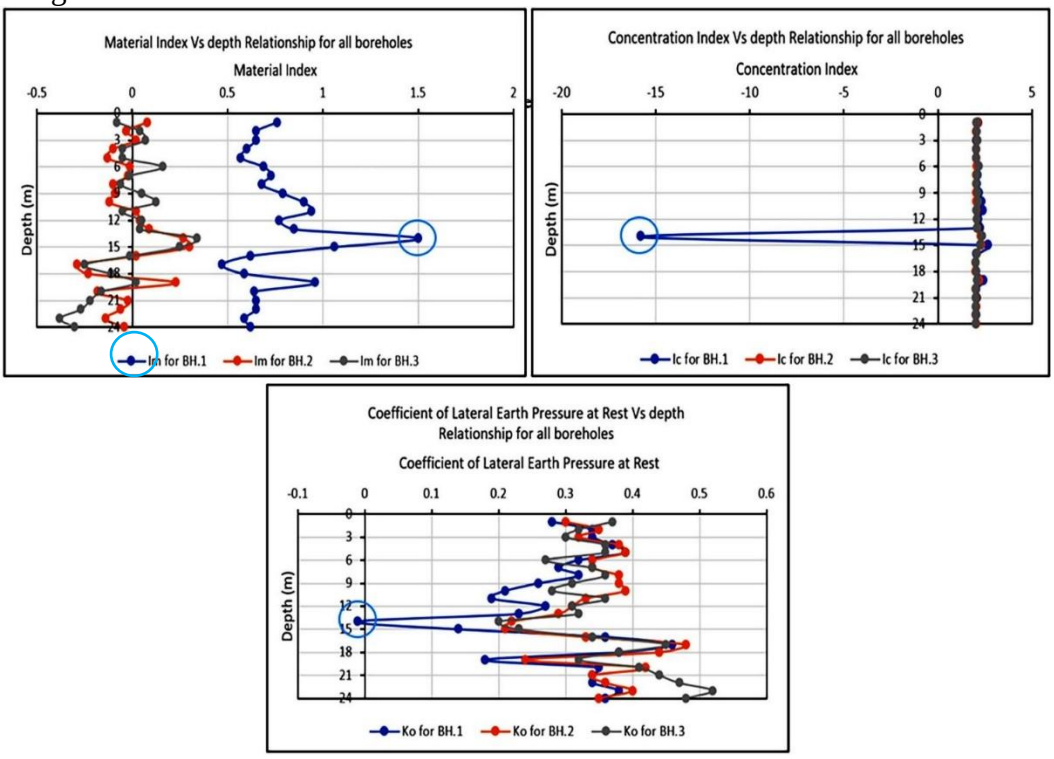


Fig. 9. Relationship between the geotechnical properties' values and depth for all boreholes in the study site, the blue circle tends to decrease these values corresponding to the third layer.

Standard Penetration Test (SPT) and Allowable Bearing Capacity (Q_{all})

The allowable bearing capacity is guessed from SPT data. The behavior of the studied geotechnical properties belonging to the average of BH.1, BH.2, and BH.3 with depth IS built separately, as demonstrated in Figure 10.

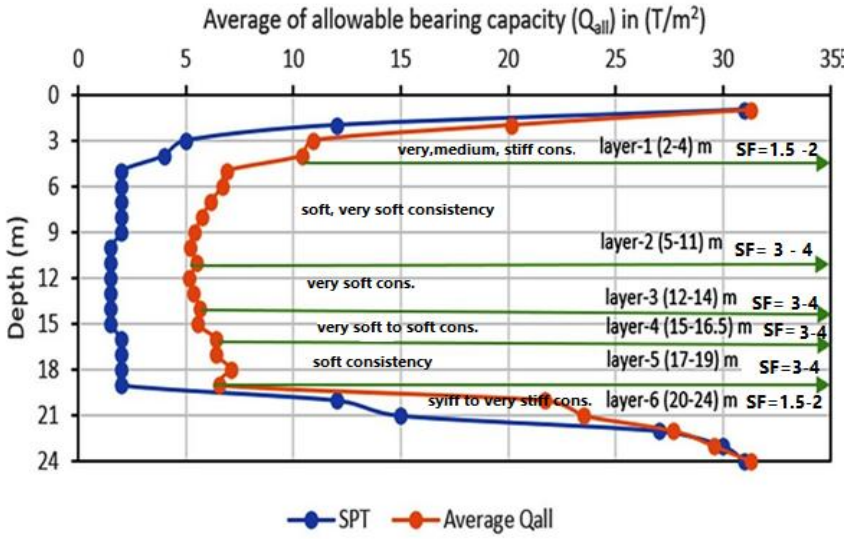


Fig. 10. Relationship between the allowable bearing capacity values and SPT with depth for all boreholes in the study site

This figure shows that six layers underlie the surface ground. Depths are indicated next to each of them. These are different results from the number of SPT and the allowable bearing capacity, which in turn comes from the variations occurring in the lithology of the soil up to a depth of 24 meters. Also, this conclusion is similar to the results we extracted by interpreting the results of seismic velocities, elastic constants, and geometrical properties.

Safety Factor (S_F)

The safety factor denotes the capacity of a design structure that can be applied beyond its projected or actual loads. The S_F of the studied site is about (1.5) and (3-4) based on Table 4. The type of soil found at the place under investigation lies within stiff to very stiff (1.5-2) and loose and soft (3-4) soil. However, the cover layer is considered a soft fill material ranging between 0 and 1 m, which should be eliminated while building. The soil type of the investigated site is lying within stiff to medium stiff (2 to 4) m, soft to very soft (5-11) m, very soft (12-14) m, very soft to soft (15-16.5) m, soft (17-19) m and stiff to very stiff (20-24) m depths described in table (3) below.

Plate Load Test Interpretation

Settlement and Allowable Bearing Capacity

The plate load test was performed at the study site in 2021. It is observed that the average values of settlement ranged between 0.17 mm in point-4 and 3.73 mm in point-2. The relationship between applied pressure and average settlement was plotted for all selected points (Fig. 11). From this figure, the allowable bearing capacity values ranged from 13 to 25.5 T/m^2 in points 3 and 5, respectively. It is also noted that these values are somewhat close to the results of allowable bearing capacity guessed from SPT data.

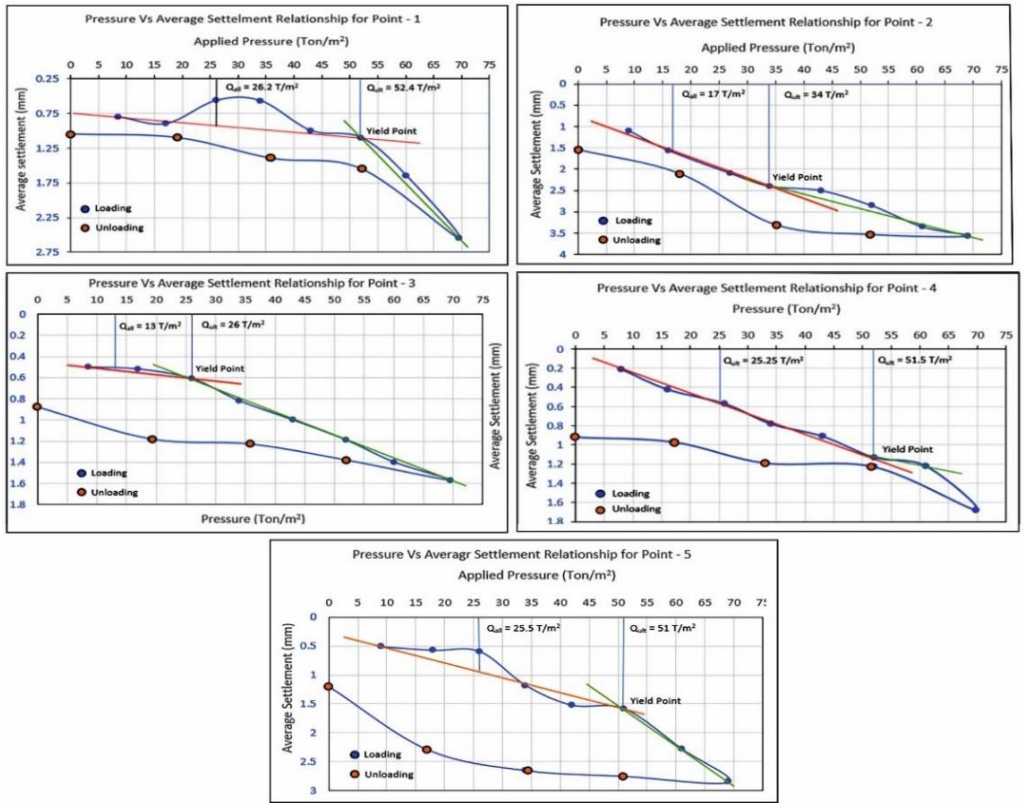


Fig. 11. The relationship between Average settlement values with applied pressure for different points in the study site

Table 3: shows the average values of Vp, Vs, elastic modulus, and geotechnical properties of the studied site

Depth (m)	Consistency	Average Values of											
		V_p	V_s	σ	μ (Mpa)	M (Mpa)	E (Mpa)	K (Mpa)	I_m	I_c	K_o	Q_{all} (Ton/m^2)	S_F
1	cover												
2		**480.4**	**276.**	**0.25**	**133.3**	**401.5**	**333.6**	**224.0**	**0.22**	**2.07**	**0.34**	**20.1**	**1.5-2**
3	**Very Stiff to medium stiff**	509	296	0.24	152.4	451.0	379.2	247.8	0.25	2.08	0.32	10.9	1.5-2
4		548.0	308	0.27	180.9	574.2	459.5	333.3	0.15	2.04	0.37	10.4	1.5-2
5	Soft to very soft	527.9	294	0.28	164.9	532.4	420.6	312.6	0.13	2.04	0.38	6.9	3--4
6		494.6	291	0.23	161.6	467.7	399.2	252.2	0.28	2.11	0.31	6.7	3--4
7		475.1	276	0.25	139.4	413.1	347.00	227.2	0.23	2.08	0.32	6.1	3--4
8		447.7	255	0.26	118.5	366.8	298.9	208.5	0.17	2.05	0.35	5.7	3--4
9		409.4	239	0.24	104.4	307.0	258.9	167.8	0.25	2.10	0.32	5.4	3--4
10		380.4	226	0.22	93.27	265.1	227.8	140.9	0.30	2.16	0.29	5.2	3--4
11		365.9	217.	0.22	82.93	235.9	202.7	125.2	0.30	2.17	0.29	5.5	3--4
12	Very soft	388.7	230	0.23	93.13	266.1	229.1	141.9	0.29	2.11	0.30	5.1	3--4
13		359.3	215.	0.22	81.70	227.2	199	118.3	0.33	2.15	0.28	5.3	3--4
14		342.2	224.	0.1	88.50	206.2	195.8	89.1	0.70	-3.72	0.14	5.7	3--4
15	Very soft to soft	373.4	237	0.16	102.3	253.7	237.4	117.3	0.54	2.42	0.19	5.5	3--4
16		401.8	231	0.25	96.83	294.1	242.9	1625.	0.21	2.07	0.34	6.4	3--4
16.5		434.3	225	0.32	92.30	343.5	242.9	220.6	-0.02	2.00	0.46	6.4	3--4
17	soft												
18		413.1	226	0.29	92.67	310.6	238.5	187.3	0.08	2.02	0.40	7.1	3--4
19		407.3	249.	0.2	116.4	310.4	278.2	155.3	0.40	2.25	0.25	6.5	3--4
20	Stiff to very stiff	417.1	230	0.28	98.87	325.3	253.2	193.7	0.10	2.03	0.39	21.7	1.5-2
21		438.5	245.	0.27	112.5	359.7	285.7	209.7	0.14	2.05	0.37	23.5	1.5-2
22		452.5	250	0.28	117.9	387	301.2	229.9	0.11	2.04	0.39	27.7	1.5-2
23		462.4	245.	0.30	114.1	404.2	296.2	252.3	0.02	2.02	0.43	29.6	1.5-2
24		477.9	262	0.28	129.6	431.8	332.1	258.6	0.09	2.04	0.40	31.3	1.5-2

Subgrade Reaction and Permanent Deformation Moduli

Table 5 shows the results tested for the selected points at the study site. Also, a logarithmic graph between the Modulus of Subgrade Reaction and the Modulus of Permanent Deformation at all studied points was constructed, illustrating a strong power relationship between these two moduli (Correlation Coefficient, $R^2 = 1$), as shown in Figure 12. This means that critical subgrade values must be achieved in the test.

Table 4: The results of Subgrade Reaction and Permanent Deformation tests of the selected points

Point No.	Modulus of subgrade reaction (Ks) (Kg/cm^2)	Modulus of permanent deformation (Kg/cm)
1	140	7875
2	142	7987.5
3	185	10406.25
4	270	15187.5
5	20	1125

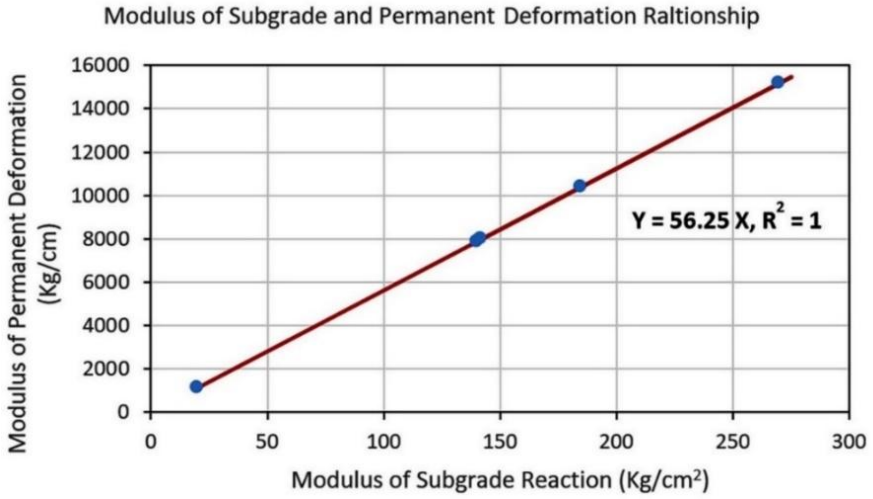


Fig. 12. Relationship between modulus of subgrade reaction and permanent deformation at the studied points of the plate late

Conclusions

1. The results of the engineering properties showed a clear correspondence with the results of Vp and the elastic constants for depths 0-24 meters, indicating the accuracy of the data obtained from fieldwork surveys at the study site.
2. From in-situ information, boring and cross-hole seismic refraction surveys show that the weak zones are subterranean surface phenomena in the research area's soil. The subsurface was divided into six soil layers according to the output results of surveys, there are: stiff to medium stiff (2 to 4) m, soft to very soft (5-11) m, very soft (12-14) m, very soft to soft (15-16.5) m, soft (17-19) m and stiff to very stiff (20-24) m depths.
3. At depths of 5-19 meters are characterized by low N-value (1.5-2), as these depth intervals represent zones of weakness in the soil of the study site, and they can't be used as foundations for building due to their inability to bear the weights coming from the structure.
4. The maximum settlement is 3.7 mm at 61 tons/m2; this indicates that the foundation soil can bear twice the expected design load without subsidence. Plate load test experiments and elasticity theory results are so close.
5. The allowable bearing capacity values ranged from 13 to 25.5 T/m^2 in points 3 and 5, respectively. It is also noted that these values are somewhat close to the results It is also noted that these values are somewhat close to the results of allowable bearing capacity guessed from SPT data.
6. A strong power relationship between Subgrade Reaction and Permanent Deformation moduli was noticed. Correlation Coefficient, R^2, is equal to 1. This means that critical subgrade values must be achieved.

7. The difference in the values of the engineering results was observed despite the small distance between the test wells due to the heterogeneity of the geometric soil properties with depth at the study site.

Acknowledgments

The authors would like to acknowledge the staff of Al-Fao Company for Engineering Testing for their efforts in assisting in all field investigations using their instruments.

References

Al-Ameri, T.K. and Al-Khafaji, A.J., 2014. Oil seeps affinity and basin modeling used for hydrocarbon discoveries in the Kifle, Merjan, and Ekheither fields, West Iraq. Arabian Journal of Geosciences, Vol. 7, No. 12, pp. 5273-5294.

Al-Ameri, T.K., Jasim, S.Y., and Al-Khafaji, A.J.S. 2011. Middle Paleolithic to Neolithic cultural history of North Iraq. Arab J Geosci 4, pp. 945–972. https://doi.org/10.1007/s12517-010-0159-5

Al-Dabbas, M.A., Tobia, F.J., and Suliaman, M.A., 1989. Water Quality and Lithological Framework for Upper Dibdibba Sediments Interaction at Safwan-Zubair Area, Southern Iraq: Proc. 5th. Sci. Conf./Scientific Research Council, Vol. 1, Part 3, pp. 10-23.

Al-Heety, A.J., Al-Khalidy, A.A., Al-Khafaji, A.J. 2016, Ground penetrating radar in civil engineering application: A case study of multistorey building foundation site to mapping subsurface features at the center of Karbala governorate, Iraq, Iraqi Geological Journal, Vol. 39-49, No. 1, pp. 49–65. https://doi.org/10.46717/igj.39-49.1.4Ms-2016-06-26

Al-Kadhimi, J.A.M., Sissakian, V.K., Fattah, A.S., and Dikran, D.B., 1996. Tectonic map of Iraq, GEOSURV, Baghdad, Iraq, (Unpubl.).

Al-Sinawi, S.A., Khorshid, S.Z.A., and Hamdi, F.A.I., 1990. Application of Compressional and Shear Wave Velocities in Solving Geotechnical Problems Associated with Gypsiferous Sediments in Central Iraq, Iraqi J. Sci. Vol. 13, No.3, pp. 591-610.

Al-Siyab, A., Al-Ansari, N., Al-Rawi, D., Al-Jassem, J., Al-Omari, F.S., and Al-Sheikh, Z., 1982. Geology of Iraq. Dar Al-Kutub Publishing House, Mosul, 160 pages.

Al-Zubaidi, M.A., Al-Khafaji, A.J., and Abeed, Q. 2022. The Mishrif Reservoir Characteristics Utilizing Well Log Data Interpretation in the Fauqi Oilfield in Maysan, Southern Iraq. Iraqi Geological Journal, Vol. 55, No. 2, pp. 82-95. https://doi.org/10.46717/igj.55.2E.5ms-2022-11-19

Ameen, N.N., 2006. Laboratory seismic study for some geotechnical properties of rocks for engineering purposes. MSC. Thesis, College of Science, University of Basra. (Unpublished), 111 P. (In Arabic).

Buday, T. and Jassim, S.Z., 1987. The Regional Geology of Iraq, Tectonism, Magmatism and Metamorphism: Vol. 2, Geological Survey and Mineral Investigation Press, Baghdad, 445 P.

Craig, R.F., 2004. Craig's Soil Mechanics: 7th Ed., Department of Civil Engineering, University of Dundee, UK. 176 P.

Dobrin, M.B. and Savit, C.H., 1988. Introduction to Geophysical Prospecting. 4th Edition. McGraw-Hill Publ. Co, New York, 730 P.

Hatzfeld, D. and Molnar, P., 2010. Comparisons of the Kinematics and Deep Structures of the Zagros and Himalaya and of the Iranian and Tibetan Plateaus and Geodynamic Implications. Reviews of Geophysics, Vol. 48, RG2005. https://doi.org/10.1029/2009RG000304.

Hunt, R.E., 1986. Geotechnical Engineering Analysis and Evaluation. McGraw-Hill Book Co., 730 P.

Jaafar, I.M., Anmar H.S., Amer A.L., and Emad H.A., 2024. Engineering Site Investigation inside Basrah City, Southern Iraq using Cross-hole Seismic Refraction Technique (A Case Study). Iraqi Geological Journal, Vol. 57, No. IE, pp. 52-57. https://doi.org/10.46717/igj.57.1E.4ms-2024-5-15.

Kennedy, S.H., Maher, A., and Iman, M.J., 2024. Evaluation of Liquefaction Based on Shear Wave Velocity Using Machine Learning. Proceedings of the 9th World Congress on Civil, Structural, and Environmental Engineering. ICGRE 155. DOI: 10.11159/icgre24.155

Mohsain, A.F., Al-Khalidy, A.A.L., 2022. Geotechnical Assessment of Dar Al Salam Complex in Hilla City, Babylon Using the Seismic Refraction. Iraqi Geological Journal, Vol. 55, No.1F, pp. 95–101. https://doi.org/10.46717/igj.55.1F.8Ms-2022-06-23.

Saify, Z.M.J., Al-khalidy, A.A.L. 2023. Engineering, Geophysical Investigation of a Multistory Building, at Hilla, Iraq, Utilizing the MASW Method. Iraqi Geological Journal, Vol. 56, No. 1, pp. 217–227. https://doi.org/10.46717/igj.56.1E.16ms-2023-5-26.

Uyanik, O., 2010. Compressional and shear-wave velocity measurements in unconsolidated topsoil and comparison of the results. International Journal of the Physical Sciences, Vol. 5, No. 7, pp. 1034-1039.

Zahraa J. and Al-Khalidy A. 2023. Comparing the Results of Geotechnical Tests with the Well Seismic Survey to Find the Dynamic Modulus of Elasticity for the Surface Soil Sections in Hilla City. Iraqi Geological Journal, Vol. 56, No. 1, pp. 228–233. https://doi.org/10.46717/igj.56.1E.17ms-2023-5-27.

Iraqi National Journal of Earth Science

www.earth.uomosul.edu.iq

Hydro-morphometric and Hydrochemical Criteria to Select the Optimal Location for Small Dam in Um Al-Shibabit Valley, Al-Shirqat, Northern Iraq

Abdulhadi Hamad Mohammed [1*], Alaa Ahmad Mohammed [2], Sabbar Abdullah Salih [3], Abdulsalam Mehdi Salih [4]

[1,2,3,4] *Department of applied geology, College of science, University of Tikrit, Tikrit, Iraq.*

Article information

Received: 05- Dec -2023

Revised: 20- May -2024

Accepted: 27- Dec -2024

Available online: 01- Jan – 2026

Keywords:
Um Al-Shibabit,
Valley,
GIS,
RS,

Correspondence:
Name: Abdulhadi Hamad Mohammed

Email: hadi_aldokhy@tu.edu.iq

ABSTRACT

In this study, a morphometric analysis of the Um Al-Shibabit Valley basin has been done. It reflects that Um Al-Shibabit Valley is of the 7th order valley consisting of two sub-basins (northern and southern). The Valleys of two parts of the basin are linked about 6 kilometers from the Tigris River. The areal, shape, discharge, and topographic properties of the basin are determined. The area, perimeter, length, and width of the basin are 295 km², 80 km, 24 km, and 14.5 km, respectively. The shape is intermediate between circular and a rectangular basin. The discharge characteristics reveal a quick access of the downstream floods during heavy rainstorms. The hydro-chemical properties of water in the valley are studied. The chemical analyses reflect a high salinity in the upstream, near Mehha Saltern. The abundant salt in this part of the valley is sodium chloride, while the salinity decreased in the midstream to reach the lowest concentration near Ain Al-Baidha Spring. The concentration returns to increase toward the downstream, where NaCl and CaSO4.2H2O are the main salts; while in Ain Al-Baidha Spring, the main salt is CaSO4.2H2O. The water of the valley is usable for animal drinking, construction, and irrigation of crops, palm, barley, and wheat. Mineralogical and chemical diagnoses reflect that quartz, calcite, feldspar, gypsum, palygorskite, kaolinite, dolomite, and halite are the abundant minerals in the transported sediments in the valley. The optimum location selected according to the hydro-morphometric, hydro-chemical, and mineralogical conclusions is considered a location for the suggested small dam. The location is near the confluence of the two main branches of the valley. The study suggests that the separated high-salinity water at the upstream can be used for salt production and other industrial uses.

DOI: 10.33899/injes.v26i1.60179, ©Authors, 2026, College of Science, University of Mosul.
This is an open-access article under the CC BY 4.0 license (http://creativecommons.org/licenses/by/4.0/).

الخصائص المورفومترية والهيدروكيميائية لاختيار الموقع الأمثل لسد صغير على وادي ام الشبابيط في قضاء الشرقاط، شمالي العراق

عبد الهادي حمد محمد [1]* ، علاء أحمد محمد[2] ، صبار عبد الله صالح[3]، عبد السلام مهدي صالح [4]

[4,3,2,1] قسم علوم الأرض التطبيقية، كلية العلوم، جامعة تكريت، تكريت، العراق.

معلومات الارشفة

تاريخ الاستلام: 05– ديسمبر –2023

تاريخ المراجعة: 20– مايو –2024

تاريخ القبـول: 27– ديسمبر –2024

تاريخ النشر الالكتروني: 01– يناير –2026

الكلمات المفتاحية:

أم الشبابيط،

الوادي،

نظم المعلومات الجغرافية،

RS،

المراسلة:

الاسم: عبد الهادي حمد محمد

Email: hadi_aldokhy@tu.edu.iq

الملخص

تم في هذه الدراسة إجراء التحليل المورفومتري لحوض وادي ام الشبابيط. تشير نتائج التحليل الى أن الوادي من الرتبة السابعة ويتكون من حوضين ثانويين (شمالي وجنوبي)، تلتقي الوديان المكونة للجزأين على بعد 6 كيلومترات عن مصب في نهر دجلة. تم حساب الخصائص المساحية والشكلية والتصريفية والتضاريسية للحوض، اسفرت النتائج ان مساحة الحوض ٢٩٥ كم ومحيطه ٨٠ كم وطوله ٢٤ كم وعرضه ١٤.٥ كم، وأن شكله يمثل حالة وسطية ما بين الدائري والمستطيل. تشير خصائصه التصريفية إلى وصول سريع للموجات الفيضية إلى المصب عند زخات المطر الشديدة. درست الخواص الهيدروكيميائية لمياه الوادي وتبين ارتفاع ملوحة المياه في اعالي الوادي قرب مملحة محة وان الملح في الوادي هو ملح كلوريد الصوديوم وخصوصا في أعاليه، أما في وسط الحوض فان الملوحة تقل تدريجيا لتكون اقل ما يمكن عند عين البيضة، ثم تعود للزيادة باتجاه المصب، وأن الملح السائد في هذه المواقع هو أيضا كلوريد الصوديوم يليه الجبس، ماعدا في عين البيضة فان الجبس هو الملح السائد، وأن مياه الحوض في جميع المواقع عدا أعالي الوادي تصلح لشرب الحيوان وللبناء والإنشاءات ولري المحاصيل والنخيل والخضار الإستراتيجية في المنطقة تم تشخيص معادن الـ (dolomite, kaolinite, palygorskite, gypsum, feldspar, calcite, quartz and Halite) كمعادن سائدة في الرسوبيات المنقولة في الوادي، وهذا ما عززته التحليلات الجيوكيميائية لرسوبيات الوديان. بناءا على المعطيات الهيدرومورفومترية والهيدروكيميائية ومعدنية الرسوبيات تم انتخاب المقطع المثالي، الذي يقترح ان ينشأ عنده السد بعد التقاء الوديان الرئيسة القادمة من جزئي الحوض الجنوبي والشمالي بعد عزل مياه أعالي الوادي ذات المحتوى الملحي العالي، واقتراح استثمار مياهه في إنتاج الملح أو الاستخدامات الصناعية الأخرى.

DOI: 10.33899/injes.v26i1.60179, ©Authors, 2026, College of Science, University of Mosul.
This is an open-access article under the CC BY 4.0 license (http://creativecommons.org/licenses/by/4.0/).

Introduction

Water has been an important factor in humanity and the emergence of civilizations because of its attraction, which has paved the way for human societies as a verified basis for their first step in residing near natural water resources (Hussein and Salih, 2024). Water crisis is a term that indicates the scarcity of suitable water for human use and water pollution. The water crisis is affected by geographical, political, economic, and cultural factors, which require the development of techniques of water use and management with scientific methods (Badawy et al., 2023). Studies indicate that the solution is to find a perfect integrated way to manage the available water sources, and one of the ways that leads to such management is to study the valley's hydrology. Developing water sources within the region is the biggest challenge facing decision-makers, given the diminishing water resources on the one hand and the increasing demands on the other. The study of valley water storage is one of the most important solutions for developing water resources and their sustainable management.

Location of Study Area

The study area is undulated, and it is located in the west and south-west of the city of Al-Shirqat, north of Iraq, between the geographic coordinates (longitudes 43° 0' 27.7" E -43° 14' 37.9" E and latitudes 35° 21' 59.1" N -35° 38' 25.9" N). The height of the basin reaches 250 m (a.s.l) in the west, and slopes to the east, reaching a height reaches 150 m (a.s.l). The valley meets with the Tigris River southeast of Al-Shirqat, which is the last drainage order in the watershed that represents the Um Al-Shibabit valley. This valley runs seasonally and reaches its peak in the winter, especially during heavy rainfall (Fig. 1). The valley dries up in the summer, which calls for thinking about storing water in the valley and recycling it during the dry period.

Geological Background

Geologically, the gypsum and clay beds are exposed within the Fatha Formation (Middle Miocene) in most of the basin, especially in its western part, and it consists of cycles of gypsum, anhydrite, and marl, in addition to friable rocks in the upper part of the formation. Moreover, there are layers of salt rock within the basin depth (Al-Juboury et al., 2001). These layers of salt rock could be the main source of table salt dissolved in water, as will come later.

The valley breaks through a sediment strip on the west bank of the Tigris River and flows into the river south of Al-Shirqat (Salih et al., 2012).

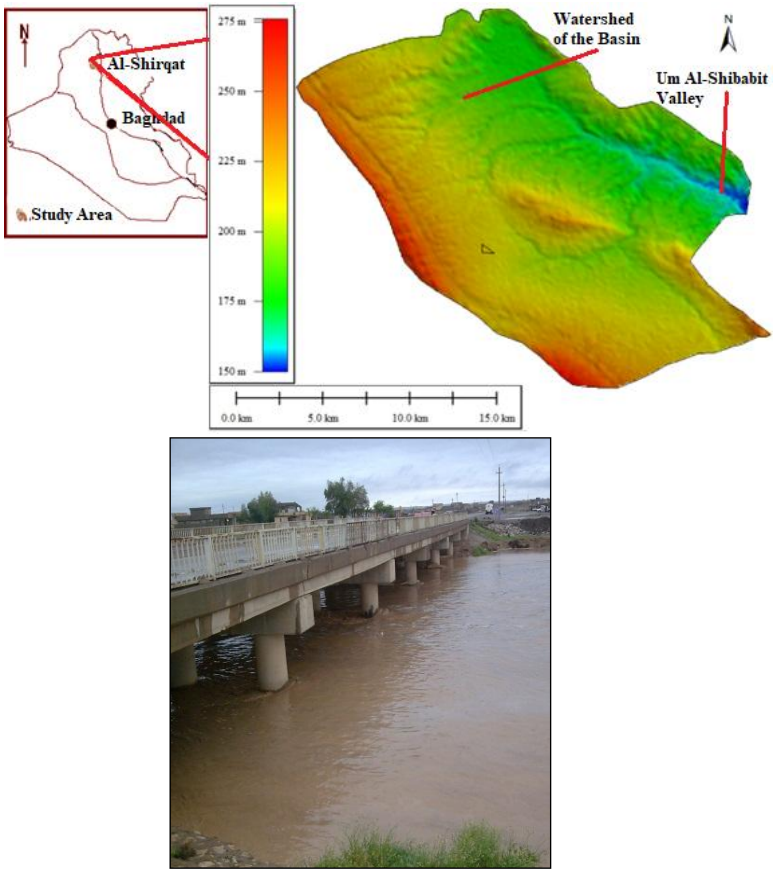


Fig. 1. Um Al-Shibabit basin location, with 2D DEM, and Um Al-Shibabit Valley bridge near Al-Khusum village during the flood.

This study is of great importance in investing in the valley's water resources to develop the region, especially in increasing the area of agricultural land and natural pastures.

The study aims to carry out morphometric analyses of the area and to diagnose the valley's orders; hence, determining the perfect locations for storing water at the convergence of the major valleys. The qualitative properties of the valleys' water have been discussed, classified, and evaluated for various purposes. The sediment and mineral load of the valley are discussed as important factors for the future problems that may occur in the suggested dam reservoir. The study also evaluates the possible uses of the clayey sediments.

Materials and Methods

The Digital Elevation Model (DEM) that covers the study location is used to extract the geomorphological and geometric features; the boundaries of the watershed were derived from the DEM produced by the United States Geological Survey (USGS) of 10X10m spatial resolution. By applying the global mapper V.13 software and the ArcGIS V. 10.8 software, these data are used to derive and distinguish the drainage orders and to determine the optimum location of the dam.

Watershed characteristics: The Arc GIS 10.8 and Global Mapper 13 systems are used to derive the outer boundaries of the river basin and its parameters, basin area, and highest and lowest points at numerous heights within the area. Then, the geographic information system ArcGIS 10.8 is used to extract layers, where each one of them represents the drainage orders of the river. These orders are extracted from the DEM and topographic maps of the area with a scale of (1:25000); then, they are checked using the American Satellite Imager Landsat-8 for the area in 2013. The number and lengths of the valleys in each order of the database of each layer, the real and ideal length, and the width of the basin are extracted.

Eight water samples from the valleys were collected during the 2nd heavy rain in the wet season from upstream towards downstream. Chemical analytics were performed at the laboratories of the General Company for Geological Survey and Mining to classify and evaluate the water samples for different uses and show the variations of the properties with the direction of flow.

Accordingly, chemical analyses are performed to determine the concentrations of major cations Ca^{++}, Mg^{++}, Na^{+}, K^{+}, and major anions NO_3^{-}, Cl^{-}, HCO_3^{-}, and SO_4^{-} in ppm. Other physicochemical parameters, such as TDS, EC, and pH, are measured as well. The analyses are accomplished in the laboratories of the General Company of Geological Survey and Mining.

Five geological samples are selected to isolate the clay's suspended loads to perform chemical, mineral, and grain size analyses in the General Company for Geological and Mineral Survey to determine its source, to evaluate it for different uses, and to treat the engineering problems that resulted in the bottom of the reservoir.

Results and discussion

Hydro-morphometric analysis

It is considered one of the most appropriate methods for quantitatively describing and classifying river basins based on capacity, parameters, length, width, and variation of land surface heights and the length and number of valleys and their branches (Strahler, 1954).

The morphometric analysis is of great importance because it provides a method of assembling the drainage of the water and the arrival of the flood waves on the side of the water drainage (Badowi et al., 2024). The morphometric characteristics are measured based on the equations of Strahler (1954; in Mohammad et al., 2024).

These numerical, longitudinal, and areal data of the basin are used to calculate all its hydro-morphometric properties (Fig. 2).

The *stream orders* are the numerical grade of the tributaries that form the basin drainage network, so each tiny stream is connected with the other to form another stream that has a higher

order, and this, in turn, connects to a symmetry system to be the highest order, etc. (Mohammad et al., 2024).

The *numbers and lengths* of the valleys were inserted within seven orders as given in Table 1, in which Um Al-Shibabit is considered to be of the seventh order. The bifurcation ratio is an important measure that controls the surface drainage rate, and it represents the ratio between the number of streams in the specified order to the number of streams in the next higher order (Al-Babawati, 1995).

The *bifurcations* remained similar (up to 2) for all the higher orders (the upstream of the basin) except the last order (which is close to the estuary) decreased to 0.36; this is because the basin consists of two sub-basins (separated by the light green line). They meet at the last order; the values of the drainage orders and the calculated drainage characteristics are listed in Table 1. The drainage density is a measure of the ability of the valleys to transport the rainwater toward the estuary. The drainage increases with the increase of the capacity, and it usually increases in areas with heavy rainfall, especially the areas that have surface clay beds with low permeability (Al-Juboury, 2009).

The *stream frequency* is calculated depending on the total ratio of valley numbers in all the orders to the basin area; it has reached 8.22 km in the basin, which is medium density according to the Strahler classification (1962), while the longitudinal drainage density (ratio of the total lengths of the valleys basin to its area) is low according to the same classification which amounted (3.36 km/km^2). As for the proportional density of the valleys, which represents the ratio of numerical density to the square of longitudinal density which reaching (0.73 valley/km). As for the low-density drainage under drought conditions and lack of rain reduces the chance of developing the upper levels of the basin river beds and increases their area. The intensity of the drainage is of great importance because it reflects the speed of the drainage waves traveling from parts of the basin towards the main channel to reach the drainage peak (Mustafa et al., 2024; Hussein and Salih, 2023). And it represents the numerical ratio between the longitudinal density and to numerical density, and the little value (0.41) means that the basin is still young and has a high drainage capacity.

River turns are evaluated by the deflection factor, which represents the ratio of the true length of the main valley to its ideal length (the shortest distance between the source and estuary of the river), as this factor reflects the problems caused by river deflections (Schumn, 1956; in Al-Juboury, 2009). The increase in the deflection means an increase in the river twists. Consequently, it increases in evaporation and leaching in the riverbed and complications in the geomorphologic situation on the deflection sides, as sedimentation occurs on one side and erosion on the other, the value of the deflection factor of the basin is very low (1.04), which shows the lack of curves.

Table 1: The river orders and calculated drainage characteristics for the Um Al-Shibabit catchment area

Order	No of Valleys	Length of Valleys (km)	Bifurcation ratio	Property	Value
1st	1819	483.312		Stream Frequency valley/km^2	8.22
2nd	456	234.707	1/2→3.99	Numerical Drainage Density km/km^2	3.36
3rd	114	125.229	2/3→4	Valleys' relative density valley/km	0.73
4th	29	72.785	3/4→3.93	Drainage intensity	0.41
5th	8	41.797	4/5→3.63	Sinuosity factor	1.04
6th	2	26.848	5/6→4		
7th	1	8.493	6/7→2		
Total	2429	993.171			

Geospatial characteristics: It specializes in the basin's geometric dimensions and the difference between them; a group of climate factors, rock types, and tectonic movements (Al-Khuzamy, 2004) affect these characteristics. They increase with the increase of water erosion and the weakness of the rocks' resistance and erosion activity, which may lead to lowering the

base level or the occurrence of river capture (Al-Muhsin and Al-Azzawi, 2002). The basin area is important because it controls the water flow and obtains quantitative relationships by evaluating the hydrology of the basin. The difference between the basin's length and width is not significant, which may cause rapid water splashes during heavy rain showers, which may be taken into consideration when designing the dam and choosing the nominated low topography for storage (Table 2).

Table 2: Area characteristics of the Um Al-Shibabit drainage basin.

The actual length km	Ideal length km	Basin width km	Parameter km	Area km^2
24.2	23.16	14.5	79.46	295.32

Shape characteristics: It is used to evaluate basin hydrology. The elongation value indicates that the basin is closer to a circular shape than a rectangular with a value close to (1), which is due to the sharp differences in the hardness of the detector of the rock layers. The sharp contrast in climatic conditions was indicated by the evaluation of the circulation (basin consistency ratio), which exceeded 0.5, showing that the basin has an irregular flow temporally and high drainage during heavy rainstorms, in addition to the high sedimentary load.

As for the formal factor, which describes how wide the basin is along the stream, is (0.5). That also shows how wide the basin is towards the splitting area. The factor decreases towards the estuary, but the existence of two central valley's divides the basin into two sub-basins. As for the fusion factor of the basin, which is judged by the relationship between the perimeter and area of the basin, its value may suggest the large meanders of the valley's perimeter.

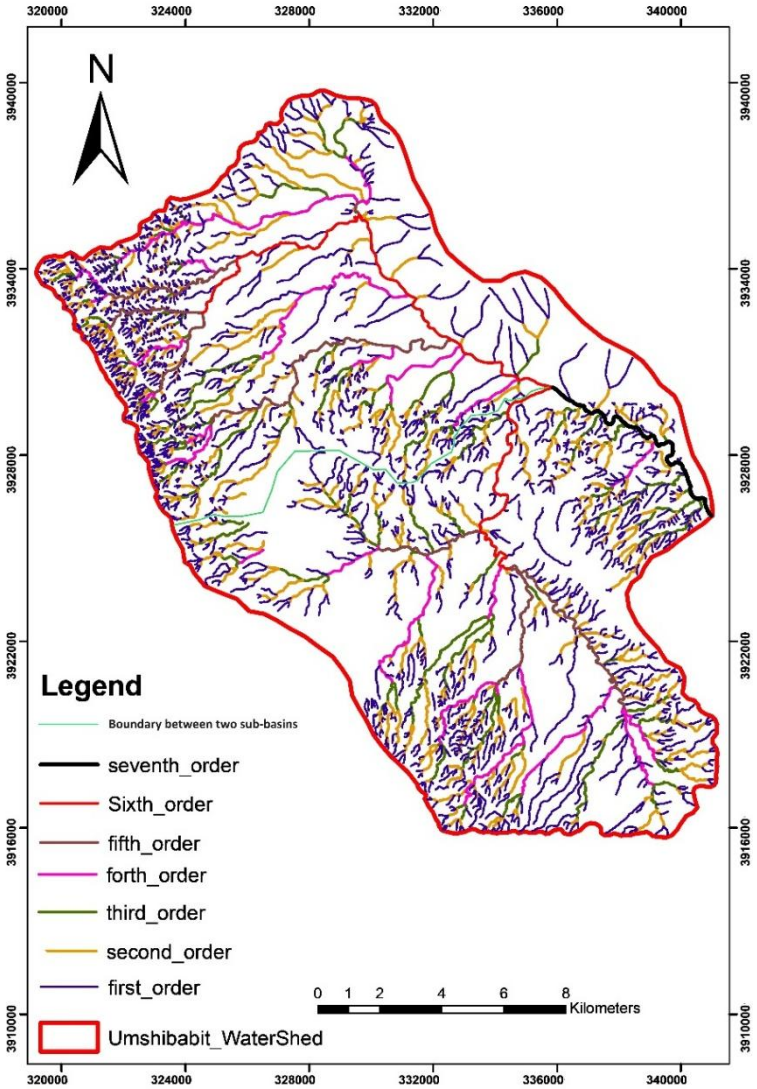


Fig. 2. Boundaries and stream orders of Um Al-Shibabit Valley and locations of the samples.

The proportion of the grip of the perimeter exceeded 1, which indicates the purpose of its staying away from the circular shape, but not to the stage that changes its rectangular shape. It means that its roundness is medium, so all these factors will control the design of the dam, and the selection of the suggested site (Table 3).

Table 3: The formal characteristics of Um Al-Shibabit Valley

elongation	rotation	shape factor	Pear shape	Integration factor	Perimeter cohesion
0.8	0.59	0.5	0.02	268.5	1.3

Terrain characteristics: Their importance lies in the evaluation of erosion activity, which depends on the nature of the basin rocks, and the high values indicate the terrain range and demolition activities (Mahsoub, 1980). The terrain ratios indicate the relationship between the basin terrain and its perimeter length, and they express its regression; the ratio rises whenever the difference between the highest and lowest points is more significant (Verstaphen, 1983). We infer from the high terrain values of the basin (107 km/km^2) that it has high terrain quality, which is an important indicator of high regression. The value of roughness increases with the increase of drainage density of the basin and the increase of terrain quality, which means the arrival of flood waves during heavy rainstorms (Mustafa, 1998). The highest and lowest points in the basin and its actual length, with an average value in the Um Al-Shibabit basin (0.005), show the high activity of sculpturing. Hypsometric integration is a criterion of the stages of the erosive cycle. Its lower value is (2.17 km/km^2) in the Um Al-Shibabit basin (Table 4). The basins have small areas, and it is still at the beginning of their erosive cycle (Abu Al-Enein, 1990; Al-Juboury, 2009).

Table 4: Terrain characteristics of the Um Al-Shibabit basin.

Terrain ratio (m/km)	Roughness value (km/km^2)	terrain average	Hypsometric integration (km^2/m)
1.7	5.75	0.005	2.17

Hydrochemistry of the water of Um Al-Shibabit

The types and concentrations of dissolved salts depend on their interaction with the rocks or soil preparation of the rocks and the speed of the water. Human activities may affect the concentrations of these materials in water, like irrigation and fertilization, and urban uses. The water quality is a primary factor of its usability for various uses, including the uses for which the dams are created. The water quality changes in different locations along the valley streams are also crucial for choosing the appropriate sites for water storage; the results of hydrochemical analyses to determine the concentrations of ions are included in Table 5.

Table 5: Concentrations of the major cations and anions in ppm units.

No.	Name	Ca^{++} ppm	Mg^{++} ppm	Na^{+} ppm	K^{+} ppm	$NO_3^{=}$ ppm	HCO_3^{-} ppm	$SO_4^{=}$ ppm	Cl^{-} ppm
1	Upstream of Um Al-Shibabit	441	221	1884	10.1	54	79	1640	3053
2	Gedhaib Valley	301	105	540	6.7	0	122	1406	710
3	Al Shouk Valley	232	8.82	574	10.1	0	79	781	710
4	Khudaira Valley	232	108	539	5.8	49	116	1028	710
5	Before Ain Al-Baidha	449	67	341	6.1	16	111	1480	355
6	Ain Al-Baidha	369	21	87	5.8	7	117	956	71
7	Jumalia Jadida	441	96	732	7.4	27	104	1661	888
8	Um Al-Shibabit Bridge	440	89	696	7.2	69	68	1640	817

pH is also measured. The Total Dissolved Solids (TDS) and the salts were measured from the total dissolved ions to demonstrate the accuracy of the analysis by their compatibility with TDS. The total hardship of TDS is calculated due to its importance in determining the usability of water for different uses (Najeeb et al., 2021). As the sum of the concentrations of the positive and negative ions concentrations are calculated in (ppm) to calculate the average of errors of the analysis by the ion balance (Mazor, 1990). Its value was lower than 1% in all samples, and the results are included in Table 6. The average error values show the accuracy of the analysis, which is acceptable according to the Mazor formula that assumes the ratio should be less than

5%; this is confirmed by the linear relationship between the CTDS and TDS concentration values with a correlation R^2=0.98 (Fig. 3).

The pH value is almost equivalent in all water samples, as the salinity was high in the upstream of the valley (near Mahha) compared to the other sites. This is due to the presence of rising salty water in the form of seepage from deep water sources in the Fatha Aquifer, which is rich with dissolved salts, as the formation is characterized by the presence of gypsum and halite salt layers or domes among its components (Jassim and Goff, 2006). The salinity starts to decrease towards the stream as a result of contributions of Kudhaib valley, Al-Shouk valley, and Khudhaira valley to Ain Al-Baidha, where the salinity decreased to the lowest limit at this spring and the other close freshwater springs. The salinity starts to increase towards the stream where the main valley meets the valleys of the southern sub-basins. Table 6 exhibits pH, dissolved salts, and intractability of Um Al-Shibabit water, and the chemical analysis error ratio.

Table 6: pH, dissolved salts, and intractability of Um Al-Shibabit water, and chemical analytics error ratio.

No.	Name	pH	TDS	TH	Cation epm	Anion epm	Error
1	Upstream of Um Al-Shibabit	6.69	7399	2006	122.37	122.44	%0.03-
2	Gedhaib Valley	7.27	3264	1183	51.70	51.30	%0.39
3	Al Shouk Valley	7.00	2440	617	37.59	37.60	%0.02-
4	Khudaira Valley	6.72	2864	1025	44.11	44.12	%0.01-
5	Before Ain Al-Baidha	7.02	2984	1398	42.93	42.91	%0.03
6	Ain Al-Baidha	7.20	1616	1009	24.11	23.94	%0.36
7	Jumalia Jadida	7.20	4080	1497	61.95	61.75	%0.16
8	Um Al-Shibabit Bridge	7.30	3940	1469	59.82	59.42	%0.34

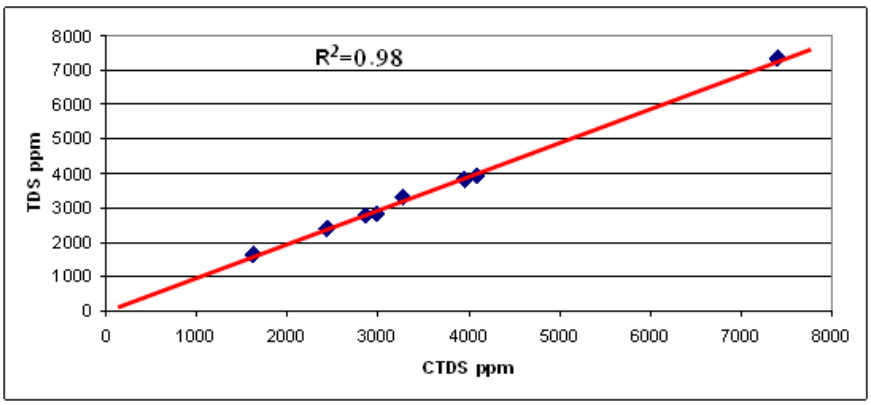


Fig.3. Linear relationship between the concentration values CTDS and TDS in different locations along the valley of Um Al-Shibabit.

The results of the chemical analyses reflect a large variation in the concentration of major ions from one site to another along the valley due to the contribution of the other tributaries to bringing water with different hydrochemical properties that reflect the watershed conditions of each tributary separately (Fig. 4).

For example, a large increase in the concentrations of sodium (positive) and chloride (negative) is observed in the upstream of the valley compared to the rest of the ions in the same site. And as for their concentrations in the rest of the sites, due to the presence of sources of rising salty water in the form of leaching from deep water in the Fatha forming reservoir, as mentioned before (Fig. 5).

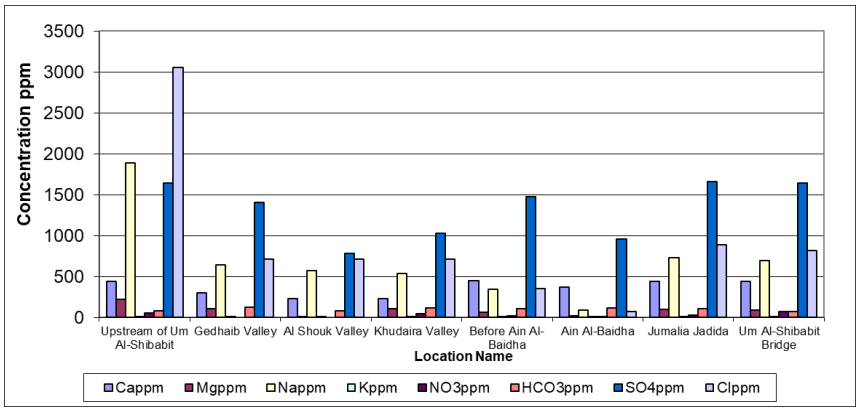


Fig.4. Variation of dissolved ion concentrations along Um Al-Shibabit valley stream.

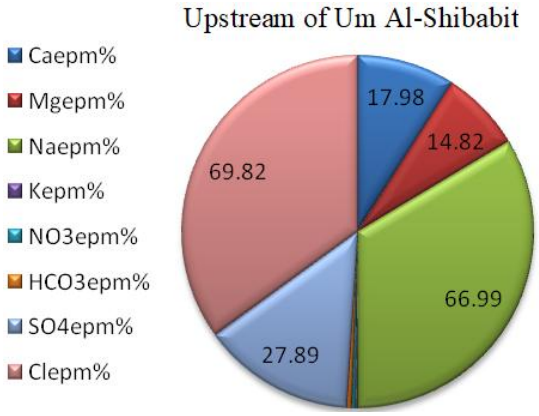


Fig.5. Prevalence of the concentration ratios of magnesium and sodium in the upstream of Um Al-Shibabit, where NaCl is the most available salt.

The prevalence of these two ions continues in the rest of the sites except in Ain Al-Baidha. As for the concentrations of calcium (positive) and sulfates (negative), they come in the second order as a result of the dissolving the gypsum rocks and they are the most common in Ain Al-Baidha where their source of nutrition is far from layers rich in salt (halite) (Fig. 6). Bicarbonate and magnesium concentrations are a little lower in the valley water as a reflect of lack of carbonate rocks within the basin outcrops. Potassium concentration is very low, which is typical for this ion that always coexists subordinately with sodium ions in salty rocks.

The chemical analyses' results are projected onto the triple Piper projection chart to classify the water at different locations and to indicate its hydrochemical potential. This chart shows that Ain Al-Baidha water is within the normal alkaline groundwater, in which sulfur mien is prevalent. In contrast, the rest samples are within alkaline water, in which chloride or chloride-sulfate is prevalent (Fig. 7).

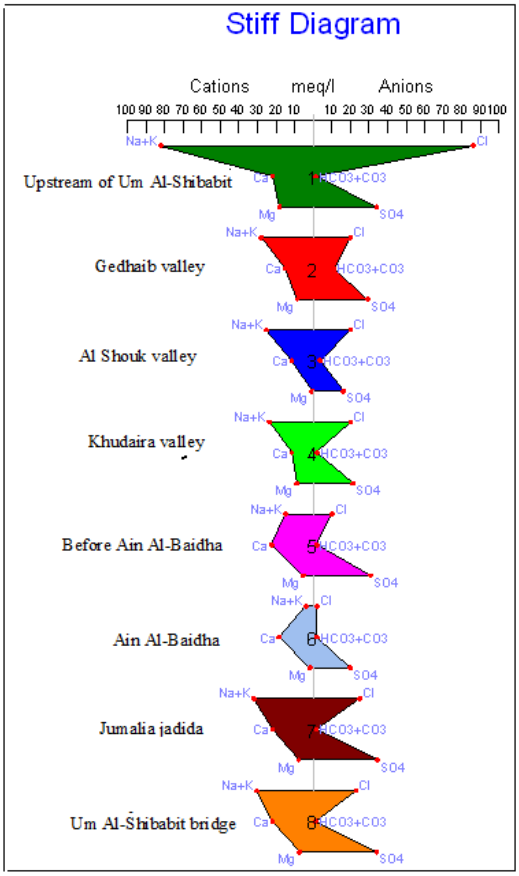


Fig. 6. Distribution of the concentration of the positive and negative ions on the Stiff Chart with meq/1 units, and the prevalence of positive (sodium) and negative (chloride) is illustrated.

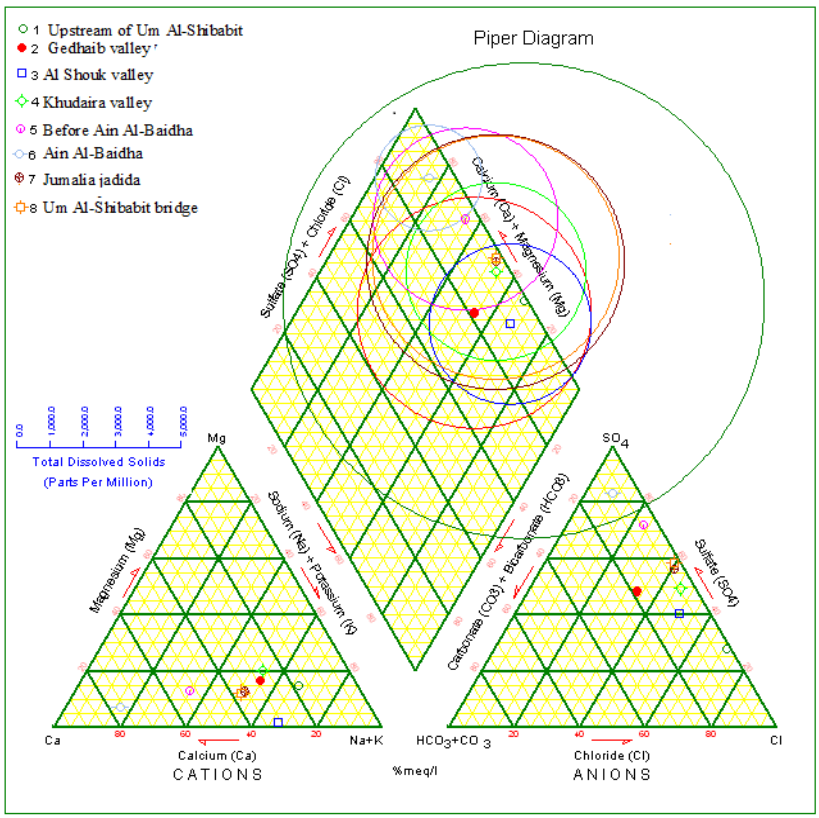


Fig. 7. Chemical ions projection on the triple Piper chart.

The ion concentrations are converted into ppm units as given in Table (6), then to epm units, then at last to epm% as listed in Table (7) to calculate the hypothetical salt combination for each mentioned used method mentioned (Collins, 1976) listed in Table (8). It is shown in this table that the prevalent default salt is NaCl, especially in the heights that reach 66.99% and may reach more than 95% after the water goes through the drying and sedimentation cycle. This makes it a promising area for investment in the salt industry or other industries, such as caustic soda, that require isolation in the case of thinking about storing water in the valley, and this site is unique in the lack of Na_2SO_4 and a low concentration of $MgSO_4$ (3.49%).

Table 7: Major ion concentrations (in epm%) dissolved in the water of Um Al-Shibabit.

No.	Name	Ca^{++} epm%	Mg^{++} epm%	Na^{+} epm%	K^{+} epm%	$NO_3^{=}$ epm%	HCO_3^{-} epm%	$SO_4^{=}$ epm%	Cl^{-} epm%
1	Upstream of Um Al-Shibabit	17.98	14.82	66.99	0.21	0.71	1.06	27.89	69.81
2	Gedhaib Valley	29.01	16.76	53.9	0.33	0	3.9	57.06	39.04
3	Al Shouk Valley	30.86	1.93	66.52	0.68	0	3.46	43.27	53.27
4	Khudaira Valley	26.3	20.22	53.15	0.34	1.79	4.31	48.5	45.4
5	Before Ain Al-Baidha	52.18	12.92	34.55	0.36	0.6	4.24	71.82	23.34
6	Ain Al-Baidha	76.32	7.31	15.75	0.62	0.47	8.02	83.14	8.37
7	Jumalia jadida	35.51	12.8	51.38	0.31	0.7	2.75	56	40.55
8	Um Al-Shibabit bridge	36.78	12.3	50.61	0.31	1.87	1.88	57.48	38.76

Table 8: Default salt combination (in epm%) from UmAl-Shibabit water.

No.	Name	$CaCO_3$	$CaSO_4$	$MgSO_4$	$MgCl_2$	Na_2SO_4	NaCl	KCl	Total
1	Upstream of Um Al-Shibabit	1.07	16.91	11.33	3.49	0	66.99	0.21	100
2	Gedhaib valley	3.90	25.11	16.76	0	15.19	38.71	0.33	100
3	Al Shouk valley	3.46	27.40	1.93	0	13.94	52.58	0.69	100
4	Khudaira valley	4.39	21.91	20.22	0	7.25	45.90	0.33	100
5	Before Ain Al-Baidha	4.27	47.91	12.92	0	11.42	23.13	0.35	100
6	Ain Al-Baidha	8.06	68.26	7.31	0	7.96	7.79	0.62	100
7	Jumalia jadida	2.77	32.74	12.8	0	10.85	40.53	0.31	100
8	Um Al-Shibabit bridge	1.92	34.86	12.3	0	11.42	39.19	0.31	100

Gypsum ($CaSO_4.2H_2O$) is the prevalent salt near Ain Al-Baidha with a ratio of 49.91% before it and 68, 26% beyond it; this indicates that the source of its sustenance is from karst cavities, cracks, and fractures of the gypsum layers in the orifice formation. Its continuous flowing and the short-term stay of its water in its middle host made the concentrations of its total salts low. As for the points confined between the upper valley and Ain Al-Baidha, the ratio of gypsum order is the second after halite, and this is expected in an area with outcrops that are rich in gypsum. As for the points after Ain Al-Baidha towards the downstream, the waters of the valleys of the sub-basin that meet the central valley raise the gypsum ratios to be close to the halite ratios, which is no more than 40% for both salts. As for Na_2SO_4 and $MgSO_4$, their ratios are low and not more than 20% at Ain Al-Baidha, where carbonates are present in a small proportion and interfere with gypsum rocks. As for sulphate salt, it is the least among all salts as its ratio does not reach 1%. This has technical benefits in the case of investing in the upper valley for the salt industry, as it is easy to separate it from halite.

To evaluate the study area waters for drinking purposes, the concentrations of dissolved and salinity ions, the pH, and total hardness listed in Tables 5 and 6 are compared with the Iraqi standards of drinking water (IQS, 2009) and with the international standard specifications of WHO (2024). It is found that this water is not suitable for human consumption, but can be used for animal drinking by comparison with the Altoviski (1962) specifications, whose classification is adopted to decide the suitability of the basin's water for construction purposes. And it is found that it is suitable in all sites for this purpose except at the top of the basin near the Mahha area.

From the comparison of different ions, solidity, and hardness with the standard specifications of the irrigation waters (Ayres and Westcot, 1989) and with the extent to which crops tolerate the concentration of salts (Todd, 1980), it can be said that this water (except at the upper valley) is suitable for irrigation of different field crops such as barley, cotton,

sunflower, corn and wheat, also vegetables such as tomato, cucumber, onion, and palm. It is preferable to use the modern irrigation methods that reduce the effect of salinity.

Analysis of clay and non-clay minerals in the recent sediments of Um Al-Shibabit valley and its branches is carried out for the untreated clay samples using X-ray diffraction (XRD). It is found that the results of the current mineral analysis show the presence of the following minerals: palygorskite, kaolinite, and non-clay minerals (quartz, feldspar, calcite, and dolomite) (Table 9). The clay minerals are distinguished depending on the base reflections and other unique reflections for each mineral, following Mustafa et al. (2022).

Palygorskite is a clay mineral that is formed in certain environments where calcite and dolomite, especially the fibrous type, are formed together (Sudo et al., 1981), as shown in Figure 8.

Kaolinite is distinguished based on the base reflection (7.13) Angstrom to the levels (0.01) and (3.58) (Carroll, 1970; Brindly and Brown, 1980) as shown in figure (8).

Clay minerals represent one of the most important essential mineral components in rocks and clay deposits, and these minerals may be either from clastic rocks origin, locally formed, or from a transformative origin and thus have great importance in knowing the prevailing climatic and environmental conditions at the time of their sedimentary deposits. To know the original rocks from which they were derived, or to know the impact of the transformation process affecting their formation.

The main clay minerals shown in the current studies are kaolinite and palygorskite, while the non-clay minerals include quartz, feldspar, calcite, and dolomite (Table 9, Fig. 8). The presence of palygorskite in the claystone sample is under study, and this indicates the local origin of this mineral. The palygorskite belongs to the group of clay minerals with fibrous textures (inosilicate double chain) and is the hydrated magnesium-aluminum silicate. Many studies have shown that this mineral is more locally formed or (informed) more than any other origin. Thus, it is considered one of the minerals that are useful in confirming the origin of the ancient climate (paleoclimatic indicators) as it is formed in dry and semi-dry soils (Singer, 1980). Special chemical conditions form it, and its presence is associated with carbonate rocks, especially dolomite, due to its prevalence of evaporation origin. Magnesium, with a high concentration and high pH, is also necessary to form this mineral (Banat, 1980).

Table 9: Results of XRD analysis representing clay and non-clay minerals in selected deposits of Um Al-Shibabit Valley.

No.	Name	XRD
1	Upstream of Um Al-Shibabit	Quartz, Calcite, Feldspar, Gypsum, Palygorskite, Kaolinite, Dolomite
2	Gedhaib Valley	Quartz, Calcite, Feldspar, Gypsum, Palygorskite, Kaolinite, Dolomite
3	Khudaira Valley	Quartz, Calcite, Feldspar, Gypsum, Palygorskite, Kaolinite, Dolomite
4	Ain Al-Baidha	Quartz, Calcite, Feldspar, Gypsum, Palygorskite, Kaolinite, Dolomite
5	Um Al-Shibabit Bridge	Quartz, Calcite, Feldspar, Gypsum, Palygorskite, Kaolinite, Dolomite, Halite

The most suitable environment for this mineral to form is underground (subaerial) (Chamley and Muller, 1991), where the appropriate environmental conditions for the presence of palygorskite are available.

As for the rest minerals, they are detrital, and this also matches with the percentage of the potassium-feldspar, which is commonly found in sandy sediments of the rocks of the upper crater unit to form the orifice, which is considered one of the most important structures exposed in the region, providing clastic deposits in the valleys (Al-Juboury, et al., 2001). As for kaolinite, it is formed from the crushing of igneous rock fragments rich in potassium feldspar. Grim (1968) showed that the kaolinite could be formed in flood environments (fluviatile) or near shore, and is formed due to the excavation of other minerals, as shown by Parham (1966), that the presence of kaolinite indicates its presence in evaporation environments. From what aforementioned previously mentioned, we note that there is a significant relationship between

the identified clay minerals and the other carbonate minerals associated with them, such as calcite and dolomite. As for quartz and feldspar minerals, they are usually formed from the excavation of sandstone in sediments of the formations exposed in the area.

The presence of the evaporite minerals such as gypsum and halite is also associated with either the crushed rocks that contain these minerals in situ and from a nearby source, or it represents one of the minerals that was formed from evaporation due to high temperature and scarcity of rain, especially since the valley flows from a low evaporative.

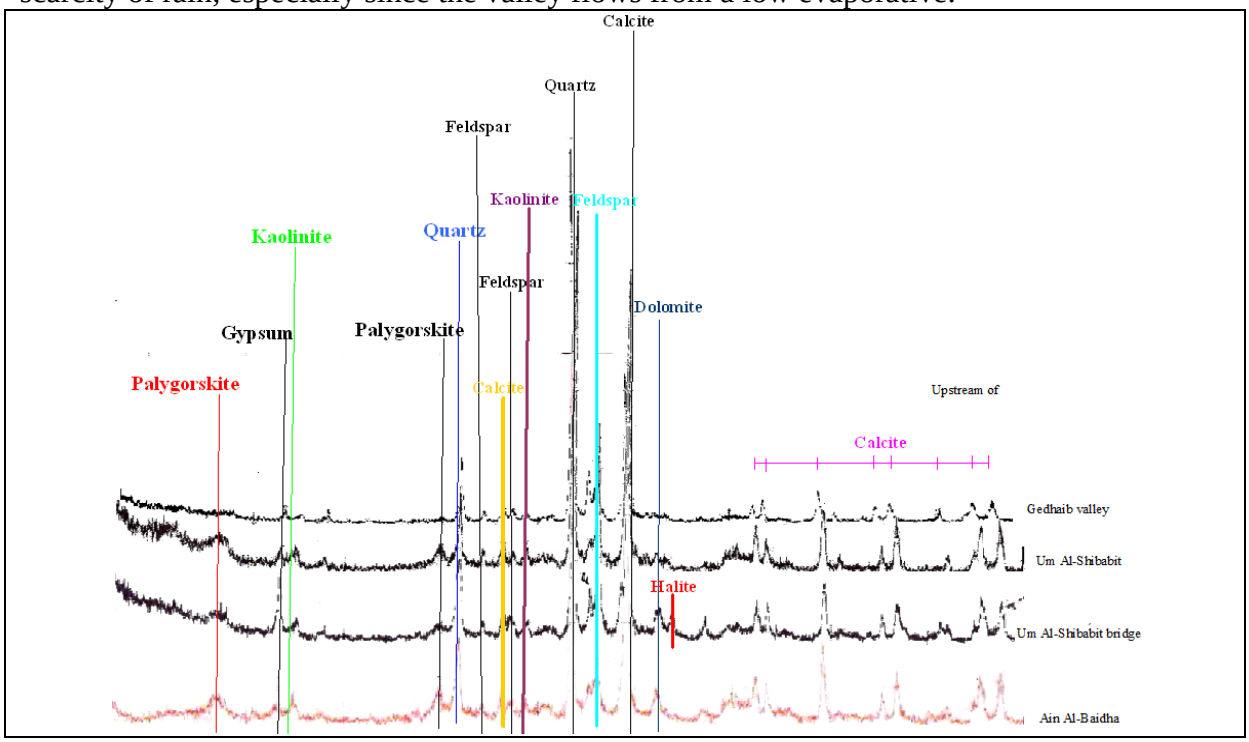


Fig. 8. Diffractograms of clay-separated components in a recent sediment sample of secondary valleys supplying Um Al-Shibabit.

The results of the geochemical analysis of the valley sediments were in agreement with the results of the mineral analysis. As the insoluble components formed the main component of the sediments, including quartz, clay minerals, and feldspar, it is noted that there is a significant ratio of silicon dioxide, a lack of salts washed into the valley's water, and a lack of organic materials (Fig. 9).

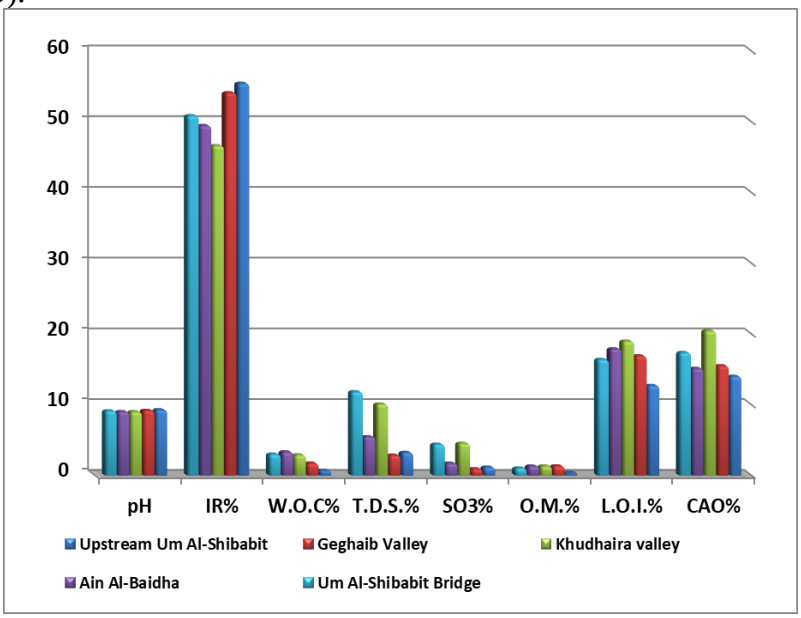


Fig. 9. Contrast of the geochemical characteristics of the sediments of Um Al-Shibabit valley.

Selection of the suggested dam site

The selection of a site for constructing a dam is not easy. It must be taken into consideration all the geomorphological, morphometric, and hydrological variables, the land ownership, land uses, groundwater conditions, and engineering conditions properties of the rocks, and the availability of dam construction materials in the presence of a topographic depression suitable for storage. These conditions may be less in the case of establishing small dams on seasonal valleys under study.

The morphometric analysis produces several data points, including the large number of orders in the basin compared to its area, as it was classified as seventh, and there were two northern and southern sub-basins, and the valley that formed them met 6 km away from the Tigris estuary.

Its shape represents a mid-shape between rectangular and circular. Its drainage characteristics show a rapid arrival of flood waves downstream in severe rainstorms. This encourages the idea of constructing the dam immediately after the meeting point to ensure the benefits of both of the sub-watersheds and also not getting closer to the Tigris River to guarantee the optimal benefit of the water storage.

The hydrochemical properties of the valley waters are studied. And the increase of the salt in the water is shown in the upper valley near Mahha. As for the middle of the basin, the salinity decreased gradually to reach the least amount in Ain Al Baidha. Then it starts to increase again until reaching the river estuary, so it is preferable to separate or isolate the salty part of the basin in the upper valley for the salt industry purposes or other industrial investments, and to avoid harming the stored waters.

The digital elevation model is used to derive the topographic section of the valley at the convergence point of the two sub-basins, which represents a topographic gorge that secures the water storage in the lower part of the basin at a depth of 5 m. The cross-sectional width reaches less than 600 m, where the cross-section is an important factor in the design and cost of dams, as for the financial and constructional material needed for this purpose (Fig. 10).

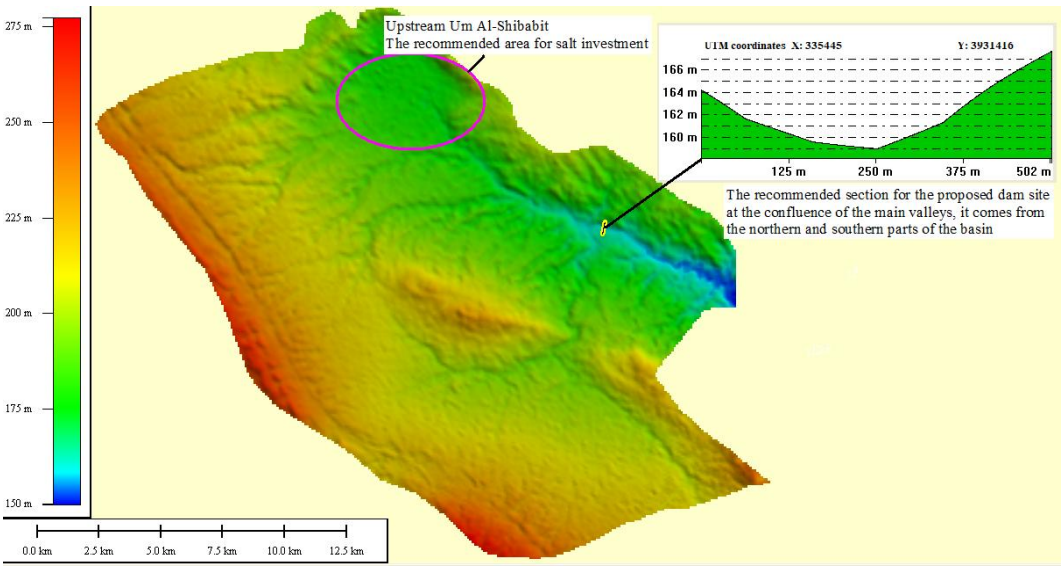


Fig. 10. Topographic section and suggested site for water storage and the nominated area for isolation in the upper area of Um Al-Shibabit

Conclusions

The areal, shape, topographic, and drainage characteristics indicated that the rapid arrival of flood peaks to the suggested dam site should be taken into consideration for the dam design. The analysis shows that the existence of two sub-basins, north and south, within the central

basin is determinant in selecting the location of the proposed dam. The hydrochemical and default salt studies show an increasing concentration of salts, especially table salt, in the upper basin, which should be separated to secure the type of water in the basin. The hydrochemical properties reflect the validity of the valley waters for agricultural and constructional purposes, as well as for human consumption, except for the upper basin. Based on the above-mentioned, the study recommends stopping the random construction and housing towards the sides of valleys and establishing factories for the production of table salt and caustic soda in sites that are rich in sodium chloride.

References

Abu Al-Enein, H.S.A., 1990. Wadi Dibba in the United Arab Emirates, natural geography and its impact on agricultural development, Kuwait University.

Al- Al-Babawati, A.A.H., 1995. Wadi Al-Ajej in Iraq and the uses of its landforms, Ph.D. Thesis, Department of Geography, College of Arts, University of Baghdad, (Unpublished).

Al- Juboury, M.Y.H., 2009. Morphology of Wadi Al-Shour Basin, a comparison of the use of multiple data sources and their technologies, PhD thesis (unpublished), Mosul University, 110 P.

Al-Juboury A.I., Al-Naqib, S.Q. and Al-Juboury, A.M., 2001. Sedimentology and mineralogy of the Upper clastic units of Fath'a Formation. South of Mosul, Iraq. Dirasat (Pure Sciences) Jordan, 28(1), pp. 80-106.

Al-Khuzamy, M.A., 2004. Geographical information systems, foundations and applications for geographers, Knowledge Facility, Alexandria, 3rd Ed.

Al-Muhsin, E.Y. and Al-Azzawi, A.A.A., 2002. The Impact of Morphometric Characteristics in Determining the Basin Area/ Khazer Basin, Journal of Education and Science, College of Education, University of Mosul, 9(2), pp. 139-153.

Altoviski, M., 1962. Handbook of Hydrogeology, Geolitzet Moscow USSR, 614 P.

Ayres, R.S. and Westcot, D.W., 1989. Water quality for Agriculture, Irrigation and Drainage (Paper No. 29), Rev.1, FAO, Rome, Italy, 174 P.

Badawy MS., Saleh SA., Abbood MR., 2023. Suggested Scenarios of Initial Filling for the Badush Reservoir, Iraq. Tikrit Journal of Engineering Sciences 30(4), pp. 134-144. http://doi.org/10.25130/tjes.30.4.14.

Badowi M.S., Saleh S.A., Abbood M.R., 2024. Dam Breakdown and Response of Protection Dam, Case Scenarios of Mosul-Badush Dams, Northern Iraq. Tikrit Journal of Engineering Sciences; 31(1), pp. 75-87. http://doi.org/10.25130/tjes.31.1.7.

Banat, K.M., 1980. Fundamentals of Clay Minerals, University of Baghdad, Baghdad, Iraq 138 P.

Brindly, G.W. and Brown, G., 1980. Crystal structures of clay minerals and X-ray identification. Miner. Soc. Monograph. No. 5. London, 495 P.

Carroll, D., 1970. Clay Minerals: A guide to their X-ray identification. Geol. Soc. Amer., Special (Paper. 126), 80 P.

Chamley, H. and Muller, D.W., 1991. Clay Mineralogy in Southeast Spain during the Late Miocene: Climatic, Paleooceanographic and tectonic events in the Eastern Betic Seaway. Geologie en Mijnbouw, 70, pp. 1-19.

Collins, A.G., 1976. Geochemistry of Oil- Field water. Development in Petroleum Science, Elesevier, Amsterdam, Holland, 1, 496 P.

Grim, R.E., 1968. Clay Mineralogy. McGraw-Hill, New York, 596 P.

Hussein A.J., Salih S.A., 2023. Unmanned Aerial Vehicle Derived DEM Using in Accurate Geometric Analysis for Water Harvesting in Small-Scale Depressions, Iraqi Geological Journal, 56(2E), pp. 82-94. http://doi.org/10.46717/igj.56.2E.6ms-2023-11-11.

Hussein A.J., Salih S.A., 2024. Quantifying the Reliability of Volumetric and Areal Calculation with UAV-Generated DEMs: A Comparative Study with Ground Truth Data. Tikrit Journal of Engineering Sciences, 31(1), pp. 43-55. http://doi.org/10.25130/tjes.31.1.5.

IQS, I.S., 2009. Iraqi Standard of Drinking Water No. 417, Second modification.

Jassim, S.Z. and Goff, C.J., 2006. Geology of Iraq, Dolin, Prague, and Moravian. Museum, Brno, 341 P.

Mahsoub, M.S., 1980. Geomorphology of landforms, Dar al-Fikr al-Arabi, Cairo.

Mazor, M., 1990. Applied chemical and isotopic groundwater hydrology, New York, 274 P.

Mohammad, J.K., Saleh, S.A. and Amin, D.A. (2024). Determining the surface drainage network causing flash floods in Central Erbil Sub-Basins in Northern Iraq using GIS and geospatial technique. The Iraqi Geological Journal, 57(1F), pp. 191-208. https://doi.org/10.46717/igj.57.1F.15ms-2024-6-24.

Mustafa, A.F., Al-Karai, N.A.K. and Saleh, S.A. 2024. Comparative Assessment of Suggested Dam Sites Using Both Analytic Hierarchy Process and Weighted Sum Method for Rainwater Harvesting in Al-Naft Valley, Eastern Diyala, Iraq. The Iraqi Geological Journal, 57(2E), pp. 78-98. https://doi.org/10.46717/igj.57.2E.7ms-2024-11-16.

Mustafa, A.I., Mansurbeg, H. and Mohialdeen, I.M. 2022. Petrography and Clay Mineral Variations Across the Cretaceous/Paleogene (K/Pg) Boundary, Sulaimani, Kurdistan Region, Iraq. The Iraqi Geological Journal, pp. 16-34. http://doi.org/10.46717/igj.55.2e.2ms-2022-11-16.

Mustafa, A.A., 1998. Contour maps, their interpretation and sectors, University Knowledge House, Alexandria University, 2nd Ed.

Najeeb, F.R., Saleh, S.A. and Abed, M.F., 2021. Hydrogeology of Al-Hamdaniya, Northern Iraq. The Iraqi Geological Journal, 54(2B), pp. 112-121. https://doi.org/10.46717/igj.54.2B.10Ms-2021-08-30.

Parham, W.E., 1966. Lateral variations in clay mineral assemblages in recent and ancient sediments. In: Proc. Inter. Clay. Conf., 1. pp. 136-145.

Salih, S., Ulaiwi, J., Al-Tarif, A. and Al-Juboury, A., 2012. Morphometric, Hydrogeologic and Hydrochemical Analyses of Solar Saltwork Pond Region, in Meha Area, Northwest Sharqat City, Iraq. Journal of Geographic Information Systems, 4, pp. 86-95. http://doi.org/10.4236/jgis.2012.42012.

Schumn, S.A., 1956. The evaluation of drainage system and slopes in badlands at Pert Amboy, New Jersey, Bull, Geol-Amer. 67, pp. 579-648.

Singer, A., 1980. The paleoclimatic interpretation of clay minerals in soils and weathering profiles. Earth Science Reviews, 15, pp. 303-326.

Strahler, A.N., 1954. Quantitative analysis of water shed, geomorphology traps, American Geophysical Union, 38, pp. 912-920.

Strahler, A.N., 1962. Geomorphology, Translated to Arabic by Al-Kashab, W., and Al-Dabbagh, A., Dar Al-Zaman Press, Baghdad, 425 P.

Sudo T., Shimoda S., Yotsumoto H. and Aita A., 1981. Electron micrographs of clay minerals, Elsevier Scientific Publishing Company Amsterdam-Oxford-New York, Kodansha Ltd, ISBN 0-44-99751-2, 31, 203.

Todd, D.K., 1980. Groundwater Hydrogeology, 2nd edition, John Wiley and Sons. Inc Toppan printing Co. (Ltd), New York, 535 P.

Verstaphen, H.T., 1983. Applied geomorphology, geomorphological survey for environmental, chapter 4, Elsevier, New York, pp. 57-83.

WHO, World Health Organization, 2024. Guideline for drinking water quality Recommendation Vol. (1), 5th Ed, https://www.who.int/publications/i/item/9789240088740.

Iraqi National Journal of Earth Science

www.earth.uomosul.edu.iq

Sedimentology of Avanah Formation (Middle-Upper Eocene) from Selected Sections within Iraqi Kurdistan Region

Amanj Ibrahim Fattah [1*], Hazhar Hasan Ahmad Perot [2]

[1]*Department of Earth Sciences and Petroleum, College of Science, University of Sulaimani, Sulaimani, Iraq.*

[2] *Directory of Oil and Mineral of Sulaimani, Kurdistan Region-Iraq.*

Article information

Received: 14- Oct -2023

Revised: 11- Nov -2024

Accepted: 11- Dec -2024

Available online: 01- Jan – 2026

Keywords:
Avanah Formation,
Benthic Foraminifera,
Microfacies Analysis,
Inner Ramp,
Shallow Open Marine,

Correspondence:

Name: Amanj Ibrahim Fattah

Email:

amanj.fattah@univsul.edu.iq

ABSTRACT

Sedimentary features, petrography, and microfacies analysis of the Avanah Formation are investigated in the current study. Two exposed outcrops (Sartak-Bamo and Belula) for the Avanah Formation are studied in detail, located in the Zagros High Folded Zone (ZHFZ), and two subsurface sections (K90 and K306) within the Zagros Low Folded Zone (ZLFZ). The Avanah Formation is composed of multi-lithological sequences (limestone, dolomitic limestone, dolostone, and marly limestone). It has been subdivided into five units based on its composition. The Khurmala Formation underlies the Avanah Formation at all the studied sections unconformably. The Pila Spi Formation at the Sartak-Bamo section conformably overlies the Avanah Formation, but the Jaddala Formation conformably overlies the Avanah Formation at the Belula section. The Fatha Formation unconformably overlies the Avanah Formation at both subsurface sections. A variety of large benthic foraminifera species have been identified, such as Nummulite spp.; Orbitolite complanatus (Lamarck); Alveolina spp.; Discocyclina spp. and Assilina spp. In addition, some other small benthic foraminifera, such as Miliolids, Rotalids, a few Mollusca, and Algae with their bioclasts, are identified in the studied sections. Based on detailed microfacies analysis, four main microfacies (Mudstone, Wackestone, Packstone, and Packstone-Grainstone) and eleven submicrofacies are determined. Three facies' associations are identified, which lead to interpreting that the Avanah Formation was deposited in a semi-lagoon, shoal (bank) to shallow open marine environment of the inner ramp and extending to the middle ramp setting.

DOI: 10.33899/injes.v26i1.60181, ©Authors, 2026, College of Science, University of Mosul.
This is an open-access article under the CC BY 4.0 license (http://creativecommons.org/licenses/by/4.0/).

دراسة رسوبية لتكوين أفانا (الايوسين الاوسط- الاعلى) في مقاطع مختارة من اقليم كردستان العراق

أمانج ابراهيم فتاح [1]* ، هەژار حسن أحمد پیرۆت[2]

[1] *قسم علوم الأرض، كلية العلوم، جامعة السليمانية، السليمانية، العراق.*

[2] *مديرية النفط والمعادن في محافظة السليمانية، السليمانية، العراق.*

معلومات الارشفة

تاريخ الاستلام: 14- اكتوبر -2023

تاريخ المراجعة: 11- نوفمبر -2024

تاريخ القبول: 11- ديسمبر -2024

تاريخ النشر الالكتروني: 01- يناير -2026

الكلمات المفتاحية:

تكوين آفانا،

المتحجرات القاعية،

تحليل السحنات المجهرية،

المنحدر الداخلي،

بيئة بحرية ضحلة مفتوحة،

المراسلة:

الاسم: ئامانج إبراهيم فتاح

Email: amanj.fattah@univsul.edu.iq

الملخص

تمت دراسة الخصائص الرسوبية، البتروغرافية، والسحنات الدقيقة لتكوين أفانا المنكشف في مقطعي (سارتك بمو وبيلولة) ضمن نطاق زاكروس للطيات العالية (ZHFZ) وكذلك بئري (K90-K306) ضمن نطاق زاكروس للطيات الواطئة (ZLFZ). إعتمادا على المكونات الصخرية، قُسم التكوين الى خمس وحدات، فالتكوين مؤلف بشكل رئيس من تتابعات صخرية تشمل صخور الحجر الجيري، الحجر الجيري المتدلمت، الحجر الدولوميتي والحجر الجيري الصلصالي. أظهرت الدراسة أن هناك سطح عدم توافق يفصل تكوين أفانا عن تكوين خورمالة الواقع اسفله ضمن المقاطع المدروسة، بينما سطحه العلوي مع تكوين بيلاسبي وجداله يعتبر سطحاً متوافقاً ضمن مقطعي (سارتك بمو و بيلولة)، بينما في مقاطع البئرين (K90-K306) فهو سطح عدم توافق مع تكوين فتحة. حددت الدراسة أنواعاً مختلفة من المنخربات القاعية الكبيرة الحجم، والتي تمثلت بالأنواع منها: Nummulite spp.; Orbitolite complanatus (Lamarck); Alveolina spp.; Discocyclina spp. and Assilina spp. بالاضافة الى ذلك تم تشخيص أنواع أخرى من متحجرات الفورامنيفيرا صغيرة الحجم مثل: المليوليد، والروتاليد وقليل من الرخويات والطحالب مع بقايا أحيائية. بناءً على تحليل السحنات الدقيقة، تم تحديد أربع سحنات دقيقة رئيسة (Mudstone، وWackestone، وPackstone، وPackstone-Grainstone) وإحدى عشر سحنًة ثانويًة. فسرت بيئة الترسيب لتكوين افانا بناءً على تجمعات السحنية facies associations))، ترسب تكوين أفانا في بيئة لاغونية شبه محصورة Semi restricted lagoon)، ومياه ضحلة (Shoal) إلى بيئة بحرية ضحلة مفتوحة للمنحدر الداخلي (shallow open marine environment of the inner ramp) وتمتد إلى بيئة المنحدر الأوسط (Middle Ramp).

DOI: 10.33899/injes.v26i1.60181, ©Authors, 2026, College of Science, University of Mosul.
This is an open-access article under the CC BY 4.0 license (http://creativecommons.org/licenses/by/4.0/).

Introduction

According to Sharland *et al.* (2004), the Avanah Formation belongs to the upper part of the AP10 tectonic mega-sequence of the Arabian plate (Early Paleocene-Late Eocene). McGinty (1953), in Bellen *et al.* (1959), first described the Avanah Formation (from Kirkuk well 116, Avanah dome). Lithologically, the Avanah Formation is composed of limestone beds, which are generally dolomitized, recrystallized, and intercalated with some beds of dolomitized limestone. This Formation is distributed along a relatively narrow belt (30-40 km) wide with different thicknesses, and lithologically it is rather uniform and can be correlated with the Dammam Formation in facies and age (Buday, 1980). Generally, the Avanah Formation represents a fore-slope marine platform facies (Al-Hashimi and Amer, 1985).

Several large benthic foraminifera have been reported from the Avanah Formation, such as Alveolina sp., Nummulites sp., Discocyclina sp., Operculina sp., *Orbitolites complanatus*

(Lamarck), *Lockhartia Alveolata* (Silvestri), *Assilina exponens* (SOWERBY) (Bellen et al., 1959; Al-Hashimi and Amer, 1985; Abawi and Sharbazheri, 1987; Ameen Lawa and Ghafur, 2015 and Pirot, 2017). The typical shoal realm's fossils are the most abundant ones (Buday, 1980). According to Karim (1997), the Avanah Formation interfingers with the Pila Spi Formation in the Sartak-Bamo area. Different microfacies and shallow depositional environments (nummulitic bank and shoal) were suggested for the Avanah Formation (Al-Temimi, 2002; Al-Mutwali and Al-Banna, 2005, and Barzani, 2016). While semi-restricted, shoal to open marine platform and ramp settings have been proposed for the Avanah depositional environment (Sharbazheri, 1983; Abdullah *et al.*, 2020; and Asaad, 2022). The Avanah Formation contains numerous species of larger benthic foraminifera that flourished and developed in the photic zone of tropical to subtropical seas. Large benthic foraminifera provide significant indications for the reconstruction of sedimentary paleoenvironments (Rahmani *et al.*, 2009; Amirshahkarami *et al.*, 2010). Nummulitic facies of the Avanah Formation form the middle to upper Eocene shelf margin, passing basinward into marls of the Jaddala Formation (Bellen *et al*., 1959; Aqrawi *et al.*, 2010).

To achieve the aims of this study, two outcrops, Sartak-Bamo and Darband Belula, and two subsurface sections (Kirkuk wells K-90 and K-306) are selected (Fig. 1). The subsurface sections are drilled at depths ranging from 846 to 973 m and 807 to 993 m, respectively (Table 1). Tectonically, the Sartak-Bamo and Darband Belula sections are located close to the boundary between the Zagros High Folded Zone (ZHFZ) and the Zagros Low Folded Zone (ZLFZ). According to Aqrawi *et al.* (2010), the boundary is sharp, and it is probably controlled by a basement lineament.

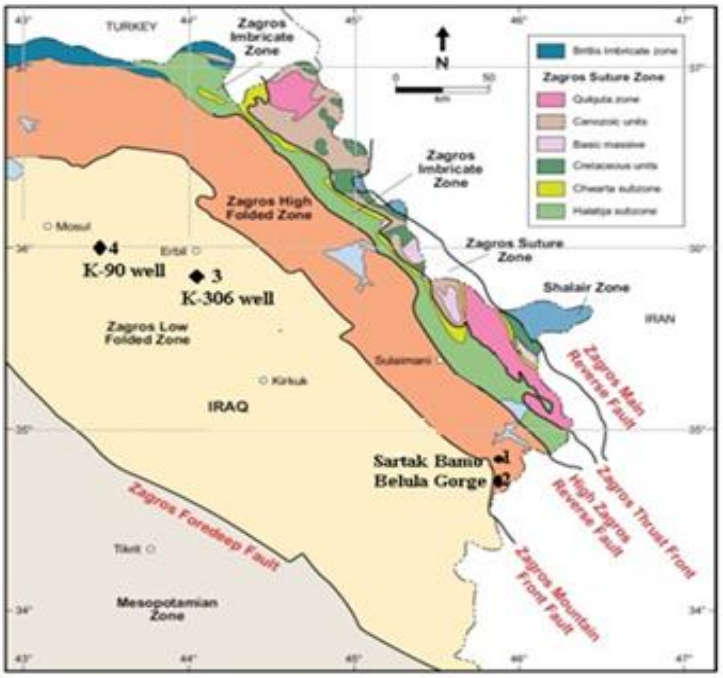


Fig. 1. Tectonic map of northern Iraq showing the locations of the studied sections (After Al-Qayim, *etal.*, 2012).

The beds at Sartak-Bamo are vertical but sometimes inclined, especially near the top of the Avanah to Pila Spi formations. Due to extensive tectonic activity, different sets of normal and reverse faults have been observed within the rock units of the Belula section. While the two subsurface sections (K-90, K-306 wells) are tectonically located within the Zagros Low Folded Zone (ZLFZ) (Fig. 1), the main objectives of the current study are to identify the sedimentological characteristics, stratigraphy, petrographic analysis, and microfacies assemblages, and to interpret the depositional environments of the Avanah Formation from the selected sections.

Table 1: Geographic coordination, names, thicknesses, and locations of the studied sections.

Sections	Types	Latitude	Longitude	Thickness	Locations
Sartak-Bamo	Outcrop	34°56'53.08" N	45°43'40.93" E	64 m	35 km southeast of Darbandikhan town, (The SW limb of the Bamo Mountain).
Belula Gorge	Outcrop	34°51'58.52" N	45°43'50.54" E	75 m	48 km southeast of Darbandikhan town, (The SW limb of the Kawella mountain).
Well K-90	Subsurface	35°47'28.99"N	43°59'06.34" E	127 m	Avanah Dome/Kirkuk structure.
Well K-306	Subsurface	35°59'01.65" N	43°42'44.68" E	186 m	Avanah Dome /Kirkuk structure

Methodology

Executing detailed field investigation within Sulaimani Governorate, northeastern Iraq, looking for well-exposed outcrops of the Avanah Formation. This work is based on field observation and data collection for determining the textural and compositional characteristics of the carbonate rocks, facies association, thickness of the beds, and nature of lithological contacts with the overlying and underlying formations. Documenting the microfacies types, their constituents, the faunal abundance, and their diversity has all been taken into consideration (especially benthic foraminifera).

Accordingly, 102 slices of thin sections from Sartak-Bamo and Belula Gorge were prepared at Sulaimani University/Department of Geology, and 286 previously prepared slices of thin sections by the North Oil Company for wells K-90 and K-306 have been studied and investigated under a binocular polarized microscope. Textural descriptions and microfacies interpretation follow (Dunham, 1962) and (Flügel, 2010).

Results

Stratigraphy of Avanah Formation

Geologically, north and northeastern Iraq represent a part of the extensive Alpine Mountain belt of the east, which developed through the collision of the Afro-Arabian and the Eurasian continents (Sharland *et al.*, 2004). Jassim and Goff (2006) divided the Middle Paleocene-Eocene Megasequence (AP10) into two sequences: The Paleocene-Early Eocene and the Middle-Late Eocene sequences. Dammam platform, Ratga fore slope, Jaddala deep basin, Avanah nummulitic shoal, Pila Spi lagoonal, and fluvial and fluviomarine (Gercus) formations along the final phase of the subduction and closing of the remnant part of the Neo-Tethys Ocean (Al-Hashimi and Amer, 1985; Jassim and Goff, 2006). The Avanah Formation, which belongs to the Middle-Late Eocene sequence, is laterally changing to the Gercus Formation in the north and northeast of Iraq (Al-Hashimi and Amer, 1985; Jassim and Goff, 2006; and Aqrawi *et al.*, 2010). Karim (1997) mentioned that the Pila-Spi and Avanah formations show homogeneous and continuous lateral extension. Ameen and Mardan (2019) reported that the Gercus Formation laterally changed to the Avanah and Sagrma formations in the south and southwest direction of the Darbandikhan area. This formation is occasionally inter-fingered with the lower part of the Pila Spi Formation in the Duhok area (Barzani, 2016). Due to the effects of depositional environments and diagenesis processes, the Avanah Formation in the studied sections is composed of different lithologies, such as limestone, dolomitic limestone, dolostone, and marly limestone.

The lower contact of the Avanah Formation, as observed across all studied sections, is marked by an unconformable surface overlying the Khurmala Formation. This boundary is characterized by abrupt changes from dark grey, highly porous, fossiliferous limestone of the Khurmala Formation, rich with organic matter, gastropod, and pelecypod shells (Fig. 2), to creamy-colored well-bedded, fine crystalline fossiliferous limestones of the Avanah Formation (Pirot, 2017) (Fig. 3). The upper part of the limestone bed of the Avanah Formation at the Sartak-Bamo section changed gradually from light gray, well-bedded fossiliferous limestone and dolomitic limestone to massive dolostone of the Pila Spi Formation (Figs. 3 and 5). In the Belula Gorge section, the contact between the Jaddala Formation and the Avanah Formation is

clearly visible (Fig. 4). The upper part of the Avanah Formation changed gradually from creamy-colored, porous, fossiliferous limestone to the overlying dark grey marly limestone, rich with planktonic foraminifera of the Jaddala Formation (Figs. 4 and 6).

While at the subsurface sections (K90 and K306 Wells), according to the internal reports of the Kirkuk North Oil Company and within the current study, the upper contact of the Avanah Formation with the Lower Fars (Fatha) Formation is unconformable, surface, and marked by a conglomerate bed that is known as the basal Fars conglomerate (BFC).

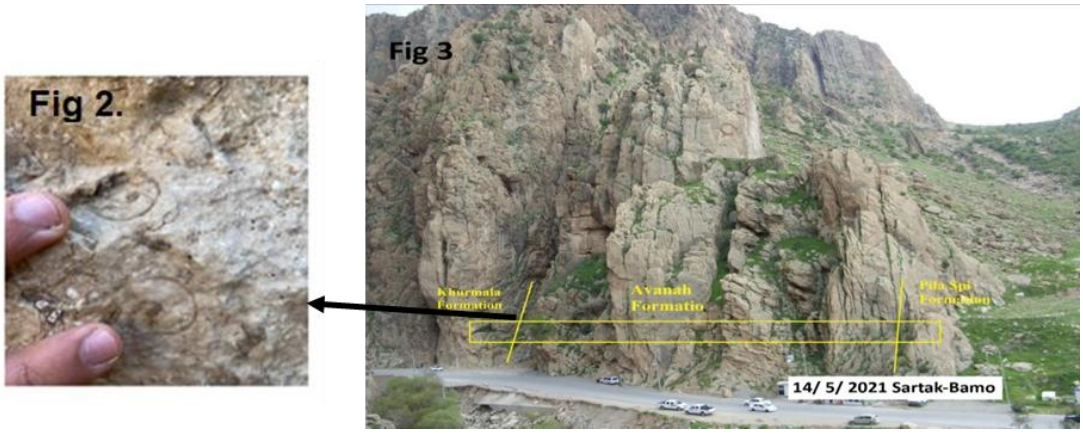


Fig. 2. (left) Dark grey, highly porous, fossiliferous limestone of Khurmala Formation, rich in organic matter, Gastropod and Pelecypod shells.

Fig. 3. (right) Field Photo showing underlying Khurmala and overlying Pila Spi formations of Avanah Formation at the Sartak-Bamo Section.

Based on field observation and petrologic study, the Avanah Formation exhibits significant lithological variability across different sections. Three distinct lithological units (A, B, and E) are recognized in the Sartak-Bamo section (Fig. 5), whereas four lithological units in the Belula section (A, B, D, and E) (Fig. 6) are identified. At the (K-90 and K-306 Wells), four lithological units (A, B, C, and E) (Figs. 7 and 8) are identified. These sedimentary units are characterized by various fossil content (large and small benthic foraminifera and other fossils).

However, according to internal reports of Kirkuk North Company (KNOC), the Avanah Formation is divided into two units based on porosity properties (the lower and upper units).

Leached zone, heavily recrystallized, partially dolomitized, fractured beds, vuggy, porous, and fossiliferous limestone, occasionally saturated with oil, are the main characteristics of the whole lithology of the Avanah Formation (at these subsurface sections).

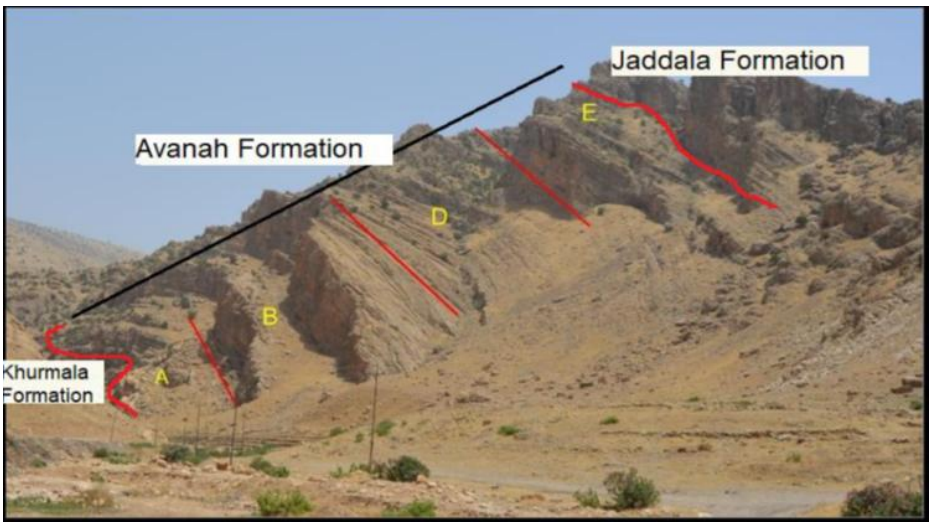


Fig. 4. Field Photo for Avanah Formation from Belula section showing the underlying and overlying formations with the four identified lithostratigraphic units.

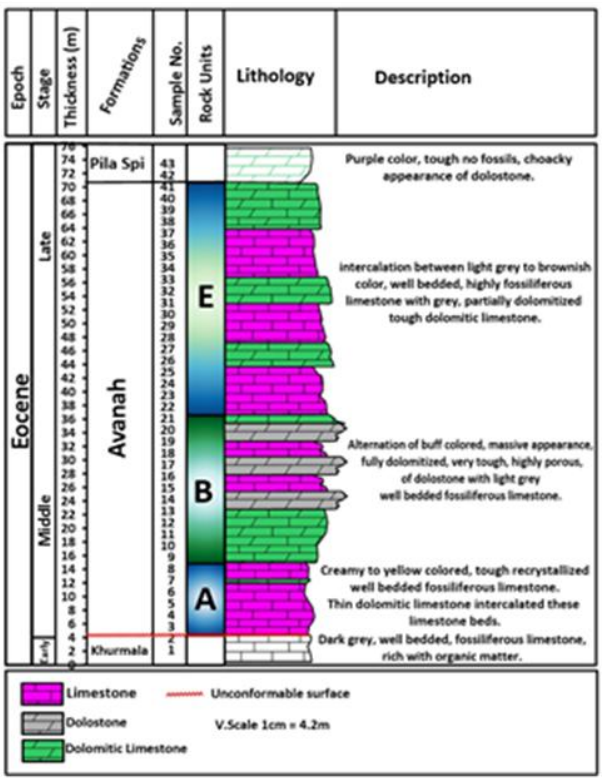


Fig. 5. Stratigraphic column of Avanah Formation at the Sartak- Bamo section

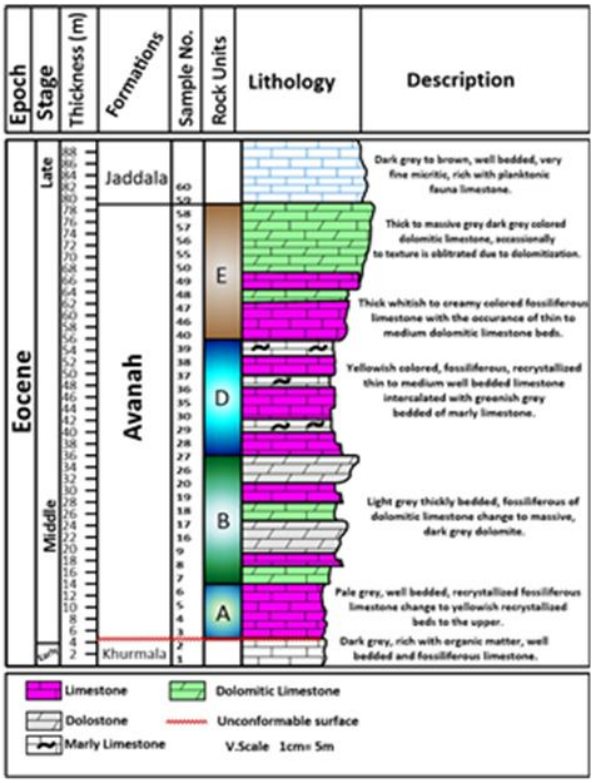


Fig. 6. Stratigraphic column of Avanah Formation at the Belula section.

Lithological units of the studied sections

Unit (A): This unit unconformably overlays the dark grey limestone beds of the Khurmala Formation. It is composed of creamy to yellowish grey, fossiliferous, well-bedded limestone, dark grey, and highly porous dolomitic limestone beds (especially at the Sartak-Bamo section) intercalated with the limestone beds. Nummulite, Alveolina, and Orbitolites are the most identified larger benthic foraminifera (LBF) of unit A. Detecting the Orbitolites complanatus at the lower part of this unit can be suggested as a valuable indicator for identifying the presence of the Avanah Formation and determining its age. Dolomitization, recrystallization, and dissolution affected different parts of unit (A).

Unit (B): This unit is characterized by the alternation of light grey, highly porous, dolomitized fossiliferous limestone of (40-70 cm) thick, with buff-colored, massive dolostone of (1-3 m) thick. Some thin to thick yellowish-colored recrystallized fossiliferous limestone beds, especially from the subsurface sections (K-90 and K-306), are identified at the lower and middle parts. The fossil assemblages of this unit are the same as in unit (A), but the Orbitolite species no longer exist.

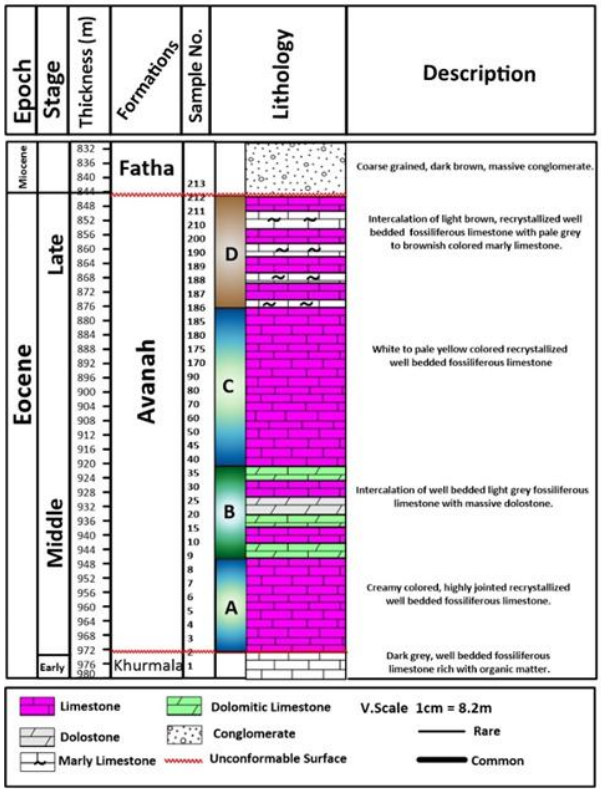


Fig. 7. Stratigraphic column of Avanah Formation at Well (K 90).

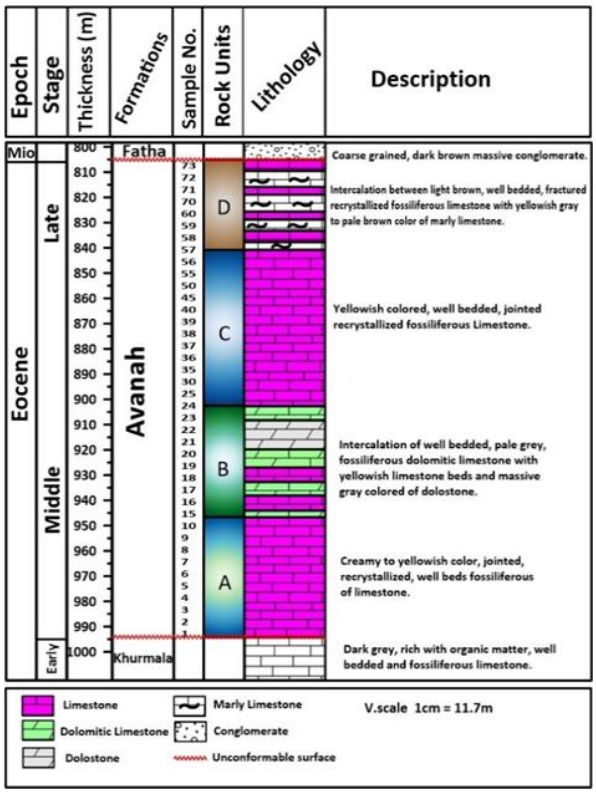


Fig. 8. Stratigraphic column of Avanah Formation at Well (K 306).

Unit (C): This unit is observed in (K-90 and K-306 Wells) with depths of (920- 876) m and (903- 842) m, respectively. It is characterized by yellow-to-brown colored well-bedded recrystallized fossiliferous limestone. Various types of porosities are detected in the lower part of this unit. Whereas the middle and the upper parts are affected by recrystallization and dissolution. Nummulites, Discocyclina, and Assilina species are the identified faunal assemblages of this unit.

Unit (D): This unit is observed at the middle part of the Belula Gorge and the upper parts of the K-90 and K-306 sections. It is characterized by yellowish to light brown, thin to medium well-bedded recrystallized fossiliferous limestone, alternated with greenish grey thin to thick marly limestone beds. Lenticular and flattened shapes, Discocyclina and Assilina species are the common recorded fossil assemblages, while Nummulite species and their bioclasts are less prevalent. The morphology test of these fossils strongly reflects the physical condition of a relatively shallow water and high-energy regime.

Unit (E): Alternation of light grey to creamy colored, medium to thick, well-bedded, fossiliferous limestone, with dark grey colored, thick to massive dolomitic limestone is the main characteristic of this unit. Nummulites, Assilina, and Discocyclina are the most identified fossil assemblages within this rock unit, in addition to small benthic foraminifera. While the Alveolina species are not observed in this unit. Recrystallization and dissolution had affected various parts of this unit.

Description and interpretation of major microfacies types (MFTs)

The facies component percentages in the studied thin sections are identified. Various large and small benthic foraminifera, such as Alveolina spp. (Fig. 9-a), Nummulites spp. (Fig. 9-b, c, and d), Discocyclina spp. (Fig. 9-e), *Orbitolites complanatus* (Lamarck) (Fig. 9-f), Assilina spp. (Fig. 10-k), Miliolids spp., Rotalids spp., calcareous algae, skeletal fragments of

echinoderms, pelecypods, and others are identified. These fossil assemblages are good indicators for detecting the sedimentary environment and age of the formation.

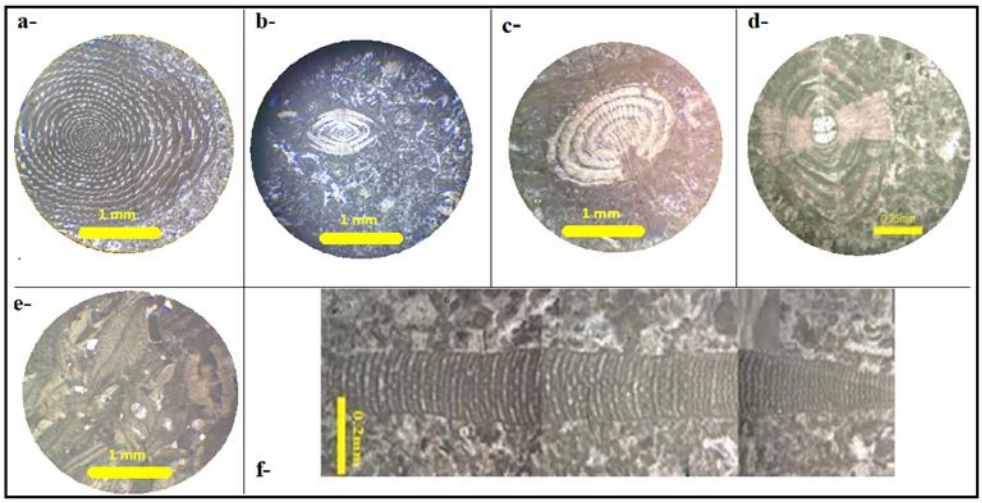


Fig. 9. Photomicrographs showing the foraminiferal taxa identified in the Avanah Formation. (a) Alveolina spp., Sartak-Bamo section, S.No.13; (b) *Nummulites* spp., Sartak-Bamo section, S.No.14; (c) *Nummulites* spp., Sartak-Bamo section, S.No.12; (d) *Nummulites* spp., Sartak-Bamo section, S. No. 21; (e) *Discocyclina* spp., Belula section; (f) *Orbitolites complanatus* (Lamarck) Sartak-Bamo section, S. No. 3.

Studying the skeletal and non-skeletal components, textural and lithological characteristics of the carbonate rocks, reveals the presence of four major carbonate microfacies that are subdivided into 11 submicrofacies types (Table 2).

Table 2: Main microfacies and submicrofacies types of the Avanah Formation.

Mudstone	Wackestone	Packstone	Packstone-Grainstone
● Micritic mudstone Submicrofacies ●Bioclastic mudstone Submicrofacies	●Miliolidal wackestone Submicrofacies ●Bioclastic wackestone Submicrofacies ●Discocyclina, Nummulite Wackestone Submicrofacies	●Alveolinal packstone Submicrofacies ●Bioclastic packstone Submicrofacies. ●Miliolidal packstone Submicrofacies ● Assilina, Discocyclina-Nummulitic packstone Submicrofacies.	● Nummulitic packstone-Grainstone submicrofacies ●Bioclastic Peloidal packstone-grainstone Submicrofacies.

1- Micritic mudstone submicrofacies (Mf 1)

Description:

Dark brown micritic groundmass and lack of fossils except some scattered fine bioclasts with a high amount of argillaceous material and organic matter are the main characteristics of this submicrofacies (Fig. 10a). This microfacies type is very common in all studied sections, especially in the two subsurface wells and Belula sections. It is observed only in the middle part of the Sartak-Bamo section. The effects of dolomitization processes are obvious in different parts of the studied sections, which occasionally cause to change in the micritic mudstone submicrofacies to dolomitic mudstone submicrofacies (Fig. 10-b).

Interpretation:

The dominance of the micritic matrix within this submicrofacies indicates that it had deposited in a low-energy and low-oxygenized setting of calm conditions with no water circulation. The fine-grained micritic groundmass is common in a deeper outer ramp and inner ramp; therefore, this submicrofacies corresponds to lagoonal environments of the inner ramp setting, and it is correlated with (RMF 19) according to a homoclinal carbonate ramp of Flügel (2010). This submicrofacies falls within the range of (FZ8) of Wilson (1975) and may have an appropriate situation with the (SMF23) of rimmed carbonate platform.

2- Bioclastic Mudstone submicrofacies (Mf 2)

Description:

This submicrofacies is recognized at the upper part of all the studied sections, and it is mostly composed of highly recrystallized bioclasts of fine to medium-sized fragments. Bioclasts of calcareous green algae and Mollusks with low diversity of some skeletal grains (such as small miliolids and rotalids) and their bioclasts are embedded in a micritic matrix (Fig. 10c). Many diagenetic processes affected this microfacies, especially dolomitization, which is the most obvious diagenetic process that obliterates some of the constituents.

Interpretation:

The prevailing bioclasts of algae and mollusks, with some skeletal grains of miliolids and rotalids, can reveal insights into the water depth, salinity, biological diversity, and environmental stability of the lagoon over time. The predominance of bioclastic shell fragments within a mud-supported microfacies indicates shallow water with limited circulation, of lagoon depositional environments (Flügel, 2010). This submicrofacies corresponds to (RMF17) of the inner ramp setting and is appropriate with the (SMF12) of rimmed platform within the range (FZ8) of Wilson (1975).

3- Miliolidal wackestone submicrofacies (Mf 3)

Description:

This microfacies is observed at different levels throughout the studied sections. Small miliolids foraminifera, with few Peneroplis and Rotalids, are embedded in the micritic groundmass of this submicrofacies (Fig. 10-d). While some skeletal debris of different fossils and algae are the subordinate components. Micritization is the abundant diagenetic process that affects the allochems and causes them to form a micritic envelope surrounding these grains.

Interpretation:

The sedimentation of this submicrofacies occurred under relatively low-energy conditions, typically found in calm, shallow water environments of the inner ramp. According to Flügel (2010), such sediments accumulate in these quiet settings, where energy levels are insufficient to transport larger particles, leading to the deposition of finer sediments. According to Hallock and Glenn (1986)Shallow-water lagoon environments are often characterized by imperforate foraminifera (e.g., miliolids, soritiidae, alveolinidae, and small rotalids). The presence of miliolids within the mud matrix confirms that these submicrofacies types were deposited in low-energy, shallow marine (lagoon) settings (Flügel, 2010). The miliolids inhabit quiet and shallow-water conditions (Khatibi Mehr and Adabi, 2014). Depending on the dominant matrix-supported rock fabric and the moderate to low diversity of the above-mentioned foraminifera, this submicrofacies correlates with the (RMF16), and it was deposited in protected and low-energy inner ramp settings. It corresponds to (FZ 7) of Wilson (1975).

4- Bioclastic wackestone submicrofacies (Mf 4)

Description:

This submicrofacies is characterized by fine to medium grain size of bioclasts with few worn skeletal grains (Fig. 10-e). This microfacies is common in the two subsurface sections (Well K90 and Well K306) and the Belula section, but is partially present in the Sartak-Bamo section. The identification of the bioclasts is difficult due to wave currents that have caused significant fragmentation.

Interpretation:

Most of the particles, which represent fine to medium shell fragments, are typically transported from high-energy to low-energy environments (such as from shallow water to

nearby deeper water). This type of sediment transport and deposition is characteristic of lagoonal environments within an inner ramp setting, and corresponds to (RMF17) (Flügel, 2010); or it corresponds to (SMF10) of Wilson (1975) and facies zone (FZ7).

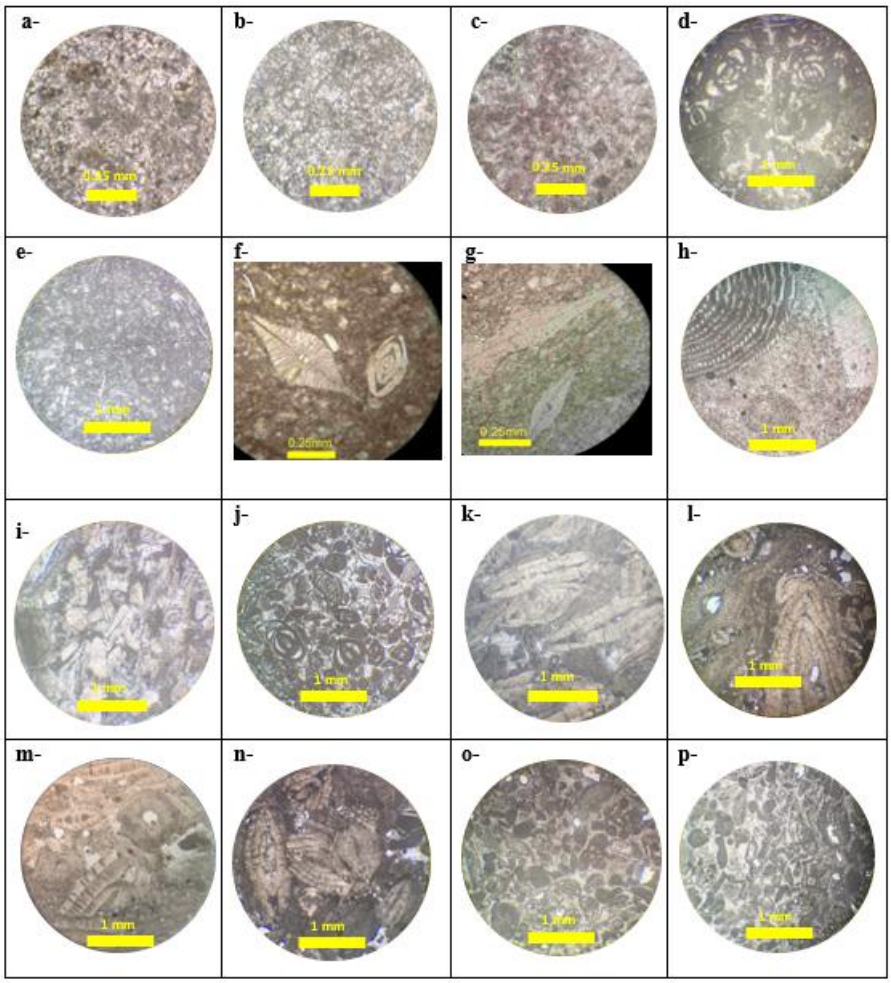


Fig.10. Photomicrographs revealing the identified submicrofacies types (MFTs) of the Avanah Formation. a- Micritic mudstone submicrofacies (Mf 1). b- Dolomitization causes to change in the micritic mudstone submicrofacies to dolomitic mudstone submicrofacies. c- Bioclastic Mudstone submicrofacies (Mf 2). d- Miliolidal wackestone submicrofacies (Mf 3). e-Bioclastic wackestone submicrofacies (Mf 4). f- Discocyclina-Nummulite wackestone submicrofacies (Mf 5). g- Actinocyclina spp. within the (Mf 5), Belula section. h- Alveolinal packstone submicrofacies (Mf 6). i- Bioclastic packstone submicrofacies (Mf 7). j- Miliolidal packstone submicrofacies (Mf 8). k and l- Assilina, Discocyclina- Nummulitic packstone submicrofacies (Mf 9). m and n- Nummulitic packstone-grainstone submicrofacies (Mf 10). o-Bioclastic Peloidal packstone-grainstone submicrofacies (Mf 11). p-Thin micritic enveloped process around some grains within (Mf 11).

5- Discocyclina-Nummulite wackestone submicrofacies (Mf 5)

Description:

This microfacies is observed in the middle part of the Belula section and the two subsurface wells (K 90 and K306) sections. The diagnostic feature of this submicrofacies is the appearance of some well-preserved and easily recognizable large lenticular benthonic foraminifera such as Discocyclina and Nummulites (Fig. 10f). These foraminifera constitute up to 25% of the components of this submicrofacies. Some other skeletal benthic forams, such as *Actinocyclina* spp. (Fig. 10-g) and *Operculina* spp., in addition to some bioclasts, are also observed, which are embedded in a micritic groundmass.

Interpretation:

The abundance of the above-mentioned biotic assemblage that disseminated in a micritic matrix and the fine-grained texture indicate a low-energy environment. Beavington-Penney and Racey (2004) and Payros *et al.* (2010) have pointed out that the Nummulites thrived in an open marine environment with a depth of (40–80 m). This submicrofacies represents a shallow open marine of the inner ramp and corresponds to (RMF 13) of Flügel (2010), and according to Wilson (1975), it corresponds to the facies zone (FZ7) and correlates with the standard microfacies type (SMF8).

6- Alveolinal packstone submicrofacies (Mf 6)

Description:

This submicrofacies is observed at the lower to middle part of the Avanah Formation, especially at the Sartak-Bamo section, and it is characterized by a grain-supported texture in which most of the grains are packed together (Fig. 10-h). Alveolina is a diagnostic large benthic foraminifer of this submicrofacies, which is associated with orbitolite, miliolids, rotalids, echinoid plates, with some bioclasts. The allochems and the groundmass of this submicrofacies, affected by recrystallization, suffered from compaction processes, which caused the packing of the grains, and deformed some of them.

Interpretation:

Alveolinids are known to tolerate a wide range of environmental conditions, particularly temperature and salinity variations. This adaptability allows them to thrive in diverse habitats within shallow-marine carbonate platforms (Hadi *et al.*, 2019).

Scheibner *et al.* (2007) regarded that microfacies dominated by alveolinids are characteristic of an inner platform. Orbitolitids, along with a high abundance of alveolinids and a micritic groundmass, often point to conditions typically found in a calm, shallow marine setting (Hottinger, 1983) and (Rasser *et al.,* 2005). The occurrence of Alveolina assemblages confirms an inner ramp depositional setting (Adabi *et al.*, 2008). This submicrofacies of the current study represents shallow open marine sedimentary environments and corresponds with (RMF 13) of the inner ramp setting, and it corresponds to the facies zone (FZ7) of Wilson (1975) and with the standard microfacies type (SMF8).

7- Bioclastic packstone submicrofacies (Mf 7)

Description:

This submicrofacies is identified within the wells K90 and K306 and Belula sections, but is less common in the Sartak-Bamo section. Several worn-out and micritized skeletal debris are distributed within a grain supporting texture of this facies (Fig. 10i). Some of these bioclasts are smashing and disturbing, and mostly they represent the bioclasts of benthonic foraminifera such as Rotalids and Nummulites with echinoid fragments. Recrystallization, micritization, leaching, and dissolution are the most common diagenetic processes that affected the allochems and the groundmass.

Interpretation:

Most of the particles are worn out and micritized, indicating that these bioclasts were transported before deposition, from high-energy settings to low-energy environments. The presence of worn medium to large-sized fragments of nummulites with other bioclasts in the studied samples indicates an open, shallow marine environment with medium salinity, (Milliman *et al.,* 1974).

This submicrofacies represents the mid-ramp setting and corresponds to the (RMF7), and according to Flügel (2010); it is equivalent to (SMF 10).

8- Miliolidal packstone submicrofacies (Mf 8)

Description:

Grain-supported texture with a few amounts of micrite between or around the allochems is the main characteristic of this facies. Miliolids are the predominant skeletal grains with some peloids and green algae bioclasts (Fig. 10-j). Micritization and recrystallization processes are the main diagenetic processes that affect the components. This submicrofacies is well developed only at the lower part of the Sartak-Bamo section, and is not recognized at Belula and the two subsurface wells sections.

Interpretation:

Miliolids are observable in shallow and restricted lagoon environments (Wilson, 1975). Diversity and abundance in a large number of miliolids are good indicators of low-energy, shallow marine, clean tropical, saline waters of the restricted inner platforms (shelf-lagoon) and inner ramp setting (Flügel, 2010).

The miliolids inhabit calm and quite shallow water conditions, and their great dominance suggests nutrient-rich and lagoonal marine conditions of the inner ramp (Racey and Simmons, 1994; Beavington-Penney *et al.,* 2006; Adabi *et al.,* 2008; Khatibi Mehr and Adabi, 2014). Miliolid foraminifera are prevalent in lagoonal environments, particularly those with elevated salinity, during the Mesozoic and Cenozoic eras, and are well-adapted to the specific conditions found in restricted inner platforms and inner ramps (Abd El-Moghny and Afifi, 2022).

Accordingly, this submicrofacies is compatible with shelf lagoons with open circulation (FZ 7) and may correlate with the standard microfacies type (SMF18-For) and (RMF 16) of the inner ramp setting.

9- Assilina, Discocyclina- Nummulitic packstone submicrofacies (Mf 9)

Description:

This submicrofacies is well identified at the lower and middle parts of the Avanah Formation at the Belula section, in addition to the lower parts of the two subsurface Wells (K90 and K306). Large benthonic forams such as *Nummulite* spp., *Discocyclina* spp., and *Assilina* spp. are the most abundant components of this submicrofacies, with their large bioclasts.

These allochems are well preserved, highly packed, and form a grain-supported texture (Fig. 10-k and l). Granular sparry calcite cement partially fills the intergranular spaces between skeletal grains.

Interpretation:

Large benthic foraminifera, prevalent throughout a grain-supported texture, indicate deposition in the mid-part of the ramp setting, below the fair-weather wave base (Mateu-Vicens *et al.,* 2012; Moallemi *et al.,* 2014).

The association of flat and discoidal shapes of large benthonic foraminifera, such as discocyclina and nummulites, generally suggests that these organisms lived in relatively deep, low-energy environments with low light conditions. (Sarkar, 2017). Flourishing of flat Nummulitic foraminifera in deeper mesophotic, clay-dominated settings reflects their adaptation to low-light, low-energy environments with fine sediments (Mateu-Vicens *et al.,* 2012). Hottinger (1997) suggested that the large benthonic foraminifera, like Assilina, with thinner tests, are typically found in environments with low water transparency or in deeper waters due to their adaptability to low-light conditions (Banerjee *et al.,* 2018).

So, the occurrence of large disc-shaped nummulites that are associated with large discocyclina and assilina within this submicrofacies of the current study was deposited below the fair-water wave base (FWWB). According to Rasser *et al.* (2005); Flügel (2010) and Hadi

et al. (2019), this facies in the current study is suggested to correspond to (RMF 8) as assigned by Flügel (2010) and it is typically deposited in a middle ramp environment open marine setting.

10- Nummulitic packstone-grainstone submicrofacies (Mf 10)

Description:

This submicrofacies is common in the middle and upper parts of the studied subsurface wells and the Belula section, but it does not appear in the Sartak-Bamo section. It is characterized by a high abundance of large, robust to flat forms of Nummulites, with a compact texture (Fig. 10-m and n). Fragments of Assilina, Discocyclina, Nummulite, algae, and echinoderms are also identified. The recrystallization process affected the micrite ground-mass, forming microsparite or pseudosparite cement between the skeletal grains.

Interpretation:

In the current study, this submicrofacies is indicative of a shallow water environment, where high-energy processes played a dominant role in sediment deposition. Racey (2001) observed that smaller and lenticular forms of Nummulites tests are more commonly found in shallower, inner platform, shelf, or ramp settings, and conversely, they are generally absent from more restricted water environments. The nummulites accumulation forms in a broad range of water depths in the inner and mid-ramp within the photic zone. According to Martín-Martín *et al.* (2021), during the middle Lutetian to Bartonian period, hyaline LBF (larger benthic foraminifera)-rich facies were prevalent, leading to the creation of extensive, thick nummulitic banks. These banks were primarily composed of large, robust to flat forms of Nummulites tests. Within these bank (shoal) environments, the shapes of Nummulites tests range from spherical and robust to more flattened forms (Fig. 11). The morphology of larger foraminifera is influenced by various environmental factors, including water depth gradients, light intensity, and hydrodynamic forces (Hottinger, 1983).

Hadi *et al.* (2016) proposed that the distinctive morphology of A-form Nummulites is characterized by their robust and ovoid tests, and they can serve as a useful indicator for identifying palaeohighs in shallow inner-ramp environments. Moreover, Attila *et al.* (2016) mentioned that the predominance of the abraded Nummulites assemblages indicates that the deposits were deposited in a shallow water environment with high hydrodynamic activity in a wave-dominant setting. Accordingly, the robust to flat nummulites of this submicrofacies in the current study can be developed in a shoal setting corresponding to (RMF 26) of a shallow inner ramp environment.

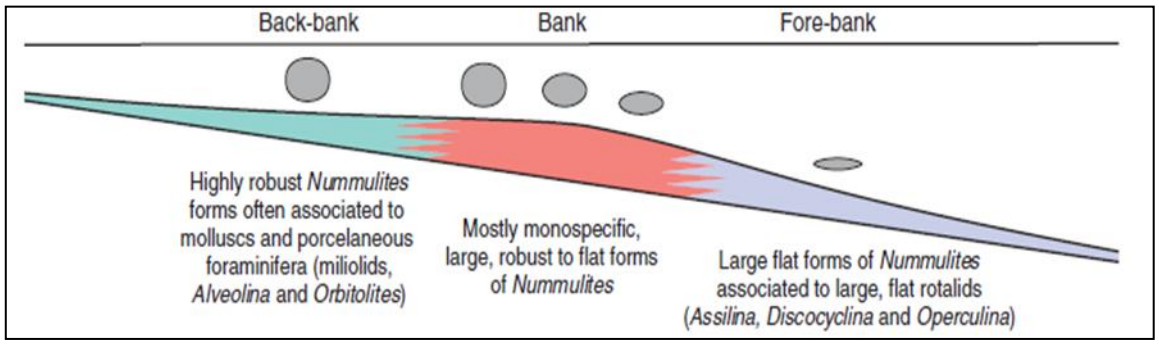


Fig. 11. General scheme of a nummulitic bank, after Mateu-Vicens *et al.* (2012).

11- Bioclastic Peloidal packstone -grainstone submicrofacies (Mf 11)

Description:

This type of submicrofacies is only observed in the Sartak-Bamo section. Sub-rounded to rounded, medium-sized allochems embedded in sparry and micritic matrix. The allochems are represented by bioclasts, peloids, intraclasts, and some small-coated foraminifera skeletal grains (miliolids) with amounts of calcareous algae (Fig. 10-o). Due to the effects of thin

micritic enveloped process around some grains, the identification of them became very difficult (Fig. 10-p). In addition to this, dissolution, recrystallization, and compaction diagenetic processes affected some allochems and parts of the groundmass. Different types of porosity (molds; intra and inter particles) are observed.

Interpretation:

The variance morphology of the allochems suggests that the deposition took place under moderate to high-energy conditions in a shallow condition of subtidal setting, which caused reworking and deposition of the sub-rounded to rounded grains within the basin. The relatively identified textures (sub-rounded to rounded, micritic outlines, grains, moderately sorted allochems, and grain-supported texture) are a good indication that these sediments of this submicrofacies could be deposited in shallow marine environments (Hashmie *et al.*, 2016) with active and winnowed hydrodynamic conditions. This submicrofacies corresponds with the (RMF 27) shoal and bank of the inner ramp setting.

Depositional environments

Integrating all collected data (depositional texture, grain types, their abundances, and their ratio to groundmass according to Dunham (1962), can be used to infer depositional environments both horizontally and vertically. Determining the microfacies is the main indicator of the carbonate platforms (Flügel, 2010; Zhang *et al.*, 2020). Different investigations were carried out, which proposed determining and interpreting the depositional environment of the Avanah Formation. Therefore, all the identified data of the current study, such as microfacies, faunal assemblages, lithological association, and the field observations, can be employed to identify and distinguish the three main facies associations that are related to energy conditions. Consequently, it can be suggested that the Avanah Formation was deposited in a carbonate ramp environment.

Detailed explanation of the depositional environments

I-Inner ramp

In the current study, three sub-environments were distinguished in the inner ramp setting.

I-A Semi-restricted lagoon facies associations

This setting comprises five microfacies as follows: 1) Micritic mudstone submicrofacies (Mf1), 2) Bioclastic Mudstone submicrofacies (Mf2), 3) Miliolidal wackestone submicrofacies (Mf3), 4) Bioclastic wackestone submicrofacies (Mf4), and 5) Miliolidal packstone submicrofacies (Mf8). At several intervals of the Avanah Formation in the studied sections, the high proportion of micrite matrix, occasionally represented by miliolids wackestone and packstone microfacies types are good indication of a low-energy environment that was deposited in a quiet environment, such as a restricted lagoon or semi-barred basin environments (Adachi *et al.*, 2004). The coexistence of Alveolina with miliolids and orbitolitids with their micritized skeletal fragments in the micritic texture has a significant role in a shallow water inner ramp- semi-restricted lagoonal setting and a back shoal setting (Boudaugher-Fadel, 2018). This situation conforms to the lower part of the Avanah Formation at the Sartak-Bamo section.

It is revealed that the above-mentioned submicrofacies were deposited within the (FZ 7 and 8) of Wilson (1975) and Flügel (2010), which represent semi-restricted platforms in inner ramp settings. Abd El-Moghny and Afifi (2022) concluded that shallow nearshore and lagoonal environments, down to about 50 m, are characterized by porcelaneous miliolid foraminifera.

I-B Shoal facies associations

The main microfacies represented in the shoal association of the current study comprise three submicrofacies: Nummulitic packstone-grainstone submicrofacies (Mf 10) and Bioclastic Peloidal packstone-grainstone submicrofacies (Mf 11).

These submicrofacies associations are characteristics of shallow water, under the influence of a moderate-to-high energy current-swept condition. They are typically suggested by the presence of coated bioclasts, nummulites assemblages, and micritized grains, which are set in a packstone-grainstone texture with low portions of mud content. This idea is consistent with Al-Hashimi and Amer (1985), that the Avanah Formation was deposited in a shoal bank.

Nummulites inhabited a wide range of open marine environments, including both ramps and shelves (Mateu-Vicens *et al.,* 2012) (Fig. 9). Racey (2001) stated that "Nummulitic banks are common in Early and Middle Eocene Tethyan shallow-marine carbonates, especially in oligotrophic settings".

While Jorry *et al.* (2006) suggested that the autochthonous Nummulites deposits can be found as in situ winnowed bioaccumulations or be accumulated offshore, onshore or alongshore, away from the original biotope according to various geological and oceanic processes.

Coated bioclastic packed-grainstone, within grain-supported textures, moderately sorted grains, and cemented material indicates a relatively high-energy setting under shoal environment agitated water (winnowed platform area) with content wave action at or situated above the fair water wave base (Flügel, 2010).

I-C Shallow open marine facies associations

This setting comprises 2 to 3 submicrofacies, such as Alveolinal packstone submicrofacies *(*Mf 6) and Discocyclina-Nummulite wackestone submicrofacies *(*Mf 5*)* types. The abrupt change from restricted to shallow open marine microfacies and again to restricted platform environments indicates the oscillation in sea-level during the deposition of the Avanah Formation.

Moderately sorted large porcelaneous foraminifera, mainly comprising sub-globular to ovoid tests of Alveolina, characterize Alveolinal packstone submicrofacies. Sub-globular to ovoidal alveolinids suggest a shallow-marine depositional setting corresponding to euphotic and oligotrophic conditions (Sarkar, 2019). Sediment rich in alveolinids/rotalids assemblages is typically habitat in inner ramp environments in non-vegetated substrates (Španiček *et al.,* 2017).

Hallock and Glenn (1986) pointed out that the larger foraminifera (such as Discocyclina and Nummulites) appear in shallow, well-lit sea bottom, and if they are not transported to the deeper basins, their appearance is indicative of depth less than 30m. Porcelaneous larger benthic foraminifera assemblages are commonly indicative of oligotrophic environments, which are the characteristics of the inner ramp setting. These foraminifera thrive in conditions of sufficient light with low nutrient levels (Martín-Martín *et al.*, 2023). So, the above-mentioned submicrofacies in the current study can be associated with and correspond to the shallow open marine environments of the inner ramp setting.

II- Middle ramp facies associations

The association of middle ramp facies consists of Bioclastic packstone submicrofacies (Mf 7) and Assilina, Discocyclina- Nummulitic packstone submicrofacies (Mf 9) types.

In the current study, the occurrence of worn-out and micritized medium to large-sized echinoid fragments with bioclasts of some benthonic foraminifera indicates that these bioclasts were transported before deposition from high-energy settings to low-energy environments.

On the other hand, the coexistence of large flat to discoidal benthic foraminifera like Assilina sp. and Discocyclina sp. with large flat Nummulites sp. suggests a range of depositional environments within the middle ramp setting. These environments are described

as spanning from the distal parts of the inner ramp to the proximal open-marine middle ramp environments.

Nummulite-rich facies with a paucity of alveolinids and orbitolitids indicate deposition below the fair-weather wave base (FWWB) and in the middle platform environment (Rasser *et al.,* 2005; Hadi *et al.,* 2019).

Discussion

Detecting microfacies types is crucial for inferring paleoenvironmental conditions and understanding sedimentological processes of the Avanah Formation. Accordingly, all the detected microfacies types of the current study are compared with the standard microfacies types in the Facies Zones (FZ) of the rimmed carbonate platform model and microfacies types in different parts of a homoclinal carbonate ramp of (Wilson, 1975; Flügel, 2010).

In general, the mudstones and wackestones microfacies are often formed and indicative of low-energy environments and revealing that the energy levels are not high enough to rework sediments, allowing for fine particles and carbonate materials to settle and accumulate. These microfacies types have a wide distribution in the semi-restricted lagoon environments of the inner ramp setting in the studied sections, and are represented by the submicrofacies (Mf 1, Mf 2, Mf 3, and Mf 4).

Whereas, the rich-miliolid packstone submicrofacies (Mf 8) that is characterized by a low-diversity of foraminiferal association, could reflect an environment protected from strong wave action, and it can be deposited in a shallow semi-restricted lagoonal environment of an inner ramp environment with low energy. This situation conforms to the lower part of the Sartak-Bamo section.

The Alveolinids tend to thrive in relatively calm, clear, and warm marine environments, and are represented by the submicrofacies (Mf 6) in the current study. It indicates shallow water, vegetation-covered substrates behind the nummulitic bank based on the abundance of Orbitolites and Alveolina species (Jorry *et al.,* 2006). This submicrofacies (Mf 6) is associated with the Discocyclina-Nummulite wackestone submicrofacies (Mf 5), which can infer the depositional environments of the Avanah Formation in the studied sections.

The combination of these submicrofacies suggests a shallow, open marine environment typical of the inner ramp setting, which is characteristic of relatively shallow depth, resulting in varied energy conditions. The packstones indicate areas of higher energy or more active sediment transport, while the wackestones point to slightly quieter conditions. These variations in sediment types and associated fauna help to paint a picture of a dynamic shallow open marine environment with both high-energy and more sheltered zones of the inner ramp setting.

The Avanah Formation shows a clear gradient from open shallow water of low-energy conditions to the more energetic conditions shoal setting with better-sorted coarser sediments.

The shoal facies association of the Avanah Formation consists of Nummulitic packstone-grainstone submicrofacies (Mf 10) and Bioclastic Peloidal packstone-grainstone submicrofacies (Mf 11).

At Sartak-Bamo, the moderate to well-sorted, sub-rounded to rounded, coated bioclastic packstone-grainstone indicates episodic events, which exhibit micritization, grain-supported texture, and cemented rims that highlight their deposition in a high-energy condition, situated above the (FWWB) in a shoal environment (Flügel, 2010). While the middle and upper parts of the Belula section and both subsurface sections (wells K90 and K306) contain large and robust to flat forms of Nummulites assemblages, indicating that these parts were deposited within shoal environments of an inner ramp setting. The Nummulites formed significant accumulations in various marine environments. Nummulites inhabited a wide range of open marine environments, including both ramps and shelves (Mateu-Vicens *et al.,* 2012). Whereas

Racey (2001) mentioned that their deposits are often found in inner and mid-ramp settings within the photic zone.

In the current study, the middle ramp facies association consists of Assilina, Discocyclina- Nummulitic packstone submicrofacies (Mf 9) and bioclastic packstone submicrofacies (Mf 7). Assilina, Discocyclina, and Nummulites forms are generally well-adapted to environments with low to moderate energy conditions. The presence of large benthic disc-shaped foraminifera such as Nummulites, Assilina, and Discocyclina in the Avanah Formation at the Belula section and both studied subsurface wells (K306 and K90) indicates that these organisms typically inhabited shallow open marine environments, particularly ranging from the inner to middle ramp settings.

Based on the evidence provided and the accumulation of the mentioned foraminiferal fossils (and other petrographic components), it suggests that the Sartak-Bamo section is characterized by environments ranging from a semi-restricted lagoon to a shoal environment at the inner ramp setting (Fig. 12). The Avanah Formation at the Belula section exhibits a progression from a low-energy, back shoal environment through a more energetic shoal setting to a shallow open marine environment within an inner to middle ramp setting (Fig. 13).

At the wells (K90 and K306), the depositional environments of the Avanah Formation show a consistent pattern of transition from shoal to shallow open marine environment, and extending from the inner to middle ramp settings (Figs. 14 and 15).

This suggests that overall, the depositional environments of the Avanah Formation at the studied areas began as semi-restricted lagoonal settings to high-energy environments (shoals), to a shallow open marine condition of the inner ramp, then extending to a middle ramp setting (Fig. 16).

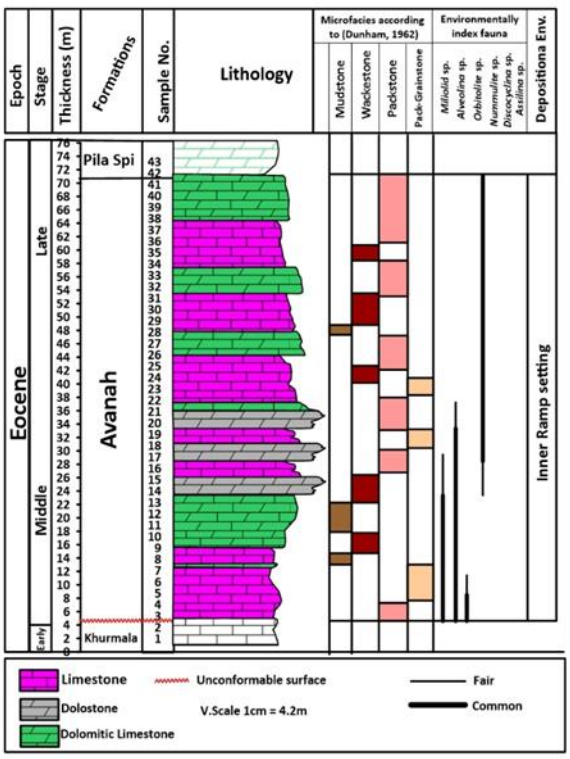


Fig.12. Sartak-Bamo Section.

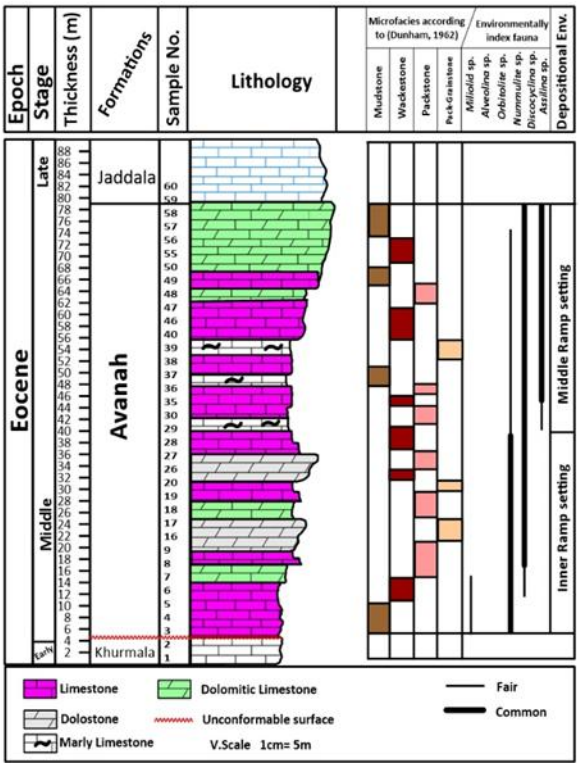


Fig. 13. Belula Section.

Microfacies types, faunal assemblages, and depositional environments of the Avanah Formation at Sartak-Bamo section (left) and Belula section (right).

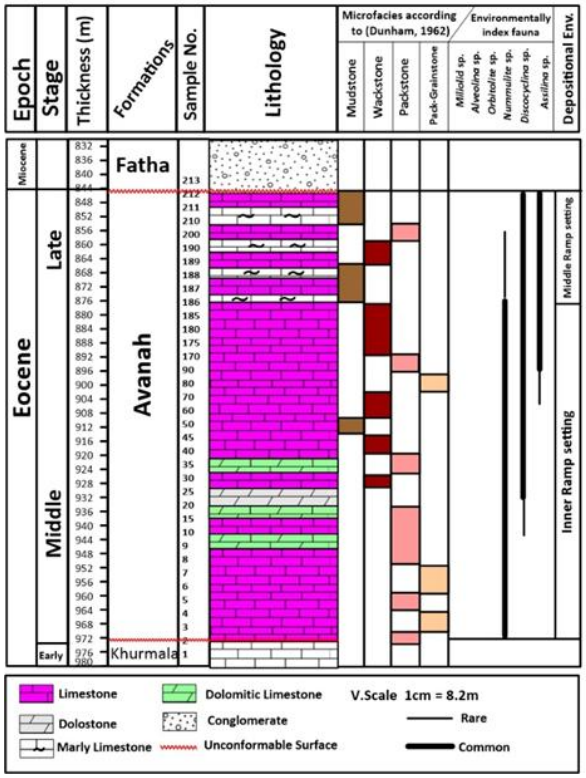


Fig. 14. Well K-90

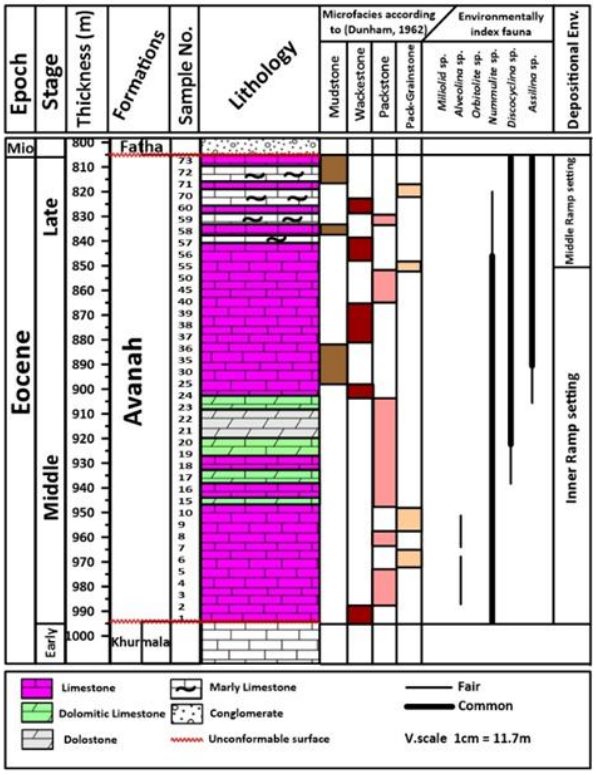


Fig. 15. Well K-306

Microfacies types, faunal assemblages, and depositional environments of the Avanah Formation at Well K90 (left) and Well K306 (right).

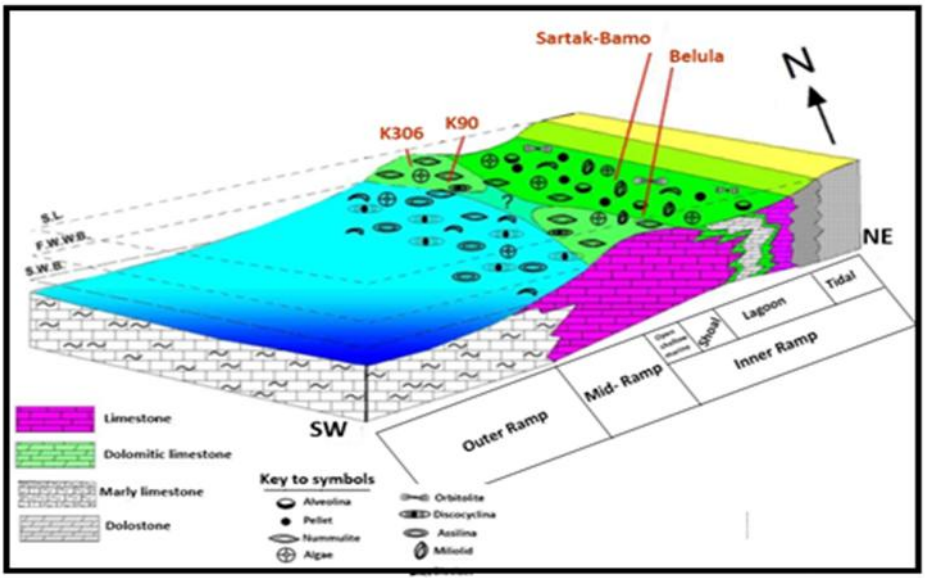


Fig. 16. Depositional and facies model of the Avanah Formation in the studied area.

Conclusion

1-The Avanah Formation shows a significant spatial variation in thickness across the studied sections. In the subsurface wells (K90 and K306), which are located in the ZLFZ, the Avanah Formation is thicker, with measurements of 127 meters and 186 meters, respectively. In contrast, the thickness of the Avanah Formation decreases towards the ZHFZ direction at surface sections, with measurements of (64 m at Sartak-Bamo and 75 m at Belula section. This pattern indicates a spatial variation in the thickness of the Avanah Formation due to various geological factors such as sedimentation, tectonic activity, or erosional processes that might be influencing the distribution and development of this formation.

2- The Avanah Formation unconformably underlain by the Khurmala Formation at all studied sections. At Wells K90 and K306, the Avanah Formation is unconformably overlain by the Fatha Formation, whereas at the Sartak-Bamo and Belula sections, the Avanah Formation has a conformable upper contact and is overlain by the Pila Spi and Jaddala formations, respectively.

3- Petrographically, the Avanah Formation is composed of micrite, cement, skeletal grains (Nummulite, Alveolina, Miliolid, Discocyclina, Assilina, Orbitolite, Alga, Bioclasts… etc.) and non-skeletal grains (Peloids, Extra clasts and Intra clasts).

4- In the studied sections, several distinct lithofacies have been identified (limestone, dolomitic limestone, dolostone, and marly limestone). Notably, the Sartak-Bamo section stands out as having thicker dolomitic limestone and dolostone lithofacies compared to the other three sections.

5- The Marly limestone lithofacies present in the middle to upper parts of the formation at the Belula section and wells (K90 and K306) reflect a deeper water environment compared to the Sartak-Bamo section, which lacks this lithofacies and may represent a shallower, more carbonate-dominated setting. This stratigraphic evidence helps in reconstructing the paleoenvironments and understanding the changes in depositional conditions over time and space within the Avanah Formation.

6- Different diagenetic processes have affected the carbonate rocks of the Avanah Formation, such as recrystallization, cementation, neomorphism, dolomitization, micritization, dissolution, and compaction.

7- Four main microfacies (Mudstone, Wackestone, Packstone, and Packstone-Grainstone) are identified, which they typically categorized into eleven submicrofacies based on their composition, texture, and fossil content.

8- The depositional environments of the Avanah Formation range from more restricted lagoonal settings to open marine conditions. Environments ranging from a semi-restricted lagoon to a shoal (bank) setting characterize the Sartak-Bamo section. The depositional environment of the Belula section, K90, and K306 Wells, starts with shoal (bank) conditions, then transitions to a shallow open marine environment extending from inner to middle ramp settings.

The depositional environment of the Avanah Formation encompassed a variety of settings ranging from the semi-restricted shallow lagoons, shoals (banks), to shallow open marine environments (of the inner ramp) and extending from the inner to the middle ramp setting.

References

Abawi, T.S. and Sharbazheri, K.M.E., 1987. Larger foraminifera from the Avanah Formation (Middle Eocene) of Dohuk Area, Northern Iraq.

Abd El-Moghny, M.W. and Afifi, A.A., 2022. Microfacies analysis and depositional environments of the Middle Eocene (Bartonian) Qurn Formation along Qattamiya-Ain Sokhna district, Egypt, Carbonates and Evaporites, 37(1), pp. 18. Doi.org/10.1007/s13146-022-00762-9

Abdullah, M.A., Hassan, F.N. and Saleh, A.M., 2020. Microfacies and Palaeoenvironment of Avanah Formation (Middle Eocene) Geli Bessri in Dohuk City/North of Iraq, Tikrit Journal of Pure Science, 25(1), pp. 85–93. Doi.org/10.25130/tjps.v25i1.217

Adabi, M.H. Zohdi A., Ghabeishavi A. and Amiri-Baxtiyar H., 2008. Applications of nummulitids and other larger benthic foraminifera in depositional environment and sequence stratigraphy: an example from the Eocene deposits in Zagros Basin, SW Iran, Facies, 54(4), pp. 499-512. Doi.org/10.1007/s10347-008-0151-7

Adachi, N., Ezaki, Y. and Liu, J., 2004. The fabrics and origins of peloids immediately after the end-Permian extinction, Guizhou Province, South China, Sedimentary Geology, 164(1–2), pp. 161–178. Doi.org/10.1016/j.sedgeo.2003.10.007.

Al-Hashimi, H.A.J. and Amer, R.M., 1985. Tertiary microfacies of Iraq. Directorate general for Geological Survey and mineral investigation.

Al-Mutwali, M.M. and Al-Banna, N.Y., 2005. Microfacies and Depositional Environment of the Interfingering Beds of Avanah Formation from Selected Sections, Sinjar Anticline, Northwest Iraq, Rafidain journal of science, 16(1A). Doi: 10:33899/rjs.2005.41362.

Al-Qayim, B., Omer, A. and Koyi, H., 2012. Tectonostratigraphic overview of the Zagros suture zone, Kurdistan region, Northeast Iraq, GeoArabia, 17(4), pp. 109–156. Doi.org/10.2113/geoarabia1704109

Al-Temimi, M.S., 2002. Foraminifera of the Sinjar and Avanah Formations (Lower Tertiary) in Northern Iraq, M.Sc. Thesis, University of Baghdad. Unpublished.

Ameen, F. and Mardan, F., 2019. Sequence Stratigraphic Analysis of the Middle Paleocene-Middle Eocene in the Sulaimani District (Kurdistan Region), North Iraq, in Paleobiodiversity and Tectono-Sedimentary Records in the Mediterranean Tethys and Related Eastern Areas: Proceedings of the 1st Springer Conference of the Arabian Journal of Geosciences (CAJG-1), Tunisia 2018. Springer, pp. 207–209.

Ameen Lawa, F.A. and Ghafur, A.A., 2015. Sequence stratigraphy and biostratigraphy of the prolific late Eocene, Oligocene and early Miocene carbonates from Zagros fold-thrust belt in Kurdistan region, Arabian Journal of Geosciences, 8, pp. 8143–8174. Doi: 10.1007/s12517-015-1817-4

Amirshahkarami, M., Ghabishavi, A. and Rahmani, A., 2010. Biostratigraphy and paleoenvironment of the larger benthic foraminifera in wells sections of the Asmari Formation from the Rag-e-Safid oil field, Zagros Basin, southwest Iran, Stratigraphy and Sedimentology Researches, 26, pp. 63–84.

Aqrawi, A.A.M., Goff, J.C., Horbury, A.D. and Sadooni, F.N., 2010. The petroleum geology of Iraq. Scientific Press Beaconsfield.

Asaad, I.S., 2022. Lithostratigraphy and microfacies analysis of Avanah Formation (Middle Eocene) in Gomaspan section northeast Erbil City, Iraqi Kurdistan region, Kuwait Journal of Science, 49(3). Doi.org/10.48129/kjs.11183

Attila, K.S., Lorand S., Gyorgy L. and Sorin F., 2016. 'Middle Eocene (Bartonian) Nummulites perforatus bank from the Transylvanian Basin, Romania: an example from a classical occurrence, Geophysical Research Abstracts Vol. 18, EGU2016-4402.

Banerjee, S., Khanolkar, S. and Saraswati, P.K., 2018. Facies and depositional settings of the Middle Eocene-Oligocene carbonates in Kutch, Geodinamica Acta, 30(1), pp. 119–136. Doi.org/10.1080/09853111.2018.1442609

Barzani, B.A., 2016. Microfacies, depositional environment and sequence stratigraphy of Avanah Formation from selected sections in Iraqi Kurdistan Region, Unpublished M.Sc. Thesis, University of Salahaddin.

Beavington-Penney, S.J. and Racey, A., 2004. Ecology of extant nummulitids and other larger benthic foraminifera: applications in palaeoenvironmental analysis, Earth-Science Reviews, 67(3–4), pp. 219–265. Doi.org/10.1016/j.earscirev.2004.02.005

Beavington-Penney, S.J., Wright, V.P. and Racey, A., 2006. The middle Eocene Seeb Formation of Oman: an investigation of acyclicity, stratigraphic completeness, and accumulation rates in shallow marine carbonate settings, Journal of Sedimentary Research, 76(10), pp. 1137–1161. Doi.org./10.2110/jsr.2006.109

Bellen, R.C., Dunnington. H.V., Wetzel, R. and MortonAsie, Fasc., 10a, Iraq, P., 1959. No Title Lexique Stratigraphic International.

Boudaugher-Fadel, M.K., 2018. Evolution and geological significance of larger benthic foraminifera. UCL Press. https://doi.org/10.14324/111.9781911576938.

Buday, T., 1980. The regional geology of Iraq, Vol. I, Stratigraphy and paleogeography. In: Kassab IIM and Jassim SZ (eds) GEOSURV, Baghdad, Iraq.

Dunham, R.J., 1962. Classification of carbonate rocks according to depositional textures.

Flügel, E., 2010. Microfacies of Carbonate Rocks: Analysis, Interpretation and Application. 2nd Ed. Springer-Verlag Berlin, Germany. Doi.org/10.1007/978-3-642-03796-2

Hadi, M., Mosaddegh, H. and Abbassi, N., 2016. Microfacies and biofabric of nummulite accumulations (Bank) from the Eocene deposits of Western Alborz (NW Iran), Journal of African Earth Sciences, 124, pp. 216–233. Doi.org/10.1016/j.jafrearsci.2016.09.012

Hadi, M., Vahidinia, M. and Hrabovsky, J., 2019. Larger foraminiferal biostratigraphy and microfacies analysis from the Ypresian (Ilerdian-Cuisian) limestones in the Sistan Suture Zone (eastern Iran), Turkish Journal of Earth Sciences, 28(1), pp. 122–145. Doi 10.3906/yer-1802-10

Hallock, P. and Glenn, E.C., 1986. Larger foraminifera: a tool for paleoenvironmental analysis of Cenozoic carbonate depositional facies, Palaios, pp. 55–64. Doi.org/10.2307/3514459

Hashmie, A., Rostamnejad, A., Nikbakht, F., Ghorbanie, M., Rezaie, P., Gholamalian, H., 2016. Depositional environments and sequence stratigraphy of the Bahram Formation (middle–late Devonian) in north of Kerman, south-central Iran, Geoscience Frontiers, 7(5), pp. 821–834. doi.org/10.1016/j.gsf.2015.07.002

Hottinger, L., 1983. Processes determining the distribution of larger foraminifera in space and time, Utrecht Micropaleontological Bulletins, (30), pp. 239–253.

Hottinger, L., 1997. Shallow benthic foraminiferal assemblages as signals for depth of their deposition and their limitations, Bulletin de la Société géologique de France, 168(4), pp. 491–505.

Jassim, S.Z. and Goff, J.C., 2006. Geology of Iraq: Dolin, Prague and Moravian Museum, Brno, Czech Republic, 5.

Jorry, S.J., Hasler, C.A. and Davaud, E., 2006. Hydrodynamic behaviour of Nummulites: implications for depositional models, Facies, 52, pp. 221–235. Doi.org/10.1007/s10347-005-0035-z

Karim, K.H., 1997. Stratigraphy of Sartaq-Bamo Area from northeastern Iraq, Journal of Iraqi Geological Society, 2(4), pp. 493–509.

Khatibi Mehr, M. and Adabi, M.H., 2014. Microfacies and geochemical evidence for original aragonite mineralogy of a foraminifera-dominated carbonate ramp system in the late Paleocene to Middle Eocene, Alborz basin, Iran, Carbonates and Evaporites, 29, pp. 155–175. Doi.org/10.1007/s13146-013-0163-4

Martín-Martín M. Guerrera F., Tosequella J. and Tramontana M., 2021. Middle Eocene carbonate platforms of the westernmost Tethys, Sedimentary Geology, 415, p. 105861. Doi.org/10.1016/j.sedgeo.2021.105861

Martín-Martín M., Tosequella J., Guerrera F., Maate A., Hilal R., Maate S., Tramontana M. and Le Breton E., 2023. The Eocene carbonate platforms of the Ghomaride Domain (Internal Rif Zone, N Morocco): a segment of the westernmost Tethys, Sedimentary Geology, 452, p. 106423. Doi.org/10.1016/j.sedgeo.2023.106423

Mateu-Vicens, G., Pomar, L. and Ferrandez-Canadell, C., 2012. Nummulitic banks in the upper Lutetian "Buil level", Ainsa Basin, South Central Pyrenean Zone: the impact of internal waves, Sedimentology, 59(2), pp. 527–552. doi.org/10.1111/j.1365-3091.2011.01263.x

Milliman, J.D., Mueller, G. and Foerstner, U., 1974. Marine Carbonates Recent Sedimentary Carbonates, Part I. Springer-Verlag, Berlin. doi.org/10.1007/978-3-642-65528-9_6

Moallemi, S.A., Daneshian, J. and Hosseinzadeh, M., 2014. Lithostratigraphy, Microfacies Investigation, and Paleoenvironmental Reconstruction of the Jahrum Formation in the West and North of the Bandar Abbas Area, South Iran, Advances in Environ. Biology, 8(4), pp. 963–974.

Payros, A., Pujalte V., Tosquella J. and Orue-Etxebarria X., 2010. The Eocene storm-dominated foralgal ramp of the western Pyrenees (Urbasa–Andia Formation): an analogue of future shallow-marine carbonate systems?, Sedimentary Geology, 228(3–4), pp. 184–204. doi.org/10.1016/j.sedgeo.2010.04.010

Pirot H.H.A., 2017. Sedimentology of Avanah Formation (M - L Eocene) from selected sections in Iraq Kurdistan Region. Unpub. MSc. Thesis. Univ. of Sulaimani.

Racey, A., 2001. A review of Eocene nummulite accumulations: structure, formation and reservoir potential, Journal of Petroleum Geology, 24(1), pp. 79–100. doi.org/10.1111/j.1747-5457. 2001.tb00662.x

Racey, A. and Simmons, M.D., 1994. Biostratigraphy and palaeobiogeographic significance of Tertiary nummulitids (foraminifera) from northern Oman, Micropalaeontology and hydrocarbon exploration in the Middle East, 343, p. 370.

Rahmani, A., Vaziri-Moghaddam, H., Taheri, A. and Ghabeishavi, A., 2009. A model for the paleoenvironmental distribution of larger foraminifera of Oligocene–Miocene carbonate rocks at Khaviz Anticline, Zagros Basin, SW Iran, Historical Biology, 21(3–4), pp. 215–227. Doi.org/10.1080/08912960903461296

Rasser, M.W., Scheibner, C. and Mutti, M., 2005. A paleoenvironmental standard section for Early Ilerdian tropical carbonate factories (Corbieres, France; Pyrenees, Spain), Facies, 51, pp. 218–232. Doi:10.1007/s10347-005-0070-9

Sarkar, S., 2017. Microfacies analysis of larger benthic foraminifera-dominated Middle Eocene carbonates: a palaeoenvironmental case study from Meghalaya, NE India (Eastern Tethys), Arabian Journal of Geosciences, 10(5), pp. 121. Doi:10.1007/s12517-017-2929-9

Sarkar, S., 2019. Alveolina-dominated assemblages in the early Eocene carbonates of Jaintia Hills, NE India: Biostratigraphic and palaeoenvironmental implications, Comptes Rendus Palevol, 18(8), pp. 949–966. Doi:10.1016/j.crpv.2019.10.006

Scheibner, C., Rasser, M.W. and Mutti, M., 2007. The Campo section (Pyrenees, Spain) revisited: Implications for changing benthic carbonate assemblages across the Paleocene–Eocene boundary, Palaeogeography, Palaeoclimatology, Palaeoecology, 248(1–2), pp. 145–168. Doi:10.1016/j.palaeo.2006.12.007

Sharbazheri, K.M.E., 1983. Study of Foraminifera and Microfacies of the Avanah Limestone (Middle Eocene), Dohuk Area, North Iraq, Unpublished MSc Thesis, Mosul University. College of Science, Iraq.

Sharland, P.R., Casey D.M., Davies R.B., Simmons M.D. and Sutcliffe O.E., 2004. Arabian plate sequence stratigraphy–revisions to SP2, GeoArabia, 9(1), pp. 199–214. Doi:10.2113/geoarabia0901199

Španiček, J., Cosovic V., Mrinjek E. and Vlahovic I., 2017. Early Eocene evolution of carbonate depositional environments recorded in the Čikola canyon (north Dalmatian Foreland Basin, Croatia), Geologia Croatica, 70(1), pp. 11–25. Doi:10.4154/gc.2017.05

Wilson, J.L., 1975. Carbonate Facies in Geologic History. Springer Verlag, Berlin. Doi:10.1007/978-1-4612-6383-8

Zhang, X., Pang X., Jin Z. and Wang K., 2020. Depositional model for mixed carbonate-clastic sediments in the middle Cambrian lower Zhangxia formation, Xiaweidian, north China, Advances in Geo-Energy Research, 4(1), pp. 29–42. Doi:10.26804/ager.2020.01.04

Iraqi National Journal of Earth Science

www.earth.uomosul.edu.iq

Assessing the Environmental Situation of Euphrates River Sediments Using Magnetic Susceptibility Techniques in Al-Muthanna Province, Southwestern Iraq

Nawrass N. Ameen [1*]

[1] *college of science, University of Al Muthanna, Al Muthanna, Iraq.*

Article information

Received: 27- Aug -2024

Revised: 20- Oct -2024

Accepted: 15- Jan -2025

Available online: 01- Jan – 2026

Keywords:
Sediment Contamination
Magnetic, Mineralogy,
Heavy Metals,

Correspondence:

Name: Nawrass N. Ameen

Email: nawrass@mu.edu.iq

ABSTRACT

Sediment contamination is one of the major challenges the Euphrates River environment faces. The Euphrates River is regarded as the main supply of water for industrial and agricultural purposes for Samawa City in Al Muthanna Province, the southwestern part of Iraq. The sewage pipeline is dumped into the river, which directly affects the water quality and subsequently the vegetation. A magnetic mineralogy study is carried out on sediments to specify the contamination by heavy metals. Magnetic properties are measured in 250 sediment samples; magnetic susceptibility, anhysteretic remanent magnetization, isothermal remanent magnetization, and thermomagnetic analyses are measured. Heavy metal analyses are performed using SEM together with energy-dispersive X-ray and X-ray fluorescence analyses to connect the results with magnetic enhancements. Statistical analyses show that the mean value of magnetic susceptibility is 3361.2 × 10-8 m3kg-1, of anhysteretic remanent magnetization is 628.9 × 10-8 m3kg-1, and thermomagnetic analyses (high and low) clearly show the typical curves of magnetite. The magnetic properties results indicate that the main magnetic phases are single-domain (SD) to multi-domain (MD) state magnetite caused by the surrounding catchment and anthropogenic activities. Results of heavy metal (HM) analysis performed on ten selected samples and then compared with the magnetic results. A correlation between HM and χ shows a positive correlation between magnetic susceptibility and Ca, Cr, Mg, Fe, Pb, and Na concentrations. The results of magnetic mineralogy indicate that the magnetic susceptibility parameter can be used as an indicator for heavy metals.

DOI: 10.33899/injes.v26i1.60182, ©Authors, 2026, College of Science, University of Mosul.
This is an open-access article under the CC BY 4.0 license (http://creativecommons.org/licenses/by/4.0/).

تقييم الوضع البيئي لرواسب نهر الفرات باستخدام تقنيات الحساسية المغناطيسية في محافظة المثنى، جنوب غربي العراق

نورس امين [1]*

[1] *كلية العلوم، جامعة المثنى، المثنى، العراق.*

معلومات الارشفة

تاريخ الاستلام: 27- اغسطس-2024

تاريخ المراجعة: 20- اكتوبر-2024

تاريخ القبول: 15- يناير -2025

تاريخ النشر الالكتروني: 01- يناير -2026

الكلمات المفتاحية:

تلوث التربة،

المعدنية المغناطيسية،

العناصر الثقيلة،

المراسلة:

الاسم: نورس امين

Email: nawrass@mu.edu.iq

الملخص

يعد تلوث الرواسب من أهم التحديات التي تواجه بيئة نهر الفرات، حيث يعتبر نهر الفرات المصدر الرئيس للأغراض الصناعية والزراعية لمدينة السماوة، محافظة المثنى والتي تقع في الجزء الجنوبي الغربي من العراق. يتم وضع خط أنابيب الصرف الصحي في النهر، مما يؤثر بشكل مباشر على جودة المياه وبالتالي على الغطاء النباتي. تم إجراء دراسة معدنية مغناطيسية على الرواسب من أجل تحديد التلوث بالمعادن الثقيلة. حيث تم قياس الخصائص المغناطيسية في 250 عينة من الرواسب؛ تم قياس الحساسية المغناطيسية، والمغناطيسية المتبقية اللاهسترية، والمغناطيسية المتبقية المتساوية الحرارة والتحليلات الحرارية المغناطيسية. تم إجراء تحليلات المعادن الثقيلة باستخدام المجهر الإلكتروني الماسح مع الأشعة السينية المشتتة للطاقة، كما تم إجراء تحليلات فلورسنت الأشعة السينية لربط النتائج بالتعزيزات المغناطيسية. تظهر التحليلات الإحصائية أن متوسط قيم القابلية المغناطيسية كانت 3361.2 × 10−8 م3كغم−1، وكانت المغناطيسية المتبقية اللاهسترية 628.9 × 10−8 م3كغم−1، كما تظهر التحليلات الحرارية المغناطيسية (العالية والمنخفضة) بوضوح المنحنيات النموذجية للمغنتايت. تشير نتائج الخصائص المغناطيسية إلى أن المراحل المغناطيسية الرئيسة هي المغنتايت أحادي المجال (Single-domain) إلى متعدد المجالات (Multi-domain) الناجم عن مستجمعات المياه المحيطة ومن الأنشطة البشرية. نتائج تحليلات المعادن الثقيلة (Heavy Metals) التي أجريت على عشر عينات مختارة تمت مقارنة نتائجها بالنتائج المغناطيسية. يُظهر الارتباط بين HM والحساسية المغناطيسية ارتباطًا إيجابيًا بين الحساسية المغناطيسية وتراكيز العناصر Ca وCr وMg وFe وPb وNa. تشير نتائج المعادن المغناطيسية إلى أنه يمكن استخدام معامل الحساسية المغناطيسية كمؤشر للمعادن الثقيلة.

DOI: 10.33899/injes.v26i1.60182, ©Authors, 2026, College of Science, University of Mosul.
This is an open-access article under the CC BY 4.0 license (http://creativecommons.org/licenses/by/4.0/).

Introduction

The river sediments are generated from bedrock weathering, organic matter, erosion, or anthropogenic activities (Perry and Taylor, 2007), which would be of great interest in carrying contaminants that reflect on humans. Anthropogenic activities, such as heavy metals, play a crucial role in polluting the environment, and they represent the majority of contaminants found in the river sediments caused by different sources such as irrigation, land use near the river, fuel combustion, industrial waste disposal, or agricultural waste (Sudarningsih et al., 2023).

Many researchers have reported monitoring heavy metals in soils and sediments using magnetic susceptibility techniques, where the magnetic susceptibility increases with increasing heavy metal concentrations. This method is considered efficient, fast, and cost-effective (Evans and Heller, 2003).

The accumulation of heavy metals has been evaluated in sediments from Sawa Lake in southern Iraq using magnetic mineralogy techniques. Selected heavy metal concentrations were measured and correlated with magnetic susceptibility concentrations. The results revealed an

insignificant correlation between magnetic susceptibility and heavy metals due to the low concentrations of magnetic signals in the lake sediments (Ameen et al., 2019).

In another study, the level of contamination in sediments from river streams collected from the Arc River (Provence, France) was assessed by rock-magnetic methods, to recognize magnetic particles produced by industrial to find a connection between magnetic pollution and heavy metal concentrations. The findings showed that human activity is the source of the magnetic variances identified in the riverbank sediments of the streams since these variances are positively correlated with Pb, Zn, Fe, and Cr concentrations (Desenfant et al., 2004).

The concentration of anthropogenic heavy metals found in both highly and slightly contaminated soil cores from a forest near a steel mill at Leoben, Austria, was measured by magnetic susceptibility analyses. In naturally contaminated soil, the magnetic susceptibility method proved to be an effective tool for semi-quantitatively defining the concentrations of heavy metals in soils. The results showed that there is a boundary depth that indicates the transition from the deeper “unpolluted” zone to the contaminated zone (Blaha et al., 2008).

This study aims to examine the magnetic signature of river sediments collected from the Euphrates River in Samawa City (Al Muthanna province) in southern Iraq, and to correlate the magnetic concentration with the heavy metals, given that heavy metal pollution could cause an increase in the magnetic concentration.

Materials and Methods

Geology and Geomorphology

The Euphrates River flows through the Mesopotamian Plain and ultimately merges with the Tigris River near the town of Al-Qurnah. The Mesopotamian Plain's sediments are mostly made of silt and clay (Sissakian and Al-Ansari, 2019). In the Mesopotamian Plain, small smooth and extremely flat depressions are frequent as morphological characteristics, having a few hundred square meters to several hundred square kilometers area, which cover different areas. The larger shallow depressions are found close to the area where the Abu Jir active fault zone links the western and southern deserts to the Mesopotamian plain; they are primarily sag depressions that show evidence of neotectonic activity (Sissakiana et al., 2021).

Study area location and sampling

The Study area is located in the Euphrates River, which crosses the city of Samawa, Al Muthanna province, with coordinates 31°19'34.80" N, 45°15'6.78" E. The type of sediments mainly consists of alluvial sediments (clay, silt) carried by rushing streams (Fig. 1).

Two hundred fifty sediment samples were collected from the bottom of the river using a shovel at intervals of one meter between the samples, and then stored in plastic bags and labeled.

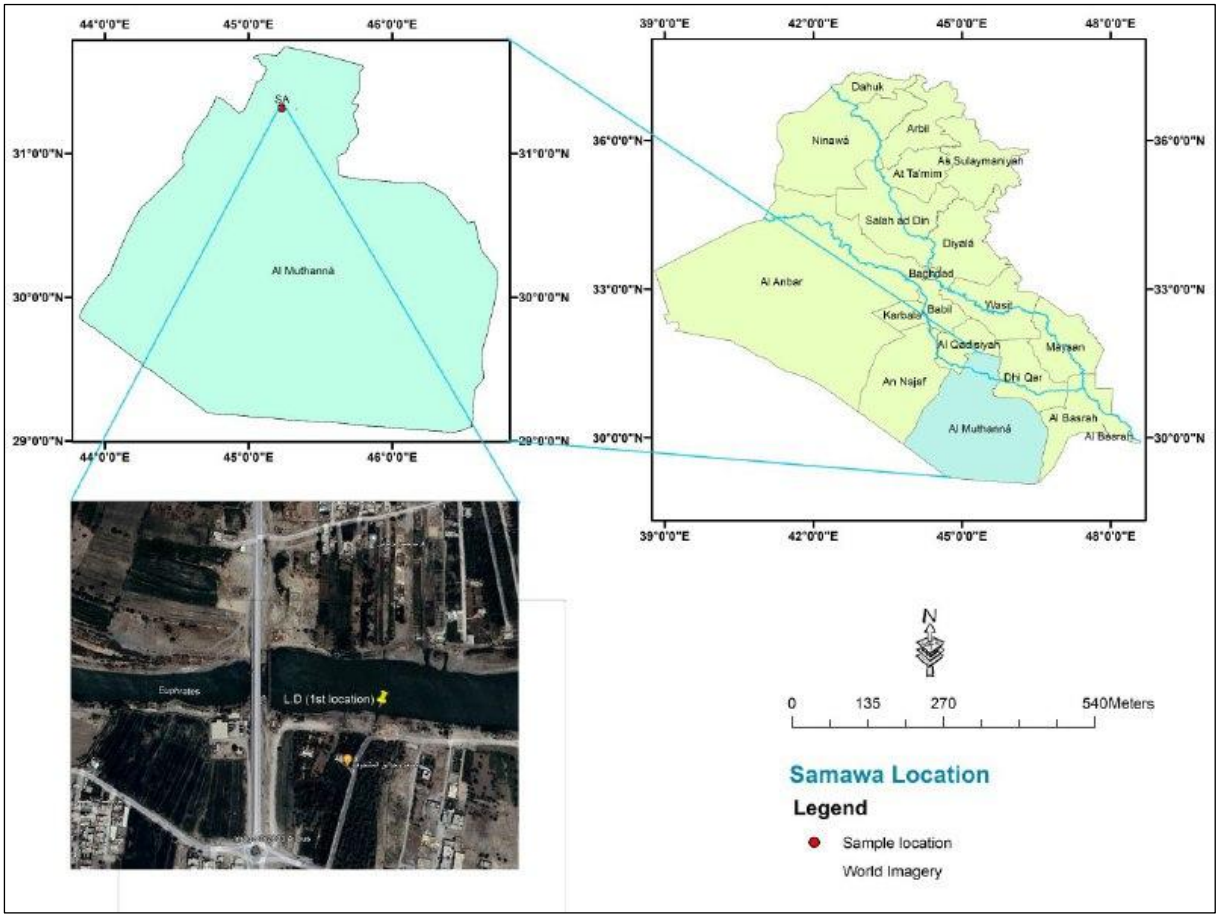


Fig. 1. Location maps of the study area

Laboratory Measurements

Magnetic measurements

The collected samples were transported to the Earth Magnetism Laboratory at the German Research Center for Geosciences (GFZ) located in Potsdam, Germany, in August 2023. Sample preparation has been performed, where the samples are air dried, sieved to remove the organic matter, and packed into small cubic plastic boxes 6 cm³, tightly closed to perform a series of magnetic measurements.

Magnetic susceptibility represents the concentrations of the ferrimagnetic minerals (such as iron-oxides, -hydroxides, and -sulphides), which expresses the dominance of magnetite. An AGICO Multi-function Kappabridge MFK1A was used to ascertain low-field susceptibility (κLF) (converted to mass-specific χ m^3kg^{-1}). Grain size distribution was estimated using several magnetic parameters, such as frequency-dependent susceptibility (κfd%) (Hanesch and Petersen, 1999; Dearing et al., 1996a) measured at five frequencies (475, 825, 1525, 2675, 4775) Hz using AGICO MFK1 Kappabridge, to identify domain state via grain sizes (Jordanova and Jordanova, 1999). An eight-sample holder from 2G Enterprises' 755 SRM long-core magnetometer was used to perform anhysteretic remanent magnetization (ARM) and normalized AF demagnetization curves of ARM. The ARM was applied along the z-axis of the samples using a 100 mT AF field and a 0.05 mT static field. The ARM was then represented as the susceptibility of ARM (χARM). A 2G Enterprises 660 pulse magnetizer was used to induce isothermal remanent magnetization (IRM), which was then measured using a Molyneux spinning magnetometer at two intensities, a backfield of 300 mT and 1000 mT, which is referred to as saturation isothermal remanent magnetization (SIRM). The S-ratio is calculated according to Bloemendal et al. (1992) equation, which is described as $\kappa fd(\%) = [(\kappa lf - \kappa hf) / \kappa lf] \times 100$. For pure hematite ($Fe_2O_3$), the S ratio is around 0; for both magnetite (Fe3O4) and

greigite (Fe3S4), it is around 1 (Rohrmüller et al., 2017). Using an AGICO Multi-function Kappabridge MFK1A, thermomagnetic analyses were carried out on bulk samples to measure low-field magnetic susceptibility versus temperature (κ–T curves) for determining the Curie temperature of magnetic minerals. Continuous measurements were performed from room temperature to 700 °C and back to room temperature using a Bartington furnace in free air (high temperature), and at low temperature using liquid nitrogen.

Heavy metal analyses

Scanning electron microscopy (SEM) and X-ray fluorescence (XRF) analyses were performed on selected samples to support the magnetic results. SEM was performed using a TESCAN MIRA3 SEM instrument. SEM can provide more details about fine grains and determine the mineralogy of the samples using SEM and energy dispersive X-ray (EDX) examinations to visualize the surface composition and shape of the extracted magnetic granules (Tamuntuan et al., 2015). XRF spectrometry was used to determine the concentration and source of the heavy metals in the study area (Oudeika et al., 2020). Concentrations (Al, Fe, Ca, Na, Si, Mg) of selected samples were measured. Heavy metal concentrations were measured using a Panalytical XRF System.

Results and Discussion

Magnetic Properties

Magnetic results are summarized in Table 1 and shown in Fig. 2. The Magnetic susceptibility of sediments is able to be employed for tracking pollutant sources. χ of sediment samples collected from the Euphrates River in Samawa City, Al Muthanna province, ranges at 2923.03×10^{-8} m^3kg^{-1} to 4039.29×10^{-8} m^3kg^{-1} with the mean value of 3361.23×10^{-8} m^3kg^{-1}. ARM and SIRM have similar distribution patterns; χ, $\chi_{ARM,}$ and SIRM displayed a similar trend with the mean values of 3361.23×10^{-8} m^3kg^{-1}, 628.98×10^{-8} m^3kg^{-1}, and 2952.60 Am^2kg^{-1}, respectively, indicating that ferromagnetic minerals are dominant.

Table 1: Magnetic parameters of sediments from the Euphrates River.

Magnetic parameters	$\chi \times10^{-8}$ [m^3/ kg^{-1}]	$\chi_{ARM} \times10^{-8}$ [m^3kg^{-1}]	SIRM [Am^2kg^{-1}]	K_{fd} [%]	S-ratio
Min.	2923.03	400.18	2390.90	0.35	0.96
Max.	4039.29	1354.12	5289.35	0.48	0.99
Mean	3361.23	628.98	2952.60	0.42	0.98
Median	3310.66	628.85	2918.06	0.42	0.98

The correlation between χ and χ_{ARM}, χ and SIRM is shown in Fig. 3. SIRM is more likely correlated with χ, with a correlation coefficient ($R^2 = 0.44$), while the correlation between χ_{ARM} and χ is less ($R^2 = 0.32$). The comparatively strong correlations show that ferrimagnetic minerals—such as magnetite and hematite—contribute more than paramagnetic minerals, such as biotite and pyrite (Sun et al., 1996).

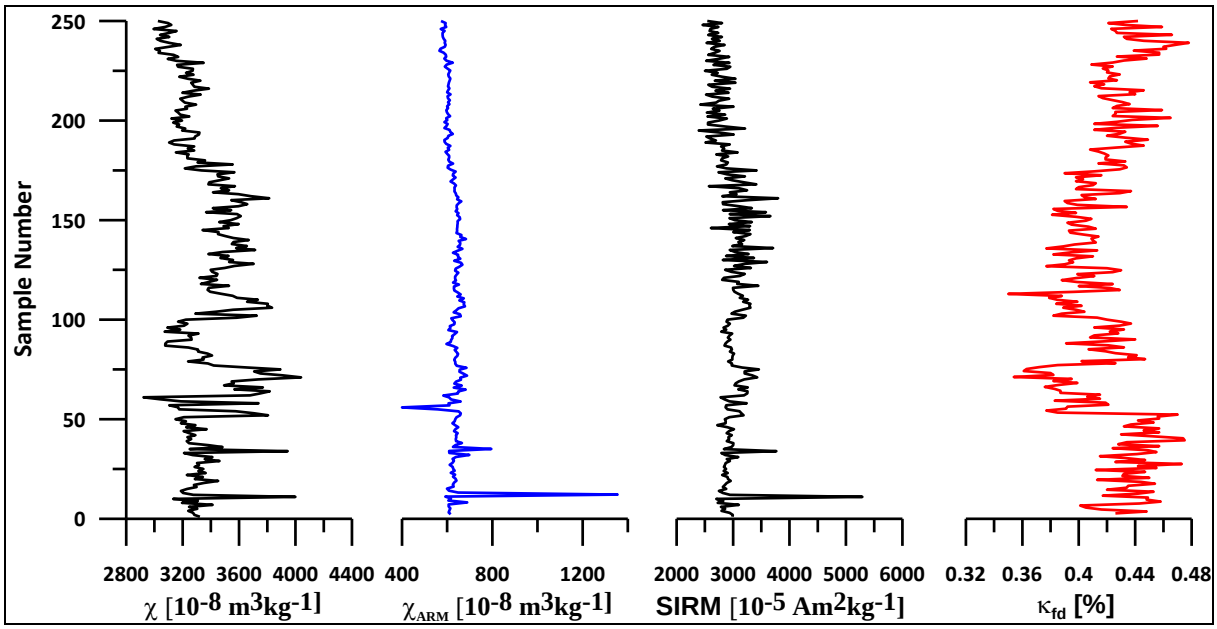


Fig. 2. Profiles of (A) mass-specific magnetic susceptibility; (B) anhysteretic susceptibility; (C) saturation isothermal remnant magnetization; (D) frequency-dependent susceptibility. All curves are versus the sample number.

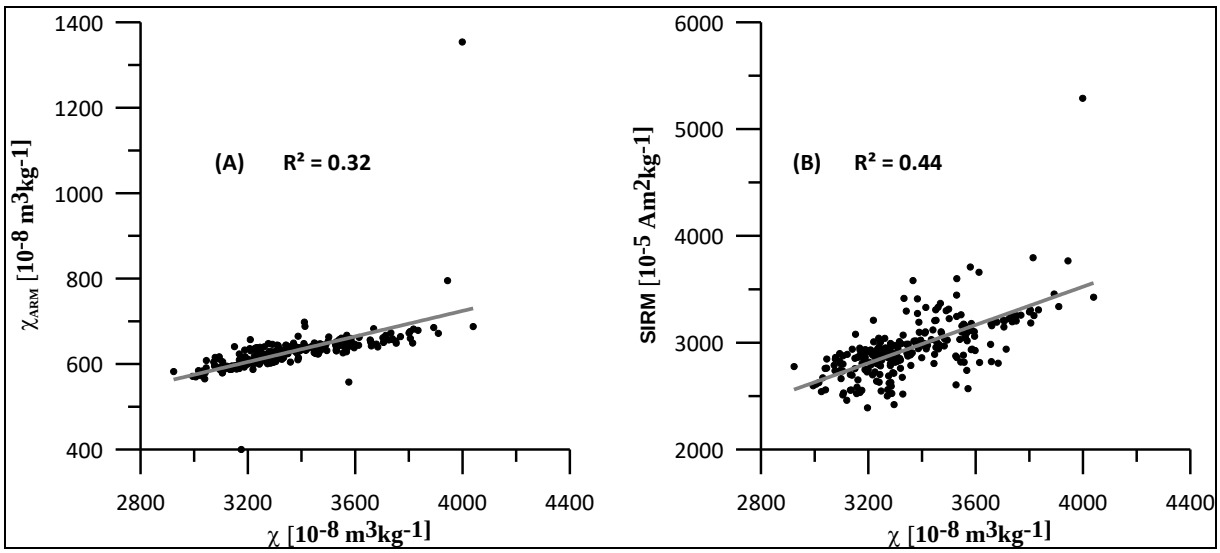


Fig. 3. Scatterplot of anhysteretic remnant magnetization and saturation isothermal remnant magnetization versus magnetic susceptibility.

Magnetic mineral grain size can be indicated by the values of χ_{ARM}/χ and SIRM/χ (Thompson and Oldfield, 1986; Evans and Heller, 2003). These ratios are frequently utilized in environmental magnetism for source identification and changes in grain size distribution as shown in Figure (4). The ratios of χ_{ARM}/χ and SIRM/χ drop as χ increases; in particular, the ratio ARM/χ exhibits a dramatic decline with increasing grain sizes and clearly defined maximum values for carriers of magnetite/maghemite in a single domain (0.03 μm). However, when magnetite grain sizes increase over 2 μm upwards, the ratio SIRM/χ progressively falls (Jordanova et al., 2014). S- ratio of sediments ranges from 0.96 to 0.99 with a mean value of 0.98 (Table 1), which indicates that soft magnetic minerals (magnetite) predominate in these samples (Shen et al., 2006). The percentage of frequency dependent susceptibility [κ_{fd}%] ranges at 0.35% to 0.48 % with a mean value of 0.42% (Table 1). As stated in Dearing et al. (1996 b), the samples with κ_{fd}% < 6% and χ_{lf} is > 0.5 × 10^{-6} m^3kg^{-1}, the sediments are most likely polluted sediments with stable-single domain (SSD) and multi-domain (MD) ferrimagnetic grains.

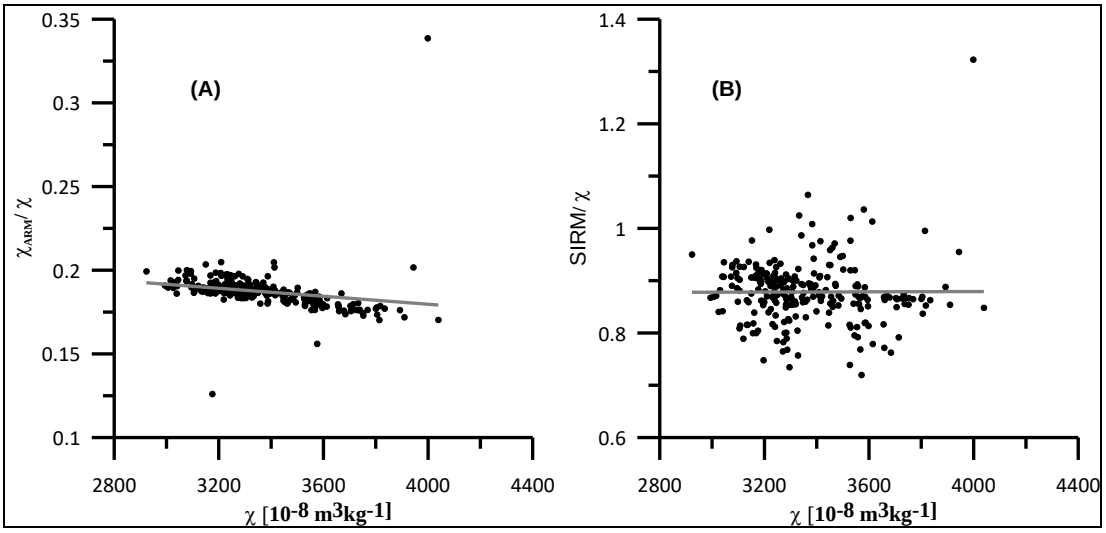


Fig. 4. Scatterplot of ratios χ_{ARM}/χ and SIRM/χ versus χ.

Temperature-dependent magnetic susceptibility measurements of selected sediment samples (κ-T) curves of low and high temperature are shown in Figure (5). Magnetic phases can be distinguished using high-temperature κ-T curves according to their Curie temperature or particularly the decomposition temperatures. High temperature-dependent magnetic susceptibility measurements can be used to identify the type of magnetic minerals based on their Curie temperature (Ju et al., 2004) as shown in Figure (5). During heating cycle, magnetic susceptibility would display a drop when reaching to 580 ºC, which represents the Curie temperature of magnetite, and reaching its baseline at around 580°C (Thompson and Oldfield, 1986) proving the presence of magnetite in the samples. According to Hu et al. (2008), heating could result in the formation of more magnetic minerals because the susceptibility increase during cooling cycle in comparison to heating cycle when the temperature lower than 500 ºC. The low temperature-dependent susceptibility (blue curves in Fig. 5) is a noticeable shift in susceptibility seen in all samples around -150 ºC, which obviously show 'Verway transition' indicating the existence of magnetite (King and Williams, 2000).

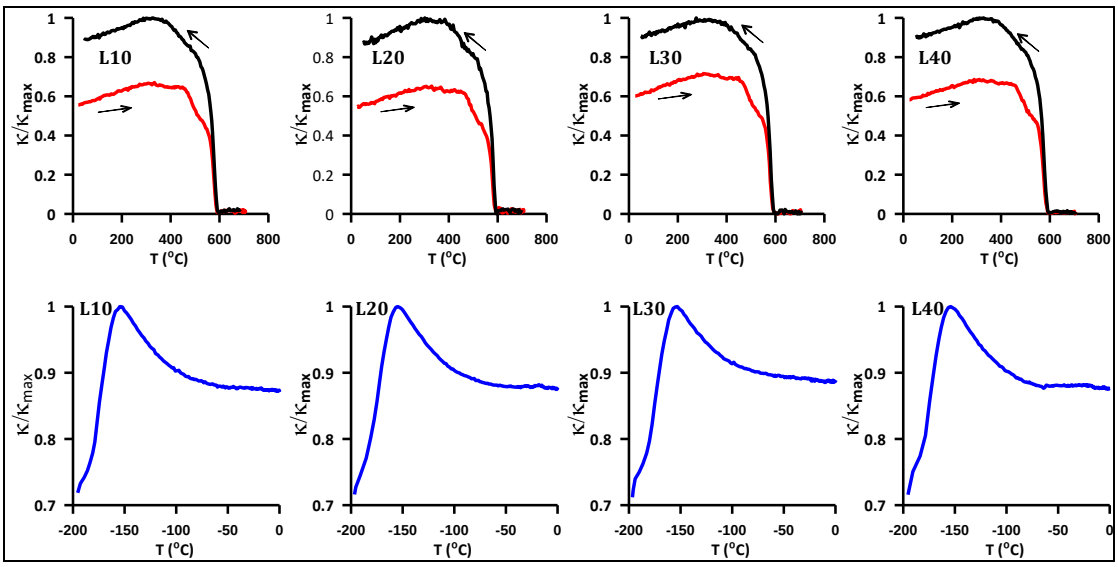


Fig. 5. Thermomagnetic analyses of selected sediment samples; the upper curves are for high temperature measurements; the red curve is for the heating cycle, and the black curve is for the cooling cycle; the lower curves are for low temperature measurements of the same samples.

Heavy metal (HM) analyses

Fig. 6 displays SEM pictures along with energy dispersive X-ray (EDX) analysis of particular samples. The X-ray indicates that the desired amount of Fe-minerals is present in Figure (6A, B), but seeing it in the image is difficult because of several issues. In contrast, Fig. 6C demonstrates the presence of a magnetic particle (spherical), indicating that the anthropogenic activities are the main source of the magnetic minerals.

Concentrations of Ca, Cr, Mg, Fe, Pb, and Na were measured using X-ray fluorescence (XRF). A correlation between χ and HM is shown in Fig. 7. χ exhibits a positive correlation with Ca, Cr, and Mg, with correlation coefficients of 0.3, 0.4, and 0.2, respectively, while the correlations of (Fe, Pb, and Na) are negative.

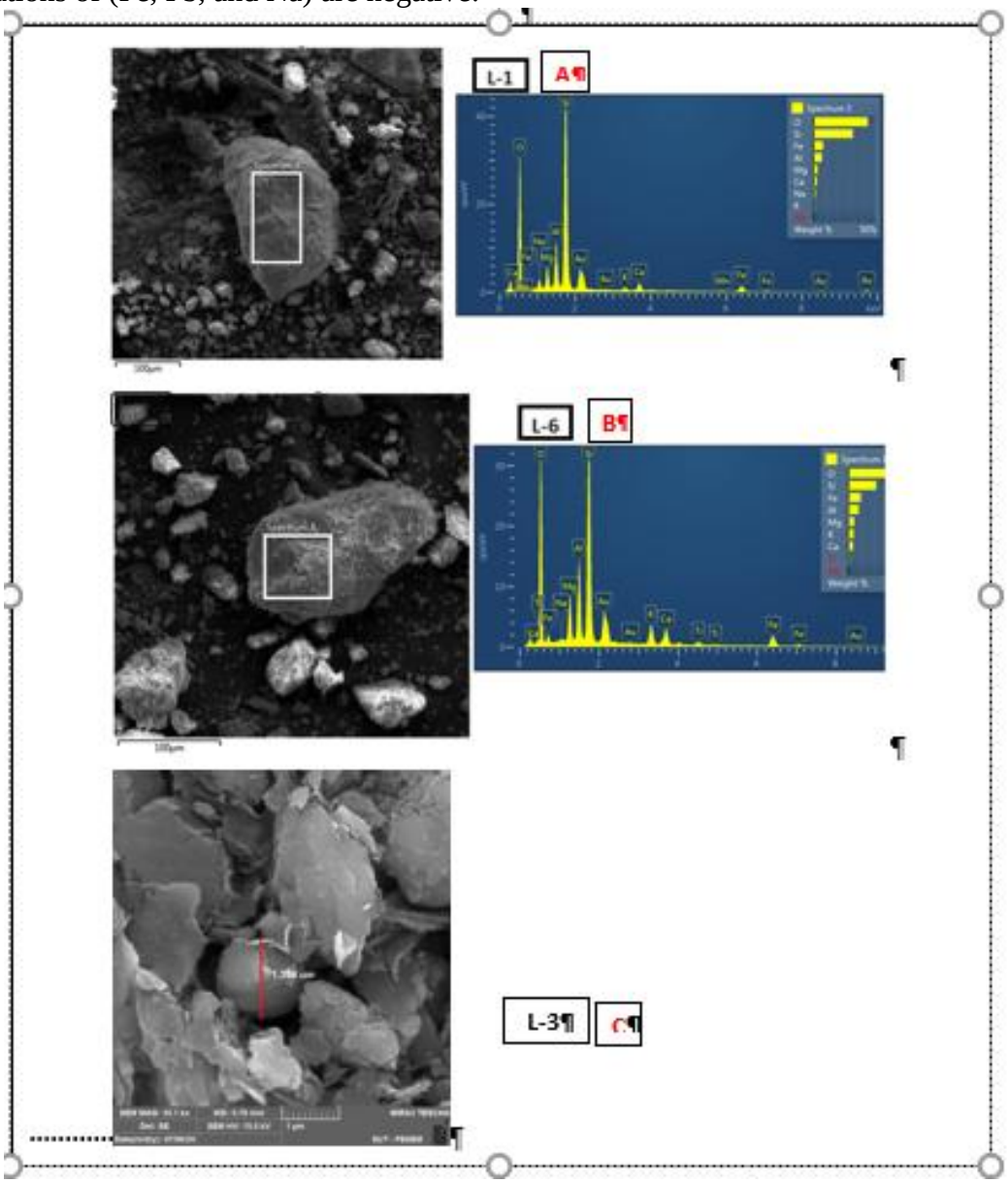


Fig. 6. Scanning Electron Microscopy images and energy dispersive X-ray analyses of selected samples: A (L1), B (L6), and C (L3) SEM micrographs showing a spherical magnetic particle of ~1.35 µm diameter.

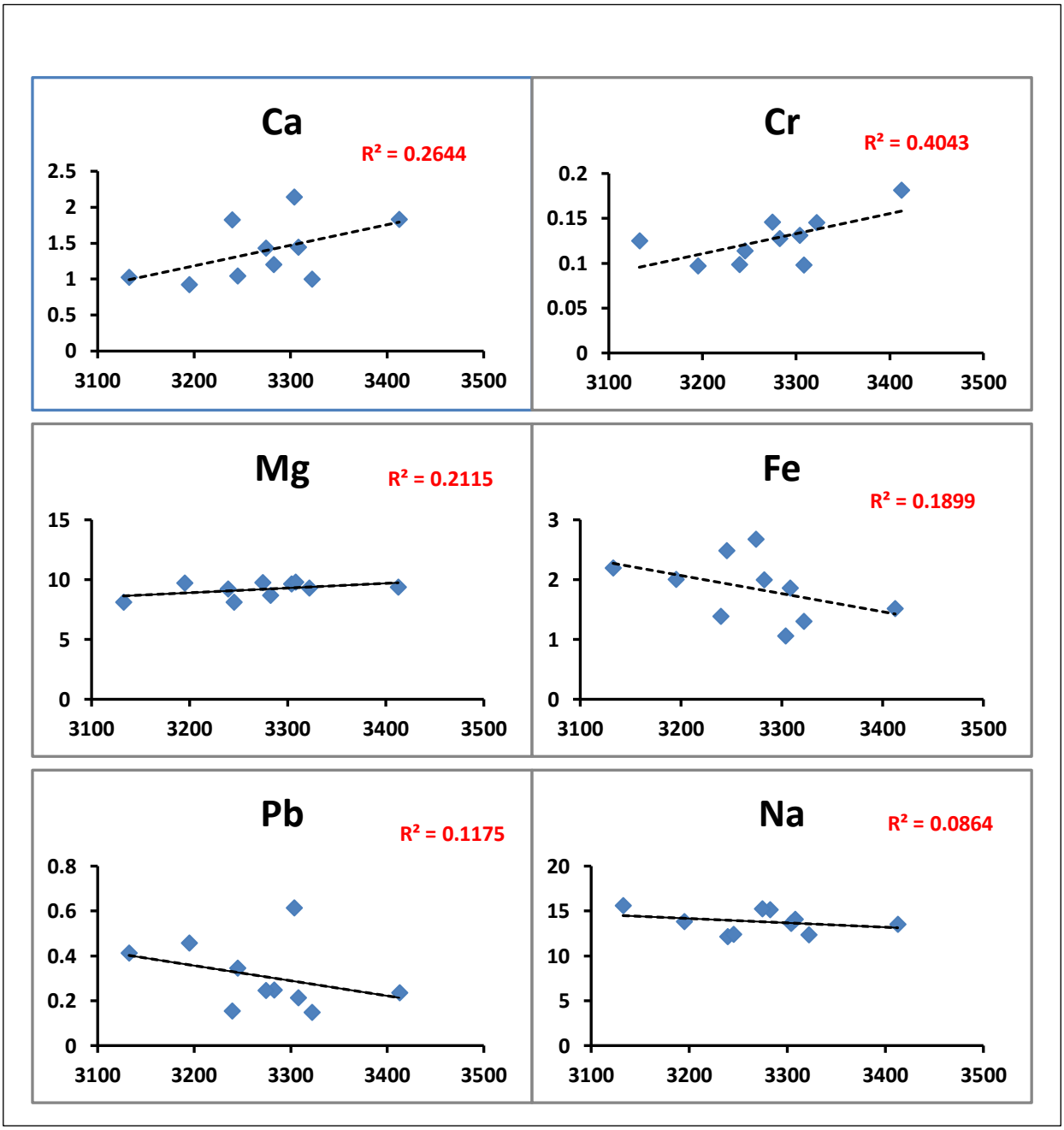


Fig. 7. Correlation of χ versus the heavy metals' concentrations of (Ca, Cr, Mg, Fe, Pb, and Na) in ppm of selected samples (L1-L10).

Conclusion

1. The concentration-dependent magnetic parameters (χ, χ_{ARM}, and SIRM) exhibit very high values. The correlation between these parameters suggests that ferrimagnetic minerals such as magnetite and hematite contribute significantly more than paramagnetic minerals.
2. 2. As χ grows, the ratios of χ_{ARM}/χ and SIRM/χ decrease. In particular, the ratio χ_{ARM}/χ shows a sharp decline with larger grain sizes and has maximum values that are well-defined for single-domain magnetite/maghemite carriers (0.03 μm). Furthermore, since the χ_{lf} is > 0.5 × 10^{-6} m^3 kg^{-1} and the κ_{fd}% < 6%. Dearing et al. (1996 b) stated that the sediments are most likely polluted with stable single-domain (SSD) and multi-domain (MD) ferrimagnetic grains.
3. Thermomagnetic measurements are of low temperature-dependent susceptibility for all samples, suggesting that susceptibility appears to transfer close to -150 ºC, clearly showing

the 'Verway transition', and indicating the existence of magnetite. High temperature is clearly shown to demonstrate the Curie temperature of magnetite (580 ℃).

4. Energy dispersive X-ray (EDX) and SEM studies of a subset of samples show the existence of a spherical magnetic particle, which suggests the effects of anthropogenic activities, and the appropriate concentration of ferrimagnetic minerals in the samples.
5. Correlation between χ and XRF analyses shows a positive correlation of χ with (Ca, Cr, and Mg), while a negative correlation between χ and (Fe, Pb, and Na).

Acknowledgements

The author would like to express gratitude to Dr. Norbert Nowaczyk from Helmholtz Centre Potsdam (GFZ), German Centre for Geoscience, Germany, for granting free entry to the magnetic laboratory and providing all the new techniques used for measurements.

Conflict of Interest

The author declares that there are no conflicts of interest regarding the publication of this manuscript.

References

Ameen, N., Rasheed, L. and Khwedim, K., 2019. Evaluation of Heavy Metal Accumulation in Sawa Lake Sediments, Southern Iraq Using Magnetic Study. Iraqi Journal of Science, Vol. 60, No. 4, pp. 781-791. http://doi.org/10.24996/ijs.2019.60.4.12.

Blaha, U., Appel, E. and Stanjek, H., 2008. Determination of Anthropogenic Boundary Depth in Industrially Polluted Soil and Semi-Quantification of Heavy Metal Loads Using Magnetic Susceptibility, Environmental pollution, Vol. 156, pp. 278–289, https://doi.org/10.1016/j.envpol.2008.02.013.

Bloemendal, J., King, J.W., Hall, F.R. and Doh, S.J., 1992. Rock Magnetism of Late Neogene and Pleistocene Deep-Sea Sediments: Relations to Sediment Source, Digenetic Process, and Sediment Lithology. Journal of Geophysical Research, Vol. 97, pp. 4361-4375. https://doi.org/10.1029/91JB03068.

Dearing, J.A., Dann, R.J.L., Hay, K., Lees, J.A., Loveland, P.J., Maher, B.A. and O'Grady, K., 1996a. Frequency-Dependent Susceptibility Measurements of Environmental Materials. Geophysical Journal International, Vol. 124, pp. 228–240. https://doi.org/10.1111/j.1365-246X.1996.tb06366.x.

Dearing, J.A., Hay, K.L., Baban, S.M.J., Huddleston, A.S., Wellington, E.M.H. and Loveland, P.J. 1996b. Magnetic Susceptibility of Soil: an Evaluation of Conflicting Theories Using a National Data Set. Geophysical Journal International, Vol. 127, pp. 728–734, 1996. https://doi.org/10.1111/j.1365-246X.1996.tb04051.x.

Desenfant, F., Petrovský, E. and Rochette, P., 2004. Magnetic Signature of Industrial Pollution of Stream Sediments and Correlation with Heavy Metals: Case Study from South France. Water, Air, and Soil Pollution, Vol. 152, pp. 297–312. https://doi.org/10.1023/B:WATE.0000015356.88243.f.

Evans, M.E. and Heller, F., 2003. Environmental Magnetism: Principles and Applications of Enviromagnetics, in: International Geophysics Series, Vol. 86, Academic Press, Amsterdam. https://doi.org/10.1144/1470-9236/04-103

Hanesch, M. and Petersen, N., 1999. Magnetic Properties of a Recent Parabrown-Earth from Southern Germany. Earth Planet. Science Letters, Vol. 169, pp. 85–97. https://doi.org/10.1016/S0012-821X%2899%2900076-X

Hu, S.Y., Duan, X.M., Shen, M.J., Blaha, U., Roesler, W., Yan, H.T., Appel, E., Hoffmann, V., 2008. Magnetic Response to Atmospheric Heavy Metal Pollution Recorded by Dust-Loaded Leaves in Shougang Industrial Area, Western Beijing. Chinese Science Bulletin, Vol. 53, No. 10, pp. 1555–1564. https://doi.org/10.1007/s11434-008-0140-9

Jordanova, D. and Jordanova, N., 1999. Magnetic Characteristics of Different Soil Types from Bulgaria. Studia Geophysica Et Geodaetica, Vol. 43, pp. 303–318. https://doi.org/10.1023/A:1023398728538.

Jordanova, D., Jordanova, N. and Petrov, P., 2014. Magnetic Susceptibility of Road Deposited Sediments at a National Scale – Relation to Population Size and Urban Pollution. Environmental Pollution, Vol. 189, pp. 239–251. https://doi.org/10.1016/j.envpol.2014.02.030.

Ju, Y.T., Wang, S.H., Zhang, Q., Wang, L.D., Deng, C.L., 2004. Mineral Magnetic Properties of Polluted Topsoils: a Case Study in Sanming City, Fujian Province, Southeast China. Chinese Journal of Geophysics, Vol. 47, No. 2, pp. 282–288. (in Chinese). http://www.geophy.cn/en/article/id/cjg_63?viewType=HTML

King, J.G. and Williams, W., 2000. Low-Temperature Magnetic Properties of Magnetite. Journal of Geophysical Research, Vol. 105, No. B7, pp. 16427–16436. https://doi.org/10.1029/2000JB900006.

Oudeika, M.S., Altinoglu, F.F., Akbay, F. and Aydin, A. 2020. The Use of Magnetic Susceptibility and Chemical Analysis Data for Characterizing Heavy Metal Contamination of Topsoil in Denizli City, Turkey. Journal of Applied Geophysics, Vol. 183, pp. 104208. https://doi.org/10.1016/j.jappgeo.2020.104208.

Perry, C. and Taylor, K., 2007. Environmental Sedimentology, Blackwell Publishing, Oxford. https://www.wiley.com/en-us/Environmental+Sedimentology-p-9781444309003

Rohrmüller, J., Kämpf, H., Geiß, E., Großmann, J., Grun, I., Mingram, J., Mrlina, J., Plessen, B., Stebich, M., Veress, C., Wendt, A. and Nowaczyk, N. 2017. Reconnaissance Study of an Inferred Quaternary Maar Structure in the Western Part of the Bohemian Massif Near Neualbenreuth, NE-Bavaria (Germany). International Journal of Earth Sciences. https://doi.org/10.1007/s00531-017-1543-0

Shen, M., Hu, S., Blaha, U., Yan, H.T. and Hoffmann, V., 2006. A Magnetic Study of a Polluted Soil Profile at the Shijingshan Industrial Area, Western Beijing, China. Chinese Journal of Geophysics, Vol. 49, No. 6, pp.1665–1673. (in Chinese). https://doi.org/10.1002/cjg2.980

Sissakian, V.K. and Al-Ansari, N., 2019. Geography, Geomorphology, Stratigraphy and Tectonics of the Euphrates River Basin. Journal of Earth Sciences and Geotechnical Engineering, Vol. 9, No. 4, pp. 315-337.

Sissakiana, V.K., Al-Ansari, N. and Adamoc, N., 2021. Geomorphology, Stratigraphy and Tectonics of the Mesopotamian Plain, Iraq: A Critical Review. *Geotectonics*, 2021, Vol. 55, No. 1, pp. 135–160.

Sudarningsih, S., Pratama, A., Bijaksana, S., Fahruddin, F., Zanuddin, A., Salim, A., Abdillah, H., Rusnadi M. and Mariyanto, M., 2023. Magnetic Susceptibility and Heavy Metal Contents in Sediments of Riam Kiwa, Riam Kanan and Martapura Rivers, Kalimantan Selatan Province, Indonesia. Heliyon, Vol. 9, Issue 6, e16425. ISSN 2405-8440, https://doi.org/10.1016/j.heliyon.2023.e16425.

Sun, Z., Hu, S. and Ma, X., 1996. A Rock-Magnetic Study of Recent Lake Sediments and its Palaeoenvironmental Implication. Acta Geophysica Sinica, Vol. 39, No. 2, pp. 178–187. (in Chinese). http://www.geophy.cn/en/article/id/cjg_4077

Tamuntuan, G., Bijaksana, S., King, J., Russell, J., Fauzi, U., Maryunani, K., Aufa, N. and Safiuddin, L.O., 2015. Variation of Magnetic Properties in Sediments from Lake Towuti, Indonesia, and its Paleoclimatic Significance. Palaeogeography, Palaeoclimatology, Palaeoecology, Vol. 420, pp. 163-172. https://doi.org/10.1016/j.palaeo.2014.12.008.

Thompson, R. and Oldfield, F., 1986. Environmental Magnetism. London: Allen and Unwin, Winchester, Mass., pp. 1–227. https://doi.org/10.1007/978-94-011-8036-8

Iraqi National Journal of Earth Science

www.earth.uomosul.edu.iq

Engineering Site Investigation Using 2D Electrical Resistivity Imaging, K3 Area, Western Anbar Governorate

Sameer Sh. Abbas [1*]

[1]*Anbar Education Directorate, Ministry of Education, Ramadi, Iraq.*

Article information

Received: 14- Oct -2024

Revised: 12- Dec -2024

Accepted: 15- Jan -2025

Available online: 01- Jan -2026

Keywords:
K3 Residential Complex, Sinkhole, Engineering Site Investigation, Weak Zones, Resistivity survey, Anbar Governorate.

Correspondence:
Name: Sameer Sh. Abbas

Email: sameershaker69@gmail.com

ABSTRACT

Subsurface cavities and weak zones have a significant influence on the long-term feasibility of infrastructure and buildings; these problems must be considered before beginning construction of buildings and town decisions. Assessing the hazard associated with these cavities requires a greater understanding of the complex behavior of the karst structure, which is best developed in a region that absences indicators on the ground surface. This study investigates the subsurface characteristics in the K3 region using 2D electrical resistivity imaging (ERI) to recognize and describe underground structures. The data acquisition has been conducted manually along four 2D traverses, each 97 m long, using a dipole-dipole array with 20 electrodes spaced at 5 m apart. The data are processed using the RES2DINV software with a robust method to generate a 2D resistivity model. The results show distinct high-resistivity anomalies; these are suggestive of several cavities with a variety of depths from 3 to 15 m below the surface, with a width of 35 m. Also, several subsurface weak zones reveal that they are more severe at depths of 1.25-5 m below the ground surface. These zones associated with subterranean channels, cavities or sinkholes lead to issues with new construction and potential foundation subsidence. The investigation successfully charted the spatial distribution, depth, and approximate size of the detected cavities and weak areas. These findings have crucial importance to the assessment of geotechnical risk and urban planning in the K3 region; the efficacy of 2D ERI in the detection of subsurface structures is demonstrated.

DOI: 10.33899/injes.v26i1.60185, ©Authors, 2026, College of Science, University of Mosul.
This is an open-access article under the CC BY 4.0 license (http://creativecommons.org/licenses/by/4.0/) .

استخدام تصوير المقاومة النوعية الكهربائية ثنائية الابعاد للتحري الهندسي الموقعي في منطقة K3، غربي محافظة الانبار

سمير شاكر عباس[1] *

[1]مديرية تربية الانبار، وزارة التربية، الرمادي، العراق.

معلومات الارشفة

تاريخ الاستلام: 14- اكتوبر-2024

تاريخ المراجعة: 12- ديسمبر-2024

تاريخ القبول: 15- يناير-2025

تاريخ النشر الالكتروني: 01- يناير-2026

الكلمات المفتاحية:

مجمع كثري السكني،
التخسفات،
تحريات هندسية موقعية،
مناطق الضعف،
مسح المقاومة النوعية،
محافظة الانبار،

المراسلة:

الاسم: سمير شاكر عباس
Email; sameershaker69@gmail.com

الملخص

التكهفات تحت السطحية والمناطق الضعيفة لها تأثير كبير على الاستدامة طويلة الأجل للبنية التحتية والمباني، ويجب تقييم هذه القضايا قبل البدء في بناء وتخطيط المدن. تقييم الخطر المرتبط بهذه الكهوف يتطلب فهمًا أعمق للسلوك المعقد لنظام الكارست، والذي يتم تطويره بشكل أفضل في منطقة تفتقر إلى المؤشرات على السطح. يهدف هذا البحث إلى التحقيق في ظروف ما تحت الأرض في منطقة K3، باستخدام التصوير بالمقاومة الكهربائية ثنائية الأبعاد (ERI) لتحديد ووصف ميزات ما تحت الأرض. تم جمع البيانات يدويًا على طول أربعة مسارات ثنائية الأبعاد، كل منها بطول 97 مترًا، باستخدام ترتيب ثنائي القطب- ثنائي القطب مع 20 قطبًا، والمسافة بين الأقطاب تبلغ 5 أمتار. تمت معالجة البيانات باستخدام برنامج RES2DINV مع طريقة روبوست لإنتاج مقاطع عرضية ثنائية الأبعاد للمقاومة النوعية. أظهرت النتائج شذوذات مقاومة عالية مميزة تشير إلى وجود العديد من التجاويف بعمق يتراوح ما بين 3 و 15 مترًا متصلة بالسطح بعرض 35 مترًا. بالإضافة إلى ذلك، تم الكشف عن عدة مناطق ضعيفة تحت السطح تكون أكثر حدة على أعماق تتراوح ما بين 1.25 و 5 أمتار تحت سطح الأرض، وهذه المناطق مرتبطة بالقنوات الجوفية أو الكهوف أو الفجوات، مما يؤدي إلى مشاكل في المشاريع الجديد واحتمالية هبوط الأساسات. نجح التحري في رسم التوزيع المكاني والعمق والحجم التقريبي للتجاويف والمناطق الضعيفة المكتشفة. هذه النتائج لها أهمية حاسمة لتقييم المخاطر الجيوتكنيكية والتخطيط الحضري في منطقة K3، وتظهر فعالية التصوير بالمقاومة النوعية الكهربائية ثنائية الأبعاد في الكشف عن التراكيب تحت السطحية.

DOI: 10.33899/injes.v26i1.60185, ©Authors, 2026, College of Science, University of Mosul.
This is an open-access article under the CC BY 4.0 license (http://creativecommons.org/licenses/by/4.0/) .

Introduction

Engineering site investigations play a crucial role in assessing the ground conditions and determining avoid risks that may be encountered on an infrastructure project. This is important, especially in the K3 region, where the structures are mostly made of carbonate rocks (limestone and dolomite). These carbonate formations are particularly sensitive to chemical weathering as well as dissolution, which causes the evolution of karst features as subsurface cavities, sinkholes, and other types of voids (Sissakian and Al-Mousawi, 2007). Such features can pose a severe danger to the construction of buildings and engineering projects, human life, and the solidity of the ground, since the failure of these voids may cause ground subsidence and the sudden formation of sinkholes. Additional human involvement in the form of building and exploiting natural resources has increased the frequency of subsidence and sinkhole development (Gutierrez et al., 2008). In site investigation, geophysical techniques, including 2D Electrical Resistivity Imaging (ERI) procedures, are used more often to identify these hazards. 2D ERI is a geophysical method used for imaging the subsurface dependent on variations in electrical resistivity (Zhou et al., 2002; Chalikakis et al., 2011; Metwaly and Alfouzan, 2013; Abbas et al., 2024a). This

technique is useful in detecting underground features such as voids, cracks, water-saturated areas, weak areas, and layers of gypsum soil (Abdulrazzaq et al., 2020; Salman et al., 2020; Al-Jumaily et al., 2022). 2D ERI offers a clear image with great resolution to determine underground features and the suitability for building (Loke, 2004; Al-Saady et al., 2022; Elawadi, 2001). Also, this procedure is very useful in evaluating the possible subsidence or collapse risks, which are dangerous in planning for infrastructure and hazards (Ahmed et al., 2022; Abbas et al., 2024b). ERI provides a broader identification of such structures that are localized, which depends on a more continuous view of the ground conditions (Van Schoor, 2002; Dahlin, 2001). Many studies explained the efficiency of 2D ERI in several geohazard assessments (Berhi and Al-Saadi, 2024; Al-Awsi and Abdulrazzaq, 2022; Abed et al., 2021).

This study aims to determine subsurface geology, the location and extent of karst features, and evaluate their potential effects on safe engineering and construction projects using two-dimensional electrical resistivity imaging.

Location of the Study Area

The studied area is located in the K3 area between Baghdadi and Haditha districts within Anbar Governorate, about 177 Km west of Ramadi City (Fig. 1). It is located in the western part of Iraq along the Euphrates River. The topographic elevation of the K3 area is about 175 meters above sea level. It is mostly flat with undulations and occasional escarpments, which have been built through layers of sedimentary rocks. Geologically, the studied area includes the Anah Formation and Euphrates Formation (Fig. 2). The Anah Formation (Late Oligocene–Early Miocene) is represented by hard recrystallized reefal limestone rocks, which are overlained by white porous limestone rocks at the top, having a thickness of about 7 m (Al-Ghreri, 2007). The base of the formation in the area is conformable, while the top contact is always of an angular unconformity with the Euphrates Formation. Euphrates Formation (Early Miocene - Middle Miocene) comprises a basal conglomerate fining upward with 3 m thick, besides the layers of oolitic limestone, dolomitic limestone in the upper part with 18 m thick (Al-Ghreri, 2007; Alrawi et al., 2023). The Formation is sitting unconformably above Oligocene layers by the basal conglomerate with a thickness ranging between 1 to 5 m. These conglomerates are composed of pebbles that originated predominantly from the Anah Formation (Al-Ghreri, 2007).

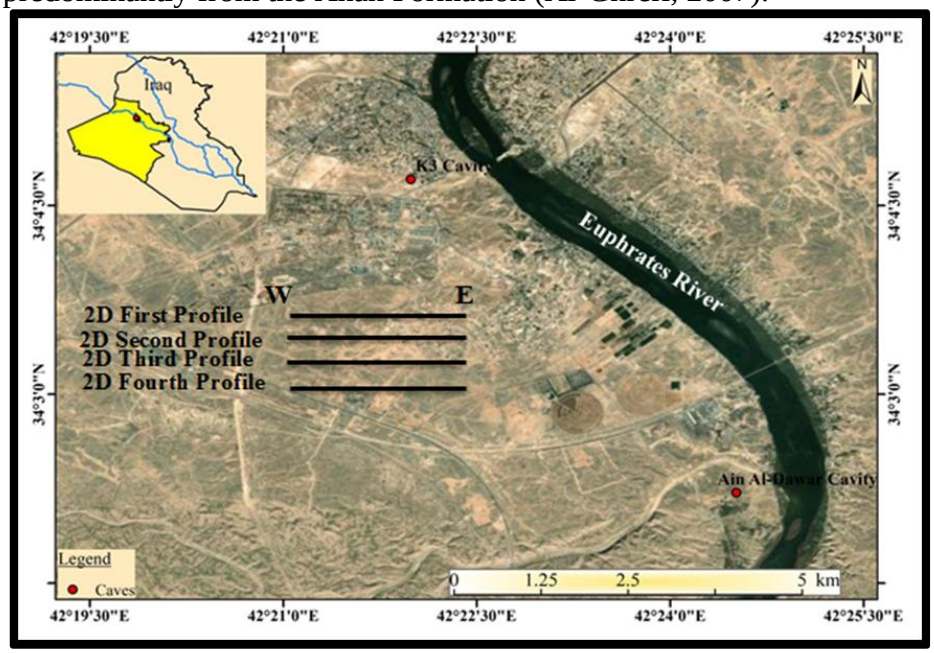


Fig. 1. Location of the studied site with a 2D resistivity profile survey.

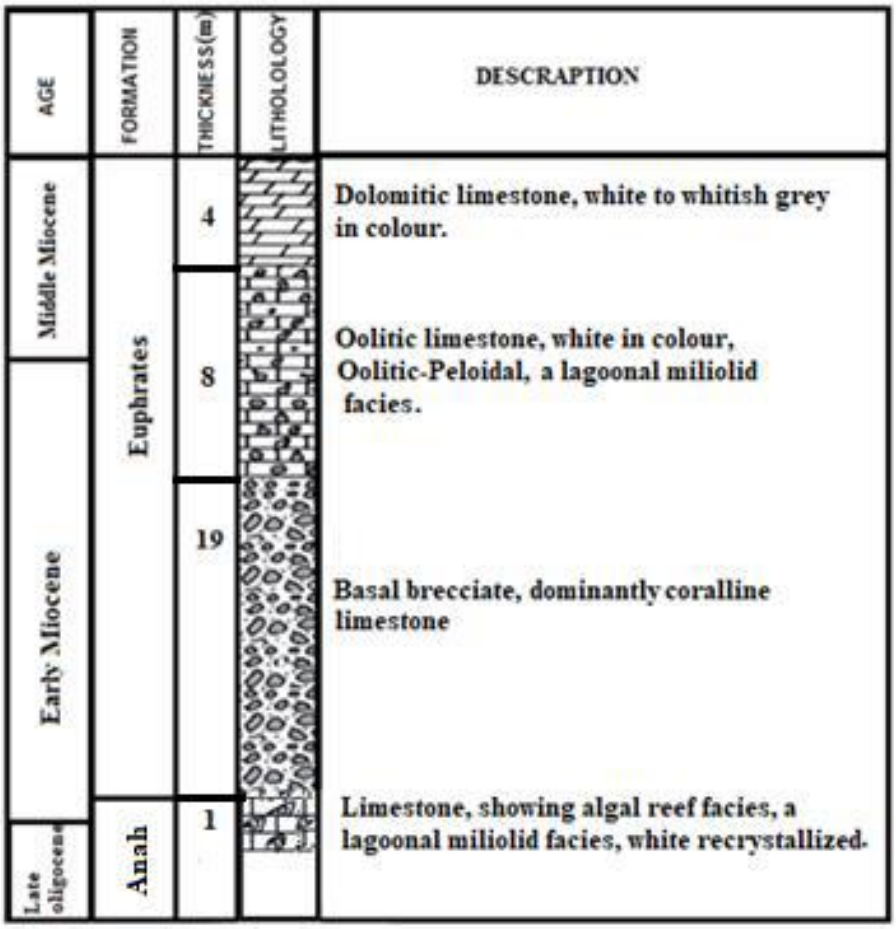


Fig 2. Stratigraphic column of the studied site (Al-Jibouri et al., 2022).

Materials and Methods

A 2D electrical resistivity imaging survey has been conducted using ABEM Terrameter SAS 4000 to delineate the subsurface condition of the studied area. Field resistivity data were acquired using four 2D imaging profiles with a dipole-dipole array (Fig. 3). The 2D resistivity data are manually created and oriented in the W-E direction. Where the number of electrodes, spacing, the distance between profiles, and n-factor are 20, 3, 15, and 6, respectively. The profile's survey depth is estimated at 19.58 m with a 97 m. These profiles were generated using the Electra Pro program. The resistivity measurements were used to construct the pseudo-section to provide a 2D image of the subsurface, and the data processing was performed using the RES2DINV program. The inversion routine is based on the smoothness-constrained least squares method using finite difference forward modeling and Quasi-Newtonian techniques (Loke et al., 2003). In these methods, the subsurface is segmented into a set of dimensional blocks, where cell size increases with depth (Fig. 4). Inversion procedures use numerical techniques to generate a subsurface resistivity model that best fits the available data set. The conventional least-squares optimization method is often used in inversion algorithms to solve the non-uniqueness problem in order to construct a good 2D inverse model to which the data should be homogeneous (Loke and Dahlin, 2002).

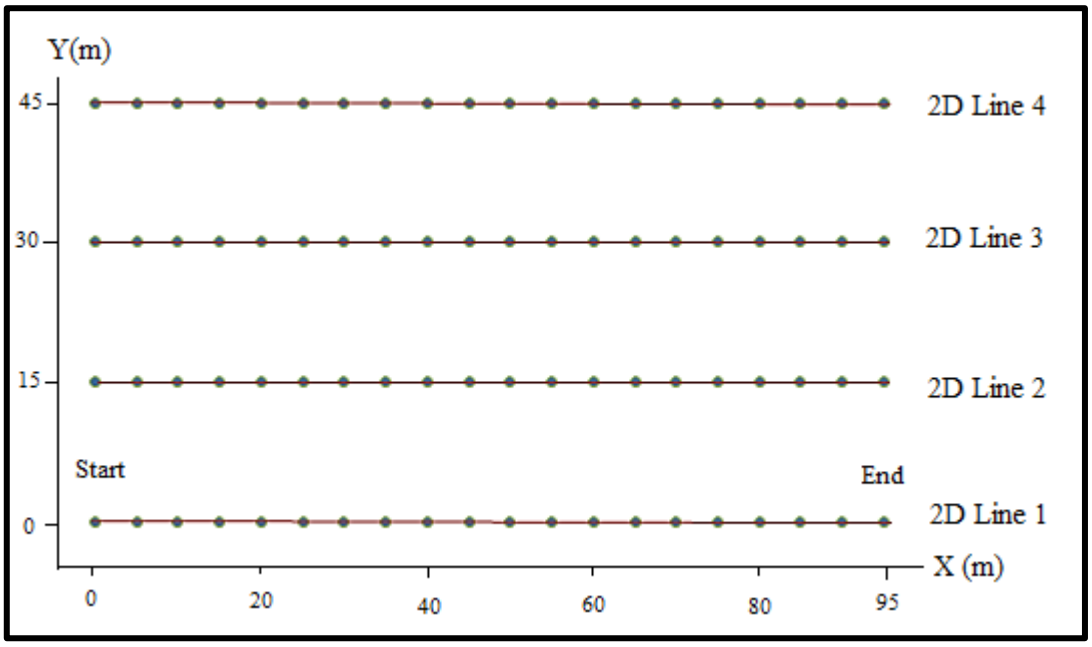


Fig 3. Four 2D imaging profiles were surveyed using a dipole-dipole array in the studied area.

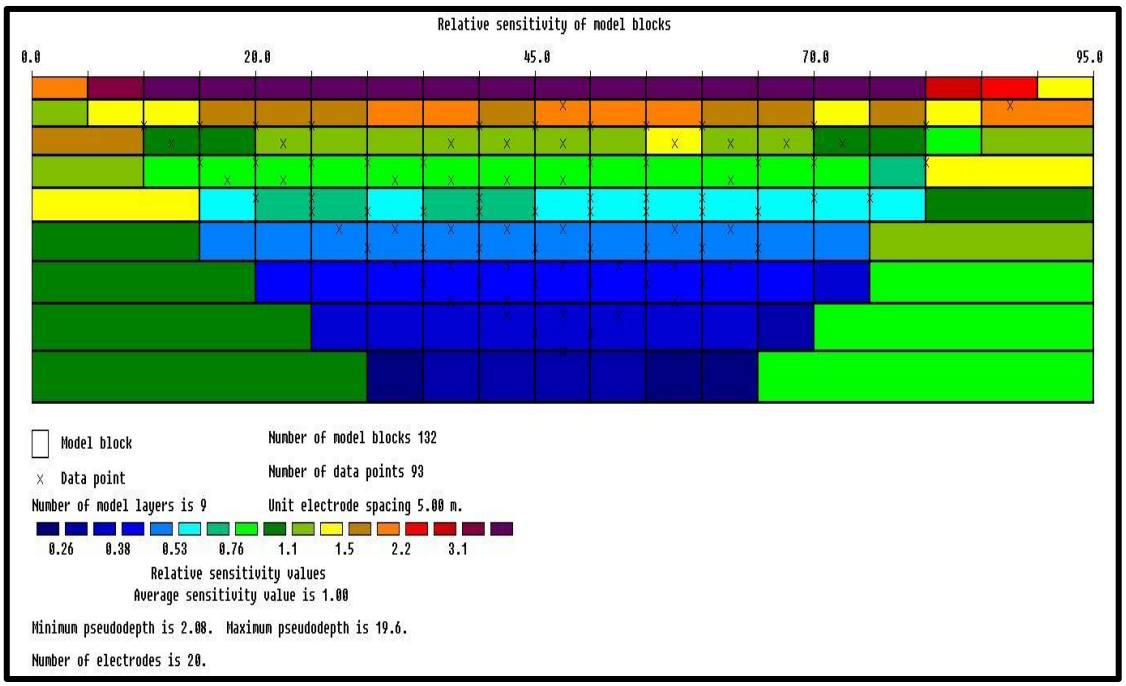


Fig 4. 2D block of subsurface studied area in profile- 2.

Results and Discussion

The first model (Fig. 5) represents a weathering zone near the earth's surface characterized by a lower resistivity value of 20.4 Ω.m. This low resistivity is due to increased water content. Areas of high resistivity values ranging from 145 to 527 Ω.m indicate the presence of voids or cavities within the subsurface. The first cavity is located to the left of the survey line and has high resistivity values ranging from 145 to 275 Ω.m. This cavity starts at a depth of about 3 m and extends to about 11 m below the surface. A larger cavity is present on the right side of the survey line, approximately 60 m to 85 m away from the starting point. This cavity extends to a depth of approximately 10 m. The high resistivity values within the cavity may be relatively dry, which has a higher resistivity than the surrounding rocks. There are some small caves in the middle of the survey line with irregular shapes and boundaries.

The limits of caves are more obvious on the left side, indicating that the voids are more distinct or better defined than those on the right side.

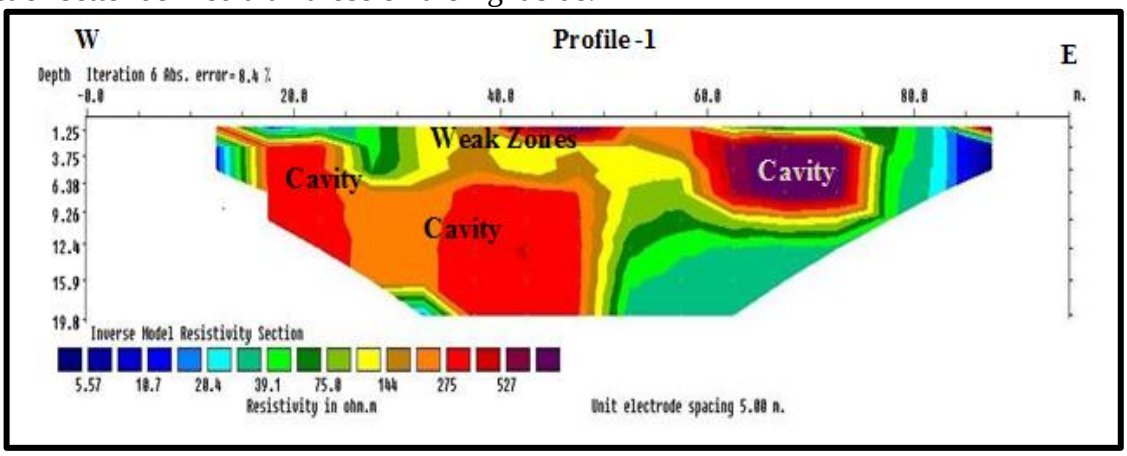


Fig 5. 2D resistivity inverted model for the first profile.

The second model (Fig. 6) reveals the presence of multiple subsurface cavities and a shallow weak zone characterized by varying degrees of resistivity. The areas in the left model exhibit high resistivity values ranging from 145 to 454 Ω.m at distances between 12-28 m and a depth of 3 -11 m, which may represent a dry cavity or a sediment-filled cavity. In the middle section of the model, there are variable resistivity values at distances of 38-55 m and a depth of 5- 15 m. These variations are interpreted as indicative of a cavity. The right side of the model shows a very high resistivity value at a distance between 60- 85 m with a depth extension of approximately 16 m. These extreme values represent a major cavity. Areas along the model with small low resistivity values are interpreted as small caves or voids, while areas with very low resistivity values are indicative of a weathered zone due to an increase in moisture content within the rocks.

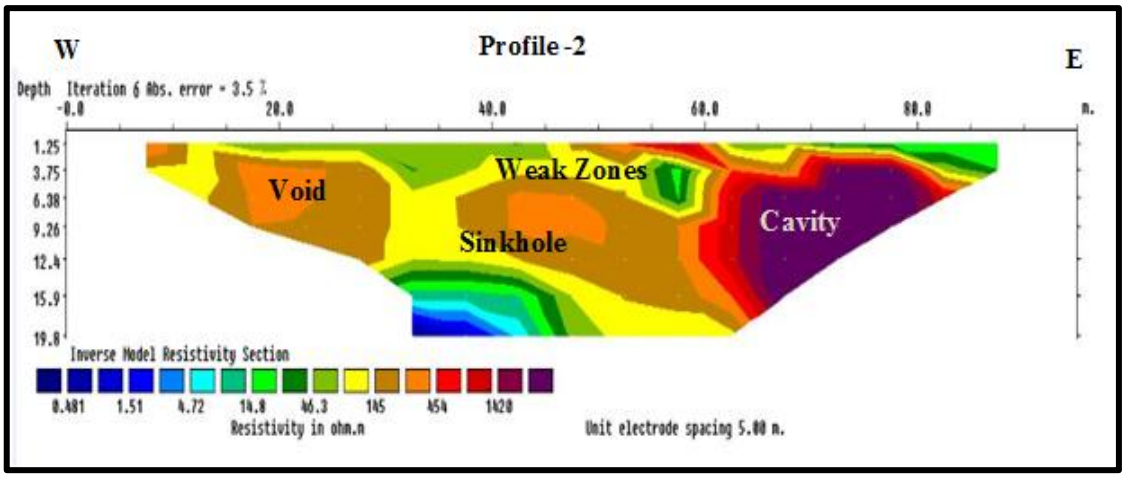


Fig 6. 2D resistivity inverted model for the second profile.

The third model (Fig. 7) indicates three main cavities. The first cavity is located on the left side of the model, recognized by a high resistivity value of 187 Ω.m. This cavity appears at a distance between 13 to 24 m and a depth of 2- 7 m. A second cavity is located in the middle section at a distance of 48- 58 m and a depth of 6 to 16 m. The last cave is found on the right side of the model, with a very high resistivity value of 389 Ω.m. It is located at a distance of 60 m to 83 m with a depth ranging from 3 to 10 m. Also, the model shows numerous weathered zones and voids on both right and left sides of the main cavities. These areas exhibit low resistivity values ranging from 0.606 Ω.m and 2.21 Ω.m.

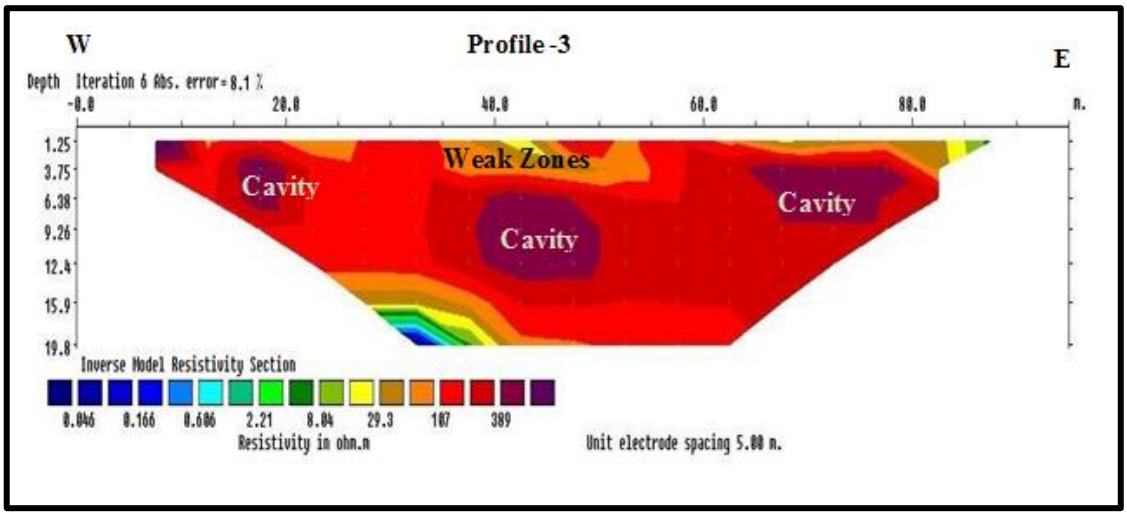


Fig 7. 2D resistivity inverted model for the third profile.

The fourth model (Fig. 8) displays two near-surface caves that are distributed over the left and right sides of the model. These caves are distinguished by high resistivity values that are greater than 345 Ω.m. It is located at distances 12-40 m and 55-82 m, respectively, with a depth of 4-16 m and 3-14 m, respectively. There are greater dangers in the meters study area for new construction stretches to a depth of about twelve meters. Resistivity begins to decrease beyond this depth.

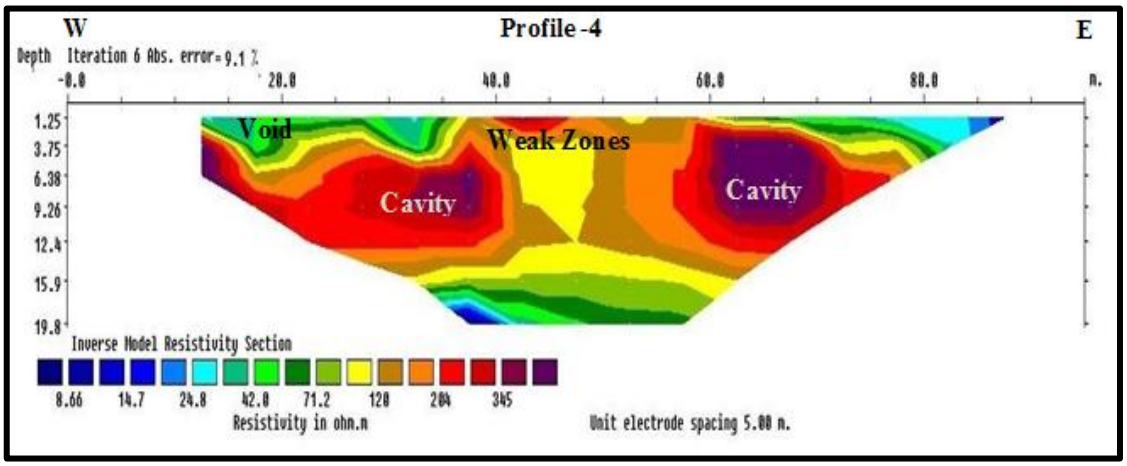


Fig. 8. 2D resistivity inverted model for the fourth profile.

Conclusion

The engineering site exploration using 2D electrical resistivity imaging has considered important findings relevant to geotechnical assessments. The studied area comprises predominantly limestone, which has an excessive increase in activity. Exploring the depth of the shallow weak zones and imaging the risk of subsurface cavities are important procedures before building and surface foundation structure. The study effectively detects differences in resistivity, which is representative of the presence of possible cavities, weak areas, voids, and cracks within the Euphrates Formation that pose risk areas for building and the safety of the structure. All 2D models suggest substantial anomalies as markers for these cavities, with several depths documented below the surface, starting from 3 m and extending down to more than 15 m. Additionally, various subsurface weak areas and cracks are designated through low and intermediate resistivity values, representative potential areas of instability. These regions are recognized to be more obvious at depths between 1.25 m and 5 m below the surface, suggesting complex geological settings that may include dissolution developments through groundwater movement. The description of underground cavity and weak zones

emphasizes areas that may comprise risks to structural integrity and require more research using geotechnical assessment.

Acknowledgements

The author would like to thank Mr. Mustafa Jumah and Mr. Saad Jumah for their valuable help in the fieldwork of this research. Also, thanks are extended to Mr. Aseel Mohamed for providing geological data of the studied area, which is essential to complete the research.

References

Abbas, S.S., Al-Saady, H.A. and Al-Mahemmdi, W.D., 2024a. An Attempt to Delineate Subsurface Ain Aldawar Cavity Using 2D Electrical Resistivity Imaging Method in Haditha Area, Western Iraq. The Iraqi Geological Journal, 57 (1F), pp. 47-52. https://doi.org/10.46717/igj.57.1F.4ms-2024-6-13

Abbas, S.S., Al-Mahemmdi, W.D. and Al-Saady, H.A., 2024b. Caves and Fractured Zones Investigation Using 2D Electrical Resistivity Imaging in an Engineering Site, Haqlaniyah, Western Iraq. The Iraqi Geological Journal, 57 (2E), pp. 33-40. https://doi.org/10.46717/igj.57.2E.3ms-2024-11-12

Abdulrazzaq, Z.T., Al-Zubedi, A.S. and Abed, A.M., 2020. Detected of gypsum soil layer by using 2d and 3d electrical resistivity imaging techniques in University of Anbar, Iraq. The Iraqi Geological Journal, 53(2C), pp. 134-144. http:// dx.doi.org/ 10.46717 /igj. 53.2c. 10Rs-2020.09.10

Abed, A.M., Thabit, J.M. and Al-Menshed, F.H., 2021. An attempt to image Um El-Adam cavity structure in the karst terrain at hit area, Western Iraq. The Iraqi Geological Journal, 54(1A), pp. 44-54. https://doi.org/10.46717/igj.54.1A.5Ms-2021-01-26

Ahmed, M.M., Abbas, S.S., Abed, A.M. and Al-Menshed, F.H., 2022. Application of 2D and 3D Electrical Resistivity Imaging Techniques for Site Investigation in Ramadi City, Western Iraq. IOP Conference Series: Earth and Environmental Science, IOP Publishing, 1080 (1), 012011. https://doi.org/10.1088/1755-1315/1080/1/012011

Al-Awsi, M.D. and Abdulrazzaq, Z.T., 2022. Implementing electrical resistivity tomography to delineate soil contamination zone, Southern Baqubah City, Iraq. Kuwait Journal of Science, 49(2), pp. 1-15. https://doi.org/ 10.48129/kjs.10674

Al-Ghreri, M., 2007. Biostratigraphic succession of the formations of Euphrates Valley between Hit and Al-Qaim in Iraq. 121 P.

Al-Jibouri, A.S., Al-Halboosi, J.M.H. and Abed, A.M., 2022. Detection of Haqlaniyah cave within carbonate stratigraphic sequence rocks using 2D resistivity imaging technique, Haditha, western Iraq. IOP Conference Series: Earth and Environmental Science. IOP Publishing, 1080 (1), 012017. http://dx.doi.org/10.1088/1755-1315/1080/1/012017

Al-Jumaily, O.H., Abed, A.M. and Ali, K.K., 2022. Detection of Shallow Cavities Using 3D Resistivity Technique in a Small Site Near Haditha City, Western Iraq. Iraqi Journal of Science, 63(4), pp. 1557-1564. https://doi.org/10.24996/ijs.2022.63.4.16

Al-Saady, H.A., Karim, H.H. and Al-Menshed, F.H., 2022. Comparison of Three Electrical Resistivity Arrays to Investigate Weak Zones in Soil, Along a Profile Southeast Baghdad City, Iraq. Iraqi Journal of Science, 63(11), pp. 4793-4798. https://doi.org /10.24996/ijs.2022.63.11.18

Alrawi, S.S., Kadhim, L.S. and Al-Hadaithy, A.A., 2023. Mineralogy and Geochemistry of Anah and Euphrates Formations and Their Suitability for Portland Cement and Noora Industry at Al-Baghdadi and Haditha Areas, Western Iraq. The Iraqi Geological Journal, 56(2D), pp. 177-186. https://doi.org/10.46717/igj.56.2D.14ms-2023-10-20

Berhi, F.Z. and Al-Saadi, O.S., 2024. Electrical Resistivity Synthetic Modeling and Field Survey for Subsurface Features Investigation of the Borsippa Archaeological Site, Babylon Governorate, Middle Iraq. The Iraqi Geological Journal, 57 (1F), pp. 33-46. https://doi.org/10.46717/igj.57.1F.3ms-2024-6-12

Chalikakis, K., Plagnesl, V., Guerin, R., Valois, R. and Bosch, F.P., 2011. Contribution of geophysical methods to karst-system exploration: an overview. Hydrogeology Journal, 19(6), pp. 1169-1180. https://doi.org/10.1007/s10040-011-0746-x

Dahlin, T., 2001. The development of DC resistivity imaging techniques. Computers and Geosciences, 27(9), pp. 1019-1029. https://doi.org/10.1016/S0098-3004(00)00160-6

Elawadi, E., 2001. Detection of Cavities Using Pole-Dipole Resistivity Technique. Kyushu University.

Gutierrez, F., Cooper, A.H. and Johnson, K.S., 2008. Identification, prediction, and mitigation of sinkhole hazards in evaporite karst areas. Environmental Geology, 53, pp. 1007-1022. http://dx.doi.org/10.1007/s00254-007-0728-4

Loke, M.H. and Dahlin, T., 2002. A comparison of Gauss-Newton and Quasi-Newton methods in resistivity imaging inversion. Journal of applied geophysics, 49(3), pp. 149-162. http://dx.doi.org/10.1016/S0926-9851(01)00106-9

Loke, M.H. 2004. Tutorial: 2-D and 3-D Electrical Imaging Surveys.

Loke, M.H., Acworth, I. and Dahlin, T., 2003. A comparison of smooth and blocky inversion methods in 2D electrical imaging surveys. Exploration geophysics, 34(1), pp. 182-187. https://doi.org/10.1071/EG03182

Metwaly, M. and Alfouzan, F., 2013. Application of 2-D geoelectrical resistivity tomography for subsurface cavity detection in the eastern part of Saudi Arabia. Geoscience Frontiers, 3(4), pp. 469-476. https://doi.org/10.1016/j.gsf.2012.12.005

Salman, A.M., Thabit, J.M. and Abed, A.M., 2020. Application of the electrical resistivity method for site investigation in University of Anbar, Ar-Ramadi City, Western Iraq. Iraqi Journal of Science, 61(6), pp. 1345-1352. https://doi.org/10.24996/ijs.2020.61.6.12

Sissakian, V.K. and Al-Mousawi, H.A., 2007. Karstification and related problems, examples from Iraq. Iraqi Bulletin of Geology and Mining, 3(2), pp. 1-12.

Van Schoor, M. 2002. Detection of sinkholes using 2D electrical resistivity imaging. Journal of applied geophysics, 50, pp. 393-399. https://doi.org/10.1016/S0926-9851(02)00166-0

Zhou, W., Beck, B.F. and Adams, A.L., 2002. Effective electrode array in mapping karst hazards in electrical resistivity tomography. Environmental geology, 42, pp. 922-928. http://dx.doi.org/10.1007/s00254-002-0594-z

Iraqi National Journal of Earth Science

www.earth.uomosul.edu.iq

Mineralogy and Geochemistry of Upper Cretaceous and Paleogene Succession in Gali and Qalbaza Sections, Northeastern Iraq: Implications for Provenance and Detecting K/Pg Boundary

Shareef T. Al-Hamed [1*], Sattar J. Al-Khafaji [2]

[1] *Department of Geology and Petroleum, College of Science, University of Mosul, Mosul, Iraq.*

[2] *Department of Geology, College of Science, University of Basrah, Basrah, Iraq.*

Article information

Received: 01- Nov -2024

Revised: 28- Nov -2024

Accepted: 18- Dec -2024

Available online: 01- Jan -2026

Keywords:
Geochemistry,
Tanjero/Kolosh,
K/Pg boundary,
Cretaceous,
Paleogene,

Correspondence:
Name: Shareef T. Al-Hamed
Email:
shareefalhamed82@gmail.com

ABSTRACT

One of the most controversial topics in geology is the K/Pg event, marked by mineralogical and geochemical evidence, as well as environmental catastrophes that led to a massive extinction. At the end of the Mesozoic, the Chicxulub meteorite impact and/or prolonged Deccan eruptions were the causes of the global mineralogical and geochemical anomalies at the K/Pg. The Gali and Qalbaza sections in Iraq represent the K/Pg between the upper Tanjero and lower Kolosh formations. The sandstones of these sections are immature lithic graywacke derived from an undissected arc-recycled orogenic provenance, and they were deposited in an arid to semi-arid paleoclimate. REE suggests that a single melt underwent differentiation to provide the source rocks that weathered and were deposited under oxic-anoxic paleoredox conditions. Quartz and K-feldspar increase and carbonate fragments decrease at 10 cm thick of both gray siltstone (sample G19 of Gali section) and red conglomerate layers (sample Q18 of Qalbaza section). The G19 and Q18 layers exhibit low calcite content and the presence of analcime, smectite, and vermiculite. Positive anomalies for SiO_2, Al_2O_3, Fe_2O_3, MgO, Na_2O, K_2O, TTEs, Zr, Zn, and Cu, and negative anomalies for CaO, MnO, LOI, Hf, Sr, and Cs are recorded at 10 cm thick G19 and Q18 layers. Elevated levels of Fe/Al, Ni/Al, Cr/Al, and SO_2/MnO are also detected at the G19 and Q18 layers. Based on the current evidence, the proposed boundaries of gray siltstone (sample G19) and red conglomerate (sample Q18) layers could represent the K/Pg boundaries, with parts of them perhaps eroded.

DOI: 10.33899/injes.v26i1.60186, ©Authors, 2026, College of Science, University of Mosul.
This is an open-access article under the CC BY 4.0 license (http://creativecommons.org/licenses/by/4.0/).

معدنية وجيوكيميائية تتابعات الكريتاسي الاعلى والباليوجين في مقطعي كَلي وكالبازا، شمال شرقي العراق: يتضمن الاصل وتحديد حد الكريتاسي/الباليوجين

شريف ثمود الحامد[1]* ، **ستار جبار الخفاجي [2]**

[1] قسم علم الارض والنفط، كلية العلوم، جامعة الموصل، الموصل، العراق.

[2] قسم علم الارض، كلية العلوم، جامعة البصرة، البصرة، العراق.

معلومات الارشفة

تاريخ الاستلام: 01- نوفمبر- 2024

تاريخ المراجعة: 28- نوفمبر- 2024

تاريخ القبول: 18- ديسمبر- 2024

تاريخ النشر الالكتروني: 01- يناير- 2026

الكلمات المفتاحية:

جيوكيميائية،

تانجيرو/كولوش،

حدود K/Pg،

كريتاسي،

باليوجين،

المراسلة:

الاسم: شريف ثمود الحامد

Email: shareefalhamed82@gmail.com

الملخص

يُعد حدث K/Pg وهو حد الكريتاسي/الباليوجين من أكثر المواضيع المثيرة للجدل في علم الأرض، والذي يتميز بأدلةٍ معدنية وجيوكيميائية وكوارث بيئية سببت انقراضاً جماعياً. ان اصطدام نيزك جيكسولوب و/او دفقات براكين ديكان طويلة الامد في نهاية الحقبة المتوسطة (Mesozoic) هي الاحداث التي تقف وراء الشذوذات المعدنية والجيوكيميائية العالمية عند حد K/Pg. يمثل مقطعا كَلي وكالبازا في العراق حد K/Pg بين تكويني تانجيرو الاعلى وكولوش الاسفل. الصخور الرملية لهذه المقاطع عبارة عن (lithic graywacke) غير ناضجة مشتقة من أصل اوروجيني قوسي معاد الترسيب، وقد ترسبت في مناخ قديم جاف الى شبه جاف. تُشير العناصر الأرضية النادرة إلى أن صهيراً مفرداً عانى من التفاضل لتوفير الصخور المصدرية التي تجوت وترسبت تحت ظروف مؤكسدة – مختزلة. يزداد المرو والفلدسبار البوتاسي وتنخفض القطع الكاربوناتية عند سمك 10 سم في طبقات كل من الغرين الرمادي (العينة G19 من مقطع كَلي) والمدملكات الحمراء (العينة Q18 من مقطع كالبازا). تُظهر طبقات G19 وQ18 محتوى منخفض من الكالسايت ووجود كل من الأنالسيم والسمكتايت والفيرميكيولايت. تم تسجيل شذوذات إيجابية لـ SiO_2 وAl_2O_3 وFe_2O_3 وMgO وNa_2O وK_2O وTTEs وZr وZn وCu، وشذوذات سلبية لـ CaO وMnO وLOI وHf وSr وCs عند طبقات G19وQ18 التي يبلغ سمكها 10 سم. تم الكشف أيضًا عن مستويات مرتفعة من Fe/Al وNi/Al وCr/Al وSO_2/MnO عند طبقات G19 وQ18. استناداً إلى الأدلة الحالية، فإن الحدود المقترحة لطبقات الغرين الرمادي (العينة G19) والمدملكات الحمراء (العينة Q18) من مقطعي كَلي وكالبازا على التوالي، يمكن أن تمثل حد الكريتاسي/الباليوجين (K/Pg)، مع احتمال تعرية أجزاءً منها.

DOI: 10.33899/injes.v26i1.60186, ©Authors, 2026, College of Science, University of Mosul.
This is an open-access article under the CC BY 4.0 license (http://creativecommons.org/licenses/by/4.0/).

Introduction

The K/Pg boundary event is currently one of the greatest contentious topics in geology due to the geochemical elemental anomalies related to these period deposits and environmental catastrophes caused the massive extinction that characterized the Cretaceous end before ~ 66 Ma, marking the end of the Mesozoic Era and the beginning of the Cenozoic Era. The Cretaceous period began 145 Ma ago and ended abruptly 66.04 Ma ago with the entrance of a new period of Paleogene that continued for 43 Ma (Coccioni and Silva, 2015). The geochemical and mineralogical anomalies across the K/Pg boundary at various places around the world were attributed to the impact of an extraterrestrial object with a diameter of 10 km on the Earth and/or the widespread, long-lasting activity of Deccan eruptions at the end of the Mesozoic (Alvarez et al., 1980; Adatte et al., 2002). Both a large asteroid-projectile (Chicxulub) impacted Earth in the Yucatán Peninsula of Mexico (mixed target) and the Deccan Traps eruptions in India caused worldwide fires, acidic rains, and dust fog-cloud that continued for a long time (Alvarez et al., 1980; Keller et al., 2012), which prevented sunlight and led to a global and abrupt fall in degrees of temperature that caused the disrubbery of the food system and mass extinction (Keller et al., 2011; Sial et al., 2019). The three events of Chicxulub impact, mass extinction, and giant pulse of Deccan eruptions possibly happened

within a hundred thousand years of one another (Sial et al., 2019). Although the Chicxulub impact and Deccan volcanism were more than 13,000 km apart, they might have cooperatively contributed to the end-Cretaceous mass extinction (Renne et al., 2015).

Although biostratigraphical studies have been conducted on the K/Pg boundary in Iraq, mineralogical and geochemical research have made relatively few and limited contributions. Therefore, this paper aims to detect the K/Pg boundary between the Tanjero and Kolosh formations in northern and northeastern Iraq by mineralogical and geochemical anomalies.

Study area

The study area is situated in the Iraqi Kurdistan Region (IKR) at the governorates of Erbil and Sulaymaniyah in the northeast of Iraq (Table 1 and Fig. 1). The Gali section lies in the Sama Qulley area, approximately 55 km east of Erbil City, 36 km southeast of Shaqlawa Town, and 11 km north of Koysinjaq Town on the northeast limb of Awagird Mountain at the plunging of the Safeen anticline in the direction of southeast, and for a distance of 1 km southeast of the Gali Village. The Qalbaza section, on the other hand, is located in the Qalbaza Village at the southern boundary of Sharazoor Plain, which is about 41 km southeast of Sulaymaniyah City, 19 km northwest of Halabja City, 12 km southeast of Halebjai Taza Town, and 11 km northeast of the Darbandikhan Lake.

According to Buday and Jassim (1987), the study area sits within the High Folded Zone of the Unstable Shelf (Fig. 2). Moreover, Figure 3 shows the geological map of the studied sections in Erbil and Sulaymaniyah areas.

Table 1: Locations and coordination of the studied sections.

Governorate	Section	Latitude	Longitude	Nearby point
Erbil	Gali	36° 10′ 51.30″ N	44° 36′ 40.80″ E	Gali Village
Sulaymaniyah	Qalbaza	35° 15′ 41.34″ N	45° 48′ 27.06″ E	Qalbaza Village

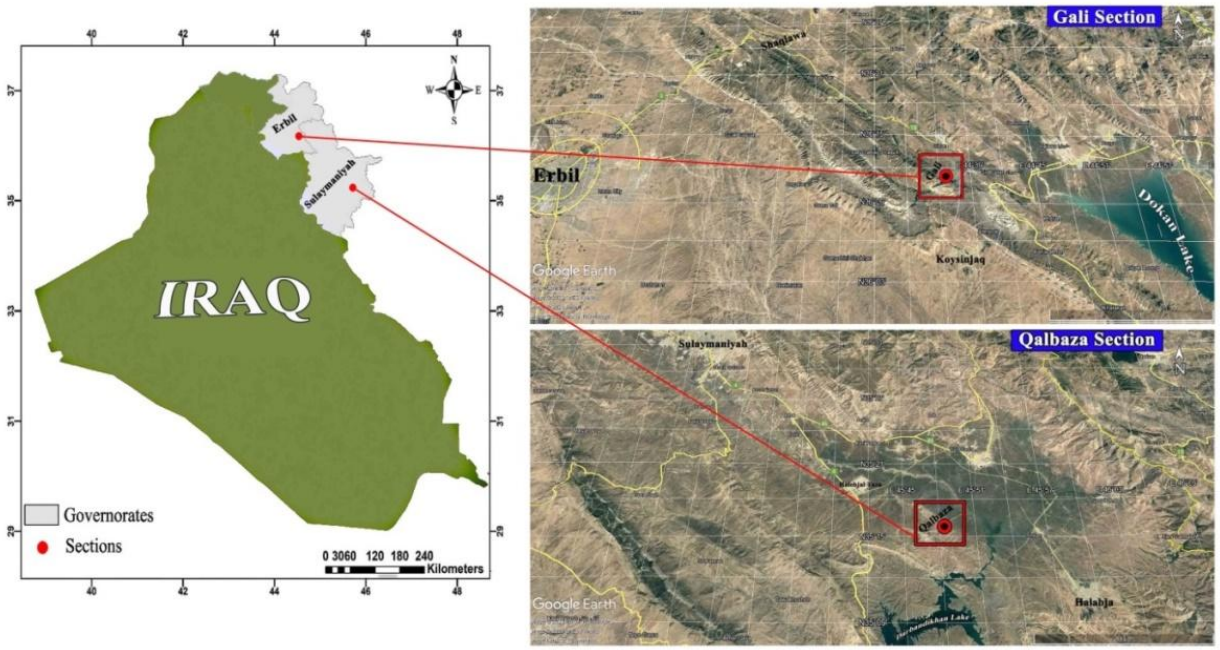


Fig. 1. Location of the studied sections.

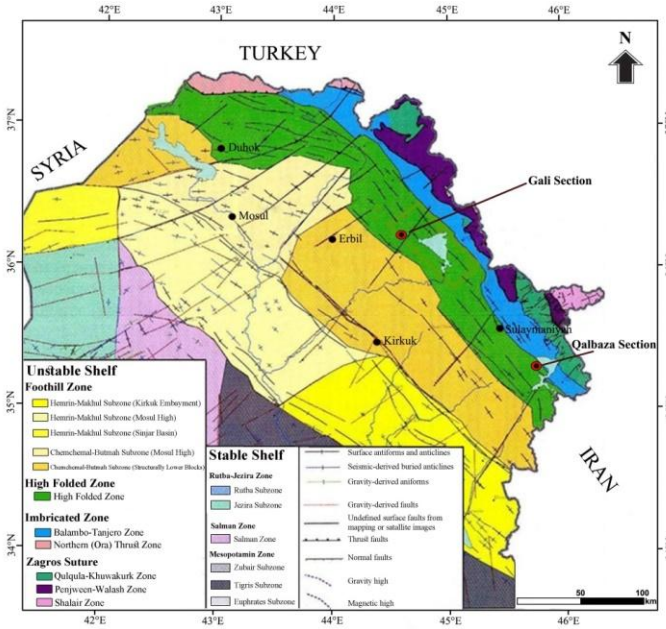


Fig. 2. Tectonic division map of Iraq showing the location of the studied area, modified from Buday and Jassim (1984).

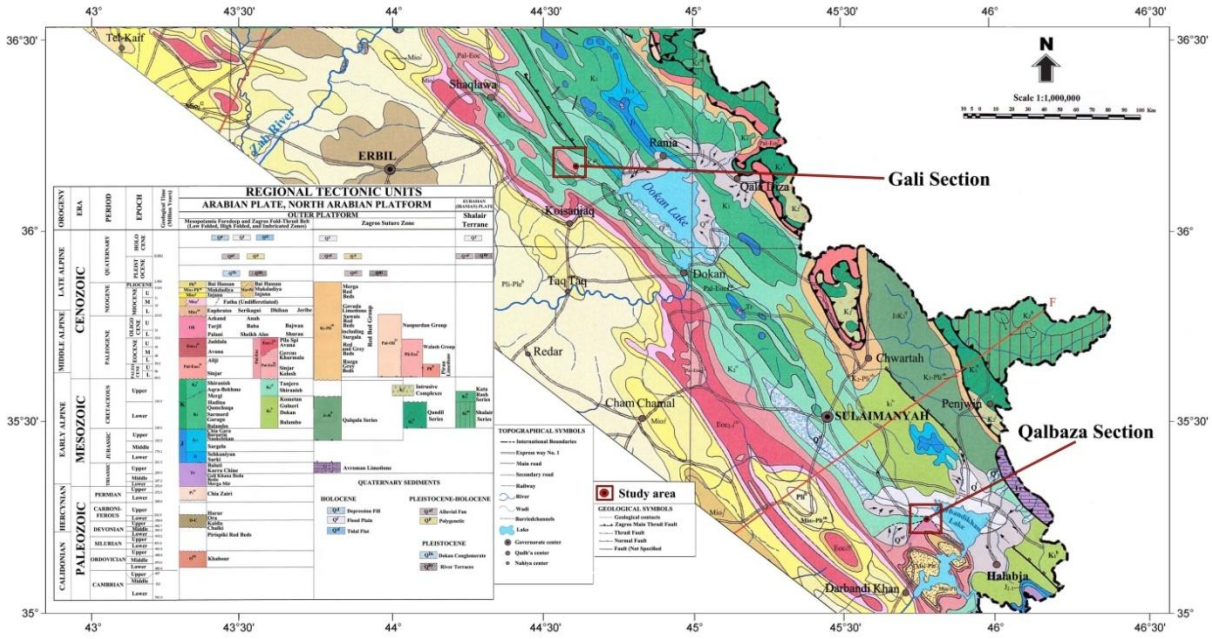


Fig. 3. Geological map of the studied area from Sissakian and Fouad (2012). The boundary between the Tanjero and Kolosh formations in the Qalbaza section has been modified.

Methodology

Fieldwork and sampling

The boundaries between the Tanjero and Kolosh formations have been proposed by the biostratigraphical studies of Sharbazheri (2008) in the Gali section and Al-Qayim et al. (2020) in the Qalbaza section. Based on changes in lithological characteristics and bed colors, 62 samples were collected (30 from the Gali section and 32 from the Qalbaza section) with sampling distances intensified to vary between 0.5 and 20 cm at the field-observed K/Pg boundary (possibly K/Pg).

However, fieldwork reveals that the total thickness of the Gali section is about 61.7 m (31.7 m for Tanjero Formation and 29.3 m for Kolosh Formation) (Fig. 4). The lower part of

the Tanjero Formation conformably overlies gray shale interbedded with gray marl of the Shiranish Formation. On the other hand, the upper part of the Tanjero Formation ends with 10 cm of gray siltstone (sample G19) (Figs. 4 and 5). The K/Pg boundary was initially marked in the field within 70 cm of gray marly limestone (sample G20), which contains limestone ball structures with diameter range of 5–15 cm (Fig. 5). These structures may be located between the Tanjero and Kolosh formations due to slump and foundering of beds or deep burial by tectonic horizontal forces and differential load pressure (Potter and Pettijohn, 1977; Karim, 2004). The biostratigraphical study of Sharbazheri (2008) determined the K/Pg boundary within 1.25 m of 1 m of oily impregnated friable-soft and weathered pale brown fine sandstone beds and 25 cm of dark organic papery shale interlayered by thin beds of dark grey marl. This case is not observed in the current investigation. Moreover, Sharbazheri (2008) reported that the boundary was difficult to identify in the field due to an erosional surface and no continuous biostratigraphic document. In the Gali section, the lower part of the Kolosh Formation conformably overlies gray marly limestone; it consists of olive sandy marlstone (sample G21, 10 cm thick) overlaid by 20 cm of olive friable sandstone (sample G22) (Fig. 4).

On the other hand, the total thickness of the Qalbaza section is about 47 m, which consists of 26.5 m of Tanjero's upper part and 20.2 m of Kolosh's lower part (Fig. 6). The upper part ends with 20 cm of gray silty marlstone (sample Q16) (Figs. 6 and 7A). The K/Pg boundary was initially determined by the appearance of two conglomerate layers (20 cm of sample Q17 and 10 cm of sample Q18, respectively) (Figs. 6 and 7). These layers are overlaid by the first layer of the Kolosh Formation (sample Q19), which consists of 1 m of dark gray sandstone with sand ball structures (2–15 cm in diameter) (Figs. 6 and 7B). The sources of these structures were illustrated when the previous section was explained. The conglomerate reveals the unconformity contact between the Tanjero and the Kolosh formations (Abawi et al., 1982), and may be the submarine fans created the conglomerate during periodic tectonic activity pulses (Karim, 2004). The biostratigraphical study of Al-Qayim et al. (2020) determined the K/Pg boundary in the Qalbaza section within the marlstone layers with no break or hiatus.

Laboratory works

Many methods and techniques are used in this work, including insoluble residue (IR), pipette analysis, polarized microscopy, X-ray diffraction (XRD), fusion X-ray fluorescence (XRF), and inductively coupled plasma-mass spectrometry (ICP-MS). For selected samples across the K/Pg boundary, IR, pipette analysis, and a petrographic study were conducted in the geochemical laboratory, Geology Department, College of Science, University of Mosul. While in the laboratories of the Iranian University of Science and Technology (IUST), Tehran, the following techniques were carried out: XRD of PW3830 type for 13 samples (6 and 7 samples for Gali and Qalbaza section respectively); fusion XRF of PW1480 type for 11 samples (5 and 6 samples for Gali and Qalbaza section respectively); ICP-MS of Agilent 7700 series type for 13 samples (7 and 6 samples for Gali and Qalbaza section respectively); and fire assay-ICP-MS (to determine the platinum group elements (PGE)) for 7 samples (3 and 4 samples for Gali and Qalbaza section respectively).

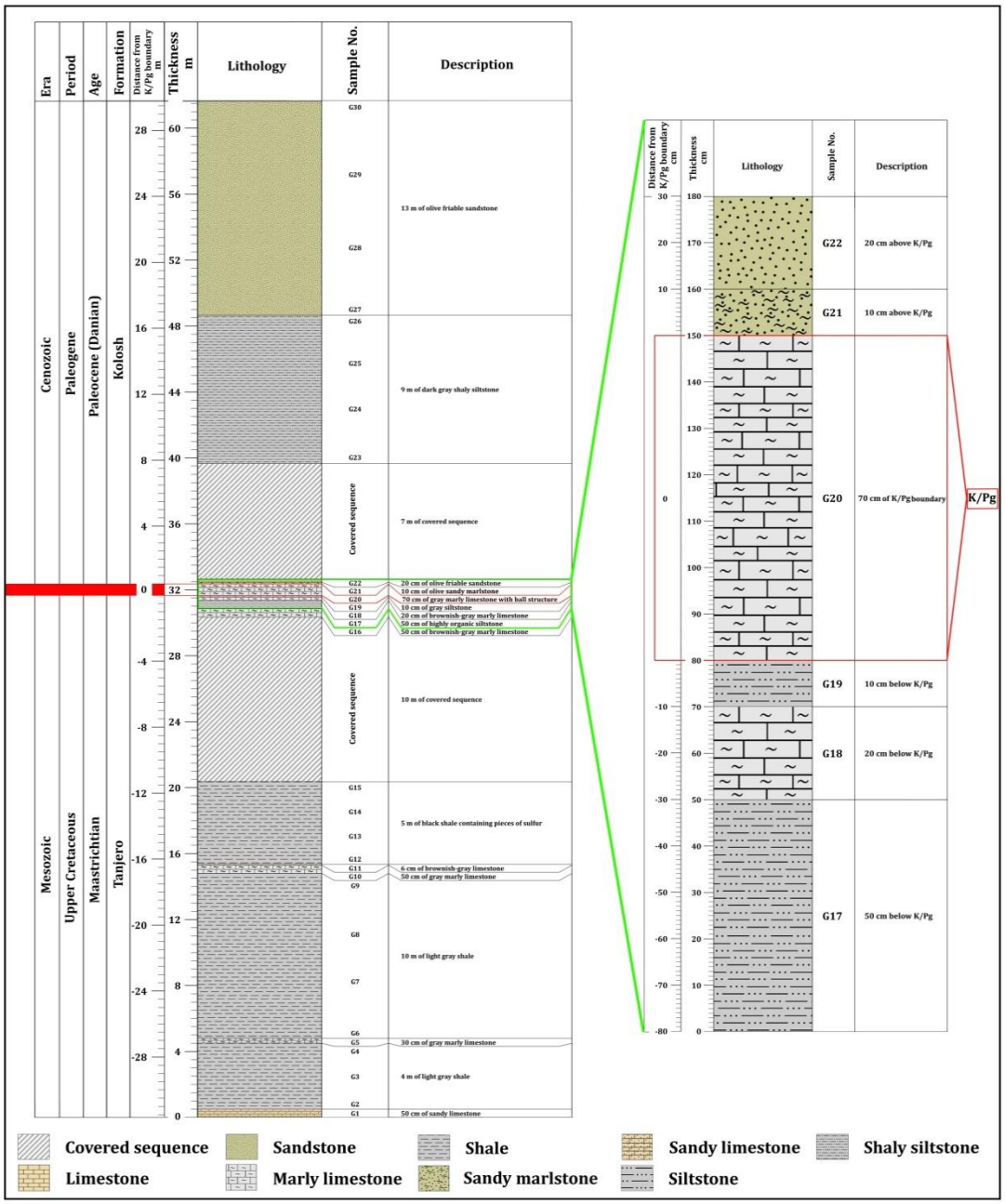


Fig. 4. Lithostratigraphic column across the K/Pg boundary in the Gali section.

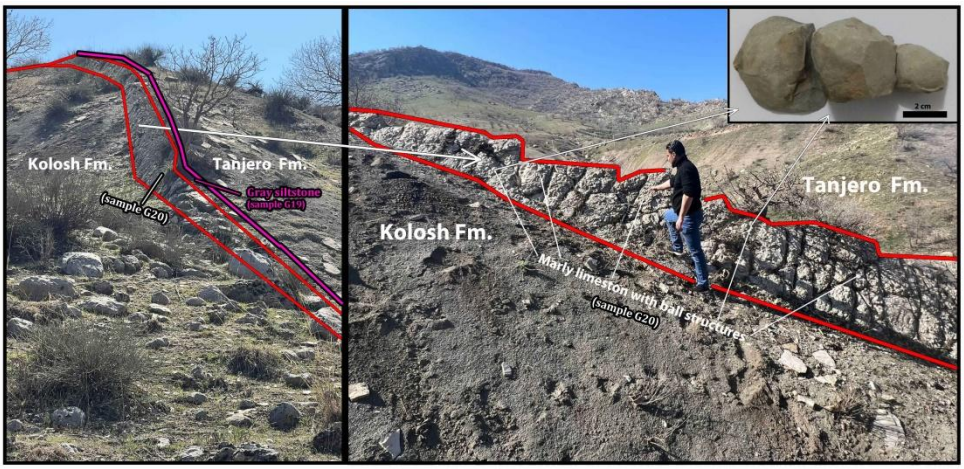


Fig. 5. Field photo from the Gali section showing the upper part of the Tanjero Formation (10 cm gray siltstone; sample G19) and the initial proposed K/Pg boundary (70 cm of marly limestone layer with ball structures; sample G20).

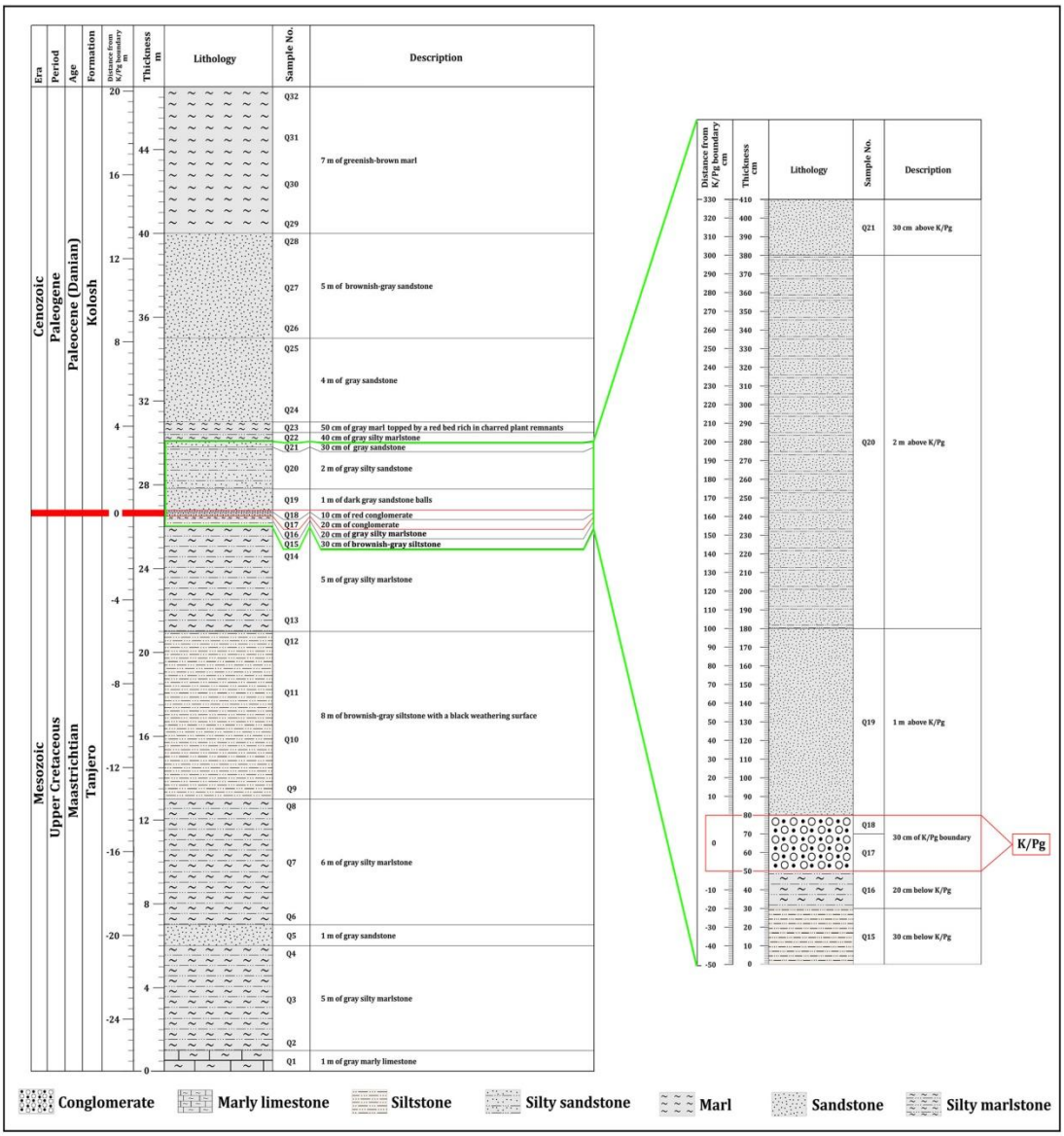


Fig. 6. Lithostratigraphic column across the K/Pg boundary in the Qalbaza section.

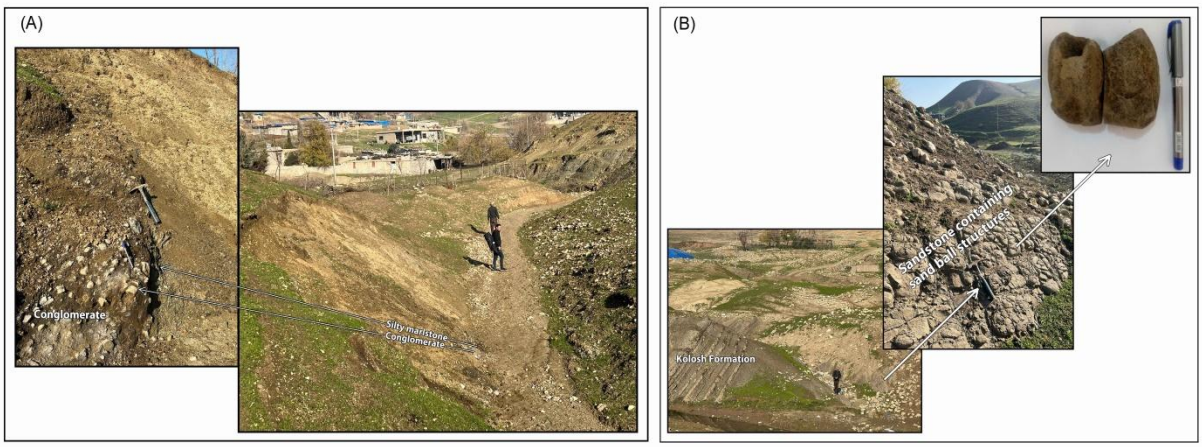


Fig. 7. Field photos from the Qalbaza section. (A) The upper part of the Tanjero Formation exhibiting 20 cm gray silty marlstone (sample Q16) with 30 cm conglomerates (samples Q17 and Q18). (B) The lower part of the Kolosh Formation displaying 1 m dark gray sandstone with sand ball structures (sample Q19).

Results and Discussion

Petrography

The petrographic study across the K/Pg boundary reveals that the Gali section comprises carbonates and sandstones. The carbonate petrography shows that sample G18 of the Upper Cretaceous consists of 10–50% globular planktonic foraminifera embedded in a micritic matrix (Fig. 8A and B) as planktonic foraminiferal lime wackestone microfacies (Dunham, 1962), which is consistent with the Tanjero microfacies that were classified by Al-Hamed and Malak (2021). On the other hand, sample G20 of the Lower Paleogene is composed of < 10% skeletal grains with about 90% micritic matrix (Fig. 8C) as fossiliferous lime mudstone microfacies (Dunham, 1962). Calcite, minor amounts of monocrystalline quartz, and iron oxides comprise the mineral composition of these two microfacies (Fig. 8 B, C, and D). The decline in foraminifera from Upper Cretaceous (~50%) to Lower Paleogene (<10%) layers could be associated with the Chicxulub impact and/or Deccan events (Smit, 1982; Keller et al., 2011), which caused one of the greatest mass extinctions (Petersen et al., 2016; Bardeen et al., 2017). After this event, little species began to emerge (Smit, 1982; Arenillas et al., 2004). Therefore, the K/Pg boundary in the Gali section could be the layer of sample G19 set between the increase and decrease in assemblages.

Sandstone constituents of the Gali and Qalbaza sections are given in Tables 2 and 3. Two varieties of quartz grains were determined, mono- and polycrystalline (Fig. 9A and B). The proposed K/Pg layers show the highest total quartz content compared to the samples below and above these boundaries (Tables 2 and 3). Quartz influx increases at K/Pg layers as sea level falls (Bourgeois et al., 1988; Smit, 1999). Both sections show a minor amount of feldspars (Tables 2 and 3; Fig. 9C and D) due to their high susceptibility to chemical breakdown during weathering and diagenetic processes to form clays (Pettijohn, 1975; Boggs, 2006). Moreover, orthoclase dominates over plagioclase in the studied samples because orthoclase is more stable during chemical weathering (Nichols, 2009). Rock fragments mainly comprise carbonate with minor amounts of chert, igneous, and metamorphic rock fragments (Fig. 9E and F; Fig. 10A and B), indicating that the Gali and Qalbaza sandstones derived from older, highly carbonate-containing formations exposed to the surface through tectonic processes (Dickinson, 1985; Zattin and Zuffa, 2004). The proposed K/Pg layers contained the lowest amount of carbonate fragments (Tables 2 and 3). Gali and Qalbaza sandstones included a high matrix proportion (Tables 2 and 3) with carbonate cement dominating these sandstones (Fig. 10A), as well as low amounts of heavy minerals such as iron oxide, hornblende, and pyroxene (Tables 2 and 3; Fig. 10A, B, C, and D). Fig. 11 shows the petrographic variation across the proposed K/Pg boundaries of the Gali (sample G19) and Qalbaza (sample Q18) sections. These boundaries reveal a decrease in carbonate rock fragments, chert, and heavy minerals, while an increase in total quartz and K-feldspar. Calcite cement increases significantly in samples located above the boundaries. Moreover, maximum matrix content can be observed at the Qalbaza K/Pg boundary and below the Gali K/Pg boundary. Detrital component variations at the boundary are possibly due to elevated global environmental stress during the Upper Cretaceous, which resulted from volcanism in the Deccan trap before the Chicxulub impact (Font et al., 2018). Consequently, samples G19 and Q18 from the Gali and Qalbaza sections could indicate the K/Pg boundary. Despite this, detecting the K/Pg boundary cannot only be done by a petrographic study. This necessitates the contribution of mineralogical and geochemical proof to determine or propose the boundary layer.

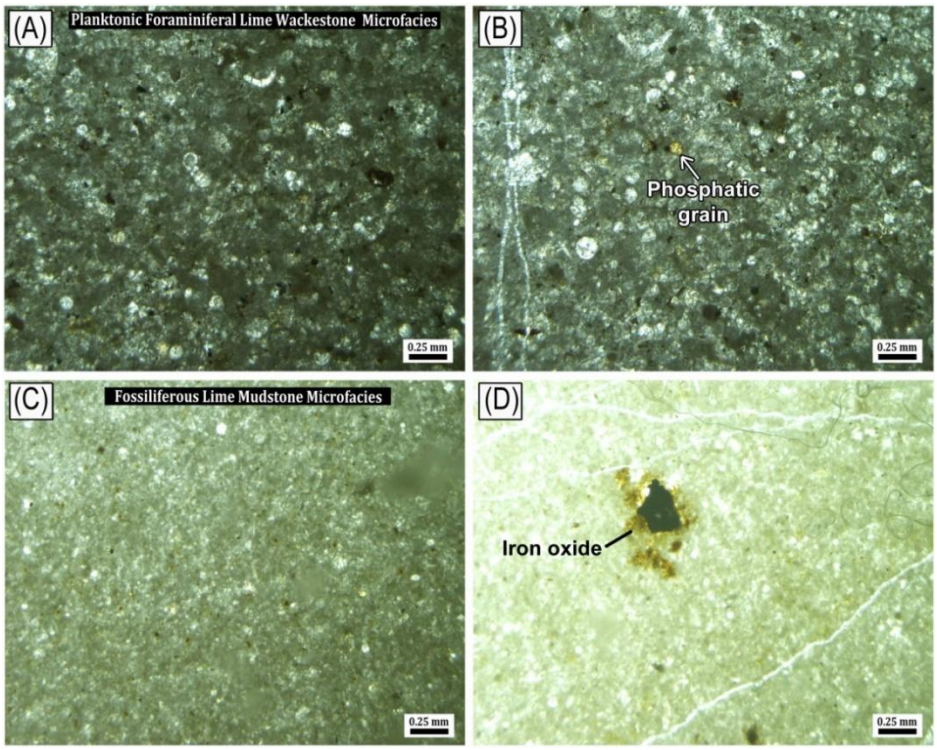


Fig. 8. Photomicrographs of Gali section carbonate samples. (A) Planktonic foraminiferal lime wackestone microfacies; sample G18 (40X). (B) Globular planktonic foraminifera, phosphatic grain, and monocrystalline quartz; sample G18 (40X). (C) Fossiliferous lime mudstone; sample G20 (40X). (D) Iron oxide; sample G20 (40X).

Table 2: The major petrographic components % of the Gali section.

Components	G22	G21	G19 (K/Pg)	G17	Min.	Max.	Average
Monocrystalline	10.50	8.00	14	11.5	8.00	14.00	11.00
Polycrystalline	2.00	2.50	5	1	1.00	5.00	2.63
K-feldspar	0.00	0.50	1	0	0.00	1.00	0.38
Plagioclase	0.00	0.50	0.5	0	0.00	0.50	0.25
Carbonate	36.00	34.00	32	35	32.00	36.00	34.25
Chert	4.50	1.50	0	0.5	0.00	4.50	1.63
Igneous and metamorphic	4.00	0.50	1	0.5	0.50	4.00	1.50
Heavy minerals	1.00	1.00	0.5	2	0.50	2.00	1.13
Matrix	37.00	34.00	36	41.5	34.00	41.50	37.13
Cement	5.00	17.50	10	8	5.00	17.50	10.13
Total	100	100	100	100			100
Quartz (Q %)	21.93	22.11	35.51	25.77	21.93	35.51	26.33
Feldspar (F %)	0.00	2.11	2.80	0.00	0.00	2.80	1.23
Rock Fragment (RF%)	78.07	75.79	61.68	74.23	61.68	75.79	72.44

Table 3: The major petrographic components % of the Qalbaza section.

Components	Q21	Q20	Q19	Q18 (K/Pg)	Q17	Q16	Q15	Min.	Max.	Average
Monocrystalline	20.50	12.00	11.50	15.00	9.00	16.5	18.25	9.00	20.50	14.68
Polycrystalline	5.25	3.50	2.50	3.00	0.50	1	2.5	0.50	5.25	2.61
K-feldspar	2.00	1.50	0.50	1.25	0.50	1.5	3	0.50	3.00	1.46
Plagioclase	1.00	1.50	1.00	1.50	2.50	2	1	1.00	2.50	1.50
Carbonate	23.50	28.00	26.50	18.00	39.00	32.5	27	18.00	39.00	27.79
Chert	4.50	2.00	7.50	3.00	4.50	1.5	2.25	1.50	7.50	3.61
Igneous and metamorphic	3.00	5.50	3.50	0.00	0.50	2	4.5	0.00	5.50	2.71
Heavy minerals	1.00	2.00	1.00	0.50	1.00	2.5	2	0.50	2.50	1.43
Matrix	36.00	42.50	40.00	56.25	41.00	35.25	38	35.25	56.25	41.29
Cement	3.25	1.50	6.00	1.50	1.50	5.25	1.5	1.50	6.00	2.93
Total	100	100	100	100	100	100	100			100
Quartz (Q %)	43.10	28.70	26.42	43.11	16.81	30.70	35.47	16.81	43.11	32.04
Feldspar (F %)	5.02	5.56	2.83	6.59	5.31	6.14	6.84	2.83	6.84	5.47
Rock Fragment (RF %)	51.88	65.74	70.75	50.30	77.88	63.16	57.69	50.30	77.88	62.49

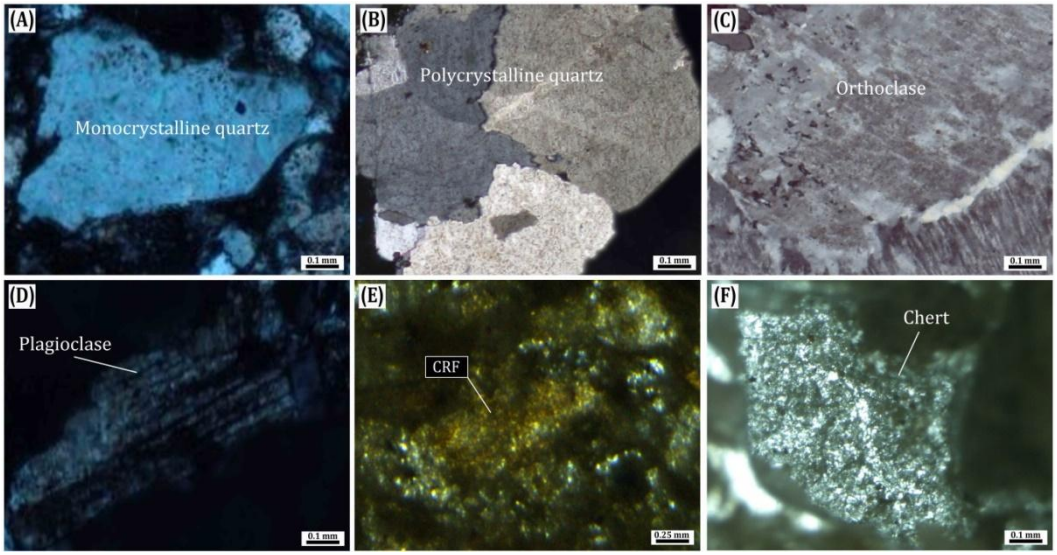


Fig. 9. Photomicrographs of Gali and Qalbaza sandstones. (A) Monocrystalline quartz; sample Q18 (100X; XPL). (B) Polycrystalline quartz; sample G19 (100X; XPL). (C) Orthoclase feldspar; sample Q15 (100X; XPL). (D) Plagioclase feldspar; sample Q18 (100X; XPL). (E) Carbonate rock fragments (CRF); sample Q21 (40X; PPL). (F) Chert rock fragment; sample G22 (100X; PPL).

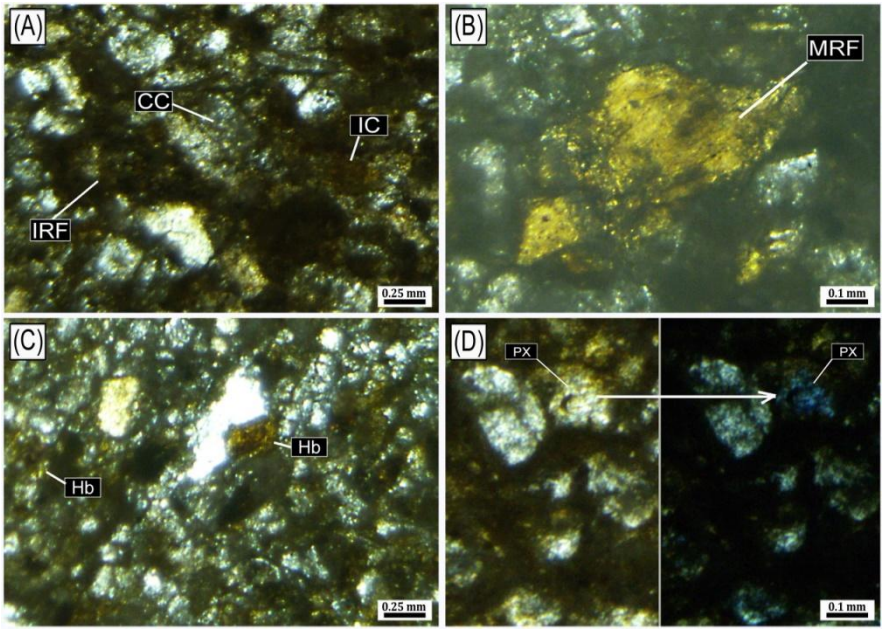


Fig. 10. Photomicrographs of Gali and Qalbaza sandstones. (A) Igneous rock fragments (IRF), carbonate cement (CC), and iron cement (IC); sample G21 (40X; PPL). (B) Metamorphic rock fragments; sample G17 (100X; PPL). (C) Hornblende (Hb); sample Q15 (40X; PPL). (D) Pyroxene (PX); sample Q20 (100X; PPL on left and XPL on right).

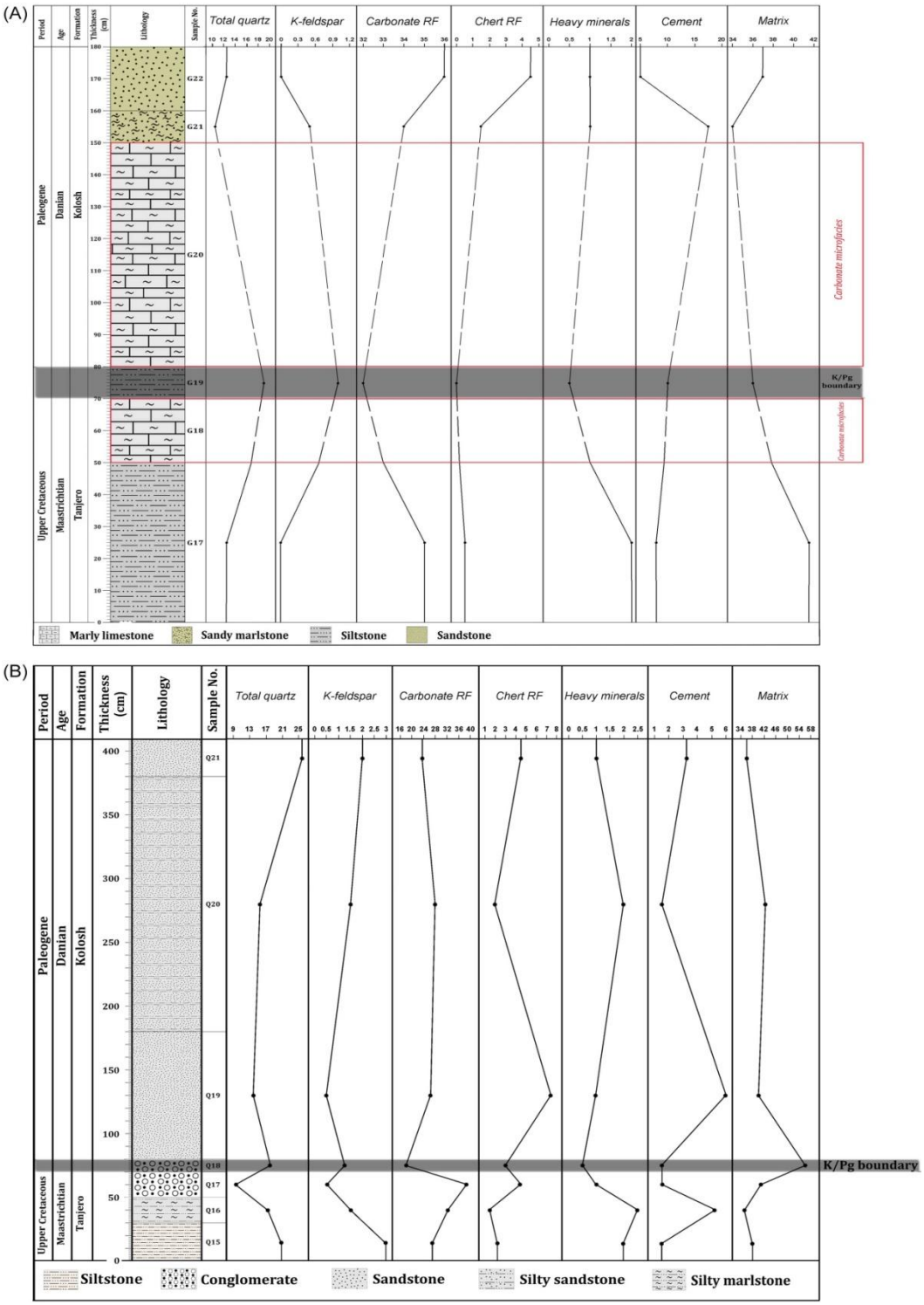


Fig. 11. Petrographic variation across the K/Pg boundary from (A) Gali section and (B) Qalbaza section.

According to Pettijohn (1975), Gali and Qalbaza sandstones are considered texturally immature due to their over 15% matrix content (Tables 2 and 3). The mineralogical maturity index (MMI) in the Gali and Qalbaza sandstones was calculated (Tables 4 and 5) using the MMI = Q / (F + RF) equation and parameters in Table 6 proposed by Nwajide and Hoque (1985). MMI values are between 0.28 and 0.55 with an average of 0.37 for Gali sandstones and between 0.20 and 0.76 with an average of 0.50 for Qalbaza sandstones (Tables 4 and 5). These calculated MMI values correspond to the categories Q = < 50% and MMI ≤ 1 in Table 6, indicating that the Gali and Qalbaza sandstones are immature sediments.

According to Dott (1964), Gali and Qalbaza sandstones are classified as lithic graywacke sandstones (Fig. 12).

Table 4: Modal composition of the sandstone and mineralogical maturity index (MMI) in the Gali section.

Components	G22	G21	G19 (K/pg)	G17	Min.	Max.	Average
Quartz (Q)	12.50	10.50	19.00	12.50	10.50	19.00	13.63
Feldspar (F)	0.00	1.00	1.50	0.00	0.00	1.50	0.63
Rock Fragment (RF)	44.50	36.00	33.00	36.00	33.00	44.50	37.38
Total	57.00	47.50	53.50	48.50	47.50	57.00	51.63
F + RF	44.50	37.00	34.50	36.00	34.50	44.50	38.00
Q %	21.93	22.11	35.51	25.77	21.93	35.51	26.33
F + RF %	78.07	77.89	64.49	74.23	64.49	78.07	73.67
MMI %	0.28	0.28	0.55	0.35	0.28	0.55	0.37

Table 5: Modal composition of the sandstone and mineralogical maturity index (MMI) in the Qalbaza section.

Components	Q21	Q20	Q19	Q18 (K/pg)	Q17	Q16	Q15	Min.	Max.	Average.
Quartz (Q)	25.75	15.50	14.00	18.00	9.50	17.50	20.75	9.50	25.75	17.29
Feldspar (F)	3.00	3.00	1.50	2.75	3.00	3.50	4.00	1.50	4.00	2.96
Rock Fragment (RF)	31.00	35.50	37.50	21.00	44.00	36.00	33.75	21.00	44.00	34.11
Total	59.75	54.00	53.00	41.75	56.50	57.00	58.50	41.75	59.75	54.36
F + RF	34.00	38.50	39.00	23.75	47.00	39.50	37.75	23.75	47.00	37.07
Q %	43.10	28.70	26.42	43.11	16.81	30.70	35.47	16.81	43.11	32.04
F + RF %	56.90	71.30	73.58	56.89	83.19	69.30	64.53	56.89	83.19	67.96
MMI %	0.76	0.40	0.36	0.76	0.20	0.44	0.55	0.20	0.76	0.50

Table 6: Maturity scale of sandstones shows limiting % of Q, (F + RF), and MMI stage (Nwajide and Hoque, 1985).

Q = ≥ 95% , (F + RF) = 50%	MMI = ≥ 19 Super mature
Q = 95-90% , (F + RF) = 5-10%	MMI = 19-9.0 Sub mature
Q = 90-75% , (F + RF) = 10-25%	MMI = 9.0-3.0 Sub mature
Q = 75-50% , (F + RF) = 25-50%	MMI = 3.0-1.0 Immature
Q = < 50%	MMI ≤ 1 Immature
(F + RF) > 50%	Extremely immature

Abbreviations: Q (quartz%), F (feldspars%), RF (rock fragments%), and MMI (mineralogical maturity index).

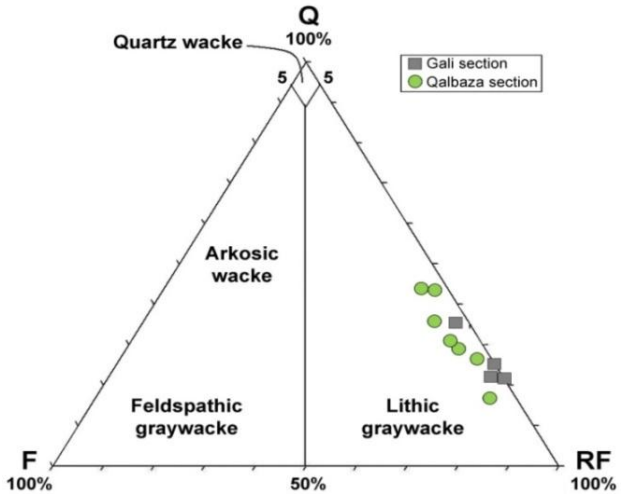


Fig. 12. Sandstone classification of the Gali and Qalbaza samples (Dott, 1964). Q (quartz), F (feldspar), and RF (rock fragments).

Furthermore, the Q-F-L ternary diagram (Fig. 13 A) illustrates that most of the Gali samples are plotted in the undissected arc field, excluding one sample (G19) in the recycled orogenic field, whereas four samples (Q15, Q16, Q18, and Q21) of the Qalbaza sandstones are plotted in the recycled orogenic field, two samples (Q19 and Q20) in the transition area between recycled orogenic and transitional arc fields, and one sample (Q17) in the undissected arc field. Moreover, the Qm-F-Lt ternary diagram (Fig. 13 B) indicates that the Gali and Qalbaza sandstones were derived from a recycled orogenic provenance. Weathered products of the elevated orogenic belt are moved to the nearby foreland basins (Dickinson and

Suczek, 1979; Dickinson, 1985; Al-Hamidi et al., 2023). As is the case in the foreland basins located on the passive margin of the Arabian Plate, which received their sediments from the northern and northeastern eroded margins of the Arabian Plate's collision zone with the Turkish-Iranian Plate, hence Tanjero and Kolosh formations are believed to be sourced from sedimentary, igneous, and metamorphic rocks (Jassim and Goff, 2006; Al-Hamidi et al., 2023). Tanjero and Kolosh source area is situated to the northeast of the basin, where tectonic forces caused this area to rise and move to the northeast, and Tanjero and Kolosh flysch deposits are a result of the Zagros Foreland Basin's creation by elevating older sedimentary rocks (Çelik and Salih, 2021). Hence, ophiolites of the Zagros suture zone, Qulqula group, and Avroman Formation carbonates were potential sources for Gali and Qalbaza sandstones. Moreover, the current study indicates that the Gali and Qalbaza sandstones were deposited in an arid to semi-arid paleoclimate (Fig. 14).

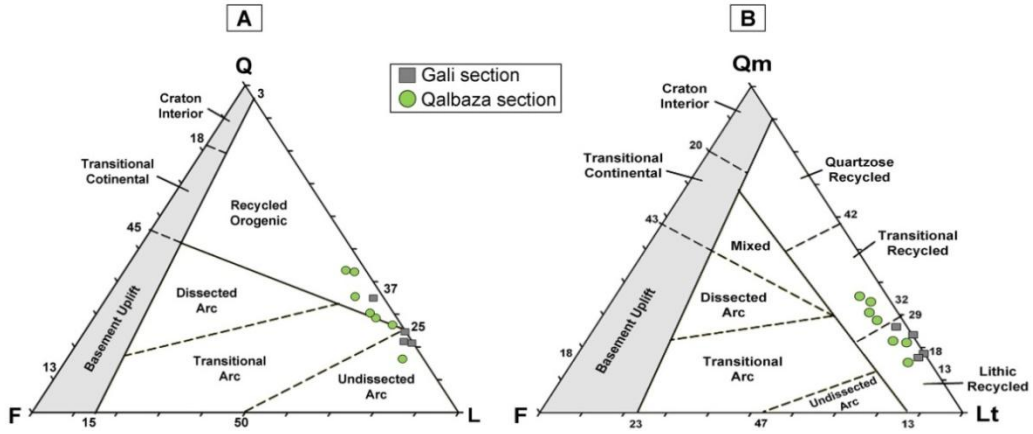


Fig. 13. Tectonic provenance ternary diagrams of Gali and Qalbaza sandstones. (A) Q-F-L (Ingersoll and Suczek, 1979). (B) Qm-F-Lt (Dickinson and Suczek, 1979). Q (quartz), F (feldspar), L (rock fragments), Qm (monocrystalline quartz), and Lt (rock fragments + polycrystalline quartz).

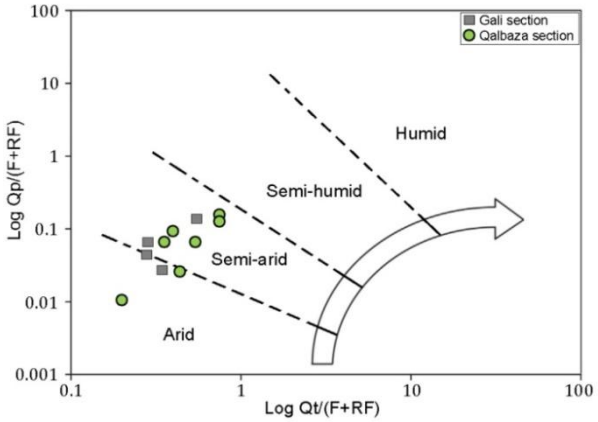


Fig. 14. Paleoclimate diagram of sandstone samples from the Gali and Qalbaza sections (Suttner and Dutta, 1986). Qt (total quartz), Qp (polycrystalline quartz), F (feldspars), and RF (rock fragments).

Mineralogy

Generally, the mineralogical composition of the Gali section is dominated by calcite, quartz, and clay minerals (Fig. 15). Sample layer G20 (carbonate facies) was proposed as the K/Pg boundary in the Gali section based on the field criteria; however, the petrographic study revealed that sample G19 may represent the K/Pg boundary; unfortunately, sample G18 was not analyzed by XRD.

In the Qalbaza section, the mineralogical composition mainly consists of quartz, calcite, and clay minerals with minor amounts of plagioclase, analcime, and muscovite (Fig. 16). Sample Q18 was proposed as the K/Pg boundary in this section based on the petrographic

study. Tables 7, 8, 9, and 10 show the semi-quantitative mineralogical proportions in the Gali and Qalbaza sections by calculating the area under the peak of reflection according to the method suggested by Carver (1971).

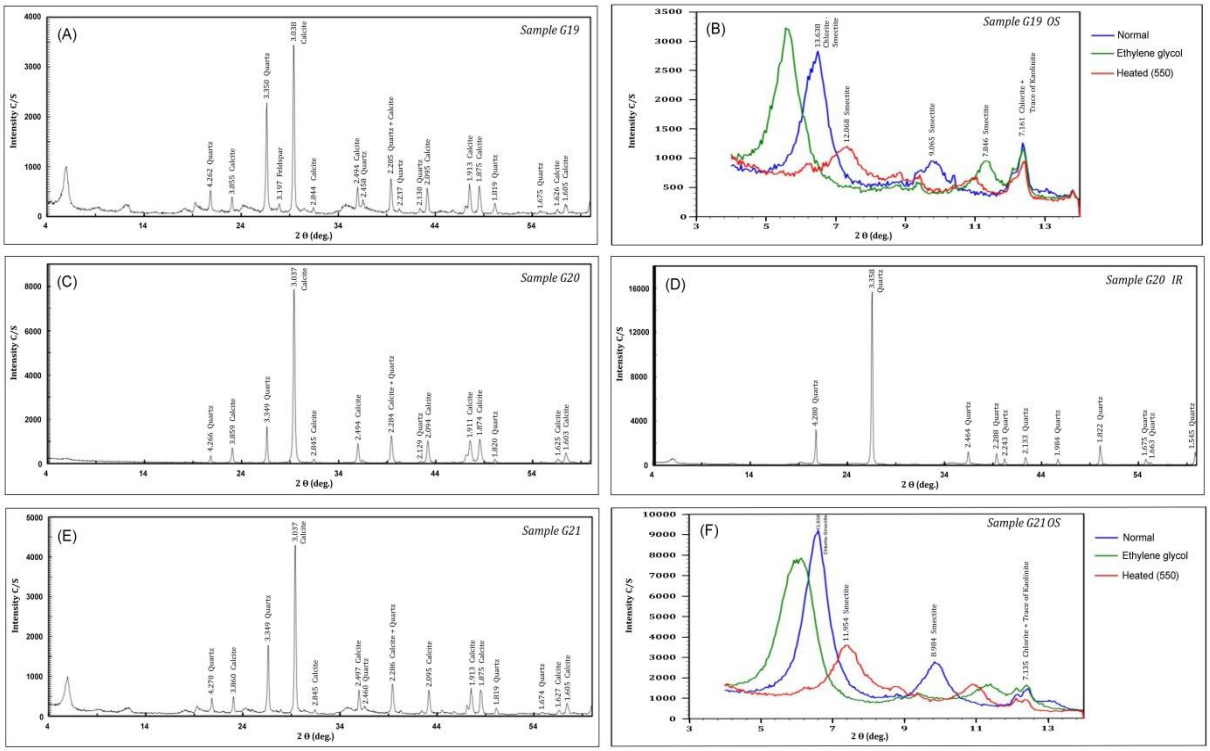


Fig. 15. XRD pattern of Gali section. (A) Bulk sample G19. (B) Oriented slide of sample G19 (G19 OS). (C) Bulk sample G20. (D) Sample G20 was processed by the insoluble residues method. (E) Bulk sample G21. (F) Oriented slide of sample G21 (G21 OS). (A) and (B) represent the proposed K/Pg boundary; (C), (D), (E), and (F) represent the Paleogene layers.

Table 7: Semi-quantitative bulk mineralogical proportions in the Gali section.

Mineralogy	Bulk Samples			The sample was processed by the insoluble residues method (IR)
	G21	G20	G19	G20 IR
Calcite %	79.53	89.84	49.79	—
Quartz %	20.47	10.16	48.88	100
Feldspar %	—	—	1.33	—
Total	100	100	100	100

Table 8: Semi-quantitative clay mineral proportions in the Gali section.

Mineralogy	G21OS	G19OS
Chlorite-Smectite %	91.73	68.32
Smectite %	5.99	20.13
Chlorite + Kaolinite %	2.28	11.55
Total	100	100

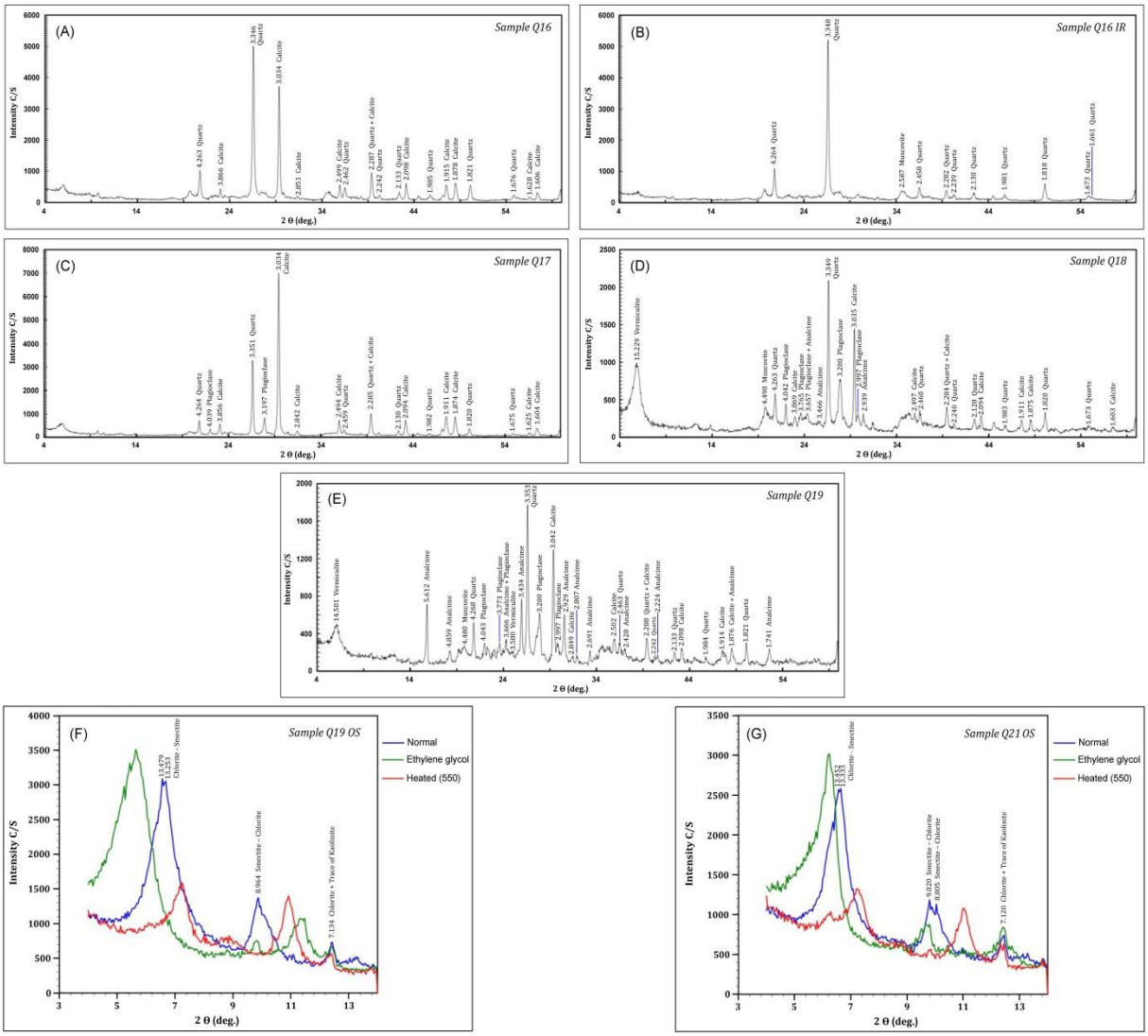


Fig. 16. XRD pattern of Qalbaza section. (A) Bulk sample Q16. (B) Sample Q16 was processed by the insoluble residues method. (C) Bulk sample Q17. (D) Bulk sample Q18. (E) Bulk sample Q19. (F) Oriented slide of sample Q19 (Q19OS). (G) Oriented slide of sample Q21 (Q21OS). (A), (B), and (C) represent the Upper Cretaceous layers; (D) represents the proposed K/Pg boundary; (E), (F), and (G) represent the Paleogene layers.

Table 9: Semi-quantitative bulk mineralogical proportions in the Qalbaza section.

Mineralogy	Bulk Samples				The sample was processed by the insoluble residues method (IR)
	Q19	Q18	Q17	Q16	Q16 IR
Quartz %	36.42	40.74	24.94	51.73	95.44
Calcite %	23.76	13.98	71.17	48.27	—
Vermiculite %	8.04	28.63	—	—	—
Plagioclase %	15.13	11.16	3.89	—	—
Analcime %	14.62	2.04	—	—	—
Muscovite %	2.03	3.45	—	—	4.56
Total	100	100	100	100	100

Table 10: Semi-quantitative clay mineral proportions in the Qalbaza section.

Mineralogy	Q21OS	Q19OS
Chlorite-Smectite %	95.76	96.97
Chlorite + Kaolinite %	4.24	3.03
Total	100	100

In the Gali section, the proposed K/Pg boundary (sample G19) possesses the lowest calcite (49.79%) and highest quartz (48.88%), where calcite increases to 89.84% and quartz decreases to 10.16% at the Lower Paleogene layer (sample G20) after the proposed K/Pg boundary (Table 7). In the Qalbaza section, calcite decreases, and quartz increases within the

proposed K/Pg layer (sample Q18), then calcite increases and quartz decreases at the Lower Paleogene layer (sample Q19) (Table 9). The lowest content or sharp decrease in the calcite, which corresponds to carbonate rock fragments decreasing (see petrography topic), at the Gali and Qalbaza K/Pg boundaries may be attributed to the change of conditions caused by Chicxulub and/or Deccan events, such as acidic rain and global temperature drops, etc., that might have cooperatively contributed to temporarily preventing the development of biogenic calcite by dissolved or inhibition of planktonic carbonate (Keller et al., 2011). Moreover, the high levels of quartz, which are consistent with the petrography study, at the K/Pg boundaries of both sections may be attributed to a quartz influx increase as sea level falls during the K/Pg event (Bourgeois et al., 1988; Smit, 1999). Analcime was diagnosed at both the K/Pg boundary and the Lower Paleogene layers (samples Q18 and Q19, respectively) of the Qalbaza section. It is a low-temperature phase that can be a replacement product from vitric tuffs, cement of pyroclastic rocks, or spherules of silica glass as an authigenic mineral in the sediments (Gribble and Hall, 1985; Liou et al., 1991). Analcime occurs in terrestrial deposits under warm, arid to semi-arid environments (Iijima and Utada, 1966; Liou et al., 1991). This phase was found at the K/Pg boundary and/or the Lower Paleogene layer in Taringatura of New Zealand (Coombs, 1954), Chicxulub impact crater (Kring et al., 2020), Western Argentina (Montano et al., 2023), and Alabama in the USA (Pitakpaivan et al., 1994). Therefore, analcime presence at both the K/Pg boundary layer and the Lower Paleogene layers of the Qalbaza section may be attributed to the Deccan eruptions and/or Chicxulub impact event.

Clay minerals of Gali and Qalbaza sections across the proposed K/Pg boundary are dominated by smectite (montmorillonite), chlorite-smectite mixed layer, chlorite + trace of kaolinite, and vermiculite (Figs. 15 B, F; 16 D, E, F, G, and Tables 8, 9, 10). The K/Pg boundary (sample G19OS) of the Gali section has a higher smectite content than the Paleogene layer (sample G21OS) (Table 8). Smectite minerals are formed by the weathering of igneous and metamorphic rocks in a semi-arid climate and alkaline water with restricted water movement (Carroll, 1970). Smectite usually reflects volcanic activities; it can be derived from a volcanic ash submarine alteration during a devitrification process (Harder, 1972). Smectite can also be derived from spherules associated with the Mexico ‘‘Chicxulub’’ impact, where the spherules may be completely replaced by smectite, calcite, or chlorite (Mateo et al., 2019), like Demerara Rise in western North Atlantic, La Sierrita in NE Mexico, and Brazos River in Texas (Mateo et al., 2019). The Gali section's Paleogene layer (sample G21OS) has higher chlorite-smectite content than the K/Pg boundary (sample G19OS) (Table 8), while the Qalbaza section's Paleogene layers (samples Q19OS and Q21OS) show a significant chlorite-smectite mixed layer (Table 10). Temperature increases cause smectite to change gradually into chlorite (Horton, 1985), indicating temperatures were restored after the K/Pg event. A significant amount of vermiculite was determined at the K/Pg boundary (sample Q18) of the Qalbaza section (Fig. 16D and Table 9). Vermiculite arises essentially from the weathering of biotite and muscovite under arid conditions (Pal et al., 1989; Srivastava et al., 1998). Vermiculite was one clay mineral identified at the K/Pg boundary between the Tanjero and Kolosh formations around Sulaimani City, Iraq (Mustafa et al., 2022).

The proposed K/Pg boundaries of both studied sections are mineralogically characterized by the low calcite, high quartz, analcime, and clay minerals of smectite and vermiculite, so they resemble all other global well-known K/Pg boundaries, such as Stevns Klint in Denmark, Blake Nose in the NW Atlantic, Agost and Caravaca in Spain, and Gubbio in Italy. Additionally, the proposed K/Pg boundaries of both studied sections differ from these typical K/Pg boundaries due to the absence of spherules and shocked quartz related to the Chicxulub event; this may be attributed to the spherules being completely replaced by smectite, calcite, or chlorite and the disappearance of shocked quartz grains gradually with

distance from the Chicxulub crater (Joanna et al., 2006), similar to the K/Pg boundaries of Hermanas hill section in western Cuba (Jorge et al., 2015) and Medetli and Gölpazari sections in northwestern Turkey (Yoji et al., 2003). Therefore, the mineralogical results indicate that the G19 and Q18 layers of the Gali and Qalbaza sections, respectively, may represent the K/Pg boundaries, while not excluding the idea that part of these boundaries may have been eroded.

Geochemistry

The chemical composition of major, trace, and rare earth elements is given in Tables 11 and 12. Chondrite-normalized REE patterns (Fig. 17) exhibit similarity with each other and show a one-package zigzag pattern; this may reflect a single melt that suffered from differentiation to provide the source rocks from which sediments were derived. Generally, the REE pattern differs from UCC and PAAS patterns and displays more enrichment than chondrite and slightly enriched light rare earth elements (LREEs) relative to heavy rare earth elements (HREEs) (Tables 11 and 12; Fig. 17), as well as elevated Tb and Tm, suggesting the REE scavenging mechanism from seawater (De Baar et al., 1985). Moreover, the sediments show positive Eu and slightly negative Ce anomalies in most samples (Tables 11 and 12; Fig. 17). The Eu anomaly is exhibited by transitioning from Eu^{3+} to Eu^{2+} under reducing conditions (Brookins, 1989). Positive Eu anomalies (Eu/Eu* > 1) have often been caused by plagioclase feldspar accumulation during magmatic differentiation (Trubelja et al., 1995), so the positive anomaly may be due to the absence and/or slight presence of plagioclase in the studied samples. The soluble Ce^{3+} oxidation to less soluble Ce^{4+} is responsible for the negative Ce anomaly (Ce/Ce* < 1) (Sholkovitz et al., 1994). Positive Eu/Eu* and slightly negative Ce/Ce* (Tables 11 and 12; Fig. 17) may suggest that the studied sediments were deposited under oxic-anoxic paleoredox conditions.

The K/Pg boundaries of Gali and Qalbaza sections are shared by a prominent positive anomaly for SiO_2, Al_2O_3, Fe_2O_3, MgO, Na_2O, K_2O, TTEs ‘‘transition trace elements’’ (Ni, Co, Cr, Sc, and V), Zr, Zn, and Cu and a prominent negative anomaly for CaO, MnO, LOI, Hf, Sr, and Cs (Figs. 18-21). The K/Pg boundary layers around the world often contain elevated concentrations of SiO_2, Al_2O_3, Fe_2O_3, MgO, Na_2O, K_2O, TiO_2, Ni, Co, Cr, Sc, V, Zr, Zn, and Cu (Alvarez et al., 1980; Smit and ten Kate, 1982; Vajda and Wigforss-Lange, 2006). Therefore, proponents of the impact theory propose that the asteroid and target zone are the source of these elements (Smit and ten Kate, 1982; Gilmour and Anders, 1989), and advocates of volcanic activity theory argue that these elements are derived from the post-fallout from the Deccan cloud (Graup et al., 1989). SiO_2, Al_2O_3, Fe_2O_3, MgO, Na_2O, and K_2O elements elevate during the K/Pg event due to vegetation decreases or sea-level fall, causing the ground to become unstable and further prone to erosional stages (Bercovici et al., 2012).

Table 11: Concentrations of major oxides (in wt%), trace elements (in ppm), and rare earth elements (in ppm) of the Gali section. Major oxides were analyzed by XRF; trace and rare earth elements were analyzed by ICP-MS. * Major oxides were analyzed by ICP-MS.

	G23	G22	G21	G20	G19 (K/Pg)	G18	G17*	Min.	Max.	Average
SiO_2		44.43	37.32	11.02	40.92	26.57		11.02	44.43	32.05
Al_2O_3	6.67*	8.48	6.11	1.01	7.48	2.66	>5.0*	1.01	8.48	5.40
Fe_2O_3	>5.0*	7.29	6.20	0.89	6.76	3.24	>5.0*	0.89	7.29	4.88
MgO	>5.0*	10.54	8.73	1.35	8.87	5.47	>5.0*	1.35	10.54	6.99
CaO	>5.0*	9.78	17.74	46.65	13.97	31.61	>5.0*	9.78	46.65	23.95
Na_2O	0.47*	0.30	0.11	0.38	0.22	0.21	1.47*	0.11	1.47	0.45
K_2O	0.60*	0.64	0.27	0.03	0.45	0.03	0.52*	0.03	0.64	0.36
TiO_2	0.27*	0.337	0.233	0.044	0.269	0.132	0.43*	0.04	0.43	0.25
P_2O_5	0.04*	0.07	0.08	0.04	0.06	0.05	0.04*	0.04	0.08	0.05
MnO	0.07*	0.132	0.115	0.242	0.122	0.135	0.08*	0.07	0.242	0.13
LOI		17.82	22.89	38.07	20.64	29.66		17.82	38.07	25.82
Total		99.82	99.80	99.73	99.76	99.77				
Ni	1110	717	562	64	598	201	827	64	1110	582.71
Co	88.24	78.67	36.68	6.72	58.27	15.78	85.94	6.72	88.24	52.90
Cr	677	418	226	22	299	63	531	22	677	319.43
Sc	19.8	25.1	16.2	2.1	19.4	6.8	32.9	2.1	32.9	17.47

V	91	119	76	17	93	33	136	17	136	80.71
Zr	71	68	92	<1	71	17	19	1	92	48.43
Hf	10.36	9.25	8.65	8.58	10.25	11.06	12.01	8.58	12.01	10.02
Nb	4.69	5.85	6.47	7.85	7.89	6.21	5.45	4.69	7.89	6.34
Ta	3.58	5.96	3.58	4.25	3.41	5.78	6.01	3.41	6.01	4.65
Th	6.25	9.21	8.25	10.25	7.65	9.74	8.25	6.25	10.25	8.51
U	2.58	1.41	3.12	6.58	4.62	4.25	2.54	1.41	6.58	3.59
Y	14.25	15.36	15.21	11.25	16.54	13.25	18.52	11.25	18.52	14.91
Ba	6147.8	1610.3	622.3	3.2	1212.3	19.2	27.3	3.2	6147.8	1377.49
Rb	14.36	16.25	17.85	13.25	11.25	14.25	13.25	11.25	17.85	14.35
Sr	198.1	234.4	328	336.1	316.7	539.6	144	144	539.6	299.56
Cs	7.14	6.25	9.01	6.58	7.58	9.59	8.21	6.25	9.59	7.77
Li	23	36	28	9	34	23	33	9	36	26.57
Ga	5.41	2.25	1.26	2.14	4.26	3.85	1.14	1.14	5.41	2.90
Pb	333.25	4.26	1.25	6.25	7.21	1.45	3.25	1.25	333.25	50.99
Ag	0.74	0.32	3.01	0.25	0.41	0.31	0.41	0.25	3.01	0.78
As	8	7	8	3	4	5	2	2	8	5.29
Be	0.28	0.34	0.64	0.89	0.25	0.41	0.89	0.25	0.89	0.53
Bi	3.25	3.07	2.01	1.47	1.25	6.21	1.25	1.25	6.21	2.64
Cd	0.47	0.62	0.14	0.25	0.56	0.14	0.21	0.14	0.62	0.34
In	0.21	0.78	0.25	0.41	0.36	0.48	0.85	0.21	0.85	0.48
Mo	1.03	0.24	1.07	1.65	0.12	1.4	0.23	0.12	1.65	0.82
S	1800	500	300	200	500	500	300	200	1800	585.71
Sb	3.58	3.25	2.58	1.47	1.25	2.85	3.58	1.25	3.58	2.65
Sn	1.89	5.32	4.98	9.95	3.58	10.47	2.52	1.89	10.47	5.53
Te	0.34	0.58	0.74	0.48	0.36	0.85	0.24	0.24	0.85	0.51
Tl	3.25	1.85	2.54	2.14	3.21	3.25	2.14	1.85	3.25	2.63
W	1.25	6.25	7.45	2.85	3.62	6.25	2.58	1.25	7.45	4.32
Cu	39.1	57.1	44.6	7.1	48.2	27.3	59.1	7.1	59.1	40.36
Zn	63.6	78.8	56.3	8.1	66.2	22.5	64.9	8.1	78.8	51.49
La	5.15	5.96	6.96	4.64	8.09	6.32	3.12	3.12	8.09	5.75
Ce	11.25	12.36	14.25	10.36	17.65	13.58	6.21	6.21	17.65	12.24
Pr	2.98	1.71	2.69	2.03	3.28	2.26	1.03	1.03	3.28	2.28
Nd	6.23	4.69	4.89	3.79	6.89	4.69	2.26	2.26	6.89	4.78
Sm	4.49	3.26	3.21	3.21	3.01	2.12	1.03	1.03	4.49	2.90
Eu	3.03	2.31	2.26	2.29	2.01	1.03	0.69	0.69	3.03	1.95
Gd	4.12	3.19	4.58	3.69	2.89	1.89	0.95	0.95	4.58	3.04
Tb	2.89	2.03	2.12	2.59	1.03	0.91	0.43	0.43	2.89	1.71
Dy	3.89	3.01	3.59	3.39	2.21	1.59	0.69	0.69	3.89	2.62
Ho	2.42	1.71	1.49	2.49	0.79	0.69	0.31	0.31	2.49	1.41
Er	3.59	2.68	3.03	3.26	1.89	1.49	0.51	0.51	3.59	2.35
Tm	2.12	1.39	1.12	2.13	0.41	0.51	0.23	0.23	2.13	1.13
Yb	3.12	2.12	2.59	2.95	1.29	1.31	0.47	0.47	3.12	1.98
Lu	1.78	1.03	0.79	1.89	0.31	0.36	0.12	0.12	1.89	0.90
LREE	33.13	30.29	34.26	26.32	40.93	30.00	14.34	14.34	40.93	29.90
HREE	23.93	17.16	19.31	22.39	10.82	8.75	3.71	3.71	23.93	15.15
LREE/HREE	1.38	1.77	1.77	1.18	3.78	3.43	3.87	1.18	3.87	2.45
ΣREE	57.06	47.45	53.57	48.71	51.75	38.75	18.05	18.05	57.06	45.05
(La/Sm)*n*	0.74	1.18	1.40	0.93	1.74	1.92	1.96	0.74	1.96	1.41
(Gd/Yb)*n*	1.09	1.24	1.46	1.03	1.85	1.19	1.67	1.03	1.85	1.36
(La/Yb)*n*	1.18	2.02	1.93	1.13	4.50	3.46	4.76	1.13	4.76	2.71
Eu/Eu*	2.16	2.19	1.80	2.04	2.09	1.58	2.14	1.58	2.19	2.00
Ce/Ce*	0.70	0.95	0.81	0.83	0.84	0.88	0.85	0.70	0.95	0.84

Table 12: Concentrations of major oxides (in wt%), trace elements (in ppm), and rare earth elements (in ppm) of the Qalbaza section. Major oxides were analyzed by XRF; trace and rare earth elements were analyzed by ICP-MS.

	Q21	**Q19**	**Q18 (K/Pg)**	**Q17**	**Q16**	**Q15**	**Min.**	**Max.**	**Average**
SiO_2	63.64	53.44	55.71	33.95	56.25	58.84	33.95	63.64	53.64
Al_2O_3	9.78	10.28	9.89	7.31	8.7	10.49	7.31	10.54	9.41
Fe_2O_3	4.34	7.85	7.55	3.3	4.17	5.26	3.30	7.85	5.41
MgO	2.8	5.64	3.49	1.76	2.68	3.14	1.76	5.64	3.25
CaO	5.83	7.24	6.73	28.22	10.31	7.77	5.83	28.22	11.02
Na_2O	1.36	0.72	1.63	0.63	0.17	0.45	0.17	1.63	0.83
K_2O	0.41	1.35	0.66	0.21	2.01	1.51	0.21	2.01	1.03
TiO_2	0.438	0.62	0.586	0.246	0.345	0.434	0.25	0.62	0.44
P_2O_5	0.057	0.056	0.038	0.062	0.106	0.087	0.04	0.11	0.07
MnO	0.064	0.119	0.078	0.334	0.085	0.07	0.06	0.33	0.13
LOI	11.12	12.41	12.99	23.84	14.97	11.66	11.12	23.84	14.50
Total	99.84	99.73	99.35	99.86	99.80	99.71			
Ni	74	64	90	60	68	64	60	90	70
Co	35.18	38.36	38.14	29.41	22.03	26.55	22.03	38.36	31.61
Cr	65	87	128	40	40	42	40	128	67
Sc	25.3	34.1	31.4	13.7	16.2	21.2	13.7	34.1	23.65

V	138	206	186	118	95	133	95	206	146
Zr	54	57	56	49	108	98	49	108	70.33
Hf	10.36	9.36	8.14	9.85	12.05	11.36	8.14	12.05	10.19
Nb	3.25	3.14	4.62	5.52	4.69	2.85	2.85	5.52	4.01
Ta	3.25	5.89	4.58	6.09	3.58	4.78	3.25	6.09	4.70
Th	9.25	10.36	11.25	10.36	9.54	4.85	4.85	11.25	9.27
U	3.74	2.78	3.58	6.35	4.87	3.69	2.78	6.35	4.17
Y	15.01	14.85	12.58	13.25	11.25	17.21	11.25	17.21	14.03
Ba	89.3	261.1	127.5	2909.6	3347.9	4795.6	89.3	4795.6	1921.83
Rb	13.85	17.25	19.21	13.69	14.25	13.25	13.25	19.21	15.25
Sr	128.8	484.3	145.6	290.1	503	328.6	128.8	503	313.4
Cs	9.85	7.85	5.98	8.14	9.21	6.28	5.98	9.85	7.89
Li	26	30	42	20	23	24	20	42	27.5
Ga	5.41	3.25	2.41	1.69	1.78	3.52	1.69	5.41	3.01
Pb	1.21	0.12	1.25	512.32	287.36	113.25	0.12	512.32	152.59
Ag	0.74	0.85	0.62	0.52	0.25	0.65	0.25	0.85	0.61
As	2	5	3	4	1	3	1	5	3
Be	0.47	0.89	0.74	0.65	1.44	0.74	0.47	1.44	0.82
Bi	4.05	1.32	1.25	6.03	1.85	1.58	1.25	6.03	2.68
Cd	0.52	0.21	0.14	0.36	0.14	0.52	0.14	0.52	0.32
In	0.45	0.31	0.36	0.14	0.62	0.25	0.14	0.62	0.36
Mo	2.25	0.21	0.14	1.04	0.21	1.22	0.14	2.25	0.85
S	900	1200	1300	2100	1000	1500	900	2100	1333.33
Sb	1.54	1.23	1.23	1.25	2.47	3.45	1.23	3.45	1.86
Sn	3.21	2.36	6.54	5.48	2.25	3.64	2.25	6.54	3.91
Te	0.52	0.47	0.91	0.68	0.18	0.52	0.18	0.91	0.55
Tl	3.25	4.14	3.25	2.58	1.78	1.25	1.25	4.14	2.71
W	93.61	34.21	45.48	60.29	5.25	4.25	4.25	93.61	40.52
Cu	37.4	95.1	35.2	26.4	55.9	65.1	26.4	95.1	52.52
Zn	37.8	73.9	43.3	31.6	70.6	64.3	31.6	73.9	53.58
La	6.12	6.36	4.14	10.20	16.67	16.45	4.14	16.67	9.99
Ce	12.01	11.25	9.21	21.25	32.25	31.25	9.21	32.25	19.54
Pr	1.29	2.12	1.89	6.36	8.96	9.25	1.29	9.25	4.98
Nd	4.23	4.21	2.89	8.48	13.25	12.69	2.89	13.25	7.63
Sm	3.26	3.03	2.03	6.25	7.96	8.69	2.03	8.69	5.20
Eu	2.36	2.14	1.23	5.01	7.03	6.25	1.23	7.03	4.00
Gd	3.96	3.02	2.58	6.18	10.58	9.09	2.58	10.58	5.90
Tb	2.12	2.03	1.03	4.56	6.25	5.36	1.03	6.25	3.56
Dy	3.25	2.89	2.12	5.39	9.36	8.03	2.12	9.36	5.17
Ho	1.89	1.58	0.91	3.78	5.15	5.03	0.91	5.15	3.06
Er	3.21	2.48	1.59	5.05	7.58	7.51	1.59	7.58	4.57
Tm	1.26	1.23	0.51	3.01	4.25	4.36	0.51	4.36	2.44
Yb	2.58	2.29	1.21	3.78	6.31	6.96	1.21	6.96	3.86
Lu	0.96	0.89	0.32	2.15	3.25	3.25	0.32	3.25	1.80
LREE	29.27	29.11	21.39	57.55	86.12	84.58	21.39	86.12	51.34
HREE	19.23	16.41	10.27	33.90	52.73	49.59	10.27	52.73	30.36
LREE/HREE	1.52	1.77	2.08	1.70	1.63	1.71	1.52	2.08	1.74
ΣREE	48.50	45.52	31.66	91.45	138.85	134.17	31.66	138.85	81.69
(La/Sm)*n*	1.21	1.36	1.32	1.05	1.35	1.22	1.05	1.36	1.25
(Gd/Yb)*n*	1.27	1.09	1.76	1.35	1.38	1.08	1.08	1.76	1.32
(La/Yb)*n*	1.70	1.99	2.45	1.94	1.89	1.70	1.70	2.45	1.95
Eu/Eu*	2.01	2.17	1.65	2.47	2.34	2.15	1.65	2.47	2.13
Ce/Ce*	1.05	0.75	0.81	0.65	0.65	0.62	0.62	1.05	0.75

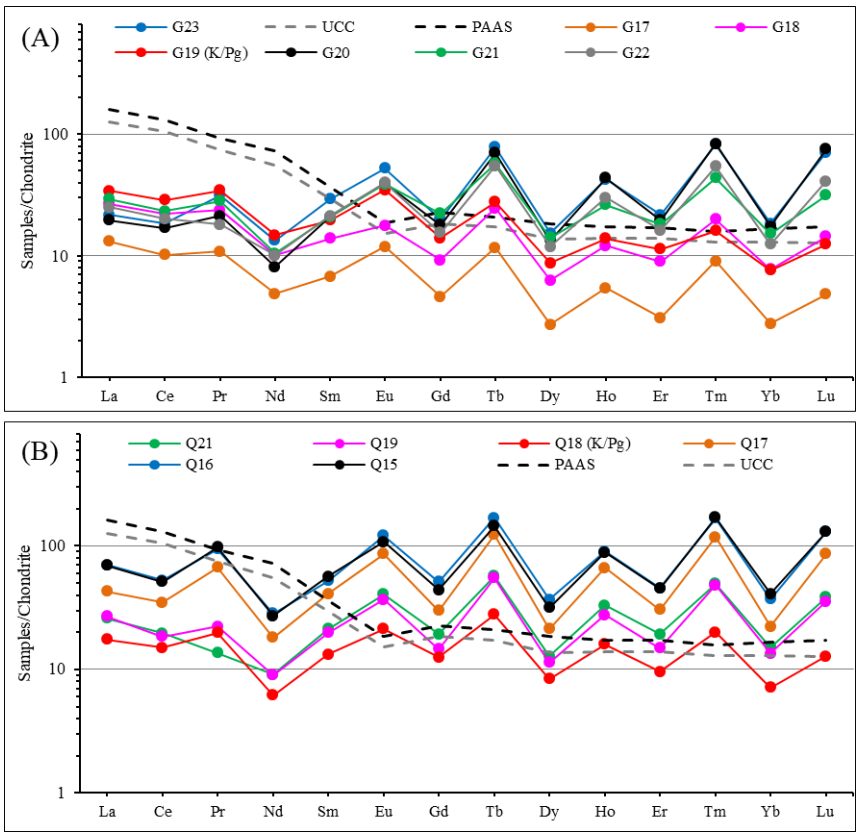


Fig. 17. Chondrite-normalized REE pattern of sediments across the K/Pg boundary in (A) Gali section and (B) Qalbaza section. Chondrite values are taken from Sun and McDonough (1989), and PAAS and UCC from Taylor and McLennan (1985).

Ni and Cr are two of the key elements to detect a K/Pg boundary (Smit and ten Kate, 1982), where high levels of Ni and Cr at the K/Pg boundary layer may be generated by an extraterrestrial origin (Smit and ten Kate, 1982). Furthermore, the elevated authigenic concentrations (element/Al) of Fe, Ni, and Cr within the proposed K/Pg layers of Gali and Qalbaza sections (Table 13) are a good indicator of these boundaries (Sosa-Montes de Oca et al., 2013; 2020). In addition, the elevated contents of Zr, Zn, and Cu may suggest that these elements derived from the rocks that were the Chicxulub target, or possibly derived from the post-fallout from the Deccan cloud (Premovic et al., 2004; Vajda and Wigforss-Lange, 2006). The Chicxculub fireball vapor cloud and/or Deccan eruptions cloud could produce an atmospheric acidity condition due to the release of amounts of SO_2, causing acidity rainfall (Prinn and Fegley, 1987), and this results in a higher SO_2/MnO ratio at the K/Pg boundary layer relative to prior and post layers (Keller, 2014; Renne et al., 2015). The K/Pg boundaries of the Gali and Qalbaza sections (samples G19 and Q18) exhibit a high SO_2/MnO ratio compared to the prior and post layers (Table 13).

PGEs anomaly proves the K/Pg boundary (Alvarez et al., 1980). Unfortunately, PGEs were undetected (< 5 pbb) in 3 samples of the Gali section (samples G19, G20, and G21) and 4 samples of the Qalbaza section (samples Q16, Q17, Q18, and Q19). As a result, this work suggests that PGEs may not be detectable at concentrations less than 5 ppb in Iraqi K/Pg boundary sites.

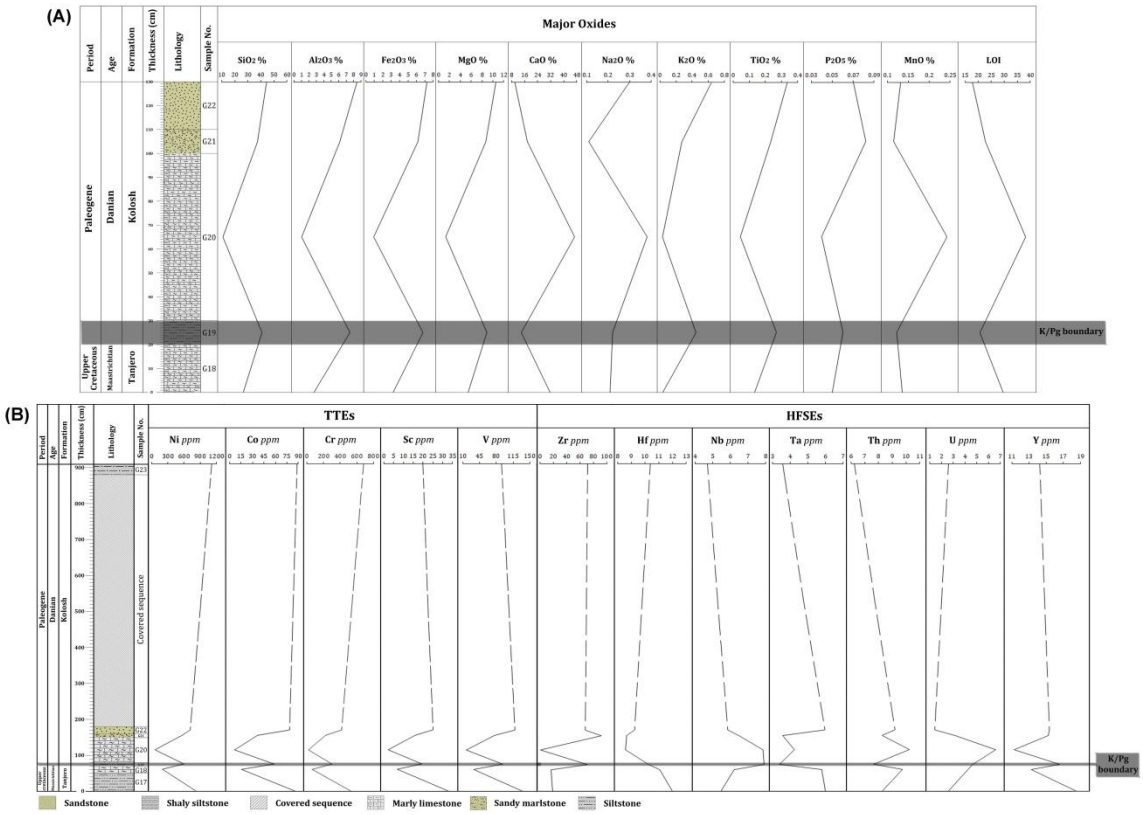


Fig. 18. Vertical distribution profile plot across the K/Pg boundary from the Gali section. (A) Major oxides with LOI. (B) Transition trace elements (TTEs) and high field strength elements (HFSEs). The gray area represents the K/Pg boundary layer.

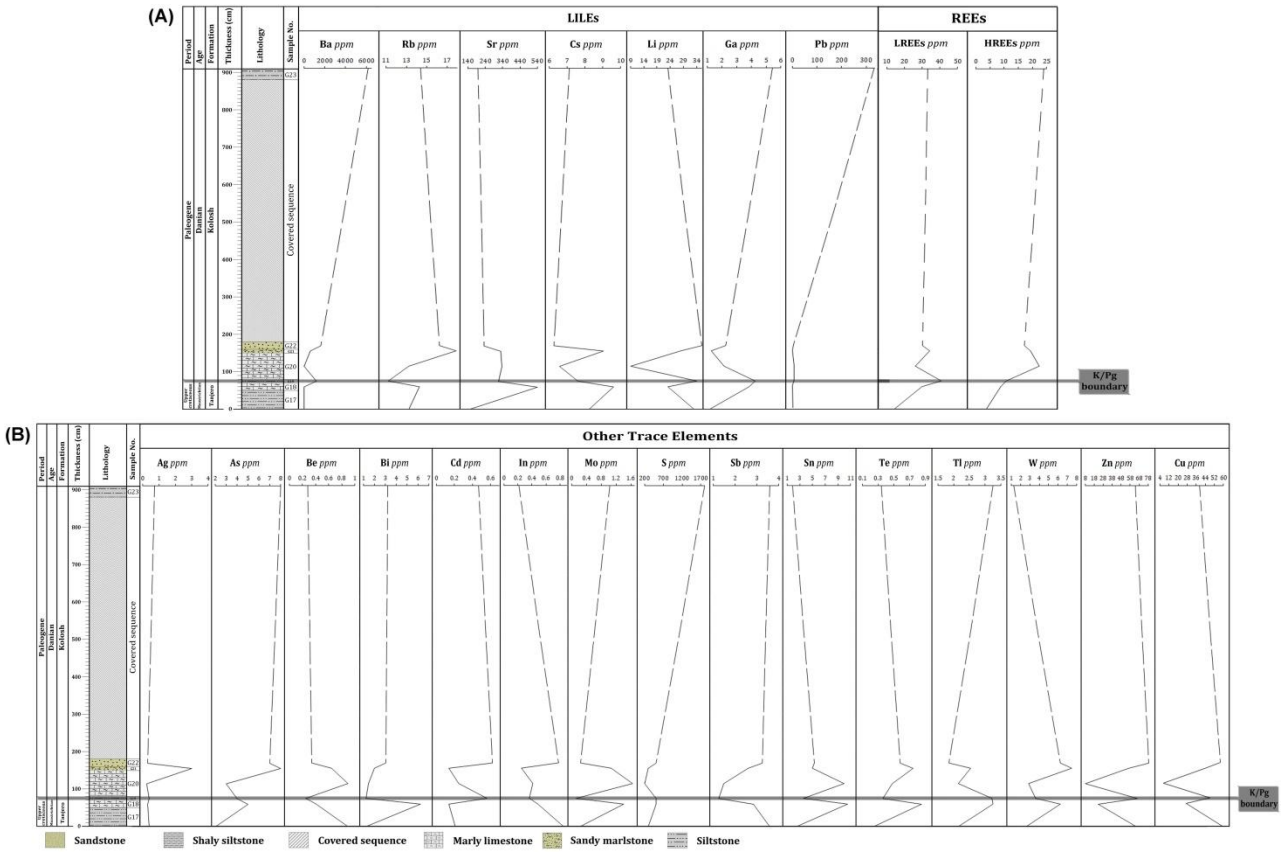


Fig. 19. Vertical distribution profile plot across the K/Pg boundary from the Gali section. (A) Large ion lithophile elements (LILEs), Light rare earth elements (LREEs), and heavy rare earth elements (HREEs). (B) Ag, As, Be, Bi, Cd, In, Mo, S, Sb, Sn, Te, Tl, W, Zn, and Cu elements. The gray area represents the K/Pg boundary layer.

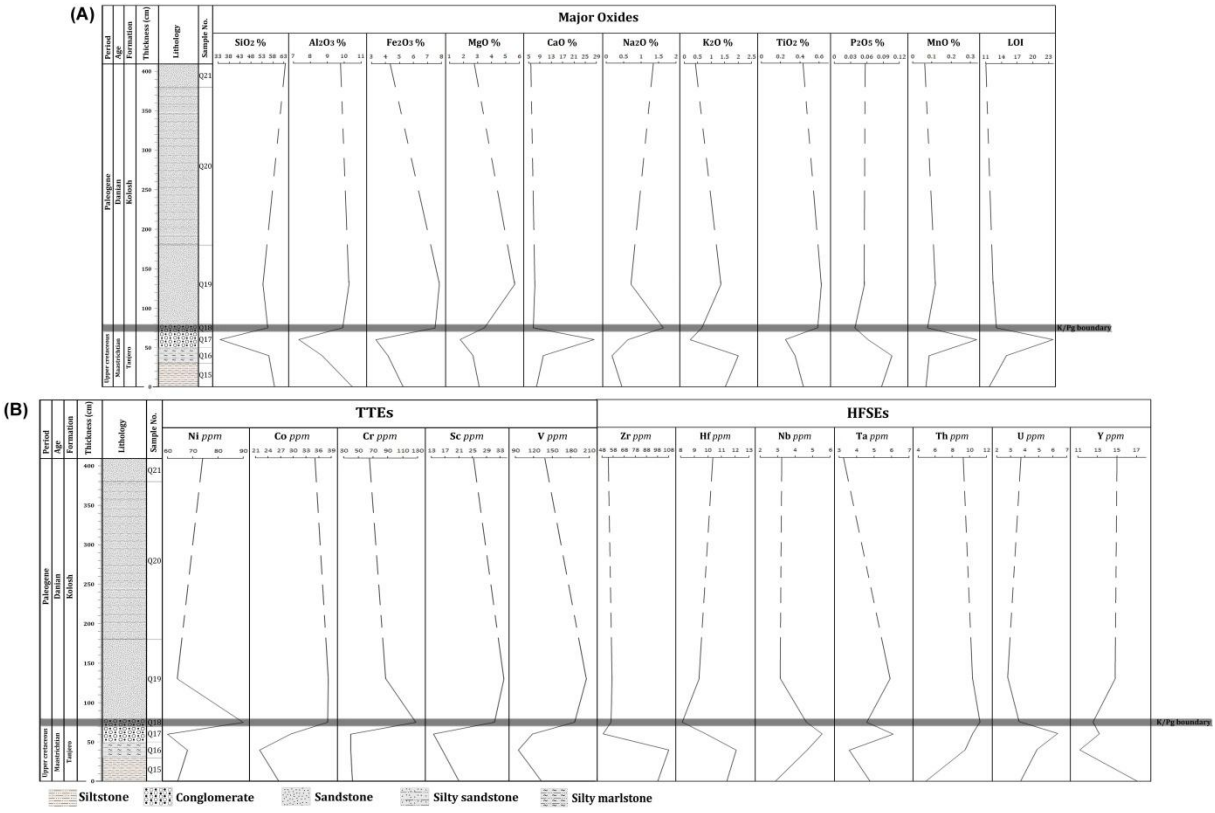


Fig. 20. Vertical distribution profile plot across the K/Pg boundary from the Qalbaza section. (A) Major oxides with LOI. (B) Transition trace elements (TTEs) and high field strength elements (HFSEs). Sample Q20 was not analyzed; the gray area represents the K/Pg boundary layer.

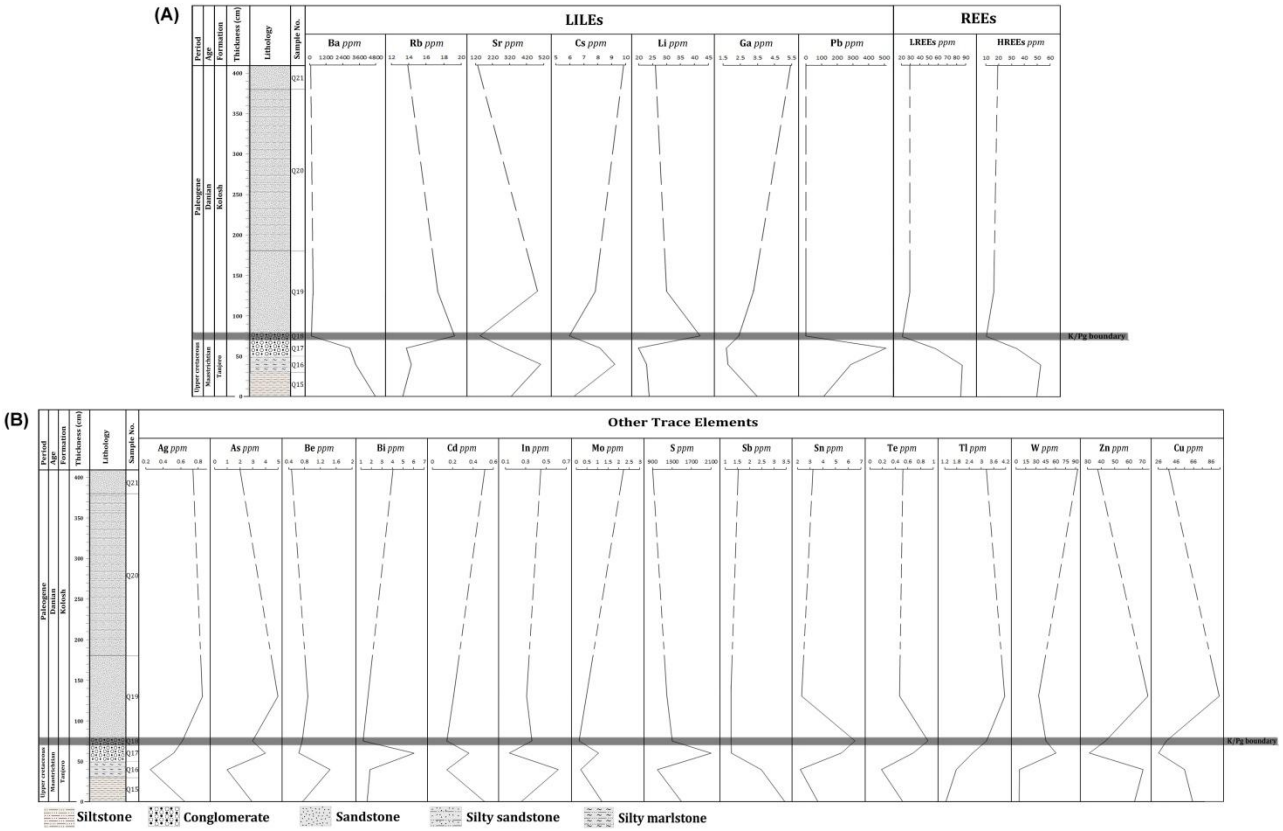


Fig. 21. Vertical distribution profile plot across the K/Pg boundary from the Qalbaza section. (A) Large ion lithophile elements (LILEs), light rare earth elements (LREEs), and heavy rare earth elements (HREEs) (B) Ag, As, Be, Bi, Cd, In, Mo, S, Sb, Sn, Te, Tl, W, Zn, and Cu elements. Sample Q20 was not analyzed; the gray area represents the K/Pg boundary layer.

Table 13: Element/Al and SO_2/MnO ratios in the studied samples across the K/Pg boundary from Gali and Qalbaza sections.

Section	Sample	Fe/Al	Ni/Al	Cr/Al	SO_2/MnO
Gali	G22	1.097	0.0154	0.0090	0.537
	G21	1.291	0.0167	0.0067	0.563
	G20	1.055	0.0108	0.0037	0.164
	G19 (K/Pg)	1.522	0.0155	0.0077	1.042
	G18	1.462	0.0130	0.0041	0.925
Qalbaza	Q21	0.586	0.0014	0.0013	9.350
	Q19	1.007	0.0012	0.0016	6.901
	Q18 (K/Pg)	1.009	0.0017	0.0024	9.791
	Q17	0.577	0.0015	0.0010	4.169
	Q16	0.660	0.0015	0.0009	5.670
	Q15	0.663	0.0012	0.0008	11.094

Moreover, a sharp reduction in CaO may be attributed to acidic rain caused by Chicxulub and/or Deccan events, which temporarily prevented the development of $CaCO_3$ during the K/Pg boundary event (Keller et al., 2011). LOI shows a strong positive correlation with CaO in the studied sections (r = 0.99 for Gali and Qalbaza sections, respectively), indicating a drop in LOI at K/Pg boundaries of the current study. The reasons behind the depletion of trace elements at low temperatures are not well understood. Depletion mechanisms are influenced by trace element solubility, oxygen fugacity, and pH in aqueous environments (Ritter et al., 2015). Consequently, we are simply describing the possibility of detecting the K/Pg boundary.

According to geochemical results, the G19 and Q18 layers of the Gali and Qalbaza sections, respectively, appear to have originated during the Cretaceous and Paleogene periods.

Conclusion

The main conclusions of this study are:

1. Gali and Qalbaza sandstones are immature lithic graywacke derived from the undissected arc-recycled orogenic provenance and deposited in an arid to semi-arid paleoclimate.
2. Vermiculite, smectite, and analcime phases support arid-semi-arid paleoclimate conditions for Gali and Qalbaza sediments.
3. Rare earth elements (REE) suggested a single melt suffered differentiation to provide the source rocks that weathered and deposited under oxic-anoxic paleoredox conditions.
4. Carbonate rock fragments, chert, and heavy minerals decreased, while total quartz and K-feldspar increased by 10 cm thick in both the grey siltstone of the Gali section and the red conglomerate of the Qalbaza section.
5. At 10 cm thick, low calcite content, high quartz content, analcime, smectite, and vermiculite have been identified in both the grey siltstone of the Gali section and the red conglomerate of the Qalbaza section.
6. Positive anomalies for SiO_2, Al_2O_3, Fe_2O_3, MgO, Na_2O, K_2O, TTEs, Zr, Zn, and Cu, and negative anomalies for CaO, MnO, LOI, Hf, Sr, and Cs were recorded at 10 cm thick in both the grey siltstone of the Gali section and red conglomerate of Qalbaza section.
7. Elevated levels of Fe/Al, Ni/Al, Cr/Al, and SO_2/MnO were detected at 10 cm thick of gray siltstone and red conglomerate layers from the Gali and Qalbaza sections, respectively.
8. Based on the current mineralogical and geochemical evidence, the proposed boundaries of gray siltstone and red conglomerate layers from the Gali and Qalbaza sections, respectively, could represent the K/Pg boundaries, with parts of them perhaps eroded.

Acknowledgements

We are grateful to the Department of Geology at Basrah University for the facilities they provide. We would also like to thank Dr. Kamal Karim, Dr. Nabaz Aziz, Mr. Madyan

Al-Gburi, and Mr. Irfan Asaad for their assistance in the fieldwork and sampling. We are very thankful to Dr. Kotayba Al-Youzbakey, Dr. Ahid Almallah, Dr. Zaid Malak, Dr. Safwan Al-Lhaebi, and Dr. Salem Hamed for their valuable discussions that supported this study. We also thank the Journal's Editor in Chief, Secretary, Technical Editors, and Reviewers for their valuable contributions and suggestions.

References

Abawi, T.S., Abdel Kireem, M.R. and Yousef, G.M., 1982. Planktonic foraminiferal stratigraphy of the Shiranish Formation, Sulaimaniah-Dokan region Northeastern Iraq, Revista Espanola de Micropaleontologia, Vol. 14, No. 1-3, pp. 153-164. https://dialnet.unirioja.es/servlet/articulo?codigo=8997713.

Adatte, T., Keller, G., Burns, S., Stoykova, K.H., Ivanov, M.I., Vangelov, D., Kramar, U. and Stuben, D., 2002. Paleoenvironment across the Cretaceous-Tertiary transition in eastern Bulgaria, in Adatte, T., Koeberl, C., and MacLeod, K.G., eds., Catastrophic Events and Mass Extinctions: Impacts and Beyond: Boulder, Colorado, Geological Society of America Special Paper 356, pp. 231–251. DOI: 10.1130/0-8137-2356-6.231.

Al-Hamed, S.T. and Malak, Z.A., 2021. Comparison Between the Classical Classification and Digital Classification for Selected Samples of Igneous and Carbonate Rocks. Iraqi Geological Journal, Vol. 54, No. 1C, pp. 16-29. Doi: 10.46717/igj.54.1C.2Ms-2021-03-22.

Al-Hamidi, R.I., Al-Hamed, S.T., Malak, Z.A. and Al-Sanjary, A.A., 2023. Mineralogy and Geochemistry of Sandstones from the Tanjero Formation, Bekhme Gorge Northeastern Iraq: Implications for Paleoweathering and Provenance. The Iraqi Geological Journal, Vol. 56, No. 1C, pp. 25-39. DOI: 10.46717/igj.56.1C.3ms-2023-3-14.

Al-Qayim, B.A., Kharajiany, S.O.A. and Sherwood, W.W.Jr., 2020. Biostratigraphic analysis of the K/Pg boundary using calcareous nannofossils from the Sulaimani Area, Kurdistan Region, Iraq. Kuwait Jour.of Sci. and Eng., Vol. 47, No. 4, pp. 92-105.

Alvarez, L.W., Alvarez, W., Asaro, F. and Michel, H.V., 1980. Extraterrestrial cause for the Cretaceous-Tertiary extinction: Experimental results and theoretical interpretation. Science, Vol. 208, No. 4448, pp. 1095-1108. DOI: 10.1126/science.208.4448.1095.

Arakawa, Y., Li, X., Ebihara, M., Meriç, E., Tansel, I., Bargu, S. and Matsumaru, K., 2003. Element profiles and Ir concentration of Cretaceous-Tertiary (KT) boundary layers at Medetli, Gölpazari, northwestern Turkey. Geochemical journal, Vol. 37, No. 6, pp. 681-693. DOI: 10.2343/geochemj.37.681.

Arenillas, I., Arz, J.A. and Molina, E., 2004. A new high-resolution planktonic foraminiferal zonation and subzonation for the lower Danian. Lethaia, Vol. 37, No. 1, pp. 79–95. DOI: 10.1080/00241160310005097.

Bardeen, C.G., Garcia, R.R., Toon, O.B. and Conley, A.J., 2017. On transient climate change at the Cretaceous-Paleogene boundary due to atmospheric soot injections. Proceedings of the National Academy of Sciences USA, Vol. 114, No. 36, pp. E7415–E7424. DOI: 10.1073/pnas.1708980114.

Bercovici, A., Vajda, V., Pearson, D., Villanueva-Amadoz, U. and Kline, D., 2012. Palynostratigraphy of John's Nose, a new Cretaceous–Paleogene boundary section in southwestern North Dakota, USA. Palynology, Vol. 36, No. 1, pp. 36-47. DOI: 10.1080/01916122.2012.678695.

Boggs, S.J., 2006. Principles of sedimentology and stratigraphy. 4th ed., Pearson Prentice Hall, Upper Saddle River, New Jersey, 662 p. Online version: 647640269.

Bourgeois, J., Hansen, T.A., Wiberg, P.L. and Kauffman, E.G., 1988. A Tsunami Deposit at the Cretaceous-Tertiary Boundary in Texas. Science, Vol. 241, No.4865, pp. 567–570. DOI: 10.1126/science.241.4865.567.

Brookins, D.G., 1989. Aqueous geochemistry of rare earth elements. In: Lipin BR, McKay GAŽ (eds) Geochemistry and mineralogy of rare earth elements. Reviews in Mineralogy and Geochemistry, Vol. 21, No. 1, pp. 201-225.

Buday, T. and Jassim, S., 1987. The Regional Geology of Iraq: Tectonics, Magmatism, and Metamorphism. In: Kassab, I.I. and Abbas, M.J., Eds, Stratigraphy, State Establishment of Geological Survey and Mineral Investigations, Baghdad, pp. 1-445.

Buday, T. and Jassim, S.Z., 1984. Tectonic Map of Iraq, Scale 1:1,000,000. GEOSURV, Baghdad. https://www.scirp.org/reference/referencespapers?referenceid=1264156.

Carroll, D.C., 1970. Clay minerals: A guide to their X-Ray identification. The Geological Society of America, Special Paper 126, Colorado Building, 80 p.

Carver, R.E., 1971. Procedures in sedimentary petrology. John Wiley and Sons, New York, 653 P.

Çelik, H. and Salih, H.M.H., 2021. Petrographic characteristics of deep marine turbidite sandstones of the Upper Cretaceous Tanjero Formation, Northwestern Sulaimaniyah, Iraq: implications for provenance and tectonic setting. Bulletin of the Mineral Research and Exploration, Vol. 164, No. 164, pp. 11-38. DOI: 10.19111/bulletinofmre.800132.

Coccioni, R. and Premoli Silva, I., 2015. Revised Upper Albian – Maastrichtian planktonic foraminiferal biostratigraphy and magnetostratigraphy of the classical Tethyan Gubbio section (Italy). Newsletters on Stratigraphy, Vol. 48, No. 1, pp. 47-90. DOI: 10.1127/nos/2015/0055.

Coombs, D.S., 1954. The nature and alteration of some Triassic sediments from Southland, New Zealand. In Transactions of the Royal Society of New Zealand, Vol. 82, No. 65, 109 p.

De Baar, H.J., Bacon, M.P., Brewer, P.G. and Bruland, K.W., 1985. Rare earth elements in the Pacific and Atlantic Oceans. Geochimica et Cosmochimica Acta, Vol. 49, No. 9, pp. 1943-1959. DOI: 10.1016/0016-7037(85)90089-4.

Dickinson, W.R. and Suczek, C.A., 1979. Plate tectonics and sandstone compositions. Aapg Bulletin, Vol. 63, No. 12, pp. 2164-2182. DOI: 10.1306/2F9188FB-16CE-11D7-8645000102C1865D.

Dickinson, W.R., 1985. Interpreting Provenance Relations from Detrital Modes of Sandstones. In: Zuffa, G.G. (eds) Provenance of Arenites. NATO ASI Series, Springer, Dordrecht, vol 148, pp. 333 -361. DOI: 10.1007/978-94-017-2809-6_15.

Dott, R.H., 1964. Wacke, greywacke and matrix; what approach to immature sandstone classification. Journal of Sedimentary Research, Vol. 34, No. 3, pp. 625-632. DOI: 10.1306/74D71109-2B21-11D7-8648000102C1865D.

Dunham, R.J., 1962. Classification of carbonate rocks according to depositional textures. In: Classification of Carbonate Rocks — A Symposium, ed. By Ham, William E. AAPG Memoir, 1. AAPG (American Association of Petroleum Geologists), Tulsa, Oklahoma, pp. 108-121. ISBN: 9781629812366.

Font, E., Adatte, T., Andrade, M., Keller, G., Bitchong, A.M., Carvallo, C., Ferreira, J., Diogo, Z. and Mirão, J., 2018. Deccan volcanism induced high-stress environment during the Cretaceous–Paleogene transition at Zumaia, Spain: Evidence from magnetic,

mineralogical and biostratigraphic records. Earth and Planetary Science Letters, 484, pp. 53-66. DOI: 10.1016/j.epsl.2017.11.055.

Gilmour, I. and Anders, E., 1989. Cretaceous-Tertiary boundary event: Evidence for a short time scale. Geochimica et Cosmochimica Acta, Vol. 53, No. 2, pp. 503-511. DOI: 10.1016/0016-7037(89)90401-8.

Graup, G. and Spettel, B., 1989. Mineralogy and phase-chemistry of an Ir-enriched pre-K/T layer from the Lattengebirge, Bavarian Alps, and significance for the KTB problem. Earth and Planetary Science Letters, Vol. 95, No. 3-4, pp. 271-290. DOI: 10.1016/0012-821X(89)90102-7.

Gribble, C.D., Hall, A.J., 1985. The non-silicates. In: A Practical Introduction to Optical Mineralogy. Springer, Dordrecht, pp. 132-172.

Harder, H., 1972. The role of magnesium in the formation of smectite minerals. Chemical Geology, Vol. 10, No. 1, pp. 31-39. DOI: 10.1016/0009-2541(72)90075-7.

Horton, D.G., 1985. Mixed-layer illite/smectite as a paleotemperature indicator in the Amethyst vein system, Creede district, Colorado, USA. Contributions to Mineralogy and Petrology, Vol. 91, No. 2, pp. 171-179. DOI: 10.1007/BF00377764.

Iijima, A. and Utada, M., 1966. Zeolites in sedimentary rocks, with reference to the depositional environments and zonal distribution. Wiley, Vol. 7. No. 4. pp. 327-357.

Ingersoll, R.V. and Suczek, C.A., 1979. Petrology and provenance of Neogene sand from Nicobar and Bengal fans, DSDP sites 211 and 218. Jour. of Sedimentary Research, Vol. 49, No. 4, pp. 1217-1228. DOI: 10.1306/212F78F1-2B24-11D7-8648000102C1865D.

Jassim, S.Z. and Buday, T., 2006. Tectonic framework. In: S.Z. Jassim and J.C. Goff (eds), Geology of Iraq. Publication of Dolin, Prague and Moravian Museum, Brno, 341 P.

Joanna M., Cristiano L., Anton K., Barry C., Claire B., Sandro M., Enrique D.M., Antonio B., and Virginio N., 2006. Analyses of shocked quartz at the global K-P boundary indicate an origin from a single, high-angle, oblique impact at Chicxulub, Earth and Planetary Science Letters, Vol. 251, No. 3-4, pp. 264-279. DOI: 10.1016/j.epsl.2006.09.009.

Jorge L. Cobiella, R., Esther M.C.G., Silvia B.B., Lourdes P.E, Santa G.G. and Yania P.R., 2015. Cretaceous-Paleogene boundary deposits and paleogeography in western and central Cuba. Revista Mexicana de Ciencias Geológicas, Vol. 32, No. 1, pp. 156-176.

Karim, K.H., 2004. Basin analysis of Tanjero Formation in Sulaimaniya area, NE-Iraq. Unpublished Ph.D. thesis, University of Sulaimani, 135 P.

Keller, G., 2014. Deccan volcanism, the Chicxulub impact, and the end-Cretaceous mass extinction: Coincidence? Cause and effect. Geological Society of America Special Papers, 505, pp. 57-89. DOI: 10.1130/2014.2505(03).

Keller, G., Adatte, T., Bhowmick, P.K., Upadhyay, H., Dave, A., Reddy, A.N. and Jaiprakash, B.C., 2012. Nature and timing of extinctions in Cretaceous-Tertiary planktic foraminifera preserved in Deccan intertrappean sediments of the Krishna-Godavari Basin, India, Earth and Planetary Science Letters, Vol. 341–344, pp. 211-221. DOI:10.1016/j.epsl.2012.06.021.

Keller, G., Bhowmick, P.K., Upadhyay, H., Dave, A., Reddy, A.N., Jaiprakash, B.C. and Adatte, T., 2011. Deccan volcanism linked to the Cretaceous-Tertiary boundary (KTB) mass extinction. New evidence from ONGC wells in the Krishna-Godavari Basin, India:

Journal of the Geological Society of India, Vol. 78, pp. 399-428. DOI:10.1007/s12594-011-0107-3.

Kring, D.A., Tikoo, S.M., Schmieder, M., Riller, U., Rebolledo-Vieyra, M., Simpson, S.L. and Yamaguchi, K.E., 2020. Probing the hydrothermal system of the Chicxulub impact crater. Science Advances, Vol. 6, No. 22, eaaz3053. DOI: 10.1126/sciadv.aaz3053.

Liou, J.G., de Capitani, C. and Frey, M., 1991. Zeolite equilibria in the system $CaAI_2Si_2O_8$-$NaAISi_3O_8$-SiO_2-H_2O. New Zealand Journal of Geology and Geophysics, Vol. 34, No. 3, pp. 293-301. DOI: 10.1080/00288306.1991.9514467.

Mateo P., Keller, G., Adatte, T., Bitchong, A.M., Spangenberg, J.E., Vennemann, T. and Hollis, J.C., 2019. Deposition and age of Chicxulub impact spherules on Gorgonilla Island, Colombia. Geological Society of America. GSA Bulletin. V. 132, No. 1-2, pp. 215-232. DOI. 10.1130/B35287.1.

Montano, D., Gasparrini, M., Rohais, S. and De Luca, R., 2023. A Lacustrine Record for the Cretaceous–Paleogene Boundary-Yacoraite Fm., (Northwest Argentina). Geosciences. Vol. 13, No. 8, 227 P. DOI: 10.3390/geosciences13080227.

Nichols, G., 2009. Sedimentary and stratigraphy, Blackwell Publishing Company, UK, 355 P. ISBN 978-1-4051-3592-4.

Nwajide, C.S. and Hoque, M., 1985. Problem of classification and maturity evaluation of a diagnostically altered fluvial sandstone. Geologic en mijnb., Vol.64, No. 1, pp. 69-77.

Petersen, S. V., Dutton, A. and Lohmann, K.C., 2016. End-Cretaceous extinction in Antarctica linked to both Deccan volcanism and meteorite impact via climate change. Nature. Communications Vol. 7, 12079 P. DOI: 10.1038/ncomms12079.

Pettijohn, F.J., 1975. Sedimentary Rocks. 3rd Edition, Harper and Row, New York, 628 P.

Pitakpaivan, K., Byerly, G.R. and Hazel, J.E., 1994. Pseudomorphs of impact spherules from a Cretaceous-Tertiary boundary section at Shell Creek, Alabama. Earth and planetary science letters, Vol. 124, No. 1-4, pp. 49-56. DOI: 10.1016/0012-821X(94)00077-8.

Potter, P.E. and Pettijohn, F.J., 1977. Paleocurrent and Basin Analysis, 2nd Edition, Springer-Verlag Berlin, 425 P.

Premović, P.I., 2004. Cretaceous-Tertiary boundary deposits in Denmark: A diachroneity. Journal of the Serbian Chemical Society, Vol. 69, No. 7, pp. 555-561. DOI: 10.2298/JSC0407555P.

Prinn, R.G. and Fegley Jr, B., 1987. Bolide impacts, acid rain, and biospheric traumas at the Cretaceous-Tertiary boundary. Earth and Planetary Science Letters, Vol. 83, No. 1-4, pp. 1-15. DOI: 10.1016/0012-821X(87)90046-X.

Renne, P.R., Sprain, C.J., Richards, M.A., Self, S., Vanderkluysen, L. and Pande, K., 2015. State shift in Deccan volcanism at the Cretaceous-Paleogene boundary, possibly induced by impact, Science, Vol. 350, No. 6256, pp. 76-78. DOI: 10.1126/science.aac754.

Ritter, X., Deutsch, A., Berndt, J. and Robin, E., 2015. Impact glass spherules in the Chicxulub K-Pg event bed at Beloc, Haiti: Alteration patterns. Meteoritics and Planetary Science, Vol. 50, No. 3, pp. 418-432. DOI: 10.1111/maps.12432.

Sharbazheri, K.M., 2008. Biostratigraphy and Paleoecology of Cretaceous/Tertiary Boundary in The Sulaimani Region, Kurdistan, NE-Iraq. Unpublished Ph.D. Thesis, University of Sulaimani, Iraq, 219 p.

Sholkovitz, S.R., Landing, W.M. and Lewis, B.L., 1994. Ocean Particle Chemistry: The fractionation of rare earth elements between suspended particles and seawater. Geochimica et Cosmochimica Acta, Vol. 58, No. 6, 1994, pp. 1567-1579. DOI: 10.1016/0016-7037(94)90559-2.

Sial, A.N., Chen, J., Lacerda, L.D., Frei, R., Higgins, J.A., Tewari, V.C., Gaucher, C., Ferreira, V.P., Cirilli, S., Korte, C., Barbosa, J.A., Pereira, N.S. and Ramos, D.S., 2019. Chemostratigraphy Across the Cretaceous-Paleogene (K-Pg) Boundary: Testing the Impact and Volcanism Hypotheses, American Geophysical Union, John Wiley & Sons, Inc. Chapter 12, Edited by Alcides N. Sial, Claudio Gaucher, Muthuvairavasamy Ramkumar, and Valderez Pinto Ferreira, pp. 223-258. DOI: 10.1002/9781119382508.

Sissakian, V.K. and Fouad, S.F., 2015. Geological map of Iraq, scale 1: 1000 000, 2012. Iraqi Bulletin of Geology and Mining, Vol. 11, No. 1, pp. 9-16.

Smit, J., 1982. Extinction and evolution of planktonic foraminifera after a major impact at the Cretaceous/Tertiary boundary, Geological Implications of Impacts of Large Asteroids and Comets on the Earth, Leon T. Silver, Peter H. Schultz, pp. 329–352. DOI: 10.1130/SPE190-p329.

Smit, J., 1999. The global stratigraphy of the Cretaceous-Tertiary boundary impact ejecta. Annual Review of Earth and Planetary Sciences, Vol. 27, No. 1, pp. 75-113. DOI: 10.1146/annurev.earth.27.1.75.

Smit, J. and ten Kate, W.G.H.Z., 1982. Trace-element patterns at the Cretaceous-Tertiary boundary—consequences of a large impact. Cretaceous research, Vol. 3, No. 3, pp. 307-332. DOI: 10.1016/0195-6671(82)90031-3.

Sosa-Montes De Oca, C, De Lange, G.J., Martínez-Ruiz, F., Ortega-Huertas, M. and Rodríguez-Tovar, F.J., 2020. Microscale trace-element distribution across the Cretaceous/Palaeogene ejecta layer at the Agost section: Constraining the recovery of pre-impact conditions. *Chemical Geology*, *533*, 119431, 10 P. DOI: 10.1016/j.chemgeo.2019.119431.

Sosa-Montes De Oca, C., Martínez-Ruiz, F. and Rodríguez-Tovar, F.J., 2013. Bottom-water conditions in a marine basin after the Cretaceous–Paleogene impact event: timing the recovery of oxygen levels and productivity. PLoS One, Vol. 8, No. 12, 7 P. DOI: 10.1371/journal.pone.0082242.

Sun, S.S. and McDonough, W.F., 1989. Chemical and isotopic systematics of oceanic basalts: implications for mantle composition and processes. Geological Society, London, Special Publications, Vol. 42, No. 1, pp. 313-345. DOI: 10.1144/GSL.SP.1989.042.01.19.

Suttner, L.J. and Dutta, P.K., 1986. Alluvial sandstone composition and paleoclimate; I, Framework Mineralogy. Journal Sedimentary Research, Vol. 56, No. 3, pp. 329-345. DOI: 10.1306/212F8909-2B24-11D7-8648000102C1865D.

Taylor, S.R. and McLennan, S.M., 1985. The Continental Crust: Its Composition and Evolution. Blackwell, Scientific Publication, Oxford. 312 P. DOI: 10.1002/gj.3350210116.

Trubelja, F., Marchig, V., Burgath, K.P. and Vujović, Ž., 1995. Origin of the Jurassic Tethyan ophiolites in Bosnia: a geochemical approach to tectonic setting. Geologia Croatica, Vol. 48, No. 1, pp. 49-66. https://hrcak.srce.hr/18012.

Vajda, V. and Wigforss-Lange, J., 2006. The Jurassic-Cretaceous transition of Southern Sweden–Palynological and sedimentological interpretation. Progress in Natural Science, Vol. 16, No. 1, pp. 31-38. DOI: 10.1080/10020070612330073A.

Zattin, M. and Zuffa, G.G., 2004. Unravelling the source rocks of Late Eocene-Miocene orogenic wedge and foredeep arenites of the northern Apennines and southern Alps. Bollettino Della Societa Geologica Italiana, Vol. 123, No.1, pp. 67-76. https://api.semanticscholar.org/CorpusID:131986124.

Iraqi National Journal of Earth Science

www.earth.uomosul.edu.iq

Groundwater Quality Assessment and Its Suitability for Agricultural Use in Al-Shirqat Area, Salahaldin Governorate

Ayad A. Khalaf [1*], Abdelhadi H. Hasan[2]

[1,2]*Department of Soil Science and Water Resources, College of Agriculture, Tikrit University, Tikrit, Iraq.*

Article information

Received: 29- Aug -2024

Revised: 18- Nov -2024

Accepted: 22- Jan -2025

Available online: 01- Jan – 2026

Keywords:
Irrigation Water Quality,
Arc GIS,
IDW,
Water Quality Indices,

Correspondence:
Name: Ayad A. Khalaf

Email: aiad2017@tu.edu.iq

ABSTRACT

The study aims to investigate the assessment of groundwater quality and its suitability for agricultural use in the Al-Shirqat area in Salahaldin Governorate. The selected (23) wells are distributed over the study area at two different locations. The first location includes 12 wells and is located within the sedimentary soil unit, while the second site includes 11 wells and is located within the calcareous soil unit. Well water samples are analyzed to measure the positive and negative dissolved ions (Ca, Mg, Na, K, HCO_3, Cl, and SO_4). The irrigation water quality criteria (SAR, Na% %, ESP, PS, Mg% % and TDS) are calculated, and spatial distribution maps are prepared. The results show that the concentrations of calcium and chloride ions exceed the permissible limits needed for irrigation, while the concentration of sodium ions is within the permissible limits according to FAO standards. The values of EC range between 3-10 dSm-1 and a low exchangeable sodium absorption ratio SAR (less than 4.48) under the S1C4 group.

DOI: 10.33899/injes.v26i1.60194, ©Authors, 2026, College of Science, University of Mosul.
This is an open-access article under the CC BY 4.0 license (http://creativecommons.org/licenses/by/4.0/).

تقييم نوعية المياه الجوفية وملاءمتها للاستخدام الزراعي في منطقة الشرقاط، محافظة صلاح الدين

اياد خلف [1*]، عبد الهادي حسن [2]

[2,1] قسم علوم التربة والموارد المائية، كلية الزراعة، جامعة تكريت، تكريت، العراق.

معلومات الارشفة

تاريخ الاستلام: 29- اغسطس -2024

تاريخ المراجعة: 18- نوفمبر-2024

تاريخ القبول: 22- يناير-2025

تاريخ النشر الالكتروني: 01- يناير-2026

الكلمات المفتاحية:

نوعية المياه الري،

نظم المعلومات الجغرافية،

تقنية وسيط المسافة المعكوسة،

مؤشرات نوعية المياه،

المراسلة:

الاسم: اياد خلف

Email: aiad2017@tu.edu.iq

الملخص

تهدف الدراسة الى تقييم نوعية المياه الجوفية وملاءمتها للاستخدام الزراعي في منطقة الشرقاط في محافظة صلاح الدين. اختير (23) اثنان وعشرون بئراً موزعة على منطقة الدراسة ومن موقعين مختلفين. اما الموقع الأول فاشتمل على 12 بئراً ويقع ضمن وحدة الترب الرسوبية، اما الموقع الثاني فاشتمل على 11 بئراً ويقع ضمن وحدة الترب الكلسية. تم جلب نماذج مياه الآبار الى المختبر لقياس وتقدير الايونات الموجبة والسالبة الذائبة فيها طبقا للطرق القياسية المتبعة في مختبرات قسم علوم التربة في جامعة تكريت. تم حساب بعض المعايير والمؤشرات وهي SAR, Mg%, ESP ،Na% ،PS ،TDS وتم اعداد خرائط توزيعها المكاني. أظهرت النتائج ان تراكيز ايوني الكالسيوم والكلوريد تجاوزت الحدود المسموح بها وفقا لمواصفة FAO، في حين كان تركيز ايون الصوديوم ضمن الحدود المسموح بها. أظهرت النتائج بان الايصالية الكهربائية كانت بين 3- 10 دسيسمنز م-1 ومنخفضة نسبة الصوديوم المتبادل SAR اذ كانت اقل من 4.48 وصنفت مياه الري ضمن (عالية الملوحة وقليلة الصوديوم S1C4).

DOI: 10.33899/injes.v26i1.60194, ©Authors, 2026, College of Science, University of Mosul.
This is an open-access article under the CC BY 4.0 license (http://creativecommons.org/licenses/by/4.0/).

Introduction

Mismanagement of water for irrigation purposes leads to soil degradation and reduced agricultural production through the toxicity of nutrients, especially in arid and semi-arid areas, if it is improperly managed and exploited (Al-Hadidi, 2009; Berhe et al., 2015; Salcedo et. al., 2021). Treder (2005) confirmed that the presence of calcium and magnesium ions in irrigation water results in high accumulation in the soil under the drip irrigation system. Herrero and Perez-Coveta (2005) studied soil salinity variations over 24 years in a Mediterranean irrigated area and explained that soil degradation from salt accumulation is a threat in irrigated regions, and salinization has often been evaluated from changing cropping types, and often the trends in the salinization process have not been quantified. The quality of groundwater is of great importance in determining its suitability for various uses, as water is considered the secret of life and existence. The extraction of groundwater is of primary importance to the people who want to use their agricultural lands, which have been affected by land degradation due to drought. This is a part of the practices of land management in arid and semi-arid regions (Ma et al., 2017, 2018; Periasamy and Ravi, 2020). The impact of salinity is not limited to agricultural production, but it has negative repercussions on the environment and direct or indirect effects on the life of society (Zhang et al., 2022). Hence, groundwater needs to be evaluated for its quality, and this requires identifying the most important specifications that must be available in this water to determine its suitability for a specific use. Some limits must be met in water to determine its suitability for agricultural use. Many studies have been conducted to evaluate water quality and its suitability for irrigation in different regions of the world (Kovda et al., 1973; Liu et al., 2015; Kaba and Majar, 2020; Dimple et al., 2022; Mohammed et. al., 2023). Locally, Abbas (2010) studied the hydrogeochemistry of

groundwater in Ummordomah in western Iraq and confirmed the possibility of using water for irrigation purposes. Ibrahim and Kashmola (2011) studied the quality properties of some wells water and the Lower Zab River. According to the American Salinity Laboratory classification, it is between (S1-C3) and (S3-C1). The dominant cations and anions were sodium, calcium, chloride, and sulphate. Therefore, it is worth paying attention to studying the quality of groundwater, the possibility of exploiting it agriculturally, and the extent of its potential impact on soil degradation. Several worldwide studies have used the SAR, EC, Cl, and TDS in the assessment of water quality (Presley et al., 2004; Meireles et al., 2010; Al-Rifaee and Al-Rubay, 2017; Abbasnia et al., 2018; Mostafa et al., 2020; Ekhmaj et al., 2021; Mahmood et al., 2022). These studies focused on evaluating the quality of water for irrigation, which is an important aspect of agricultural land management and raising its production efficiency.

The main goal of the present study is to evaluate the groundwater quality and its suitability for agricultural use in the Al-Shirqat area of Salahaldin Governorate based on the International Food and Agriculture Standards.

Materials and Methods

Study Area

Al-Shirqat is a district in Salahaddin Governorate in northern Iraq; its center is the city of Shirqat. It is located 115 km south of Nineveh Governorate, 125 km north of Tikrit, and 135 km west of Kirkuk Governorate. The total area of Al-Shirqat District is approximately 1,568 km^2, in which two locations are identified to evaluate the quality of groundwater in agricultural lands. The first site is located between longitudes (43°18'15.229" E and 43°19'17.511" E) and latitudes (35°23'32.155" N and 35°23'55.828" N). Twelve wells are selected within the physiographic unit of the alluvial plain affected by the sediments of the Tigris River, characterized by the cultivation of wheat, barley, and corn crops (Fig. 1). The second site is located between longitudes (43°24'59.756"E and 43°28'37.361"E) and two latitudes (35°26'1.696"N and 35°25'14.314" N). Eleven wells are selected that are distributed over the area of the study; this site is characterized by lands cultivated with wheat and maize crops. The study area is located within the arid and semi-arid areas with high temperatures in summer, which reach about 50°C, leading to burning of field crops due to the high concentration of salts in the soil resulting from the quality of well water with high temperature.

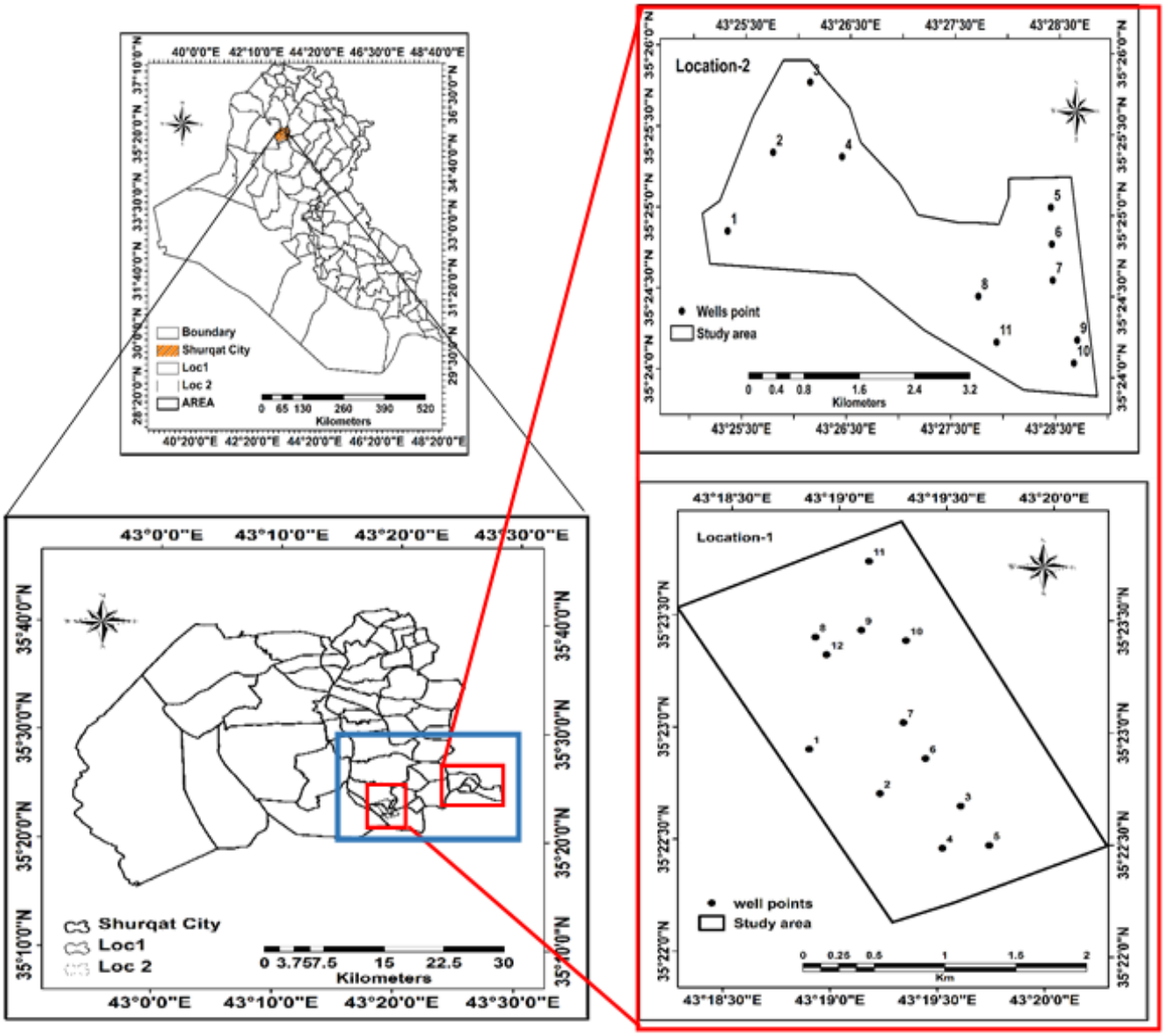


Fig. 1. Maps of study locations.

Laboratory work

Water samples were collected on October 5, 2023, and their geographic coordinates were recorded using GPS. The laboratory work includes measuring the EC and pH according to the method described by Page et al. (1982). The dissolved positive ions, calcium and magnesium, are determined by titration with EDTA (Jackson, 1969). Sodium and potassium ions are estimated using the flame photometer. Chloride is determined by precipitation with silver nitrate, while bicarbonate and carbonate are determined by titration with 0.01 M sulfuric acid (Jackson, 1969). Ayers and Westcot's (1985) classification is used in the assessment of irrigation water quality (Table 1).

Table 1: Irrigation water quality criteria according to Ayers and Westcot (1985).

Properties	EC	pH	TDS	SAR	Ca^{++}	Mg^{++}	Na^{+}	K^{+}	Cl^{-}	$SO_4^{=}$	HCO_3^{-}
Critical	dSm^{-1}		$mg\ l^{-1}$		meq/l						
	3	6.5-8.4	2000	15	20	5	9	2	10	20	10

Ayers and Westcot (1989, 1994): https://www.fao.org/4/t0234e/T0234E01.htm#tab2; Islam et al., 2016)

Water Quality Criteria

Several indices are used in this study as follows:

1 – **Total Dissolved Salts (TDS):** It is calculated after knowing the degree of electrical conductivity, and expressed as in the following equation (Thorne and Thorne, 1954).

$$TDS(mg/L) = EC(dS\,m^{-1}) \times 640 \quad \text{…….. 1}$$

2 - Sodium Hazard (Na%): It is calculated according to Todd (1980) (Table 2).

$$Na\% = \frac{Na+K}{Ca+Mg+Na+K} \times 100 \quad \text{…… 2}$$

3- Sodium Adsorption Ratio (SAR): It is an expressive value of the concentration of sodium to the (calcium and magnesium concentration) in milliequivalents of charge per liter using the following equation (Richards, 1954) (Fig. 2; Table 2).

$$SAR = \frac{Na}{\sqrt{\frac{Ca + Mg}{2}}} \text{.....3}$$

4- Exchangeable Sodium Percentage of water (ESP): It refers to the proportion of exchange sites occupied by sodium ion and calculated by the following formula (Richards, 1954).

$$ESP = \frac{100 \times (-0.0126 + 0.01475\,SAR)}{1 + (-0.0126 + 0.01475\,SAR)} \text{… … … … 4}$$

5- Potential Salinity (PS). It is calculated according to the following equation suggested by Doneen (1971), who considered its values in the range of (5-20) for good soil permeability, (15-3) for moderate soil permeability, and (7-3) meq/l is suitable for low permeable soils (after Al-Zubaidi, 1989) (Table 2).

$$\boldsymbol{PS(meq\,l^{-1}) = Cl + \frac{1}{2} \times SO_4} \text{…… 5}$$

6- Magnesium Hazard (Mg%): When its value exceeds 50%, it is considered unsuitable for irrigation (Kovda et al., 1973). It is calculated by the following formula (Table 2).

$$\boldsymbol{Mg\% = \frac{Mg}{Ca + Mg} \times 100} \text{… … … … 6}$$

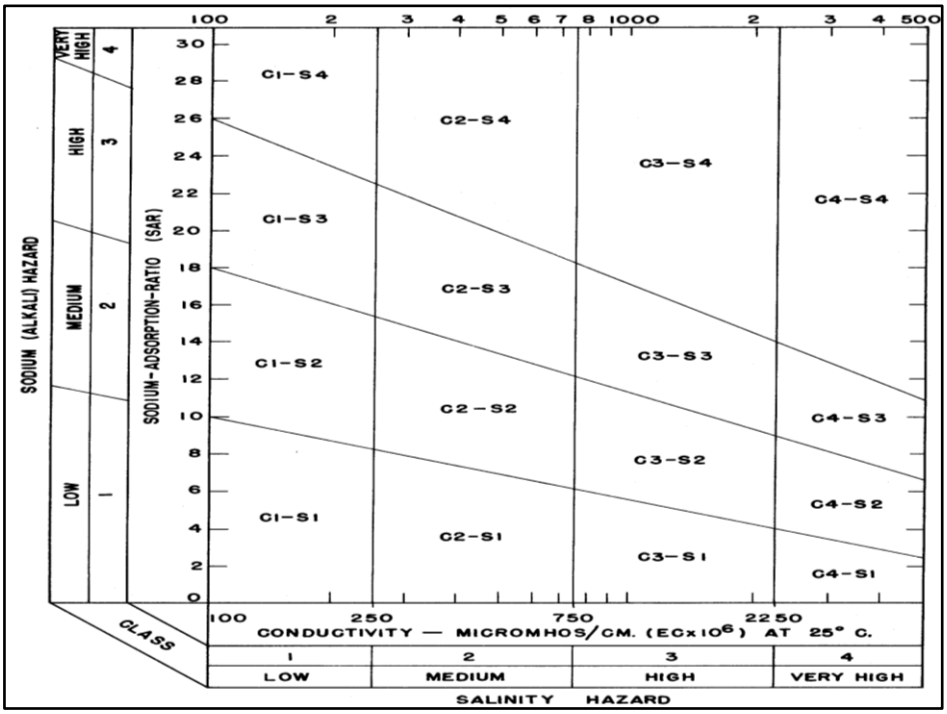


Fig. 2. Classification of irrigation waters.

Table 2: Irrigation water quality criteria for assessing groundwater in the study area.

Indicator	Class	Range	Quality	Reference
EC (dSm^{-1})	1	<0.7	High	Ayers and Westcot (1985)
	2	0.7-2.25	Moderate	
	3	2.25-5.00	Low	
	4	>5.00	Very low	
SAR	1	<3	Very High	Ayers and Westcot (1985) * Reprinted 1989, 1994)
	2	3-6	High	
	3	6-12	Moderate	
	4	12-20	Low	
	5	20-40	Very low	
TDS	1	< 450	Non	Ayers and Westcot (1985)
	2	450-2000	Slightly to Moderate	
	3	> 2000	Sever	
Na %	1	60	Excellent to good	Doneen (1954)
	2	60 - 75	Good to injurious	
	3	>75	Injurious to unsatisfactory	
PS	1	<3	Suitable	Awad et al. (2022)
	2	>3	Unsuitable	
Mg %	1	<50%	Suitable	Kovda et al. (1973)
	2	>50%	Unsuitable	

Maps and Descriptive Statistics Analysis

ArcGIS program tools are used in preparing of mapping of the soluble ions and water quality indices using Inverse Distance Weighting (IDW). Descriptive statistics values (mean, SD, minimum, maximum, and coefficient of variation, CV%) are calculated using the Excel program.

$$\boldsymbol{Mean} = \frac{\sum \boldsymbol{xi}}{\boldsymbol{n}} \quad \ldots\ldots\ldots \quad 7$$

$$\boldsymbol{Standard\ deviation\ (SD)} = \sqrt{\frac{\sum(\boldsymbol{xi} - \bar{\boldsymbol{x}})^{\boldsymbol{2}}}{\boldsymbol{n-1}}} \ldots\ldots\ldots \mathbf{8}$$

$$\textit{Coefficient of Variance } (\boldsymbol{CV}\%) = \frac{\boldsymbol{SD}}{\bar{\boldsymbol{x}}} \times \mathbf{100} \ldots\ldots\ldots\ldots \mathbf{9}$$

Results and Discussion

EC, TDS, and pH

Table 3 indicates the variation of well water in the degree of electrical conductivity. Through the results of descriptive statistics, the well water values for the first site range between 3.80-10 dSm^{-1} with a mean of 6.27; the standard deviation value is 2.13, and the coefficient of variance (CV) is 34.04%. While in the second site, it ranges between 4.20-7.70 dSm^{-1} with a mean of 5.70; the value of the standard deviation is 1.10, and the coefficient of variance (CV) of 19.22%. Compared to the standard specifications, the well water exceeds the permissible limits for irrigation water, which is 3 $dS.m^{-1}$ EC. The electrical conductivity causes an increase in the osmotic pressure of the liquid soil phase to affect the ability of plants to absorb water and nutrient elements, which can decrease productivity in the long term. It is the most important parameter in determining the suitability of water for irrigation, and is generally measured as the electrical conductivity (EC) of water or the concentration of total dissolved salts (TDS). The results of Fig. 3 show that the total dissolved salts (TDS) in the first site range from 2432.0 to 6400.0 mg/l, with a CV of 34.04 %. As for the second site, they range between 2688.00 and 4928.00 mg l^{-1}, with a CV of 19.22%. According to the FAO classification, they are severe. Table 3) exhibits the pH values for the first site, ranging between 6.60 and 7.20 with an average of 7.01, and the standard deviation is 0.19, with a coefficient of variance of 2.70%. While the second site, the degree of interaction ranges between 6.20 and 6.90 with an average of 6.60, with a standard deviation value of 0.21, and the CV% is 3.25%.

Table 3: Descriptive Statistics of pH, EC, TDS, and soluble ions of well water.

Statistics	pH	EC	TDS	Ca^{+2}	Mg^{+2}	Na^{+1}	K^{+1}	HCO_3^{-1}	Cl^{-1}	SO_4^{-2}
		dSm^{-1}	mg l^{-1}				meq/l			
Site-1										
Min	6.60	3.80	2432.00	22.50	7.50	9.70	0.06	2.30	6.75	26.57
Max	7.20	10.00	6400.00	67.50	28.00	23.39	0.27	8.20	33.00	64.03
Mean	7.01	6.27	4010.67	35.38	14.92	14.35	0.17	5.43	18.33	41.05
SD	0.19	2.13	1365.39	13.65	6.55	4.74	0.07	1.79	7.80	13.02
CV %	2.70	34.04	34.04	38.59	43.86	33.04	42.48	32.97	42.56	31.72
Site-2										
Min	6.20	4.20	2688.00	19.00	8.00	9.43	0.11	2.10	8.25	30.60
Max	6.90	7.70	4928.00	43.00	21.00	15.78	0.22	7.50	25.50	45.18
Mean	6.60	5.70	3648.00	32.25	12.68	12.58	0.15	5.18	16.91	35.56
SD	0.21	1.10	701.08	7.41	4.39	1.99	0.04	1.90	6.31	4.40
CV%	3.25	19.22	19.22	22.98	34.61	15.83	25.02	36.74	37.29	12.36

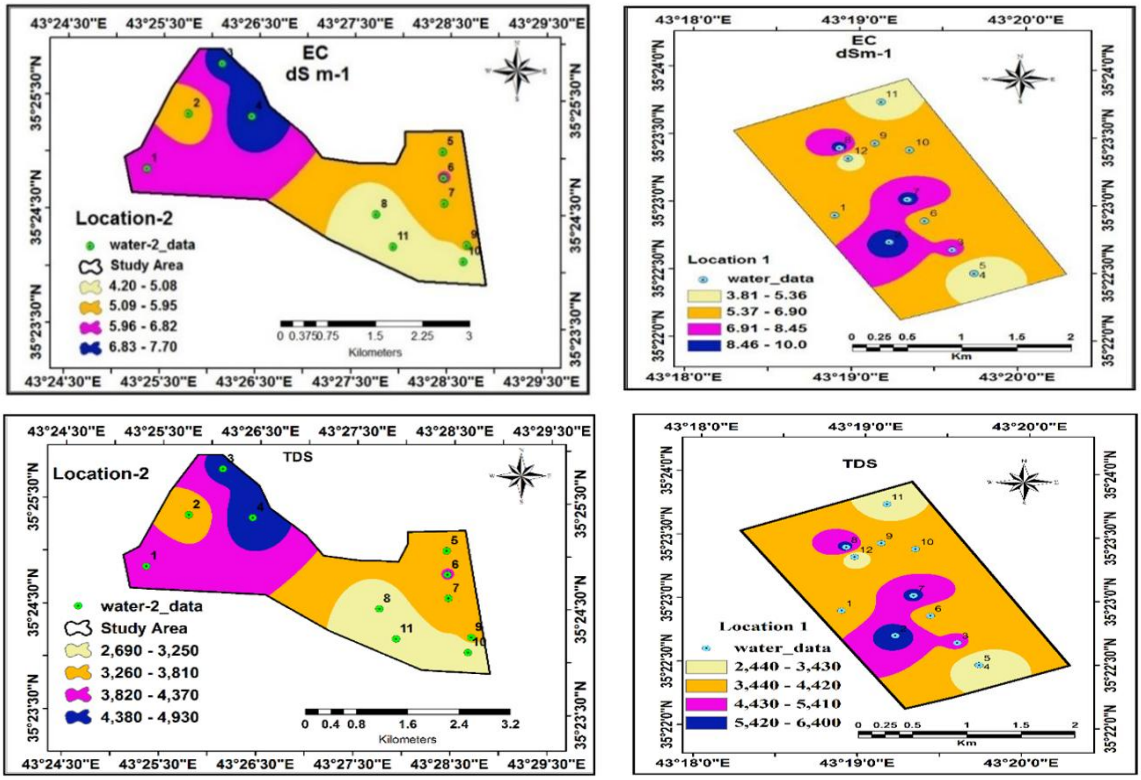


Fig. 3 Maps of electrical conductivity in the study area.

Cations

The calcium ion concentrations in the first site range from 22.50 to 67.50 meq/l with a mean of 35.38 meq/l, a standard deviation value of 13.65, with a dispersion coefficient of 38.59%. The calcium concentrations in the second site range between 19.00 and 43.00 with a mean of 32.25 meq/l, with a standard deviation of 7.41, and a coefficient of variance of 19.22%. According to the classification of Ayers and Westcot (1985) the concentration of calcium is considered unacceptable for irrigation purposes (20 meq/l or 400 mg/l) (Fig. 4). The magnesium ion concentration ranged between 7.50 and 28.00, with an average of 14.92 meq/l; the value of the standard deviation was 6.55, with a coefficient of 43.68%. The concentration of magnesium in the second site ranged between 8.00 and 21.00, with an average of 12.58, a standard deviation of 4.39, and a coefficient of variance of 34.61%. It was noted that the wells of the study sites fell within the impermissible limits of 5 meq/l. The concentration of Ca and Mg in groundwater is derived from weathering of calcite or dolomite. The ions Calcium and Magnesium, and bicarbonate originate primarily from calcite and dolomite minerals (Avaci et al., 2018) (Fig. 4; Table 3).

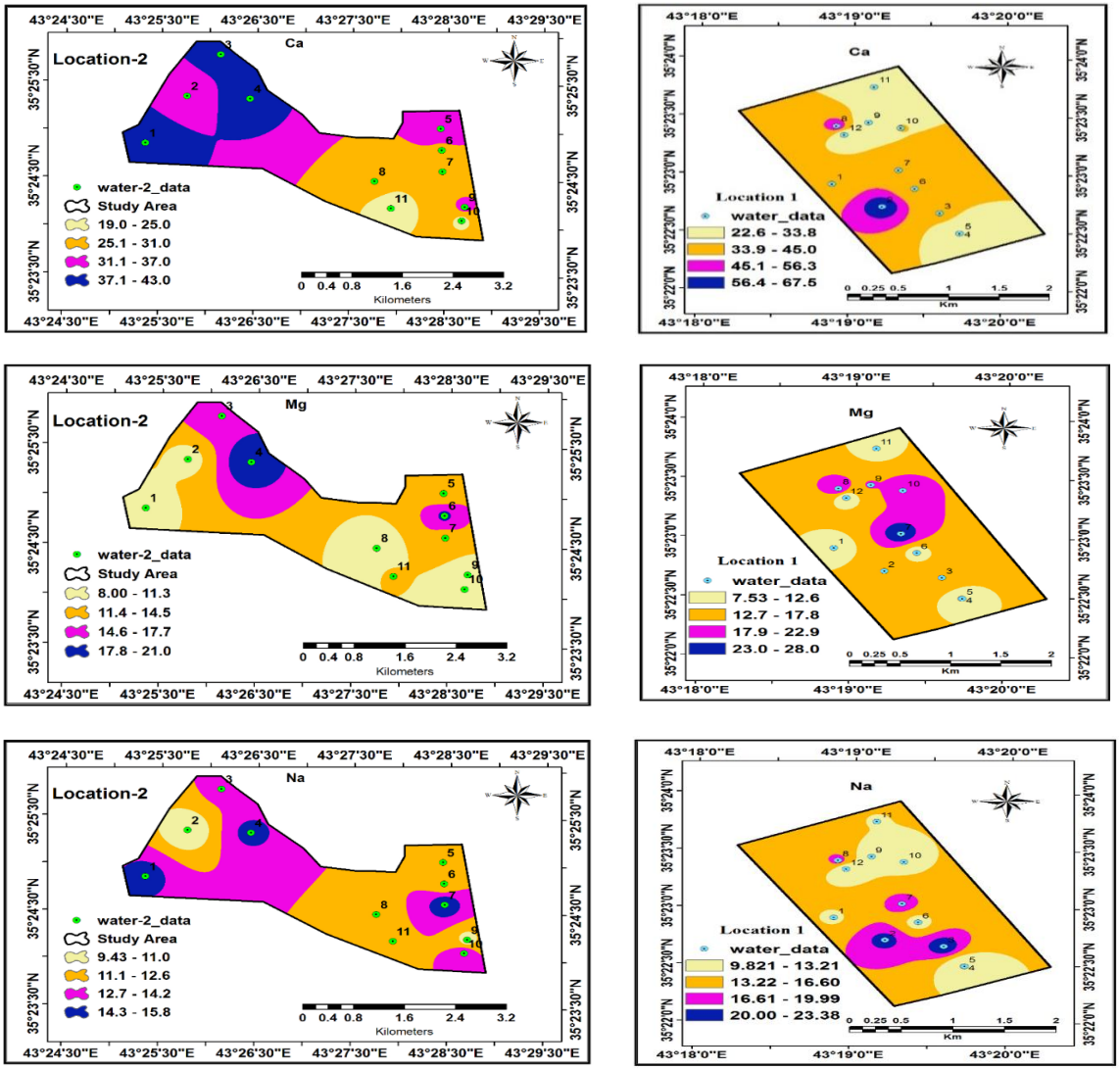


Fig. 4 Spatial distribution of positive soluble ions concentration in well water.

The sodium ion concentrations range from 9.70 to 23.39 with a mean of 14.92 meq/l, and the standard deviation value is 4.74, with a dispersion coefficient is 33.04%. As for the second site, the sodium concentrations range between 9.43 and 15.78 with a mean of 12.58, with a standard deviation of 1.99, and a coefficient of variance of 15.83% (Table 3; Fig. 4). The results of table (3) show that the potassium ion concentrations in the first location range between 0.06 to 0.27 meq/l, and according to the dispersion coefficient, it is observed that the well water had a dispersion coefficient of 42.48%, with a standard deviation of 0.07. This is due to the variation occurring like the rock material and geological formations, which are the main storehouse of nutrients and their quantity dissolved in water. As for the second location, the potassium ion concentrations range between 0.11 and 0.22 meq/l, according to the dispersion coefficient, it is noted that the well water had a dispersion coefficient of 25.02, with a standard deviation of 0.04.

Anions

Fig. (5) shows that the chloride content in the first location range between 6.75 to 33.00 meq/l, and the value of the dispersion coefficient is 42.56%, with a standard deviation of 7.80. In the second site, the chloride contents range between 8.25 and 25.50, and the dispersion coefficient value is 37.29, with a standard deviation of 6.31 (Table 3). Most of the samples in the study area are within the limits that are not permissible for irrigation purpose. Table (3) and Fig. (5) show that the sulfate contents in the first site range from 26.57 to 64.03 meq/l, and the value of the dispersion coefficient reached 31.72%, with a standard deviation of 13.02. As for

the site second, sulphates range between 30.6 and 45.18 meq/l, and the dispersion coefficient value reaches 12.36, with a standard deviation of 4.40. Therefore, compared to the classification standards, most of the samples in the study area are within the impermissible limits. The results of Table 3 show that the bicarbonate (HCO_3) concentrations in the first site range between 2.30 and 8.2 with a mean of 5.43 meq/l, and the value of the dispersion coefficient is 32.97%, with a standard deviation of 1.7. In the second site, the bicarbonate concentrations range between 2.10 and 7.50 meq/l, and CV reaches 36.74%, with a standard deviation of 1.90. Compared with Table 1, both sites are within the permissible limits. The HCO_3 is unstable at high temperature (100 C°), and sometimes converted to H_2O and CO_2 (Avaci et al., 2018).

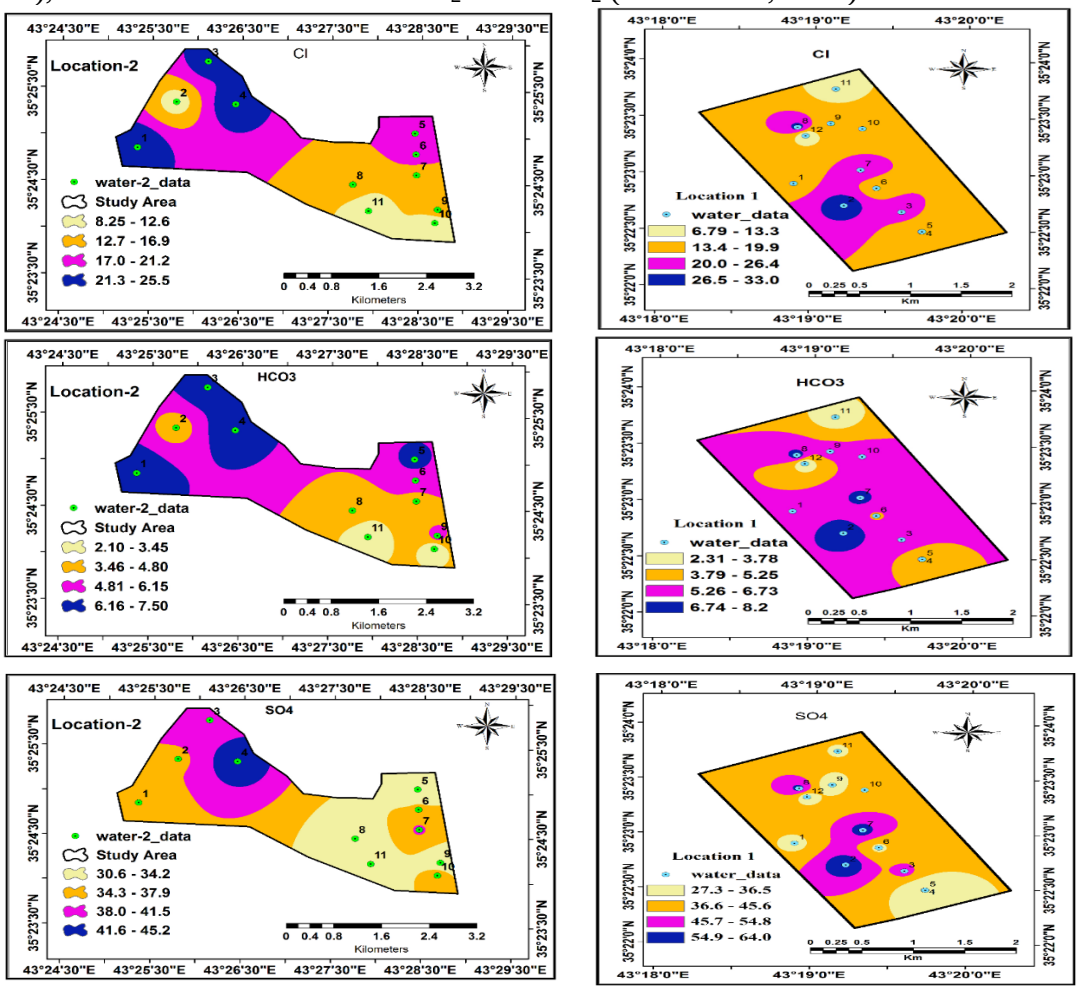


Fig. 5. Maps of negative soluble ions concentration in the study area.

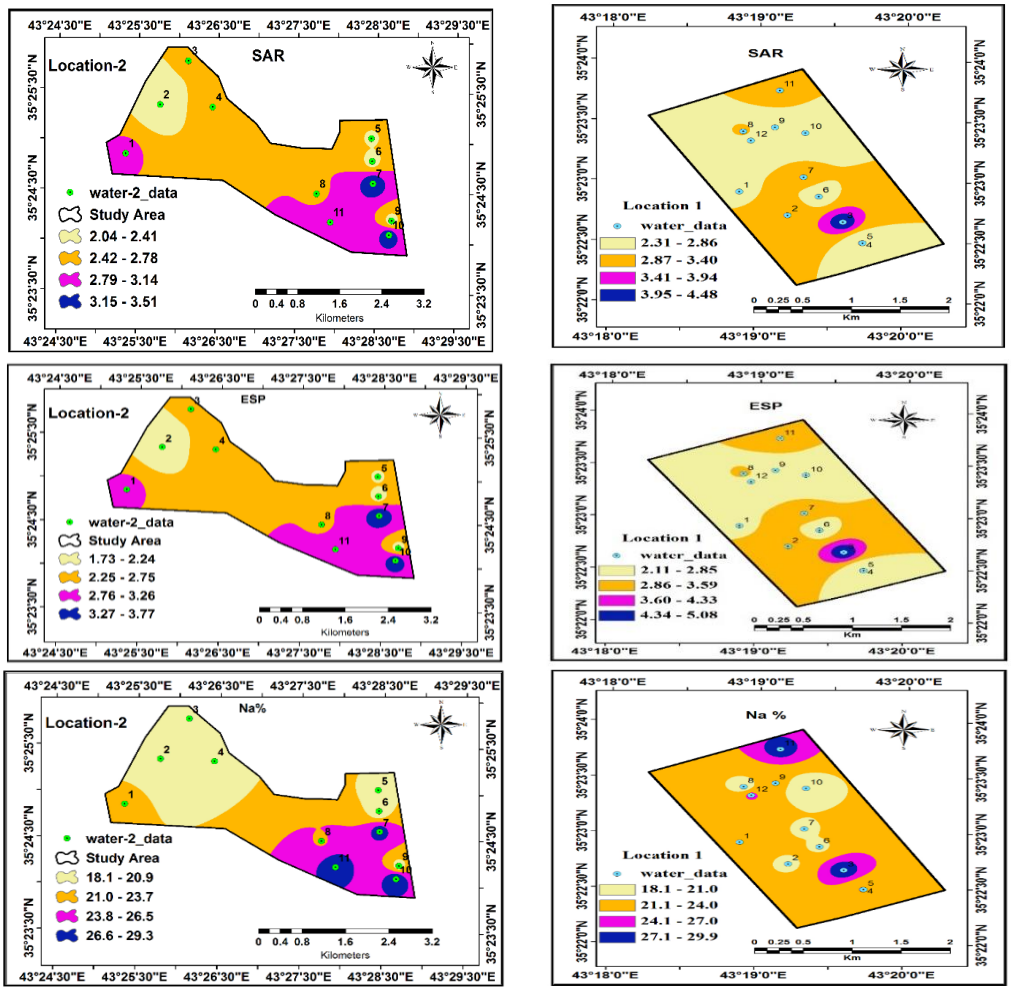
SAR, ESP, and Na%

Table (4) and Fig. (6) display the variation in the sodium adsorption rate, which represents the degree of saturation of the irrigation water solution with the sodium concentration at the expense of the concentration of magnesium and calcium ions. In the first location, it ranges from 2.31 to 4.48, and according to the standards of descriptive statistics and CV of 21.95% compared with Fig. 2, all study sites are located within S1 (sodium is low) and C4 (EC is high). As for the second site, the sodium adsorption rate ranges between 2.04 and 3.51, with a CV of 18.00%. The well water of both study sites fell within the permissible limits. The results of Table 4 and Fig. 6 indicate that the percentage of exchangeable sodium percentage (ESP) in the first site ranges from 2.11 to 5.08, and the value of the dispersion coefficient is 30.10% with a standard deviation of 0.86. In the second site, the ESP ranges between 1.73 and 3.77, and the value of the CV reaches 25.64%, with a standard deviation of 0.68. Table 4 shows that the Na% in the first site ranges from approximately 18 to 30%, and the value of the standard deviation reaches 3.62, and the dispersion coefficient is 16.14%. As for the second site, the percentage of sodium hazard ranges between 18.10 and 29.31, with a dispersion coefficient of 19.75%, and

the value of the standard deviation reaches 4.39. SAR is one of the valuable parameters for evaluating the suitability of groundwater for irrigation because it is responsible for the sodium hazard. Because SAR is concerned with salt absorption on the soil surface, it provides a good foundation for evaluating the sodium damage degree in irrigation water. Moreover, sodium from irrigation water reaches the soil and replaces the absorbed calcium and magnesium, resulting in a reduction in permeability and poor drainage in the soil (Alaya et al., 2013).

Table 4: Criteria for evaluating the quality of well water at the study sites.

Stat.	PS	SAR	Na%	ESP	(MH)	Group
			Site-1			
Min	17.74	2.31	18.07	2.11	18.60	C4-S1
Max	40.22	4.48	29.96	5.08	43.90	C4-S1
Mean	25.95	2.86	22.44	2.87	29.64	C4-S1
SD	7.99	0.63	3.62	0.86	7.94	C4-S1
CV%	30.79	21.95	16.14	30.10	26.78	C4-S1
			Site-2			
Min	18.37	2.04	18.10	1.73	18.10	C4-S1
Max	29.89	3.51	29.31	3.77	37.99	C4-S1
Mean	22.96	2.69	22.25	2.63	28.24	C4-S1
SD	3.33	0.48	4.39	0.68	6.98	C4-S1
CV%	14.51	18.00	19.75	25.64	24.71	C4-S1



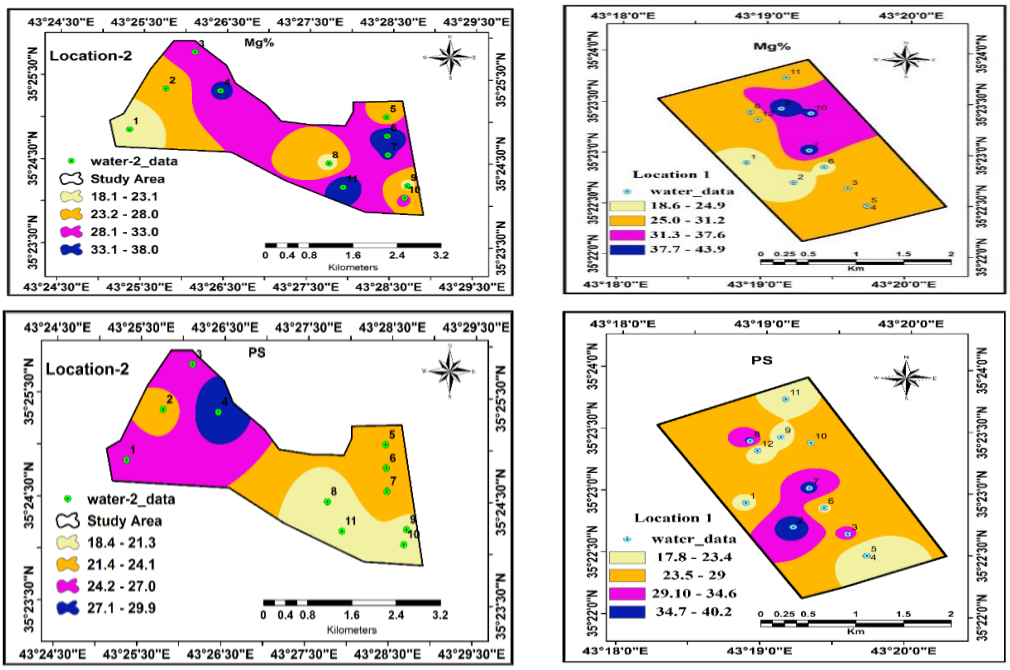


Fig. 6. Maps of SAR, ESP, Na%, and MH in the study area.

PS and Mg %

The results of Table 4 and Fig. 6 show that the PS values in the first site range from 17.74, as the lowest effect of the magnesium hazard ratio, to approximately 40, as the highest PS ratio. The value of the dispersion coefficient reaches 30.79 with a standard deviation of approximately 8.00. As for the second location, the PS percentage ranges between 18.37 and 29.89, and the dispersion coefficient value reaches 18.83%, with a standard deviation of 7.28.

A potential salinity is less than 3 meq/l, illustrating that the water can be used for irrigation (Doneen, 1954; Avaci et al., 2018; Awad et al., 2022). The PS values of all collected samples are estimated as high values. The results of Fig. 6 show that the risk percentage of magnesium in the first site ranges from 20.65 to 43.94%, with a standard deviation value of 8.81 and a dispersion coefficient of 28.14%. As for the second site, the risk rate of magnesium ranges between 22.35 and 39.36%, with a dispersion coefficient of 20.54, and the standard deviation value is 6.10. These values are less than 50 meq/l, indicating that all samples are suitable for irrigation and have no effect on crop yield (Zhao et al., 2021).

Conclusion

The results confirm that the electrical conductivity concentration is relatively high in some study areas, while we did not notice an increase in the exchangeable sodium ratio, which is less than 10. The results also confirm that the concentration of total dissolved salts reaches more than 6000 mg/l in some areas, while we note that the other indicators had good results for agricultural use. Research has shown significant differences in water quality even between wells located just a few kilometers apart. Therefore, each well must be studied independently based on its unique characteristics. In general, groundwater in this area is suitable for irrigating crops that are moderately resistant to desertification, such as wheat during the winter season. Groundwater can also be used as a supplementary source of irrigation when rainfall is interrupted for short periods during the agricultural season. However, it is crucial to avoid overusing this water as excessive use, which may lead to salt accumulation in the soil and degrade its quality over time, negatively affecting agricultural productivity and contributing to desertification.

References

Abbas, F.H., 2010. Hydrogeochemical study of groundwater wells in formation Ummordomah – western of Iraq. Journal of University of Anbar for Pure Science, Vol. 4, Issue 1, pp. 143-149. https://www.iasj.net/iasj/article/15455

Abbasnia, A., Radfard, M., Mahvi, A.H., Nabizadeh, R., Yousefi, M., Soleimani, H. and Alimohammadi, M., 2018. Groundwater quality assessment for irrigation purposes based on irrigation water quality index and its zoning with GIS in the villages of Chabahar, Sistan and Baluchistan, Iran. Data in Brief, 19, pp. 623–631. https://doi.org/10.1016/j.dib.2018.05.061

Alaya, M.B., Saidi, S., Zemni, T. and Zargouni, F., 2013. Suitability assessment of deep groundwater for drinking and irrigation use in the Djeffara aquifers (Northern Gabes, southeastern Tunisia). Environmental Earth Sciences, 71(8), pp. 3387–3421. DOI: 10.1007/s12665-013-2729-9.

Al-Hadidi, A.S., 2009. Evaluation of irrigation water quality and its effect on the chemical properties of some calcareous soils. Tikrit Journal of Agricultural Sciences. Vol. 9, Issue 2, pp. 442-447. https://iasj.rdd.edu.iq/journals/journal/issue/10116

Al-Rifaee, M.K.I. and Al-Rubay, A.A.M., 2017. Effect of Adding Irrigation Water Quality Index to Medulas Model on Environmental Sensitivity to Desertification in Sheika Saad Project Lands/ Wasit Governorate. Iraqi Journal of Agricultural Research, Vol. 22, No.1, pp. 101-116.

Al-Zubaidi, A.H., 1989. Soil Salinity: Theoretical and Applied Foundations. University of Mosul, Ibn Al-Atheer Printing and Publishing Press, 308 P.

Avaci, H., Dokuz, U.E. and Avci, A.S., 2018. Hydrochemistry and groundwater quality in a semiarid calcareous area: an evaluation of major ion chemistry using a stoichiometric approach. Environmental Monitoring and Assessment, 190 (11). 10.1007/s10661-018-7021-8

Awad, E.S., Imran, N.S., Albayati, M.M., Snegirev, V., Sabirova, T.M., Tretyakova, N.A., Alsalhy, Q.F., Al-Furaiji, M.H., Salih, I.K. and Majdi, H.S., 2022. Groundwater Hydrogeochemical and Quality Appraisal for Agriculture Irrigation in Greenbelt Area, Iraq. Environments, 9, 43, pp. 1-20. https://doi.org/10.3390/environments9040043.

Ayers, R.S. and Westcot, D.W., 1985. Water quality for Agriculture. Irrigation and Drainage paper 29, Rev.1, FAO, Rome, Italy, 174 P. (Reprinted 1989, 1994). https://www.fao.org/4/t0234e/T0234E01.htm#tab2.

Berhe, B.A., Çelik, M. and Dokuz, U.E., 2015. Investigation of Irrigation Water Quality of Surface and Groundwater in the Kütahya Plain, Turkey. Bull. Min. Res. Exp. 150: pp.145-162. https://www.researchgate.net/publication/279174241

Dimple, Rajput, J., Al-Ansari, N. and Elbeltagi, A., 2022. Predicting Irrigation Water Quality Indices Based on Data-Driven Algorithms: Case Study in Semiarid Environment. Journal of Chemistry. Volume, Article ID 4488446, pp. 1-17. https://doi.org/10.1155/2022/4488446

Doneen, L.D., 1954. Salination of soil by salts in the irrigation water. Transactions, American Geophysical Union, 35(6), pp. 943-950. https://doi.org/10.1029/TR035i006p00943

Doneen, L.D., 1971. Irrigation practice and water management irrigation and drainage. Paper (1), FAO, Rome, 84 P.

Ekhmaj, A.I., Alriyani, A.A. and Dulayoum, M.M., 2021. Evaluation of Groundwater Quality in the South of Tripoliand its suitability for Irrigation Using Irrigation Water Quality Index (IWQI). Al-Mukhtar Journal of Sciences. 36 (1): pp. 80-97. https://www.researchgate.net/publication/352560896.

Herrero, J. and Peres-Coveta, O., 2005. Soil salinity changes over 24 years in a Mediterranean irrigated district. Geoderma, 125, pp. 287-308. https://doi.org/10.1016/j.geoderma.2004.09.004.

Ibrahim, A. and Kashmola, M.S., 2011. Study of quality properties of some wells water and Lower Zap stream and their fitness to different uses. Mesopotamia Journal of Agriculture, Volume 39, Issue (4), pp. 75-94. https://www.iasj.net/iasj/article/28225

Islam, M.M., Azad, A.K., Ara, M.H. Rahman, M., Hassan, N., Swarnokar, S.C. and Rabeya, I., 2016. Environmental Study on a Coastal River of Bangladesh with Reference to Irrigation Water Quality Assessment: A Case Study on Shailmari River, Khulna. Journal of Geoscience and Environment Protection, 4, pp. 41-64. http://dx.doi.org/10.4236/gep.2016.410003.

Kaba, R. and Majar, A., 2020. Spatial and Temporal Variability Analyses of Water Quality in Jaghjagh River, Syria. Jordan Journal of Earth and Environmental Sciences. 11(1), pp. 62-70. https://jjees.hu.edu.jo/files/Vol11No1/JJEES_Vol_11_No_1_P7.pdf.

Kovda, V.A., van den Berg, C. and Hagan, R.M., 1973. Irrigation drainage and salinity. An International Source Book. HUTCHINSON/FAO/UNESCO Publication, Ltd., London, 510 P.

Liu, F., Song, X., Yang, L., Han, D., Zhang, Y., Ma, Y. and Bu, H., 2015. The role of anthropogenic and natural factors in shaping the geochemical evolution of groundwater in the Subei Lake basin, Ordos energy base, Northwestern China. Science of the Total Environment, Vol. 538, pp. 327–340. http://dx.doi.org/10.1016/j.scitotenv.2015.08.057

Ma, L.G., Ma, F.L., Li, J.D., Gu, Q., Yang, S.T., Wu, D., Feng, J. and Ding, J.L., 2017. Characterizing and modeling regional-scale variations in soil salinity in the arid oasis of Tarim Basin, China. Geoderma, 305, pp. 1–11. https://doi.org/10.1016/j.geoderma.2017.05.016

Ma, L.G., Yang, S.T., Simayi, Z., Gu, Q., Li, J.D., Yang, X.D., Ding, J.L., 2018. Modeling variations in soil salinity in the oasis of Junggar Basin, China. Land Degrad. Dev. 29, pp. 551–562. http://dx.doi.org/10.1002/ldr.2890

Meireles, A.C.M., Andrade, E. M., Chaves, L.C.G., Frischkorn, H. and Crisostomo, L.A., 2010. A new proposal of the classification of irrigation water. Revista Ciência Agronômica, Vol. 41, No. 3, pp. 349-357. https://www.scielo.br/j/rca/a/4QHKYxG6bXZQRSVSwFf7vxd/?format=pdf&lang=en

Mohammed, A.I., Naimi, S. and Dawood, A.S., 2023. Evaluation of the Drinking and Irrigation Quality of Groundwater in Basrah, Iraq. Journal of Ecological Engineering. Vol. 24, No. (9), 260–271. http://dx.doi.org/10.12911/22998993/169177

Mostafa A. M., Abd El-Kawy, O.M. Mohamed, Y.I. and Khaled, N.A.N., 2020. Desertification Sensitivity Analysis East of Siwa Using GIS and Remote Sensing. Alexandria Science Exchange Journal, Vol. 41, No. 1, pp. 1-14. DOI:10.21608/ASEJAIQJSAE.2020.70346.

Page, A.L., Miller, R.H. and Keeney, D.R., 1982. Methods of Soil Analysis. Part 2. Chemical and Microbiological Properties, second edition. American Society of Agronomy. Inc. Soil Science Society of America, Inc., No. 9 (part 2) in the series, 1159.

Periasamy, S. and Ravi, K.P., 2020. A novel approach to quantify soil salinity by simulating the dielectric loss of SAR in three-dimensional density space. Remote Sensing of Environment, 251, 112059. https://doi.org/10.1016/j.rse.2020.112059.

Presley, D.R., Ransom, M.D., Kluitenberg, G.J. and Finnell, P.R., 2004. Effects of Thirty Years of Irrigation on the Genesis and Morphology of Two Semiarid Soils in Kansas. Soil Science Society of America Journal, 68(6), 1916. http://dx.doi.org/10.2136/sssaj2004.1916.

Jackson, M.L.R., 1969. Soil chemical analysis. Verlag: Prentice Hall, Inc., Englewood Cliffs, NJ. 1958, 498 S. DM 39.40. Zeitschrift Für Pflanzenernährung, Düngung, Bodenkunde, 85(3), 895 P. https://doi.org/https://doi.org/10.1002/jpln.19590850311

Richards, L.A., 1954. Diagnosis and Improvement of Saline and Alkali Soils. Agriculture Handbook No. 60, Washington 25 DC, 159, USDA. https://www.ars.usda.gov/ARSUserFiles/20360500/hb60_pdf/hb60complete.pdf

Salcedo, F.P., Cutillas, P.P., Cabanero, J.J.A. and Vivaldi, A.G., 2022. Use of remote sensing to evaluate the effects of environmental factors on soil salinity in a semi-arid area. Science of The Total Environment. 815, 152524. https://doi.org/10.1016/j.scitotenv.2021.152524

Thorne, D.W. and Thorne, J.P., 1954. Changes in Composition of Irrigated Soils as Related to the Quality of Irrigation Waters. Soil Science Society of America Journal, 18(1), 92. pp. 92-97. https://doi.org/10.2136/sssaj1954.03615995001800010023x.

Todd, D.K., 1980. Groundwater Hydrology. 2nd edition, John Wiley, New York, 552 P.

Treder, W., 2005. Variation soil pH, Calcium and magnesium status influenced by drip irrigation and fertigation. Journal of Fruit and Ornamental Plant Research Vol. 13: pp. 59-70. https://www.inhort.pl/files/journal_pdf/journal_2005/full2005_6.pdf

Zhang, Y.T., Hou, K., Qian, H., Gao, Y.Y., Fang, Y., Xiao, S., Tang, S.Q., Zhang, Q.Y., Qu, W.A. and Ren, W.H., 2022. Characterization of soil salinization and its driving factors in a typical irrigation area of Northwest China. The Science of the Total Environment. 837, 11. https://doi.org/10.1016/j.scitotenv.2022.155808.

Zhao, X., Guo, H., Wang, Y., Wang, G., Wang, H., Zang, X. and Zhu, J., 2021. Groundwater hydrogeochemical characteristics and quality suitability assessment for irrigation and drinking purposes in an agricultural region of the North China plain. Environmental Earth Sciences, 80(4). DOI: 10.1007/s10661-018-7021-8.

Iraqi National Journal of Earth Science

www.earth.uomosul.edu.iq

Sedimentological analysis of the Dokan Formation (Cenomanian) in Goizha Section, Azmar Anticline, Northeastern Iraq

Noor T. Al-Taee [1*]

[1]*Department of Geology, College of Science, University of Mosul, Mosul, Iraq.*

Article in Formation

Received: 13- Oct -2024

Revised: 14- Nov -2024

Accepted: 25- Dec -2024

Available online: 01- Jan – 2026

Keywords:
Cenomenian,
Microfacies,
Shelf Environments,
Dokan Formation,
Iraq,

Correspondence:
Name: Noor T. Al-Taee
Email: noortalal@uomosul.edu.iq

ABSTRACT

The Dokan Formation (Cenomanian) has been studied within the Azmar anticline in Sulaymaniyah Governorate (about 4 km northeast of the city center). The field description shows that the Dokan Formation is composed mainly of light-gray limestone rocks and lead-gray marly limestone with thin beds of dark-gray shale. The thickness of the Formation in the studied section is 18 m; The lower and upper contacts of the Dokan Formation are conformable with the Balambo Formation and the Gulneri Formation, respectively. The petrographic study of (55) thin sections reveal the following components: planktonic and benthonic foraminifera, calcospheres, some echinoderm bioclasts, and lesser proportions of ostracods. Many diagenetic processes (dissolution, cementation, chemical and physical compaction, etc.) affected the rocks of the Formation. Two main microfacies are distinguished: the first one is lime mudstone microfacies, and the second is lime wackestone microfacies; these, in turn, are divided into six sub-microfacies. Comparing all microfacies with the standard microfacies indicates that the Dokan Formation was deposited in the zone that extended from the outer shelf to the upper slope environments.

DOI: 10.33899/injes.v26i1.60198, ©Authors, 2026, College of Science, University of Mosul.
This is an open-access article under the CC BY 4.0 license (http://creativecommons.org/licenses/by/4.0/).

التحليل الرسوبي لتكوين دوكان (السنوماني) في مقطع كويزة، طية ازمر، شمال شرقي العراق

نور طلال الطائي [1*]

[1] *قسم علوم الأرض، كلية العلوم، جامعة الموصل، الموصل، العراق.*

معلومات الارشفة

تاريخ الاستلام: 13- اكتوبر-2024

تاريخ المراجعة: 14- نوفمبر-2024

تاريخ القبـول: 25- ديسمبر-2024

تاريخ النشر الالكتروني: 01- يناير-2026

الكلمات المفتاحية:

سينومينيان،
سحنات الدقيقة،
الرصيف البحري العميق،
تكوين دوكان،
العراق،

المراسلة:

الاسم: نور طلال الطائي

Email: noortalal@uomosul.edu.iq

الملخص

تمت دراسة تكوين دوكان (السنومينيان) ضمن طية ازمر، شمال شرقي العراق في محافظة السليمانية، وتحديدا ضمن طية ازمر والتي تبعد حوالي 4 كم عن شمال شرقي مركز المدينة. لوحظ من خلال الوصف الصخري حقلياً، أن تكوين دوكان يتألف من تتابعات من الصخور الجيرية ذات اللون الرصاصي الفاتح وبنسبة اقل صخور المارل الرصاصية اللون وصخور الطفل المترقق داكنة اللون. يبلغ سمك التكوين في المقطع المختار 18 متراً. ويكون حدا التماس السفلي والعلوي متوافقين مع كل من تكويني بالامبو وكولنري على التوالي. ومن خلال الدراسة البترورغرافية وبالاعتماد على الشرائح الصخرية تم تمييز الفورامنيفرا الطافية والقاعية والكالسوسفيرات بشكل رئيس وبعض الفتاتات الحياتية وشوكيات الجلد والاوستراكود بنسب اقل، متأثرة بالعديد من العمليات التحويرية (الاذابة السمنتة الانضغاط الكيمائي والفيزيائي وغيرها). سحنيا، تم تمييز سحنتين رئيستين هما سحنة الحجر الجيري الطيني وسحنة الحجر الجيري الواكي الرئيسة والتي بدورها قُسمت الى ست سحنات ثانوية دقيقة. بعد مقارنتها بالسحنات القياسية الدقيقة، وجد ان تكوين دوكان قد ترسب ضمن بيئة الرصيف المفتوح القريب من المنحدر.

DOI: 10.33899/injes.v26i1.60198, ©Authors, 2026, College of Science, University of Mosul.
This is an open-access article under the CC BY 4.0 license (http://creativecommons.org/licenses/by/4.0/).

Introduction

Dokan Formation Late Cretaceous (Cenomanian) was first described by Lancaaster Jones (1957; in Bellen *et al*., 1959), typically at the Dokan area in Sulaymaniyah City within the high folded zone, northeastern Iraq. It consists of light-gray to white oligosteginal limestone. In Subsurface, the Dokan Formation includes dark grey and often argillaceous limestone. The thickness of the formation reaches about 150 m to the southwest in the Chamchamal wells, and reaches 5-30 m in Kirkuk, Bai Hassan, Demir Dagh, and Qara Ash-Shuq areas. The current study is conducted on the Dokan Formation due to the lack of sedimentary studies on the formation, so it includes a detailed study of the petrography and facies reaching the sedimentary environment. The lower and upper contacts of the formation are unconformable in the type section area. The upper contact is with the Gulneri Formation and in some areas with Kometan Formation, while the lower contact is with Qamchuqa Formation or Jawan Formation. The Dokan Formation is one of the important formations in the Late Tithonian-Early Turonian cycle, which is a part of the mega sequence (AP8) (Sharland *et al*., 2001). This cycle includes these formations (Dokan, Gulneri, Jawan, Qamchuqa, Garagu, Balambo, Sarmord, Chia Gara). Previous studies have shown that the environment of the Dokan Formation was within an open marine environment (Ditmar and the Iraqi-Soviet Team, 1971; in Jassim and Goff, 2006). It was later studied by Al-Juboury *et al*. (2002), who deduced the open shelf environment near the lower slope and the slope front environment in wells within Kirkuk Governorate. However, in this study, the aim is to clarify the depositional environment in the studied section; so, it is

necessary to address the sedimentary and biological evidence and their link together to reach the identification and well-accepted conclusion of the depositional environment.

According to Abawi and Hammoudi (2010), the age of the Dokan Formation is Cenomanian, and the age of the formation at the Jebel Azmar area is Middle-Late Cenomanian assigned by *Rotalipora cushmani* Zone Abawi and Hammoudi (2010). This refers to a major hiatus between the Dokan Formation and the older Balambo Formation (Middle-Late Albian) in this area.

All sedimentological and stratigraphical studies of the Dokan Formation indicate that it has been deposited in the deep marine environment (e.g., Al-Juboury *et al*., 2002). Karim *et al.* (2013) studied the stratigraphic analysis of the Goizha anticline by nannofossils.

Al-Sheikhly *et al*. (2015) mentioned that the Dokan Formation had been deposited in an open-marine deep shelf environment; it could have been deposited at a deeper shelf to slope and basinal.

This study aims to identify the main petrographic components and diagenesis affecting the Dokan Formation, then determine the microfacies to reconstruct the depositional environment of the formation in the studied area.

Geological Setting

The study area is located in the northeastern part of Iraq within Sulaymaniyah Governorate at the Azmar anticline at latitude 35° 40' 00" N and longitude 45° 25' 00" E. The Azmar anticline denotes the area of the Imbricated Zone within the Foreland belt of the Zagros collision zone (Numan, 1997; Jassim and Goff, 2006) (Fig. 1A). The main Azmar anticline includes a group of secondary folds, namely Bekhola, Harut, Azmar, and Goizha, which were affected by several faults. The length of the Azmar anticline is 91 km, and its width is 1-4.5 km (Karim *et al*., 2013). The Azmar and Goizha are two connected mountains that are located to the north and northeast of Sulaimaniyah City, respectively (Karim *et al*., 2013).

Tectonically, according to Fouad (2015), the selected section is located within the Arabian shelf at the Azmar anticline of the Zagros Orogenic Belt, located within the Imbricated Zone. The selected section is situated at the Arabian Shelf within the Azmar anticline of the Zagros Orogenic Belt, which lies in the Imbricated Zone (Fig. 1B) that arose between the northeast of the edge of the Arabian plate and the Eurasian plate in the form of a Druze belt. While the Arabian and Anatolian plates are connected by the Bitlis range section. The geographical location map is exhibited in Fig. 1C. Aljumaily and Adeeb (2011) also confirmed in their correlation diagram of the Azmar-Goizha anticlines the occurrence of the Dokan Formation in the Goizha anticline. Al-Hakari (2011) also studied the geological setting through his correlation diagram, declaring the connection between the Azmar-Goizha anticlines and the Dokan Formation in the Goizha anticline. Within the Azmar anticline, many exposed formations from oldest to youngest are: Balambo (Valanginian-Albian), Dokan (Cenomanian), Gulneri (Turonian), Kometan (Campinian), Shiranish (Campinian-Maastrichtian), and Tanjero (Maastrichtian).

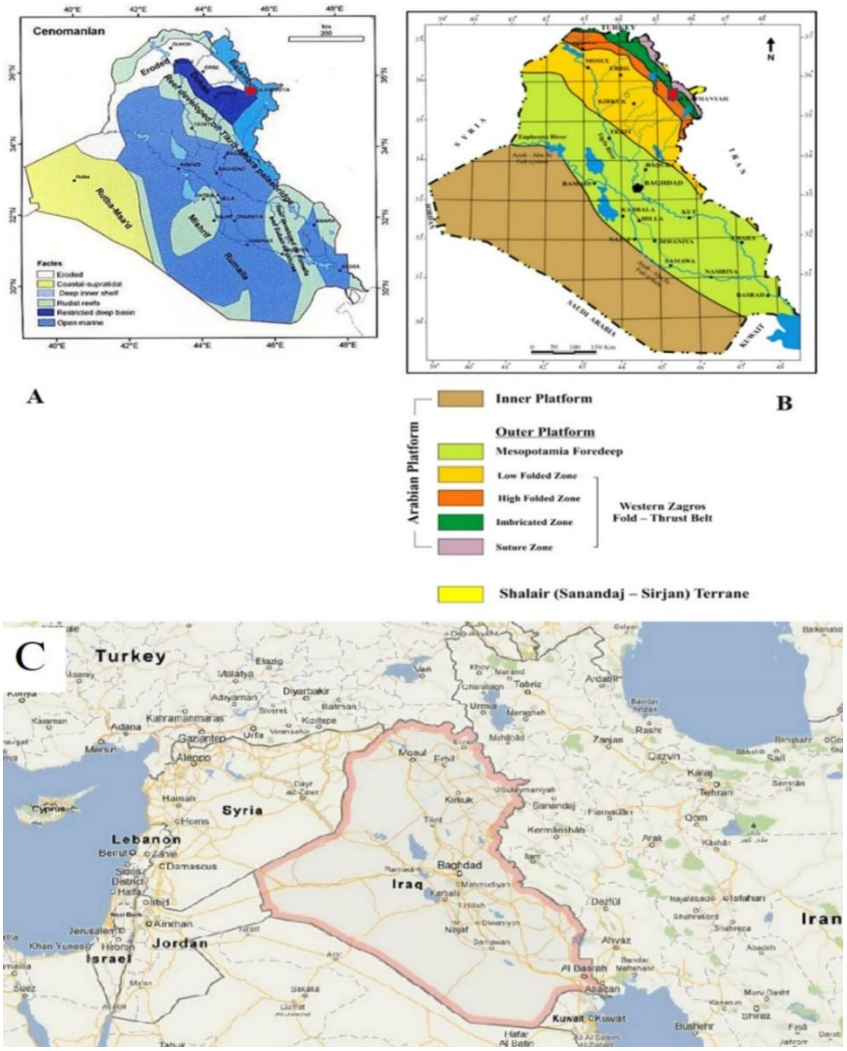


Fig. 1. A. Paleogeography of the Dokan Formation deposits (Jassim and Buday, 2006); B. Modern tectonic division of Iraq from Fouad (2015) showing the current study section; C. Geographical location map.

Materials and Methods

The study methods include the field and laboratory works; in the field work, the description of the exposed rocks of the Dokan Formation is achieved in some selected outcrops in order to obtain a detailed lithological description. The sampling process is based on the facies change and color contrast.

In the laboratory, rock slices (thin sections) of 25 rock samples are prepared and studied under a polarizing microscope (Swift type) in order to determine the petrographic components, diagenesis, and microfacies.

Results

Lithostratigraphy

The lower and upper contacts of the Dokan Formation are conformable with Balambo and the Gulneri, respectively (Fig. 2). The thickness of the Dokan Formation is about 18 meters. The first exposed part of the formation begins with flat-bedded light lead-colored to white limestone rocks with a thickness of 4m (Fig. 3). They are followed by thin successions of yellowish-white flat-bedded marly limestone beds with a thickness of 2m; the succession ended by a bed of gray-colored thin shale with a thickness of 1m. Then, another succession of light grey limestone flat beds with 4m thick starts, followed by a bed of 1m thick grey shale,

continued by a succession of grey-white limestone beds with 4m thick, then a bed of grey marly limestone with 60 cm thick occurs, and finally returns to limestone at the contact with Gulneri Formation.



Fig. 2. A. Lower contact of the Dokan Formation with the Balambo Formation; B. Upper contact with the Gulneri Formation.

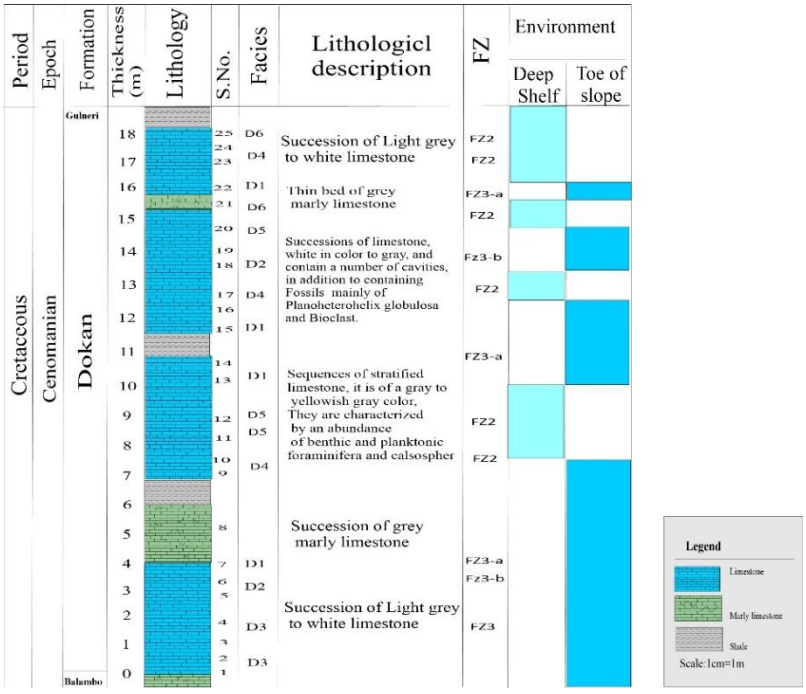


Fig. 3. Lithological column showing the rock sequence of Dokan Formation.

Petrography

The petrographic examination of the Dokan Formation reveals a diversity in grain size; each type of grain reflects specific environmental and sedimentary conditions, and can reveal features of the diagenetic processes that affected it. According to Tucker (1981, 2003), skeletal grains encompass all types of fossils, which are either complete in form (biomorpha) or in the form of bioclasts of varying shapes and sizes. The Dokan Formation is known to be rich in fossil content. The presence of well-preserved fossils allows researchers to identify various species and to determine the environmental conditions. This formation can provide insights into the evolutionary history of the region, as well as the paleoecological dynamics during the period it represents. This formation also offers valuable insights into the region's evolutionary history and the paleoecological dynamics of its period. The main skeletal grains are Foraminifera, including both planktonic and benthonic. The planktonic includes: Globigerinelloides bentonensis (Plate 1-A), Globigerinelloides ultramicus (Plate 1-B,2-F), Rotalipora cushmani (Plate 1-C), Planoheterohelix globulosa (Plate 1-D), Rotalipora ticinensis (Plate 1-E), Whiteinella archeoeretacea, Rotalipora sp. (Plate 1-F), Favusella washitensis.

Benthic foraminifera are identified in the study area sequences in very small amounts; this presence is important in the microfacies analysis to infer the sedimentary environment, whether the marine environments are shallow or deep (Flügel, 2004). According to Milliman (1974), the small percentage of benthic foraminifera in the sediments generally indicates deep marine environments (Wilson and Evans, 2002), and they include both Textularia sp. (Plate 2-A) and Nodosaria sp. (Plate 2-B). The association of benthic foraminifera with the planktonic ones indicates an open shelf environment (Bishop, 1972). The other fossil grains are Calcispheres that indicate limestone deposition in the deep-sea environment (Flügel, 2010). The calcispheres are identified generally by small size, spherical to oval in shape, and their diameter ranges between 30-33 microns. They are well preserved and filled with spary calcite, and their percentage is around 70% in the study sediments (Plate 2-C). Bivalve or oval-shaped shells belonging to freshwater, mixed, and marine environments (Abawi et al., 2000) generally characterize ostracods. Ostracods occur in very small proportions and are often affected by modification processes (Plate 2-A). Echinoderms are also identified in the current study in very small amounts (Plate 2-D). In general, it is believed that most of the bioclasts identified in the current study are due to the debris of the shells of foraminifera, in addition to Calcispheres, Echinoderms, and Ostracods (Plate 2-E). They are peloid grains may be present but not identified. They may be within a bioclast.

The examined rocks are predominantly characterized by the presence of micrite groundmass as a matrix between and within the grains and microfractures of the rocks. Micrite is mechanically deposited in the marine environments that are characterized by low energy, where currents and strong waves have minimal impact (Friedman, 1985). Where micrite is found as a pale, opaque, black, or dark color groundmass, depending on the percentage of organic matter or even the type of clay materials (Plate 2-A).

The **most important diagenetic processes** diagnosed in the current study are:

Compaction: The mechanical and chemical compaction affects the formation deposits. The intensity of mechanical compaction varies in contact, as in (Plate 4-A, C), such as the breakage of shells, the presence of their debris, or the elongation of limestone balls (Plates 1-E, 4-D). Some shells exposed to compaction (Plate 1-D) show fullness microfractures or are filled with organic materials. Chemical compaction is indicated by the dissolution lines in the form of the porosity of the matrix (Plate 3-A). fractures (Plate 3-C) due to the presence of affecting digenesis.

Recrystallization: It is a process noticed by the microspar spots in the micrite floor (Plate 2-E), and in some fossil shells were affected by the recrystallization process (Plate 1-B).

Cementation: Carbonate minerals appear within the rocks of the formation either within fossils or filling voids, cracks, fractures, and veins. The main texture types of cementations are granular cement (Plate 3-C), which is one of the types of late-forming cement (Flügel, 1982; Bathurst, 1975). Blocky cement, which consists of large and fully faceted crystals that have no direction in growth, may be formed after the dissolution of granules or carbonate cement or by late diagenesis (Boggs, 2006). Blocky cement is abundant in the deposits of the formation (Plate 3-B), formed by late diagenesis and filling either fossils or vugs and cracks (Plates 1-D,3-D).

Dissolution: is a process that affects the Dokan Formation deposits through partial dissolution of the non-skeletal components and skeletal shells. It results in the formation of many types of pores, including intragranular porosity. These pores are formed inside some skeletal grains as a result of dissolving the soft parts of fossils (Plates 3-A, 4-A). Also, vuggy porosity appears as gaps of different shapes and sizes associated with mold porosity and often cuts the groundmass and grains (Plate 3-A).

Micritization: This process may include the entire grain (Boggs, 2006), where the micrite is not limited to the outer bed of the grain, but rather extends to its internal parts, leading to the obliteration of the internal features of the grain (Plate 4-B).

Authigenesis: It is recorded through pyrite mineral as one of the authigenic minerals scattered in the deposits of the Dokan Formation, and it is characterized by its isotropic appearance and dark brown color (Plates 1-E,3-E). Neither replacement nor alteration is observed.

Facies analysis

Detailed field description and petrographic analysis of the carbonate rocks of the Dokan Formation reveal that these rocks could be organized into two major microfacies and six submicrofacies.

A- Lime Mudstone Microfacies

The mudstone microfacies is one of the common facies that have been diagnosed within the deposits of the Dokan Formation. This facies occurs within the lower beds of the studied section and consists mainly of the micritic matrix and a small number of grains that do not exceed 10% of the components of the facies, including planktonic foraminifera and calcispheres, which can be subdivided into three submicrofacies depending on the petrographic components:

1. **Planktonic Foraminiferal Lime Mudstone Submicrofacies (D1)**

   This microfacies is predominantly made up of micrite and Planktonic Foraminifera (Plate 4-A) represented by: *Globigrinelloides bentonensis* and *Globigerinelloides*; it is affected by diagenetic processes like dissolution and cementation, distributed in all parts along the formation, but increased towards the top. This microfacies is equivalent to the standard Microfacies (SMF3) according to Flügel (2004), which is deposited within the facies zone (FZ3-a), the outermost slope known as the deep-water zone (Open Sea Shelf environment) near the slope.

2. **Calcispheres Lime Mudstone Submicrofacies (D2)**

   Micritic matrix is the most abundant in this microfacies, followed by Calcisphere grains (less than 10%) and some Planktonic Foraminifera (4-B). The main diagenetic processes of this microfacies are cementation and micritization with the presence of pyrite authigenesis. This microfacies occurs at the middle and upper deposits of the formation; it is equivalent to the standard Microfacies (SMF3) according to Flügel (2004) and is deposited within the facies zone (Fz3-b), which is known as the proximal deep-water zone (Open Sea Shelf environment) near the slope.

3. **Bioclastic Lime Mudstone Submicrofacies (D3)**

   The grain components in this microfacies consist of foraminifera shell fragments and Calcispheres, representing about 10% of the microfacies (Plate 1-B), with the presence of pyrites; it is affected by the recrystallization process within the groundmass and shells.

This microfacies is locally present at the lower part of the formation, which is equivalent to the standard Microfacies (SMF3) according to Flügel (2004) and is deposited within the facies zone (FZ3) known as the deep zone near the slope.

B- Lime Wackestone Microfacies

Generally, these facies are composed of skeletal grains that exceed (10%) and do not exceed (50%) of the facies components and micritic matrix. Planktonic foraminifera and calcispheres and their debris (10%) represent the grains. These facies can be divided depending on the petrographic components into:

1. ***Planoheterohelix globulosa*** **Lime Wackestone Submicrofacies (D4)**

Planktonic organisms, particularly Planoheterohelix globulosa, are the most abundant, followed secondarily by the ultramicud Globigerinelloides. These organisms are present in the limestone beds, specifically within the middle and upper parts of the formation. The identified diagenetic processes here are compaction and cementation (Plate 4-C). This facies is equivalent to the standard microfacies (SMF8) according to Flügel (2004), which is deposited within the facies zone (FZ2) known as the open sea shelf environment near the lower slope.

2. ***Globigerinelloids*** **Lime Wackestone Submicrofacies(D5)**

Globigerinelloids are the major common constituent of the grains in this microfacies (Plate 4-D). The Ground is composed mainly of micrite. This microfacies has been affected by the diagenetic processes: cementation, dissolution, and compaction. The microfacies is represented within the limestone deposits in the middle of the formation. It corresponds to the standard microfacies (SMF8) (Flügel, 2004), deposited within the facies zone (FZ2) known as the open sea shelf environment near the lower slope.

3. **Bioclastic Lime Wackestone Submicrofacies (D6)**

This microfacies contains bioclasts of foraminifera and echinoderms; the bioclasts constitute 35% of the facies, affected by micrization and compaction (Plate 2-B), and are found at the end of the upper beds of the formation. This microfacies is equivalent to the standard microfacies (SMF2) according to Flügel (2004) and is deposited within the facies zone (FZ2) known as the outer shelf environment near the lower slope.

Discussion

Depositional Environment

The following is a list of the most important sedimentary and biological evidence that are relied upon in formulating the depositional environment:

Facies Sedimentological evidence

All the identified microfacies are composed primarily of micrite with only a small percentage of sparite, suggesting deposition in calm and low-energy environments situated below the wave base level. The alternation of limestone beds with shale and marly limestone, further with flat-bedding, indicates a deep and tranquil sedimentary setting. Additionally, the presence of authigenic minerals such as pyrite points to a deep-water environment with low oxygen levels (Nichols, 1999).

Facies Biological evidence

Three biological evidences refer to the deep marine environment; the first is the abundance of planktonic fossils and the lack of benthic fossils within the rocks (Murray, 2006); the second is the association of planktonic fossils and calcispheres; and the third is the lack of bioclasts identified within the studied rocks. Nevertheless, the association of both Textularia sp. and Nodosaria sp. indicates an open shelf environment (Murray, 2006).

Depending on the biological, sedimentological evidence, and microfacies analysis data compared with the standard microfacies listed in Wilson (1975) and Flügel (1982, 2004), the microfacies of the Dokan Formation in the studied section include (SMF2, SMF3, and SMF8). They are deposited within the two facies zones (FZ2, FZ3) interpreted to be located within the toe of slope and the deep shelf margin (Table 1). In the outer shelf (100-200 m deep), the living organisms are planktonic foraminifera and a few benthic foraminifera, whereas in the toe of slope environment, there is an increase in planktonic foraminifera and calcispheres.

Table 1: Microfacies and facies zone of the Dokan Formation in the studied section.

Microfacies of the Dokan Formation	SMF of Flügel (2010) and FZ of Wilson (1975)		
	SMF	FZ (Wilson, 1975)	Location of SMF (Flügel, 2010)
Planktonic Foraminiferal Lime Mudstone Submicrofacies (D1)	(SMF3)	(FZ-3)	Toe of slope
Calcispheres Lime Mudstone Submicrofacies	(SMF3)	(FZ-3)	Toe of slope
Bioclastic Lime Mudstone Submicrofacies (D3)	(SMF3)	(FZ-3)	Toe of slope
Planoheterohelix globulosa Lime Wackestone Submicrofacies(D4)	(SMF8)	(FZ-2)	Deep Shelf
Globigerinelloids Lime Wackestone Submicrofacies(D5)	(SMF8)	(FZ-2)	Deep Shelf
Bioclastic Lime Wackestone Submicrofacies (D6)	(SMF2)	(FZ-1)- (FZ-2)	Deep shelf

The lime mudstone and lime wackestone contain planktonic foraminifera, calcispheres, and bioclasts, with a lack of sedimentary structures. These characteristics are related to the deep marine environment, ranging from the slope environment to the open sea environment (Brandly and Krause, 1998). The presence of the genus *Globigerinelloides* indicates the open marine environment and may reach the outer shelf environment (Abdel-Kireem, 1983). The disappearance of Rotalipora cushmani is linked to a significant turnover in marine organisms, affecting both planktonic and benthic foraminifera, as well as calcareous nannofossils (Abdel-Kireem, 1983). This event occurred shortly before the onset of Oceanic Anoxic Event 2 (OAE 2), which represents the sedimentary signature of the global late Cenomanian anoxic event (Coccioni et al., 2016). The presence of *Planoheterohelix globulosa* indicates its deposition in the open marine environment under the influence of waves (Rahimpour-Bonab *et al*., 2012; Omidvar *et al*., 2014; Gowhari *et al*., 2020), and may have been broken up in lower environmental sites represented by the open sea shelf.

Depending on the aforementioned, the current study suggests that Dokan Formation rocks were deposited in the open sea deep shelf environment extending to the toe of slope environment. These environmental conditions are calm, below the level of the base of the wave. Regarding the climate, northeastern Iraq during the Cenomanian period was located within a tropical climate zone (Beydoun, 1991). The suggested model for the Dokan Formation is illustrated in Fig. 4.

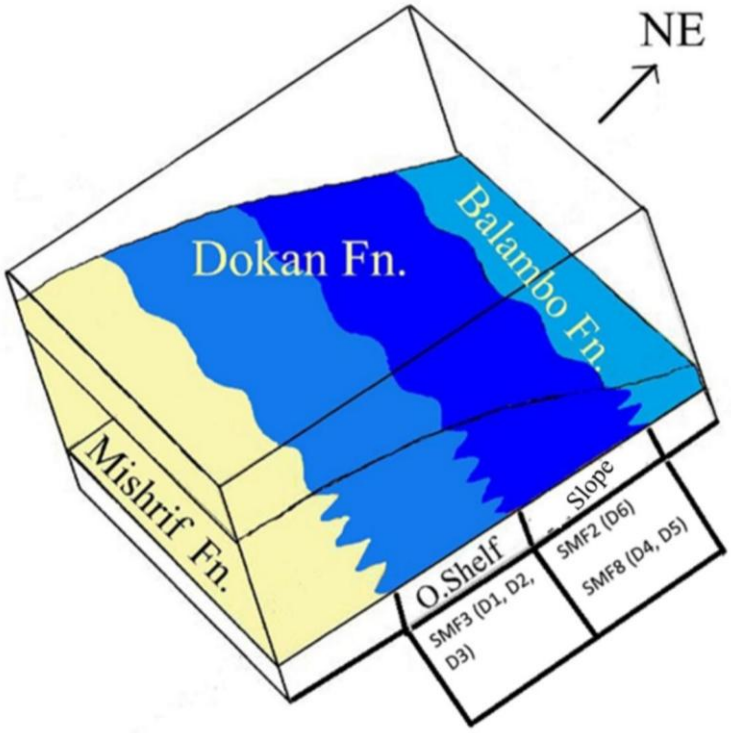


Fig. 4. Sedimentary model of the Dokan Formation in the study area under a tropical climate.

Conclusions

The thickness of the Dokan Formation exposed in the studied section is about 18m. It consists mainly of limestone sequences alternating with marly limestone beds and thin shale beds. The lower and upper contacts of the Dokan Formation are conformable with the Balambo Formation and the Gulneri Formation, respectively. Petrographically, foraminifera, calcisphere, and some bioclastics are distinguished as grains merged in micritic matrix, affected by many diagenetic processes (dissolution, cementation, chemical and physical compression, etc.).

Two mains distinguished microfacies (lime mudstone microfacies and lime wackestone microfacies) are divided into six secondary submicrofacies after comparing them with the standard facies.

The current study indicates that the deep shelf environment is represented by the open shelf environment near the lower slope, which is calm, below the level of the base of waves, and the environment of the slope. This is confirmed by the presence of calcispheres and Foraminifera. Through environmental analysis of the formation deposits, a microfacies and petrographic compatibility is found, represented in the slope environment towards the open sea. Based on these details, a sedimentary model is constructed that explains the formation deposit.

The Dokan Formation had been deposited in an isolated basin between the Balambo basin to the northeast and the Mishrif basin to the southwest. A fluctuation in the sea level variation is observed depending on the environmental variation between the Toe of the slope and the Deep Shelf environment.

References

Abawi, T.S. and Hammoudi, R.A., 2010. Stratigraphy of the Dokan Formation (Upper Cretaceous), Jebel Azmer-Sulaimaniya Area, Northeastern Iraq. Iraqi Journal of Earth Sciences, Vol. 10, No. 1, pp.1-10.

Abawi, T.S., Nader, A.D. and Khalaf, S.K., 2000. Micropaleontology, Dar Al-Kutub for Printing and Publishing, University of Mosul, 416 P.

Abdel-Kireem, M.R., 1983. A study of the palaeoecology and bathymetry of the foraminiferal assemblages of the Shiranish Formation (Upper Cretaceous), northeastern Iraq. Palaeogeography, palaeoclimatology, 43(1-2), pp.169-180.

Al-Hakari, S.H.S., 2011. Geometric Analysis and Structural Evolution of NW Sulaimani Area, Kurdistan Region, Iraq. Unpublished PHD Thesis, University of Sulaimani, pp. 309.

Al-Juboury, A.I., Al-Jwainy, Q.S. and Hadad, S.N., 2002. Facies analysis of Dokan Formation in Selected Wells at Jambur Oil Field, Rafidain Journal of Science. Northeast Iraq, Vol. 13, pp. 62-77

Aljumaily, I.S. and Adeeb, H.G., 2011. Some structural features of Azmar Anticline, NE Iraq. Journal of Mineral Research and Exploration, 143, pp. 37 – 52.

Al-Sheikhly, S.S., Tamar-Agha, M.Y. and Mahdi, M.M., 2015. The facies analysis of the Cenomanian-Turonian succession of Surdash – Shaqlawa area, NE. Iraq. Iraqi Journal of Science, Vol. 56, No. 1C, pp. 767-773.

Bathurst, R.G.C., 1975. Carbonate sediments and their diagenesis: Development in Sedimentology-12, Elsevier Scientific Publ. Com. Amsterdam, 658 P.

Bellen, V.R.C., Dunnington, H.V., Wetzel, R. and Morton, D.M., 1959. Lexique Stratigraphique International. V. III, Asie, Fascicule, 10a, Iraq, Central National deal Recherches Scientifique, Paris, 333 P.

Beydoun, Z.R., 1991. Arabian plate hydrocarbon, geology and potential – A plate tectonic approach. American Association of Petroleum Geologists, Studies in Geology, Vol. 33, 77 P.

Bishop, B.A., 1972. Petrography and origin of Cretaceous limestones – Sierra De Picachos and Vicinity, Nuevo Leon, Mexico. Journal of Sedimentology Petroleum, 42(2). pp. 270-286.

Boggs, S.J., 2006. Principles of Sedimentology and Stratigraphy (4th Ed.), Pearson Prentice-Hall, 662 P.

Brandly, R.T. and Krause, E.E., 1998. Carboniferous upwelling thermoclins and wave sweeping. Amer. Assoc. Petrolieum Geol.Bull, pp. 365-390.

Coccioni, R., Sideri, M., Frontalini, M. and Montanari, M., 2016. The Rotalipora cushmani extinction at Gubbio (Italy): Planktonic foraminiferal testimonial of the onset of the Caribbean large igneous province emplacement? The Stratigraphic Record of Gubbio: Integrated Stratigraphy of the Late Cretaceous–Paleogene Umbria-Marche Pelagic Basin, Doi: https://doi.org/10.1130/2016.2524(06)

Flügel, E., 1982. Microfacies Analysis of Limestone, Springer Verlag, Berlin, 633 P.

Flügel, E., 2004. Microfacies of carbonate rocks: analysis, interpretation and application, Springer Verlag: 984.

Flügel, E., 2010. Microfacies of carbonate rocks: analysis, interpretation, and application, 2nd ed. Springer, Berlin: 929 P.

Fouad, S., 2015. Tectonic map of Iraq, scale 1:1000 000, 3rd Edition. Iraqi Bulletin of Geology and Mining, Vol. 11, pp. 1-7.

Friedman, G.M., 1985. The term micrite or micrite cement is a contradiction–discussion of micritic cement in microborings is not indicator. J.S.P., Vol. 55, pp. 777-784.

Gowhari, S.A., Ahmadi, V., Saroea, H. and Yazdgerdi, K., 2020. Depositional environment, sequence stratigraphy and biostratigraphy of the Gurpi Formation in Fars zone, Zagros Basin (SW Iran), Carbonates and Evaporites, 35:86, pp.15.

Jassim, S.Z. and Buday, T., 2006. Unit of the Unstable Shelf and the Zagros Suture, in: Jassim, S.Z. and Goff, J. C. Geology of Iraq, Published by Dolin Prague and Moravian Museum, Brno, pp. 71-83.

Jassim, S.Z. and Goff, J.C., 2006. Geology of Iraq. Prague and Moravian Museum, Brno: 341 P.

Karim, K.H., Salih, A.O. and Ahmad, S.H., 2013. Stratigraphic Analysis of Azmar-Goizha anticline by Nannofossils. Journal of Zankoy Sulaimani- Part A (JZS-A), Vol. 15 (2), pp. 22.

Milliman, J.D., 1974. Marine Carbonates, Springer-Verlag, Berlin, 375 P.

Murray, J.W., 2006. Ecology and Applications of Benthic Foraminifera, Cambridge University Press, UK, 426 P.

Nichols, G., 1999. Sedimentology and Stratigraphy. Blackwell Science Ltd., Oxford, 355 P.

Numan, N.M.S., 1997. A plate tectonic scenario for the Phanerozoic succession in Iraq. Journal of Geological Society of Iraq, Vol. 30, pp.85 – 119. Scholle, P.A and Ulmer- Scholle, D.S., 2003. A Color Guide to The Petrography of Carbonate Rocks: Grains, Textures, Porosity, Diagenesis, AAPG Memoir- 77, Tulsa, Oklahoma, U.S.A., 474 P.

Omidvar, M., Mehrabi, H., Sajjadi, F., Bahramizadeh-Sajjadi, H., Rahimpour-Bonab, H. and Ashrafzadeh, A., 2014. Revision of the foraminiferal biozonation scheme in Upper Cretaceous carbonates of the Dezful Embayment, Zagros, Iran: integrated palaeontological, sedimentological and geochemical investigation. Revue de Micropaleontologie, Vol. 57, pp. 97-116.

Rahimpour-Bonab, H., Mehrabi, H., Enayati-Bidgoli, A.H. and Omidvar, M., 2012. Coupled imprints of tropical climate and recurring emersions on reservoir evolution of a mid-Cretaceous carbonate ramp, Zagros Basin, SW Iran, Cretaceous Research, Vol. 37, pp. 15-34.

Sharland, P.R., Archer, R., Casey, D.M., Davis, R.B., Hall, S.H., Heward, A.P., Horbury, A.D. and Simmons, M.D., 2001. Arabian Plate Sequence Stratigraphy. Geo Arabia, Special publication, no. 2. 372 P.

Tucker, M.E., 1981. Sedimentary Petrology: An Introduction, Vol. 3, Blackwell Scientific Publishing, Oxford, 252 P.

Tucker, M.E., 2003. Sedimentary Rocks in the Field, Wiley, England, 234 P.

Wilson, J.L., 1975. Carbonate Facies in Geologic History, Springer–Verlag, New York, 475 P.

Wilson, M. and Evans, M., 2002. Sedimentology and diagenesis of Tertiary carbonates on the Mangkalihat Peninsula, Borneo: Implications for subsurface reservoir quality. Marine and Petroleum Geology - Mar Petrol Geol. Vol. 19, pp. 873-900. DOI. https://doi.10.1016/S0264-8172(02)00085-5.

Plate 1

A: *Globigerinelloides bentonensis* found in the central parts section.

B: *Globigerinelloides ultramicus* for planktonic foraminifera, Bioclastic Lime Mudstone Submicrofacies in the upper parts section affected by the recrystallization process indicated by the arrow.

C: *Rotalipora cushmani* in the central parts with scattered pyrite.

D: *Planoheterohelix globulosa* in the upper parts section, presence of granular cement inside the fossils, compaction.

E: *Rotalipora ticinensis* in the central parts section, presence of pyrite and compaction.

F: Rotalipora sp. in the central parts section.

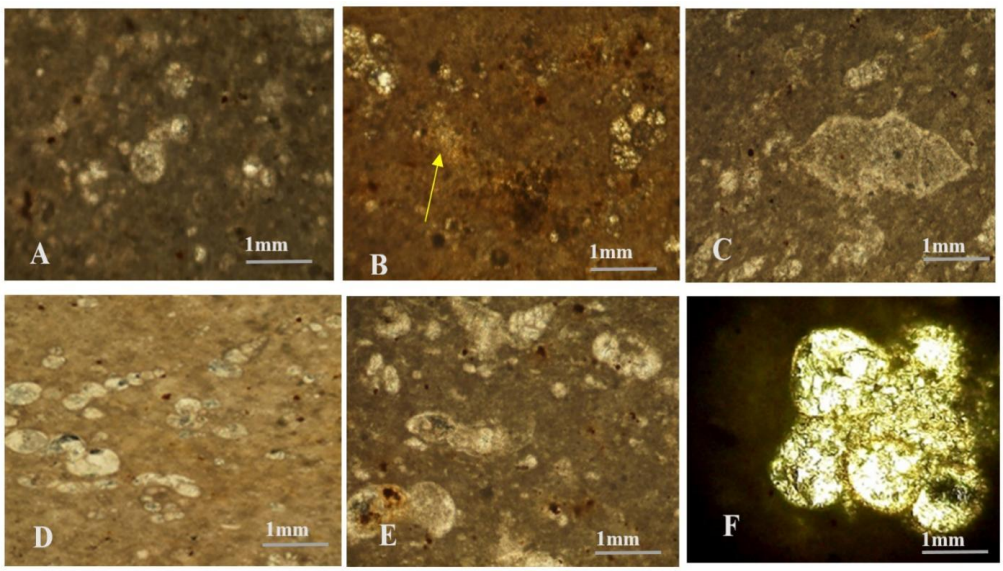


Plate 2

A: Textularia sp. of benthic foraminifera with calcospheres and ostracoda within a micrite in the middle parts section.

B: Nodosaria sp. of benthic foraminifera, Bioclastic Lime Wackestone Submicrofacies in the upper parts section.

C: Calcospherite in upper parts section.

D: Echinoderms in upper parts section.

E: Bioclast with recrystallization in the upper parts section.

F: *Globigerinelloides* ultramicus with micrit (m) and sparite (s) in the upper parts section.

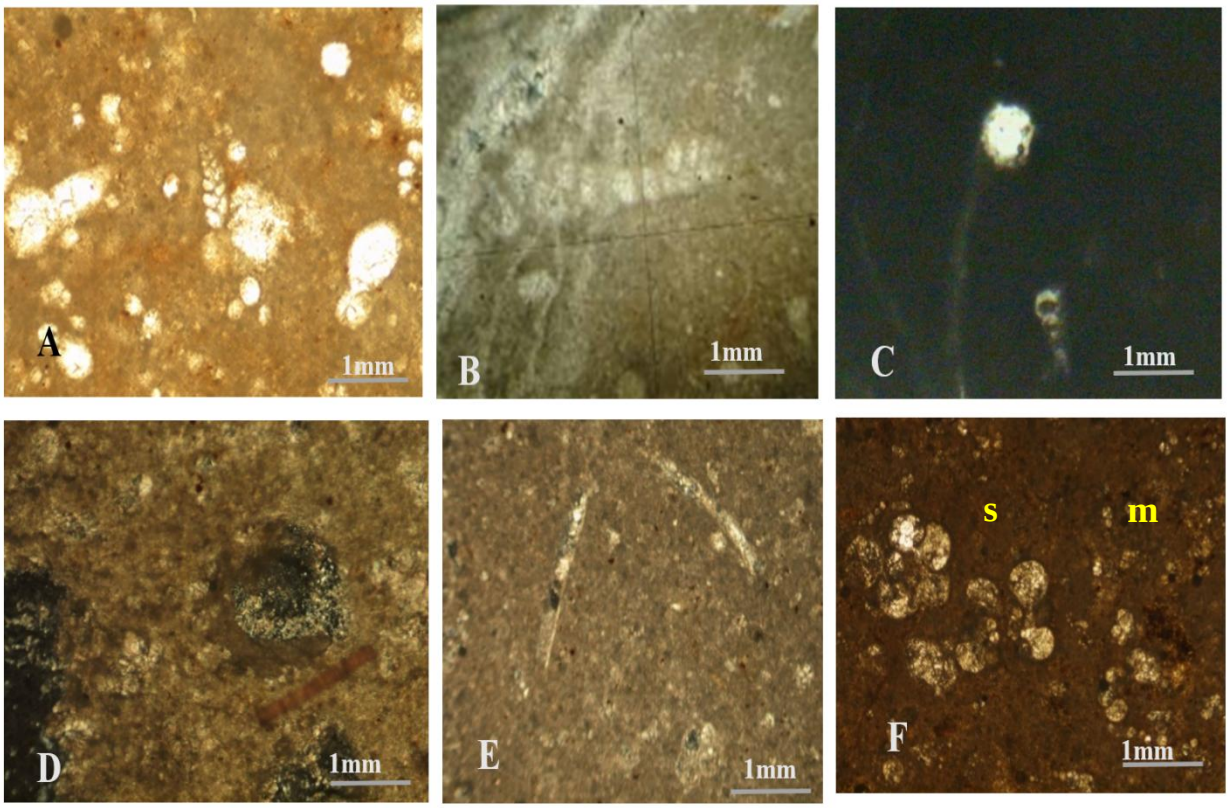


Plate 3

A: Mold porosity, dissolution.

B: Cement in the form of blocky cement is one of the most common types of cement under study.

C: Fractures: due to the presence of chemical solutions, cement.

D: A vein of calcite-filling voids.

E: Presence of localized minerals as well represented by scattered pyrites.

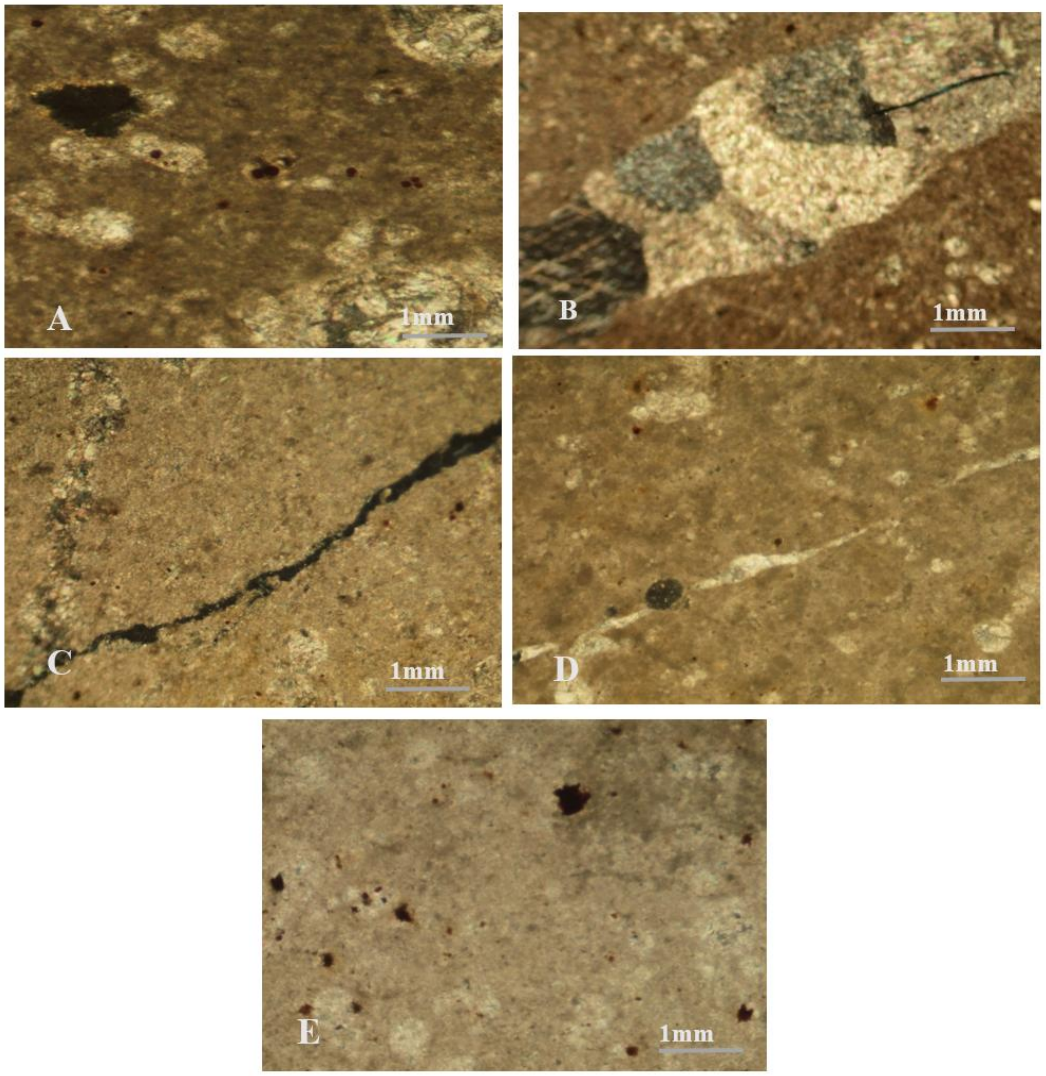


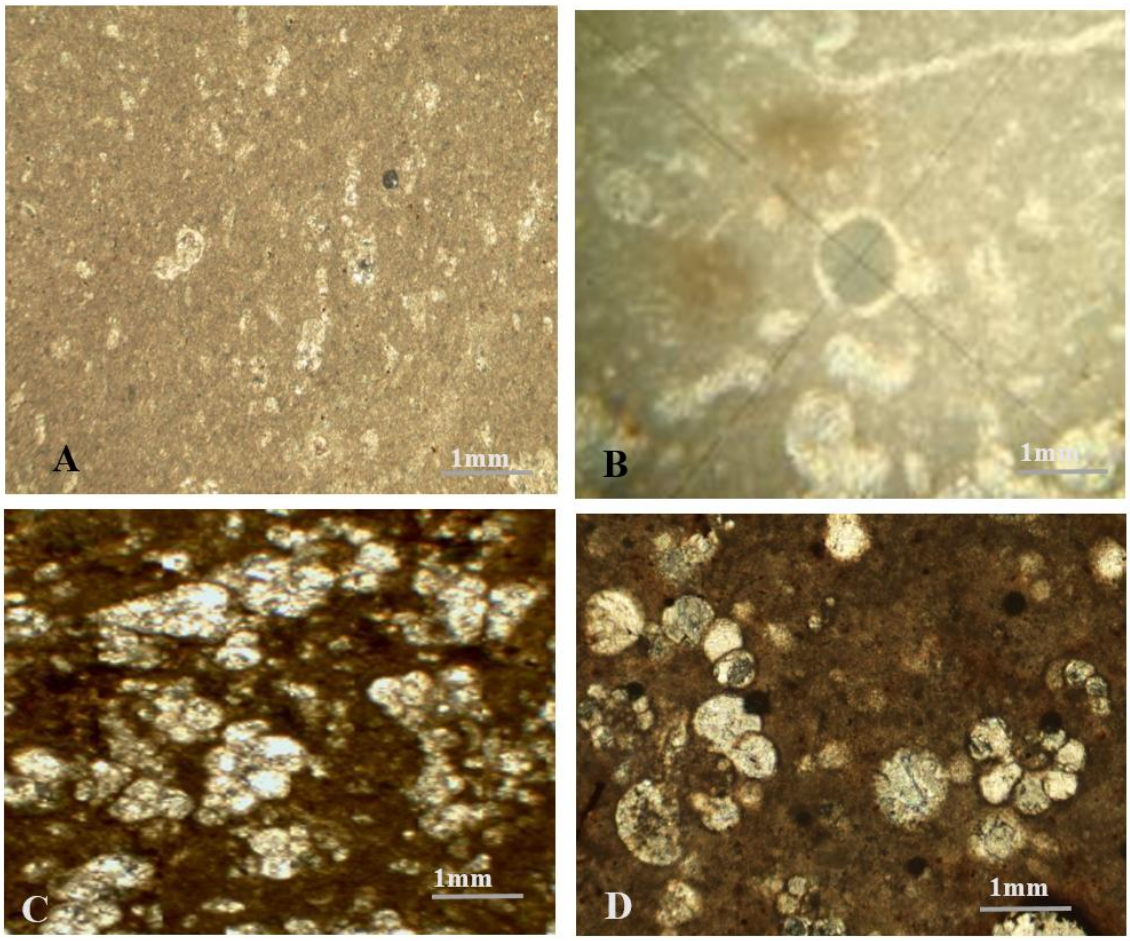
Plate 4

A: Planktonic Foraminiferal Lime Mudstone Submicrofacies.

B: Calcispheres Lime Mudstone Submicrofacies.

C: *Planoheterohelix globulosa* Lime Wackestone Submicrofacies.

D: *Globigerinelloids* Lime Wackestone Submicrofacies.



Iraqi National Journal of Earth Science

www.earth.uomosul.edu.iq

Environmental Significance of the First Appearance of *Porosononion martkobi* in Southern Iraq Sediments

Bushra Majeed Issa [1*]

[1]*Department of Geology, College of Science, University of Basrah, Basrah, Iraq.*

Article information

Received: 20- Sep -2024

Revised: 12- Dec-2024

Accepted: 02- Feb -2025

Available online: 01- Jan – 2026

Keywords:
Porosononion martkobi,
Southern Iraq,
Late Holocene,
Foraminifera,
North Basrah,

Correspondence:

Name: Bushra Majeed Issa

Email:
bushra.issa@uobasrah.edu.iq

ABSTRACT

The study aimed to identify a new species that was observed for the first time in Iraq, particularly in the southern region of it, where the recent sediments from the late Holocene period are located in the north of Basrah Governorate. Eighteen samples were collected from nine sites north of Basrah Governorate (Qaryat Nasr). The texture of recent sediments for these samples was determined. As well as the diagnosis of the foraminifera species and the relative abundance of the species in the study area. The results of the grain size analysis of the studied sites' sediments showed that the study area contains five types of sediment texture: clay, sandy silt, sandy clay, mud, and sandy mud. Clay sediment is the most common type in the sediments of the region. As for the species of foraminifera that was identified, it was represented by *Porosononion martkopi*. It is one of the benthic foraminifera species that live in marine environments, so its appearance in the study area was clear environmental evidence of the exposure of southern Iraq to marine influence, which was identified in this study within the sediments of the Late Holocene period. The species *Porosononion martkopi* also showed high relative abundance where the sediments were of fine grain size, that is, the sedimentary ecosystem was quiet, which in turn provided an environment in which the species thrived.

DOI: 10.33899/injes.v26i1.60199, ©Authors, 2026, College of Science, University of.
This is an open-access article under the CC BY 4.0 license (http://creativecommons.org/licenses/by/4.0/).

الأهمية البيئية للظهور الأول لـ *Porosononion martkobi* في رواسب جنوب العراق

بشرى مجيد عيسى [1]*

[1] *قسم علم الارض، كلية العلوم، جامعة البصرة، البصرة، العراق.*

معلومات الارشفة

تاريخ الاستلام: 20- سبتمبر -2024

تاريخ المراجعة: 12- ديسمبر -2024

تاريخ القبول: 02- فبراير -2025

تاريخ النشر الالكتروني: 01- يناير -2026

الكلمات المفتاحية:

النوع *Porosononion martkobi*،

جنوب العراق،

الهولوسين المتأخر،

المنخربات،

شمال البصرة،

المراسلة:

الاسم: بشرى مجيد عيسى

Email: bushra.issa@uobasrah.edu.iq

الملخص

هدفت الدراسة إلى التعرف على نوع جديد تم رصده لأول مرة في العراق وخاصة في المنطقة الجنوبية منه حيث تتواجد الرواسب الحديثة من فترة الهولوسين المتأخرة في شمال محافظة البصرة، وقد تم جمع ثمانية عشر عينة من تسعة مواقع شمال محافظة البصرة (قرية نصر)، وتم تحديد نسيج الرواسب الحديثة لهذه العينات، وكذلك تشخيص أنواع المنخربات والوفرة النسبية للأنواع في منطقة الدراسة، وقد أظهرت نتائج تحليل حجم الحبيبات لرواسب المواقع المدروسة أن منطقة الدراسة تحتوي على خمسة أنواع من نسيج الرواسب وهي الطين ، والغرين الرملي والطين الرملي والوحل والوحل الرملي، وتعد الرواسب الطينية النوع الأكثر شيوعاً في رواسب المنطقة. أما عن نوع المنخربات الذي تم التعرف عليه فقد تمثل بالنوع *Porosononion martkopi* وهو من أنواع المنخربات القاعية التي تعيش في البيئات البحرية لذا فإن ظهوره في منطقة الدراسة كان دليلاً بيئياً واضحاً على تعرض جنوب العراق للتأثيرات البحرية والذي تم التعرف عليه في هذه الدراسة ضمن رواسب فترة الهولوسين المتأخرة كما أظهر النوع *Porosononion martkopi* وفرة نسبية عالية حيث كانت الرواسب ذات حجم حبيبات دقيقة أي أن النظام البيئي الرسوبي كان هادئاً مما وفر بدوره بيئة ازدهر فيها هذا النوع.

DOI: 10.33899/injes.v26i1.60199, ©Authors, 2026, College of Science, University of.
This is an open-access article under the CC BY 4.0 license (http://creativecommons.org/licenses/by/4.0/).

Introduction

Southern Iraq, commonly known as Lower Mesopotamia, is a region rich in history and cultural importance. This area is recognized as one of the cradles of civilization, where ancient cultures flourished between the Tigris and Euphrates rivers. Notably, the area is distinguished by its marshlands, specifically the Ahwar of Southern Iraq, which encompass numerous archaeological sites. The climate in this region exhibits considerable differences from other areas of Iraq, possessing distinct features that have shaped its environment (Saad, 2024). Complex implications of neotectonic activities, sea-level fluctuations, and differential sedimentation rates, in addition to the climatic changes during the Holocene, have resulted in the formation and preservation of these unique marshlands (Aqrawi, 2001).

One significant environmental alteration impacting southern Iraq was the rise in temperatures that caused the sea level to rise from the end of the Pleistocene era and during the Holocene (Al-Jumaily, 1994). The impact of these climatic and environmental changes appeared in the Quaternary period in southern Iraq through the influence of marine transgression that caused the formation of marine sediments at the beginning of the Holocene period (Al-Jubouri, 1997). Numerous studies have recorded the marine impact in Southern Iraq by studying the remains of faunal shells in sediments. Hudson and colleagues (1957) conducted research on marine ostracods and bivalves in the near of Basrah. Similarly, Dance and Eames (1966) focused their studies on marine bivalves found in the Basrah and Amarah regions. As for MacFadyen and Vita-Finze (1978) examined the foraminifera, ostracoda, and

bivalves found in the subsurface boreholes located in the Amarah and Garmet Ali (in Basrah) regions.

One of the most important pieces of evidence that reflected the effect of seawater on the sediments of southern Iraq is foraminifera species that proved the validity of that (Issa, 2010, 2024), the two studies successfully validated and substantiated the influence of seawater, attributed to sea level changes during the Holocene period, on the sediments found in northern Basrah (Southern Iraq). This analysis was based on the documented presence and abundance of various marine foraminifera species in the area.

Foraminifera are sensitive to environmental conditions and can adapt to a particular environment. Many studies have shown that environmental factors are the main tool that controls the distribution of foraminifera, and therefore, this type of fossil is valuable in the field of reconstructing the ancient environment (Vu, 2020). Thus, paleoenvironmental inference by using foraminifera is an essential factor for any study that intends to explore the environment of any region during a specific period of time, which is what was used in the current study, especially with the recording of the appearance of species for the first time in the sediments of the region. It also reinforces the confirmation of the impact of the paleoenvironmental conditions in the study area.

Aim of the study

The study aimed to identify a new species observed in southern Iraq (north of Basrah Governorate) where late Holocene sediments are found, and to confirm its identity as a benthic foraminifera species known as *Porosononion martkobi* and to reveal its environmental significance that led to its appearance in the study area, which in turn contributes to ultimately enhances the understanding of the paleoenvironment associated with late Holocene sediments.

Materials and Methods

The study was implemented in July 2018 in southern Iraq, Basra Governorate, south of Qaryat Nasr (Fig. 1), where sediment samples were collected using a shovel from nine sites with depths ranging between 0.5m and 1.10m according to the variation in the sediment color appearing at each depth.

To identify the type of sediments existing in the study area sites, 100 grams were taken from each sample of the mentioned sites, and a grain size analysis was performed by wet sieving on a 0.0625 mm sieve to isolate the sand from silt and clay, and to conduct the Pipette analysis based on Folk (1980).

As for the study of the foraminifera species, the wet samples were washed through a 0.0625 mm sieve to remove silt and clay, then dried and the species picked up and fixed on slides, to determine the foraminifera species was using a binocular stereoscopic microscope. The species was imaged using a scanning electron microscope (FE-SEM) Nova Nano SEM 450 in the Department of Physics, University of Basrah. The taxonomy of foraminifera was based mainly on Yanko and Troitskaja (1987), with the assistance of Cimerman and Langer (1991), and the classification of higher taxonomic categories was based on the WoRMS (World Register of Marine Species) website.

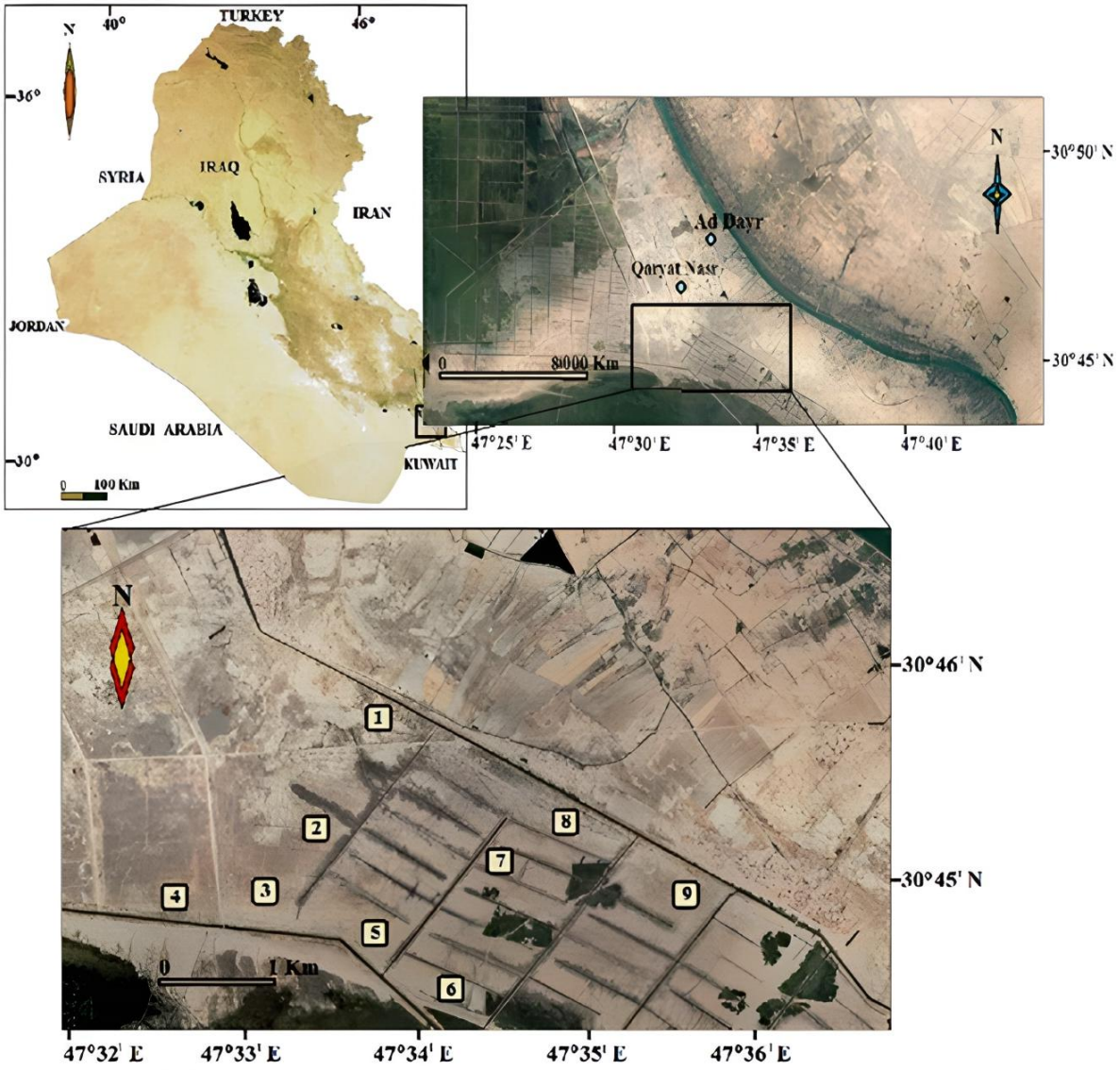


Fig. 1. Satellite image showing the studied area and location of samples

Results

Sediments texture

The results of the grain size analysis according to the classification of Folk (1980), as shown in Figure 2 and Table 1, clay sediment is very high in the study area, which forms about 44%, while sandy silt formed 17%, and also sandy clay 17%. As for the sediments of mud and sandy mud, the percentage of each of them was 11%.

In general, it is noted that the fine fraction, represented by clay, is concentrated at great depths, while the coarse fraction, sand, appears at lower depths. The variation in the distribution of fine and coarse fractions may be due to the nature of study area location, where the drying process that the area was exposed to facilitated the role of erosion on its surface, which in turn assisted in increasing the percentage of aeolian sediments that are active in the area, in addition to the proximity of the study area to river water and swamps. As well as the role of marine sediments during the Holocene period, where sea level rose and its effect on the area (Issa, 2010).

The main goal of grain size analysis is to determine the type of environment and energy associated with the transport mechanism at the time of deposition; thus, gaining a deeper understanding of the paleoenvironmental features and the conditions of deposition (López,

2017). The significance of grain size analysis extends beyond this aspect; it also plays a crucial role in understanding the relationship between the abundance of foraminifera species and particular sediment types. Foraminifera thrive in specific sediment types, with their abundance often correlated with sediment grain size. Finer sediments, such as silt and clay, tend to support higher densities of foraminifera due to better nutrient retention and organic matter availability. In contrast, coarser sediments may lead to instability and lower food quality, negatively affecting foraminiferal populations (Naik et al.,2023; El Bakkali et al., 2024).

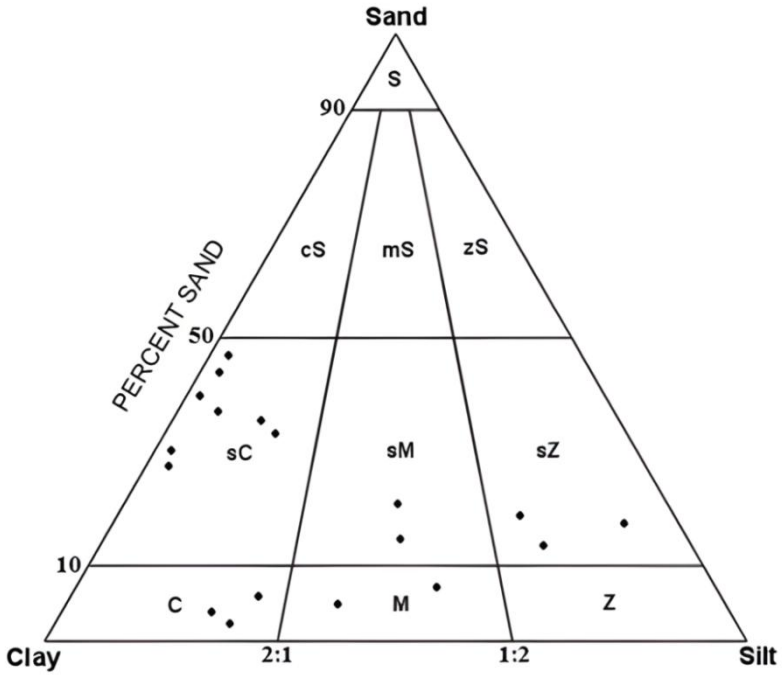


Fig. 2. Sand, silt, and clay percentage ternary diagram of the studied samples

Table 1: Sediment texture and the percentage of sand, silt, and clay in the sediment samples

Site	Sample depth (m)	Sand %	Silt %	Clay %	Sediment texture
1	0.7	14	65	21	Sandy silt
	1.0	7	52	41	Mud
2	0.8	21	40	39	Sandy mud
	0.95	4	39	57	Mud
3	0.77	44	2	54	Sandy clay
	0.96	4	20	76	Clay
4	0.5	38	6	56	Sandy clay
	0.95	40	3	57	Clay
5	0.75	38	10	52	Clay
	1.0	31	3	66	Clay
6	0.8	35	12	53	Clay
	1.05	2	28	70	Clay
7	0.5	20	58	22	Sandy silt
	1.10	47	4	49	Sandy clay
8	0.6	15	43	42	Sandy mud
	1.0	6	66	28	Clay
9	0.7	17	73	10	Sandy silt
	0.95	3	27	70	Clay

Foraminiferal species

The species *Porosononion martkobi* identity was determined as shown in Figure 3, which was prominently observed in the study area, exhibiting a dominant presence over the other remaining few foraminifera species, which were four species of benthic foraminifera (Fig. 4). Table 2 shows the relative abundance and dominance of the species *Porosononion martkobi* in the study area sites compared to the remaining foraminifera species.

The remaining species (Fig. 4) were not well defined, with some exhibiting morphological changes and others suffering from inadequate preservation, resulting in their classification as relatively minor compared to the previously mentioned species. The taxonomic system for Porosononion martkobi is outlined as follows:

Kingdom: Chromista CAVALIER-SMITH, 1981

Subkingdom: Harosa CAVALIER-SMITH, 2010

Infrakingdom: Rhizaria CAVALIER-SMITH, 2002

Phylum: Foraminifera d'ORBIGNY, 1826

Class: Globothalamea PAWLOWSKI, HOLZMANN, and Tyszka, 2013

Subclass: Rotaliana MIKHALEVICH, 1980.

Order: Rotaliida DELAGE and HEROUAD, 2013

Superfamily: Rotalioidea EHRENBERG, 1839

Family: Elphidiidae GALLOWAY, 1933

Subfamily: Elphidiinae GALLOWAY, 1933

Genus *Porosononion* PUTRYA IN VOLOSHINOVA, 1958

Porosononion martkobi BOGDANOVICH,1947

(Fig. 3)

1947*Nonion martcobi* Bogdanowicz; p. 30, pl. 1v, figs. 4a-c.

1987 *Porosononion martcobi* Bogdanowicz; Yanko and Troitskaya, p.52, pl.18, figs 1-4.

1991 *Porosononion* sp.1; Cimerman and Langer, p. 81, pl. 84, figs 9-12.

2002 *Porosononion martkobi* Bogdanowicz; Kaminski et al., p. 178, pl. V, figs. 9a, b.

2020 *Porosononion martkobi* Bogdanowicz; Grizelj et al., p. 162, pl. 7, fig 17.

2024 *Porosononion martkobi* Bogdanowicz; Peryt et al., p. 5, pl. 3, fig. G.

Morphological characteristics: The shell exhibits a rounded to oval shape on its sides, characterized by a weakly lobed outline and a narrowly oval form on the aperture side. The peripheral margin is rounded, and the shell typically contains 7 to 8 chambers, with 7 being the most common. The chambers are slightly convex, except the last two, with bluntly rounded umbilical ends that do not close in the umbilical region. The sutures are deepened, superficial on the peripheral margin and expanding towards the umbilical region, which gives the latter the appearance of an irregular star with short rays. The umbilical region is wide, flattened, and covered with granules of various sizes and shapes. Granulation extends into the deepened parts of the sutures and onto the lower part of the broadly oval septal surface. The aperture is sieve-shaped, covered with granulation, and the foramen is in the form of large openings on the septum and in the form of a slit at its base. The wall is coarse-pored, radially radiant.

Distribution: The species *Porosononion martkobi* is documented in various formations and deposits from many parts of the world and during geological periods Miocene to Modern (Table 3).

Ecology: The studies have documented a general trend of decreasing salinity in sediment profiles where *Porosononion martkobi* is found (Koubová and Hudáčková,2010; Filipescu et al., 2011), indicating that the study of Yanko and Troitskaja (1987) indicated that

Porosononion martkobi is of narrowly euryhaline warm-water species, where it was recorded in the Black Sea at salinity from 11‰ in estuaries to 18-21‰ on the western shelf of it.

As the species *Porosononion martkobi* is associated with shallow marine environments where salinity levels fluctuated significantly. The coexistence of *Porosononion martkobi* with other foraminifera species in conditions ranging from hypersaline to marine is evidence of its adaptation to different salinity levels (Peryt and Peryt, 2009). The ecological implications of these findings suggest that *Porosononion martkobi* thrived in environments where salinity was influenced by factors such as evaporation and water depth fluctuations, characteristic of marginal seas or lagoons (Koubová and Hudáčková, 2010; Filipescu et al., 2011). Overall, the ecological context indicates that *Porosononion martkobi* is adapted to a range of salinity levels typical of the sedimentary environments.

In the current study, it was observed that the species *Porosononion martkobi* emerged as the predominant species among the limited benthic foraminifera identified in the study area, which comprised a total of four species. Most of these species were found to exhibit poorly preserved shells, characterized by significant alterations in their morphology, alongside the occurrence of shell fragments. While none of these signs were seen on *Porosononion martkobi*, individuals of this species appeared in their normal forms without any morphological changes and with similar sizes.

The aforementioned factors, particularly the reduction in both species diversity and abundance, alongside the prevalence of opportunistic species such as *Porosononion martkobi* within the assemblage, serve as significant indicators of paleoecological stress in the study area, which results from the transitions between different environmental states. (Gustiantini et al., 2016; Dayong and Nagarajan, 2023).

It has been noted that the abundance of the species *Porosononion martkobi* is found in sites characterized by a high percentage of fine sediments, specifically silt and clay, as this species is prevalent in regions abundant in fine sediments, which provide a significant supply of nutrients (Temelkov, 2008; Lo Giudice Cappelli et al., 2019; Yanko, 2020).

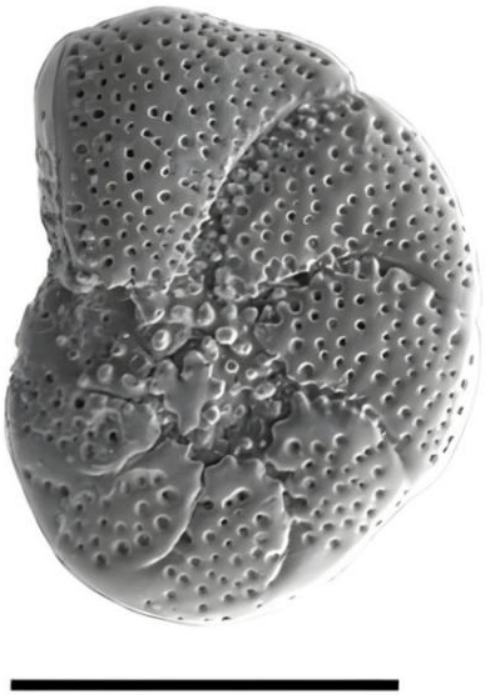


Fig. 3. Scanning electron micrographs (SEM) of the identified *Porosononion martkobi* in this study. The scale bar is 100 µm

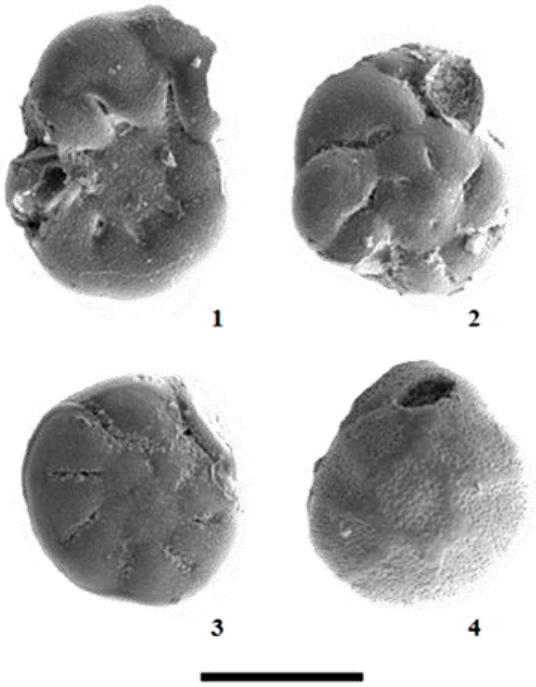


Fig. 4. Scanning electron micrographs (SEM) images of unidentified foraminifera species 1-4. Scale bar=100 µm

Table 2: Relative abundance of *Porosononion martkobi* and unidentified foraminifera species in the study area sites.

Site	Sample depth (m)	*Porosononion martkobi* %	Unidentified foraminifera species %
1	0.7	70	30
	1.0	88	12
2	0.8	80	20
	0.95	84	16
3	0.77	65	35
	0.96	71	29
4	0.5	65	35
	0.95	74	26
5	0.75	66	34
	1.0	71	29
6	0.8	64	36
	1.05	76	24
7	0.5	78	22
	1.10	79	21
8	0.6	64	36
	1.0	71	29
9	0.7	66	34
	0.95	77	23

Table 3: Distribution of *Porosononion martkobi* in the regions and geological periods.

Formation or Sediment	Region	Period	Source
Underwater sediments	Southern Romanian	Modern	Yanko-Hombach et al.,2014
Underwater sediments	Black Sea	Modern	Yanko (1990)
Azov Sea	Between Russia and Ukraine	Modern	Yanko and Troitskaja(1987)
Northwestern shelf sediments	Black Sea	Holocene	Yanko and Troitskaja(1987)
Azov Sea	Between Russia and Ukraine	Holocene	Yanko and Troitskaja(1987)
The Bosphorus Strait-exit delta	Marmara Sea	Holocene	Kaminski et al. (2002)
Cape Tuzla area	Romanian coast	Late Pleistocene	Yanko and Troitskaja(1987)
Taman Peninsula sediments	Krasnodar Krai, Russia.	Late Pleistocene	Yanko and Troitskaja(1987)
Sarmatian deposits	Georgia	Late Miocene	Shatilova et al. (2020)
Transylvanian Basin	Romania	Miocene	Silye(2015)
The middle and lower Sarmatian deposits	Crimean-Caucasia	Miocene	Bogdanovich (1947)

Discussion

Porosononion martkobi was first described by Bogdanovich in 1947 as *Nonion martkobi* (Bogdanovich,1947). This species is primarily identified from Neogene Miocene deposits in the Transylvanian Basin, particularly around areas like Jimbor and Sibiel (Silye, 2015). It is considered a typical species of both the Konkian and Sarmatian basins; it assisted in stratigraphic correlation (Koiava et al., 2017). Often, the biozones established for Sarmatian sediments face challenges due to the diverse facies' conditions, but the presence of *Porosononion martkobi*, along with other foraminiferal species, provides insights into the micropaleontological content of these sediments that the assemblages can vary significantly, reflecting changes in environmental conditions over time (Filipescu, 2005; Maissuradze et al., 2006).

Outside the boundaries of the Black Sea and Mediterranean areas, *Porosononion martkobi* was recognized in the northern Adriatic Sea as part of foraminiferal communities located within an intertidal pool (Koubová and Hudáčková, 2010). Additionally, in the Middle Miocene sediments of the Central Paratethys, which includes regions that are now Austria, Hungary, and Slovakia, *Porosononion martkobi* has been recorded in association with a variety of other benthic foraminiferal species (Peryt et al., 2024). The appearance of the species in these studies, in association with other benthic foraminifera species, together indicated the fluctuation in salinity and tolerance of euryhaline conditions (Koubová and Hudáčková, 2010; Peryt et al., 2024).

The significance of *Porosononion martkobi* studying has increased more than with time, particularly during the Holocene period, which has been identified in Holocene sediments, especially in marine environments such as the Marmara Sea and the Black Sea (Yank et al., 1999; Kaminsk et al., 2002). *Porosononion martkobi* holds significant importance in the study of Holocene sediments due to its role as a bioindicator of past environmental conditions. As a benthic foraminifer, this species is sensitive to changes in environmental conditions such as salinity, temperature, and organic matter availability. Thus, its presence in sediment can indicate historical marine environments and shifts in ecological conditions during the Holocene (Geslin et al., 2000).

The species has contributed through its distribution can assist in tracing historical connections between marine bodies, such as the Black Sea and the Mediterranean Sea. The presence of *Porosononion martkobi* in sediments has been linked to periods of marine transgression and the establishment of estuarine conditions, which are crucial for understanding past hydrological changes and biotic interactions in these regions (Kaminski et al.,2002; Khameiss and Zubi, 2024).

The presence of *Porosononion martkobi* in a given region serves as an indicator that the area has been influenced by marine conditions (Koubová and Hudáčková, 2010l; Filipescu et al., 2011; Peryt et al., 2024), suggesting that seawater once inundated the region, thereby facilitating the species' stabilization within its sediments. This observation leads to the inference that the study area experienced marine transgression during the Holocene, particularly in the late Holocene period (Aqrawi, 2001). Furthermore, Issa (2010) corroborated this by stating that the southern region of Iraq, where the current study area is situated, underwent fluctuations in sea level in the Late Holocene (3000-2000 years ago). Additionally, Issa (2016) reported that the boundaries of the range corresponding to this period are situated approximately less than two meters from the surface of the study area.

What contributed to confirming the marine water impact in the study area was that revealed by the sediment grain size analysis revealed a reduction in the proportion of coarse grains, with fine grains being the most prevalent in the sediment samples. This shift in grain size distribution is likely associated with the lack of riverine influence (Sadough et al., 2013).

Furthermore, the increased presence of the species *Porosononion martkobi* in depths characterized by fine sediments reinforces the notion that marine water conditions are the dominant environment in these sediments.

The species is not only important as an environmental indicator but also provides insights into sedimentary processes and paleoenvironmental reconstructions. It was observed that *Porosononion martkobi* is often dominant in the fine-grain sediments like silt-sand and silt (Temelkov, 2008; Yanko, 2020), where this species is found more commonly in environments characterized by calm depositional settings, such as areas with low energy, where the accumulation of organic-rich sediments, which are essential for the sustenance of foraminiferal populations (Lo Giudice Cappelli et al.,2019; Binczewska et al., 2023).

The present study findings are consistent with previous results, that the relative abundance of the *species Porosononion martkobi* exhibited an increase in regions with finer sediment sizes. This observation was made by comparing the proportion of species (Table 2) against the sediment type at each site within the study area in Table 1.

Conclusion

- Identified five sediment types within the study area are clay, sandy silt, sandy clay, mud, and sandy mud. Where clay sediment was the most common type.
- The micropaleontological study depended on one species that was dominant in the study area, which is *Porosononion martkobi*.
- The initial appearance of *Porosononion martkopi* was documented in southern Iraq during the Late Holocene period.
- This study is the first in identifying the species *Porosononion martkopi* in Iraq.
- The importance of the species *Porosononion martkobi* is evident in revealing the paleoenvironment and thus interpreting the environmental events at that time in the studied area.
- The paleoenvironmental indication for the presence of the species *Porosononion martkopi* showed that the study area has been influenced by marine conditions, especially marine transgression in the late Holocene period.
- The current study showed that the relative abundance of the species *Porosononion martkopi* increases with the fineness of the grain size of the sediments of the study area.

Conflict of Interest

The author declares that there is no conflict of interest regarding the publication of this manuscript.

References

Al-Jubouri, B.S., 1997. Palynological evidence of the climatic and environmental changes during the Quaternary period in the Mesopotamian plain, southern Iraq, unpublished master's thesis, Baghdad University, 79 P. (In Arabic)

Al-Jumaily, W.A.,1994. Quaternary Ostracodes in Southern Iraq, PhD Thesis (unpublished), Baghdad University, 117 P.

Aqrawi, A.A., 2001. Stratigraphic signatures of climatic change during the Holocene evolution of the Tigris–Euphrates delta, lower Mesopotamia, Global and Planetary Change, 28(1-4): pp. 267-283. DOI:10.1016/S0921-8181(00)00078-3

Bogdanovich, A.K., 1947. Results of the study of the Miocene foraminifera from the Crimean-Caucasian region. Microfauna of the oil deposits of Caucasus, Emba**,** and Central Asia. ВНИГРИ - Oil Research Geological Institute (VNIGRI), Leningrad, pp. 5-34. **(**in Russian**).** http://marbef.org/data/aphia.php?p=sourcedetails&id=300376

Cimerman, F. and Langer, M.R.,1991. Mediterranean Foraminifera, Slovenska Akademija Znanosti in Umetnosti, Akademia Scientiarum et Artium Slovenica, Ljubljana, 118 P. https://www.researchgate.net/profile/Martin-Langer-3/publication/46958692

Dance, S.P. and Eames, F.E., 1966. New Molluscs from Recent Hammar Formation of South-East Iraq. Proc. Malac. Soc. London, 37, pp. 35-43. DOI:10.1093/oxfordjournals.mollus.a064973

Dayong, V. and Nagarajan, R., 2023. Interpretation of paleoenvironment using benthic foraminifera from Tertiary rocks, northern Sarawak. In MATEC Web of Conferences, 377 P., EDP Sciences. DOI:10.1051/matecconf/202337701002

Filipescu, S., Silye, L. and Krézsek, C., 2005. Sarmatian micropaleontological assemblages and sedimentary paleoenvironments in the southern Transylvanian Basin, Acta Palaeontologica Romaniae, 5: pp. 173-179. https://adatbank.ro/vendeg/htmlk/pdf7672.pdf

Filipescu, S., Wanek, F., Miclea, A., DeLeeuw, A. and Vasiliev, I., 2011. Micropaleontological response to the changing paleoenvironment across the Sarmatian-Pannonian boundary in the Transylvanian Basin (Miocene, Oarba de Mures section, Romania), Geologica Carpathica, 62(1): pp. 91-102. DOI:10.2478/v10096-011-0008-9

Folk, R.L., 1980. Petrology of Sedimentary Rocks, Hemphill, Texas, 184 **P**. https://repositories.lib.utexas.edu/bitstreams/4537855d-d386-4794-bfbc-0f24715e64dc/download

Geslin, E., Stouff, V., Debenay, J.P. and Lesourd, M., 2000. Environmental variation and foraminiferal test abnormalities, In Environmental micropaleontology: the application of microfossils to environmental geology, Boston, MA: Springer, USA, pp. 191-215. DOI:10.1007/978-1-4615-4167-7_10

Grizelj, A., Milošević, M., Bakrač, K., Galović, I., Kurečić, T., Hajek-Tadesse, V., Avanić, R., Miknić, M., Horvat, M., Čaić Janković, A. and Matošević, M., 2020. Paleoecological and sedimentological characterisation of Middle Miocene sediments from the Hrvatska Kostajnica area (Croatia), Geologia Croatica, 73(3): pp. 153-175. DOI:10.4154/gc.2020.15

Gustiantini, L., Dewi, K.T., Muller, A. and Praptisih, P., 2016. Paleoenvironmental Reconstruction from Benthic Foraminiferal Assemblages of Early Holocene, Shallow Marine Deposits in Gombong, Central Java, Bulletin of the Marine Geology, 22(1): pp. 16-27. DOI: 10.32693/bomg.v22i1.2

Hudson, R.G.S., Eames, F.E. and Wilkins, G.L., 1957. The fauna of some Recent marine deposits near Basrah, Iraq, Geol. Mag., 94, pp. 393-401. DOI: 10.1017/S0016756800069429

Issa, B.M., 2010. Depositional environments and biofacies of selected sediments, north Basrah, Journal of Basrah Research (Sciences), 36(5) A: pp. 1-14. https://www.iasj.net/iasj/download/08dad357ddb0c657

Issa, B.M., 2016. Ostracoda and Charophyte as indicators of environmental varity in the marshland area of Southern Iraq. Journal of Basrah Researches (Sciences), 42(2)A: pp. 148-159. https://www.academia.edu/download/51709979/14.pdf

Isaa, B.M., 2024. Benthic Foraminifera and *Bithynia* sp. Opercula as Indicators of Depositional Environment of Late Holocene in Eastern Hammar Marsh, Southern Iraq, Kirkuk Journal of Science, 19(3): pp. 36-47. DOI: 10.32894/kujss.2024.152718.1174

Kaminski, M.A., Aksu, A., Box, M., Hiscott, R.N., Filipescu, S. and Al-Salameen, M., 2002. Late Glacial to Holocene benthic foraminifera in the Marmara Sea: implications for Black Sea–Mediterranean Sea connections following the last deglaciation, Marine Geology, 190(1-2): pp. 165-202. DOI:10.1016/S0025-3227(02)00347-X

Khameiss, B. and Zubi, H., 2024. Diversity, Ecology and Environmental Significance of Foraminifera in Al Hamama and Susah Coastal Regions, Northeastern Libya: Insights from Holocene Sediments, Journal of Environmental Protection, 15(01): pp. 13-25. DOI:10.4236/jep.2024.151002

Koiava, K., Kvaliashvili, L., Maissuradze, L., Mauvilly, J. and Mosar, J., 2017. Species of the genus *Porosononion* from Sarmatian deposits of Georgia and their stratigraphic significance, In the 15th Swiss Geoscience Meeting, Davos, Switzerland, pp. 181-182. DOI:10.13140/RG.2.2.13115.11049

Koubová, I. and Hudáčková, N., 2010. Foraminiferal successions in the shallow water Sarmatian sediments from the MZ 93 borehole (Vienna Basin, Slovak part), Acta Geologica Slovaca, 2(1): pp. 47-58. https://www.researchgate.net/profile/Natalia-Hudackova/publication/301956751

Lo Giudice Cappelli, E., Clarke, J.L., Smeaton, C., Davidson, K. and Austin, W.E.N., 2019. Organic-carbon-rich sediments: benthic foraminifera as bio-indicators of depositional environments. Biogeosciences, 16(21): pp. 4183-4199. https://bg.copernicus.org/articles/16/4183/2019/

López, G.I., 2017. Grain size analysis. Encyclopedia of geoarchaeology, pp. 341-348. DOI:10.1007/978-1-4020-4409-0_18

Macfadyen, W.A. and Vita-Finzi, C., 1978. Mesopotamian: The Tigris – Euphrates Delta and the Holocene Hammar fauna, Geological Magazine, 115: pp. 287-300. DOI:10.5194/bg-16-4183-2019

Maissuradze, L. and Koiava, K., 2006. New Data on Distribution of Sarmatian Foraminifera in the Sediments of Kakheti. Georgian Oil and gas, 19: pp. 50-62. https://www.researchgate.net/publication/259661618

Peryt, D. and Peryt, T., 2009. Environmental changes in the declining Middle Miocene Badenian evaporite basin of the Ukrainian Carpathian Foredeep (Kudryntsi section). Geologica Carpathica, 60(6): pp. 505-517. DOI:10.2478/v10096-009-0037-9

Peryt, D., Gedl, P., Worobiec, E., Worobiec, G. and Peryt, T.M., 2024. Foraminiferal and Palynological Records of an Abrupt Environmental Change at the Badenian/Sarmatian Boundary (Middle Miocene): A Case Study in Northeastern Central Paratethys, Geosciences, 14(3): pp. 1-38. DOI: 10.3390/geosciences14030086

Saad, K.S., 2024. Marshes of Southern Iraq and Some Economic Activities of its inhabitants, Journal of Misan Researches, 19(39): pp. 359 - 381. DOI: 10.52834/jmr.v20i39.236

Sadough, M., Ghane, F., Manouchehri, H., Moghaddasi, B. and Beikaee, H., 2013. Identification and abundance of benthic foraminifera in the sediments from Fereidoonkenar to Babolsar of Southern Caspian Sea. Turkish Journal of Fisheries and Aquatic Sciences, 13(1), pp. 79-86. DOI: 10.4194/1303-2712-v13_1_10

Shatilova, I.I., Maissuradze, L.S., Koiava, K.P., Kokolashvili, I.M., Bukhsianidze, M.G. and Bruch, A.A., 2020. The environmental history of Georgia during the Late Miocene based of foraminifera and pollen, Georgian National Museum: Tbilisi, Georgia, pp.1-84. DOI: 10.5281/zenodo.13680652

Silye, Lóránd, 2015. Sarmatian foraminiferal assemblages from southern Transylvanian Basin and their significance for the reconstruction of depositional environments. Cluj−Napoca: Presa Universitară Clujeană, 2015. 229 P. https://www.researchgate.net/profile/Lorand-Silye/publication/279917900

Temelkov, B.K., 2008. Ecological characteristics of the foraminiferal fauna (Protozoa: Foraminifera) of the Bulgarian South Black Sea area, Acta zoological Bulgarica, Supplementary, 2: pp. 275-282. https://www.researchgate.net/publication/265982612

Trogrlić, A.M., 2018. Sarmatski paleookoliši lokaliteta Vranović (kamenolom Našicecement) na osnovu foraminifera, PhD thesis, Zagreb University, Faculty of Science, Department of Geology, Croatia,.41 P. https://urn.nsk.hr/urn:nbn:hr:217:283928

Vu, A.T., 2020. Foraminiferal assemblages of Cretan beaches (Greece)-proxy for tsunami deposits, PhD thesis, RWTH Aachen University, 196 P. DOI: 10.18154/RWTH-2021-00155

World Register of Marine Species. URL: https://www.marinespecies.org/2019

Yanko, V.V., 1990. Stratigraphy and paleogeography of the marine Pleistocene and Holocene deposits of the southern seas of the USSR, Mem. Soc. Geol. Ital., 44: pp. 167-187. https://www.researchgate.net/profile/ValentinaYanko/publication/281479633_Stratigraphy

Yanko-Hombach, V.V., Kondaryuk, T.O., Likhodedova, O.G., Akindinova, O.V. and Motnenko, I., 2014. Evaluating the influence of river discharge on marine benthic ecosystems using benthic foraminifera and lithology as the main tools. In Proceedings of the Second Plenary Conference. IGCP 610 Second Plenary Conference and Field Trip: "From the Caspian to Mediterranean: Environmental Change and Human Response during the Quaternary" (A. Gilbert and V. Yanko-Hombach, eds.), Baku, Azerbaijan, pp. 12-20. https://gpimo.nas.gov.ua/sites/default/files/91-117.pdf

Yank, V., Kennett, J., Coral, H. and Cornfield, J., 1999. Stable isotopic evidence from Holocene Sea of Marmara sediments for two-way watermass interchange between the Black Sea and the Mediterranean Sea, South African Journal of Science, 95(4): pp. 201-204. https://www.researchgate.net/profile/Joel-Kronfeld/publication/286415348

Yanko, V.V. and Kondariuk, T.O., 2020. Origin and taxonomy of the Neopleistocene–Holocene Ponto-Caspian benthic foraminifera. Geological magazine, (1): pp. 17-33. DOI: 10.30836/IGS.1025-6814.2020.1.196975

Yanko, V.V. and Troitskaja, T.S., 1987. Late Quaternary Foraminifera of the Black Sea. Trudy Instituta Geologii i Geo¢siki, Akademiya Nauk SSSR, Novosibirsk, 694: 111 P. (in Russian). https://www.marinespecies.org/foraminifera/aphia.php?p=sourcereq&id=261696

Iraqi National Journal of Earth Science

www.earth.uomosul.edu.iq

Forecasting PM2.5 Daily Concentration in Baghdad, Iraq Based on Improving Random Forest Algorithm

Zakariya Nafi Shehab [1*], Zakariya Yahya Algamal [2], Raid Mahmood Faisal [3]

1 Department of Environmental Systems and Information, Environmental Research Center, University of Mosul, 41002 Mosul, Nineveh, Iraq.
2 Department of Statistics and Informatics Science, College of Computer Science and Mathematics, University of Mosul, 41002 Mosul, Nineveh, Iraq.
3 Department of Environmental Technology, College of Environmental Sciences, University of Mosul, 41002 Mosul, Nineveh, Iraq.

Article information

Received: 15- Nov-2024

Revised: 16- Dec -2024

Accepted: 07- Jan -2025

Available online: 01- Jan -2026

Keywords:
Coati Optimization Algorithm,
Random Forest Algorithm,
PM2.5,
Air Pollution,
Forecasting,

Correspondence:
Name: Zakariya Nafi Shehab

Email:
zakariyashehab@uomosul.edu.iq

ABSTRACT

Forecasting air quality in urban areas is complex due to difficulties in accurately defining emission flux density and the meteorological fields. Combustion gases from human and social activities are the most significant sources of PM 2.5, which is a major air pollutant. Accurate and reliable prediction of PM 2.5 levels is crucial for assessing health risks. Forecasting PM2.5 daily concentration, in general, has been predicted by Random Forest (RF) as a machine learning algorithm. However, the RF performance is highly sensitive to the choice of its hyperparameters, which usually necessitates careful tuning. Consequently, searching for the optimal set of RF hyperparameters constitutes an essential step when attempting to improve model efficiency. Various techniques have come into view for effective hyperparameter tuning of RF. Meta-heuristic optimization methods, with their strong local search abilities, can prevent the training network from getting trapped in local optima and increase the likelihood of identifying the global optimum. This paper proposes employing the Coati Optimization Algorithm (COA), a meta-heuristic approach, to improve RF hyperparameter determination, and, consequently, forecasting PM 2.5 concentrations. Daily PM 2.5 concentrations in Baghdad, Iraq, from 2019 to 2023 are gathered to train RF models and assess the proposed COA performance. The effectiveness of COA is estimated using several metrics. Overall, our proposed COA approach demonstrates superior performance in terms of evaluation criteria compared to other methods in both training and testing daily PM 2.5 concentrations.

DOI: 10.33899/injes.v26i1.60200, ©Authors, 2026, College of Science, University of Mosul.
This is an open-access article under the CC BY 4.0 license (http://creativecommons.org/licenses/by/4.0/).

التنبؤ بالتركيز اليومي لـ PM2.5 في بغداد، العراق بناءً على خوارزمية الغابات العشوائية المحسنة

زكريا نافع محمود شهاب [1*]، زكريا يحيى الجمال [2]، رائد محمود فيصل [3]

[1] قسم النظم والمعلومات البيئية، مركز بحوث البيئة، جامعة الموصل، الموصل، نينوى، العراق.

[2] قسم الإحصاء وعلوم المعلومات، كلية علوم الحاسوب والرياضيات، جامعة الموصل، الموصل، نينوى، العراق.

[3] قسم تقانات البيئة، كلية العلوم البيئية، جامعة الموصل، الموصل، نينوى، العراق.

معلومات الارشفة

تاريخ الاستلام: 15– نوفمبر – 2024

تاريخ المراجعة: 16– ديسمبر – 2024

تاريخ القبول: 07– يناير – 2025

تاريخ النشر الالكتروني: 01– يناير – 2026

الكلمات المفتاحية:

خوارزمية التحسين الكواتي،

PM2.5،

خوارزمية الغابة العشوائية،

تلوث الهواء،

التنبؤ،

المراسلة:

الاسم: زكريا نافع شهاب

Email: zakariyashehab@uomosul.edu.iq

الملخص

يعد التنبؤ بجودة الهواء في المناطق الحضرية أمرًا معقدًا بسبب الصعوبات في تحديد كثافة تدفق الانبعاثات بدقة وتأثير مجالات الأرصاد الجوية. وتُعد غازات الاحتراق الناتجة عن الأنشطة البشرية والاجتماعية أهم مصادر انبعاثات PM 2.5، وهي ملوث رئيس للهواء. يعد التنبؤ الدقيق والموثوق بمستويات PM 2.5 أمرًا بالغ الأهمية لتقييم المخاطر الصحية. وقد تم التنبؤ بالتركيز اليومي لـ PM2.5 بشكل عام بواسطة الغابة العشوائية (RF) كخوارزمية للتعلم الآلي. ومع ذلك، فإن أداء الترددات اللاسلكية حساس للغاية لاختيار المعلمات المفرطة التي تتطلب عادةً ضبطًا دقيقًا. وبالتالي، فإن البحث عن المجموعة المثلى من المعلمات التشعبية للترددات اللاسلكية يشكل خطوة أساسية عند محاولة تحسين كفاءة النموذج. وقد ظهرت تقنيات مختلفة لضبط المعلمات الفائقة الفعالة للترددات اللاسلكية. يمكن لطرائق التحسين الفوقية المجتهدة، بقدراتها القوية في البحث المحلي، أن تمنع شبكة التدريب من الوقوع في فخ التفاوتات المحلية وتزيد من احتمالية تحديد المستوى الأمثل العالمي. تقترح هذه الورقة البحثية استخدام خوارزمية كواتي للتحسين (COA)، وهو نهج مجتهد– متغاير، لتحسين تحديد المعلمات المفرطة للترددات اللاسلكية، وبالتالي التنبؤ بتركيزات PM 2.5. تم جمع التركيزات اليومية لـ PM 2.5 في بغداد بالعراق من عام 2019 إلى عام 2023 لتدريب نماذج الترددات اللاسلكية وتقييم أداء COA المقترح. تم تقدير فعالية COA باستخدام عدة مقاييس. بشكل عام، يُظهر نهجنا المقترح لتقييم أداء النماذج المقترحة أداءً متفوقًا من حيث معايير التقييم مقارنة بالطرق الأخرى في كل من التدريب واختبار تركيزات جسيمات 2.5 اليومية.

DOI: 10.33899/injes.v26i1.60200, ©Authors, 2026, College of Science, University of Mosul.
This is an open-access article under the CC BY 4.0 license (http://creativecommons.org/licenses/by/4.0/).

Introduction

Air pollution gives rise to environmental issues such as global warming, depletion of the ozone layer, and the occurrence of acid rain. Air quality degradation, particularly in urban regions, arises from swift industrialization, infrastructure expansion, and urban development. While these advancements aim to accommodate the rapid population growth in these areas, they concurrently generate detrimental effects on human health and the environment equally (Jamil and Shehab, 2021; Wood, 2022).

In this regard, high population density is normally linked to high air quality degradation resulting from increased energy consumption, which can be attributed to both residential and industrial activities. Some major sources of this problem are the use of fossil fuels for power generation and heating purposes, which leads to the release of greenhouse gases (such as ozone, methane, carbon dioxide, nitrogen oxides), sulphur oxides, and particulate matter into the atmosphere (Wang et al., 2019). Moreover, increasing numbers of vehicles across cities, which has become the cause of congestion, worsened air quality and have strong effects on locals

(Mohd Shafie et al., 2022). Exposure to outdoor air pollution, largely due to PM2.5, has led to an estimated 3.3 million premature deaths annually across the globe, with a possible doubling of that number by 2050 (Lelieveld et al., 2015).

PM 2.5 is among the major environmental air contaminants, characterized by small size, high toxicity, easy diffusivity, and long suspension time in the air (Xu et al., 2022), which seriously threatens the environment, human health, and socio-economic contexts. PM2.5 not only carries harmful compounds but also travels extensively across distances, carrying an appreciable effect on air quality and visibility (Tsurumi and Managi, 2020). Exposure to PM2.5 raises the risk of cancer, respiratory, and cardiovascular diseases, which are major threats to human health.

Precise and efficient prediction of future PM2.5 levels holds considerable importance in environmental management (Wang et al., 2024). Human activities associated with fossil fuel consumption in transportation, power generation, heating/cooling, and various industrial processes are primary sources of anthropogenic PM2.5. Additionally, events like crop-residue burning, human-induced forest fires, and deforestation-related dust storms intermittently contribute significantly to PM2.5 levels in specific regions (Tian et al., 2021; Wood, 2022). The complexity of atmospheric conditions, including temperature inversion layers and thermal updrafts, significantly influences the accumulation or dispersion of air pollutants. However, these intricacies often elude customary meteorological measurements (Murthy et al., 2020).

PM2.5 concentration forecasting models have gained increasing interest and have been continuously updated and redeveloped in recent years. For environmental protection supervision, it is critically required that PM2.5 concentrations are continuously monitored in real time, which requires reliable methods for forecasting to determine whether air quality standards are met (Wu et al., 2022). The accurate forecast of spatiotemporal variations of air pollution requires intricate algorithms in addressing the complexities of tracking this type of pollution (Muthukumar et al., 2022). Researchers cited the need for strong estimation models that would analyse levels of air pollution to give meaningful insights and aid in informed policy formulation (Southerland et al., 2022). Therefore, it is very critical to adopt new data-driven methodologies so as to achieve high accuracy in air quality predictions.

Of late, deep learning as well as machine learning have been placed among the most important tools in earth and environmental sciences (Faisal and Shehab, 2025; Shehab and Faisal, 2025; Zhong et al., 2021)**.** They were applied to many complex tasks, like urban flood prediction (Kao et al., 2021), estimation of water quality (Algamal et al., 2025; Jamil and Shehab, 2021; Najah Ahmed et al., 2019; Shehab et al., 2024), and regional air pollution forecasting (Wong et al., 2021). These technologies have greatly improved the ability to forecast PM 2.5 levels and issue warnings on air pollution. Some algorithms of machine learning, namely SVM as well as RF, have already shown a huge potential in PM 2.5 forecasting because of their excellent ability to learn complex variable patterns and relationships. That capacity easily permits the perfect capturing of nonlinear dynamics within the PM 2.5 concentration series and, therefore, better accuracy in its forecasting (Wang et al., 2024). Such models can clearly be a great alternative to the traditional atmospheric models, which are inventory-based because they use statistics and are not limited by the presence of extensive inventories (Feng et al., 2020). An ensemble learning method, the RF algorithm is employed in this research due to its great flexibility in PM 2.5 forecasting. On that note, its strength in adaptability to handle complex relationships within data averts overfitting, a common problem in most machine learning models.

This research thus aims to go beyond the limitations associated with short-term and coarse temporal resolution in prediction and provide a method that will enable the building of a robust model for the prediction of daily variations reliably and accurately. This paper focuses on the development and extension of precise models for the forecasting and prediction of PM 2.5

concentrations using an RF model based on environmental and meteorological variables. For this purpose, daily data are used from a ground-level sensor at Baghdad U.S. Embassy, located in one of the most highly congested areas within Baghdad, Iraq. This dataset will form the basis for training, testing, and validation of the model proposed herein. This dataset contains daily measurements of PM 2.5 for four years.

Data and methods

Study area

The daily PM2.5 average concentration dataset was compiled from the Baghdad U.S. Embassy air quality monitoring station from 1st March 2019 to 1st June 2023. Undoubtedly, the data obtained from the singular monitoring post are solely indicative of the immediate conditions of the city centre, providing a comprehensive urban outlook but struggling to identify specific pollution hotspots within the city. Baghdad stands as the largest urban centre in Iraq (Fig. 1), accounting for about 22% of the national population, and therefore encounters substantial air pollution threats stemming from different sources such as vehicle emissions, industrial activities, power generation, open burning, and waste disposal. This has led to an upward trend in average yearly PM 2.5 concentration spanning over the previous ten years. Baghdad was ranked among the most polluted cities, depending on PM2.5 concentrations globally in 2022.

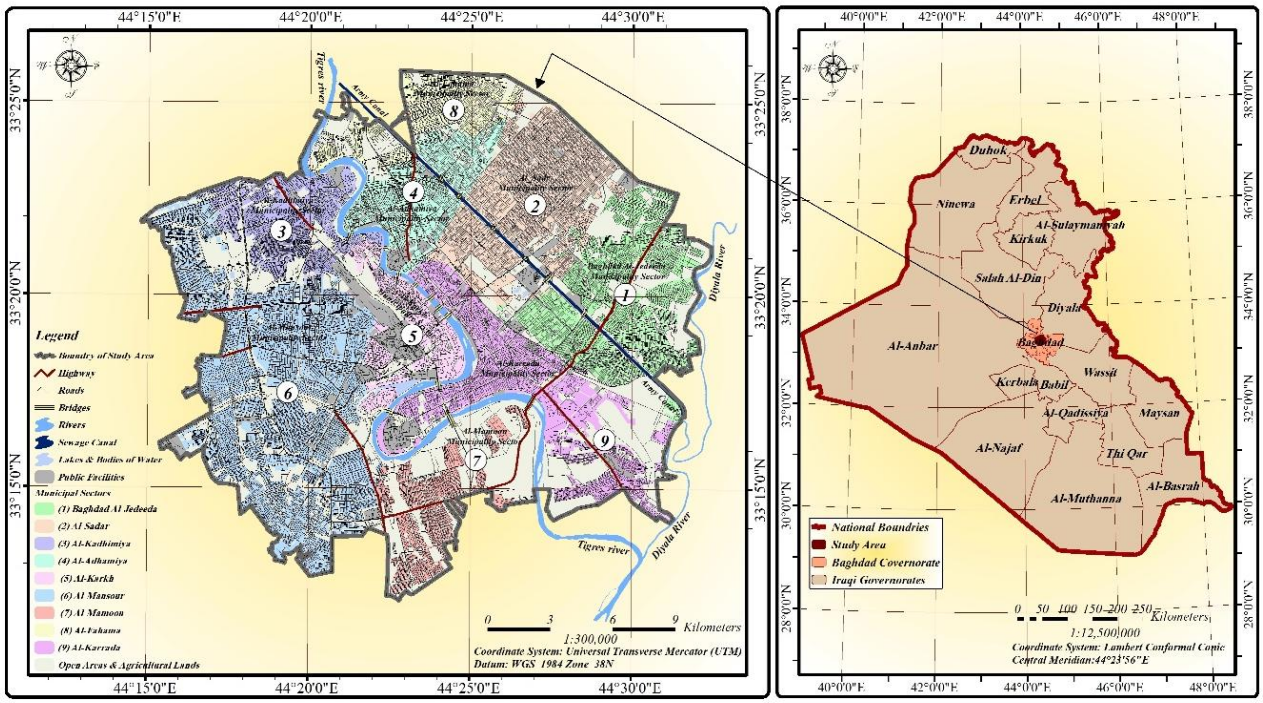


Fig. 1. Map of Baghdad highlighting metropolitan areas and municipalities.

Random Forest algorithm

RF has developed into a robust as well as versatile tool in the machine learning landscape, demonstrating remarkable performance in diverse applications and employed in regression and classification tasks equally (Hasnain et al., 2023). This technique gains from the power of ensemble learning by creating an ensemble of decision trees, each of them trained on a dissimilar random subset of training data. This will then merge the predictions of multiple decision trees, reducing overfitting, generally providing an increase in accuracy and a boost in the robustness of the model. The algorithm creates multiple bootstrap samples around the training data by randomly drawing subsets of it with replacement. A decision tree is built for each bootstrap sample. Inherent in the tree induction process: at each split, instead of

considering all features, the algorithm randomly selects a subset of features to consider at each node. This randomness in features goes a step further in reducing overfitting and increasing the variety of the forest. In prediction, each tree in the forest casts a vote (Josso et al., 2023). For classification, it chooses the most common class among the trees as a prediction. It uses the average of all trees' predictions for regression. RF is found to be at par with other state-of-the-art performance measures across a wide array of tasks all the time. Its ensemble nature reduces overfitting and improves generalizability, hence more reliable predictions. Besides, it is resistant to noise and outliers in data, retaining its accuracy even on challenging datasets (Yang et al., 2020). The RF also gives the significance of distinct features so that one can see the logic of the model's decision process. Then, the power of RF is that, with its adaptability and flexibility, it can be employed for both regression and classification tasks, which very much extends the domains of problems it is useful for.

The proposed improvement

Hyperparameters are those parameters that require defining before implementing an algorithm or before running an algorithm (Khalid and Javaid, 2020). In the case of Data Science, tuning of hyperparameters is one of the significant stages in the workflow. Done correctly, hyperparameter tuning can indeed take a worthless model and turn it into a model ready for production to make real decisions (Probst et al., 2019; Singh et al., 2021).

The identification of the appropriate hyperparameters plays a crucial part in the RF prediction accuracy and learning time (Daviran et al., 2021). However, the decision-making of the right combination of hyperparameters is very critical and consumes a lot of time (Zhu et al., 2022).

Tuning hyperparameters manually consumes a lot of time, and at the same time, a manual process needs a deeper understanding of the RF algorithm as well as its hyperparameters. As for the issues regarding the manual specification of hyperparameters, it is necessary to use hyperparameter optimization to search for the best configuration automatically (Ge et al., 2023). The methods to apply to find the values of the hyperparameters include randomized search (RS), Bayesian optimization (BO), cross-validation (CV), and grid search (GS). This process was previously conducted for all the possible combinations of hyperparameters, and the set of hyperparameters that yielded the best results in the chosen criterion was returned. However, these approaches are computationally expensive, and they do not exhaust all the possible combinations of hyperparameters (Abdulsaed et al., 2023).

Hence, there is a need for better and more effective methods for hyperparameter tuning for RF. Over the last few years, metaheuristic optimization algorithms have been extensively applied for solving the problem of hyperparameter tuning (Abdulsaed et al., 2023; Algamal et al., 2021). Recently, various new nature-inspired algorithms were proposed by researchers to extend and upgrade the exploration and exploitation of the existing algorithms. The Coati Optimization Algorithm (COA) has emerged as one of the most popular because of its high efficiency (Dehghani et al., 2023; Jia et al., 2023).

COA is a population-based metaheuristic approach, where each coati represents an individual within the population. The location of each coati within the search space affects the decision variables' values. Therefore, in COA, coatis serve as potential solutions to the problem at hand. Initially, the coatis are randomly placed within the search space as defined thereafter (Dehghani et al., 2023):

$$X_i : X_{i,j} = Lb_j + r * (Ub_j - Lb_j), \quad i = 1, 2, ..., N ; j = 1, 2, ..., m \tag{1}$$

One interesting behavior in this exploration phase is that one group of coatis climbs the tree to scare the iguana down to ground level, where others are waiting to capture it. This behavior shows the ability of the algorithm to explore or examine certain aspects in a particular context. The algorithm mimics the behavior based on the notion that half the population climbs

the trees to force the iguana down, and the remaining half wait at ground level to catch the iguana as it falls, and it looks like the following Eq. (2).

$$X_i^{new} : X_{i,j}^{new} = X_{i,j} + r*(I_j - \vartheta * X_{i,j}), i = 1,2,.....,[N/2]; j = 1,2.....,m \quad (2)$$

Once the iguana drops to the ground, it is assigned a random position (I^G) within the search space, and the coatis under the tree adjust their position according to Eqs. (3) and (4). If the objective function value at the new position calculated for each coati is an improvement over the current value, the new position is accepted. Conversely, if the new position yields a worse objective function value, the coati remains in its original position (Eq. 5) (Dehghani et al., 2023).

$$I^G : I_j^G = Lb_j + r*(Ub_j - Lb_j), j = 1,2,.....,m \quad (3)$$

$$X_i^{new} : X_{i,j}^{new} = \begin{cases} X_{i,j} + r*(I_j^G - \vartheta * x_{i,j}), F(I^G) < F(X_i) \\ X_{i,j} + r*(X_{i,j} - I_j^G), else \end{cases} \quad (4)$$

with $i = \left\lfloor \frac{N}{2} \right\rfloor + 1, \left\lfloor \frac{N}{2} \right\rfloor + 2,.....,N$, $j = 1,2,.....,m$

$$X_i = \begin{cases} X_i^{new}, F(X_i^{new}) < F(X_i) \\ X_i, else \end{cases} \quad (5)$$

where: X_i is the current position of the ith coati, X_i^{new} is the newly calculated position for the ith coati, I^G is the randomly generated position of the iguana, F is the objective function value.

In the next phase, the exploitation phase, the behavior of coatis employing a predator-escape strategy is described. This strategy keeps the coati close to its current position and in a safe stance, enhancing the algorithm's exploitation capability. To accomplish this, a random position is created near each coati using Eqs. (6) and (7). If this newly generated position results in an improved objective function value, the coati assumes the new position; otherwise, it retains its original position (Eq. 5).

$$Lb_j^{local} = \frac{Lb_j}{t}, Ub_j^{local} = \frac{Ub_j}{t}, t = 1,2,.....,T \quad (6)$$

$$X_i^{new} : X_{i,j}^{new} = X_{i,j} + (1-2*r)*(Lb_j^{local} + r*(Ub_j^{local} - Lb_j^{local})), i = 1,2,...,N, j = 1,2,..,m \quad (7)$$

To optimize the hyperparameters of RF using COA as an improvement proposition, the position vector *X* of each coati is defined as a vector with dimension *D*, representing the coati's position in the COA. Consequently, each vector *X* corresponds to a specific configuration of the RF, with each dimension of *X* representing a distinct hyperparameter of the RF. Therefore, we have five positions that each coati in the swarm will search for them. Consequently, our proposed improvement is as follows:

Step 1: The number of coatis, N_{coati} , is set to 30, and the maximum number of iterations is T =500.

Step 2: The positions of each coati are randomly specified. For the number of trees in the forest (N_{trees}), the position is randomly generated from a uniform distribution between 10 and 100. While for the minimum number of samples at leaf node (MN_{leaf}) and for the minimum

number of samples considered to split an internal node ($MN_{internal}$), the position for each one is randomly generated from a uniform distribution within the range [1,25] and range [2,20], respectively. Further, the position of the maximum depth of the tree (M_{tree}) is randomly generated from a uniform distribution between 1 and 200. Finally, the number of features ($N_{features}$) taken for the best split is considered depending on the number of lags of the series. A representation of the coati position (Fig. 2).

Step 3: The fitness function is defined as

$$\text{fitness} = \min\left[\frac{1}{n}\sum_{i=1}^{n}(y_i - \hat{y}_{i\,(N_{trees}, MN_{leaf}, MN_{internal}, M_{tree}, N_{features})})^2\right]. \quad (8)$$

Step 4: The positions of the coati are updated using Eq. (4) and Eq. (7), respectively.

Step 5: Steps 3 and 4 are repeated until a T is reached.

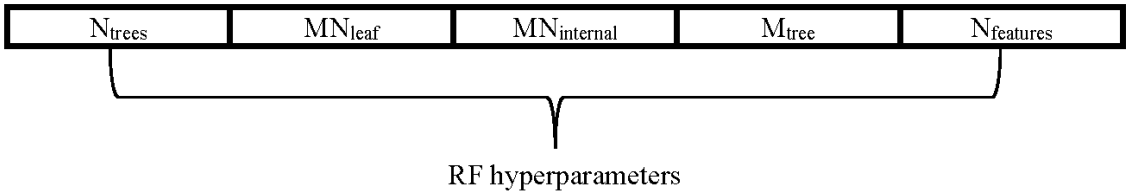


Fig. 2. Position of each coati in the COA algorithm.

Forecasting evaluation criteria

Four assessment measures, RMSE, MAE, direction accuracy (DA), and R^2 are adopted in this research to estimate the effectiveness of the projected forecasting method. Their simple mathematical expressions (Table 1).

Table 1: Forecasting evaluation criteria.

Evaluation criterion	Mathematical formula
MAE	$\frac{1}{n}\sum_{t=1}^{n}\lvert y_t - \hat{y}_t\rvert$
RMSE	$\sqrt{\frac{1}{n}\sum_{t=1}^{n}(y_t - \hat{y}_t)^2}$
DA	$\frac{1}{n}\sum_{t=1}^{n} z_t, \quad z_t = \begin{cases} 1, & \text{if } (y_{t+1} - y_t)(\hat{y}_{t+1} - \hat{y}_t) \geq 0 \\ 0, & \text{otherwise} \end{cases}$
R^2	$1 - \left[\sum_{t=1}^{n}(y_t - \hat{y}_t)^2 \Big/ \sum_{t=1}^{n}(\hat{y}_t - \bar{y}_t)^2\right]$

Results analysis

Our goal in using our proposed approach, COA, is to demonstrate that an adequate choice of hyperparameters can produce better PM2.5 daily concentration forecasting. Comprehensive comparison tests using RS, BO, CV, and GS are used to examine the forecasting performance of our proposed algorithm, COA.

The data are divided into two sets: the training data set, including 1270 PM2.5 daily concentrations (from 1 March 2019 to 31 December 2022), and the testing data set, including 151 PM2.5 daily concentrations (from 1 January 2023 to 1 June 2023). Figures (3 and 4) depict the daily PM2.5 concentrations' pattern over time for the training and testing data sets. Both figures proved that the daily PM2.5 concentration pattern is nonlinear and non-stationary over

time. The descriptive statistics for both training and testing data sets (Table 2) were used to investigate the behavior of daily PM2.5 concentrations. The daily PM2.5 concentrations' pattern has trend, fluctuation, asymmetry, and intermittency.

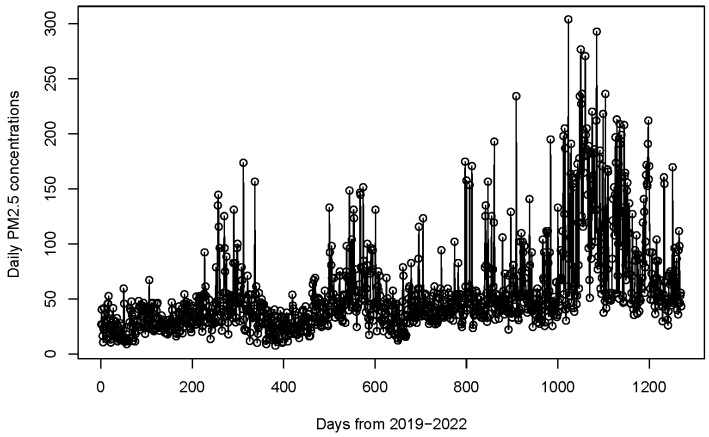


Fig. 3. Time series of the daily PM2.5 concentrations for the training data set.

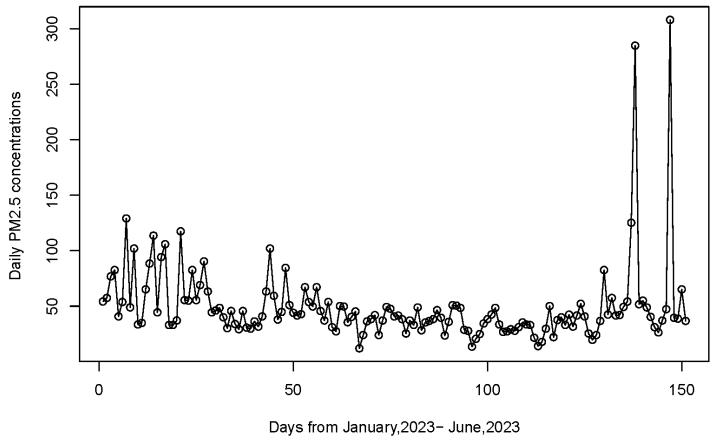


Fig. 4. Time series of the daily PM2.5 concentrations for the testing data set.

Table 2: Statistical descriptive daily PM2.5 concentrations.

	Training data set	Testing data set
Mean	55.51	49.19
Standard deviation	42.47	35.83
Skewness	2.27	4.74
Kurtosis	5.77	29.51
Minimum	7.44	12.00
Maximum	303.98	308.02

The forecasting performances of the COA, RS, BO, CV, and GS models in terms of evaluation criteria (Tables 3 and 4) for training and testing data sets, respectively. According to the results of Tables 3 and 4, it can be shown from the forecasting results of daily PM2.5 concentrations that the suggested approach, COA, may significantly improve forecasting accuracy and generalization capacity because it has lower MAE, RMSE, greater DA, and greater R^2 values. COA performs better than the RS, BO, CV, and GS methods. From Table (3), compared to RS, BO, CV, and GS, the reduction in terms of MAE and RMSE of COA is 87.26%, 85.53%, 86.01%, 86.55% and 87.22%, 86.75%, 86.99%, and 87.16% respectively.

Similarly, for the testing data set (Table 4) compared to RS, BO, CV, and GS, the corresponding criteria, in terms of MAE, decreased by 87.61%, 86.67%, 86.91%, and 87.21% respectively. While in terms of RMSE, it decreased by 83.61%, 83.05%, 83.34% and 83.54% respectively.

Meta-heuristic algorithms perform well in predicting, even in the absence of data processing, except for the traditional techniques; RS, BO, CV, and GS performance could be caused by the arbitrary hyperparameter settings. Moreover, in the comparison between CV, RS, and GS in estimating the best hyperparameters of RF, the results of the evaluation indicators based on the training set show that the CV method is superior to the RS and GS methods. In addition, the application of the RS method revealed that RS obtained non-satisfactory results.

Table 3: Forecasting results of the COA and the benchmark approaches RS, BO, CV, and GS for the training set.

	COA	RS	BO	CV	GS
MAE	0.124	0.974	0.857	0.886	0.922
RMSE	1.308	10.237	9.877	10.057	10.189
DA	0.984	0.651	0.694	0.681	0.663
R^2	0.988	0.614	0.711	0.704	0.625

Table 4: Forecasting results of the COA and the benchmark approaches RS, BO, CV and GS for the testing set.

	COA	RS	BO	CV	GS
MAE	0.205	1.655	1.538	1.567	1.603
RMSE	1.789	10.918	10.558	10.738	10.87
DA	0.964	0.635	0.678	0.665	0.647
R^2	0.972	0.598	0.695	0.688	0.609

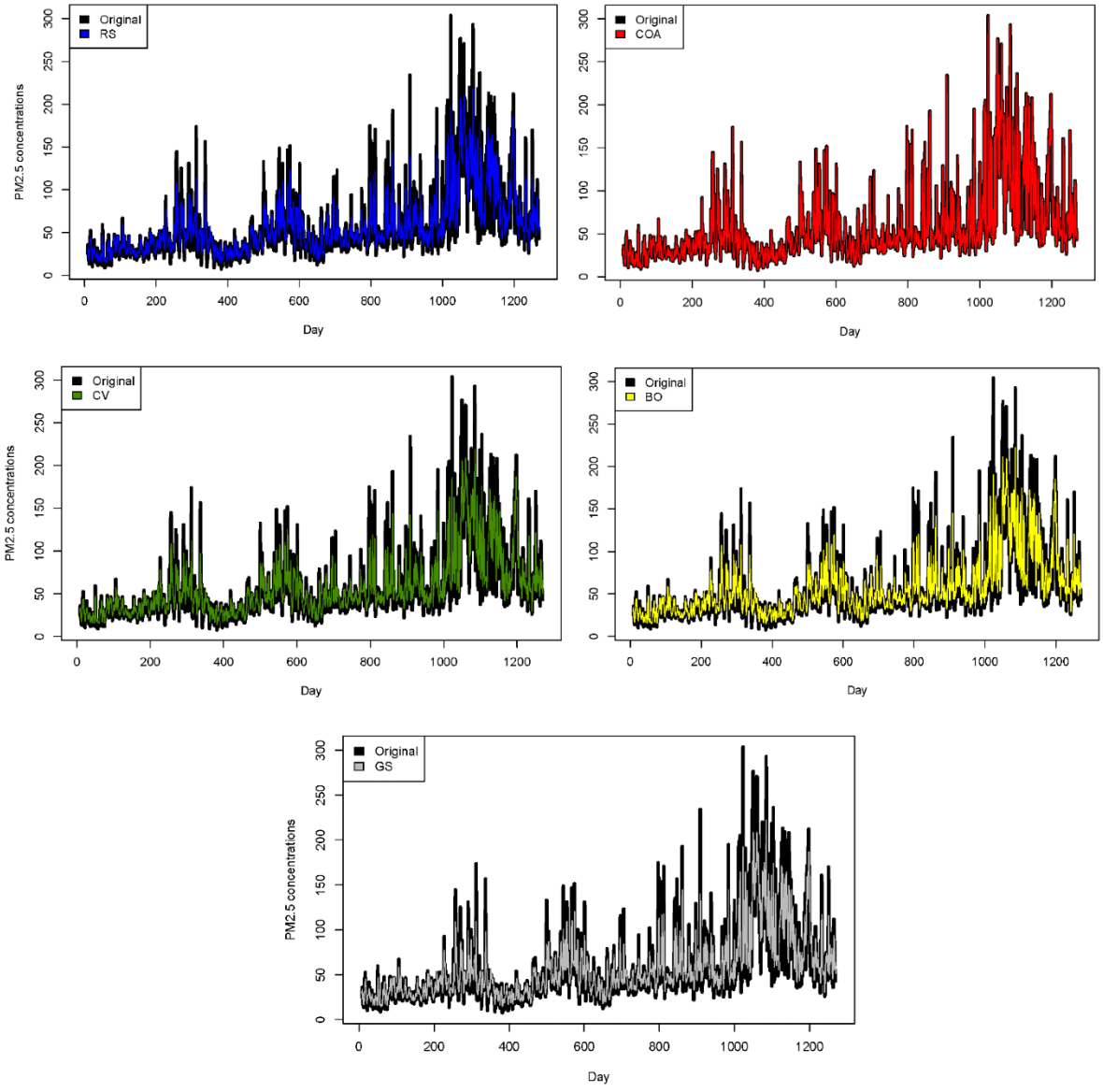


Fig. 5. Forecasting results in the training data set based on methods used.

From time-series plots of forecasting, the model accuracy of RF based on the COA algorithm is stable and superior to others for both the training and testing datasets. As demonstrated in Figures 5 and 6, the COA model's predicted daily PM2.5 levels are essentially in line with the actual values, demonstrating the high quality of the model's forecast. In addition, training and testing PM2.5 concentrations greatly increase the prediction capacity of COA. This is combined with the rather smooth time series of the COA. As a result, the COA model predicts daily PM2.5 concentrations with remarkable accuracy. Moreover, as shown in Figures 5 and 6, the PM2.5 concentrations forecast depending on CV are slightly closer to the actual value in comparison to the BO method. On the other hand, the PM2.5 concentrations forecast of RS method performs poorly in their forecasts over time.

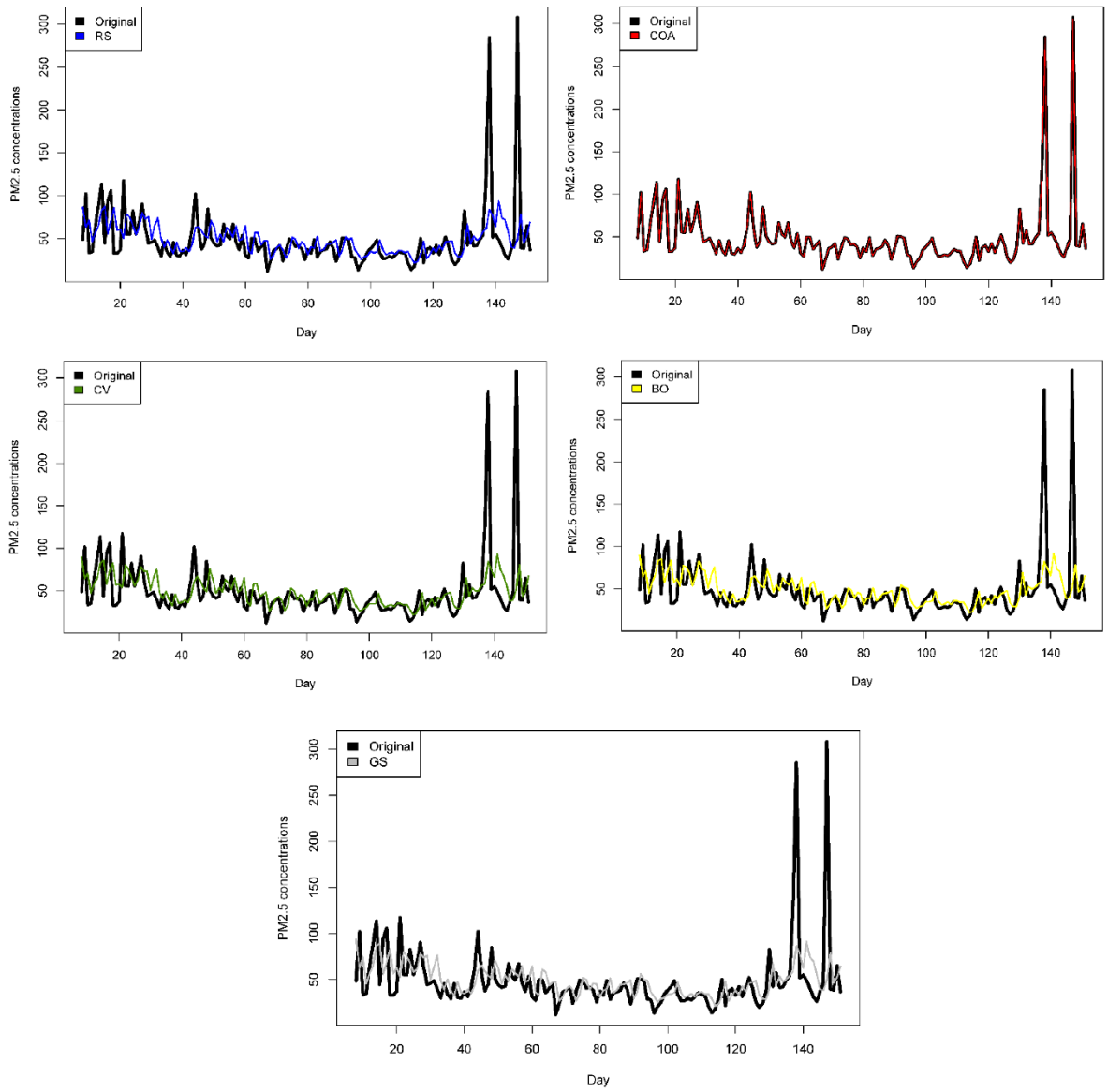


Fig. 6. Forecasting results in the testing data set based on the methods used.

Conclusion

The novelty of this approach is, in fact, the accurate estimation of PM2.5 concentrations. This study combines the RF model with a meta-heuristic optimization algorithm to estimate daily variations in PM2.5 concentrations within Baghdad, Iraq. This further enhances the exploration and exploitation capabilities of the COA to carry out hyperparameter optimization within RF. The results indicate that the COA-based methodology is superior compared to other RS, BO, CV, and GS methods, improving the predictive accuracy of the RF model significantly.

In particular, COA shows a better performance for all the metrics used to evaluate its performance, including MAE, RMSE, DA, and coefficient of determination (R^2). In the future, hybrid models and other meta-heuristic optimization algorithms may be developed to study the increased accuracy of PM2.5 forecasting to devise highly useful environmental policies.

The accurate prediction of PM2.5 concentration has a very critical role in the protection of public health and the management of the environment. This enhanced COA, as employed in this study for improving the prediction accuracy of daily PM2.5 levels, provides a potent tool for policymakers and health officials. With increased reliability in the forecasts, the authorities can initiate timely warnings and measures to decrease exposure, such as traffic restrictions, control over emissions by industries, and public advisories.

References

Abdulsaed, E.H., Alabbas, M. and Khudeyer, R.S., 2023. Hyperparameter Optimization for Convolutional Neural Networks using the Salp Swarm Algorithm. Informatica (Slovenia), 47(9), pp. 133–144. https://doi.org/10.31449/inf.v47i9.5148

Algamal, Z.Y., Qasim, M.K., Lee, M.H. and Mohammad Ali, H.T., 2021. Improving grasshopper optimization algorithm for hyperparameters estimation and feature selection in support vector regression. Chemometrics and Intelligent Laboratory Systems, 208. https://doi.org/10.1016/j.chemolab.2020.104196

Algamal, Z.Y., Shehab, Z.N. and Faisal, R.M., 2025. Spatiotemporal variation analysis of Tigris River water quality in Mosul, Iraq during 2020–2023 based on environmetric techniques. Environmental Earth Sciences, 84(2), 69. https://doi.org/10.1007/s12665-024-12086-z

Daviran, M., Maghsoudi, A., Ghezelbash, R. and Pradhan, B., 2021. A new strategy for spatial predictive mapping of mineral prospectivity: Automated hyperparameter tuning of random forest approach. Computers and Geosciences, 148. https://doi.org/10.1016/j.cageo.2021.104688

Dehghani, M., Montazeri, Z., Trojovská, E. and Trojovský, P., 2023. Coati Optimization Algorithm: A new bio-inspired metaheuristic algorithm for solving optimization problems. Knowledge-Based Systems, 259. https://doi.org/10.1016/j.knosys.2022.110011

Faisal, R.M. and Shehab, Z.N., 2025. Integrating GIS and comparative multi-criteria decision-making techniques for landslide susceptibility assessment. Progress in Physical Geography. https://doi.org/10.1177/03091333251380439

Feng, R., Gao, H., Luo, K. and Fan, J. ren., 2020. Analysis and accurate prediction of ambient PM2.5 in China using Multi-layer Perceptron. Atmospheric Environment, 232. https://doi.org/10.1016/j.atmosenv.2020.117534

Ge, D.M., Zhao, L.C., and Esmaeili-Falak, M., 2023. Estimation of rapid chloride permeability of SCC using hyperparameters optimized random forest models. Journal of Sustainable Cement-Based Materials, 12(5), pp. 542–560. https://doi.org/10.1080/21650373.2022.2093291

Hasnain, A., Sheng, Y., Hashmi, M.Z., Bhatti, U.A., Ahmed, Z. and Zha, Y., 2023. Assessing the ambient air quality patterns associated to the COVID-19 outbreak in the Yangtze River Delta: A random forest approach. Chemosphere, 314. https://doi.org/10.1016/j.chemosphere.2022.137638

Jamil, N.R. and Shehab, Z.N., 2021. Landscape Perspective to River Pollution: A Study of Bentong River, Malaysia. In Water Pollution and Management Practices. https://doi.org/10.1007/978-981-15-8358-2_2

Jia, H., Shi, S., Wu, D., Rao, H., Zhang, J. and Abualigah, L., 2023. Improve coati optimization algorithm for solving constrained engineering optimization problems. Journal of Computational Design and Engineering, 10(6), pp. 2223–2250. https://doi.org/10.1093/jcde/qwad095

Josso, P., Hall, A., Williams, C., Le Bas, T., Lusty, P., and Murton, B., 2023. Application of random-forest machine learning algorithm for mineral predictive mapping of Fe-Mn crusts in the World Ocean. Ore Geology Reviews, 162. https://doi.org/10.1016/j.oregeorev.2023.105671

Kao, I.F., Liou, J.Y., Lee, M.H. and Chang, F.J., 2021. Fusing stacked autoencoder and long short-term memory for regional multistep-ahead flood inundation forecasts. Journal of Hydrology, 598. https://doi.org/10.1016/j.jhydrol.2021.126371

Khalid, R. and Javaid, N., 2020. A survey on hyperparameters optimization algorithms of forecasting models in smart grid. In Sustainable Cities and Society (Vol. 61). Elsevier Ltd. https://doi.org/10.1016/j.scs.2020.102275

Lelieveld, J., Evans, J.S., Fnais, M., Giannadaki, D. and Pozzer, A., 2015. The contribution of outdoor air pollution sources to premature mortality on a global scale. Nature, 525(7569). https://doi.org/10.1038/nature15371

Mohd Shafie, S.H., Mahmud, M., Mohamad, S., Rameli, N.L.F., Abdullah, R. and Mohamed, A.F., 2022. Influence of urban air pollution on the population in the Klang Valley, Malaysia: a spatial approach. Ecological Processes, 11(1). https://doi.org/10.1186/s13717-021-00342-0

Murthy, B.S., Latha, R., Tiwari, A., Rathod, A., Singh, S. and Beig, G., 2020. Impact of mixing layer height on air quality in winter. Journal of Atmospheric and Solar-Terrestrial Physics, 197. https://doi.org/10.1016/j.jastp.2019.105157

Muthukumar, P., Cocom, E., Nagrecha, K., Comer, D., Burga, I., Taub, J., Calvert, C.F., Holm, J. and Pourhomayoun, M., 2022. Predicting PM2.5 atmospheric air pollution using deep learning with meteorological data and ground-based observations and remote-sensing satellite big data. Air Quality, Atmosphere and Health, 15(7). https://doi.org/10.1007/s11869-021-01126-3

Najah Ahmed, A., Binti Othman, F., Abdulmohsin Afan, H., Khaleel Ibrahim, R., Ming Fai, C., Shabbir Hossain, M., Ehteram, M. and Elshafie, A., 2019. Machine learning methods for better water quality prediction. Journal of Hydrology, 578. https://doi.org/10.1016/j.jhydrol.2019.124084

Probst, P., Wright, M.N. and Boulesteix, A.L., 2019. Hyperparameters and tuning strategies for random forest. In Wiley Interdisciplinary Reviews: Data Mining and Knowledge Discovery, Vol. 9, Issue 3, Wiley-Blackwell. https://doi.org/10.1002/widm.1301

Shehab, Z.N. and Faisal, R.M., 2025. Harnessing wind for hydrogen: comparative MCDM-GIS assessment of optimal plant locations. Journal of King Saud University – Engineering Sciences, 37(6), 30. https://doi.org/10.1007/s44444-025-00025-7

Shehab, Z.N., Faisal, R.M. and Ahmed, S.W., 2024. Multi-criteria decision making (MCDM) approach for identifying optimal solar farm locations: A multi-technique comparative analysis. Renewable Energy, 237. https://doi.org/10.1016/j.renene.2024.121787

Shehab, Z.N., Farhhan, A.F. and Faisal, R.M., 2024. Spatial variation influence of landscape patterns on surface water quality across an urbanized watershed in Mosul city, Iraq. Sustainable Water Resources Management, 10(5), 181. https://doi.org/10.1007/s40899-024-01162-8

Singh, P., Chaudhury, S. and Panigrahi, B.K., 2021. Hybrid MPSO-CNN: Multi-level Particle Swarm optimized hyperparameters of Convolutional Neural Network. Swarm and Evolutionary Computation, 63. https://doi.org/10.1016/j.swevo.2021.100863

Southerland, V.A., Brauer, M., Mohegh, A., Hammer, M.S., van Donkelaar, A., Martin, R.V., Apte, J.S., and Anenberg, S.C., 2022. Global urban temporal trends in fine particulate matter (PM2·5) and attributable health burdens: estimates from global datasets. The Lancet Planetary Health, 6(2). https://doi.org/10.1016/S2542-5196(21)00350-8

Tian, M., Gao, J., Zhang, L., Zhang, H., Feng, C. and Jia, X., 2021. Effects of dust emissions from wind erosion of soil on ambient air quality. Atmospheric Pollution Research, 12(7). https://doi.org/10.1016/j.apr.2021.101108

Tsurumi, T. and Managi, S., 2020. Health-related and non-health-related effects of PM2.5 on life satisfaction: Evidence from India, China and Japan. Economic Analysis and Policy, 67. https://doi.org/10.1016/j.eap.2020.06.002

Wang, J., Wu, T., Mao, J. and Chen, H., 2024. A forecasting framework on fusion of spatiotemporal features for multi-station PM2.5. Expert Systems with Applications, 238, 121951. https://doi.org/10.1016/j.eswa.2023.121951

Wang, W., Zhao, S., Jiao, L., Taylor, M., Zhang, B., Xu, G. and Hou, H., 2019. Estimation of PM2.5 Concentrations in China Using a Spatial Back Propagation Neural Network. Scientific Reports, 9(1). https://doi.org/10.1038/s41598-019-50177-1

Wong, P.Y., Lee, H.Y., Zeng, Y.T., Chern, Y.R., Chen, N.T., Candice Lung, S.C., Su, H.J. and Wu, C.Da., 2021. Using a land use regression model with machine learning to estimate ground level PM2.5. Environmental Pollution, 277. https://doi.org/10.1016/j.envpol.2021.116846

Wood, D.A., 2022. Trend decomposition aids forecasts of air particulate matter (PM2.5) assisted by machine and deep learning without recourse to exogenous data. Atmospheric Pollution Research, 13(3). https://doi.org/10.1016/j.apr.2022.101352

Wu, A., Harrou, F., Dairi, A. and Sun, Y., 2022. Machine learning and deep learning-driven methods for predicting ambient particulate matters levels: A case study. Concurrency and Computation: Practice and Experience, 34(19). https://doi.org/10.1002/cpe.7035

Xu, Z., Niu, L., Zhang, Z., Hu, Q., Zhang, D., Huang, J. and Li, C. 2022. The impacts of land supply on PM2.5 concentration: Evidence from 292 cities in China from 2009 to 2017. Journal of Cleaner Production, 347. https://doi.org/10.1016/j.jclepro.2022.131251

Yang, L., Xu, H. and Yu, S., 2020. Estimating PM2.5 concentrations in Yangtze River Delta region of China using random forest model and the Top-of-Atmosphere reflectance. Journal of Environmental Management, 272. https://doi.org/10.1016/j.jenvman.2020.111061

Zhong, S., Zhang, K., Bagheri, M., Burken, J.G., Gu, A., Li, B., Ma, X., Marrone, B.L., Ren, Z.J., Schrier, J., Shi, W., Tan, H., Wang, T., Wang, X., Wong, B.M., Xiao, X., Yu, X., Zhu, J.J. and Zhang, H., 2021. Machine Learning: New Ideas and Tools in Environmental Science and Engineering. Environmental Science and Technology, 55(19), pp. 12741–12754. https://doi.org/10.1021/acs.est.1c01339

Zhu, N., Zhu, C., Zhou, L., Zhu, Y. and Zhang, X., 2022. Optimization of the Random Forest Hyperparameters for Power Industrial Control Systems Intrusion Detection Using an Improved Grid Search Algorithm. Applied Sciences (Switzerland), 12(20). https://doi.org/10.3390/app122010456

Iraqi National Journal of Earth Science

www.earth.uomosul.edu.iq

Evaluation of Spatio-Temporal Forest Health of Bangladesh Using Google Earth Engine

Md. Shahadad Hossain [1*], Nobonita Shobnom [2], Umme Sumaiya Shams [3], Rezaul Roni [4]

[1,2,3,4] Department of Geography and Environment, Social Science faculty, Jahangirnagar University, Savar-1342, Dhaka, Bangladesh.

Article information

Received: 25- Aug -2024

Revised: 11- Oct -2024

Accepted: 07- Dec -2024

Available online: 01- Jan -2026

Keywords:
Forest Health,
Google Earth Engine,
Remote Sensing,
Seasonality,
Spatio-temporal Variability,

Correspondence:
Name: Md. Shahadad Hossain

Email: shahadat.46@geography-juniv.edu.bd

ABSTRACT

Bangladesh has a significantly low and steadily declining land covered in forest compared to the required one-third. Therefore, it is essential to explore the condition of the forest cover in Bangladesh. In recent years, remote sensing techniques have become increasingly popular for assessing the health of forests. The research evaluates the forest health seasonality and spatiotemporal variability. Landsat 7 ETM+, Landsat 8 OLI, and Sentinel-2 images for 2002-2021 and seven vegetation indices are used in the Google Earth Engine platform as it is widely accepted and convenient. The results reveal the time series analysis of vegetation indices; they show a maximum value of 0.8107 for SAVI in Sundarban and a minimum value of 0.0146 for NDVI in the Dinajpur and Hill Tract areas. Also, spatial variability illustrated a maximum value of 0.8107 for SAVI in Sundarban and a minimum value of 0.0146 for NDVI in the Dinajpur area. Moreover, Seasonal patterns are also identified where forest health is best observed during the monsoon season (July - October). Furthermore, the assessment indicates that the south and southeastern portions of the research region, Sundarban, and the Hill Tract area have healthier forest cover than the others. This study could be considered a comprehensive reference for managing and planning forests.

DOI: 10.33899/injes.v26i1.60201, ©Authors, 2026, College of Science, University of Mosul.
This is an open-access article under the CC BY 4.0 license (http://creativecommons.org/licenses/by/4.0/).

تقييم الصحة الحراجية (صحة الغابات) المكانية–الزمانية لبنغلاديش باستخدام محرك جوجل إيرث

محمد شهادات حسين [1*]، **نوبونيتا شبنم** [2]، **أمية سمية شمس** [3]، **رضا الروني** [4]

[1،2،3،4] *قسم الجغرافيا والبيئة، كلية العلوم الاجتماعية، جامعة جاهانجيرناغار، سافار–1342، دكا، بنغلاديش.*

معلومات الارشفة

تاريخ الاستلام: 25– اغسطس– 2024

تاريخ المراجعة: 11– اكتوبر– 2024

تاريخ القبول: 07– ديسمبر– 2024

تاريخ النشر الالكتروني: 01– يناير– 2026

الكلمات المفتاحية:

صحة الغابات،

محرك جوجل إيرث،

الاستشعار عن بُعد،

الموسمية،

التباين المكاني والزماني،

المراسلة:

الاسم: م د شهادات حسين

Email: shahadat.46@geography-juniv.edu.bd

الملخص

مقارنةً بالثلث المطلوب، تمتلك بنغلاديش مساحة منخفضة جداً ومتناقصة باطراد من الأراضي المغطاة بالغابات. ولذلك، من الضروري استكشاف حالة الغطاء الغابي في بنغلاديش. في السنوات الأخيرة، أصبحت تقنيات الاستشعار عن بعد شائعة بشكل متزايد لتقييم صحة الغابات. يقيّم هذا البحث التباين الموسمي والمكاني–الزماني لصحة الغابات. تم استخدام صور Landsat 7 ETM+ ، وLandsat 8 OLI ، و Sentinel-2للفترة ما بين 2002–2021، وسبعة مؤشرات نباتية، على منصة محرك جوجل إيرث (Google Earth Engine) نظراً لكونها مقبولة على نطاق واسع ومريحة. تكشف النتائج عن تحليل السلاسل الزمنية للمؤشرات النباتية؛ حيث تُظهر قيمة قصوى بلغت 0.8107 لمؤشر (SAVI) في منطقة السندربان، وقيمة دنيا بلغت 0.0146 لمؤشر (NDVI) في مناطق ديناجبور ومنطقة التلال .(Hill Tract) كما أوضح التباين المكاني قيمة قصوى بلغت 0.8107 لمؤشر (SAVI) في منطقة السندربان، وقيمة دنيا بلغت 0.0146 لمؤشر (NDVI) في منطقة ديناجبور. علاوة على ذلك، تم تحديد الأنماط الموسمية حيث تُلاحظ صحة الغابات بأفضل شكل خلال موسم الرياح الموسمية (يوليو – أكتوبر). بالإضافة إلى ذلك، يشير التقييم إلى أن الأجزاء الجنوبية والجنوبية الشرقية من منطقة البحث، وهي السندربان ومنطقة التلال، تتمتع بغطاء غابي أكثر صحة من المناطق الأخرى. يمكن اعتبار هذه الدراسة مرجعاً شاملاً لإدارة الغابات وتخطيطها.

DOI: 10.33899/injes.v26i1.60201, ©Authors, 2026, College of Science, University of Mosul.
This is an open-access article under the CC BY 4.0 license (http://creativecommons.org/licenses/by/4.0/).

Introduction

The creation of forest conditions that directly meet human needs and the resilience, recurrence, persistence, and biophysical processes that result in sustainable ecological conditions have been used to describe forest health. The spatial size also affects how we define and comprehend forest health. Forests cover roughly 30 percent of Earth's land area and play an important role in atmospheric regulation of carbon dioxide (CO_2) and oxygen (O_2) soil conservation providing habitat for many species, and providing a source of many useful products like wood and food (Xie et al., 2008; Chaturvedi et al., 2011; Rudel et al., 2005; Vega et al., 2012). On the surface of the earth, the forest essentially encompasses any natural resources, such as wood or solar energy, that can be naturally renewed through time and can be a healthy ecosystem (Sahana et al., 2015). The influence of anthropogenic and physical forces on the regions that encompass the majority of these surfaces has steadily increased in the preserved habitats over the last few decades. The primary driver of anthropogenic habitat fragmentation, however, is a rising population that requires more land for residence, agriculture, urban habitat expansion, the construction of more roads and railroads, and industrial activities (Carroll et al., 2004). In forested ecosystems, the hydrological cycle or surface force equilibrium actively contributes to the regulation of the biosphere (Rogan et al., 2002). Most forests are fragmented in wealthy countries, while on the other side of this fragmentation trend,

the area covered by forests is growing at an alarming rate in other emerging nations (Talukdar et al., 2019). Forest health primarily defines the origin of forest conditions that depend on nature and humans (Kayet et al., 2019). The monitoring of forest products and assessing changes in ecological function are crucial assessments of the factors in forest health (King, 2000). The effects on forest health are mostly caused by the reduction of changes in both temperature and carbon dioxide. Because temperatures rise in the warmer season, forest persecution increases in the cooler season. The decline in forest health is caused by invading species in addition to an increase in temperature (Nandi and Sarkar, 2021). Density and fragmentation models are useful for assessing the health of a forest in a given area. Several studies have used the Landsat TM data analysis guide for mapping and analyzing forest canopy density, whose model can help in assessing forest degradation (Jaiswal et al., 2002). If a forest is in good shape, it could be a reliable indicator of the local environment (Allen et al., 2010). Both abiotic stresses, notably drought (Macpherson et al., 2017) and biotic disturbances, such as logging and fires (Lausch et al., 2017), are rising within the world's forests. The effectiveness and efficiency of a city's ecosystem are directly linked to the condition of its forests (Xiao and McPherson et al., 2002).

Land use, land cover, and vegetation mapping for both urban and rural forests have made extensive use of remote sensing data (Erikson, 2004; Xiao et al., 2004; Pouliot et al., 2002; Ustin and Xiao, 2001). Forward the resolution data from the Advanced Very High-Resolution Radiometer (AVHRR) (Tucker et al., 1985) and the Moderate Resolution Imaging Spectroradiometer (MODIS) (Huete et al., 2002) provide comprehensive findings. Researchers have devoted a great deal of time and resources to studying and creating novel approaches to silviculture (Moore et al., 2017; Watt et al., 2017), tree breeding programs (Klapste et al., 2017; Li et al., 2015), nutrition in forests (Maggard et al., 2017), and remote sensing techniques for better forest management to increase productivity in the world's plantations of trees (Watt et al., 2015; Watt et al., 2016; Pearse et al., 2017). Spatio-temporal portraits of medium-to-long-term (years to decades) vegetation dynamics are from space-based remote sensing instruments. The article explains that common vegetation indices like the Normalized Difference Vegetation Index (NDVI) can pick up on seasonal fluctuations in the amount of fractional cover and leaf area index (LAI) across different forest types, which contributes to the emphasis on structure (Wang et al., 2017). A study demonstrated that deforestation prevention policies and management strategies benefit from a better understanding of forest spatial patterns and the processes that shape them (Fuller et al., 2006). The ability to monitor seasonal or annual variations in tree health and trace the spread of disease is another focus of this study. In addition, it offers data on tree health that is crucial for analyzing the environmental, social, and economic benefits that urban forests provide to their communities (Xiao and McPherson, 2005).

National grasslands and forests must be in good condition if we accomplish our mission of helping people and conserving the environment. The Forest Service strives to maintain, enhance, and restore healthy forest conditions in the nation's forests and grasslands. According to the World Bank Country Climate and Development Report in 2022, Bangladesh is one of the most susceptible countries to climate change, which may prove to be crucial in maintaining healthy forests in the future. A healthy forest protects coastal communities from bad weather and sea level rise, in addition to absorbing greenhouse gases and managing water flows. They provide access to healthy habitats for migratory plant and animal species, too. The significance of vegetation in preserving the ecological biota and environmental balance must be understood. As a result, to evaluate vegetation status, it is necessary to consider ecological dynamism, enough soil nutrients, plant health, as well as effective coping mechanisms and management measures that can assist in reducing risks and sustaining forest health (Allen et al., 2010). Consequently, healthy forests can perform their functions more effectively than unhealthy ones. It is crucial to safeguard and maintain forests to provide integrated and sustainable drainage and sustainable management of agroforestry features.

An important facet of environmental policy and resource allocation is the assessment and evaluation of forest health. The root reasons for the detrimental effects on the health and vitality of forests differ from location to location, and it is difficult to gauge their scope and longevity. It is challenging to understand how these components interact with one another, as well as how they affect the health and vitality of forests. Wide-ranging indirect effects could have social, economic, and environmental implications. The main issues facing Bangladesh's forest resources are the fast-growing population's exponentially expanding consumption and dependence on forest products and services, as well as the weak enforcement of forest laws. Expansion of industrialization, tobacco cultivation, and land grabbing for the real estate industry, i.e., housing, and other new industrial expansions include different chemical and garment industries (Sal Forest), ship breaking and shrimp cultivation (Planted Mangrove), and so on. An increase in encroachment and illegal deforestation in forests is another reason for the diminution of the forest area. Following that, this exploration aims to evaluate the forest health along with seasonality and spatio-temporal variability to achieve: a) assessing the forest health from 2002 through 2021, b) identifying the spatio-temporal variability, and c) evaluating the seasonality of forest health, which are set as objectives.

Study Area

The present study has been done in Bangladesh, which is a South Asian country located between latitudes 20″34′ and 26″38′ North and longitudes 88″01′ and 92″41′ East. It is situated on the Bay of Bengal, east of India, and is surrounded by the Indian states of Tripura and Mizoram to the east, West Bengal to the west and north, Assam to the north, Meghalaya to the north and northeast, and West Bengal to the west and northwest. Its border with Myanmar (Burma) is shared to the southeast (Chowdhury, 2014). As our research area, we have selected five areas from the different regions of Bangladesh. These sample sites are: Sundarbans in the southern region and coastal area, Hill tracts in the southeastern region, Lawchara in the northeastern region, Madhupur in the central-northern region, and Dinajpur area in the northwestern region (Fig. 1) (Rahman, 2012).

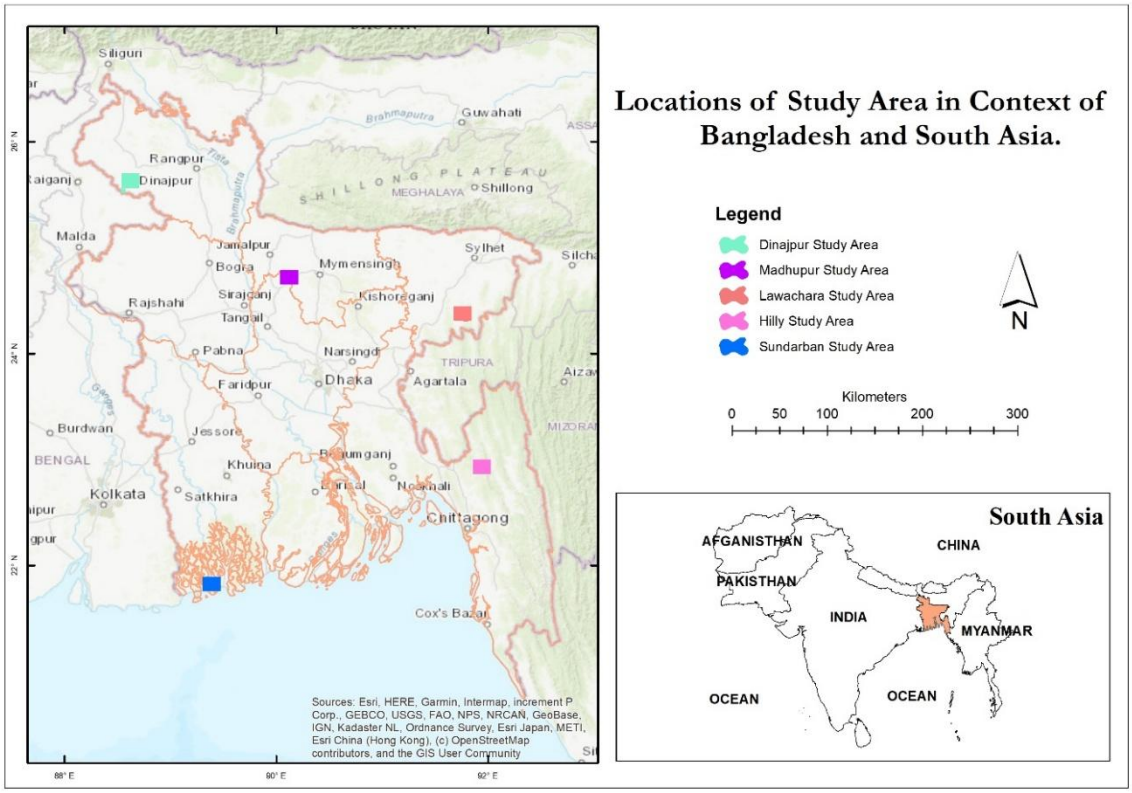


Fig. 1. The study area of Bangladesh with five sample locations of forest cover.

Materials and methods

Data type and sources

To analyze mapping and track deforestation, intra-annual availability of cloud-free land satellite data is required. The Landsat missions are equipped with a multispectral passive optical sensor that measures radiation from the Earth's surface on several arbitrarily broad electromagnetic channels known as spectral bands. The Copernicus Sentinel-2 mission comprises two identical satellites orbiting in the same orbit. Each satellite of Sentinel-2 is equipped with a cutting-edge wide-swath high-resolution multispectral imager with 13 spectral bands to provide a new viewpoint on our land and vegetation. TM, OLI, Sentinel and Blue, red, NIR, SWIR1, and SWIR2 are all similar across all frequently used spectral strips. Vegetation-sensitive bands (Table 1).

Table 1: Vegetation sensitive bands that are used in the analysis.

Landsat 7	Landsat 8	Sentinel-2
Band 1 - Blue	Band 2 - Blue	Band 4 – Red
Band 2 - Green	Band 3 - Green	Band 8 – NIR
Band 3 - Red	Band 4 - Red	
Band 4 - Near-Infrared	Band 5 - Near Infrared (NIR)	
Band 5 - Short-wave Infrared	Band 6 - SWIR 1	
Band 6 - Thermal	Band 7 - SWIR 2	
Landsat 7	Band 10 - Thermal Infrared (TIRS) 1	

Imaging of Landsat TM (Path-136, 137, 138, Row-43, 44, 45), OLI (Path-136, 137, 138, Row-43, 44, 45), and Sentinel-2 is used through Google Earth Engine. The number of imagery accessible each year in the study region, as in the other tropical covers, is restricted; nonetheless, at least one cloud-free Landsat image is available every season. The images had been geometrically rectified in Level and atmospherically corrected in the Solar Spectrum using the radio-transmission approach of the second satellite signal simulation. Their key advantage over higher-resolution imaging is that they may be used as archive data for an extended period of time. Images with greater than 10% cloud coverage are avoided and not included in the research (Mozgeris and Balenovic, 2021; Calders et al., 2020).

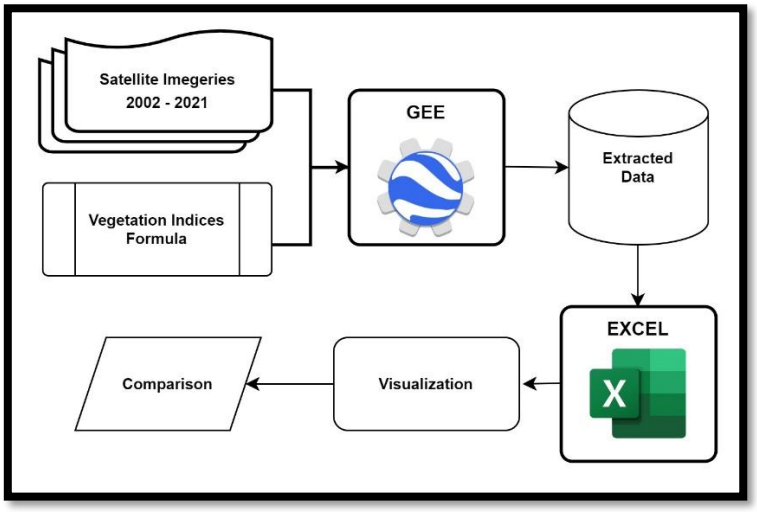


Fig. 2. A detailed flowchart of the method.

The key goal of this study is to evaluate how the sample areas of Bangladesh have changed over time. This section explains the overall methods utilized to collect and process data in achieving the aim of the study. As previously indicated, the Google Earth Engine (GEE) hosts satellite imaging data and provides computational services via a simple web-based interface. The Earth Engine Code Editor is used in this study to access this facility through interactive JavaScript coding. From 2002 to 2021, GEE satellite imagery from Landsat 7 and Landsat 8 was used. Then, the data are filtered to remove any digital photos with clouds, fog,

or haze. The GEE computing module is then provided with the shortlisted and cleaned dataset, which is responsible for recognizing the forest cover initially. Following that, using pixel counting, the minimum, maximum, mean, and standard deviation values of vegetation indices are extracted as datasets. Next, extracted datasets are imported to MS Excel to filter, rearrange, combine, and make graphical representations. The meaningful visualization of the vegetation indices data helps to better understand the condition of the vegetation health, pattern, and trends to discuss causes and consequences. Figure 2 summarizes the entire procedure.

Vegetation indices

To evaluate the forest health of Bangladesh, seven VI were initially analyzed (Table 2), namely the Normalized Difference Vegetation Index (NDVI), Normalized Difference Moisture Index (NDMI), Greenness Index (GI), Soil-Adjusted Vegetation Index (SAVI), Perpendicular Vegetation Index (PVI), Enhanced Built-Up and Bareness Index (EBBI), and Leaf Area Index (LAI). These indices are used to produce the health status and vigor of a forested area. The vegetation indices were measured using reflectance values at various wavelengths to increase information relevant to vegetation while considering environmental conditions and shadow.

Table 2: Vegetation indices used in this analysis.

Vegetation Index	Equation	Reference
NDVI	$\frac{NIR-Red}{NIR+Red}$	(McDaniel,1982)
NDMI	$\frac{NIR-SWIR}{NIR+SWIR}$	(Dutta, 2020)
GI	$((0.2728 * \text{Blue}) - (0.2174 * \text{Green}) - (0.5508 * \text{Red}) + (0.7221 * \text{NIR}) + (0.0733 * \text{SWIR1}) - (0.1648 * \text{SWIR2}))/100$	(Yuan, 1996)
SAVI	$\frac{NIR-Red}{NIR+R+0.5} * (1.5)$	(Ren, 2018)
PVI	$\frac{\sqrt{(0.355\,NIR-0.149\,RED)^2-(0.355RED-0.852NIR)^2}}{100}$	(Rajan, 2009)
EBBI	$\frac{SWIR-Red}{10*\sqrt{(SWIR+TIR)}}$	(Baranwal, 2022)
LAI	0.57 * exp (2.33 * NDVI)	(Bajocco, 2022)

Google Earth Engine (GEE)

Google Earth Engine, the platform adopted for this research, is a cloud platform that hosts a multi-petabyte database of satellite images and geographic information, as well as planetary-scale analytic capabilities. Utilizing GEE aids in minimizing the pre-processing and data-obtaining procedures, which would otherwise demand significant computing power and large data storage capacity (Kong et al., 2019). The technique presented in this paper requires the collection of spatiotemporal data over a period of 20 years. Multi-petabyte datasets are easily accessible and are mostly pre-processed on Google Earth Engine. Second, high-performance computing resources enable users to utilize a machine-learning technique to obtain verified results. Data extraction for this analysis is based on the collection of Landsat, Sentinel data and integrated vegetation indices. Selected imagery, vegetation-sensitive bands, and index equations are arranged into a GEE Image Collection object. We applied "reducers," a sophisticated feature in GEE that allows us to compute at the pixel level across a stack of images or inside a specific region of space. We utilized the EE. Reduce method to compute descriptive statistics such as minimum, maximum, mean, and standard deviation. Finally, the data are saved to CSV files and evaluated with the MS Excel program. Although applying the formulas for vegetation indices for various satellite band combinations during data extraction presented certain challenges, we made an effort to reduce these. For instance, while evaluating the greenness index with Landsat 8, we can choose SWIR1, SWIR2, or Landsat 7, which utilize the SWIR band.

Statistics

Data collection and analysis are phases in the statistical analysis process, which is used to find patterns and trends. It is a technique for reducing bias from data evaluation by numerical

analysis (Candiago et al., 2015). In this work, we have generated statistics for the indices for assessing forest health in the study region. We have presented comparison graphs of vegetation indices using the extracted data as well, which help us in understanding how they change over time. The difference in scale ratio, however, prevented us from including LAI in this comparison. As we know, vegetation indices such as NDVI, NDMI, GI, PVI, SAVI, and EBBI vary from -1 to +1, while LAI goes from 1 to 4.5. To evaluate seasonality, a quarter graph is produced. We have also conducted trend analysis by linear regression to understand spatial variability and time series analysis, which reveals changes in forest cover over time in various places.

Seasonality

The temporal profiles of the vegetation indicators for the five sites under investigation are displayed in Fig. 3. The average VI values are plotted month by month. The seasonal VI fluctuation between dry and rainy seasons, as well as the appearance of green vegetation, is measured between January and December. The resemblance can be observed in the NDVI, NDMI, and GI indices. The Normalized Vegetation Index (NDVI) measures the amount and how notably the vegetation on the surface has grown. While the Greenness Index (GI) provides information on the quality of the greenery since the green area is covered with grasses, trees, and different plants, the Normalized Moisture Index (NDMI) reveals the moisture level in the vegetation (Brando et al., 2010). If we look at the lines of NDVI, NDMI, and GI, we can see that their values rise and show the maximum value from August to November, gradually decrease and show a mid-range from December to February, and afterwards display the lowest value from March to July. In contrast, PVI and SAVI show a similarity, where PVI is used to represent the level of soil brightness, and SAVI is used to correct NDVI for the effects of soil brightness where vegetation cover is low. As shown by the X and Y lines, the values are lowest from September to January, grow to a mid-range from February to May, and are highest from June to August. Particularly with respect, EBBI has a line that counts both built-up and bare space. Since there is little variation in this line, seasonality is not given considerable weight.

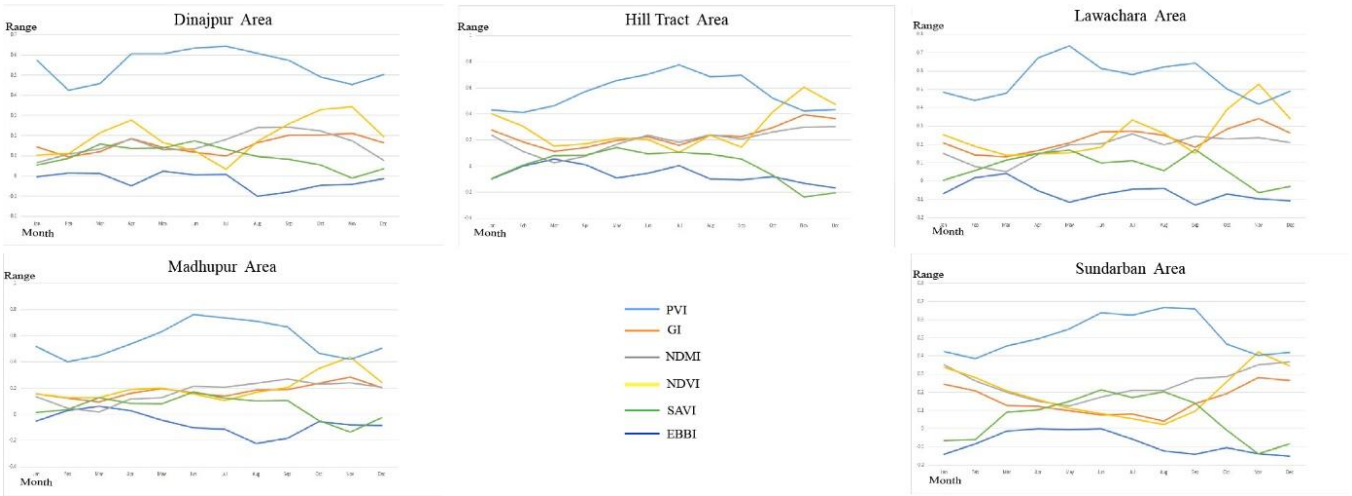


Fig. 3. Comparison of the monthly mean of different vegetation indices.

Spatio-temporal variability

The variability change patterns are defined by spatial and temporal fluctuations. The spatial parameters are the locations and frequency of change, whereas the temporal parameters are the time of occurrence and length of each change event (Quiring and Ganesh, 2010). According to Fig. 4, the yearly average NDVI varies between 0 and 0.5 in different locations. In the Lawachara region, the NDVI of the vegetation-covered area demonstrates significant variations between 2002 and 2021. The NDVI of the Madhupur vegetation-covered areas has been considerably increasing since 2017, with other regions exhibiting a minimal decline. The

vegetation-covered regions' annual average NDMI varies from 0.1 to 0.4. In the Sundarban region, the NDMI of the vegetation-covered area shows greater changes between 2002 and 2014. The GI lines appear to vary from -0.1 to 0.4, while the EBBI lines appear to range from -0.2 to 0. The GI and EBBI of the Dinajpur and Hill Tract region remain relatively stable over time, although variations are observed in other locations. PVI values vary from 0.4 to 0.7, whereas SAVI values range from -0.5 to 0.3. All of the sample locations showed little fluctuation in PVI, while the Sundarbans region showed a modest rise from 2019 to the present. SAVI showed a linear trend across all of the zones, with the hill tract recording the lowest value in 2007.

However, the variations didn't reflect a consistent pattern as we used satellite data from two separate periods; the inaccuracy is related to the discrepancy in the wavelength scale of the bands.

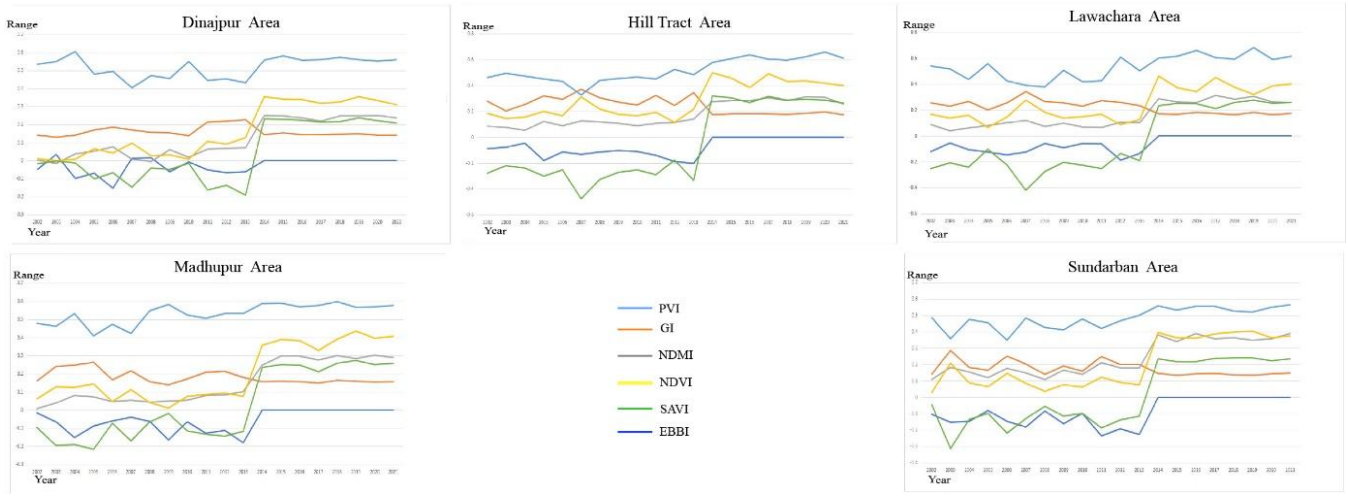


Fig. 4. Comparison of the yearly mean of different vegetation indices.

Results

Seasonality

The findings of the graph (Fig. 5) provide a good understanding of the seasonal variance. Several vegetation indices, including NDVI, GI, SAVI, and PVI, demonstrate good variability for all of the study sites. It is also interesting that these indices exhibit maximum values from July to October, during the monsoon season, minimum values from November to February (winter), and medium values from March to April (the pre-monsoon season). As we inspect the EBBI lines, we can observe that a parallel scenario is portrayed rather than much of a tendency toward growth or deterioration. Therefore, EBBI's seasonality is of little real consequence for any location.

We can bring to light some intriguing points if we carefully observe the NDMI curves. Although NDMI does not show much variation for all the sites, its major shift is observed in the Dinajpur region. This assists us in comprehending how effectively this measure reflects seasonality in geographical areas with less forest cover.

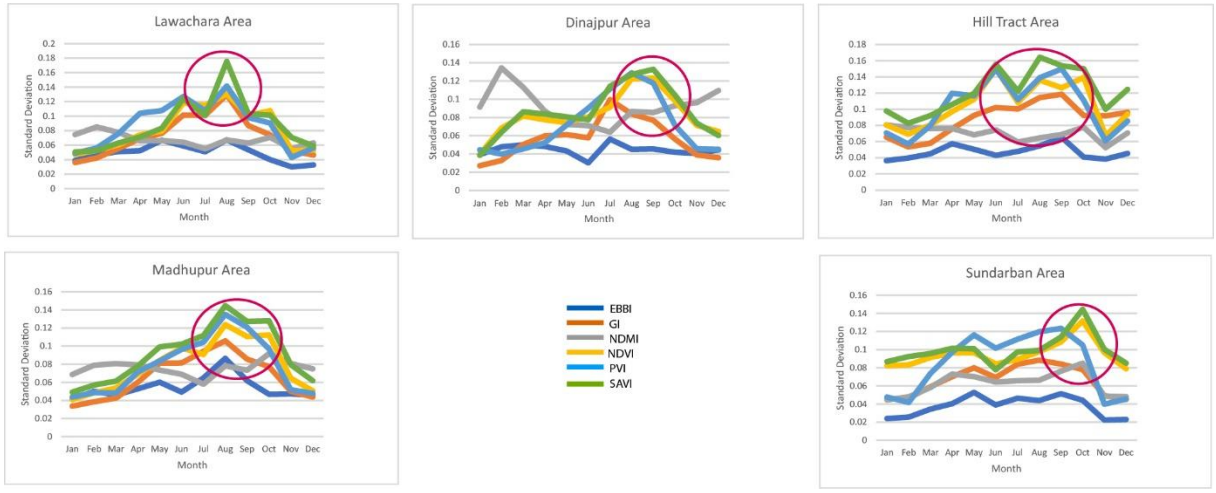


Fig. 5. Seasonal variability of different vegetation indices.

Spatio-temporal variability

For the Spatio-temporal evaluation of vegetation indices (Fig. 6), trend lines are generated using linear regression models to show how they vary over time, along with y-intercepts as statistical measures. Here, we will observe how each vegetation index has evolved for all five sample areas over the past 20 years.

We begin by reviewing EBBI, which has significantly decreased across all locations. The Sundarban Mangrove Forest has had the lowest decline, whereas the Dinajpur area has experienced the highest. The best-fitting line is detected for the Dinajpur region with a value of 0.7447. Second, we find a significant drop in GI as well. The Hill tract region is indicated by the best-fitting line with a value of 0.8. However, GI is least deteriorated in the Dinajpur region and is most degraded in the hill tract. Then, during the course of the time, all NDMI lines exhibited a modest rise. Dinajpur has the best-fitting NDMI line, with a value of 0.5562 and it has also shown a little growth compared to other areas. The NDVI patterns show a mixed situation. It increases slightly in the Dinajpur and Sundarbans regions, while exhibiting a minor decline in Lawachara, Madhupur, and the Hill Tract. However, the best-fitted line is identified for Lawachara with a value of 0.3918.

PVI and SAVI demonstrate a somewhat similar dropping tendency across all the geographic areas, as can be seen. The Sundarban mangrove forest is represented by the best-fit curve for PVI and SAVI, with values of 0.4695 and 0.8107, respectively.

Finally, we'll concentrate on LAI's illustrations. As we know, the Leaf Area Index (LAI) involves measuring how much leaf material is there in a forest cover. In all regions, LAI is going up concurrently. But with several 0.592, the Dinajpur region demonstrates the best-fit line.

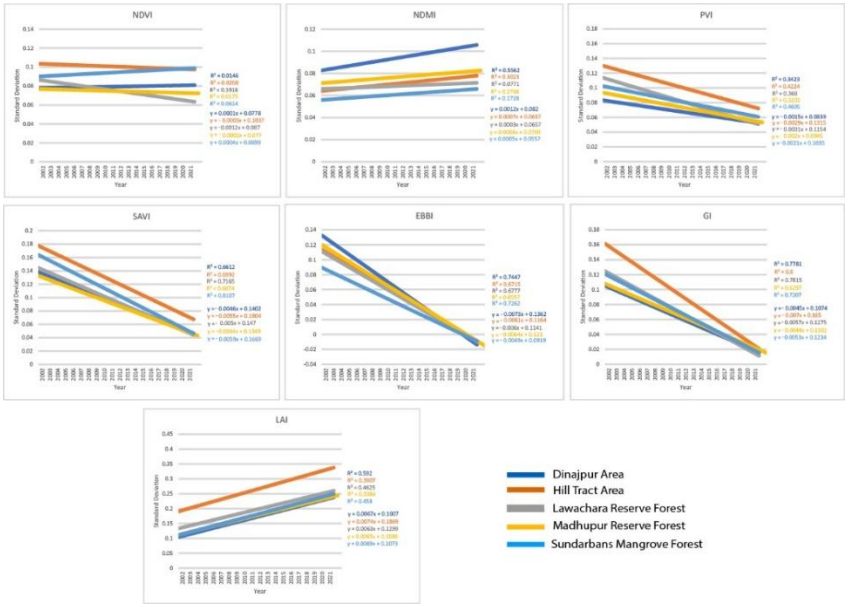


Fig. 6. Spatial variability among the areas based on different vegetation indices.

Trend analysis

We have presented the time series analysis trend of all vegetative indicators for each specific sample location for the 20 years from 2002 to 2021, according to Figure 7. We will be able to understand the past and the present condition and make predictions about how it could be in the future from this. Initially, if we investigate the vegetation indices in the Dinajpur region. We can discover that NDVI and NDMI are marginally rising while the remaining indices, such as GI, PVI, SAVI, and EBBI, are somewhat falling. The perfect fit line among them is given by GI with a value of 0.7781. As we can see in the second graph, the hill tract region's NDMI and NDVI exhibit very mild increases and decreases, respectively, whereas the trends for GI, PVI, SAVI, and EBBI reflect a considerable decline. SAVI's value of 0.6992 indicates that this region's line of best fit.

The patterns in the vegetation indices for the Lawachara and Madhupur regions are quite comparable to those in the Hill tract regions. However, the best-fit line for Lawchara is shown by GI and SAVI for Madhupur, whose values are 0.7815 and 0.6674, respectively. The last part is the Sundarbans, where all the areas covered by the indices follow the pattern of the indices, but significantly, NDVI is only rising in this area. However, the best fit in this region shows a value of 0.8107.

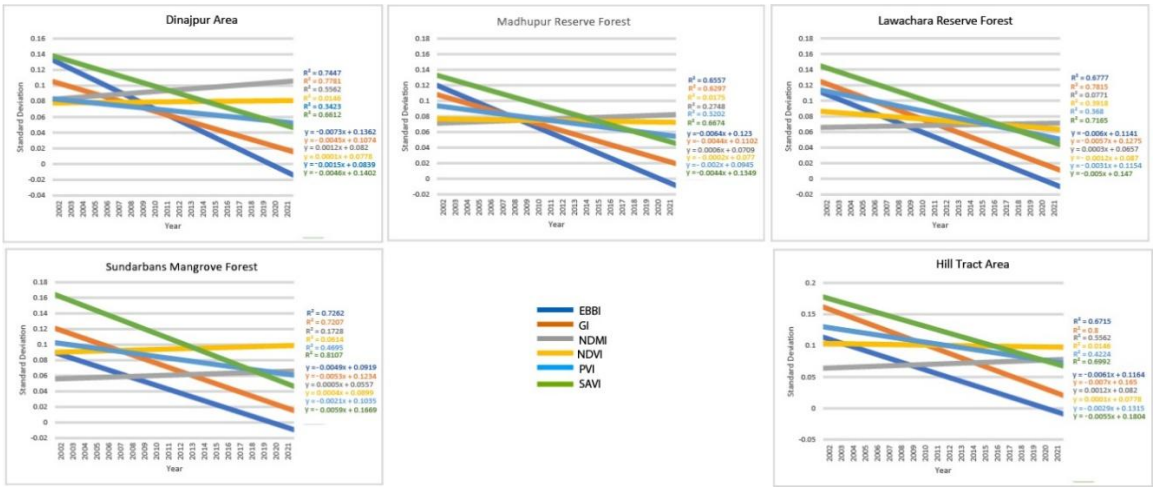


Fig. 7. Time series analysis of vegetation indices: 2002-2021.

Discussion

To determine the Bangladesh forest health status and how it has evolved, we have used seven vegetation indicators in this article. Seasonal trends and any indicators that exhibited strong sensitivity to vegetation were also discovered. In our inspection, we identified seasonality in the condition of the forest cover in Bangladesh, where the monsoon season lasts from July to August. During this time, there is a lot of rain, which improves the forest's health. According to our data, the months of July to October have the largest NDVI, GI, PVI, and SAVI values, while March to April have the pre-monsoon season's median values.

Among the sample places in Bangladesh, our studied research region, Hill Tract, Lawchara Reserve Forest, and Sundarban Mangrove Forest, are in reasonably good condition and have not changed significantly over the years. However, the state of the Madhupur Reserve Forest and the Dinajpur region has more or less degraded, and the time series analysis shows a significant diminution.

First, we observe high points of SAVI, PVI, NDVI, and GI for seasonality in the Dinajpur region. While EBBI continues a flat line and the NDMI shows somewhat fluctuation. For spatio-temporal variability, NDMI and LAI represent an increase, while PVI, SAVI, EBBI, and GI turn downwards. In time series analysis, all the indices climbed except for the NDVI.

Next, in Lawachara Reserve Forest, our investigation has found inflated seasonality lines for SAVI, PVI, NDVI, and GI, while the other two lines remained horizontal. The remaining data in the variability analysis show a downswing, but the LAI and NDMI show modest increases. However, trend analysis shows that leftovers are smooth while SAVI, PVI, GI, and EBBI decrease for this site.

Thirdly, the Hill tract region is identified in this study as having peak values in periodic analysis for SAVI, PVI, NDVI, and GI. Regarding spatiotemporal variability, PVI, SAVI, EBBI, and GI appear to decline, while LAI, NDMI, and NDVI seem to rise. In terms of on-time interval assessment, the rest decrease, while SAVI, PVI, GI, and EBBI show an increase.

Fourthly, the sporadic inspection of Madhupur Reserve Forest shows an improvement in all vegetation indices. For the LAI, NDMI, and NDVI, spatiotemporal data demonstrate an upturn, while the spare depicts a downturn. When compared to the rest, the time-period inquiry displays a growth for the NDVI and NDMI.

Lastly, this study has found that all vegetation indices—aside from EBBI—had higher values in the Sundarban Mangrove Forest area. In the context of spatiotemporal findings, PVI, SAVI, EBBI, and GI are diminished, while NDMI, NDVI, and LAI are intensified. When it comes to time series investigation, the NDVI and NDMI exhibit significant values, while the others are alternative.

We have acknowledged that all indices that reflect sensitivity, but are dependent on the amount of forest cover, are used when it comes to categorizing vegetation sensitivity bands. Except for EBBI, the other indices exhibit substantial reflectance in places with higher forest cover, although in areas with less forest cover, the relevance of EBBI has also been noted. However, considerable inconsistencies in accuracy have been noted due to the difference in the wavelength of the bands, due to the usage of data from two satellites at identical times.

Conclusion

The current study attempted an integrated approach for rapid satellite-based monitoring of changes in the forest region. This study demonstrates the ability of Landsat time series data acquired between 2002 and 2021 to identify anomalies, temporal trends, and confirm the pattern of changes over time. Vegetation indices in forest health evaluation demonstrated their

sensitivity in our research locations, and seasonal patterns were observed. Additionally, we note both positive and negative trends in the spatiotemporal analysis for various locations.

The primary drawback of Landsat data is its intra-year and inter-year availability, which means that seasonal variation in vegetation conditions is unlikely to be assessed. Thus, an integrated method is used, which combines coarse spatial resolution satellite data (Landsat) with high spatial resolution satellite data (Sentinel). During the investigation, we discovered that using data from two satellites at the same time highlights discrepancies. It is advised for future research to conduct scrutiny to reduce the discrepancies.

The assessment revealed a spatiotemporal distribution of changes (physical and stress-induced) across Bangladesh's forest cover, and the methodologies used in this study might be easily applied to extract first-hand knowledge when conducting field verifications.

References

Allen, C.D., Macalady, A.K., Chenchouni, H., Bachelet, D., McDowell, N., Vennetier, M. and Cobb, N., 2010. A global overview of drought and heat-induced tree mortality reveals emerging climate change risks for forests. Forest ecology and management, 259(4), pp. 660-684. https://doi.org/10.1016/j.foreco.2009.09.001

Bajocco, S., Ginaldi, F., Savian, F., Morelli, D., Scaglione, M., Fanchini, D. and Bregaglio, S. U.M., 2022. On the use of NDVI to estimate LAI in field crops: Implementing a conversion equation library. Remote Sensing, 14(15), 3554. https://doi.org/10.3390/rs14153554

Baranwal, E., Ahmad, S. and Mudassir, S.M., 2022. New independent component-based spectral index for precise extraction of impervious surfaces through Landsat-8 images. Geocarto International, 37(27), pp. 15935-15963. https://doi.org/10.1080/10106049.2022.2102244

Brando, P.M., Goetz, S.J., Baccini, A., Nepstad, D.C., Beck, P.S. and Christman, M.C., 2010. Seasonal and interannual variability of climate and vegetation indices across the Amazon. Proceedings of the National Academy of Sciences, 107(33), pp. 14685-14690. https://doi.org/10.1073/pnas.0908741107

Candiago, S., Remondino, F., De Giglio, M., Dubbini, M. and Gattelli, M., 2015. Evaluating multispectral images and vegetation indices for precision farming applications from UAV images. Remote sensing, 7(4), pp. 4026-4047. https://doi.org/10.3390/rs70404026

Calders, K., Jonckheere, I., Nightingale, J. and Vastaranta, M., 2020. Remote sensing technology applications in forestry and REDD+. Forests, 11(2), 188. https://doi.org/10.3390/f11020188

Carroll, C., Noss, R.F., Paquet, P.C. and Schumaker, N.H., 2004. Extinction debt of protected areas in developing landscapes. Conservation Biology, 18(4), pp. 1110-1120. https://doi.org/10.1111/j.1523-1739.2004.00083.x

Chaturvedi, R.K., Gopalakrishnan, R., Jayaraman, M., Bala, G., Joshi, N.V., Sukumar, R. and Ravindranath, N.H., 2011. Impact of climate change on Indian forests: a dynamic vegetation modeling approach. Mitigation and adaptation strategies for global change, 16, pp. 119-142. https://doi.org/10.1007/s11027-010-9257-7

Chowdhury, M.S.H. (Ed.)., 2014. Forest conservation in protected areas of Bangladesh: policy and community development perspectives. Springer, 20. https://doi.org/10.1007/978-3-319-08147-2

Dutta, S., Rehman, S., Sahana, M. and Sajjad, H., 2021. Assessing forest health using geographical information system based analytical hierarchy process: evidences from

southern West Bengal, India. Spatial modeling in forest resources management: Rural livelihood and sustainable development, pp. 71-102. https://doi.org/10.1007/978-3-030-56542-8_3

Erikson, M., 2004. Species classification of individually segmented tree crowns in high-resolution aerial images using radiometric and morphologic image measures. Remote Sensing of Environment, 91(3-4), pp. 469-477. https://doi.org/10.1016/j.rse.2004.04.006

Fuller, D.O., 2006. Tropical forest monitoring and remote sensing: A new era of transparency in forest governance? Singapore Journal of Tropical Geography, 27(1), pp. 15-29. https://doi.org/10.1111/j.1467-9493.2006.00237.x

Huete, A., Didan, K., Miura, T., Rodriguez, E.P., Gao, X. and Ferreira, L.G., 2002. Overview of the radiometric and biophysical performance of the MODIS vegetation indices. Remote sensing of environment, 83(1-2), pp. 195-213. https://doi.org/10.1016/S0034-4257(02)00096-2

Jaiswal, R.K., Mukherjee, S., Raju, K.D. and Saxena, R., 2002. Forest fire risk zone mapping from satellite imagery and GIS. International journal of applied earth observation and geoinformation, 4(1), pp. 1-10. https://doi.org/10.1016/S0303-2434(02)00006-5

Kayet, N., Pathak, K., Chakrabarty, A., Singh, C.P., Chowdary, V.M., Kumar, S. and Sahoo, S., 2019. Forest health assessment for geo-environmental planning and management in hilltop mining areas using Hyperion and Landsat data. Ecological Indicators, 106, 105471. https://doi.org/10.1016/j.ecolind.2019.105471

Klápště, J., Suontama, M., Telfer, E., Graham, N., Low, C., Stovold, T. and Dungey, H., 2017. Exploration of genetic architecture through sib-ship reconstruction in advanced breeding population of Eucalyptus nitens. PLoS One, 12(9), e0185137. https://doi.org/10.1371/journal.pone.0185137

Kong, D., Zhang, Y., Gu, X. and Wang, D., 2019. A robust method for reconstructing global MODIS EVI time series on the Google Earth Engine. ISPRS Journal of Photogrammetry and Remote Sensing, 155, pp. 13-24. https://doi.org/10.1016/j.isprsjprs.2019.06.014

Lausch, A., Erasmi, S., King, D. J., Magdon, P. and Heurich, M., 2017. Understanding forest health with remote sensing- Part II: review of approaches and data models. Remote Sensing, 9(2), 129. https://doi.org/10.3390/rs9020129

Li, Y., Xue, J., Clinton, P.W. and Dungey, H.S., 2015. Genetic parameters and clone by environment interactions for growth and foliar nutrient concentrations in radiata pine on 14 widely diverse New Zealand sites. Tree Genetics and Genomes, 11, pp. 1-16. https://doi.org/10.1007/s11295-014-0830-1

Macpherson, M.F., Kleczkowski, A., Healey, J.R., Quine, C.P. and Hanley, N., 2017. The effects of invasive pests and pathogens on strategies for forest diversification. Ecological modelling, 350, pp. 87-99. https://doi.org/10.1016/j.ecolmodel.2017.02.003

McDaniel, K.C. and Haas, R.H., 1982. Assessing mesquite-grass vegetation condition from Landsat. Photogrammetric Engineering and Remote Sensing, 48(3), pp. 441-450. https://pubs.usgs.gov/publication/70142200

Maggard, A.O., Will, R.E., Wilson, D.S., Meek, C.R. and Vogel, J.G., 2017. Fertilization can compensate for decreased water availability by increasing the efficiency of stem volume production per unit of leaf area for loblolly pine (Pinus taeda) stands. Canadian Journal of Forest Research, 47(4), pp. 445-457. https://doi.org/10.1139/cjfr-2016-0422

Moore, J.R., Dash, J.P., Lee, J.R., McKinley, R.B. and Dungey, H.S., 2018. Quantifying the influence of seedlot and stand density on growth, wood properties and the economics of

growing radiata pine. Forestry: An International Journal of Forest Research, 91(3), pp. 327-340. https://doi.org/10.1093/forestry/cpx016

Mozgeris, G. and Balenovic, I., 2021. Operationalization of Remote Sensing Solutions for Sustainable Forest Management. MDPI AG. https://doi.org/10.3390/rs13040572

Nandi, D. and Sarkar, S., 2021. Non-Timber Forest Products Based Household Industries and Rural Economy-A Case Study of Jaypur Block in Bankura District, West Bengal (India). Spatial Modeling in Forest Resources Management: Rural Livelihood and Sustainable Development, pp. 505-528. https://doi.org/10.1007/978-3-030-56542-8_21

Olthof, I. and King, D.J., 2000. Development of a forest health index using multispectral airborne digital camera imagery. Canadian Journal of Remote Sensing, 26(3), pp. 166-176. https://doi.org/10.1080/07038992.2000.10874767

Pearse, G.D., Morgenroth, J., Watt, M.S. and Dash, J.P., 2017. Optimising prediction of forest leaf area index from discrete airborne lidar. Remote Sensing of Environment, 200, pp. 220-239. https://doi.org/10.1016/j.rse.2017.08.002

Pouliot, D.A., King, D.J., Bell, F.W. and Pitt, D.G., 2002. Automated tree crown detection and delineation in high-resolution digital camera imagery of coniferous forest regeneration. Remote sensing of environment, 82(2-3), pp. 322-334. https://doi.org/10.1016/S0034-4257(02)00050-0

Quiring, S.M. and Ganesh, S., 2010. Evaluating the utility of the Vegetation Condition Index (VCI) for monitoring meteorological drought in Texas. Agricultural and forest meteorology, 150(3), pp. 330-339. https://doi.org/10.1016/j.agrformet.2009.11.015

Rahman, S., 2012. Climate Change and Forest in Bangladesh: Growth, Survivability, Stress Adoption and Spatial Shift to Forest Species Due to Climate Change. Van Haren Publishing, Netherlands, 250 P.

Rajan, N. and Maas, S.J., 2009. Mapping crop ground cover using airborne multispectral digital imagery. Precision agriculture, 10, pp. 304-318. https://doi.org/10.1007/s11119-009-9116-2

Ren, H., Zhou, G. and Zhang, F., 2018. Using negative soil adjustment factor in soil-adjusted vegetation index (SAVI) for aboveground living biomass estimation in arid grasslands. Remote Sensing of Environment, 209, pp. 439-445. https://doi.org/10.1016/j.rse.2018.02.068

Rogan, J., Franklin, J. and Roberts, D.A., 2002. A comparison of methods for monitoring multitemporal vegetation change using Thematic Mapper imagery. Remote sensing of environment, 80(1), pp. 143-156. https://doi.org/10.1016/S0034-4257(01)00296-6

Rudel, T.K., Coomes, O.T., Moran, E., Achard, F., Angelsen, A., Xu, J. and Lambin, E., 2005. Forest transitions: towards a global understanding of land use change. Global environmental change, 15(1), pp. 23-31. https://doi.org/10.1016/j.gloenvcha.2004.11.001

Sahana, M., Sajjad, H. and Ahmed, R., 2015. Assessing spatio-temporal health of forest cover using forest canopy density model and forest fragmentation approach in Sundarban reserve forest, India. Modeling Earth Systems and Environment, 1, pp. 1-10. https://doi.org/10.1007/s40808-015-0043-0

Talukdar, N.R., Ahmed, R., Choudhury, P. and Barbhuiya, N.A., 2009. Assessment of forest health status using a forest fragmentation approach: A study in Patharia Hills Reserve Forest, northeast India. Modeling Earth Systems and Environment, 6, pp. 27-37. https://doi.org/10.1007/s40808-019-00652-5

Tucker, C.J., Townshend, J.R. and Goff, T.E., 1985. African land-cover classification using satellite data. Science, 227(4685), pp. 369-375. https://doi.org/10.1126/science.227.4685.369

Ustin, S.L. and Xiao, Q.F., 2001. Mapping successional boreal forests in interior central Alaska. International Journal of Remote Sensing, 22(9), pp. 1779-1797. https://doi.org/10.1080/01431160118269

Vega Orozco, C., Tonini, M., Conedera, M. and Kanveski, M., 2012. Cluster recognition in spatial-temporal sequences: the case of forest fires. Geoinformatica, 16, pp. 653-673. https://doi.org/10.1007/s10707-012-0161-z

Wang, R., Chen, J.M., Liu, Z. and Arain, A., 2017. Evaluation of seasonal variations of remotely sensed leaf area index over five evergreen coniferous forests. ISPRS Journal of Photogrammetry and Remote Sensing, 130, pp. 187-201. https://doi.org/10.1016/j.isprsjprs.2017.05.017

Watt, M.S., Dash, J.P., Bhandari, S. and Watt, P., 2015. Comparing parametric and non-parametric methods of predicting Site Index for radiata pine using combinations of data derived from environmental surfaces, satellite imagery and airborne laser scanning. Forest Ecology and Management, 357, pp. 1-9. https://doi.org/10.1007/s11295-014-0830-1

Watt, M.S., Dash, J.P., Watt, P. and Bhandari, S., 2016. Multi-sensor modelling of a forest productivity index for radiata pine plantations. New Zealand Journal of Forestry Science, 46, pp. 1-14. https://doi.org/10.1186/s40490-016-0065-z

Watt, M.S., Kimberley, M.O., Dash, J.P. and Harrison, D., 2017. Spatial prediction of optimal final stand density for even-aged plantation forests using productivity indices. Canadian Journal of Forest Research, 47(4), pp. 527-535. https://doi.org/10.1139/cjfr-2016-0220

Xiao, Q. and McPherson, E.G., 2002. Rainfall interception by Santa Monica's municipal urban forest. Urban ecosystems, 6, pp. 291-302. https://doi.org/10.1023/B:UECO.0000004828.05143.67

Xiao, Q., Ustin, S.L. and McPherson, E.G., 2004. Using AVIRIS data and multiple-masking techniques to map urban forest tree species. International Journal of Remote Sensing, 25(24), pp. 5637-5654. https://doi.org/10.1080/01431160412331291224

Xiao, Q. and McPherson, E.G., 2005. Tree health mapping with multispectral remote sensing data at UC Davis, California. Urban Ecosystems, 8, pp. 349-361. https://doi.org/10.1007/s11252-005-4867-7

Xie, Y., Sha, Z. and Yu, M., 2008. Remote sensing imagery in vegetation mapping: a review. Journal of Plant Ecology, 1(1), pp. 9-23. https://doi.org/10.1093/jpe/rtm005

Yuan, D. and Elvidge, C.D., 1996. Comparison of relative radiometric normalization techniques. ISPRS Journal of Photogrammetry and Remote Sensing, 51(3), pp. 117-126. https://doi.org/10.1016/0924-2716(96)00018-4

Iraqi National Journal of Earth Science

www.earth.uomosul.edu.iq

Use of Remote Sensing and GIS to Study the Expansion of Sands and Vegetation in the Draa Region (Morocco) From Landsat Satellite Images

Otman Tamri [1*], Allal Labriki [2], Soukaina el Idrissi [3], Mohammed Amine Zerdeb [4], Saïd Chakiri [5]

[1,4,5]*Geosciences and Natural Resources Laboratory, University of Ibn Tofaïl, Kenitra, Morocco.*
[2]*Department of Geology, College of Geosciences and Applications, University of Sciences Ben M'Sik, Casablanca, Morocco.*
[3] *Department of Geology, College of Geosciences, University of Ibn Tofaïl, Kenitra, Morocco.*

Article information

Received: 14- Aug -2024

Revised: 09- Nov -2024

Accepted: 14- Feb -2025

Available online: 01- Jan–2026

Keywords:
Remote sensing,
GIS,
Landsat images,
Change map,
Draa region (Morocco),

Correspondence:
Name: Otman Tamri

Email: otman.tamri5@gmail.com

ABSTRACT

The Draa region, located in the southern part of Morocco, has been faced with a significant increase in desertified surfaces, sand deposits, and a decrease in vegetation cover. The region's ability to develop is hampered by this issue. Through a spatio-temporal study, this project aims to contribute to the comprehension and quantitative assessment of these potential risks. Understanding the dynamics of land use is made possible by the merging of remote sensing and geographic information systems techniques. For this diachronic analysis, two multidate satellite images are employed (Landsat 7 ETM+ 2001 and Landsat 9 OLI 2023). After all the necessary processing of these images, a map of changes is generated by the difference between the two land use maps, which correspond to the two dates of the time interval considered in the project. This allows us to make a diachronic analysis and highlight the change in each component of the studied environment. The obtained results are validated by contrast with other climatic data and by examining the correlations between the remote sensing parameters. The changes are important, especially for the vegetation cover and the migration of sands in the considered area. This is due to the influence of climatic factors. After digitization, it is evident that in comparison to 2001, there was a 43.46% decline in vegetation in 2023. By 2023, living sand will have taken over 20.90% of the area that was covered by vegetation in 2001, posing the biggest threat to the palm oasis.

DOI: 10.33899/injes.v26i1.60202, ©Authors, 2026, College of Science, University of Mosul.
This is an open-access article under the CC BY 4.0 license (http://creativecommons.org/licenses/by/4.0/).

استخدام الاستشعار عن بُعد ونظم المعلومات الجغرافية لدراسة توسع الرمال والغطاء النباتي في منطقة درعة (المغرب) من مرئيات الأقمار الصناعية لاندسات

عثمان التامري[1]* ، علال لبريكي[2] ، سكينة الإدريسي[3] ، محمد أمين زردب[4] ، سعيد شكيري[5]

[1،4،5] مختبر علوم الأرض والموارد الطبيعية، جامعة ابن طفيل، القنيطرة، المغرب.

[2] قسم علوم الأرض وتطبيقاتها، كلية العلوم بن مسيك، جامعة الحسن الثاني، الدار البيضاء، المغرب.

[3] قسم علوم الأرض، كلية العلوم، جامعة ابن طفيل، القنيطرة، المغرب.

معلومات الارشفة

تاريخ الاستلام: 14- اغسطس-2024

تاريخ المراجعة: 09- نوفمبر-2024

تاريخ القبول: 14- فبراير-2025

تاريخ النشر الالكتروني: 01- يناير- 2026

الكلمات المفتاحية:

الاستشعار عن بعد،

نظم المعلومات الجغرافية،

مرئيات لاندسات،

خريطة التغيير،

(المغرب) منطقة درعة،

المراسلة:

الاسم: عثمان التامري

Email: otman.tamri5@gmail.com

الملخص

على مدى العقود القليلة الماضية شهدت منطقة درعة في جنوب المغرب زيادة كبيرة في المناطق المتصحرة والترسبات الرملية وانخفاض الغطاء النباتي. وقد أعاقت هذه المشكلة قدرة المنطقة على التنمية. ويهدف هذا المشروع من خلال دراسة مكانية وزمانية إلى المساهمة في فهم هذه المخاطر المحتملة وتقييمها كمياً. وقد أصبح ممكنا فهم ديناميكيات استخدام الأراضي من خلال دمج الاستشعار عن بعد ونظم المعلومات الجغرافية. وقد استُخدمت مرئيتان من مرئيات الأقمار الصناعية متعددة التواريخ لهذا التحليل الزمني (لاندسات 7 2001 ETM+ ولاندسات 9 2023 OLI). وبعد إجراء جميع المعالجات اللازمة لهذه المرئيات، تم إنشاء خريطة للتغييرات من خلال الفرق بين خريطتي الغطاء الأرضي المطابقة للتاريخين في الفترة الزمنية التي تم أخذها في الاعتبار في المشروع. يمكّننا ذلك من إجراء تحليل زمكاني وتسليط الضوء على التغيرات في كل مكون من مكونات البيئة المدروسة. يتم التحقق من صحة النتائج التي تم الحصول عليها من خلال مقارنتها ببيانات مناخية أخرى ومن خلال فحص الارتباطات بين معاملات الاستشعار عن بعد. كانت التغيرات كبيرة خاصة بالنسبة للغطاء النباتي وهجرة الرمال في المنطقة قيد الدراسة. ويرجع ذلك إلى تأثير العوامل المناخية. بعد ترقيم وحدات استخدام الأراضي المختلفة في عامي 2001 و2023، يمكن ملاحظة أن الغطاء النباتي قد تناقص بنسبة 43.46% في عام 2023 مقارنة بعام 2001. إن أخطر ما يهدد واحة النخيل هو أن 20.90% من المساحة التي كان يغطيها الغطاء النباتي في عام 2001 قد استعمرتها الرمال الحية بحلول عام 2023 مما يشكل تهديدا لواحة النخيل.

DOI: 10.33899/injes.v26i1.60202, ©Authors, 2026, College of Science, University of Mosul.
This is an open-access article under the CC BY 4.0 license (http://creativecommons.org/licenses/by/4.0/).

Introduction

Observing the Earth from space increasingly becomes an indispensable tool in the development of a multitude of scientific disciplines. This technique allows us to track the dynamic changes and metamorphoses undergone by the globe through diachronic analysis (Kieffer and Serradj, 2013). As a corollary, the launch of several satellite constellations has been observed, taking continuous images to predict catastrophes and occurrences and to plan appropriate and sustainable territorial development (Ahmed, 2022).

Due to the prolonged periods of drought that have affected the Draa region over the past few decades, it is currently experiencing enormous difficulties (Ben Salem and El Alami El Filali, 2024).

This area is currently experiencing a process of desertification that manifests as the degradation of the vegetative cover, which mostly occurs in the oasis where the majority of the population derives its primary economic support. This degradation is primarily the result of sand migration and a decrease in water storage (Karmouji *et al*., 2022; Oussedik *et al.*, 2003).

This study has two main goals. On the one hand, it attempts to demonstrate the potential of the employment of remote sensing and GIS for monitoring the evolution of the major components of land use between 2001 and 2023. In contrast, the creation of spatial information layers and cartographic supports provides local representatives, leaders, and decision-makers with accurate information on the state of the environment and resources of the area (Al-Zahraa *et al*., 2021). In the framework of the conservation and integrated management of the ecosystem in the region.

Presentation of the study area

The study area addressed in this work is located in southern Morocco, covering an area of 14,767 km², representing 2.08% of the national territory (Fig. 1). It is limited to:

- at the north by the region of Beni Mellal-Khenifra

- at the south by Algeria

- at the east by the region of Tafilalet

- at the west by the region of Souss-Massa

This study zone is diversified, including plateaus in the desert, acacia forests, mountains, and valleys. One of the largest palm plantations in Africa and Wadi Drâa in the middle can be seen to the east of the sand dunes.

Draa has long, heated summers and extremely moderate winters during the daytime but freezing winters at night, which is typical of the Moroccan desert. With an average annual rainfall of just 61 mm, the climate is extremely arid throughout the year. Summer temperatures are intense and persistently hot, usually exceeding 40°C (Sefiani and Kettab, 2018).

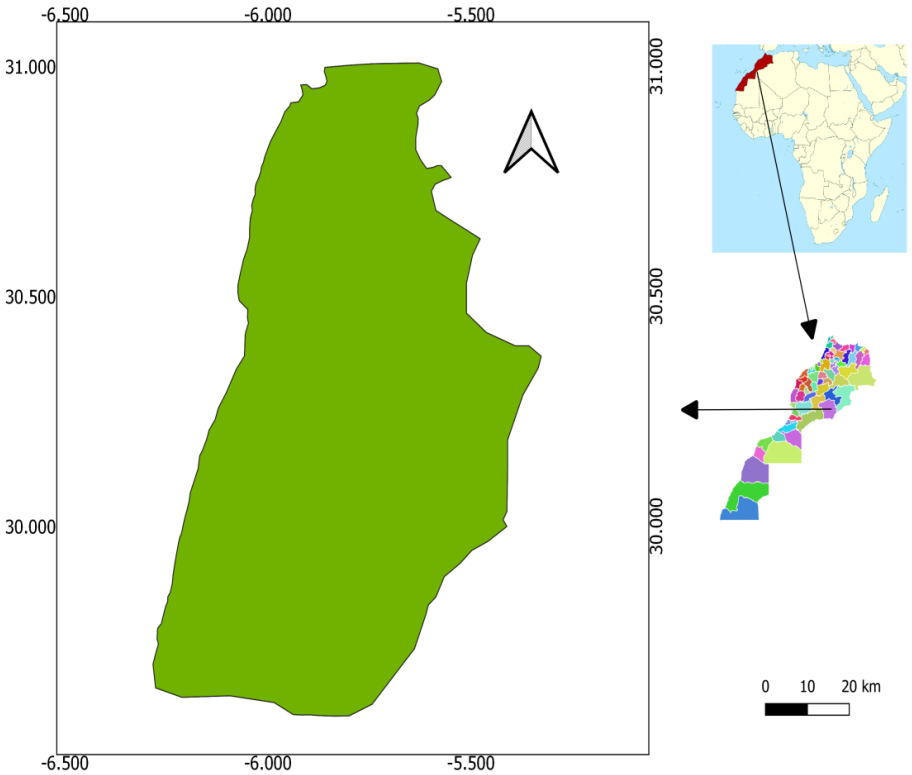


Fig. 1. Geographic Location of Study Area.

Materials and Methods

Data Selection and Acquisition

• On two different dates, datasets of two Landsat satellite acquisitions were collected, both in the years 2023 and 2001, available for free download on the USGS website (https://earthexplorer.usgs.gov/).

However, using Landsat satellite images for long-term studies has several advantages compared to other satellite data. This archive allows for the analysis of land changes over decades, making it ideal for monitoring long-term trends like in our case, such as climate change.

Landsat's consistent data stream over many years ensures comparability across time, but the disadvantage is that the resolution is low. As our study does not involve the classification of fine objects, we have accepted this type of resolution by introducing a panchromatic layer with a resolution of 15 m (Roy and Boschetti, 2016).

The (Landsat Collection 1 Level-1 data) (L1T) are freely available (Ghobadi *et al*., 2012). However, the primary issue with optical images is the existence of clouds, which is ignored at this level of processing. This explains our decision to only acquire data during the summer or when the sky is often clear. In order to obtain photographs of the region with the lowest percentage of clouds, the cloud coverage percentage has been set at 10%.

To fully cover the study region, two scenes were acquired for each acquisition. The following Table 1 lists the characteristics that describe two acquisitions.

Table 1: Characteristics of the Images.

Image 2001	Image 2023
Landsat 7 ETM+ C1 Level-1 ETM+ (Enhanced Thematic Mapper Plus) Resolution: 30 m Panchromatic band: 15 m	Landsat 9 OLI/ TIRS C2 Level-1 OLI (Operational Land Imager) Resolution: 30 m Panchromatic band: 15 m

- Land use maps
- The climatic data of the region (temperature, rainfall, humidity, wind ...) come from the High Commission for Water and Forests and the fight against desertification in Zagora: http://www.eauxetforets.gov.ma/SitePages/Index.aspx

Software

The satellite data are processed, and the land use maps are created using two software programs (ENVI and QGIS).

- Image data are processed using the ENVI (Environment for Visualizing Images) software. It enables the analysis and visualization of big data sets in a variety of forms. Its primary benefit is its capacity to manipulate several multispectral images.
- QGIS is a GNU General Public License-compliant Geographic Information System (GIS) that is simple to use. It supports various uses that exploit geographic data and is frequently used.
- Google Earth is a software application that enables any user to fly over the Earth and zoom in on a specific location. The information is more or less precise depending on the geographic zone (Gore and Hu, 2012).

Using ENVI and QGIS together allows for a more robust and complete approach to remote sensing projects. While ENVI excels at advanced analysis and processing of raw satellite data, QGIS provides the flexibility to combine and visualize that data in a geographic context, making it ideal for spatial analysis and map creation (Lillesand *et al*., 2015).

Working method

This section will describe the steps used, from data collection to final results confirmation, to create a cartography of the components of the occupation of our interested land using Landsat data (Bachir and El Zerey, 2014). The methodology used is shown in the organizational structure in Fig. 2.

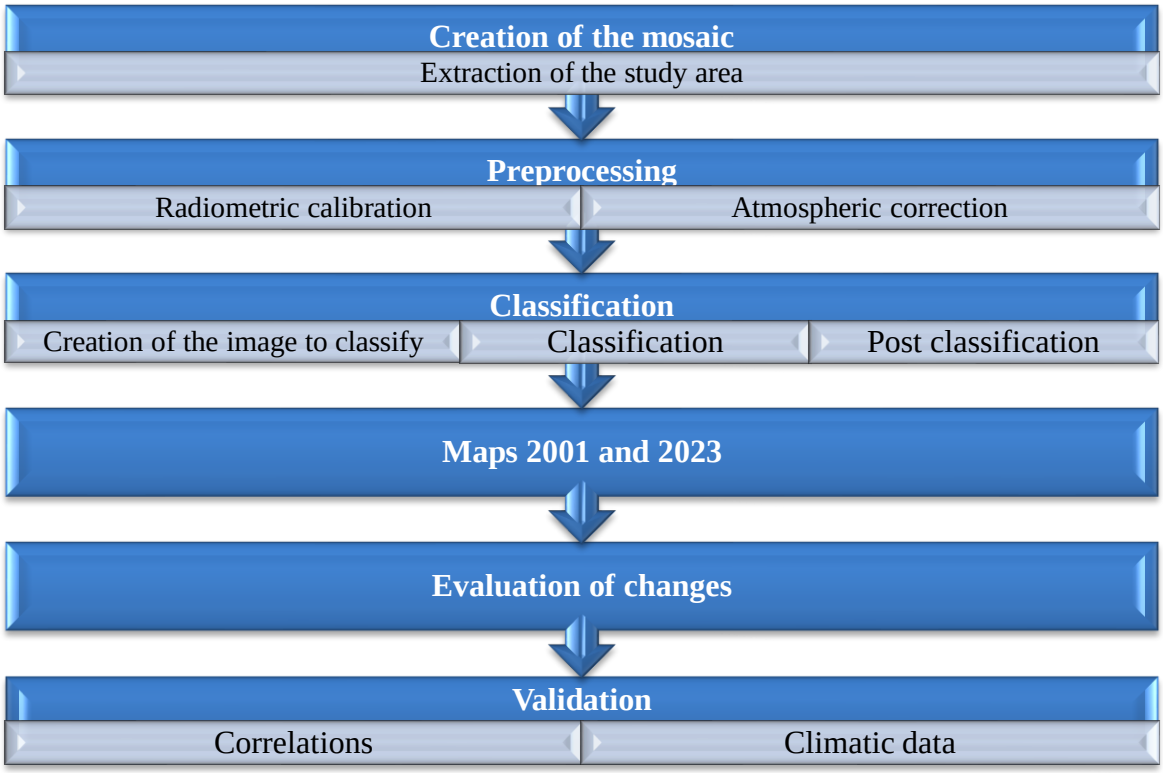


Fig. 2. General outline of the methodology.

Extraction of the Study Area

The creation of satellite image mosaics is a method for putting together scenes that were captured continuously from the same orbit or from two parallel orbits whose paths overlap. To cover the entire research area, a mosaic is created using the two scenes from each acquisition.

In this instance, the projection was used: Projection: UTM Zone 30 North; Datum: WGS 84

The desired study area is extracted using a georeferenced shapefile projected onto the mosaic of scenes.

Preprocessing

Landsat satellite images must first be pre-processed to remove possible faults before they can be used successfully. These images are pre-processed mostly through radiometric calibration and atmospheric correction procedures.

Radiometric calibration

This process involves converting the pixel numerical counts into radiance values and subsequently into the apparent reflectance at the atmosphere's top (Bildgen *et al*., 1990).

Atmospheric correction

It is carried out because the two shooting dates did not have the same atmospheric conditions.

The relative approach of atmospheric correction, on the other hand, is applied based on the choice of a priori invariant objects in the image. The relationship between the numerical counts of the two images on the two dates is straightforward to explain (Teferi et al., 2010).

Spectral sharpening

Using a high spatial resolution panchromatic band, the PC spectral sharpening model is employed to modify a low spatial resolution multi-band image (in our case, 30m). The technique assumes that the panchromatic band with a high spatial resolution (in our case 15m) corresponds to the low spatial resolution spectral bands. Since our images are georeferenced, both datasets may be co-registered instantly by ENVI by resampling (Baker and Williams, 2014).

Classification

Creation of the image to classify

The strategy based on the calculation of neo bands is used to reduce class confusion. This basic technique's idea is to create new bands using the pre-processed image's original bands as a starting point. Two new bands, corresponding to the two primary classifications of land cover vegetation (through the calculation of the normalized difference vegetation index (NDVI) and sand by the gloss index (IB) were established, as the goal of our study is to produce land cover maps. While Principal Component Analysis is used to create the other bands' sound (PCA).

- IB is the index of brightness that represents the image's average brightness. It is sensitive to the brightness of the soil, which is related to its moisture and salt content. The following formula generates this index:

$$\boldsymbol{IB} = (\boldsymbol{PIR} \times \boldsymbol{PIR} + \boldsymbol{R} \times \boldsymbol{R})^{\boldsymbol{1/2}} \quad (1)$$

- NDVI is the most famous and extensively utilized vegetation index. It is a metric that describes the chlorophyll greenness, relative density, and vegetation health of each pixel in a satellite image (Yu *et al*., 2017; Zhou *et al*., 2015). This index has been defined using the following basic variant:

$$\boldsymbol{NDVI} = \frac{\boldsymbol{PIR} - \boldsymbol{R}}{\boldsymbol{PIR} + \boldsymbol{R}} \quad (2)$$

where:

$\boldsymbol{R}$ – red band.
$\boldsymbol{PIR}$ – near infrared band.

After the establishment of the neo-bands in the preceding step, they must be combined into a single image with QGIS for classification. The result of this processing is an image made up of the NDVI, IB, and PCA bands (Fig. 3). The reason for combining the NDVI, IB, and PCA bands is to create a more informative multi-dimensional representation of the landscape, which enhances the classification process. To merge multiple bands, a “Build Virtual Raster” in QGIS can be used (Jensen, 2007).

NDVI, IB, and PCA play a crucial role before classification.

The NDVI is used to:

- enhance class separability: This helps in differentiating bare soil, water, and vegetation.
- improve supervised classification by distinguishing forests from agricultural lands.
- feature selection: It is used as an additional band to improve classification accuracy.

The Brightness Index (IB) can help in separating built-up areas from natural landscapes.

The PCA is used to:

- reduce redundancy: It removes correlations between spectral bands.
- improve computational efficiency: i.e., fewer dimensions mean faster processing.
- enhance class discrimination: That is, the first components contain the most relevant information.

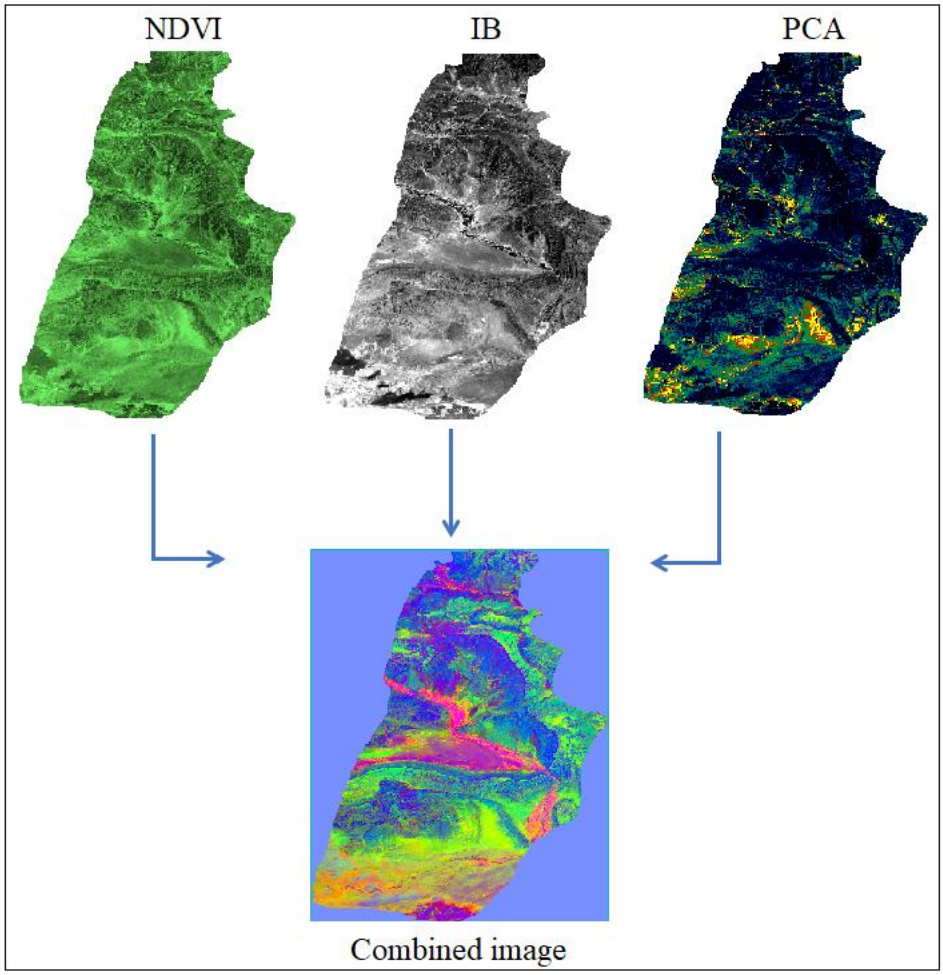


Fig. 3. Creation of the image to classify.

Classification

A **compréhensive** and accurate classification of land cover in this study area is achieved through the application of supervised classification. Before initiating the classification process, a thorough understanding of the land under investigation was developed using various data sources. Google Earth imagery provided high-resolution satellite images**,** allowing for an initial visual inspection of the area. Additionally, field trips were conducted to collect ground-truth data, which ensured that the classifications would be based on accurate real-world observations. These combined efforts helped to refine the boundaries and characteristics of different land cover types within the study area.

With this foundational understanding, we proceeded to supervised classification based on the Maximum Likelihood Classification (MLC) algorithm, a commonly used technique in remote sensing (Jemberie et al., 2016). Supervised classification involves manually selecting training samples **from** specific regions in the image that are representative of the different land cover classes you wish to identify. These training samples serve as the basis for the classification algorithm, which uses them to "learn" how to categorize the pixels in the entire image.

The MLC algorithm assigns each pixel in the image to a specific class based on the probability that it belongs to that class. It does so by analyzing the spectral signatures of the training samples. Each land cover class is associated with a set of statistical parameters, such as the mean and variance of pixel values within the training samples. These parameters describe how the spectral values of a given class are distributed across different image bands (red, green, blue, and near-infrared). Once the statistical properties of each class have been established, the

MLC algorithm assigns each pixel in the image to the class that has the highest probability given in its spectral values (Li *et al*., 2016).

This method is especially effective for working with multispectral satellite imagery, where multiple bands provide different types of information. It is particularly useful in cases of low-resolution images like those used in our study, which have a spatial resolution of 15 meters. Although low-resolution data may have a reduced ability to capture fine spatial details. The MLC algorithm compensates for this by analyzing the statistical relationships between the spectral bands and making class assignments based on overall patterns in the data rather than on fine-scale spatial features. This makes MLC an appropriate choice for datasets with relatively coarse spatial resolution.

One of the key advantages of using the MLC algorithm in this context is that it accounts for the variability of each class's spectral signature. This means that even if some pixels exhibit mixed characteristics or fall on the boundaries between different classes, the algorithm can still assign them to the most likely class based on the statistical likelihood.

After the classification process, the results are evaluated for accuracy. This is done through an accuracy assessment**,** like the global precision and kappa coefficient**,** used to quantify the accuracy and reliability of the classification results (Lillesand et al., 2015).

Global Precision is a simple and direct measure of the correct classification rate in the results. It compares the number of correctly classified pixels to the total number of pixels in the confusion matrix.

$$\boldsymbol{Global\ precision} = \frac{\boldsymbol{Number\ of\ Correctly\ Classified\ Pixels}}{\boldsymbol{Total\ Number\ of\ Pixels}} \quad (3)$$

Kappa Coefficient is a more advanced measure that accounts for the possibility of random chance agreement. It compares the observed accuracy to the expected accuracy.

The kappa statistic is especially useful when dealing with imbalanced data (where some classes dominate the classification) (Congalton, 1991).

$$\boldsymbol{Kappa\ coefficient} = \frac{\boldsymbol{P_0 - P_e}}{\boldsymbol{1 - P_e}} \quad (4)$$

where P_0 is the observed accuracy, and P_e is the expected accuracy by chance.

Table 2: Confusion Matrix (2001).

Actual Class \ Predicte Class	Sand	Vegetation	Dune	Other	Total
Sand	2800	250	200	125	3375
Vegetation	200	1150	80	70	1500
Dune	250	120	1100	155	1625
Other	125	90	150	5637	6002
Total	3375	1500	1625	6002	12502

Table 3: Confusion Matrix (2023).

Actual Class \ Predicted Class	Sand	Vegetation	Dune	Other	Total
Sand	3180	70	80	45	3375
Vegetation	60	775	20	20	875
Dune	140	40	1390	55	1625
Other	80	30	110	5782	6002
Total	3460	875	1600	5902	12502

Table 4: Results of classification.

Classification	Global Precision	Kappa coefficient
2001	(11302/12502) =89 %	(0,89-0,31)/ (1-0,31) =0.84
2023	(11560/12502) =92.45 %	(0,92-0,125)/ (1-0,125) =0.91

Post classification

Following the classification procedure, a small number of isolated pixels are usually left, usually misclassified or unclassified, and frequently located at the boundary of two distinct assignment ranges (Moutaz and Hussain, 2016). These give the image a "pointillist" appearance, which can be embarrassing for a cartographic representation. The classification should then be homogenized by reassigning these pixels to one of two classes. Filtering techniques are also used to accomplish this.

- **Classification aggregation**

This tool connects smaller adjacent class regions to a larger region. Aggregation is a useful cleaning process when the classification result includes a large number of small regions (this is the case for our classification) (Jensen, 2016).

The aggregation equation is typically:

$$\boldsymbol{Aggregated\ value} = \sum_{\boldsymbol{i=1}}^{\boldsymbol{n}} \boldsymbol{C_i} \times \boldsymbol{A_i} \qquad (5)$$

Where: *Ci*: Classification value (class label, such as forest, water, or urban); *Ai*: Area or pixel count of class; *n*: Total number of classes in the classification.

- **Clumping classes**

Our classification images suffer from a lack of spatial coherence (spots and holes in the classified areas). Similarly, clumping classes will be used to group adjacent areas using morphological operators (Prakasam, 2010).

To mathematically express clumping or reclassification, we can use the following equation:

$$\boldsymbol{C_i^{new}} = \sum_{\boldsymbol{K \in G_i}} \boldsymbol{C_K} \qquad (6)$$

Where:

C_i^{new}: The new merged class label; G_i: The group of original classes that are clumped into a new class; C_K: The original class labels.

- **Majority Analysis**

The majority analysis will be used to modify the spurious pixels within a single large class. A kernel size is selected, and the center pixel in the kernel is replaced by the class value that has the majority of pixels in the kernel (Lillesand *et al*., 2015).

The majority rule equation can be expressed mathematically as:

$$\boldsymbol{C_{i,j}} = \boldsymbol{arg\ max_k} \left(\sum_{\boldsymbol{m,n \in N(i,j)}} \boldsymbol{\delta(C_{m,n}, k)} \right) \qquad (7)$$

Where:

$\boldsymbol{C_{i,j}}$: The new class assigned to the central pixel (i, j); *k*: Possible class values; *N(i, j)*: The neighborhood (usually a 3×3, 5×5, or 7×7 window**)** centered on pixel (i, j); $\boldsymbol{C_{m,n}}$: The class label of the pixel at location (m, n) within the neighborhood; $\boldsymbol{\delta(C_{m,n}, k)}$: Indicator function, defined as:

$$\boldsymbol{\delta(C_{m,n}, k)} = \begin{cases} \boldsymbol{1}, \boldsymbol{if\ C_{m,n} = k} \\ \boldsymbol{0}, \boldsymbol{otherwise} \end{cases} \qquad (8)$$

The argmax function selects the class *k* that appears most frequently in the neighborhood.

Results and Discussion

The results announcement is presented in the form of 2 maps of desired land use components which are vegetation and sands in 2001 and 2023 (Fig. 4).

Furthermore, a visual comparison of the two classifications to clearly show the changes in the Draa area.

The quantitative calculation of land use changes was established by the difference between the two classified maps.

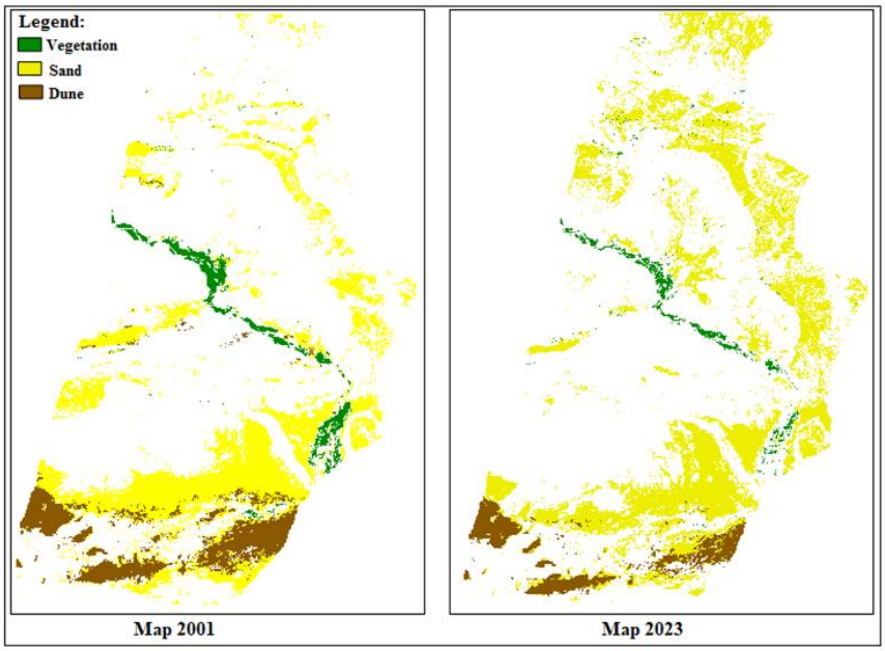


Fig. 4. Land use maps in 2001 and 2023.

Vegetation Dynamics

Following the digitization of the various land use units in 2001 and 2023. It can be seen that the vegetation has decreased by 43.46% in 2023 compared to 2001 (Fig. 4).

The most dangerous threat to the palm oasis is that 20.90 % of the space covered by vegetation in 2001 has been colonized by living sand by 2023 (Fig. 5).

The NDVI classes indicate a decrease in vegetation production, which is mainly made up of date palms. This decrease is related to the distribution of rainfall in the treated years. The rainiest year, 2001, has the highest chlorophyll activity with a value of NDVI max of about 0.26; on the other hand, the driest year, 2023, has the lowest activity, justified by its maximum NDVI of 0.17. Also, the negative impact of the long periods of severe drought that affected it between the two treated dates. The spectral signatures are also used to validate these results.

It can be concluded that there is a retreat of vegetation space, which is already very limited in a desert environment dominated by soils and dunes that feed the living sand. Also, by calculating the NDVI index from a satellite image, a sustainable development can be valued as a nation's indicator of sustainable development. Rainfall and NDVI have a powerful link. Many authors have already noted the strong relationship between these two variables (Pal, 2005).

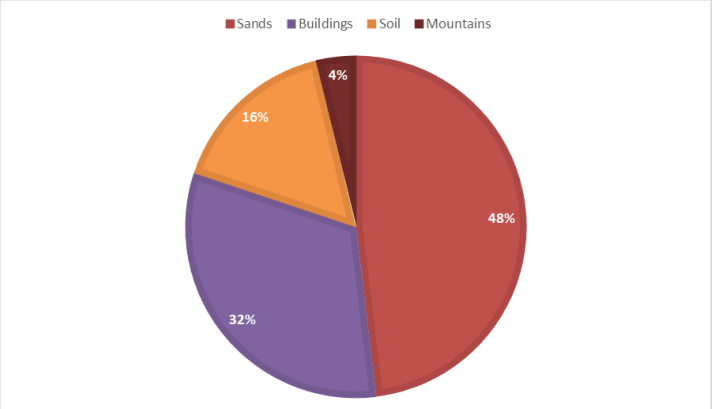


Fig. 5. Percent of vegetation colonized by other soil components between 2001 and 2023.

Silting Dynamics

The mobile sands are a persistent threat to Draa's oasis. This research allows for mapping the evolution of silting from an image archive (Landsat 7 ETM+ and Landsat 9 OLI) to the red sands that are the final product of soil stripping. The recognition of the sands by supervised classifications is enabled by the iron index image, which allows us to precisely locate them due to their ferric nature (Karnieli *et al*., 2002).

The land use change map shows that there is a 19.1 % increase in sand between 2001 and 2023. Sand dunes precisely feed these massive amounts of sand (Fig. 4).

Large quantities of these displaced live sands have taken the place of vegetation cover, making the problem more dangerous (Fig. 5).

It has been demonstrated that sand distribution and migration are affected by climatic conditions such as humidity, wind speed, and precipitation. The year 2023, which was the driest in terms of precipitation, saw a greater migration of sands; whereas the year 2001, which was the wettest, saw a less significant movement.

According to Coude-Gaussen and Rognon (1993); Wang and Liu (2013), the problem of silting has become very acute in semi-arid and arid countries, particularly in Morocco, where the effect is developing particularly in the south and southeast of the country: in the east of the High Atlas, in the basin of the middle and lower Ziz, around Errachidia, Goulmima, Erfoud, and southward in the Tafilalet and the Draa basin, particularly in the province of Zagora.

It should be noted that the work of Lemsanni (1999) about the monitoring of desertification in Morocco from NOAA AVHRR images, and Desjardins (2005), who highlighted the advance of dunes in several locations in southeastern Morocco using remote sensing data for the characterization of the desertification phenomenon. This is achieved because of the free availability of satellite data and open-source processing software.

Correlation Between Remote Sensing Parameters

In this regard, and to assist surveyors in better interpreting remote sensing variables, and to validate our results, we developed a correlation method that allows us to investigate the relationships between the following parameters: normalized difference vegetation index (NDVI), brightness index (IB), and land surface temperature (LST) (Wan and Li, 1997).

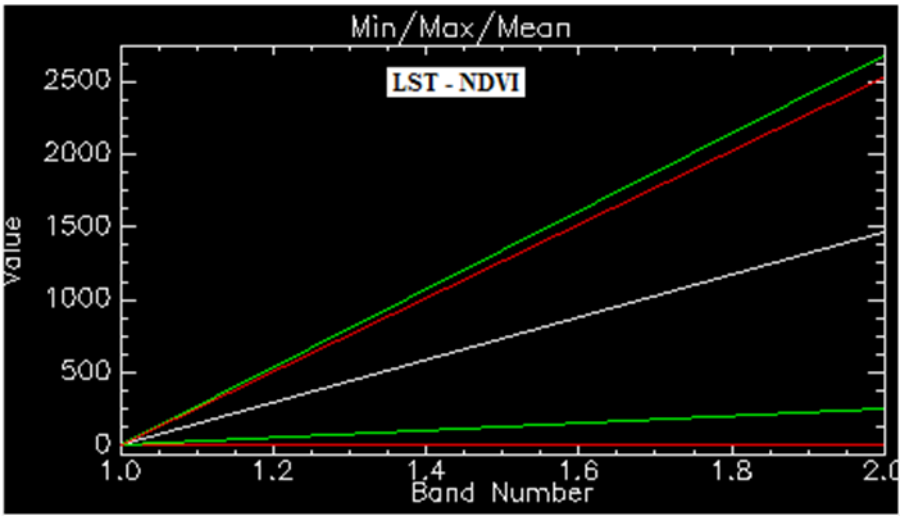


Fig. 6. Correlation between NDVI and LST.

An inverse correlation between surface temperature and vegetation index is obtained in the year 2023 (Fig. 6), especially for areas with high vegetation cover, which is -0.85.

The results reveal that the environment's chlorophyll activity is strongly related to the land surface temperature.

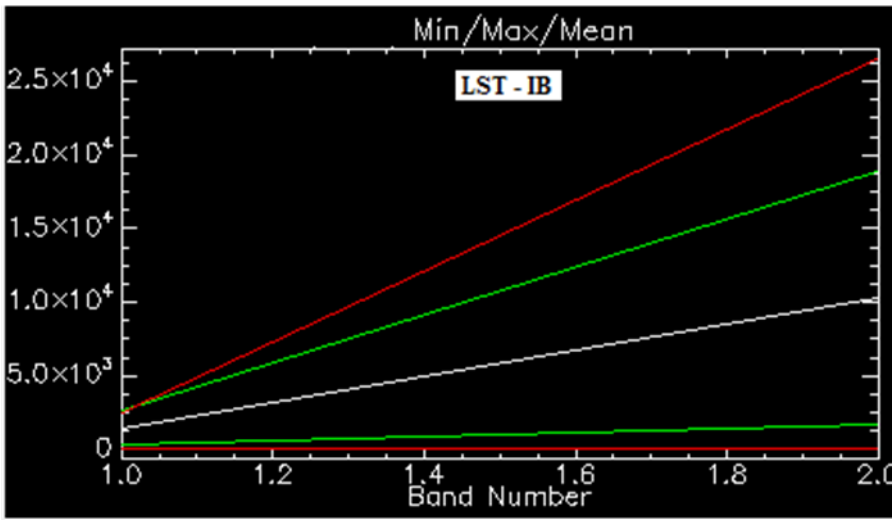


Fig. 7. Correlation between LST and IB.

Fig. 7 illustrates the correlation result for the year 2023 image as an example, showing a significant link between LST and IB of 0.96, especially in areas with low vegetation cover, soil, and sand, which provides optimal conditions for sand migration.

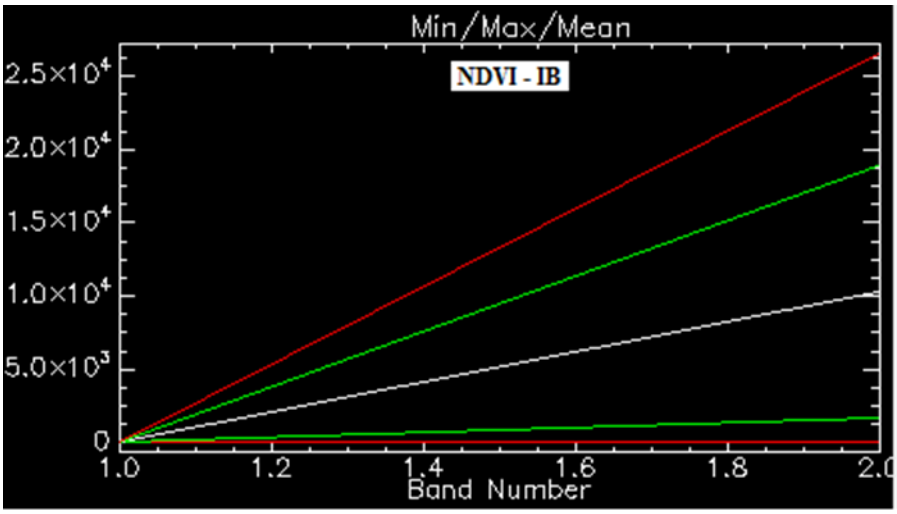


Fig. 8. Correlation between NDVI and IB.

The analysis of 2 bands of NDVI and IB shows that there is a strong negative correlation of -0.83 between these bands (Fig. 8), which explains the dominance of vegetation cover with low chlorophyll activity, as well as the large spaces occupied by the soil and the salty sands that have a high brightness value.

The analysis of remote sensing data (NDVI, LST, and IB) through the GIS for this study allows to conclude that the Draa area is characterized by a dominance of bare soil, sand, low vegetation cover, and high-temperature values.

These resource distributions create favorable conditions for desertification and silting, and have a negative influence on the Draa oasis.

Conclusion

With the increasing frequency of recurrent droughts and growing demographic pressure, it is crucial to monitor the natural resources of the Draa region for sustainable and rational

management. In this context, remote sensing serves as a powerful tool for data collection, resource monitoring, and decision-making in long-term environmental management.

This study employed diachronic analysis using Landsat ETM+ (2001) and Landsat 9 OLI/TIRS (2023) imagery to assess land-use changes over 22 years. The results reveal a 43.46% decline in vegetation cover and a 19.1% increase in sand migration, highlighting the expansion of desertification. These findings underscore the importance of integrating Geographic Information Systems (GIS) for a more detailed analysis of spatial and temporal changes.

The study further confirms the vulnerability of the oasis ecosystem to climate change, where reduced rainfall and prolonged dry periods significantly impact both agricultural productivity and sand encroachment. While Landsat imagery provides valuable insights for land cover mapping and decision-making, the use of Sentinel-2 images (not available for the year 2001) with a higher spatial resolution (<10 m) and free accessibility could enhance classification accuracy. However, given the study's objective of analyzing long-term changes, Landsat data remain indispensable for historical assessments (Sekertekin et al., 2017).

While remote sensing is undeniably a powerful tool for large-scale environmental monitoring, it is important to recognize that its effective use depends on the context, resources, and technical expertise available. Remote sensing excels in applications like urban planning and environmental monitoring, offering large-scale insights and enabling efficient data collection over time. However, it can be more challenging to adopt for small-scale projects or in resource-constrained settings, where high costs and specialized technical expertise may limit its effectiveness. In such cases, improving the accessibility of remote sensing tools such as using freely available Sentinel-2 imagery, can help overcome these challenges, especially for smaller-scale studies in developing regions.

Future research should explore a comparative study of optical and radar remote sensing for land use and land cover mapping in the Draa region, where such analyses remain limited (Wang et al., 2012). This approach could improve classification accuracy and provide deeper insights into environmental changes in arid regions. By balancing the advantages of remote sensing with its limitations, future studies can maximize its potential while addressing resource constraints and ensuring its effective use in different contexts.

Acknowledgements

The authors would like to acknowledge the insightful study on the topic of desertification. Their thorough investigation into the factors contributing to desertification in the Draa region has shed light on the complex interactions between climate change, human activities, and ecological resilience.

The findings presented in their study highlight the urgent need for sustainable land management practices and effective policy interventions to mitigate the adverse effects of desertification. By identifying key indicators and mapping vulnerable areas, their research provides a valuable foundation for developing targeted strategies to conserve and restore ecosystems affected by desertification.

Conflict of Interest

The authors declare that there are no conflicts of interest regarding the publication of this manuscript

References

Ahmed, B.K., 2022. Using Remote Sensing and Geographic Information Systems to Study the Change Detection in Temperature and Surface Area of Hamrin Lake. Baghdad Science Journal. 19(5): pp. 1130-1139.

Al-Zahraa, A.M., Monim, H.J. and Yaseen, K.T., 2021. Investigating the Aerodynamic Surface Roughness Length over Baghdad City Utilizing Remote Sensing and GIS Techniques. Baghdad Science Journal. Vol. 18, No.2, pp. 1048-1055.

Bachir Bouidjra, S.E. and El Zerey, W., 2014. The use of multi sources data for mapping of sensitive areas to hydrous erosion in the mountains of Tessala (Northern Algeria). *International Journal of Environment*, 3, 3, 321-331.

Baker, M.R. and Williams, M.O., 2014. High-resolution panchromatic image fusion with multi-spectral bands: A case study using Landsat data. Geoscience and Remote Sensing, IEEE Transactions on, 52(12), pp. 8067-8075.

Ben salem, A. and El Filali, A. El., 2024. Addressing Climate Change and Building Resilience in the Draa-Tafilalet Region.

Bildgen, P., Gilg, J.P., Boulegue, J. and Mabrukt, K., 1990. Use of MSS TM and SPOT spectral data expressed in exo-atmospheric reflectance values for the diachronic study of the evolution of soils, mining areas or vegetation cover. Second Bondy Remote Sensing Day, Paris December 4-6, 7 P.

Congalton, R.G., 1991. A review of assessing the accuracy of classifications of remotely sensed data. Remote Sensing of Environment, 37(1), pp. 35-46. A review of assessing the accuracy of classifications of remotely sensed data - ScienceDirect

Coude-Gaussen and Rognon, P., 1993. Seminar courses in Médenine (Tunisia) and Agadir (Morocco). Désertification et aménagement au Maghreb. Désertification et aménagement au Maghreb | WorldCat.org

Desjardins, R., 2005. Monitoring desertification in Morocco from NOAA AVHRR images, Lausanne, University Agency of the Francophonie, 2000, 171 P.

Ghobadi, Y., Pradhan, B., Kabiri, K., Pirasteh, S., Shafri, H.Z.M. and Sayyad, G.A., 2012. Use of Multi-Temporal Remote Sensing Data and GIS for Wetland Change Monitoring and Degradation, IEEE Colloquium on Humanities, Science and Engineering Research (CHUSER 2012), December 3-4, 2012, Kota Kinabalu, Sabah, Malaysia.

Gore, A.T. and Hu, J., 2012. Google Earth: A virtual globe for Earth observation and mapping. International Journal of Remote Sensing, 33(19), pp. 5850-5863.

High Commission for Water and Forests and the Fight Against Desertification (HCEFLCD). 2023. Climatic data for Zagora region. Available from: http://www.eauxetforets.gov.ma/SitePages/Index.aspx

Jemberie, M., Gebrie, T., Gebremariam, B., 2016. Evaluation of land use land cover change on stream flow: a case study of Dedissa sub basin, Abay basin, South Western Ethiopia. *Evaluation IJIERT* 3: pp. 44-60.

Jensen, J.R., 2007. Remote Sensing of the Environment: An Earth Resource Perspective (2nd ed.). Pearson Prentice Hall.

Jensen, J.R., 2016. Introductory Digital Image Processing: A Remote Sensing Perspective (4th Ed.). Pearson. Introductory Digital Image Processing: A Remote Sensing Perspective

Karmouji, A., Ben Salem, A., El Jaafari, S., Chaachouay, H., Moumane, A. and Hajji, L., 2022. Exploring the land use and land cover change in the period 2005–2020 in the province of Errachidia, the pre-sahara of Morocco. https://DOI: 10.3389/feart.2022.962097

Karnieli, A., Gabai, A., Ichoku, C., Zaady, E. and Shachak, M., 2002. Temporal dynamics of soil and vegetation spectral responses in a semi-arid environment. *International Journal of Remote Sensing*. 23(19): pp. 4073–4087. (PDF) Temporal dynamics of soil and vegetation spectral responses in a semi-arid environment (researchgate.net)

Kieffer, E. and Serradj, A., 2013. Remote sensing in the service of urban studies: expansion of the city of Pondicherry between 1973 and 2009. Géomatique Expert, No. 95, pp. 68-79. geo95_pp68-79.pdf (geomag.fr)

Lemsanni, A., 1999. Monitoring desertification in Morocco using NOAA AVHRR images , : Remote sensing in 297 French-speaking countries : critical analysis and outlook, scientific news, Lausanne, French-speaking University Agency, 2000, pp. 171-176. Lamsanni A., 2000, Suivi de la désertification... - Google Scholar

Li, L., Lu, D. and Kuang, W., 2016. Examining Urban Impervious Surface Distribution and its Dynamic Change in Hangzhou Metropolis. Remote Sens-Basel 8(3). Remote Sensing | Free Full-Text | Examining Urban Impervious Surface Distribution and Its Dynamic Change in Hangzhou Metropolis (mdpi.com)

Lillesand, T., Kiefer, R.W. and Chipman, J., 2015. Remote Sensing and Image Interpretation (7th Ed.). Wiley. Remote Sensing and Image Interpretation - Thomas Lillesand, Ralph W. Kiefer, Jonathan Chipman - Google Livres

Moutaz, A.D. and Hussain, Z.A., 2016. Geomorphological Mapping of Razzaza–Habbaria Area using Remote Sensing Techniques. Baghdad Science Journal. 13(1), pp. 155-166. View of Geomorphological Mapping of Razzaza–Habbaria Area using Remote Sensing Techniques (uobaghdad.edu.iq)

Oussedik, A., Iftene and T. and Zegrar, A., 2003. Realization by remote sensing of the Algerian desertification sensitivity map, Sécheresse, 14, 3, pp. 195-201. Réalisation par télédétection de la carte d'Algérie de sensibilité à la désertification* | Semantic Scholar

Pal, M., 2005. Random forest classifier for remote sensing classification. *International Journal of Remote Sensing*, 26 :1, pp. 217-222. https://doi.org/10.1080/01431160412331269698.

Prakasam, C., 2010. Land use and land cover change detection through remote sensing approach: A case study of Kodaikanal Taluk, Tamil Nadu, India. International Journal of Geomatics and Geosciences 1: 150. Land use and land cover change detection through remote sensing approach: Acass study of Kodaikanal taluk, Tamil nadu | Request PDF (researchgate.net)

Roy, D.P., Boschetti, L. and Ju, J., 2016. Landsat-8: Science and product vision for the future. Remote Sensing of Environment, 185, pp. 17-23. Landsat-8: Science and product vision for terrestrial global change research - ScienceDirect

Sefiani, M. and Kettab, M., 2018. The Draa River Basin: A geographical overview. Journal of Arid Land Studies, 28(2), pp. 99-110.

Sekertekin, A., Marangoz, A.M. and Akcin, H., 2017. Pixel-based classification analysis of land use land cover using Sentinel-2 and Landsat-8 data. The International Archives of the Photogrammetry, Remote Sensing and Spatial Information Sciences, Volume XLII-4/W6, *4th International GeoAdvances Workshop*, 14–15 October 2017, Safranbolu, Karabuk, Turkey. isprs-archives-XLII-4-W6-91-2017.pdf (copernicus.org)

Teferi, E., Uhlenbrook, S., Bewket, W., Wenninger, J. and Simane, B., 2010. The use of remote sensing to quantify wetland loss in the Choke Mountain range, Upper Blue Nile basin, Ethiopia, Hydrol. Earth Syst. Sci., 14, pp. 2415–2428, *www.hydrol-earth-syst-sci.net*/14/2415/2010/.https://doi.org/10.5194/hess-14-2415-2010

U.S. Geological Survey (USGS), 2023. Landsat satellite imagery [Data set]. U.S. Department of the Interior. Available from: https//earthexplorer.usgs.gov/

Wan, Z. and Li, Z.L., 1997. A physics-based algorithm for retrieving land-surface emissivity and temperature from EOS/MODIS data, IEEE Transactions on Geoscience and Remote Sensing, 35, pp. 980-996. A physics-based algorithm for retrieving land-surface

emissivity and temperature from EOS/MODIS data | IEEE Journals and Magazine | IEEE Xplore

Wang, D., Morton, D., Masek, J., Wu, A., Nagol, J. and Xiong, X., 2012. Impact of sensor degradation on the MODIS NDVI time series. Remote Sensing of Environment 119: pp. 55-61. Impact of sensor degradation on the MODIS NDVI time series - ScienceDirect

Wang, T. and Liu, S., 2013. Regionalization for Regulating Oasification and Desertification in the Arid Regions of China: A Program. J. Desert Res, 8, pp. 959–966. Regionalization for Regulating Oasification and Desertification in the Arid Regions of China: A program | Semantic Scholar

Yu, Y., Notaro, M., Wang, F., Mao, J., Shi, X. and Wei, Y., 2017. Observed positive vegetation-rainfall feedbacks in the Sahel dominated by a moisture recycling mechanism. *Nature Communications* 8: 1873. Observed positive vegetation-rainfall feedbacks in the Sahel dominated by a moisture recycling mechanism | Nature Communications

Zhou, D., Zhao, X., Hu, H., Shen, H. and Fang, J., 2015. Long-term vegetation changes in the four mega-sandy lands in Inner Mongolia, China. Landsc. Ecol. 13, pp. 1613–1626. (PDF) Spatial–temporal variations of NDVI and its response to climate in China from 2001 to 2020 (researchgate.net)

Iraqi National Journal of Earth Science

www.earth.uomosul.edu.iq

Rooftop Rainwater Harvesting for Mosul City as Water Resources Using GIS

Mohammed Muwafaq Yahya [1*], Mohamed H. Alsalmani [2], Qusai Y. AL-Kubaisi [3]

[1] *Department of Geology and Petroleum, College of Science, University of Mosul, Mosul, Iraq.*

[2] *Education Directorate of Al-Anbar, Ministry of Education, Iraq.*

[3] *Department of Geology, College of Science, University of Baghdad, Baghdad, Iraq.*

Article information

Received: 18- Sep -2024

Revised: 15- Jan -2025

Accepted: 16- Mar -2025

Available online: 01- Jan – 2026

Keywords:
Harvesting,
Roofs,
Rainwater,
Precipitation,

Correspondence:
Name: Mohammed Muwafaq Yahya
Email: mohmed.m.m@uomosul.edu.iq

ABSTRACT

The collection of rainwater from rooftops is a sustainable and widely practiced technique in many countries. This approach is designed to capture rainwater from building roofs, enabling its storage and efficient use to address water scarcity in urban areas. In this study, Mosul is chosen as a case study for rooftop rainwater harvesting. An analysis of the city's climate over 30 years (1984–2014) shows that the average annual precipitation was 352.1 mm. Using advanced software, the total rooftop area in the city is determined to be 63.292 Km², providing an accurate measure of the potential collection area during the rainy season. To estimate the rainwater harvesting potential, the Gould and Nissen formula was applied. The calculation reveals that rooftops in the study area could collect approximately 21.170×10^9 liters of water annually. This corresponds to an estimated 39.42 liters per capita per day, which meets international standards. According to these standards, a daily per capita allocation of 20 liters is considered adequate to meet basic human water needs.

DOI: 10.33899/injes.v26i1.60208, ©Authors, 2026, College of Science, University of Mosul.
This is an open-access article under the CC BY 4.0 license (http://creativecommons.org/licenses/by/4.0/).

تقييم إمكانية حصاد مياه الأمطار من أسطح المنازل في مدينة الموصل باستخدام تطبيقات نظم المعلومات الجغرافية

محمد موفق يحيى [1*]، محمد حسين السلماني [2]، قصي يوسف الكبيسي [3]

[1] *قسم علوم الأرض والنفط، كلية العلوم، جامعة الموصل، الموصل، العراق.*

[2] *مديرية تربية الانبار، وزارة التربية، العراق.*

[3] *قسم علوم الأرض، كلية العلوم، جامعة بغداد، بغداد، العراق.*

معلومات الارشفة

تاريخ الاستلام: 18– سبتمبر –2024

تاريخ المراجعة: 15– يناير –2025

تاريخ القبول: 16– مارس –2025

تاريخ النشر الالكتروني: 01– يناير –2026

الكلمات المفتاحية:

حصاد

أسطح

مياه الأمطار

هطول الأمطار

المراسلة:

الاسم: محمد موفق يحيى

Email: mohmed.m.m@uomosul.edu.iq

الملخص

يُعَدُّ جمع مياه الأمطار من أسطح المباني تقنية مستدامة تُطبَّق على نطاق واسع في العديد من دول العالم، إذ تهدف هذه الطريقة إلى استغلال مياه الأمطار المتساقطة على الأسطح من خلال تخزينها واستخدامها بكفاءة لمعالجة مشكلات شح المياه في المناطق الحضرية. في هذه الدراسة، تم اختيار مدينة الموصل كحالة تطبيقية لنظام حصاد مياه الأمطار من الأسطح. أظهر تحليل المناخ في المدينة خلال فترة ثلاثين عامًا (1984–2014) أن متوسط الهطول السنوي بلغ 352.1 ملم. وبالاعتماد على برامج تحليل متقدمة، تم حساب المساحة الإجمالية لأسطح المباني بدقة لتبلغ 63.292 كم²، وهو ما يمثل المساحة الممكن الاستفادة منها خلال موسم الأمطار. ولتقدير إمكانات حصاد المياه، تم استخدام طريقة Gould and Nissen. وقد بينت النتائج أن أسطح المباني في منطقة الدراسة يمكن أن تجمع نحو 21.170×10^9 لتر من المياه سنويًا، أي ما يعادل 39.42 لترًا للفرد يوميًا، وهو معدل يتماشى مع المعايير الدولية التي تعتبر أن توفير 20 لترًا يوميًا للفرد كافٍ لتغطية الاحتياجات الأساسية من المياه.

DOI: 10.33899/injes.v26i1.60208, ©Authors, 2026, College of Science, University of Mosul.
This is an open-access article under the CC BY 4.0 license (http://creativecommons.org/licenses/by/4.0/).

Introduction

The world's population is growing, cities are growing, and more water is needed to meet their demands. especially cities that lack groundwater or surface water. Rainwater harvesting is a method for gathering, storing, and utilizing rainwater for irrigation, groundwater recharge, household water supply, and other uses (Singh and Devi, 2017). The harvesting process for rainwater and surface runoff is one of the most important aspects of investment that can correspond to the climatic conditions and the nature of the studied area (Al-Kubaisi and Al-Kubaisi, 2023).

The relationship between precipitation intensity and surface temperature has emerged in response to the growing worry over human-induced global warming (Al-Sekar and Al-Dabbas, 2022). Freshwater reserves worldwide are drying out, especially in developing countries, due to population growth, urbanization, changes in land use, and climate change (Khatri et al., 2008).

The Tigris River, dividing Mosul City into two halves, relies to a significant extent on water originating from northern Iraq. This water primarily comes from rainfall and melting snow, which are essential for recharging groundwater. Consequently, rainfall in Mosul serves as a secondary water source. Therefore, future strategies must focus on maximizing the

utilization of rainwater that falls within the city's boundaries by capturing and storing it instead of allowing it to evaporate from solid surfaces. This captured rainwater can act as a supplementary resource to the city's primary water supply.

To achieve this, it is crucial to study and evaluate the rainfall on urban rooftops using specific methodologies aligned with practical and effective water management strategies. Water availability has been significantly affected, particularly in arid and semi-arid regions, due to the overexploitation of various water resources, which has, in turn, heightened the demand for sustainable water solutions (Jones et al., 2009).

Rainwater harvesting, an ancient practice rooted in the traditions of early civilizations, aims to make optimal use of rainfall by capturing it where it falls and preventing it from draining away. Given the favorable properties and intrinsic quality of rainwater, this traditional method has gained renewed importance in modern times (Dwivedi and Bhadauria, 2006).

The collection of rainwater from rooftops aims to meet the growing demand for water due to population increases and to calculate the potential volume of water that can be harvested annually. This approach helps alleviate the strain on drainage systems during periods of heavy rainfall, thereby minimizing urban flooding. Furthermore, it offers the possibility of directing collected rainwater towards replenishing groundwater reserves. An additional benefit includes the purification of rainwater from contaminants, making it suitable for agricultural and industrial applications.

Study area

Mosul City is the center of the Nineveh Governorate and a significant city in northern Iraq. After the capital Baghdad, the city is regarded as the second-largest in terms of population.

The study area is located between longitudes 43°14′57.573″ E and 43°02′43.102″ E and latitudes 36°24′57.109″ N and 36°16′42.038″ N. The area of Nineveh Governorate is estimated at 37,303 Km². In comparison, the area of the city of Mosul is estimated at 743.6 Km² according to the Ministry of Planning report in 2021 (Spatial Development Gaps Report, Nineveh Governorate, 2021) (Fig. 1).

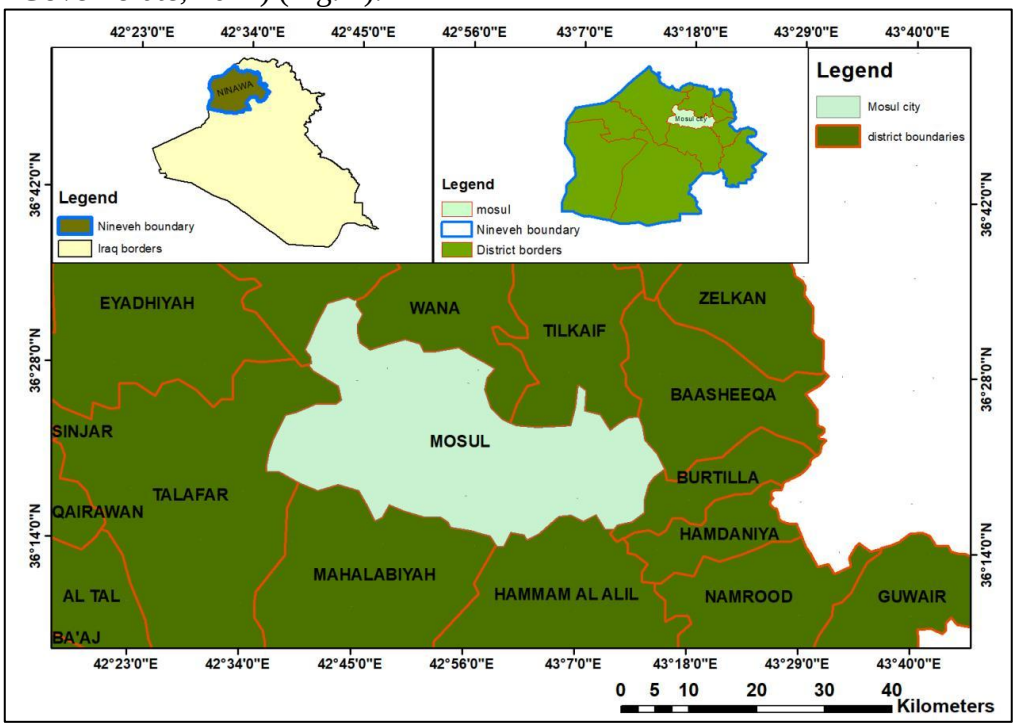


Fig. 1. Location of the study area.

Based on the research, the percentages of land use in the city of Mosul show that the rate of residential land use reaches about 34.5%, which amounts to approximately 93.4 km² according to the Urban Planning Directorate of Nineveh Governorate and the basic design for the city of Mosul for the year 2021 (Al-Qaba, 2022).

Materials and Methods

Data Collection

Climatic data are one of the important and main factors on which research is based in achieving its results, and the Mosul station is used for this purpose. The climatic factors and their effects on the study area between 1984 and 2014 are investigated. It is important to note that the recording of the climate data in the study area has problems because of battles that happened from 2014 to 2017, which caused a pause in the collection of climate data.

Summers in Mosul are hot and dry, and winters there are cold with rare frost, according to meteorological data that covered the years 1984-2014, the total annual precipitation was 352.1 mm, the relative humidity was 51.4%, the monthly average temperature was 20.47 °C, the evaporation was 173.6 mm, the wind speed was 1.1 m/s, and the sunlight duration was 8.3 hours per day (Fig. 2).

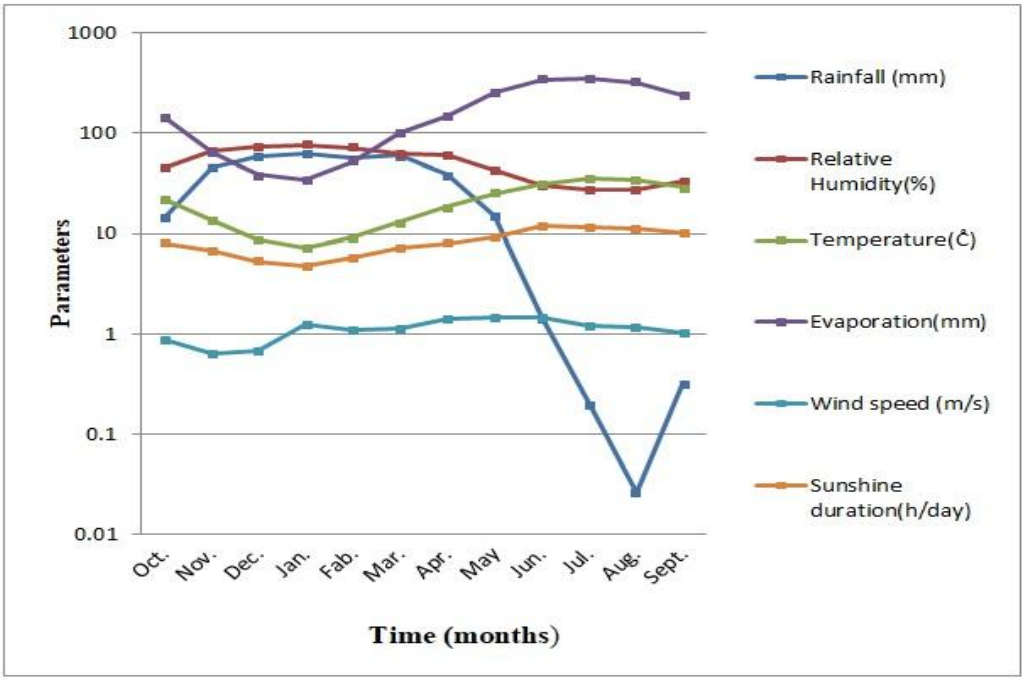


Fig. 2. Relations between various climate elements in the study area for a period of 1984-2014.

The process of collecting data in a large and wide city such as Mosul City is considered a very difficult process, especially since there are no accurate statistics for the roof areas of buildings and unbuilt areas. Therefore, in the process of data collection, it is required to draw the boundaries of all buildings within the city by using satellite visuals of the city and drawing on them. The analysis is conducted using ArcGIS 10.4 software. (Fig. 3).

After drawing the boundaries of the roofs of the buildings, it is found through some software operations that the area of all these roofs is 63.292 Km². This area is the total of the roofs that can be considered areas for collecting water from rain in the rainy season (Figs. 4, 5).

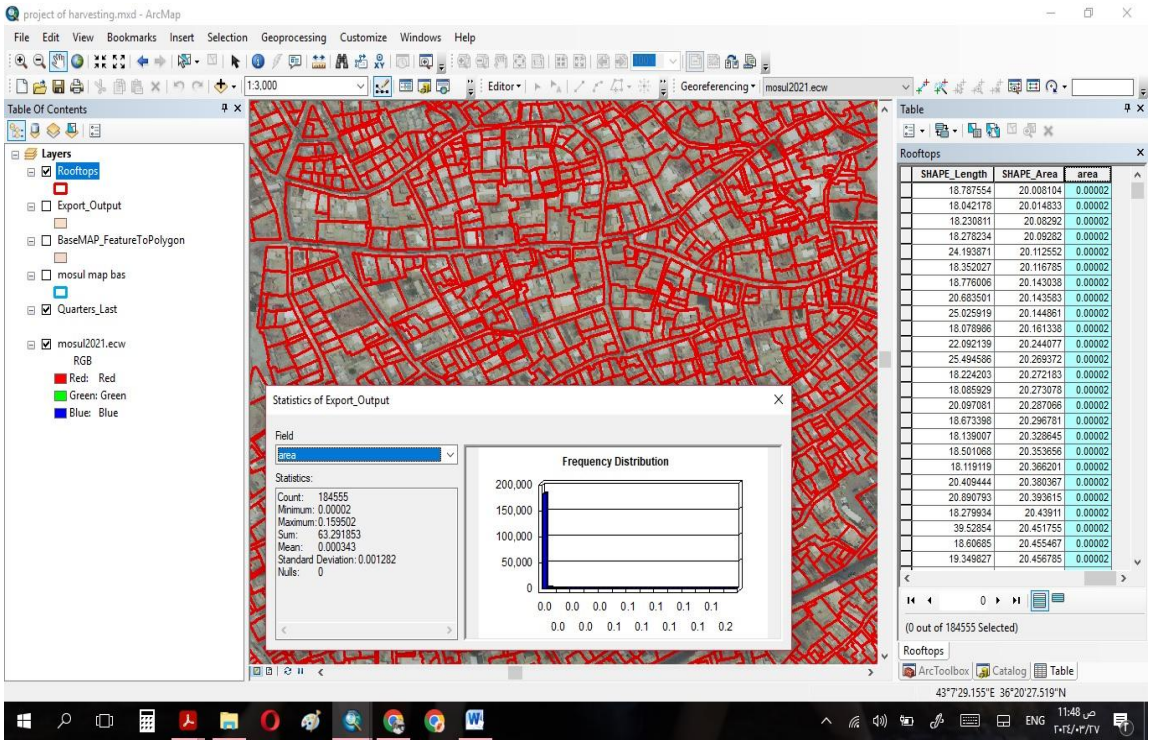


Fig. 3. Shapefiles of Mosul City in ArcGIS.

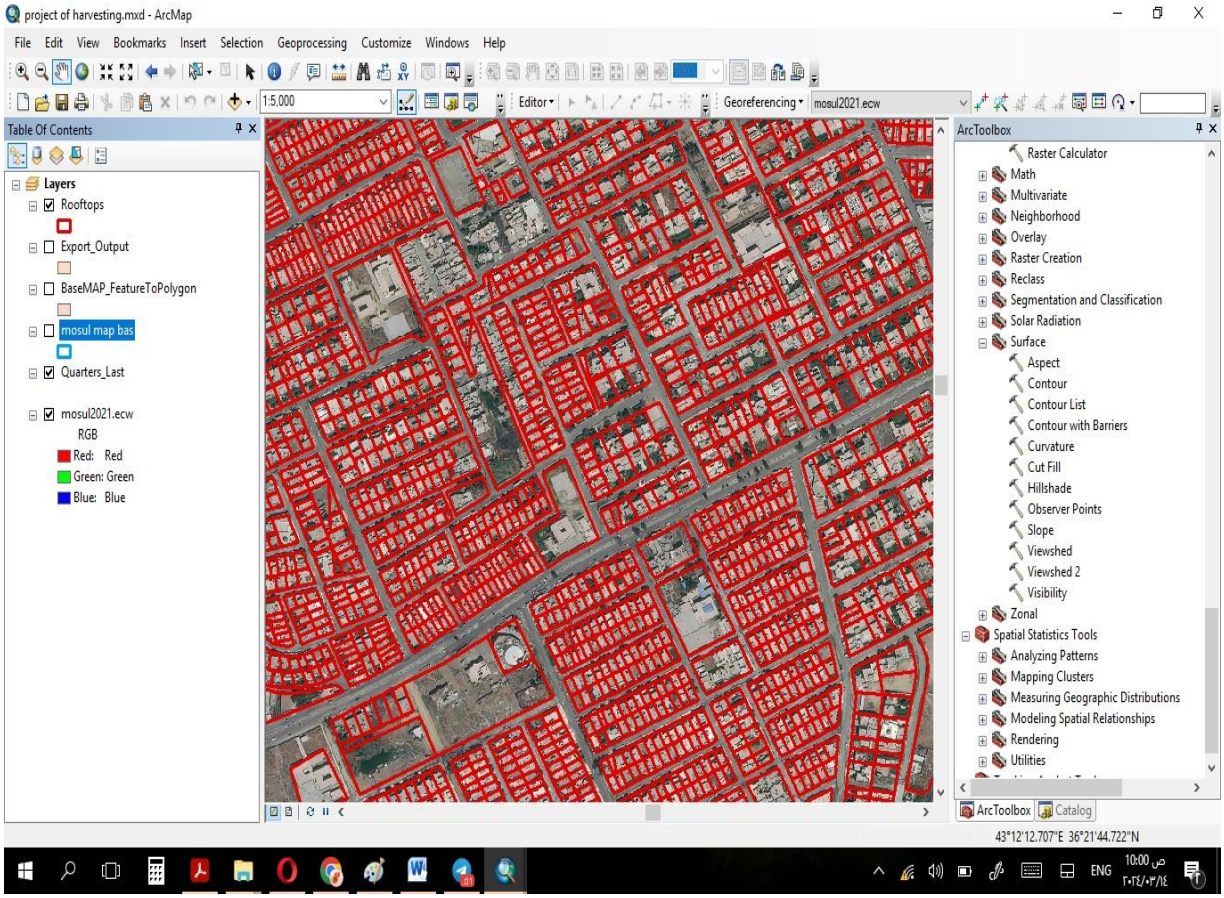


Fig. 4. Digitizing the rooftop of the building to calculate the area in GIS.

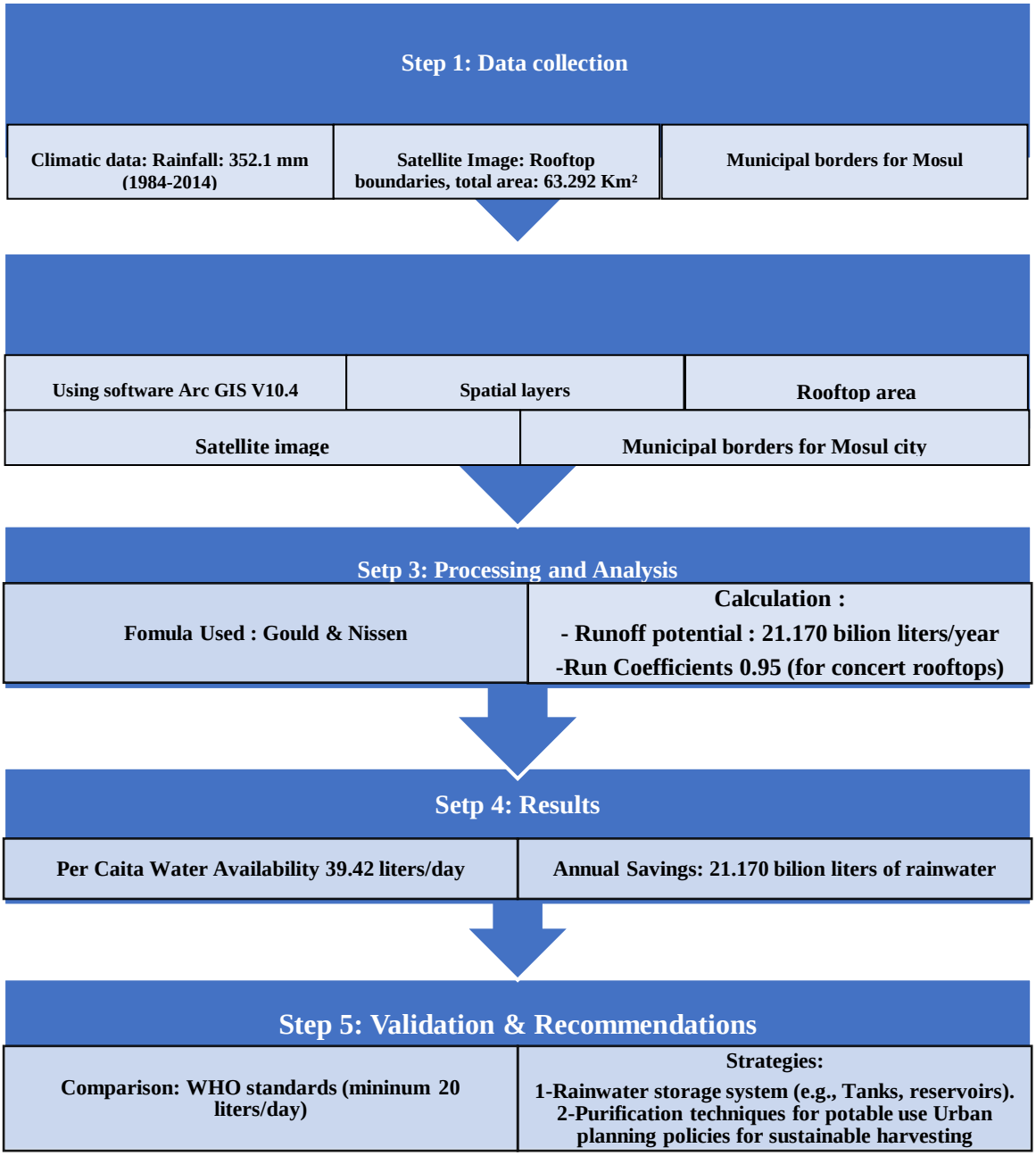


Fig. 5. Flowchart for the steps of rooftop rainwater harvesting for Mosul City.

Results

Evaluation of the potential of harvesting rainwater

The Gould and Nissen Formula (1999) is used to determine the potential of the study area's rooftops for rainwater harvesting :

$$S = R*A*Cr \qquad \text{(Hari, 2019) ……. (1)}$$

Where:

S = Potential of roof rainwater harvesting (In cu. m); R = Average annual rainfall in m. A = Roof area in Sq. m. Cr = Coefficient of Runoff

Coefficient of runoff (Cr)

The proportion of water that runs off to the total amount of rain that falls on the rooftop is known as the Coefficient of Rooftop (Cr) for any catchment. The potential for collecting rainwater from rooftops is determined by different sorts of runoff coefficients, which depend on the surface type (Table 1) (Hari et al., 2018).

Table 1: Potential rooftop rainwater harvesting in Mosul City.

Type of Roof	Area (m²)	Runoff Coefficients	Annual Rainfall in (mm)	(S=R*A*Cr) Runoff (cu. m)	(S=R*A*Cr) Runoff (liters)
Concrete Roof	63,292	0.95	352.1	21,170,857.54	21,170,857,540

Quantity of water requirement

The process of determining the amount of water required for human consumption in any city is determined by many criteria. Therefore, some researchers suggested, based on these criteria, that the amount of water required per person per day be 15 liters, if this amount is considered a major indicator of meeting the minimum standards of disaster relief (Howard et al., 2003)

The Department of International Development (United Kingdom) also prepared a guideline in which Well (1998) mentioned that the minimum needed amount of water per person is 20 liters per day.

From the aforementioned, it can be concluded that the least amount of water a person can need in the city of Mosul is 20 liters per day in harsh conditions to cover drinking and household activities. According to a report issued by the Nineveh Governorate's Statistics Directorate, the population of Mosul District was 1,471,353 in 2021 (Al-Qaba, 2022).

Water per capita

According to the data obtained from the foregoing, the per capita share of water per day collected from rooftop Rainwater harvesting is:

$$Per - Capita\ demand = \frac{Value\ of\ roof\ rainwater\ harvesting}{number\ of\ population\ of\ Mosul\ city} \ldots\ldots\ldots (2)$$

$$\text{Per} - \text{Capita demand} = 14388.7 \text{ Liters annually for every person}$$

$$\text{Per} - \text{Capita demand} = 14388.7 \div 365 = 39.42 \text{ Liters per day per person}$$

Discussion

Domestic Water Requirements and the Potential of Rooftop Rainwater Harvesting

This section examines the domestic water requirements in the study area and evaluates the potential for water savings and storage through the implementation of rooftop rainwater harvesting (RRWH). Additionally, it analyzes the disparity between per capita water availability in the study area and the World Health Organization's (WHO) recommended minimum water requirement.

Rainwater collected from rooftops in Kathmandu’s urban districts is primarily used for non-potable purposes, such as cleaning, laundry, and toilet flushing. According to survey findings (Mishra and Dev, 2021), none of the respondents reported using harvested rainwater for drinking due to a lack of awareness regarding filtration and purification methods. This

presents a significant opportunity to enhance the usability of RRWH through the integration of accessible and cost-effective water treatment systems.

Domestic Water Availability and Requirements

The study determined that per capita domestic water availability from RRWH reached 39.42 liters per day, which is 19.42 liters higher than the WHO's recommended minimum of 20 liters per day for survival. This substantial difference indicates that even if harvested rainwater availability were reduced by half, it would still meet the WHO's survival threshold.

Given that the average urban domestic water demand ranges between 50 and 100 liters per person per day, these findings suggest that RRWH can serve as a valuable supplementary source to conventional water supplies, thereby reducing dependence on surface and groundwater resources. Furthermore, with the incorporation of appropriate filtration systems, harvested rainwater could be safely utilized for potable purposes, further bridging the gap between demand and availability.

Water Savings and Storage Potential

The study's findings highlight the potential for water savings and long-term storage through RRWH:

• Daily Water Collection per Household: With an average of 39.42 liters per person, a household of five could collect approximately 197 liters per day.

• Annual Storage Potential: Assuming a rainy season of four months, the total harvested rainwater per household could reach approximately 23,640 liters, which could be stored for use during the dry season.

Although comprehensive climate data from 2014 to 2023 is unavailable, anecdotal evidence suggests that these years experienced drier conditions compared to previous decades. This further underscores the importance of rainwater harvesting as a supplementary water resource. Implementing effective storage solutions, such as rooftop tanks or underground reservoirs, can enable surplus water collection during the rainy season, enhancing water security in drier months.

Future Considerations and Policy Implications

The study emphasizes the critical role of RRWH in addressing domestic water scarcity, particularly in urban regions with limited access to conventional water sources, such as Kathmandu and similar arid regions, including Iraq. To maximize the effectiveness of RRWH, the following measures should be prioritized:

•Public Awareness and Education: Conducting community-based awareness programs to educate residents about water filtration, purification, and safe reuse of harvested rainwater.

•Investment in Storage Infrastructure: Expanding access to high-capacity storage tanks and underground reservoirs to preserve harvested rainwater for dry seasons.

•Policy Integration and Urban Water Management: Incorporating RRWH into national and municipal water management strategies as a sustainable, cost-effective, and reliable alternative water source.

By implementing these recommendations, RRWH can play a pivotal role in enhancing urban water resilience, reducing over-reliance on groundwater and municipal supplies, and mitigating the impacts of climate variability on water availability.

Although climate data from 2014 to 2023 is unavailable, anecdotal evidence suggests these years were drier than previous periods. This further emphasizes the importance of rainwater harvesting as a supplementary water source. By adopting effective storage

solutions, such as rooftop tanks or underground reservoirs, surplus water collected during the rainy season can be preserved for future use, enhancing water security during drier months.

Future Considerations

The study underscores the crucial role of rooftop rainwater harvesting in meeting domestic water needs, particularly in water-scarce regions like Kathmandu and similar areas, including Iraq. To maximize the benefits of this system, the following measures should be considered:

- *Public Awareness Campaigns*: Educating communities about rainwater filtration methods and safe reuse.
- *Investment in Storage Infrastructure*: Prioritizing the construction of tanks and reservoirs.
- *Policy Integration*: Incorporating rainwater harvesting into urban water management strategies as a sustainable and reliable resource.

Conclusions

1. The results of the study indicate that rooftop rainwater harvesting in Mosul City is a sustainable and effective solution for meeting the basic water needs of the population, as the collected water exceeds the minimum amount recommended by the World Health Organization.
2. Rainwater harvesting serves as a supplementary water source, helping to reduce pressure on traditional water resources, especially during periods of rainfall scarcity.
3. Proper storage systems for rainwater harvesting enhance the city's water security, particularly during dry periods, ensuring a reliable water supply when natural water sources are low.
4. It is essential to increase public awareness about the importance of rainwater harvesting systems and to develop technological solutions to ensure water treatment and make it suitable for various household purposes.
5. Rainwater harvesting should be integrated into future urban water management strategies, with improved infrastructure for water storage and appropriate policies to ensure the long-term sustainability of the system.

Acknowledgments

Thanks to God, we dedicate this research to academics and researchers. As well as we are grateful to the Iraqi Meteorological and Seismological Authority for providing us with climate data. We would also like to express our gratitude to Engineer Ahmed Nazim of the Nineveh Planning Directorate.

Reference

Al-Kubaisi, M.H. and Al-Kubaisi, Q.Y., 2023. Selection of dam sites for rainwater harvesting in western desert of Iraq: A case study in Wadi Al-Mohammadi Basin. The Iraqi Geological Journal, 56(1F), pp. 38–50. https://doi.org/10.46717/igj.56.1F.3ms-2023-6-11

Al-Qaba, A.H.A., 2022. Spatial-based analysis of Mosul Road network using artificial intelligence (Doctoral dissertation, University of Mosul, College of Humanities, Human Geography). https://iqdr.iq/search?view=4d44e90bd9d1fa

Al-Sekar, H.M. and Al-Dabbas, M., 2022. The influence of the Tigris River discharge on the hydrochemistry with time, from Baghdad to Amara, southern Iraq. Iraqi Journal of Science, 62(12), pp. 140–156. https://doi.org/10.24996/ijs.2021.62.12.13

Dwivedi, A.K. and Bhadauria, S.S., 2006. Domestic rooftop water harvesting: A case study. Ground Water, 4(6), pp. 31–38.

Great Britain. Department for International Development and WELL, 1998. Guidance manual on water supply and sanitation programmes. WEDC, Loughborough University.

Hari, D., 2019. Estimation of rooftop rainwater harvesting potential using applications of Google Earth Pro and GIS. International Journal of Innovative Technology and Exploring Engineering, 8(9), pp. 1122–1127. https://doi.org/10.35940/ijitee.I7853.078919

Hari, D., Reddy, K.R., Vikas, K., Srinivas, N. and Vikas, G., 2018. Assessment of rainwater harvesting potential using GIS. IOP Conference Series: Materials Science and Engineering, 330(1), 012119. https://doi.org/10.1088/1757-899X/330/1/012119

Howard, G., Bartram, J., Water, S. and World Health Organization, 2003. Domestic water quantity, service level and health. World Health Organization. https://iris.who.int/handle/10665/67884

Jones, A., Stolbovoy, V., Rusco, E., Gentile, A.R., Gardi, C., Marechal, B. and Montanarella, L., 2009. Climate change in Europe: Impact on soil—A review. Agronomy for Sustainable Development, 29(3), pp. 423–432. https://doi.org/10.1051/agro:2008067

Khatri, K., Vairavamoorthy, K. and Porto, M., 2008. Challenges for urban water supply and sanitation in developing countries. In J. Feyen, K. Shannon, and M. Neville (Eds.), Water for a changing world: Developing local knowledge and capacity, pp. 93–112. CRC Press. https://doi.org/10.1201/9780203878057.ch7

Mishra, K. and Joshi, G.D., 2021. Prospects of rooftop rainwater harvesting: A case from Nepal. Indo American Journal of Multidisciplinary Research and Review, 5(1). https://doi.org/10.5281/zenodo.4774881

Singh, L.K. and Devi, S.R., 2017. Rooftop rainwater harvesting for domestic water demand and supply management and designing of optimum rainwater harvesting structure in Imphal West District, Manipur. Indian Journal of Hill Farming, 29(2), pp. 153–159. https://epubs.icar.org.in/index.php/IJHF/article/view/66695

Nineveh Governorate Development Plans Series, 2021. Spatial development gaps report: Nineveh Governorate 2021.

Iraqi National Journal of Earth Science

www.earth.uomosul.edu.iq

Overpressure and Under-Compaction Mechanism Effect on Pore and Fracture Pressure Development of Mauddud Formation, Badra Oil Field, Eastern Iraq

Mohammed Almojahed Farooq Abdalla [1*], Nagham Jasim Al-Ameri [2]

[1,2] Petroleum Engineering Department, College of Engineering, University of Baghdad, Baghdad, Iraq.

Article information

Received: 01- Nov-2024

Revised: 30- Nov -2024

Accepted: 20- Dec -2024

Available online: 01- Jan -2026

Keywords:
Compaction Mechanism,
Overburden Pressure,
Pore Pressure,
Fracture Pressure,
Microfacies analysis,

Correspondence:
Name: Mohammed Almojahed Farooq Abdalla

Email: muhammed.farooq2208m@coeng.uobaghdad.edu.iq

ABSTRACT

Accurate pore and fracture pressure detection is a major step in successful drilling operations design. The overestimation of these parameters absolutely leads to serious problems throughout and after well drilling. This study is concerned with the characterization and analysis of the most significant diagenetic processes that degrade or improve the reservoir characteristics of the Mauddud Formation in the Badra oil field. The primary goal of this research is to estimate the pore pressure and fracture pressure using well logging data by Techlog 2015 software in order to assess the impact on the estimation of the mud weight window (MWW). The estimated values of formation pressures are then analyzed according to different diagenetic processes affecting the reservoir under study. These important reasons, such as sedimentary texture and original structure, have been analyzed in this study based on the images of both Scanning Electron Microscopy (SEM) and thin section (TS) of many samples taken at different depths of the studied reservoir to cover the vertical changes of the formation. The results show that the value of the safe mud weight window must range from 2.3 to 3.4 ppg, and it becomes narrower and more dangerous when the wells cross the edge of the anticline structure of the reservoir.

DOI: 10.33899/injes.v26i1.60209, ©Authors, 2026, College of Science, University of Mosul.
This is an open-access article under the CC BY 4.0 license (http://creativecommons.org/licenses/by/4.0/).

تأثير آلية الضغط الزائد ونقص الضغط على تطور ضغط المسام والكسر في تكوين مودود، حقل بدرة النفطي، شرق العراق

محمد المجاهد عبدالله [1*] ، نغم جاسم [2]

[2,1] قسم هندسة النفط، كلية الهندسة، جامعة بغداد، بغداد، العراق.

معلومات الارشفة

تاريخ الاستلام: 01- نوفمبر- 2024

تاريخ المراجعة: 30- نوفمبر- 2024

تاريخ القبول: 20- ديسمبر- 2024

تاريخ النشر الالكتروني: 01- يناير- 2026

الكلمات المفتاحية:

آلية الضغط،

الضغط الزائد،

ضغط المسام،

ضغط الكسر،

تحليل السحنات الدقيقة،

المراسلة:

الاسم: محمد المجاهد عبدالله

Email: muhammed.farooq2208m@coeng.uobaghdad.edu.iq

الملخص

يعد الكشف الدقيق عن ضغط المسام والكسر خطوة رئيسة في تصميم عمليات الحفر الناجحة. إن المبالغة في تقدير هذه المتغيرات تؤدي بالتأكيد إلى مشاكل خطيرة أثناء حفر الآبار وبعدها. تهتم هذه الدراسة بتوصيف وتحليل أهم العمليات التحويرية التي تؤدي إلى تحلل أو تحسين الخصائص المكمنية لتكوين مودود في حقل بدرة النفطي. الهدف الأساس من هذا البحث هو تقدير ضغط المسام وضغط الكسر باستخدام بيانات تسجيل الآبار بواسطة برنامج (Techlog 2015) من أجل تقييم التأثير على تقدير نافذة وزن الطين (MWW). ومن ثم تم تحليل القيم المقدرة لضغوط التكوين وفقا لتأثيرات العمليات التحويرية المختلفة على المكمن قيد الدراسة. تم تحليل هذه الأسباب المهمة مثل النسيج الرسوبي والبنية الأصلية في هذه الدراسة بناءً على صور كل من المجهر الإلكتروني الماسح (SEM) والشرائح الصخرية الرقيقة (TS) للعديد من العينات المأخوذة من أعماق مختلفة من المكمن المدروس لتغطية التغييرات الرأسية للتكوين. وتبين النتائج أن قيمة نافذة وزن الطين الآمن (MWW) يجب أن تتراوح مابين 2.3 إلى 3.4 باوند لكل غالون، وتصبح هذه القيمة ضيقة وأكثر خطورة عندما تقترب الآبار من حافة هيكل طية التكوين.

DOI: 10.33899/injes.v26i1.60209, ©Authors, 2026, College of Science, University of Mosul.
This is an open-access article under the CC BY 4.0 license (http://creativecommons.org/licenses/by/4.0/).

Introduction

At a certain depth in a studied formation, the stress that actually affects is made up of vertical stress, maximum horizontal stress, and minimum horizontal stress. Pore pressure is the force that acts on liquids inside the pores of rocks. Pore pressure is an important part of the mechanical factors used in the drilling plan and geological and geomechanical studies to determine the horizontal stresses (Rasouli et al., 2011; Bandara and Al-Ameri, 2024). According to Aadnoy and Looyeh (2011). The rocks are porous materials with a rocky matrix and liquid. Not all formation stresses are carried by the rock matrix; some are carried by the fluids in the rock's pores (Aman et al., 2018). Hence, the effective stress is the percentage of stress that the rock matrix bears.

The diacritical pore pressure in shale formation may be determined using sonic and resistivity logs, as stated by Rasouli et al. (2011). Pore pressure is classified into three classes according to its magnitude, as mentioned by Zhang (2013), as follows: first, the normal pore pressure, which is the pressure generated by the fluid column from the formation's surface to the bottom. It varies due to the kind of fluid, temperature gradient, gases present, and dissolved solids content; therefore, it is not constant. Second, the abnormal pore pressure, which refers to pore pressure greater than the hydrostatic pressure of the formation. Abnormal pressure is

assumed to be caused by extranormal hydrostatic or increased pressure. Third, the subnormal pore pressure, in which the formation pressure for the stated depth is lower than the hydrostatic fluid pressure.

There are two methods for determining pore pressure (direct and indirect). In permeable formations, methods like Drill Stem Testing (DST), Repeated Formation Testing (RFT), and Modular Dynamic Formation Tester (MDT) can be used to determine the normal pore pressure of the formation (Najibi et al., 2005).

To estimate pore pressure from logs, geophysical measurement is used. This method is commonly used because the direct methods are costly, risky, time-consuming, and provide poor measurements in some intervals. Furthermore, direct methods cannot quantify pore pressure in shale (impermeable zone) or clay rocks (Aadnoy and Ong, 2003). Therefore, the geophysical measurement provides a continuous pore pressure profile along the interval of interest. To minimize suspicion, the determined pore pressure can be matched with the point of formation pressure, which is measured by a direct method, and then the profile is calibrated for direct pressure measurements to minimize suspicion in the determined pore pressure.

Formation breakdown pressure, as mentioned by Chen (2017), or fracture pressure, as mentioned by Aadnoy and Looyeh (2011), is required to cause rock fracture at a depth. The fracture pressure may be less than the minimum horizontal stress if the rocks already have pre-existing flaws (Chen, 2017). The maximum fracture pressure for unaffected rocks will occur following the initiation of a tensile failure and the occurrence of mud loss. When the tensile strength and the least hoop stress are equivalent, the fracture pressure can be determined using Kirsch's solution (Haimson and Fairhurst, 1969).

In the current study, four wells (A, B, C, and D), which are dispersed along the Badra oil field anticline structure, have been used to investigate different formation pressures, including overburden, pore, and fracture pressure, to estimate the safe mud weight window.

Geological Background

One of the major carbonate reservoirs found in the Arabian Plate region is present in the Mauddud Formation (Cross et al., 2010). Across the Arabian plate, the formation is thick and has a regional distribution (Sadooni and Alsharhan, 2003). Oil is produced from limestone units in the Badra oil field in eastern Iraq by the Mauddud Formation (Faisal and Mahdi, 2020b). Limestone with a thin coating of dolomite, stylolitic dolomite, and detrital and chalky limestone make up the Mauddud Formation in the Badra oil field. A wealth of fossils supports an Albian age. Initially, it was believed that the formation continued into the Cenomanian due to the frequent appearance of certain Orbitolina concave group species; the formation was deposited in a neritic, occasionally shoal environment (Ghafor et al., 2023).

The Mauddud Formation has a conformable and gradational lower contact with Nahr Umr, Lower Balambo, and Lower Sarmord formations. The top contact is characterized by a break and is either nonsequential or unconformable; it represents an unconformity in north central-, northern-, and northeastern Iraq (Jassim and Goff, 2006).

The Badra field is situated in eastern Iraq, as shown in Fig. 1A, close to the borders between Iraq and Iran. It lies between the Mesopotamian Zone (Tigris subzone) and the Foothill Zone (Himreen-Makhul subzone). The Mesopotamian zone is the easternmost unit of the Stable Shelf. The zone likely underwent uplift during the Hercynian deformation, but it declined in the Late Permian period. Beneath the Quaternary cover, the zone is made up of buried faulted structures that are divided by wide synclines. As illustrated in Fig. 1B, some NE-SW trending fold structures exist; in the eastern part of the zone, the fold structures mainly go NW-SE, while in the southern part, they trend N-S. (Jassim and Goff, 2006). The Tigris, Euphrates, and Zubair subzones are the three subzones that make up the Mesopotamian Zone.

The largest and most mobile Mesopotamian Zone unit is the Tigris Subzone. Long normal faults go alongside broad synclines and small anticlines that trend NW-SE. The zone has an EW transversal trend and two sets of low-amplitude, NW-SE trending buried anticlines linked to longitudinal faults (Faisal and Mahdi, 2020a).

This portion of the Unstable Shelf is called the Foothill Zone. The zone contains extremely thick Miocene-Pliocene molasses sediments (3 km thick) and the lowest Precambrian basement in Iraq (13 kilometers). The zone's two longitudinal components are the Makhul-Hemrin Subzone in the southwest and the Subzone Butmah-Chemhemal in the northeast. The Foothill Zone's structurally deepest area is the Makhul-Hemrin Subzone. Long, conspicuous NW-SE or E-W trending anticlines with decollement thrust faults make up the Subzone. The Subzone's anticlines extend more than 100 kilometers (Jassim and Goff, 2006). The Badra field structure is an asymmetrical NW-SE anticline trending, with a more gradual NE flank and a sharply descending SW flank (Kareem, 2020).

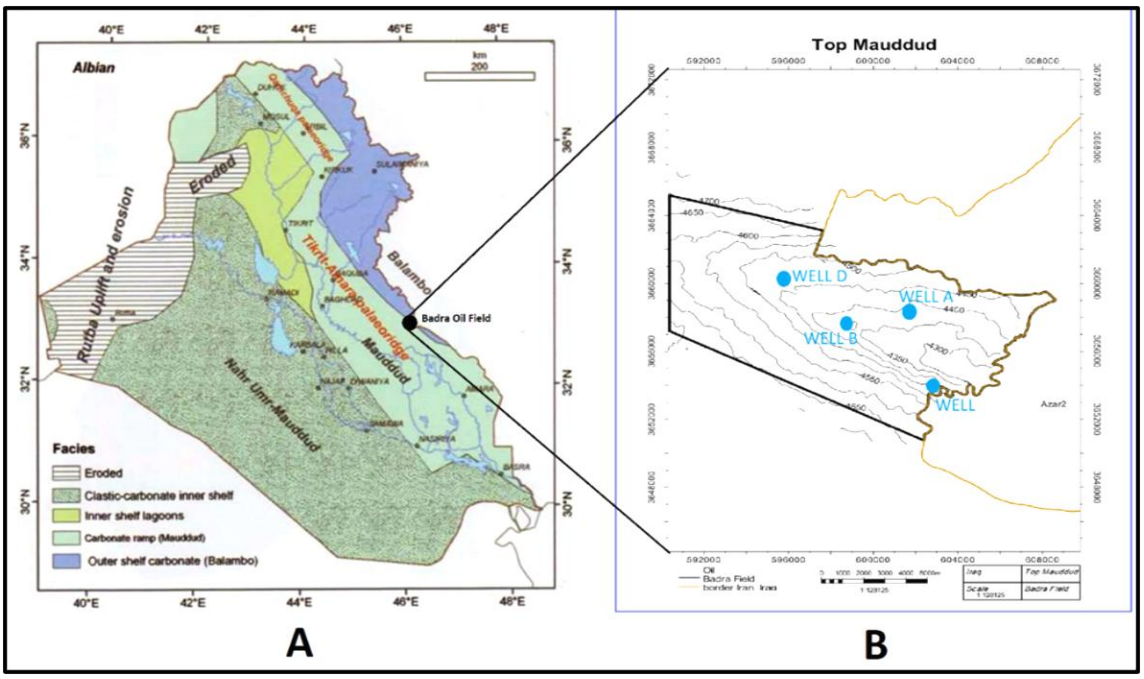


Fig. 1. A. Iraqi geological map (Jassim and Goff, 2006), B. Top Mauddud formation (Kareem, 2020).

Diagenesis Processes in Mauddud Formation

The physical, chemical, and biological processes that result in alterations, such as compaction, cementation, recrystallization, and others, are referred to as diagenesis. Diagenetic processes have significance for several reasons. They have the power to alter the content and texture of sediment significantly, and in some cases, they can even destroy the original structures. The porosity and permeability characteristics of sediment, which regulate the sediment's ability as a reservoir for water, gas, or oil, are likewise impacted by diagenesis. The above processes might be involved in generating or obstructing porosity. The Mauddud Formation has processes including neomorphism, dissolution at some points, cementation, micritization, compaction, and dolomitization. An overview of these procedures is seen below:

Micritization

It is the most frequent process that affects the skeletal pieces in the Mauddud Formation's bioclastic packstones and bioclastic wackestone microfacies. Blue-green algae or fungus significantly affects the micritization process in a stagnant marine phreatic zone. Micritization is an early diagnostic process that mostly affects benthonic foraminifera, particularly Orbitolinids and Miliolids. It is highly prevalent in the facies of the Mauddud Formation (Al-Dabbas et al., 2010).

Cementation

An essential diagnostic process minimizes pores by filling the space created by cement between the main and/or secondary porosity (Longman, 1980). The Mauddud Formation contains calcite cement. It completely or partially obstructs pores. The Mauddud Formation has been found to include the following forms of calcite cement:

a) Drusy Cement

The production of drusy mosaic cement is distinguished by calcite crystals that fill pore spaces, whose size increases toward the center of interparticle voids or pores (Flügel and Munnecke, 2010). Anhedral and subhedral crystals, which fill the moldic porosity, are characteristic of the cement type mentioned above. This cement's properties suggest a quick cementing process (Longman, 1980). It is widespread in the Mauddud Formation's microfacies and significantly decreases the secondary porosity, as shown in Fig. 2 (Sample A).

b) Granular -Blocky- Cement

Blocky cement is created in the later stages of diagenesis processes, frequently after sediments have been exposed to pressure from the ocean and lithified. Transparency and anhedral or subhedral calcite crystals with sizes ranging from 10 to 60 mm are characteristics of blocky cement (Flügel, 2012). The high crystal sizes in saturated solution indicate slow crystallization speeds (Flügel and Munnecke, 2010). The Mauddud Formation's mud and grain-supported microfacies include these huge cement crystals, as shown in Fig. 2 (Sample B).

c) Syntaxial Rim Cement

Within the microfacies of the Mauddud Formation, syntaxial rim cement is formed when crystals grow around echinoderm plate fragments to form optically continuous crystals. These crystals have an early diagenetic origin and are formed of either aragonite or calcite. This suggests the early formation of freshwater phreatic cement (Flügel and Munnecke, 2010). This kind of cement decreases the porosity between particles, especially in grain-supported microfacies, as shown in Fig. 2 (Sample C).

Neomorphism

A term first used by Folk (1965) to describe escalating neomorphism is the process by which a few giant crystals grow into and replace the micritic matrix, converting tiny crystals to massive ones (Scholle and Ulmer-Scholle, 2005). Both micrite and fossils from the microfacies undergo recrystallization. When skeletal grains recrystallize, they lose their original structure. Microspar or pseudospar is a neomorph of micrite. The degree of preservation demonstrates that neither micrite nor neomorphic skeletal grains developed a significant porosity.

Dissolution

The primary diagenetic process that enhances the porosity and permeability of the Mauddud Formation is dissolution. This appears to be affected by the solubility of minerals. For example, calcium carbonate is more soluble when transitioning from aragonite and high-magnesium to low-magnesium calcite. Different types of pores, such as moldic and vuggy ones, are created by dissolution (Choquette and Pray, 1970). These varieties, which range in size as shown in Fig. 3 (Sample C), were discovered in the Mauddud Formation. The widespread vugs and molds in the Mauddud Formation are evidence of significant disintegration occurrences. Certain skeletal grains, like echinoderms, are neither dissolved nor dolomitized and are composed of magnesium calcite (Enos, 1988).

Dolomitization

Dolomitization is transforming lime mud, either wholly or partially, into dolomite by substituting magnesium carbonate ($MgCO_3$) for $CaCO_3$ by the action of magnesium-containing water (Flügel and Munnecke, 2010). Dolomitization is even more widespread in mud-

dominated microfacies in the Mauddud Formation, where skeleton grain fragments from the original microfacies can still be seen, as shown in Fig. 2 (Samples F and E).

Compaction

Compaction causes the thickness of the overlying sediments to decrease, which lowers porosity and rock volume. There are two compaction-process categories (mechanical and chemical) (Croizé, 2010). Soon after deposition, mechanical compaction may start, resulting in micrite envelopes' collapse, elongated bioclasts' flattening toward the bedding plane, and tighter packing of grains. Stylolite, created by mixing dissolution and compaction, and in all carbonate rock textures, is a chemical compaction symbol. Pressure solution produced Stylolites, which result from the solution around grain contact sites that react to pressure as shown in Fig. 2 (Sample D).

Fracturing

In carbonate rocks, fractures are often significant secondary structures that arise from either compaction or the local tectonic regime (Flügel, 2012). Fracture has a small effect on the Mauddud Formation and is mostly observed in the rudistid facies. They can be filled with calcite cement, as shown in Fig. 3 (Sample D), or left open.

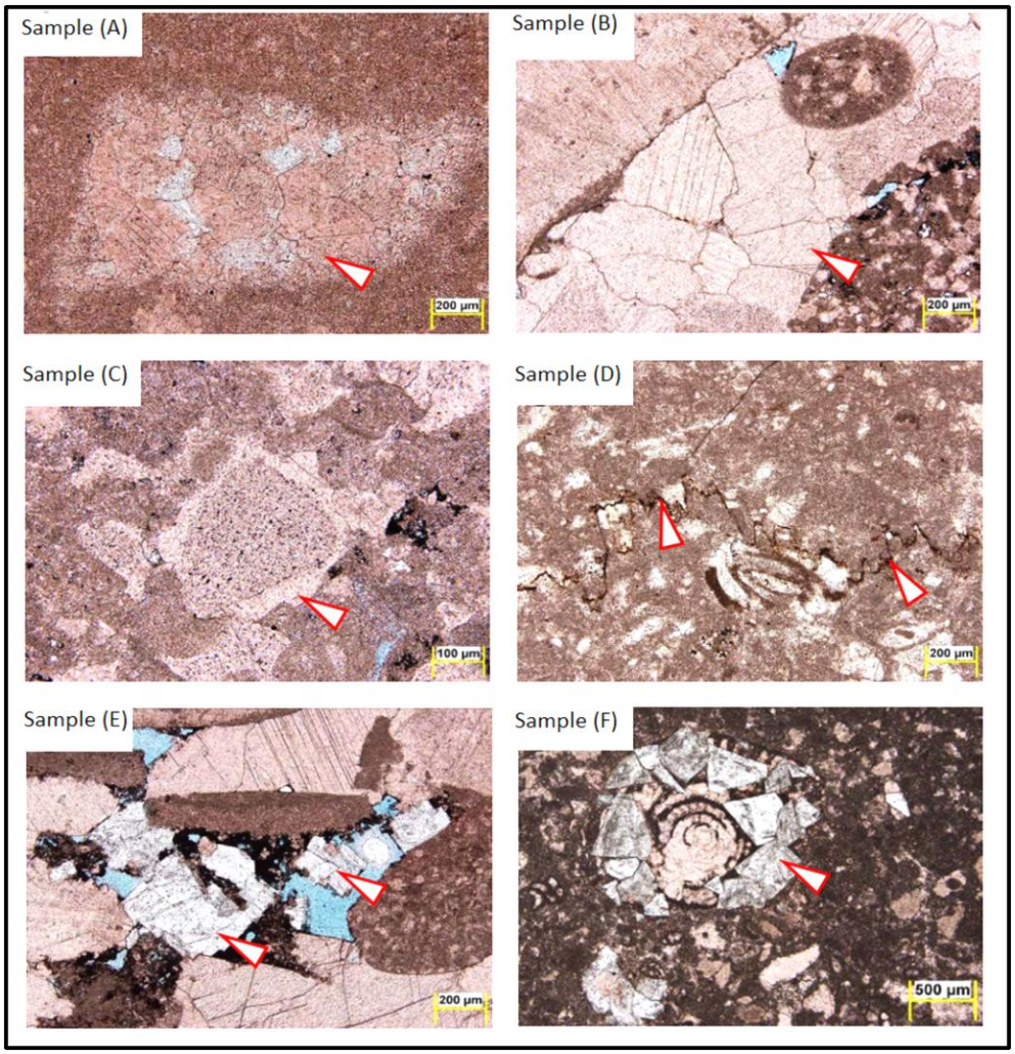


Fig. 2. Photomicrographs showing main diagenetic processes in well A: Sample A: 4593.57 m: Drusy calcite cement. Sample B: 4595.34 m: Blocky calcite cement. Sample C: 4599.45 m: Syntaxial calcite overgrowth around echinoderm plate. Sample D: 4594.24 m: Irregular stylolite with organic matter concentrated on the stylolite surface. Photo E, 4595.34 m: Euhedral dolomite rhombs partially filling Intergranular pores. Photo F, 4594.24 m: Subhedral to euhedral dolomite rhombs partially replacing foraminifera.

Materials and methods

Distinguishing the Pore Types

The Mauddud Formation's microfacies display a variety of pore types. They may be classified as primary or secondary. A number of them are listed below, as mentioned by:

a) ***Interparticle* (*Intergranular*)**: among them are the pores seen in between the grains, as shown in Fig. 3 (Sample A); the intragranular porosity is present mainly within foraminiferal tests and rudist shells, as shown in Fig. 3 (Sample B).

b) ***Moldic***: This porosity is formed after the dissolution of unstable fragments of shells such as Trocholina sp., bivalves, etc., as shown in Fig. 3 (Sample C). Interparticle pores are connected to them. However, most moldic porosity is reduced or completely plugged with calcite and/or dolomite cements.

c) ***Fracture***: Tectonic tensions within the rock cause cracks. Calcite cement can be poured into fracture pores, as shown in Fig. 3 (Sample D), or left open in another one.

d) ***Vuggy***: The breakdown of the fundamental components of limestone, including intergranular sparry calcite cement and allochems, is the cause of the vuggy pores' asymmetrical form (Al-hamdani et al., 2023). The pores are prevalent in mud- and grain-supported microfacies, cutting the matrix and the grains (Al-Dabbas et al., 2010).

There are also porosity types in the Mauddud Formation, such as channel and cavernous. These different types of pores are detected in the Mauddud Formation microfacies by categorizing pore types (Choquette and Pray, 1970).

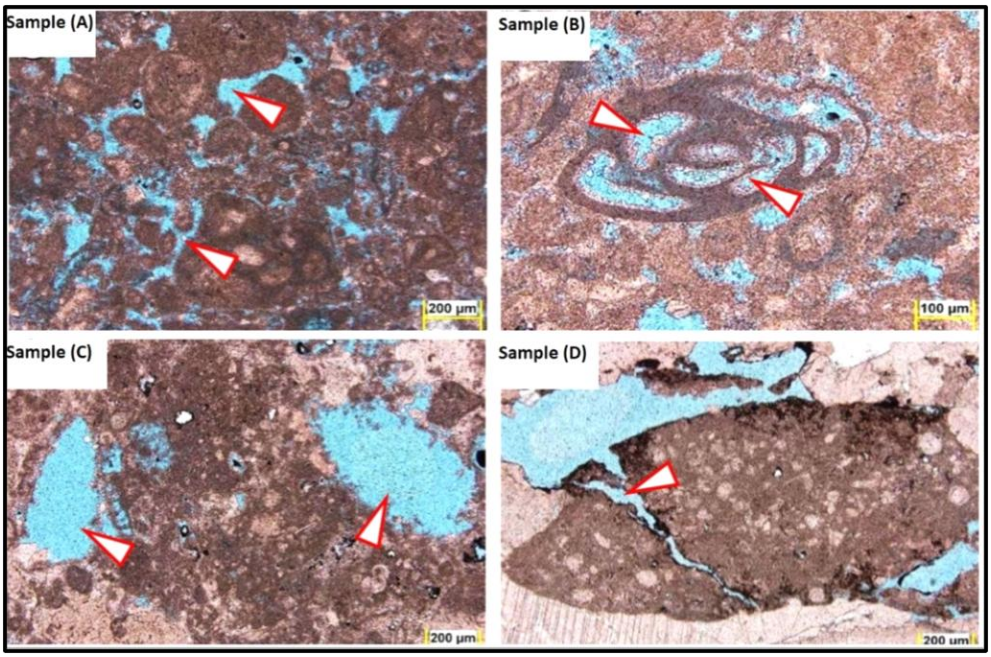


Fig. 3. Common pore types in well A: Sample. A: 4590.49 m: Intergranular porosity between fossils. Sample B: 4590.49 m: Intragranular porosity within foraminiferal tests. Sample: C: 4527.34 m: Moldic porosity through dissolution of bioclasts. Sample: D: 4595.3m: Fracture porosity due to shattering of grains.

Overburden Stress

The overburden stress, known as vertical stress, is brought on by the weight of the formations above (Zaidan et al., 2024). The overburden stress (σ_V) can be computed as follows :

$$\sigma v = \rho a * g * Z \quad \ldots\ldots\ldots 1$$

where: ρa is the average density of the underlying; g is the acceleration caused by gravity, and Z is the depth.

The vertical stress σv can be determined by integrating the densities to the depth of interest, *Z*, if the densities of the formation vary, i.e.,

$$\boldsymbol{\sigma v = \rho w * g * Zw + g \int_{zw}^{z} \rho b \, Zdz} \ldots\ldots\ldots 2$$

where: Zw is the water depth (for onshore drilling, Zw = 0); ρw is the density of seawater; and ρb is the formation bulk density as a function of depth, which can be determined from the density log.

However, density logs are usually not monitored at shallow depths. A shallow formation's bulk density can be calculated by extrapolation of the density log from the surface to the top of the log.

Pore Pressure

The total pressure effect on a certain point in a formation is the summation result of effective pressure and pore pressure (Aman et al., 2018; AlHusseini and Hamed-Allah, 2023). The effective stress will decrease with increased pore pressure, increasing the probability of failure (Zhang, 2019). Therefore, effective stress can be defined as the difference between the externally applied stress and the internal pore pressure, as established by Terzaghi (1943), or as the net stress applied to the rock skeleton:

$$\boldsymbol{\sigma` = \sigma - Pp} \ldots\ldots\ldots\ldots 3$$

where: σ` = effective stress, σ = total stress, $\boldsymbol{Pp}$ = pore pressure.

The poroelastic (α) or biot coefficient is the difference between bulk and pore volumes and explains the inter-grain connections between grains. Next, the effective stress equation is written as follows (Hettiaratchi, 1988):

$$\boldsymbol{\sigma` = \sigma - \alpha \, Pp} \ldots\ldots\ldots\ldots 4$$

The poroelastic constant has a value between zero and one; if the rocks are low-stiff, the biot coefficient (α) equals zero, and if the rocks are stiff (α=1), then the pore fluid is most effective at reducing effective stress. According to (G, 2015). The most popular approach for predicting pore pressure in the oil and gas sector is Eaton's technique (Eaton, 1975), who proposed an empirical connection to calculate pore pressure using compressional transit time data by Terzaghi (Terzaghi, 1943). According to this approach, the overburden pressure is assumed to be supported by both pore pressure and vertical effective stress, with the disequilibrium of compaction being identified as the main cause of overpressure. In this work, the non-shale zone *Pp* is computed using equation 5:

$$\boldsymbol{Pp = \sigma v - (\sigma v - Ppn) * a * \left(\frac{\Delta tn}{\Delta t}\right)^{n}} \ldots\ldots\ldots\ldots 5$$

where: Δt is the compressional transit time or slowness from the sonic log, and Δtn is the compressional transit time or slowness in shales at normal pressure. Fitting factors "a" and "n" are called the Eaton exponent and Eaton factor, respectively. The initial values are n=3 and a=1. Ppn denotes hydrostatic pore pressure.

Fracture Pressure

Fracture pressure is the point at which a rock formation cracks or breaks, potentially causing drilling fluids to leak into nearby formations. Eaton calculated the fracture pressure using the formation's Poisson's ratio and the Hubbert and Willis idea of the lowest injection pressure (Eaton, 1969; AlHusseini and Hamed-Allah, 2023):

$$\boldsymbol{Pf = \frac{v}{1-v}(\sigma v - \alpha \, Pp) + \alpha \, Pp} \ldots\ldots\ldots\ldots 6$$

where: *Pf* = the fracture pressure (psi), *v* = Poisson's ratio.

Mud Weight Window

Controlling the well mud density during drilling is crucial for ensuring safe drilling and maintaining the wellbore stability (Al-Hlaichi and Al-Mahdawi, 2023). Pore and fracture pressure are the primary variables determining the mud density value. Both static and dynamic drilling mud pressures must be lower than the fracture pressure. However, this pressure range above pore pressure is known as the mud weight window (MWW) (Charlez, 1999). It is necessary to apply mud weight within a certain range to preserve borehole stability. As shown in Fig. 4, the borehole failures can be broadly classified into four categories (Zhang, 2013):

a) Mud weight is significantly less than pore pressure, causing washouts or fluid kicks to the wellbore.
b) Mud weight being very low causes breakouts or shear failures.
c) Mud weight is too high, causing loss or lost circulation mud and resulting in tensile failure (hydraulic fractures).
d) Slide or rock failures caused by pre-existing fractures.

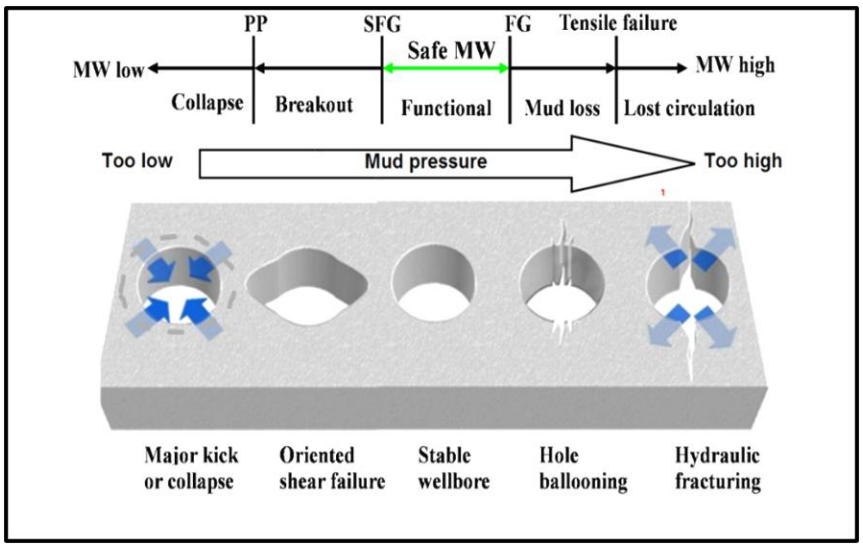


Fig. 4. Connection between borehole failures and mud pressure (mud weight, MW) (Zhang, 2013).

Microfacies Analysis of Mauddud Formation

In this study, 40 thin sections, which represent the rock core sample and cuttings, are examined, providing the information for the comprehensive study of Mauddud Formation, which was taken from four oil wells (A, B, C, and D). They are employed in the current investigation to evaluate the various depositional environments and to determine the sedimentary and stratigraphic frameworks of the sedimentary basin through the use of microfacies analysis. Five primary microfacies are found in the Mauddud sequence. These microfacies' distinctive grain types and sedimentary textures allowed for identifying the paleoenvironment; another researcher also improved this (Dunham, 1962; Flügel and Munnecke, 2010). These are:

A. Microfacies A: Wackestone-Packstone Orbitolina

Together with echinoderm and calcareous green algae, the initial microfacies contain some bioclasts from mollusks and rudists. It also contains Orbitolina sp. This could be about the deposition found in Fig. 5 (Sample A), the shallow open maritime habitat. The minute details in the Badra oil field a distributed in the middle and upper portions of the sequence under study.

B. Microfacies B: Miliolids Wackestone

These microfacies are primarily made up of pellets containing calcareous green algae, echinoderm, and orbitolinids with miliolids, in addition to bioclasts of mollusks.

The deposition in the shallow open maritime environment (Fig. 5, Sample B) is referred to as facies B. These microfacies appear in the lowest portion of the Badra oil field investigated succession.

C. Microfacies C: Bioclast, Mollusk, and Echinoderm Wackestone-Packstone

Nezzazata sp. and other bioclasts, together with mollusk and echinoderm bioclasts, are the principal constituents of this facies. These microfacies (Fig. 5, Sample C) reflect the deposition confined to semi-restricted environments. These microfacies are visible in the wells under study in the middle and upper parts of the Mauddud Formation.

D. Microfacies D: Wackestone/Bioclastic Packstone

Intraclasts, echinoderms, and fragmented rudist bioclasts are the microfacies seen in the succession, in addition to little benthic foraminifera. The slope environment is represented by microfacies (D) (Fig. 5, Sample D). The uppermost portion of the Mauddud Formation has these microfacies.

E. Microfacies E: Foraminifera/Planktonic Packstone

This less common phenomenon appears in the middle part of the Mauddud succession, composed of calcisphere and ooze with shall and marly limestones (Fig. 5, Sample E). It can be identified by high gamma ray well log reflection values and thin section diagnostics.

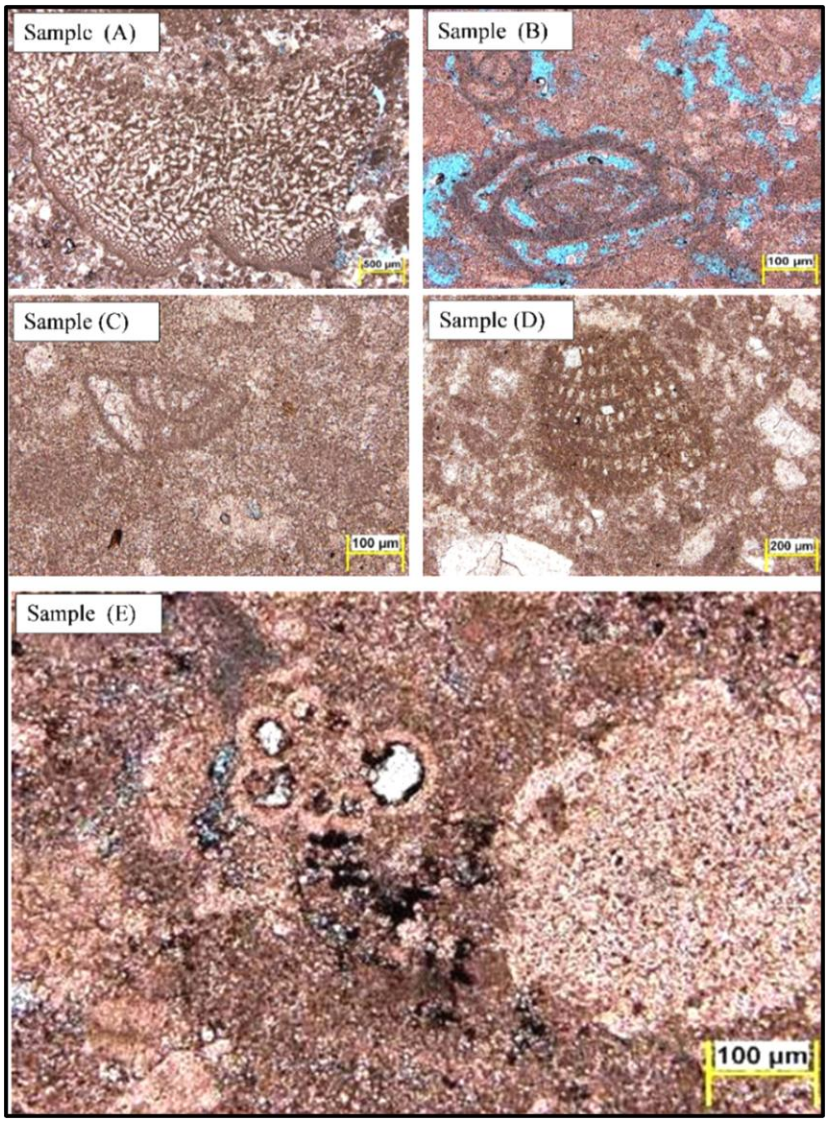


Fig. 5. Common types of Mauddud Microfacies in Badra oil felid.

Results and Discussion

Studying the pressure results of well A (Fig. 6), it seems that the values of the fracture pressure (FPRS_EATON in the third track) of the Mauddud Formation range from 9625 psi at a depth of 4485 m to 11393 psi at a depth of 4700 m. The values of fracture pressure reflect the possibility of breaking the formation; the lower value reflects an increased possibility of cracking the formation at this depth, which means the possibility of many problems, such as lost circulation, formation damage, and mud pressure decline. While high fracture pressure values reduced the possibility of mud fracturing, they increased problems such as gas/oil kicks, pipe sticking, and collapse. The overburden stress values mentioned as (SVERTACAL_EXT in the third track) range from 15346 psi at the top of the formation to 16681 psi at the bottom. Studying the results of pore pressure (PPRS_EATON_S in the third track) explains that it ranges from 8000 psi at 4485m to 10027 psi at 4700 m. The obtained pore pressure values of the current study are close to the measured values mentioned in previous research literature (Kareem, 2020). The high pore pressure calculated at different levels of the Mauddud Formation is mainly caused by compaction. Compaction leads to reduced porosity and volume of rocks resulting from overburdened sediment thickness. The formation structure appears to be a narrow NW-SE trending anticline accompanied by long normal faults. The area contains two NW-SE trending sets of low amplitude buried anticlines associated with longitudinal faults and a transverse EW trend. High formation pressure results from the Foothill zone, part of an unstable shelf (Kareem, 2020).

The suggested value of this well's Mud Weight Window (MWW), which indicates the difference between pore pressure and fracture pressure values, is about (2.7-2.9 ppg) and is considered a safe value for drilling the interested formations.

Analyzing the results of different pressures across the field provides an important estimation of the real situation of the anticline structure of the reservoir. This can be done by analyzing the results of other wells in different locations over the field. Pressure analysis of well B (Fig. 7) shows that the values of the fracture pressure (FPRS_EATON in the third track) range from 10240 psi at a depth of 4456 m to 11525 psi at a depth of 4621 m. The values of overburden stress (SVERTACAL_AVG in the third track) range from 14580 psi at 4454 to 15680 psi at 4763m. The pore pressure results (PPRS_EATON_S in the third track) show that they range from 8063 psi at 4456m to 9703 psi at 4621m. The estimated Mud Weight Window for this well is about (2.7-3.4 ppg).

On the other hand, the results of well C (Fig. 8) show that the values of the fracture pressure (FPRS_EATON in the third track) range from 10561 psi at a depth of 4470 m to 12082 psi at a depth of 4606 m. At the same time, the values of overburden stress (SVERTACAL_EXT in the third track) range from 15788 psi at 4470 to 17050 psi at 4824 m. Studying pore pressure results (PPRS_EATON_S in the third track) explains that the pressure ranges from 7947 psi at 4470 m to 9986 psi at 4606 m. The estimated Mud Weight Window for this well is about (2.3-2.8 ppg).

In the fourth well D (Fig. 9), it is found that the values of the fracture pressure (FPRS_EATON in the third track) range from 10420 psi at a depth of 4539 m to 12467 psi at a depth of 4919 m. While the values of overburden stress (SVERTACAL_EXT in the third track) range from 15122 psi at 4539 to 16498 psi at 4921 m. Studying pore pressure results (PPRS_EATON_S in the third track) shows that the pressure ranges from 8070 psi at 4539 m to 10457 psi at 4919 m. The estimated Mud Weight Window for this well is about (2.4-3.1 ppg).

A comprehensive study of the four wells shows that the lowest value for the fracture pressure is recorded in well A, which means that the well is the most exposed to the fracturing problem. The σ_V values are almost high, and the pressure gradient value is more than 1 psi/ft,

which causes the problem of instability of layers and thus stuck pipe in most wells. The largest value of σ_V is observed in well C. Accordingly, this well is the most exposed to this problem.

If the value of the pore pressure is greater than the fracture pressure in specific areas of the Mauddud Formation, this will lead to a kicking problem, and therefore, the pressure of the drilling mud in those areas must be increased. The highest value of pore pressure recorded in the well D (Fig. 9) is 10457 psi at a depth of 4919 m. This explains the relative difference between the measured mud density (MW_meas in the fourth track) and the equivalent calculated mud density (PPMW_EATON_S).

Finally, the widest MWW is estimated in well B, located at the crest of the anticline structure of the field, and is considered the best well relative to safety drilling operations. In contrast, the safe mud weight window becomes narrower and more dangerous for other wells located near the edge of the anticline structure of the fields.

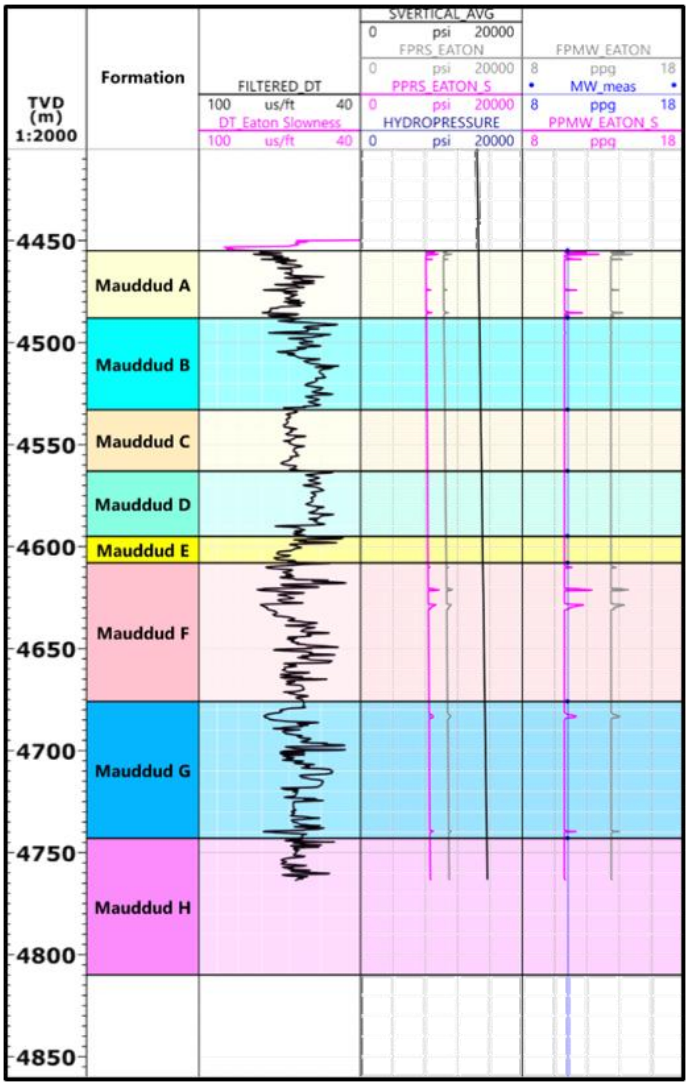


Fig. 6. Pore and fracture pressures in well A.

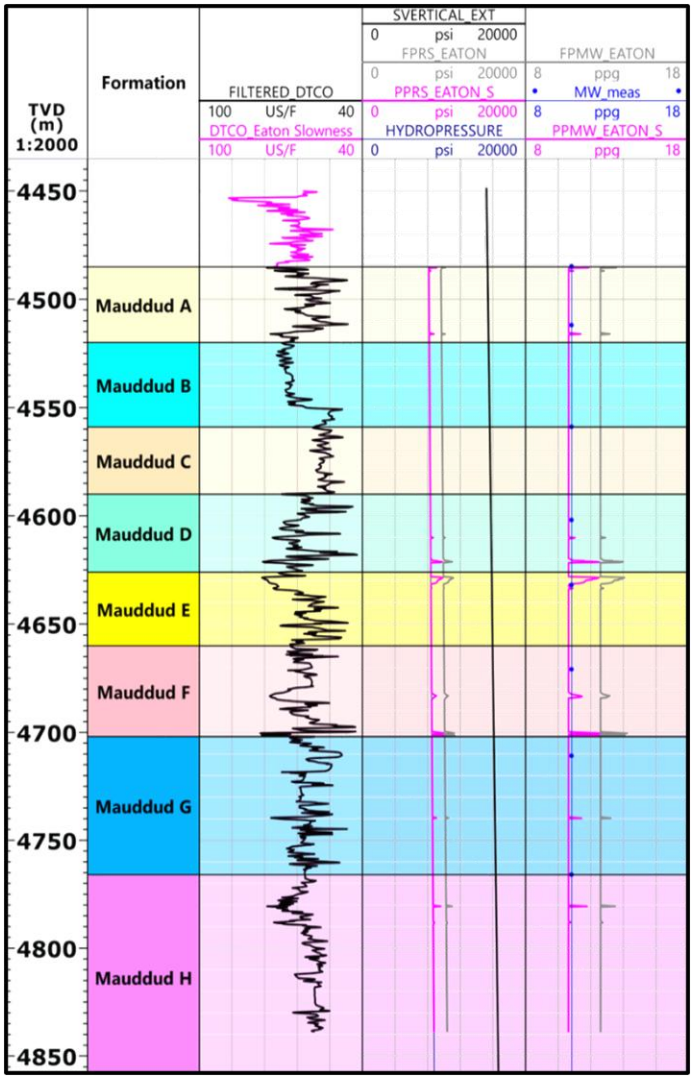


Fig. 7. Pore and fracture pressures in well B.

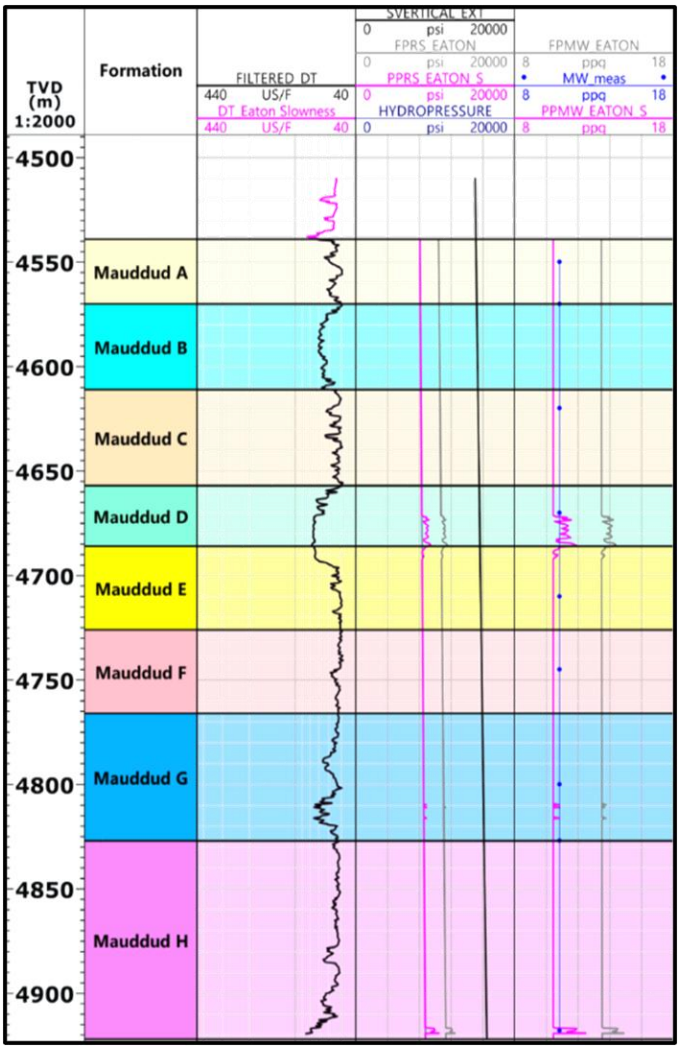


Fig. 8. Pore and fracture pressures in well A.

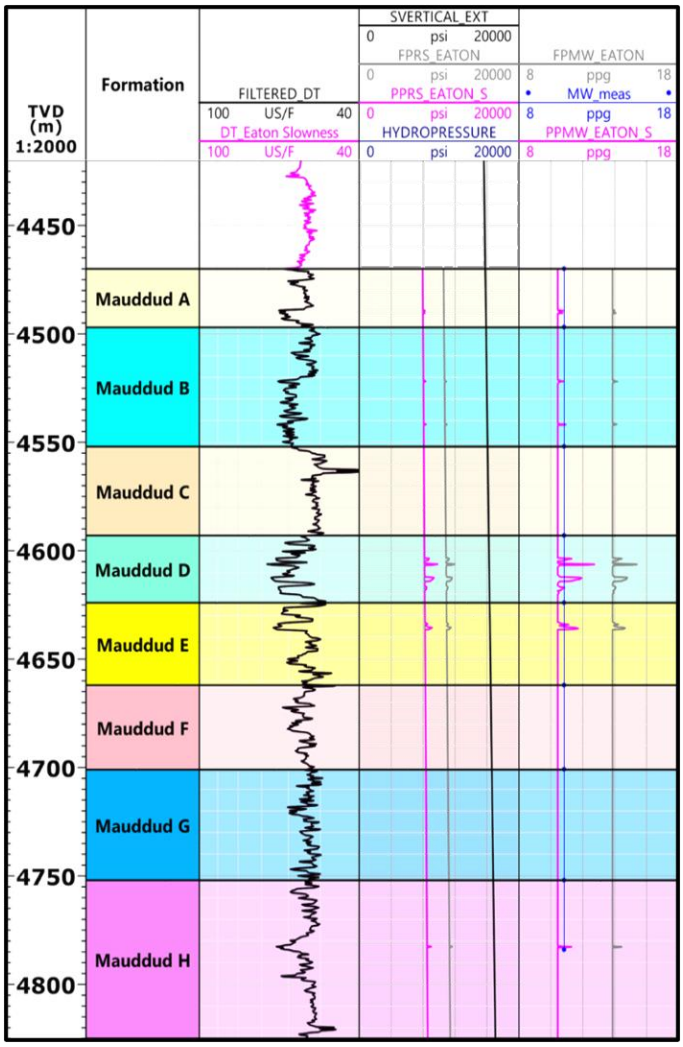


Fig. 9. Pore and fracture pressures in well D.

Conclusions

This section highlights the main investigation from the estimated results of different pressure types of the Badra oil field interval Mauddud Formation. It is concluded that the prediction of mud weight along the studied formation shows that the value of a safe mud weight window must range from 2.3 to 3.4 ppg and becomes narrower and more dangerous when the wells cross the edge of the anticline structure of the reservoir. This result is acceptable since the higher difference between the maximum and minimum horizontal stress values is concentrated at the edge of the geological structure. In other words, drilling the wells near the crest of the studied formation is recommended to avoid the narrow mud weight window expected in the formation's structural edge.

References

Aadnoy, B.S. and Ong, S., 2003. Introduction to the special issue on borehole stability. Journal of Petroleum Science and Engineering, Vol. 38, No. 3, pp.79–82. https://doi.org/10.1016/S0920-4105(03)00022-6

Aadnoy, B.S. and Looyeh, R., 2011. Petroleum Rock Mechanics: Drilling Operations and Well Design, 1st Edition. In Oxford: Gulf Professional Publishing. https://www.scribd.com/book/413520471/Petroleum-Rock-Mechanics-Drilling-Operations-and-Well-Design

Al-Dabbas, M.A., Jassim, J.A. and Qaradaghi, A.I., 2010. Sedimentological and depositional environment studies of the Mauddud formation, central and southern Iraq. Arabian Journal of Geosciences, 5(2), pp. 297–312. https://doi.org/10.1007/s12517-010-0256-5

Al-hamdani, D.M., Abdullah, M.H., Al-Hameedy, R. and Al Hamdani, S.A., 2023. Porosity Type Determination Using the Velocity Deviation Technique for The Sheikh Allas Formation in The Kirkuk Oil Field, Northeastern Iraq. Iraqi National Journal of Earth Science (INJES), 23(2), pp. 20–36. https://doi.org/10.33899/earth.2023.139106.1059

Al-Hlaichi, S.K. and Al-Mahdawi, F.H.M., 2023. Drilling Optimization by Using High Drilling Techniques: A Review. AIP Conference Proceedings, 2839(1), pp. 53–64. https://doi.org/10.1063/5.0167961

AlHusseini, A.K. and Hamed-Allah, S.M., 2023. Estimation Pore and Fracture Pressure Based on Log Data; Case Study: Mishrif Formation/Buzurgan Oilfield at Iraq. Iraqi Journal of Chemical and Petroleum Engineering, 24(1), pp. 65–78. https://doi.org/10.31699/ijcpe.2023.1.8

Aman, M., Espinoza, D.N., Ilgen, A.G., Major, J.R., Eichhubl, P. and Dewers, T.A., 2018. CO2-induced chemo-mechanical alteration in reservoir rocks assessed via batch reaction experiments and scratch testing. Greenhouse Gases: Science and Technology, 8(1), pp. 133–149. https://doi.org/https://doi.org/10.1002/ghg.1726

Bandara, M.K. and Al-Ameri, N.J., 2024. Wellbore Instability Analysis to Determine the Safe Mud Weight Window for Deep Well, Halfaya Oilfield. Iraqi Geological Journal, 57(1D), pp. 153–173. https://doi.org/10.46717/igj.57.1D.13ms-2024-4-23

Charlez, P.A., 1999. The concept of mud weight window applied to complex drilling. SPE Annual Technical Conference and Exhibition, SPE-56758. https://doi.org/https://doi.org/10.2118/56758-MS

Chen, S., 2017. Petroleum Production Engineering. Springer Handbook of Petroleum Technology, pp. 501–516. https://doi.org/https://link.springer.com/chapter/10.1007/978-3-319-49347-3_14

Choquette, P.W. and Pray, L.C., 1970. Geologic nomenclature and classification of porosity in sedimentary carbonates. AAPG Bulletin, 54(2), pp. 207–250. https://doi.org/10.1306/5D25C98B-16C1-11D7-8645000102C1865D

Croizé, D., 2010. Mechanical and chemical compaction of carbonates: an experimental study. University of Oslo, Norway. https://doi.org/https://www.duo.uio.no/bitstream/handle/10852/12547/2/PhD-Croize.pdf

Cross, N., Goodall, I., Hollis, C., Burchette, T., Al-Ajmi, H.Z.D., Johnson, I.G., Mukherjee, R., Simmons, M. and Davies, R., 2010. Reservoir description of a mid-Cretaceous siliciclastic-carbonate ramp reservoir: Mauddud Formation in the Raudhatain and Sabiriyah fields, North Kuwait. GeoArabia, 15(2), pp. 17–50. https://doi.org/https://archives.datapages.com/data/specpubs/carbona2/data/a038/a038/0001/0100/0108.html

Dunham, R.J., 1962. Classification of carbonate rocks according to depositional textures. https://onepetro.org/JPT/article-abstract/21/10/1353/164490

Eaton, B.A., 1969. Fracture gradient prediction and its application in oilfield operations. Journal of Petroleum Technology, 21(10), pp. 1353–1360. https://doi.org/onepetro.org/JPT/article-abstract/21/10/1353/164490

Eaton, B.A., 1975. The equation for geopressure prediction from well logs. SPE Annual Technical Conference and Exhibition, SPE--5544. https://doi.org/10.2118/5544-MS

Enos, P., 1988. Evolution of pore space in the Poza Rica trend (Mid-Cretaceous), Mexico. Sedimentology, 35(2), pp. 287–325. https://doi.org/10.1111/j.1365-3091.1988.tb00950.x

Faisal, M.J. and Mahdi, T.A., 2020a. Diagenetic processes overprint and pore types of Mauddud formation, Badra oil field, Central Iraq. Iraqi Journal of Science, 61(6), pp. 1353–1361. https://doi.org/10.24996/ijs.2020.61.6.13

Faisal, M.J. and Mahdi, T.A., 2020b. Geological model of Mauddud Formation in Badra Oilfield. The Iraqi Geological Journal, pp. 58–67. https://doi.org/10.46717/igj.53.1a.R4.2020.01.28

Flügel, E., 2012. Microfacies analysis of limestones. Springer Science and Business Media. https://doi.org/10.1007/978-3-642-68423-4

Flügel, E. and Munnecke, A., 2010. Microfacies of carbonate rocks: analysis, interpretation and application, Vol. 976, Springer. https://doi.org/10.1007/978-3-662-08726-8

Folk, R.L., 1965. Some aspects of recrystallization in ancient limestones. https://onepetro.org/ARMAUSRMS/proceedings-abstract/ARMA69/All-ARMA69/130984abstract/ARMA69/All-ARMA69/130984

G, Z.U., 2015. An overview of pore pressure prediction using seismicallyderived velocities. Journal of Geology and Mining Research, 7(4), pp. 31–40. https://doi.org/10.5897/JGMR15.0218

Ghafor, I., Fatah, A. and Khafaf, A.A.L., 2023. Biostratigraphy and Microfacies of the Mauddud Formation (Late Albian–Early Cenomanian) in Musaiyib Well No. 1, Central Iraq. Iraqi Bulletin of Geology and Mining, 19(2), pp. 37–56. https://doi.org/https://doi.org/10.59150/ibgm1902a03

Haimson, B. and Fairhurst, C., 1969. In-situ stress determination at great depth by meansing hydraulic fracturing. ARMA US Rock Mechanics/Geomechanics Symposium, ARMA-69. https://doi.org/10.1016/0167-1987(88)90005-0

Hettiaratchi, D., 1988. Theoretical soil mechanics and implement design. Soil and Tillage Research, 11(3–4), pp. 325–347. https://doi.org/10.1306/2F918A63-16CE-11D7-8645000102C1865D

Jassim, S.Z. and Goff, J.C., 2006. Geology of Iraq. DOLIN, sro, distributed by the Geological Society of London. https://doi.org/https://www.sciencedirect.com/science/article/pii/0167198788900050

Kareem, K.A., 2020. Optimization of Water Injection for Badra Oil Field. 53(1), pp. 13–28. https://doi.org/10.46717/igj.53.1B.2Rz-2020-03-02

Longman, M.W., 1980. Carbonate diagenetic textures from nearsurface diagenetic environments. AAPG Bulletin, 64(4), pp. 461–487. https://doi.org/https://books.google.com/books

Najibi, A.R., Ghafoori, M., Lashkaripour, G.R. and Asef, M.R., 2017. Reservoir geomechanical modeling: In-situ stress, pore pressure, and mud design. Journal of Petroleum Science and Engineering, 151, pp. 31-39.

Rasouli, V., Pallikathekathil, Z.J. and Mawuli, E., 2011. The influence of perturbed stresses near faults on drilling strategy: a case study in Blacktip field, North Australia. Journal of Petroleum Science and Engineering, 76(1–2), pp. 37–50. https://doi.org/10.1306/04220301111

Sadooni, F.N. and Alsharhan, A.S., 2003. Stratigraphy, microfacies, and petroleum potential of the Mauddud Formation (Albian–Cenomanian) in the Arabian Gulf basin. AAPG Bulletin, 87(10), pp. 1653–1680. https://doi.org/10.1306/04220301111

Scholle, P.A. and Ulmer-Scholle, D., 2005. A Color Guide to the Petrography of Carbonate Rocks: Grains, Textures, Porosity, Diagenesis. AAPG Memoir, 77, 486 P. https://doi.org/10.1306/M77973

Terzaghi, K., 1943. Theoretical soil mechanics. https://doi.org/libarch.nmu.org.ua/bitstream/handle/GenofondUA/19513/fe8e4061e420c7a5c38e39e9774911c0.pdf?sequence=1

Kareem, K.A., 2020. Optimization of water injection for Badra oil field Wasit, southern Iraq. The Iraqi Geological Journal, Vol. 53, No. 1B, pp. 13-28. https://doi.org/10.46717/igj.53.1B.2Rz-2020-03-02

Zaidan, A.F., Hadi, F.A. and Klempa, M., 2024. Investigation of Wellbore Instability in Southern Rumaila Oil Field. Iraqi Journal of Chemical and Petroleum Engineering, 25(2), pp. 17–31. https://doi.org/10.31699/ijcpe.2024.2.2

Zhang, J., 2013. Borehole stability analysis accounting for anisotropies in drilling to weak bedding planes. International Journal of Rock Mechanics and Mining Sciences, 60, pp. 160–170. https://doi.org/10.1016/j.ijrmms.2012.12.025

Zhang, J.J., 2019. Applied Petroleum Geomechanics. In Loess and Loess Geohazards in China. https://doi.org/10.1201/9781315177281-4

Iraqi National Journal of Earth Science

www.earth.uomosul.edu.iq

Impact of Diagenetic Processes and Dolomitization on the Dammam Formation in Central Iraq

Basma A. Al-Samarraie [1 *] , Mohanad H. Al-Jaberi [2]

[1,2] Department of Geology, College of Science, University of Basrah, Basrah, Iraq.

Article information

Received: 15- Oct -2024

Revised: 16- Nov -2024

Accepted: 11- Dec -2024

Available online: 01- Jan -2026

Keywords:
Dammam Formation,
Dolomitization
Karstification,
Mixing zone,
Carbon and oxygen isotope,

Correspondence:
Name: Basma A. Al-Samarraie

Email: basma1984t@gmail.com

ABSTRACT

This study examines the diagenetic processes that affect the Dammam Formation, with a focus on the dolomitization mechanism of limestone rocks within Al-Najaf Governorate, Central Iraq. The Dammam Formation is composed of dolostone, limestone, and dolomitic limestone. The results of XRD analysis show the presence of primarily non-clay minerals (calcite, dolomite, quartz, and feldspar) and clay minerals (palygorskite, montmorillonite, and kaolinite) as secondary minerals. In addition to the dolostone facies, six types of limestone microfacies are identified. Most of them indicate sparse to intense dolomitization. Three facies' associations are distinguished in the Dammam Formation. Each represents a distinct depositional environment, including shallow restricted, shallow open marine, and shoal environments. Several diagenesis processes have affected the Dammam Formation, with dolomitization being the predominant one. Five major textural patterns of dolomite are distinguished: microcrystalline, planar-euhedral, planar-subhedral to euhedral, planar-porphyrotopic, and planar void-filling. Petrographic investigations, geochemical data, and isotope analysis indicate that the dolomitization of the Dammam Formation has formed in a mixing zone. The paleo-temperature of dolomite in Dammam Formation, measured based on $\delta^{18}O$, ranges from (42.2-67.1°C). Accordingly, its deposition by mixing meteoric-sea water associated with low temperature and shallow burial conditions becomes more probable. The recorded depletion in $\delta^{13}C$ value of (-7.97‰). At depth 34 m in BH3, there is a sea-level fall, and exposure of the Dammam Formation was in the late Eocene. The diagenetic history of the limestones can be subdivided into early, middle, and late stages.

DOI: 10.33899/injes.v26i1.60210, ©Authors, 2026, College of Science, University of Mosul.
This is an open-access article under the CC BY 4.0 license (http://creativecommons.org/licenses/by/4.0/) .

تأثير العمليات التحويرية والدلمتة على تكوين دمام في وسط العراق

بسمة اسعد السامرائي [1*]، مهند حامد الجابري [2]

[1،2] قسم علوم الارض، كلية العلوم، جامعة البصرة، البصرة، العراق.

معلومات الارشفة

تاريخ الاستلام: 15- اكتوبر- 2024

تاريخ المراجعة: 16- نوفمبر- 2024

تاريخ القبول: 11- ديسمبر- 2024

تاريخ النشر الالكتروني: 01- يناير- 2026

الكلمات المفتاحية:

تكوين الدمام،

الدلمتة،

الكارست،

نطاق الاختلاط،

نظائر الكاربون والاوكسجين،

المراسلة:

الاسم: بسمة اسعد السامرائي

Email: basma1984t@gmail.com

الملخص

تناقش هذه الدراسة العمليات التحويرية التي أثرت على تكوين دمام، وتركز على آلية دلمتة الصخور الكاربوناتية ضمن محافظة النجف في وسط العراق. يتكون تكوين دمام من الحجر الجيري المتدلمت والحجر الجيري والدولومايت. أظهرت نتائج تحليل الاشعة السينية وجود المعادن غير الطينية وهي الكالسايت والدولومايت والكوارتز والفلسبار، بينما تعتبر المعادن الطينية معادن ثانوية وتشمل (الباليجورسكيت والمونتموريلونيت والكاولينيت). إلى جانب سحنات الدولستون المدروسة، تم التعرف على ستة سحنات دقيقة من الحجر الجيري. قدمت معظم هذه السحنات الدقيقة أدلة على وجود الدلمتة المتناثرة والمنتشرة. تم تحديد ثلاث مجاميع ترسيبية لتكوين دمام. يمثل كل منها بيئة ترسيبية متميزة، بما في ذلك البيئات البحرية الضحلة المحصورة والبيئة البحرية الضحلة المفتوحة والحاجز المتضحل. أثرت العديد من عمليات التحوير على تكوين دمام، لكن عملية الدلمتة هي السائدة. تم التعرف على خمسة انواع من الانسجة الرئيسة من الدولومايت: الدقيق التبلور، والمستوي أحادي السطوح، وشبه المستوي إلى المستوي، المسطح البورفيروتوبي، والمستوي الذي يملأ الفراغ. أشارت الدراسة الصخرية والبيانات الجيوكيميائية وتحليل النظائر إلى أن عملية الدلمتة في تكوين دمام ربما حدثت في منطقة الخلط. درجة الحرارة القديمة للدولومايت في تكوين دمام والتي تم قياسها على أساس $\delta\ ^{18}O$ تتراوح مابين (42.2-67.1) درجة سليزية. وعليه فإن احتمالية تكوين الدولومايت عن طريق خلط مياه البحر النيزكية تحت ظروف درجات الحرارة المنخفضة وعلى عمق دفن ضحل يصبح أكثر احتمالا. يشير الاستنزاف المسجل في قيم $\delta\ ^{13}C$ (7.97-‰) على عمق 34 مترًا في BH3 إلى انخفاض مستوى سطح البحر وانكشاف تكوين دمام في أواخر العصر الأيوسيني. يمكن تقسيم التاريخ التحويري للحجر الجيري إلى ثلاث مراحل (مبكرة ومتوسطة ومتأخرة).

DOI: 10.33899/injes.v26i1.60210, ©Authors, 2026, College of Science, University of Mosul.
This is an open-access article under the CC BY 4.0 license (http://creativecommons.org/licenses/by/4.0/) .

Introduction

The Eocene Epoch in Iraq belongs to the Middle Paleocene-Eocene of the tectono-stratigraphic megasequence (AP l0), which is an important stratigraphic unit in the stratigraphic column of Iraq. The Eocene-Miocene formations in the study area, in ascending order, are Rus, Dammam, and Euphrates Formations. The Dammam Formation covers large areas in the southern desert of Iraq and occurs at different depths. Bramkamp (1941; in Bellen et al., 1959) was the first to describe the Dammam Formation from the Dammam dome in East Saudi Arabia, where it consists of limestone (chalky, organodetrital, or dolomitic), dolomites, marls, and shales. In Iraq, an accessory type section was suggested by Owen and Nasr (1958) in the well Zubair-3 in southern Iraq, where the formation consists mainly of dolomitized and locally chalky limestone, with a shale layer often occurring near the base of the formation. Al-Hashimi and Amer (1985) assumed a typical dominated lagoonal environment for the deposition of the Dammam Formation, which is distinguished by

dolomitic limestone and the dominant occurrence of Miliolids and Peneroplis. According to Mahdi and Youkhanna (1996), the middle member of the Dammam Formation was deposited in a tropical-subtropical shallow marine with a depth of nearly 100 m or less. Jassim and Goff (2006) found that the Dammam Formation is composed of shoal limestone, often recrystallized and/or dolomitized. The limestone is characterized by the common occurrence of nummulites in the lower part and miliolids in the upper part. Maziqa et al. (2024) found that the Dammam Formation was deposited in a variety of settings, including peritidal inner ramp, lagoon, shoal, restricted-marine platform, and open interior platform.

Geological Setting and Stratigraphy

The sedimentary succession in the study boreholes consists of Rus, Dammam, and Euphrates formations, ranging in age from Early Eocene to Middle Miocene. The Dammam Formation is composed of limestone, fossiliferous limestone, dolomitic limestone, marl, crystalline limestone, and crystalline dolostone facies that were deposited in shallow restricted, shallow open marine, and shoal environments. It consists of three members: lower, middle, and upper, according to lithological variations and assemblage fauna. The absence of the upper member in most boreholes and the variation in its thickness in others indicate the difference in the intensity of erosion from place to another. In general, the upper member thickness is inversely proportional to the intensity of weathering and erosion. In the present work, the boundary between the Rus and Dammam formations is taken at the first appearance of massive gypsum. The upper boundary between the Upper Member of Dammam Formation and Euphrates Formation is unconformable and marked by pseudobrecciated limestone at the bottom of Euphrates Formation. The study of the upper boundary of the Dammam Formation reveals that there is karstification and a late stage of dolomitization below the unconformity. The paleokarst zone of the Dammam Formation developed as a result of exposure during Oligocene–Early Miocene time.

This study interprets the origin of the dolomitization process for the Dammam Formation based on its stratigraphic distribution, petrographic characteristics, XRD, chemistry analysis, and oxygen and carbon isotope analysis, to propose a model for dolomitization in the Al-Najaf area. In addition, the diagenetic history related to the Dammam-Euphrates unconformable boundary is studied in the same area.

The study location lies in the southern desert of Iraq, within Al-Najaf Governorate (Fig. 1). Four boreholes are selected with the geographic coordinates shown in Table 1. Structurally, the study area lies within the Arabian inner platform, Southern Desert (Fouad, 2015).

Table 1: Location coordinates of the studied wells and depth intervals of the Dammam Formation.

BH. No.	Eastern	Northern	Depth (m).	Thickness m.	Number of samples
BH2	450311	3480676	10-125	115	41
BH3	443606	3488661	35-115	80	43
BH16	391077	3538969	10- 140	130	26
BH21	423789	3506144	10-183	173	60

Materials and methods

Detailed petrographic study of core samples collected from four boreholes within Al-Najaf Governorate, which were drilled by the Iraq Geological Survey (GEOSURV). Petrographic study includes the microscopic examination of 170 thin sections of selected samples under a polarizing microscope to provide details of the petrographic components and diagenetic processes that affect the rocks. All thin sections are stained with Alizarine Red S following the procedure of Friedman (1959) to differentiate between calcite and dolomite in the thin section. The classification of (Dunham, 1962) is used to describe and classify the carbonate rocks of the formation, whereas dolostone textures are defined according to crystal

size following (Chatalov, 2013). The mineralogy of six samples was identified by using chemical analysis and X-ray diffraction (XRD). Five samples were studied with a Scanning Electron Microscope (SEM) in Al-Khora Company (Baghdad) to identify the microporosity. Carbon and oxygen isotope ($\delta\ ^{18}O$ and $\delta\ ^{13}C$) analyses were performed for eight samples in the laboratories of the Institute of Geology, Mineralogy and Geophysics at the Ruhr-University Bochum to provide information about paleoenvironmental such as temperature and salinity variations of the seawater.

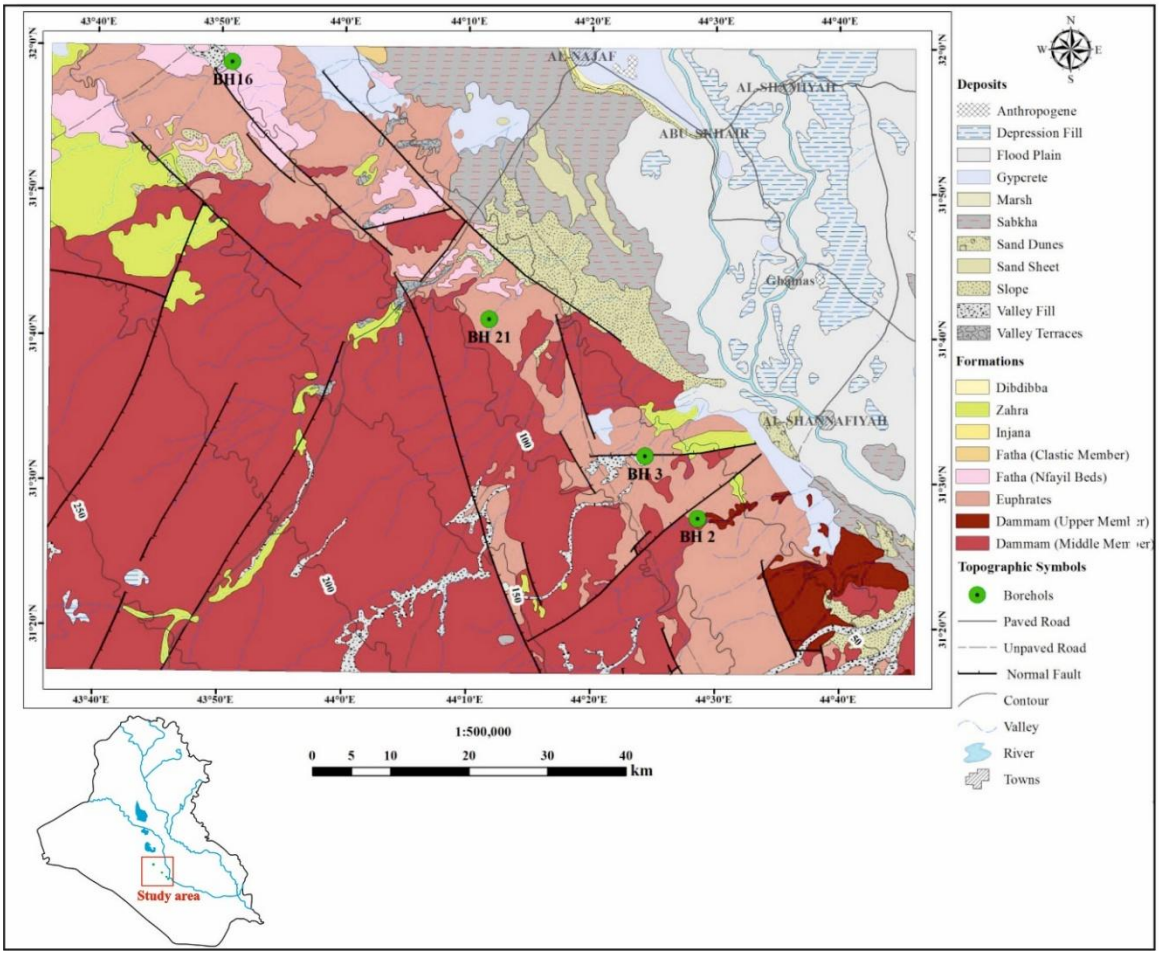


Fig. 1. Geological and location map of the studied boreholes (after Hassan *et al.*, 1995).

Results

Mineralogy and geochemistry

The main rocks of the Dammam Formation are limestone, dolostone, and dolomitic limestone. The result of XRD analysis show the presence of non-clay minerals is calcite, dolomite, quartz and feldspar, whereas clay minerals as secondary minerals including (palygorskite, montmorillonite and kaolinite) (Fig. 2). The clay minerals of Dammam Formation are various including terrigenous (detrital) like kaolinite that may formed during regressive period from the continent, and authigenic such as palygorskite (Table 2). Since kaolinite does not form in a marine environment, it has a detrital origin (Swadi et al., 2023).

Table 2: Samples and results of the XRD Test.

Ser. No.	Sample name	Depth (m)	Formation	Clay minerals	Non-clay minerals
1	BH3/A10	22	Euphrates	---	Calcite
2	BH3/A11	26	Euphrates	Palygorskite and montmorillonite	Calcite and dolomite
3	BH3/A12	35	contact	Palygorskite and montmorillonite	Calcite, quartz and feldspar
4	BH3/A15	44	Dammam	---	Calcite and dolomite
5	BH3/A19	54	Dammam	Montmorillonite and Kaolinite	Calcite and quartz
6	BH3/A26	74	Dammam	---	Calcite and dolomite

7	BH3/A30	84	Dammam	Palygorskite and	Montmorillonite	Dolomite, quartz and feldspar
8	BH3/A34	94	Dammam	Montmorillonite and Palygorskite		Calcite, quartz and dolomite
9	BH3/A40	110	Dammam	---		Dolomite and quartz
10	BH3/A41	115	Dammam	---		Dolomite
11	BH3/A42	120	Rus	---		Dolomite and gypsum

The analysis of major oxides shows that the average of SiO_2 is 5.14% and it ranges from 0.02 % to 18.3%. Aluminum oxide average is 0.69%, with a range between 0.04% and 2.18 %. Silica (SiO_2) and alumina (Al_2O_3) originate from clay minerals and detrital quartz (Table 3).

The highest values of silica and aluminum in some samples were pointed out in the sandy limestone layer found above the contact within the Euphrates Formation. The average of Fe_2O_3 is 0.30% and it ranges from 0.02% to 0.88%. Sulfate oxide (SO_3) reflects values from 0.03% to 0.09%, with an average of 0.06%. Sulfate is hard to find in carbonate rocks, while the values of SO_3 are found in strata that contain gypsum cement. On the contrary, CaO, MgO, and LOI reveal high values compared with other major oxides. The average of CaO is 36.55%, and its range is between 31.03% and 44.97 %. The average of MgO is 13.74%, and it ranges from 0.77% to 20.79% (Fig. 3). The average of LOI is 43.58% and its range is between 35.15% and 47.5%. The high percentage of CaO is due to the high content of carbonate rock in the Dammam Formation, which is mainly composed of calcite. Meanwhile, the high percentage of MgO is related to dolomitization, which affects limestone poetically in the upper part of the middle member of the Dammam Formation.

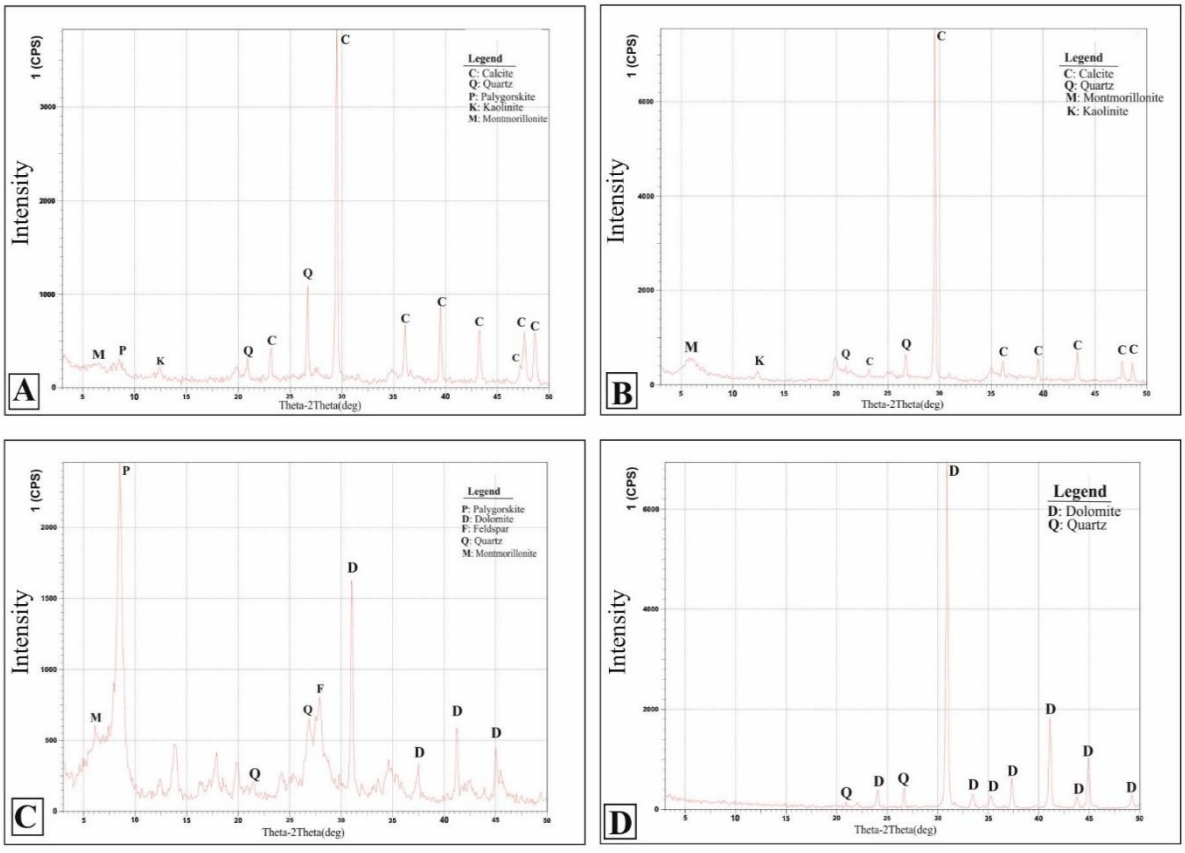


Fig. 2. X-ray diffractograms show the peak reflections of the minerals; (A) BH3/A12, 35m depth; (B) BH3/A19, 54m depth; (C) BH3/A30, 84m depth; (D) BH3/A41, 115m depth.

Table 3: Percentage of chemical analysis for Dammam Formation rocks, BH2.

Ser. No.	Sample name	Depth m.	SiO_2%	Fe_2O_3 %	Al_2O_3%	CaO%	MgO %	SO_3%	LOI%	Total
1	BH2/A1	5	18.30	0.30	2.18	42.89	0.77	0.03	35.15	99.62
2	BH2/A5	10	13.88	0.36	1.79	44.97	1.38	0.04	37.22	99.64
3	BH2/A9	20	0.81	0.10	0.55	32.9	18.58	0.06	46.99	99.99
4	BH2/A14	30	0.10	0.04	0.08	37.46	15.75	0.06	46.50	99.99

5	BH2/A20	41	0.74	0.10	0.22	31.03	20.79	0.06	47.5	100.44
6	BH2/A25	52	0.06	0.02	0.05	34.04	18.65	0.09	47.07	99.98
7	BH2/A29	60	0.04	0.25	0.06	33.08	19.54	0.08	46.07	99.12
8	BH2/A33	70	0.02	0.49	0.05	34.10	20.01	0.09	44.81	99.57
9	BH2/A42	81	0.90	0.88	0.20	32.0	18.58	0.06	47.10	99.72
10	BH2/A47	90	0.36	0.02	0.04	37.19	15.87	0.09	46.41	99.98
	Min		0.02	0.02	0.04	31.03	0.77	0.03	35.15	99.12
	Max		18.3	0.88	2.18	44.97	20.79	0.09	47.5	100.4
	Average		5.14	0.30	0.69	36.55	13.74	0.06	43.58	99.83

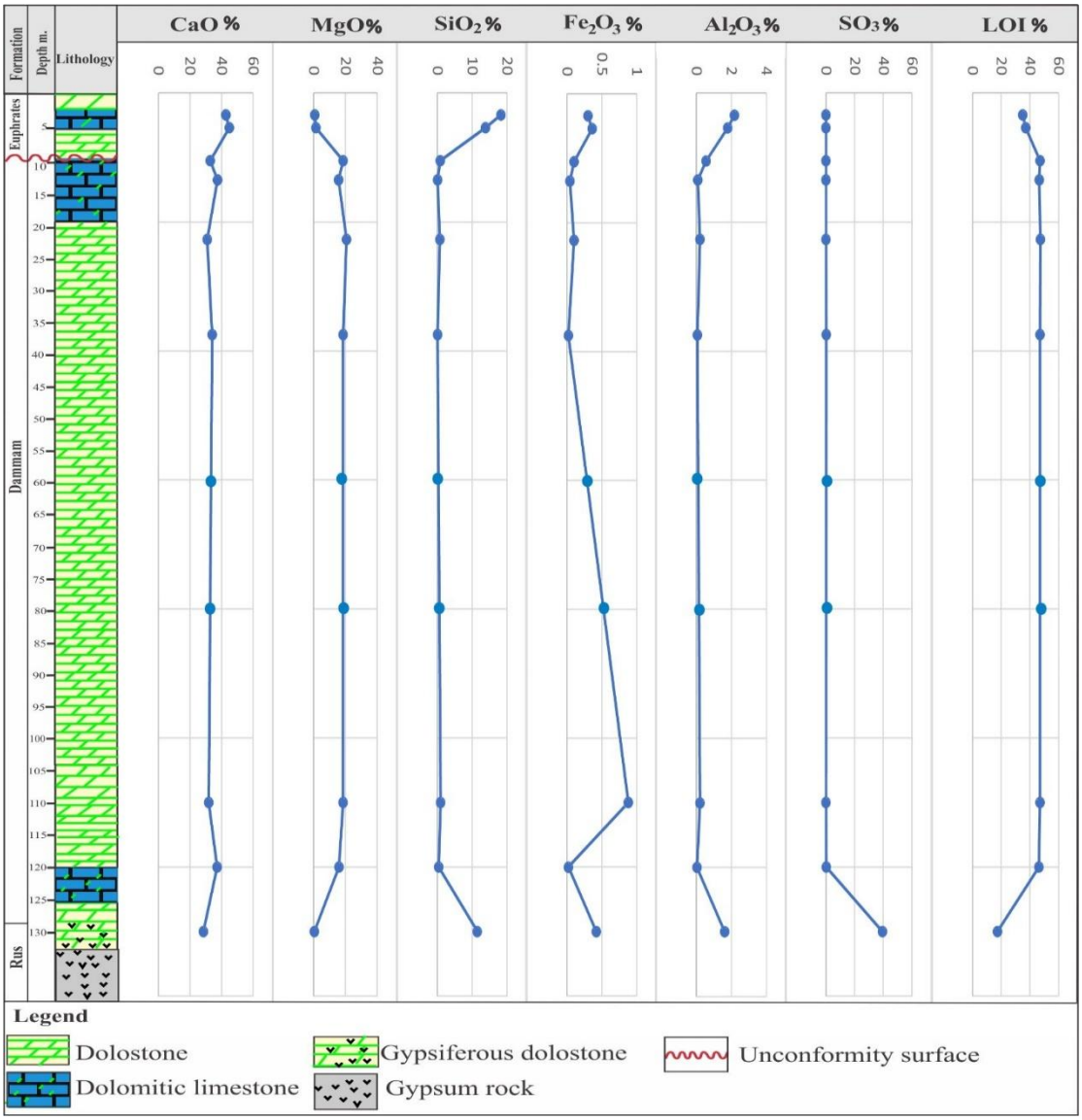


Fig. 3. Chemostratigraphy of major oxides of Dammam formation in BH2.

Oxygen and carbon isotopes

The stable oxygen isotope composition ($\delta^{18}O$) of a precipitated carbonate depends mainly on the isotope composition, salinity, and temperature of the host fluid, whereas the stable carbon isotope composition ($\delta^{13}C$) reflects the source of CO_2 for precipitation, such as meteoric or seawater, shell dissolution, or various biochemical origins, including microbial oxidation of organic matter and methane. Consequently, plots of $\delta^{18}O$ versus $\delta^{13}C$ for carbonate materials can help identify their depositional and/or diagenetic environments (Nelson and Smith, 1996).

Eight samples of limestone and dolomitic limestone are analysed for oxygen and carbon isotopes. The values of $\delta^{18}O$ and $\delta^{13}C$ for Dammam Formation vary from -9.09‰ to -5.13‰ and -7.97‰ to -5.28‰ respectively, while the values of $\delta^{18}O$ and $\delta^{13}C$ for Euphrates

Formation vary from -10.48 ‰ to -0.59‰ and -7.40‰ to 0.20‰ respectively (Fig. 4). The calcite paleotemperature equation is used to calculate the "isotope temperature" of the formation. Epstein et al. (1953; in Taha and Abdullah, 2019) used the $\delta^{18}O$ value of the water responsible for calcite precipitation, known as:

$$T=16.5 - 4.3\,\delta + 0.14\,\delta^2$$

Where: T is the temperature in °C.

The paleotemperature of the Dammam carbonates ranges from (42.2- 67.1 °C) in the studied borehole (BH3) (Table 4).

Table 4: The analytical results of $\delta^{18}O$ and $\delta^{13}C$ show the temperature of calcite precipitation, T and Z values.

Sample Name	Depth (m)	Formation	Lithology	$\delta^{13}C^{PDB}$ [‰]	$\delta^{18}O^{PDB}$ [‰]	T (°C)	Z	Salinity
BH3/A1	2.3	Euphrates	Calcite	-0.65	-10.48	76.9	120.7	marine
BH3/A6	15	Euphrates	Calcite+ dolomite	0.20	-0.59	19.1	127.4	marine
BH3/A11	24	Euphrates	Calcite	-7.40	-5.44	44.1	109.4	Meteoric-marine
Min				-7.40	-10.48			
Max				0.20	-0.59			
Average				-3.01	-5.51			
BH3/A12	35	Contact	Calcite	-7.97	-8.70	64.5	106.6	Meteoric-marine
BH3/A14	42	Dammam	Calcite	-6.66	-8.17	60.9	109.5	Meteoric-marine
BH3/A26	74	Dammam	Calcite	-5.42	-9.09	67.1	111.6	Meteoric-marine
BH3/A35	94	Dammam	Calcite+ dolomite	-5.28	-5.13	42.2	113.9	Meteoric-marine
Min				-7.97	-9.09			
Max				-5.28	-5.13			
Average				-6.43	-7.55			
BH3/A41	118	Rus	Dolomite	-1.96	0.89	12.7	123.7	marine

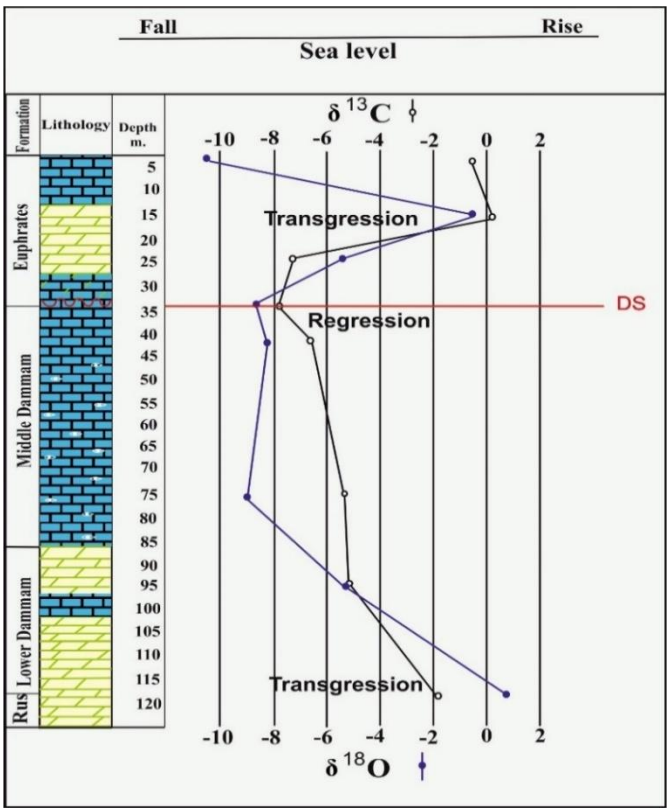


Fig. 4. The variations of δ¹³C and δ¹⁸O values for limestone and dolostone lithologies versus depth in wells BH3.

To differentiate between marine and freshwater limestone, the following equation is used (Keith and Weber, 1964):

The paleo-salinity (Z values) = $2.048(\delta\ ^{13}C + 50) + 0.498(\delta\ ^{18}O + 50)$

Where both $\delta^{13}C$ and $\delta^{18}O$ are measured as ‰ PBD. The Z values above 120 for carbonate rocks would be classified as marine, while the values below 120 as freshwater. The Z values for the Dammam carbonate samples range from 106.6 to 113.9 in the studied area. The Z value less than 120 indicates that regional regression caused the exposure of the study area. The exposed sediments were subjected to fresh water diagenesis, with aragonite dissolution, cementation by calcite spar, and sediment stabilization to low-Mg calcite, taking place in vadose and phreatic zones.

Discussion

Facies associations of Dammam Formation

Three facies' associations are distinguished in the Dammam Formation. Each represents a distinct depositional environment, including restricted, shallow open marine, and shoal environments (Table 5). In addition, diagenetic carbonate facies are identified.

Table 5. Facies associations in the Dammam Formation.

Facies association	Microfacies	Skeletal and non-skeletal	Diagenesis
Restricted	Bioclastic mudstone and dolomitic bioclastic mudstone	fossils <10% with carbonate mud matrix. Benthonic foraminifera	Early dolomitization, dissolution, and porosity developments such as intercrystalline.
	Dolomitic intraclastic mudstone	Intraclasts consist of microcrystalline dolomite and range in size from fine to medium sand (0.2–0.4 mm)	Early dolomitization
	Dolomitic foraminiferal bioclastic wackestone	Fossils (15-20 %) with carbonate mud matrix. The bioclasts include *Coskinolina* sp., miliolids,	Dolomitization, micritization, dissolution and porosity development such as intraparticle, vugs, biomolds, and

		Peneroplis sp., *Elphidum* sp., *Textularia* sp.	intercrystalline and selective silicification of some fossils
Open marine	Bioclastic nummulitic wackestone- packstone	Fossils (15-20 %) with carbonate mud matrix. The bioclasts include *Nummulites bayhariensis*, *Nummulites gizehensis*, *Nummulites perforatus*, *Nummulites* sp., *Coskinolina* sp. echinoderm plates, and echinoid spines. Other bioclasts are relatively rare, including ostracods, a few gastropods and broken shell fragments	Partial dolomitization, micritization, neomorphism (recrystallization and inversion), dissolution and porosity development (vugs, intercrystalline, and intraparticle), cementation by granular calcite, and selective silicification of shell fragments
Shoal	Nummulitic packstone	Fossils (40-50) % with carbonate mud matrix. The recorded bioclasts (30–50%) consist of *Nummulites gizehensis*, *Nummulites perforates*, *Nummulites planulatus*, and *Nummulites* sp.	Neomorphism (recrystallization and inversion affecting fossils), physical compaction, dissolution, and porosity development (intraparticle and intercrystalline).
	Bioclastic nummulitic grainstone	Fossils (50-60) % with sparry calcite cement. The recorded bioclasts consist of *Nummulites gizehensis*, *Nummulites bayhariensis*, *Nummulites millecaput*, *Nummulites* sp. and bryozoa.	Dissolution and porosity development (intraparticle, intercrystalline, and vugs), cementation of some pores by secondary calcite such as granular, syntaxial rim, and isopachous rim cement, and neomorphism (inversion affecting fossils).

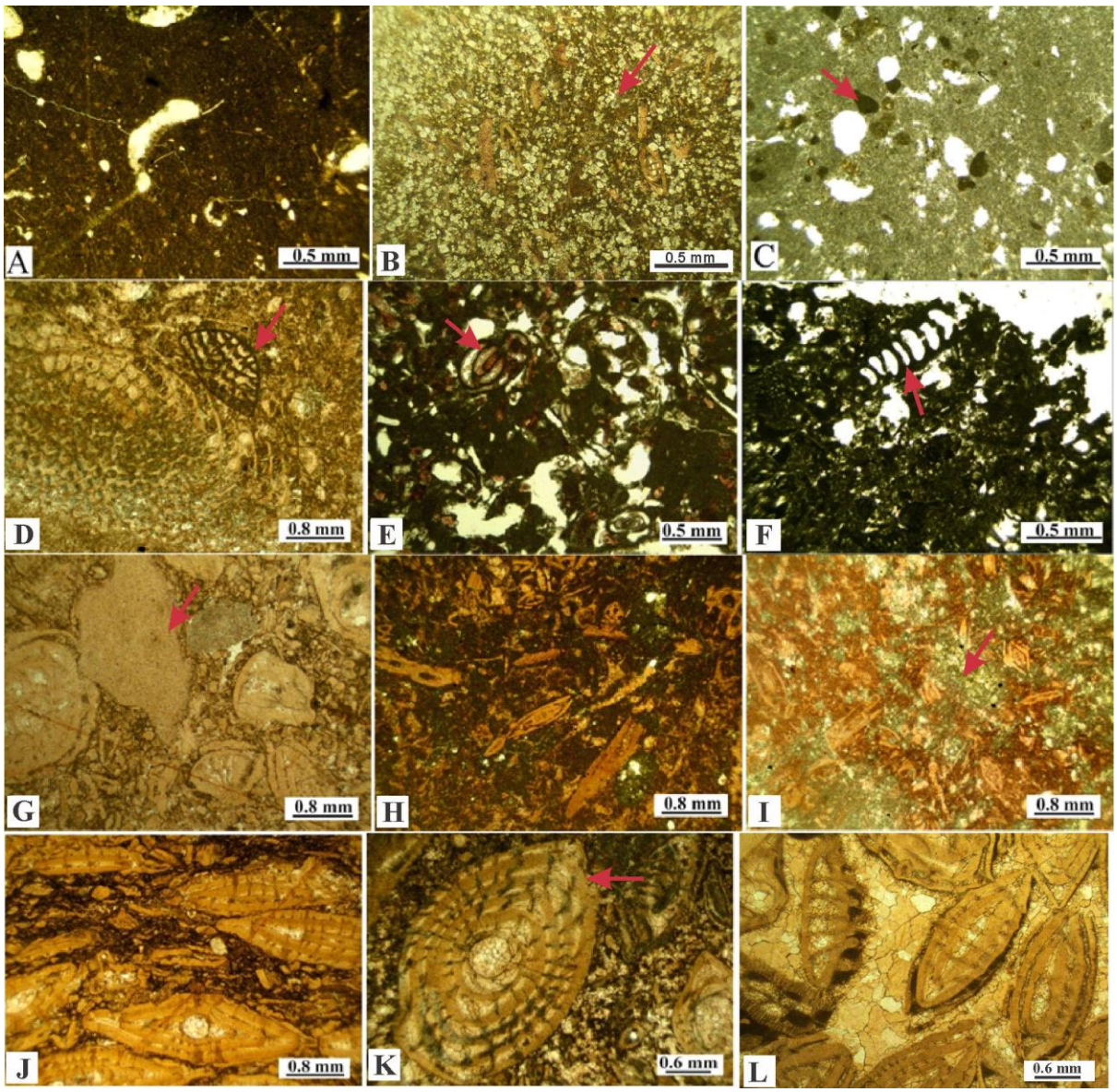


Fig. 5. Microfacies of the Dammam Formation; (A) Bioclastic mudstone, BH21, 106 m depth, PPL.; (B) Dolomitic bioclastic mudstone BH21, 81m depth, PPL; (C) Dolomitic intraclastic mudstone, BH21, 177 m depth, PPL.; (D) *Coskinolina* sp., BH3, 53 m depth, PPL.; (E) Dolomitic foraminiferal bioclastic wackestone showing miliolids, BH3, 96m depth; F) *Peneroplis* sp., BH16, 120m depth, PPL.; (G) Bioclastic nummulitic wackestone-packstone showing Echinoderm plate, BH3, 43 m depth; H) Fragments of *Nummulites* sp., BH3, 80 m depth, PPL.; (I) Dolomitization selectively affects groundmass, BH3, 60m depth PPL.; (J) Nummulitic packstone showing packed nummulites which affected by physical compaction, BH3, 61 m depth, PPL.; (K) *Nummulites perforatus*, BH3, 70 m depth, PPL.; (L) Bioclastic nummulitic grainstone, BH3, 50m depth, PPL.

Diagenetic carbonate facies

In addition to the above-mentioned microfacies, three diagenetic facies within the Dammam Formation are recognized. These facies are not included in the facies associations as they were affected by diagenetic changes that severely affected the original textures and structures of the rocks, as well as the fauna. The diagenetic facies include crystalline dolostone, biomoldic fine to medium crystalline dolostone, and crystalline limestone.

1. Fine to medium crystalline dolostone

The rocks assigned to these facies are varicolored (beige, grey, yellowish white, and greyish white), mostly tough and very tough. Petrographic investigation reveals that dolomite is considered the main component (98.5–100 %). It is present as fine to medium (0.04-0.14) mm, subhedral to euhedral and rhombohedral tightly interlocking crystals, most of which

show zoning. The zoning indicates the changes in fluid geochemistry of the formation during the growth of dolomite crystals. These facies are severely affected by diagenetic processes, such as late dolomitization, dissolution, and porosity development (intercrystalline, vugs, and intracrystalline), cementation by different types of cement including secondary calcite such as granular, blocky and poikilotopic enclosing fine to medium rhombic dolomite (Fig.12 G and H), and then selective silicification of shell fragments by chalcedony (Fig. 13 G).

2. Biomoldic fine to medium crystalline dolostone

The rocks that belong to these facies are white, grayish white, chalky, tough to very tough, and enclose a large number of biomolds. These facies are identified by the occurrence of abundant biomolds (10–35%) with fine to medium (0.04 and 0.12) mm, euhedral to rhombohedral intergrown dolomite crystals. Most of the fossils are dissolved and remain as biomolds. These molds represent the spaces resulting from dissolved fossils (mostly nummulites and pelecypod-shaped molds) (Fig. 7F).

3. Crystalline limestone

In these facies, calcite forms the main constituent occurring as anhedral interlocking crystals and forming a sort of mosaic texture with variable sizes ranging from fine to coarse. The sparry calcite of this facies is probably produced by recrystallization of the micritic matrix. Most of the original depositional textures and constituents are obliterated. This facies is observed in the uppermost part of the Dammam Formation, and it indicates the exposure of the formation in the late Eocene. Recrystallization from micrite to coarse sparry calcite depends on changes in temperature, pressure, water chemistry, and rates of flow in fresh water vadose and/or phreatic environments (Longman, 1980). This facies is formed in supratidal and intertidal flats under subaerial exposure and during fluctuations in sea level (sea-level regression) (Flügel, 2004).

Diagenetic Processes

The diagenetic processes and products are identified by petrographic study and chemical analysis. Several diagenetic processes affect the rocks of the Dammam Formation, including dolomitization, which appears widespread, micritization, leaching, cementation, neomorphism, silicification, physical compaction, and dedolomitization. These observations (Figs. 14 and 15) are discussed below:

Dolomitization

The Dolomites can be subdivided into primary and secondary based on mode of formation (Pichler and Humphrey, 2001). Usually at or close to room temperature (20–35°C), primary dolomite precipitates straight from aqueous solution without $CaCO_3$ dissolution required (Wells, 1962). But dolomite can also be formed as a subsequent phase that replaces the precursor mineral calcite. These diagenetic processes highly affect the middle members of the Dammam Formation in the study boreholes (Figs. 14 and 15).

Dolomite-rock textures

Five dolomite-rock textures are distinguished and classified according to crystal-boundary shape (planar or non-planar) and crystal-size, using the dolomite-rock classification scheme of Sibley and Gregg (1987) and Chatalov (1971).

1. Microcrystalline dolomite: This type consists of very fine-grained, unimodal, and euhedral crystals of dolomite (Fig. 6A).
2. Planar-euhedral dolomite: this type consists mostly of limpid and euhedral to rhombohedral crystals of dolomite ranging in size from fine to coarse (0.2-0.6) mm (Fig. 6 B and C). In some samples, dolomite has zoning with a cloudy center and clear rim (CCCR) (Fig. 6E). The center of dolomite crystals is cloudy because of high calcite inclusion. The presence of

subhedral to euhedral and zoned crystals of dolomite suggests a major, probably long-lasting dolomitization event during a marine-meteoric mixing zone environment under low temperature and pressure (Chafetz, 1972). The zoning indicates changes in the geochemistry of formation fluids during the growth of dolomite crystals. This process is formed under a hypersaline environment.

3. Planar-subhedral to euhedral dolomite: These crystals are subhedral with straight and scarcely curved boundaries ranging in size from fine to medium (0.15-0.4) mm with low inter-crystalline porosity (Fig. 6D).

4. Planar void-filling dolomite: The dolomite crystals are euhedral, lining pores or vugs (Fig. 6F). At the late stage, dissolution is followed by reprecipitation of dolomite occurs as pore-filling dolomite, which is known as dolomite cement.

5. Planar- porphyrotopic dolomite: It occurs as euhedral crystals floating within micritic matrix (Fig. 7A).

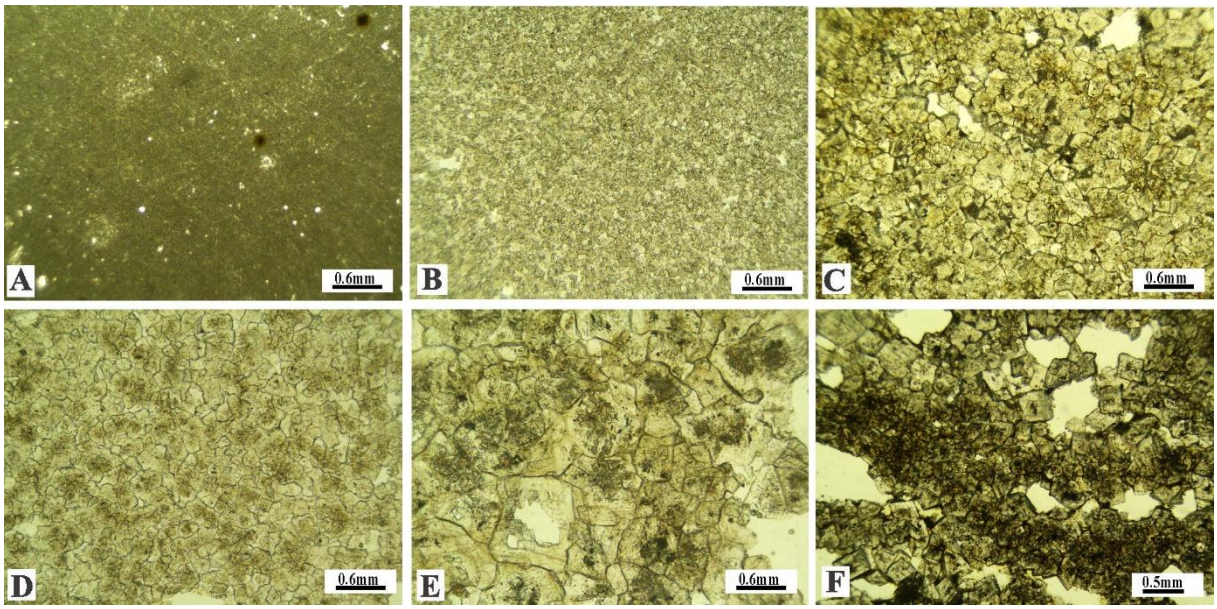


Fig. 6. (A) Non planar- microcrystalline dolomite, BH3, 87m. depth, PPL; (B) Fine crystalline planar-subhedral dolostone, BH21, 36m. depth, PPL; (C) Medium crystalline planar-subhedral-euhedral dolostone, BH16, 65m. depth, PPL; (D) Medium crystalline planar subhedral dolostone, BH21, 56m. depth, PPL; (E) Coarse crystalline planar- euhedral dolostone, BH16, 55m. depth, PPL; (F) Planar void-filling dolomite with cloudy center and clear ream (CCCR), BH16, 50m. depth, PPL.

Replacive dolomite

Many dolostones in the stratigraphic record contain fossils that suggest typical marine habitats of deposition, which is a sign of dolomitization as a result of the partial and total replacement process of mineral calcite or aragonite (Nichols, 2009; in Mahdi et al., 2023). Replacive dolomite usually occurs at the early and middle stages, where dolomite replaces limestone with enough amount of Mg^{2+} source. Replacive dolomite usually retains the original texture of precursor limestone. This process is the dominant type in the Dammam Formation and is verified by the occurrence of very finely crystalline dolomite that is wholly or partly replaced by micritic matrix and fossils (Fig. 7).

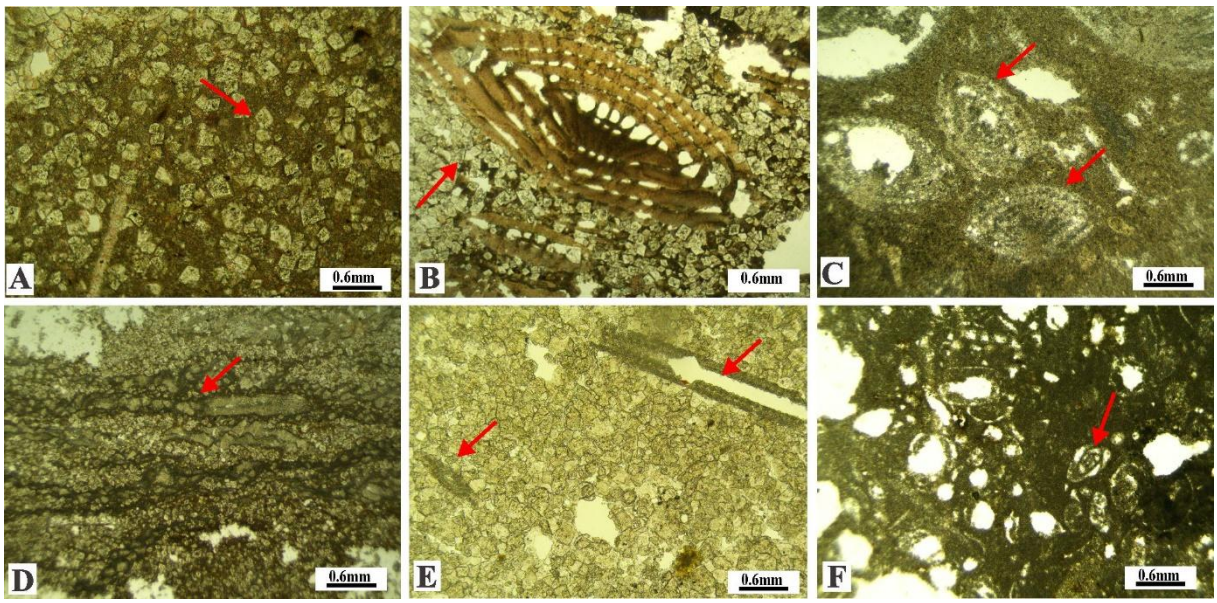


Fig. 7. Replacive dolomite (A) Scatter rhomb of planar- porphyrotopic dolomite in the matrix, BH21, 112m. depth, PPL; (B) Selective dolomitization affecting groundmass of dolomitic nummulitic wackestone, BH21, 78m. depth, PPL; (C) Pervasive dolomitization affecting fossils and groundmass, BH16, 42m. depth, PPL; (D) Dolomitization completely affects groundmass and nummulite, BH16, 45 m. depth, PPL. (E) Dolomitization affecting groundmass and echinoid spine, BH21, 115m depth, PPL; (F) Pervasive dolomitization affecting groundmass and fossils such as miliolids.

Dolomite origin

Dolomite $CaMg(CO_3)_2$ can be deposited by two different mechanisms (Machel, 2004): (1) by substitution of $CaCO_3$ by $CaMg(CO_3)_2$ (replacive dolomite) and (2) by deposition of dolomite from aqueous solution in primary or secondary pores (dolomite cement). Dolomite can form as a hydrothermal phase, a diagenetic replacement, or a primary mineral; all that is needed is sufficient magnesium and fluid movement. Tucker and Wright (1990) and Warren (2000) proposed five models to explain the dolomitization process: seepage-reflux, burial, evaporative (penecontemporaneous; in hypersaline sabkha/supratidal), seepage-zone, and seawater models. The first and second models occur on a lower scale, while the rest models occur in large-scale dolomitization (Nichols, 2009). Petrographic investigations, geochemical data, and isotope analysis show that the dolomitization of the Dammam Formation occurred in a mixing zone. These observations are shown in Figure 8, and as explained below:

1. Petrographic investigation shows the common occurrence of planar (euhedral, subhedral) dolomite texture and the lack of non-planar (anhedral) dolomite, which specifies that the dolomitization took place under low salinity and temperature conditions (Gregg and Sibley, 1984). The crucial roughening temperature for dolomites is between 50 and 60 °C, which is the range around which planar crystals form (Gregg and Sibley, 1984). These are lower than the temperatures that are expected to arise when limestones are dolomitized at hydrothermal water (100–220 °C) or deep burial temperature (70–90 °C) (Warren, 2000). The paleotemperature of dolomite in Dammam Formation, which is calculated based on $\delta^{18}O$, ranges from (42.2-67.1°C). Consequently, the likelihood of its development by the mixing of meteoric sea water in situations of low temperature and shallow burial depth increases.
2. The studied dolostones do not include evaporite minerals, according to thin-section observations, chemical analysis, and XRD analysis. This suggests that the examined dolomite is typically not compatible with the dolomitization model in environments with brine reflux or evaporitic supratidal (sabkha) (Machel, 2004). Thus, the dolomitization of the Dammam Formation probably occurred in a mixing zone at shallow burial depth. It is mainly developed during major sea-level fall periods in the carbonate platform. The sea-level fall is associated with the progradation of the meteoric-marine mixing zone.

3. Dolomite formed in equilibrium with normal seawater has $\delta^{18}O$ values of 1-3‰, while hypersaline water has $\delta^{18}O$ values greater than +3‰ (Land, 1985; Warren, 2000). Thus, the values of oxygen isotope in the dolomite samples at depths 94-118 m (-5.13 to +0.89‰) indicate that dolomitization was unlikely resulted from hypersaline or seawater. Therefore, the reduction in the oxygen values (-5.13 to +0.89‰) implies that the dolomitization was caused by a seawater-meteoric water mixture.
4. The depletion in $\delta^{13}C$ values (-7.97‰) at depth 34 m in BH3-NJ indicates sea-level fall, and exposure of the Dammam Formation in the Late Eocene (Fig. 4).
5. The Late Eocene sea-level fall that affected the carbonate platform of the Dammam Formation in the study area supports the mixing meteoric-seawater model of Tucker and Wright (1990).

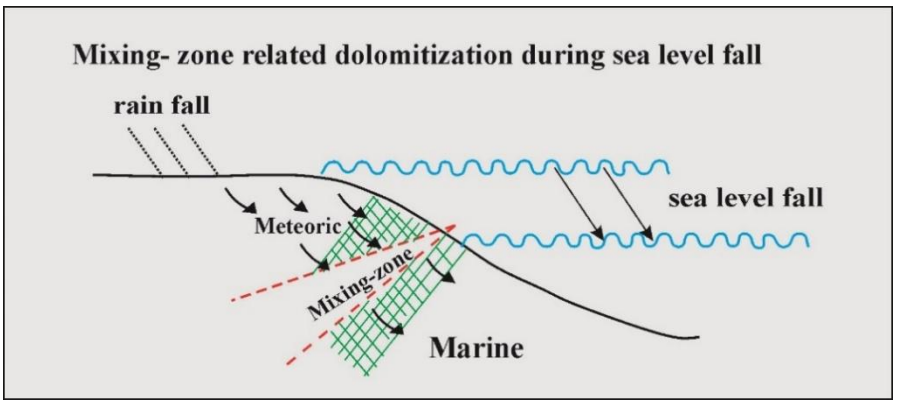


Fig. 8. Suggested dolomitization model (after Wright, 1993) for the Dammam Formation based on petrographic, mineralogical, and geochemical characteristics of Dammam dolostone.

Dissolution and porosity evolution

This process occurs when the pore-fluids are undersaturated relative to carbonate minerals, leading to dissolution of metastable carbonate grains and cement. This process affects shallow near-surface meteoric environments, and according to Choquette and Pray (1970), it resulted in the development of three types of pores. They are:

1. Fabric-selective pores:

This is related to the components of the carbonate rock. These pores are classified into different types:

A. Moldic pores

The moldic pores are caused by the solution of whole fossils. It is the most common type of porosity in the upper Dammam Formation, and appears clearly in biomoldic dolostone facies. Certain molds (nummulites and pelecypod-shaped molds) depict the spaces left by the majority of fully dissolved skeleton grains (Fig. 9A). This kind of pore is typical in meteoric-phreatic zones and is widely distributed in shallow marine carbonates.

B. Intraparticle pores

This type of pore is formed by solution within individual particles or grains, mainly within the chambers of skeletal grains (Fig.9 B). The majority of submicrofacies exhibit this phenomenon to varying degrees. Meteoric vadose and phreatic conditions influence the development of this kind of solution.

C. Intercrystalline

The intercrystalline pores result from dolomitization (Fig. 9C) that causes an increase in porosity as limestone facies are dolomitized.

2. Non-fabric selective pores

These pores occur where they are formed, independent of original textures. They are:

A. Vugs

These pores are irregular without a definite shape. They represent solution enlargement of fabric-selective pores presumably due to the interface of meteoric water with seawater in the subsurface environment.

B. Cavern pores

The term cavern is used for larger openings of channel or vug shapes developed mainly by karstic solution processes. These pores are recorded in the karst zone, which is located below the contact between the Dammam and the Euphrates Formations (Fig. 10C).

C. Veins and fractures

They are dominant in the upper part of the Dammam Formation and filled with granular calcite cement (Fig. 12F).

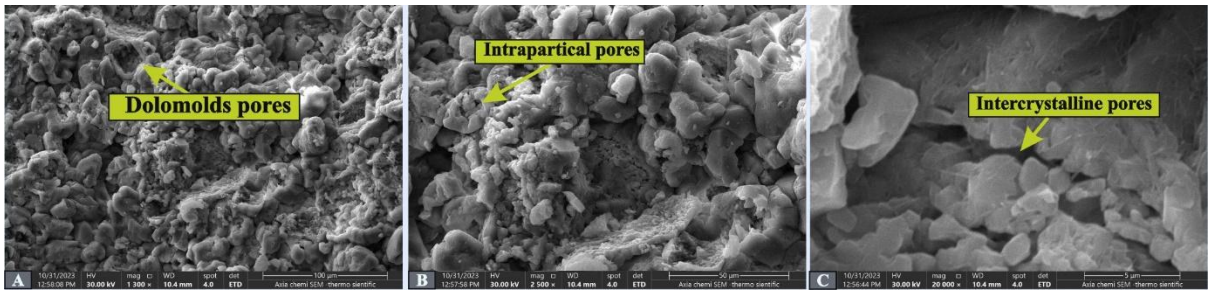


Fig. 9. SEM microphotograph showing rhomb's dolomite in crystalline dolostone; (A) Dolomolds pores; (B) Intraparticle porosity; (C) Intercrystalline porosity.

Karstification

Groundwater enriched with carbon dioxide seeps through carbonate rocks, dissolving portions of the formations and creating solution pipes, sinks, and caverns. The geomorphological features developed by the solution process are referred to as karst features. In this study, the Dammam Formation is subdivided into three members: upper, middle, and lower, with a paleokarst zone at the top. The paleokarst zone is formed when the Dammam Formation was exposed during Oligocene–Early Miocene time. This study includes a detailed investigation of the paleokarst zone, which is located below the contact between the Dammam and Euphrates formations, as noted in the Al-Najaf borehole (BH3). Petrographic evidence for subaerial exposure includes dolocrete features, mixing zone dolomites, and secondary porosity. These observations are shown in Figure 10 and are explained below:

A. The exposed upper part of the Dammam Formation consists of chalky microcrystalline dolostone. The Dammam Formation is extensively fractured. The dolomite is replaced by dolocrete in the weathered zone. A pseudobreccia occurs near the contact zone as a result of the difference in color and texture of dolomite and dolcrete (Fig. 10A). It is observed in BH3, Najaf at 20-25 m depth.

B. Solution vugs and cavities range in size from 4–8 cm and are partially or fully filled with calcite (Fig.10 B).

C. Fractures and small caves occur within the Dammam Formation below the dolomitized zone (Fig. 10C).

D. Friable sediments filling the cave and vugs (Fig. 10D).

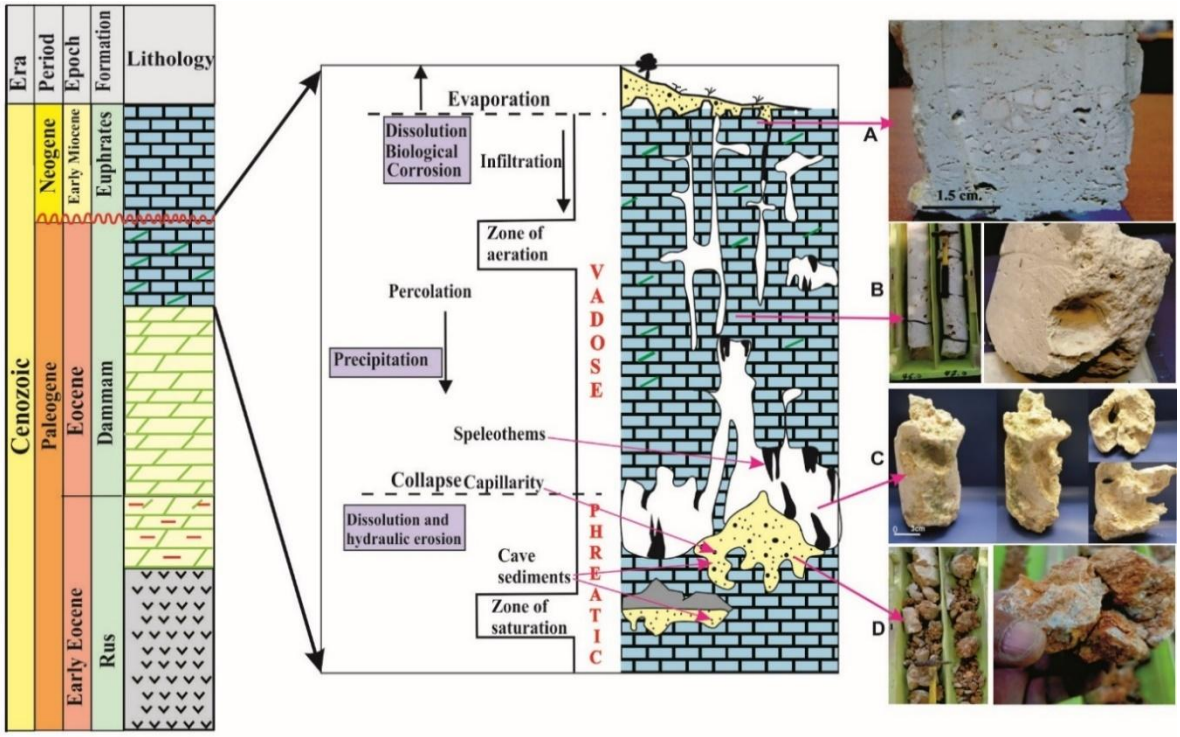


Fig. 10. Paleokarst zone, BH3, compared with Boggs (2009); (A) Pseudobreccia at the top of Dammam Formation, 25 m. depth; (B) Dissolution affects the rocks, which are represented by vugs and cavities, 31m depth; (C) Small caves are present as a result of dissolution at 34-36m depth; (D) Cave sediments filling vugs, 35m depth.

The results of XRD analysis show that the soft sediments filling vugs consist of non-clay minerals such as calcite, quartz, and feldspar, whereas clay minerals include palygorskite and montmorillonite (Fig.11). This indicates that the detrital sediment supply, such as quartz and feldspar, occurred during the exposure stage.

Cementation

It represents the process of precipitation of minerals in primary or secondary pores. This process takes place when the pore fluids are supersaturated with respect to the minerals. In the study boreholes, calcite is the common cementing mineral in the carbonate facies, whereas silica and gypsum are less common cements. Calcite cement includes granular (Fig.12. A), blocky (Fig.12. B), poikilotopic calcite cement (Fig.12. C), and syntaxial overgrowth cement (Fig. 12.D).

Micritization

This process is common in the Dammam Formation. It is the first diagenetic alteration (early marine diagenesis) seen in the studied boreholes and occurred soon after deposition since it predates all other diagenetic features, producing a micritic envelope surrounding skeletal grains, which is composed of high Mg calcite. The occurrence of a micrite envelope is important for the grain shape. Most fossils affected by this process include *Peneroplis* sp. and Miliolids (Fig. 13A). Such a process occurred in the shallow marine environment (Tucker and Wright, 1990).

Neomorphism

This process involves inversion of aragonite to calcite and mainly calcite to recrystallized calcite (Bathurst, 1983). The neomorphic replacement of micritic matrix and fossils is by microsparite calcite (Fig.13. B). In an aqueous environment, inversion occurs when aragonite is gradually replaced by calcite via solution and in situ precipitation. Radial calcite preserves the original aragonitic fossils (Fig.13. C).

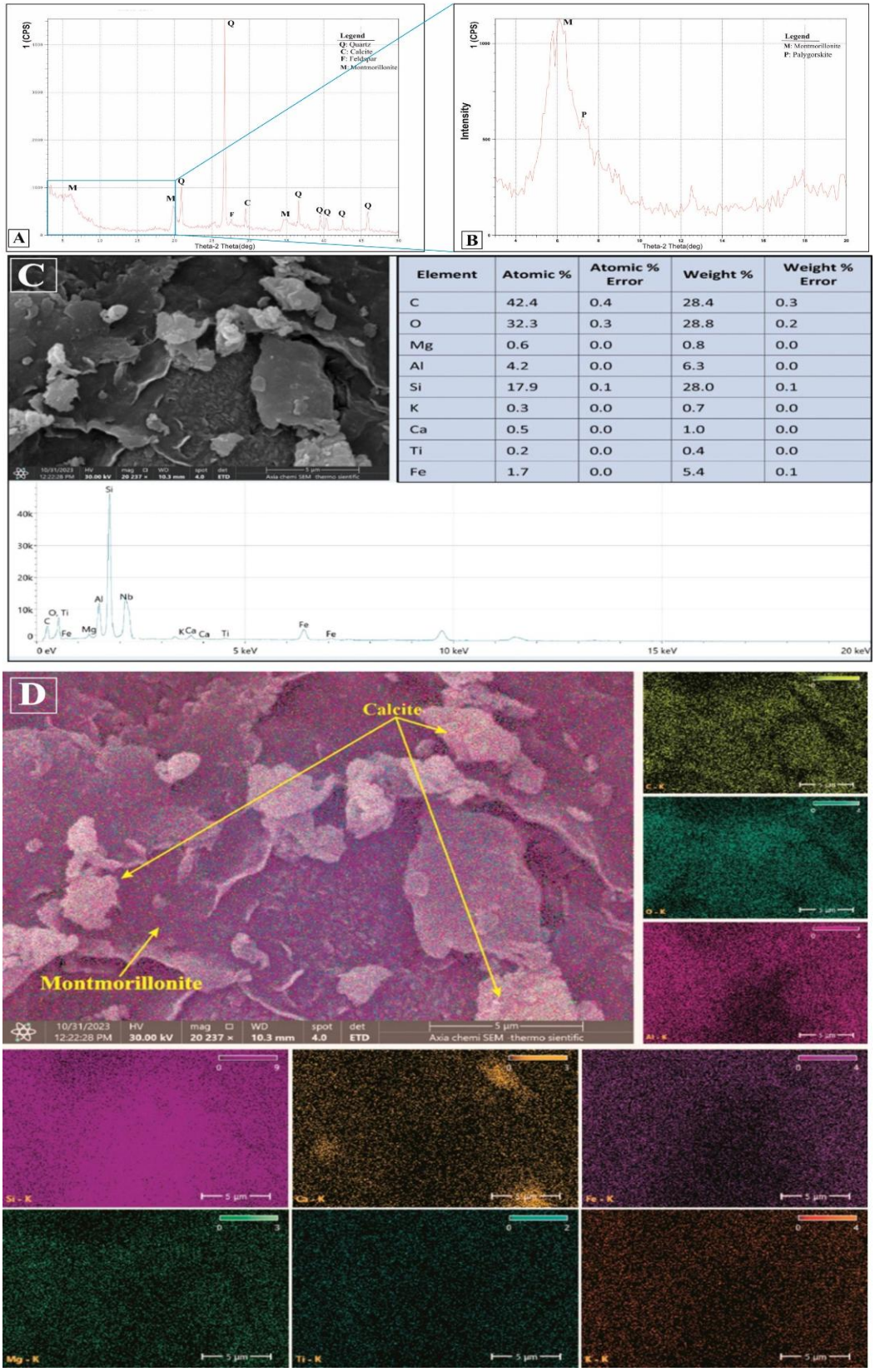


Fig. 11. Soft sediment in unconformity contact between Dammam and Euphrates Formations, 35m depth, BH3 (A) X-ray diffractograms show the peak reflections of the minerals including quartz, calcite, feldspar and montmorillonite; (B) The same of (A) but showing the peak reflections of the clay minerals; (C) SEM image and EDS test result of soft sediment; (D) EDX colour mapping showing carbon, oxygen, aluminium, silicon, calcium, iron, magnesium, titanium and potassium.

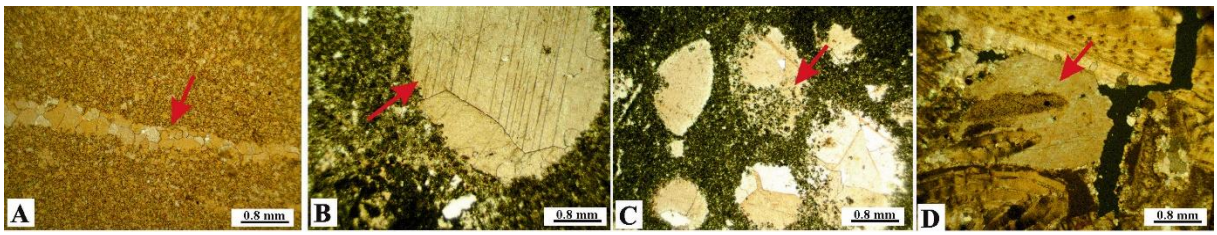


Fig. 12. (A) Fracture filled with granular calcite cement; (B) Blocky calcite cement filling biomolds, PPL.; (C) Poikilotopic calcite cement consists of coarse crystals of calcite enclosing fine and rhombic crystals of dolomite, PPL.; (D) Syntaxial overgrowth cement, BH3, 46m depth, XPL.

Silicification

In the Dammam Formation, the effect of silicification on carbonate rocks involves the partial or complete replacement of shell fragments by silica as well as the precipitation of pore-filling silica cement. The shell fragments of pelecypods are found to be among the most affected bioclasts by selective silicification and either completely or partially replaced by fibrous chalcedony with a preferred orientation parallel to the shell microstructures (Fig.13D).

Dedolomitization

Dedolomitization is the diagenetic replacement of dolomite by calcite to produce a limestone again. Dedolomitization is considered a surface or near-surface process resulting from the interaction between sulphate-rich solution and dolomite. This process is most effective in the uppermost part of the Dammam Formation, and it indicates the exposure of the formation in the late Eocene. The widespread occurrence of dedolomitization is indicated by the following identifiable textures:

- The presence of well-developed composite calcite rhombohedra as pseudomorphs of calcite after dolomite (Fig.13E).
- Remnants of dissolved dolomite are preserved inside the pseudomorphs of calcite or at their boundaries.
- The development of some rhombohedral pores is evidence for dedolomitization in limestone.

Compaction

In the present study, the carbonate rocks of Dammam are subjected to physical compaction. The criteria used to estimate the effect of physical compaction are the preferred orientation of skeletal grains parallel to the bedding, fragmentation of shell fragments, and deformation of fossils such as Nummulites sp. (Fig. 13F).

Paragenesis

The Eocene carbonates of the Dammam Formation in the Al-Najaf area were sampled to study their diagenetic history. These carbonates were cyclically deposited in a shallow water environment and are characterized by extensive dolomitization. The diagenetic history of the limestones can be subdivided into early, middle and late stages (Fig. 16). The term early diagenesis refers to the diagenesis formed immediately after deposition (Berner, 1980; in Flügel, 2010), while the late diagenesis occurs a long time after deposition, when sediments are more compacted into a rock due to burial processes acting in the subsurface over a long geological time (Flügel, 2010). These subdivisions in the Dammam Formation are characterized by porosity evolution, cement type, and recrystallization events, and are separated by periods of dissolution and secondary porosity development. The early stage of diagenesis occurred in a near-surface setting and is characterized by reduction of primary porosity (such as intragranular and intercrystalline pores), micritization, and marine cementation. The middle and late stages reflect post-depositional modification in shallow

meteoric to deep burial settings. Middle stages are characterized by neomorphism, secondary porosity, silicification, and formation of equant calcite spar cements. The late stage of diagenesis occurred in a deep burial environment and is represented by blocky cement, dolomite cement, compaction, and dedolomitization.

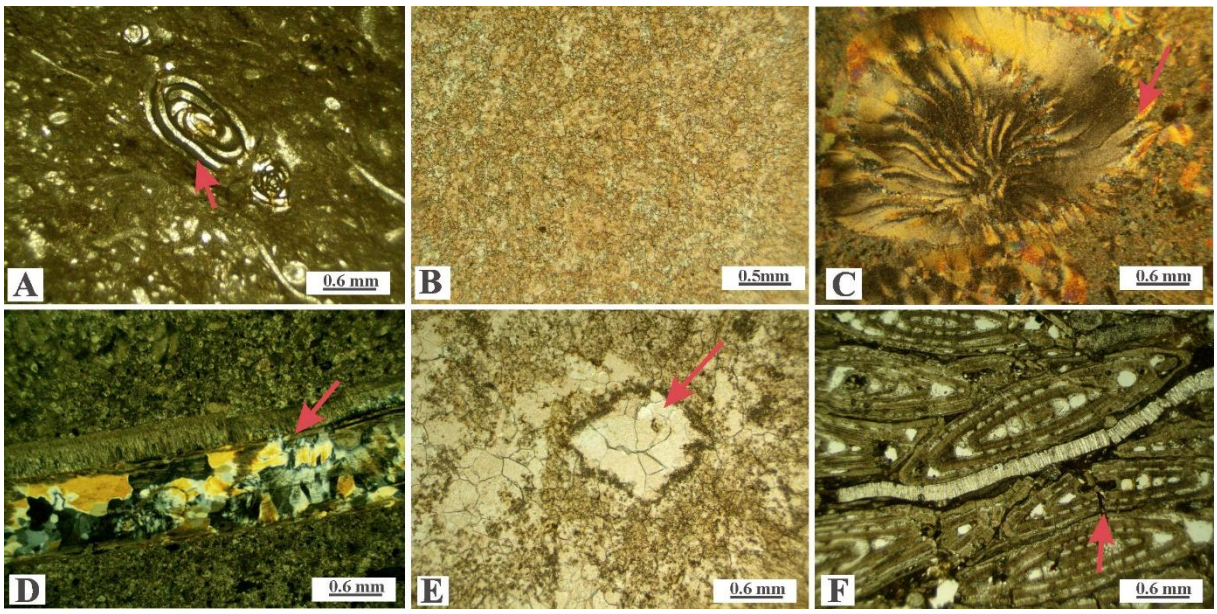


Fig. 13. (A) Micritization affects Miliolids, BH3, 17m depth, PPL.; (B) Crystalline limestone from micrite to microsparite, BH2, 12m depth, XPL.; (C) Inversion affects nummulite, XPL. (D) Complete replacement of shell fragments by silica (fibrous chalcedony); (E) Dedolomitization affects groundmass, pseudomorphs of calcite after dolomite; (F) Nummulitic bioclastic packstone showing deformed nummulite due to physical compaction, PPL.

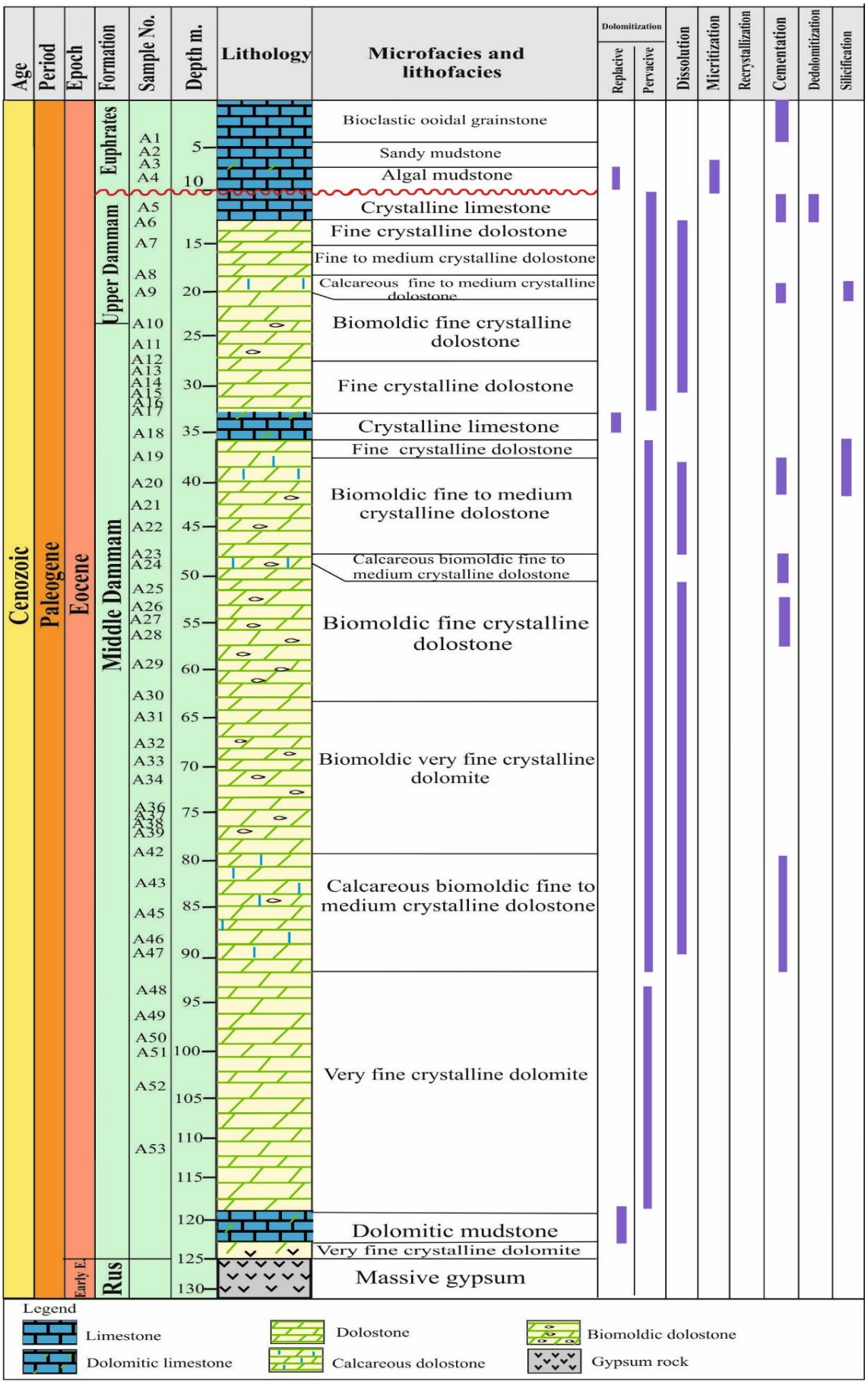


Fig. 14. Stratigraphic column of BH2 illustrating facies and diagenetic processes.

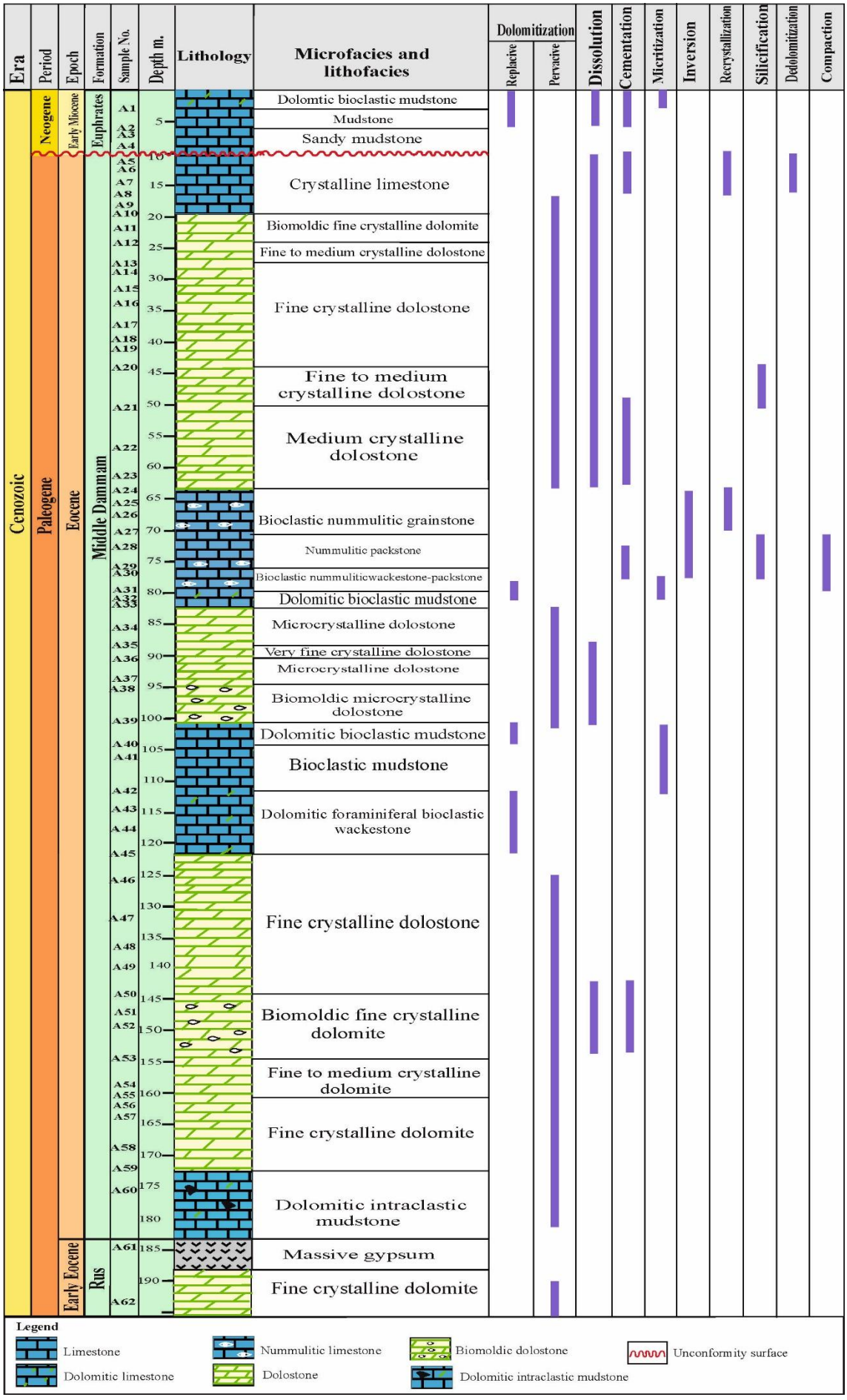


Fig. 15. Stratigraphic column of BH21 illustrating facies and diagenetic processes.

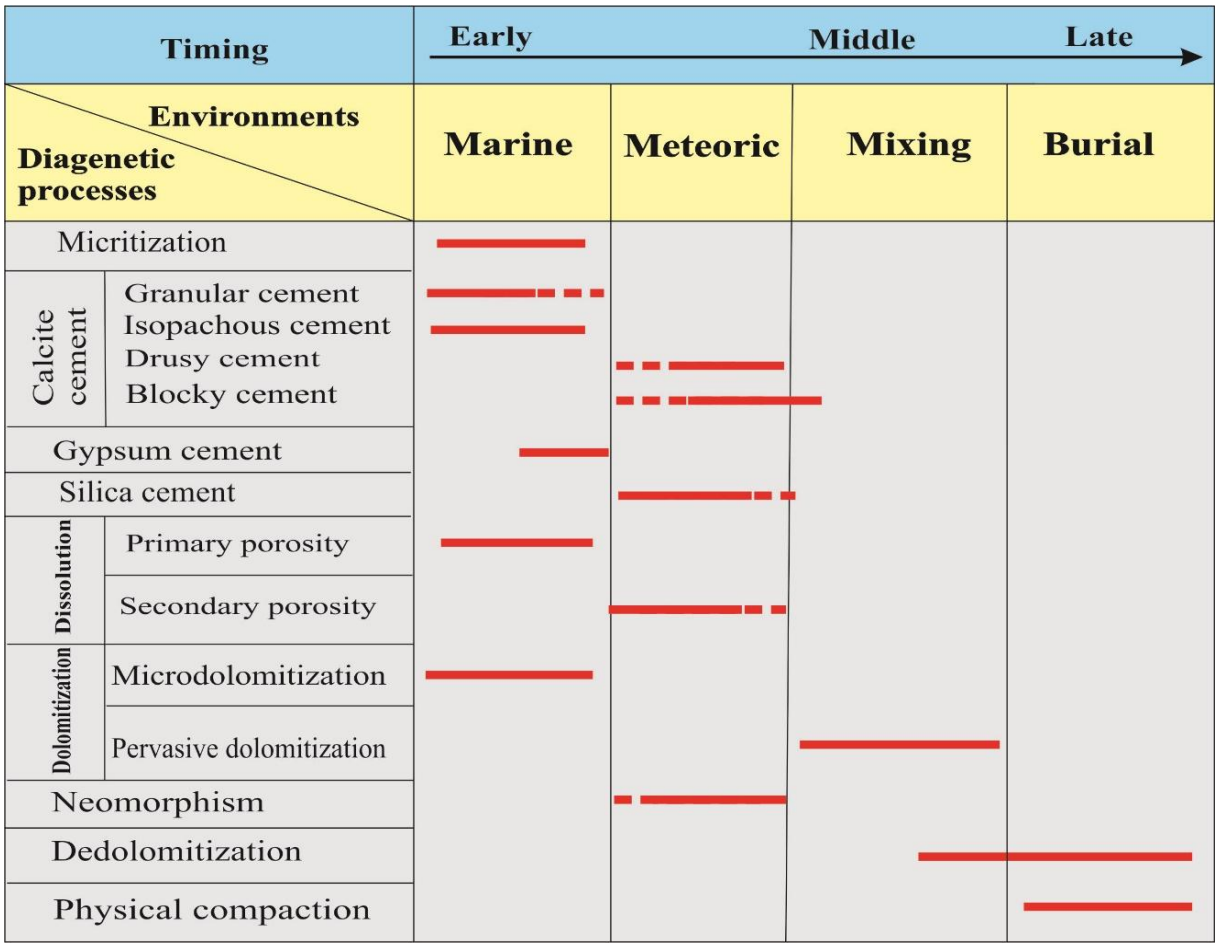


Fig. 16. The main diagenetic processes that affect the Dammam Formation in the study boreholes.

Conclusions

In this study, the Dammam Formation is subdivided into three members: upper, middle, and lower, with a paleokarst zone at the top. The paleokarst zone formed when the Dammam Formation was exposed during Oligocene–Early Miocene time. The results of XRD analysis show the presence of non-clay minerals (calcite, dolomite, quartz, and feldspar), whereas the clay minerals, as secondary minerals, include palygorskite, montmorillonite, and kaolinite.

Six microfacies are distinguished in the Dammam Formation, in addition to dolostone and crystalline limestone facies. Each represents a distinct depositional environment, including restricted, shallow open marine, and shoal environments. Most of these microfacies show indications of scarce to prevalent dolomitization. Five main textural types of dolomites are identified: microcrystalline dolomite, planar-euhedral dolomite, planar-subhedral to euhedral dolomite, planar-porphyrotopic dolomite, and planar void-filling dolomite. The dominance of planar textures and lack of non-planar textures indicates dolomitization under low temperature and salinity conditions. Petrographic investigations, geochemical data, and isotope analysis indicate that the dolomitization of the Dammam Formation was developed in a mixing zone. The decrease of $\delta^{13}C$ values (-7.97‰) at depth 34 m in BH3 indicates sea-level fall, and exposure of the Dammam formation in the late Eocene. During the Late Eocene, the sea-level fall along the carbonate platform of the Dammam Formation supports the model mixing of meteoric-seawater. The paleotemperature of dolomite in Dammam Formation, which is calculated based on $\delta^{18}O$, ranges from (42.2-67.1 °C). Therefore, dolomite deposition by mixing meteoric seawater with low temperature conditions at shallow burial depth becomes a more probable mechanism. The diagenetic history of the limestones can be

subdivided into early, middle, and late stages. The early stage of diagenesis occurred in a near-surface setting and is characterized by reduction of primary porosity, micritization, and marine cementation. The middle and late stages reflect post-depositional modification in shallow meteoric to deep burial settings. The middle stage is characterized by neomorphism, secondary porosity, silicification, and formation of equant calcite spar cements. The late stage of diagenesis occurred in a deep burial environment and is represented by blocky cement, dolomite cement, compaction, and dedolomitization.

Acknowledgments

The authors extend their thanks to Mr. Mustafa A. Ali (Assistant Chief Geologist) and Dr. Younus Al-Saady (Senior Chief Geologist) from the Iraqi Geological Survey for their help in drawing the location map of the study area.

References

Al-Hashimi, H.A.J. and Amer, R.M., 1985. Tertiary microfacies of Iraq. Iraqi Geological Survey (GEOSURV), Baghdad, 56 Pages, 159 Plates.

Bathurst, R.G.C., 1983. Neomorphic spar versus cement in some Jurassic grainstones: Significance for evaluation of porosity evolution and compaction. Journal of the Geological Society, Vol. 14, pp. 229-237. https://doi.org/10.1144/gsjgs.140.2.0229

Bellen, R.C., Daunnigton, H.V., Wetzel, R. and Morton, D., 1959. Lexique Stratigraphic International, Asia, Face 10a, Iraq, Paris. 333 P.

Boggs, S.J. 2009. Petrology of sedimentary rocks, 2nd Edition, Cambridge University Press, New York, 600 P.

Chafetz, H. S., 1972. Surface diagenesis of limestone, Journal of Sedimentary Research, Vol. 42, No. 2, pp. 325–329. https://doi.org/10.1306/74D7253B-2B21-11D7-8648000102C1865D

Chatalov, A.G., 1971. Schemes for the size of textural elements in carbonate rocks, Review of the Bulgarian Geological Society, Vol. 32, pp. 374–377 (in Bulgarian).

Chatalov, A.G., 2013. Flowchart for micropetrographic description and classification of Dolostones, Carbonates and Evaporites, Vol. 28, No. 4, pp. 447 – 456. https://doi.org/10.1007/s13146-013-0140-y

Choquette, P.W. and Pray, L.C., 1970. Geologic nomenclature and Classification of porosity in Sedimentary carbonate, American Association of Petroleum Geologists Bulletin, Vol. 54, No. 2, pp. 207-250.

Dunham, R.J., 1962. Classification of carbonate rocks according to depositional texture, in: Ham, W.E. (ed.) Classification of carbonate rock, American Association of Petroleum Geologists Bulletin, Memoir, No. 1, pp.108-121.

Flügel, E., 2004. Microfacies of Carbonate Rocks, Springer – Verlag Berlin Heidelberg New York, 976 P.

Flügel, E., 2010. Microfacies of Carbonate Rocks, Second edition, Springer Heidelberg, 1006 P.

Fouad, S.F., 2015. Tectonic Map of Iraq, Scale 1:1000 000, 3rd edition, 2012, Iraqi Bulletin of Geology and Mining, Vol. 2, No. 1, pp. 1-7.

Friedman, G.M., 1959. Identification of carbonate minerals by staining methods, Journal of Sedimentary Research, Vol. 29, No. 1, pp. 87 – 97. https://doi.org/10.1306/74D70894-2B21-11D7-8648000102C1865D

Gregg, J.M. and Sibley, D.F., 1984. Epigenetic dolomitization and the origin of xenotopic dolomite texture, Journal of Sedimentary Petrology, Vol. 54, No. 3, pp. 908–931. https://doi.org/10.1306/212F8535-2B24-11D7-8648000102C1865D

Hassan, K.M., Yacoub, S.Y., and Amir, E.A., 1995. The Geology of Al-Salman Quadrangle (NH–38– 6), scale 1:250000, Iraqi Geological Survey (GEOSURV), Internal Report No. 2404.

Jassim, S.Z. and Goff, J.C. (Editors), 2006. Geology of Iraq, Dolin, Prague, and Moravian Museum, Brno, 341 P.

Keith M.L. and Weber Y.N., 1964. Carbon and oxygen isotopic composition of selected limestone and fossils, Geochimica et Cosmochimica Acta, Vol. 28, No. 10-11, pp. 1787-1816. https://doi.org/10.1016/0016-7037(64)90022-5

Land, L.S., 1985. The origin of massive dolomite, Journal of Geological Education, Vol. 33, No. 2, pp. 112-125. http://dx.doi.org/10.5408/0022-1368-33.2.112

Longman, M.W., 1980. Carbonate Diagenetic Textures from Nearsurface Diagenetic Environments, American Association of Petroleum Geologists Bulletin, Vol. 64, No. 4, pp. 461-487.

Machel, H.G., 2004. Concepts and models of dolomitization: a critical reappraisal, Geological Society, London, Special publication, Vol. 235, No. 1, pp. 7-63. https://doi.org/10.1144/GSL.SP.2004.235.01.02

Mahdi, A.I. and Youkhanna, R.Y., 1996. The geology of Shithatha quadrangle, Sheet NI-38-13(GM25), Scale 1: 250 000. Iraqi Geological Survey (GEOSURV), Internal Report No. 2414.

Mahdi, M.M., Al-Shawi, Z.A. and Hannina, S.E., 2023. Microfacies and Depositional Model of the Shuaiba Formation (Lower Cretaceous), in Selected Wells, Southern Iraq, Iraqi Bulletin of Geology and Mining, Vol. 19, No. 2, pp. 69-79. https://doi.org/10.59150/ibgm1902a05

Maziqa, F.H., Mahdi, M.M., and Mohammed, A.H., 2024. Nummulite Biozonation of Dammam Formation During the Eocene Epoch from Samawa and Nasiriya Cities, Southwestern Desert of Iraq, Iraqi National Journal of Earth Science, Vol. 24, No. 2, pp.100-124. https://doi.org/10.46717/igj.56.2A.16ms-2023-7-25

Nelson, C.S. and Smith, A.M., 1996. Stable oxygen and carbon isotope compositional fields for skeletal and diagenetic components in New Zealand Cenozoic nontropical carbonate sediments and limestones: A synthesis and review, New Zealand Journal of Geology and Geophysics, Vol. 39, No. 1, pp. 93-107. https://doi.org/10.1080/00288306.1996.9514697

Nichols, G., 2009. Sedimentology and Stratigraphy, second edition, John Wiley and Sons, Ltd., Publication, 41 P.

Owen, R.M. and Naser, S.N., 1958. The Stratigraphy of Kuwait – Basrah area. In: Weeks, L.G. (Editor): Habitat of Oil, a Symposium. American Association of Petroleum Geologists Bulletin, pp. 1252-1278.

Pichler, T. and Humphrey, J.D., 2001. The formation dolomite in island-arc sediments due to gas-seawater-sediment interaction, Journal of Sedimentary Research, Vol. 71, No. 3, pp. 394-399. https://doi.org/10.1306/2dc4094d-0e47-11d7-8643000102c1865d

Sibley, D.F. and Gregg, J.M. 1987. Classification of dolomite rock textures, Journal Sedimentary Petrology, Vol. 57, No. 6, pp. 967-975.

Swadi, N.H., Al-Jaberi, M.H., and Alsultan, H.A., 2023. Clay minerals of Shiranish Formation in Erbil, Duhok, northern Iraq, IOP Conference Series: Earth and Environmental Science, pp. 1-6. DOI 10.1088/1755-1315/1300/1/012029

Taha, T.M. and Abdullah, E.J., 2019. Reconstruction of Paleo depth and Paleo temperature from C- O stable isotope records of Mishrif Formation, southern Iraq. Iraqi Journal of Science, Vol. 60, No. 8, pp. 1730-1742. https://doi.org/10.24996/ijs.2019.60.8.10

Tucker, M.E. and Wright, V.P., 1990. Carbonate Sedimentology. Blackwell Scientific Publications, London, 182 P.

Warren, J., 2000. Dolomite: occurrence, evolution and economically important associations, Earth-Science Reviews, Vol. 52, No. 1, pp. 1-81. https://doi.org/10.1016/S0012-8252(00)00022-2

Wells, A.J., 1962. Recent Dolomite in the Persian Gulf, Nature, Vol. 194, pp. 274–275.

Wright, V.P., 1993. Sedimentology Review/1. Blackwell Scientific Publications, Oxford, 142 P.

Iraqi National Journal of Earth Science

www.earth.uomosul.edu.iq

Assessment of Rock Slope Stability in Khanuqa Anticline, Northern Iraq

Waeal Mohammed Khazel [1*], **Mohammed Rashed Abood** [2]

[1,2]*Department of Applied Geology, College of Science, University of Tikrit, Tikrit, Iraq.*

Article information

Received: 01- Dec -2024

Revised: 29- Jan -2025

Accepted: 01- Mar -2025

Available online: 01- Jan -2026

Keywords:
Kinematic Analysis,
Failure,
Stability,
Plane Sliding,
Flexural Toppling,

Correspondence:
Name: Waeal Mohammed Khazel

Email: waeal.mohammed@st.tu.edu.iq

ABSTRACT

Rock failures are a very frequent phenomenon, especially on slopes that cut off roads in mountainous areas. The road leading to the village of Al-Naml, which is located north of Tikrit City, is considered the most important road that connects this village to the neighboring areas and cities. This road sometimes experiences several rock failures that cause difficulty in transportation for people, especially in winter and spring. Therefore, evaluating the stability of rocky slopes on such a road is very necessary. Four slope stations are selected along this road to evaluate the stability of rocky slopes using different techniques. The selection of slope stations is based on the difference in the pattern of discontinuities, the change in the morphology of the slope, and the difference in the type of failures. The failure that occurred in the area is a rockfall, while the expected one is direct toppling. The information taken from the field has been analyzed to determine the degree of stability probability through engineering analysis (Kinematic analysis) using the DIPS-v6.008 program, as well as through the system of giving values to the slope mass rating (SMR) using the SMRTool-V205 program. The engineering analysis (kinematic analysis) showed that wedge sliding is possible at all stations (1,2,3,4), while plane sliding, flexural, toppling, and direct toppling are not likely to occur. The values of SMR for both Discrete-SMR and Continuous-SMR for the slopes of all stations range from (37-1) and (37-5), respectively. It is observed that the values at stations (1,2,3) are within a completely unstable range with a probability of failures of about (0.9), while the value at station (4) is within the unstable range with a probability of failure of about (0.6).

DOI: 10.33899/injes.v26i1.60211, ©Authors, 2026, College of Science, University of Mosul.
This is an open access article under the CC BY 4.0 license (http://creativecommons.org/licenses/by/4.0/).

تقييم إستقرارية المنحدرات الصخرية في طية خانوكة المحدبة، شمال العراق

وائل محمد خزعل[1]* ، **محمد راشد عبود[2]**

[2,1]قسم علوم الارض التطبيقية، كلية العلوم، جامعة تكريت، تكريت، العراق.

معلومات الارشفة

تاريخ الاستلام: 01- ديسمبر- 2024

تاريخ المراجعة: 29- يناير- 2025

تاريخ القبول: 01- مارس- 2025

تاريخ النشر الالكتروني: 01- يناير- 2026

الكلمات المفتاحية:

التحليل الهندسي،

انهيار،

الإستقرارية،

انزلاق مستوي،

انقلاب انثنائي،

المراسلة:

الاسم: وائل محمد خزعل

Email: waeal.mohammed@st.tu.edu.iq

الملخص

تعتبر الانهيارات الصخرية من الظواهر التي تحدث بصورة متكررة جدا خصوصاً في المنحدرات التي تقطع الطرق في المناطق الجبلية. يعتبر الطريق المؤدي الى قرية النمل الذي يقع شمالي مدينة تكريت الطريق الاهم الذي يربط هذه القرية بالمناطق والمدن المجاورة لها. تقع في هذا الطريق أحيانا عدد من الأنهيارات الصخرية التي تسبب صعوبة في النقل والمواصلات للناس، وخصوصا في فصلي الشتاء والربيع. لذلك ان تقييم استقرارية المنحدرات الصخرية في مثل هذا الطريق يكون ضرورياً جداً. تم اختيار أربع محطات انحدار على امتداد هذا الطريق وذلك لتقييم استقرارية المنحدرات الصخرية بتقنيات مختلفة. يكون اختيار محطات الانحدار على أساس الاختلاف في نمط الانقطاعات والتغير في مورفولوجيا المنحدر والاختلاف في نوع الانهيار. إنَّ الانهيار الحاصل في المنطقة هو السقوط الصخري، اما المتوقع حدوثه فهو الانقلاب المباشر، وقد تم تحليل المعلومات المأخوذة من الحقل لمعرفة درجة احتمالية الإستقرارية من خلال التحليل الهندسي (التحليل الحركي) باستخدام برنامج DIPS-v6.008 وكذلك من خلال نظام اعطاء القيم لكتلة الانحدار Slope Mass Rating (SMR) (باستخدام برنامجSMRTool-V205) الذي يستخدم لتحديد استقرارية المنحدر. اظهر التحليل الهندسي (التحليل الحركي) بأن الانزلاق الاسفيني هو الممكن حدوثه في جميع المحطات (1,2,3,4)، اما الانزلاق المستوي والانقلاب الانثنائي والمباشر فلا توجد احتمالية حدوثها. أن قيم كتلة الانحدار لكل من Discrete-SMR و46 Continuous-SMR لمنحدرات كل المحطات تتراوح مابين (1-37) و (5-37) على التوالي. وقد لوحظ بأن القيم في المحطات (1,2,3) تقع ضمن نطاق غير مستقر تماماً مع احتمالية حدوث الأنهيار بحدود (0.9)، أما قيمة في المحطة (4) فتقع ضمن النطاق غير المستقر مع احتمالية الأنهيار بحدود (0.6).

DOI: 10.33899/injes.v26i1.60211, ©Authors, 2026, College of Science, University of Mosul.
This is an open access article under the CC BY 4.0 license (http://creativecommons.org/licenses/by/4.0/).

Introduction

The stability of rocky inclines is regarded as a crucial subject in the realm of engineering geology due to its significance in assessing and understanding the stability of mountainous regions that host a multitude of engineering structures including highways, rock excavations for tunnels, mining operations, agricultural terraces, and various forms of construction; along with its material relevance and its influence on human existence (Qader and Syan, 2021). Moreover, the stability of rock slopes stands as one of the primary hazards and challenges confronting geologists, who complement the efforts of civil engineers, as these challenges manifest as landslides on slopes supporting railways and roads, as well as essential public infrastructure, and during the road construction process for vehicle transit (Aboud et al., 2017). Landslides represent one of the most perilous varieties of environmental calamities that individuals living in mountainous regions face, occurring when the conditions for them are met. The failure may transpire gradually or abruptly. Numerous factors contribute to landslides, with gravity being the most significant (Bromhead, 1992). When the resistance of the rock masses is comprising, i.e., the slope matches or exceeds the gravitational force, it indicates a state of equilibrium, meaning the rock mass is stable. However, any disruption of this balance results in instability within the rock masses, leading to a collapse of the slope through various mechanisms (Al-Jawadi, 2024). The landslides represent the movement of

land masses in the form of rocks, debris, or other earth materials towards the bottom of the slope. So, we can define slope failure as the movement of land masses under the influence of their weight towards the bottom of the slope. Instability of these slopes may result from changes in the conditions of the rock masses that form these slopes, as well as external factors such as slope water and seismic activities. The most important factor, which is considered the basic factor in the failure of rock slopes, is the presence of joints, faults, and surfaces that are applied within the surfaces of the discontinuities of the rock masses. Rock failures are classified into four types (plane failure, wedge slide, overturning, and rotational failure) according to Wyllie and Mah (2005).

The objective of this study is a comprehensive work of the engineering geological survey of rock slopes beyond a traditional engineering geological survey that focuses specifically on the slopes adjacent to the road within the designated study area, intending to identify and analyze thoroughly the various factors that significantly influence the stability of these slopes. While also pinpointing the precise locations where collapses have previously occurred, as well as those areas that may be at risk of future collapses, and assessing their potential impacts through the application of a systematic slope classification methodology known as the slope mass rating (SMR) system. All of these will be executed using the advanced SMRTool-v205 program; furthermore, we will employ the kinematic analysis technique to anticipate probable failures using the DIPS-v6.008 program.

Location of the Study Area

The research location resides in the Salahaldin Governorate in northern Iraq, positioned approximately 120 kilometers north of Tikrit City, specifically within the Khanuqa anticline, adjacent to the roadway leading to the village of Al-Naml situated between the northing (3904000 - 3907000) and easting (350000 - 348000) in the UTM coordinate system, within the Khanuqa anticline as illustrated in Figure (1).

Tectonic and Structural Geology

Tectonically, the research area is located in northern Iraq within the Low Folded Zone of the Unstable Shelf (Buday and Jassim, 1984). The Khanuqa anticline runs in a northwest-southeast orientation and is identified as a semi-symmetric double-plunging anticline. It is flanked by the adjacent Makhoul anticline by a syncline known as Wadi Al-Jafr, which is broad at its center and narrow at its plunge (Fouad, 2002). According to Darwish (2010), the Khanuqa anticline is designated as an open fold (gentle fold) following the classification of Fleuty (1964). This fold, akin to other formations in the vicinity, emerged during the second phase of the Alpine orogeny in the Pliocene epoch (Dewey et al, 1973). The area exhibits fractures induced by tectonic activities, including joints and fissures with sets of fractures present within the gypsum-holding formation (the Fatha Formation), filled with clay materials. The fracture sets are also present within the sandstone strata of the Injana Formation. The region showcases numerous surface and subsurface structures resulting from the aforementioned structural dynamics, with the formation of ground elevation intricately linked to the mountain-building processes occurring in the Zagros Highlands (Al-Lahebi, 2023).

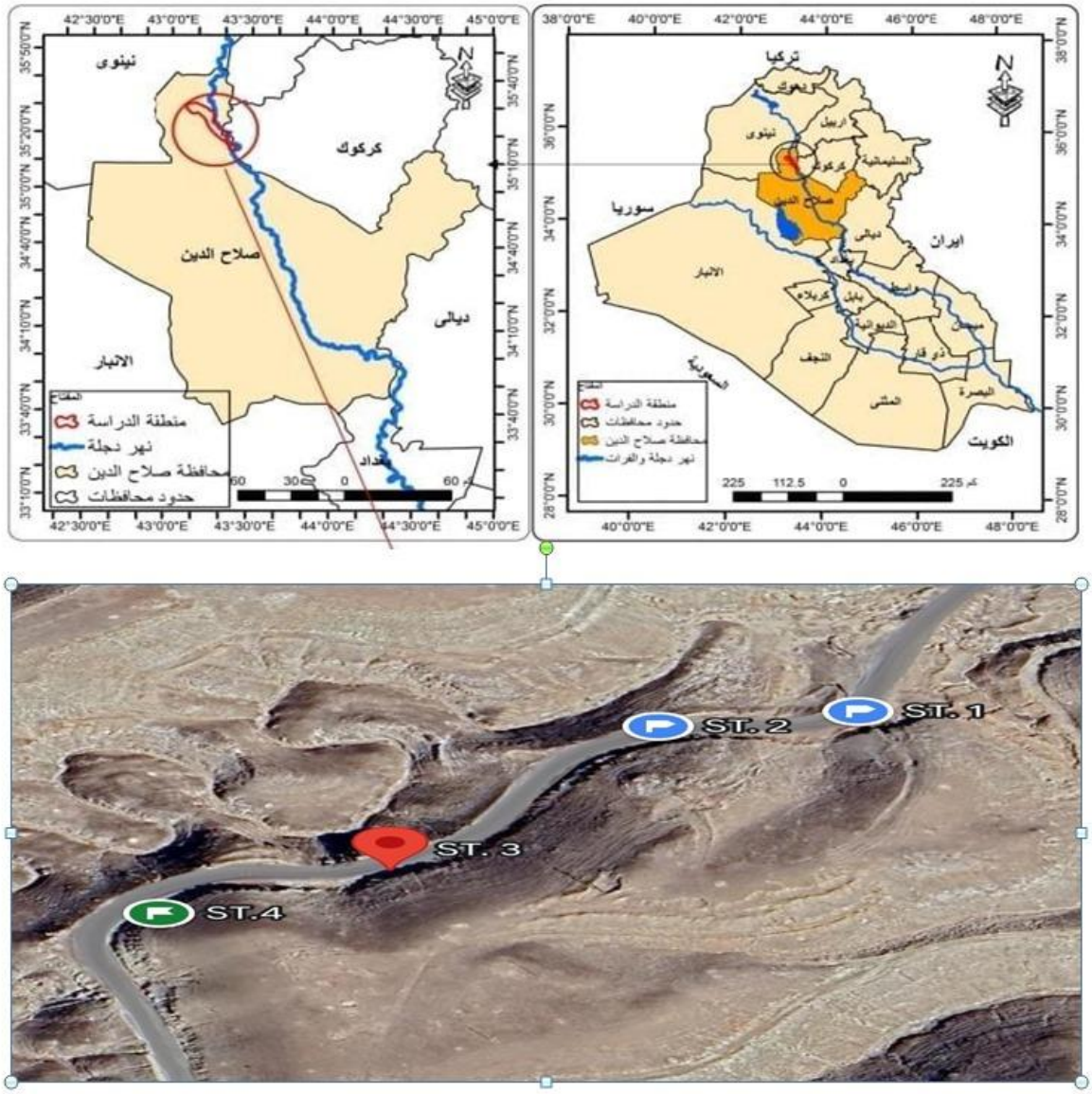


Fig. 1. Location of the study area and selected locations.

Stratigraphy of the Study Area

The geological field of the designated region focused solely on the strata outcrops in the study area, revealing the Fatha Formation (Middle Miocene), alongside the Injana Formation (Late Miocene), as well as Quaternary deposits.

Fatha Formation:

(Middle Miocene) manifests as a plethora of rocky outcrops across the study area, comprising alternating sedimentary sequences where substantial layers of gypsum intersperse with marl, marly limestone, limestone, and additional marl strata. This formation is dated to the Middle Miocene (Bellen et al., 1959). Many scholars, including Buday (1980), concur that this formation accumulated in shallow, highly saline coastal basins, resulting in a notable lack of fossils, primarily represented by micro foraminifera and ostracodes found within the limestone.

Injana Formation:

(Upper Miocene) is initially described in the Fars region of southwestern Iran by Busk and Mayo (1918), as noted by Buday and Jassim (1987), this formation dates back to the

Upper Miocene (Bellen et al., 1959), previously referred to as Upper Fars (Adeeb, 2006), but later renamed to Injana Formation after selecting a prime section in the Injana area within the southern Hamrin anticline south of Tuz (Al-Rawi, 1981) corresponding to the Upper Miocene period. This formation is prevalent as deposits at the onset of the Alpine molasses and is widespread across northern Iraq, while in the southern regions, these deposits vanish, giving way to the Dibdiba Formation. It consists of exemplary sequences of sandstone, alluvial, and clay deposits (Buday and Jassim, 1987), with the exposures in the study area comprising sequences of sandstone and clay.

Quaternary Sediments:

include floodplain sediments, alluvial fans, and river terraces. Flood sediments are a blend of coarse-grained materials (gravel and sand) and fine-grained constituents (clay and silt) along the banks of perennial streams, where the grain size diminishes as moving away from the river channel, as these sediments emerge during flood events (Thornburt, 1969; Ritter, 1986).

Geomorphology of the Study Area

The study area is characterized by the presence of some geomorphic phenomena related to its structure and geological conditions, as well as the occurrence of erosional and weathering processes (Al-Ani, 1997; Al-Talib, 2021). Several factors contribute to the appearance of these phenomena, including erosional phenomena caused by rock erosion processes, rock erosion and ground heights, or fluvial phenomena, namely valleys formed by fluvial sedimentary processes extending along the river channel, and valleys formed by geomorphic erosional processes, or structural phenomena represented by geomorphic factors that cause the movement of rock masses (Al-Jabouri, 2005). Another characteristic of the study area is the presence of strike valleys, whose extension is parallel to the strike of the folds (northwest-southeast) and are characterized by their relative decline resulting from the erosion of weak layers in the formation of the opening. There are also transverse valleys, i.e., perpendicular to the strike of the fold.

Materials and Methods

As seen below, the work techniques comprised many stages, ranging from data collection to the outcomes stage.

Data Collecting:

This stage includes collecting information about the study area by reviewing and reading many reports, theses, and research to evaluate the slopes related to the study area and benefit from them during field work. Maps and pictures related to the study area are also collected to obtain information about the geology of the area.

Fieldwork:

This stage lasted three days (July 29-31, 2024). First, the study area was surveyed (4 stations), where failures could occur, identified, as well as studying the structure, stratigraphy, and geomorphology of the area. Second, the necessary information was collected for each station, including the coordinates and attitude of slopes, layers, and joints, as follows:

1- The coordinates of each station were determined using GPS equipment and UTM units.
2- The attitude of slopes, layers, and joints was determined using a geological compass.
3- The width and height of the slope were measured.
4- The thickness of the layer was measured at each station.
5- The conditions of discontinuities (dip direction and dip amount), spacing, frequency, openings, and filling materials of discontinuities were studied in detail.
6- Measuring the width of the street, the distance between the street and the slope, the number of cars passing per hour, and their speed.

7- Identifying the types of existing and probable failures, as well as the types of slopes.
8- Collecting rock samples representing each station to conduct laboratory tests.
9- Taking photographs to document the sampling process.

Laboratory Work:

This stage includes preparing and setting up the samples of the four stations to test the uniaxial compressive strength according to Brook (1985) and ISRM (1985). This is achieved by point load testing, one of the most important and widely used tests due to its ease of implementation and the ease of preparing and setting up the sample. The sample is equipped with dimensions (D, W, L), where (D) represents the thickness of the sample between the two tips of the device, (W) represents the width of the sample, and (L) represents the length. The distance from the top of the sample to the point of the device must be less than half the height (L < 0.5 D). Afterward, the sample is loaded in compression until it reaches failure, and the uniaxial compressive strength (σc) is calculated (Table 1) to represent the results of this test for the studied stations and the type of rocks according to Anon (1977).

Table 1. Test results of studied stations and the type of rocks according to Anon (1977).

Station No.	Type of rock	D(mm)	L(mm)	W(mm)	F(KN)	$A(mm)^2=D\times W$	$De=\sqrt{\frac{4A}{\pi}}mm$	$De^2=\frac{4A}{\pi}mm^2$	$Is=F/De^2$	$F=(\frac{De}{50})^{0.45}$	$Is_{(50)}=Is\times f$ (Mpa)	$\sigma c=21\times Is_{(50)}$ (Mpa)	Classification of rock according to Anon,1977
1	Gypsum	70	50	90	4.18	6300	89.58	8025.4	0.520	1.300	0.676	14.2	moderately strong
2	Gypsum	60	40	70	3.62	4200	73.14	5350.3	0.676	1.293	0.874	18.35	moderately strong
3	Gypsum	70	50	100	3.54	7000	94.43	8917.19	0.396	1.331	0.527	11.1	Moderately weak
4	Gypsum	80	60	90	2.76	7200	95.77	9171.9	0.300	1.339	0.401	8.421	Moderately weak

Office Work:

This stage includes the presentation of the data obtained in the field and the results of the laboratory tests, as follows: The coordinates of each station in the study area were projected onto a location map using a program (GIS). The program (SMRTool-v205) was also used to determine the degree of stability of each landslide type. The program (Dips v6.008) was also used to determine the probable failure. This study focuses on the assessment of the stability of rock slopes through dynamic analysis, the Slope Mass Rating system (SMR), and the continuous slope Mass Rating (CSMR). Kinematic analysis is the simplest analysis of a failure, given the data such as the attitude of joint sets, layer attitude, slope, and internal friction angle measured by the field slope method. (Bruce et al., 1989) These collected data were presented using the program DIPS v6.008. Kinematic analysis is a simple method to determine the possible failure modes (plane, wedge, and toppling) and failure directions in a rock mass based on the angular relationship between the discontinuity and the slope surface (Hoek and Bray, 1981). The Slope Mass Rating (SMR) proposed by Romana is a system for determining the stability of rock slopes. The method is based on the rock mass classification (RMR) system introduced by Bieniawski in 1989. The RMR system is based on field and office studies and includes the unconfined compressive strength (UCS) of the intact rock, the rock quality designation (RQD), the discontinuity spacing, the discontinuity condition, and the groundwater conditions. The classifications are then added to obtain the RMRb value (basic RMR). RMR plays an essential role in calculating SMR and CSMR. The average spacing between all discontinuities was calculated from the inverse relationship with the average frequency of all discontinuities (Bieniawski, 2011). Remote sensing analysis and geographical information systems GIS are used in many studies of rock mass sliding by identifying lineaments that mostly represent discontinuity density in the rock masses (Bety et al., 2022). The rock quality designation (RQD) was calculated according to Palmstrom (2005) using the number of volumetric discontinuities (Jv) (the number of discontinuities per unit volume), and thus the RQD is equal to 110-2.5Jv. (Table 2) shows the different stability classes and experimentally discovered limit values of SMR associated with different failure

modes proposed by Romana (1985). Thomas (2007) also developed a continuous SMR (CSMR), which is a modification of Romana's discrete SMR technique. CSMR provides a unique value for each adjustment factor, unlike the range in discrete SMR. SMR is calculated using RMRb with some adjustment factors proposed by Romana (1985) as shown in the following equation:

$$SMR = RMRb + (F1.\ F2.\ F3) + F4 \ldots\ldots(1)$$

Table 2: Description of slope mass rating (SMR) (Romana, M. 1985)

Classes	V	IV	III	II	I
SMR	0-20	21-40	41-60	61-80	81-100
Description	Very bad	Bad	Normal	Good	Very good
Stability	Completely unstable	Unstable	Partially stable	Stable	Completely stable
Failures	Big planar or soil -like	planar or big wedges	Some joints or many wedges	Some blocks	None
Failure probability	0.9	0.6	0.4	0.2	0

Results and Discussion

This study includes an engineering geological survey of four stations represented by rock slopes in the Khanuqa anticline within the Fatha Formation. The attitude of these stations in terms of slope attitude, layer, joints, and friction angle is shown in Table 3, which consists of sequences of clay layers followed by a gypsum layer, then a marl layer, then a limestone layer, and then a clay layer. When the clay layer is exposed to weathering, it makes the gypsum layers overhang, which leads to the possibility of toppling when the center of gravity exceeds the support base, when the cohesion across the discontinuities is zero (Al-Jawadi, 2021). At the same time, the resulting failure is of the rockfall type due to the presence of vertical and overhanging slopes, where the rock masses fall due to their weight when the cohesion becomes zero across the discontinuities. The results of the kinetic analysis using the DIPS-v6.008 program showed that the failure probable to occur at the four stations is of the (wedge-sliding) type due to the intersection point of the joint sets J1andJ2 occurring in the area of potential sliding, and its direction for the four stations is as follows, respectively (153, 158, 147, and 128), and there is no possibility of plane sliding, flexural toppling, or direct toppling as in (Figures, 2, 3, 4, and 5), and the letters (a, b, c and d) represent plane sliding, wedge sliding, flexural toppling, and direct toppling, respectively, and SF represents the slope face, So represents the bedding plane, J1 the first set of joints, and J2 the second set of joints.

Table 3: Attitude of slope face, bedding planes, and joints in the stations of road-cut slopes and friction angle.

Station no. (Slope site)	**Slope Dip direction / Dip angle (Average)**	**Bedding plane Dip direction/ Dip angle (Average)**	**Join set (J1) Dip direction/ Dip angle (Average)**	**Joint set (J2) Dip direction/ Dip angle (Average)**	**friction Angle (ϕ)**
1	320/90-OH	070/06	253/87	341/75	39
2	332/90-OH	230/11	01/63	285/70	32
3	335/90-OH	219/06	020/67	297/59	43
4	284/90-OH	195/03	258/70	312/60	43

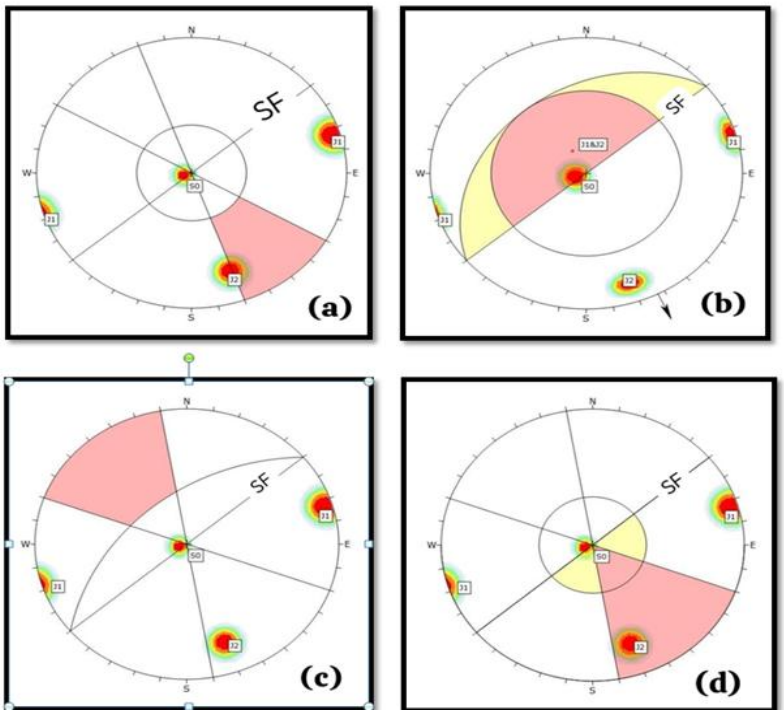


Fig. 2. Results of kinematic analysis of station No. (1), (a) no plane sliding, (b) wedge sliding towards 153, (c) no flexural toppling, (d) no direct toppling.

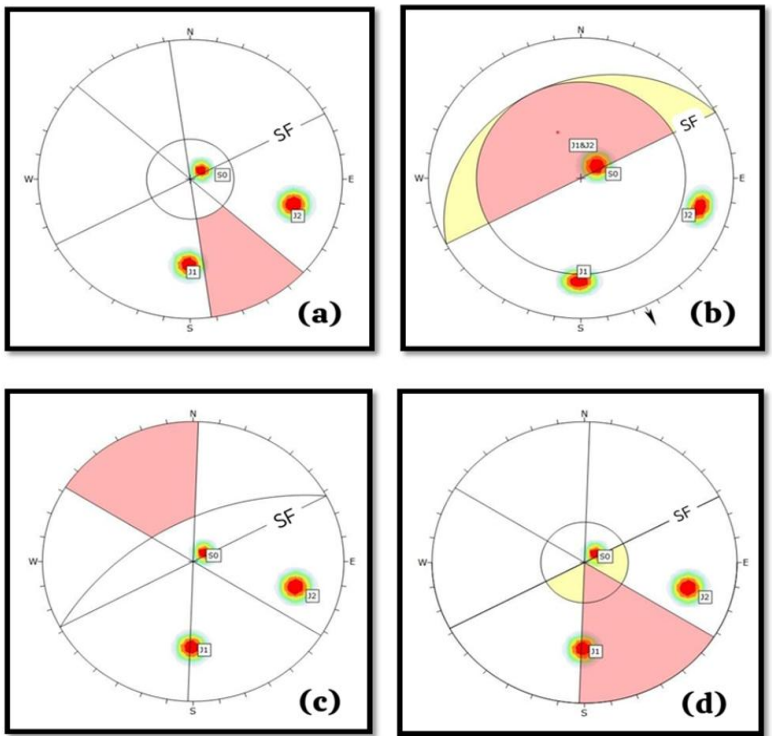


Fig. 3. Results of kinematic analysis of station No. (2), (a) no plane sliding, (b) wedge sliding in the direction of 158, (c) no flexural toppling, (d) no direct toppling.

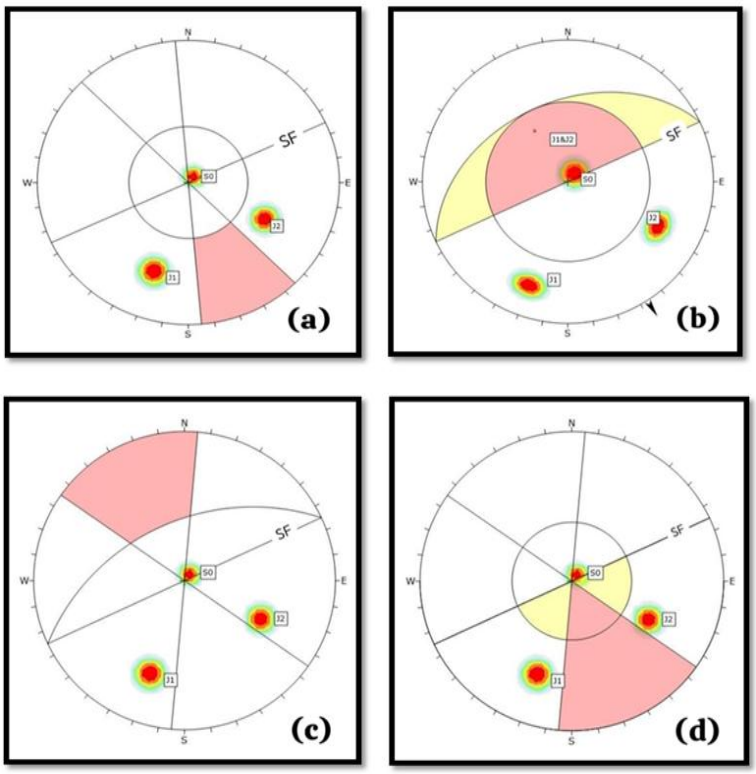


Fig. 4. Results of kinematic analysis of station No. (3), (a) no plane sliding, (b) wedge sliding towards 147, (c) no flexural toppling, (d) no direct toppling.

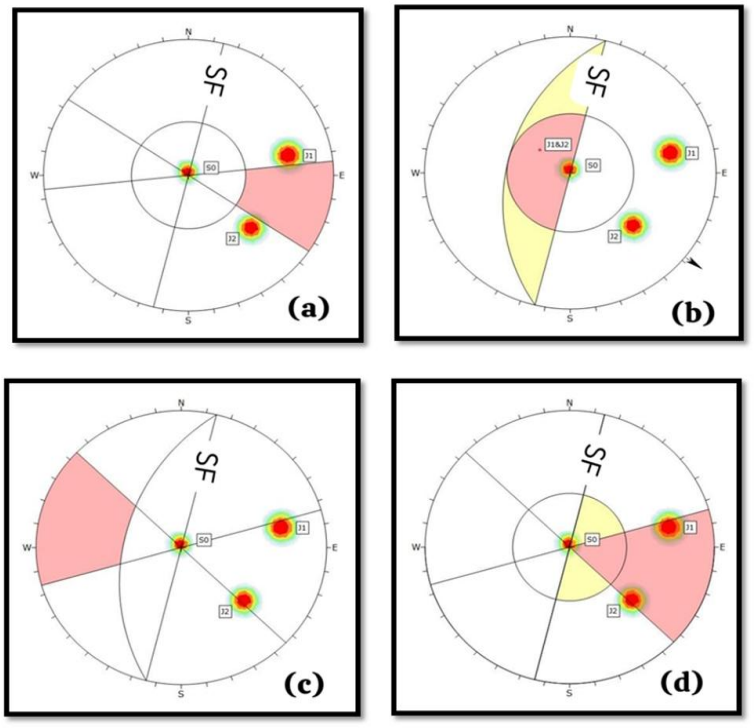


Fig. 5. Results of kinematic analysis of station No. (4), (a) no plane sliding, (b) wedge sliding in the direction of 128, (c) no flexural toppling, (d) no direct toppling.

The results of the SMRTool-v205 program identified one type of failure using the kinematic analysis of structurally controlled rock masses, which is wedge sliding, and its results were used in the slope classification system. The RMRb was calculated according to (Bieniawski, 1989). The unconfined compressive strength UCS was obtained indirectly from the point load test, which was performed according to (After Brook, 1985; ISRM, 1985), where the UCS value ranges from 8.421 MPa to 18.35 MPa, i.e., moderately weak -

moderately strong, as shown in Table 1. The rock quality designation RQD was obtained from the relationship between RQD and the number of volumetric joints (Jv) (RQD=110-2.5 Jv), Palmstrom, 2005 (Table 4), which has a value of 99.70, and the average spacing between all discontinuities was obtained from the inverse of the average frequency of all discontinuities (Bieniawski, 2011), which ranges from 697.6mm to 736.7mm, as shown in (Table. 5).

Table 4: Volumetric joint count (Jv), rock quality designation (RQD), and average spacing of all discontinuities measurements from joint sets observed in the Gypsum rocks at station no. (1).

Discontinuities	Set spacing and frequency					
	Spacing (m)		Max.	Min.	Average	Average
Bedding plane and Joints	Min	Max	frequency	frequency	spacing(m)	frequency*
(So)	0.3	1.3	3.33	0.769	0.8	1.25
(J1)	0.4	0.9	2.5	1.11	0.65	1.538
(J2)	0.5	1	2	1	0.75	1.33
random joints**						
Jv=Frequencies (joints/m3)						4.118
RQD = 110 – 2.5 Jv		99.70				
Average frequency of all discontinuities = Jv / 3						1.3726
Average spacing of all discontinuities (m) = (1 / average frequency) = 3 / Jv					0.7285m=728.5mm	

*Average frequency=1/Average spacing Palmstrom, A., 2005
**For random joints, a spacing of 5m for each random joint is used in the Jv calculation.
-RQD = 110 -2.5 Jv Palmstrom, A., 2005
-Average frequency of all discontinuities=Jv/3 Bieniawski, Z.T., 2011
-Average spacing of all discontinuities (m)=1/average frequency Bieniawski, Z.T., 2011
Were So: Bedding plane, J1: Joint set 1, J2: Joint set 2, Jv: Volumetric joint count, RQD: Rock Quality Designation.

Finally, by Rock mass characterization in the rock slopes of stations 1, 2, 3 and 4 (Table. 6) the RMRb (1989) values of the rock mass were determined at all slope stations, RMRb (1989) is basic rock mass Rating, without adjustment factor for discontinuity direction, (Table. 7), which shows that the RMRb value at all stations is equal to (61). This data is represented in the SMRTool-v205 program, (Fig. 6), where the SMRTool-v205 program showed that the discrete SMR and continuous SMR values are at their worst (i.e. the lowest SMR value) for the wedge slide at stations (1, 2, and 3) where they range from (1-19), which indicates that the rock mass is within the fifth category (V), i.e. it has very low stability and its condition is very unstable. As for the fourth station, the SMR value is (37), which indicates that the rock mass is within the fourth category (IV), i.e. it has low stability and its condition is unstable (Table 8) and (Table 9).

Table 5: Rock quality designation RQD, volumetric joint (Jv), and average spacing of all discontinuities measurements from joint sets observed in study stations.

Station no.	Jv (Joints/m^3)	RQD	Average spicing of all discontinuities (mm)
1	4.118	99.70≈100	728.5
2	4.235	99.41≈99	708.38
3	4.30	99.25≈99	697.6
4	4.072	99.82≈100	736.7

Table 6: Rock mass characterization in the rock slopes of study stations.

					Remarks
Stability station	**1**	**2**	**3**	**4**	
Elevation (a.s.l) (m)	179	194	210	212	
Rock type	Gypsum	Gypsum	Gypsum	Gypsum	From Field
Strength of intact rock material UCS (50) (MPa)	14.196	18.35	11.067	8.421	
RQD (%)	100	99	99	100	
Average spacing (mm)	728.5	708.38	697.6	736.7	
Surface condition of discontinuities	moderately weathered, Rough moderately, fine filling < 5mm, Aperture:5cm, persistence:>20m	moderately weathered, Rough moderately, fine filling < 5mm, Aperture:5cm, persistence:>20m	moderately weathered, Rough moderately, fine filling < 5mm, Aperture:5cm,persistence>20m	moderately weathered, Rough moderately, fine filling < 5mm,Aperture:6cm, persistence>20m	From field description
Ground water	Dry	Dry	Dry	Dry	From field

condition	(Summer)	(Summer)	(Summer)	(Summer)	description

Table 7: Rating values of RMRb (1989) and RMR- parameters for the rock masses in the rock slopes of study stations.

Slope station		1	2	3	4
Elevation above sea level (m)		179	194	210	212
Rating of parameters	Strength of intact rock (UCS)	2	2	2	2
	RQD	20	20	20	20
	The average spacing of all discontinuities	15	15	15	15
	Condition of discontinuities	9	9	9	9
	Ground water condition	15	15	15	15
RMRb (1989)		61	61	61	61

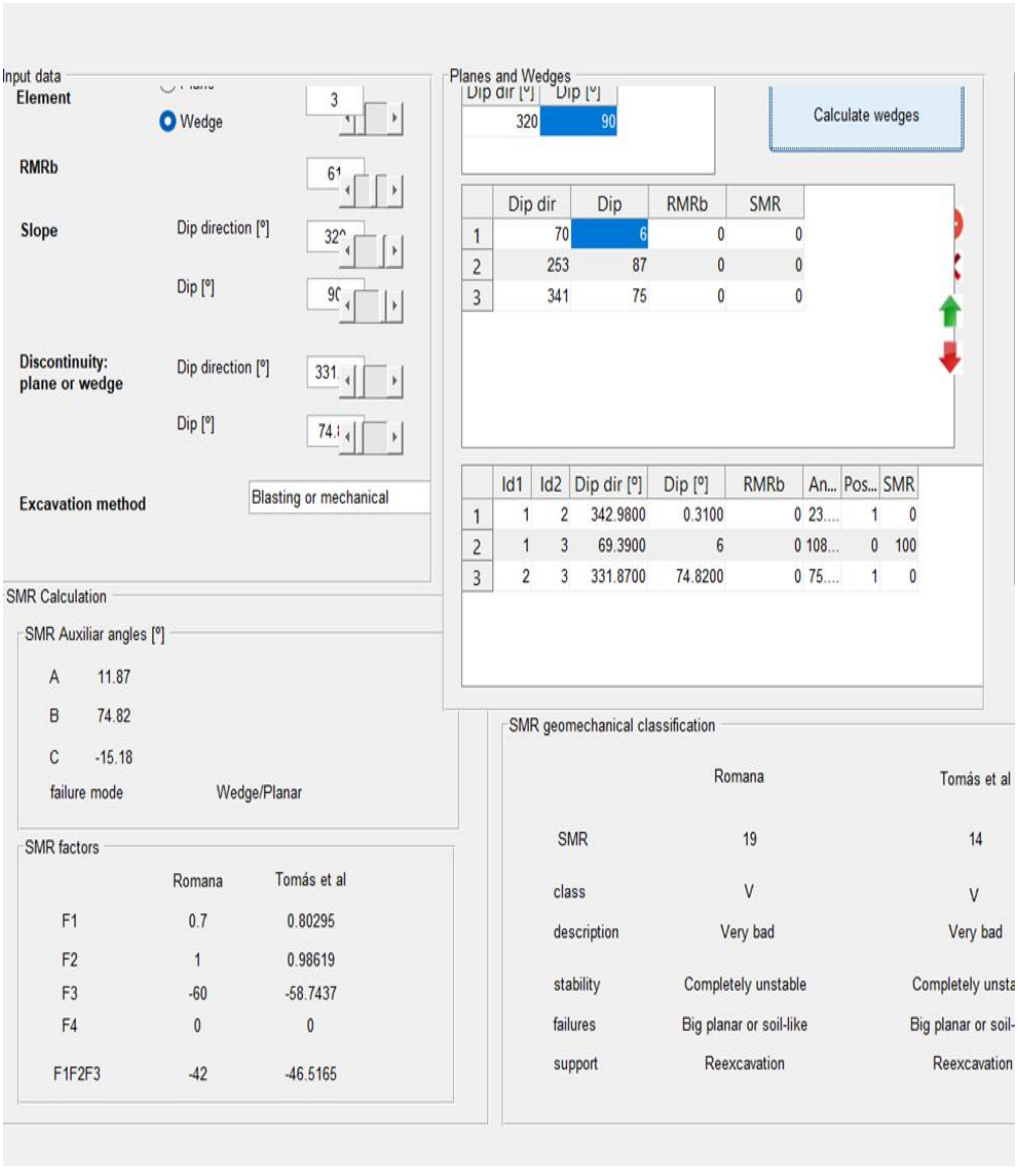


Fig. 6. Evaluation of the stability of the rock slopes of station No. (1) showing wedge sliding using the SMRTool-v205 program.

Table 8: SMR separate slope mass classification results using SMRTool-v205.

Station No.	Attitude of slope	Value RMRb	Type of Failure	Direct of Failure	F1	F2	F3	F4	F1.F2.F3	value SMR	Classification of stability according to Romana, M. 1985
1	320/90	61	b)WS	153	0.7	1	-60	0	-42	19	V/Unsta.
2	332/90	61	b)WS	158	1	1	-60	0	-60	1	V/Unsta.
3	335/90	61	b)WS	147	0.85	1	-60	0	-51	10	V/Unsta.
4	284/90	61	b)WS	128	0.4	1	-60	0	-24	37	IV/Unsta.

Table 9: Continuous (CSMR) value results using (SMR Tool).

Where: WS: represents wedge sliding; (F1, F1, F2, F3 and and F4): represents

Station No.	Attitude of slope	Value RMRb	Type of Failure	Direct of Failure	F1	F2	F3	F4	F1. F2. F3	value SMR	Classification of stability according to Romana, M. 1985
1	320/90	61	b)WS	153	0.80295	0.98619	-58.7437	0	-46.5165	14	V/Co.Unsta.
2	332/90	61	b)WS	158	0.96631	0.96902	-59.3537	0	-55.5773	5	V/Co.Unsta.
3	335/90	61	b)WS	147	0.90119	0.95792	-59.4528	0	-51.3235	9	V/Co.Unsta.
4	284/90	61	b)WS	128	0.40846	0.96816	-59.3643	0	-23.476	37	IV/Unsta.

correction coefficients for SMR; Unsta.: means unstable; Co.Unsta.: means very unstable., the letter (b) represents failure from wedge sliding.

Conclusion

This study reached the following conclusions: the failure occurring in the field is a rock fall, while the expected one in the field is a direct toppling. The kinetic analysis using the DIPS-v6.008 program revealed that the failure that may occur is a wedge sliding, which is expected to occur at all stations (1, 2, 3, and 4). It also showed that in the worst conditions, the values of the discrete SMR and continuous CSMR range from (1-37) and (5-37), respectively. This indicates that the rock mass at stations (1, 2, and 3) falls within the fifth category (V), meaning that it has a very bad slope and its condition is completely unstable. As for station (4), the rock mass falls within the fourth category, meaning that it has a bad slope and its condition is unstable. When comparing the results of the discrete SMR and continuous SMR, it is noted that the slope stability classification at stations (1, 2, and 3) differs between the discrete and continuous SMR, as the results of the discrete SMR show that these stations are unstable, while the results of the continuous SMR show that these stations are completely unstable, i.e. the CSMR model has given a more accurate assessment than the discrete SMR model in terms of slope stability degrees in terms of quantitative numbers. By comparing the SMR results with the slope mass classification description table, we find that the probability of failure at stations (1, 2, and 3) is (0.9), while at the station (4) the probability is (0.6).

Acknowledgments

I would like to extend my thanks and appreciation to Tikrit University, represented by the University President, in addition to the Deanship of the College of Science, Department of Applied Geology, and Dr. Mohammed Rashid Abboud for their support of this research.

References

Adeeb, H.G., 2006. The tectonic structure of the Alpine Molasses Basin - Northern Iraq. Unpublished PhD Thesis. Department of Geology, College of Science, University of Mosul. (In Arabic)

Al-Ani, A.A.R., 1997. Optimal investment of groundwater in Al-Fatha Basin - Samarra MSc. Thesis, College of Science, University of Baghdad. (In Arabic)

Al-Jubouri, D.K.H., 2005. Wadi Al-Fada Basin in the Wavy Region of Iraq, Master's Thesis (unpublished), College of Education, Tikrit University, 130 P. (In Arabic).

Al-Jawadi, A.S., 2024. Predicting Slip Surfaces for Slope Stability Assessment Along Highway 80 in Mosul, Northern Iraq, Geotechnical and Geological Engineering, 42, pp. 2997–3008, https://doi.org/10.1007/s10706-023-02713-0

Al-Jawadi, A.S., 2021. Theoretical Models of Slope Stability Analysis in The Maqlub Mountain Rock Cut Routes, North Iraq, 2021, The Iraqi Geological Journal, 54 (1A), pp. 55-68, https://10.46717/igj.54.1A.6Ms-2021-01-27

Al-Lahibi, S.A.T., 2023. Evaluation of selected sites for establishing a geopark between Makhoul Mountain and the Tigris River in central Iraq, Master's thesis in the Department of Geology, College of Science, Tikrit University. (In Arabic)

Al-Rawi, I.K., 1981. Sedimentology and petrology of the Tanjero clastic Formation North and Northeastern Iraq. Unpub. Ph.D. Thesis, Baghdad University,

Al-Talib, S.A., Al-Jawadi, A.S. and Al-Sanjari, A.A., 2021. Impact of Gercus Formation Erosion and Rock Sliding on Duhok Dam Reservoir – Northern Iraq, Iraqi Journal of Science, Vol. 62, No. 5, pp. 1562-1569, DOI: https://10.24996/ijs.2021

Anon., 1977. The description of rock masses for engineering purposes, Report by the Geological Society Engineering Group Working Party, Quarterly Journal of Engineering Geology, Vol. 10, pp. 355-388.

Bellen, R.C. Van, Dunnington, H.V. Wetzel, R. and Morton, D., 1959. Lexique Stratigraphique Internal, 0310 Asie (Iraq), 333 P. Reprinted electronically and on paper by Gulf Petrolink in 2005, by permission of CNRS Editions, France.

Bety, A.Kh.S., Al-Jawadi, A.S. and Ismaeel, O.A., 2022. Lineament Analysis by Using Remote Sensing and GIS Technique of Sangaw Area, Kurdistan Region, NE Iraq, Iraqi Geological Journal, 55 (2C), pp. 150-161, DOI: https://10.46717/igj.55.2C.11ms-2022-08-24.

Bieniawski, Z.T., 2011. Misconceptions in the applications of rockmass classifications and their corrections, ADIF Seminar on Advanced Geotechnical Characterization for Tunnel Design, Madrid, Spain, June 29. http://www.geocontrol.es/publicaciones/EB189._

Biniawski, Z.T., 1989. Engineering rock mass classification. John Wiley, New York.

Bromhead, E.N., 1992. The Stability of Slopes, 2nd Ed., Blackie Academic and Professional, Great Britain, 410 P.

Brook, N., 1985. The equivalent core diameter method of size and shape correction in point load testing. Int. J. Rock Mech. Min. Sci. and Geomech. Abstr. Vol. 22, pp. 61-70.

Bruce, I.G. Cruden, D.M. and Eaton, T.M., 1989: Use of a tilting table to determine the basic friction angle of hard rock samples, Can. Geotech. J. 26, pp. 274-279.

Buday, T. and Jassim S.Z., 1987. The Regional Geology of Iraq, Tectonism, Magmatism and Metamorphism, D.G. of Geol. Surv. and Min. Inves, Baghdad, Iraq, V.2.

Buday, T. and Jassim, S.Z., 1984. Final report and the regional geological survey of Iraq unable. Report S.O.M. Library, Vol. 2 Tectonic Frame Work.

Buday, T., 1980, The regional geology of Iraq" Vol.1(Stratigraphy and Paleogeography, D.G. of Geol. Surv. and Min. Inv. Published., Baghdad, 445 P.

Busk, H.G., Mayo, H.T., 1918. Some notes on the geology of the Persian oil welds",Journal Institute Petroleum Technology. Carbonate rock slope stability in selected sites north of Jordan, Proc.8 th. Int. Cong. of IAEG, Vancouver, Canada, A.A. Balkema, Rotterdam: Vol. 5, pp. 3095-3100.

Darwish, H.A, 2010. Geomorphology and structure of the Khanuqa anticline, northern Iraq/Al-Fatha - Baiji, Master's thesis, College of Science - University of Basra, 102 P. (In Arabic)

Dewey, J.F., Pitamn, W.C., Byan, W.B.F. and Bonnin, J., 1973. Plate Tectonic and The Evolution of the Alpine System, Am. Bull, 84 P.

Fluety, M.J., 1964. The Description of Folds. Proceedings of the Geologist' Association, 75, pp. 461-492. http://dx.doi.org/10.1016/S0016-7878(64)80023-7.

Fouad, S.F., 2002. Detailed Geological Survey of Khanuga area, Geosurv, Baghdad, Iraq, internal report, 132 P.

Hoek, E. and Bray, J.W., 1981. Rock Slope Engineering, 3rd. ed., Institution of Mining and Metallurgy, London, 358 P.

ISRM, P.L.T. 1985. Suggested method for determining point load strength. Int J Rock Mech Min Sci Geomech Abstr, 22(2), pp. 51-60.

Mohammed, R.A., Amira, I.H. and Marwan A.M., 2017. Stability study of rock slopes of exposed formations in the northeastern end of the Bor anticline/Northern Iraq. Department of Applied Earth Sciences, College of Science, Tikrit University, Tikrit, Iraq, Tikrit Journal of Pure Science, 22 E-ISSN: pp. 2415-1726 (In Arabic)

Palmstrom, A., 2005. Measurements of and correlations between block size and Rock Quality Designation (RQD), Journal of Tunneling and Underground Space Technology, Vol. 20, pp. 362-377

Qader, R.M., Syan, S.H.A., 2021. Rock slope stability assessment along Rawanduz main road, Kurdistan Region. The Iraqi Geological Journal, pp. 79-93.

Ritter, D.F., 1986: Process geomorphology, 2nd Edition, Wm. C. Brown Publishers, Iowa, USA, 579 P.

Romana, M., 1985. New adjustment ratings for application of Bieniawski classification to slopes, in: Proceedings of the International Symposium on the Role of Rock Mechanics in Excavations for Mining and Civil Works. International Society of Rock Mechanics, Zacatecas, pp. 49-53.

Thornbury, W.D., 1969: Principles of geomorphology (2nd ed.). John Wiley and Sons, Inc., New York, 594 P.

Tomas, R., Delgadob, J. and Seron, J.B., 2007. Modification of slope mass rating (SMR) by continuous functions. International Journal of Rock Mechanics and Mining Sciences, Vol. 44, No. 7, pp. 1062-1069.

Iraqi National Journal of Earth Science

www.earth.uomosul.edu.iq

Conditions of Depositional Environment of the Sargelu Formation in Rania Area Based on Geochemical Data

Mohamed Ali Alrashedi [1*], Falah A. Al-Miamary [2], Zaid A. Malak [3]

[1]*Department of Petroleum and Refining Engineering, College of Petroleum and Mining Engineering, University of Mosul, Mosul, Iraq.*
[2,3] *Department of Geology and Petroleum, College of Science, University of Mosul, Mosul, Iraq.*

Article information

Received: 03- Feb-2025

Revised: 05- Mar -2025

Accepted: 07- Apr -2025

Available online: 01- Jan -2026

Keywords:
Sargelu Formation,
Sedimentary Condition,
Rania Area,
Geochemical data,

Correspondence:
Name: Mohammed Ali Alrashedi

Email: dr.mohammed.ali@uomosul.edu.iq

ABSTRACT

The sequence of the Sargleu Formation (Middle Jurassic) in the Hangira section is located at the northwestern Sulaymaniyah Governorate center in Rania City, northeastern Iraq. The studied successions consist of well-bedded limestone and dolomitic limestone, gray in color, interbedded with thin beds of argillaceous limestone rich in organic matter and intertwined at the top of this succession by thin beds of brown chert rich in ammonite fossils. The aforementioned beds are followed by a succession of thin-bedded limestone, brown color alternating with beds of argillaceous limestone and thin beds of chert. The selected section has been studied in terms of geochemical data of some major and trace elements and the ratio between them for ten samples to elucidate the paleoenvironmental conditions, including paleoproductivity, oxidation and reduction conditions, provenance, hydrodynamic conditions, and detrital input. The productivity record of (P/Al, P/Ti, Ba/Al ratios) indicates high paleoproductivity. Redox proxies for trace elements (V/V+Ni), (U/Th), and (Ni/Co) suggest anoxic to oxygen-deficient conditions. The provenance proxies (Al2O3/TiO2 ratio) indicate that the source rocks of the Sargelu Formation are intermediate igneous rocks. The (Zr/Rb ratio) values indicate a deposition in conditions with low water energy. The high ratios of (Si/Al and Ti/Al) indicate a high clastic flow in the sedimentation basin of the Sargelu Formation due to the presence of detrital quartz or organic silica of organisms with a silicate wall, such as Radiolaria. While the high ratio of (K/Al) is attributed to the role of the wind source of clastic flow in the deposits of the formation, or to the nature of the clay minerals present in the deposits of the Sargelu Formation.

DOI: 10.33899/injes.v26i1.60213, ©Authors, 2026, College of Science, University of Mosul.
This is an open-access article under the CC BY 4.0 license (http://creativecommons.org/licenses/by/4.0/).

ظروف البيئة الترسيبية لتكوين ساركلو في منطقة رانيا بالاعتماد على البيانات الجيوكيميائية

محمد علي الراشدي[1]*، فلاح عبد المعماري [2]، زيد عبد الوهاب ملك [3]

[1] قسم هندسة النفط والتكرير، كلية هندسة النفط والتعدين، جامعة الموصل، الموصل، العراق.

[3،2] قسم علوم الارض والنفط ، كلية العلوم، جامعة الموصل، الموصل، العراق.

معلومات الارشفة

تاريخ الاستلام: 03– فبراير – 2025

تاريخ المراجعة: 05– مارس– 2025

تاريخ القبول: 07– ابريل– 2025

تاريخ النشر الالكتروني: 01– يناير – 2026

الكلمات المفتاحية:

تكوين ساركلو

الظروف الترسيبية

منطقة رانيا

البيانات الجيوكيميائية

المراسلة:

الاسم: محمد علي الراشدي

Email: dr.mohammed.ali@uomosul.edu.iq

الملخص

تتألف تتابعات تكوين ساركلو بعمر (الجوراسي الأوسط) في مقطع هانجيرا الواقع في (مدينة رانية) شمال غربي مركز محافظة السليمانية، شمال شرقي العراق من صخورالحجر الجيري المتطبقة والحجر الجيري الدولوميتي، رمادي اللون، تتخللها طبقات رقيقة من الحجر الجيري الطيني الغني بالمواد العضوية، تتعاقب معها في أعلى هذ التتابع طبقات رقيقة من الصوان البني الغني بمتحجرات الأمونايت. تعلو الطبقات المذكورة آنفاً طبقات رقيقة من الحجر الجيري البني اللون بالتناوب مع طبقات من الحجر الجيري الطيني وطبقات رقيقة من الصوان. اجريت دراسة جيوكيميائية لبعض العناصر الرئيسة والعناصر الأثرية والعلاقة بينها لعشرة عينات كمؤشر لظروف البئية القديمة بما في ذلك الإنتاجية القديمة وظروف الأكسدة والاختزال والمصدرية والظروف الهيدروديناميكية ومدخلات الحطام. يشير سجل الإنتاجية (P/Al, P/Ti, Ba/Al) إلى إنتاجية قديمة عالية. تشير مؤشرات الأكسدة والاختزال للعناصر الأثرية (V/V+Ni)، (U/Th) و(Ni/Co) إلى ظروف نقص الأوكسجين. تشير مؤشرات المصدرية (Al2O3/TiO2) إلى أن الصخور المصدرية للتكوين كانت صخوراً نارية متوسطة. تشير قيم نسبة (Zr/Rb) إلى ترسبها في ظروف ذات طاقة مائية منخفضة. بينما تشير نسب (Si/Al وTi/Al) إلى تدفق حطامي مرتفع في الحوض الترسيبي لتكوين ساركلو، والذي قد يكون ارتفاعه بسبب وجود الكوارتز الفتاتي أو السيليكا العضوية للكائنات الحية ذات الجدار السيليكاتي، مثل الراديولاريا. بينما تُعزى نسبة (K/Al) إلى دور الرياح كمصدر للتدفق الحطامي في رواسب التكوين أو إلى طبيعة المعادن الطينية الموجودة في رواسب التكوين.

DOI: 10.33899/injes.v26i1.60213, ©Authors, 2026, College of Science, University of Mosul.
This is an open-access article under the CC BY 4.0 license (http://creativecommons.org/licenses/by/4.0/).

Introduction

The Sargelu Formation was initially documented in its type section by Wetzel (Wetzel, 1948 in Bellen et al., 1959), and its name originates in Sargelu village, situated in the Surdash Anticline, in the region of Sulaymaniyah Governorate, Northeastern Iraq. In lithology, thin, black cherty and bituminous limestones, and thin, argillaceous limestones intercalated with thin black cherty ones, dominate in thin forms, most prominently in the upper parts. In terms of its position in a stage, its base of the stratigraphical interval corresponds with the stage of Bajocian, and its top with the stage of Bathonian, according to its fossil associations in the unit. The Sargelu Formation ranks amongst the most economically significant in Iraq, with high contents of organic matter, and thus, such a formation is a key source rock for generating a source of petroleum in its upper Jurassic and lower Cretaceous rocks (Jafar, 2010).

According to Bolton (1958), the Sargelu Formation in the Rania region is composed of black shaly limestone with thin stratification, with cherty black bands, and with accompanying brown dolomitized marls. On the basis of the dominant faunas prevalent, the Sargelu Formation is located in the Bajocian and Bathonian stages. (Hamza,1971 in Al-Hadithi et al., 1976)" describe the Sargelu Formation in the Benafi region, and pointed out

that it consists of bluish-gray to black, well-bedded organic limestone and dolomitic in some parts."

Buday (1980) refers that the Sargelu and Muhaiwir Formations were deposited as a result of marine advances during the Middle Jurassic and identified the environment of the Sargelu Formation in its type section as an open marine environment extending to the shallow marine environment, and pointed out that the Sargelu Formation was deposited in a toxic marine environment but some of its beds show good aeration conditions.

(Al-Ahmed, 2001) studied the Sargelu Formation in Northern Iraq and explained that the formation with high organic content is an oil exporter in Iraq, and that the conditions of the sedimentary environment of the formation are deep marine. (Balaky, 2004) while studying the formation in selected sections of Erbil and Dohuk governorates in Northern Iraq, indicated that the abundance of silica in the upper beds of the Sargelu Formation reflects its organic sedimentary origin.

The geochemical study of sediments and knowing the proportions of some elements in them is of great importance in predicting ancient environmental conditions (Tribovillard et al., 2006; Chang et al., 2016). The information obtained from geochemical studies (major and trace elements) in sedimentary successions can also be widely used to obtain important information about clastic flow, oxygenic conditions, and other depositional conditions (Tribovillard et al., 2006).

Many studies have been carried out on the Sargelu Formation, including: (Al-Ahmed, 2006; Sherwani and Balaky, 2006; Al-Fariji, 2008; Jafar, 2010; Al-Taie, 2013; Al-Asi, 2016; Al-Atroshe, 2018; Akram et al., 2021; Al-Dolaimy et al., 2021; Al-Tarim and Al-Shakiri, 2022). This research aims to study the concentrations of some major and trace elements and the proportions between them to deduce some sedimentary conditions during the deposition of the Sargelu Formation.

Location of the Study Area

The Sargelu Formation was studied in the Hanjira village, located within the borders of Sulaymani Governorate, Northeastern Iraq. The Hanjira section is located 95 km Northwest of the Sulaymani center, specifically 1.97 km Northwest of the Rania town, which is located on the Southwestern limb of the Shaweri anticline, at the intersection point (44°50'55'E) and (36°16'50'N) (Fig. 1).

Geological Setting

Jurassic successions are exposed in different areas, northern and northeastern Iraq, and are concentrated within the High Folded Zone and the Imbricated Zone as well as the Thrust Zone (Buday, 1980). The Sargelu Formation in the studied section is located within the Imbricated Zone (Fouad, 2015) (Fig. 1).

The Sargelu Formation is one of the formations that make up the Great Arabian Plate (Late Toarcian- Early Tithonian Megasequence-AP7) (Jassim and Buday, 2006).

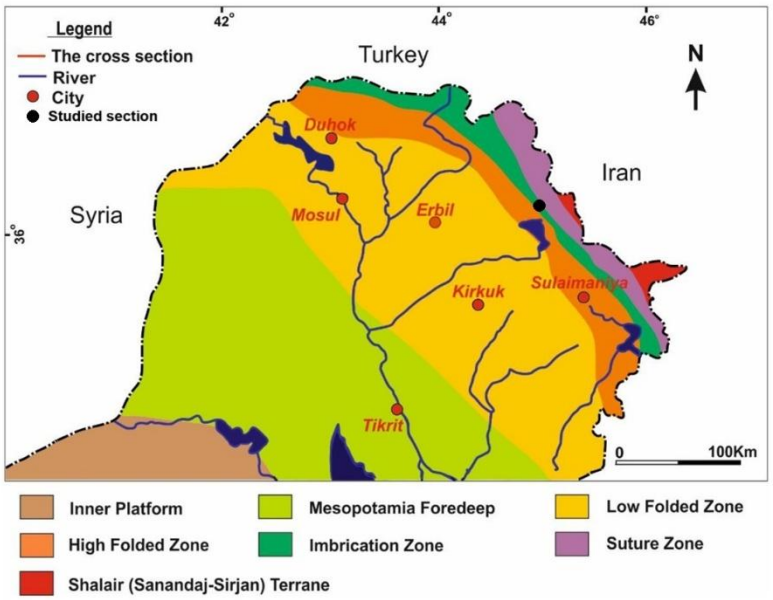


Fig. 1. Tectonic and location map of the study area (after Fouad, 2015).

It includes two sub-sequences, the late Jurassic and the Middle Jurassic. The Saggar, Cotnia, Najma, Naokelekan, and Barsarin formations were deposited in the late Jurassic, while the middle Jurassic sequences included the Sargelu and Muhaiwer formations (Jassim and Buday, 2006; Sharland et al., 2001).

The form of sedimentary basins in the Middle East during the Middle Jurassic (Bajocian and Bathonian) after tectonic movements that led to a significant marine decline during the late Triassic (Sharief, 1982), it began to develop and originate in most areas of Iraq seas within the continent, then deposition of Muhaiwer Formation facies occurred in its shallow parts, while the facies of the Sargelu Formation deposited in its deep parts (Rabu et al., 1990).

In the study area, the Sargelu Formation is bounded at the bottom by the Sehkaniyan Formation and at the top by the Naokelekan Formation. The Sehkaniyan Formation (Upper Liassic) was first described by Wetzel and Morton 1950 in Bellen et al. (1959) in the Sordash anticline near the village of Sehkaniyan, northeastern Iraq.

The Sehkaniyan Formation consists of hard and dark gray dolostone rocks. The formation is located below the Sargelu Formation, and the contact surface between them appears as a conformable surface (Bolton, 1958). The Naokelekan Formation (Late Oxfordian - Early Kimmeridgian) is described in the typical section by Wetzel and Morton (1950 in Bellen et al., 1959), which is located near the village of Naokelekan in northeastern Iraq. The formation consists of thick-bedded light brown limestone interspersed with thin beds of gray-colored carbonate rocks intertwined with thin black shales. The formation is underlain by the Sargelu Formation, and the contact surface between them is sedimentologically conformable (Buday, 1980).

Methods and Materials

The field work involved a number of site trips to the field location in Hanjira village. On-site, ten samples were collected from the Sargelo Formation with regard to rock variation in character. In detail, observations regarding rock bed criteria, including thickness, color, and relation in terms of stratigraphy, were recorded. All indications of presence and life activity, and the presence of bituminous matter, were noted, and proper photograph documentation was conducted. In the laboratory, thin sections of samples collected and prepared in the geologic workshop in the Department of Geology, University of Mosul, and analyzed with a polarized microscope. An analysis and attempt to assess the composition, texture, and the impact of a diagenesis process in rock samples. Besides, X-ray fluorescence (XRF) analysis

with the (ADX 2700) device is carried out for ten samples in the University of Baghdad, College of Science. The geochemical analysis is an attempt to assess concentrations of major and trace elements in the Sargelu Formation in order to calculate an elemental proportion as well.

The thickness of the Sargelu Formation in the Hangira section is 40 meters beginning with a succession of 28 meters thick (Fig. 2), which consists of well-bedded limestone and dolomitic limestone, gray in color, interspersed with beds of argillaceous limestone (10-30 cm thick) rich in organic matter, intertwined at the top of this succession by thin beds of brown chert rich in ammonite fossils.

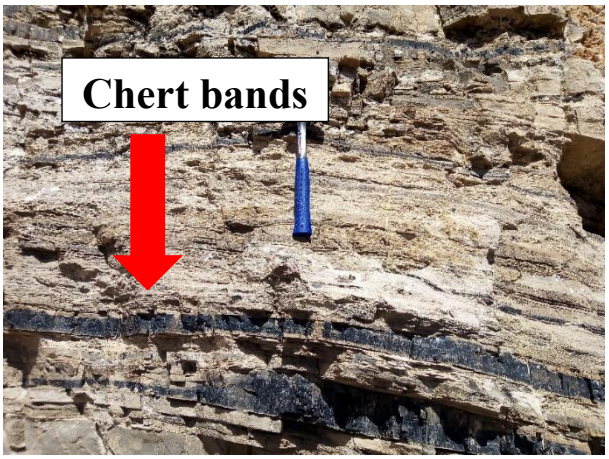


Fig. 2. Field photo showing well-bedded limestone, dolomitic limestone, and chert beds, Hanjera section.



Fig. 3. Field photo showing limestone beds interbedded with chert bands, Hanjera section.

The aforementioned beds followed by another succession of 12 meters thick consisting of well-bedded limestone with a bed thickness of (10-40 cm) of brown color alternating with beds of argillaceous limestone and thin beds of chert with thickness (5-10 cm) (Fig. 3). The above sequences end in brown, thick limestone beds belonging to the Naokelekan Formation (Fig. 4).

According to Al-Shammary et al. (2023b), three dominant microfacies constitute the formation: namely lime mudstone, lime wackestone, and lime packstone. These three microfacies have eight respective subdivisions as in Table 1. Siliceous microfossil occurrences, namely radiolarian tests, which in these microfacies serve as a dominant marker for pelagic depositional environments. All these indications, according to Mohammed Sajed

et al. (2024), strongly validate that the depositional environment of the formation is a deep-shelf system with a deep-sea basin.

Table 1: Main and submicrofacies of the Sargelu Formation.

Microfacies	Submicrofacies
Lime mudstone microfacies	Radiolarian lime mudstone
	Bioclastic lime mudstone
Lime wackestone microfacies	Radiolarian lime wackestone
	Bioclastic filaments lime wackestone
	Bioclastic lime wackestone
Lime packstone microfacies	Bositra lime packstone
	Ostracoda lime packstone
	Filaments lime packstone

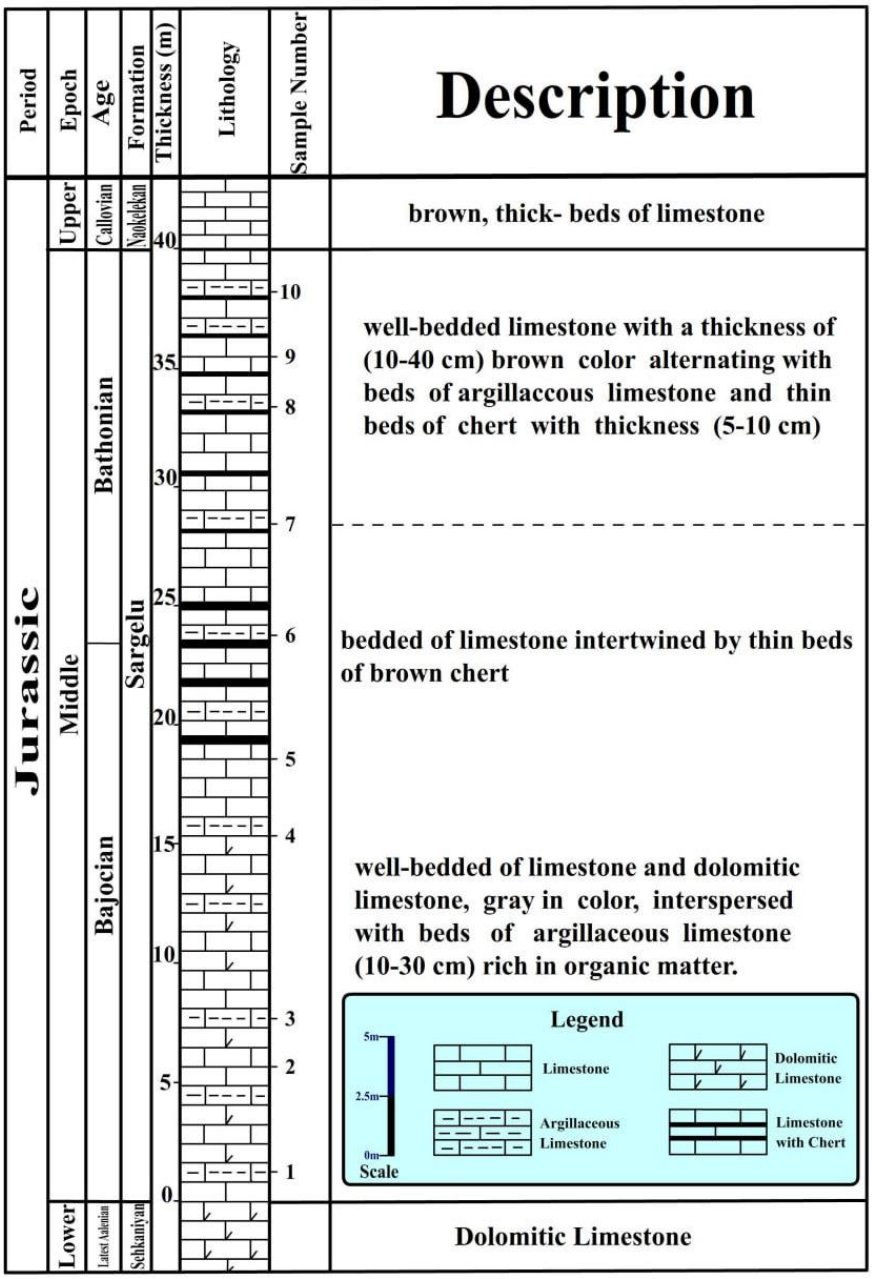


Fig. 4. Columnar lithology of Sargelu Formation in Hanjira section.

Results and Discussion

Paleoproductivity

The concentrations of some major and trace elements, as well as the ratios between them, are determined for ten samples distributed across the Sargelu Formation to extrapolate

certain conditions of its depositional environment that accompanied the deposition of the Sargelu Formation. Table 2 shows these ratios.

Phosphorus (P)

Phosphorus is a life-supporting element for all living forms on the planet, acting as an important nutrient for living beings in view of its role in a variety of processes in living forms (Shen et al., 2015; Tribovillard et al., 2006). In addition, it forms an integral part of soft skeletal structures responsible for assimilation of phosphorus in tissue development (Shen et al., 2015; Tribovillard et al., 2006). Phosphorus in sediments has a strong relation with productivity at the surface, and it is buried with organic matter during the decomposition of living forms. In reduced environments, phosphorus can become mobilized in organic matter, and even in areas with high productivity in living forms, its depletion can occur (Schenau et al., 2005). High concentrations of phosphorus in sediments in upwelling allow for increased cycling of nutrients, and in consequence, high organic productivity with organic compounds, including calcareous deposits (Böning et al., 2004; Schenau et al., 2005).

Phosphorus deposition is preferentially mineralized over organic carbon and subsequently mobilized in pore water during its migration in the water column. In a secondary stage, endogenous phosphate can form too. To exclude, at least in part, the role of terrestrial detrital contribution, productivity in terms of phosphorus is conventionally considered in terms of (P/Ti) or (P/Al) and not in terms of absolute concentrations of phosphorus (Algeo et al., 2011).

Table 2: Some elemental ratios of depositional Conditions of the Sargelu Formation.

Sample No.	P/Al	P/Ti	Ba bio	V/(V+Ni)	U/Th	Ni/Co	Al_2O_3/TiO_2	Zr/Rb	Si/Al	Ti/Al	K/Al
M1	0.06	0.68	77.29	0.46	1.12	12.33	13.39	2.21	2.92	0.08	0.27
M2	0.14	2.47	32.40	0.65	2.93	24.40	20.16	3.66	2.61	0.06	0.24
M3	0.05	0.61	31.94	0.63	3.86	40.34	12.91	1.98	11.77	0.09	0.30
M4	0.14	1.70	38.10	0.47	8.15	86.94	13.38	1.69	7.25	0.08	0.33
M5	0.09	1.53	34.93	0.48	1.38	13.02	18.40	1.94	2.50	0.06	0.45
M6	0.02	0.31	80.56	0.62	4.19	12.16	15.75	1.98	2.59	0.07	0.49
M7	0.05	0.55	40.84	0.46	8.76	111.44	13.52	1.64	6.77	0.08	0.60
M8	0.04	0.56	37.83	0.69	4.67	25.32	15.90	1.07	3.03	0.07	0.38
M9	0.04	0.42	92.05	0.67	5.36	93.19	10.52	2.62	2.66	0.11	0.42
M10	0.06	0.57	74.38	0.74	8.92	35.01	11.63	1.63	3.14	0.10	0.40
Ave.	0.07	0.94	54.03	0.59	4.93	45.41	14.56	2.04	4.52	0.08	0.39
Max	0.14	2.47	92.05	0.74	8.92	111.44	20.16	3.66	11.77	0.11	0.60
Min	0.02	0.31	31.94	0.46	1.12	12.16	10.52	1.07	2.50	0.06	0.24

P/Al Ratio

The results of this work confirm that the mean (P/Al) value is approximately 0.07, with a range between 0.02 and 0.14, as in Table 2. These observations confirm that in this work, the mean (P/Al) value is larger in comparison with its documented mean in shales, and it is 0.008 according to Wedepohl (1971). That confirms high productivity in Sargelu Formation samples. These observations agree with (Hetzel et al., 2009; Liu et al., 2019), who regarded (P/Al) values are high in a range between (0.01 and 0.03). Thus, observations evidently confirm that the Sargelu Formation accumulated under high productivity in terms of its biological productivity.

P/Ti Ratio

The (P/Ti) values in the Sargelu Formation range between (0.31 and 2.47) with an average of (0.94) as in Table 2. All these values point to high productivity in samples under consideration in consonance with productivity values postulated by Algeo et al. (2011). Specifically, a (P/Ti) value less than (0.34) signifies low productivity, and a value exceeding (0.79) signifies high productivity. Ratios between (0.34 and 0.79) represent indicative intermediate productivity. In general, phosphorus enrichments in black horizons are most

frequently accompanied by augmented primary productivity supported through augmented availability of nutrients.

Organic Barium (Ba) (Ba/Al Ratio)

Barium in marine environments is present in a variety of forms, including the form of the mineral barite, in living beings' skeletal structures, and in organic matter. In such forms, its presence is a result of marine organism metabolic processes, in which barium is taken in and incorporated, or adsorbed onto, a silica or a carbonate skeleton, or transported with organic matter, possibly derived from detrital sources. There is a strong organic carbon-barium association (Dymond et al., 1992; Tribovillard et al., 2006). Organic barium (Ba_{bio}) is a well-established proxy for initial organic productivity (Dymond et al., 1992; Francois et al., 1995), and reflects specifically incorporated barium through living activity, and can therefore discriminate between incorporated barium derived through processes not living in origin, such as through hydrothermal activity, and through incorporation with detrital matter associations (Martinez-Ruiz et al., 2014; Eagle et al., 2003; Ding et al., 2018). Quantitation of organic barium (Ba_{bio}) is most commonly calculated through the use of the following equation:

$$Ba_{bio}=Ba_{total}-(Al_{total}*Ba/Al_{alum.}) = Ba_{total}-(Al_{total}*0.0075)$$

Where the value of the (Ba/Al_{alum}) ratio in detrital aluminum silicates is (0.0075) in the rocks of the Earth's crust (Dymond et al., 1992), and when the values are positive, the productivity is high, and when they are negative or very little, they indicate low productivity. The percentage of organic barium (Ba_{bio}) in the Sargelu Formation has positive values ranging between (31.94-92.05) with an average of (54.03). Note Table (2). These positive values indicate high old productivity.

Oxidation and reduction conditions

V/(V+Ni) Ratio

Vanadium is a minor, oxidation state-sensitive element, and its abundance increases under anoxia (Jones and Manning, 1994; Hatch and Leventhal, 1992; Tribovillard et al., 2006). Meunier (1994) reported that vanadium can occur in substitution for aluminum in clays in an octahedral position during diagenesis processes (Tribovillard et al., 2006). Hatch and Leventhal (1992) even constructed a (V/(V+Ni)) value that with a value > 0.84 is indicative of toxic environments, 0.54 < (V/(V+Ni)) < 0.84 indicative of depletion in oxygen, 0.46 < (V/(V+Ni)) < 0.54 indicative of semi-oxygen (dysoxical) environments, and (V/(V+Ni)) at and below 0.46 indicative of high concentrations of oxygen environments.

In the current study, the ratio (V/(V+Ni)) ranges between (0.46-0.74) at a rate of (0.59) (Table 2); and therefore, most of the rocks of the Sargelu Formation were deposited under anoxic to semi-oxygen (dysoxic) environmental conditions.

U/Th Ratio

The chemical behavior of uranium is similar to thorium, and U/Th is utilized in terms of checking for oxidation-reduction state. Any value of U/Th > 1.25 signifies an environment with a lack of oxygen, and values between 0.75 and 1.25 denote a dysoxic-suboxic environment (Jones and Manning, 1994; Zhang et al., 2019). Conversely, a value < 0.75 signifies an environment with an abundance of oxygen (Jones and Manning, 1994; Zhang et al., 2019). In Sargelu Formation samples, U/Th values range between 1.12 and 8.95 with an average of 4.93 (Table 2). All such values are about 0.38 in excess of the general U/Th in a shale (Wedepohl, 1971). High U/Th values in the current study mean that the Sargelo Formation had been deposited in an oxygen-lacking environment.

Ni/Co Ratio

The nickel/cobalt (Ni/Co) ratio can also be used as an indication of the conditions of deposition in terms of the abundance of oxygen. If the ratio is greater than (7.0), then the depositional conditions are of scarce or no oxygen (anoxic), and if they are between (5.0-7.0) the conditions are moderate in terms of the abundance of oxygen (dysoxic), but if the ratio is less than (5.0), the conditions are abundant in oxygen (Dypvik, 1984; Jones and Manning, 1994).

This percentage in the Sargelu Formation samples is at a rate of (45.41) with a range between (12.16-111.44) (Table 2), and these values indicate deposition in oxygen-scarce conditions.

Provenance

Al_2O_3/TiO_2 Ratio

The (Al_2O_3/TiO_2) ratio is commonly used for source rock determination (Hayashi et al., 1997; Zeng et al., 2019). In general, a value exceeding 21 signifies felsic acid igneous rocks, a value between 8-21 signifies intermediate igneous rocks, and a value less than 8 signifies basic igneous rocks. For Sargelu Formation samples, (Al_2O_3/TiO_2) value ranges between (10.52) and (20.16) with an average of (14.56) (Table 2). This signifies that Sargelu Formation source rocks have predominantly an intermediate igneous character.

Hydrodynamic Conditions

Hydrodynamic conditions represent an integrated system that includes the influence of water depth, wave base, and current speed. The quantitative preservation of organic matter increases with a decrease in water energy (Liu et al., 2006). The hydrodynamics of the basin can be inferred through the ratio (Zr/Rb), which can reflect the changes occurring in hydrodynamic conditions. Zircon enrichment usually occurs in coarse sediments, but is depleted in fine sediments. As for the element Rubidium, it is generally deposited in low-energy environments and is associated with fine-grained minerals such as clay minerals. Therefore, if the ratio (Zr/Rb) is high, it usually indicates an environment with high hydroenergy, while if this ratio is low, it indicates an environment with low energy (Liu et al., 2006), as the ratio of values that are Less than (2) and at a rate of (0.9) to low water capacity with the presence of thinning and black color of the sediments (Liu et al., 2006).

The ratio (Zr/Rb) in the models of the Sargelu Formation ranges between (1.07-3.66) with an average of (2.04) (Table 2), and these values may indicate that the Sargelu Formation was deposited in conditions with low water energy, which is associated with the deposition of thinned black chert.

Detrital input

Si/Al Ratio

Silicon (Si) and aluminum (Al) are generally immobile elements during diagenetic processes and are often used as evidence of clastic flow (Sageman and Lyons, 2005; Tribovillard et al., 2006). Silicon is mainly found in the siliciclastic (quartz) part and the organic part (Kidder and Erwin, 2001). As for aluminum, its presence is limited to the fine part of aluminum silicate and is rich in kaolinite and smectite, and is formed as a result of severe chemical weathering under the influence of humid and warm climate conditions (Yeasmin et al., 2017).

The Si/Al ratio has been used in many studies as a means of determining clastic flow, as it represents the ratio of quartz to clay (Murphy et al., 2000; Rimmer, 2004), and changes in the Si/Al ratio are preferably interpreted to reflect changes in silicon flow (Si) which is independent of alluvial processing (Werne et al., 2002). This ratio in the samples of the Sargelu Formation ranges between (2.5-11.77) at a rate of (4.52) (Table 2), and these values are higher than its value in the shale rate (3.11) (Wedepohl, 1971), which indicates a high

clastic flow in the sedimentation basin of the Sargelu Formation, whose high values may be due to the presence of detrital quartz or organic silica of organisms with a silicate wall such as Radiolaria.

Ti/Al and K/Al Ratios

The assessment of detrital preparation is determined via (Ti/Al and K/Al) ratios (Tribovillard et al., 2006; Rakociński et al., 2018). The origin of titanium comes through wind flow (aeolian inputs), and (Ti/Al, therefore, is an expression of wind activity (aeolian activity (Challands et al., 2009) and weathering of adjacent volcanic rocks (Boström, 1970). In Sargelu Formation samples, the (Ti/Al) ratio ranges between (0.06-0.11) with an average of (0.8), and the (K/Al) ratio ranges between (0.24-0.60) with an average of (0.39) (Table 2). For comparison, (Ti/Al and K/Al in the composition of shale) are (0.05 and 0.34, respectively (Wedepohl, 1971). Higher values, in contrast to (in shale), could be an expression of wind clastic flows' impact in Sargelu Formation deposits, or the specific character of clays in Sargelu Formation sediment.

Conclusion

The findings of the current study can be synthesized below:

1. The studied section of the Sargelu Formation in Hanjira, northeastern Iraq, consists predominantly of dolomite and limestone, with organic matter-enriched argillaceous limestone and thin chert intercalation.

2. Geochemical analyses of rock units in the formation have been performed in an attempt to evaluate paleoproductivity, oxidation and reduction, provenance, hydrodynamic, and detrital input. Ratios of P/Al, P/Ti, and Ba/Al in general imply high productivity values.

3. Redox proxies for trace metalloelement (e.g., V/(V + Ni), U/Th, and Ni/Co) record anoxia to semi-oxygenated (dysoxia).

4. The Al_2O_3/TiO_2 proportion suggests that the source rocks for the Sargelu Formation are intermediate igneous rocks in general.

5. The Zr/Rb ratio proves that the Sargelu Formation had been accumulated in an environment with low-energy water.

6. Ratios of Si/Al, Ti/Al, and K/Al indicate high clastic contribution in the Sargelu Formation sedimentary basin, with a dominant source of clastic material being driven by wind.

Acknowledgements

The authors wish to express their sincere appreciation to the College of Science, University of Mosul, for offering the necessary resources that significantly contributed to enhancing the quality of this research. The authors also extend their gratitude to the Editor-in-Chief, Prof. Dr. Rayan Ghazi, the editorial board members, and the technical editors for their dedicated efforts and insightful feedback.

References

Akram, R., Edilbi, A.N., Mamaseni, W.J., Sherwani, G.H. and Al-Ansari, N., 2021. Source rock evaluation and 1-D basin modelling approach for the Sargelu Formation, Atrush-2 Well, Kurdistan Region-Iraq. Open Journal of Geology, 11(3), pp. 49-60. DOI:10.4236/ojg.2021.113004

Al-Ahmed, A., 2001. Palynofacies indications of depositional environment and source potential for hydrocarbon (middle Jurassic) Sargelu Formation Northern Iraq. Unpublished M.Sc. thesis, Baghdad University, 100 P.

Al-Ahmed, A., 2006. Organic geochemistry palynofacies and hydrocarbon potential of Sargelu Formation (Middle Jurassic) Northern Iraq. Unpublished Ph.D. thesis, Baghdad University, 120 P.

Al-Asi, B.B.H., 2016. Sedimentary study of the Sargelu Formation rocks and determination of organic content in them for selected wells in Butma and Ain Zala field/Northern Iraq, Unpublished M.Sc. thesis, Tikrit University, 95 P.

Al-Atroshe, R.K.H., 2018. Investigation of Properties of Sedimentology and Petroleum Possibilities of Middle–Late Jurassic Rock Units in Regions of Northern Iraq, süleyman demirel Üniversitesi, Fen Bilimleri Enstitüsü, Mühendisliği Anabilim Dalı'nda, ISPARTA, 197 P.

Al-Dolaimy, A.M., Al-Beyati, F.M. and Al-Mallah, A.Y., 2021. Distribution of steranes and triterpanes biomarkersas indication of depositional environment and maturity of Sargelu and Kurrachine Formations in different wells Northern Iraq. The Iraqi Geological Journal, pp. 87-100. DOI:10.46717/igj.54.1C.7Ms-2021-03-27

Al-Fariji, Sh.H.M., 2008. biostratigraphy and sedimentary study of the Sehkaniyan and Sargelu Formations in Northeastern Iraq, Unpublished M.Sc. thesis, University of Baghdad, 106 P.

Algeo, T.J., Kuwahara, K., Sano, H., Bates, S., Lyons, T., Elswick, E., Hinnov, L., Ellwood, B., Moser, J. and Maynard, J.B., 2011. Spatial variation in sediment fluxes, redox conditions, and productivity in the Permian-Triassic panthalassic ocean. Palaeogeography, Palaeoclimatology, Palaeoecology. Vol. 308, pp. 65-83. DOI:10.1016/j.palaeo.2010.07.007

Al-Hadithi, H., Pesl. V. and Isaac, E.A., 1976. Geology of the middle part of the Northern Thrust Zone, S.O.M. Library, Baghdad.

Al-Shammary, M., Malak, Z. and Al-Jwary, M., 2023. Sedimentological Study of Exposed Successions of the Sargelu Formation, Middle Jurassic, Northeastern, Iraq, Iraqi Geological Journal, 56(1B), pp. 51-63. DOI: 10.46717/igj.56.1B.5ms-2023-2-13

Al-Taie, A.J.M., 2013. Sedimentary basin analysis of Sargelu and Muhaiwir Formations (Bajocian – Bathonian) in Iraq, Unpublished Ph.D. Thesis, University of Mosul, 220 P.

Al-Tarim, H.A.F. and Al-Shakiri, A.J., 2022. Field description and lithostratigraphic study of Sargelu Formation in Rania and Sargelu sections, Northern Iraq. Iraqi Journal of Science, pp. 583-595. DOI: 10.24996/ijs.2022.63.2.15

Balaky, S.M., 2004. Stratigraphy and sedimentology of Sargelu Formation (Middle Jurassic) in selected sections in Erbil and Duhok Governorates- Iraqi Kurdistan region. Unpublished M.Sc. thesis, University of Salahaddin, 110 P.

Bellen, R.C.V., Dunnington, H.V., Wetzel, R. and Morton, D., 1959. Lexique Stratigraphique International Asie, Iraq. Vol. 3C, No. 10a, 333 P. https://api.semanticscholar.org/CorpusID:128726684

Bolton, C.M.G., 1958. The geology of the Ranya area site Inv., Co., Report S.O.M. Library. No. 271, Baghdad, Report.

Böning, P., Brumsack, H.J., Bottcher, M.E., Schnetger, B., Kriete, C., Kallmeyer, J. and Borchers, S. L., 2004. Geochemistry of Peruvian near surface sediments. Geochem. Cosmochim. Acta, Vol.68, pp. 4429–4451. doi:10.1016/j.gca.2004.04.027

Boström, K., 1970. Submarine volcanism as a source for iron. Earth and planetary science letters, Vol. 9. pp. 348-354.

Buday, T., 1980. The Regional Geology of Iraq: Stratigraphy and Paleogeography, Dar Al-Kutub Publ. House, Mosul, 445 P.

Challands, T.J., Armstrong, H.A., Maloney, D.P., Davies, J.R., Owen, W.D. and Owen, A. W., 2009. Organic-carbon deposition and coastal upwelling at mid-latitude during the Upper Ordovician (Late Katian): a case study from the Welsh Basin, U.K. Palaeogeography, Palaeoclimatology, Paleoecology. Vol. 273, pp. 395–410. Doi: 10.1016/j.palaeo.2008.10.004

Chang, C., W. Hu, Q. Fu, J. Cao, X. Wang. and Yao, S., 2016. Characterization of trace elements and carbon isotopes across the Ediacaran-Cambrian boundary in Anhui province, South China: implications for stratigraphy and paleoenvironment reconstruction. Journal of Asian Earth Sciences, Vol. 125, pp. 58-70. https://doi.org/10.1016/j.jseaes.2016.05.014

Ding, J., Zhang, J., Tang, X., Huo, Z., Han, SH., Lang, Y., Zheng, Y. Li. and Liu, T., 2018. Elemental geochemical evidence for depositional conditions and organic matter enrichment of black rock series strata in an Inter-Platform Basin: The Lower Carboniferous Datang Formation, Southern Guizhou, Southwest China. Minerals, Vol. 8, pp. 1-29. https://doi:10.3390/min8110509

Dymond, J., Suess, E. and Lyle, M., 1992. Barium in deep-sea sediment: a geochemical proxy for paleoproductivity. Paleoceanography. Vol. 7, pp 163–181. https://doi.org/10.1029/92PA00181

Dypvik, H., 1984. Geochemical compositions and depositional conditions of upper Jurassic and lower Cretaceous Yorkshire clays, England. Geological Magazine, Vol. 121, pp. 489-504. https://doi.org/10.1017/S0016756800030028

Eagle, M., Paytan, A., Arrigo, K.R., Van Dijken, G. and Murray, R.W., 2003. A comparison between excess barium and barite as indicators of carbon export. Paleoceanography, Vol. 18, pp. 2101–2113. DOI: 10.1029/2002PA000793

Fouad, S.F.A., 2015. Tectonic Map of Iraq. Scale 1: 1000000, 3rd Edition, Iraqi Bulletin of Geology and Mining, Iraq, Vol. 11, No.1, pp. 1-7.DOI:https://ibgm-iq.org/ibgm/index.php/ibgm/article/view/262.

Francois, R., Honjo, S., Manganini, S.J. and Ravizza, G.E., 1995. Biogenic barium fluxes to the deep sea: Implications for paleoproductivity reconstruction. Glob. Biogeochemical Cycles, Vol. 9, pp. 289–303.https://doi.org/10.1029/95GB00021

Hatch, J.R. and Leventhal, J.S., 1992. Relationship between inferred redox potential of the depositional environment and geochemistry of the Upper Pennsylvanian (Missourian) Stark Shale Member of the Dennis limestone, Wabaunsee country, Kansas, USA. Chemical Geology. Vol. 99, pp. 65–82. https://doi.org/10.1016/0009-2541(92)90031-Y

Hayashi, K.I., Fujisawa, H., Holland, H. D. and Ohmoto, H., 1997. Geochemistry of ~1.9 Ga sedimentary rocks from northeastern Labrador, Canada. Geochim. Cosmochim. Acta. Vol. 61, pp. 4115–4137. https://doi.org/10.1016/S0016-7037(97)00214-7

Hetzel, A., Böttcher, M.E., Wortmann, U.G. and Brumsack, H.J., 2009. Paleo-redox conditions during OAE 2 reflected in Demerara Rise sediment geochemistry (ODP Leg

207) Palaeogeography, Palaeoclimatology, Palaeoecology. Vol. 273, pp. 302–328. https://doi.org/10.1016/j.palaeo.2008.11.005

Jafar, M.S.A., 2010. Hydrocarbon sources and oil accumulation in Cenomanian–Early Turonian Mishrif Formation reservoir, in Selected fields, Southeastern Iraq. Unpublished PhD Thesis, University of Baghdad, 203 P.

Jassim, S.Z. and Buday, T., 2006. Late Toarcian – Early Tithonian (Mid-Late Jurassic) Megasequence AP7. In: Jassim, S.Z. and Goff, J.C., (eds.), Geology of Iraq, Dolin, Prague and Moravian Museum, Brno. pp. 124-140.

Jones, B. and Manning, D.A.C., 1994. Comparison of geochemical indices used for the interpretation of paleoredox conditions in ancient mudstones. Chem. Geol. Vol. 111, pp. 111–129.

Kidder, D.I. and Erwin, D.H., 2001. Secular Distribution of Biogenic Silica Trough the Phanerozoic: Comparison of Silica-Replaced Fossil and Bedded Cherts at the Series Level. Journal of Geology, 109: pp. 509-522. https://doi.org/10.1086/320794

Liu, W. Q., Yao, J. X., Tong, J.N., Qian, Y. and Chen, Y., 2019. Organic matter accumulation on the Dalong Formation (Upper Permian) in western Hubei, South China: constraints from multiple geochemical proxies and pyrite morphology. Palaeogeography, Palaeoclimatology, Palaeoecology, Vol. 514, pp. 677–689.

Martinez-Ruiz, F., Kastner, M., Gallego-Torres, D., Rodrigo-Gamiz, M., Nieto-Moreno, V. and Ortega-Huertas, M., 2014. Paleoclimate and paleooceangraphy over the past 20.000 yr in the Mediterranean Sea basins indicated by sediment elemental proxies. Quaternary Science Reviews. Vol. 107, pp. 25–46. https://doi.org/10.1016/j.quascirev.2014.09.018

Meunier, J.D., 1994. The composition and origin of vanadium-rich clay minerals in Colorado Plateau Jurassic sandstones. Clays and Clay Minerals, 42(4), pp. 391-401. https://doi.org/10.1346/CCMN.1994.0420403

Mohammed Sajed, O.K., Glover, P.W., Alrashedi, M.A. and Collier, R.E.L., 2024. Quantification of the effect of fracturing on heterogeneity and reservoir quality of deep-water carbonate reservoirs. Journal of African Earth Sciences 218 (2024) 105383. https://doi.org/10.1016/j.jafrearsci.2024.105383

Murphy, A.E., Sageman, B.B., Hollander, D.J., Lyons, T.W. and Brett, C.E., 2000. Black shale deposition and faunal overturn in the Devonian Appalachian basin: clastic starvation, seasonal water-column mixing, and efficient biolimiting nutrient recycling. Paleoceanography, Vol. 15, pp. 280-291. DOI:10.1029/1999PA000445

Rabu, D., Le Metour, J., Bechennec, F., Beurrier, M., Villey, M. and DE Grissac, C.H., 1990. Sedimentary aspects of the Arabian Platform. In: Robertson, A.H.F., Serale, M.P. and Ries, A.C. (eds), The Geology and Tectonics of Oman Region. Geo. Soc., London, Spec. Publ., Vol. 49, pp. 49-68.

Rakociński, M., Zatoń, M., Marynowski, L., Gedl, P. and Lehman, J. 2018. Redox conditions, productivity, and volcanic input during deposition of uppermost Jurassic and Lower Cretaceous organic-rich siltstones in Spitsbergen, Norway. Cretaceous Research, Vol. 89, pp. 126-147. DOI:10.1016/j.cretres.2018.02.014

Rimmer, S.M., 2004. Geochemical paleoredox indicators in Devonian–Mississippian black shales, Central Appalachian Basin (USA). Chem. Geol. Vol. 206, pp. 373–391. https://doi.org/10.1016/j.chemgeo.2003.12.029

Sageman, B.B. and Lyons, T.W., 2005. Geochemistry of fine-grained sediments and sedimentary rocks. In: Mackenzie, F. (Ed.), Treatise on Geochemistry 7. Elsevier, New York, pp. 115–158. https://doi.org/10.1016/B0-08-043751-6/07157-7

Schenau, S.J., Reichart, G.J. and De Lange, G.J., 2005. Phosphorus burial as a function of paleoproductivity and redox conditions in Arabian Sea sediments. Geochim. Cosmochim. Acta, Vol. 69, pp. 919–931. https://doi.org/10.1016/j.gca.2004.05.044

Sharief, F.A., 1982. Lithofacies distribution of the Permian -Triassic rocks in the Middle East: J. Petr. Geo., Vol. 4, pp. 299-310.

Sharland, P.R., Archer, R., Casey, D.M., Davies, R.B., Hall, S.H., Heward, A.P., Houbury, A. D., and Simmons, M. D., 2001. Arabian Plate Sequence Stratigraphy, Geo Arabia, Spec. Publ., No. 2, Petrolik Manama, Bahrain, 371 P.

Shen, J., Schoepfer, S.D., Feng, Q.L., Zhou, L., Yu, J. X., Song, H.Y., Wei, H.Y. and Algeo, T.J., 2015. Marine Productivity Changes During the End-Permian Crisis and Early Triassic Recovery, Earth Science Review, Vol. 149, pp. 136–162. DOI: 10.1016/j.earscirev.2014.11.002

Sherwani, G.H. and Balaky, S.M.H., 2006. Black chert, An Interesting petrographic component within the Upper part of Sargelu Formation (Middle Jurassic) – North and Northeastern Iraqi. Iraq Bull. Geo. Min., Vol. 2, No.1, pp. 77 -88.

Liu, W., Xu, Y., Chen, J., Hu, K. and Gao, C., 2006. Comprehensive Geochemical Identification of Highly Evolved Marine Hydrocarbon Source Rocks: Organic Matter, Paleoenvironment and Development of Effective Hydrocarbon Source Rocks. Chinese Journal of Geochemistry, 25(4), pp. 333-340. https://doi.org/10.1007/s11631-006-0332-4.

Tribovillard, N., Algeo, T.J., Lyons, T. and Riboulleau, A., 2006. Trace-metals as paleoredox and paleoproductivity proxies: an update. Chemical Geology, Vol. 232, pp.12–32. DOI:10.1016/j.chemgeo.2006.02.012

Wedepohl, K.H., 1971. Environmental influences on the chemical composition of shales and clays. In: Ahrens, L.H., Press, F., Runcorn, S.K., Urey, H.C. (Eds.), Physics and Chemistry of the Earth, Pergamon, Oxford, Vol. 8, pp. 305–333.

Werne, J.P., Sageman, B.B., Lyons, T.W. and Hollander, D.J., 2002. An integrated assessment of a ‘‘type euxinic’’ deposit: evidence for multiple controls on black shale deposition in the Middle Devonian Oatka Creek formation. Am. J. Sci. Vol. 302, pp. 110-143. https://doi.org/10.2475/ajs.302.2.110

Yeasmin, R., Chen, D., Fu, Y., Wang, J.G., Guo, Z.H. and Guo, C., 2017. Climatic oceanic forcing on the organic accumulation across the shelf during the Early Cambrian (Age 2 through 3) in the mid-upper Yangtze Block, NE Guizhou, South China. J. Asian Earth Sci., Vol. 134, pp. 365–386. DOI:10.1016/j.jseaes.2016.08.019

Zeng, S., Wang, J., Chen, W., Fu, X., Feng, X., Song, C., Wang, D. and Sun, W., 2019. Geochemical characteristics of Early Cretaceous marine oil shale from the Changshe Mountain area in the northern Qiangtang Basin, Tibet: Implications for palaeoweathering, provenance, tectonic setting, and organic matter accumulation. Geological Journal, Vol. 55, pp. 3229-3246. DOI:10.1002/gj.3579

Zhang, X.L., Wang, Y., Liu, J.B., Rong, J.Y., Li, R.Y., Zhan, R.B., Wu, R.C. and Tang, P., 2019. Connecting the marine red beds with the onset of the Great Ordovician Biodiversification Event: a case study from the Laojianshan Formation of western Yunnan, Sibumasu Massif. Palaeoworld, Vol. 28, pp. 211–223. DOI:10.1016/j.palwor.2018.04.003

Iraqi National Journal of Earth Science

www.earth.uomosul.edu.iq

Studying the Spatial and Temporal Changes of the Surface Urban Heat Island Using Geographic Information Systems (GIS) and Remote Sensing (Mosul City as a Model)

Waleed Shabeeb [1*], Sahar Altaee [2], Kossay Al Ahmady [3]

[1,2] Department of Geography, College of Education of Human Sciences, University of Mosul, Mosul, Iraq.

[3] Department of Environmental Engineering, College of Environmental Sciences, University of Mosul, Mosul, Iraq.

Article information

Received: 13- Aug-2024

Revised: 10- Sep-2024

Accepted: 06- Oct-2024

Available online: 01- Jan -2026

Keywords:
Surface Urban Heat Island,
Climate Change,
Gis,
Mosul City,
Urban Areas,

Correspondence:
Name: Waleed Shabeeb

Email: waleed.22ehp124@student.uomosul.edu.iq

ABSTRACT

Surface heat islands are formed due to the increase in surface temperatures of the earth alongside air temperature within urban areas compared to the surrounding suburban and rural areas. This increase is primarily attributed to the concentration of various human activities and prevalent land uses. This study aims to analyze the spatial and temporal variation of surface temperature across different seasons and the reasons for their concentration in specific locations within the study area. In this study, satellite imagery from Landsat-8 was used. The researcher examined all images from the year 2023 for all seasons to select a set of images that align with the nature of the study to determine the surface temperature of the Earth, providing a true representation of the surface heat island in the city of Mosul using Geographic Information Systems (GIS) and remote sensing. Thermal map results showed that surface heat islands. vary from season to season, with the highest values recorded in the fall, ranging between (42-48.6°C). In contrast, the lowest surface temperatures were recorded in the winter, reaching (13.6-17.1°C). The study also indicated that areas with high population density and desert lands are among the regions that fall within the highest temperature ranges compared to others. Furthermore, it was observed that areas adjacent to the Tigris River and forest areas with dense vegetation cover are less hot, indicating a negative relationship where the surface temperature decreases with an increase in vegetation cover.

DOI: 10.33899/injes.v26i1.60214, ©Authors, 2026, College of Science, University of Mosul.
This is an open-access article under the CC BY 4.0 license (http://creativecommons.org/licenses/by/4.0/).

دراسة التغيرات المكانية والزمانية لجزيرة الحرارة الحضرية السطحية باستخدام نظم المعلومات الجغرافية (GIS) والاستشعار عن بُعد (مدينة الموصل أنموذجًا)

وليد شبيب[1*]، سحر الطائي[2]، قصي الاحمدي[3]

[1،2] قسم الجغرافيا، كلية التربية للعلوم الانسانية، جامعة الموصل، الموصل، العراق.

[3] قسم الهندسة البيئية، كلية العلوم البيئية، جامعة الموصل، الموصل، العراق.

معلومات الارشفة

تاريخ الاستلام: 13- اغسطس- 2024

تاريخ المراجعة: 10- سبتمبر- 2024

تاريخ القبول: 06- اكتوبر- 2024

تاريخ النشر الالكتروني: 01- يناير- 2026

الكلمات المفتاحية:

الجزر الحرارية السطحية الحضرية،

تغير المناخ،

نظم المعلومات الجغرافية،

مدينة الموصل،

المناطق الحضرية،

المراسلة:

الاسم: وليد خالد محمد شبيب

Email: waleed.22ehp124@student.uomosul.edu.iq

الملخص

تتشكل الجزر الحرارية السطحية نتيجة لارتفاع درجات حرارة سطح الأرض بالتزامن مع درجات حرارة الهواء داخل المناطق الحضرية، وذلك مقارنةً بالمناطق شبه الحضرية (الضواحي) والريفية المحيطة بها. ويُعزى هذا الارتفاع بشكل أساسي إلى تركز الأنشطة البشرية المختلفة واستعمالات الأرض السائدة. تهدف هذه الدراسة إلى تحليل التباين المكاني والزماني لدرجة حرارة السطح عبر الفصول المختلفة، والكشف عن أسباب تركزها في مواقع محددة داخل منطقة الدراسة. وقد استُخدمت في هذه الدراسة مرئيات فضائية من القمر الصناعي (Landsat-8)، حيث قام الباحث بفحص جميع مرئيات عام 2023 ولكافة الفصول لاختيار مجموعة منها تتوافق مع طبيعة الدراسة؛ بغية تحديد درجة حرارة سطح الأرض بما يوفر تمثيلاً حقيقياً للجزر الحرارية السطحية في مدينة الموصل باستخدام نظم المعلومات الجغرافية (GIS) وتقنيات الاستشعار عن بعد. وقد أظهرت نتائج الخرائط الحرارية أن الجزر الحرارية السطحية تبايناً فصلياً للجزر الحرارية السطحية؛ إذ سُجِّلت أعلى القيم خلال فصل الخريف، حيث تراوحت بين (42-48.6) درجة مئوية. وفي المقابل، سُجِّلت أدنى درجات حرارة للسطح خلال فصل الشتاء، حيث بلغت (13.6-17.1) درجة مئوية. كما أشارت الدراسة إلى أن المناطق ذات الكثافة السكانية المرتفعة والأراضي الصحراوية (الجرداء) تقع ضمن النطاقات الحرارية الأعلى مقارنةً بغيرها. علاوةً على ذلك، لوحظ أن المناطق المحاذية لنهر دجلة ومناطق الغابات ذات الغطاء النباتي الكثيف تكون أقل حرارة، مما يؤشر إلى وجود علاقة ارتباطية عكسية؛ حيث تنخفض درجة حرارة السطح بزيادة كثافة الغطاء النباتي.

DOI: 10.33899/injes.v26i1.60214, ©Authors, 2026, College of Science, University of Mosul.
This is an open-access article under the CC BY 4.0 license (http://creativecommons.org/licenses/by/4.0/).

Introduction

Urban planning significantly impacts daily temperatures, whereas temperatures within cities differ from those in open rural areas due to various factors such as weather conditions, wind speed, sunlight intensity, humidity, and the structural layout of the city, this includes building density, the ratio between building heights and the spaces between them, different construction materials and their colors, street width, and pollution influenced by urban planning and the urban fabric. These factors contribute to increased temperatures. The surface temperature of the earth in the study differs greatly from the temperatures commonly reported in weather forecasts, which refer to the free air surface temperature measured at heights ranging from 1.25 to 2m above the ground (Ismail, 2023), and accordingly the land surface temperature (LST) is an important parameter for studying surface energy balance, climate change, and various physical and chemical processes on Earth (Ullah et al., 2023). (LST), It is a phenomenon in which urban areas experience higher temperatures than surrounding rural areas (Richard and Abah, 2019). The Earth's surface absorbs shortwave solar radiation and

then emits longwave radiation toward the atmosphere, which retains most of it, allowing only a small portion to escape into space. Although atmospheric components absorb only a very small percentage of the shortwave solar radiation passing through it, the atmosphere is capable of retaining a very large percentage of the longwave terrestrial radiation reflected from the Earth's surface. Water vapor and carbon dioxide are primarily responsible for this latter function. Therefore, studying the Earth's thermal changes is one of the most important climatological studies due to its direct impact on various living organisms and urban planning (Ahmad, 2018).

Materials and Methods

Study area

The city of Mosul serves as the administrative center of Nineveh Governorate, located in the northwestern part of Iraq, within the middle basin of the Tigris River (northern Iraq). The Tigris River divides the city into two unequal parts in terms of shape, area, and population (Al-Janabi, 1996). Geographically, the city is bordered by agricultural lands and villages extending to the Tal Kaif district and the Hamidat sub-district to the north and northwest, the Bartella and Bashiqa sub-districts to the east and northeast, the Tal Afar district to the west, and the Hamam al-Alil sub-district to the south (Adnan, 2022). The study area is situated between the latitudes of (36°, 24′,10″ - 36°, 14′, 40″) north and two longitudes (43°, 18′, 10″- 43°,05′,30″) east. The total area of the study area is 4409 km2 (Ismail, 2023), out of the total area of Nineveh Governorate, which is 36767.97 km2. Geospatial location of the city of Mosul (Fig. 1).

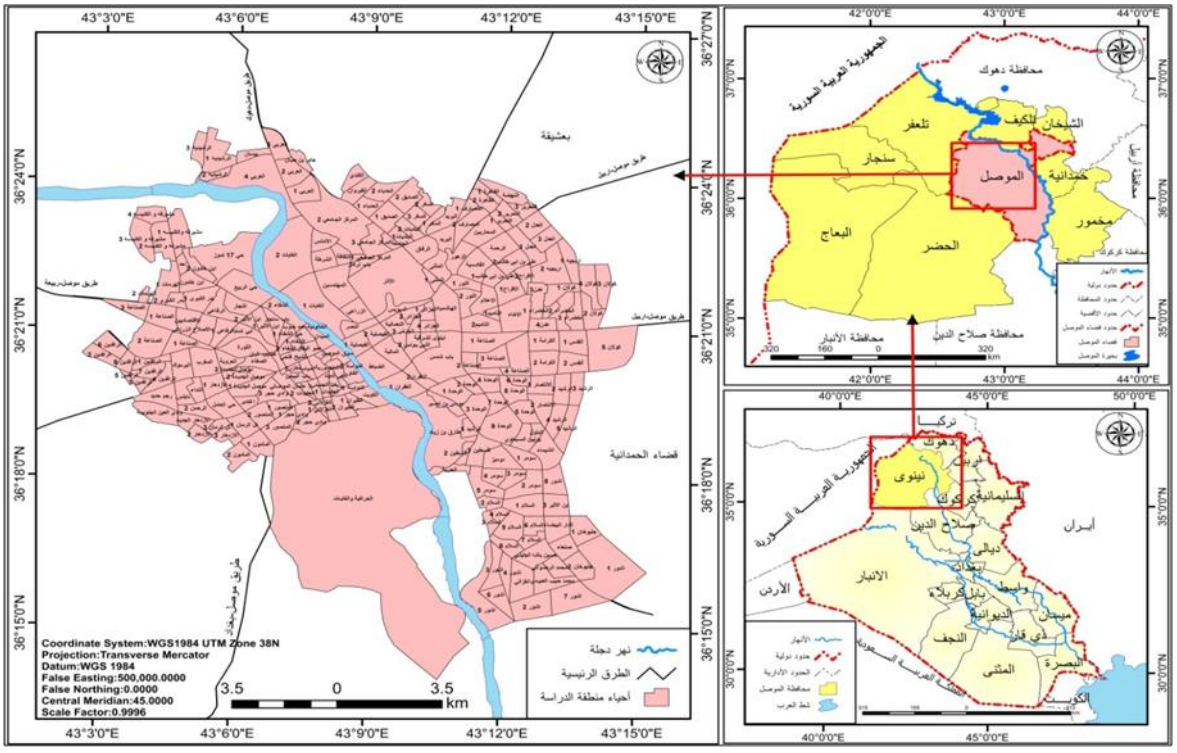


Fig. 1. The geographical and astronomical location of the city of Mosul

Source: Work of the researcher based on Nineveh Governorate, Nineveh Municipalities Directorate, Planning Department, unpublished data, 2022, and ARC MAP program.

2.2 Data sets and methods

The image satellites were downloaded from the US Geological Survey (https://www.usgs.gov/). The researcher examined all the satellite imagery dates according to the specified time period for the study area, which is the year 2023, to select the set of images that best fit the nature of the study. Accordingly, satellite images from Landsat-8 were used

for different seasons of the year to determine the surface temperature, which will provide an accurate depiction of the surface urban heat island in the study area, as illustrated in Table 1 and Fig. 2.

Table 1: Characteristics of the visuals used in the study (Source: https://www.usgs.gov)

Sequence	Satellite name	Date the photo was taken	The chapter that the image represents
1	LANDSAT 8	25/1/2023	winter season
2	LANDSAT 8	30/3/2023	spring season
3	LANDSAT 8	28/7/2023	summer season
4	LANDSAT 8	22/9/2023	Autumn season

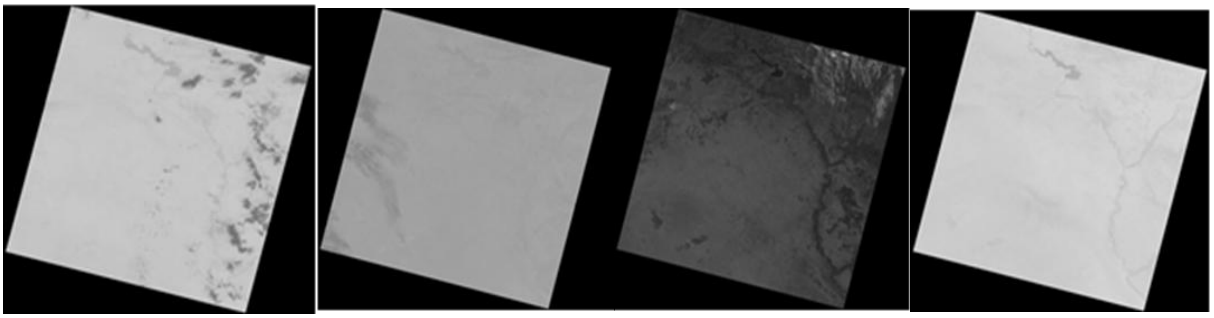


Fig. 2. The image satellite adopted in the study (Source: https://www.usgs.gov)

After acquiring the satellite imagery for the study area, the bands used in the study are identified as follows:

The Band (10) file, which reflects thermal infrared radiation (TIRS1), is included in the Landsat (8) satellite imagery and is used to extract the Earth's surface temperature.

The thermal spectral radiance in LANDSAT-8 is calculated using several equations, as follows:

First step: create a file that reflects the radiation value at the top of the atmosphere (Top of Atmosphere) (TOA), spectral radiance. Through this step, the (raw spectral) value in the band (10) is converted to the radiation value at the top of the atmosphere through the following equation:

$$L\lambda = ML * QCAL + Al \quad \text{..... (1)}$$

Whereas ML = the value of the multiplier scale factor, which is obtained from the metadata file (MTL), QCAL = calorific value of the tenth band, Al = the value of the additional scaling factor, which is obtained from the metadata file (TML), QI = 10th band correction factor, fixed value (0.29).

-The second step: Create a file representing the brightness temperature value: (Brightness temperature) (BT) according to the following equation:

$$T_{(K)} = \frac{K2}{\ln\left(\frac{K1}{L\lambda} + 1\right)} \quad \textbf{-273.15..... (2)}$$

Since ln = logarithm, k1, k2 = fixed values for the thermal transfer obtained from the metadata file (MTL). They are fixed values and vary depending on the satellite, and their value for the Landsat 8 satellite is shown in Table 2.

Table 2: Constants used for Landsat satellite (8)

Sequence	Heat packs	Value	Constants
1	10	799.0284	K1
2	10	1329.2405	K2
3	10	3.3420E-04	ML
4	10	0.10000	AL

From the researcher's work using visual data

TOA = Lλ, the value 273.15 is a constant value for converting from Kelvin temperature to Celsius temperature.

The third step: Create a Normalized Difference vegetation Index (NDVI) file:

To determine the amount of vegetation cover by measuring the difference between the near infrared light reflected by the vegetation cover and the red light absorbed by the vegetation cover, through the equation:

$$NDNI = \frac{NIR(BAND5) - RED(BAND4)}{NIR(BAND5) + RED\ (BAND4)} \quad \text{.....(3)}$$

Fourth step: Create a file calculating the percentage of vegetation cover (PORPORTION OF VEGETATION) (PV) according to the equation:

$$\mathbf{Pv} = \left(\frac{\mathrm{NDVI} - \mathrm{NDVImin}}{\mathrm{NDVImax} - \mathrm{NDVImin}}\right) \text{.....(4)}$$

Step five: Create a file to calculate emissions values from the Earth's surface: Land surface Emissivity (LSE) or (ε) according to the equation:

(ε = 0.004* pv + 0.986).....(5)

Step Six: Create a file that reflects the Earth's surface temperature in the city of Mosul according to previous time periods, through the equation:

$$LST = \frac{BT}{\{1+[(\lambda BT/P)Ln\varepsilon_{\lambda}]\}} \quad \text{.....(6)}$$

Whereas Lst = Land surface temperature, BT = Land surface emissivity value, and where ph = 14388 and h = (Planck's constant), and C = (Boltzmann constant) is one of the physical constants to obtain the relationship between the energy of the atom or molecule in the gaseous state and the temperature. The symbol $\boldsymbol{\sigma}$ represents the speed of light (Muhammad, 2023).

Results and Discussion

Land surface temperature during the winter

It is observed from Fig. 3, cold colors, specifically dark and light green, which indicate lower surface temperatures, have shown a notable increase in area coverage during the winter season compared to previous periods. In the first instance, they covered an area of 53,819 m^2 within the study area, with temperatures ranging between 6.9°C and 9.2°C, encompassing many neighborhoods, including Mushayrifa, Al-Kaneesa 1, Al-Najjar, Al-Rifa'i, Al-Muthanna, Nabi Yunus 2, Al-Shurta, Al-Andalus, and Al-Arabi 2. Meanwhile, the light green color covered the largest area, reaching 59,030 m^2, with temperatures ranging between 9.3°C and 10.4°C. This mostly covered the neighborhoods on the left side of the city compared to the right side. The observed increase is attributed to natural factors related to weather and climate elements previously mentioned, as well as a noticeable expansion of vegetative cover recently, driven by the increased attention from government and civil bodies. In contrast, warm colors (dark red, orange, and yellow) covered substantial areas. Dark red occupied 13,924 m^2, with temperatures ranging from 13.6°C to 17.1°C, mostly covering the southern, southeastern, and southwestern parts of the study area. Orange covered an area of 33,905 m^2, with temperatures varying between 11.9°C and 13.5°C, including southeastern and southwest-southern parts of the city and several neighborhoods. Yellow occupied 33,905 m^2, with temperatures ranging from 10.5°C to 11.8°C, covering various neighborhoods on both sides of the city, such as Wadi Hajar, Al-Ta'mim Industry 3, Industry 1, Salam 8, and Tal Al-Rumman 2. Regarding the Tigris River, cold colors (dark and light green) dominated the largest areas. Dark green covered 4,227 m^2, with temperatures ranging from 8.4°C to 9.7°C, mostly in the northern and central parts of the river. Light green covered 3,566 m^2, with temperatures between 9.8°C and 10.6°C, distributed along the river's course, particularly in

its lower sections. On the other hand, warm colors (dark red, orange, yellow) occupied limited areas, with yellow covering 2,095 m^2, with temperatures ranging from 10.7°C to 11.9°C, mostly in the southern sections and some small patches in the northern parts of the river. Orange ranked second, occupying 0.956 m^2, with temperatures between 12°C and 13.6°C, mostly in the lower sections of the river, while dark red occupied 0.450 m^2, with temperatures ranging from 13.7°C to 16.1°C, confined to the southern sections of the river's course. Table 3 illustrates the colors included in the classification of Earth's surface temperature, along with the area represented by each color and the corresponding temperature, as well as the number of regions covered by each classification.

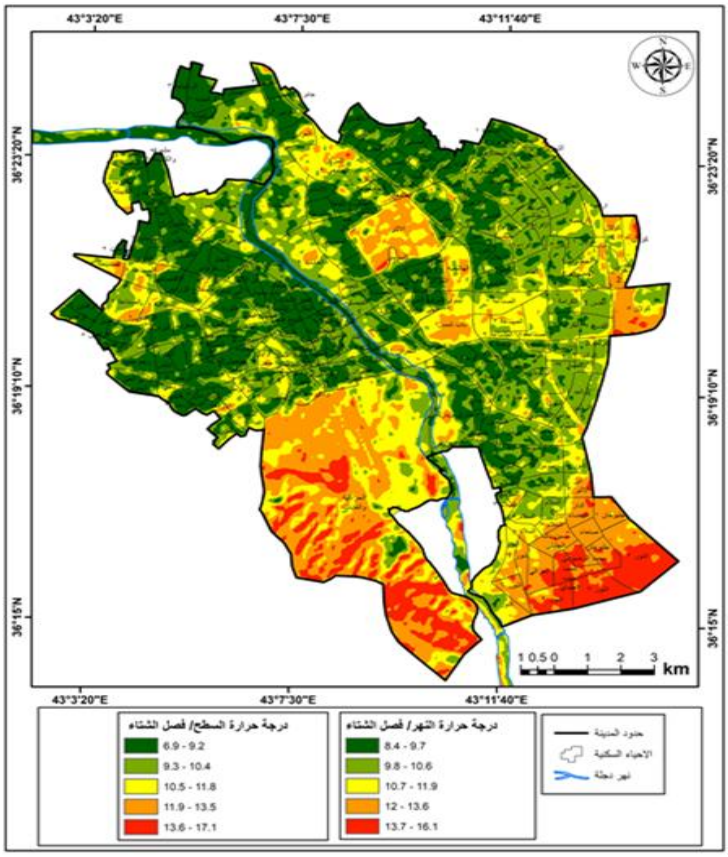


Fig. 3. Surface temperature during the winter Land

Source: Based on Landsat-8 satellite imagery (2023) of the city of Mosul

Table 3: Illustrates the colors, areas, temperatures, and number of regions included in the classification of Earth's surface temperature during the winter

sequence	Color	area	temperature	Covered areas
1	Dark green	53,819m^2	(6.9°C to 9.2°C)	(Meshirfa and Al-Kanisa 1, Al-Najjar, Al-Rifai, Al-Muthanna, Nabi Yunus 2, Al-Shurta, Al-Andalus, Al-Arabi 2),
2	Light green	59 ,030m^2	(9.3°C to 10.4°C)	(Jerusalem 1, Al-Karamah, Al-Afrah 2, Al-Sinaa 2, Arbajiyeh, Al-Salam 6)
3	Dark red	13,924m^2	(13.6°C to 17.1°C)	(mostly covering the southern, southeastern, and southwestern parts of the study area)
4	color orange	33,905m^2	(11.9° to 13.5°C)	(Ashur 4, Jalikhan 1, Bab Shams, Antiquities, Al-Arabi 2, Ibn Al-Athir 3)
5	Yellow color	33.905 m^2	(10.5°C to 11.8°C)	(Wadi Hajar, Al-Ta'mim Industry 3, Industry 1, Salam 8, and Tal Al-Rumman 2)

Source: Based on Landsat-8 satellite imagery (2023) of the city of Mosul

Land surface temperature during the spring

In spring, as observed in Fig. 4, the proportions of cool color areas (dark green and light green) have decreased after being high during the winter season. The first color occupied an area of 3.047 m^2 with temperatures ranging from 10.5 to 16.3°C, covering parts of the green spaces adjacent to the Tigris River and portions in the southeastern parts of the study area.

Meanwhile, the second color (light green) covered an area of 16.018 m², with temperatures ranging between 16.4 and 18.2°C, including the southeastern, southern, and southwestern parts of the city, along with limited areas as shown on the thermal map. In contrast, the spatial coverage of warm colors (dark red, orange, yellow) increased, with the first color occupying an area of 40.476m² and temperatures varying between 20.2 and 25°C, mainly in the southern, southwestern, and eastern parts, while the remaining areas covered various city neighborhoods, such as Sin'a 2, Al-'Urubah, Nabi Shayt, Sin'a al-Ta'mim 3, Al-Jami'ah, and Al-Faisaliyah. The second color (orange) occupied a larger area, 88,703 m², with temperatures ranging from 19.3 to 20.1°C, covering a substantial number of neighborhoods, including Al-Islah al-Zira'i, Al-Rifai 1, Al-Rafidayn, Al-Wahda 1, Al-Quds, Al-Tahrir, Al-Adl, and Al-Masaref 2. The third color (yellow) occupied an area of 53.981 m², with temperatures varying between 18.3 and 19.2°C, covering the southern, southeastern, northern, and northwestern parts of the study area, in addition to scattered spots across neighborhoods such as Al-Hashimiyah, Al-Zuhur, Al-Muhandisin, Al-Tayran, Rajm Hadid, and Al-Harmat 1. Along the river, the cool colors (dark green and light green) covered extensive areas, with the first color covering 2,819 m² and temperatures ranging from 13.1 to 14.8°C, distributed along the watercourse, particularly in its northern and central parts. The second color (light green) occupied 2,085 m² with temperatures ranging between 14.9 and 16°C, primarily covering the southern, central, and northern parts of the upper river course, along with some limited areas in the river's northern sections. In contrast, the warm colors (dark red, orange, yellow) covered significant areas. The first color registered 662 m², with temperatures ranging from 18.9 to 21.3°C, mainly covering the lower parts of the river. The second color (orange) occupied an area of 2.644 m², with temperatures varying from 17.4 to 18.8°C, including the northern and southern sections of the river. Lastly, the third color (yellow) covered a wide portion of the area, amounting to (3.085 m²) with temperatures ranging from 16.1 to 17.3°C, covering the three main parts of the river (upper, middle, and lower) within the administrative boundaries of the study area, Table (4) illustrates the colors included in the classification of Earth's surface temperature, along with the area represented by each color and the corresponding temperature, as well as the number of regions covered by each classification.

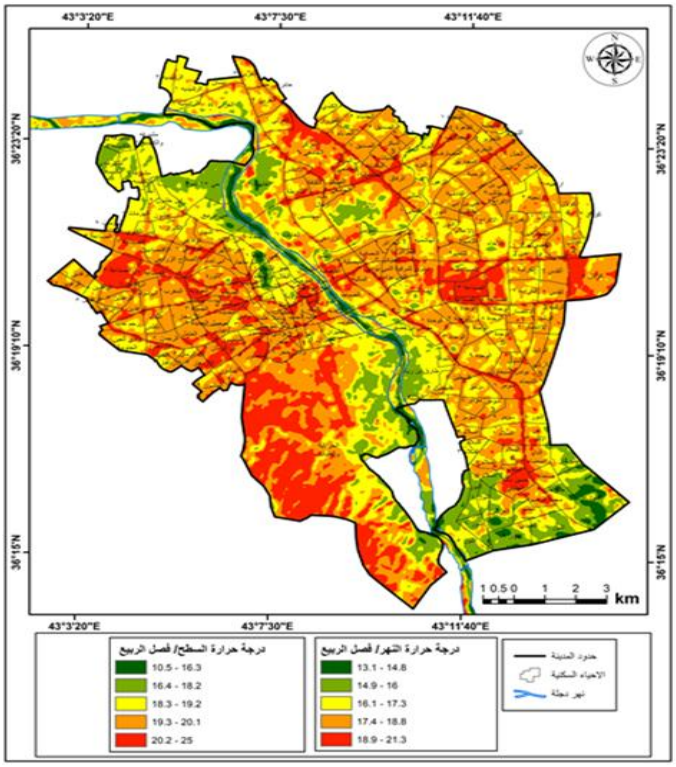


Fig. 4. Land surface temperature during the spring
Source: Based on Landsat-8 satellite imagery (2023) of the city of Mosul

Table 4: Illustrates the colors, areas, temperatures, and number of regions included in the classification of Earth's surface temperature during the spring

Sequence	Color	Area	Temperature	Covered areas
1	Dark green	3.047 m^2	10.5-16.3°C	covering parts of the green spaces adjacent to the Tigris River and portions in the southeastern parts of the study area
2	Light green	16.018m^2	16.4-18.2°C	including the southeastern, southern, and southwestern parts of the city
3	Dark red	40.476m^2	20.2-25°C	Sin'a, Al-'Urubah, Nabi Shayt, Sin'a al-Ta'mim, Al-Jami'ah, and Al-Faisaliyah
4	color orange	88.703m^2	19.3-20.1°C	Al-Islah al-Zira'i, Al-Rifai, Al-Rafidayn, Al-Wahda, Al-Quds, Al-Tahrir, Al-Adl, and Al-Masaref
5	Yellow color	53.981m^2	18.3-19.2°C	Al-Hashimiyah, Al-Zuhur, Al-Muhandisin, Al-Tayran, Rajm Hadid, and Al-Harmat

Source: Based on Landsat-8 satellite imagery (2023) of the city of Mosul

Land surface temperature during the summer season

In the summer, as observed in Fig. 5, the observed area occupied by warm colors (dark red, orange, yellow) is increasing. The first of these, dark red, covers an area of 49.222 m^2, with temperatures varying between 36.4°C and 42°C. This color is concentrated in the southern, southwestern, and southeastern parts of the city and includes several neighborhoods such as Sanaye2, Al-Athar, Bab Shams, and Al-Arabi1. The second color, orange, occupies an area of 55.476 m^2, with temperatures ranging from 31.4° to 36.3°C, covering a wide range of neighborhoods across both sides of the city, such as New Mosul3, Qadib Al-Ban, Al-Sanaye, Arabiya2, University Center3, Kulan5, and Nabi Yunus1. This area is characterized by a diverse, highly active environment, encompassing both industrial and commercial activities with constant vehicular movement throughout the day, contributing to higher temperatures and the phenomenon under study. It is worth noting that these neighborhoods will also be examined in the following section, which addresses air pollutant measurements for the specified elements. These areas recorded the highest levels in previous classifications and now exhibit the highest temperatures. The third color, yellow, has temperatures ranging between 27.6° and 31.3°C and spans an area of 88.713 m^2, covering much of the study area. Most of this area is concentrated on the left side of the city. As for the cool colors (light and dark green), their area has increased compared to the previous section. Light green occupies an area of 5.946 m^2, with temperatures ranging from 24° to 27.5°C, predominantly in the lands adjacent to the lower parts of the river, along with some patches noticeable on the thermal map, representing green spaces within the study area. Dark green, on the other hand, covers an area of 2.895 m^2, with temperatures ranging between 20.1° and 23.9°C, restricted to small patches in the study area. From another perspective, the cool colors (light and dark green) registered the highest values along the river, with the former covering an area of 3.3399 m^2 and temperatures between 20.1° and 26.9°C, mainly concentrated in the northern and central parts of the river.

The latter (light green) spans an area of 2.3589 m^2, with temperatures between 27° and 32.4°C. Its distribution pattern is similar to that of dark green, extending along most of the river course. On the other hand, the warm colors (dark red, orange, yellow) cover substantial areas, with dark red occupying 1.2051 m^2 and temperatures ranging between 39° and 44°C, primarily concentrated in the southern parts of the river, as well as small patches observed in the northern sections of the river course. Orange covers an area of 1.7199 m^2, with temperatures between 36° and 38.9°C, distributed between the upper and lower sections of the river course. Finally, yellow occupies an area of 2.7108 m^2, with temperatures ranging from 32.5° to 35.9°C, extending across vast parts of the river course, particularly in the upper sections. Table 5 illustrates the colors included in the classification of Earth's surface temperature, along with the area represented by each color and the corresponding temperature, as well as the number of regions covered by each classification.

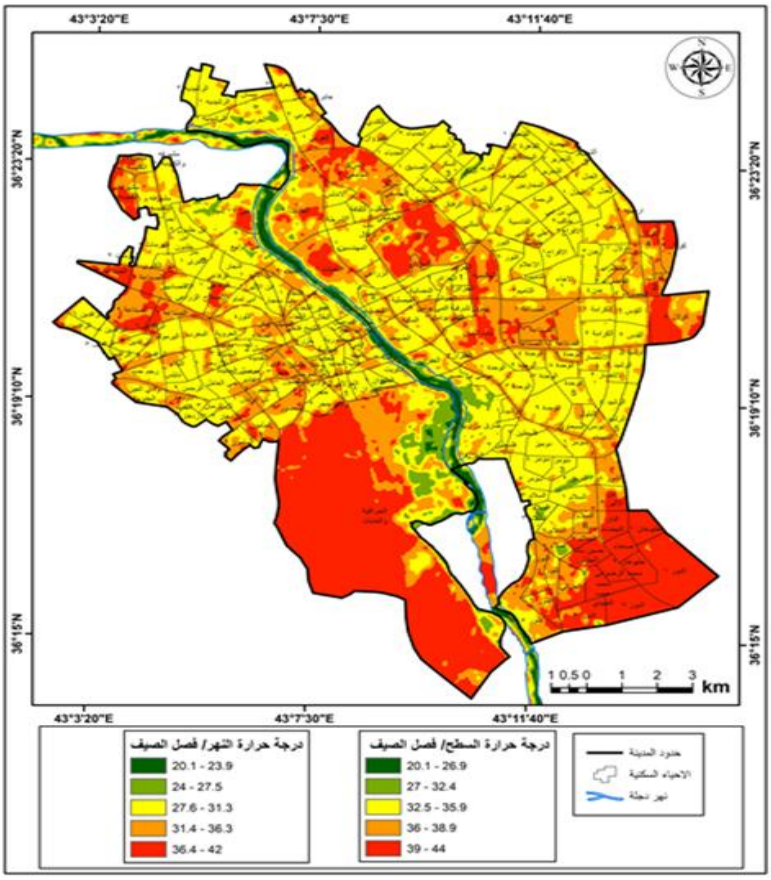


Fig. 5. Land surface temperature during the summer season

Source: Based on Landsat-8 satellite imagery (2023) of the city of Mosul

Table 5: illustrates the colors, areas, temperatures, and number of regions included in the classification of Earth's surface temperature during the summer

sequence	Color	area	temperature	covered areas
1	Dark green	(2.895) m^2	20.1° to 23.9°C	(restricted to small patches in the study area)
2	Light green	(5.946) m^2	24° to 27.5°C	(Limited predominantly in the lands adjacent to the lower parts of the river, along with some patches noticeable on the thermal map, representing green spaces within the study area. Dark green)
3	Dark red	(49.222) m^2	36.4° to 42°C	(Sanaye2, Al-Athar, Bab Shams, Al-Arabi1)
4	color orange	(55.476) m^2	31.4° to 36.3°C	(New Mosul3, Qadib Al-Ban, Al-Sanaye, Arabiya2, University Center3, Kulan5, Nabi Yunus1)
5	Yellow color	(88.713) m^2	27.6° to 31.3°C	(Al-Qadisiyah, Al-Zuhur, Al-Intisar, Al-Wahda 1, Al-Rifai, Al-Najjar, Nablus, Mosul Jadida 1)

Source: Based on Landsat-8 satellite imagery (2023) of the city of Mosul

Land surface temperature during the autumn

In the autumn season, as shown in Fig. 6, through satellite imagery analysis, the most severe heat zones were observed in the southern, southwestern, and eastern parts of the study area, where dark red areas cover a surface area of 39,929 m² with temperatures ranging between 42 °C and 48.6°C. These high-heat zones extend across several neighborhoods on both sides of the city, represented by red spots on the thermal map. The color orange ranks second in terms of high surface temperature coverage, occupying an area of 37,808 m² with temperatures between 38.9°C and 41.9°C, and it spans relatively large sections within city neighborhoods. Following this, yellow areas cover (53,880) m² with temperatures ranging between 36.4° and 38.8°C, as shown on the map, and extend over a significant portion of the study area, including neighborhoods such as Al-Shifa 2, Al-Safa, Al-Faisaliah, Al-Sina'a 4, and the University Center 2. On the other hand, the cooler colors, dark green and light green, occupy relatively large areas. The dark green covers 3,318 m² with temperatures between 22° and 30.9°C, mainly along parts of the riverbank. Light green spans 67,311 m² with

temperatures between 31° and 36.3°C, predominantly on the city's left side compared to the right. Along the Tigris River, the hot colors (dark red, orange, yellow) cover considerable areas. Dark red accounts for 0.972234 m² with temperatures between 38.8° and 44.9°C, limited to the lower river sections. The orange covers 1,964 m² with temperatures between (33.4° and 38.7°C), distributed across the upper and lower parts of the river. Yellow occupies (2,768) m² with temperatures between 29.7 °C and 33.3°C, representing the northern and southern sections of the river. The cooler colors, light green and dark green, cover larger river areas, with light green occupying 2,191 m² and temperatures between 26.1° and 29.6°C, while dark green extends over 3,411 m² with temperatures from 22° to 26°C, distributed across the middle, upper, and lower river sections, Table 6 illustrates the colors included in the classification of Earth's surface temperature, along with the area represented by each color and the corresponding temperature, as well as the number of regions covered by each classification.

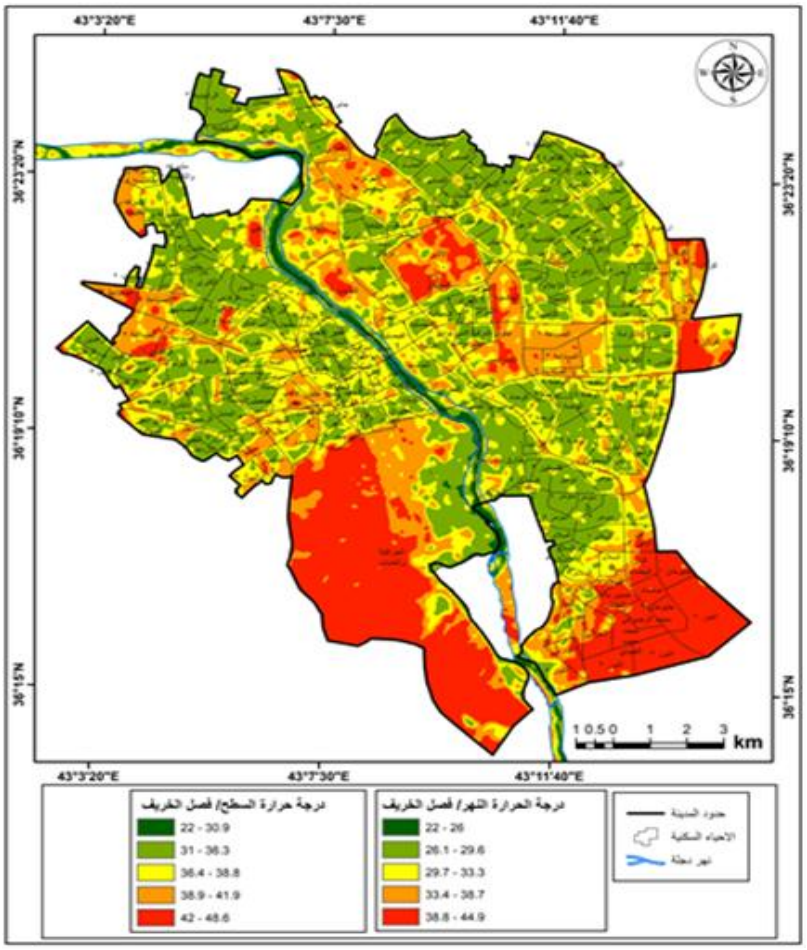


Fig. 6. Land surface temperature during the Autumn

Source: Based on Landsat-8 satellite imagery (2023) of the city of Mosul

Table 6: Illustrates the colors, areas, temperatures, and number of regions included in the classification of Earth's surface temperature during the Autumn

sequence	Color	area	temperature	covered areas
1	Dark green	3.318 m^2	22° to 30.9°C	(Limited parts of the lands adjacent to the river)
2	Light green	67.311 m^2	31° to 36.3°C	(Al-Najjar, Al-Rafai, New Mosul, Al-Muthanna, Al-Zahour, Al-Hadba 1, Unit 7)
3	Dark red	39.929 m^2	42° to 48.6°C	(Al-Rafidain 1, Al-Rifai, Al-Sinaa 3, Bab Shams, Al-Athar, Kulan 3, Al-Ghabat 1, Al-Arabi 1)
4	color orange	37.808 m^2	38.9° to 41.9°C	(Industry 3, Industry 2, Tel Al-Rumman 1, Mushairfa and the Church, Al-Shimaa, Al-Ezdehar)
5	Yellow color	53.88 m^2	36.4° to 38.8°C	(Ibn Al-Atheer, Al-Faisaliah 1, Ashur 8, Al-Salam District 8, Al-Salam District 6, New Mosul 2)

Source: Based on Landsat-8 satellite imagery (2023) of the city of Mosul

Conclusions

The surface temperature of the Earth is distributed heterogeneously in the city of Mosul due to the topography of the area, so the surface temperatures of the earth rise in the southern, southeastern and western parts of the city of Mosul in particular, these areas are areas almost completely devoid of vegetation and facing the sun as well as the main roads passing through them, while the surface temperature of the Earth decreases in areas adjacent to the Tigris River as a result of being affected by the influences coming from it, and the relationship between the surface temperature of the Earth and the vegetation index Normalized Difference Vegetation Index (NDVI) is an inverse relationship, as areas with dense vegetation cover can reduce the thermal difference. The thermal difference of surface temperatures between desert and barren areas and vegetation cover areas ranges between 10-18 °C in the city of Mosul during the summer. Moreover, due to the diversity of land cover in the study area, the single pattern of heat islands does not appear consistently across large areas, but rather intermittently with other patterns of heat islands, resulting from varying environmental activities, as well as population and urban variations.

References

Muhammad, I.A.I., 2023. Spatial Variation of Land Surface Temperature and the Impact of Some Variables in Cairo City 2022, The Egyptian Geographical Journal, NUM (181), pp. 12-22. https://Doi.org/10.23953/cloud.ijarsg.48

Ullah, W., Ahmad, K., Ullah, S., Tahir, A.A., Javed, M.F., Nazir, A. and Mohamed, A., 2023. Analysis of the relationship among land surface temperature (LST), Land use and Land cover (LULC), and Normalized Difference Vegetation Index (NDVI) with topographic elements in the lower Himalayan region, Helion, 9 NUM (2), pp. 13-25. https://Doi.org/10.1016/j.heliyon.2023.e13322

Richard, J.U. and Abah, I.A., 2019. Derivation of land surface temperature (LST) from Landsat 7 & 8 imageries and its relationship with two vegetation indices (NDVI and GNDVI), Int J Res Granthaalayah,7 NUM (2), 109 P. https://Doi.org/10.29121/granthaalayah.v7.i2.2019.1013

Ahmad, M.M., 2018. A Study of Thermal Changes in the West Bank, Palestine, Using Geographic Information Systems and Remote Sensing: 1985-2017. Master's Thesis.An-Najah National University, Graduate Studies, pp. 31-43. https://www.researchgate.net/publication/315662833_An_Evaluation_of_Satellite_Remote_Sensing_for_Crop_Area_Estimation_in_the_West_Bank_Palestine

Al-Janabi, S., 1996. Locational Geographical Characteristics of the City of Mosul, Journal of the Iraqi Geographical Society, Baghdad, No. 32, pp. 96-112.

Adnan, Y.A., 2022. Using geomatics techniques to conduct a comparative study of the amount of environmental pollution for the cities of Mosul and Hamdaniya as a model, Higher Diploma Thesis, College of Education for Human Sciences, University of Mosul, pp. 7-23.

Ismail, I.A., 2023. Variation of land surface temperature and the impact of some variables in Cairo City, Arab Geog J, NUM (181), pp. 5-6.

Iraqi National Journal of Earth Science

www.earth.uomosul.edu.iq

Evaluation of Hydrochemistry of Kirkuk Irrigation Project, Kirkuk, Northern Iraq

Hiba Hasan Sultan [1*], Soran Nihad Sadiq [2]

[1,2]*Department of Applied Geology, College of Science, University of Kirkuk, Kirkuk, Iraq.*

Article information

Received: 22- Nov-2024

Revised: 29- Dec-2024

Accepted: 04- Feb -2025

Available online: 01- Jan -2026

Keywords:
Irrigation Project,
Hydrochemical,
Heavy Elements,
CWQI,
Kirkuk,

Correspondence:
Name: Hiba Hasan Sultan

Email: hibahasansultan@gmail.com

ABSTRACT

The irrigation project is considered one of the important projects in Iraq, as the study area is one of the important agricultural areas, which mostly depends on groundwater wells as well as surface water from the Kirkuk Irrigation Project. This study aims to estimate the irrigation project for drinking, agriculture, and irrigation purposes. (46) Water samples were collected in humid and dry seasons in (2023-2024) and analyzed; several methods and classifications were used, including comparison with Canadian standards, Piper hydrochemical facies classification, and classifications for irrigation purposes. The major and minor elements and heavy metals were analyzed. The physical properties were measured, including pH, electrical conductivity, total dissolved solids, turbidity, and total hardness. It indicates that the Piper scheme of the hydrochemical facies is calcium-magnesium-bicarbonate. The results show, according to the Canadian water quality index, that the water is poor and unsuitable for human use, and does not have an excellent water condition due to turbidity and calcium concentration, pH, and magnesium values exceeding the permissible limit according to WHO and IQS, so it is considered unsafe for drinking. The results show, according to the classifications of SAR, MH, %Na, SP, salinity hazard, and Wilcox, that the study area is generally suitable and good for irrigation and agricultural uses for most soils and agricultural crops. Analyzed Pearson's correlations in some of the studied parameters in both seasons reveals that the correlation coefficient is strong and significant positive and negative.

DOI: 10.33899/injes.v26i1.56019, ©Authors, 2026, College of Science, University of Mosul.
This is an open-access article under the CC BY 4.0 license (http://creativecommons.org/licenses/by/4.0/) .

التقييم الهيدروكيميائي لمشروع ري كركوك، شمالي العراق

هبه حسن سلطان [1*] ، سوران نهاد صادق [2]

[2,1]قسم علوم الارض التطبيقية، كلية العلوم، جامعة كركوك، كركوك، العراق.

معلومات الارشفة

تاريخ الاستلام: 22- نوفمبر- 2024

تاريخ المراجعة: 29- ديسمبر- 2024

تاريخ القبول: 04- فبراير - 2025

تاريخ النشر الالكتروني: 01- يناير- 2026

الكلمات المفتاحية:
مشروع الري،
هايدروكيميائية،
العناصر الثقيلة،
المؤشر الكندي،
كركوك،

المراسلة:

الاسم: هبه حسن سلطان

Email: hibahasansultan@gmail.com

الملخص

يعد مشروع الري من المشاريع المهمة في العراق حيث تعد منطقة الدراسة من المناطق الزراعية المهمة والتي تعتمد في الغالب على المياه المأخوذة من الآبار الجوفية وكذلك المياه السطحية من مشروع ري كركوك. هدفت هذه الدراسة إلى تقييم المشروع لأغراض الشرب والزراعة والري. تم جمع (46) عينة مياه في الموسمين الرطب والجاف في (2023-2024) وتم تحليلها, وتم استخدام عدة طرق وتصانيف منها المقارنة مع المعايير الكندية وتصنيف بايبر للسحنات الهيدروكيميائية وعدة تصانيف لأغراض الري. تم تحليل العناصر الرئيسية والثانوية والثقيلة وتم قياس الخصائص الفيزيائية ومنها الرقم الهيدروجيني والتوصيلية الكهربائية والمواد الصلبة الذائبة الكلية والعكورة والصلابة الكلية. ويشير مخطط بايبر إلى أن السحنات الهيدروكيميائية كانت كالسيوم-مغنيسيوم-بيكربونات. وأظهرت النتائج أن مؤشر جودة المياه كان من الفئة الرديئة وغير صالحة للاستخدام البشري ولم يكن المياه في حالة ممتازة بسبب العكورة وتركيز الكالسيوم وقيم الأس الهيدروجيني والمغنيسيوم التي تجاوزت الحد المسموح بها حسب (WHO و IQS) والتي تعتبر غير آمنة للاستخدامات البشرية. وأظهرت النتائج حسب التصانيف SAR و MH و Na% و SP و Salinity Hazard و Wilcox أن منطقة الدراسة مناسبة بشكل عام وجيدة للري و للاستخدامات الزراعية لاغلب الترب والمحاصيل الزراعية. وتم تحليل ارتباط بيرسون في بعض المتغيرات المدروسة في كلا الموسمين وأظهر ارتباطاً إيجابياً وسلبياً قوياً وذو دلالة إحصائية.

DOI: 10.33899/injes.v26i1.56019, ©Authors, 2026, College of Science, University of Mosul.
This is an open-access article under the CC BY 4.0 license (http://creativecommons.org/licenses/by/4.0/)

Introduction

Water quality depends largely on the intended uses of water for assessing water quality and the methods for comparing and analyzing results (Babiker et al., 2007). Therefore, understanding the basics of water is mainly to assess its suitability for different uses. Furthermore, it is possible to conclude the change in quality due to (water-rock) interaction (weathering) or another kind of human effect (Todd, 1980). Water pollution affects water quality, thereby threatening human health, economic development, and social welfare (Singh, 2014; Chandra et al., 2014). A hydrogeochemical study of surface water within the Kirkuk irrigation project is conducted to evaluate the main ion chemistry and water quality index for drinking and irrigation uses. For this purpose, samples from the project water were collected and analyzed for pH, electrical conductivity (EC), total dissolved solids (TDS), turbidity, total hardness (T.H.), main cations (Ca^{2+}, Mg^{2+}, Na^{+}, and K^{+}) and main anions (HCO_3^{-}, Cl^{-}, NO_3^{-}, and SO_4) (Milovanovic, 2007). A major contribution to the development of the Water Quality Index, a model proposed by the Canadian Council of Ministers for the Environment (CCME) (Khan et al., 2003). In the current study, the quality index is relied upon, which is one of the most effective methods for assessing the environmental status of water resources (Kong et al., 2017; Ebrahimi et al., 2015). In this paper, binary correlation coefficients are used to determine the geochemical association between heavy elements and ions in different ranges for the purpose of determining the geochemical association between heavy elements, major ions (positive and negative), total dissolved solids, and pH values (Odat, 2015). This water is used

in agriculture, industry, or for irrigation purposes, and measures the Kellies ratio (KR), sodium percentage (SP), and sodium adsorption ratio (SAR). The study aims to evaluate the hydrogeochemical water of the Kirkuk Irrigation Project by stating the geochemical relationships that link these elements, classifying Kirkuk Irrigation Project water according to the international standard specifications, and evaluating the suitability of the project water for drinking, agricultural, and irrigation purposes in the region.

A previous study by Al-Kilabi (2013) examined groundwater and the effect of a suitable period for irrigation on its assessment of the quality in the Al-Hawija area, Kirkuk, Iraq. It was found that the surface groundwater in the study area is not suitable for drinking, especially during the period of abstinence, but is suitable for animals to drink. Most of the pure water samples are not suitable for irrigation under normal conditions, while most of the surface water samples are suitable for irrigation. Al-Hamdani (2009) studied the relationship between groundwater and irrigation and drainage projects in the Daquq Basin, south of Kirkuk, and the sources of pollutants, their quantities, and their changes in the high-water season. He found that the water of the Daquq Basin is suitable for drinking, industry, construction, livestock and irrigation.

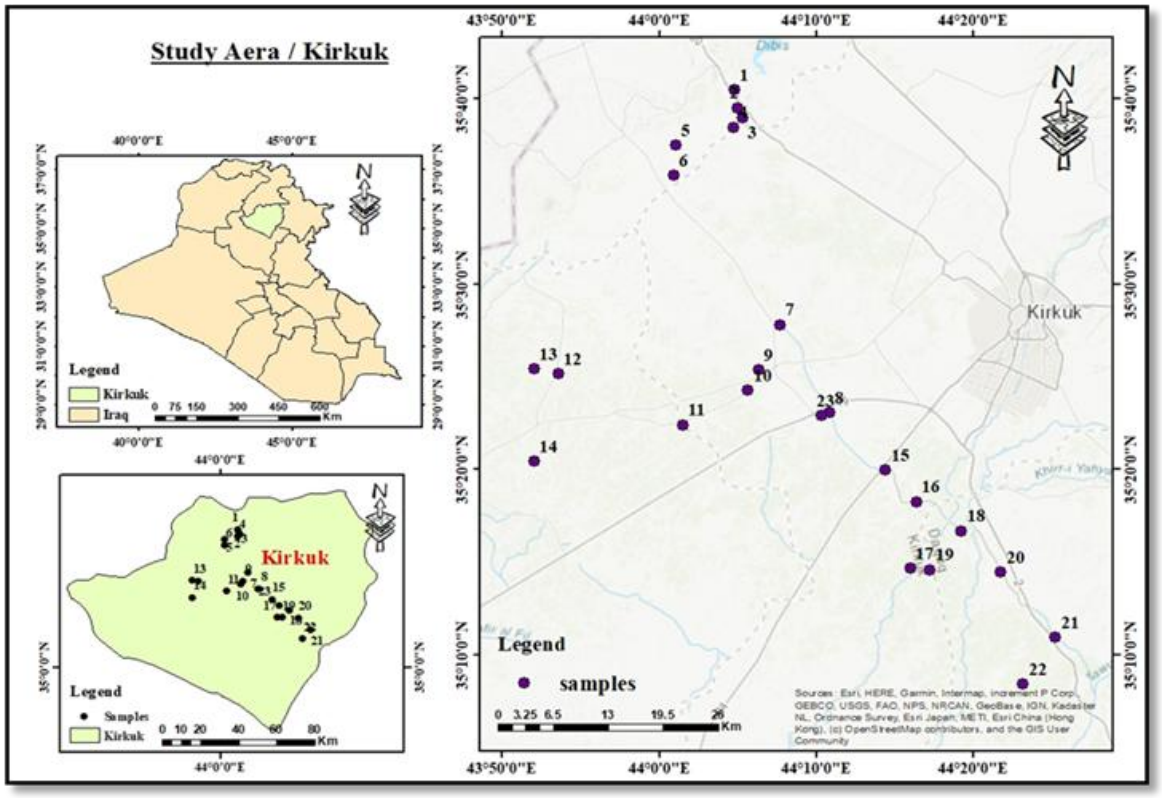


Fig. 1. Map of the Study area.

Location of the study area

The area of study is located in Kirkuk Governorate, northeastern Iraq, between latitudes (35°14’00”21-35°67’79”1) N and longitudes (43°86’41”20-44°42’09”59) E, which lies in zone (38N) in UTM (Fig. 1). The Lesser Zab River passes through northwest, in addition to some seasonal rivers such as the Khassa River, which goes along the middle of Kirkuk. The area of interest is represented by the Kirkuk Irrigation Project, which extends from northwest of Kirkuk Governorate from the Dibis Dam to the south of Kirkuk Daquq City (Fig. 2). The project is considered a part of the irrigation system in the region passing through the area of Dibis and Mulla Abdullah**,** and also passing through the area of Maktab Khalid and then to Taza and Daquq Town. It aims to improve agriculture and save water.

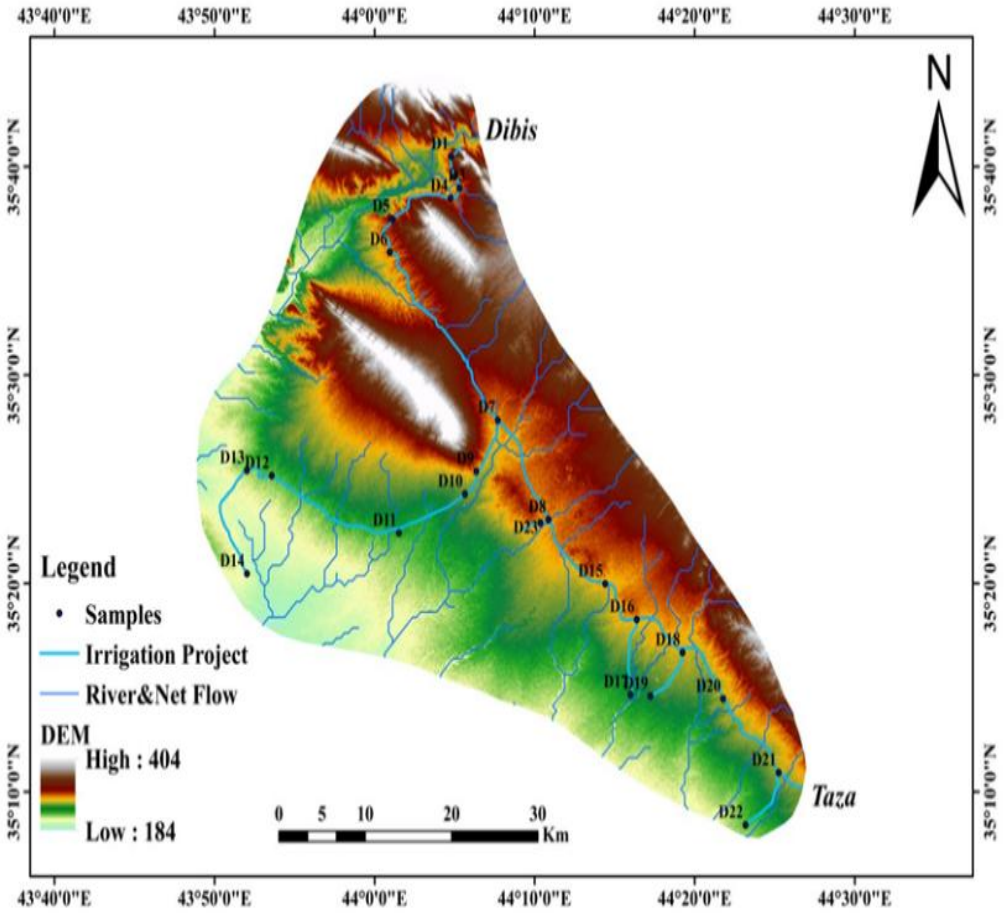


Fig. 2. Map of the DEM of the study area.

Geological and hydrogeological setting

Generally, the study area is mostly covered by Tertiary-age rock formations represented by exposed rocks of the Fatha, Injana, Muqdadiyah, and Bai Hassan formations, which are covered by Quaternary and Recent sediments. The stratigraphy is composed mainly of chemical sedimentary and clastic rocks dating back to the Cenozoic era, and these sedimentary rocks are represented by sandstone, siltstone, claystone, limestone, gypsum, and salt (Buday, 1980) of (Pliocene-Pleistocene- Middle Miocene) (Jassim and Goff, 2006). The surface of Kirkuk Governorate is characterized by a variety of terrain features, including hills, plateaus, and plains. Elevation varied between 212 m and 266 m (Stevanovic and Markovic, 2004). The study region is located within the unstable shelf in the low folded or foothill subzone (Makhul subzone) (Al-Kadhimi et al., 1996) (Fig. 3).

The hydrogeological water source for the project is the Lesser Zab River. Two dams were built on the Lesser Zab River, namely Dukan Dam and Dibis Dam. Dibs Dam is located 40 km north-west of Kirkuk, used to feed the Kirkuk Irrigation Canal. All the valleys in the region flow towards the Lesser Zab, while in the Taza and Daquq regions, they flow into the seasonal Khassa and Daquq rivers and from there into the Tigris River.

The described climate of the study area is a Mediterranean climate (Soran, 2008), as it is hot and dry in summer and cold and humid in winter. By monitoring the climate information of Kirkuk Governorate for the period between (1992-2022), it is characterized by the amount of precipitation falling at a rate in January (64.3mm) annually, and at a temperature in July (43.9 Cº) and a minimum in January (5.2 Cº), and at an annual rate of evaporation in July (427.3 mm) (Meteorological Authority - Kirkuk Station data) (Table 1).

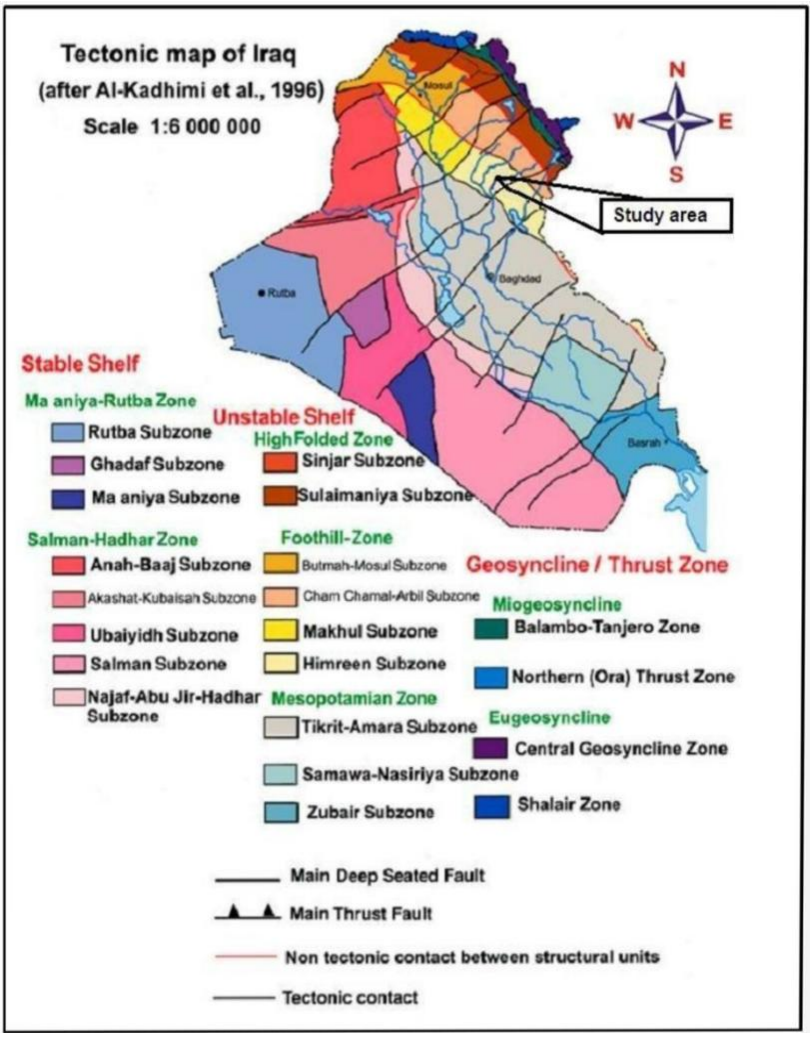


Fig. 3. Tectonic Map of Iraq (after Al-Kadhimi et al., 1996).

Table 1: Monthly and annual mean of climate elements from (1992-2022), Directorate of Meteorological - Kirkuk Station.

Months	Temperature (C°)	Rainfall (mm)	Evaporation (mm)
October	33.8	13.3	219.9
November	23	44.5	106
December	16.8	51.5	64.9
January	14.5	64.3	65.1
February	16.7	51.3	78.13
March	21	47.6	124.2
April	27.3	35.7	182.8
May	34.6	13.4	278.1
June	40.8	0.1	374.7
July	43.9	0.3	427.3
August	43.7	0	410.9
September	38.7	0.7	315.3
Mean	29.4	26.6	220.6

Materials and Methods

Sampling

The fieldwork included collecting water samples at the humid season from the Kirkuk Irrigation Project in December (2023) and the dry season in May (2024). Samples were collected from different places along the Kirkuk Irrigation Project for the purpose of conducting chemical and physical analyses to determine their suitability for their purpose, while the element concentrations were analyzed in the laboratory in Kirkuk, Iraq, and the heavy element and trace elements were analyzed by ICP-MS in the University Lab of Ankara, Turkey. The

accuracy results indicate that there is a great convergence between the measured results and those of the analytical accuracy (Table 2).

Table 2: Analytical accuracy as a comparison between certified and measured concentration.

Elements (ppb)	Certified Concentration µg/l	Measurement Concentration µg/l
Al (ppb)	52	**50.3**
As (ppb)	26.67	**25.91**
B (ppb)	301.1	**300.6**
Cu (ppb)	85.2	**87.3**
Co (ppb)	20.28	**21.2**
Cr (ppb)	38.6	**37.7**
Fe (ppb)	34.3	**31.2**
Mn (ppb)	121.5	**119.6**
Ni (ppb)	27.4	**28.1**
Pb (ppb)	27.89	**28.8**

Water Quality Index (WQI) Calculation

It is calculated using the Canadian Council of Ministers for the Environment Water Quality Index (CCME-WQI, 2001) method along the Kirkuk Irrigation Project for assessment of the water quality for human drinking compared with Iraqi Standards (2009). The method is calculated through three factors: range F1, frequency F2, and amplitude F3. The equations are calculated through the following coefficients:

Factor 1, Scope, where, F1= Number of Failed Variables/Total Number of Variables x100 …1

Factor 2, Frequency, where, F2= Number of Failed Tests/Total Number of Tests × 100 …. 2

Factor 3, Amplitude:

Step 1 where, Excursions = (Failed Test /Value Objective)-1 ….3

Excursion = (Value Objective /Failed Test)-1 ….4

Step 2 where NSE= ∑Excursion /Total Number of Tests …5

F3= NSE /0.01NSE + 0.01 f, where, CCME WQI = 100- [√F1+F2 + F3/ 1.732] …6

The CCME WQI categorization scheme is given in Table 3 for aquatic.

Table 3: Classification of water quality according to CWQI (2001).

Values	Water type
95-100	Excellent
80-94	Good
65-79	Fair
45-64	Marginal
0-44	Poor

Suitability of water for Irrigation purposes

To evaluate the suitability of water for irrigation and agriculture, the calculated indicators are: SAR, MH, salinity hazard, SP, KR, and Wilcox. The spatial distribution of various CWQls was carried out effectively to find water components suitable for human purposes and improve water quality (Abbas and Hassan, 2018). These indices are:

Sodium Percentage (Na%), where all concentrations are expressed in meq/l and can be determined using the following formula of Todd (1995):

$$Na\% = rNa + rK / (rCa + rMg + rNa + rK) \times 100 \quad \text{.....7}$$

Kelley ratio (KR), by which irrigation is evaluated following Kelley's (1940) measured level of sodium versus calcium-magnesium. All concentrations are expressed in meq/l determined using the following formula:

$$KR = Na+/(Ca^{+2} + Mg^{+2}) \quad \text{.... 8}$$

SAR Sodium Absorption Ratio (SAR), The sodium absorption ratio is used to evaluate whether it is suitable for irrigation. It is expressed in meq/l and is calculated using the formula shown below (Raghunath, 1987):

$$SAR = Na/(\sqrt[2]{Ca + Mg/2}) \qquad \text{.....9}$$

Magnesium hazard (MH), by detecting Mg over Ca. used to determine whether project water is suitable for purposes (Raghunath, 1987). Magnesium hazard expressed as meq/l is calculated using the following formula:

$$MH = [Mg^{+2}/(Ca^{+2} + Mg^{+2})] \times 100 \qquad \text{..... 10}$$

Results and discussion

Canadian Water Quality Index (CWQI)

It is noted that there is a variation in values between the average global quality index for the winter season, range of '62.61', and that in the summer season, '58.14' (Table 3). It is noted in the wet season that it falls into the third category 'Fair' and the dry season in the fourth category 'Marginal' according to the classification of CCME WQI (2001). As for the values of the remaining sites, they mostly fell between 'Fair, Marginal, and Poor' (Table 4) due to turbidity exceeding the permissible limit, increasing the pH to alkalinity, and high Ca values above the permissible limit. In the wet season, site W17 is within the 'Good' category.

During the dry season, in the final result, it is found through the index that the quality assessment is unsuitable and poor water with high risks for human use and drinking due to the presence of pollutant concentrations in the sites within the water project. The good category also needs simple treatment, while the rest of the categories need advanced treatment, and the last category is poor, which is unacceptable (Kennish, 1992) (Fig. 4). At present, anthropogenic inputs of pollutants have exceeded natural inputs. Turbidity in water results from suspended particles such as clay, silt, fine organic matter, plankton, and other microorganisms (Charles, 1970). When the water is clear, it refers to turbidity. Increased turbidity is indicative of most human activities occurring in the Irrigation project (WRC, 2003).

Table 4: Measurement value of CCME WQI in wet and dry seasons.

Sample No.	F1	F2	NSE	F3	CWQI	Classes	Sample No.	F1	F2	NSE	F3	CWQI	Classes
W1	18.18	18.18	1.96	66.33	40.7	poor	D1	18.18	18.18	1.22	55.036	47.2288	Marginal
W2	9.09	9.09	0.91	47.69	40.97	poor	D2	18.18	18.18	3.2	76.1904	35.015	poor
W3	18.18	18.18	0.09	9.15	73.71	Fair	D3	18.18	18.18	2.49	71.5787	37.6776	poor
W4	18.18	18.18	0.12	11	72.65	Fair	D4	18.18	18.18	1.007	50.36	49.9286	Marginal
W5	18.18	18.18	0.10	9.66	73.42	Fair	D5	27.27	27.27	1.73	63.6849	31.7377	poor
W6	18.18	18.18	0.65	39.72	56.07	Marginal	D6	18.18	18.18	0.84	45.6521	52.6468	Marginal
W7	18.18	18.18	0.82	45.07	52.98	Marginal	D7	18.18	18.18	1.57	61.1945	43.6731	Poor
W8	18.18	18.18	0.58	36.92	57.68	Marginal	D8	9.09	9.09	0.0109	1.0792	88.8793	Good
W9	18.18	18.18	1.61	61.99	43.21	poor	D9	18.18	18.18	0.48	32.6756	60.139	Fair
W10	18.18	18.18	0.69	40.96	55.35	Marginal	D10	18.18	18.18	0.68	40.4762	55.6352	Marginal
W11	18.18	18.18	0.46	31.91	60.58	Fair	D11	18.18	18.18	0.15	13.4347	71.248	Fair
W12	18.18	18.18	0.40	28.87	62.33	Fair	D12	18.18	18.18	0.098	9.0183	73.7979	Fair
W13	9.09	9.09	0.21	17.82	79	Fair	D13	9.09	9.09	0.0078	0.7722	89.0565	Good
W14	18.18	18.18	1.87	65.22	41.34	poor	D14	9.09	9.09	0.0085	0.8465	89.0136	Good
W15	18.18	18.18	0.31	23.92	65.19	fair	D15	18.18	18.18	1.52	60.3174	44.1795	poor
W16	9.09	9.09	0.40	28.7	72.93	fair	D16	18.18	18.18	1.107	52.4739	48.7081	Marginal
W17	18.18	18.18	0.25	20.53	67.14	fair	D17	18.18	18.18	1.572	61.1945	43.6731	poor
W18	9.09	9.09	0.71	42	65.24	fair	D18	9.09	9.09	3.72	78.9661	43.9099	poor
W19	9.09	9.09	0.003	0.37	89.28	Good	D19	9.09	9.09	0.45	31.3448	71.4049	Fair
W20	9.09	9.09	0.27	21.47	77.1	fair	D20	9.09	9.09	0.909	47.8421	61.8799	Fair
W21	18.18	18.18	0.12	11.03	72.63	fair	D21	27.27	27.27	5.0057	83.4283	20.3385	poor

W22	18.18	18.18	0.18	15.9	69.82	fair	D22	9.09	9.09	0.001	0.1	89.4411	Good
W23	18.18	18.18	0.97	49.29	50.54	marginal	D23	9.09	9.09	0.022	2.196	88.2345	Good
Average					62.61							58.14	

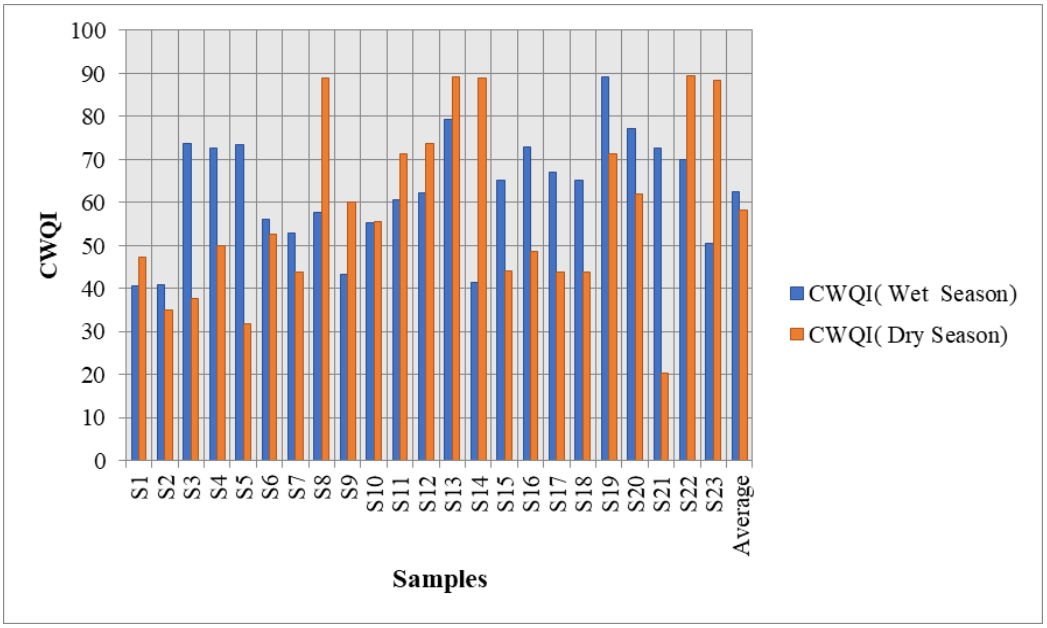


Fig. 4. CWQI for human purposes in an irrigation project.

Physicochemical Characteristics for Irrigation

Descriptive statistics of the physical and chemical parameters of river water samples, including mean, range, and standard deviation, are performed as shown in Tables 5 and 6. The average pH in the wet and dry seasons is 8.44 and 8.48, respectively, with ranges of 7.2-9.6 and 7.7-10.6, respectively. This refers to the water sample that is almost neutral to alkaline and, in some locations, is alkaline in nature. TDS is within the permissible limits for irrigation. Salts possess an effect on soil structure for plant growth as well as directly influencing it (Matthess, 1982). It is found that wet and dry period samples classified as 'Good' are permissible according to Don (1995), as shown in Table 9. Most of the values are higher than the permissible limit according to the IQS (2009) and WHO (2017) standards of 5 NTU. Turbidity was classified following, and it is found that they are all bad because irrigation water is affected by agricultural and human activities, pollutants, rain in the winter season, and the project is fed from the dam, so it is in a state of continuous impurity. Total hardness is one of the main parameters for determining the quality of water if we rely on the classifications of Al-Safawy et al. (2018). It is found in both seasons that it has 'hard-very hard' classes. The temperature in the wet season was 14.5 C° with a range between (13-16 C°). In the dry season, it was 24.21 C° with a range between 20-27°C. As shown in Figure 2 and Tables 5 and 6, it is clear that there is a variation in the temperatures, and there is no abnormal temperature recorded. Some of the major and minor elements exceed the limits of WHO (2017); some of the heavy metals (As, Cr, Pb, Ni) are also more than the standard of WHO (2017) and IQS (2009), caused by the pollution from the agriculture and industrial activities (Kadhim et al., 2018).

Table 5: Descriptive statistics in the wet season, physical-chemical parameters.

wet	PH	EC	TDS	Turb.	T.H	Ca	Mg	Na	K	HCO3	SO4	CL	NO3
N Valid	23	23	23	23	23	23	23	23	23	23	23	23	23
Mean	8.4	382.21	248.34	40.31	168.73	45.52	24.82	7.99	1.02	110.13	74	32.17	5.03
Median	8.3	381	248	36.89	170	48	19.5	8.6	1	104	82	32	4.20
Mode	8.1[a]	302[a]	196	.00[a]	170[a]	60	4.90[a]	2.90[a]	.80	97.60	78.00[a]	32	4
Std. Deviation	.505	68.47	44.470	29.48	24.88	17.20	18.63	3.49	.33	23.1	29.74	7.77	1.97
Kurtosis	1.192	2.06	2.06	1.01	1.98	-1.19	.79	-.749	.485	-.60	-1.15	.16	2.23

Std. Error of Kurtosis	.93	.93	.93	.93	.93	.93	.93	.93	.93	.93	.93	.93	.93
Range	2.40	295.00	192.	112	120	56	73.50	11.90	1.50	83	94.00	30.00	8.00
Sum	194.2	8791	5712	927.1	3881	1047	570.8	183.9	23.6	2533	1702.2	740	115.80

Table 6: Descriptive statistics in dry season, physical-chemical parameters.

	PH	EC	TDS	Turb.	T.H	Ca	Mg	Na	K	HCO3	SO4	CL	NO3
N Valid	23	23	23	23	23	23	23	23	23	23	23	23	23
Mean	8.54	920	644	70.45	208.43	50.43	19.97	12.07	.69	137.56	88.95	17.17	7.3874
Median	8.4	920	644	55	200	54	17.6	13.8	.80	138	90	18	8.8000
Mode	8.3	590[a]	413.00[a]	4.00	200	56	14.00[a]	3.00[a]	0.0	146.40[a]	78[a]	18.00	10.00
Std. Deviation	.58	203.46	142.42	72.88	30.47	12.92	7.91644	5.34	.67	38.51	30.59	2.55	3.32299
Kurtosis	6.37	-1.2	-1.2	2.07	-.55	-.45	1.756	-.66	-1.6	-.233	-.60	-.84	-.379
Std. Error of Kurtosis	.93	.93	.93	.93	.93	.93	.93	.93	.93	.93	.93	.93	.93
Range	2.90	660	462.00	280	112	47	34.00	17	1.90	155.4	116	8	11.27
Sum	196.44	21160	14812.00	1620.52	4794	1160	459.50	277.7	16	3164	2046	395	169.91

Water Suitability for Agricultural Purposes

It is found that the Kirkuk irrigation project, which represents the study area, can use its water because it is suitable for growing most types of crops (Table 7).

Table 7: Suitability of using the project's water for agricultural purposes according to Ayres and Westcot (1994) classification.

Crop Department	Low salt tolerance EC(µs/cm)	Medium salt tolerance EC (µs/cm)	High salt tolerance EC(µs/cm)
Fruit crops	3000-0 Avocado, Lemon, Strawberry, Peach, Orange, Apple, Grapefruit.	4000-3000 Date, Olive, Fig.	**00010-4000 Date palm.**
Vegetable crops	4000-3000 Green beans. Celery.	10000-4000 Cucumber, Peas, Onion, Potatoes, Broccoli. Tomato, Bell pepper, Sweet corn.	**10000-12000 Spinach, Asparagus, and Garden Beet.**
Field crops	6000-4000 Field beans	10000-6000 Castor beans, Sunflower, Corn, Rice, Wheat	**16000-10000 Cotton, Sugar beet, Rape.**

Hydrochemical facies

Piper Diagram: This diagram is shown in figure (5 A-B) that the predominant waters are alkaline terrestrial with bicarbonate dominance, and a few are alkaline terrestrial with bicarbonate dominance and little sulfate. The water samples fall into the bicarbonate types in the anion triangle, while calcium-magnesium is the predominant type in the cation triangle. The order is $Ca^{+} > Mg^{+}$, Na^{+}, K^{+}, although the anions order is $HCO_3 > SO_4$, Cl^{-}.

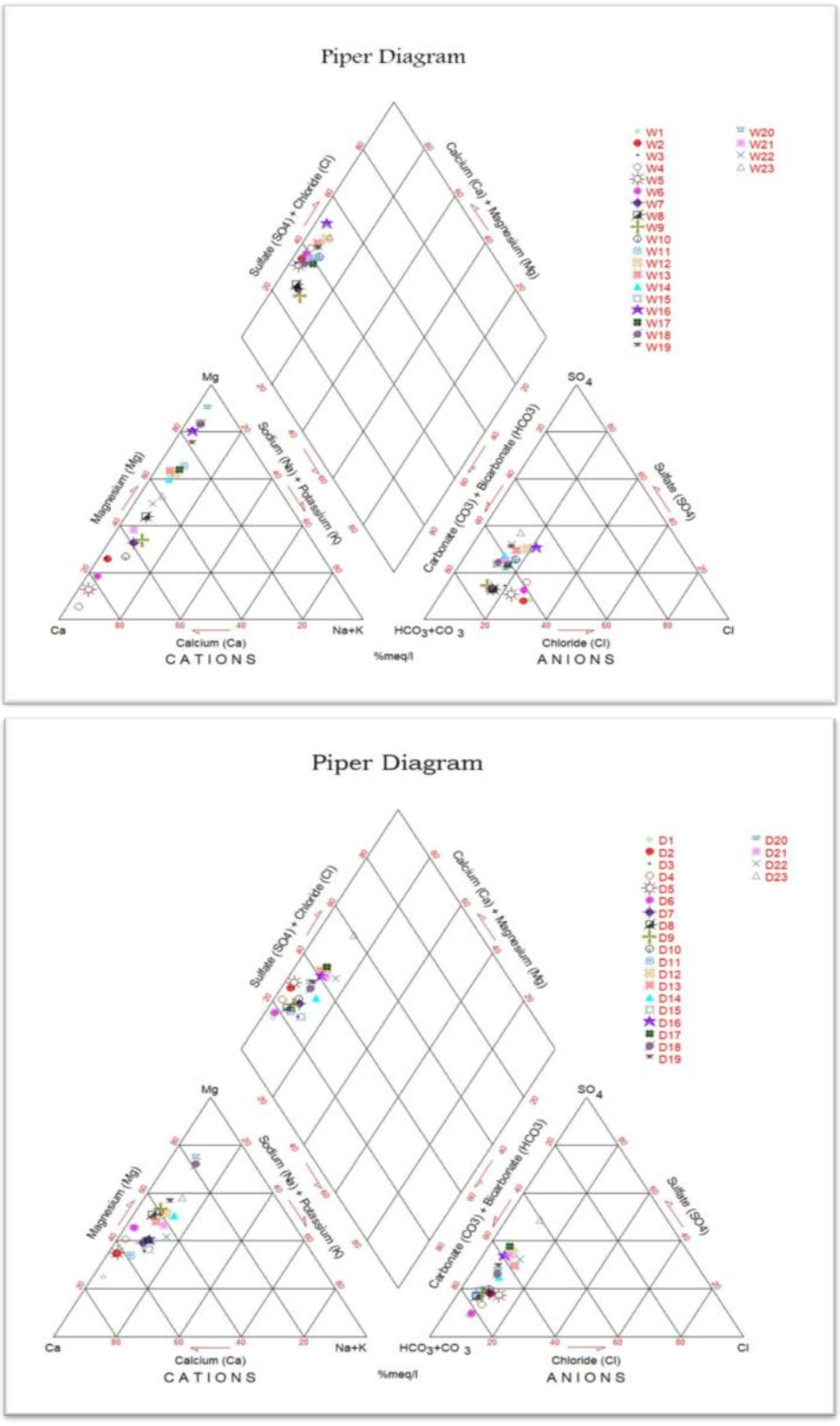


Fig. 5. Piper Diagrams, (Top) for the wet season, (Bottom) for the dry season.

Irrigation Water Quality Analysis

There are many classifications used to assess the quality of water for irrigation purposes by means of several variables (Qanam, 2003)**,** including cations, anions, electrical conductivity, total salts, pH, SAR, (Na%)**,** and SP and KR, MH (Al-Manmi, 2008), as follows:

SAR: The results in Table 8 display that all values are less than 10 and categorized as 'excellent' for irrigation, as listed in Table 9.

Sodium Percentage (Na%): Table 8 shows the sodium percentage values of water samples based on Don's (1995) classification. The sodium percentage was in the wet period 'Good-Excellent' category (Table 9). It is observed in the dry season 'Excellent-Good' category, then classified as having 'good' for irrigation.

KR: The result shows that all samples for both seasons are less than 1, and the sample sites are suitable for irrigation.

MH: It is observed that the results show a difference and variation in values; it is found that in the wet season from the site (W1-W10) were less than 50, suitable for irrigation, while the sample sites (W12-W23) show that these sites had an increase in magnesium risk values that were more than 50. As for the dry season, most of them are suitable for irrigation, ranging from (17.5-45.9), while the rest (D18, D19, D20, D23) have more than 50, which are not suitable according to the classification of Raghunath (1987) as shown in Tables (8,9). If water contains high levels of magnesium that degrade soil alkalinity, it will reduce crop productivity. Magnesium concentrations affect crops more seriously than calcium concentrations.

Table 8: Results of Irrigation parameters (wet and dry) seasons.

Sample No.	SAR	KR	SP (%)	MH	Sample No.	SAR	KR	SP%	MH
W1	0.103	0.0396	4.15	11.85	D1	0.085	0.0374	5.04	17.57
W2	0.097	0.0371	4.04	18.09	D2	0.068	0.0377	5.24	24.21
W3	0.07	0.0238	3.57	18.17	D3	0.294	0.1588	21.12	29.03
W4	0.153	0.046	4.39	3.52	D4	0.078	0.0378	6.76	29.92
W5	0.132	0.0387	4.06	8.47	D5	0.082	0.0401	6.42	25.62
W6	0.115	0.0407	3.98	12.56	D6	0.073	0.0423	8.11	35
W7	0.202	0.1023	13.73	25.16	D7	0.299	0.1714	16.55	31.43
W8	0.168	0.0981	14.12	35.14	D8	0.161	0.1161	13.94	41.77
W9	0.211	0.1518	19.92	26.94	D9	0.184	0.135	15.61	45.43
W10	0.205	0.1158	14.79	20.19	D10	0.184	0.1481	15.55	44.14
W11	0.186	0.1448	22.95	60.17	D11	0.163	0.223	13.72	26.17
W12	0.168	0.1162	21.24	55.12	D12	0.227	0.1863	22.64	44.67
W13	0.121	0.0741	17.65	54.65	D13	0.227	0.1666	18.79	40.59
W14	0.151	0.0984	17.17	51.65	D14	0.311	0.24	27.71	45.97
W15	0.091	0.0798	18.84	81	D15	0.232	0.3076	21.75	30
W16	0.082	0.0657	18.42	75.09	D16	0.243	0.2411	20.51	33.84
W17	0.161	0.1287	22.51	57.56	D17	0.245	0.2396	20.32	32.52
W18	0.086	0.089	22.63	77.17	D18	0.199	0.1565	24.57	67.03
W19	0.105	0.1083	22.74	70.79	D19	0.242	0.1607	23.29	50.15
W20	0.075	0.0719	22.12	89.91	D20	0.154	0.1197	29.06	71.87
W21	0.168	0.0752	6.68	29.25	D21	0.211	0.2261	21.86	43.21
W22	0.142	0.0906	10.34	40.15	D22	0.233	0.2226	22.89	36.85
W23	0.192	0.1187	15.46	44.55	D23	0.227	0.1471	24.09	56.23

Table 9: Irrigation parameters indices and percentage of water samples.

Parameters	Values	Water type
Na% (Wilcox 1955)	<20	Excellent
	20-40	Good
	40-6	Permissible
	60-8	Doubtful
	>80	Unsuitable
MH (Raghunath 1987)	<50	Suitable
	>50	Unsuitable
SAR	<10	Excellent
	10-8	Good
	18-26	Doubtful
	>26	Unsuitable
EC (Don 1995)	250	Excellent
	250-750	Good
	750-2000	Permissible
	2000-3000	Doubtful
	>3000	Unsuitable
KR (Killyes 1963)	<1	Good
	>1	Unsuitable

Wilcox Diagram: Surface water samples collected from both seasons assess the suitability for irrigation based on their Wilcox chart (Fig. 6, A-B).

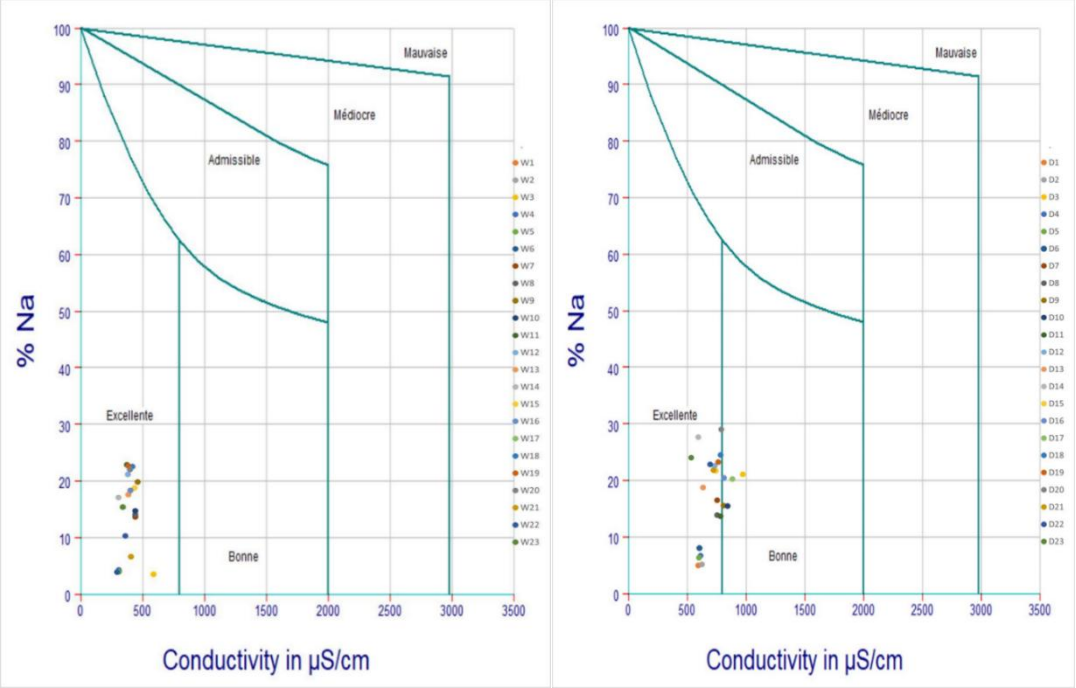


Fig. 6. Wilcox Diagrams, (Left) for the wet season, (Right) for the dry season.

Correlation Coefficient Analysis

Wet season: Fig. (7) shows strong negative correlations between Al and each of Fe (−0.614), Mn (−0.687), Fe (−0.677), and Mn (−0.635), respectively, suggesting that as Al concentration increases, Fe and Mn concentrations tend to decrease. This may suggest that higher Al levels may inhibit the presence or availability of Fe and Mn, which may impact overall water quality and ecosystem health (Hodge and Krenitsky, 2020). Boron has a strongly positive wet period correlated with sodium (0.712), potassium (0.427), HCO_3 (0.630), SO_4 (0.562), electrical conductivity (0.789), and total dissolved solids (0.791). This may be due to the presence of geochemical associations between them, or they are from the same sources. In the wet period, a strong positive correlation between chromium and iron is found. Chromium shows a strong positive correlation with iron (0.828) and manganese (0.703). A moderate positive correlation is also found between chromium and copper (0.445). This suggests a strong relationship that could reflect similar environmental or geological processes. This may indicate common sources or similar geochemical behaviors (Hubert and Wolkersdorfer, (2015).

Dry season: Iron is positively correlated strongly with manganese in wet (0.784) and in dry season (0.773); iron is moderately correlated with bicarbonate (0.459) (Table 8), Fe in the dry season with Zn (0.512), K (0.542) and HCO_3 (0.554) moderately positive; increased levels of zinc, potassium and bicarbonate are associated with higher levels of iron. Iron is negatively correlated moderately with sodium (-0.529) and negatively correlated strongly with SO_4 (-0.643) and with pH (-0.640), EC (-0.640), and TDS (-0.640). Iron solubility decreases under alkaline conditions, limiting its availability (Baker, 1987). Manganese has a moderate positive correlation with zinc (0.461). Simultaneous increases in manganese and zinc may indicate pollution or changes in agricultural land use practices that affect both minerals. Nickel and pH correlation of 0.659 reveals a strong positive relationship. Positive correlations between them suggest that these elements may originate from similar sources or be affected by similar environmental conditions. This is particularly important in agricultural runoff (Es-sahbany et al., 2019). Pb has a moderately negative correlation with zinc (-0.462). The inverse relationship may indicate competition between lead and zinc for uptake in biological systems, such as plants or aquatic organisms. High levels of lead may inhibit the uptake of zinc, which is essential for many biological functions. The negative correlation may mean that lead and zinc originated

from different sources or underwent different movement processes in the environment (APHA et al., 2017). The correlation coefficient in the dry period indicates a moderate negative relationship between the other (Senthilkumar et al., 2019).

Persones Correlations (W.)

W.	Al	As	B	Cu	Co	Cr	Fe	Mn	Ni	Pb	Zn	Ca	Mg	Na	K	HCO3	SO4	Cl	NO3	PH	EC	TDS
Al	1																					
As	-.255	1																				
B	-.389	-.042	1																			
Cu	-.223	.290	-.188	1																		
Co	-.087	.370	.404	-.047	1																	
Cr	-.343	.311	.082	.445*	.095	1																
Fe	-.614**	.343	.292	.392	.218	.828**	1															
Mn	-.687**	.213	.396	.282	.143	.703**	.784**	1														
Ni	-.283	-.002	.188	-.184	-.171	.238	.177	.269	1													
Pb	.221	.431*	-.231	-.043	.079	-.254	-.164	-.285	-.061	1												
Zn	-.386	-.266	-.070	.236	-.052	.355	.314	.461*	-.017	-.462*	1											
Ca	.146	.158	-.216	.050	.119	-.051	-.012	-.174	-.372	.205	-.070	1										
Mg	.418*	-.391	.169	-.254	-.008	-.275	-.271	-.339	-.012	-.003	-.286	-0.648	1									
Na	-.269	-.177	.712**	-.246	-.076	.045	.076	.348	.575**	-.134	-.049	-.436*	.152	1								
K	-.173	.025	.427*	-.237	.257	.295	.323	.257	.448*	-.228	-.020	-.260	.185	.271	1							
HCO3	-.268	.022	.630**	-.020	.183	.300	.459*	.329	-.265	-.244	.094	.004	.086	.308	.205	1						
SO4	-.327	-.283	.562**	-.311	.112	-.278	-.154	.214	.438*	-.213	.048	-.622**	.335	.642**	.382	-.050	1					
Cl	.125	.130	-.328	.085	.054	-.076	.037	-.271	-.455*	.270	-.069	.373	.030	-.579**	-.278	-.059	-.582**	1				
NO3	-.268	-.018	.295	-.009	-.246	-.051	.219	.110	-.274	-.073	-.034	-.195	.218	.147	.108	.602**	.137	-.040	1			
PH	.067	.019	-.006	-.200	-.262	-.051	-.303	.071	.659**	.212	-.147	-.441*	.081	.591**	.115	-.381	.463*	-.542**	-.290	1		
EC	-.324	.013	.789**	-.010	.464*	.119	.370	.394	-.340	-.195	.076	.053	.002	.294	.241	.715**	.241	-.075	.418*	-.429*	1	
TDS	-.321	.013	.791**	-.013	.466*	.117	.368	.393	-.339	-.193	.074	.050	.006	.296	.242	.714**	.244	-.077	.417*	-.427*	1.000**	1

**. Correlation is significant at the 0.01 level (2-tailed). *. Correlation is significant at the 0.05 level (2-tailed).

Persons Correlations D.

D.	Al	As	B	Cu	Co	Cr	Fe	Mn	Ni	Pb	Zn	Ca	Mg	Na	K	HCO3	SO4	Cl	NO3	PH	EC	TDS
Al	1																					
As	-.336	1																				
B	.186	-.245	1																			
Cu	.088	.254	-.088	1																		
Co	-.132	-.231	-.094	-.070	1																	
Cr	.038	-.052	-.108	-.080	.088	1																
Fe	-.677**	.165	-.535**	-.120	.257	.053	1															
Mn	-.635**	.192	-.279	.171	.164	.052	.773**	1														
Ni	.555**	-.263	-.150	-.014	-.162	.266	-.211	-.112	1													
Pb	.201	-.127	.014	.401	.159	-.048	.069	.130	.348	1												
Zn	-.480*	.274	-.043	-.274	.208	-.211	.512*	.486*	-.454*	-.263	1											
Ca	.028	.001	-.062	.120	.185	-.060	.393	.331	.170	.390	.224	1										
Mg	-.105	.024	.048	-.151	-.127	-.036	-.224	-.072	-.002	-.305	.019	-.551**	1									
Na	.239	-.153	.175	.223	-.220	-.107	-.529**	-.249	.416*	.133	-.455*	-.184	.508*	1								
K	-.084	-.091	-.310	-.144	.281	.318	.542**	.539**	.125	-.028	.380	.520*	-.317	-.540**	1							
HCO3	-.251	.108	-.406	.155	.222	-.048	.554**	.579**	.084	.191	.306	.601**	.082	-.088	.600**	1						
SO4	.287	-.128	.498*	-.075	-.288	-.137	-.643**	-.434*	.216	-.079	-.245	-.235	.557**	.804**	-.615**	-.357	1					
Cl	-.170	.079	-.351	-.267	.164	.324	.362	.083	.058	-.192	.133	.024	.084	-.227	.329	.127	-.220	1				
NO3	-.366	.119	.052	.144	.205	-.215	.215	.226	-.394	.018	.365	.244	.298	-.048	.042	.449*	.076	.053	1			
PH	.263	-.256	.158	-.182	-.200	.195	-.483*	-.500*	-.050	-.212	-.277	-.626**	.028	.079	-.365	-.780**	.247	-.281	-.476*	1		
EC	-.010	-.071	.190	.073	-.014	-.046	-.023	.222	.373	.204	-.047	.394	.396	.657**	.032	.507*	.523*	-.002	.271	-.537**	1	
TDS	.157	-.034	.291	.077	-.302	-.200	-.640**	-.529**	-.071	-.208	-.254	-.600**	.536**	.679**	-.798**	-.569**	.787**	-.226	.068	.479*	.090	1

**. Correlation is significant at the 0.01 level (2-tailed). *. Correlation is significant at the 0.05 level (2-tailed).

Fig.7. Pearson's correlation of parameters of irrigation in the, (Top) for the wet Season, (Bottom) for the dry Season.

Conclusions

To assess the quality of water in the Kirkuk irrigation project for drinking purposes and irrigation, agricultural lands are assessed on several physical and chemical criteria, and analyses of heavy and trace elements. The water in the two wet and dry seasons varied between neutral, sub-alkaline, and alkaline, and it is shown that the pH is neutral in the north and gradually changed to alkaline towards the southern part, indicating that the dissolution processes were prevalent in the northern part. Most of the physical parameters are within their standard limits except for turbidity, which exceeded the permissible limit, and the pH in the southern areas of the project water is increasing towards alkalinity. Calcium is somewhat exceeded and magnesium. Fertilizers are another source of calcium, and from carbonate sedimentary rocks, it is found that all heavy elements are within the permissible limits. The Pearson correlation coefficient is used in continuous bivariate data to determine whether there are strong positive and strong negative relationships, and some are neutral positive and negative. As for drinking

applications, they were not suitable. As for irrigation applications, it is generally predicted that the indicators show that they are suitable, 'excellent', and 'good' except for MH, which is found to be exceeded and became unsuitable for irrigation, as irrigation water containing high levels of magnesium leads to deterioration and reduces crop productivity. Piper and Wilcox's are suitable for irrigation in all types of soils.

Acknowledgment

The authors would like to express their gratitude to the University of Kirkuk, College of Science, for providing all of the required facilities, which contributed to the improvement of the quality of this work.

References

Abbas, A.A., Hassan, F.M., 2018. Water quality assessment of Euphrates River in Qadisiyah province (Diwaniyah River), Iraq Iraqi Journal of Agricultural Sciences 49(2), pp. 152-162.

Al-Hamdani, J.A., 2009. Hadrochemical effect of groundwater due to irrigation and drainage projects in Tawuq sub-basin, MSc Thesis, College of Science, University of Baghdad.

Al-Kadhimi, J.A., Sissakian, V.K., Fattah, A.S., and Deikran, D.B., 1996. Tectonic map of Iraq, S.E. of Geological Survey and Mining National Library. No. (10/1990), Baghdad. Iraq.

Al-Kilabi, J.A., 2013. Hydrogeochemistry of groundwater and the probable effect of Kirkuk irrigation project on its quality in Al-Hawija area, Iraq. MSc Thesis, College of Sciences, University of Baghdad.

APHA, AWWA, and WEF, 2017. Standard Methods for the Examination of Water and Wastewater, 23rd Edition. American Public Health Association.

Ayres, R.S., and Westcot, D.W., 1994. Water quality for agriculture, FAO Irrigation and Drainage Paper 29, Rev. 1. Rome: Food and Agriculture Organization of the United Nations.

Babiker, I.S., Mohamed, M.A.A., and Hiyama, T., 2007. Assessing groundwater quality using GIS. Water Reso. Manage 21, pp. 699–715. https://doi.org/10.1007/s11269-006-9059-6

Baker, A.J.M., 1987. Interactions of iron and pH in aquatic systems.

Buday, T., 1980. The regional geology of Irradhaaq: stratigraphy and paleogeography (Vol. 1). State Organization for Minerals, Directorate General for Geological Survey and Mineral Investigation.

CCME, 2001. Canadian Council of Ministers of the Environment, Canadian water quality guidelines for the protection of aquatic life: CCME Water Quality Index 1.0. Technical Report. In: Canadian Environmental Quality Guidelines, Canadian Council of Ministers of the Environment, Winnipeg.

Chandra, S., Khan, S., Avula, B., Lata, H., Yang, M.H., Elsohly, M.A., Khan, I.A., 2014. Assessment of total phenolic and flavonoid content, antioxidant properties, and yield of aeroponically and conventionally grown leafy vegetables and fruit crops: a comparative study. Evid Based Complement Alternat Med.; 2014:253875. Doi: 10.1155/2014/253875.

Charles, E.R., 1970. Investigating Water Problems: A Water Analysis Manual, Published by LaMotte Chemical Products Company, Chestertown, Maryland.

Don, C.M., 1995. A grows guide to water quality. University College Station, Texas.

Es-sahbany, H., Berradi, M., Nkhili, S., Hsissou, R., Allaoui, M., Loutfi, M., Bassir, D., Belfaquir, M., and El Youbi, M., 2019. Removal of heavy metals (nickel) contained in

wastewater-models by the adsorption technique on natural clay: Materials Today: Proceedings, Vol. 13, pp. 866-875.

Hodge, J.W. and Krenitsky, D., 2020. Correlation between Metal Concentrations in Aquatic Systems, Journal of Environmental Monitoring, 22(3), pp. 154-167.

Hubert, E. and Wolkersdorfer, C., 2015. Establishing a conversion factor between electrical conductivity and total dissolved solids in South African mine waters. Water SA 41 (4) 490-500. https://doi.org/10.4314/wsa.v41i4.08.Iraqi Standard, 2009. Iraq Standard of Drinking Water No.417, Second Modification.

Jassim, S.Z. and Goff, T., 2006. Phanerozoic development of the northern Arabian Plate, In: Jassim S.Z., Goff, J. C., Geology of Iraq, publication of Dolin, Prague and Moravian Museum, Brno, 341 P.

Kelley, W.P. 1940. Permissible composition and concentration of irrigation waters. Proc. Am. Soc. Civil Eng. 66, pp. 607–613.

Kennish, M.J., 1992. Ecology of Estuaries. Anthropogenic effects. Boca Raton, USA: CRC Press.

Khan, F., Hussain, T., and Lumb, A., 2003. Water quality evaluation and trend analysis in selected watersheds of the Atlantic regions of Canada, J. of Environmental Monitoring and Assessment 88, pp. 221–248.

Matthess, G., 1982: The Properties of Groundwater, John Wiley and Sons, New York, U.S.A., 397 P.

Milovanovic, M. 2007. Water quality assessment and determination of pollution sources along the Axios / Vardar River, Southeast Europe. Desalination 213: pp. 159-173.

Kadhim, L.S., Sadiq, S.N. and Heas, M.H., 2018, Major and Trace Elements of Water and Sediments of Dibis Dam –Iraq. Sustainable Resources Management Journal118-113 (2) 2018, 31324179 http://doi.org/10.5281/zenodo.

Senthilkumar, R., Prasad, D. R., Govindarajan, L., Saravanakumar, K., and Prasad, B. N., 2019, Green alga-mediated treatment process for removal of zinc from synthetic solution and industrial effluent: Environmental technology, v. 40, no. 10, p. 1262-1270.

Singh, A., 2014. Conjunctive use of water resources for sustainable irrigated agriculture, Journal of Hydrology, Vol. 519, Part B, pp. 1688-1697, ISSN 0022-1694, https://doi.org/10.1016/j.jhydrol.2014.09.049.

Soran, N.S., 2008, Hydrogeochemical properties of groundwater in the vicinity of Al-Hawija plain SE-Kirkuk, Iraq, Journal of Kirkuk University-Scientific Studies, Vol.3, No.2, DOI: 10.32894/kujss.2008.47139.

Todd, D.K., 1980. Ground Water Hydrology 2nd Ed., Hoboken, NJ: John Wiley and Sons, 535 P.

Todd, D.K., 1995. Groundwater Hydrology, 3rd Ed. John Wiley and Sons Publications, New York, NY, USA.

WHO (World Health Organization), 2017. Guidelines for Drinking-water Quality. 4th Edition, incorporating the first addendum. Brazil, World Health Organization, 518 P.

Wilcox, L.V., 1955. Classification and Use of Irrigation Water. US Department of Agriculture, Circular 969, Washington, DC, USA.

WRC, Water Resources Commission, 2003. Ghana Raw Water Criteria and Guidelines. Vol. 1. Domestic Water. CSIR-Water Research Institute, Accra, Ghana.

Iraqi National Journal of Earth Science

www.earth.uomosul.edu.iq

Spatial Simulation of Future Changes in the LULC for Babil Governorate Using Cellular Automata (CA)−Markov Model

Hayder Hameed Jassoom[1*], Rabab Saadoon Abdoon [2]

[1,2] *Department of Physics, Collage of Science, University of Babylon, Babil, AL-Hilla, 51002, Iraq.*

Article information

Received: 21- Sep -2024

Revised: 03- Dec -2024

Accepted: 11- Feb -2025

Available online: 01- Jan -2026

Keywords:
Remote sensing (RS),
land use and land cover (LULC),
Cellular Automata-Markov (CA–Markov),
Geographic Information System (GIS),
Babil governorate,

Correspondence:
Name: Hayder Hameed Jassoom

Email: sci685.hadiar.hamied@student.uobabylon.edu.iq

ABSTRACT

Babil Governorate has witnessed radical changes in land use and land cover (LULC) over the past few decades, driven by rapid population growth and economic development. Despite this, knowledge remains limited regarding land use patterns and the mechanisms of change driven by human activities. Therefore, there is an urgent need to study the transformations of LULC in Babil Governorate to determine the factors influencing these changes, and to predict their future trajectories. This study aims to assess LULC changes during the period 1990-2020 and to predict the expected changes up to 2050 by analyzing land use and land cover data for 1990, 2000, 2010, and 2020. By applying the LULC transition matrix and the Markov model, the study could simulate the expected LULC patterns for the study area in the future. The study results show that the region will experience substantial changes in LULC during the period 2030-2050. Urban areas are expected to increase gradually, while bare land is expected to decline significantly. Water bodies are also expected to grow, and vegetation lands are expected to remain relatively stable. These changes reflect the intertwined effects of urban expansion, climate change, water inflows from neighboring countries, and shifts in land use patterns. The results indicate that current LULC trends will continue over the next three decades. This study can provide decision-makers with the necessary tools to develop sustainable land and water management policies.

DOI: 10.33899/injes.v26i1.60218, ©Authors, 2026, College of Science, University of Mosul.
This is an open-access article under the CC BY 4.0 license (http://creativecommons.org/licenses/by/4.0/) .

المحاكاة المكانية للتغيرات المستقبلية في استخدام الأراضي والغطاء الأرضي لمحافظة بابل باستخدام نموذج الخلية الآلية لماركوف

حيدر حميد جسوم [1*] ، رباب سعدون عبدون [2]

[2،1] قسم الفيزياء، كلية العلوم، جامعة بابل، بابل، الحلة، 51002، العراق.

معلومات الارشفة

تاريخ الاستلام: 21- سبتمبر- 2024

تاريخ المراجعة: 03- ديسمبر- 2024

تاريخ القبول: 11- فبراير- 2025

تاريخ النشر الالكتروني: 01- يناير- 2026

الكلمات المفتاحية:

الاستشعار عن بعد،

الاستخدام الأرضي والغطاء الارضي،

الأوتوماتا الخلوية-ماركوف،

نظم المعلومات الجغرافية،

محافظة بابل،

المراسلة:

الاسم: حيدر حميد جسوم

Email: sci685.hadiar.hamied@student.uobabylon.edu.iq

الملخص

شهدت محافظة بابل تغييرات جذرية في استخدامات الأراضي وتغطية الأراضي (LULC) على مدى العقود القليلة الماضية بدافع النمو السكاني السريع والتنمية الاقتصادية. على الرغم من ذلك، لا تزال المعرفة محدودة فيما يتعلق بأنماط استخدام الأراضي وآليات التغيير المدعمة بالأنشطة البشرية. لذلك، هناك حاجة ملحة لدراسة تحولات LULC في محافظة بابل وتحديد العوامل المؤثرة على هذه التغيرات والتنبؤ بمساراتها المستقبلية. يهدف هذا البحث إلى تقييم تغييرات LULC خلال الفترة 1990–2020 والتنبؤ بالتغيرات المتوقعة حتى عام 2050 من خلال تحليل بيانات استخدامات الأراضي وتغطية الأرض لعام 1990 و2000 و2010 و2020. من خلال تطبيق مصفوفة انتقال LULC ونموذج ماركوف، يمكن للدراسة محاكاة أنماط LULC المتوقعة لمنطقة الدراسة في المستقبل. أظهرت نتائج الدراسة أن المنطقة ستشهد تغييرات كبيرة في LULC خلال الفترة 2030–2050. من المتوقع أن تزداد المناطق الحضرية تدريجياً، بينما من المتوقع أن تنخفض الأراضي الجرداء بشكل كبير. ومن المتوقع أيضًا أن تنمو المسطحات المائية، ومن المتوقع أن تظل أراضي الغطاء النباتي مستقرة نسبيًا. تعكس هذه التغييرات الآثار المتداخلة للتوسع الحضري وتغير المناخ وتدفق المياه من البلدان المجاورة وتحولات أنماط استخدام الأراضي. تشير النتائج إلى أن الاتجاهات الحالية لـ LULC ستستمر على مدى العقود الثلاثة المقبلة. يمكن أن توفر هذه الدراسة لصانعي القرار الأدوات اللازمة لتطوير سياسات مستدامة لإدارة الأراضي والمياه.

DOI: 10.33899/injes.v26i1.60218, ©Authors, 2026, College of Science, University of Mosul.
This is an open-access article under the CC BY 4.0 license (http://creativecommons.org/licenses/by/4.0/) .

Introduction

LULC refers to changes in land use and land cover resulting from human activities (Riggio *et al*., 2020). These modifications have seriously affected the ecological balance at different local (study area) and international levels. As a result, this matter has become a focus of the international community due to its impact on our planet (Anwar *et al*., 2022). As a solution to this issue, geospatial models and open-source geospatial data have proven to be powerful tools for monitoring and tracking the status and changes in land use and land cover. This approach can effectively support efforts to protect the environment and sustainably manage land (Rai *et al*., 2018). Due to the increase in income and population, cities and urban areas have experienced significant expansion, which is natural with increasing human activity.

Land use patterns in these areas are influenced by various factors (industrial, technological, globalization, economic, and administrative) (Fei *et al*., 2021). It is important to know that rapid urban expansion significantly impacts the economic conditions of cities. This widespread phenomenon, often resulting from poor urban planning, causes negative side effects such as deforestation, decreased agricultural land, and the conversion of pastures into built-up

areas (Feng *et al*., 2021). The forthcoming years will witness multiple and interconnected challenges in land use due to the expected increase in demand for goods and services, which will lead to the depletion of limited land resources (Popp *et al*., 2017). Therefore, making the right decisions about the environment and long-term sustainable development is conditional on the availability of accurate data on land use and land cover change. Consequently, this data is essential for evaluating studies and discussions on current global changes. Given the expected increase in demand for products and services, which puts increasing pressure on limited land resources, the world will face new and intertwined challenges in land use in the near future (Cuevas *et al*., 2016).

This study aims to analyze the spatial distribution of land use and land cover types in Babil Governorate and to provide detailed information to support decision-making related to natural resource management. Additionally, the study aims to evaluate the efficiency of the Cellular Automata-Markov model in predicting future changes in land use.

Related work

A variety of spatial simulation models have been employed, including the conversion of land use and its effects on a model developed by Das *et al*. (2019) and the future land use simulation model proposed by Lin *et al*. (2020), to predict dynamic changes in land surface cover over time and space.

Among the most prominent models that have received widespread attention in this field is the CA-Markov model, which combines the power of Markov chains in representing temporal changes with the flexibility of cellular automata in simulating spatial interactions, making it a powerful tool for understanding the dynamics of complex spatial changes (Wang *et al*. 2021). Furthermore, studies have shown that the CA-Markov model provides a powerful tool for analyzing the complex spatial changes and offers valuable insights to support decision-making in the field of spatial planning. For example, Ruben *et al*. (2020) and Kisamba and Li (2023) successfully used this model to predict land cover changes, and they proposed sustainable land use policies.

In a previous study, Matlhodi *et al*. (2021) compared the performance of the Cellular Automata-Markov and GEOMOD models in predicting future land use changes in the Nepalese Fewa Lake watershed. Their results showed that the Cellular Automata-Markov model outperformed in simulating future scenarios.

Liu *et al.* (2017) proposed a novel Future Land Use Simulation (FLUS) model to forecast changes in land use and land cover in the future. The model integrates top-down and bottom-up approaches to accurately simulate the complex interactions between human activities and climate change. The FLUS model was tested on a Chinese case study and outperformed existing models in predicting future land use patterns under various scenarios. This innovative model provides valuable insights for sustainable urban planning and policymaking.

Based on the promising results shown by the CA-Markov model in previous studies, we applied this model for the first time in Babil Governorate to assess current land use change patterns and to predict its future distribution until 2050. Thus, this study introduces a new scientific contribution in this field at the level of Babil Governorate. A comprehensive study is conducted on historical LULC change data in Babil Governorate. Changes in LULC were assessed over different periods, and their causes were identified. Future land use in the study area is also projected. The results of this study are expected to enhance the sustainable use of natural resources in the study area.

Study Area

Babil Governorate is situated in the center of Iraq, south of the capital Baghdad, and is the cradle of ancient civilizations. It is the fifth-largest governorate in Iraq in terms of

population, with approximately two million inhabitants as of 2018 (Hashim *et al.*, 2022). Geographically, it extends between longitudes 43° 58' 10" and 44° 38' 35" East, and latitudes 32° 7' 25" and 33° 0' 35" North, covering an area of approximately 5119 km^2 (Talib and Laffta, 2024). It is bordered by Baghdad Governorate to the north, Wasit Governorate to the east, Karbala and Anbar Governorates to the west, and Najaf and Qadisiyah Governorates to the south (Talib and Laffta, 2024) (Fig. 1).

Babil Governorate experiences a hot and arid continental climate with summer temperatures exceeding 50 °C. Despite these harsh climatic conditions, Babylon has managed to develop a thriving agricultural economy through an extensive network of irrigation canals that supply agricultural lands. This network contributes to the production of a variety of crops, including grains, vegetables, and fruits, making agriculture a cornerstone of the local economy (Hashim *et al.*, 2022).

Administratively, the governorate is divided into six districts: Hilla (the governorate center), Al-Mahawil, Al-Musayyib, Al-Hashimiyah, Al-Hamza Al-Gharbi, and Kothi (Hashim *et al.*, 2022).

Babil is renowned for its ancient historical sites dating back to the Sumerian and Babylonian civilizations, making it the most important tourist destinations in Iraq for tourists from all over the world. It is the place where visitors come to enjoy the beauty of its archaeological sites and to learn more about its ancient history. https://en.wikipedia.org/wiki/Babylon_Governorate).

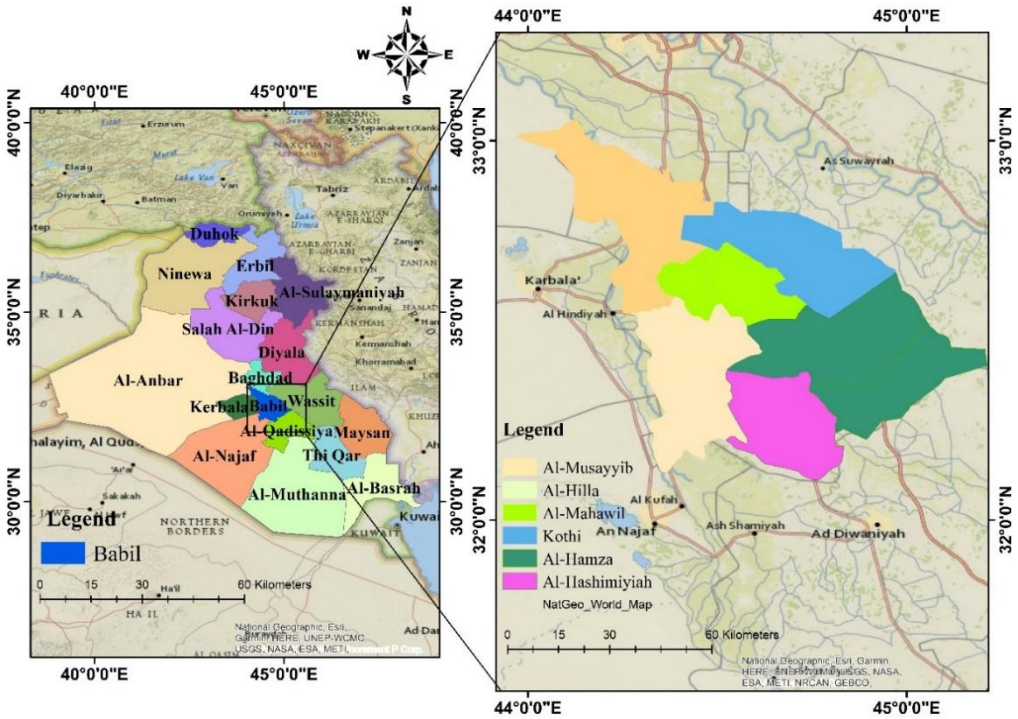


Fig. 1. Geographical map illustrating the location of Babylon Governorate and its administrative divisions in the central part of Iraq

Materials and Methods

Opted method

A comprehensive methodology integrating satellite image processing, land use classification, and Markov modeling is employed to predict future land use changes as illustrated in Fig. 2.

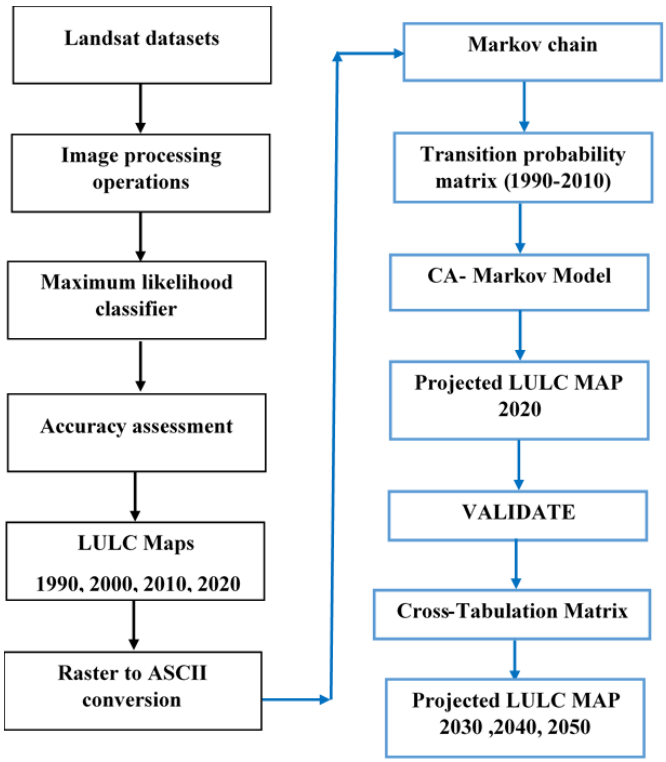


Fig. 2. Flow chart of the correction procedures.

Landsat datasets

A precise methodological framework is employed to analyze satellite imagery spanning multiple temporal periods. Key considerations encompassed the selection of cloud-free images, the assurance of high spatial resolution, and the maintenance of consistent acquisition dates (Marti *et al*., 2016). Subsequently, the images are projected using the Universal Transverse Mercator projection (UTM). Their geographic location is accurately determined using the World Geodetic System 1984 (WGS84) and the ellipsoid (Okiemute *et al*., 2018).

Landsat 7 (+ETM) and Landsat 8 (OLI) datasets (Table 1) are carefully selected for the study, considering the criteria above, pertinent scientific references, and the common use of Landsat imagery in LULC studies. Land cover and land use dynamics are investigated using four Landsat satellite images with a 10-year time interval (Table 1). The Landsat scenes are obtained from the United States Geological Survey (USGS) Earth Explorer website (http://earthexplorer.usgs.gov/).

Table 1: Remote sensing imagery used in this study.

Path	Row	Landsat 7 (+ETM)			Landsat 8 (OLI)
168	37	12 / July / 1990	1 / July / 2000	10 / July / 2010	13 / July / 2020
168	38	12 / July / 1990	1 / July / 2000	10 / July / 2010	13 / July / 2020
169	37				20 / July / 2020

Image processing operations

Initial image processing is carried out using ENVI 5.6 and ArcGIS desktop software (Nath et al., 2022). This includes radiometric and atmospheric correction, as well as repairing distortions caused by the Landsat 7 scan line corrector failure. To address missing data (approximately 22% in the 2010 image), the Nearest Neighbor Interpolation technique is employed. Spatially consistent spectral bands from Landsat 7 and 8 are merged to enhance spectral information. Subsequently, the images are mosaicked and clipped to the study area.

Google Earth imagery is used as a reference to establish ground control points for accurate georeferencing of the Landsat images. To ensure accurate classification, a comprehensive training dataset is created. For the years 1990, 2000, 2010, and 2020, training sites are identified using on-screen digitization techniques on Landsat imagery and Google Earth Pro. To minimize the impact of mixed pixels, homogeneous polygons are chosen as training sites. A stratified random sampling technique is employed to generate 250 sample points per class from these polygons. Additionally, independent validation samples (approximately 25 points per class) are collected to assess classification accuracy.

A maximum likelihood classifier is employed to categorize the pixels into various LULC classes. The unique spectral signatures of each LULC class are compared on the maps to identify the specific land cover types in different areas of Babil Governorate. The classified LULC classes are then compared to the corresponding types observed in Google Earth Pro imagery. The classified images are converted from TIF to ASCII format using the "Raster to ASCII" command for input into IDRISI Selva. The CA-Markov model is applied to analyze historical LULC changes and to predict future trends.

Assessment of the accuracy of classification

Evaluating the accuracy and reliability of image classification methodologies is a crucial stage in the research process (Lu and Lu, 2023). To guarantee reliability and discrimination, it is advised that the accuracy level for LULC classification exceeds 90% as per previous studies (Junaid *et al*., 2023). Studies have emphasized the importance of validating the model and its accuracy in conducting a reliable LULC survey (Ruuska *et al*., 2018). This study relied on Kappa statistics and total accuracy to evaluate the effectiveness of classification maps. Google Earth images and satellite images are used to verify the results. An error matrix combined the land use map, classified land cover, and ground reference information. Several metrics were identified, such as product accuracy, user accuracy, overall accuracy, and Kappa coefficient (Foody, 2020). The proportion of correctly classified pixels in the confusion matrix determined overall accuracy, and the Kappa index indicated the degree of agreement between the classified map and the reference data used (Twele *et al*., 2016). The following equations are used to calculate these two measures:

$$Overall\ accuracy = \frac{D}{T} * 100\% \qquad (1)$$

where: *D* represents the total number of correct calls as summed along the major diagonal, and *T* represents the total number of correct calls in the error matrix. While the Kappa index ($\widehat{k}$) is calculated as follows:

$$\widehat{k} = \frac{T \sum_{n=1}^{r} Y_{nn} - \sum_{n=1}^{r} (Y_{n+} * Y_{+n})}{T^2 - \sum_{n=1}^{r} (Y_{n+} * Y_{+n})} \qquad (2)$$

where: *T* represents the total number of cells in the error matrix, *r* represents the number of rows in the matrix, Y_{nn} represents the total number of correct cells in a class (i.e., value in row *n* and column *n*), Y_{n+} represents the total for row *n*, Y_{+n} represents the total for column *n*.

Kappa indices are an essential tool for evaluating the accuracy of maps as they provide information about how closely the results match. If the kappa value is greater than or equal to 75%, the maps are highly consistent; if it is between 50% and 75%, the agreement is average; if it is less than or equal to 50%, it is poor (El Baroudy, 2016; Wan *et al*., 2015). As a result, to assess the CA-Markov model's ability to accurately simulate future land use and land cover conditions, Wang and Zheng (2023), after simulating land use and land cover for 2020 using classified images from 1990 and 2020, validated the CA-Markov model. Two map agreements (actual and simulated for 2020) were evaluated using the Kappa index of agreement (K_{IA}) (Mathanraj *et al*., 2021), such as no information Kappa (K_{no}), location Kappa ($K_{location}$), and standard Kappa ($K_{standard}$), using the CROSSTAB module in IDRISI Selva software.

Additionally, the simulated and actual areas of each land use and land cover class are compared using the validate module. Therefore, the Kappa index is a suitable indicator; thus, land use and land cover can be predicted for 2030, 2040, and 2050.

Methods

Land use and land cover change detection

Analyzing Land Use and Land Cover Change (LULCC) is essential to identify the particular changes in different land use categories (Spruce *et al.*, 2020). The land cover change detection map is used to assess and examine the temporal changes in land use and land cover within the defined area. The equation mentioned below is applied to estimate the size of the changes that occurred in each category:

$$C_i = R_i - B_i \qquad (3)$$

where: C_i represents the change in extent for the class i, B_i denotes the base image, and R_i is the most recent image.

The percentage change for each LULC class is calculated using the following equation:

$$P_i = \frac{R_i - B_i}{B_i} \qquad (4)$$

where: P_i denotes the percentage shift for the class i, and B_i denotes the base image, and R_i is the most recent image.

Land Use and Land Cover (LULC) Change Prediction Using Cellular Automata-Markov Model

The Cellular Automata-Markov (CA-Markov) model is a methodology that combines cellular automata and Markov chains. This approach aims to predict future trends and characteristics of LULC change. The cellular automata model looks at the uncertainty that comes from several sources, such as the relationships between model components, the design of the model, and the quality of the data used as input (Palmate *et al.*, 2022). On the other hand, the CA-Markov approach concentrates on the local interactions of cells, considering their behavior in space and time. This method benefits from suitable computational capabilities for dynamic simulation and visualization.

One of the most critical applications of the CA-Markov model involves analyzing the transition probabilities among different LULC classes across various periods (Nouri *et al.*, 2019). By examining these transition probabilities, insights can be gained into the driving forces behind land use changes and their potential future trajectories. This knowledge facilitates predicting LULC characteristics and their potential environmental, natural resource, and landscape implications (Deafalla, 2022). Leveraging the strengths of both Markov models and cellular automata, the CA-Markov model has proven effective in simulating land use change in previous studies (Abdelkarim, 2023). This model identifies potential spatial distributions of transitions (Wang *et al.*, 2021; Rimal *et al.*, 2018).

The following stages are implemented throughout the process: the base map and LULC maps for the period (1990-2020) at ten-year intervals, in addition to transition probability images used to create LULC maps for 1990, 2000, 2010, and 2020. Using IDRISI Terrset software, the transition probability and prospective transition images are processed. Subsequently, a potential transition map for 2000–2010 is established to duplicate the land use land cover map for 2020, and the Markov transition probability estimation technique is used to model land use land cover maps for the period (2030-2050) at ten-year intervals based on 2010−2020. The CA-Markov model utilizes the time factor to identify patterns and factors that contribute to future modification:

$$S(t, t+1) = f(S(t), n) \qquad (5)$$

where: n operates, representing the occurrence rate at any given moment, and $S(t+1)$ means the system status at the instant of $(t, t+1)$.

The CA-Markov model is frequently employed to anticipate future stability and change in LULC in a particular area, as well as to conduct ecological modeling and LULC monitoring. The following formula is employed to forecast future changes in LULC:

$$S(t, t+1) = S(t) * P_{ij} \qquad (6)$$

where: $S(t+1)$ is the system status at the time $t+1$ and, $S(t)$ is the system status at time t, P_{ij} is the transition probability matrix in a state, which is defined as:

$$= \left|\left|P_{ij}\right|\right| = \left\| \begin{matrix} P1,1 & P1,2 & P1,n \\ P2,1 & P2,2 & P2,n \\ Pn,1 & Pn,2 & Pn,n \end{matrix} \right\| (\,0 \leq P_{ij} \leq 1) \qquad (7)$$

where P represents the transition probability, P_{ij} represents the probability that a particular state will persist at any given time, and Pn represents the probability that it will transit from one state to another in the future.

A high transition probability is closer to (1) than a low transition probability (Nath *et al.*, 2023). A Markov chain analysis is conducted to generate a LULC transition matrix quantifying the probability of land cover changes between 1990-2000, 2000-2010, 2010-2020, and 1990-2020. This transition matrix served as a foundation for projecting future LULC dynamics. However, the Markov chain model exhibits limitations in capturing spatial dependencies, needing a mechanistic explanation for change processes and disregarding the spatial distribution of LULC, which are critical factors in simulating land cover patterns (Pandey *et al.*, 2021).

The cellular automata model is widely employed for the prediction of LULC due to its ability to simulate and regulate the dynamics of intricate spatial systems. A CA model comprises cells, cell space, neighborhood, time, and rules. It predicts new LULC patterns by considering the previous states of neighboring cells (Castro *et al.*, 2022). The influence of a neighbor on a cell's change is determined by their spatial proximity, with closer neighbors exerting a more significant impact. These weights are combined with transition probabilities to estimate the likelihood of changes in neighboring cells, preventing solely random predictions. Integrating Markov chain principles, the CA model incorporates the preceding LULC state and utilizes the conditions of neighboring cells to define transition rules (Koko *et al.*, 2020). The model's suitability for dynamic modelling within Geographic Information Systems and remote sensing environments is attributed to its analytical capabilities (Chuvieco, 2020). However, the CA model necessitates refinement to establish clear transition rules and modelling frameworks. As a result, integrating it with dynamic and other empirical models, like the Cellular Automata-Markov model, is essential for conducting a comprehensive analysis of LULC (Lacher *et al.*, 2023).

The procedures for running the CA-Markov model in the IDRISI-Selva program involve the following steps: The first stage entailed the execution of two models using land-cover maps for the periods 1990-2000, 2000-2010, 2010-2020, and 1990-2020. This process generated a transition probability matrix and a transition area matrix. The transition probability matrix is determined through cross-tabulation of multiple pairs of temporal images. Over a predetermined period, this matrix exhibits the likelihood of each land cover class transitioning to another. The transition area matrix contains the anticipated number of pixels that may transit from one land cover class to another over a specified number of time units. Simultaneously, the conditional probability map denotes the probability that each pixel of a land cover class will be situated at a site with a specific class after a particular time (Aneesha Satya *et al.*, 2020).

Transition probability matrices for periods 1 and 2 are generated by employing a variety of historical land use scenarios for the periods 1990-2000 and 2000-2020. The second stage entailed using a standard 5x5 adjacency filter to ascertain the perimeter of each cell. The scenario-based approach is implemented to simulate the prospective land use pattern during the final stage. LULC maps classified for 1990 and 2000 are employed to calibrate and refine the Markov algorithm. Time 1 is utilized in 1990, while time 2 is utilized in 2000. Transition probabilities between time one and time two are employed to simulate the land use pattern in 2020. The cellular automata Markov model is validated to assess the accuracy of its predictions for the year 2020. This process involves a statistical method to differentiate between locational and quantitative errors by comparing two images (Zhang *et al.*, 2021). The Kappa statistic index is employed to ascertain the degree of concordance between the actual and forecast 2020 land cover maps. An acceptable Kappa index is obtained, indicating reliable land use modelling and prediction. Subsequently, the classified land cover map of 2020 is utilized as a baseline for predicting potential land use in 2030, 2040, and 2050.

The Markov chain model determines the change in land area from the base year to the projected year. This model generates prospective probabilities of land cover and land use and a more comprehensive understanding of how to adapt factors that influence land cover and land use change, which benefits decision-makers (Tadese *et al.*, 2021). This model clarifies the dynamics of land cover and land use, which is crucial for developing and planning various land use policies that will improve the management of appropriate land cover and land use (Getu and Bhat 2022). The model effectively anticipates future land use shifts by analyzing the underlying causes of land use alterations, the suitability of different land use combinations, and other influential elements like transportation infrastructure, waterways, and urban centers. This model is particularly effective in simulating land use patterns in dispersed regions. In addition, the research has demonstrated that the CA-Markov model is more effective than other models in accurately simulating land use patterns and landscapes including the Artificial Neural Networks-Cellular Automata (ANN-CA) model, the Future Land Use Simulation (FLUS) model, and the Conversion of Land Use and its Effects (CLUE) model (Nath *et al.*, 2020; and Wang *et al.*, 2021).

Model Calibration and Validation

In the absence of accurate evaluation data, it becomes necessary to make future adjustments to the procedures for assessing prediction accuracy, model calibration, and validation to improve the modeling process. In a study conducted by Nath *et al.* (2020), the chi-square test (χ^2) was used to verify the accuracy of estimated land use images compared to real-world data for 2020. However, this comparison alone may not be sufficient to accurately assess the spatial distribution of land use classes in the study area. Therefore, researchers resorted to using the Kappa index, a more accurate statistical tool, to handle this issue (Debnath *et al.*, 2023). This technique involved calculating three types of Kappa index: location Kappa ($K_{location}$), quantity Kappa ($K_{quantity}$), and no information Kappa (K_{no}), to distinguish between spatial and quantitative errors in the predicted and actual images. These indices are used to evaluate the accuracy of the CA-Markov model, where higher values show a higher level of concordance between the model and reality. Kappa index values range from 0 to 1, as values closer to 1 indicate perfect agreement. According to Beroho and colleagues (2024) (Beroho *et al.*, 2023), a Kappa value of less than 0.5 indicates poor agreement, while a value of 0.75 indicates moderate agreement, and a value greater than 0.75 indicates strong agreement.

Results and Discussion

Changes in LULC categories in Babil Governorate

The study area exhibited four LULC classes, with an assessment revealing historical transformations and change patterns for each. The main LULC types in the study area include urban lands, bare soil land, water bodies, and vegetation lands, and the total quantity has

actually changed over the period 1990-2020. However, an evaluation of the transformations between these land cover categories showed a significant shift between them, as shown in Fig. 3 and Table 2. Babil Governorate faced several challenges, including urban expansion, loss of vegetation lands, and a decrease in water bodies.

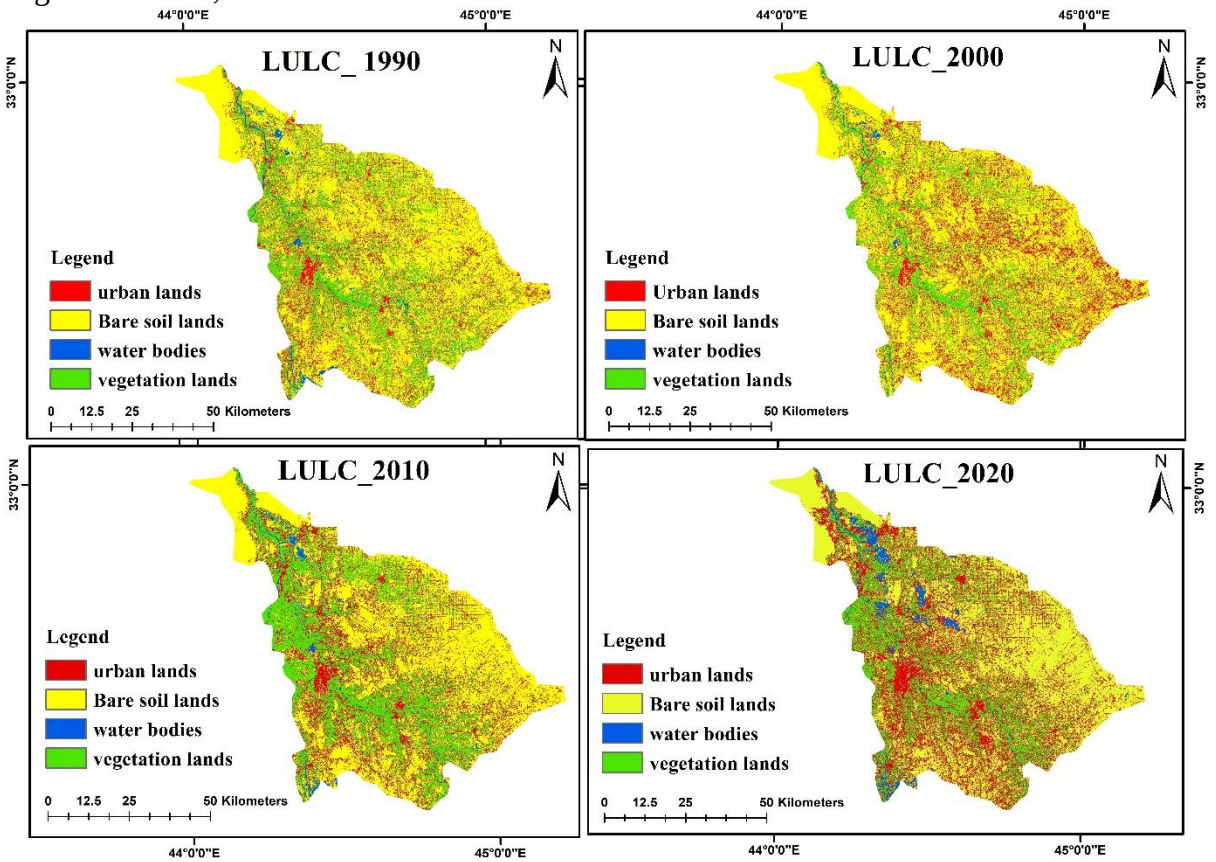


Fig. 3. LULC Changes in the Babil Governorate for 1990, 2000, 2010, and 2020.

Table 2: Distribution of LULC in Babil Governorate in 1990, 2000, 2010, and 2020.

Classes	1990		2000		2010		2020	
	Area (km^2)	Area %	Area (km^2)	Area %	Area (km^2)	Area %	Area (km^2)	Area %
Urban lands	921.8394	17.2770	1168.7976	21.9054	1160.6328	21.7524	1638.1863	30.7026
Bare soil lands	3034.5714	56.8735	3160.9935	59.2429	2525.7564	47.3373	2321.6850	43.5127
Water bodies	82.3518	1.5434	32.7924	0.6146	73.9260	1.3855	161.1567	3.0204
Vegetation lands	1296.8910	24.3061	973.0701	18.2371	1575.3384	29.5248	1214.6256	22.7643
Total	5335.6536	100	5335.6536	100	5335.6536	100	5335.6536	100

Table 2 presents data on land cover and land use in the region between 1990 and 2020, showing a significant increase in the area of urban land from 921.8394 km² to 1638.1863 km², attributed to population growth and urban expansion. Conversely, the area of bare soil land experienced a significant decrease from 3034.5714 km² to 2321.6850 km², as a result of conversion to other uses such as agriculture or construction. The area of water bodies also experienced fluctuations during the study period, depending on the volume of water imports from neighboring countries for the Euphrates River, as well as monthly releases from the governorate's water allocation and climate changes. The areas of vegetation land witnessed noticeable fluctuations between increases and decreases, mainly due to the expansion plans for crop cultivation implemented by the concerned authorities.

Overall, the data show significant shifts in land use between 1990 and 2020, represented by an expansion of urban and vegetation areas at the expense of a decrease in the area of bare soil land, reflecting population growth, urban expansion, and an increase in marketing plans for agricultural crop cultivation.

Cross-Tabulation Matrix Results

Based on the validation using Kappa indices, the CA-Markov model is deemed suitable for simulating the land cover and land use map for 2050 using transition probabilities from 1990 to 2020 and the 2020 class map as a baseline. Therefore, the model is deemed suitable for this application. The metrics are determined by employing the subsequent equations (Gasirabo *et al.*, 2023):

$$K_{no} = \frac{G_{(v)}\, H_{(n)}}{S_{(s)} - H_{(n)}} \quad (8)$$

$$K_{location} = \frac{G_{(v)}\, H_{(n)}}{S_{(v)} - H_{(v)}} \quad (9)$$

$$K_{standard} = \frac{G_{(v)}\, H_{(n)}}{S_{(s)} - H_{(v)}} \quad (10)$$

where: $G_{(v)}$, $H_{(v)}$, and $S_{(v)}$ provide moderate grid cell-level information, while $H_{(v)}$, $S_{(v)}$ and $S_{(s)}$ offer precise grid cell-level information across the topography.

An assessment is implemented to identify the components of agreement or disagreement (Table 3), and these reasons were categorized into two main classes: spatial distribution errors (0.1181) and quantity errors (0.0520). Thus, the results suggest that the primary cause of the discrepancy between the recorded and actual data was spatial distribution errors rather than quantity issues (refer to Fig. 4). Fig. 4 shows the simulation results. The results show a good similarity between the actual LULC of Babil Governorate in 2020 and the simulated land use and land cover. The model's performance in forecasting LULCCs was verified by simulating land use and land cover for 2020, utilizing transition probabilities for the period 1990-2000. Subsequently, the simulated results were compared to classified land use and land cover data for 2020, with differences in Kappa values employed as an accuracy measure.

The simulation analysis demonstrated a high level of agreement among the results, with Kappa indices of 0.79 for both K_{no}, and $K_{location}$, and 0.72 for $K_{standard}$, as shown in Table 4. This indicates the reliability and effectiveness of the model in predicting future land cover and land use in the biosphere. Furthermore, visual inspection reveals a relatively close match between the land cover and land use classes in the simulated data and the classified data for 2020. These findings suggest that the modeling outcomes are reliable and that the broad patterns of modeled land cover and land use closely align with real-world patterns.

Table 3: Validation assessment determines levels of agreement and disagreement between the two images.

Agreement / Disagree	Value	Value %
Agreement Chance	0.2000	20.00
Agreement Quantity	0.1853	18.53
Agreement Strata	0.0000	00.00
Agreement Grid cell	0.4445	44.45
Disagree Grid cell	0.1181	11.81
Disagree Strata	0.0000	00.00
Disagree Quantity	0.0520	5.20

Table 4: Validate the simulated 2020 Land Use Land Cover image.

Coefficient	Value	Value %
K_{no}	0.79	79 %
$K_{location}$	0.79	79 %
$K_{standard}$	0.72	72 %

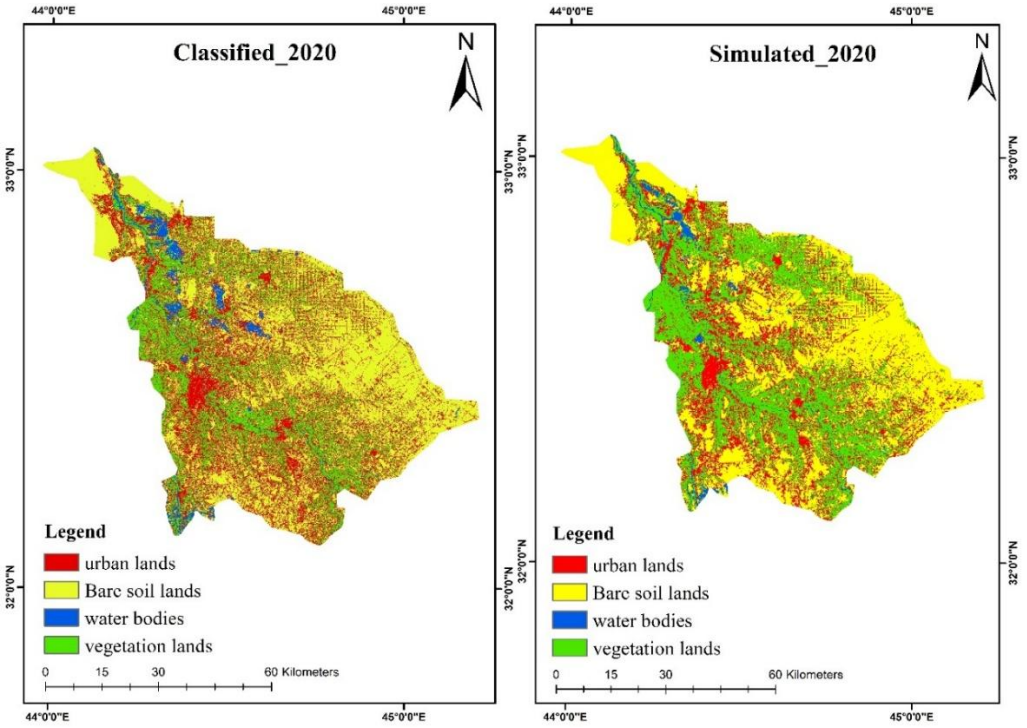


Fig. 4. Classified and simulated LULC maps for 2020: modelled and annotated.

LULCC Prediction Results in the Coming 2030, 2040 and 2050 years

A transition probability matrix is calculated to model the likelihood of land cover changes between 1990 and 2020 (Table 5). This matrix is then used to predict future land cover and land use patterns in the years 2030, 2040, and 2050.

Table 5. Transition probability matrix over the period 1990–2020.

	2020			
1990	**Urban lands**	**Bare soil lands**	**Water bodies**	**Vegetation lands**
Urban lands	0.4517	0.3515	0.0165	0.1804
Bare soil lands	0.2805	0.5894	0.0352	0.095
Water bodies	0.0929	0.1088	0.5885	0.2098
Vegetation lands	0.3631	0.1606	0.0203	0.4559

The presented matrix shows the probability of land use changes between 1990 and 2020. The matrix indicates an increased probability of other land use types transforming into urban areas between 1990 and 2020. This trend is driven by factors such as population growth, urban expansion, and economic transformation. The matrix shows a probability of urban land transforming into bare soil land (0.3515) due to the security instability and military operations between 2003 and 2017 in the governorate. The matrix shows a probability of bare soil land transforming into urban land (0.2805). This may reflect changes in the direction of urban expansion due to the unstable security situation. The matrix indicates a low probability of water bodies transforming into other land-use types. This may be due to the importance of water bodies for ecosystems and the existence of laws to protect them. The matrix shows a probability of vegetation lands transforming into urban lands (0.3631) due to population growth and urban expansion. These changes are taken into account when forecasting future transformations in 2030, 2040, and 2050. Based on the ongoing changes, changes in LULC are designed, and a change map for the years 2030, 2040, and 2050 is obtained. From Fig. 6, it can be observed that the changes will occur mainly in water bodies and barren lands, and how their extent will expand. The study predicts a gradual increase in urban areas, a sharp decline in barren lands, and a significant growth in water bodies, with relative stability of green areas, reflecting the impacts of urban expansion, climate change, and changing land use patterns. In 2030, the area of urban land will reach approximately 0.2231847 square kilometers, increasing to 1875.1473

square kilometers in 2040, and then decreasing slightly to 2793.1860 square kilometers in 2050. These results indicate a trend towards urban expansion, which is common in many areas due to population growth and economic development. In contrast to urban areas, barren lands are expected to experience a significant decrease in their area. In 2030, the area of barren land will be approximately 2156.8860 square kilometers, decreasing to 2089.2600 square kilometers in 2040, and then decreasing further to 1810.1160 square kilometers in 2050. This decrease may be attributed to several factors, such as urban expansion or changing land use for other purposes. Regarding water bodies, they are expected to experience a significant increase in their area. In 2030, the area of water bodies will be approximately 228.1797 square kilometers, increasing to 259.7607 square kilometers in 2040, and then experiencing a significant jump to 554.4297 square kilometers in 2050. This significant increase may be the result of the construction of dams and reservoirs, changes in rainfall patterns, or other factors affecting the water cycle. On the other hand, green areas are expected to experience relatively minor changes during the projected period. In 2030, the area of land covered by vegetation will be approximately 1103.5656 square kilometers, increasing slightly to 1111.4856 square kilometers in 2040, and then decreasing slightly to 1110.8286 square kilometers in 2050. These results indicate a relative stability in the area of green land with some minor fluctuations (Fig. 5 and Table 6).

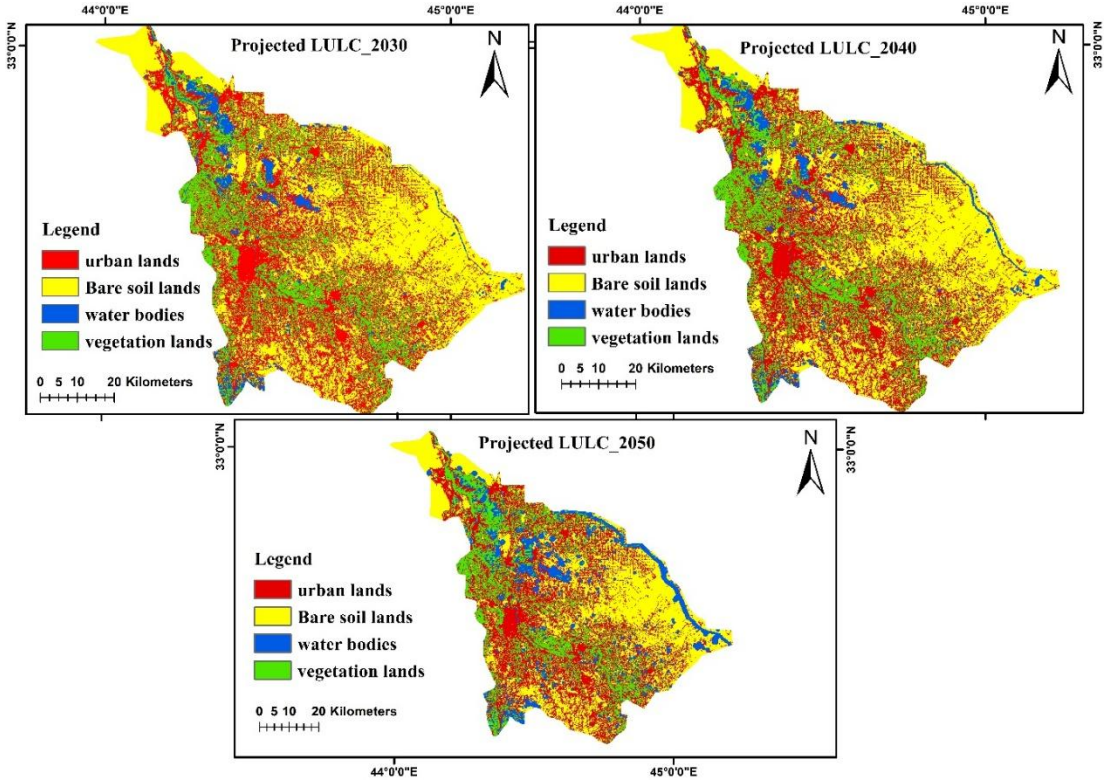


Fig. 5. Projected LULC for 2030, 2040, and 2050.

Table 6. Statistical distribution of the modeled LULC in 2020, 2030, 2034, and 2050.

Classes	2020		2030		2040		2050	
	Area (km^2)	Area %	Area (km^2)	Area %	Area (km^2)	Area %	Area (km^2)	Area %
Urban lands	1638.1863	30.7026	1847.0223	34.6166	1875.1473	35.1437	1860.2793	34.8651
Bare soil lands	2321.6850	43.5127	2156.8860	40.4240	2089.2600	39.1566	1810.1160	33.9249
Water bodies	161.1567	3.0204	228.1797	4.2765	259.7607	4.8684	554.4297	10.3910
Vegetation lands	1214.6256	22.7643	1103.5656	20.6829	1111.4856	20.8313	1110.8286	20.8190
Total	**5335.6536**	**100**	**5335.6536**	**100**	**5335.6536**	**100**	**5335.6536**	**100**

The results indicate the likelihood of significant transformations in Land Use and Land Cover (LULC) patterns within the study area as demonstrated by the Cellular Automata-Markov (CA-Markov) model. This model has proven highly efficient in simulating spatiotemporal changes in LULC patterns, confirming the area's exposure to varying levels of

dynamics and change. Therefore, strategic land use planning and water resource management are of paramount importance under these circumstances. Studying how land is used and how it has changed in the past, along with the reasons for these changes, is crucial for predicting how land will be used in the future. Science supports this hypothesis, and this is precisely the approach taken in this study (Keshtkar and Voigt, 2016). Therefore, documenting these transformations is essential to support future decision-making. However, given this study's focus on direct driving factors, uncertainty about future LULC patterns necessitates the integration of additional factors into the modeling process, such as population changes, changes in the climate, natural disasters, and the state of the economy. This would contribute to a deeper understanding of the complex LULC change processes and thus the development of more comprehensive and effective management strategies.

Conclusion

This study aims to assess and predict future changes in Land Use and Land Cover (LULC) in Babil Governorate. In order to achieve this goal, a hybrid-integrated model combining cellular automata and Markov chains is employed. GIS techniques and multi-temporal satellite data are used to monitor changes in LULC from 1990 to 2020.

By reviewing the transformation of LULC changes in Babil Governorate from 1990 to 2020, it reveals a significant increase in urban area, primarily due to population growth and urban expansion. Conversely, barren lands experienced a noticeable decline as they were converted to other uses such as agriculture and construction. Water bodies, on the other hand, exhibited fluctuations in their area during the study period, influenced by climate changes and water imports from neighboring countries. Additionally, the area of green lands increased due to the rise in marketing plans for crops. Overall, these results demonstrate substantial transformations in land use within the governorate, with urban and green areas expanding at the expense of barren lands, reflecting the demographic, economic, and environmental changes experienced by the governorate.

The study divides the LULC maps into four primary classes: urban areas, barren lands, water bodies, and green areas. This detailed classification enabled a comprehensive understanding of the spatial distribution of different land use types in the governorate, facilitating the prediction of future scenarios. The accuracy of the simulated LULC map for 2020 is assessed using the Kappa index, and the evaluation results show agreement with the map extracted from satellite images, confirming the efficiency of the model used in the simulation. The analysis reveals that the factors influencing LULC changes vary with the type of cover and evolve.

The advanced CA-Markov model is used to simulate LULC patterns in the governorate until 2050. The simulation results demonstrate the model's ability to generate accurate future LULC scenarios, indicating its high efficiency in this field. Despite the promising results obtained by the study, it is essential to emphasize the importance of integrating the latest local population statistics into future simulation models. This is because population growth is a significant factor influencing land use changes, and neglecting it could reduce the accuracy of predictions. Therefore, future studies should focus on analyzing the complex relationship between population growth and LULC changes for a more comprehensive understanding of long-term environmental change processes and their impact on the sustainability of natural resources.

Acknowledgments

We would like to express our sincere gratitude to all those who contributed to the success of this research, especially the Hindiya Dam Irrigation Project Directorate in Babil and the Babil Municipality Directorate, for providing us with valuable information and data that contributed to the completion of this work.

References

Abdelkarim, A.J.G., 2023. Monitoring and forecasting of land use/land cover (LULC) in Al-Hassa Oasis, Saudi Arabia based on the integration of the Cellular Automata (CA) and the Cellular Automata-Markov Model (CA-Markov). Geology, Ecology, and Landscapes, pp. 1-32. https://doi.org/10.1080/24749508.2022.2163741

Aneesha Satya, B., Shashi, M. and Deva, P., 2020. Future land use land cover scenario simulation using open-source GIS for the city of Warangal, Telangana, India. Applied Geomatics, 12(3), pp. 281-290. https://doi.org/10.1007/s12518-020-00298-4

Anwar, Z., Alam, A., Elahi, N. and Shah, I., 2022. Assessing the trends and drivers of land use land cover change in district Abbottabad lower Himalayan Region Pakistan. Geocarto International, 37(25), pp. 10855-10870. https://doi.org/10.1080/10106049.2022.2040604

Beroho, M., Briak, H., Cherif, E.K., Boulahfa, I., Ouallali, A., Mrabet, R., Kebede, F., Bernardino, A. and Aboumaria, K., 2023. Future scenarios of land use/land cover (LULC) based on a CA-Markov simulation model: case of a Mediterranean watershed in Morocco. Remote Sensing, 15(4), 1162. https://doi.org/10.3390/rs15041162

Castro, M.L., Machado, P., Santos, I., Rodriguez-Fernandez, N., Torrente-Patiño, A. and Carballal, A., 2022. State of the art on artificial intelligence in land use simulation. Complexity, 2022(1), 2291508. https://doi.org/10.1155/2022/2291508

Chuvieco, E., 2020. Fundamentals of satellite remote sensing: An environmental approach. CRC Press: Boca Raton, FL, USA. https://doi.org/10.1201/9780429506482

Cuevas, S.C., 2016. The interconnected nature of the challenges in mainstreaming climate change adaptation: evidence from local land use planning. Climatic change, 136(3), pp. 661-676. https://doi.org/10.1007/s10584-016-1625-1

Das, P., Behera, M.D., Pal, S., Chowdary, V.M., Behera, P.R. and Singh, T.P., 2019. Studying land use dynamics using decadal satellite images and Dyna-CLUE model in the Mahanadi River basin, India. Environmental monitoring and assessment, 191, pp. 1-17. https://doi.org/10.1007/s10661-019-7698-3

Deafalla, T., 2022. Integrative Assessment and Modelling of the Non-Timber Forest Products Potential in Nuba Mountains of Sudan by Field Methods, Remote Sensing and GIS, Ph.D. Thesis, Unterkünfte in der Nähe, Dresden, Germany. https://tud.qucosa.de/api/qucosa%3A78638/attachment/ATT-0/

Debnath, J., Sahariah, D., Lahon, D., Nath, N., Chand, K., Meraj, G., Kumar, P., Singh, S.K., Kanga, S. and Farooq, M., 2023. Assessing the impacts of current and future changes of the planforms of river Brahmaputra on its land use-land cover. Geoscience Frontiers, 14(4), 101557. https://doi.org/10.1016/j.gsf.2023.101557

El Baroudy, A.A., 2016. Mapping and evaluating land suitability using a GIS-based model. Catena, 140, pp. 96-104. https://doi.org/10.1016/j.catena.2015.12.010

Fei, R., Lin, Z. and Chunga, J., 2021. How land transfer affects agricultural land use efficiency: Evidence from China's agricultural sector. Land Use Policy, 103, 105300. https://doi.org/10.1016/j.landusepol.2021.105300

Feng, B., Zhang, Y. and Bourke, R., 2021. Urbanization impacts on flood risks based on urban growth data and coupled flood models. Natural Hazards, 106(1), pp. 613-627. https://doi.org/10.1007/s11069-020-04480-0

Foody, G.M., 2020. Explaining the unsuitability of the kappa coefficient in the assessment and comparison of the accuracy of thematic maps obtained by image classification. Remote sensing of environment, 239, 111630. https://doi.org/10.1016/j.rse.2019.111630

Gasirabo, A., Xi, C., Hamad, B.R. and Edovia, U.D., 2023. A CA–Markov-Based Simulation and Prediction of LULC Changes over the Nyabarongo River Basin, Rwanda. Land, 12(9), 1788. https://doi.org/10.3390/land12091788

Getu, K. and Bhat, H.G., 2022. Dynamic simulation of urban growth and land use change using an integrated cellular automata and Markov chain models: a case of Bahir Dar city, Ethiopia. Arabian Journal of Geosciences, 15(11), 1049. https://doi.org/10.1007/s12517-022-10304-1

Hashim, A.H., Jasim, O.Z. and Salih, M.M., 2022. The Establishing of Geospatial Database for Agricultural Lands of Islamic WAQF In Iraq: Case Study Babil Province. In IOP Conference Series: Earth and Environmental Science 961(1), 012025. IOP Publishing. https://doi. 10.1088/1755-1315/961/1/012025

Junaid, M., Sun, J., Iqbal, A., Sohail, M., Zafar, S. and Khan, A., 2023. Mapping LULC dynamics and its potential implication on forest cover in malam jabba region with landsat time series imagery and random forest classification. Sustainability, 15(3), 1858. https://doi.org/10.3390/su15031858

Keshtkar, H. and Voigt, W., 2016. A spatiotemporal analysis of landscape change using an integrated Markov chain and cellular automata models. Modeling Earth Systems and Environment, 2, pp. 1-13. https://doi.org/10.1007/s40808-015-0068-4

Kisamba, F.C. and Li, F., 2023. Analysis and modelling urban growth of Dodoma urban district in Tanzania using an integrated CA–Markov model. Geo Journal, 88(1), pp. 511-532. https://doi.org/10.1007/s10708-022-10617-4

Koko, A.F., Yue, W., Abubakar, G.A., Hamed, R. and Alabsi, A.A.N., 2020. Monitoring and predicting spatio-temporal land use/land cover changes in Zaria City, Nigeria, through an integrated cellular automata and Markov chain model (CA-Markov). Sustainability, 12(24), 10452. https://doi.org/10.3390/su122410452

Lacher, I., Fergus, C., McShea, W.J., Plisinski, J., Morreale, L. and Akre, T.S., 2023. Modeling alternative future scenarios for direct application in land use and conservation planning. Conservation Science and Practice, 5(7), e12940. https://doi.org/10.1111/csp2.12940

Lin, W., Sun, Y., Nijhuis, S. and Wang, Z., 2020. Scenario-based flood risk assessment for urbanizing deltas using future land-use simulation (FLUS): Guangzhou Metropolitan Area as a case study. Science of the Total Environment, 739, 139899. https://doi.org/10.1016/j.scitotenv.2020.139899

Lu, Z. and Lu, Y., 2023. Enhancing the reliability of image classification using the intrinsic features. Knowledge-Based Systems, 263, 110256. https://doi.org/10.1016/j.knosys.2023.110256

Liu, X., Liang, X., Li, X., Xu, X., Ou, J., Chen, Y., Li, S. and Pei, F., 2017. A future land use simulation model (FLUS) for simulating multiple land use scenarios by coupling human and natural effects. Landscape and Urban Planning, 168, pp. 94–116. http://dx.doi.org/10.1016/j.landurbplan.2017.09.019

Marti, R., Gascoin, S., Berthier, E., De Pinel, M., Houet, T. and Laffly, D., 2016. Mapping snow depth in open alpine terrain from stereo satellite imagery. The Cryosphere, 10(4), pp. 1361-1380. https://doi.org/10.5194/tc-10-1361-2016

Mathanraj, S., Rusli, N. and Ling, G.H.T., 2021. Applicability of the CA-Markov model in land-use/land cover change prediction for urban sprawling in Batticaloa Municipal Council, Sri Lanka. In IOP Conference Series: Earth and Environmental Science (Vol. 620, No. 1, p. 012015). IOP Publishing. https://doi.org/10.1088/1755-1315/620/1/012015

Matlhodi, B., Kenabatho, P.K., Parida, B.P. and Maphanyane, J.G., 2021. Analysis of the future land use land cover changes in the Gaborone dam catchment using CA-Markov model: Implications on water resources. Remote Sensing, 13(13), 2427. https://doi.org/10.3390/rs13132427

Mohan, C., Western, A.W., Wei, Y. and Saft, M., 2018. Predicting groundwater recharge for varying land cover and climate conditions–a global meta-study. Hydrology and Earth System Sciences, 22(5), 2689-2703. https://doi.org/10.5194/hess-22-2689-2018.

Nath, B., Choudhury, N. and Mitra, A.K., 2022. Observing tectonic-geomorphological changes along the Dawki Fault and adjoining areas of Sylhet, Bangladesh from 1980 to 2020 using remote sensing and GIS techniques. Journal of Earth System Science, 131(3), 160. https://doi.org/10.1007/s12040-022-01900-6

Nath, B., Wang, Z., Ge, Y., Islam, K., P. Singh, R. and Niu, Z., 2020. Land use and land cover change modeling and future potential landscape risk assessment using Markov-CA model and analytical hierarchy process. ISPRS International Journal of Geo-Information, 9(2), 134. https://doi.org/10.3390/ijgi9020134

Nath, N., Sahariah, D., Meraj, G., Debnath, J., Kumar, P., Lahon, D. and Kanga, S., 2023. Land use and land cover change monitoring and prediction of a UNESCO world heritage site: Kaziranga eco-sensitive zone using cellular automata-Markov model. Land, 12(1), 151. https://doi.org/10.3390/land12010151

Nouri, H., Faramarzi, M.M. and Sadeghi, S.H., 2019. Impact of regional rangeland cover degradation on increasing dusty days in West of Iran. Journal of Rangeland Science, 9(3), pp. 286-299. https://oiccpress.com/journal-of-rangeland-science/article/impact-of-regional-rangeland-cover-degradation-on-increasing-dusty-days-in-west-of-iran/

Okiemute, E.S., Oduyebo, O.F. and Olulade, S.A., 2018. On the determination of NTM and UTM positions from post processing of static DGPS observations on the Nigeria Minna Datum. Eteje SO, Oduyebo OF and Olulade SA (2018): On the Determination of NTM and UTM Positions from Post Processing of Static DGPS Observations on the Nigeria Minna Datum. International Journal of Engineering Research and Advanced Technology (IJERAT), 4(10), pp. 10-24. http://doi.org/10.31695/IJERAT.2018.3332

Palmate, S.S., Wagner, P.D., Fohrer, N. and Pandey, A., 2022. Assessment of uncertainties in modelling land use change with an integrated cellular automaton–Markov chain model. Environmental Modeling and Assessment, pp. 1-19. https://doi.org/10.1007/s10666-021-09804-3

Pandey, S., Kumar, P., Zlatic, M., Nautiyal, R. and Panwar, V.P., 2021. Recent advances in assessment of soil erosion vulnerability in a watershed. International Soil and Water Conservation Research, 9(3), pp. 305-318. https://doi.org/10.1016/j.iswcr.2021.03.001

Popp, A., Calvin, K., Fujimori, S., Havlik, P., Humpenöder, F., Stehfest, E., Bodirsky, B.L., Dietrich, J.P., Doelmann, J.C., Gusti, M. and van Vuuren, D.P., 2017. Land-use futures in the shared socio-economic pathways. Global Environmental Change, 42, pp. 331-345. https://doi.org/10.1016/j.gloenvcha.2016.10.002

Rai, P.K., Chandel, R.S., Mishra, V.N. and Singh, P., 2018. Hydrological inferences through morphometric analysis of lower Kosi River basin of India for water resource management based on remote sensing data. Applied water science, 8, pp. 1-16. https://doi.org/10.1007/s13201-018-0660-7

Riggio, J., Baillie, J.E., Brumby, S., Ellis, E., Kennedy, C.M., Oakleaf, J.R., Tait, A., Tepe, T., Theobald, D.M., Venter, O., Watson, J.E. M. and Jacobson, A.P., 2020. Global human influence maps reveal clear opportunities in conserving Earth's remaining intact terrestrial ecosystems. Global Change Biology, 26(8), pp. 4344-4356. https://doi.org/10.1111/gcb.15109

Rimal, B., Zhang, L., Keshtkar, H., Haack, B.N., Rijal, S. and Zhang, P., 2018. Land use/land cover dynamics and modeling of urban land expansion by the integration of cellular automata and markov chain. ISPRS International Journal of Geo-Information, 7(4), 154. https://doi.org/10.3390/ijgi7040154

Ruben, G.B., Zhang, K., Dong, Z. and Xia, J., 2020. Analysis and projection of land-use/land-cover dynamics through scenario-based simulations using the CA-Markov model: A case study in Guanting Reservoir Basin, China. Sustainability, 12(9), 3747. https://doi.org/10.3390/su12093747

Ruuska, S., Hämäläinen, W., Kajava, S., Mughal, M., Matilainen, P. and Mononen, J., 2018. Evaluation of the confusion matrix method in the validation of an automated system for measuring feeding behaviour of cattle. Behavioural processes, 148, pp. 56-62. https://doi.org/10.1016/j.beproc.2018.01.004

Spruce, J., Bolten, J., Mohammed, I.N., Srinivasan, R. and Lakshmi, V., 2020. Mapping land use land cover change in the Lower Mekong Basin from 1997 to 2010. Frontiers in environmental science, 8, 21. https://doi.org/10.3389/fenvs.2020.00021

Tadese, S., Soromessa, T. and Bekele, T., 2021. Analysis of the current and future prediction of land use/land cover change using remote sensing and the CA-Markov model in Majang forest biosphere reserves of Gambella, Southwestern Ethiopia. The scientific world journal, 2021(1), 6685045. https://doi.org/10.1155/2021/6685045

Twele, A., Cao, W., Plank, S. and Martinis, S., 2016. Sentinel-1-based flood mapping: a fully automated processing chain. International Journal of Remote Sensing, 37(13), pp. 2990-3004. https://doi.org/10.1080/01431161.2016.1192304

Talib, Z.R. and Laffta, S.J., 2024. Analysis of the Agricultural Drought Causes in Babylon Province. Iraqi Journal of Science, pp. 4667-4676. https://doi: 10.24996/ijs.2024.65.8.43

Wan, T.A.N.G., Jun, H.U., Zhang, H., Pan, W.U. and Hua, H.E., 2015. Kappa coefficient: a popular measure of rater agreement. Shanghai archives of psychiatry, 27(1), 62. https://doi.org/10.11919%2Fj.issn.1002-0829.215010

Wang, Q., Guan, Q., Lin, J., Luo, H., Tan, Z. and Ma, Y., 2021. Simulating land use/land cover change in an arid region with the coupling models. Ecological Indicators, 122, 107231. https://doi.org/10.1016/j.ecolind.2020.107231

Wang, S.W., Munkhnasan, L. and Lee, W.K., 2021. Land use and land cover change detection and prediction in Bhutan's high-altitude city of Thimphu, using cellular automata and Markov chain. Environmental Challenges, 2, 100017. https://doi.org/10.1016/j.envc.2020.100017

Wang, S. and Zheng, X., 2023. Dominant transition probability: Combining CA-Markov model to simulate land use change. Environment, Development and Sustainability, 25(7), pp. 6829-6847. https://doi.org/10.1007/s10668-022-02337-z .

Zhang, Z., Hu, B., Jiang, W. and Qiu, H., 2021. Identification and scenario prediction of degree of wetland damage in Guangxi based on the CA-Markov model. Ecological Indicators, 127, 107764. https://doi.org/10.1016/j.ecolind.2021.107764

https://en.wikipedia.org/wiki/Babylon_Governorate

Iraqi National Journal of Earth Science

www.earth.uomosul.edu.iq

Sedimentological Study and Age Determination of the Shiranish Formation in Perat Anticline, Northern Iraq

Mohammed W. Al-Abbasi [1*], Omar A. Al-Badrani [2], Majid M. Al-Mutwali [3], Zaid A. Malak [4]

[1]*College of Environmental Sciences, University of Mosul, Iraq.*
[2,4] *Department of Geology and Petroleum, College of Science, University of Mosul, Mosul, Iraq.*
[3] *Collage of Petroleum and Mining Engineering, University of Mosul, Iraq.*

Article information

Received: 23- Nov -2024

Revised: 30 -Dec -2024

Accepted: 19- Feb -2025

Available online: 01- Jan -2026

Keywords:
Shiranish Fn,
Nannofossils,
Foraminifera,
Perat,
Iraq,

Correspondence:
Name: Mohammed W. Al-Abbasi

Email: mws3000@uomosul.edu.iq

ABSTRACT

A sedimentological and nannofossil biostratigraphical study of the Shiranish Formation focuses on an exposed section of the Perat anticline's northern limb. The formation consists of limestone, marl, and marly limestone. It produces a diverse range of calcareous nannofossils, planktic foraminiferal fauna, and some bioclasts. The calcareous nannofossil's stratigraphic distribution allows for the identification of three distinct biozones. These are Uniplanarius trifidus Interval zone (cc22), Tranolithus phacelosus Interval zone (Part) (cc23), and Reinhardites levis Interval zone (cc24), which indicate that the age of the studied Shiranish Formation in Perat anticline is estimated to span from Late Campanian to Early Maastrichtian. On the other hand, the studied section is composed of Globular Planktic Foraminiferal lime wackestone microfacies (Sh1), Keeled Planktic Foraminiferal lime wackestone microfacies (Sh2), Bioclastic lime wackestone microfacies (Sh3), Argillaceous Planktic Foraminiferal lime packstone microfacies (Sh4), and Marl lithofacies (Sh5). The formation's depositional habitats extend from the middle shelf to the upper bathyal based on the distinctive characteristics of these facies.

DOI: 10.33899/injes.v26i1.60219, ©Authors, 2026, College of Science, University of Mosul.
This is an open-access article under the CC BY 4.0 license (http://creativecommons.org/licenses/by/4.0/) .

دراسة رسوبية وتحديد عمر تكوين شرانش في طية بيرات المحدبة، شمالي العراق

محمد وليد العباسي[1*] ، عمر احمد البدراني[2]، ماجد مجدي المتولي[3]، زيد عبدالوهاب ملك[4]

[1] *كلية العلوم البيئية، جامعة الموصل، الموصل، العراق.*

[2،4] *قسم علوم الأرض والنفط، كلية العلوم، جامعة الموصل، الموصل، العراق.*

[3] *كلية هندسة النفط والتعدين، جامعة الموصل، الموصل، العراق.*

معلومات الارشفة

تاريخ الاستلام: 23– نوفمبر – 2024

تاريخ المراجعة: 30– ديسمبر – 2024

تاريخ القبول: 19– فبراير – 2025

تاريخ النشر الالكتروني: 01– يناير – 2026

الكلمات المفتاحية:

تكوين شرانش،

النانو،

الفورامينفرا،

بيرات،

العراق،

المراسلة:

الاسم: محمد وليد العباسي

Email: mws3000@uomosul.edu.iq

الملخص

اجريت دراسة رسوبية وطباقية حياتية لمقطع سطحي من تكوين شرانش الذي يقع ضمن الطرف الشمالي من طية بيرات المحدبة. تتألف صخارية التكوين في منطقة الدراسة من طبقات الحجر الجيري والحجر الجيري المارلي وصخور المارل، والتي امتازت بمحتواها الجيد من متحجرات النانو الكلسية وحشود الفورامنيفرا الطاقية مع القليل من حطام الاصداف. وقد افرزت دراسة الطباقية الحياتية لمتحجرات النانو تشخيص ثلاثة انطقة حياتية وهي: *Uniplanarius trifidus* Interval zone (cc22), *Tranolithus phacelosus* Interval zone (Part) (cc23), *Reinhardites levis* Interval zone (cc24). ومن خلال مقارنة هذه الانطقة مع الانطقة العالمية والمسجلة في مناطق متفرقة، تم تحديد عمر التكوين بالكامباني المتأخر–الماسترختي المبكر. من جهة أخرى فقد قسمت صخور التكوين الى خمسة سحنات رسوبية وهي: سحنة الحجر الجيري الواكي الحاملة لمتحجرات الفورامنيفرا الطافية ذات الحجرات الكروية (Sh1) وسحنة الحجر الجيري الواكي الحاملة لمتحجرات الفورامنيفرا الطاقية ذات الجؤجؤ (Sh2) وسحنة الحجر الجيري الواكي الحاملة لحطام الاحياء (Sh3) وسحنة الحجر الجيري–الطيني الواكي الحاملة لمتحجرات الفورامنيفرا الطاقية (Sh4) والسحنة الصخارية للمارل (Sh5) . هذه السحنات قد عكست صفات ومحتويات البيئة الترسيبية للتكوين في منطقة الدراسة والتي امتدت من الرصيف الأوسط – الباثيال الأعلى.

DOI: 10.33899/injes.v26i1.60219, ©Authors, 2026, College of Science, University of Mosul.
This is an open-access article under the CC BY 4.0 license (http://creativecommons.org/licenses/by/4.0/).

Introduction

Around the village of Shiranish Islam, which is located 17 kilometers northeast of Zakho City, (Henson 1940; in Bellen et al., 1959) first described the Shiranish Formation. Within the type section of the formation, there are two units: the upper unit (99 m) is composed of blue marl, while the bottom one (128 m) is thinly bedded with blue limestone. However, Al-Qayim et al. (1986) separated the type section into three parts, where the marly- and shaly-limestone make up the lower part (65 m), the sandstone and limestone make up the middle part (20 m), and the bluish marly shale makes up the upper part (100 m). It is reported that the formation environment is located far from the shore in a deep, open ocean environment. Al-Badrani (2001) examined the Ammonites of the lower Shiranish Formation in the Sinjar area and concluded that the depositional environment of the formation represents the upper continental slope. According to the examination of microfacies, Al-Atroshi (2007) deduced that the upper-middle bathyal and outer shelf environments are the depositional settings of the Shiranish Formation in the Duhok region. Furthermore, the age of the formation in the same area (Duhok) was determined to be Late Campanian-Maastrichtian (Al-Mutwali and Al-Juboury, 2005; Bamarni, 2010) through their studies of the foraminifera and biostratigraphy of the formation. Alrashedi (2013) used the study of planktic foraminifera to examine the biostratigraphy of the Shiranish Formation on the southern limb of the Perat anticline within the Bekhma area. He concluded

that the formation extends from the Late Campanian–Early Late Maastrichtian period. Finally, the depositional habitat of the Shiranish Formation, which is middle Campanian in age, ranges from the outer shelf to the upper bathyal according to research done by Al-Dulaimi et al. (2023) on the litho- and biostratigraphy of the Shiranish Formation in the Diana area.

Given the lack of research on the studied formation at the northern limb of Perat anticline, this study goals to identify the fossil species of calcareous nannofossil, to determine their biostratigraphic zones for age determination, and to conclude the paleoenvironmental context based on facies analysis.

Studied Section

Location: It is located near the Bekhma Dam tunnel on the northern limb of the Perat anticline to the southwest of the residential complex (Fig. 1). Within the Unstable Shelf's High Folded Zone, the section's midpoint is located at latitude (36° 42′ 00″) and longitude (44° 17′ 00″).

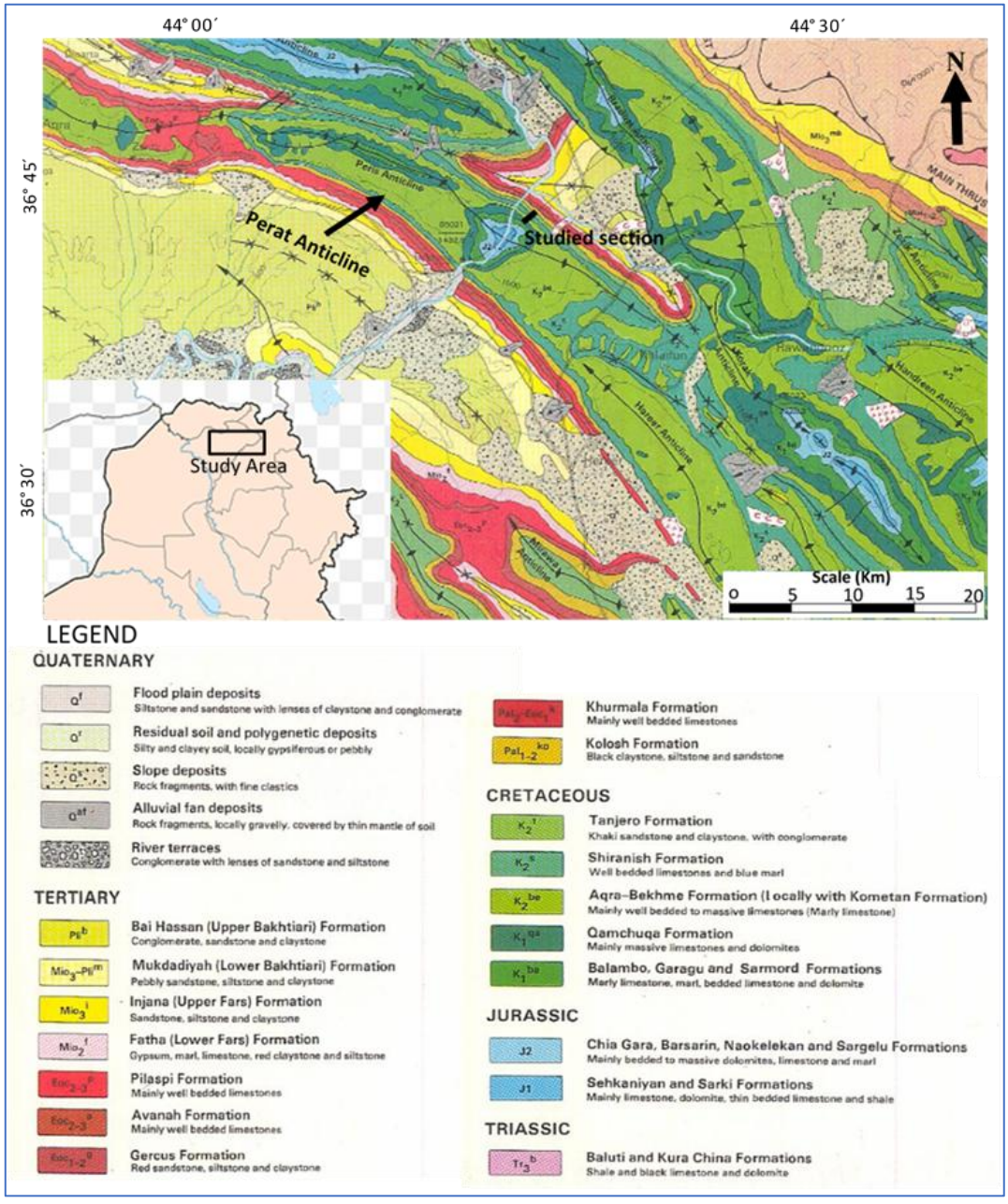


Fig. 1. Geological map of the studied area (after Sissakian et al., 1997).

Lithology: The studied section's thickness is approximately 154 m (Fig. 2). The lower contact of Shiranish Formation with Bekhma Formation is not clear due to its coverage by recent sediments. Gray marly limestone and pale gray limestone (30-150 cm thick) are intercalated by thin beds of pale green marl, which represent the bottom portion of the formation (Fig. 3), followed by sequences of pale green marl that are roughly 20 m thick. The middle portion is made up of a series of beds that are 40 cm to 2 m thick of pale grey argillaceous limestone, 30 cm to 3 m thick of greenish grey marly limestone, and 30 cm to 5 m thick of greenish marl (Fig. 4). Whereas the upper portion is distinguished by a predominance of greenish-grey marl beds mixed with a very small number of limestone beds, each is not thicker than 10 cm, and on its top, there are thick beds of light grey limestone (Fig. 5). The upper boundary is comfortable with the Tanjero Formation.

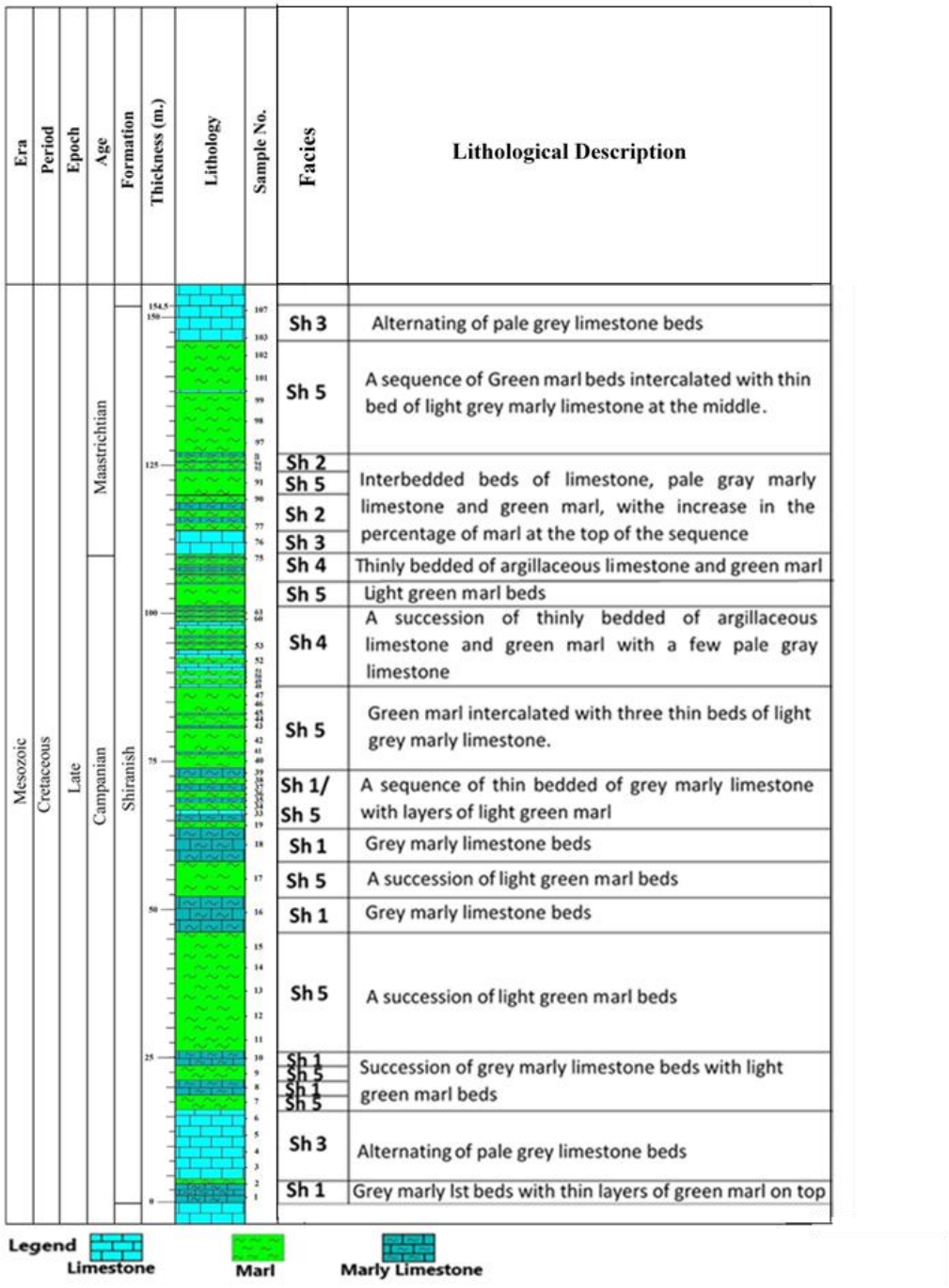


Fig. 2. Lithological column and facies types in the studied section.



Fig. 3. Lower part of Shiranish Formation in the study section.

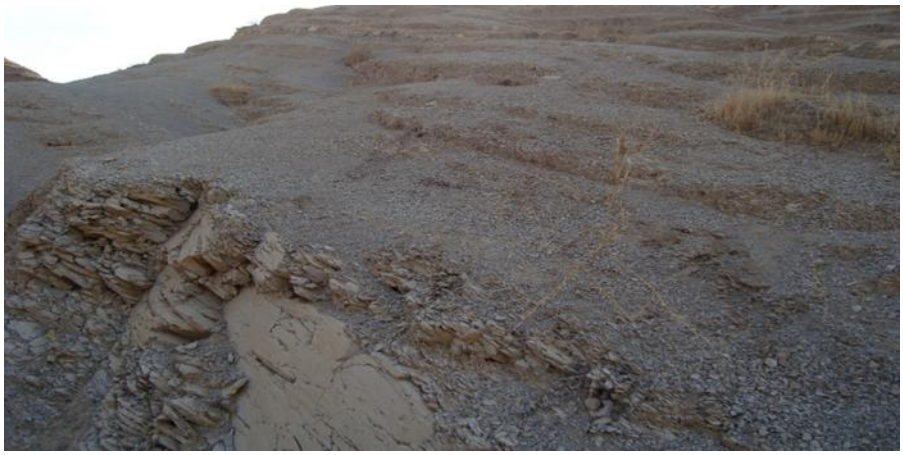


Fig. 4. Middle part of Shiranish Formation in the study section.



Fig. 5. Uppermost part of Shiranish Formation in the study section

Materials and Methods

Based on changes in lithology between 50 cm and 4 m intervals, 107 samples were collected from the study area. An analysis is conducted on approximately fifty thin sections accomplished in the Department of Geology workshop, Mosul University, for petrographical description and facies analysis, which forms the basis of the current investigation. In addition, numerous samples are selected in order to examine the calcareous nannofossils and ascertain the age of formation. Armstrong and Brasire's (2005) techniques, as well as the transmitted light microscope (Italy, POL353-B Optika), are used for this purpose. The atlas map of Young and Bown (1997) is utilized for comparison with the results.

Facies Analysis

Sedimentological hints are utilized to ascertain the depositional environment for each of the five facies that make up the Shiranish Formation, which are identified as Sh1 through Sh5. This facies are as follows:

1- Globular Planktic Foraminiferal lime wackestone microfacies (Sh1)

The allochems make up roughly 40% of the facies' overall contents, and they are extensively distributed throughout the lower and middle portions. With a minor number of bivalvia and bioclasts, the majority is composed of globular foraminifera (Fig. 6A) such as *Heterohelix* and *Pseudotextularia*, with minimal keeled planktic foraminifera genera. The distribution of these materials is in a fine micrite ground. This facies are impacted at some levels by the dissolution process, which dissolved some fossils, and some are to be filled with calcite crystals in the form of sparse cement inside fossil skeletons. As a result, the overall evidence for this microfacies points to its deposition within middle-outer shelf settings (Leicke, 1987).

2- Keeled Planktic Foraminiferal lime wackestone microfacies (Sh2)

It is well documented in the formation's upper parts, with fossils making up roughly 30–40% of the facies' overall composition. Large and well-preserved keeled foraminifera make up the majority of this facies (*Globotruncana* and *Globotruncanita*), with a small number of globular forms (Fig. 6B). Moreover, a very few benthic foraminifera and bioclastics with some irregular quartz crystals (chalcedony) are seen. Occasionally, certain diagenetic processes affect this facies, such as recrystallization into microspar and cementation in the form of spary calcite crystals inside the fossil shells. The sedimentological and biological evidences of this microfacies indicate that it was deposited in the upper bathyal zones (Leicke, 1987; Koutsoukos and Hart, 1990).

3- Bioclastic lime wackestone microfacies (Sh3)

Hard limestone beds with a pale grey color make up this facies, which are found in all the formation's parts (lower, middle, and upper). Although a few bivalve shells and planktic foraminifera are present, the shell debris makes up the majority of this facies' composition (up to 20–30% of the total) (Fig. 6C). This facies are affected by some diagenetic processes, especially neomorphism resulting from recrystallization of micrite, and the presence of spary cement in a scattered manner within the micrite, in addition to documenting the effect of the dissolution process on some shells. According to Flügel (2004), this microfacies was deposited in the uppermost regions of the outer shelf.

4- Argillaceous Planktic Foraminiferal lime packstone microfacies (Sh4)

This facies consists of limestone beds with a tiny quantity of clay in the micritic matrix, and it is located in the middle and upper parts of the formation, primarily composed of globular planktic foraminifera, which make up roughly 50% of the total components (Fig. 6D). There are also some rock fragments and a tiny amount of shell debris in addition to iron oxides in a fair percentage. The existence of fractures and vugs porosity in this facies indicates that it is impacted by the dissolution process to some extent (Al-Fandi et al., 2023). The sedimentary and skeletal criteria of this microfacies suggest the middle shelf environment (Gibson, 1989; Flügel, 2004).

5- Marl lithofacies (Sh5)

The thickness of this facies ranges from 1-20 m, and is evidently the dominant property among the formation sequences as reported throughout the studied section. This facies are composed of light green friable marl sequences that are occasionally intercalated with thin beds of pale grey marly limestone. These beds are distinguished by a high percentage of planktic foraminifera up to 40%. At certain levels, the dominance of keeled-shaped planktic foraminifera

is observed, while the prevalence of globular planktic foraminifera is predominant at other levels. This facies were deposited within a sedimentary range that extends from upper bathyal to outer shelf (Gibson, 1989; Flügel, 2004).

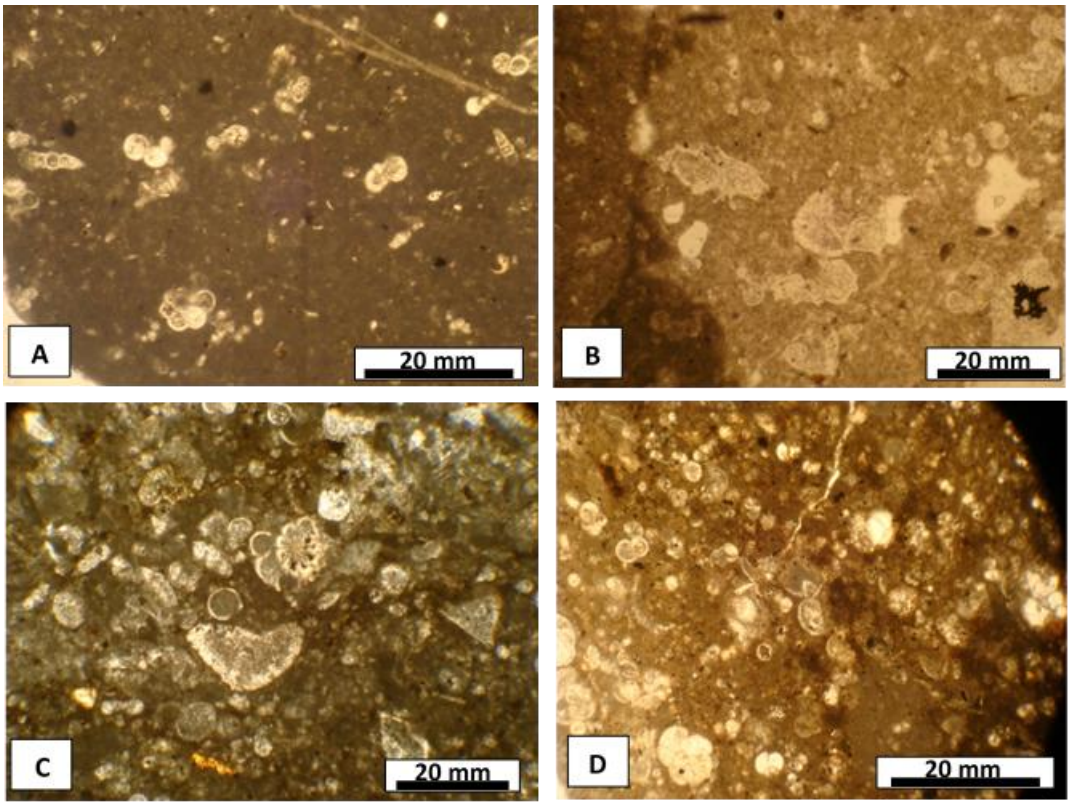


Fig. 6. Studied facies, A-Sh1, B-Sh2, C-Sh3, and D-Sh4.

Nannobiostratigraphy

In this investigation, twenty-four species from sixteen genera and ten families are identified. They are: *Ahmuellerella alboradiata, Reinhardtitus levis, Tranolithus phacelosus, Zeugrhabdotus embergeri, Eiffellithus collis, Eiffellithus eximius, Cribrosphaerella ehrenbergii, Prediscosphaera columnata, Retecapsa crenulata, Retecapsa schizbrachiata, Retecapsa ficula, Watznaueria barnesae, Watznauria coronate, Watznauria biporta, Broinsonia parca, Calculites obscurus, Lithraphidites quadratus, Microrhadulus decuratus, Micula decussate, Micula staurophora, Uniplanarius trifidus, Ceratolithoides aculeus, Ceratolithoides prominens and Ceratolithoides sagittatus*. (Figs. 7 and 8).

The detected calcareous nannofossil taxa in the examined section (Fig. 9) can be classified into three biozones based on their correlation with other places of the world (Sissingh, 1977) (Fig. 10); these zones are;

1- *Uniplanarius trifidus* Interval Biozone (cc22) (part)

Definition: The time interval is between the first occurrence of *Uniplanarius trifidus* (Vekshina, 1959) and the last recorded *Eiffelithius eximius* Stover, 1966.

Thickness: 46 m.

Discussion and Boundaries: The bottom boundary of this biozone, which is not exposed in the area under study, is marked by the first appearance of *Quadrun trifidum* Vekshina (1959), while the last occurrence of *Eiffelithius eximius* Stover, 1966, marks the upper boundary. The last occurrence of *Eiffelithius eximius* Stover, 1966, coincided with the first occurrence of *Reinhardites anthophorus* (Deflandre, 1959). This zone is similar to

the *Quadrun trifidum* biozone described by Bukry and Bramlette (1970), which was broadened by Sissingh (1977) to include the Late Campanian period (Ogg et al. 2016).

2- *Tranolithus phacelosus* Interval Biozone (cc23) (Part)

Definition: The time interval is between the last recorded instance of *Eiffelithius eximius* Stover, 1966, and the last recorded instance of *Tranolithus phacelosus* Stover (1966).

Thickness: 64 m.

Discussion and Boundaries: The lower contact is marked by the last recorded *Eiffelithius eximius* Stover, 1966; the upper contact was indicated by the last documented data of *Tranolithus phacelosus* Stover (1966). This zone exhibited a correlation with Sissingh's (1977) *Tranolithus phacelosus* zone, which was dated as the Latest Campanian to Early Maastrichtian period (Ogg et al. 2016).

3- *Reinhardites levis* Interval Biozone (cc24) (part)

Definition: an interval is between the last recorded instance of *Tranolithus phacelosus* Stover (1966) and the last recorded instance of *Renhardites levis* (Sissingh, 1977).

Thickness: 44.5 m.

Discussion and Boundaries: the lower boundary is indicated by the last recorded instance of *Tranolithus phacelosus* Stover (1966); the upper limit is not included in the section under study. This zone is similar to *Renhardites levis* (cc24) by Perch-Nielsen (1979) and Sissingh (1977), *Arkhangeskilla cymbiformis* by Doeven (1983), and *Lithraphidites praequardatus* by Roth (1978), aged Early Maastrichtian. Therefore, the age of this zone is Early Maastrichtian (Ogg et al. 2016).

Depositional Environment

The evidence of the five sedimentary facies previously described in the facies analysis section will be the main emphasis of the discussion of the depositional environment of the studied formation, as follows:

In general, the high and diverse proportions of planktic foraminifera in the current study samples indicate an outer shelf environment (Berggren and Miller, 1989; Gibson, 1989). Additionally, the greater frequency of globular planktic foraminifera compared to keeled planktic foraminifera (Sh1) implies the existence of this facies on the continental shelf and in warm waters (Leicke, 1987). An environment near the coast is also suggested by the rise in *Heterohelix* individuals in some parts of this facies (Leicke, 1987). As a result, the overall evidences for facies (Sh1) point to its deposition within middle-outer shelf settings. Conversely, in the other parts of the studied section, high and varied proportions of keeled planktic foraminifera (Sh2) are exhibited, indicating deep marine settings distant from the shore, particularly in the upper bathyal zones (Leicke, 1987; Koutsoukos and Hart, 1990; Omana, 2006). On the other hand, the dominance of shell debris in microfacies (Sh3) suggests that this facies were deposited on the uppermost regions of the outer shelf (Wilson, 1975; Scholle et al., 1983; Flügel, 2004). However, the existence of argillaceous limestone facies with planktic foraminifera (Sh4) suggests the deposition in the middle shelf environment (Gibson, 1989; Flügel, 1982 and 2004). The distribution of the marl facies (Sh5) with its two types of planktic foraminifera, which are globular in some areas and keeled in others, suggests that this facies was deposited within a sedimentary range that reaches the upper bathyal from the outer shelf. (Berggren and Miller, 1989; Gibson, 1989; Samir, 2002).

As previously aforementioned, the Shiranish Formation's depositional environment on the northern limb of the Perat Anticline stretches from the middle shelf to the upper bathyal.

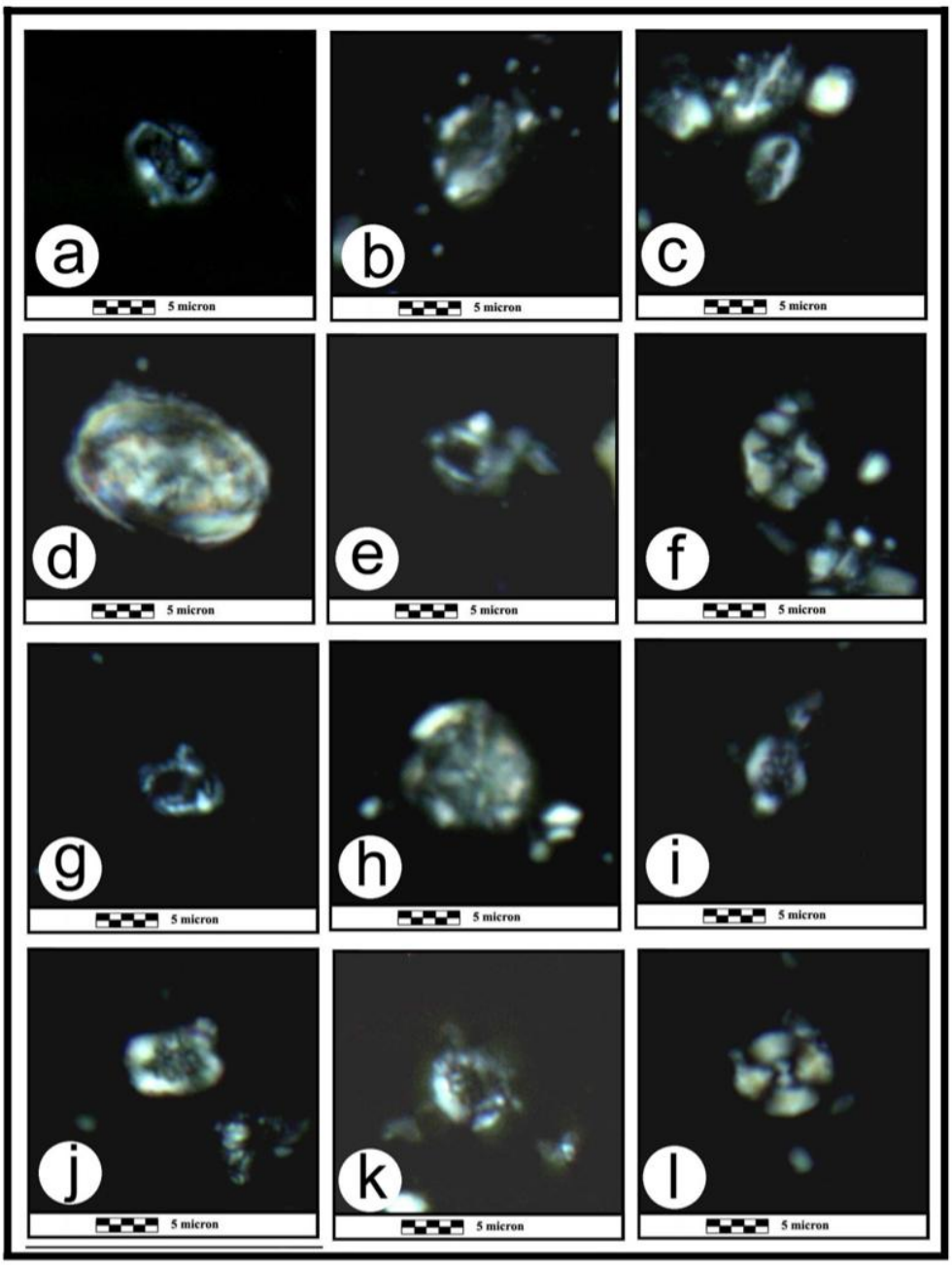


Fig. 7. Distinguished calcareous nannofossils from the studied Formation. (a) Ahmuellerella alboradiata; (b) Reinhardtitus levis; (c) Tranolithus phacelosus; (d) Zeugrhabdotus embergeri; (e) Eiffellithus collis; (f) Eiffellithus eximius; (g) Cribrosphaerella ehrenbergii; (h) Prediscosphaera columnata; (i) Retecapsa crenulata; (j) Retecapsa ficula; (k) Retecapsa schizbrachiata; (l) Watznaueria barnesae.

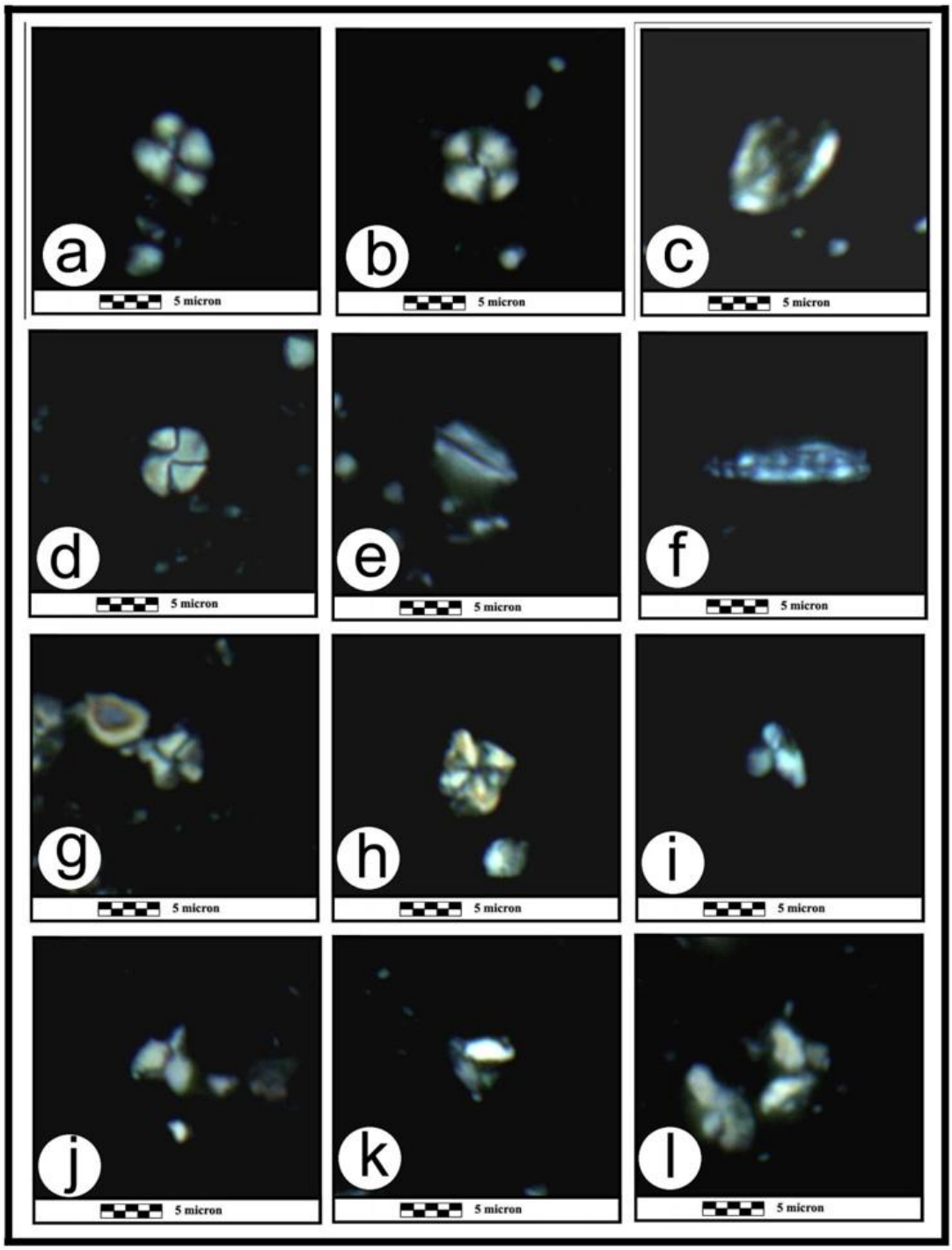


Fig. 8. Significant calcareous nannofossil taxa from the studied Formation. (a) Watznauria biporta; (b) Watznauria coronate; (c) Broinsonia parca; (d) Calculites obscurus; (e) Lithraphidites praequadratus; (f) Microrhadulus decoratus; (g) Micula decussate; (h) Micula staurophora; (i) Uniplanarius trifidus; (j) Ceratolithoides aculeus; (k) Ceratolithoides prominens; (l) Ceratolithoides sagittatus.



Fig. 9. Distribution chart of calcareous nannofossils for the study section.

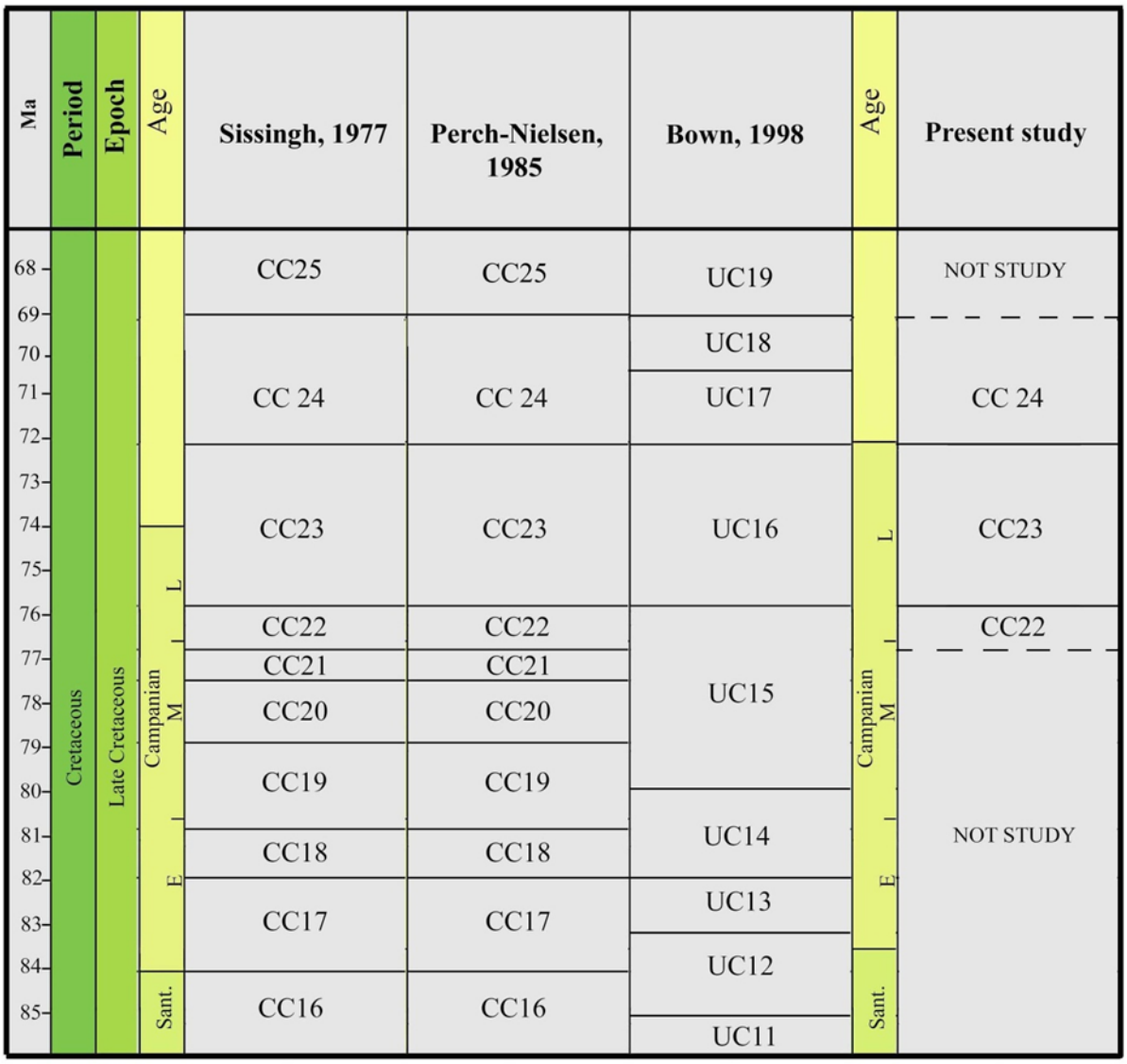


Fig. 10. Biozones of calcareous nannofossils and their age correlation chart (Ogg et al., 2016).

Conclusions

The Shiranish Formation is classified into three biozones according to the distribution of the calcareous nannofossil assemblage. These biozones are: the *Uniplanarius trifidus* Interval Biozone (cc22), *Tranolithus phacelosus* Interval Biozone (Part) (cc23), and *Reinhardites levis* Interval Biozone (cc24). They are dated from Late Campanian to Early Maastrichtian. On the other hand, the study of sedimentary facies has revealed the diagnosis of five microfacies, which are: Globular Planktic Foraminiferal lime wackestone microfacies (Sh1), Keeled Planktic Foraminiferal lime wackestone microfacies (Sh2), Bioclastic lime wackestone microfacies (Sh3), Argillaceous Planktic Foraminiferal lime packstone microfacies (Sh4), and Marl lithofacies (Sh5). The distinctive feature of the microfacies under study indicates that the Shiranish Formation, which is located in the northern limb of the Perat anticline, was deposited on the middle shelf to the upper bathyal.

Acknowledgements

For providing facilities that enhanced the caliber of this study, the authors are appreciative to the College of Environmental Sciences, College of Sciences, and College of Petroleum and Mining Engineering, University of Mosul.

References

Al-Atroshi, R. Kh., 2007. Facies analysis and sedimentary model of Shiranish Formation successions in Dohuk area. Unpublished MSc Thesis, College of Science, University of Mosul, 131 P.

Al-Bdrani, O.A., 2001. Biostratigraphy and paleoecology of Upper Cretaceous ammonites for the lower part of Shiranish Formation northwest Iraq. MSc Thesis, University of Mosul, Iraq. 104 P.

Al-Fandi, E.I., Al-Abbasi, M.W. and Malak, Z.A., 2023. Porosity Evolution and Sequence Stratigraphy of Khasib Formation (Late Turonian-Coniacian) in Selected Oilfields, Central Iraq. Iraqi Geological Journal, Vol. 56, (2E), pp. 244-255. DOI: 10.46717/igj.56.2E.17ms-2023-11-22

Al-Mutwali, M.M. and Al-Juboury, F.N., 2005. Litho and Biostratigraphy of the Shiranish Formation (Late Campanian-Late Maastrichtian) In Sinjar Area, Northwestern Iraq. Rafidain Journal of Science, Vol. 16, No. 1, pp. 152-176.

Al-Dulaimi, A.M., Al-Haj, M.A., Al-Badrani, O.A. and Al-Juboury, A.I., 2023. Lithostratigraphy and Biostratigraphy of the Shiranish Formation (Late Campanian-Maastrichtian) in Diana area, Northern Iraq. Iraqi Journal of Science, Vol. 64, No. 3, pp. 1268-1284. https://doi.org/10.24996/ijs.2023.64.3.22

Al-Qayim, B., Habib, H.R. and Al-Dyni, N., 1986. Petrology and geochemistry of Shiranish Formation (type section) towards sedimentary facies interpretation. Journal Geological Society of Iraq, Vol. 19, No.3, pp. 123-136.

Al-Rashidi, M.A., 2013. Sedimentological and Stratigraphical Study of Upper Cretaceous (Late Campanian –Maastrichtian Successions in Selected Areas, Northern Iraq. Unpublished Ph. D. Thesis, University of Mosul, 240 P. (In Arabic).

Armstrong, H. and Brasier, M., 2005. Microfossils, Blackwell Publishing, 296 P.

Bamarni, A.A., 2010. Biostratigraphy Of the Shiranish Formation in The Subsurface Section of Khanke Well No.1, Duhok Area, North of Iraq. Unpublished MSc Thesis, College of Science, University of Mosul, 111 P.

Bellen, Van R.C., Dunnington, H.V., Wetzel, R. and Morton, D.M., 1959. Laxique statigraphique international Asia, Fascicule, 10a, Iraq, Paris, 333 P.

Berggren, W.A. and Miller, K.G., 1989. Cenozoic bathyal and abyssal calcareous benthonic foraminiferal zonation. Micropaleontology, Vol. 35, No. 4, pp. 308-320.

Bown, P.R., 1998. Calcareous Nannofossil Biostratigraphy. British Micropalaeontological Society Publications Series. Chapman and Hall, London, pp.132-199.

Bukry, D. and Bramlette, M.N., 1970. Coccolith age determination Leg 3. Deep Sea Drilling Project. Initial Rep. Deep Sea drill. Proj., 3. Pp. 589-611.

Deflandre, G., 1959. On calcareous nannofossils and their systematics. Rev. Micropaleontology, Vol. 2, No. 3, pp. 127-152.

Doeven, P.H., 1983. Cretaceous nannofossil stratigraphy and paleoecology of the Canadian Atlantic Margin. Bull. Geol Surv. Can., 356, pp. 1-70.

Flügel, E., 1982. Microfacies analysis of limestone. Springer-Verlag, Berlin, 663 pages.

Flügel, E., 2004. Microfacies of Carbonate Rock, Analysis, Interpretation and Application, Springer-Verlag, Berlin, 976 P.

Gibson, T.G., 1989. Planktic benthonic foraminiferal ratios: Modern patterns and Tertiary application. Marine Micropaleontology, vol. 15, pp. 29-52.

Koutsoukos, A.M. and Hart, M.B., 1990. Cretaceous foraminiferal morphogroup distribution patterns, paleocommunities and trophic structures: A case study from the Sergipe Basin. Brazil Transactions of the Royal Society of Edinburgh, Earth Science, Vol. 81, pp. 221-246.

Leicke, R.M., 1987. Paleoecology of mid-Cretaceous planktic foraminifera: A comparison of open ocean and epicontinental sea assemblages. Micropaleontology, Vol. 33, No.2, pp. 164-176.

Ogg, J.G., Ogg, G. and Gradstein, F.M., 2016. A Concise Geologic Time Scale: Amsterdam, Elsevier, 240 P.

Omana, L., 2006. Late Cretaceous (Maastrichtian) foraminiferal assemblage from the inoceramid beds, Ocozocoaulta formation, central Chiapas. Ciencias Geologicas, Vol. 23, No. 2, pp. 125-132.

Perch-Nielsen, K., 1979. Calcareous nannofossils from the Cretaceous between the North Sea and the Mediterranean. Aspekte der Kreide Europas, IUGS Series A, Vol. 6, pp. 223-272.

Perch-Nielsen, K., 1985. Validation of new combinations. Newsletter of the International Nannoplankton Association, Vol. 6, No. 1, pp. 42-46.

Roth, P.H., 1978. Cretaceous nannoplankton biostratigraphy and oceanography of the Northwestern Atlantic Ocean. Initial Rep. Deep Sea drill. Proj., 44, pp. 731-59.

Samir, A.M., 2002. Biostratigraphy and paleoenvironmental changes in the Upper Cretaceous-Early Paleogene deposits of Gabal Samara section, southwestern Sinai, Egypt. Journal of Paleontology, Vol. 2, pp. 1-40.

Scholle P.A., Arther M.A. and Ekdale A.A., 1983. Pelagic environment, in: Scholle P.A., Bebout, D.G. and Moore, C.H., Carbonate depositional environments. American Association of Petroleum Geologists Memoir 33, pp. 620-681.

Sissakian, V. K., Mahdi, A. I., Amin, R. M. and Mohammed, B.S., 1997. The Nfayil Formation. A new lithostratigraphic unit in Iraq. Iraqi Geol. Jour., Vol. 30, No. 1.

Sissingh, W., 1977. Biostratigraphy of Cretaceous Calcareous Nannoplankton. In Bolli, H.M., Saunders, J.B., and Perch-Nielsen, K. (eds.), 1985. Plankton Stratigraphy. Cambridge University Press, Cambridge, pp. 329 – 426.

Stover, E., 1966. Cretaceous coccoliths and associated nannofossils from France and Netherlands. Micropaleontology, Vol. 12, No. 2, pp. 133-167.

Vekshina, V.N., 1959. Coccolithophoridae of the Maastrichtian deposits of the West Siberian lowland. Trudy Sibir. Nauch-Issled. Inst. Geol. Geofiz. Min. Syrya, Vol. 2, pp. 56-81.

Wilson, J.L., 1975. Carbonate facies in geological history. Springer- Verlag, Berlin, 471 P.

Young, J.R. and Bown, P.R., 1997. Cenozoic Calcareous Nannoplankton Classification, Journal of Nannoplankton Research, Vol. 19, pp. 36-47.

Iraqi National Journal of Earth Science

www.earth.uomosul.edu.iq

Prediction and Prospection of Groundwater in the Iraqi Western Desert Using Remote Sensing and GIS

Ahmed Abbas Hasan [1*], Shahad Adil Al-Qaraghuli [2], Linaz Anis Fadhil [3], Aymen Muwafaq Ahmed [4]

[1,2,3,4] *Remote Sensing Department, College of Remote Sensing and Geophysics, AlKarkh University of Science, Baghdad, Iraq.*

Article information

Received: 19 -Jul -2024

Revised: 30 -Sep -2024

Accepted: 19- Jan -2025

Available online: 01- Jan -2026

Keywords:
Groundwater,
Lineaments,
Iraqi Western Desert,
Remote Sensing,
GIS.

Correspondence:
Name: Ahmed Abbas Hasan

Email: ahmad.a.h@kus.edu.iq

ABSTRACT

Groundwater resources are receiving a lot of attention, especially in arid and semi-arid areas, as a result of the growing demands for water brought on by urbanization, population growth, and agricultural development. Finding the most significant contributing parameters, such as lineament density, frequency, and junction nodes that reveal the groundwater potential, is the foundation of this investigation. To determine suitable sites for drilling wells, analysis of linear structures is necessary to detect and exploit groundwater sustainably. This study highlights the importance of geospatial systems, including remote sensing and geographic information system technologies, to effectively explore and manage groundwater resources. To identify linear structures in the study area, different image enhancement techniques are applied, such as band composite (BC) and high-pass filtering (HPF). These methods work well, and they are suitable for identifying these structures. The results show that the area contains a large number of short and long fractures, most of which have an orientation from northwest to southeast, and that it is possible to explore groundwater in areas with a high density of areas with intersections in linear structures. The area, where groundwater occurrence is most promising for sustainable use of groundwater, has been identified within the region. Using remote sensing (RS) data and geographic information systems (GIS), a thematic map of each parameter is created. The final groundwater potential zones of the studied region are created by combining these input layers using the GIS Raster Calculate Module. Different groundwater prospective potential zones are depicted on the final output map: very high (49 km^2), high (261 km^2), and moderate (1041 km^2).

DOI: 10.33899/injes.v26i1.56113, ©Authors, 2026, College of Science, University of Mosul.
This is an open-access article under the CC BY 4.0 license (http://creativecommons.org/licenses/by/4.0/) .

التنبؤ والتنقيب عن المياه الجوفية في الصحراء الغربية العراقية باستخدام الاستشعار عن بعد ونظم المعلومات الجغرافية

احمد عباس حسن[1*] ، شهد عادل فاضل القرغولي[2]، لينا ز انيس فاضل[3]، ايمن موفق احمد[4]

[1،2،3،4] قسم الاستشعار عن بعد، كلية الاستشعار عن بعد والجيوفيزياء، جامعة الكرخ للعلوم، بغداد، العراق.

معلومات الارشفة

تاريخ الاستلام: 19- يوليو- 2024

تاريخ المراجعة: 30- سبتمبر- 2024

تاريخ القبول: 19- يناير- 2025

تاريخ النشر الالكتروني: 01- يناير- 2026

الكلمات المفتاحية:

المياه الجوفية،

التراكيب الخطية،

الصحراء الغربية العراقية،

الاستشعار عن بعد،

نظم المعلومات الجغرافية.

المراسلة:

الاسم: احمد عباس حسن

Email: ahmad.a.h@kus.edu.iq

الملخص

تحظى المياه الجوفية باهتمام واسع، ولا سيما في المناطق القاحلة وشبه القاحلة، بسبب ازدياد الطلب على المياه الناتج عن التوسع العمراني ونمو السكان وتطور الزراعة. يعتمد هذا البحث على تحديد أهم المؤشرات المرتبطة بالمياه الجوفية، مثل كثافة الخطوط، وتكرارها، ونقاط التقاطع بينها، لأنها تساعد في الكشف عن المناطق ذات الإمكانات الجيدة للمياه الجوفية. يعدّ تحليل التراكيب الخطية أمرًا مهمًا لتحديد المواقع المناسبة لحفر الآبار، لأنه يساعد في الكشف عن المياه الجوفية واستثمارها بصورة مستدامة. وتركّز هذه الدراسة على دور التقنيات الجغرافية المكانية، مثل الاستشعار عن بعد ونظم المعلومات الجغرافية، في استكشاف وإدارة موارد المياه الجوفية بشكل فعّال. لتحديد التراكيب الخطية في منطقة الدراسة، جرى تطبيق عدة تقنيات لتحسين الصور، مثل التركيب اللوني (BC) للنطاقات والترشيح عالي التمرير (HPF) نجحت هذه الأساليب وكانت مناسبة لتحديد التراكيب الخطية. وأظهرت النتائج أن منطقة الدراسة تحتوي على عدد كبير من الكسور القصيرة والطويلة، ويتجه معظمها من الشمال الغربي إلى الجنوب الشرقي. كما تشير النتائج إلى إمكانية استكشاف المياه الجوفية في المناطق التي تزداد فيها كثافة هذه التراكيب ونقاط تقاطعها. تم تحديد المناطق الأكثر وعدًا لوجود المياه الجوفية من أجل الاستغلال المستدام داخل منطقة الدراسة. وباستخدام بيانات الاستشعار عن بعد (RS) ونظم المعلومات الجغرافية(GIS) ، تم إعداد خريطة لكل عامل من العوامل المدروسة، ثم جرى دمج هذه الخرائط باستخدام وحدة الحساب الراستري في GIS Rasterللحصول على خريطة إمكانات المياه الجوفية النهائية. وقد بينت الخريطة وجود ثلاث فئات من إمكانات المياه الجوفية: عالية جدًا (49 كم^2)، وعالية (261 كم^2)، ومتوسطة (1041 كم^2). عالية جدًا (49 كم^2)، وعالية (261 كم^2)، ومتوسطة (1041 كم^2).

DOI: 10.33899/injes.v26i1.56113, ©Authors, 2026, College of Science, University of Mosul.
This is an open-access article under the CC BY 4.0 license (http://creativecommons.org/licenses/by/4.0/) .

Introduction

Groundwater potential studies have been increasingly popular across the world in recent years because of the requirement of achieving Sustainable Development Goal #6. Most of these investigations depend on the techniques of remote sensing, geographic information systems, and geophysics; however, some of these studies (Al-Djazouli et al., 2021**;** Saadi et al., 2021**;** Owolabi et al., 2020**;** Mpofu et al., 2020**;** Adeyeye et al., 2019**;** Magaia et al., 2018**;** Delgado**,** 2018) depend on data from the borehole.

A lot of consideration goes into choosing locations for groundwater exploration while doing lineament analysis. It should be mentioned that areas where many fractures converge frequently experience strong water flow and fractures (Coulibaly et al., 2021). To explore groundwater resources, linear structural studies are now essential (Dembele and Ye, 2017). This

study aims to identify possible locations for water drilling sites in the investigated area by utilizing drilling flows.

Elongations are natural linear structures of geological origin with a long extension that exceeds 10 km and reaches more than 1000 km. They are observed from satellite images in a straight or slightly curvature direction, and their presence is linked to geological structures (faults and folds) (AlFasatwi and Dijk, 1990). Linear structures are two-dimensional and their inclination is difficult to determine on satellite images. Therefore, they are considered to have vertical or nearly vertical surfaces, reflecting deep subsurface structures that may reach the basement rocks (Siegel and Gillespie, 1980).

Most previous studies of the region were limited to detailed studies conducted in the Western Desert region of Iraq. One of these studies was conducted by Al-Amiri in 1978 using satellite images to study the tectonics of the region extending from the west of the Euphrates to the international border and through the analysis of linear phenomena. The researcher used the same data in 1979 to determine the importance of these structures and drew a map of the linear structures. Another previous study of the region was the study carried out by Al-Hiti in 1985, which included a field study of the microseismicity of the Al-Kaara area. Al-Rawi (1986) studied the use of spectral technology to estimate the depth of basement rocks. As for Al-Sulaiman (1989), he studied fracture systems in the Western Desert using satellite images in addition to a field study of fractures in selected areas. Regarding Al-Azzawi (1988), he used data from remote sensing to examine the tectonics of the area west of the Euphrates River. There are other studies carried out by Abdul Qadir (2002) and Al-Jaf (2008) in which satellite data were used to identify active areas containing groundwater in the Western Desert of Iraq, in addition to studying some of the geological phenomena and the mineral deposits in the Western Desert of Iraq. Al-Moaden (2009) studied the northern part of the Iraqi Western Desert structurally using satellite images. Hasan et al. (2022) also studied the deformation in the drainage pattern, which was investigated using remote sensing data. A variety of distinct drainage pattern types were identified, and the patterns were examined using various satellite images at various scales.

The study region is located in the elevated part of the Rutba-Jazira region and the western desert of Iraq (Fig. 1). This region falls within Iraq's stable shelf (Jassim and Goff, 2006). The research region, which covers 3151 square kilometers, is situated between longitudes (40°30´ - 41°30´) east and latitudes (32°30´ - 33°30´) north. At a maximum elevation of 734 meters and a minimum elevation of 363 meters above sea level, the Earth's surface progressively rises from east to west.

Geological formations in the study area date back to the Paleozoic, Mesozoic, and Cenozoic eras (Fig. 2). The oldest formation in the region is the Ga'ara, which is dated to the Permian age (Sissakian and Mohammed, 2007).

Materials and Methods

In the study, linear structures are identified and inferred using a Landsat-7 satellite image. The ETM+ sensor image is used for this investigation due to the vastness of the study area and the spatial resolution of the available satellite images. With a resolution of 30 meters, linear structures are visible in this image. Three distinct software packages (ERDAS IMAGINE version 11, ArcGIS version 10.8, and ROCK WARE version 15) are employed in this investigation since no one program could handle every step of the study. The ArcGIS application is utilized for linear structural analysis, whereas the ERDAS IMAGINE program handles all satellite image processing tasks. The Rose diagram is created using the ROCK WARE software to comprehend the linear structures.



Fig. 1. Map of the study region.

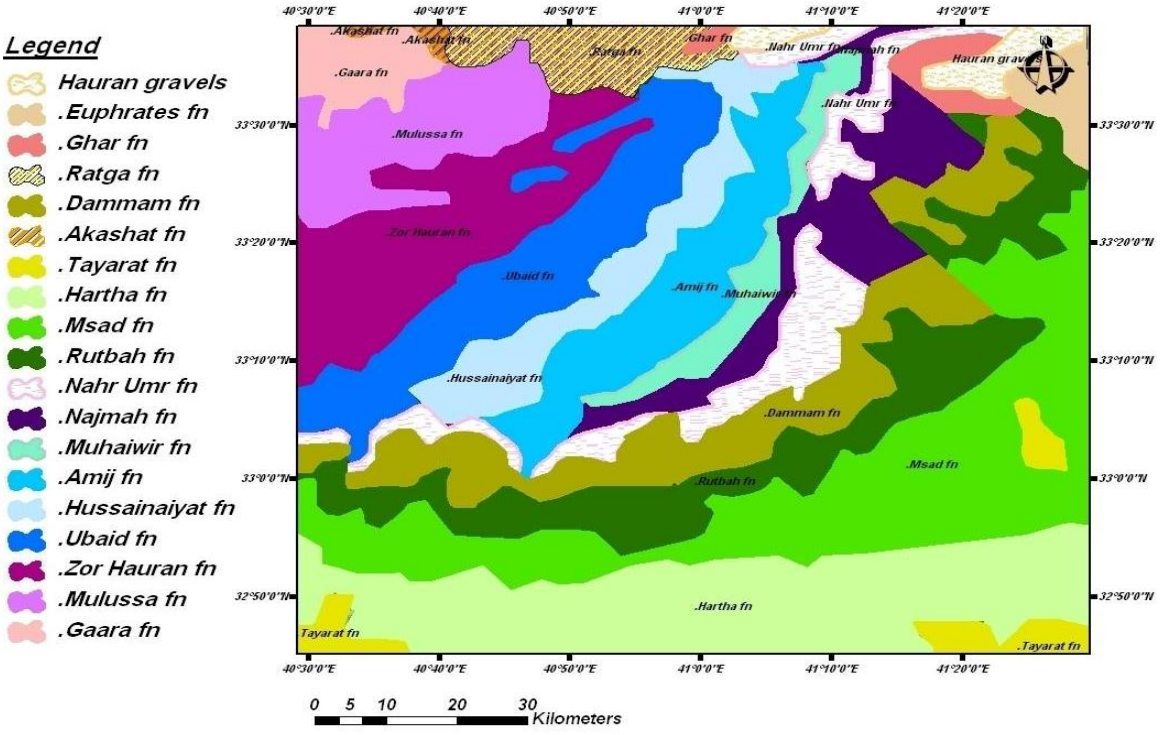


Fig. 2. Geologic map of the studied area (Sissakian, 2000).

Determining linear structures

The Earth's crust's linear features have fascinated Earth scientists and hydrologists. Faults, folds, and fractures are examples of linear features that might provide information for groundwater and mineral resource research. They are also crucial in various technical applications, such as building highways, power plants, and dams, and identifying potential locations for new settlements (Maina and Tudunwada, 2017).

Linear structures are important and key to drawing regional structures and studying regional tectonic analysis to use them in petroleum and mineral exploration and hydrological studies. The process of interpreting linear structures is considered one of the most important elements of analyzing satellite images in geological and tectonic studies, as they represent the surface appearance of deep subsurface fault systems and are areas where hydrocarbons, mineral ores, and groundwater collect (AlFasatwi and Dijk, 1990).

Maps, satellite images, and aerial photos may all be used to identify elongations, which are topographic characteristics that are linear and indicate areas of structural weakness. It is regarded as the main tool for analyzing regional tectonics, creating regional geological maps, and using the results in hydrological and structural studies, and mineral and oil exploration. After processing the digital image, linear structures are visually interpreted and retrieved from the satellite images. In satellite images, these structures appear as straight lines. The interpreter's experience is the key point in identifying these structures, especially in connecting unconnected parts with a longer line (Wang, 1990). However, some key features assist in identifying linear structures such as straightness in parts of major valleys, variation in the intensity of color and texture of soil or rock due to variation in moisture and water content, linear arrangement of vegetation, and sudden change in drainage networks, ridges, or slopes. Straight lines and sudden changes in rock exposures were identified (Lillisand et al., 2015).

According to Lloyd (1999) and Youan Ta (2008), geomorphological features like aligned ridges and valleys, displacement of ridge lines, escarpments, straight drainage channels, breaks in rock masses, and aligned surface depressions are commonly used in geological structural investigations**,** including lineament mapping.

Several image enhancement techniques can contribute to manually identifying linear compositions. In this study, filtering and band composite processes are used to prepare the final linear structure map.

Filtering process (FP)

Lineament detection is accomplished by the use of high-pass filters. The most common filters for hydrogeologic research are gradient or high-pass filters (Meijerink et al., 2007).

A characteristic of satellite images that sets them apart is the spatial frequency parameter, which may be described as the quantity of brightness value variations per unit distance for a specific area of the image. A section of an image is said to have low frequency if there are relatively few variations in the brightness value over that area. On the other hand, this is a region of high-frequency detail if brightness levels vary dramatically over short distances (Jensen, 1996). Thus, the significance of spatial frequency in the image can be emphasized or diminished by the application of filtering procedures. The frequency in question can be explained by the existence of local lineages. Stated differently, the filtering procedure will make the distinctions between neighboring units clearer.

The main drawback of the filtering process is the ability to efficiently extract linear structures in low-contrast areas, where structures extend in sun-parallel directions and in mountain shadows (Koike et al., 1995).

Moving a window with specified kernel sizes (3*3, 5*5, 7*7, etc.) is a typical filtering procedure. As seen in Fig. 5, a new numerical value is computed beneath each pixel in the

output file (resulting image) and substituted with the window's center pixel. High-frequency spatial components, which comprise the majority of the visual information, are preserved while the high-pass filter (HPF) (Sarp 2005), selectively enhances large-scale phenomena, or low-frequency components. Figures (3, 4, and 5) display the results of the 3*3, 5*5, and 7*7 high-pass filters.

Band composite (BC)

A brief foray into color-coded band combinations is helpful since a large portion of the hydrogeologic implementation of remote sensing data involves visual interpretation. For the best picture fusion, such as integrating three multi-spectral bands with an orthophoto or high-resolution panchromatic satellite image, some knowledge of color and intensity information is required (Meijerink et al., 2007).

This technology relies on collecting three multispectral bands and displaying them over a range of visible wavelengths to be visible to the human eye. This technology displays three spectral bands, each band has a specific color: red (0.7-0.6), and green (0.6-0.5). The blue color (0.5-0.4) micrometers are called RGB. The basis for displaying beams depends on the intensity of the reflectivity of the metal to be shown in that beam. Beam mixing is a spectroscopic technique applied in the studied area to digitally enhance images. It is one of the basic methods of image usage in first-order analysis of remote sensing data (Mustard and Sunshine, 1999). To highlight severe spectral anomalies and make the image easier to comprehend, spectral data are stored in several bands that are then integrated by merging them into a single band (Zumsprekel and Prinz, 2000).

Three images (bands) are combined to generate color composites. The first band is shown in various red tones, while the remaining two bands are shown in various green and blue tones.

Because they make the data easier to read, false color graphics are created to interpret lines. The highest visual quality is achieved using a fake color image employing three bands, 4, 3, and 2 (red, green, and blue, respectively), after experimenting with different combinations of the three bands. It is simpler to recognize linear vegetation patterns, river channels, geological weakness zones, and limits of geological formations using this fake color combination. Fig. 6 displays the operation's outcome.

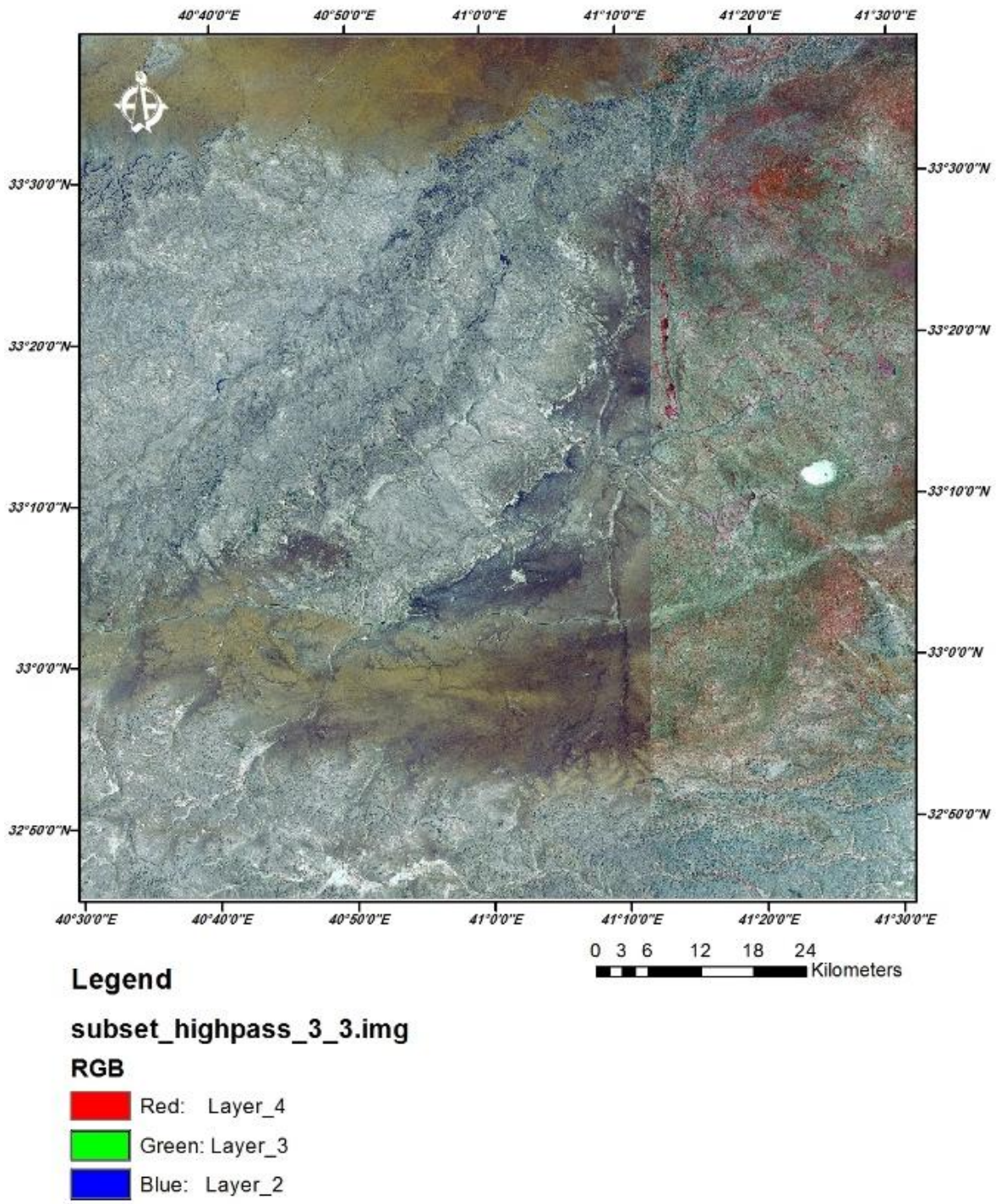


Fig. 3. Image of the high-pass filtering, kernel (3*3).

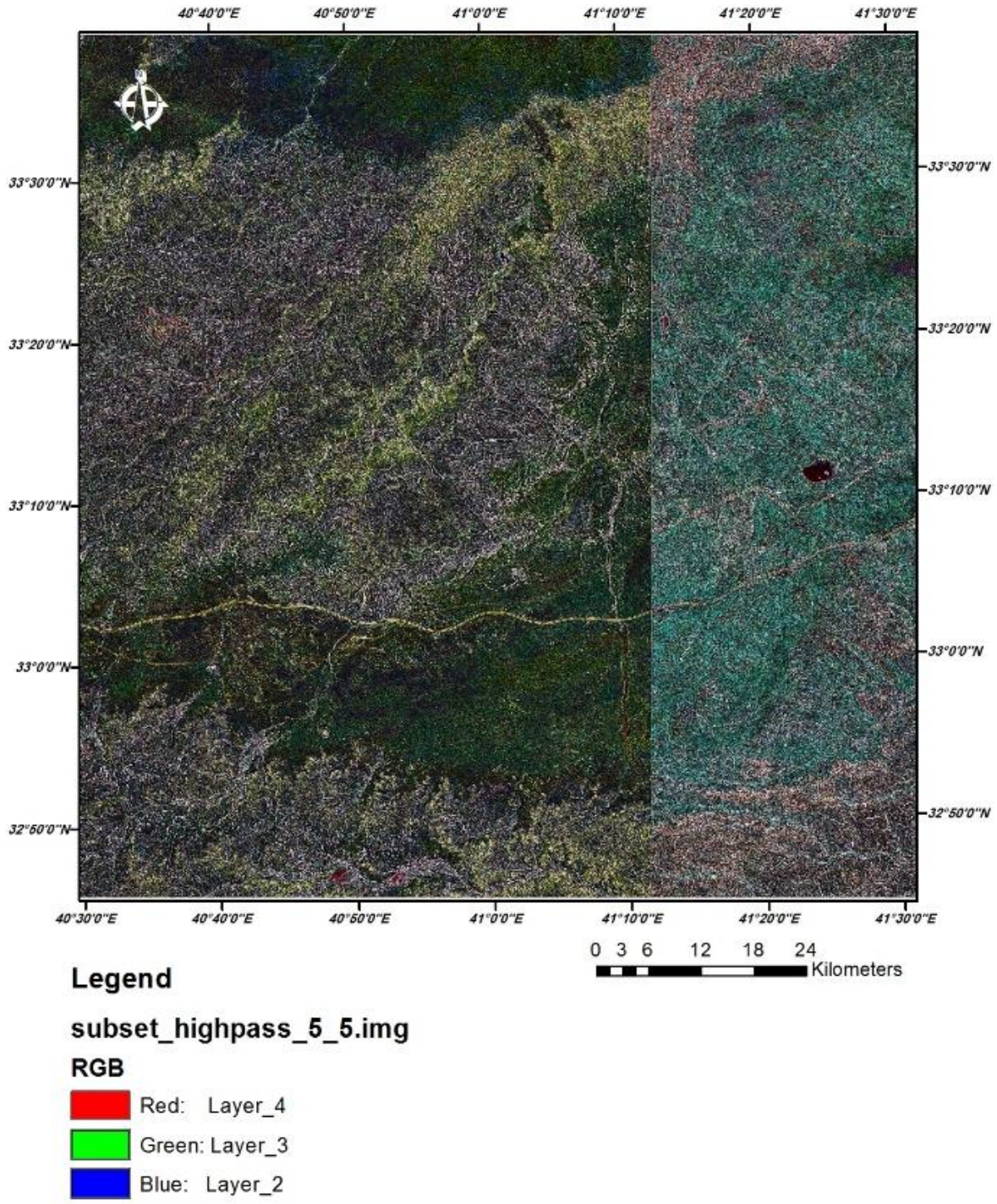


Fig. 4. Image of the high-pass filtering kernel (5*5).

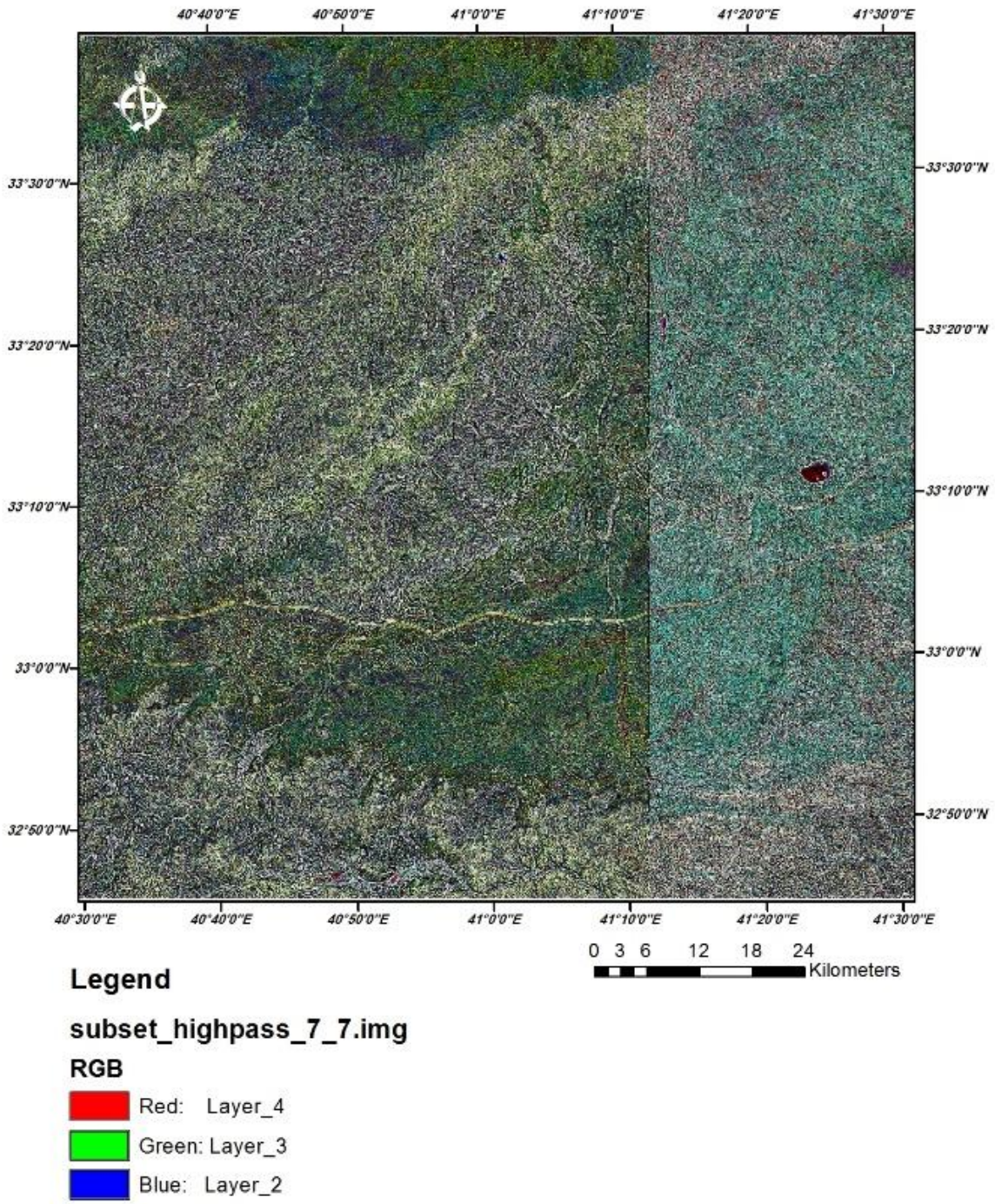


Fig. 5. Image of the high-pass filtering kernel (7*7).

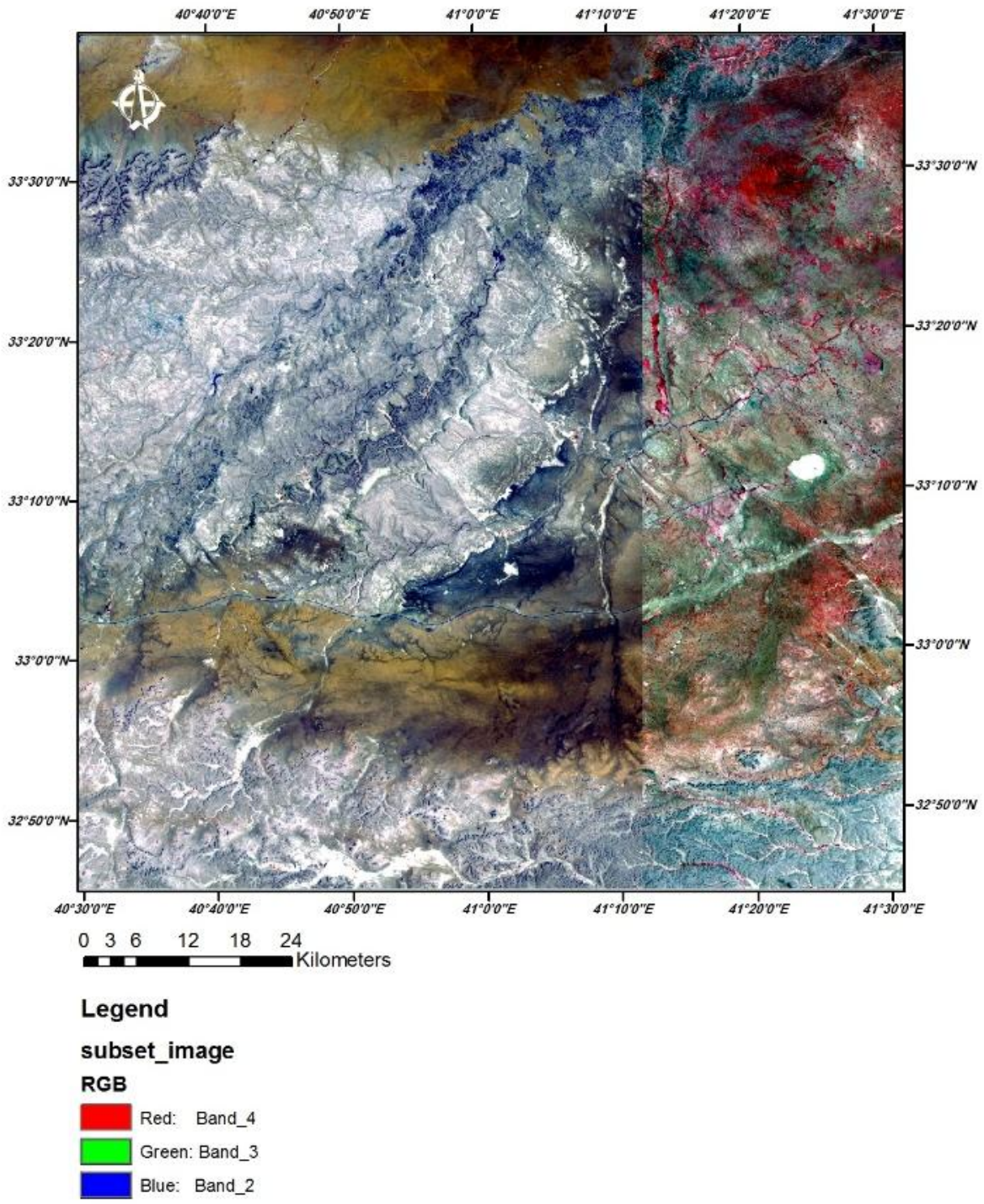


Fig. 6. Color composite of the band 4 (Red), 3 (Green), 2 (Blue).

Linear structure analysis

The most important element of analyzing space visuals in tectonic studies is the analysis of linear structures, as they represent the surface appearance of deep subsurface fault systems (AlFasatwi and Dijk, 1990). The final lineaments map is created after adding all the linear structures and deleting those that matched the roads (Fig. 7). The total number of inferred linear structures found through various methods is 354 linear structures in the region. The linear structures in the region are categorized based on El-Etr's (1974) categorization as well as on their lengths (Fig. 8), which is a function of the depth of their extension within the rock units into:

- Structures longer than 2 km are marked in red.

- Structures less than 2 km long are marked as blue.

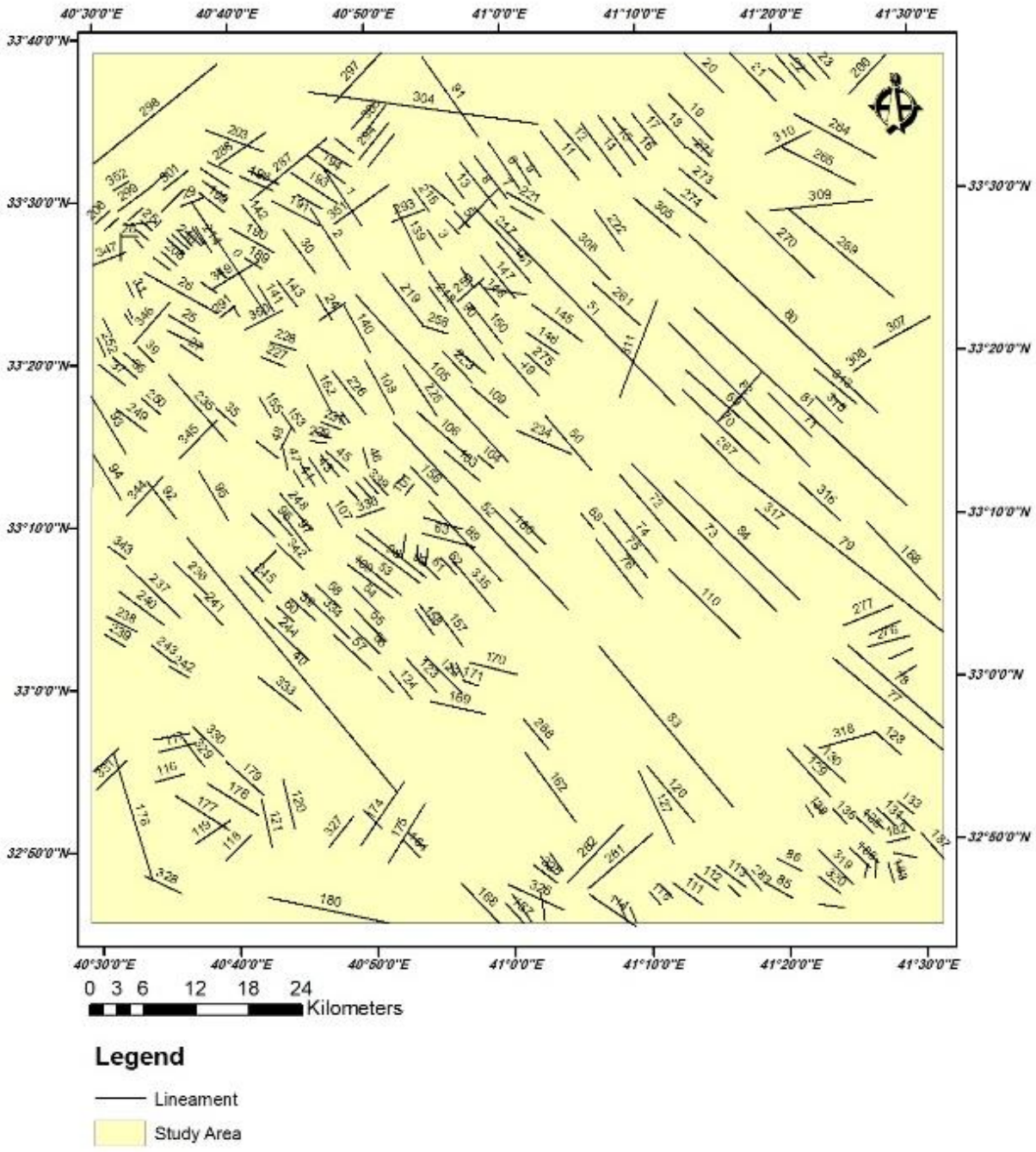


Fig. 7. Final map of linear structures.

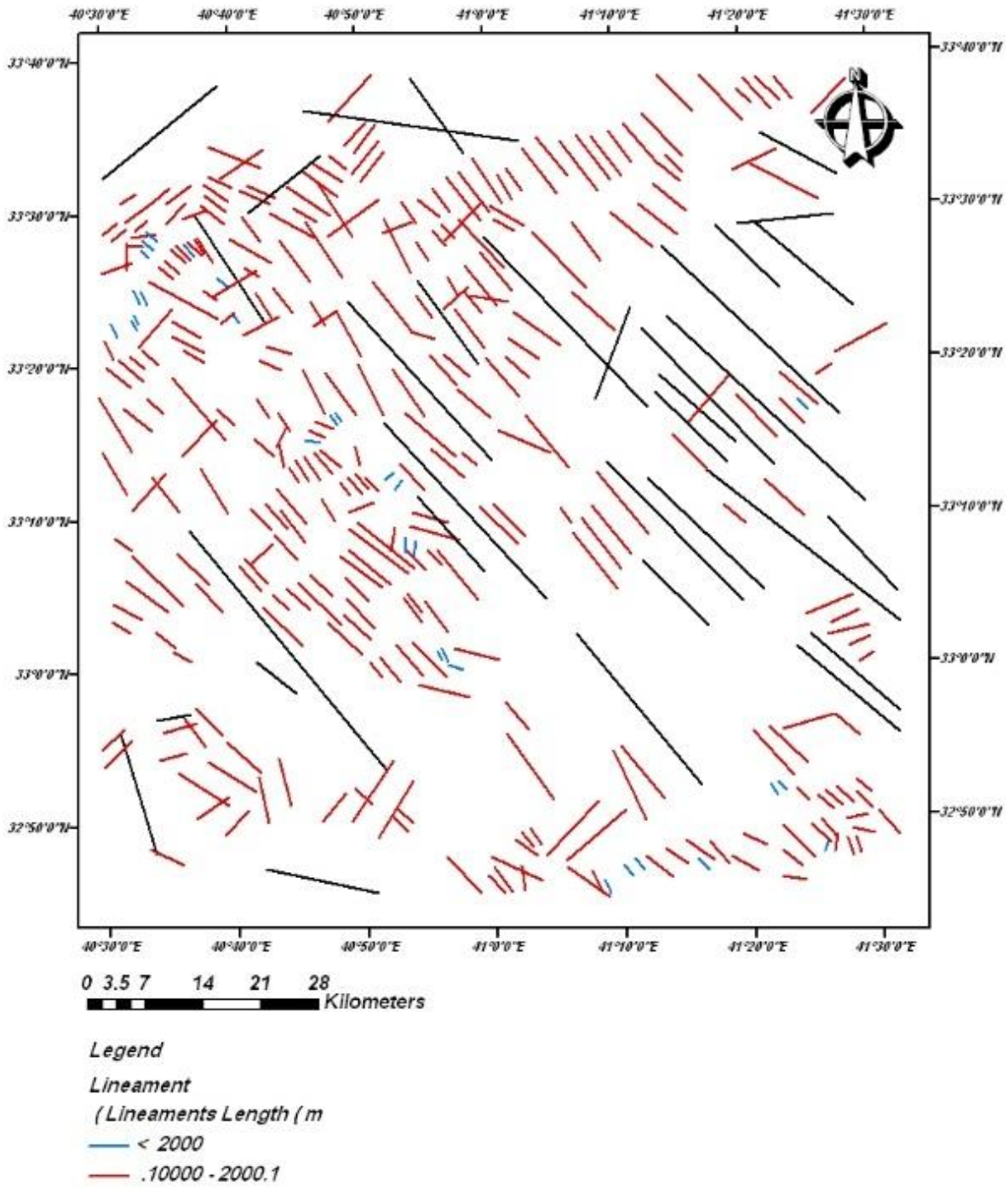


Fig. 8. Classification of linear structures within the study area.

The lineaments' azimuths are also measured and plotted as rose diagrams. The lineament orientations within the research region are well mapped as seen in Fig. 9. The rose diagram shows that the linear structures are concentrated in the main direction within the studied area, which is N 40° W, while the minor directions are (N 15° W, N 50° E, and N 55° W) (Fig. 9). The groups of linear structures are approximately parallel to each other. 354 lines are discovered and digitized in the entire study area. Based on the interpretation of satellite imagery, the structures show surface evidence for possible deep faults in the basement rocks.

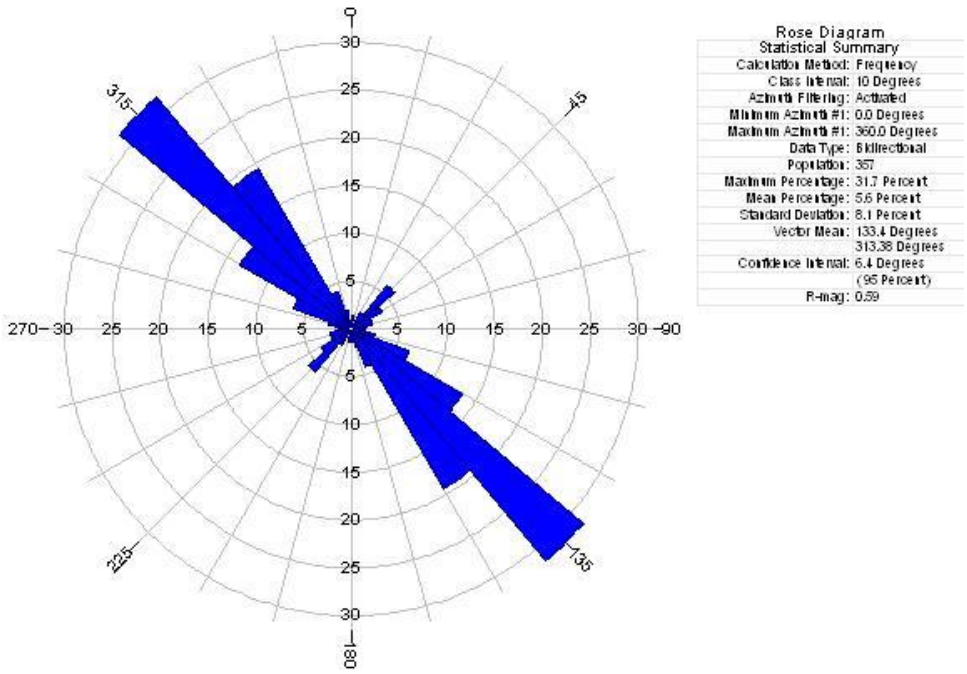


Fig. 9. Rose diagram of the linear structures within the study area.

Results and Discussion

In fractured aquifers, lineaments serve as groundwater drainage systems (Koita, 2010; Brunner et al., 2007). Because smaller lineaments may be missed during the manual extraction process, it is subjective and challenging to apply to a large region (Saepuloh et al., 2018).

Linear features like faults, fractures, and geological linkages between different lithologies can cause the water to seep into the soil and migrate through the aquifer system, perhaps using the lineaments as a path. According to Pradhan and Kim (2014), lineaments are geologic structures that symbolize underlying surface fractures. These structures have the potential to improve the definition of already existing aquifers, identify new reservoirs close to highly inhabited regions that facilitate fluid movement to the bottom, and provide information about water penetration and flow along lineaments (Benjmel et al., 2020).

It is believed that as lineament density increases, so does the quantity of water penetration; hence, lineament density may act as an indirect predictor of groundwater potential (Magesh et al., 2012). Satellite data may be used to map fractures, bedding planes, and geological boundary contacts, all of which will be correlated with these lineaments to assist the groundwater potential analysis (Jhariya et al., 2016).

According to Subba Rao (2006), lineaments are the surface manifestations of underlying geological features that indicate the permeability and porosity of the underlying rocks. The main routes for groundwater flow and storage on Earth are fractures in impermeable rocks (Preeja et al., 2011). Both on-site observations and satellite imagery are used in this work to identify the lineaments in the investigated region. Most of the fractures have NW–SE trends. A map of lineament density is made using the line density approach. The lineament density map (Fig. 10) was made after lineaments were digitized from satellite images. Then, based on Natural Breaks intervals, it is split into five classes: 0 to 2.064, 2.064 to 4.129, 4.129 to 6.194, 6.194 to 8.258, and 8.258 to 10.323 (Table 1). Groundwater development is beneficial in areas with high lineament density, except in the remaining hill environment. The research region is divided into five distinct hydrogeological potential zones, which are depicted as patches in Fig. 10. Table 1 provides a summary of the zones.

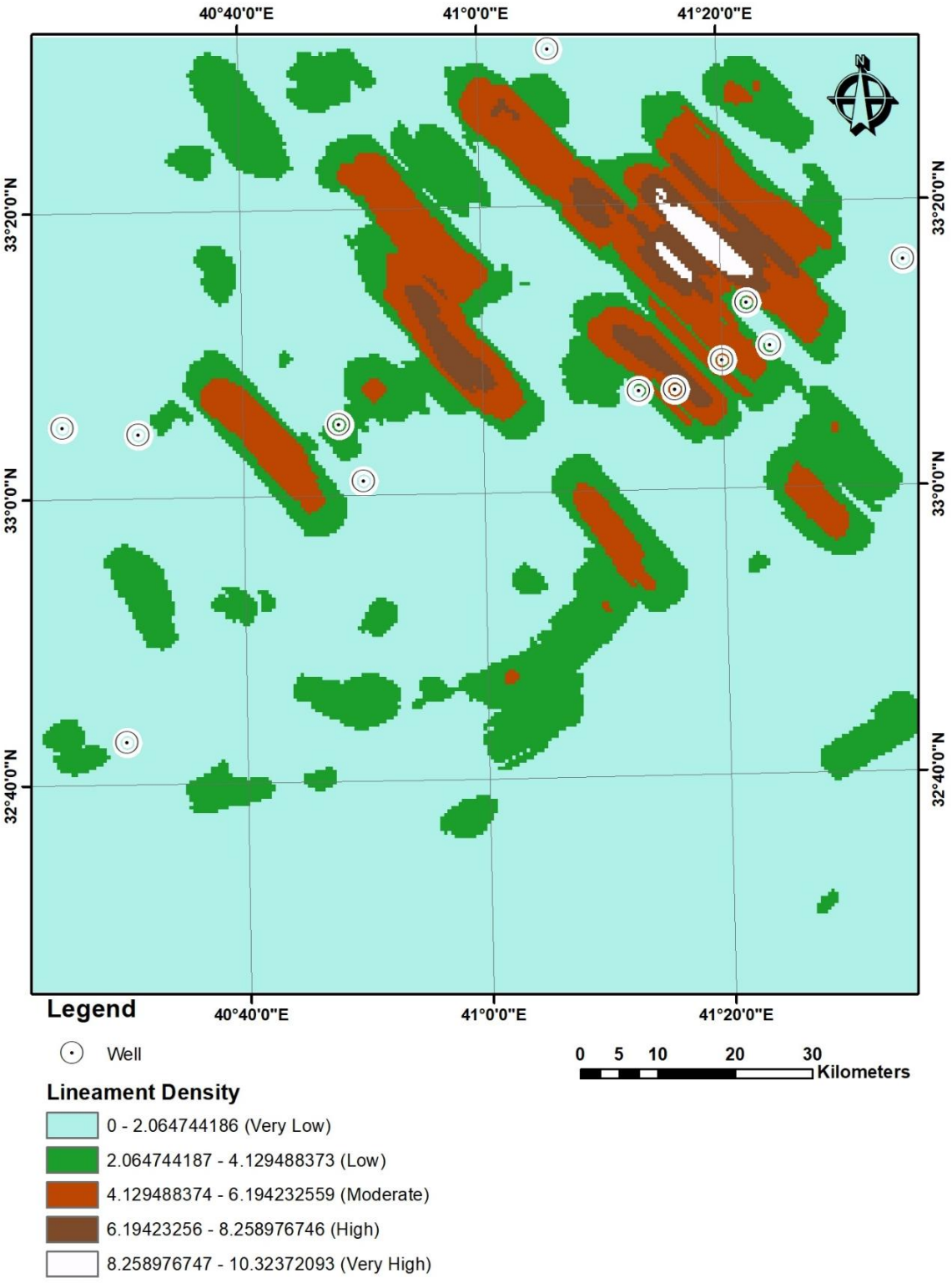


Fig. 10. Lineament density map of the studied area.

Table 1: Research areas' groundwater prospecting depending on lineament density.

Lineaments Density Range (km/km^2)	Groundwater Prospecting
0 to 2.064	Very low
2.064 to 4.129	Low
4.129 to 6.194	Moderate
6.194 to 8.258	High
8.258 to 10.323	Very high

As Fig. 10 illustrates, the lineament density is much lower in the research area's southeast and considerably higher in the study area's northern portion as compared to the other locations. In the site with low lineament density, there is a lower groundwater infiltration rate, whereas in the region with high lineament density, there is a higher groundwater infiltration rate.

A lineament frequency map indicates how many lineaments there are in a square kilometer grid region, with more lineaments indicating excellent groundwater potentiality (Naidu et al., 2015). By calculating the number of lineaments per square kilometer grid, a weighted lineament frequency map is created. Five zones, from high to poor, are used to classify the research region based on lineament frequency. Fig. 11 illustrates that a high zone in this research region denotes a modest groundwater potential.

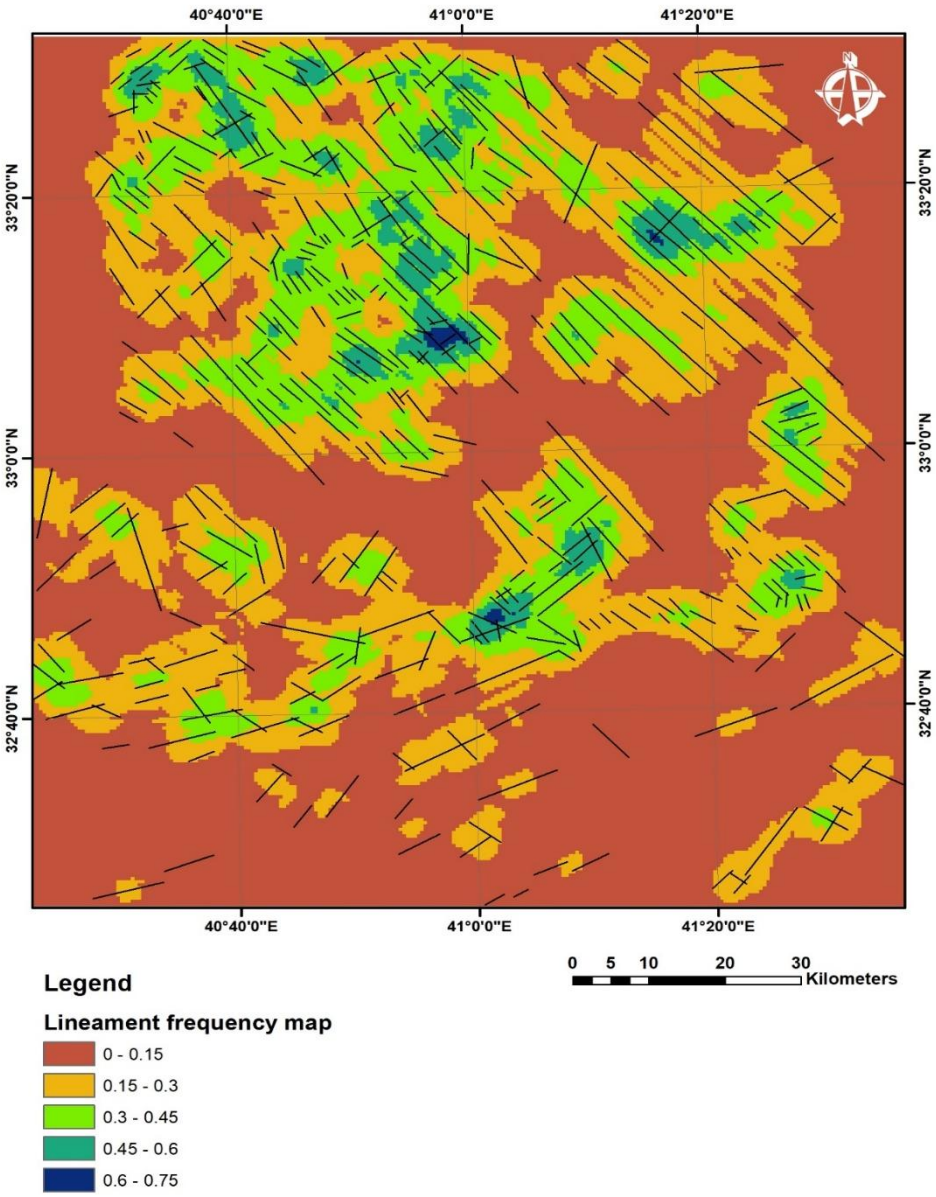


Fig. 11. Lineament Frequency map of the studied area.

According to Fig. 12, there are many lineament junction nodes in the land located in the north and south portions of the research region, but there are few or none in other places. Since groundwater originates within faults and fractures in the rocks, these previously indicated regions might offer strong groundwater potentials in terms of groundwater exploration due to their large concentration of lineament intersections.

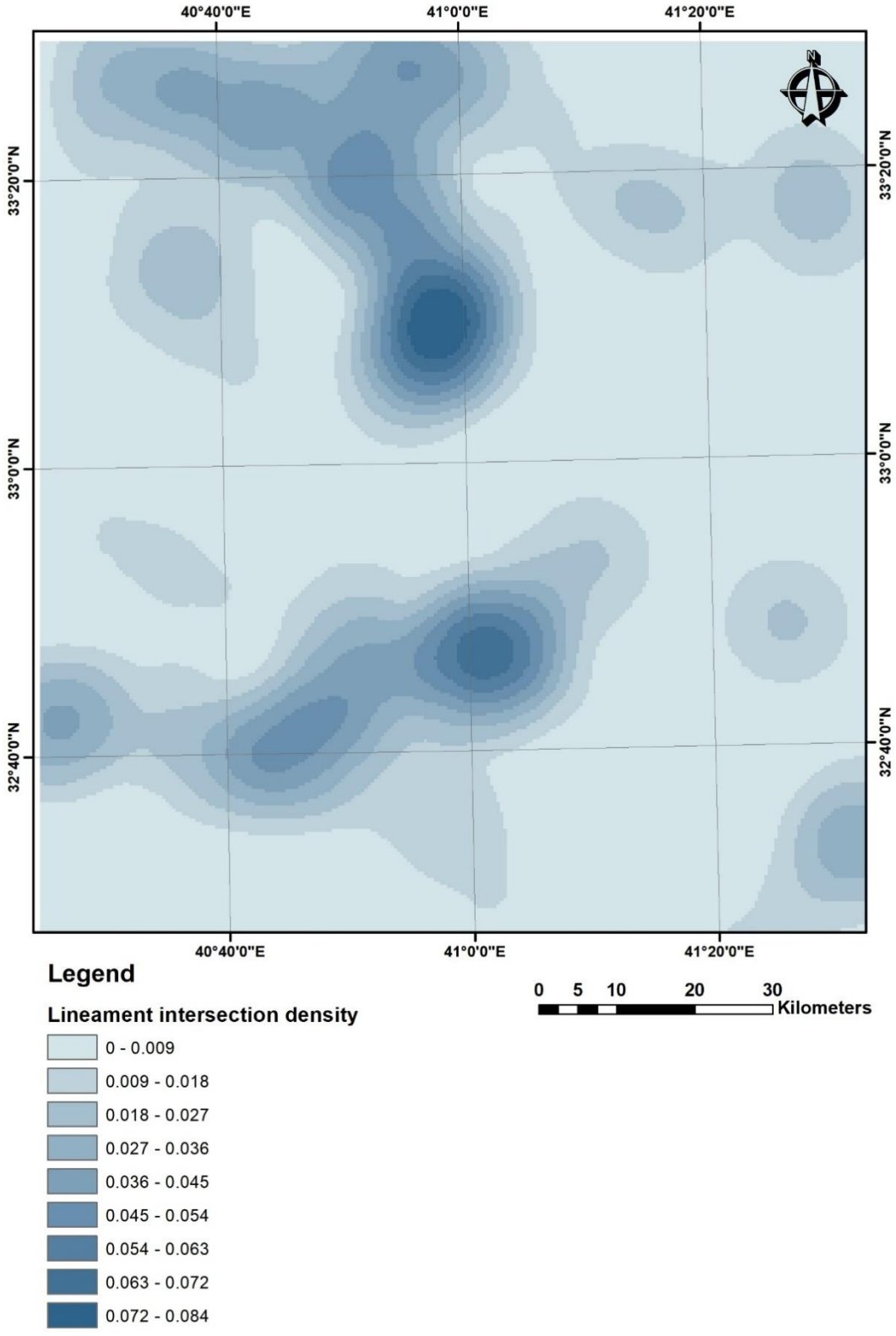


Fig. 12. The Study area's density map of lineaments intersecting.

Conclusion

Groundwater investigations on hard formations frequently necessitate data extraction from satellite imagery and GIS. Because of the lack of available data, maps of the lineaments and structural features are crucial materials for identifying locations of the groundwater recharge and discharge, flow, and development. Specifically, the lineaments related to

fractures, faults, and joints are primarily responsible for groundwater occurrences in hard rocks. Moreover, the concentration and distribution of groundwater discharge locations are strongly associated with lineament distribution.

For geologic and tectonic research in desert regions like the study region, where rocks are well exposed, and field visits are challenging, remote sensing is a potent tool. Most geological formations, including faults, can be understood and analyzed through the use of satellite images. This study presents the results of lineament extraction from Landsat-7 satellite images in identifying groundwater areas in the Iraqi Western Desert. Filtering and band composite processes are applied to the final lineament extraction in the studied area. Combining several image-enhancing methods, such as color composite (CC) and filtering, proved useful and appropriate for spotting linear structures.

To effectively acquire a thorough general perspective of the tectonic stress direction in this area, the orientation analysis of the lineament findings shows that the primary orientations of the lineaments are N 40° W, with the minor directions being N 15° W, N 50° E, and N 55° W.

Groundwater wells in the investigated region are projected on a lineament density map; most of these wells matched the areas with a high density of linear structures. The research region has been divided into five groups based on lineament frequency, density, and intersect maps (Figures 10, 11, and 12); they are: very low, low, moderate, high, and very high. Groundwater potential is highest in areas in the high and very high categories. According to the study, 1351 km^2 of zones have very good, medium, and moderate groundwater potential.

References

Abdul-Qadir, A.M., 2002, Integration of remote sensing and GIS for optimal Utilization of water resources in the western desert of Iraq, PhD Thesis, Univ. of Baghdad, Iraq, 152 P.

Adeyeye, O.A., Ikpokonte E.A., Arabi, S.A., 2019. GIS-based groundwater potential mapping within Dengi area, North Central Nigeria, The Egyptian Journal of Remote Sensing and Space Science, Vol 22, 2, pp. 175-181, ISSN 1110-9823, https://doi.org/10.1016/j.ejrs.2018.04.003 .

Al Rawi, F., 1986. Basement Depth Estimation in the Western Desert of Iraq using the power spectrum technique, Journal. Geol. Soc. Iraq, Vol. 19, No.2. pp. 17-22.

Al-Amiri, H.M., 1978. Structural interpretation of Landsat satellite imagery for western Desert, Iraq, Unpub. Rep., No.923, GEOSURV, Iraq, 60 P.

Al-Azzawi, T.M., 1988. Tectonics of the western Euphrates through interpretation of satellite images and geological information, unpublished master's thesis, College of Science, University of Baghdad, 108 P.

Al-Djazouli, M.O., Elmorabiti, K., Rahimi, A., Amellah, O. and Fadil, O.A.M., 2021. Delineating of groundwater potential zones based on remote sensing, GIS and analytical hierarchical process: a case of Waddai, eastern Chad, GeoJournal, https://doi.org/10.1007/s10708-020-10160-0 .

AlFasatwi, Y.A. and Dijk, P.M., 1990. Lineament and geomorphic analysis of remote sensing data as an aid to hydrocarbon exploration, Sirt basin, Libya, ITC Journal, Vol. 2, pp. 137-144. http://ezproxy.utwente.nl:2048/login?url=https://webapps.itc.utwente.nl/library/1990/general/vandijk_lin.pdf.

Al-Hiti, I.A., 1985, Microseismic of the Gaara area - Western Desert, unpublished master's thesis, College of Science, University of Baghdad, 145 P.

Al-Jaf, A.O., 2008. Remote sensing and GIS for studying some geological phenomena and mineral deposits in the western desert in Iraq, unpublished MSc. Thesis, Univ. of Baghdad, Iraq.

Al-Muthen, A.A., 2009. Regional structural study of Ga'ara area in western desert of Iraq using Landsat image data, unpublished MSc. Thesis, Univ. of Baghdad, Iraq.

Al-Sulaiman, F.A., 1989. Structural study of fracture systems in the Western Desert using remote sensing data, unpublished master's thesis, College of Science, University of Baghdad, 125 P.

Benjmel, K., Amraoui, F., Boutaleb, S., Ouchchen, M., Tahiri, A.; Touab, A., 2020. Mapping of groundwater potential zones in crystalline terrain using remote sensing, GIS techniques, and multicriteria data analysis (case of the Ighremregion, western Anti-Atlas, Morocco). Water, pp. 12, 471.

Brunner, P., Hendricks Franssen, H.J., Kgotlhang, L., 2007. How can remote sensing contribute in groundwater modeling. Hydrogeol. J. 15 (1), pp. 5–18. https://doi.org/10.1007/s10040-006-0127-z.

Coulibaly, H.S.J.P., Honoré, C.T.J., Naga, C., Kouadio, K.C.A., DIDI, S.R.M., Diedhiou, A. and Savane, I., 2021. Groundwater exploration using extraction of lineaments from SRTM DEM and water flows in Béré region. The Egyptian Journal of Remote Sensing and Space Sciences 24 (3), pp. 391–400. https://doi.org/10.1016/j.ejrs.2020.07.003.

Delgado, A.C.G., 2018. A new method to map groundwater potential at a village scale, based on a comprehensive borehole database. An application to Sikasso, Republic of Mali.

Dembele, A. and Ye, X., 2017. Spatial Analysis of Linear Structures in the Exploration of Groundwater. International Journal of Geo Information. https://doi.org/10.3390/ijgi6110335.

El-Etr, H., 1974, Proposed terminology for natural linear features, Proceeding of the 1st inter. Conference on the new basement tectonics, Utah Geol., Assoc., Publ., No. 53, pp. 480-489.

Hasan, A.A., Ali, F.M., Fadil, L.A., Amine, A., Abdullah, L.H. and Mosquera, C.D., 2022. The study of drainage patterns distortion in the Iraqi western desert using remote sensing data. AIP Conference Proceedings. 2437, 020181. https://doi.org/10.1063/5.0092975.

Jassim, S.Z. and Goff, J.C., 2006. Geology of Iraq. Dolin, Czech Republic: Prague and Moravian Museum.

Jensen, J.R., 1996. Introductory Digital Image Processing: A Remote Sensing Perspective. 2nd Edition, Prentice Hall, Inc., Upper Saddle River, NJ.

Jhariya D., Kumar T, Gobinath M, Diwan P, Kishore N., 2016. Assessment of groundwater potential zone using remote sensing, GIS and multi criteria decision analysis techniques. J Geol Soc India 88: pp. 481-492. https://doi.org/10.1007/s12594-016-0511-9.

Koike, K., Nagano, S. and Ohmi, M., 1995. Lineament analysis of satellite images using a Segment Tracing Algorithm (STA). Computers and Geosciences, 21(9), pp. 1091–1104. https://doi:10.1016/0098-3004(95)00042-7.

Koita M., 2010. Characterization and modeling of the hydrodynamic functioning of a fractured aquifer in a basement zone. Dimbokro-Bongouanou region (east-central Ivory Coast). 3rd cycle thesis, Monptpellier II University, 235 P.

Lillisand, T.M., Kiefer, R.W. and Chipman, J., 2015. Remote sensing and Image Interpretation, John Wiley, 7th Edition, 736 P.

Lloyd, J.W., 1999. Water Resources in Hard Rock Aquifers in Arid and Semi-Arid Areas," UNESCO Studies and Reports in Hydrogeology No. 58, United Nations Educational, Scientific and Cultural Organization (UNESCO), Paris.

Magaia, L.A., Goto, Tn., Masoud, A.A. and Koike, K., 2018. Identifying Groundwater Potential in Crystalline Basement Rocks Using Remote Sensing and Electromagnetic Sounding Techniques in Central Western Mozambique. Nat. Resour. Res. 27, 275– 298. https://doi.org/10.1007/s11053-017-9360-5.

Magesh, N.S., Chandrasekar, N., Soundranayagam, J.P., 2012. Delineation of groundwater potential zones in Theni district, Tamil Nadu, using remote sensing, GIS and MIF techniques. Geosci Front 3: pp. 189-196. https://doi.org/10.1016/j.gsf.2011.10.007.

Maina, M. and Tudunwada, I., 2017. Lineament Mapping for Groundwater Exploration in Kano State, Nigeria. Journal of Advances in Agricultural and Environmental Engineering. (IJAAEE) Vol. 4, Issue 1, pp. 226-229.

Meijerink, A.M., Bannert, D., Batelaan, O., Lubczynski, M.W., Pointet, T., 2007. Remote sensing applications to groundwater. United Nations Educational, Scientific and Cultural Organization (UNESCO). 304 P. http://unesdoc.unesco.org/images/0015/001563/156300e.pdf

Mpofu, M., Madi, K. and Gwavava, O., 2020. Remote sensing, geological, and geophysical investigation in the area of Ndlambe Municipality, Eastern Cape Province, South Africa: Implications for groundwater potential, Groundwater for Sustainable Development, Vol 11, 100431, ISSN 2352-801X, https://doi.org/10.1016/j.gsd.2020.10043.

Mustard, J. F, Sunshine, J. M., 1999. Spectral analysis for earth science: investigations using remote sensing data. Remote sensing for the earth science - Wiley, New York.

Naidu, C.K., Reddy B.V. and Mouli, C.C., 2015. Delineation of Groundwater Potential Zones using Remote Sensing and GIS Techniques: A Case Study of Sarada Gedda Sub Watershed. International Journal of Engineering Research and Technology (IJERT). Vol. 4 Issue 11.

Owolabi, S.T., Madi, K., Kalumba, A.M. and Orimoloye, I.R., 2020. A groundwater potential zone mapping approach for semi-arid environments using remote sensing (RS), geographic information system (GIS), and analytical hierarchical process (AHP) techniques: a case study of Buffalo catchment, Eastern Cape, South Africa. Arab J Geosci 13, 1184. https://doi.org/10.1007/s12517-020-06166-0.

Pradhan, A.M.S., Kim, Y. T., 2014. Relative effect method of landslide susceptibility zonation in weathered granite soil: A case study in Deokjeok-ri Creek, South Korea. Nat. Hazards, 72, pp. 1189–1217.

Preeja, K. R., Joseph, S., Thomas, J. and Vijith, H., 2011. Identification of groundwater potential zones of a tropical river basin (Kerala, India) using remote sensing and GIS techniques. J. Indian Soc. Remote Sensing 39, pp. 83–94. https://doi:10.1007/s12524-011-0075-5.

Saadi, O., Nouayti, N., Nouayti, A., Dimane, F. and Elhairechi, K., 2021. Application of remote sensing data and geographic information system for identifying potential areas of groundwater storage in middle Moulouya Basin of Morocco, Groundwater for Sustainable Development, Vol. 14, 100639, ISSN 2352-801X, https://doi.org/10.1016/j.gsd.2021.100639.

Saepuloh A., Haeruddin H., Heriawan M., Kubo T., 2018. Geothermics application of lineament density extracted from dual orbit of synthetic aperture radar (SAR) images to detecting fluids paths in the Wayang Windu Geothermal field (West Java, Indonesia). Geothermics 72, pp. 145–155.

Sarp, G., 2005. Lineaments analysis from satellite images, north–west of Ankara, MSc. Thesis, The Graduate School of Natural and Applied Sciences of Middle East Technical University, 76 P.

Siegal, B.S., Gillespie, A.R. and Siegal, B.S., Eds., 1980. Remote sensing in geology (p. 702). New York: Wiley.

Sissakian, V.K., 2000. Geological Map of Al-Ramadi Quadrangle, sheet N1-38-9. GEOSURV, Baghdad, Iraq.

Sissakian, V.K. and Mohammed, B.S., 2007. Geology of Iraqi western desert; Stratigraphy, Iraqi Bull. Geol. Min. Special Issue, pp. 51-124.

Subba Rao, N., 2006. Groundwater potential index in a crystalline terrain using remote sensing data. Environ. Geol. 50, pp. 1067–1076.

Wang, J., 1990. Use of the Hough Transform in Automated Lineament Detection, IEEE Transactions on Geoscience and Remote Sensing, Vol. 28, No. 4, pp. 561-566. https://DOI: 10.1109/TGRS.1990.572949.

Youan Ta., M., 2008. Contribution of remote sensing and geographic information systems to the hydrogeological prospecting of the Precambrian basement of West Africa: The case of the Bondoukou region, Northeast Côte d'Ivoire. PhD Thesis, University of Cocody-Abidjan, 236 P. (in French)

Zumsprekel, H. and Prinz, T., 2000. Computer-enhanced multispectral remote sensing data: A useful tool for the geological mapping of Archean terrains in (semi)arid environments. Computer and Geosciences, 26: pp. 87-100. https://doi.org/10.1016/S0098-3004(99)00042-4.

Iraqi National Journal of Earth Science

www.earth.uomosul.edu.iq

Climate Change in Jordan: A Case Study of Rajeb Basin

Moath Qudah[1], Kamel Alzboon[2*]

[1] *Department of Water and Environmental Engineering, Huson College, Irbid. Jordan.*

[2] *Department of Water and Environmental Engineering, Al-Balqa Applied University, Irbid. Jordan.*

Article information

Received: 18- Oct -2024

Revised: 02- Jan -2025

Accepted: 04- Mar -2025

Available online: 01- Jan – 2026

Keywords:
Climate Change,
Jordan,
Rajeb Basin,
SDSM,
SWAT,
RCPs,

Correspondence:
Name: Kamel Alzboon

Email: alzboon@bau.edu.jo

ABSTRACT

Rajeb Basin is one of the most important basins in Ajloun Governorate in Jordan. This study aims to assess the effect of climate change on the Rajeb basin using the software of the climate indices (Rclimdex) model for three rainfall stations and three meteorological stations. The future impact of climate change is determined using the statistical downscaling model (SDSM) and the second-generation model for the Earth System (CanESM2) for different emission scenarios. Additionally, the study aims to predict the potential future impact of climate change on the flow of the Rajeb basin at the end of the current century using the Soil and Water Assessment Tool (SWAT) model. Regarding temperature, the results show a significant trend for 9 out of 16 extreme indices for all stations. The hot days increased by 12 days between 1982-2020, and the hot nights increased by 10 nights for the same period. The cool days decreased by 15 days between 1982-2020, and the cool nights decreased by 17 nights for the same period. The summer days (Tmax>25°C) increased by 26 days, and the tropical nights (Tmin>20°C) increased by 61 nights for the same period. It is predicted that the temperature will increase 2100 by 0.2°C, 0.57°C, and 1.4°C based on RCP 2.6, 4.5, and 8.5 scenarios, respectively. The precipitation is predicted to decrease 2100 by 10.8%, 23%, and 43%, for the three scenarios, respectively. Regarding the expected streamflow, SWAT forecast results indicate a decrease in streamflow by 8.1%, 38%, and 69.2% between 2018- 2100 based on RCP 2.6, 4.5, and 8.5, respectively. According to the study, local organizations and decision-makers need to take into consideration the effects of climate change on the Rajeb basin. Pumping operations from the basin must be monitored to ensure the sustainability of water resources.

DOI: 10.33899/injes.v26i1.60221, ©Authors, 2026, College of Science, University of Mosul.
This is an open-access article under the CC BY 4.0 license (http://creativecommons.org/licenses/by/4.0/).

التغير المناخي في الأردن: دراسة حالة لحوض راجب

معاذ قضاة[1] ، كامل الزعبون[2]*

[1] *قسم هندسة المياه والبيئة، كلية الحصن، إربد، الاردن.*

[2] *قسم هندسة المياه والبيئة، جامعة البلقاء التطبيقية، إربد، الاردن.*

معلومات الارشفة

تاريخ الاستلام: 18- اكتوبر-2024

تاريخ المراجعة: 02- يناير-2025

تاريخ القبول: 04- مارس-2025

تاريخ النشر الالكتروني: 01- يناير -2026

الكلمات المفتاحية:

تغير المناخ،

الأردن،

حوض راجب،

SDSM،

SWAT،

RCPs،

المراسلة:

الاسم: كامل الزعبون

Email: alzboon@bau.edu.jo

الملخص

يُعد حوض راجب أحد أهم الأحواض في محافظة عجلون في الأردن. تهدف هذه الدراسة إلى تقييم تأثير التغير المناخي على حوض راجب باستخدام نموذج مؤشرات المناخ (RClimdex) لثلاث محطات أمطار وثلاث محطات أرصاد جوية. يتم تحديد التأثير المستقبلي للتغير المناخي باستخدام نموذج التصغير الإحصائي (SDSM) ونموذج الجيل الثاني لنظام الأرض (CanESM2) لسيناريوهات انبعاثات مختلفة. بالإضافة إلى ذلك، تهدف الدراسة إلى التنبؤ بالتأثير المستقبلي المحتمل للتغير المناخي على تدفق حوض راجب في نهاية القرن الحالي باستخدام نموذج تقييم التربة والمياه.(SWAT) فيما يتعلق بدرجة الحرارة، تُظهر النتائج اتجاهاً كبيراً لتسعة من أصل 16 مؤشراً متطرفاً في جميع المحطات. زادت الأيام الحارة بمقدار 12 يوماً بين (1982-2020)، وزادت الليالي الحارة بمقدار 10 ليالٍ لنفس الفترة. انخفضت الأيام الباردة بمقدار 15 يوماً والليالي الباردة بمقدار 17 ليلة لنفس الفترة. زادت أيام الصيف (الحد الأقصى لدرجة الحرارة > 25 درجة مئوية) بمقدار 26 يوماً، وزادت الليالي الاستوائية (الحد الأدنى لدرجة الحرارة > 20 درجة مئوية) بمقدار 61 ليلة لنفس الفترة. ومن المتوقع أن ترتفع درجات الحرارة في عام 2100 بمقدار 0.2 درجة مئوية، و 0.57 درجة مئوية، و 1.4 درجة مئوية، بناءً على سيناريوهات RCP 2.6 ، و 4.5، و 8.5 على التوالي. ويُتوقع أن تنخفض معدلات الهطول المطري في عام 2100 بنسبة 10.8%، و 23%، و 43%، للسيناريوهات الثلاثة على التوالي. بالنسبة للتدفق المتوقع للمجرى المائي، تشير نتائج توقعات نموذج (SWAT) إلى انخفاض في تدفق المجرى المائي بنسبة 8.1%، و 38%، و 69.2% بين عامي 2018 و 2100 بناءً على سيناريوهات RCP 2.6، و 4.5، و 8.5 على التوالي. ووفقاً للدراسة، يجب على المنظمات المحلية وصناع القرار أخذ تأثيرات التغير المناخي على حوض راجب بعين الاعتبار. كما يجب مراقبة عمليات الضخ من الحوض لضمان استدامة الموارد المائية.

DOI: 10.33899/injes.v26i1.60221, ©Authors, 2026, College of Science, University of Mosul.
This is an open-access article under the CC BY 4.0 license (http://creativecommons.org/licenses/by/4.0/).

Introduction

Climate change is one of the global problems that receives attention at all political, scientific, and economic levels (Hansen and Sato, 2012). Climate change is a long-term change in the weather patterns that appears after millions of years. It differs from the natural distribution of the prevailing climate condition (US Environmental Protection Agency, 2014). The major greenhouse gases are water vapor, CO_2, CH_4, N_2O, and O_3. Water vapor (H_2O) with an average atmospheric concentration of 10 ppm is emitted from water bodies such as seas and oceans. Carbon dioxide (CO_2) with a long-term atmospheric concentration of 412 ppm is primarily emitted through the burning of fossil fuels and deforestation. Methane (CH_4) with an atmospheric concentration of 1860 ppb is produced during natural processes like wetland decay, as well as through human activities such as livestock farming and the extraction of fossil fuels. Nitrous oxide (N_2O), with a very low atmospheric concentration of 1332 ppb, is released from agricultural and industrial activities, combustion of fossil fuels, and natural processes in soils and oceans. Additionally, fluorinated gases, including hydrofluorocarbons (HFCs) with an atmospheric concentration of 5 ppb, perfluorocarbons (PFCs), and sulfur hexafluoride (SF6) with an atmospheric concentration of 10 ppt, are synthetic gases used in various industrial

applications (US Environmental Protection Agency, 2021). Since 1750, concentrations of greenhouse gases such as CO_2, CH_4, and N_2O have increased by 150 percent, 20 percent, and 40 percent, respectively (Intergovernmental Panel on Climate Change, 2014). This resulted from a rise in industrial activity, fuel combustion, and population growth. This has led to a change in the rate and trend of rainfall, drought, and heat waves. The contributions of greenhouse gases in climate change are 36-72%, 9-26%, 4-9%, and 2-7% for water vapor, carbon dioxide, methane, and ozone, respectively (European Environment Agency, 2020). The increase in emissions, especially carbon dioxide, has a significant impact on the atmosphere's growing temperature. The average global temperature increased significantly when compared to the base period (1901–2000). Since 1850, the average global temperature has risen by 1.1 to 1.2 °C. By 2100, the average global temperature is projected to increase by 2 °C, and 4.2 °C by the year 2400 (Malhi et al., 2021). Therefore, this change is a major reason affecting the quality and quantity of water and causes the transfer of sediment due to severe floods and depletion of water resources (Al Qatarneh et al., 2018). Additionally, Climate change is a major threat to global agriculture. Traditional farming methods are disrupted by rising temperatures, changes in precipitation patterns, and an increase in the frequency of extreme weather events. Reduced crop yields, more water scarcity, and the spread of diseases and pests are the results of these changes (Intergovernmental Panel on Climate Change, 2021). Declining agricultural productivity can lead to an increase in poverty levels, food price instability, and rural-to-urban migration. Based on the A1B scenario, which depicts a future world characterized by very rapid economic growth, low population growth, and sharp use of alternative energy, by the year 2050, 0.5 to 3.1 billion people will suffer from water scarcity because of an increase in temperature by two degrees Celsius (Gosling and Arnell, 2016).

Jordan receives an average of 7,200 million cubic meters (MCM) per year of rainfall, decreasing to 6,000 MCM in dry years and doubling in wet years. About 1.3% of Jordan received more than 500 mm of rainfall, 1.8% received between 300 and 500 mm, 3.8% received about 200 to 300 mm of rainfall, and between 100 and 200 mm of rainfall accounts for 12.5%; the remaining regions received less than 100 mm (Salameh, 2018). Jordan suffers from a water shortage, and this shortage has become a major challenge due to the abnormal increase in the population, due to immigration, as well as climate change. The available water resources in Jordan decreased from 3600 m^3/c.y in the mid-1950s to 125 m^3/c.y in 2016 (Ministry of Water and Irrigation, 2016). It also continued to decrease to 35 m^3/c.y in 2020 (UNHCR, 2020). This is below the water poverty index of 1000m^3/c.y (Al-Tabbal and Alzboon, 2012). Numerous studies demonstrated the substantial effects of climate change in Jordan. Al-Dahmsha et al. (2018) utilized the RClimdex program to analyze temperature and precipitation trends across six climate stations in various regions. Their findings revealed a notable decline on the account of cold days, amounting to an 11.7% reduction. Abdullah (2020) employed the SDSM model and historical meteorological data from 1961 to 2014 from eight stations in Jordan to forecast the future impacts of climate change on temperatures and rainfall. Projections indicated a 17% decrease in precipitation, and the temperature will rise, ranging from 2.5 to 5°C by the end of the century. Al Smadi (2006) analyzed T_{min} and T_{max} trends using data from Jordanian meteorological stations from 1922 to 2005, revealed a temperature increase of 0.03°C/year.

In Ajloun Governorate, the Rajeb basin is recognized as one of the most crucial sources of water resources. This basin supports the region economically and is considered one of the agricultural and tourist basins. Water resources in this basin have undergone a significant change over the past few decades. Therefore, this study aims to identify this effect to provide the decision-makers with scientific data on this issue and to address climate change in water resources strategies. To the best of the author's knowledge, this is the first study related to climate change in the Rajeb basin. Using the RClimdex program, the study will analyze data from three meteorological stations and three rainfall stations. Furthermore, using the results of the statistical downscaling model (SSD) and the second-generation Earth System Model

(CanESM2), the Soil and Water Assessment Tool (SWAT) model will be used to forecast future effects on water resources.

Methodology

The Study Area

Rajeb Basin is one of the most important basins in Ajloun Governorate. Its area is about 16% of the total area of the governorate. Rajeb basin is a perennial flow fed by numerous valleys, the most significant one among them is Al-Suq Valley, which begins with the spring of Umm Al-Jaloud in the east and then travels to the south. It represents a significant water source for the nearby agricultural plains (Gharaibeh, 2023). As shown in Figure (1), Rajeb basin is positioned astronomically in northern Jordan, south of Ajloun Governorate, between the longitudes of 32° 13' and 32°19' E and latitudes 35°40' - 35°49' N. The basin has a Mediterranean climate defined by dryness, hot summers, cold winters, and rainy autumns (Alshraifat, 2021). Its length and width are 15.8 km and 3.76 km respectively (Jalabneh and Ananzeh, 2022).

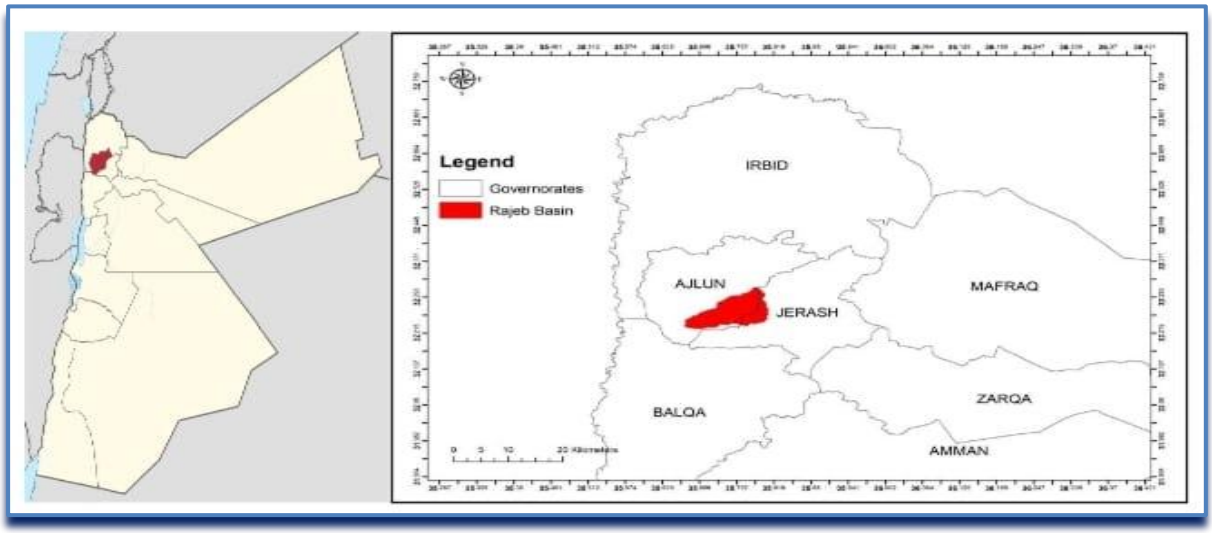


Fig. 1. Location Map of the Study Area

Data Used 1. Topography

The delineated process is carried out using a digital elevation model (DEM) downloaded from the USGS (http://earthexplorer.usgs.gov/) with a 30 m resolution (Fig. 2). The highest point of the basin is more than 1,200 meters above sea level, and the lowest point is located at the basin's outlet, at a height of about 84 meters above sea level.

2. Land use and soil

Land use maps are freely available from several space agencies, such as the European Space Agency and the National Aeronautics and Space Administration (NASA) (Wulder et al., 2018). Land use of the study area is classified as forest, crops, urban, bare ground, and rangeland, as shown in Figure 3 and Table 1. The Land cover (use) maps in this research were downloaded from the Sentinel-2 10 m land cover time series of the world from 2017–2021, produced by Microsoft, Esri, and Impact Observatory (https://www.arcgis.com/home/item.html?id= d3da5dd386d140cf93fc9ecbf8da5e31). The Digital Soil Map of the World, version 3.6, which was produced by the Food and Agriculture Organization of the United Nations (FAO/UNESCO), is shown in Figure 4 and Table 2. The research region's soil is mostly loam, but there is also clay soil that covers the eastern part (http://www.fao.org/geonetwork/srv/en/metadata. show?id=14116).

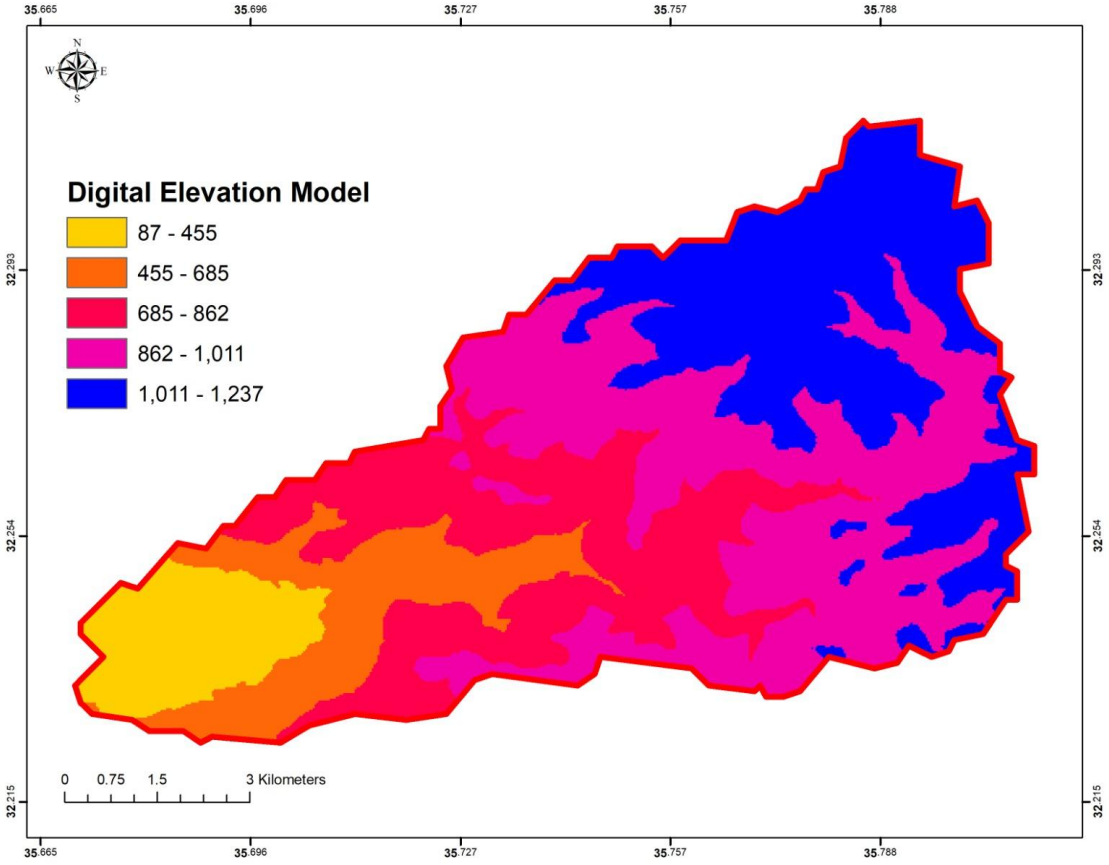


Fig. 2. Topography of the study area using Digital Elevation Model (m above sea level).

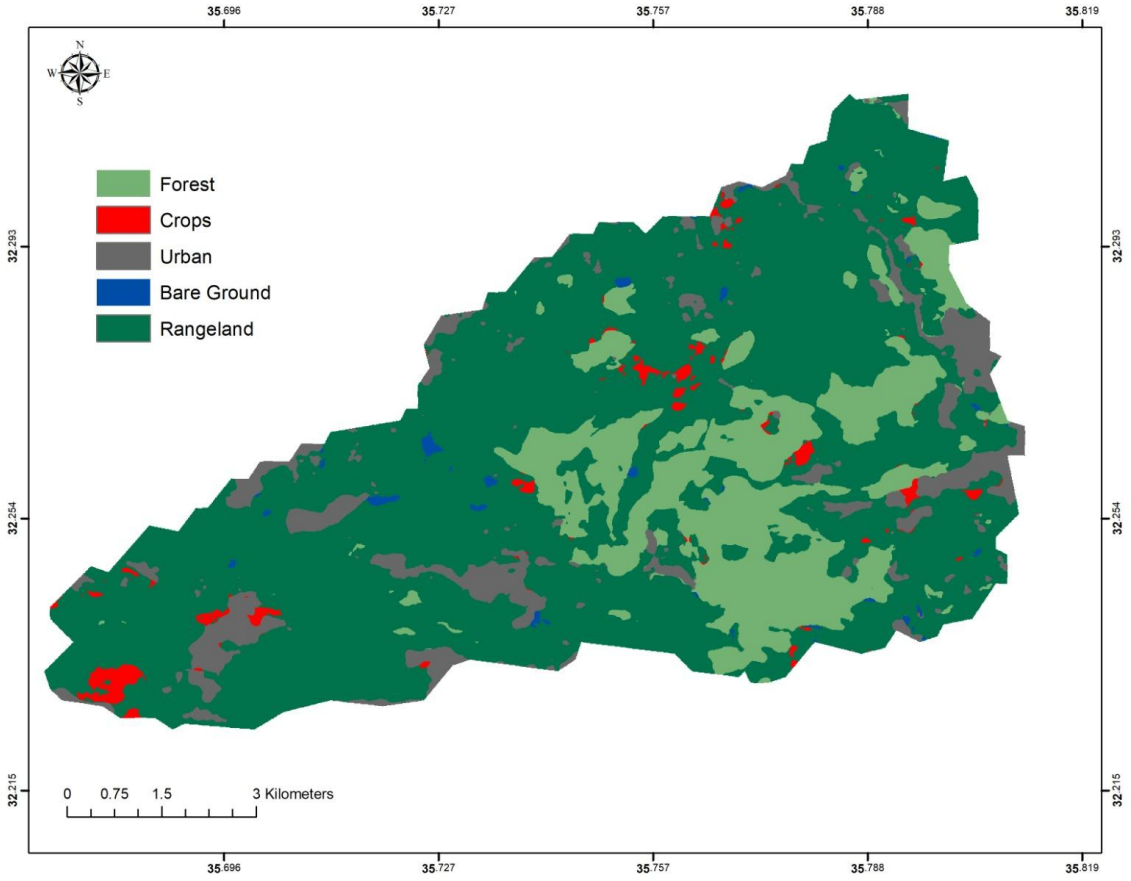


Fig. 3. Land use map of the study area.

Table 1: Classification of the land use in the study area.

Class Name	Land Use (%)
Rangeland	65.7
Forest	19.3
Urban	7.8
Crops	5.8
Bare Ground	1.4

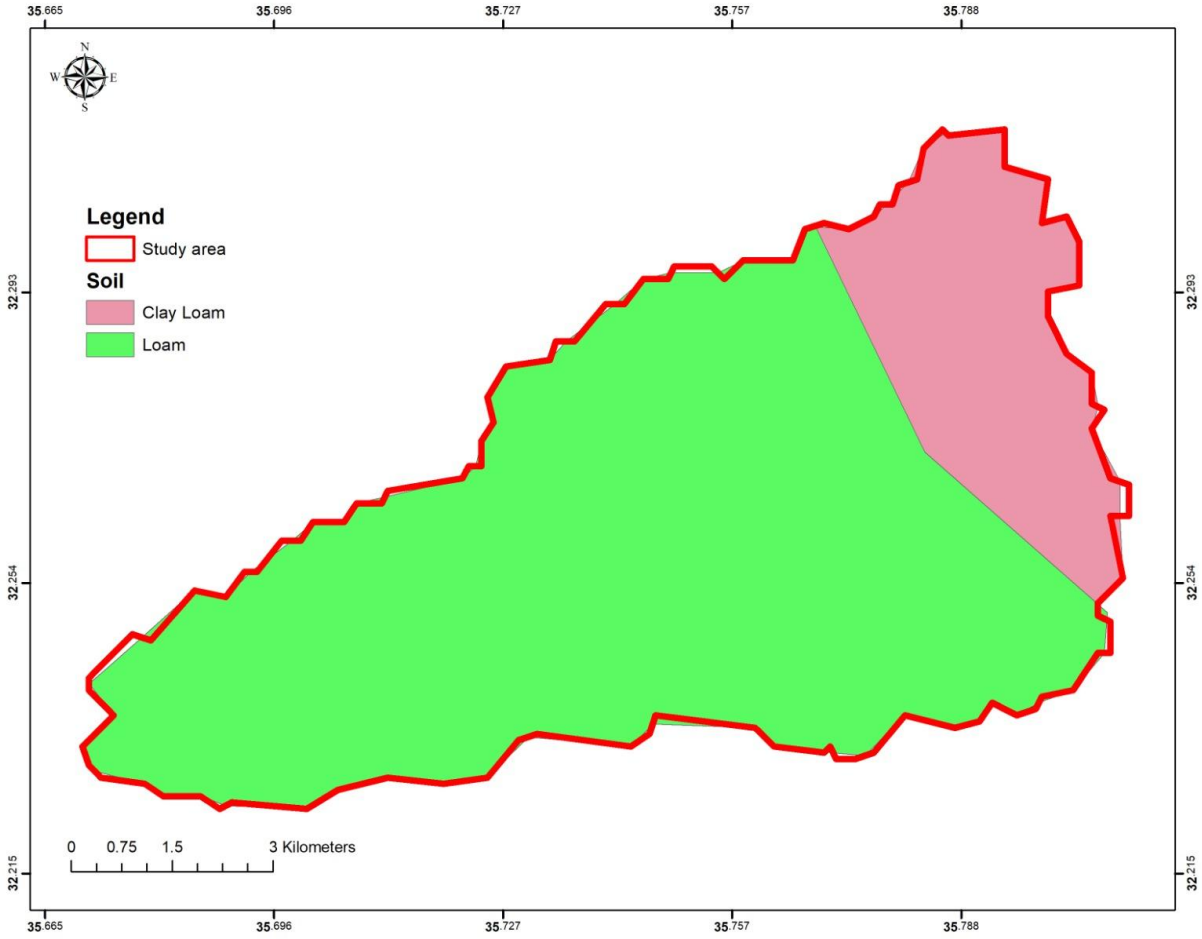


Fig. 4. Soil Map of the Study Area.

Table 2: Soil characteristics in the study area.

Soil Class	Soil ratio (%)	FAO Soil Class	Ks*(mm/hr)	Bulk Density (g/m³)	Hydrology group	Clay (%)	Silt (%)	Sand (%)
Clay Loam	24.6	Be36-3bc-5154	12.49	1.2	C	36	37	27
Loam	75.4	Ao55-2bc-5125	11.23	1.3	C	23	28	49

*Ks is the saturated hydraulic conductivity (mm/h).

3. Climate Data

Two data types are used: hydrological (rainfall and streamflow) and meteorological (maximum and minimum temperatures, relative humidity, and wind speed). Data were obtained from two sources: the Ministry of Water and Irrigation (MWI) and the Data Access Viewer website (DAV)(Larc.NASA, 2023) (https://power.larc.nasa.gov/data-access-viewer/). The effects of global warming on temperature, rainfall, and streamflow were investigated using three meteorological stations, three rainfall stations, and one streamflow gauge station. In this study, data on maximum temperature, minimum temperature, precipitation, wind speed, relative humidity, and discharge will be used to determine the impact of climate change in the study area.

4. Data quality control

Homogeneity tests are employed to assess whether a dataset exhibits uniformity in distribution and maintains consistent statistical characteristics. In climate studies, the utilization of dependable data is essential to ensure the elimination of erroneous trends or fluctuations. One method to ascertain data reliability involves comparing a climatic series with adjacent stations, which are used as the foundational principle for all relative homogeneity tests. In this study, Pettitt's test, the standard normal homogeneity test (SNHT), and von Neumann's test are utilized to assess the homogeneity of meteorological and hydrological data, with analysis conducted using the XLSTAT program (Al Qatarneh et al., 2018).

Models used

1. RClimdex Program

Numerous researchers in different countries used Rclimdex to calculate climate change indices (Al-Dahamsheh et al., 2018; Bashabsheh and Alzboon, 2024). It was created by Byron Gleason at the National Climate Data Centre (NCDC) in the United States (Zhang and Yang, 2004). Daily rainfall data and daily maximum and minimum temperatures were used in the Rclimdex program to calculate the basic climatic indices.

Before computing the core indices, the data should be homogeneous. In addition, Rclimdex performs data quality control by replacing invalid values and missing data with (-99.9), such as daily precipitation levels below zero and daily maximum temperatures below daily minimum temperatures (Zhang and Yang, 2004). The significant trend is tested with a p-value and a comparison of the estimated slope with the error slope. A significant trend will be recognized if the p-value $< \alpha$ and the estimated slope is larger than the slope error value (Berhane et al., 2020). The core indices that are displayed with their definitions and units in Table (3) are necessary to assess potential climate change during the study period.

Table 3: Climate Indices Terms and Definitions (Zhang and Yang, 2004; Alzboon et. al., 2021).

ID	Indicator name	Definitions	Units
FD0	Frost days	Annual count when TN (daily minimum) < 0°C	Days
SU25	Summer days	Annual count when TX (daily maximum) > 25°C	Days
ID0	Ice days	Annual count when TX (daily maximum) < 0°C	Days
TR20	Tropical nights	Annual count when TN (daily minimum) > 20°C	Days
GSL	Growing season length	Annual (1st Jan–31st Dec in NH, 1st July–30th June in SH) count between first span ≥6 days with TG>5°C and first span after July 1 with TG<5°C	Days
TXx	Max Tmax	Monthly maximum value of daily maximum temp	°C
TNx	Max Tmin	Monthly maximum value of daily minimum temp	°C
TXn	Min Tmax	Monthly minimum value of daily maximum temp	°C
TNn	Min Tmin	Monthly minimum value of daily minimum temp	°C
TN10p	Cool nights	Percentage of days when TN < 10th percentile	Days
TX10p	Cool days	Percentage of days when TX < 10th percentile	Days
TN90p	Warm nights	Percentage of days when TN > 90th percentile	Days
TX90p	Warm days	Percentage of days when TX > 90th percentile	Days
WSDI	Warm spell duration indicator	Annual count of days with at least 6 consecutive days when TX > 90th percentile	Days
CSDI	Cold spell duration indicator	Annual count of days with at least 6 consecutive days when TN < 10th percentile	Days
DTR	Diurnal temperature range	Monthly mean difference between TX and TN	°C
RX1day	Max 1-day precipitation	Monthly maximum 1-day precipitation	mm
RX5day	Max 5-day precipitation	Monthly maximum consecutive 5-day precipitation	mm
SDII	Simple daily intensity index	Annual total precipitation divided by number of wet days (PR ≥1.0mm)	mm/day
R10	Number of heavy precipitation days	Annual count of days when PR ≥10mm	Days
R20	Number of very heavy precipitation days	Annual count of days when PR ≥20mm	Days
Rnn	Number of days above nn mm	Annual count of days when PR ≥ nn mm (user defined)	Days
CDD	Consecutive dry days	Maximum number of consecutive days with RR <1mm	Days
CWD	Consecutive wet days	Maximum number of consecutive days with RR ≥1mm	Days

2. Statistical Downscaling Model (SDSM)

SDSM was used successfully in many international studies to predict future climate change. In this research, the daily precipitation, maximum, and minimum temperature data for Ajloun, Kufranja, and Wadi Al-Rayyan stations from 2000 to 2018 are used for this purpose. The historical climatic data are divided into two time periods: the calibration period from 2000 to 2015, and the validation period from 2015 to 2018. The SDSM applies the multiple regression method to analyze the relation between the daily climate data at local locations and the large-scale predictors supplied by GCM simulations. Three RCPs (RCP2.6, RCP4.5, and RCP8.5) are considered in this study. Representative Concentration Pathways (RCPs) are the concentrations of greenhouse gases that the IPCC adopted in 2014 for its Fifth Assessment Report (AR5). In general, RCP 8.5 calls for an enormous rise in the use of fossil fuels for energy by the end of the century and no mitigation to keep CO_2 concentrations under control, while RCP 4.5 predicts an increase in energy use until 2040, then decline, and by 2050, renewable energy resources will have grown significantly (Intergovernmental Panel on Climate Change, 2014). The second generation of the Earth System Model (CanESM2) is a tool for evaluating how the climate will change. It generates climate change scenarios using different RCPs. The rainfall, maximum, and minimum temperatures for the period (2018–2100) were predicted using the SDSM, climatic data for the base period (2000–2018), and the outputs of the CanESM2 model based on three scenarios (RCP 2.6, RCP 4.5, and RCP 8.5).

3. SWAT Model

The SWAT model is used in the hydrological model to determine the impact of climate change on the streamflow of the Rajeb basin. The model outputs show a good similarity with the observed data (1981 to 2018), with a coefficient of determination (R^2) exceeding 0.6.

Streamflow is simulated up to the year 2100 to forecast changes in streamflow based on average maximum and minimum temperatures and precipitation under three emission scenarios (RCP2.6, RCP4.5, and RCP8.5). RCPs delineate the trajectory of pollutant concentration up to the year 2100, with RCP2.6, RCP4.5, and RCP8.5 corresponding to radiative forcing pathways of 2.6, 4.5, and 8.5W/m^2 in 2100, respectively. The Arc SWAT-ArcGIS interface is employed in this study. The SWAT is developed to forecast the effects of land management techniques on water, sediment, and agricultural chemical yields in large, complex watersheds with different types of soils, land use, and management situations over extended periods. Based on the characteristics of land use and soil, each watershed is first classified into subbasins, and then into hydrologic response units (HRUs). SWAT can calculate the amount of sediment carried by surface runoff from soil particles and other chemical and chemical mixtures (Arnold et al., 2013). In this study, the runoff curve number (CN) method is used for estimating direct runoff.

4. XLSTAT Program

XLSTAT is a powerful statistical analysis software add-in for Microsoft Excel. In this research, Pettitt's test, SNHT, and von Neumann's tests are used to evaluate the homogeneity of meteorological and hydrological data. Any substantial change or break in a time series can be found using the Von Neumann test, which also shows when the change did not occur. Pettitt's test is used to determine significant changes or breaks in a time series. On the other hand, SNHT is employed to evaluate if there is a considerable shift in the mean between different years. Von Neumann, Pettit, and SNHT tests are performed using the XLSTAT program for time series with a significance level of 0.05. The test hypotheses are:

-Ho indicates homogeneous data.

- Ha indicates nonhomogeneous data.

The Ho hypothesis is accepted if P is greater than 0.05. Conversely, the Ha hypothesis is accepted at (P < 0.05). Additionally, if the data passes two out of the three checks, it is considered acceptable.

Results and Discussions

Quality Control and Data Analysis

The Ho hypothesis is accepted if P is greater than 0.05. Conversely, the Ha hypothesis is rejected if P < 0.05. Additionally, if the data passes two out of the three checks, it is considered acceptable. All stations in this research passed the homogeneity tests as shown in Tables 4, 5, and 6. Therefore, the data are considered homogenous, and no further fitting process is required. The data series are acceptable and can be utilized in trend analysis and modeling.

Table 4: Results of the homogeneity test for annual rainfall data.

Station Name	Station ID	Pettitt's Test			standard normal homogeneity test (SNHT)			Von Neumann's Test		
		α	P	Check	α	P	Check	A	P	Check
Ajloun	AJ0001	0.05	0.277	Ok	0.05	0.965	Ok	0.05	0.871	Ok
Kufranja	AJ0002	0.05	0.523	Ok	0.05	0.906	Ok	0.05	0.909	Ok
Wadi Al-Rayyan	AH0002	0.05	0.349	Ok	0.05	.337	Ok	0.05	0.247	Ok

Table 5: Results of the homogeneity test for mean annual temperature data.

Station ID	Pettitt's Test			standard normal homogeneity test (SNHT)			Von Neumann's Test		
	α	P	check	A	P	Check	A	P	check
Ajloun	0.05	0.246	Ok	0.05	0.362	Ok	0.05	0.772	Ok
Kufranja	0.05	0.239	Ok	0.05	0.361	Ok	0.05	0.769	Ok
Wadi Al-Rayyan	0.05	0.240	Ok	0.05	0.366	Ok	0.05	0.775	Ok

Table 6: Results of the homogeneity test for stream data Series.

Station ID	Pettitt's Test			(standard normal homogeneity test) SNHT			Von Neumann's Test		
	A	P	Check	A	P	Check	A	P	Check
AH0002	0.05	0.016	Not.ok.	0.05	0.433	Ok	0.05	0.131	Ok

Climate Change Trend Analysis

Rclimdex is used to calculate 27 core indices (16 temperature indices and 11 rainfall indices) to determine climate change trends in the study area, as displayed in Tables 7 and 8.

1. Temperature Trend Analysis

Table 7 presents the results of significant tests for temperature indices. The test is conducted with a 95% confidence interval and α = 0.05. All stations exhibit a significant decreasing trend in the cold days (TX10p) index, with slopes of 0.33, 0.33, and 0.401/year for Ajloun, Kufranja, and Wadi Al-Rayyan stations, respectively. This indicates a reduction in the number of cold days by 13, 13, and 15 days, respectively, during the study period (1982-2020). Similarly, there is a significant decrease in the number of cold nights (TN10p) across all stations with a slope of 0.44/year, indicating a reduction of approximately 17 nights during the study period.

The warm days and warm nights (TX90p and TN90p) exhibit a significant positive trend, indicating an increase in the number of hot days by 9-11 days and hot nights by 12-13 nights. Additionally, the monthly maximum value of the daily maximum temperature (TXx) index demonstrates a statistically significant increasing trend in Wadi Al-Rayyan with a slope of 0.057, corresponding to an increase of 2.17°C. Similarly, the monthly minimum value of the daily maximum temperature index (TNx) shows a statistically significant increasing trend in all stations with an average slope of 0.05, implying an increase of 1.9°C.

Regarding the extreme climate indices, there has been a significant increase in the number of summer days with a daily maximum temperature exceeding 25°C (SU25) and tropical nights

with a minimum temperature exceeding 20°C (TR20), reaching up to 28 days and 69 nights for SU25 and TR20, respectively. This trend indicates a notable tendency towards warmer temperatures, with a more pronounced increase observed for hot nights compared to hot days. Al Qatarneh et al. (2018) showed a positive trend in TR20 in the Azraq basin, with temperature analyses revealing increases ranging between 0.847 and 0.424°C per year. Similarly, Abdullah (2020) noted that temperatures in Jordan exhibited an upward trend during the period 1961 – 2014, with the minimum temperature experiencing a more significant increase compared to the maximum temperature.

The annual count of days with at least six consecutive days with TX> 90th percentile (WSDI) reflects the increasing frequency and intensity of heat waves. WSDI is an indicator of hot days with a daily maximum temperature greater than 90th, and represents the warm days over 6 consecutive days. The results of this research show a significant increase in Ajloun and Kufranja stations with an average slope of 0.254/year, indicating a rise in the number of days with at least 6 consecutive days with Tx>90th percentile (Table 7).

Table 7: Results of the significant tests for extreme temperature indices.

Indices	Ajloun			Kufranja			Wadi Al-Rayyan		
	A	P-value	Slope	α	P-value	Slope	α	P-value	Slope
SU25	0.05*	0.001*	0.676	0.05*	0.001*	0.668	0.05*	0.001*	0.715
TR20	0.05*	0*	1.493	0.05*	0*	1.477	0.05*	0.00049*	1.831
FD0	0.05	0.338	-0.03	0.05	0.129	-0.049	0.05	0.143	-0.042
GSL	0.05	0.285	0.015	0.05	0.457	0.009	0.05	0.418	0.012
TXx	0.05	0.081	0.05	0.05	0.081	0.05	0.05*	0.019*	0.057
TXn	0.05	0.417	0.02	0.05	0.417	0.024	0.05	0.392	0.024
TNx	0.05*	0.006*	0.055	0.05*	0.006*	0.055	0.05*	0.006*	0.05
TNn	0.05	0.214	0.036	0.05	0.214	0.036	0.05	0.186	0.038
TX10p	0.05*	0.0003*	-0.33	0.05*	0.0005*	-0.338	0.05*	0.0004*	-0.425
TX90p	0.05*	0.0002*	0.242	0.05*	0.0009*	0.237	0.05*	0.00049*	0.284
TN10p	0.05*	0.003*	-0.44	0.05*	0.0004*	-0.441	0.05*	0.0003*	-0.44
TN90p	0.05*	0.006*	0.335	0.05*	0.0004*	0.333	0.05*	0.0005*	0.311
WSDI	0.05*	0.045*	0.261	0.05*	0.02*	0.299	0.05	0.114	0.201
CSDI	0.05*	0.001*	-0.34	0.05*	0.002*	-0.33	0.05*	0*	-0.478
DTR	0.05	0.307	0.006	0.05	0.307	0.006	0.05	0.293	0.013

*Significant at P≤0.5

2. Rainfall Trend Analysis

The PRCPTOT index (annual total precipitation in wet days) represents the total accumulated precipitation from "wet days" (days with precipitation greater than or equal to 1 mm) within a specific period. The PRCPTOT index shows a significant trend (P=0.021) in Wadi Al-Rayyan station with a negative slope (-2.968), indicating that total precipitation decreased by 112 mm during the study period, while the other stations show an insignificant trend. Days with heavy precipitation (R10mm) show a significant increasing trend in Wadi Al-Rayyan with a slope equal to 0.103 during the study period.

As shown in Table 8, there are no significant changes in any of the indicators at Kufranja station. However, the CDD indicator shows a significant decrease in the Ajloun station, which expresses successive dry days in which the amount of precipitation is less than 1 mm, with a slope of 0.821 per year and a decrease of 31 days during the study period. The results also show that (R10mm and PRCPTOT) had significant changes for the Wadi Al-Rayan station. R10mm index, which indicates days with heavy precipitation, shows a significant increasing trend in Wadi Al-Rayyan with a slope equal to 0.103 and a decrease by 4 days

Models Calibration and Validation

1. Statistical Downscaling Model (SDSM)

The historical climatic data are divided into two time periods: the calibration period from 2000 to 2015 and the validation period from 2015 to 2018, as shown in Table 9. The model's performance is considered acceptable if R^2 is greater than 0.65. The values of R^2 for the maximum and minimum temperature and precipitation are greater than 0.82 for all stations, so

the model's performance is considered acceptable. All stations show higher R^2 for temperatures than for precipitation, which could be related to the annual variability in precipitation.

Regarding the limitations of SDSM, the spatial resolution of SDSM may not be sufficient to capture local-scale variations in climate within the study area, leading to potential biases in local-scale predictions. Additionally, SDSM relies mainly on historical relationships between large-scale climate variables and local observations. Changes in these relationships due to climate change can limit the model's accuracy in future projections. Emission scenarios (RCPs) are based on assumptions about the future, including technological change, energy use patterns, and population growth. These assumptions are uncertain and can significantly impact future greenhouse gas emissions and climate change projections.

Table 8: Results of the significant tests for extreme precipitation indices.

Indices	Ajloun			Kufranja			Wadi Al-Rayyan		
	A	P-value	Slope	α	P-value	Slope	α	P-value	Slope
RX1day	0.05	0.89	0.02	0.05	0.44	-0.11	0.05	0.21	-0.25
RX5day	0.05	0.67	-0.15	0.05	0.20	-0.38	0.05	0.06	-0.69
SDII	0.05	0.69	0.01	0.05	0.89	0.00	0.05	0.44	-0.02
R10mm	0.05	0.43	-0.06	0.05	0.12	-0.08	0.05*	0.05*	-0.10
R20mm	0.05	0.56	-0.02	0.05	0.56	-0.02	0.05	0.17	-0.03
R25mm	0.05	0.33	0.02	0.05	0.61	0.01	0.05	0.69	0.01
CDD	0.05*	0.046*	-0.88	0.05	0.12	-0.78	0.05	0.10	-0.80
CWD	0.05	0.19	-0.03	0.05	0.55	-0.01	0.05	0.16	-0.03
R95p	0.05	0.82	0.19	0.05	0.64	-0.30	0.05	0.22	-0.85
R99p	0.05	0.64	0.23	0.05	0.94	0.35	0.05	0.14	-0.73
PRCPTOT	0.05	0.45	-1.17	0.05	0.13	-1.82	0.05*	0.021*	-2.97
*Significant									

Table 9: SDSM performance during the calibration and validation stages.

Model	Parameter	Calibration			Validation		
		Ajloun	Kufranja	Wadi Al-Rayyan	Ajloun	Kufranja	Wadi Al-Rayyan
		R^2			R^2		
SDSM	T max	0.97	0.96	0.95	0.97	0.95	0.94
	T min	0.97	0.93	0.96	0.96	0.96	0.96
	Precipitation	0.92	0.93	0.84	0.93	0.87	0.82

2. SWAT Model

The results of the hydrological model (SWAT) are not accurate but give a clear indication of the current and future status of water resources in the Rajeb Basin. It is difficult to identify the outputs of the SWAT model because the model requires wide-ranging inputs such as meteorological data, soil properties, and land use. Many parameters in SWAT are uncertain and have a significant impact on model results. Sensitivity analyses are used in this study to assess the impact of parameter uncertainty on model results. A total of thirty-six years of streamflow data are utilized for calibration (1985-2000) and validation purposes (2011-2018).

Table 10 lists the most sensitive parameters used in model calibration. These parameters and their values are determined via a sensitivity analysis based on relevant literature (Arnold et al., 2012; Feyereisen et al., 2007).

According to Santhi et al. (2001), the model is considered acceptable when its R^2 value is greater than 0.6, and its Nash–Sutcliffe model efficiency coefficient (NSE) value is greater than 0.5. The values of R^2 and NSE for the calibration period are 0.95 and 0.88, respectively, and 0.9 and 0.83 for the validation period. This indicates that the model is calibrated and can be used for future projection of streamflow (Fig. 5).

Table 10: SWAT model calibration parameters.

Parameter	Calibrated value	Estimated value	Range	Unit	Definition
CN2	77	83	0-100	----	Curve number
Gw_Delay	420	300	----	days	Groundwater delay time
Sol_Awc	0.13	0.1	----	mm/ mm	Soil effective Water content
Sol_K1	12.5	3.5	0-100	mm/hr.	Hydraulic conductivity parameter
Sol_Z2	1300	300	0-2000	mm/hr.	Soil depth parameter

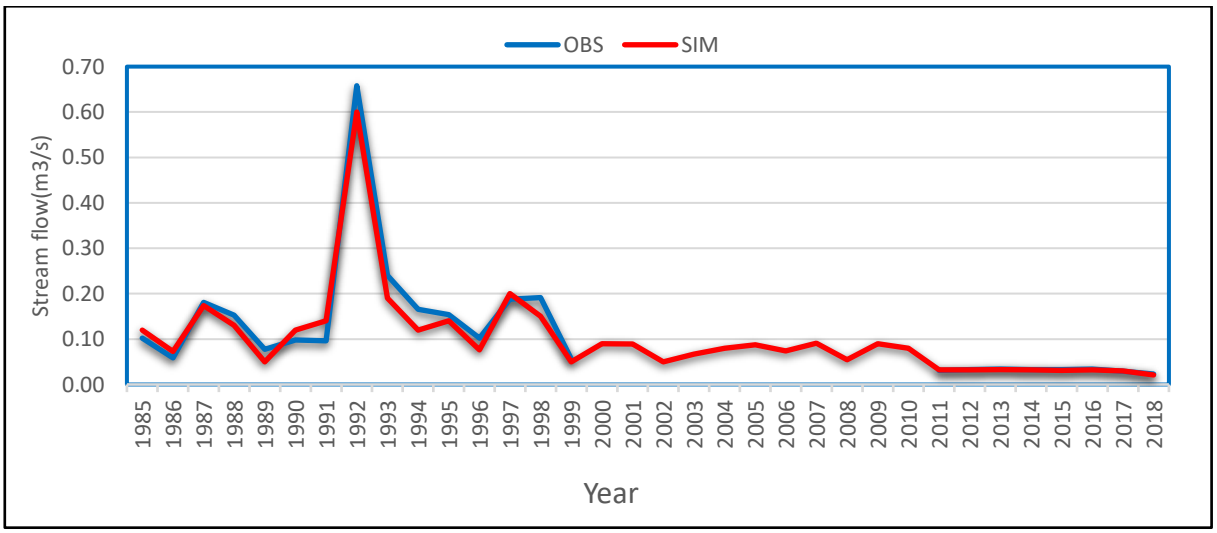


Fig. 5. Observed Streamflow (OBS) versus Simulated Streamflow (SIM) in the basin.

Models Prediction

1. Future Climate Prediction (SDSM)

As shown in Figure 6, the model predicts an increase in the maximum temperature of Ajloun station for the RCP 2.6 scenario by 0.33°C, 0.34°C, and 0.32°C for years 2050, 2075, and 2100, respectively. Similarly, the increase in Kufranja station will be 0.3°C, 0.3°C, and 0.29°C for the years 2050, 2075, and 2100, respectively. In Wadi Al-Rayyan station, the maximum temperature will increase by 0.31°C, 0.33°C, and 0.3°C for the same periods. For the RCP 4.5 scenario, the maximum temperature of Ajloun station will increase by 0.45°C, 0.52°C, and 0.56°C for the years 2050, 2075, and 2100, respectively. The increase in Kufranja station will be 0.4°C, 0.54°C, and 0.6°C for the years 2050, 2075, and 2100, respectively. In Wadi Al-Rayyan station, the maximum temperature will increase by 0.41°C, 0.57°C, and 0.64°C for the same years. For the RCP 8.5 scenario, the maximum temperature of Ajloun station will increase by 0.6°C, 0.89°C, and 1.48°C for years 2050, 2075, and 2100, respectively. The increase in kufranja station will be 0.62°C, 0.98°C, and 1.46°C for the years 2050, 2075, and 2100, respectively. In Wadi Al-Rayyan station, the maximum temperature will increase by 0.64°C, 1.1°C, and 1.56°C for the same years, respectively.

As shown in Figure 7, the minimum temperature for Ajloun station based on the RCP 2.6 scenario will increase to 0.27°C, 0.29°C, and 0.28°C for years 2050, 2075, and 2100, respectively. The increase in Kufranja station will be 0.25°C, 0.24°C, and 0.25°C for the years 2050, 2075, and 2100, respectively. In Wadi Al-Rayyan station, the minimum temperature will increase by 0.25°C, 0.23°C, and 0.21°C for the same years, respectively. According to the RCP 4.5 scenario, the minimum temperature of Ajloun station will increase by 0.35°C, 0.46°C, and 0.54°C for the years 2050, 2075, and 2100, respectively. The increase in Kufranja station will be 0.37°C, 0.44°C, and 0.48°C for the years 2050, 2075, and 2100, respectively. In Wadi Al-Rayyan station, the minimum temperature will increase by 0.3°C, 0.46°C, and 0.52°C for the same years, respectively. RCP 8.5 predicted that the minimum temperature of Ajloun station will increase by 0.55°C, 0.9°C, and 1.39°C for the years 2050, 2075, and 2100, respectively. The increase in Kufranja station will be 0.58°C, 0.94°C, and 1.33°C for the years 2050, 2075, and 2100, respectively. In Wadi Al-Rayyan station, the maximum temperature will increase by 0.45°C, 0.92°C, and 1.37°C for the same years, respectively. The temperature rise will increase the evaporation rate, decrease the soil moisture, and increase soil salinity, leading to an extremely high rate of land degradation, which intensifies desertification and creates soils lacking in nutrients. Food and Agriculture Organization (FAO) reported that if the current trend of climate change continues, the production of wheat and rice in 2100 will decline by 5-50% and 20-30% respectively (Arora, 2019).

The future precipitation trend suggests a significant decrease. As shown in Figure 8, the model predicted a decrease in the precipitation of Ajloun station for the RCP 2.6 scenario by 8%, 10.4% and 10.5% for years 2050, 2075, and 2100, respectively. The decrease in Kufranja station will be 10%, 10.3% and 10.6% for the years 2050, 2075, and 2100, respectively. In Wadi Al-Rayyan station, the precipitation will decrease by 9.8%, 10% and 10.8% for the same years. RCP 4.5 predicted that the precipitation of Ajloun station will decrease by 10.4%, 20% and 22% for years 2050, 2075, and 2100, respectively. The decrease in Kufranja station will be 11.6%, 20% and 25% for the years 2050, 2075, and 2100, respectively. In Wadi Al-Rayyan station, the precipitation will decrease by 10%, 20% and 21% for the same years. In the RCP 8.5 scenario, the precipitation at Ajloun station will decrease by 16%, 33%, and 44% for the years 2050, 2075, and 2100, respectively. The decrease in Kufranja station will be 13.6%, 33% and 44% for the years 2050, 2075, and 2100, respectively. In Wadi Al-Rayyan station, the precipitation will decrease by 14%, 33% and 42% for the same years. This reduction in rainfall will cause a significant decline in streamflow in the basin up to 69.6% in 2100, as discussed before. Reduction in streamflow will cause a deficiency in the basin's water budget, affecting water supply for different purposes.

All stations exhibited increases in both maximum and minimum temperatures, with no significant variation observed among the stations. Among the emission scenarios, RCP2.6 demonstrated lower impacts compared to RCP4.5 and RCP8.5, underscoring the importance of adhering to this scenario to mitigate the adverse effects associated with high emissions. These findings are consistent with previous studies conducted in the same area or neighboring regions. For instance, a study on climate change in Ajloun Governorate utilizing Global Climate Models (GCMs) projected a rise in maximum temperature by 1.7°C, minimum temperature by 2.2°C, and a decrease in precipitation by 18.7% by 2050 (Raggad et al., 2016). Similarly, Bashabsheh and Alzboon (2023) investigated the impact of climate change in the Yarmouk River Basin using SDSM and GCMs, reporting an increase in average temperatures ranging from 0.427°C to 1.52°C by 2100 under RCP2.6 and RCP8.5 scenarios, respectively. Precipitation was forecasted to decrease by 11.4% to 43.2% by 2100 under both scenarios. Additionally, a prediction by the US Agency for International Development (USAID) (2017) suggested a 2°C increase in the annual average temperature in Jordan by 2050.

Table 11: Predicted average rainfall drops in the study area (%).

Year	RCP 2.6	RCP 4.5	RCP 8.5
2018	0	0	0
2050	-9.3	-10.8	-15.9
2075	-11.3	-19.2	-32.3
2100	-11.4	-23.4	-44.2

Table 12: Predicted average temperature increase in the study area (%).

Year	RCP 2.6	RCP 4.5	RCP 8.5
2018	0	0	0
2050	0.28	0.41	0.64
2075	0.3	0.53	0.96
2100	0.30	0.57	1.47

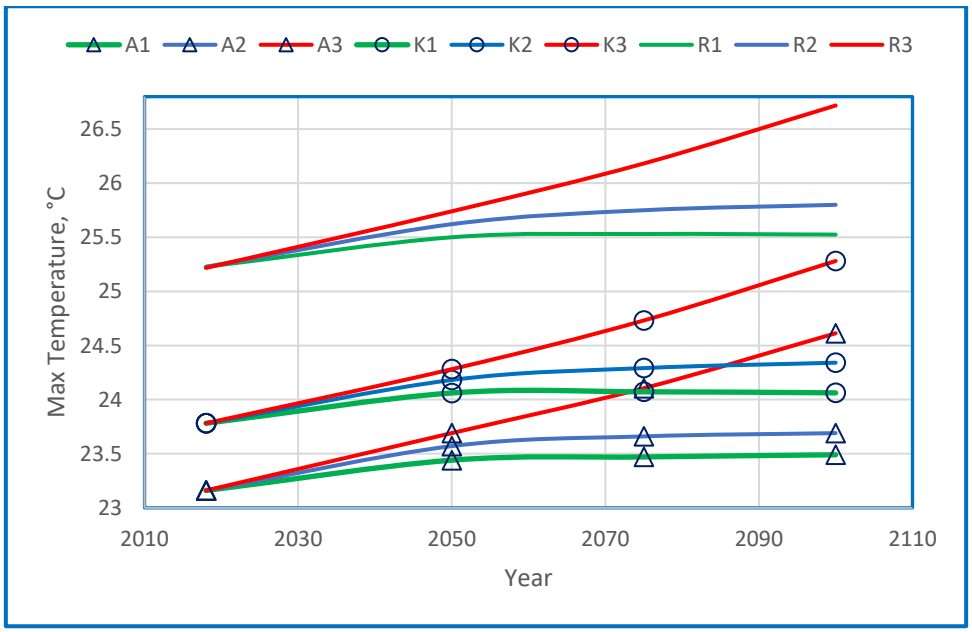


Fig. 6. Projection of the Max. temperature trend (A, K, R refers to Ajloun, Kufranja, and Wadi Al-Rayyan stations respectively; 1,2,3 refer to the RCP2.6, RCP4.5, and RCP 8.5 respectively).

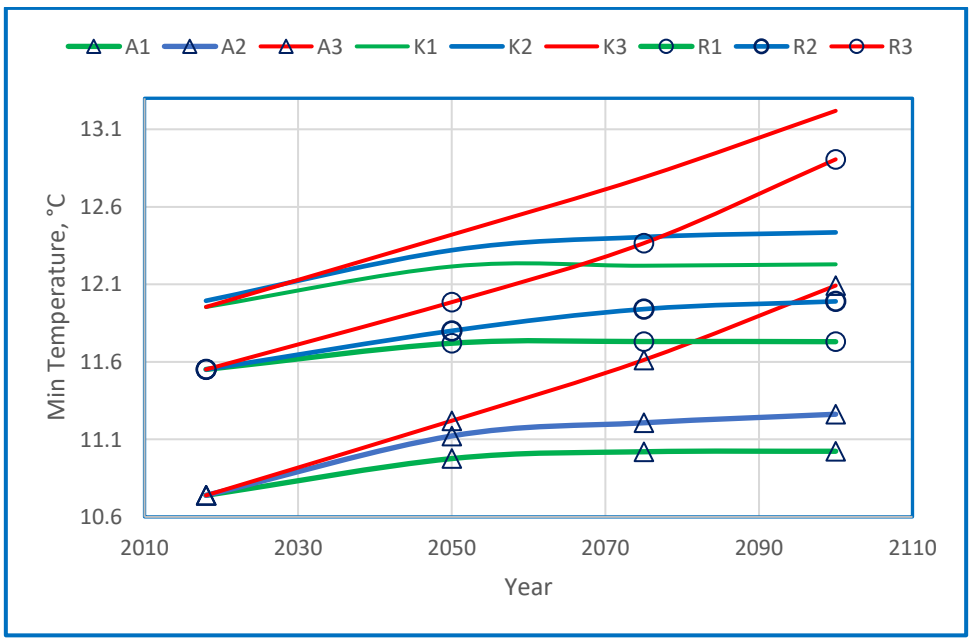


Fig. 7. Projection of the Min temperature trend (A, K, R refers to Ajloun, Kufranja, and Wadi Al-Rayyan stations respectively; 1,2,3 refer to the RCP2.6, RCP4.5, and RCP8.5 8.5 respectively).

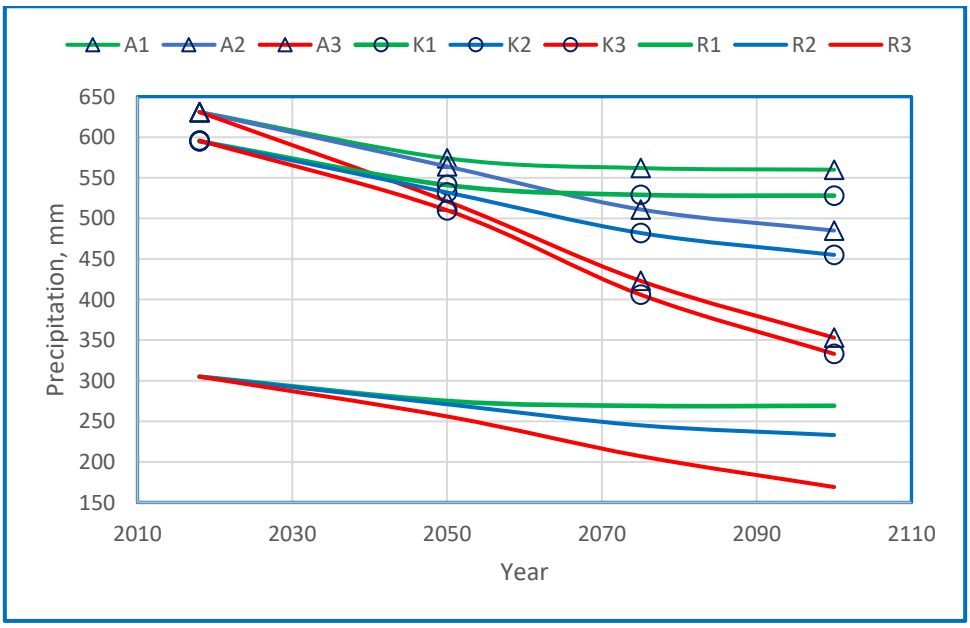


Fig. 8. Projection of precipitation trend (A, K, R refers to Ajloun, Kufranja, and Wadi-Al-Rayyan stations respectively; 1,2,3 refer to the RCP2.6, RCP4.5, and RCP8.5 8.5 respectively).

2. Prediction of Climate Change Impact on Streamflow (SWAT)

It is anticipated that the streamflow will decline across all research periods, with reductions ranging from 8.0% to 69.6% according to the SWAT forecast results. As illustrated in Figure 9, under the RCP2.6 scenario, the streamflow is projected to decrease by 8% between 2018 and 2050, 9.5% between 2051 and 2075, and 16% between 2076 and 2100. Conversely, the RCP4.5 scenario indicated a streamflow decrease of 9% between 2018 and 2050, 31% between 2051 and 2075, and 38% between 2076 and 2100. Moreover, the RCP8.5 scenario predicted a more substantial reduction in streamflow with declines of 22% between 2018 and 2050, 40% between 2051 and 2075, and 69.6% between 2076 and 2100. These findings underscore the severe impacts of climate change on basin water resources, highlighting the urgent need for mitigation measures.

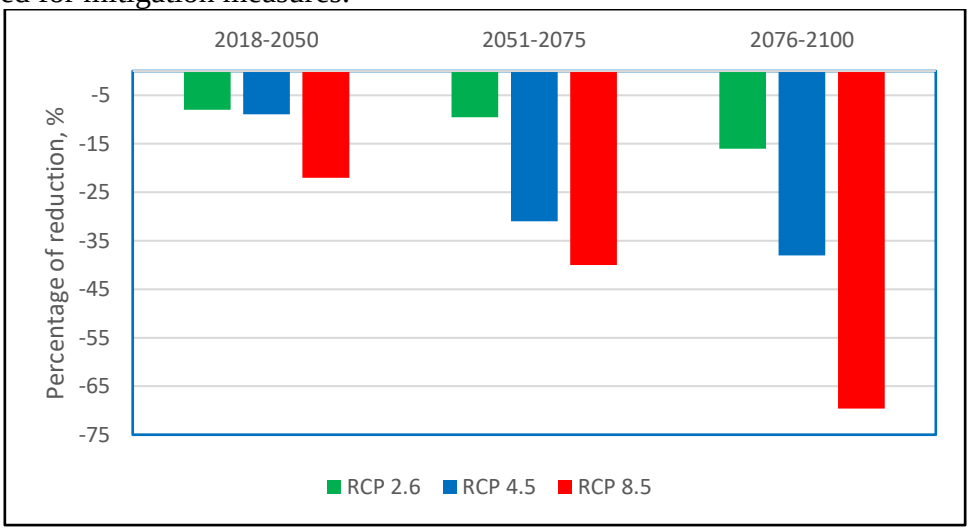


Fig. 9. Projection of changes in streamflow (%).

Conclusion and Recommendation

This study has examined the potential repercussions of climate change on an important basin within Ajloun Governorate employing RClimDex, SDSM, and SWAT models. According to the study's findings, the basin is greatly impacted by climate change, with hot days, hot nights, summer days, and tropical nights increasing dramatically between 1982 and 2000, while

cool days, cool nights, and frost days fall significantly. It is predicted that the average temperatures will increase in 2100 by 0.29℃, 0.57℃, and 1.46℃ based on RCP 2.6, 4.5, and 8.5 scenarios, respectively, while precipitation will decrease in 2100 by 10.8%, 23% and 43% based on the same scenarios, respectively. The SWAT prediction results show a reduction in the streamflow during the period (2018-2100) by 8.1% to 69.2% based on RCP scenarios (2.6 and 8.5), respectively.

After conducting a study on the impact of climate change on water resources in Rajeb Basin, there is an urgent need for a set of comprehensive recommendations to address emerging challenges and protect this vital resource. These recommendations aim to develop an integrated strategy that contributes to achieving sustainability in water resource management in the basin, considering expected climate changes. The proposed strategy consists of the following pillars:

- Development of an advanced monitoring system to obtain accurate and comprehensive data on the status of water and climate resources in the basin, and track changes that occur over time.
- Researchers must have access to the climate change data they need.
- Planting of drought-resistant types.
- Using modern technology in irrigation to save water resources.
- Development of climate change-adapted crops.
- Change planting dates to avoid exposure to drought periods and take advantage of longer growing seasons.
- Modifying the crop rotation and planting types to require less water and be less sensitive to drought.
- Modifications to farming methods, such as the use of agroforestry and conservation tillage
- Promote research on climate change and water use efficiency.
- Fostering an engaging policy environment for climate change adaptation.
- The decision-makers and local organizations need to take into consideration the evident impacts of climate change on the Rajeb basin.
- Additional projects and financial support are necessary to control the impact of climate change.
- Pumping operations in the Rajeb basin require monitoring to ensure water resource sustainability.

Acknowledgments

I am grateful to the Deanship of Scientific Research at Al-Balqa Applied University for the support provided during this research program.

References

Abdulla, F., 2020. 21st-century climate change projections of precipitation and temperature in Jordan. Procedia Manufacturing, 44(1), pp. 197-204. https://doi.org/10.1016/j.promfg.2020.02.222

Al-Dahamsheh A., Wedyan M. and Alhasant M.B., 2018. Climate change impact assessment on rainwater in Jordan. International Journal of Advanced and Applied Sciences, 5(1), pp. 148-155. https://doi.org/10.21833/ijaas.2018.01.020

Al Qatarneh, G.N., Al Smadi, B., Al-Zboon, K. and Shatanawi, K.M., 2018. Impact of climate change on water resources in Jordan: a case study of Azraq basin. Applied Water Science, 8(50), pp. 1-14. https://doi.org/10.1007/s13201-018-0687-9

Alshraifat, H., 2021. Assessment of soil erosion susceptibility in Wadi Rajeb basin using RUSLE. An-Najah University Journal for Research-B (Humanities), 37(5), pp. 981-1002. https://doi.org/10.35552/0247.37.5.2012

Al-Tabbal, J.A. and Al-Zboon, K.K., 2012. Suitability assessment of groundwater for irrigation and drinking purposes in the northern region of Jordan, Journal of Environmental Science and Technology, 5(5), 274-290. https://doi.org/10.3923/jest.2012.274.290

Alzboon, K.K., La'aly, A. and Alrawashdeh, K.A.B., 2021, Climate Change Indicators in Jordan: A New Approach Using Area Method, Jordan Journal of Civil Engineering 15(1), 142-155.

Alzboon, K.K., La'aly, A. and Alrawashdeh, K.A.B., 2021. Climate change indicators in Jordan: A new approach using area method. Jordan Journal of Civil Engineering, 15(1).

Arnold, J.G., Moriasi, D.N., Gassman, P.W., Abbaspour, K.C., White, M.J., Srinivasan, R. and Jha, M.K., 2012. SWAT: Model use, calibration, and validation. Transactions of the ASABE, 55(4), pp. 1491-1508. https://doi.org/10.13031/2013.42256

Arora, N.K., 2019. Impact of climate change on agriculture production and its sustainable solutions. Environmental Sustainability, 2, pp. 95–96. https://doi.org/10.1007/s42398-019-00078-w

Bashabsheh, A.Q. and Alzboon, K.K., 2024. Impact of climate change on water resources in the Yarmouk River Basin of Jordan. Journal of Arid Land, 16(12), pp. 1633-1647. https://doi.org/10.1007/s40333-024-0069-0

Berhane, A., Hadgu, G., Worku, W. and Abrha, B., 2020. Trends in extreme temperature and rainfall indices in the semi-arid areas of Western Tigray, Ethiopia. Environmental Systems Research, 9(1), pp. 1-20. https://doi.org/10.1186/s40068-020-00165-6

U.S. Environmental Protection Agency, 2021. Overview of greenhouse gases: fluorinated gases. https://www.epa.gov/ghgemissions/overview-greenhouse gases#flourinated

U.S. Environmental Protection Agency, 2014. Climate change indicators in the United States. (3rd Ed.). https://www.epa.gov/sites/default/files/2016-07/documents/climateindicators-full-2014.pdf

European Environment Agency, 2020. Greenhouse gas emissions. https://www.eea.europa.eu/data-and-maps/data/greenhouse-gas-emission-projections-for-6

Feyereisen, G.W., Strickland, T.C., Bosch, D.D. and Sullivan, D.G., 2007. Evaluation of SWAT manual calibration and input parameter sensitivity in the Little River watershed. Transactions of the ASABE, 50(3), pp. 843-855. https://doi.org/10.13031/2013.23149

Gharaibeh, G., 2023. Water resources in Ajloun. Jordanian Ministry of Culture. https://ich.gov.jo/node/26717

Gosling, S.N. and Arnell, N.W., 2016. A global assessment of the impact of climate change on water scarcity. Climatic Change, 134, pp. 371-385. https://doi.org/10.1007/s10584-013-0853-x

Hansen, E. and Sato, M., 2011. Paleoclimate implications for human-made climate change. In Climate Change: Inferences from Paleoclimate and Regional Aspects, pp. 21–47. Springer. https://doi.org/10.1007/978-3-7091-0973-1_2

Intergovernmental Panel on Climate Change, 2014. Climate change 2014: Synthesis report. https://www.ipcc.ch/report/ar5/syr/

Intergovernmental Panel on Climate Change, 2021. Climate change 2021: The physical science basis. Cambridge University Press. https://doi.org/10.1017/9781009157896.004

Jalabneh, O. and Al-Ananzeh, A., 2022. Morphometric analysis of Kufranjeh and Rajab basins in Ajloun Governorate using geographic information systems (GIS). Jerash for Research and Studies Journal, 23(2), Article 49. https://digitalcommons.aaru.edu.jo/jpu/vol23/iss2/49

Malhi, G.S., Kaur, M. and Kaushik, P., 2021. Impact of climate change on agriculture and its mitigation strategies: A review. Sustainability, 13(3), pp. 1-21. https://doi.org/10.3390/su13031318

Ministry of Water and Irrigation, 2016. National water strategy 2016-2025: water demand management policy. https://faolex.fao.org/docs/pdf/jor156264E.pdf

Raggad, M., Salameh, E., Magri, F., Siebert, C., Roediger, T. and Moller, P., 2016. Groundwater recharge in a semi-arid environment under high climatic variability and over-pumping: Ajloun Highlands example, Jordan. EGU General Assembly Conference Abstracts. https://ui.adsabs.harvard.edu/abs/2016EGUGA..1810292R/abstract

Salameh, E.S., 2018. Water resources of Jordan: political, social and economic implications of scarce water resources. (1st Ed.). Springer International Publishing. https://doi.org/10.1007/978-3-319-77748-1

Smadi, M.M., 2006. Observed abrupt changes in minimum and maximum temperatures in Jordan in the 20th century. American Journal of Environmental Sciences, 2(3), pp. 114-120. https://doi.org/10.3844/ajessp.2006.114.120

United Nations High Commissioner for Refugees (UNHCR), 2020. Step 3: water at Za'atari Camp. https://www.unhcr.org/7steps/en/water

U.S. Agency for International Development, 2017. Climate change risk profile: Jordan-Fact sheet.

Wulder, M.A., Coops, N.C., Roy, D.P., White, J.C. and Hermosilla, T., 2018. Land cover 2.0. International Journal of Remote Sensing, 39(12), pp. 4254-4284. https://doi.org/10.1080/01431161.2018.1452075

Zhang, X. and Yang, F., 2004. RClimDex (1.0) user manual. Climate Research Branch Environment Canada (22), pp. 1-21. https://rcc.acmad.org/procedure/RClimDexUserManual.pdf

Iraqi National Journal of Earth Science

www.earth.uomosul.edu.iq

Studying the Effect of Morcemcolor Cement as Stabilizing Material on Unconfined Compressive Strength on Compressed Earth Block Produced from Daquq Area, South of Kirkuk, Northen Iraq

Shajan Ali Shukur Al-Bayti [1*], **Aomed Ahmed Mohammed Tokmachy** [2]

[1,2] *Department of Applied Geology, College of Science, University of Kirkuk, Kirkuk, Iraq.*

Article information

Received: 28- Nov -2024

Revised: 05- Jan -2025

Accepted: 18- Feb -2025

Available online: 01- Jan -2026

Keywords:
Compressed Earth Block,
Morcemcolor,
Unconfined Compressive Strength (U.S.C),
Iraq,
Daquq,

Correspondence:
Name: Shajan Ali Shukur Al-Bayti

Email: scgm23007@uokirkuk.edu.iq

ABSTRACT

Since the Mesopotamian civilization, one of the oldest civilizations in history, soil has been used to construct buildings that still stand today. Soil is undoubtedly one of the most widely used building materials in the world. Man built the first houses made of soil. Clay and soil are still used as building materials. However, some soils have problems and need to be treated by adding other materials, such as cement. Soil samples were taken from northern Iraq, specifically the Daquq area, south of Kirkuk. The method of work includes conducting laboratory tests of the raw components of the soil before preparing the samples. Then, preparing the models to make compressed earth blocks under a pressure of 15 MPa with or without the addition of Morcemcolor cement as stabilizing material, which represents colored, water-repellent, and additive mortar with mixed binders, characterized by high fineness and plasticity. Then, geotechnical tests are conducted for (7, 14, 21, and 28) days to determine the extent of its effect on the unconfined compressive strength (UCS). The results show that the use of cement increases the UCS, resulting in very strong and safe brick blocks for construction, according to the safety and security conditions for building materials.

DOI: 10.33899/injes.v26i1.56091, ©Authors, 2026, College of Science, University of Mosul.
This is an open-access article under the CC BY 4.0 license (http://creativecommons.org/licenses/by/4.0/) .

دراسة تأثير إضافة أسمنت Morcemcolor كمواد مثبتة على المقاومة الانضغاطية اللامحصورة للطابوق الترابي المضغوط المنتج من منطقة داقوق, جنوبي كركوك, شمالي العراق

شجن علي شجن البياتي[1]*، اوميد احمد محمد توكمجي [2]

[2,1]قسم علوم الارض التطبيقية، كلية العلوم، جامعة كركوك، كركوك، العراق.

معلومات الارشفة

تاريخ الاستلام: 28- نوفمبر- 2024

تاريخ المراجعة: 05- يناير- 2025

تاريخ القبول: 18- فبراير- 2025

تاريخ النشر الالكتروني: 01- يناير- 2026

الكلمات المفتاحية:

طابوق ترابي مضغوط،

Morcemcolor،

مقاومة انضغاطية لا محصورة،

العراق،

داقوق،

المراسلة:

الاسم: شجن علي شجن البياتي

Email: scgm23007@uokirkuk.edu.iq

الملخص

منذ حضارة بلاد ما بين النهرين وهي واحدة من أقدم الحضارات في التاريخ، استخدمت التربة لبناء المباني التي لا تزال قائمة حتى اليوم، فإن التربة بلا شك واحدة من أكثر مواد البناء استخدامًا على نطاق واسع في العالم. بنى الإنسان أول منازل كانت مصنوعة من التربة. ولا يزال الطين والتربة يستخدمان كمواد بناء. ومع ذلك، فإن بعض التربة تعاني من مشاكل وتحتاج إلى علاج بإضافة مواد أخرى، مثل الأسمنت. تم أخذ العينات من شمالي العراق، تحديدا منطقة داقوق، جنوبي كركوك. تضمنت طريقة العمل اجراء الفحوصات المختبرية للمكونات الخام للتربة في المختبر قبل تحضير العينات ومن ثم تهيئة النماذج لصنع طابوق ترابي مضغوط تحت ضغط 15 ميكا باسكال مع أو بدون إضافة أسمنت Morcemcolor كمادة مثبتة والتي تمثل ملاطًا ملونًا مقاومًا للماء ومضافًا إليه مواد رابطة مختلطة، ويتميز بدرجة عالية من الدقة والمرونة. ثم يتم إجراء الاختبارات الجيوتقنية لمدة (7 و 14 و 21 و 21)يومًا لتحديد مقدار تأثير ذلك على المقاومة الانضغاطية اللامحصورة (U.S.C). أظهرت النتائج أن استخدام الأسمنت يزيد من المقاومة الانضغاطية اللامحصورة (U.S.C) مما ينتج عنه طابوق ترابي مضغوط قوي جدًا وآمن للبناء حسب شروط الامان والسلامة لمواد البناء.

DOI: 10.33899/injes.v26i1.56091, ©Authors, 2026, College of Science, University of Mosul.
This is an open-access article under the CC BY 4.0 license (http://creativecommons.org/licenses/by/4.0/) .

Introduction

Since the day of creation, food, clothing, and shelter have been among the basic human requirements. Therefore, providing and meeting these basic needs is the basis for all technological progress initiatives. However, housing is the most expensive and challenging necessity. As a result, the construction of cheap housing complexes is a problem everywhere. The shortage of building materials, their high cost, and the pollution they cause to the environment during preparation are the main obstacles to finding a solution to the housing crisis (Kabiraj et al, 2011). Over the past forty years (Houben, 1998), the use of compressed earth blocks in the construction of affordable houses has gained popularity over the past fifty years (Walker and Stace, 1997) and (Houben et al., 1998), to denote affordable houses. Since compressed earth blocks are made from readily available local earth resources, they boost the local economy, and by low-cost homes, we mean that the compressed earth blocks are made from abundant and locally available earth materials, which boosts the local economy instead of having to purchase imported materials (Zami and Lee, 2009). In addition, since production is done locally, at work sites, transportation costs are reduced (Waziri et al., 2013). According to AS 1:2007, compressed earth blocks (CEB) are the smallest structural unit with regular, cohesive, and reinforced qualities. Its definition is a result of the pressure used during

manufacturing when the earth blocks are crushed while they are still wet. Furthermore, structures made from this type of brick are widely recognized as environmentally friendly because they use less energy during the manufacturing process. In addition, during manufacturing, less carbon dioxide is produced, resulting in less waste and no direct environmental pollution (2011). Since compressed earth blocks can absorb moisture from the atmosphere and the surroundings during the day and thus slowing down the rate of heat loss and sound transmission, they also provide strong thermal and acoustic insulation properties (Arumal and Gondal, 2007; Anon, 2007; Walker et al., 1997). It does not produce direct environmental pollution. A healthy and balanced climate is produced inside buildings by evaporation, which helps release the heat that has been stored throughout the night (Riza et al., 2011). This is especially true in dry places where the weather is cool in summer and warm in winter. Therefore, construction with these types of clay bricks is suitable in subtropical and tropical climates (Vroomen, 2007). However, according to others (Geuttala et al., 2002), using earth resources directly without adding reinforcing materials has disadvantages that affect the compressive strength. However, by including stable and reinforcing elements, the strength of clay bricks can be increased and improved, Therefore, it was necessary to study the effect of adding Morcemcolor cement on the compressive strength, which is what the research study addressed, Study the effect of adding Morcemcolor cement as stabilized material to compressed earth blocks and whether it is possible to improve the compressive resistance of the block by adding it to benefit from it in construction works economically and successfully.

Location of Study Area

The research area is located in Daquq District, 45 km south of Kirkuk in northern Iraq, near the Ottoman Bridge. Samples were collected from the study site, which is located at a latitude (44°49’07”34) E and longitude (35°16’38”66) N. Demonstrating that the soil is suitable for making compressed earth blocks and that it can produce highly effective blocks with and without the use of cement, at a reduced cost (Fig. 1).

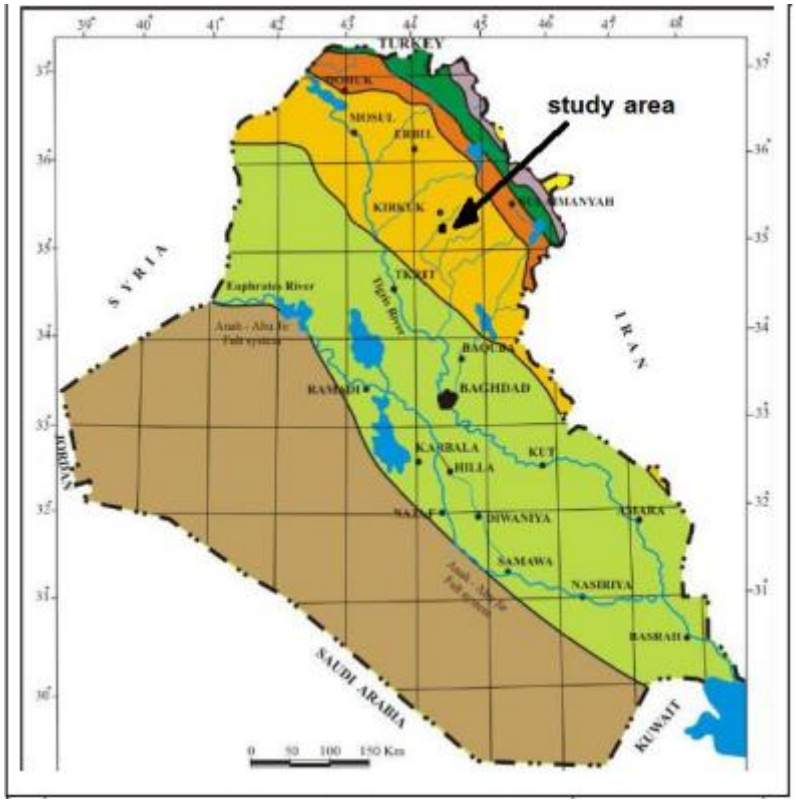


Fig. 1. Location of study area

Materials and Methods

Collection samples:

The stage included collecting soil samples from the study site in the Injana Formation in the Daquq area of Kirkuk to better understand the economic scope and enhance the properties of compacted earth blocks to which different types of cement were added.

It included collecting two soil samples from one site to prevent any abnormalities in the test results for the raw materials used in manufacturing, which may differ from the original location due to distortions caused by external factors such as litter, organic pollutants, or other distortions that alter the results.

The soil was taken from one meter below the surface to avoid soil exposed to weeds, organic debris, weathering, and erosion. For geotechnical tests and confirm the geotechnical properties of the soil, a quantity of soil was extracted and packed in polyethylene bags to prevent moisture loss.

Analysis of Soil Samples:

a) **Laboratory work stage:** When evaluating raw materials used in brick construction, their geotechnical properties must be evaluated in accordance with international standards for geotechnical testing of raw materials. Therefore, two models were taken from the study site in Daquq, southeast of Kirkuk, Iraq, and then evaluated in the laboratory to determine the possibility of using them in the manufacture of blocks**.**

It included: Dry density and moisture content, specific gravity based on the American standard (ASTM-D, 854, 2004; Ibrahim and Tokmachy, 2023), Particle size analysis, according to the American standard (ASTM, D-421, 2004), as steps, and texture of the soil (plastic limit & liquid limit). Based on the American international standard ASTM-D4318–00,2004) and American Specification (ASTM-D4318–00,2004), test (Proctor) compaction based on the standard (ASTM, D 1557-2004).

b) Chemical analyses included: Gypsum Content Based on the British Standard (B.s 1377/1990), pH measurement according to British Standard (B.S.1377:1990) (CaCO3%) According to the method mentioned in (B.S.1377:1990), organic materials according to British Standard (B.S.1377:1990), the percentage of dissolved salts According to the method mentioned in (B.S.1377:1990), Organic Materials content according to British Standard (B.S.1377:1990).

c) Geotechnical tests for compressed earth blocks: including: Verify the amount of moisture, density measurement, verifying the compressive strength without confinement, before and after adding Morcemcolor cement (Morcemcolor is a high-performance jointing mortar typically used for grouting tiles. Its chemical composition is primarily based on high-resistance cement, high-purity aggregates, pigments, and special additives that enhance performance. The additives improve its water-repellent properties and resistance to microbial growth, such as fungi and algae. This type of mortar is also designed to resist cracking and abrasion, with low water absorption, making it ideal for both indoor and outdoor use, including in areas prone to moisture like swimming pools (GRUPO PUMA).

Preparing and manufacturing blocks:

Which takes place in several stages without and with the addition of cement types (Morcemcolor):

After classifying the soil and knowing its properties, the soil was prepared for the manufacture of compressed earth blocks by lightly grinding the soil with a mortar without affecting the crystalline structure of the soil. After the soil classification and identification of its properties, the soil was prepared for the manufacture of compacted earth blocks by lightly

grinding the soil with mortar without damaging the crystalline structure of the soil, taking 8 kg of soil and adding 12% water to it, and then rubbing it by hand to allow the water to penetrate well between the soil particles. The prepared samples were placed in polyethylene bags to prevent water loss and left to ferment for 24 hours. Then, the process of making compressed earth blocks is carried out, as stated in (Houben et al., 1998; Aya and Aomed (2024), according to the international standards (ASR 674, 1996; ASR 671, 1996). Where a quantity of fermented soil is taken after 24 hours and placed in a pressing device (CINVA-RAM) and pressed by 15MP with dimensions (2.5cm, 6cm, and 8.8cm) (Fig. 2). Then, leave it to dry naturally for 28 days, after which geotechnical tests are conducted to determine its suitability for construction

At the same time, compressed earth blocks are made by adding Morcemcolor cement by mixing an amount of 8 kg of soil with 0.20 g of Morcemcolor cement, with the addition of water at a rate of 12%. They are made as happened in the compressed earth blocks without addition, and then the geotechnical properties are evaluated. For both types of blocks and comparison between them, w hich was conducted in the Engineering and Geotechnical Laboratory - College of Science - Applied Geology - University of Kirkuk. (Figs. 3, 4, and 5).

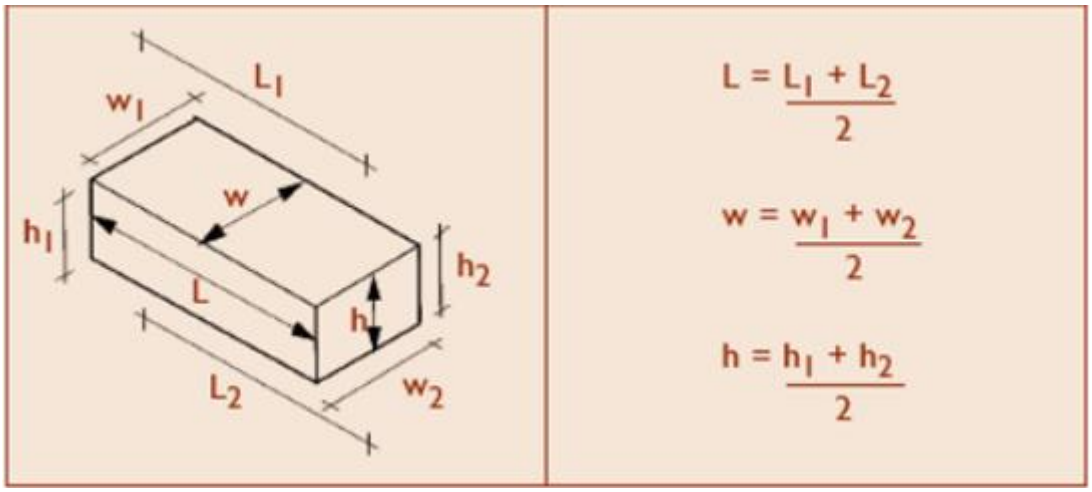


Fig. 2. The method of calculating the dimensions of compressed earth blocks (Adem and Agib, 2001)



Fig. 3. The stages of production of compressed earthen bricks without and with the addition of cement.



Fig. 4. Compressed earth blocks without additives.



Fig. 5. Compressed earth blocks with Morcemcolor cement.

Results and Discussion

The results of the geotechnical evaluation of the raw materials;

Table 1: Physical Properties

No	Dry density	Moisture content	Specific gravity	Grain Size distribution	Atterberg limits
1	1.847g/cm³	11.6%	2.82	Gravel 0%	L.L =32.47
				Sand 5%	P.L =21.81
				Silt 70%	P.I =10.67
				Clay 25%	
2	1.902g/cm³	13.7%	2.83	Gravel 0%	L.L =34.95
				Sand 5%	P.L =20.53
				Silt 68%	P.I =14.42
				Clay 27%	

The result of the chemical analysis:

Table 2: chemical analyses

No	Gypsum Content	pH measurement	T.D.S	(CaCO3%)	organic materials
1	6.92	6.11	7.86	2.88	1.02%
2	6.19	6.32	8.93	3.22%	1.1%

After drying the samples during the drying period specified according to the classification, which is 28 days, the geotechnical properties of the produced bricks were examined, and the results were as follows:

Table 3: geotechnical evaluation of the bricks

	Type of sample	M.C%	Density	Gravel	Sand	Silt	Clay	U.S.C(MP)
1	Without addition	7days =12.5 14day =11.7 21day= 10.9 28day= 9.4	7day= 1.98 14day= 1.99 21day =2.04 28day 1=.99	0	5%	(68-70)%	(25-27)%	7day=16.6 14day =21.6 21day= 24.6 28 day =28.8
2	With addition of Morcemcolor	7day =1.99 14day =1.94 21day 1=.60 28 day 1.=95	7day= 10.2 14 day= 7.33 21 day =6.01 28 day 5=.37	0	5%	(68-70)%	(25-27)%	7day =26.33 14 day =30.30 21 day= 38 28 day =41.33

After conducting the necessary tests on the raw materials of the soil to determine its suitability for the production of compressed earth blocks, the soil was classified according to international standards and it was found that the specific gravity of the soil in the study area was (2.83-2.82), i.e. within the range of clay and silt according to the classification (Das, 1985), where the percentage of clay and silt reached 95% and their presence is very important for the production of compressed earth blocks. The soil was also classified into (low fluidity soil) according to the classification (Kerbs and Walker, 1971) and (medium plasticity soil) according to the classification (Budnikov, 1964), where it falls within the CL range according to the plasticity chart for soft soils according to the unified classification (U.S.C.S.), which falls within the permissible range for the production of compressed earth blocks. As for the chemical analyses: the organic matter had no effect on the soil according to the classification (Scott, 1974), the effect of dissolved salts was unclear according to the classification (Al-Asha, 1991), the percentage of calcium carbonate was harmless according to the classification (Al-Adly, 1998), the soil was slightly acidic according to the classification (Al-Kahlout, 2015), and the soil was classified according to its gypsum content as (slightly gypsum) according to the classification (Al-Barzanji, 1973). According to the results shown above, the soil of the Daquq site near the Ottoman Bridge was within the permitted plan for the production of compressed earth blocks, i.e., it is suitable for the production of compressed earth blocks without and with the addition of Morcemcolor cement. Geotechnical and engineering tests of the bricks produced without and with the addition of cement showed that in terms of water content, the compressed earth blocks without additions retained the most water, unlike the compressed earth blocks with the addition of cement, which had a very low water content due to their interaction with water or water expulsion, as their water content after breaking after 28 days reached (5.37%) Fig.9, while the compressed earth blocks without additives were (9.4%) (Fig. 8), but the density increased with the passage of days during the drying period (28 days) of the compressed earth blocks without additives, while the density of the compressed earth blocks with additives decreased with the passage of days during the drying period (28 days). As for the unconfined compressive strength, we notice that it increased over time for both types, but with the addition of cement, the unconfined compressive strength was much higher, reaching (41.33 MP) for the compressed earth blocks with the addition of cement, while for the compressed earth blocks without addition, it reached (28.8 MP) (Figs.10 and 11). There is also an inverse relationship between water content and compressive strength; as the water content decreases, the compressive strength increases (Figs. 6 and 7).

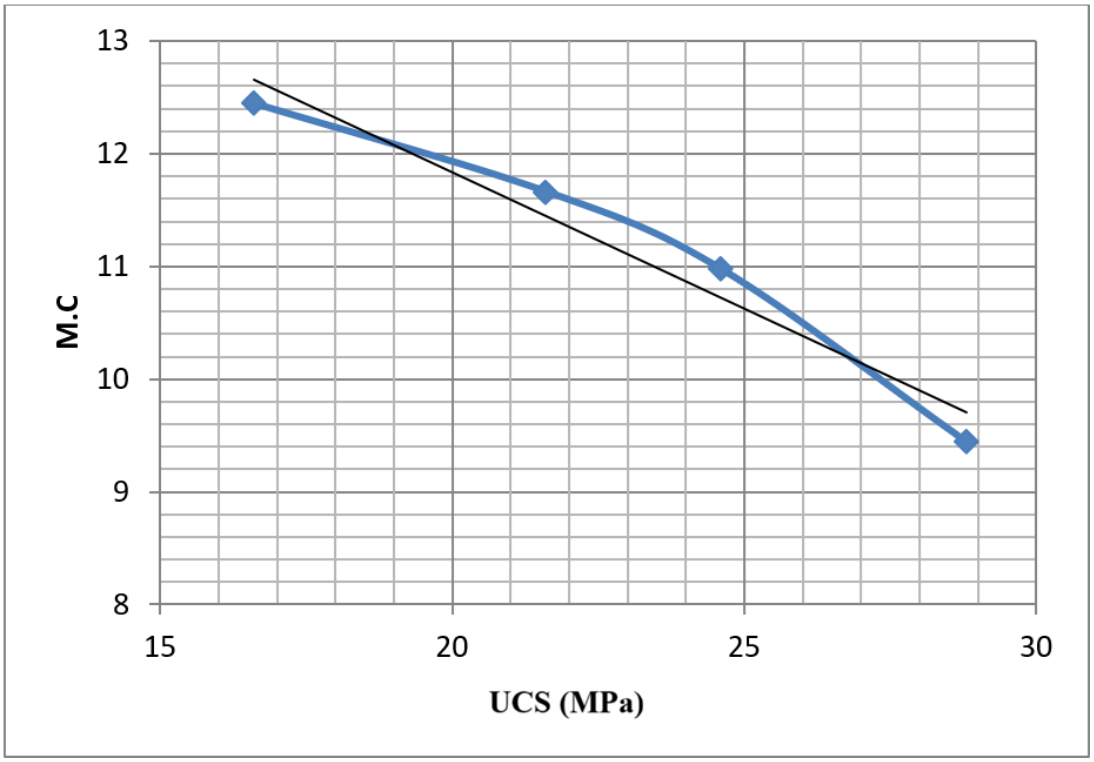


Fig. 6. U.S.C. and M.C.% for compressed earth blocks without additives

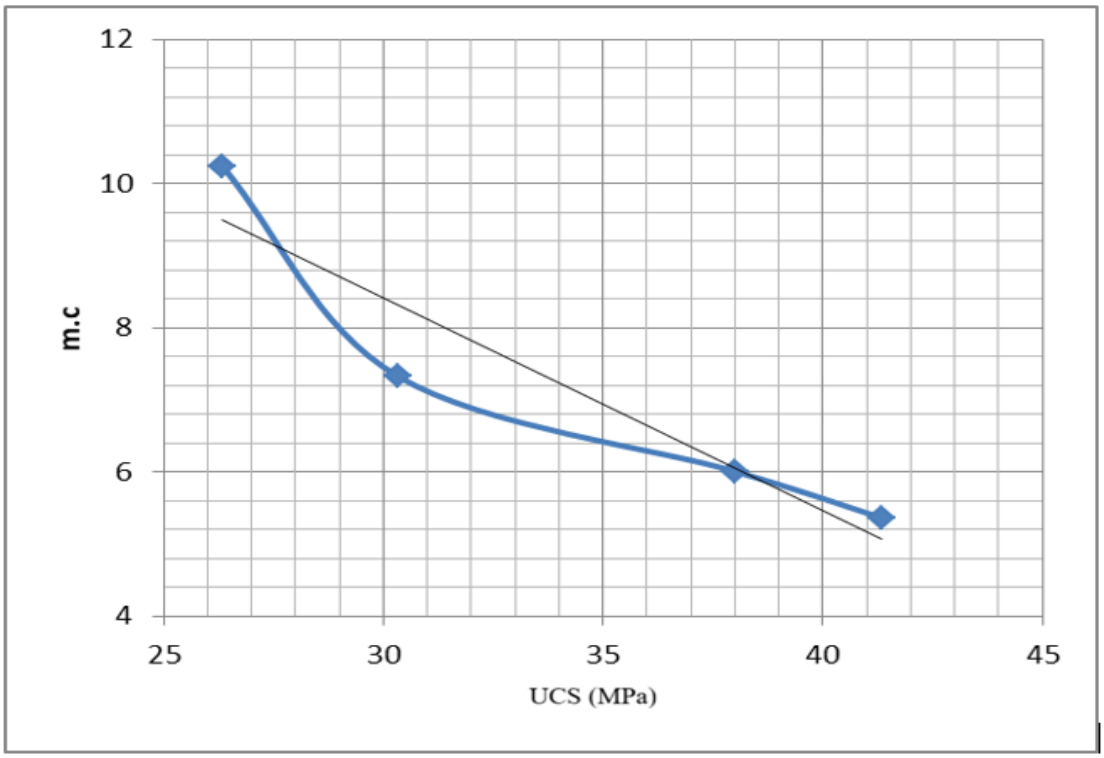


Fig. 7. UCS and M.C.% for compressed earth blocks by addition of Morcemcolor cement

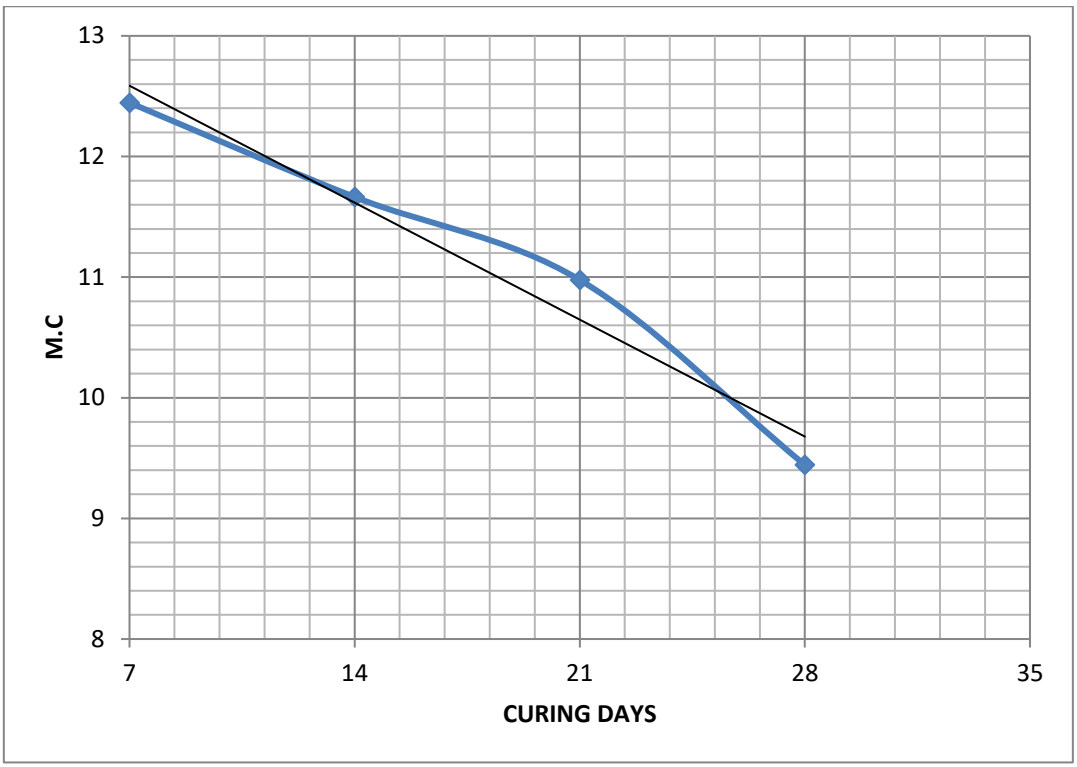


Fig. 8. M.C. and Curing days for compressed earth blocks without additives

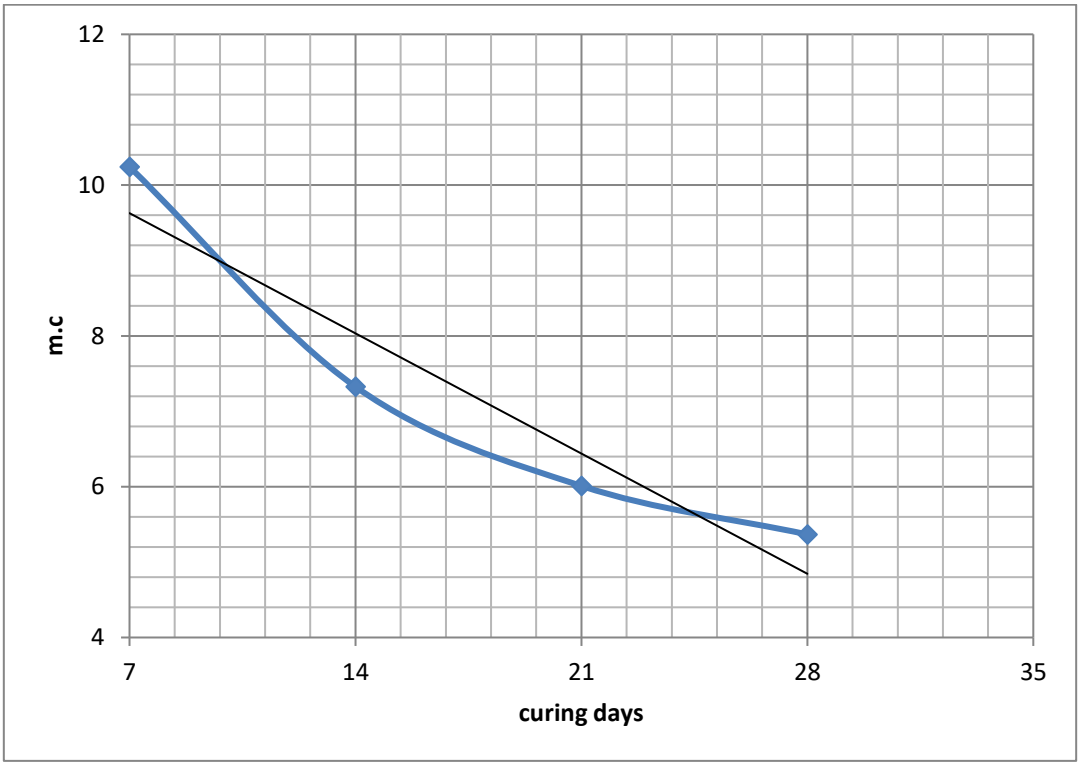


Fig. 9. M.C. and Curing days for compressed earth blocks by the addition of Morcemcolor cement

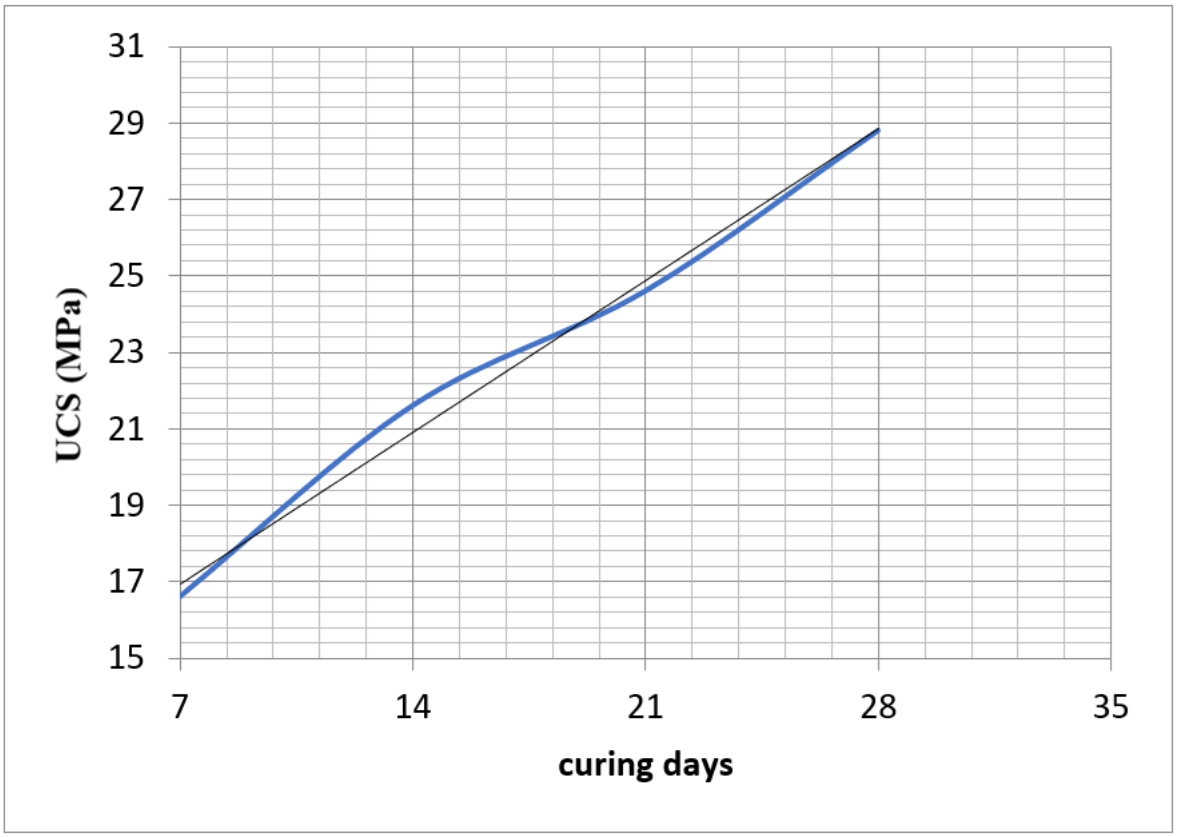


Fig. 10. UCS and Curing days for compressed earth blocks without additives

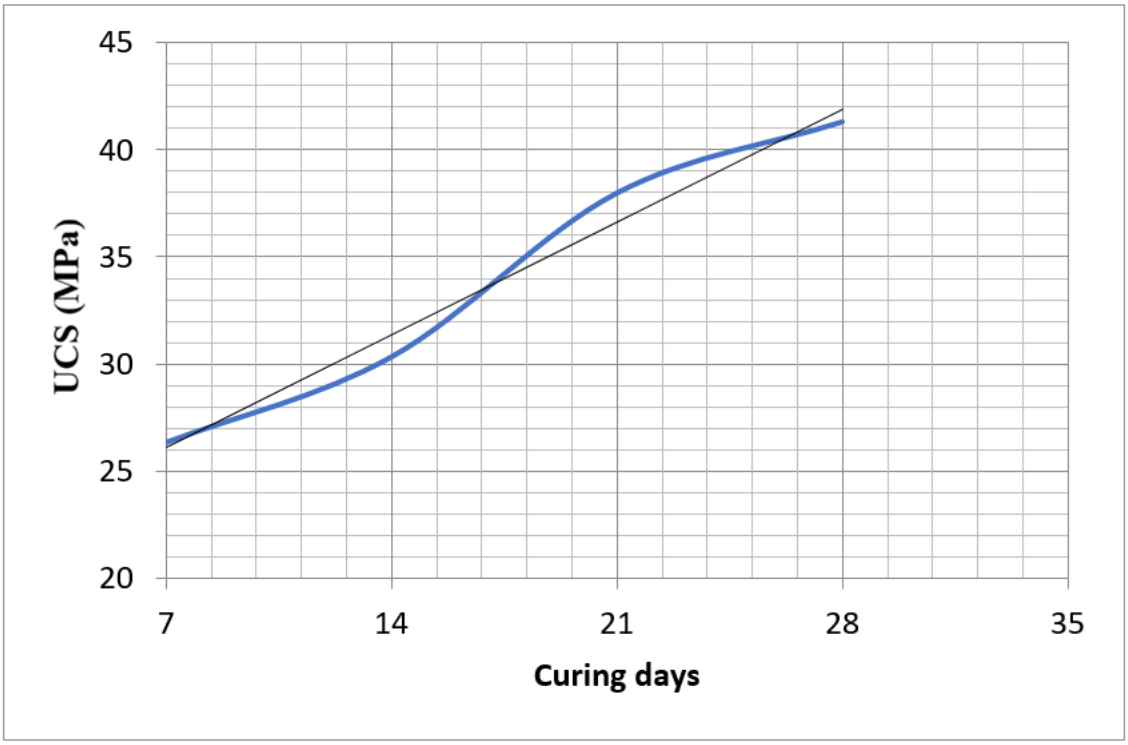


Fig. 11. UCS and Curing days for compressed earth blocks by the addition of Morcemcolor cement

Conclusion

The relationship between water content and drying days of compressed earth blocks is inverse. As the number of drying days increases, the water content of the block's decreases, which also leads to an increase in the unconfined compressive strength of the blocks, as it is inversely proportional to the water content and directly proportional to the drying days.

Therefore, the unconfined compressive strength of the compressed earth blocks to which Morcemcolor cement was added was more compressive than the compressed earth blocks without addition, and the water content was less than the earthen blocks without addition. Also, adding cement led to a reduction in the density of the earth blocks because cement has low density, which leads to a reduction in the total mass of the produced block over the days during the drying period. Therefore, by adding Morcemcolor cement, the unconfined compressive strength of the compressed earth blocks was improved, which meets the safety and security requirements for construction.

Acknowledgments

The University of Kirkuk, College of Science, is to be thanked by the writers for providing the necessary facilities that allowed the quality of their work to be improved.

References

Al-Adli A.S., 1998. Geotechnical evaluation of Baghdad city soil depressions and their treatment, unpublished doctoral thesis, University of Baghdad, College of Science, 148 P. (in Arabic).

Al-Ashaw M.O., 1991. Principles of Soil Mechanics, Dar Al-Kutub for Printing and Publishing, University of Mosul, 574 P. (in Arabic).

Al-Kahlout F.F., 2015. Soil salinization in northern Gaza, published master's thesis, Faculty of Arts, Islamic University, Gaza, Palestine, 104 P. (in Arabic).

Anon, 2007. Introduction to The Production of Compressed Stabilized Earth Block (CSEB) using any way soil block, Auroville Earth Institute, 35 P.

ARS 674, ARS (671), 1996. African standard of compressed earth blocks.

Arumala, J.O. and Gondal, T., 2007. Compressed Earth Building Blocks for Affordable Housing, RICS, 19 P.

AS-1, 2007. Standard of compressed earth blocks (Solid Environmental Solution)

ASTM D1557, 2004. Standard Test for Laboratory Compaction Characteristics of Soil Using Modified Effort.

ASTM D.422-63, 2004. Standard Test Method for particle-size Analysis of soil.

ASTM D.4318-00, 2004. Standard Test Methods for liquid limit, plastic limit and plasticity Index of Soils

ASTM D.854-02, 2004. Standard Test Methods for Specific Gravity 81.

Mohammed, A.K. and Tokmachy, A.A., 2024. Evaluation of geotechnical characteristics of surface soil for compressed earth block industry in Shuwan area northern of Kirkuk, International Journal of Geography, Geology and Environment; 6(1): pp. 230-237 DOI: https://doi.org/10.22271/27067483.2024.v6.i1d.224.

B.S 1377-3-T3, 1990. Method of determination of organic Matter of soil.

B.S 1377-3-T9, 1990. Method of determination of pH value of soil.

B.S.1377-3, 1990. Methods of Testing Soil for Civil Engineering Purposes, British Standards Institution, London.

Barzanji, A.F., 1973.Gypsiferous soils of Iraq, PhD Thesis, University of Ghent, Belgium.

Budnicov, P.P., 1964. The Technology of Ceramic and Refractoriness, Massachusetts Institute of Technology, Cambridge, 647 P.

Guettala, A.H., Houari, B. and Mezghiche, R.C., 2002. Durability of lime stabilized earth blocks. Courrier du Savoir, 02: pp. 61-66.

Houben H., 1998. Compressed Earth Blocks Standards Guide, series technologies, Belgium

Houben, H., Rigassi, V. and Garnier, P., 1998. Compressed Earth Blocks Standards CDI and CRATerre-EAG Publication.

Johanson, R.B. and Degraf, J.V., 1988.Principles of Engineering Geology, John Wiley & Sons Inc., USA, 497 P.

Kabiraj, K. and Mandal, U.K., 2011. Stabilized compacted earth block for affordable housing, The Indian Concrete Journal, 85(8), pp. 52-60

Kerbs, R.D. and Walker, R.D., 1971. Highway Material, 1st Ed., McGraw-Hill Book Inc. USA, 428 P.

Ibrahim, R.A. and Tokmachy**,** A**.**A., 2023. Study of Geotechnical Properties of Clays in the Laylan Region and their Suitability in the Brick Industry in Northeastern Kirkuk, Northern Iraq, Iraqi Geological Journal; 56(2E), pp. 37-47. https://doi.org/10.46717/igj.56.2E.3ms-2023-11-8DOI:

Riza, F.V., Rahman, I.A. and Zaidi, A.M.A., 2011. Preliminary study of compressed stabilized earth brick (CSEB). Australian Journal of Basic and Applied Sciences, 5(9): pp. 6-12.

Scott, C.R., 1974. An Introduction to Soil Mechanics and foundations, 2nd Ed., Applied science, Ripple Road, Essex, England, 361 P.

Vroomen, R., 2007. Gypsum stabilized earth: Research on the properties of cast gypsum-stabilised earth and its suitability for low-cost housing construction in developing countries. MSc Thesis in Architecture, Building & Planning, Eindhoven University of Technology, The Netherlands.

Walker, P. and Stace, T., 1997. Properties of cement stabilized compressed earth block and mortars, Springer, Netherlands, 30(9), pp 545-551.

Walker, P.J., 1995. Strength, durability and shrinkage characteristics of cement stabilized soil blocks. Cement and Concrete Composites, 17(4): pp. 301-310 .

Waziri, B.S. and Lawan, Z.A., 2013. Properties of Compressed Stabilized Earth Blocks (CSEB) For Low-Cost Housing Construction: A Preliminary Investigation, Civil and Water Engineering. University of Maiduguri, Maiduguri, Nigeria.

Zami, M. S. and Lee, A., 2009. Use of Stabilized Earth in The Construction of Low-Cost Sustainable Housing in Africa – An Energy Solution in the Era of Climatic Changes. International Journal of Architectural Research, 3(2): pp. 51- 65.

contents

Monitoring Changes of Rivers Using Remote Sensing Technique: Articles Review

Kareem Tarik Jayed, Hussein Kareem Shather 1

Assessment of Rock Masses Exposed at the Khanas Dam Site in the Southeastern Part of Sheikhan Anticline, Northern Iraq.

Safwan Taha Yasin Al-Habity, Mohammed Rashid Abood, Ibrahim saad Ibrahim Aljumaily 17

Integrating Geophysical and Geotechnical Methods to Optimize Foundation Design of a Power Station Site in Basrah, Iraq

Iman M. Jaafar, Emad H. Al-Khersan, Amer A. Al-Khalidy , Amer J. Al-Khafaji 34

Hydro-morphometric and Hydrochemical Criteria to Select the Optimal Location for Small Dam in Um Al-Shibabit Valley, Al-Shirqat, Northern Iraq

Abdulhadi Hamad Mohammed, Alaa Ahmad Mohammed, Sabbar Abdullah Salih, Abdulsalam Mehdi Salih 48

Sedimentology of Avanah Formation (Middle-Upper Eocene) from Selected Sections within Iraqi Kurdistan Region

Amanj Ibrahim Fattah, Hazhar Hasan Ahmad Perot.....65

Assessing the Environmental Situation of Euphrates River Sediments Using Magnetic Susceptibility Techniques in Al-Muthanna Province, Southwestern Iraq ….

Nawrass N. Ameen.....88

Engineering Site Investigation Using 2D Electrical Resistivity Imaging, K3 Area, Western Anbar Governorate

Sameer Sh. Abbas 100

Mineralogy and Geochemistry of Upper Cretaceous and Paleogene Succession in Gali and Qalbaza Sections, Northeastern Iraq: Implications for Provenance and Detecting K/Pg Boundary

Shareef T. Al-Hamed, Sattar J. Al-Khafaji..... 109

Groundwater Quality Assessment and Its Suitability for Agricultural Use in Al-Shirqat Area, Salahaldin Governorate

Ayad A. Khalaf , Abdelhadi H. Hasan.....138

Sedimentological analysis of the Dokan Formation (Cenomanian) in Goizha Section, Azmar Anticline, Northeastern Iraq

Noor T. Al-Taee 152

Environmental Significance of the First Appearance of *Porosononion martkobi* in Southern Iraq Sediments

Bushra Majeed Issa.....167

Forecasting PM2.5 Daily Concentration in Baghdad, Iraq Based on Improving Random Forest Algorithm

Zakariya Nafi Shehab, Zakariya Yahya Algamal , Raid Mahmood Faisal 180

Evaluation of Spatio-Temporal Forest Health of Bangladesh Using Google Earth Engine

Md. Shahadad Hossain, Nobonita Shobnom, Umme Sumaiya Shams, Rezaul Roni.....193

Use of Remote Sensing and GIS to Study the Expansion of Sands and Vegetation in the Draa Region (Morocco) From Landsat Satellite Images

Otman Tamri, Allal Labriki , Soukaina el Idrissi , Mohammed Amine Zerdeb,Saïd Chakiri 208

Rooftop Rainwater Harvesting for Mosul City as Water Resources Using GIS

Mohammed Muwafaq Yahya, Mohamed H. Alsalmani, Qusai Y. AL-Kubaisi 224

Overpressure and Under-Compaction Mechanism Effect on Pore and Fracture Pressure Development of Mauddud Formation, Badra Oil Field, Eastern Iraq

Mohammed Almojahed Farooq Abdalla, Nagham Jasim Al-Ameri..... 234

Impact of Diagenetic Processes and Dolomitization on the Dammam Formation in Central Iraq

Basma A. Al-Samarraie, Mohanad H. Al-Jaberi..... 250

Assessment of Rock Slope Stability in Khanuqa Anticline, Northern Iraq

Waeal Mohammed Khazel , Mohammed Rashed Abood..... 275

Conditions of Depositional Environment of the Sargelu Formation in Rania Area Based on Geochemical Data

Mohamed Ali Alrashedi, Falah A. Al-Miamary, Zaid A. Malak..... 289

Studying the Spatial and Temporal Changes of the Surface Urban Heat Island Using Geographic Information Systems (GIS) and Remote Sensing (Mosul City as a Model)

Waleed Shabeeb, Sahar Altee, Qusay Kamal Al-din..... 303

Evaluation of Hydrochemistry of Kirkuk Irrigation Project, Kirkuk, Northern Iraq

Hiba Hasan Sultan, Soran Nihad Sadiq..... 314

Spatial Simulation of Future Changes in the LULC for Babil Governorate Using Cellular Automata (CA)-Markov Model

Hayder Hameed Jassoom, Rabab Saadoon Abdoon..... 329

Sedimentological Study and Age Determination of the Shiranish Formation in Perat Anticline, Northern Iraq

Mohammed W. Al-Abbasi, Omar A. Al-Badrani, Majid M. Al-Mutwali, Zaid A. Malak 347

Prediction and Prospection of Groundwater in the Iraqi Western Desert Using Remote Sensing and GIS

Ahmed Abbas Hasan, Shahad Adil Al-Qaraghuli , Linaz Anis Fadhil , Aymen Muwafaq Ahmed..... 361

Climate Change in Jordan: A Case Study of Rajeb Basin

Moath Qudah, Kamel Alzboon..... 381

Studying the Effect of Morcemcolor Cement as Stabilizing Material on Unconfined Compressive Strength on Compressed Earth Block Produced from Daquq Area, South of Kirkuk, Northen Iraq

Shajan Ali Shukur Al-Bayti, Aomed Ahmed Mohammed Tokmachy 399

IRAQI NATIONAL JOURNAL OF EARTH SCIENCE

Vol. 26 January 2026 No. 1

Editor-in- Chief

Prof. Dr. Rayan Ghazi Thannoun

Managing Editor

Assistant Prof. Dr. Azealdeen Salih Al-Jawadi

Editorial Board

Prof. Dr. Majid Majdi Al- Mutwali
Prof. Dr. Moez Ben Fadhel (Tunisia)
Prof. Dr. Haji Rahab (Algeria)
Prof. Dr. Sherif Farouk (Egypt)
Prof. Dr. Ezzadin N. Baban
Prof. Dr. Basem Sayed Nabawy (Egypt)
Prof. Dr. Alain Preat (Belgium)
Prof. Dr. Masdouq M. Al-Taj (Jordan)
Prof. Dr. Sawsan Hameed Faisal Al-Hazaa
Prof. Dr. Sattar Gabar Rasheej Al-khafagi
Prof. Dr. Rafee Ibraheem Al Hamedi
Assistant Prof. Dr. Aahed Younis Al-Mallah
Assistant Prof. Dr. Mohammed Fawzy Omer
Assistant Prof. Dr. Namam Mohammed Saleh
Assistant Prof. Dr. Omar Abdullah Ismail
Assistant Prof. Dr. Falah Abdul M. Al-Maamari
Dr. Haitham I. Hamid
Assistant Prof. Dr. Saddam Essa Al-khatony
Assistant Professor Dr. Mehdi Rahnama (Iran)
Assistant Professor Dr. Rashid Pourmirzaei (Iran)
Assistant Professor Dr. Bashar Aziz Mahmoud

Managing the Electronic System of the Magazine

Assistant Prof. Dr. Saddam Essa Al-Khatony

Technical Affairs, Coordination, and Publication

Myasar Samir Mahmoud Al-Siraj

Management Coordinator: Saja Salim Abd AL-Hade

Published by: College of Science / University of Mosul

p-ISSN: 1682-3222

e-ISSN: 2664-2816

E-mail: injes@uomosul.edu.iq

Website: http://www.iasj.net

https://earth.uomosul.edu.iq/

Mobile: 009647701610916